GSI

GSI Report 2007-1
June 2007

SCIENTIFIC REPORT 2006

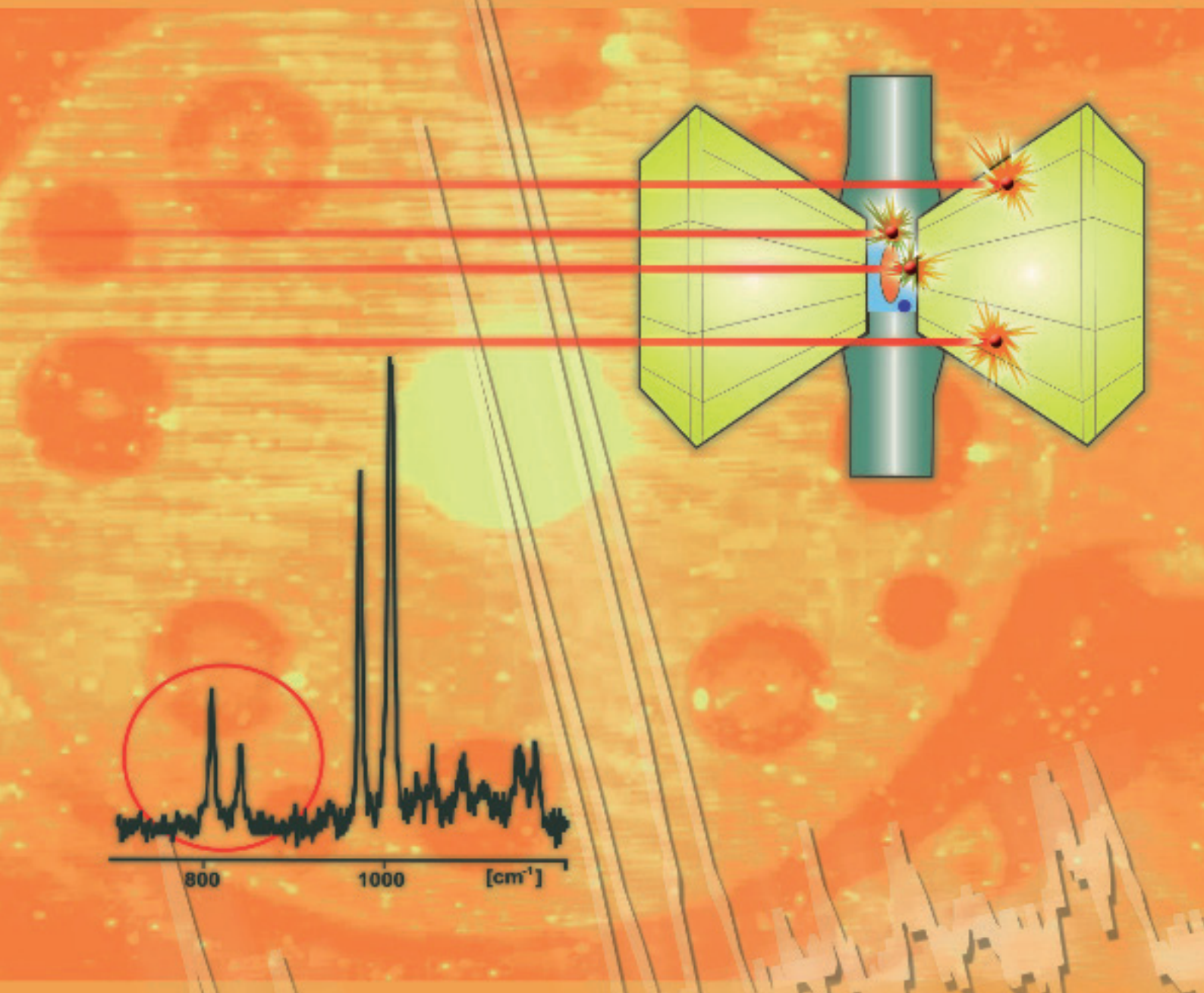

Gesellschaft für Schwerionenforschung mbH Darmstadt

Member HELMHOLTZ GEMEINSCHAFT

A small solid sample, located in the central aperture of a metal gasket and squeezed from two sides by diamond anvils, is irradiated with relativistic heavy ions from the SIS heavy ion synchrotron. The simultaneous exposure to high pressure and to the very rapid deposition of energy transferred from the decelerating ions triggers drastic structural alterations which are not caused by applying high pressure or ion beam irradiation alone. The mineral zircon, for example, transforms to a high-pressure phase at pressure values much lower than those required without simultaneous ion beam irradiation. The new phase is revealed by additional lines (indicated by the red circle) observed in the Raman spectrum of zircon.
The background displays a head-on view of the metal housing of a diamond anvil cell in the moment when an ion pulse traverses the cell. The front diamond responds with a bright flash of light emission visible in the center.

GSI Scientific Report 2006

GSI Report 2007-1
<http://www.gsi.de/library/GSI-Report-2007-1/>

ISSN: 0174-0814
and GSI Report 2007-1

Publisher: Gesellschaft für Schwerionenforschung mbH, GSI
Planckstr. 1, 64291 Darmstadt, Germany, <http://www.gsi.de>
GSI is a member of the Helmholtz association of national research centres <http://www.helmholtz.de>.

Publication dates: June 2007 (online) and August 2007 (print)
Editor: Katrin Große,
Cover: Bauer & Guse GmbH, Mühltal, Germany,
Technical Team at GSI for the printed and the Internet versions: I. Giese, K. Große, U. Meyer, V. Schaa and K. Schiebel.

Limited edition.
Copies are available by order (gsilibrary@gsi.de, phone: +496159 712610, fax: +496159 713049).

Printed by: typographics GmbH, Darmstadt, Germany.

For the production of this report templates and scripts of the JACoW collaboration (Joint Accelerator Conferences on Web <http://www.jacow.org>) were used.

The complete scientific report is also available with supplementary colored figures and illustrations on the Internet: <http://www.gsi.de/library/GSI-Report-2007-1/>

Foreword

The cover page of this year's Scientific Report illustrates a new experiment to study bulk matter at high pressure. A beam of heavy ions, energetic enough to penetrate the massive walls of a diamond anvil cell, is used to irradiate single crystals. Quite different behaviours are observed. For example, in the mineral zircon the ions trigger the formation of the high-pressure phase reidite, not induced by pressure or ions alone. In contrast, in apatite one finds less damage compared to ambient conditions and stabilization of the lattice under pressure. In addition to the basic understanding of radiation damage under such conditions, the results are useful for simulating the situations that fission tracks experience in the interior of the Earth and for their application in thermochronology. This is one of many examples in this Report that illustrate the broad range of research areas pursued with ion beams at the GSI accelerator facilities.

The central mission of the Laboratory is, of course, the microscopic study of matter in the regime of the strong force. This involves the properties of the atomic nucleus, up to nuclei only transiently created in star explosions yet key stepping stones to the matter we are made of. It addresses nuclear matter as it exists in the interior of stars and at the birth of the universe. And it searches for the underlying quark and gluon structure and the understanding of its fundamental role in shaping the many-body systems of the strong interaction: hadrons, nuclei, and nuclear and quark matter.

However, as shown by the cover page, the unique properties of the ion-beam facilities operating at GSI also provide opportunities for a wider research program, be it atomic physics studies of highly stripped atoms and ultra-high electromagnetic fields, the dense and hot bulk plasmas that can be created with ion beams, or the radiation effects induced in solids and biological materials over a wide range of ion-beam conditions.

The Scientific Report intends to provide an overview of the research and technical development work in progress at the Laboratory. It summarizes important advances and achievements made in 2006, addressing both scientific results and highlights from the various research programs and important technical (and - to some extent - also science-political) developments with respect to the Laboratory's medium- and long-term future.

The most important activity directed toward the future – and indeed, the Report begins with this Chapter – is the extensive work performed in preparation for FAIR (Facility for Antiproton and Ion Research). Last year two important milestones were reached: in July the FAIR Baseline Technical Report (BTR) was finalized and accepted by the FAIR International Steering Committee (ISC) as the defining document for 'The Project', i.e. for the scientific goals and technical performance characteristics of its accelerators and experimental stations/ detectors, and for its cost structure and timeline. Towards the end of the year, the FAIR-ISC founded an interim international project group, the FAIR Joint Core Team (FAIR-JCT), whose task it is to coordinate preparation and development of all necessary information and documents needed for the foundation of the FAIR company.

At present, 14 countries have signed a Memorandum of Understanding stating their commitment to join efforts in the preparatory activities for FAIR and the intent to collaborate in the construction and operation. About 2400 scientists and engineers from 44 countries have co-authored the Baseline Technical Report. It contains a wide range of R&D efforts that have been supported by pre-project funds from the German Federal Government and from the State of

Hessen, the European Union, and through institutional funds at the various partner institutions worldwide. In this Report brief summaries are given of many of these activities.

The scientific program at GSI, while predominantly carried out at its own accelerators, also has important components at other facilities: longer-term programs, for example, exist in ion-trap work at ISOLDE and in the construction (soon experiments) of the ALICE detector at CERN, in data analysis by staff previously involved in the BABAR experiment, and in a broad range of collaborations both in theory and in technical R&D. All of these activities are addressed in this Report.

While tempted to describe now in more detail some of the research highlights and major technical achievements of the past year, I will limit myself to a brief statistical account of the work done.

In total, the GSI accelerators provided more than 11500 hours beam on target (UNILAC 5208 h, SIS 4937 h, ESR 1382 h). The beam species again covered the full range from protons to uranium, with many secondary ion beams in addition. This excellent performance has to be seen before the background of substantial accelerator R&D for FAIR and the major efforts from the accelerator and infrastructure staff last year in constructing the heavy-ion therapy facility HIT at the Heidelberg Clinics (plus contributions to the injector linac for ion therapy facility in Pavia (Italy). HIT is now being commissioned.

The accelerators are still heavily subscribed. Despite the substantial number of hours that could be provided to the experiments last year, backlogs exist of more than one year for the UNILAC and two years for SIS. At the recent meeting of the GSI Program Advisory Committee requests for beam time were a factor of two (UNILAC), respectively three (SIS) higher than what could be approved. A promising development is the success in raising beam intensity, which has now nearly reached space charge limit for light and medium-heavy ions. Also faster cycling times are now possible because of the new GSI power-grid connection completed last year. The new link to a local power station, exclusively used by GSI, enables fast ramping of the SIS magnets up to 4.5T/s.

The research and R&D results were published last year in about 500 papers altogether (of these more than 360 in refereed (WoS listed) journals). Close to 50 PhD's out of a total of more than 100 thesis papers (bachelor, diploma/ masters, PhD) were completed last year.

The science community at GSI has a dominant fraction of users from outside GSI. This is also reflected by the number of authors, more than 1400, who have contributed to this annual scientific report and summary of the activities at and with GSI! To all of them, their sponsors, and all the others who have, through their involvement and contributions, been instrumental to the success of the many activities and projects at GSI, a most sincere 'thank you' and the wish of continued and successful future collaboration.

Walter F. Henning
Scientific Director

Contents

The FAIR project

Overview of the FAIR Project

FAIR Joint Core Team

GSI, Darmstadt, Germany

In spring 2006 the FAIR Baseline Technical Report (BTR) [1] was presented to the International Steering Committee (ISC) of FAIR. The BTR was accepted by the ISC as technical description and scope of the FAIR project and basis for the international negotiations for the creation of the FAIR GmbH.

The negotiations commenced in autumn 2006. In parallel the working groups on Administrative and Financial Issues (AFI) and Science and Technical Issues (STI) prepared the documents that are necessary for the establishment of the FAIR company. This task was completed by the end of 2006.

The ISC established the Joint Core Team which has the task to manage the FAIR project until the formal creation of the FAIR GmbH.

Great effort has been put into consolidating the ion-optical layout of the facility as well as the design and specifications of the various accelerator elements, shown in the figure below. The current status in this area is presented in the section of the FAIR division in this report.

The BTR defines the initial scientific program of FAIR. The corresponding experiments are listed in the table below. PAX/ASSIA and AIC have to prove their feasibility but provisions in the accelerator design and civil construction will be made for them.

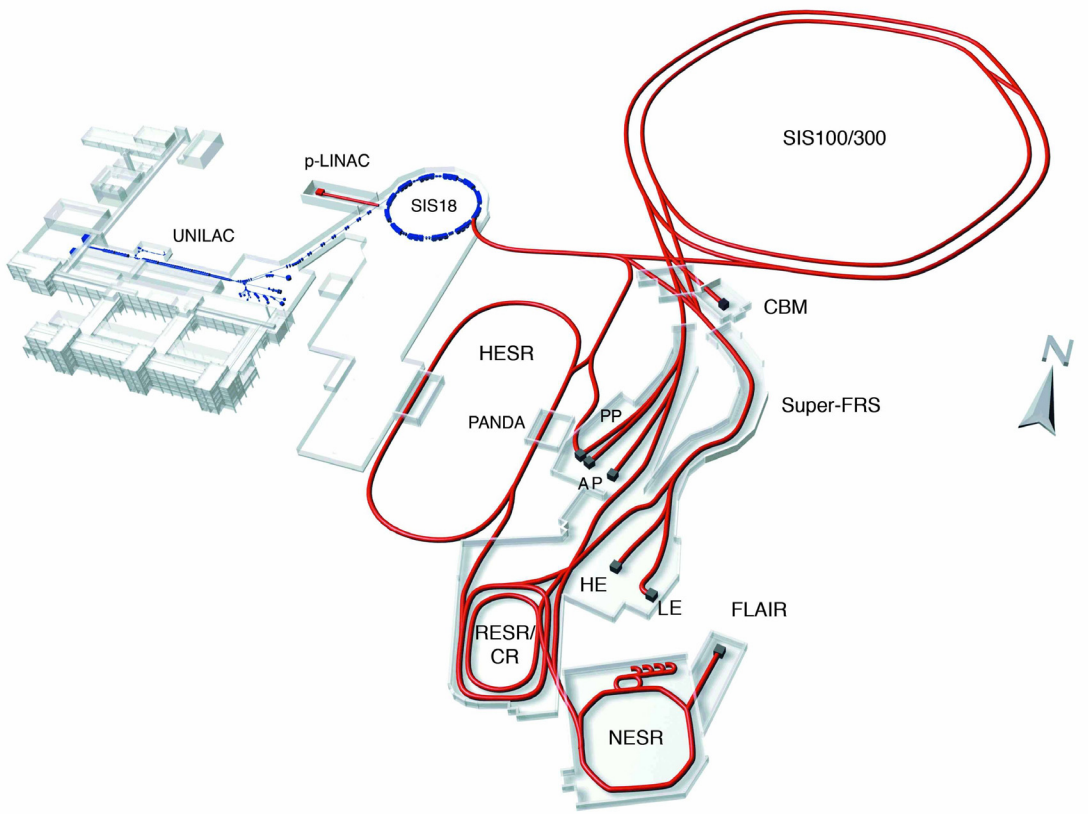

Layout of the FAIR complex. The accelerator consists of the double ring synchrotron SIS 100/300, the injection complex UNILAC, p-LINAC and SIS 18, and the storage rings (NESR, RESR/CR and HESR). The other acronyms characterize positions of experiments listed in the table on the next page. The NUSTAR experiments (light grey in table) behind the Super-FRS will be located in areas HE, LE and the NESR, HEDgeHOB and WDM in area PP and BIOMAT in AP. The SPARC experiment will involve target positions over the entire complex. CBM, PANDA and FLAIR are shown in situ.

Experiment	Research Program	Technical Facility
R3B	Nuclear reactions in inverse kinematics reaction studies with relativistic radioactive ion beams	Large reaction set-up allowing complete kinematics reaction experiments
HISPEC/ DESPEC	High resolution, high efficiency particle and gamma spectroscopy of nuclei far off stability	State-of-the-art γ-detectors (AGATA) plus set-ups for charged particle and neutron detection
LASPEC	Laser spectroscopy of radioactive ion species	Multi-purpose laser spectroscopy station
MATS	High precision, high efficiency mass and lifetime measurements on radioactive nuclei	Combined set-up of an electron beam ion trap (for charge breeding), ion traps (for beam preparation) and a precision Penning trap system.
ILIMA	Mass and lifetime measurements of stored and cooled radioactive ion beams	Devices for Schottky mass and isochronous mass spectroscopy at CR/NESR
EXL	Inverse kinematics light ion reactions on radioactive nuclei	In-ring reaction set-up to be installed at the NESR
AIC	Measurements of mass radii of nuclei far off stability	Antiproton (radioactive) ion collider
ELISe	Measurements of elastic, inelastic and quasi-free electron scattering of nuclei far off stability	Electron-ion collision device including a high resolution electron spectrometer at the NESR
PANDA	QCD and hadron physics studies with cooled high energy antiproton beams at the HESR	Large state-of-the-art internal target detector system covering almost the full solid angle
CBM	Studies of the QCD phase diagram in high-energy nucleus-nucleus collisions	Large state-of-the-art fixed target detector system covering almost the full solid angle
PAX/ASSIA	QCD and hadron physics studies with polarized antiproton beams	State-of-the-art collider detector system covering a large solid angle
FLAIR	(Precision) studies with low energy or stopped antiproton ion beams	Various stations including an ultra-low energy electrostatic storage ring, a Penning trap, low energy antiproton target stations
SPARC	Atomic physics spectroscopy and collision studies with (stored) high energy ion beams	Various fixed target and in-ring experiments
BIOMAT	Applications of ion and antiproton beams in biophysics, biology, materials research and other disciplines	Various multi-purpose target stations
HEDgeHOB/ WDM	Investigations of warm and dense bulk matter produced by intense ion and/or laser pulses	Various plasma physics experimental stations

The experiment collaborations of FAIR have worked hard on the necessary R&D for their detectors. Reports about the progress of the various collaborations are presented in this section of this report. These efforts will lead in due time to various technical design reports that are prerequisite for the start of construction of the respective experiments. However it should be noted that only a small fraction of the full activities of the experiments are reported here, as this is the Annual Report of GSI and the vast majority of collaborators are external.

References

[1] FAIR Baseline Technical Report,
ed. H.H. Gutbrod. I. Augustin, H. Eickhoff, K.D. Groß, W.F. Henning, D. Krämer, G. Walter,
ISBN 3-9811298-0-6,
http://www.gsi.de/fair/reports/btr.html

Further information can be found at
http://www.fair-center.de

A data analysis and simulation framework for the PANDA collaboration

PANDA Computing Group[1]

[1] FZJ, Jülich, Germany; GSI, Darmstadt, Germany; Jagellonian University, Cracow, Poland; JLU, Gießen, Germany; KVI/University of Groningen, Groningen, The Netherlands; LPP, Dubna, Russia; Ruhr-University, Bochum, Germany; Politecnico di Torino, Torino, Italy; Soltan Institute for Nuclear Studies, Warsaw, Poland; Technical University of Dresden, Dresden, Germany; Technische Universität München, Garching, Germany; University of Basel, Basel, Switzerland; University of Ferrara and INFN, Ferrara, Italy; University of Frankfurt, Frankfurt, Germany; University of Frascati and INFN, Frascati, Italy; University of Glasgow, Glasgow, United Kingdom; University of Pavia and INFN, Pavia, Italy; University of Torino and INFN, Torino, Italy; Uppsala University, Uppsala, Sweden

In the near future, precision anti-proton proton annihilation experiments will be conducted to provide a systematic study of the strong force which binds all hadronic matter, such as protons and neutrons. A large-scale detector system, PANDA, is being developed, which will be installed at the international research facility FAIR. The research program with the PANDA detector will be conducted by a collaboration of more than 400 physicists from 48 institutions world wide.

In preparation for these experiments, large-scale simulations need to be performed in the upcoming years for the design of the PANDA detector, to determine analysis strategies and, eventually, for the interpretation and calibration of the experiment results. For this, a computing framework is needed to perform Monte-Carlo simulations and analyses of simulated as well as experimental data. Such a framework will be used together with an AliEN[2] Grid network layer, which is presently being employed at various sites and adapted to the needs of the PANDA collaboration.

In 2006, the PANDA collaboration evaluated various computing frameworks used by several collaborations. In September, the PANDA coordination board decided to pursuit the development of a PandaRoot framework as an extension of the CBM/FAIR-root framework developed at GSI.

The PandaRoot framework is based on the object-oriented data analysis framework, ROOT [1], which is presently being developed and maintained at CERN and commonly used within the high-energy, particle, and nuclear physics communities. In addition, PandaRoot features the concept of Virtual Monte Carlo [2], which allows to use Geant3, Geant4, and Fluka transport codes via a transparent interface.

In the past year, a mature model of the PANDA setup have been implemented in the PandaRoot framework. Figure 1 depicts part of model for the target spectrometer together with the magnet structures of the PANDA setup which is presently included within the framework. A tool to convert CAD step-files to ROOT geometry definitions has meanwhile been embedded in the framework, which provides an advanced and efficient method for the implementation of detector components.

In a synergetic collaboration with the CBM and HADES computing teams, various developments of the PandaRoot framework are presently taken place. For example, the GEANE track follower [3] and the EvtGen event generator [4] have been fully integrated into the PandaRoot framework. In addition, various software tools which were developed within a Babar-like computing framework [5] are presently being migrated such as an advanced Kalman filter and various detector-related reconstruction codes. Plans are made to enrich the PandaRoot framework by computing tools for the electro-magnetic shower reconstruction, channel compositions, kinematic fitting, and many more.

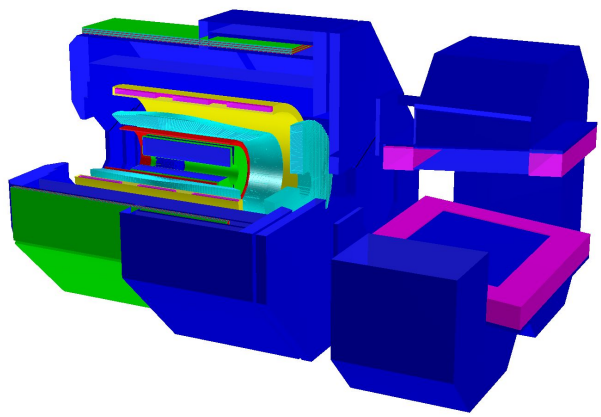

Figure 1: A sketch of the target spectrometer with the magnetic structures of PANDA as implemented in PandaRoot. The various colors or shades correspond to different detector elements (silicon vertex detector, straw-tube tracker, electro-magnetic calorimeter, muon detectors, Cherenkov detector, solenoid and dipole magnets). Optionally, a time projection chamber can be used as central tracker, which is not shown in the figure.

References

[1] http://root.cern.ch.

[2] http://root.cern.ch/root/vmc.

[3] CERN report W5013 (1991).

[4] http://www.slac.stanford.edu/~lange/EvtGen/.

[5] http://www.slac.stanford.edu/BFROOT/www/Computing/.

Low noise preamplifier ASIC for the PANDA EMC*

Peter Wieczorek[1] and Holger Flemming[1]
[1]Gesellschaft für Schwerionenforschung

Introduction

For the electromagnetic calorimeter (EMC) of the PANDA experiment a preamplifier and shaper is under development. Studies of lead tungstate ($PbWO_4$) for the first time done in the low energy region have shown that an extreme low noise front-end is mandatory. The charge sensitive amplifier (CSA) is optimized for the readout of APDs with a capacitance of 300 pF and has to cope with an event rate of over 300 kHz. Test results of a first prototype realized in a 350 nm CMOS process show an excellent noise performance and good agreement to simulation results.

Concept

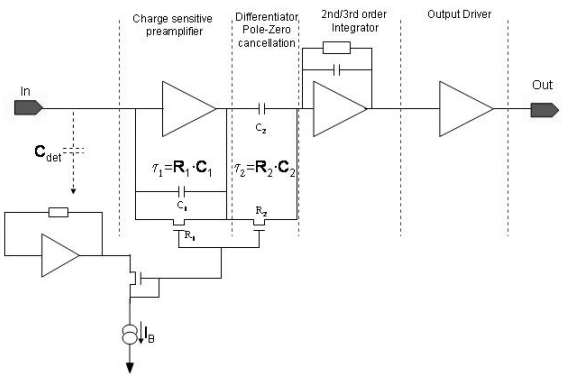

Figure 1: Principle diagram of the readout electronics

First calculations done in end of 2005 have shown the possibility of fulfilling the strong PANDA requirements for the EMC in CMOS technology. Based on this calculations design and simulation of a first prototype was started in early 2006. Figure 1 shows a principle diagram of the readout electronics. It consists of a low noise charge sensitive amplifier, an active pulse shaper and an output buffer. The dominant noise contributor is the input transistor of the preamplifier. Here large design effort was made to keep this noise contribution small. To handle the large event rate a quick discharging of the feedback capacity is necessary which is realized with a MOS transistor as feedback resistor. In addition a pole-zero-cancellation network is included to avoid undershoots.

The shaper is realised in two stages and performs a second or third order semigausian shaping with a peaking time of 230 ns. Among a non amplifying buffer which covers the whole dynamic range a second output buffer with an amplification of ten is foreseen to allow precise noise measurements. Four of these readout paths are implemented in a 350 nm CMOS technology. This ASIC was submitted in July 2006 via the Europractice program.

Measurements

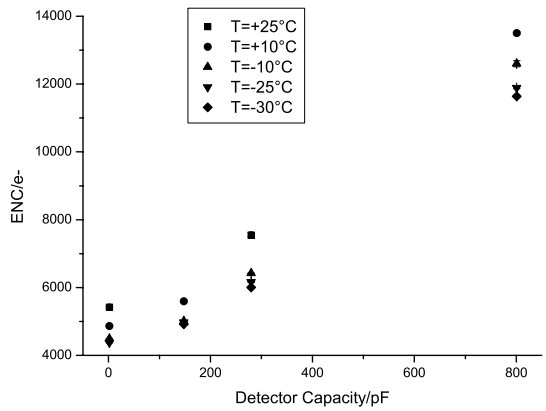

Figure 2: Results of the noise measurements

After the manufactured chips arrived at GSI in September various tests are carried out. In particular noise and dynamic range are measured at different temperatures and detector capacities. As shown in Figure 2 the noise increases with increasing temperature and detector capacitance C_{Det}. At -25 °C and $C_{Det} = 280$ pF an equivalent input noise charge of 6174 e^- ± 17 e^- was measured.
The maximum input charge the chip can cope with is 2 pC and the power consumption is 20 mW / channel.

Conclusions

The test results of the first prototype are in excellent agreement to simulations and fulfil the PANDA requirements. In spring 2007 tests with avalanche photo diodes (APD) are designated. In a second prototype which will be designed in 2007 among some other optimizations the main focus will be on signal shaping and the output stages.

* Work supported by EU (contact number: RII3-CT-2004-506078)

Large Area APD-readout of LYSO crystals*

H. Nowak[1], B. Lewandowski[1], A. Wilms[1], and K. Peters[1]
[1]GSI, Darmstadt, Germany

Introduction

For the PANDA detector a fast and compact electromagnetic calorimeter (EMC) for the detection of photons and electrons is forseen. To fulfill the requirements, defined by the EMC group, like low threshold energy, a very good energy resolution and a high compactness, the scintillator material should offer a short radiation length, a small molière radius and a high light yield. Two scintillator types have been under investigation, bismuth germanate (BGO) and lead tungstate (PWO). Since a short time there is a new scintillator on the market: $Lu_{18}Y_2SiO_5$:Ce (LYSO). This material has also to be investigated as an option for the EMC.
Large area avalanche photodiodes with the active area of 10×10 mm^2 (LAAPDs) represent the envisaged photo devices for the EMC readout.

Properties of LYSO

LYSO is a dense inorganic scintillator with a small temperature coefficient, a very high light output and energy resolution. The properties of LYSO compared to the properies of the other investigated materials are listed in table 1. LYSO is a lutetium based material, that means it contains naturally radioactive isotopes. This causes a background spectrum at low energies, especially for crystals of large size. This does not prevent its application in HEP experiments, where the readout is using trigger.

Property	BGO	LYSO	PWO
Density $[\mathrm{g/cm^3}]$	7.13	7.1	8.28
Rad. length. $[\mathrm{cm}]$	1.12	1.2	0.89
Molière rad. $[\mathrm{cm}]$	2.33	2.4	2.19
Decay time $[\mathrm{ns}]$	60-300	41	5-15
Max. emission $[\mathrm{nm}]$	480	420	420-440
Temp. coef. $[\%/^\circ\mathrm{C}]$	-1.6	$+0.04$	-2
Light Yield [ph./MeV]	9000	$4 \cdot 10^4$	100

Table 1: Properties of dense inorganic scintillators.

Longitudinal light response uniformity measurement with LYSO

For the measurement of the light response umiformity a LYSO crystal with the dimensions of $20 \times 20 \times 200$ mm^3 has been coupled to a photomultiplier. A sodium source has been moved in 10 mm intervals along the crystal (away from the photomultiplier) and the corresponding peak maxima (see fig. 1) have been measured.

* Work supported by EU (contact number: RII3-CT-2004-506078)

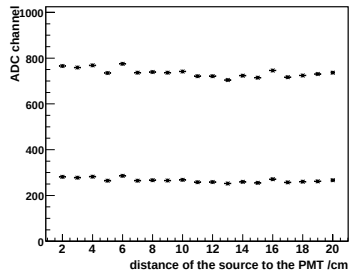

Figure 1: The ADC channel positions of the maxima of the annihilation peak at 511 keV (lower values) and the photo peak at 1274.53 keV (upper values) depending on the distance between the source and the PMT.

As it can be seen from the plot the longitudinal uniformity of the crystal is ensured.

Energy resolution of LYSO measured with LAAPD

To determine the energy resolution of the crystal, spectra have been taken with three different sources: sodium, cobalt and caesium. The positions of the annihilation and the photo peak maxima of each source were used as reference points for the energy calibration. One background spectrum has also been taken to study the effect of lutetium on the energy resolution of the crystal.

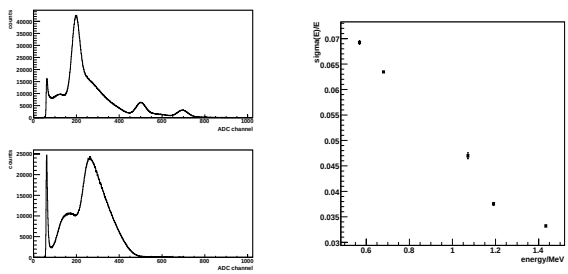

Figure 2: Sodium spectrum (top) and background spectrum (below) (left). The measured energy resolution of the annihilation and photo peaks for sodium, caesium and cobalt detected with a large crystal and a LAAPD (right).

Results

LYSO offers very high light output and energy resolution as it can be seen in figure 2. A background spectrum exists and it is dominated by the beta decay of lutetium. But there is no influence on HEP experiments. From the presented results it can be concluded that LYSO read out by APDs is a good option for electromagnetic calorimeters.

Developmentstatus of the APDs for the PANDA electromagnetic calorimeter*

A. Wilms[1], B. Lewandowski[1], H. Nowak[1], K. Peters[1,2], and N. Pitz[2]
[1]GSI, Darmstadt, Germany; [2]IKF, University Frankfurt, Germany

Introduction

The PANDA electromagnetic calorimeter (EMC) will consist of nearly 22,000 lead tungstate (PWO) crystals.They will be read out with avalanche photodiodes (APDs) at a temperature of $T \approx -25°C$. Due to the great effort in development and fabrication of those photo detectors achieved during the last years, the reachable size of the device active area is still getting larger. For the readout of the barrel part of the PANDA-EMC APDs with an active area of $(10 \times 10)mm^2$ (large area APDs (LAAPDs)) will be used. Due to the great amount of LAAPDs used in PANDA a laboratory for characterization and optimization of these devices related to the EMC specifications has been build up at Frankfurt University.

Recent activities

For the characterization and monitoring of the devices different properties of them have to be measured. The characterization of the manufacturer is done at room temperature; therefore each measurement has to be done at room temperature (to exert or vitiate the manifacturers specifications) and at operating temperature of $T \approx -25°C$. This is leading to several special requirements for the quality assurance of the whole number of APDs used in the PANDA-EMC. During the R&D phase several measuring equipments were designed and deal with the characterization and quality assurance of the LAAPDs in different specific aspects.

Characterization

Several device properties will be measured at the new APD laboratory. The capacitance and the dark current are an important input for the preamplifiers designed by the ASIC group at GSI as well as the noise of the devices. The latter parameter will be evaluated by measuring the excess noise factor of the LAAPDs at the two relevant temperatures. The quantum efficiency depending on the light wavelength and the uniformity of the device internal gain over the whole active area will also be measured.
All specification of the APDs will also be determined depending on their wafer positions as well as in terms of specification fluctuations corresponding to different wafers delivered by the manufacturer.

Radiation hardness

The radiation hardness of the available prototypes has to be determined for protons/photons as well as for neutron irradiation. The proton irradiation is done at the KVI Groningen and a setup for neutron irradiation was designed for the APD laboratory in Frankfurt to study the increase of the device dark current during irradiation. This latter measurement will be done at several temperatures which leads to a very complex design of the apparatus to fulfill all safety requirements for this kind of radiation studies. First results of this measurements will be available in the near future.

APD mounting

Another aspect of the APD activities of our group is the realization of the APD mounting procedure on the rear side of the crystals. For that reason a capsule has been designed to mount the APDs, the preamplifier, the light guides of the light pulser system as well as a temperature sensor properly on the crystal surface (see fig.1).

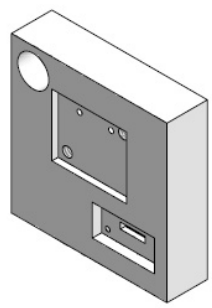

Figure 1: Capsule for one LAAPD from the back side: Shown are the gaps for the preamplifier- and thermistor-PCBs as well as a hole forseen for light guide mounting.

The material of this capsule has to be an electric shielding meanwhile its heat conductivity has to be good enough to ensure the cooling of the APDs during the measurement. Therefore we have chosen poly-ether-ether-ketone (PEEK) for the first capsule prototype production.

The evaluation of different kinds of glues has also started during the last month and the measuring equipment for the screening procedure of the splice between APD and crystal is under development.

Acknowledgment

We would like to thank Herbert Löhner from KVI for the very friendly and familar atmosphere and help during several LAAPD irradiation beamtimes.

* Work supported by EU/FP6 HADRONPHYSICS (see Annex) and GSI

The CBM experiment at FAIR*

V. Friese, W.F.J. Müller, P. Senger, GSI Darmstadt, and the CBM Collaboration

CBM physics and detector setup

The planned Compressed Baryonic Matter (CBM) experiment at FAIR offers unique possibilities to investigate baryonic matter at highest densities in the laboratory. The most promising observables from nucleus-nucleus collisions in the FAIR energy range are particles containing charm quarks (D-mesons and charmonium), low-mass vector mesons decaying into dilepton pairs (ρ, ω and ϕ mesons), and hyperons (Λ, Ξ, Ω and their antiparticles). This includes the measurement of (event-by-event) fluctuations, correlations, and collective flow of hadrons. A systematic and comprehensive investigation of these observables, in particular their excitation functions, will permit to extract information on the equation-of-state of baryonic matter at high densities, on the location of the phase boundary between hadronic and partonic matter (including the QCD critical endpoint), and on the restoration of chiral symmetry at high net-baryon densities.

The experimental task is to identify hadrons and leptons in collisions with up to 1000 charged particles at event rates of up to 10 MHz. A particular experimental challenge is the identification of D-mesons which is based on the selection of secondary vertices with high accuracy. The measurements require a high-speed data acquisition (DAQ) architecture and an appropriate high-level event-selection concept.

A schematic view of the proposed CBM detector concept is shown in figure 1. Inside a large aperture dipole magnet there is a Silicon Tracking and Vertexing System which consists of two parts: a Micro-Vertex Detector (MVD, 2 silicon pixel layers) and the Silicon Tracking System (STS, several layers of silicon microstrip detectors). The Silicon detector array has to provide the capabilities for track reconstruction, determination of primary and secondary vertices, and momentum determination. Electrons from low-mass vector-meson decays will be identified with a Ring Imaging Cherenkov (RICH) detector. The TRD detector will provide charged particle tracking and the identification of high energy electrons and positrons. The ECAL will be used for the identification of electrons and photons. As an alternative to the RICH detector a muon detection/hadron absorber system is under investigation. If the RICH will be replaced by a muon detector the TRD will be converted into a tracking detector for hadron measurements together with the timing RPC. Then the TOF-RPC detector serves for two purposes: for background suppression during muon measurements with absorbers, and for hadron identification with muon absorbers removed.

* Work supported by EU/FP6 HADRONPHYSICS (see Annex) and by INTAS

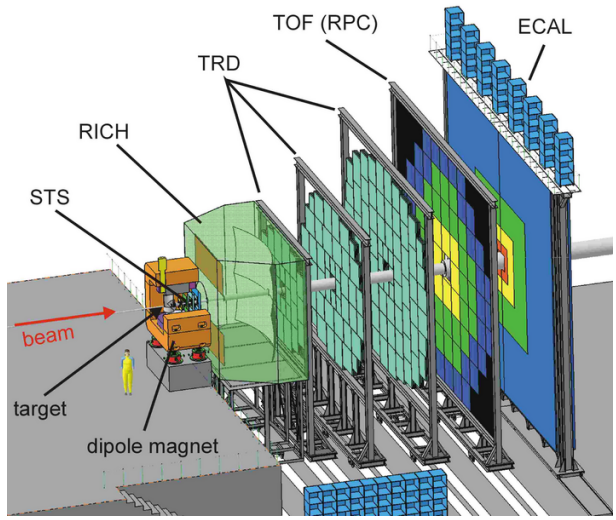

Figure 1: Schematic view of the Compressed Baryonic Matter (CBM) experiment planned at FAIR. The setup consists of a high resolution Silicon Tracking System (STS), a Ring Imaging Cherenkov detector (RICH), three stations of Transition Radiation Detectors (TRD), a time-of-flight (TOF) system made of Resistive Plate Chambers (RPC) and an Electromagnetic Calorimeter (ECAL).

Track reconstruction and STS development

The feasibility studies were performed within the CBM software framework which has been developed further (see M. Al-Turany et al., this report). The routines for track and vertex reconstruction have been improved and used for optimization of the layout of the Silicon Tracking System (see I. Kisel et al, this report). Track reconstruction efficiencies of above 95% can be obtained with a fast and radiation-hard detector system which consists either of two Silicon hybrid pixel detector stations together with 4 double-sided Silicon Strip detector layers, or of 6 Strip-sensor layers only (see J.M. Heuser et al., this report). The STS can be used as a stand-alone tracker for high-rate measurements and for the identification of hyperons (see E. Kryshen, this report). The Micro-Vertex Detector (MVD) - which is close to the target and has limitations in radiation hardness and read-out speed - will be installed only for open charm measurements which requires high-precision vertexing.

Detector R&D concentrates on the design of a prototype STS which includes double-sided sensors, the cables, the read-out chip and the mechanical structure. First prototype sensors have been designed and are being fabricated (see J.M. Heuser et al., this report). Moreover, a fast self-triggered read-out chip has been developed and is being tested (see C.J. Schmidt et al., this report).

Hadron identification via TOF

Hadron identification in the CBM experiment is performed using the time-of-flight measurement in the RPC detector wall located about 10 m downstream of the target. This requires track reconstruction and momentum determination in the Silicon Tracking System, track following through the TRD stations, and matching of reconstructed tracks to the hits in the RPCs. The total reconstruction efficiency for hadrons (STS-TRD-RPC) is well above 80 %. This result is based on realistic detector layouts and performances (see D. Kresan et al., this report). The R&D on prototype timing RPCs concentrates on high rate capability, low resistivity material, long term stability and the realization of large arrays with overall excellent timing performance (see D. González-Diaz et al., this report).

D meson identification and vertex detector

D mesons will be identified via their hadronic decay into one or two charged pions and a kaon. In order to suppress the overwhelming combinatorial background of promptly emitted pions and kaons one has to determine the D meson decay vertex with an accuracy of about 50 μm ($\tau(D^0)$ = 123 fm/c, $\tau(D^{\pm})$ = 312 fm/c). This measurement requires an extremely thin and highly granulated pixel detector. We are developing a Micro-Vertex Detector (MVD) consisting of two layers of Monolithic Active Pixel Sensors (MAPS) with a pixel size of 40x40 μm^2 and a thickness of 100 μm. Both vertex resolution and radiation damage increase with decreasing distance from the target. Simulations have been performed in order to optimize signal-to-background, efficiency, distance and detector lifetime (see I. Vassiliev et al., this report). According to these studies it is possible to record 3.6×10^5 D mesons in 10^{12} minimum bias Au+Au collisions at 25 AGeV within the lifetime of a MAPS. With a collision rate of 100 kHz the first MAPS station would have to be replaced after 120 days of running. The R&D on the MVD concentrates on the improvement of radiation hardness and readout speed of the MAPS, and on system integration (see S. Amar-Youcef et al., this report).

Electron identification with RICH and TRD

Electrons and positrons are identified with the RICH detector and with the TRD. The simulations are based on reconstructed tracks in STS and TRD, on ring recognition in the RICH photon detector, on ring-track matching, and on the statistical analysis of the energy loss signal in the TRD (see C. Höhne et al., this report). With information only from RICH the pions can be suppressed by a factor of about 500 up to a momentum of about 9 GeV/c. Taking into account additional information from the TRD the total pion suppression factor is larger than 10^4 for momenta above 1 GeV/c in central Au+Au collisions at 25 AGeV. This value will be sufficient to discard misidentified pions from the combinatorial electron background in vector-meson measurements.

The major challenge in the identification of low-mass vector mesons via their di-electronic decay is to reject the physical background of electron-positron pairs from Dalitz decays and gamma conversion. The optimization of background rejection strategies based on electron identification by RICH and TRD, using an improved track reconstruction method for low momentum particles, is in progress (see T. Galatyuk et al., this report). The combinatorial background in the mass range of the J/ψ meson can be dramatically reduced by the requirement of a high transverse momentum of the electrons. For example, when requiring electron transverse momenta of $p_t \geq 1.2$ GeV/c for central Au+Au collisions at 15 (25, 35) AGeV, signal-to-background ratios of S/B = 0.8 (1.7, 14.5) and efficiencies of ϵ = 0.09 (0.12, 0.14) can be achieved for J/ψ mesons (see A. Maevskaya et al., this report). TRD R&D is focused on the development of highly granular and fast gaseous detectors which can stand the high-rate environment of CBM. Prototype gas detectors (based on MWPC and GEM technology) have been built and tested with particle rates of up to 100 kHz/cm^2 without deterioration of performance (see M. Petrovici et al. and A. Andronic et al., this report).

Muon measurements with hadron absorbers

As an alternative approach to the dielectron measurement we have studied the possibility of detecting vector mesons (ρ, ω, ϕ, J/ψ) via their decay into $\mu^-\mu^+$ pairs. The idea is to suppress the hadrons with several absorber layers located behind the Silicon Tracking System. In order to match the muons which pass the absorber to the tracks measured by the Silicon tracker (which defines the momentum) one has to track all charged particles through the absorber. This is done by highly granulated and fast detectors which are located in each gap between the absorber layers.

The simulations are based on track reconstruction algorithms taking into account a realistic response of the STS and a position resolution of the muon chambers of σ = 100 μm (see A. Kiseleva et al., this report). The studies demonstrate that for example the ω meson can be measured in central Au+Au collisions at 15 (25, 35) AGeV with a signal-to-background ratio of S/B = 0.16 (0.14, 0.14) and with an efficiency of ϵ = 0.022 (0.033, 0.044). J/ψ mesons can be identified with a signal-to-background ratio of about 100 and an efficiency of ϵ = 0.13 for central Au+Au collisions at 25 AGeV. Such a number would be sufficient for the identification of ψ' mesons in Au+Au collisions. For the charmonium experiments the total thickness of the hadron absorber has to be increased as compared to measurements of low-mass vector mesons.

The challenge for the muon chambers and for the track reconstruction algorithms is the huge particle density of up to 1 hit/cm^2 per event in the first detector layers. Therefore, detector R&D concentrates on the design of fast and highly granulated gaseous detectors based on GEM technology.

Event reconstruction and hadron identification in the CBM experiment*

V. Friese[1], S. Gorbunov[1,2], I. Kisel[2,3], D. Kresan[1], V. Lindenstruth[2], W. F. J. Müller[1], I. Vassiliev[1], and the CBM collaboration

[1]GSI, Darmstadt, Germany; [2]KIP, Universität Heidelberg, Germany; [3]LIT, JINR Dubna, Russia

The physics programme of the CBM experiment at FAIR includes a systematic investigation of hadron production in heavy-ion reactions as function of collision energy and system size. Of particular interest are event-by-event fluctuations in the particle ratios as well as directed and elliptic flow. For this purposes, excellent identification of pions, kaons and protons is indispensable. It will also help to reduce the background for the measurements of open charm and hyperons detected by their weak-decay topology.

Hadron identification in CBM will be performed by a time-of-flight (TOF) wall situated about 10 m downstream of the interaction target. It thus requires track reconstruction and momentum determination in the STS, track following through the TRD system, and matching of the track to the measured TOF hit.

The track reconstruction procedure in the STS is based on the Cellular Automaton algorithm and has been improved with respect to speed and efficiency. An efficiency of about 96 % is obtained for primary tracks in central Au+Au collisions at 25 AGeV. Track fitting is based on the Kalman filter. This algorithm has been optimised with respect to memory access and speed by using a local polynomial approximation of the magnetic field instead of the full calculated field map. The momentum resolution is about 1 % almost independent of momentum as shown in figure 1, demonstrating the dominant effect of multiple scattering.

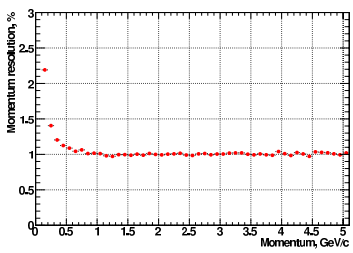

Figure 1: Momentum resolution as function of momentum for the standard STS geometry

A 3-D track following method based on a Kalman filter is employed to prolong the tracks throughout the TRD system, yielding an efficiency of about 94 %. The global track is then extrapolated towards the TOF wall, and the nearest TOF hit is attributed to it. Fig. 2 shows the efficiency of TOF hit matching (left) and the total TOF efficiency (right), including STS and TRD reconstruction efficiencies, as a function of momentum. These results were obtained with a realistic description of the RPC coordinate resolution, taking into account the single gap response also in case of mutiple hits and inclined tracks. The losses in TOF-track matching of about 7 % are dominated by particle decays and double hits in the RPCs. The latter contribution amounts to some 2 % and can be reduced by resolving double hits in the RPC strip readout. Optimisation of the RPC pad/strip sizes is ongoing in order to reduce the number of electronic channels while roughly keeping the performances.

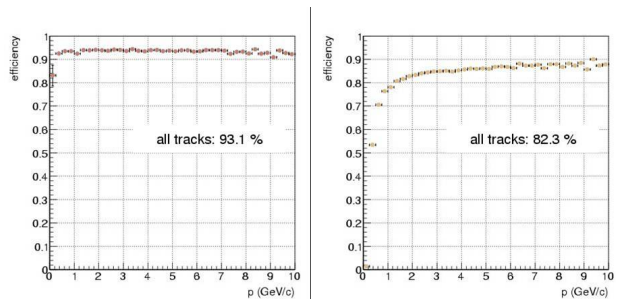

Figure 2: Efficiency of (left) matching a TOF hit with a global track and (right) total TOF reconstruction efficiency as function of momentum

This global event reconstruction scheme, developed in the course of the last year in the CBMROOT software framework, gives path to feasibility studies of physics observables. As an example, fig. 3 (left) shows the reconstructed squared particle mass from the time-of-flight, track length and momentum, as a function of momentum, for an assumed time resolution of 80 ps. The reconstructed mass spectrum at $p = 3\,\mathrm{GeV}$ is shown on the right side of the figure. With an overall efficiency of 80 % to 90 %, separation of kaons and pions can be achieved up to laboratory momenta of about 3.5 GeV, while protons can be identified up to 7 GeV.

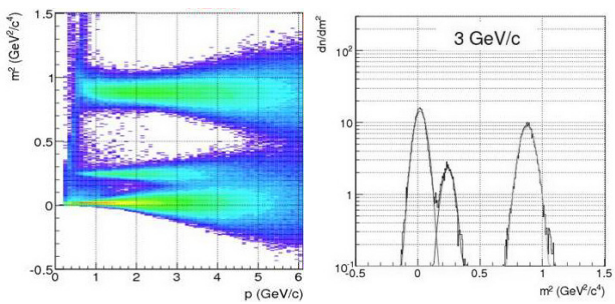

Figure 3: (Left) reconstructed particle mass from the TOF measurement as function of momentum; (right) mass spectrum derived from TOF at $p = 3\,\mathrm{GeV}$

* Work supported by EU-FP6 HADRONPHYSICS

Electron pair reconstruction in CBM*

T. Galatyuk[1], S. Das[1], C. Höhne[1], and the CBM collaboration
[1]GSI, Darmstadt, Germany

The reconstruction of low-mass vector mesons (ρ, ω, ϕ) emitted out of the hot and dense phase of relativistic heavy ion collisions is one of the experimental goals of the CBM experiment. In this contribution the status on feasibility studies for their measurement will be summarized. Dominant background sources are random combinations of e^- and e^+ from π^0-Dalitz decay and γ conversion, the latter mostly in the target and to a smaller extent in the tracking stations, the beam pipe and the magnet yoke. In order to minimize electrons from conversions a single 25 μm gold target was assumed. A characteristic feature of conversion and π^0-Dalitz decays is the moderate decay momentum of the electron pair. This generally leads to small opening angles and comparatively small laboratory momenta. A special challenge of the current concept is the fact that electron identification is not provided in front of the magnetic field. By adding correction coils it is possible to suppress the field between the target and first Silicon Tracking Station. The excellent two hit resolution in the MAPS detector ($< 100\mu$m) gives then a chance to reject close pairs. To increase the acceptance for low momentum particles the magnetic field was reduced to B_{max} = 0.7 T and the size of STS 1 to 6 was increased. The strategy of background rejection described in [1] was applied. The invariant mass

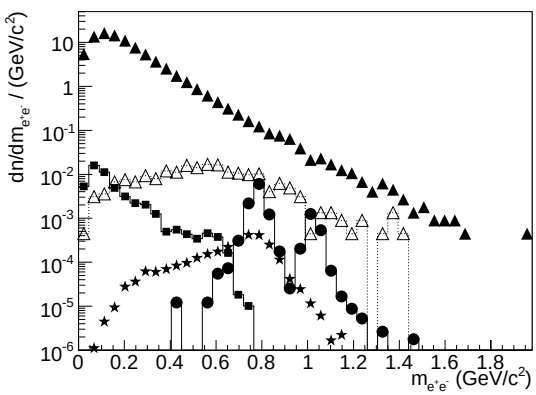

Figure 1: Di-electron invariant mass spectra for $Au + Au$ collision system at a beam energy of 25 AGeV, zero impact parameter, ideal particle ID. Close triangle: accepted combinatorial background, open triangle: after cuts. Square: γ, π^0, η and ω-Dalitz, circle: ω and ϕ, star: ρ^0.

spectrum arising after applying all cuts is shown in Figure 1. The S/B ratio in a ± 1.4 σ_m range around the vector meson peaks are 0.5 for ω with signal efficiency 15%, 0.6 for ϕ (23% efficiency), 3 for π^0-Dalitz. The optimised geometry of the STS detector and changes in the magnetic field were taken into account, however, no track reconstruction or particle identification algorithms were used.

A more realistic simulation will include track reconstruction in the STS and particle ID in the RICH detector. Considerable efforts went into the problem of tracking in the STS for low momentum tracks because a large fraction of soft tracks suffers significant multiple scattering in the detector material. The track reconstruction efficiency is 90 %. After track model improvements it is possible to reconstruct tracks with momenta down to 80 MeV (see Figure 2). To reconstruct the track parameters, tracks were fitted with electron mass using a routine based on a Kalman filter. The reduction of the magnetic field to 70 % of its nominal value results in a momentum resolution still well below 2 %. In order to reject low momentum tracks, which

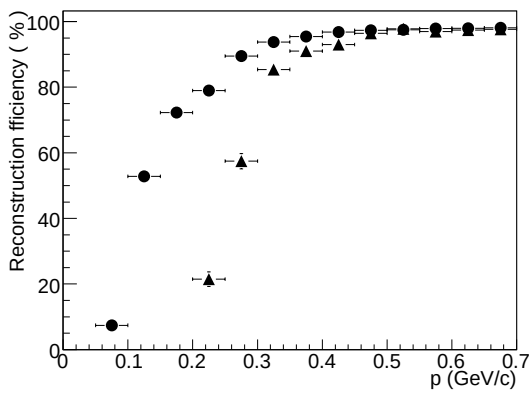

Figure 2: Track reconstruction efficiency as a function of momentum. Triangle: standard tracking algorithm, circle: improved tracking on low momentum tracks.

have been reconstructed in STS but left the acceptance before the RICH detector, it is important to have a high purity of identified electrons. The currently estimated pion suppression using only the RICH detector is about a factor 500 below 8 GeV. This suppression factor can be improved to more than 10^4 for tracks with momenta above 1 GeV when using TRD and TOF information in addition (C. Höhne et al., this report).

Invariant mass spectra of dielectron pairs including full event reconstruction and electron identification will be available in the near future.

References

[1] T.Galatyuk et al., see GSI Scientific Report 2005/FAIR-QCD-CBM-06.

* Work supported by EU/FP6 HADRONPHYSICS (see Annex)

Progress in the CBM-TOF wall, R&D and simulation*

D. González-Díaz[1], M. Ciobanu[1], E. Cordier[2], A. Semak[3], and the CBM collaboration
[1]GSI, Darmstadt, Germany; [2]Physikalisches Institut, Universität Heidelberg, Germany; [3]IHEP, Protvino, Russia

The CBM-TOF group aims at providing high π/k separation (more than 2-σ in the reconstructed mass) in Au+Au central collisions at 25 GeV/A, with a coverage of mid-rapidity by at least 1 unit in y and 1 GeV in p_T. These PId capabilities are needed for probing the QGP phase, through the study of such fundamental observables as the dynamical fluctuations of the kaon yield, kaon flow, hyperon production close to threshold and open charm.

Based on simulation, it was shown that the mentioned requirements can be satisfied by a tRPC (timing Resistive Plate Chamber) wall placed at 10 m distance from the target with 25-30° coverage in θ ($\sim$150 m^2), featuring a time resolution of 80 ps and an occupancy per cell below 5% ($\sim$ 60.000 cells). In order to cope with the high beam luminosity, the tRPC must handle rates up to 20 kHz/cm^2, while the FEE must process the very fast GHz signals from the tRPC at an interaction rate up to 10 MHz.

The CBM spectrometer benefits from the excellent overall PId capabilities of the TOF wall: for example, the π/e separation in time of flight is 3-σ for p=1.1 GeV, that provides extra π suppression (apart from that of RICH and TRD detectors) in view of di-electron spectroscopy.

Current R&D activities [1, 2, 3, 4, 5] focus on the development of high rate capability tRPCs, aiming at extending their working principle from few hundreds of Hz/cm^2 up to the required rate of 20 kHz/cm^2, for CBM usage. But also improvements on the description of the timing properties of the detector at high rates have been recently accomplished [6]. As a consequence of the latter, the idea that the deterioration of tRPC performances at high rates is mainly driven by the DC column resistivity ρd (resistivity times the resistive plate thickness per gap) is now more sound.

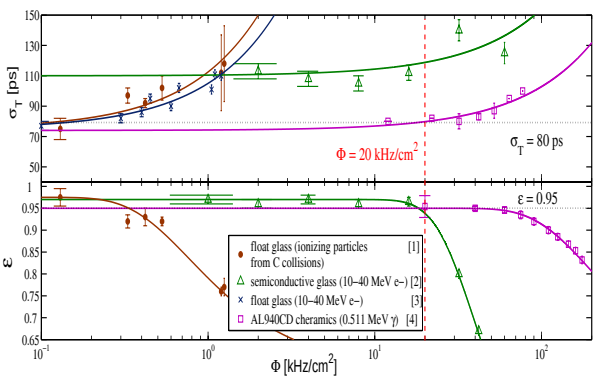

Figure 1: Compilation of different measurements.

A number of measurements was performed at different rates under different conditions: with ionizing particles from carbon collisions at GSI-SIS [1], with 10-40 MeV electrons at the ELBE LINAC [2, 3] and with γ sources [4]. Among the more promising candidates for the resistive plates of high rate tRPCs, semi-conductive glasses [2] and ceramics [4] must me mentioned, whereas the possibility of using warm thin glass deserves also consideration [5]. A compilation of results is shown in Figure 1, together with the dependence on rate Φ obtained in [6]:

$$\varepsilon \simeq \frac{\varepsilon_o}{1 + Ae^{-B/\Phi}}\ , \quad \sigma_T \simeq \sigma_o(1 + C\Phi) \qquad (1)$$

where ε_o, σ_o, A, B, C are obtained from the fit to data.

The current theoretical and experimental understanding of the detector has been used to better model the detector geometry and its response. Starting from the simulation of the gap response, a realistic description of the position resolution, inclined tracks and multiple hits have been provided for the first time. The studies performed after full tracking through CBM confirm the statements of paragraph 2 (see D. Kresan et al., this report) and open the path to a detailed comparison between pad and strip technologies that are currently existing for the tRPC readout. A first approach to the final mechanical structure has also been accomplished, where the distribution of the wall in towers looks by now the more suited solution, providing a high flexibility and a comfortable distribution of the weight (Figure 2).

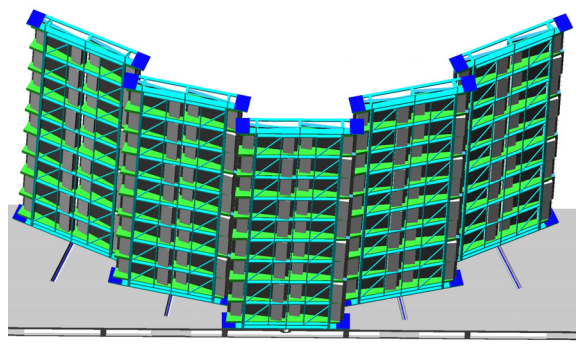

Figure 2: Rear view of the TOF wall, divided into towers.

For the read-out, an ASIC based PreAmplifier-DIscriminator chip (PADI) was developed and tested together with the TACQUILA3 digitizer (developed for the FOPI upgrade), showing a global resolution $\sigma_T < 10$ ps.

References

[1] H. Alvarez-Pol et al., NIM A, 535(2004)277.
[2] F. Dohrmann, talk at VIII CBM coll. meeting.
[3] R. Kotte et al. NIM A, 564(2006)155.
[4] L. Lopes et al., Nucl. Phys. B, (Proc. Suppl), 158(2006)66.
[5] P. Fonte et al., PoS(HEP2005)376.
[6] D. Gonzalez-Diaz et al., Nucl. Phys. B, (Proc. Suppl), 158(2006)111.

* Supported by JRA12 of EU/FP6 Hadronphysics (see annex), INTAS Ref. Nr. 03-54-3891 and German BMBF contract 06 HD190I.

Layout studies and sensor prototypes for the CBM Silicon Tracking System*

J. M. Heuser[1], R. Karabowicz[1], E. Kryshen[2], Chr. J. Schmidt[1], and the CBM Collaboration
[1]GSI, Darmstadt, Germany; [2]St. Petersburg State Polytechnic University, Russia

The Silicon Tracking System (STS) is the central detector of the CBM experiment. It serves for track reconstruction with good momentum measurement (of about of 1%) of all charged particles produced in high multiplicity nuclear reactions at the target [1]. For this task a low-mass silicon tracking detector system of high granularity is needed. We are currently studying the arrangement of the tracking stations and designing the prototype of the micro-strip silicon detectors.

The STS concept, schematically shown in Fig. 1, comprises 6 detector stations for the track measurement, made of micro-strip silicon detectors. Each station is divided into sensors, with short strips close to the beam line (compare Fig. 2) and with longer strips, realized either on single wafers or by chaining two or more sensors, in the regions further outside. The reading of the individual sensors may be realized by routing the strips' analog signals from every sector through thin flat multi-line cables to front-end electronics at the periphery of the stations (see current R&D effort in [2]). The projective coordinate measurement of the sensors leads to a significant fraction of combinatorial or fake hits, a challenge to the reconstruction algorithms. In alternative approach two first stations may consist of LHC-type hybrid pixel detectors, although those are relatively thick and presumably require active cooling in the aperture. For high-resolution vertex measurements, e.g. open charm detection, the STS is supported with a Micro-Vertex Detector (MVD) consisting of two very thin and fine-pitch MAPS pixel detector stations close to the target.

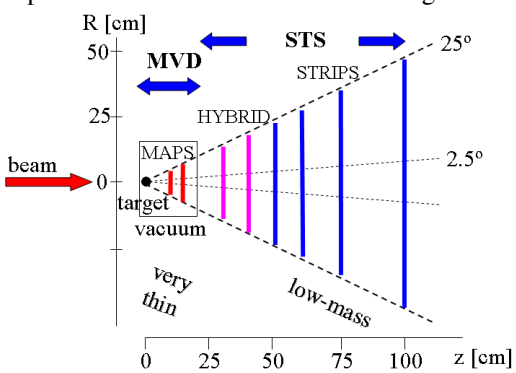

Figure 1: Schematics of the STS + MVD detector systems.

The micro-strip sensor is intended to be double-sided, with the strips oriented along the module's long axis in the front layer, and a "stereo" direction (with 15° stereo angle) on the second side, The design, shown in Fig. 3, addresses in particular connectivity issues, so that both sensor sides can be contacted both at the top and the bottom edge. The first micro-strip sensors, to be produced in 2007 [3],

* Supported by EU/FP6 HADRONPHYSICS (see Annex) and INTAS

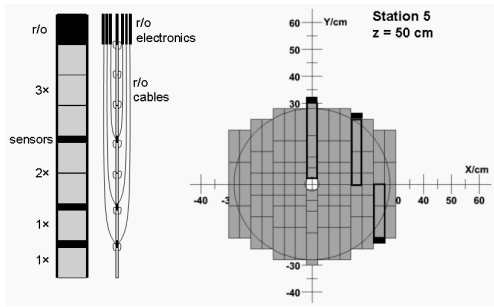

Figure 2: Silicon micro-strip sensors arranged into modules of different lengths building up a tracking station.

will have a thickness of 200–300 μm. The prototype will use chained sensors, readout electronics [4] and mechanical support. The studies will address radiation hardness, minimization of inactive area near the edges. Readout cables, made from fine-pitch aluminum traces on polyimide material will be developed.

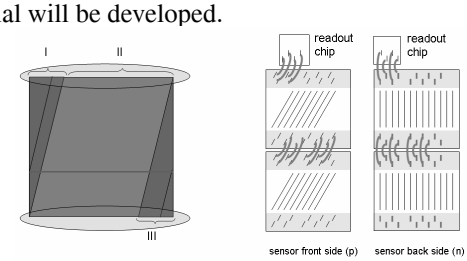

Figure 3: (Left) Schematics of the sensor's stereo side. (Right) Chained sensors and their interconnections.

The detector stations has been implemented in the simulation framework CBMROOT as discs of silicon, and were segmented into 50 × 50 μm^2 pixels or 50 μm pitch strips, for hybrid or micro-strip stations, respectively. Reconstruction efficiencies of about 97% (92%) for primary (all) tracks exceeding 1 GeV/c momentum, and a momentum resolution of 1.2% demonstrate the feasibility of the track measurement with the proposed detector concept.

Current performance studies investigate the effects of different strip lengths and stereo angles on the track reconstruction. Other detector configurations where e.g. the hybrid pixel stations are replaced with pairs of micro-strip stations are considered. Next steps will use more realistic parametrization of the STS, implementing sensor wafers arranged into modular structures and mounted on mechanical supports.

References

[1] I. Kisel et al., *Event Reconstruction in the CBM Experiment*, this report

[2] J. M. Heuser et al., GSI document DOC-2006-Dec-19

[3] CiS Institut für Mikrosensorik gGmbH, Erfurt, Germany

[4] Chr. J. Schmidt et al., this report

Electron identification and J/ψ detection in CBM *

C. Höhne[1], A. Maevskaya[2], S. Das[1], S. Lebedev[2], A. Ayriyan[2], P. Stolpovsky[3], G. Ososkov[2], V. Ivanov[2], and the CBM collaboration

[1]GSI, Darmstadt, Germany; [2]JINR-LIT, Dubna, Russia; [3]IHEP Protvino, Russia

The observation of low-mass dilepton pairs and charmonium in the CBM experiment is one of the key measurements for the study of compressed baryonic matter in heavy ion collisions. The standard setup of CBM [1] foresees the measurement of electrons using particle identification with a ring imaging Cherenkov (RICH) detector and transition radiation detectors (TRD). In this report first results on the performance of the CBM detector concerning electron identification and pion suppression including complete event reconstruction and particle identification will be presented. As important application also results on a feasibility study of a charmonium measurement in the dielectron decay channel will be discussed.

The simulations were performed for central Au+Au collisions at 15, 25, and 35 AGeV beam energy generated by UrQMD [2]. Decay electrons from J/ψ mesons were mixed into these events; for final spectra their multiplicities were taken from the HSD model [3]. These events were tracked through the CBM detector using GEANT, the transition radiation in the TRD was approximated by an external model. The event reconstruction starts with tracking in the STS, requiring a minimum of 4 STS hits. The tracks are then extrapolated to the RICH photodetector plane, to TRD and TOF. Rings are found using ring reconstruction algorithms. Ring-track as well as TOF hit-track matching were applied choosing pairs having the closest distance. This way fully reconstructed events with information on RICH, TRD, and TOF signals for each track are available.

For ring reconstruction in the RICH detector the most crucial parameter is the quantum efficiency of the photodetector, here existing MAPMTs from Hamamatsu were implemented (H8500-03) yielding about 21 hits per electron ring. Ring finding efficiencies are about 85 % with less then one fake ring per event. These fake rings are further rejected applying a set of quality criteria. A further important cut is the requirement of a maximum distance between ring center and track. Placing a cut at 1 cm rejects only 5 % of good rings with $p > 2$ GeV/c but reduces the background by about an order of magnitude. For lower momenta, however, the allowed distance would have to be increased in order to keep this good efficiency, unfortunately at a loss of purity. As for the J/ψ meson tracks at higher momenta are of prime interest, this is no issue here. Electrons are then selected choosing a range of radii of $\langle \mathrm{R} \rangle \pm 3\sigma$, with $\langle \mathrm{R} \rangle$ = 6.17 cm and σ = 0.14 cm. Pions leak into this band and will be identified as electrons only from 8-10 GeV/c on. After all cuts the efficiency of electron identification is about 70 % in the momentum range from 2-7 GeV/c. Figure 1 (left) shows the resulting pion suppression defined as $\frac{\pi \text{ identified as e}}{\pi \text{ in RICH acceptance}}$. Up to momenta of about 8 GeV/c pion misidentification is solely due to ring-track mismatches; from 8 GeV/c on pions leaking into the radius cut become dominant. Mismatches of proton tracks to electron rings can be fully eliminated using TOF information. Pions are further rejected using energy loss information from the TRD. The summed energy loss in the 12 TRD layers is taken into account as well as the result of a statistical analysis of the energy loss spectrum in each layer [4]. The combined pion suppression in RICH and TRD reaches values larger than 10^4 for $p > 1$ GeV/c.

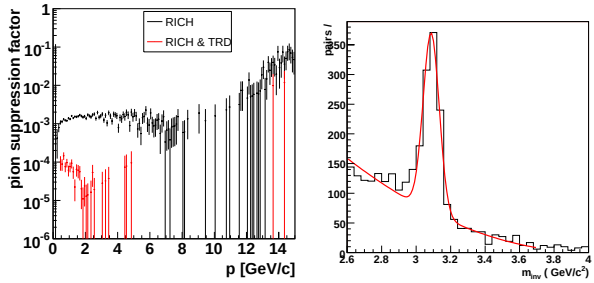

Figure 1: Results of simulations of central Au+Au collisions at 25 AGeV beam energy. Left: Pion suppression for electrons identified in CBM. Right: Invariant mass spectrum of reconstructed J/ψ mesons.

Figure 1 (right) shows the invariant mass spectrum extracted after event reconstruction and electron identification as described above. In order to suppress the physical background, a cut on transverse momentum is applied ($p_t > 1.2$ GeV/c) on each track which shows only negligible effect on the J/ψ signal due to the high momenta of the decay electrons. The most crucial factor for a good signal-to-background ratio is the purity of the electron identification. Earlier simulations have shown that a factor 10^4 pion suppression is needed which is nicely fulfilled by this simulation. Within the current simulation, J/ψ reconstruction efficiencies and signal-to-background ratios are 9 %, 12 %, 14 % and 0.8, 1.7, 14.5 for central Au+Au collisions at 15, 25, 35 AGeV beam energy, respectively.

References

[1] V. Friese et al., *The CBM experiment at FAIR*, this report.

[2] S.A. Bass et al., Prog. Part. Nucl. Phys. 41 (1998) 255.

[3] W. Cassing et al., Nucl. Phys. A 674 (2000) 249.

[4] P.V. Zrelov, V. Ivanov, NIM A 310 (1991) 623.

* Supported by EU/FP6 HADRONPHYSICS (see Annex) and partly (A. Ayriyan, S. Lebedev) by RFBR grant No 05-01-00645-a.

Vector meson detection via $\mu^+\mu^-$ decays in CBM *

A. Kiseleva[1], R. Dzhigadlo[2], S. Gorbunov[3], I. Kisel[3], and I. Vassiliev[1]
[1]GSI, Darmstadt, Germany; [2]University, Kiev, Ukraine; [3]University, Heidelberg, Germany

As an alternative approach to the dielectron measurement we have investigated the possibility to detect vector mesons ($\rho, \omega, \phi, J/\psi$) via their decay into $\mu^+\mu^-$ pairs. The muon detection system is located downstream the STS. The actual design of the muon system consists of 5 hadron absorber layers made of tungsten, iron and carbon of variable thickness, and of 16 detector layers with 100 μm position resolution. The first detector layer is positioned in front of the first (tungsten) absorber, three sensitive layers are located in each gap between two absorbers, and three detectors are located behind the last absorber. For the muon simulation we take in to account not only STS and the muon system, but also two stations of the Transition Radiation Detectors (TRD) and the time-of-flight (TOF) system.

The vector meson decays were simulated with the PLUTO generator assuming a thermal source with a temperature of 130 MeV. The ω multiplicity for central $Au + Au$ collisions at 15, 25 and 35 AGeV beam energies is taken from the HSD transport code [1]. The background was calculated with the UrQMD event generator. Both signal and background are transported through the detector setup using the transport code GEANT3 within the cbmroot simulation framework. The L1 tracking procedure [2] has been used for the track finding at STS and muon system, and for momentum reconstruction at STS. The time information from the TOF detector was used for suppression of punch-through protons and kaons. It turns out that the resulting background is dominated by muons from weak decays of charged pions and kaons.

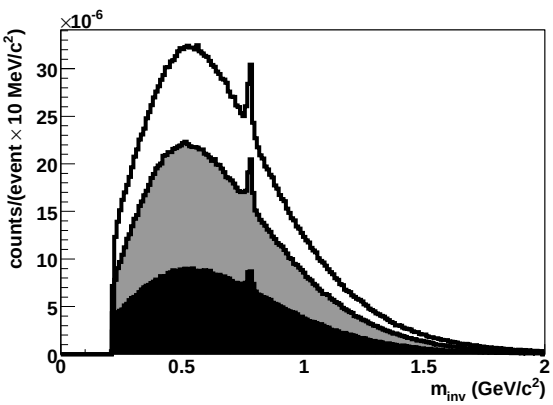

Figure 1: Dimuon invariant mass spectra for different beam energies: black - 15 AGeV, gray - 25 AGeV, and solid line - 35 AGeV. As a signal only the ω meson is included.

* Work supported by EU/FP6 HADRONPHYSICS (see Annex) and by INTAS

beam energy (AGeV)	15	25	35
S/B ratio	0.16	0.14	0.14
efficiency (%)	2.2	3.3	4.4

Table 1: Signal-to-background ratio and efficiency for ω detection in $Au + Au$ collisions at different beam energies.

Figure 1 shows the dimuon invariant mass spectra for central $Au + Au$ collisions at different beam energies. As a signal only the ω meson was included. The signal-to-background ratio (calculated in a $\pm 2\sigma$ window around the signal peak) and the efficiency for ω meson detection is listed in table 1 for different beam energies.

Figure 2 shows the dimuon invariant mass spectrum in the region of the J/ψ peak for semi-peripheral $Au+Au$ collisions at 25 AGeV. In this case the thickness of all hadron absorbers was increased by 15%. The background was suppressed by requiring muon transverse momenta of $p_t \geq 1$ GeV/c, and by kinematical cuts. The resulting signal-to-background ratio is about 100 and the efficiency is 13%.

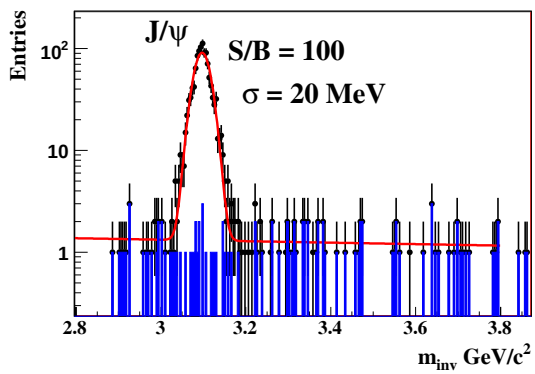

Figure 2: Dimuon invariant mass spectrum in the region of the J/ψ peak for semi-peripheral $Au + Au$ collisions at 25 AGeV after cuts (see text).

The simulation results demonstrate the feasibility of dimuon measurements using hadron absorbers in $Au + Au$ collisions at FAIR beam energies. In order to further suppress the muon background from weak decays we will study a more compact muon detection system. Moreover the hadron absorbers will be optimized separately for low mass vector mesons and charmonium.

References

[1] W. Cassing, et al., Nucl. Phys. A 691 (2001) 74.
[2] S.Gorbunov, et al., CBM-PHYS-note-2005-001.

High efficiency Transition Radiation Detectors for high counting rate environments

M. Petrovici, M. Petriş, I. Berceanu, V. Simion, D. Moisă, A. Radu, D. Bartoş,
V. Cătănescu, A. Herghelegiu, C. Măgureanu, NIPNE-Bucharest
M. Hoppe, A. Wilk, J.P. Wessels, University of Münster
A. Andronic, C. Garabatos, R. Simon, F. Uhlig, GSI-Darmstadt

One of the options currently considered for lepton identification with the CBM experiment [1] for FAIR is a shell of multiple layers of Transition Radiation Detectors (TRD).

Being a heavy-ion fixed target experiment in the energy range of 5-35 A·GeV the goal of CBM is to look for rare probes using the unique performance of FAIR in terms of high intensity heavy ion beams. This requires a high granularity TRD with good performance specifically engineered for a high counting rate environment. In this context, the optimization of the e/π rejection factor relative to the number of layers and electronic read-out channels is a challenging requirement. Various prototypes [2] based on Multiwire Proportional Chambers (MWPC) were designed, built and tested. Up to intensities of 100 kHz/cm^2, no major deterioration of their performance in terms of pulse height and position resolution has been observed.

However, this performance was reached at the expense of a low conversion efficiency for transition radiation in such a single layer MWPC based TRD. In order to circumvent this aspect, we designed and built several variants of a new prototype of TRD based on a double sided pad read-out electrode[3] with gas volumes on either side. Neglecting about 15% absorption in the central electrode, the double sided configuration is equivalent to a detector of 12 mm gas thickness, preserving the time response of the one of half the thickness [4].

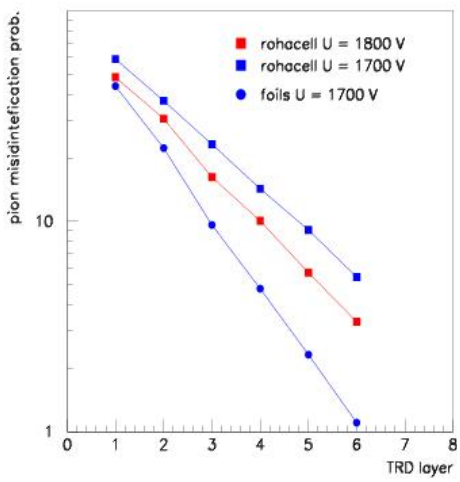

Figure 1: Pion efficiency at 90% electron efficiency at 1.5 GeV/c momentum as a function of number of layers

The prototype was tested in-beam at the SIS. The pion rejection factor was extracted using the likelihood on integrated energy deposit [5]. The pion efficiency at 90% electron efficiency at 1.5 GeV/c momentum as a function of number of layers for a Rohacell radiator is depicted in Fig. 1. The obtained pion efficiency for 6 layers is 3.32% for an anode voltage of 1800 V. For one run we used a polypropylene foil stack (120 foils, 20 μm thickness, 500 μm spacing) as radiator. For an anode voltage of 1700 V the obtained pion efficiency is (1.1%). The pion efficiency using Rohacell radiator at the same anode voltage is 5.43%, i.e. the regular foil radiator improves the pion rejection by almost a factor of five. If this improvement factor is applied to the measurement obtained at 1800 V anode voltage, a final pion efficiency of 0.67% is obtained for a 6 layer stack with a regular foil radiator.

Fig. 2 shows the pulse height distributions of pions and electrons, respectively for 26·10^3, 65·10^3, 110·10^3 and 220·10^3 particles/(s·cm^2) counting rate.

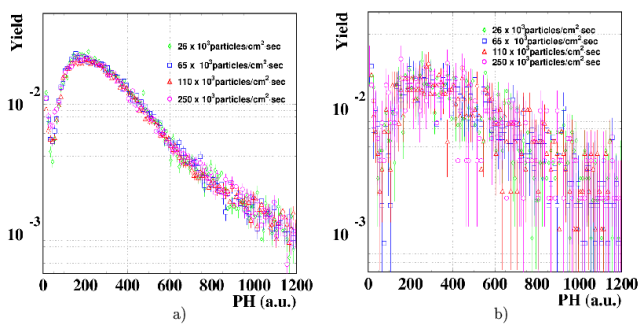

Figure 2: Pulse height distributions for a) protons and pions and b) electrons as a function of rate

Within experimental errors we conclude that these detectors preserve their pion efficiency performance up to counting rates of ∼200·10^3 particles/(s·cm^2).

Given the performance in terms of counting rate and pion efficiency this new principle of TRD commends itself as a viable solution for high counting rate environments. For a given pion efficiency and granularity it provides an optimum material budget at a reduced number of readout channels.

References

[1] CBM - Technical Status Report, 2005

[2] A. Andronic et al, GSI Ann. Rep. 2005-1, INSTMETH-33

[3] M. Petrovici et al. GSI Sci.Rep. 2006-1, p.67

[4] M. Petris et al,CBM Coll. Meet., March 9-12, 2005, GSI

[5] A.Büngener et al., Nucl. Instr. Meth. 214, 1983, p.261

Implementation of a Hough Tracker for CBM*

C. Steinle[1], A. Kugel[1], and R. Männer[1] and the CBM Collaboration
[1]University of Mannheim, Department of Computer Engineering V, 68131 Mannheim, Germany

Abstract: In this report we describe an adaptation of the Hough Transform for the tracking of particles in the CBM STS detector, together with a possible implementation of the algorithm in hardware using FPGAs.

Hough Transform

The Hough transform is a global method for track finding. All STS detector hits have to be transformed into a parameter space according to the components of the track momentum p (θ, $-q/p_{xz}$, m). This leads to our 3D Hough transform [1].

The goal of the implementation is to process the tracking with maximum speed, e.g. to process one detector hit per clock cycle. Therefore the complicated calculations of the Hough transform according to the real detector geometry and the real magnetic field are implemented with look-up tables (LUTs). Since the calculation of the LUTs is done offline, any sufficiently precise algorithm can be used.

Unfortunately a direct implementation of the 3D Hough space requires a huge amount of memory. This can be avoided by the decomposition into several 2D layers, where the number of parallely computed layers can be adjusted to the existing hardware resources (see figure 1).

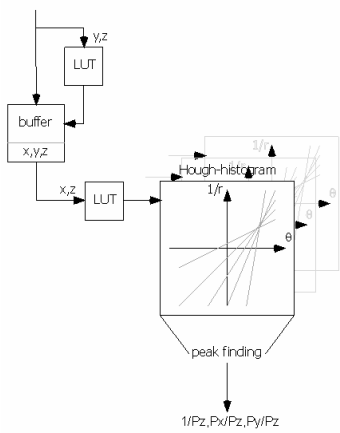

Figure 1: Hough Tracker algorithm structure

Figure 2 shows the realization of the buffer between the LUTs. The main elements are a dual-ported RAM (DP-RAM) and a register for each layer. The task of this unit is to store the information from the first LUT together with the information needed for the second LUT (see figure 1). Further on this data has to be stored in linked lists, while one list is needed for each layer. To this each entry of a list must have the ability to be moved to a list afterwards. Within this context the registers store the DP-RAM address of the actual processed entry of the list, while the DP-RAM stores the information combined with the address of the previous entry (link) of the list. So by processing the Hough entries one has just to modify the registers with addresses and to update the corresponding list addresses in the DP-RAM, if an entry has to be moved to a consecutive list. So the same Hough entry is prevented to occur more than once in the DP-RAM, even if it is used in more than one list and accordingly more than one layer.

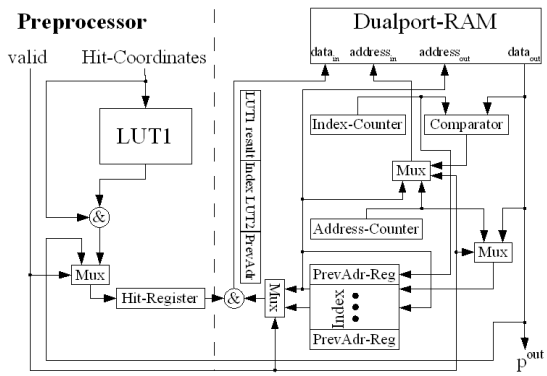

Figure 2: Hardware structure of the buffer

At present the Hough transform is further developed, in particular the adjustment of a good algorithm to produce the LUTs. We started with the formulas:

$$m = 100 \bullet 2 \frac{z \sin\gamma - y \cos\gamma}{\left(y \sin\gamma + z \cos\gamma\right)^2} \tag{1}$$

$$-\frac{q}{p_{xz}} = 10000 \bullet 0.3 \frac{2\left(z \sin\theta - x \cos\theta\right)}{B\left(x \sin\theta + z \cos\theta\right)^2} \tag{2}$$

Important is in Formula 2 the constant B which represents originally a homogenous magnetic field. Within the software framework we use instead of the correct inhomogeneous magnetic field an optimal constant factor for B at each detector plane. Our next step was to use the inhomogeneous field directly in the formula. This can be done by building the average of the integral of the magnetic field from the target to the actual plane. But surprisingly the algorithm's efficiency is decreased. So our next step is to use the 4th order Runge-Kutta method to improve the track model. This should end up in a better efficiency. We are able to use such a method because both sides of our transformation are digital and we are using LUTs.

References

[1] J. Gläss, C. Steinle, R. Männer, "Tracking in the Silicon Tracker System of the CBM Experiment using Hough Transform", 14th IEEE-NPSS REAL TIME Conference, June 2005, Stockholm, http://www.sysf.physto.se/RT2005/

* Work supported by EU/FP6 HADRONPHYSICS

Open charm measurement in the CBM experiment*

I. Vassiliev[1], S. Gorbunov[1,2], I. Kisel[2,3], and the CBM Collaboration

[1]GSI, Darmstadt, Germany; [2]KIP, Ruprecht-Karls University, Heidelberg, Germany; [3]LIT, Joint Institute for Nuclear Research, Dubna, Russia

One of the major experimental challenges of the CBM experiment is to trigger on the displaced vertex of the D-meson hadronic decay in the environment of a heavy-ion collision. This task requires fast and efficient track reconstruction algorithms and high resolution secondary vertex determination. Particular difficulties in recognizing the displaced vertex of the rare D meson decays are caused by weak K^0_S and hyperon decays which produce displaced vertices close to the target (the mean life time of the D^0 mesons is $c\tau = 122.9$ μm), very low multiplicity and branching ratio of the D meson production ($5.8 \cdot 10^{-6}$) for the central Au+Au collision at 25AGeV, and multiple scattering in the beam pipe and detectors.

To study the feasibility of open charm mesons measurement in the CBM experiment 10^4 central Au+Au UrQMD events at 25 AGeV have been simulated. K^- and π^+ pairs from D^0 decays have been added to each event in order to simulate a signal in the environment of background hadrons. A realistic STS geometry with 2 MAPS, one hybrid and 4 double-sided strip detectors has been used. The first MAPS detector have been placed at 10 cm downstream the target in order to reduce radiation damage. The primary vertex was reconstructed with high accuracy (5.7 μm in z direction, 1.0 μm in x and y) from about 450 tracks fitted in the STS with a non-homogeneous magnetic field by the Kalman filter procedure [1]. The resolution in the z distribution of the secondary vertex of 54 μm as achieved by the fitting procedure is sufficient to separate detached secondary vertices from the primary vertex.

Because of originating from a displaced decay vertex, the D^0 meson daughter tracks have a non-vanishing impact parameter at the target plane. Since the majority of the primary tracks have very small impact parameter, a significant part of the combinatorial background can be rejected using a cut on their χ^2 distance to the primary vertex. The combinatorial background is suppressed as well by the z-vertex cut to select detached vertices, the requirement for the D meson momentum to point to the primary vertex, the p_t-cut and the vertex χ^2 cut for good quality secondary vertices. After applying all cuts the background is suppressed by a factor of 10^5 in the signal mass region, and the D^0 reconstruction efficiency is 8.2% . The shape of the background in the signal IM region has been estimated using the event mixing technique. The resulting background plus D^0 signal spectrum is shown in Figure 1. The signal to background ratio is about 0.8 .

A novel algorithm has been developed to reconstruct the D^0's life time and the decay length together with their corresponding errors. The algorithm first finds the primary vertex using all reconstructed tracks, and then the D^0 meson is reconstructed from its two daughter particles K^- and π^+ using the primary vertex as the production point. The accuracy of the life time is 9.8 μm/c, showing that the reconstructed D^0 particles are well separated from the primary vertex. Figure 2 gives the distribution of the reconstructed D^0 life time with the fitted mean value of (122.8 ± 2.0) μm.

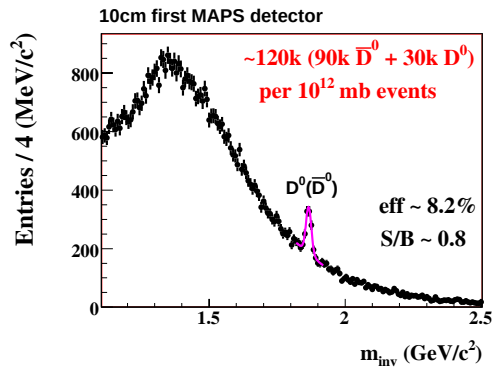

Figure 1: The D^0 and background invariant mass spectrum. The estimated spectrum corresponds to $2.5 \cdot 10^7$ minimum bias events.

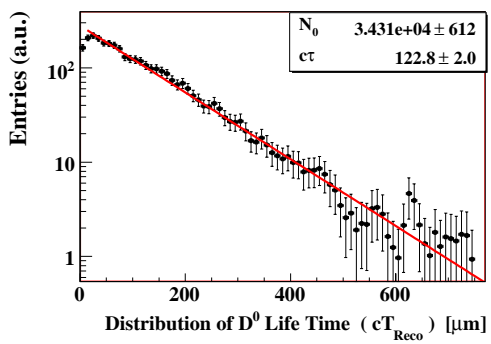

Figure 2: Distribution of the reconstructed D^0 mesons life time.

References

[1] S. Gorbunov, I. Kisel and Iouri Vassiliev, Analysis of D^0 Meson Detection in Au+Au Collisions at 25 AGeV, CBM-PHYS-note-2005-001, June 2005.

* Work supported by EU-FP6 HADRONPHYSICS (see Annex)

Achievements of CMOS Pixels for the CBM Micro-Vertex Detector (MVD)

S.Amar-Youcef[1], A.Besson[2], G.Claus[2], M.Deveaux[1,2,3], A.Dorokhov[2], W.Dulinski[2], S.Heini[2], A.Himmi[2], K.Jaaskelainen[2], Ch.Müntz[1], F.Rami[2], J.Stroth[1], I.Valin[2], and M.Winter[2]

[1]J.W.Goethe Universität, Frankfurt; [2]IPHC and Université L.Pasteur, Strasbourg; [3]GSI, Darmstadt

It was already established that CMOS sensors provide the single point resolution and reduced material budget required for the ambitioned MVD vertexing performances. Achieving these performances in the CBM running conditions is however challenging, especially because of the required radiation tolerance and read-out speed. Important steps addressing these issues were made in 2006. Moreover, a new generation of real size sensors was fabricated, to be used for thinning and system integration studies [1].

Fast read-out architecture

The fast read-out architecture developed for the CBM MVD extrapolates from the MIMOSA-8 prototype, designed for the ILC vertex detector. The sensor includes correlated double sampling micro-circuits and discriminators, and delivers discriminated binary signals [2]. Its single point resolution was evaluated in Summer 2006 at the CERN-SPS. A resolution of $\lesssim 7\ \mu m$ was found, i.e. slightly better than the intrinsic resolution ($\sim 7.2\ \mu m$) reflecting the pixel pitch (25 μm). This result indicates that integrated ADCs may not be mandatory to get a single point resolution as small as $\sim 5\ \mu m$, provided the pixel pitch is kept small enough (typically $\lesssim 18\ \mu m$). This perspective coincides with the need for a small pitch in order to enhance the sensor tolerance to bulk damage, by reducing the distance the signal charges have to cross in order to reach a sensing diode.

MIMOSA-8 was manufactured in TSMC 0.25 technology, which features a $\lesssim 7\ \mu m$ thick epitaxial layer. The chip was translated in 2006 into the AMS 0.35 OPTO technology (MIMOSA-16), where the layer is $\sim 11\ \mu m$ thick. Besides a larger signal amplitude, MIMOSA-16 also includes other improvements: enhanced tolerance to ionising radiation (MIMOSA-15 pixel architecture [2]), as well as pixels incorporating high gain amplification micro-circuits.

Since it is not yet clear whether integrating an ADC at the end of each column may be avoided, various ADC architectures are being developed, in synergy with the ILC requirements. The first ADC prototypes (5-bit Wilkinson and 4-bit successive-approximation) designed at IPHC were submitted to fabrication in Autumn 2006. Prominent design challenges include compactness, aspect ratio, signal processing speed and power dissipation.

Radiation tolerance

Radiation tolerance studies started with MIMOSA-15 in 2005 [2] were complemented in 2006 with ~ 5 GeV/c e^- beam tests at DESY.

A sensor exposed to an integrated dose of ~ 1 MRad (obtained with a 10 keV X-Ray source) was observed to still exhibit a S/N ratio of 19 (it was 27 before irradiation), and a detection efficiency of ~ 99.9 % at a coolant temperature of -20°C (180 μs integration time). These performances validate the pixel architecture implemented against parasitic leakage current generated by ionising radiation.

MIMOSA-15 chips irradiated with 1 MeV neutrons were studied on the same beam. A sensor exposed to $\sim 2{\cdot}10^{12} n_{eq}/cm^2$ still exhibited a detection efficiency above 99 % at a coolant temperature of -20°C. For a fluence of $\sim 6{\cdot}10^{12} n_{eq}/cm^2$, the detection efficiency dropped to ~ 80 %. Given the available room from improvement, these results indicate that fluences $\gtrsim 10^{13} n_{eq}/cm^2$ per MVD layer are likely to be tolerable.

Improvements include pixel design optimisation and fabrication process choices which reduce the diffusion path of the signal electrons before reaching a sensing diode. Efforts were made in 2006 towards this goal, on the one hand by designing pixels featuring L-shaped sensing diodes and on the other hand by fabricating a sensor in a BiCMOS process featuring an epitaxial layer with a relatively high resistivity expected to allow for substantial depletion.

New generation of real size sensors

The most attractive fabrication technology characterised so far is the AMS-0.35 OPTO process. Excellent tracking performances were obtained with 5 consecutive small prototypes fabricated in this technology since late 2003, which was chosen for the sensors currently developed for short term tracking applications (STAR HFT, EUDET beam telescope). The latter triggered an engineering run in 2006, which was used to produce simultaneously a real size, multi-purpose sensor, intended to equip a first generation MVD demonstrator. The sensor, which features 256x256 pixels of 30 μm pitch, is read out in $\lesssim 1$ ms. It was fabricated in 2 different versions, one where the epitaxial layer is $\sim 11\ \mu m$ thick (default value) and one where it is expected to be $\gtrsim 16\ \mu m$ (new commercial option). The engineering run was also motivated by the possibility to study the fabrication yield and to have a stock of real size sensors available for thinning and system integration studies.

References

[1] M.Winter, "Status of CMOS sensor R&D", talk presented at the CBM collaboration meeting, Sept. 2005, GSI/Darmstadt;

[2] 2005 GSI Annual Report and references therein.

Development of Microstrip Sensors for the CBM Silicon Tracking System*

J. M. Heuser, Chr. J. Schmidt, GSI, Darmstadt, Germany, and the CBM Collaboration

We have designed the first prototype of a silicon micro-strip sensor that can serve as a building block of detector modules for CBM's Silicon Tracking System.

Tracking Stations

The tracking stations are planar arrangements of micro-strip sensors, grouped into several modules of either the same or different length, that cover at given positions downstream of the target the fiducial area approximately between 2.5 and 25 degrees polar angle. Figure 1 visualizes this station concept with a vertical orientation of the modules and the long direction of the strips perpendicular to the bending plane of the magnet for best momentum measurement. The first and smallest station may be as close as 30 cm to the target. The last and largest station will be in about one meter distance from the target. One of the key requirements of the Silicon Tracking System is a low-mass design to achieve momentum measurement with about 1% resolution. Silicon micro-strip detectors are compatible with a low-mass design as the sensors themselves are thin. With an appropriate module structure, active readout electronics with its cooling requirements and material involved may be avoided in the aperture. The strongly inhomogeneous track density profile makes a sectorized module structure necessary. Close to the beam line, a module must comprise sensors with short strips. Longer strips, realized either on single wafers or by chaining two or more sensors, can be employed in the regions further outside. Those different "sectors" must be read out individually. This may be realized by routing the strips' analog signals from every sector through thin flat multi-line cables to front-end electronics at the periphery of the stations.

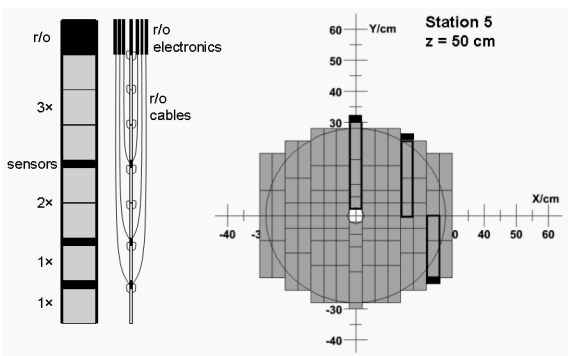

Figure 1: Silicon micro-strip sensors arranged into modules of different lengths building up a tracking station.

* Supported by EU/FP6 HADRONPHYSICS (see Annex) and INTAS

Sensor Design

We focused on a sensor compatible with this detector module structure. The design, shown in Fig. 2, addresses in particular connectivity issues. We intend to employ double-sided sensors with one strip orientation along the module's long axis, and a "stereo" direction on the second side. We strived to accomplish that both sensor sides can be contacted both at the top and the bottom edge. On the stereo side, this requires interconnections on a second metal layer between the strips of the two corner regions. This layout will enable us to chain several sensors, thus forming long strip sectors for the outer regions of the tracking stations. A staggered arrangement of the contact pads was applied allowing a wire-bonding scheme that conserves the correlation of neighbouring channels through the chain up to the readout electronics. Small stereo angles are preferred as unavoidable dead area on the sensor sides is kept small.

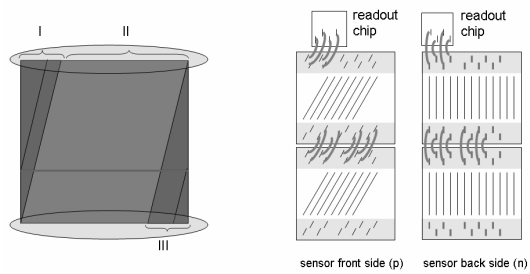

Figure 2: (Left) Schematics of the sensor's stereo side. (Right) Chained sensors and their interconnections.

Detector R&D

The first sensors, to be produced in 2007 [1], will have a thickness of 200–300 μm, are double-sided with 2×1024 AC-coupled strips of 50 μm pitch and feature a 15° stereo angle between front and back side. They will be utilized for the construction of a prototype detector module: an assembly of chained sensors, readout electronics [2] and mechanical support. Forthcoming prototypes will address radiation hardness, the minimization of inactive area near the edges, and will touch e. g. the biasing technique and the layout of the guard rings structure. The development of readout cables, made from fine-pitch aluminum traces on polyimide material for minimum material budget, is a particular important task. The capacitance of sensor and cable at the input of the front-end electronics must be small enough to achieve a sufficiently large signal-to-noise ratio.

References

[1] CiS Institut für Mikrosensorik gGmbH, Erfurt, Germany

[2] Chr. J. Schmidt et al., this report

Feasibility of hyperon detection in the CBM experiment*

E. Kryshen[1], V. Friese[2], and the CBM collaboration
[1]SPbSPU, St. Petersburg, Russia; [2]GSI, Darmstadt, Germany

The measurement of hyperons will enable the CBM experiment to characterise the strangeness content of the fireball created in high-energy nucleus-nucleus reactions, one of the key observables to access the collision dynamics. CBM aims at multi-differential measurements (spectra, flow) as function of collision energy and system size, which is a challenging task in particular for the rare Ω close to its elementary production threshold.

Hyperon detection is performed in the tracking system of CBM (STS, see J. Heuser et al., this report) exploiting the topology of weak decays into charged hadrons. The feasibility studies are based on transport through the field and detector geometry, simulation of the anticipated detector response and reconstruction of tracks and secondary vertices in the STS (see I. Kisel et al., this report), all inside the software framework CBMROOT (see M. Al-Turany et al., this report).

Details about simulation and analysis can be found in [1]. The hyperon detection feasibility was studied for central Au+Au collisions at 25 AGeV using an improved STS layout and digitisation scheme (2 hybrid pixel stations and 6 double-sided strip stations with 50 μ m strip pitch and 5° stereo angle) and an advanced secondary track finding algorithm. In addition, the topological analysis was refined with respect to that presented in [1]. The main cut parameters to suppress the combinatorial background of uncorrelated pions and kaons are the track impact parameter in the target plane, the distance of closest approach of the track pair, the impact parameter of the reconstructed mother track, and the position of the fitted decay vertex along the beam axis.

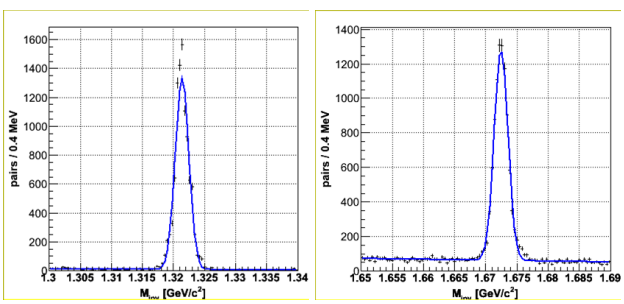

Figure 1: Invariant mass signals for (left) $\Xi^- \to \Lambda\pi^-$ and (right) $\Omega^- \to \Lambda K^-$ for central Au+Au collisions at 25 AGeV after acceptance and topological cuts

The invaraint-mass signals for Ξ^- and Ω^- obtained after all topological cuts are shown in figure 1. The hyperons can be reconstructed almost background-free due to the excellent performance of the tracking system. Table 1 shows the obtained geometrical acceptance, reconstruction efficiencies and signal-to-background ratio for Λ, Ξ^- and Ω^- after track reconstruction and all topological cuts.

	Acceptance	Efficiency	S/B
Λ	0.171	0.56	110
Ξ^-	0.065	0.26	39
Ω^-	0.075	0.36	86

Table 1: Geometrical acceptance, reconstruction efficiency and signal-to-background ratio for hyperons in central Au+Au collision at 25 AGeV

Lately, it has been proposed that the CBM experiment could in addition be operated at SIS-100 for beam energies between 2 and 10 AGeV. Thus, the study has been extended towards smaller collision energies. Here, the measurement becomes tedious because of the extremely low hyperon production rates, e. g. about 10^{-3} for Ω^- in central Au+Au at 6 AGeV. The ΛK^- invariant mass distribution after all cuts for this collision system is shown in fig. 2 (left). It is clearly dominated by the background. However, assuming perfect PID of the secondaries, a significant signal can be obtained (fig. 2, right). Thus, a measurement of the Ω at this sub-threshold energy is still possible provided the charged daughter particles can be identified by means of the CBM-TOF detector (see D. González-Diaz et al., this report).

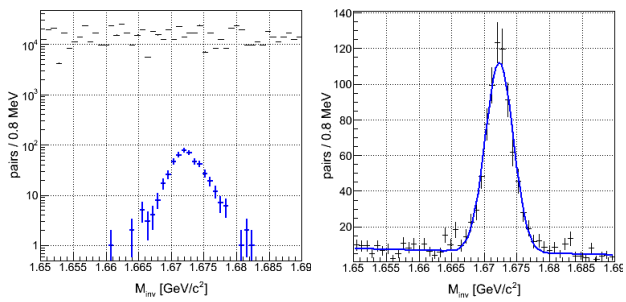

Figure 2: Invariant mass signals $\Omega^- \to \Lambda K^-$ for central Au+Au collisions at 6 AGeV after acceptance and topological cuts. The left panel shows the distribution without PID, the right panel with perfect identification of the secondaries.

References

[1] E. Kryshen and Y. Berdnikov, CBM-PHYS-note-2005-002, http://www.gsi.de/documents/DOC-2005-Aug-35.html

* Work supported by EU-FP6 HADRONPHYSICS

Detection of Fast Neutrons for R^{3}B at FAIR*

D. Rossi[1], K. Mahata[2], K. Boretzky[2], U. Datta Pramanik[3], K. D. Hildenbrand[2], N. Kalantar-Nayestanaki[4], M. Kis[2], L. Popescu[4], C. Rigollet du Toit[4], A. Schüttauf[2], H. Simon[2], M. Vencelj[4], and H. Wörtche[4] for the R^{3}B Collaboration

[1]Institut für Kernchemie, Universität Mainz, D-55128 Mainz; [2]GSI, D-64291 Darmstadt; [3]SINP, I-700067 Kolkata; [4]KVI, University of Groningen, NL-9747 AA Groningen

The R^{3}B project at the FAIR facility at GSI aims for investigations of unstable nuclei by means of reactions with high-energy radioactive beams in inverse kinematics [1]. The physics program of this project includes studies of reactions involving the emission of neutrons with projectile-like velocities. In order to perform kinematically complete measurements, a high energy neutron detector is required. For this purpose, the high resolution neutron time-of-flight spectrometer NeuLAND is being developed.

The desired neutron momentum resolution of NeuLAND is $\Delta p/p = 10^{-3}$, which is similar to that for the measurement of charged particles. Since the neutron flight path will range from 10 to 35 m, this momentum resolution can be reached at a time-of-flight resolution of $\sigma_t < 100$ ps and a position resolution of $\sigma_{x,y,z} \simeq 1$ cm. For measurements involving the maximum flight length of 35 m, an invariant-mass resolution of about $\Delta E = 30$ keV at 1 MeV above the neutron threshold can be achieved for medium-mass nuclei at beam energies of about 500 MeV per nucleon. The design parameters also ask for a neutron detection efficiency of more than 90%.

The existing neutron detector LAND [2] uses organic scintillator as detection medium and iron as passive converter. With this configuration, a time resolution of about $\sigma_t \leq 250$ ps and a position resolution of $\sigma_{x,y,z} \simeq 3$ cm is observed. For NeuLAND, the feasibility of using multigap Resistive Plate Chambers (RPC) is being investigated, since they offer time resolutions down to 50 ps for minimum ionizing particles. Neutrons that interact with the iron converter will produce hadronic showers, dominated by protons at various energies. Since up to now, the response of RPCs to non-minimum ionizing particles is not well known, a test experiment with proton beams has been carried out at KVI in Groningen (Netherlands).

Two different RPC types have been investigated during this experiment with proton beams at 190 MeV, 120 MeV, and at several energies between 80 and 30 MeV. The first RPC, built by the FOPI collaboration [3], was a 90 × 4.6 cm^2, 2 × 4 gap RPC (220 μm gaps), with a 16-strip anode. The second RPC was a shielded 2 × 2 gap RPC [4], a technology also foreseen for the HADES RPC TOF wall, provided by LIP-Coimbra and composed of five 60 × 2 cm^2 structureless electrodes that define 300 μm gaps. The standard RPC gas mixture was used for both RPCs with a total gas flow of approximately 3.6 l/h. Typical high voltage values were -9.5 kV for the FOPI RPC and +6.25 kV for the LIP-Coimbra RPC. A 5 mm round collimator was placed in front of the setup, and the beam rate was kept at 100-200 counts per second. Futhermore, two plastic-scintillator counters were used for the trigger logic and time reference.

Figure 1 shows the time spectrum of strip 4 of the FOPI RPC for 120 MeV protons and an operating voltage of -9.5 kV. A time resolution of $\sigma_t \simeq 45$ ps was observed. The time resolution stays at reasonable values ($\sigma_t \simeq 60$ ps) down to the lowest possible energy for the given setup ($E_{prot} \simeq 30$ MeV). In case of the FOPI RPC efficiency, we could determine a lower limit of 90% for all proton energies used.

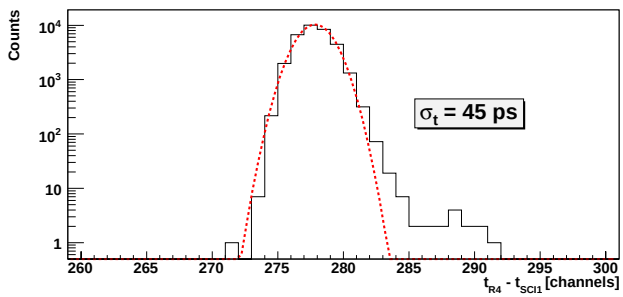

Figure 1: Time resolution of a FOPI RPC strip with 120 MeV protons. TDC conversion factor $\simeq$ 40 ps/channel.

Although the electronic readout was optimized for the FOPI RPC, the measurement with the LIP-Coimbra RPC yielded time resolutions of $\sigma_t \simeq$ 80-100 ps and efficiencies of nearly 100%.

These results demonstrate the feasibility of the neutron detection concept using converter plus RPCs for charged-particle detection. A dedicated prototype adapted to the NeuLAND concept and geometry will be developed and tested in the near future.

References

[1] R^{3}B technical proposal; http://www-land.gsi.de/r3b

[2] Th. Blaich *et al.*, NIM A314 (1992) 136-154

[3] A. Schuettauf, NIM A533 (2004) 65-68

[4] H. Alvarez-Pol *et al.*, NIM A533 (2004) 79-85

* Work supported by BMBF (contract no. 06MZ222I) and EU, EURONS (contract no. 506065).

First tests of RPC prototypes for the ToF wall of the R^{3}B experiment

E. Casarejos* , H. Alvarez, J. Benlliure, I. Duran, N. Montes, A. Morales, and D. Perez
University of Santiago de Compostela, Spain

The R^{3}B experimental program related to the investigation of reaction mechanisms with heavy beams (fission, fragmentation or multi-fragmentation) requires a high-resolution time-of-flight detector (ToF-wall) for residual nuclei identification. The main requirements of this detector are to cover the full acceptance of all charged particles and ions produced in relativistic heavy-ion collisions (50 mrad), a good granularity and an excellent time-of-flight resolution to fully identify nuclei around mass 200. For a 15 m flight path the detector should cover a surface close to 2 m^2 with individual detection cells of few cm^2. The flight path, together with the bending power of the R3B magnet and the position resolution of the tracking detectors (200 μm) impose a time resolution for the ToF measurement around 50 ps (σ).

The technical solution adopted for the construction of this ToF-wall is based on the use of resistive-plate chambers (RPCs). These gas detectors have been proved to provide excellent time resolution and good efficiency with minimum ionising particles [1]. However, they have never been used with heavy ions, requiring thus an important R&D effort.

At the University of Santiago de Compostela we initiated a year ago a program for construction and test of RPC prototypes with ion beams. Several designs and construction materials are being employed to produce different prototypes. In particular, we have constructed and tested prototypes built with four layers of 1 mm thickness soda-lime float glass with a surface of 60$\times$5 cm^2 defining two gaps of 300 μm. The signal is picked up from a common inner copper electrode with a thickness of 2.5 cm while the outer layers are grounded. This structure is surrounded by fibreglass (G10) acting as mechanical support [2]. Moreover, an active impedance adaptor placed close to the RPC electrode pickup is used to improve the quality of the signals.

These prototypes were tested with cosmic rays and a ^{12}C beam at 400 A MeV at GSI. Two plastic scintillators placed in front and behind the RPCs provided the trigger for timing and efficiency determination. The signals were recorded with a 4 GHz Tektronix oscilloscope (TDS 7404) set at 10 Gs/s.

The signals recorded during the irradiation of the RPC prototype with a ^{12}C beam at 400 A MeV, an intensity of with few 10^2 ^{12}C/s and a beam spot of about 25$\times$25 mm^2 at the RPC position, show a typical amplitude of 10 mV with a noise level around 0.5 mV (RMS) allowing to define a clear threshold discrimination. The efficiency of the measurement was determined selecting events with good correlation between the charge integral and the amplitude of the signals as shown in Fig. 1. This criterion allowed us to determine a detection efficiency higher than 80% for operation voltages between 4.4 and 5.0 kV. Considering the uncertainties due to the geometrical overlap between the scintillators and the RPC electrode, and the profile of the beam we can conclude that the two-gaps RPC presents an excellent detection efficiency for highly ionising particles such as ^{12}C.

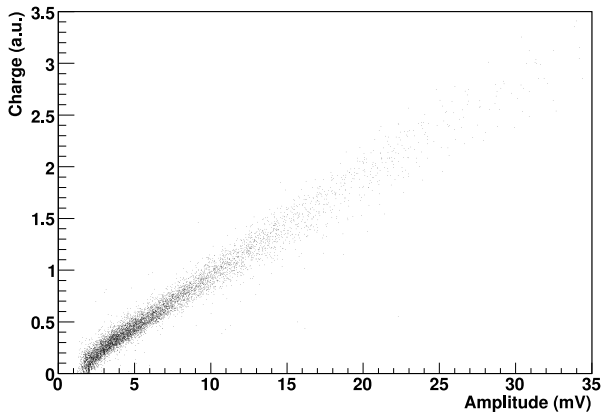

Figure 1: Scatter plot of the correlation between the charge integral and the amplitude of the signals produced by the RPC prototype described in the text, during the irradiation with a ^{12}C beam at 400 A MeV.

The present measurements yield a time resolution around 250 ps for the combined RPC+trigger system. This value is largely affected by the fact that the discrimination electronics for the scintillator signals and the recording oscilloscope were placed outside the experimental cave, 20 meters away from the detectors. Therefore, this results will be easily improved in future measurements with a better definition of the trigger timing.

In the next future we foreseen to continue our R&D program developing multi-strip RPC layers coupled to the TAQUILA[3] readout cards developed by the DVEE department at GSI for the FOPI experiment.

References

[1] RPC2005 workshop, Nucl. Phys. B 158 (2006)

[2] H. Alvarez-Pol et al. Nucl. Phys. B 158 (2006) 186

[3] A. Schuttauf, Nucl. Instr. and Meth. A 533 (2004) 65

* casarejo@usc.es

Fragment tracking with Si microstrip detectors*

M. Stanoiu[1,2,#], O.A. Kiselev[1,3], E. Cortina Gil[4], J. Hoffmann[1], N. Kurz[1], W. Ott[1], A. Chatillon[1], M.Heil[1], and K. Sümmerer[1] for the R3B Collaboration

[1]GSI, Darmstadt, Germany; [2]IFIN-HH, Bucharest, Romania; [3]Inst. f. Kernchemie, Univ. Mainz; [4]CIEMAT, Madrid, Spain

The performance of a new set-up of double-sided silicon micro-strip detectors (DSSD) developed for the R3B project [1] has been investigated in a production run aimed at measuring two-proton fragmentation of ^{20}Mg and ^{17}Ne [2].

To record simultaneously protons and the residual nuclei in micro-strip detectors requires both low-noise and wide-range integrated-circuit amplifiers. The present front-end electronics [3] uses VA64_hdr9 chips from IDEAS, Norway. The serialized differential linear output signals are fed into newly developed NIM modules (SIDEREM [4]) that digitize the signals, perform pedestal and common-noise subtraction and send the data via the serial data bus (GTB) to a universal VME interface module (SAM5) for integration into the standard GSI data-acquisition system, MBS.

Our experimental results show that both protons and heavy ions can be identified with good signal-to-noise ratio and high resolution. In Fig. 1 we show the energy-deposition spectra of ions ranging from protons to Mg corrected for variations in the gain of the individual channels and in the charge-collection efficiency dependent on the inter-strip hit position. The correction is different for the junction (S) side and the ohmic (K) side.

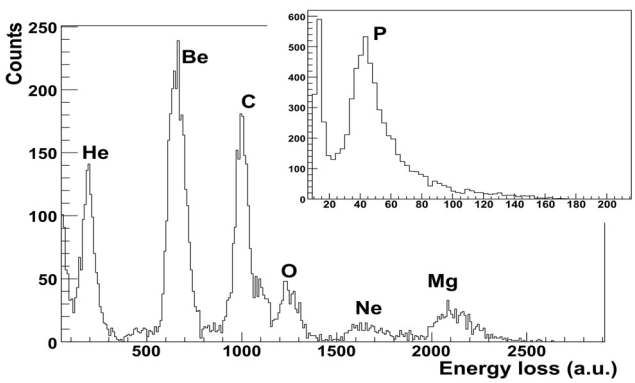

Figure 1: DSSD energy-loss spectrum, S-side. In the insert we show the proton spectrum detected in coincidence with ^{17}Ne fragments obtained from ^{20}Mg break-up.

Due to capacitive coupling between neighbouring strips the width of a hit cluster (defined as the number of adjacent strips showing a charge collection above 2σ of the noise level) depends on the total energy deposited in a cluster, i.e., on the atomic number *Z* of the ion. In Fig. 2 we plot the observed cluster widths as a function of *Z*. It is obvious that protons (which mostly fire a single strip) can be detected together with heavy ions only if they are well separated from the heavy-ion-peak centroid. The energy window for which the detectors show linear energy response is from minimum ionising particles up to 16 MeV for the K-side and 23 MeV for the S-side.

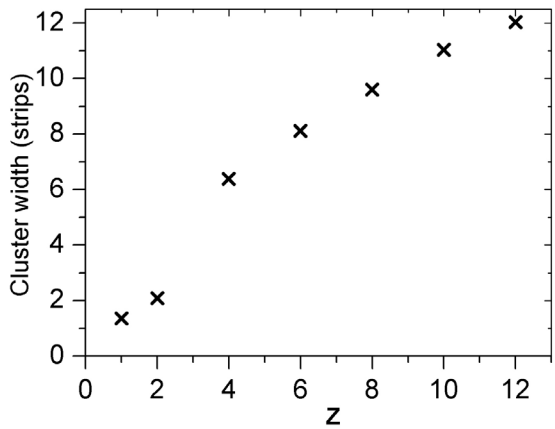

Figure 2: Cluster width as a function of Z.

The DSSD setup will be used in 2007 in astrophysical experiments (Coulomb breakup on Pb targets as time-reversed p-capture) and for quasi-free-scattering experiments on CH_2 targets. In the latter case, four detectors form a box around the beam axis covering an angular range of 15 to 75 degrees to detect protons from both target and projectile in (p,2p) reactions. This detection system serves as a prototype for the R3B recoil detector, which will be composed of a two-layer Si-strip tracker enabling the use of extended, thick liquid-H targets for quasi-free-scattering experiments with low-intensity radioactive beams.

References

[1] O.A. Kiselev *et al.*, GSI Scientific Report 2005, FAIR-NUSTAR-R3B-01.
[2] I. Mukha *et al.*, contribution to this report.
[3] http://dpnc.unige.ch/ams/GSItracker/www.
[4] J.Hoffmann *et al.*, contribution to this report.

* Work supported by EU, EURONS contract No. 506065.
# m.stanoiu@gsi.de

CALIF a Calorimeter for in-flight detection of γ-rays and light charged particles for the R^{3}B@FAIR experiment

D. Cortina-Gil, H. Alvarez-Pol, T. Aumann, J. Benlliure, E. Casarejos, I, Durán, S. España, J. Gerl, M. Gascón, O. Kiselev, I. Kojouharov, R. Lemmon, A. Maira-Vidal, N. Montes, S. Tashenov, O. Tengblad, M. Turrión, J.M. Udias and R. Wolski for the R^{3}B collaboration

A calorimeter for in-flight detection of γ-rays and light charged particles is one of the main detection systems of the R^{3}B experiment at FAIR. This detector will be used in most of the physical cases presented in the R^{3}B Technical proposal [1], though the requirements differ significantly from one case to the other. In some cases it is the γ-ray sum energy that is required ($\sigma(E_{sum})/\langle E_{sum}\rangle < 10\%$), while in others the detector has to be able to provide γ-ray multiplicities ($\sigma(N_\gamma)/\langle N_\gamma\rangle < 10\%$) and individual γ-ray energies (2-3 % ΔE/E) for spectroscopic purposes. As a key requirement the detector has also to act as the calorimeter for the target Silicon recoil detector described in [1, 2]. Hence, the detector has to stop and measure the total energy of high-energy light charged particles, i.e. protons up to 300 MeV, with good energy resolution (2-3 % ΔE/E).

The main properties of this device, high total absorption efficiency ($\geq 80\%$ for γ's at 15 MeV in the laboratory frame) and good angular resolution(≈ 1 deg for $\Theta \approx 35$ deg), are imposed by the very particular kinematics of energetic γ-rays (up to 30 MeV in the CM system) emitted by sources moving with relativistic velocities and by the typically low intensities of the secondary beams involved. In order to ensure these nominal values in all the angular domain, the polar angular segmentation and the thickness of the scintillation material will be optimise for separate angular regions. All these considerations determine the choice of the device geometry.

Several options are under study to guarantee the polar segmentation. In a first design, we propose a detector divided into small frustum-like crystals. The dimensions and type of scintillator used would depend on the γ-ray emission angle (finger-like solution). Each crystal will be coupled to an individual readout device, being the final angular resolution determined by the crystal entrance area. Another posible solution is based on larger area crystals coupled to several readout devices and where the final angular resolution will be deduced from the combined information from the different sensors. Finally, a third solution would consider two detection stages, the first one made of thin detectors with very high granularity, providing the angular resolution, and the second one with larger area and thick crystals ensuring the total absorption function.

Extensive simulations using the GEANT4 package and based on the first geometrical approach have been performed. In the present design (Figure 1), around 5000 crystals will surround the reaction target with a total length of 130 cm, 35 cm of internal radius and external variable radius ranging between 46-77 cm. We distinguish a central part or BARREL, with cylindrical shape, covering polar angles between 40 and 130 degrees, and an ENDCAP, with semi-spherical shape, for polar angles between 7 and 40 degrees. The crystals have the form of pyramidal frustum with rectangular base, with the axis orientated approximately towards a fixed point (the target, in coincidence with the center of coordinates of the system from which the polar angles are measured). The amount, size and form of the crystals are fixed to ensure the angular segmentation needed and to get a complete circle (ring). There are 5 different types of crystals in the BARREL and up to 24 in the zone of the ENDCAP, where at low polar angles, it is complicated to close a volume without gaps.

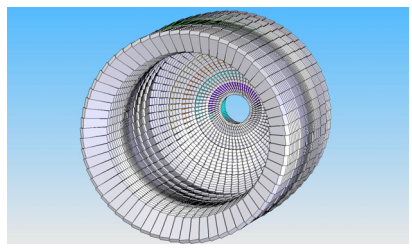

Figure 1: Graphical representation of a preliminary geometrical design of the R^{3}B calorimeter.

The selection of the appropriate scintillation material and readout device is another critical parameter that would determined the nominal energy resolution of the detector. Presently, several inorganic scintillators are under study, namely $LaCl_3$(Ce), $LaBr_3$(Ce), CsI(pure) and CsI(Tl). The first three materials have a rather good intrinsic resolution (in the order of 3% for 662 keV γ's) what coupled with an appropiated readout device will match the detector requirements. However, they present some disadventages: the first two are at present rather expensive and highly hygroscopic and the third one needs to be cooled down to LN2 temperatures to achieve this value. Those factors justify the study of CsI(Tl) crystals coupled to adecuate sensors (APD or PM) that with a moderate energy resolution (lower than 5% for 662 keV γ's) could be a plausible solution, at least for backward angles (BARREL).

This work is partially supported through EURONS (EU contract No 506065) and the Spanish Research and Science Ministry (FPA2005-00732 and FPA2005-02379).

References

[1] http://www-land-gsi.de/r3b/docu/R3B-TP-Dec05.pdf.

[2] http://www.gsi.de/informationen/wti/library/scientificreport2005/FAIR-NUSTAR-R3B-01.pdf

Detector systems for the ELISe interaction zone*

V. Nedorezov[1], Yu. Grishkin[1], N.Rudnev[1], A.Turinge[1], A.Mushkarenkov[1], V.Lisin[1], A.Polonski[1], and H. Simon[2,#], for the ELISe collaboration
[1]INR-RAS, PNLAB, Moscow, Russia,[2]GSI, Darmstadt, Germany

The achievable resolution for the ELISe spectrometer system [1] is governed by the properties, i.e. resolution and induced straggling, of its constituting tracking detectors. The requirements of operating the detectors within the proposed setup pose serious demands on the reliability and ability to be mounted in a self-supported way in vicinity to the NESR/EAR interaction zone. The material budget in the path of the electrons emerging from the interaction zone is of major concern. Straw tubes seem to fulfil most of these requirements. A prototype assembly has been put into operation in the GSI detector laboratory. A second straw tube array has been built and will be used together with the existing one in a test experiment at the S-DALINAC electron accelerator in Darmstadt. The experiment is going to be carried out there in within the first half of 2007 in collaboration with the Institute of Nuclear Physics.

In addition to an earlier described method to measure the performance of the detectors [2] we propose a second independent one that will help to improve the accuracy of the position determination. The procedure is based on using 2 sets of the straw tubes (see Fig.1). For the simulation calculation, the energy and diameter of the electron beam were chosen to be 70 MeV, and 1 mm, respectively. The thickness of the target and the thickness of the aluminum foil are assumed to be 0.5 mm, and 0.1 mm. The distance between the first detector and output window was set to be 1 cm, the diameter of each straw tube is 8 mm, the thickness of the mylar shell 0.11 mm. A mixture of argon (80%) and CO_2 (20%) with atmospheric pressure inside the detectors was assumed. A 20cm thick layer of air between output window and second detector group is taken into account.

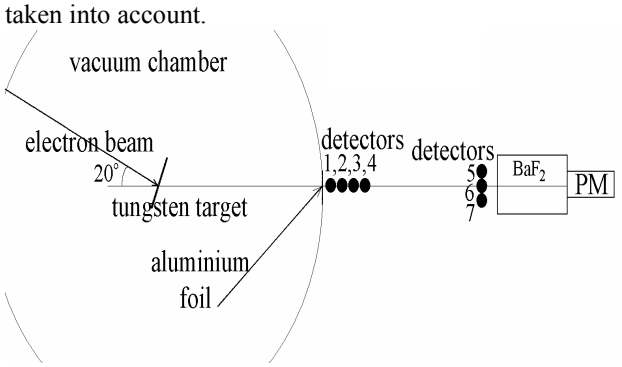

Figure 1: Test set-up for straw tube performance tests.

To exclude low energy background contributions, a BaF_2 scintillator detector will be used. Its size is 10 x 5 x 4 cm^3; diameter of the photocathode of PM is 16 mm. The distance between the center of the BaF_2 detector and the axis of the drift detector 6 is 10 cm.

* Work supported by EU, INTAS contract No. 03-54-6545
#h.simon@gsi.de

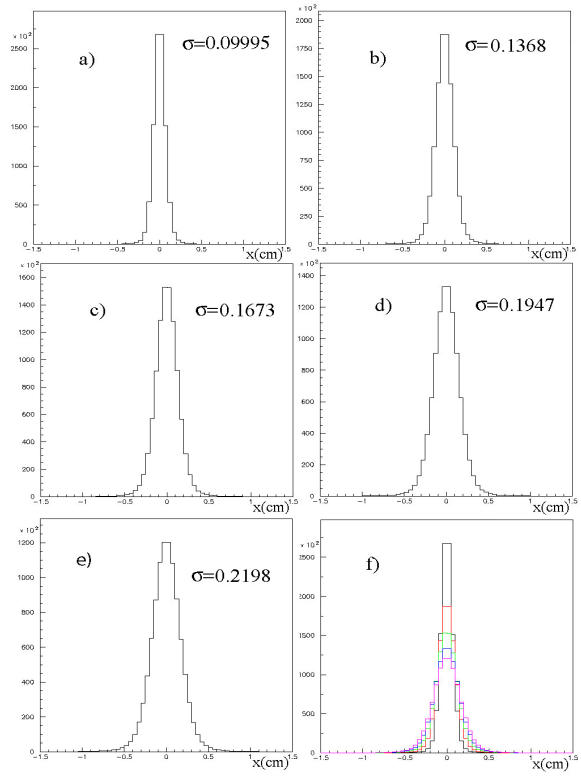

Figure 2: Simulated coordinate distributions in the second detector group depending on the number of detectors 0-4 corresponding to the labels a)-e) respectively. A summary plot is shown in panel f).

GEANT simulations have been performed for the whole setup. As a result a suppression of the low energy tail to one percent and an estimate for the multiple scattering contribution per detector (see Fig. 2) of about 4,7 mrad at 70MeV electron energy is found. Scaled to the electron energy of the collider, this value will be sufficiently small.

The experimental verification of these results will allow to confidently use simulation calculations in order to optimize the number of straw tube layers, i.e. the achievable detection efficiency, with respect to the possible resolution of the electron spectrometer.

References

[1] Technical Proposal for the Design, Construction, Commissioning, and Operation of the ELISe setup: http://www.gsi.de/documents/DOC-2006-Mar-118-1.pdf

[2] A.D. Belayev, V.M. Ionov, V.G. Nedorezov, N.V. Rudnev. Coordinate calibration method for high energy electrons. Proc. XI. Int. Sem. EMIN2006, INR Moscow(2006).

Thick Si(Li) coaxial detectors for registration of intermediate energy heavy ions*

A.G. Artyukh[1], Yu.G. Teterev[1], Yu.M. Sereda[1],L.A. Popeko[2], I.M. Kotina[2], G.A. Shishkin[2], and H. Simon[3,#], for the ELISe collaboration

[1]JINR, Dubna, Russia; [2]PNPI, Gatchina, Russia;[3]GSI, Darmstadt, Germany

The detection and identification of ions in the ring-arc sections of the NESR being used as spectrometers is one of the common instrumentation issues for the FAIR in-ring experiments (AIC, EXL, ELISe, SPARC).

The characterization of long-range particles which are produced in nuclear collisions at intermediate and high energies is here at interest. The range of these particles is in the order of several tens of cm (for example in Si solids). At present, in order to register long-range fragments mainly CsI detector walls are used, which provide an energy resolution order 1%. However, it is problematic to operate CsI detectors in vacuum (especially in ultra-high vacuum).

The objectives of this paper is to show the results of a carried out evaluation of available detector systems and techniques which could be used for detecting high-ionizing particles in a wide energy region (i.e. from several MeV/u up to several 100 MeV/u) with a high energy resolution (order 10^{-3}), in order to be able to distinguish projectile-like fragments from the non-reacting ion beam, that are expected to fall very close in their magnetic rigidity. We also aim for a 100% detector efficiency and reliable (Z,A) identification power.

For this a Si detector type was chosen as being widely available and satisfying indicated above requirements. An advantage of thick silicon detectors in comparison with HPGe is the low atomic number which is responsible for a suppression of the gamma ray background through Compton scattering. We used sufficiently low cost industrially produced high resistively silicon (1000–2500 Ω cm). A coaxial lithium drift technology was applied. In contrast to planar technology it uses a radial electric field to drift Li from the detector surface onto the center following the applied electric field gradient.

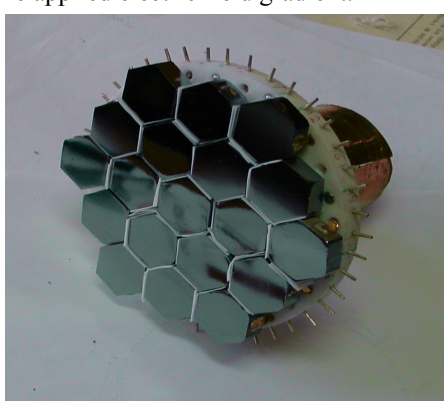

Figure 1: View of a wall of 22 hexagonal Si detectors.

* Work supported by BMBF and EU, INTAS contract No. 03-54-6545.

#h.simon@gsi.de

The detectors (Fig. 1.) under investigation [1-3] have the following dimensions: 28–30mm in diameter, 9 mm of length (100 mm was also made), the drift thickness is 12 mm; the sensitive volume is up to 90%. Insensitive parts of the detector are: a diffusion lithium layer 0.3mm thick situated on the crystal surface, and the central core. The lithium layer and the p-type core form n^- and p^+ of a diode, respectively. The main steps of the production process are: lapping, etching and washing of the crystal; applying the lithium on a side surface of the crystal and lithium diffusion; lithium drift in radial electric field at a temperature of 140^0C for 250h for a thickness of 12 mm; clean etching and test measurements.

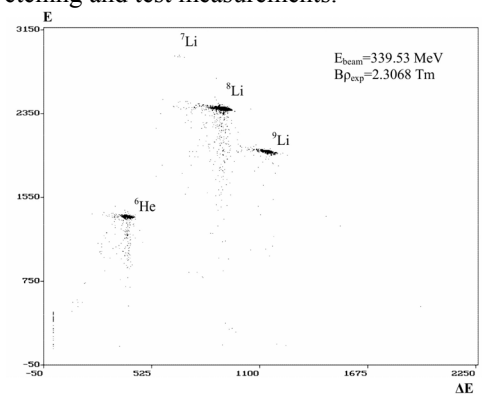

Figure 2: ΔE,E Separation plot for different light isotopes.

The totally depleted Si(Li) coaxial detectors are made of HR industrial Si and were studied under difference temperature and voltage treatment conditions. Detection of monochromatic radioactive beams ^{6}He and $^{7-9}$Li with energy from 150 till 300 MeV, carried out at the COMBAS separator [4] coupled to the U-400M cyclotron at JINR, Dubna show (Fig. 2.) that Si(Li) coaxial detectors reach an energy resolution in the range from 0.5% to 0.7%.

The results of measurements also indicate that the resolution crucially depends on the energy losses in the entrance window of the detector system and should be kept below 100 KeV. We have also prepared telescopes made of a ΔE coaxial detector (0.2 mm) and E coaxial detector (10 and 100 mm, respectively) to extend the studies of detector performance (i.e. resolution, efficiency) and identification power to the measurement of more complex isotopic spectra.

References

[1] L. Popeko, A.Derbin, A. Cherny, G. Shishkina, Sov. JETPH Lett. 50 (1989) 222.
[2] L. Popeko et al., Sov. JETPH Lett.57 (1993) 755.
[3] L.A. Popeko et al., Nucl.Inst.Meth. A535 (2004) 438.
[4] A.G. Artukh et al., Nucl.Inst.Meth. A426 (1999) 605.

The High-resolution in-flight spectroscopy (HISPEC) project

Zs. Podolyák[1], B. Rubio[2], J. Gerl[3], M. Górska[3], W. Korten[4]
[1]Univ. Surrey, UK, [2]IFIC, Valencia, Spain, [3]GSI, Darmstadt, Germany [4] CEA Saclay, France for the HISPEC/DESPEC collaboration

HISPEC [1,2] deals with a versatile, high-resolution, high-efficiency spectroscopy set-up to address questions in nuclear structure, reactions and astrophysics using radioactive beams with energies of 3-150 MeV/u. The HISPEC setup will be located at the low-energy branch of the SuperFRS, with the possibility to be mounted both before or behind the planned energy buncher. The experimental techniques to be used can be grouped together in relation to two different energy regimes (see Table 1).

Table 1: Experimental techniques for high-resolution spectroscopy at the low-energy branch.

Beam-energy range	Experimental method
E/A ~ 100 MeV	Coulomb excitation, Secondary fragmentation
E/A ~ 5 MeV; (Coulomb barrier)	Coulomb excitation, direct and deep-inelastic, fusion evaporation reactions

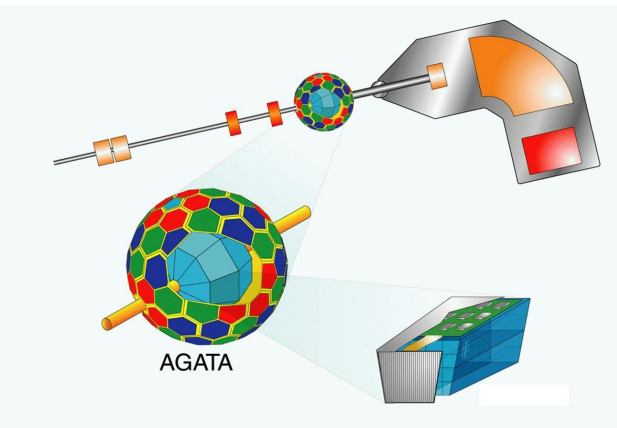

Fig.1 Schematic view of the HISPEC set-up.

The HISPEC set-up (figure 1) will comprise beam tracking and identification detectors placed before and behind the secondary target, the AGATA Ge array, charged particle detectors [3], a plunger, a magnetic spectrometer and other ancillary detectors. It can be combined for recoil decay studies, with the decay detectors of the DESPEC [4] project.

The HISPEC set-up has at its core AGATA [5], the next generation gamma-ray tracking array, with a resolving power hugely exceeding the presently available Ge-arrays. AGATA (Advanced Gamma Tracking Array) is designed to be a 4π detector consisting of 180 germanium detectors. Each detector crystal will be segmented 36 ways. Within each detector pulse shape analysis will be used to determine the interaction positions of the gamma rays to an accuracy of ~2 mm. Tracking algorithms will be used to reconstruct the paths of gamma rays passing through the detectors.

The effect of ancillary detectors (charged particle arrays, plunger) to be used in conjunction with AGATA has been simulated. Special emphasis was given to the uncertainties in energy, position and angle of the γ-ray emitting particles. The requirements with respect to the beam tracking detectors has been determined [6,1], and this performance can, in principle, be reached with existing technology.

The AGATA demonstrator, consisting of five triple cluster modules (15 Ge crystals) will start to operate in Legnaro in 2008. It is envisaged that AGATA will be moved to the SIS-FRS facility in around 2010 for an early implementation physics programme within the HISPEC project. The five units of the AGATA demonstrator will be placed at a distance of ca. 15 cm at forward angles. The detectors will form a ring subtending an angular range from about 8°to 44°. According to calculations the efficiency at $M_\gamma = 3$ (20) amounts to about 8.6% (6.1%) at 100 A·MeV/u. The position resolution of the AGATA detectors ensures an energy resolution after Doppler correction of ≈0.5% (taking into account the remaining uncertainty in the particle position and velocity).

The AGATA sub-array will complemented by the 105 Ge detectors of RISING [7]. The efficiency as well the energy resolution of the AGATA part of the proposed layout is almost three times better then what is achieved with the current RISING set-up. Keeping in mind the low to moderate multiplicities expected the gain in sensitivity and selectivity is substantial. Combining both systems enables e.g. for the first time highly selective γγ-coincidences to be measured in fragmentation reactions.

References

[1] Zs. Podolyák, Int. J. of Mod. Phys. E15 (2006) 1967.
[2]www.gsi.de/fair/experiments/NUSTAR/hispec_e.html
[3] I.Martel et al, GSI Scientific Report 2006.
[4] B.Rubio, Int. J. of Mod. Phys. E15 (2006) 1979.
[5] "AGATA Technical Proposal", ed. J Gerl and W. Korten, GSI Darmstadt 2001
[6]E. Farnea et al., LNL-INFN Ann. Rep 202/2004 p158; F. Recchia LNL-INFN Ann. Rep. 202/2004 p.160.
[7] H.-J. Wollersheim et al, NIM A537 (2005) 637.

DEcay SPECtroscopy (DESPEC) at the new FAIR-NUSTAR facility

B. Rubio[1], Zs. Podolyák[2], M. Górska[3], J. Gerl[3], W. Korten[4]
[1]IFIC, Valencia, Spain, [2]Univ. Surrey UK, [3]GSI, Darmstadt, Germany, [4] CEA-Saclay, France

For the HISPEC/DESPEC collaboration

This contribution describes DESPEC [1] (DEcay SPECtroscopy) which together with HISPEC [2] constitutes one of the proposed and accepted joint experiments of NuSTAR. Decay studies of implanted activities will be vital for our understanding of nuclear structure and astrophysics far from stability where FAIR will produce the most exotic beams of nuclei with short half-lives. Decay studies of isomeric levels is also a central part of the experimental plan. Another very interesting application of DESPEC is to work in combination with HISPEC for recoil tagging experiments. Last year we described the scientific motivation for DESPEC. In the present report we will rather focus on the "core" experimental set-up which is presented in Fig.1. Most of the experiments planned at DESPEC will involve radioactive beams from

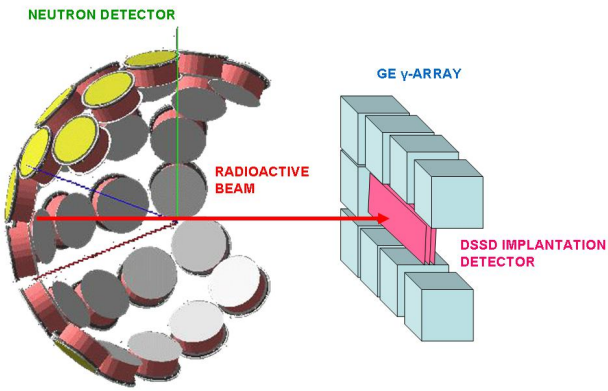

Figure 1: DESPEC "core" experimental set-up

the Super –FRS Low Energy Branch decelerated to 50 to 70 Mev/A, their deep implantation in an active stopper and the subsequent measurement of the emitted radiation, in general ß-particles, protons or neutrons and γ-rays. Extensive simulations of the beam optics and detector design were performed in 2006 which led to the following outcome given for three detector types.

Implantation detector

We envisage 8 detector units, 24cm x 8cm comprising three 1 mm thick DSSD 8cm x 8cm detectors within a common PCB support structure. In addition an upstream and a downstream single plastic detectors of 24cm x 8cm and 2mm thickness will provide the dE and the veto signals respectively. The segmentation required of the silicon strip detectors is determined by the implantation rate, the maximum half-lives of interest and the need to reduce the input loading (capacitance and leakage current) of the instrumentation to achieve good noise (low threshold) performance. In the process of optimizing the segmentation of the setup to be suitable for large variety of experiments we decided that each DSSD will consists of 128 p+n junction and 128 n+n Ohmic strips which means that each 24cm x 8cm detector comprises 3x128x128=49152 quasi-pixels.

High resolution γ-detection array

We propose two alternative solutions for the gamma array. a) An array consisting of 24 stacks of three planar double-sided Ge strip detectors. b) Six TIGRESS type CLOVER detectors [3]. The first solution will have higher granularity and better performance at low energy while the second will be clearly better for high energy γ-rays often present in β-decays with high Q-values. A Montecarlo simulation of the efficiencies and the peak-to-total ratios using Geant4 for the two proposed set-ups was presented last year [4]. Preliminary studies of tracking capabilities of the planar set up will be presented in a separate contribution to this report [5]. A prototype of a planar stack of two Ge planars is being developed.

Neutron detectors

The goal of an ideal beta delayed neutron experiment is to measure individual neutrons with high efficiency, good energy resolution and in coincidence with the gamma rays measured with a high resolution gamma-ray set-up. At DESPEC we plan to have two complementary neutron set-ups. a) A moderator based 4JI detector with more than 30% efficiency over a broad range of energies for neutron branching ratio measurements. Such detector has a marginal energy resolution and is unsuited for prompt coincidence with the gammas due to the large moderation times of 10 to 100 ms after the neutron emission. b) A much faster set-up for measuring the neutron energies based on NE213/BC501 liquid scintillators arranged in the way shown in the figure. Using the detection of the beta particle as a trigger signal, the energy of the neutron is reconstructed by means of time-of-flight (TOF). The non negligible gamma ray sensitivity of the scintillators to the gamma-rays can be suppressed using discrimination techniques based on the pulse shape analysis.

References

[1] B. Rubio, Int. J. of Mod. Phys. E15 (2006) 1979.
[2] Zs. Podolyák, Int. J. of Mod. Phys. E15 (2006) 1967.
[3] H.C. Screggs et al, Nucl.Instr. and Meth 16 A453 (2005)431
[4] A. Algora et al, GSI Scien. Rep 2005 (2006)31
[5] A. Algora et al, GSI Scien. Rep 2006

Imaging algorithm for background suppression in the planned gamma tracking array of DESPEC

S. Tashenov[1] and J. Gerl[1]
[1]GSI, Darmstadt, Germany

In the context of the DEcay SPECtroscopy project (DESPEC) a high resolution gamma-ray tracking cluster based on the Ge planar detector technology is being designed [1]. It should cover all types of decay experiments with implanted radioactive ions. In experiments where decay times are longer than typically 100 μs, the standard "implantation particle - decay γ correlation" method of the background suppression is not effective due to increased random coincidences. As an alternative the imaging capability of the planned detector array can be exploited to trace the origin of the gamma rays back to the implantation target. The applied method is based on a kinematical relation of the scattered photon energy $\hbar\omega^{'}$ (and therefore an energy of the recoil electron $\Delta E = \hbar\omega - \hbar\omega^{'}$) to the scattering angle θ

$$\hbar\omega^{'} = \frac{\hbar\omega}{1 + \frac{\hbar\omega}{m_e c^2}(1 - \cos\theta)} \, . \qquad (1)$$

When the origin of the photon is known, a redundant information about it's first scattering angle θ in the detector can be obtained. On one side it can be determined from the positions of the interactions ($\theta_{geometrical}$), on the other side from the initial and deposited energy of the photon using formula 1 ($\theta_{kinematical}$). In figure 1 one sees the simulated angular difference $\Delta\theta = \theta_{geom} - \theta_{kin}$ for the case of a detector with an ideal energy and position resolution, and for the real detector with 1 mm position resolution.

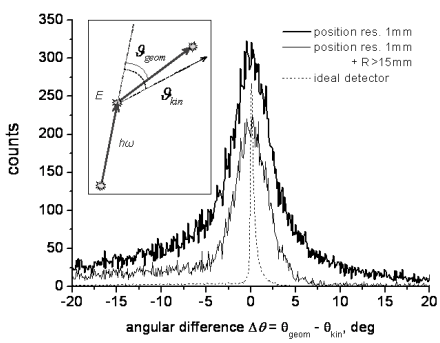

Figure 1: Distribution of the angular difference $\Delta\theta$.

With a loss of statistics one may improve the angular resolution by considering only the scattering events where the photon travels a significant distance after the scattering (a long "lever arm"). For the case of the scattering distance R more than 15 mm an example distribution is shown. Note that for background photons originating from random positions the angles θ_{geom} and θ_{kin} will not match, and these events will not contribute to the $\Delta\theta$ angle peak. Therefore the selection of the true events can be accomplished by setting up a window condition on this peak. The width of this window determines the amount of the events kept in the photopeak as well as the background suppression factor and therefore its a subject of an optimization. A dependance of the background suppression factor on the statistics is plotted in figure 2.

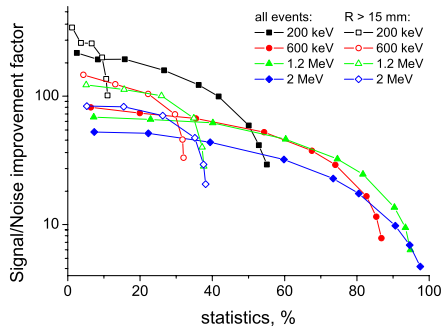

Figure 2: Compromise between the background suppression factor and the statistics. Open symbols: an additional condition was applied on the first scattering distance R > 15 mm.

An additional possibility to further increase the peak-to-background ratio in the spectrum *without* a concomitant loss of the statistics is to exploit the fact that photons deposit their energy preferably close to the surface of the detector. Based on this a weighting factor $exp(-r/r_0(E))$ was applied for every point in the energy spectrum, where r is the part of the the distance between the gamma source and the first interaction in the detector, which photon passes *inside* Ge, and $r_0(E)$ is an energy dependent Compton mean free path of a photon in Ge. An improvement of the Signal/Noise ratio due to this factor is $\sim$ 1.3 for 2 MeV photons and $\sim$ 3.8 for 200 keV photons. This weighting factor is already applied in figure 2.

Monte-Carlo simulations of the imaging capabilities of the prototype detector unit for the DESPEC Ge array show its high background suppression capabilities. The peak-to-background ratio can be improved by a factor of 10 while keeping 80 % of statistics. Compromising the kept statistics this factor can rise up to 100 or more.

References

[1] NUSTAR Letter of Intent http://www.gsi.de/fair/experiments/NUSTAR/index.html

The HYDE detector for the study of direct nuclear reactions at the Low Energy Branch of the new FAIR facility

J.M. Andujar[1], R. Berjillos[1], J. Dueñas[1], J.L. Flores[1], I.Martel[1], D. Rodríguez[1], P. Salmerón[1]

for the HYDE collaboration

[1]University of Huelva, Spain

The energy range provided at the Low-Energy Branch (LEB) allows to investigate the effect of Coulomb and nuclear fields at time scales which are most relevant for the structure of exotic nuclei. Here it is proposed to study direct nuclear reactions, elastic and inelastic scattering, break-up, and transfer reactions of exotic nuclei using an efficient charged particle detector, the HYbrid DEtector array (HYDE). Such studies will provide complementary information for B(Eλ) values, quadrupole deformations, spectroscopic values, collective phenomena and nucleon-nucleon correlations for very exotic nuclei with half lives down to the microsecond.

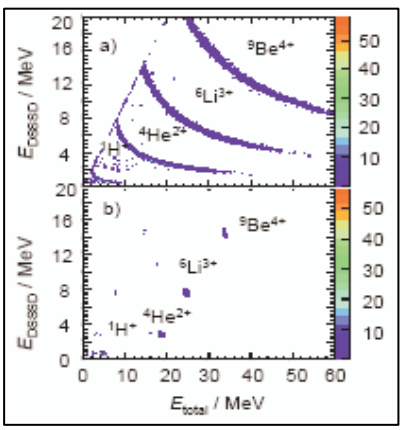

Figure 1: Simulations of the performance of a particle telescope (40 um DE and 2 mm E) in the scattering of a 5MeV/u beam of light ions from a 208Pb target. The upper and lower plots show the effect of an efficient tracking device.

To achieve this goal the HYDE array should provide maximum solid angle with good angular, energy, charge and mass resolution for the reaction fragments. Preliminary simulations of detector performance using silicon detector telescopes have been carried out. The results indicate that it is possible to achieve an efficient mass and charge identification if a fast tracking system (<100 ps) is implemented (figure1). The mechanical design will be such that the array could be used in combination with other detectors, like the gamma detector array AGATA.

Following a traditional (conceptual) design, the HYDE array would be build of several telescope detector units, each one composed of two layers of segmented silicon detectors, and one unit of CsI(Ta). Nevertheless additional detector materials and configurations should be investigated.

A recent test of diamond detectors was performed last June 2006 at the C.N.A Tandem accelerator in Seville, Spain. In this experiment time and energy response of both poly and single crystal CVD diamond materials were investigated. Diamond detectors are also of interest for the construction of fast tracking devices.

An important research effort is also dedicated to the development of efficient pulse shape analysis (PSA) techniques for particle identification with silicon detectors. Activity already started by building a data base of pulse shapes. This task is complemented by an active working group developing tools for shape classification using neural networks (Figure 2).

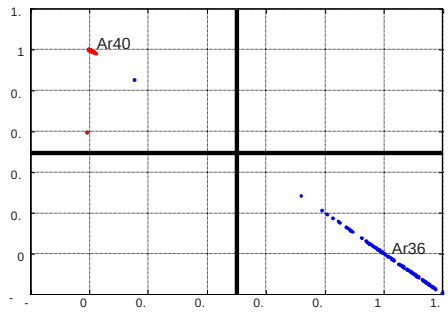

Figure 2: Isobaric separation of Ar isotopes at 5 MeV/u using PSA with neural networks (data from FAZIA collaboration).

Complementary to this activity is the development of specific ASIC for the front end electronics, fast digital signal processors for PSA in combination with an efficient data acquisition system. Part of the R&D work is being carried out in collaboration with SPIRAL2 working groups. HYDE is part of the HISPEC/DESPEC collaboration of the Low Energy Branch.

HYDE Collaboration (only one chairman per institute)

C. Angulo. CRC-Université Catholique de Louvain, Louvain la Neuve, Belgium.

M.J. G. Borge. Instituto de Estructura de la Materia - CSIC, Madrid, Spain.

W. Catford. University of Surrey, United Kingdom.

A. Fomichev. Flerov Laboratory of Nuclear Reactions, JINR, DUBNA, Russia

J. Gerl. GSI, Darmstadt, Germany

J. Gómez–Camacho. University of Sevilla, Sevilla, Spain

I. Martel. University of Huelva, Huelva, Spain (project coordinator)

K. Rusek. The A. Soltan Institute for Nuclear Studies, Warsaw, Poland.

P. Van Duppen. IKS-University of Leuven, Leuven, Belgium

R. Wolsky. The H. Niewodniczanski Institute of Nuclear Physics PAN, Cracow, Poland.

Study of the performance of tracking algorithms for the DESPEC planar setup

A. Algora *[1], B. Rubio[1], S. Tashenov[2], J. Gerl[2], B. Quintana[3], M. Doncel[3], F. Lorenzo[3], and A. Jungclaus[4]

[1]IFIC, CSIC-Univ. de Valencia, Valencia, Spain; [2]GSI, Darmstadt, Germany; [3]Univ. de Salamanca, Salamanca, Spain; [4]Univ. Autonoma de Madrid, Madrid, Spain

DESPEC is one of the experiments of the low-energy branch project of the future installations at FAIR (GSI). The main goal of this experiment is to study the decay properties of exotic nuclei. The basic instrumentation of this setup includes a set of implantation detectors, a Ge array and neutron detectors. Presently the collaboration is considering two possible setups for the Ge array. One possibility is to use an array of stacks of planar Ge detectors specifically designed for DESPEC. The other alternative is to use standard segmented Ge detectors of EXOGAM [1] or TIGRESS [2] type. The R&D phase requires the realization of Monte Carlo (MC) simulations to determine the optimal setup for the future facility.

In this annual report we present a preliminary study of the application of tracking techniques to the results of the simulations. The idea is to apply the recent developments for the tracking array AGATA to exploit maximally the possibilities of the new array for DESPEC. To perform this study a new MC code was developed which generates a list-mode output that can be used in combination with the tracking programs and algorithms developed for AGATA. This output resembles the ones obtained in a real experiment after using the pulse shape technique and contains information on the position of the interactions and the deposited energy in the sensitive parts of the array after the interaction with radiation.

The results obtained for the planar setup are presented here. This setup consists on an array of 24 composite planar detectors. Each detector unit is formed by a stack of three planar Ge detectors with dimensions $72 \times 72 \times 22$ mm^3 with an active Ge volume of $68 \times 68 \times 22$ mm^3. The distance between the planars is 3 mm and the stack is encapsulated in an Al capsule of 1.5 mm thickness. The composite detectors are positioned around a focal plane of 240×80 mm^2. The described geometry has been implemented using the MC code GEANT4 [3].

In this work the tracking code MGT developed by D. Bazzacco was used [4]. The MGT code has several ingredients: first a preprocessing of the interaction points is done in order to take into account the effects of a non-ideal pulse shape analysis, next the interaction points are clustered and a reconstruction process is applied (forward tracking) and finally the results of the reconstruction process are accepted or rejected according to a validation criteria.

The results, presented in Table 1, correspond to the application of the MGT code to simulation data of centered, point-like monoenergetic gamma sources. The first column shows the energy of the emitted gamma rays. The second presents the maximum peak efficiency that can be obtained with the setup (acting as a total absorption spectrometer). The third and fourth columns show the peak to total ratio obtained in case the planar and the stack detectors are considered individually. The fifth column shows the peak to total ratio obtained after the application of the tracking code. Finally the last column presents the efficiency of the tracking code.

Table 1: Results of the simulations for monoenergetic gamma rays (see text for details).

E (MeV)	Eff. Peak	P/T planar	P/T stack	P/T Track	Track. Eff.
0.10	47.1	85	89	89	99
0.25	38.2	44	55	69	96
0.50	26.7	19	32	48	96
1.00	18.4	11	21	36	94
2.00	13.2	7	16	28	92
5.00	6.8	3	7	13	81

As part of our work (not presented here) the effect of the emission of gamma cascades on the tracking efficiency has also been considered. The next step of our work will be the study of the performance of tracking algorithms for the segmented CLOVER setup.

Acknowledgments: A. A acknowledges the collaboration of Prof. D. Bazzacco and Dr. E. Farnea in the realization of this work.

References

[1] http://www.ganil.fr/exogam/

[2] H. C. Scraggs *et al.*, Nucl. Inst. and Meth. A543 (2005) 431

[3] S. Agostinelli *et al.*, Nucl. Inst. and Meth. A506 (2003) 250; http://wwwasd.web.cern.ch/wwwasd/geant4/geant4.html

[4] D. Bazzacco, The MGT code, unpublished.

* on leave from MTA ATOMKI, Debrecen, Hungary

Simulation of EXL Silicon Particle Array Response*

A. Zalite[1,4], A. Bracco[1], G. Colo[1], P. Egelhof[2], O. Kiselev[2,3], J.P. Meyer[2], Yu. Zalite[4], and the EXL collaboration†

[1]INFN, Milano, Italy; [2]GSI, Darmstadt, Germany; [3]Mainz University, Germany; [4]PNPI, Gatchina, Russia

The silicon target-recoil detector - EXL Silicon Particle Array (ESPA) - is designed to detect light recoil particles in experiments measuring elastic and inelastic scattering, charge-exchange, transfer reactions and quasi-free scattering. The EXL project objective is to study the structure of exotic nuclei in light-ion scattering experiments in inverse kinematics at the NESR storage ring. The ESPA will be a part of the setup which also includes gamma-ray and slow-neutron detectors, forward detectors for fast ejectiles and an in-ring heavy-ion spectrometer.

The ESPA surrounds the internal gas-jet target and is divided into 6 regions: D, C, B, A, E', E [1]. It consists of arrays of thin double-sided silicon strip detectors (DSSD) and thick lithium drifted silicon detectors (Si(Li)). Regions D and C (tracking section, $10° < \theta < 75°$) include two layers of thin DSSDs, regions B and A (non-tracking section, $75° < \theta < 89°$) - only one layer.

A simulation program was developed for modelling the ESPA response to the tracks of particles in the regions D, C, B, A using the Geant4 framework (Figure 1). The structure of the program makes it possible to add silicon detectors from other regions (E', E) in the same way and to include an interface to external event generators.

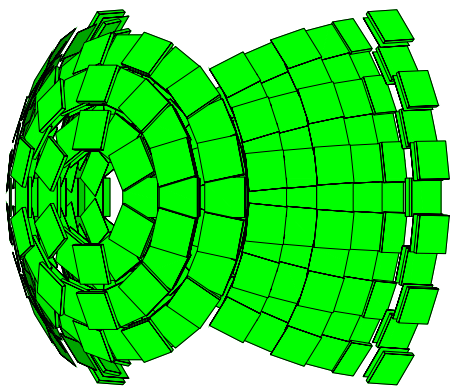

Figure 1: Part of ESPA geometry (regions A, B, C and D) in Geant4.

Geometry parameters are not "hard-coded" inside the program code. The set of basic geometry parameters, material properties and parameters that control the initialization stage, geometry building and the run of the program are read in from ASCII files and stored in a multimap container. All necessary internal geometry parameters are derived from the basic set. This structure permits to change input to any database.

The program permits to make different changes in geometry building and run conditions without recompilation. Setup geometry may be built without thick silicon detectors and without some regions. There is also possibility to build geometry without the first layers of thin DSSDs in the regions D and C. There are options for primary vertex displacement and smearing using the Gaussian distributions. The simulation program writes event headers and hits to the binary file. There is possibility to write output to the ROOT file.

The simulation output file is read in by the digitization program. All hits which belong to the same silicon detector are grouped and energy deposits are summed. For thin DSSDs local coordinates of the primary particle entry point are corrected taking into account the strip pitch. Obtained values of energy losses and time-of-flight are folded with resolutions taken from the known test results.

The simulation and digitization programs are designed to simulate events for investigation of angular and energy resolution and particle identification. The aim is to optimize the detector geometry. In particular, it was shown that for expected value of vertex spread for gas-jet target (σ = 0.5 mm) the increase of strip pitch to 0.5 mm does not worsen considerably the angular resolution (about 0.06°) in the non-tracking section - the target size defines the resolution (Figure 2). In case of droplet target with vertex spread σ = 0.05 mm the achievable resolution is much better (up to 0.015°) and there is a dependence from strip pitch. For the tracking section the angular resolution depends very crucially on the thickness of the first DSSD layers and particle energy because of the multiple Coulomb scattering. Detailed investigation demands use of external event generators for the reactions of interest.

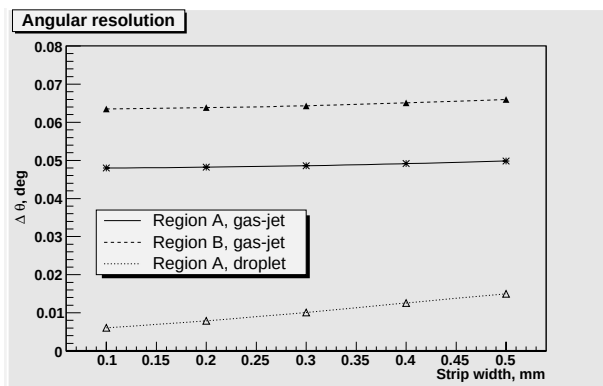

Figure 2: Angular resolution in regions A and B as function of silicon strip width for expected vertex spread.

References

[1] EXL Technical Proposal. http://www-linux.gsi.de/∼wwwnusta/tech_report/05-exl.pdf

* Work supported by EU, EURONS contract No. 506065.

† http://ns.ph.liv.ac.uk/∼mc/EXL/ns-instrum-exl.html

Position-Sensitive Si(Li) Transmission Detectors for the EXL-Experiments at GSI-Darmstadt

D. Protić, T. Krings, S. Niessen, FZ Jülich, Germany
P. Egelhof, GSI, Darmstadt, Germany
E. C. Pollacco, CEA Saclay, France
M. Müller-Veggian, FH Aachen, Abteilung Jülich

A large target-recoil detector will be constructed for the future EXL-experiments (EXotic nuclei studied in Light-ion induced reactions) at the NESR storage ring of the future FAIR project at GSI-Darmstadt [1]. As a part of the recoil detector, position-sensitive Si(Li) transmission detectors (5 to 9 mm thick) are intended for construction of ΔE-E charged-particle telescopes. Si(Li) detectors of transmission type has been an important aspect concerning the total-energy measurement for target recoils transversing the silicon ΔE-E telescopes and stopped in inorganic scintillators placed behind the telescopes.
Two ~6.5 mm thick Si(Li) transmission detectors equipped with 8 pads on the implanted p+-contact have been prepared for the test measurements at ESR (GSI-Darmstadt). To relieve the efforts for the first experiments a telescope configuration and position-sensitive structure very similar to that of the MUST2 experiment (SACLAY, ORSAY and GANIL) have been applied [2], but with UHV-capable components.

The schematic view of the Si(Li) transmission detector is presented in Fig. 1. The Si(Li) detector in the UHV-compatible housing is shown in Fig. 2.

Figure 1: Schematic view of the Si(Li) transmission detector.

The results of the test measurements in the laboratory confirm that the predetermined specifications, listed in Table 1, have been fulfilled.

Some of these results were presented at IEEE Nucl. Sci. Symp., San Diego, Nov. 2006. Test measurements in UHV environment will be performed inside the ESR-ring at GSI-Darmstadt.

Figure 2: The Si(Li) detector in the UHV-compatible housing.

- transmission type Si(Li) detector
  - ~ 6.5 mm thick
- 8 pads on the boron-implanted contact
  - the same structure as for the Si(Li) detectors for the MUST2-setup
- thin Li-diffused contact
  - effective thickness below 5 μm
  - without position-sensitive structure
- operating bias: ≧ 700 V
- energy resolution [FWHM] for 5.8 MeV α-particles: < 50 keV
- reverse current / pad: < 250 nA
- resistance pad - neighbourhood: > 1 MΩ

T = 273 K

- housing / frame:
  - design is identical to the MUST2-design
  - all components have to be UHV-compatible

Table 1: Predetermined specifications of the Si(Li) detectors.

References:

[1] www.gsi.de
[2] E. C. Pollacco et al., to be published in Nucl. Instr. Meth.
[3] D. Protić and T. Krings, "Development of transmission Si(Li) detectors", IEEE Trans. Nucl. Sci., vol. 50, pp. 1008-1012, August 2003.

Progress Report on the FLAIR Facility

A. Braeuning-Demian[1], H. Danared[2], A. Källberg[2], W. Quint[1], A. Simonsson[2], C.P. Welsch[3,4] and E. Widmann[5]

[1]GSI, Darmstadt, Germany; [2]MSL, Stockholm, Sweden; [3]MPI-K, Heidelberg, Germany; [4]CERN, Geneva, Switzerland; [5]SMI, Vienna, Austria

The low-energy physics program with antiprotons and highly charged ions proposed to be carried out at the FLAIR facility requests new developments for both the beam deceleration and cooling and new, complex experimental setups. The deceleration concept, as presented in the Baseline Technical Report [1] foresees a three-step beam manipulation: the first deceleration in the NESR, one intermediate deceleration step from the lower NESR energy of 30 MeV to 300 keV and the final deceleration which will provide beams of antiprotons with energies of 20 keV and below. The last two steps will be performed by the Low-energy Storage Ring (LSR) and two additional installations, the Ultra-low Energy Storage Ring (USR) [2] and/or HITRAP [3].

The recent activities within the FLAIR collaboration mainly focussed on preliminary experimental and theoretical investigations of the feasibility of the deceleration concept.

The Low-energy Storage Ring

Tests with deceleration of protons have been performed at CRYRING in order to verify that the present machine configuration is adequate for antiproton deceleration at FLAIR [4]. More specifically, the aim of the tests was to show that CRYRING can decelerate a sufficiently large number of particles, through the full energy range from 30 MeV to 300 keV, with acceptable particle losses.

CRYRING has already been used for deceleration in a few cases where users have requested light ions at energies lower than the injection energy of 300 keV per nucleon, as given by the RFQ. Since this injection energy is fixed, tests of deceleration of protons from 30 MeV must be made by first accelerating the particles from 300 keV to 30 MeV. This does not imply, however, that deceleration can be performed just by reversing the magnet and rf ramps used for acceleration. Remanence and hysteresis effects in the magnets make the deceleration process dependent on the acceleration.

Fig. 1 shows an example of beam current and corresponding particle number during an acceleration–deceleration cycle. The beam current was measured using a DC current transformer. To get a sufficiently good reading of the current, many injection pulses were accumulated at 300 keV. Protons were injected in batches every 0.5 s while the electron cooling was on, moving the particles away from the injection orbit and continuously increasing the beam current and the phase-space density of the beam. The resulting stepwise increase of the particle number can be hinted in the figure. Acceleration starts at time zero when the current has reached 4.9 μA, corresponding to 2.1×10^8 stored particles.

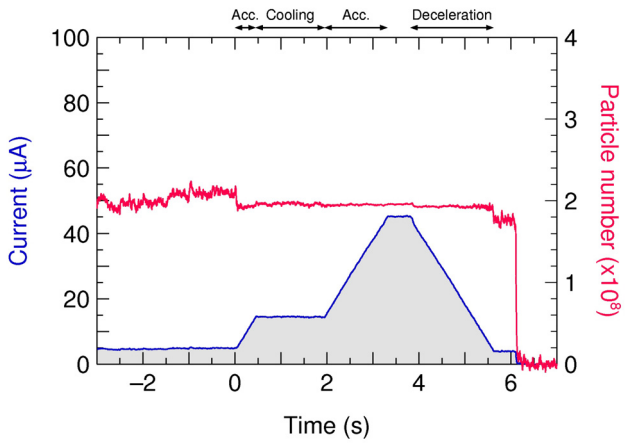

Figure 1: Particle number (upper curve) and proton beam current (lower curve) as function of time during acceleration and deceleration. The curves are averages from many machine cycles.

The beam was accelerated first from 300 keV to 3 MeV, and at that energy it was cooled again during 1.5 s while staying bunched before it was accelerated up to 30 MeV. The intermediate cooling was necessary in order to minimize the losses during the deceleration. During acceleration, the current increases with the beam velocity, whereas the particle number should stay constant if there are no losses. It is seen from the figure that there was a small loss of particles at the start of the acceleration, but that the rest of the acceleration and the cooling were made without losses.

The beam was stored for 0.5 s at 30 MeV, still bunched, and then decelerated back to 300 keV in 1.8 s without further cooling. At 6.1 s, the beam was dumped, and a new cycle started. A very small loss occurred at the start of the deceleration, and somewhat more particles were lost when the deceleration ramp met the flat bottom level. The result was that 1.8×10^8 protons remained when the beam was back at 300 keV. For FLAIR it is the efficiency in deceleration from 30 MeV to 300 keV that is important, and it is thus shown that this deceleration can be made with at least 90% efficiency given the beam properties at 30 MeV of this experiment.

With a higher injected current, the number of decelerated particles increased, although the losses also became larger. During the short time available for optimization of

the deceleration ramps, about one day, it was possible to reach up to 2.8×10^8 protons decelerated to 300 keV.

According to the present planning for FAIR, the end of the commissioning period and the start of operations at FLAIR is defined to occur when 1×10^8 antiprotons have been decelerated to 300 keV. This limit was exceeded by almost a factor three in these tests.

The Ultra-low energy Storage Ring

The USR is a new development and will be the first energy-variable electrostatic cooler synchrotron installed within a large accelerator facility. It will decelerate the antiprotons and exotic ions to lowest energies of 20 keV/q, which will allow e.g. for direct injection into traps. It is also intended to enable in-ring experiments with event rates of at least six orders of magnitude higher than in single pass setups and should, last but not least, open the way for nuclear physics studies with slow extracted, quasi-DC antiproton beams.

Ring Layout

The symmetric, four-sided machine consists of three cylinder deflectors (two times 10° and one 70° deflector) in the corner sections and quadrupole doublets that are used for transverse modulation of the beam. As can be seen in Fig. 2, the experimental sections and the integrated electron cooler mainly determine the overall size of roughly 8m x 8m of the storage ring. Single-turn injection of the beam will be realized by a pulsed deflector. Both slow and fast extraction will be available over the complete energy range. An rf operated drift tube with voltages below 100 V is used in combination with an electron cooler to shape short bunches along the longitudinal direction for in-ring experiments. Details about the USR lattice, its optical elements and the envisaged experiments are given in [4]. The main parameters of the storage ring are listed in Table 1.

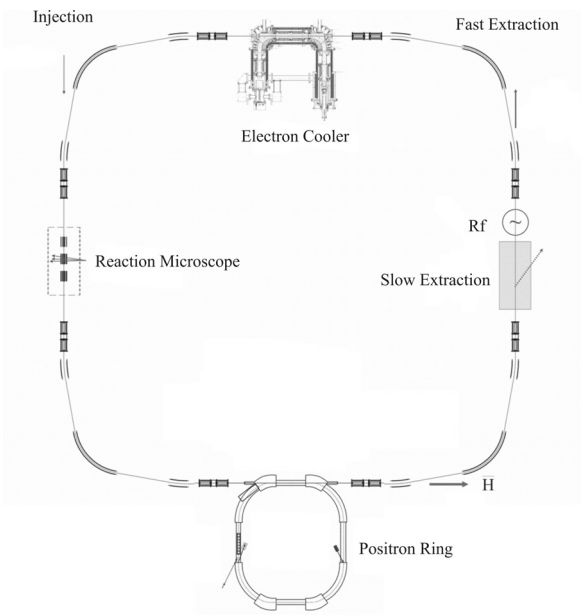

Figure 2: Preliminary layout of the ultra-low energy storage ring. The positron ring is a possible future extension that would allow for in-flight antihydrogen creation.

Table 1: Main parameters of the USR.

General Parameters	
Energy range	20 keV – 300 keV
Circumference	34.7 m
Base pressure	$< 5\cdot10^{-13}$ mbar
Operating Temperature	4 K
Machine Parameters	
space charge limit (20 keV)	$2\cdot10^7$
Q_x	2.38
Q_y	1.14
10° deflectors	
Height	240 mm
Radii	1940 mm and 2060 mm
Voltage |U|	< 20 kV
70° deflectors	
Height	160 mm
Radii	970 mm and 1030 mm
Voltage |U|	< 20 kV
Quadrupoles	
Length	200 mm
Distance between lenses	150 mm
Aperture Radius	50 mm
Voltage	+/- 6 kV
Steerer Length	100 mm
Steerer Plate Distance	120 mm

Electron Cooling at 20 keV

In the limit of such small beam energies, the realization of efficient electron cooling, employing electron energies of only few eVs (or maybe even fractions of an eV) is a new challenge. It is currently taken up in the Cryogenic Storage Ring (CSR) project at the MPI-K [5] and the experience gained there will be available to the USR. In particular, cryogenic GaAs photocathodes have already been shown to provide initial electron temperature of ~10 meV at the electron source, much lower than the 100 meV for thermoemission cathodes. This was demonstrated by the operation of a cold electron beam target from GaAs photocathodes at the TSR (MPI-K) [6, 7].

Cooling times in the USR were estimated using the BETACOOL code [8,9]. The resulting equilibrium momentum distribution and transverse emittances as a function of cooling time are shown in Fig. 3

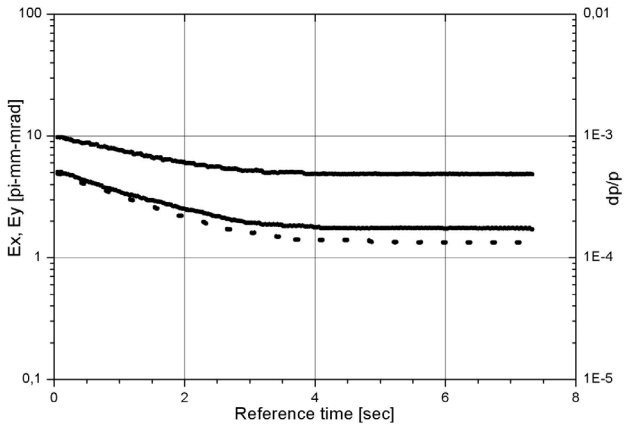

Figure 3: Evolution of the momentum spread (upper curve) and.of the horizontal (continuous line) and vertical (dashed line) emittance during the cooling process [9].

Other activities

Conceived as a multi-user facility, FLAIR will be a combination between the decelerators and a large number of different small experiments using ion and antiproton beams. Therefore, an important issue of the facility is the integration in the FAIR frame of the different FLAIR installations, part of which exist already today (at CERN, Stockholm, and GSI) and the ones which will be developed in the next future. A workshop dedicated to LSR was organized in March 2006 at GSI where aspects related to the adaptation of the CRYRING to the new task for FLAIR have been discussed by the expert groups from MSL Stockholm and GSI.

The progress of the HITRAP construction [3] prompted the discussion about the status of the new experimental setups which are planned to be used for the upcoming studies with highly charged ions and, later, also with antiprotons at FLAIR. Detailed planning of the new experiments were discussed and presented by the working groups at the HICAPE1 Workshop organized in November at GSI [9]. Starting with 2008,the present GSI facility offers the opportunity for tests, commissioning and production runs for a part of the experiments which will be installed at FLAIR.

These experiments require cw and pulsed beams, in a broad range of energies and intensities. A parallel operation of the experiments, which will assure a high duty cycle of the installation, implies a high degree of complexity of the beam sharing. This should be reflected also in the design of the facility building. The layout presented in Fig. 3 is the result of a careful planning under the aspects of functionality, safety and cost optimisation. The building includes the experimental caves, the laboratories, the electronics and control rooms spread over two levels.

Two collaboration meetings, held in Mai and December 2006, were devoted mainly to administrative and .financial issues of the collaboration.

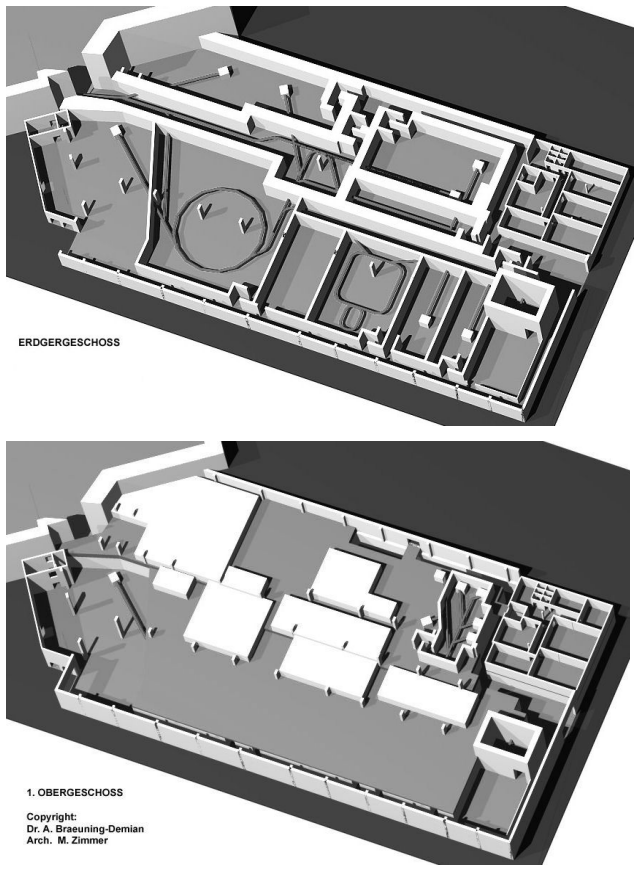

Figure 4: 3D-view of the FLAIR building: the ground level (top) and the upper level (bottom).

References

[1] FAIR Baseline Technical Report, July 2006, http://www.gsi.de/fair/reports/btr.html.

[2] C.P. Welsch, M. Grieser, J. Ullrich, A. Wolf, "An ultra-low-energy storage ring at FLAIR", NIM A 546 (2005) 405–417.

[3] W. Barth et al., HITRAP Report, see this volume.

[4] H. Danared, A. Källberg and A. Simonsson., Proc. EPAC 2006, Edinburgh, p. 249 (2006).

[5] A. Wolf, et al., "The Heidelberg CSR: Low-Energy Ion Beams in a Cryogenic Electrostatic Storage Ring", AIP Conf. Proc. 821 (2006), p.473-477.

[6] S. Pastuszka et al., J. Appl. Phys. 88, 6788 (2000).

[7] D. Orlov et al., Appl. Phys. Lett. 78, 2721 (2001).

[8] http://Lepta.jinr.ru/Betacool.htm.

[9] C.P. Welsch, A. Smirnov, "Cooling Rates at Ultra-low Energy Storage Rings", Proc. European Part. Acc. Conf, Edinburgh, UK (2006).

[10] HICAPE1, http://www-aix.gsi.de/conferences/hicape1/.

Spherical compression with low-Z shells as a target concept for the WDM-collaboration

An. Tauschwitz[1], J.A. Maruhn[1], F. Rosmej[2], D. Riley[3], A. Tauschwitz[4], and J. Jacoby[1]

[1]University of Frankfurt; [2]Université de Provence, France; [3]Queens University of Belfast, UK; [4]GSI, Darmstadt

The combination of intense energetic ion beams and a high-energy high-power laser at GSI and FAIR offers unique possibilities to investigate material at high energy densities. The "WDM" (Warm Dense Matter) collaboration proposes to study radiation properties of ion beam heated matter by means of the Thomson scattering [1]. The PHELIX laser will be used to produce X-rays of several keV energies. The choice of the materials for ion beam targets is therefore restricted to low-Z materials by the envisaged scattering diagnostics. A special target configuration, the dynamic confinement scheme, was proposed by the authors to produced homogeneous samples of WDM heated isochorically with the SIS-18 ion beam. In dynamically confined targets the conditions of the isochoric heating are provided by employing a thin low-Z tamper heated with the wings of the ion beam. The use of a low-Z tamper make the suggested targets accessible for the diagnostic X-rays. An extension of this work to spherical geometry beneficial for the scattering diagnostics is reported in [2]. Using energetic ion beams one can prepare not only isocorically heated samples of WDM, but also compress extended volumes of heated matter. The spherical target geometry can be optimized to achieve compression of the core target material. To show the capabilities of SIS-18 to compress matter in a way suitable for the X-ray scattering, we considered a solid hydrogen core surrounded by a carbon shell with a density of 2.25 g/cm^3. The ion beam consists of 10^{11} ions of U^{28+} with 200 MeV/u focused down to 1 mm spot ($FWHM$). A parabolic temporal profile of 100 ns length is assumed. The initial radius of hydrogen is $r_0 = 350\,\mu$m, the tamper has a thickness of 150 μm. Figure 1 shows the distributions of the normalized density of the core ρ/ρ_0 in length-radius plane for $t = 50, 80$ and 100 ns; ρ_0 is the initial density of hydrogen. During the heating time the pressure in the carbon shell exceeds the pressure in the hydrogen core and the H/C interface moves inwards. This pressure gradient launches a weak shock propagating towards the center of the core ($t = 50$ ns). Later, at $t = 80$ ns the reflected shock moves back. It arrives at the H/C interface before the end of the ion beam pulse, so that at $t = 100$ ns the compressed core is very homogeneous as it can be seen at Fig. 2. The hydrogen is compressed by about a factor of 2 and has according to the calculations an almost uniform temperature of 0.6 eV. The expanded low-Z tamper allows X-ray scattering diagnostics. The proposed compression scheme utilizes a Gaussian ion beam profile without special beam shaping. In comparison to cylindrical targets, spherical targets can be used at lower ion energies.

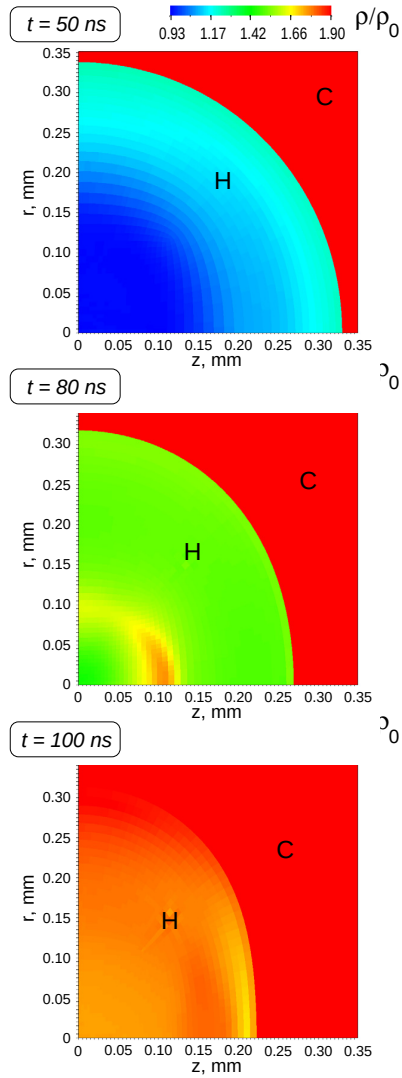

Figure 1: Distribution of the normalized density in length-radius plane for $t = 50$, 80, and 100 ns. Direction of the ion beam is the z-axis.

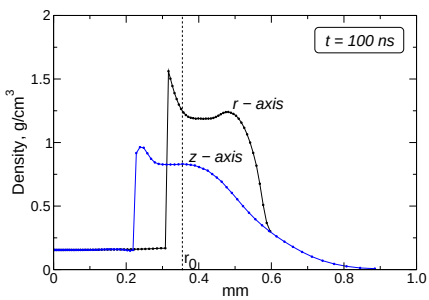

Figure 2: Density profiles along the beam axis (z) and radius(r); r_0 is the initial radius of the hydrogen core

.

References

[1] http://www.gsi.de/phelix/Experiments/FAIR/WDM/

[2] An. Tauschwitz et al., submitted to High Energy Density Physics.

Ground Based Investigations of Biological effects of Space Radiation using the BIOMAT facility at FAIR

M. Durante[1]
for the BIOMAT collaboration

[1]University Federico II, Naples, Italy

Biological experiments at the BIOMAT cave will have important applications in space radiation protection. In fact, it has been long acknowledged that more biological experiments using high-energy heavy ions are necessary to predict radiation risk in space and to develop effective countermeasure to allow safe colonization of the Solar System. In USA, NASA funded and built the NASA Space Radiation Laboratory (NSRL), which is currently supporting biological experiments performed at the Brookhaven National Laboratory (Long Island, NY). The European Space Agency (ESA) has recently established an ambitious exploration program (AURORA), and within this program (Figure 1) it has been decided to include a space radiation research program. Europe has a long tradition in radiobiology research at accelerators, generally focussing on charged-particle cancer therapy. This expertise can be adapted to address the issue of space radiation risk. To support research in this field in Europe, ESA issued a call for tender in 2005 for a preliminary study of Investigations into Biological Effects of space Radiation (IBER). The study has been completed in December 2006 with recommendations for facilities to be targeted for cooperation by ESA, and a detailed experimental campaign. The IBER team has strongly recommended GSI as the main facility to develop a European space radiation health research project. In fact, GSI has been for years the leading European facility for studying biological effects of heavy ions and for testing of space instruments. For example, for the ALTEA project (Figure 2) detectors have been calibrated on ground at the GSI facilities [1], and additional information on ion-induced light flashes has been obtained from animal studies with mice [2].

Since the ESA research program is expected to start in 2008, SIS-18 will be the main facility in the 1st phase. FAIR is expected to become the main ESA program facility in the 2nd phase (starting 2012), and will be in principle superior to any other ground-based space radiation simulator, including NSRL. Considering the importance of this facility for future manned space programs, IBER has recommended ESA to become an observer of FAIR. (The IBER webpage is: http://iber.na.infn.it)

Figure 1: The ESA exploration program AURORA in an artist's view. AURORA fosters European participation in the exploration and colonization of the moon and Mars

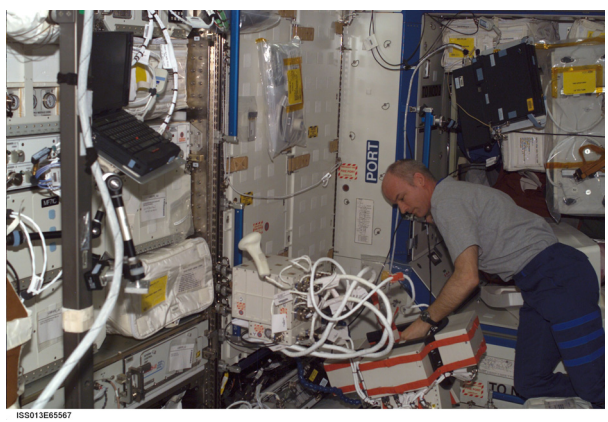

Figure 2: An astronaut installing the ALTEA facility on the International Space Station ISS in July 2006. ALTEA is a sophisticated detector used to investigate light flashes in astronauts produced by charged-particle traversals of the retina or brain. The detector has been calibrated on ground at GSI accelerators.

References

[1] L. Narici, ALTEA: FM Particle Telescope tested at GSI, GSI Scientific Report 2005, GSI report 2006-1, 382

[2] W.G. Sannita et al., Effects of heavy ions on visual function and electrophysiology of rodents: the ALTEA-MICE project. Adv. Space Res. 33 (2004), 1347-51

Novel Concept for a Beam Preparation and Manipulation System for High Precision Experiments at the LEB of the Super-FRS*

W.R. Plaß[1], M. Petrick[1], T. Dickel[1], T. Fleckenstein[1], H. Geissel[1,2], C. Jesch[1,2], C. Scheidenberger[1,2]
[1]Justus-Liebig-Universität Giessen, Germany; [2] GSI, Darmstadt, Germany

A novel system consisting of RF quadrupole and time-of-flight sections is proposed, in which ions can be cooled, bunched, mass separated with a resolution sufficient to select single isobars, and guided to different experimental setups. It also enables multiplexed operation of several connected experiments. Such a system could be employed advantageously at the LEB of the Super-FRS at FAIR. The schematic figure of the proposed system is shown in Fig. 1. Novel elements are described below.

RFQ Ion Beam Distribution System

RF quadrupoles (RFQs) allow for an efficient ion transport at significant residual gas pressure (< 0.1 mbar) and at low kinetic energy (~ 1 eV) and are thus ideally suited for applications in the vicinity of gas-filled stopping cells. Ion injection (e.g. for introduction of calibrants for mass spectrometry) and ion distribution to different directions (e.g. to different experiments or for diagnostics) can be realized [1]. As a proof of principle, an RFQ system consisting of straight and curved RFQs, which guide ions to three different directions, has been built and characterized. A transfer efficiency of 80% to 95% independent of the beam direction has been measured (Fig. 2).

Multiplexer RFQ System

For multiplexed operation of several experiments, mass-selective transfer from an RF trap can be used. While all incoming ions are accumulated and stored in the trap, ions with a selected mass number can be transmitted to an experiment, retaining all other ions in the RF trap. During successive cycles, different nuclides can be transferred, enabling multiplexed (different ion species measured at different experiments) or interleaved (different ion species measured alternatingly at one experiment) operation of the facility. Thus the efficiency can be increased by making use of several nuclides rather than just of one.

Isobar Separator

Isobar separation is performed in two stages, which consist of a low resolution RFQ mass filter and a high-resolution multiple-reflection time-of-flight mass spectrometer (MR-TOF-MS) with a cycle time on the order of 1 ms. A test version of such a MR-TOF-MS has been developed for this purpose [2].

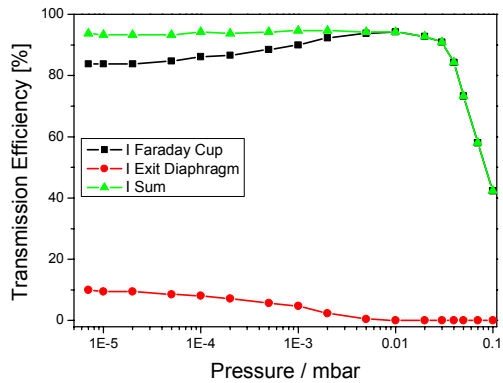

Figure 2: Transmission efficiency of the RFQ ion beam distribution system as a function of the pressure. The current measured on a Faraday cup behind the exit diaphragm and the current measured on the exit diaphragm is given relative to the current going into the system. The sum of both values is also shown.

References

[1] M. Petrick et al., GSI Scientific Report 2004, p. 330.
[2] T. Dickel et al., this volume.

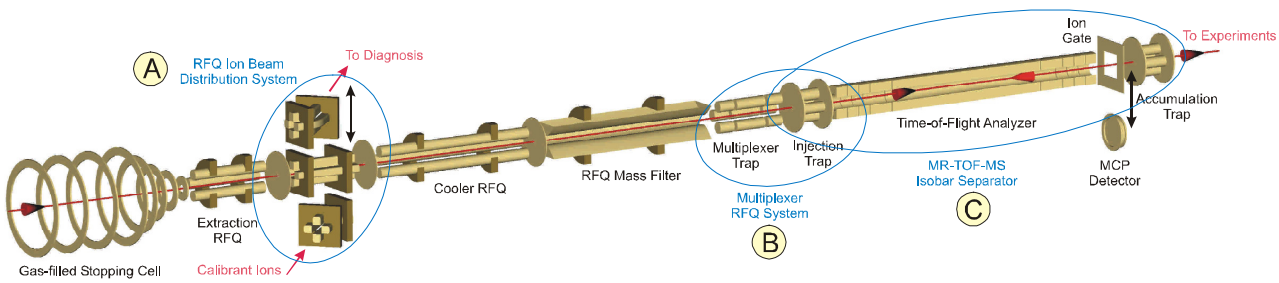

Figure 1: Schematic figure of the proposed system. Ions, which have been slowed-down and thermalized in a gas-filled stopping cell, are extracted and guided to different directions (e.g. for diagnosis or to different experiments), and reference ions are introduced by curved RFQs (A). Ion cooling and mass number selection occurs in a cooler RFQ and an RFQ mass filter. In an RFQ multiplexer system, different ion species are provided at selected times (B). A time-of-flight mass spectrometer serves for isobar separation and for direct mass measurements of very short-lived nuclei (C). In an accumulation trap, the ions are bunched, and after reacceleration made available to experiments further downstream.

* Work supported by GSI and the Helmholtz Association (contract number VH-NG-033), by the BMBF (contract number 06GI185I) and by the European Community (FP6 design study DIRACsecondary-Beams - contract number 515873).

Results from the FRS Ion Catcher experiment

M. Petrick[2], K. H. Behr[1], A. Brünle[1], L. Caceres[1], G. Chubaryan[3], J. A. Clark[4], Z. Di[2], S. Eliseev[2], H. Geissel[1,2], W. Hüller[1], M. Huyse[5], C. Karagiannis[1], R. Knöbel[1], Y. Kudryavtsev[5], T. Levand[4], Y. Litvinov[1], M. Maier[1], I. Mukha[5], D. Morrissey[6], G. Münzenberg[1], W. R. Plaß [2], M. Portillo[6], G. Savard[3], C. Scheidenberger[1,2], N. Scielzo[4], P. Van Duppen[5], H. Weick[1], M. Winkler[1], Z. Wang[2], B. J. Zabransky[3]

[1]GSI, Darmstadt, Germany; [2]JLU Giessen, Germany; [3]Texas A&M University, USA;
[4]Argonne National Laboratory, USA; [5]KU Leuven, Belgium; [6]Michigan State University, USA

The FRS Ion Catcher [1] was tested successfully in an online experiment. Its primary goal was to test the efficiently stopping process of exotic nuclei in a helium-filled gas cell and to provide different experimental setups with this cooled low-energy beam.

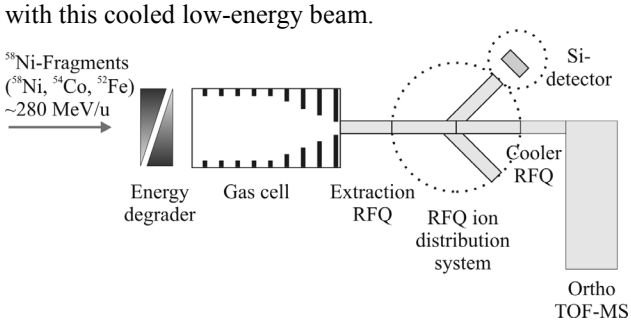

Figure 1: Schematic view of the experimental setup.

Figure 1 shows the final setup used in the beamtime. Exotic nuclei were produced by projectile fragmentation of ^{58}Ni primary beam in an Al target. Fragments with N=Z were separated with the FRS and energy-focused [2] with the wedge-shaped degrader at its exit. The various N=Z-fragments have different ranges. Due to the energy focusing, the range differences exceed the range straggling. This imposes an additional separation and thus, varying the degrader thickness allows to stop isotopically pure beam in the gas cell. This gas cell, developed at ANL [3], is the key component of the experimental setup. Equipped with different DC –and RF fields and a pressure of 100mbar helium gas inside, it guides and extracts the stopped ions to the distribution system [4]. This system allows to distribute the ion beam most efficiently to different detectors. While the experiment a silicon detector and a time of flight detector were used to diagnose the exotic ion beam.

As described, the experimental run was successful. For instance the half –life of the of the ground state ^{54}Co was measured with 198±4ms and shows the potency of this system.

To investigate the time-scale of the extracted ions, the SIS was run in a fast extraction mode. This allows to get information about the time that the ions need to be extracted after being stopped in the gas cell. Triggered with the extracting-puls from the SIS, mass-spectras were taken behind the stopping device with the Orthogonal-time-of-flight mass-spectrometer (Ortho TOF-MS) [5]. An analyse of this data represents the complete mass over averaged time scale, as shown in figure 2. Two different extracting DC-field strengh were applied to the helium-filled gas cell. As a result of the time scale measurement, the extraction time for atomic ions can be given with approximately 50ms.

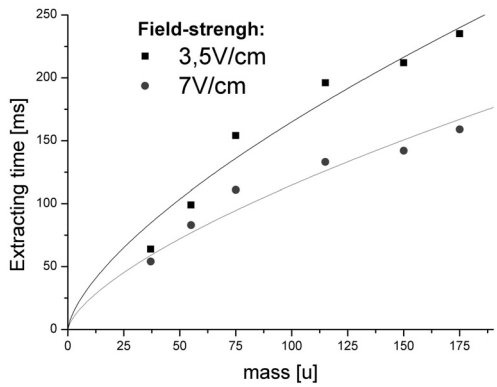

Figure 2: Extracting time of the Ion-Catcher device for two different extracting DC-field strengh supplied to the helium-filled gas cell.

References

[1] M. Maier et al., GSI Report 2005-1, 331 (2005)
[2] C. Scheidenberger et all., Nucl. Instr. Meth. B204, 119 (2003)
[3] G. Savard et al., Nucl. Instr. Meth. B204, 582 (2003)
[4] M. Petrick et al., GSI Report 2005-1, 330 (2005)
[5] S. Eliseev, PhD Thesis, Univ. Giessen (2004)

Beam Profile Detectors for the Super-FRS*

C. Nociforo[1], B. Achenbach[1], K.-H. Behr[1], A. Brünle[1], H. Geissel[1], W. Hüller[1], R. Janik[2], C. Karagiannis[1], M. Pikna[2], A. Prochazka[1], C. Scheidenberger[1], H. Simon[1], B. Sitar[2], P. Strmen[2], K. Sümmerer[1], I. Szarka[2], H. Weick[1] and M. Winkler[1]

[1]GSI, Darmstadt, Germany; [2]Comenius University, Bratislava, Slovakia.

Abstract: Gas beam profile detectors for slow and fast-extracted ion beams have been developed for the Super-FRS, and tested at the FRS with heavy ion beams at relativistic energies and intensities ranging from a few kHz up to a few MHz.

Introduction

Within the task NUSTAR 3 of the FP6 EU Design Study, beam profile detectors (BPD) for fast-extracted ion beams have been proposed and designed by the Bratislava group for future experiments at the Super-FRS [1].

For beams with a spill length as short as 50 ns a single ion tracking is not achievable anymore but only measurements of the bunch profile can be performed. This problem arises from the large amount of charge (up to several nC) which is deposited in the detector. The use of a gas detector leads to a long integration time which is needed for charge collection (≈μs). This causes a spreading of the charge and thus strongly affects the measurement of the beam profile. For this reason the use of fast electronics and lower gas pressure (around 1 mbar) has been proposed.

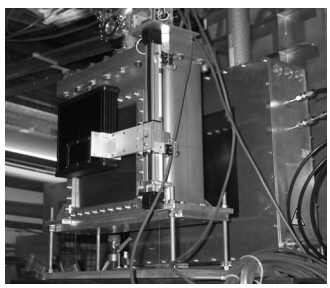

Figure 1: The BPD protoype mounted at the FRS (S2).

Another challenging feature of the BPD is related to the dynamic range of the ions to be detected which requires the use of a dedicated electronics.

Prototype design

The BPD prototype (see Fig. 1) is conceptually developed as a gas proportional wire chamber. The detector volume is filled with a gas of Ar+10%CO_2. The active area is 100 x 100 mm^2 and contains 3 x 50 wires. The detector is equipped with 2 integrated delay lines directly connected to the cathode wires for x and y position measurements simultaneously. Variable gas pressure conditions are obtained by using a gas pressure control system [2]. Adjustable preamplifiers have been constructed with a gain factor of 2V/pC. This allows to use the BPD as in-beam detectors for experiments using slow-extraction beams, similar to the time projection chamber (TPC) detectors [3]. In this case the detector is working as position-sensitive detector recording single ions.

* Work supported by the European Community under the FP6 DESIGN STUDY (contract 515873 - DIRACsecondary-Beams).

Prototype test

A first beam test of the BPD prototype has been performed in November 2006. The detector has been tested at the second focus station of the FRS (S2) with a slow-extracted ^{136}Xe beam at 470 MeV/u. The detector response has been investigated at a gas pressure of 500–900 mbar increasing the beam intensity gradually up to 3 MHz. New electronics with fast shaping signals (adjustable preamplifiers, zero crossers, etc.) have been tested. For the digitalization a standard electronics, based on VME TDC and ADC, was used. For fast-extracted beams, the use of faster digitalization was foreseen, by setting a FADC SIS3301. The trigger was given by the time signal provided by a plastic scintillator behind the BPD.

Detector calibrations were performed with the use of scintillating fibers (red by PMT) forming a grid by 3x3 (6 mm apart) in front of the detector window. One of the results of calibration in y direction is shown in Fig. 2a.

In Fig. 2b the beam profile of ^{136}Xe ions in y direction at 1 MHz intensity is shown.

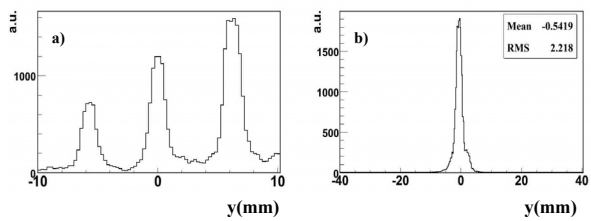

Figure 2: a) Calibration and b) beam profile in y direction.

Outlook

In view of the larger intensity beam foreseen for the FAIR facility further tests at higher intensity of slow and fast extracted beams in larger chambers with faster electronics will be prepared.

References

[1] H. Geissel et al., Nucl. Instr. Meth. B204 (2003) 71.
[2] http://www-win.gsi.de/FRS_GasSupply/.
[3] V. Hlinka et al., Nucl. Instr. Meth. A419 (1998) 503.

The FAIR Accelerator Complex*

D. Krämer for the FAIR Technical Divsion
GSI, Darmstadt, Germany

Project Status

One major milestone for the FAIR Project was achieved in finalising the Baseline Technical Report (FBTR) in spring 2006. This document [1] was handed over to the International Steering Committee (ISC) and defines the basic layout as well as the fundamental system parameters of the FAIR accelerators and experiments. Approving this document, the international partners agreed on "the project" within the financial ceiling scrutinized by the cost review groups which gave their final reports in the period under report.

However, strong focus of the ongoing work is laid on further detailing of the technical work packages. Those specifications will serve as basis for the negotiations with the international partners of FAIR to take on specific work packages. To assist and counsel in this process the In-Kind Advisory Board (IKAB) was initiated in 2006. To attract industrial partners the preparation of an International FAIR Industry Forum started in 2006.

Topology Refinements

Topology revisions and adjustments were mainly driven by the finalisation of the lattice design of both the synchrotrons and the storage rings, modifications of the Super-FRS, and the demand to shift the HESR southwards. This movement by 30 m allows for a later upgrade of the HESR to accommodate experiments with polarised antiprotons. Compared to the situation presented in the FBTR in early 2006 the topology remains primarily the same as shown in Figure 1.

This layout together with a first iteration of the load list for media demands within the different buildings provides a stable basis for further detailing of the civil construction planning.

Distinguished Technical Developments

Within this annual report all major developments presently under way of FAIR accelerators are covered. This report will flashlight on the main technological advancements.

SIS100 and SIS300 Dipole Magnets

The outcome of the R&D work for the straight SIS100 dipole magnets showed that the required parameters cannot be reached safely. Thus a reduction of the aperture and the maximum field strength was decided. The new bent magnet design was specified within 2006. One prototype magnet each - bend and straight design - was ordered at Babcock Noell Nuclear GmbH and the BINP.

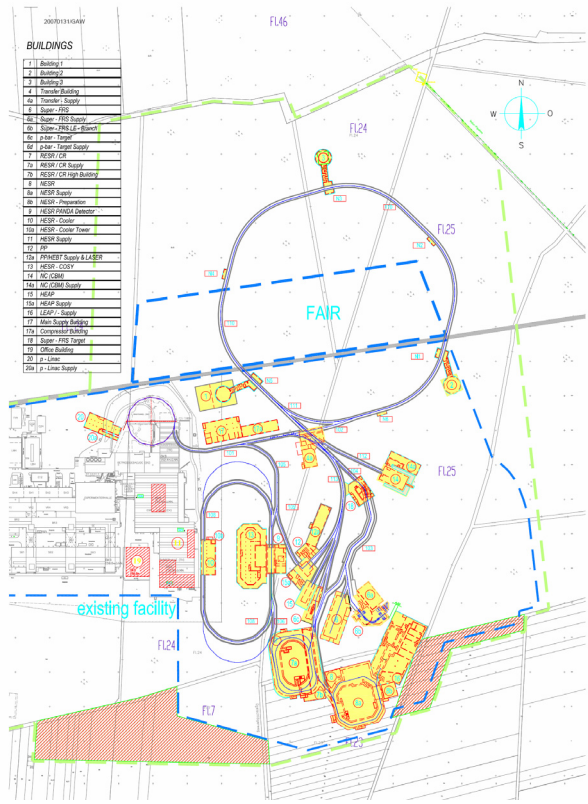

Figure 1: Topology of the FAIR facility as of Dec. 2006 compared to the one presented it the FBTR.

At the same time the R&D for the SIS300 dipole magnets focuses on bent magnets with the reduced maximum flux density of 4.5 T instead of 6 T. The development is borne by INFN. The investment cost are shared by INFN and GSI (3.7 M€ and 1 M€), whereas the workload of approx. 40 person years are covered by INFN.

Frequency Chance for the Proton Linac

It was further decided to adjust the rf-frequency of the p-linac from 352 MHz to 325 MHz. The call for tender for the klystron was issued at the end of 2006. Various arguments led to the change resulting in considerable cost cuttings not only for the proton linacs rf-system but also for the civil construction costs due to reduced space requirements. As a consequence the proton RFQ and the DTL section had to be re-designed.

References

[1] H.H. Gutbrod et al, FAIR Baseline Technical Report, GSI Darmstadt, September 2006, ISBN 3-9811298-0-6A.

* Work supported by EU, EU contract 515873 DIRACsecondary-Beams and EU contract 515876 DIRAC-PHASE-1

SIS100/300 Design Status Report

P. Spiller, K. Blasche, U. Blell, O. Boine-Frankenheim, H. Eickhoff, P. Forck, G. Franchetti, H. Klingbeil, A. Krämer, G. Moritz, C. Omet, N. Pyka, H. Ramakers, H. Reich, H. Ramakers, A. Redelbach, J. Stadlmann, H. Welker, GSI, Darmstadt, Germany, A.D. Kovalenko, JINR, Dubna, Russia

SIS100

Lattice Structure and Main Magnets

The SIS100 lattice structure is described in the FBTR. However, basic properties of the main dipole- and quadrupole magnets have been optimized. Due to the large apertures required in both types of magnets, the AC losses, which were substantially reduced by the magnet R&D program, exceeded significantly the original goal values. In addition, the quench protection system became more and more demanding due to the higher stored energy. In both magnets, field strength requirements were finally at the tolerable limits, with undesirable consequences for the field quality. Therefore it was decided to reduce the apertures and the maximum field strength. The development of the main dipole magnet, which was originally assumed to be straight, is focussed on a bent magnet allowing a reduction of aperture and field strength. Due to the bending, the length of the dipole can be increased without affecting the beam acceptance. The length of the quadruple was also increased and consequently the maximum gradient reduced.

Finally, beside the activities in the frame of the EU FP6 design studies, two full scale model dipoles have been initiated.

System Design

The technical planning of the six sections and the lattice cells was further detailed. The distribution and positioning of all accelerator components has been finished, allowing us to enter into the planning of the technical infrastructure. The planning of the supply buildings has been continued, with updates of the floor space requirements and drawings of the distribution of the supply units in the individual building levels.

Technical Systems

A technical design study has been completed in collaboration with BINP for a ferrite loaded acceleration cavity.

The collaboration has been continued with an engineering study with the goal to prepare start of a prototype production within 2007. According to the ion optical layout the injection- and extraction devices have been specified and design studies were started for the bipolar kicker magnets. In parallel, experimental investigations were conducted with pulse forming networks in collaboration with the Technical University of Darmstadt. HV pseudo spark switches as replacement for thyratron switches are under development in cooperation with the University of Erlangen. The hardware, firmware and software for the digital control of dynamic high precision power converters has been developed and is in practical use in the power converters of the therapy accelerator of HICAT in Heidelberg. Because of the high requirements for the quench protection of SIS 100 dipole magnets an electronic DC circuit breaker has been developed. A prototype DC circuit breaker is under construction in TU-Darmstadt.

SIS300

Lattice Structure and Main Magnets

The required length of the six straight sections in SIS100, especially needed for Rf devices, defines (at a given circumference) the remaining length of the arcs. Since SIS100 and SIS300 are situated in the same tunnel on top of each other, this ratio between arc and straight section length is also valid for SIS300. However, the required slot length of s.c. cosΘ magnets for a given effective field length is much bigger than the one of super ferric magnets. Therefore, the arc length, indirectly defined by SIS100, provides not sufficient space for the originally foreseen doublet focusing structure. In order to save space in each lattice cell the doublet structure has been replaced by a FODO structure [1]. A further difficulty could be solved which was caused by the lateral displacement of the straight sections of both rings. The missing dipole lattice concept was applied for SIS300 as well, leading to an almost perfect matching of both ring geometries. By removing the displacement of the straights we could resolve the collision of the vertically extracted SIS100 beam with the SIS300 cryostat. Furthermore, as in SIS100 it was decided to continue the dipole R&D with bent dipoles with lower maximum flux density of 4.5 T instead of 6 T and preferably a single layer coil. First design studies on a bent SIS300 dipole magnet have been performed by INFN [2] and BNG. However, the introduction of the missing dipole lattice requires an additional short magnet design for the ends of the arcs. A MoU for the development and production of such a short SIS300 prototype dipole magnet has been signed by INFN and GSI.

Technical Systems

A first conceptual design study has been completed for the s.c. high field extraction septum of SIS300 in collaboration with the BINP. The design study showed the feasibility of such a 3.5 T septum magnet. The 2D layout could be integrated as a 3D CATIA model into the drawings of the extraction and emergency dumping system.

References

[1] P. Spiller and J. Stadlmann, Evolution of the SIS300 lattice design and options for increased heavy ion beam intensities, GSI internal note (2007)

[2] F. Alessandria et. al., Preliminary studies of a 4.5 T curved 7.78 m long dipole option for SIS300, INFN (2006)

Design Status of the FAIR Beam Transport System

S. Ratschow[1], F. Hagenbuck[1], P. Spiller[1], and F. Hinterberger[2]
[1]GSI, Darmstadt, Germany; [2] Helmholtz-Inst. f. Strahlen- und Kernphysik Bonn, Germany

The conceptual design and the ion optical layout of the FAIR High Energy Beam Transport System were summarized in detail in the FAIR Baseline Technical Report (FBTR). However, the status of the project required continued revisions and follow up activities. Adoptions in the lattice design of the FAIR synchrotrons, storage rings and their extraction and injection systems and modifications of the Super-FRS had to be comprised. The layout of the connecting beam line between FAIR and the existing facility has been reoptimized and the extraction magnet which provides the link was selected. Furthermore, in order to allow a later extension, the HESR was moved slightly towards the south. With respect to the level concept it was considered to shift all ground level installations except the HESR down by 1 m to save building costs. To realize this option two additional vertical transitions (in the beam line from SIS18 to SIS100 and from SIS18 to PP2perp) were added. Table 1 summarizes all modifications in the HEBT system since publishing of the FBTR.

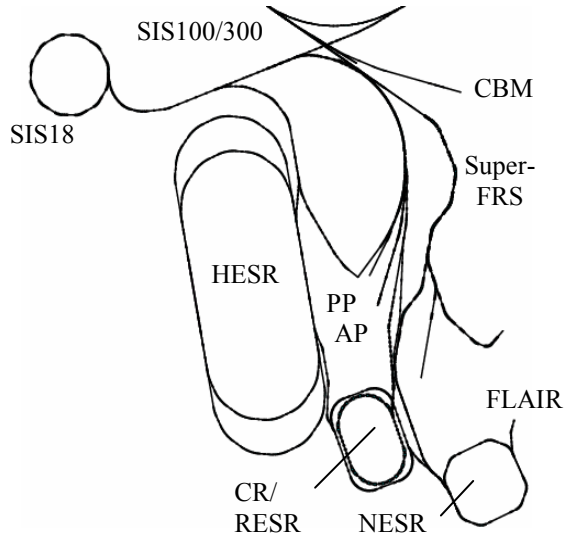

Figure 1: Modified FAIR HEBT system.

Table 1: Adoptions in the beam line topology of FAIR

Ring/beam line section		Adoptions compared to FBTR
HESR		HESR was shifted 30 m towards the south. Injection angle and position changed along the straight section. Upgrade option increases length of HESR straight sections by 60 m.
CR		Increase in size and injection angle.
RESR		Increase in width by 1.5 m due to larger CR. Extraction to NESR further south.
from	to	
NESR	FLAIR	Additional angle of approx. 6° included in the beam line to resolve spacial conflict between the FLAIR cave and the Super-FRS low energy cave.
RESR	HESR	New layout. Unfavourable geometrical constraints from HESR upgrade option.
RESR	NESR	New layout according to new extraction point.
PBAR-Target	CR	New layout.
Super-FRS		Symmetric pre-separator with 66° angle. New layout of the low energy branch.
SFRS	CR	New layout.
SFRS	NESR	Less space for matching at the NESR injection system due to 1.5 m larger lateral distance between NESR and RESR.
SIS18 Extr.		Present SIS18 extraction system is used. Deflection towards FAIR will be realized by the TS1MU1 dipole, which must be operated as a bipolar magnet.
SIS18	HESR	New layout according to completely changed boundary conditions.
SIS18	NESR	Beam line bypassing the antiproton target guided through the tunnel of the end of the Super-FRS ring branch.
SIS18	PP2perp	New layout.
SIS100	HEAP, PBAR, PP1, PP2	Layout adapted to normal conducting magnets, leading to a displacements of the beam line and their end points.
SIS100	Dump	New layout with horizontal bend. Uncompensated dispersion in both planes prevents small beam size at the beam dump.
SIS100	SFRS	New, long drift space behind extraction system to avoid conflict with SIS300.
SIS300	Dump	New layout with horizontal bend.
SIS300	CBM	Adapted to optimized SIS300 dipole parameters.
SIS300	SFRS	Upper part of vertical transition matched to SIS100 to SFRS beam line.

Design Work for the High-Energy Storage Ring (HESR)*

A. Lehrach[1,#] for the HESR Consortium
[1]Institut für Kernphysik, Forschungszentrum Jülich, Germany

Abstract

The HESR is being designed to accelerate and to store antiprotons in the momentum range between 1.5 and 15 GeV/c [1]. An important feature of this new facility is the combination of phase space cooled beams and dense internal targets, which results in demanding beam parameter requirements to reach high luminosities and high momentum resolution. The status of beam dynamics studies and R&D design work is reported.

Introduction

The HESR is being realized by a consortium consisting of IKP at Forschungszentrum Jülich, TSL at Uppsala University, and GSI Darmstadt. It will be built to exploit the research areas of charmonium spectroscopy, hadronic structure, and quark-gluon dynamics [2]. An important feature of this new facility is the combination of phase-space cooled beams and dense internal targets, comprising challenging beam parameter in two operation modes: high-luminosity mode with beam intensities up to 10^{11}, and high-resolution mode with a momentum spread down to 10^{-5}, respectively [1]. Powerful electron and stochastic cooling systems are necessary to meet the experimental requirements.

The layout of the HESR is shown in Fig. 1, including key components. The HESR lattice is designed as a racetrack shaped ring, consisting of two 180° arc sections connected by two long straight sections. One straight section will mainly be occupied by the electron cooler. The other section will host the experimental installation with internal H_2 pellet target, RF cavities, injection kickers and septa. For stochastic cooling pickup and kicker tanks are also located in the straight sections, opposite to each other. To improve longitudinal stochastic cooling a third pickup location in the arc is presently being investigated.

Special requirements for the lattice are dispersion free straight sections and small betatron amplitudes in the range of a few meters at the internal interaction point. In addition the betatron amplitudes at the electron cooler are adjustable within a large range.

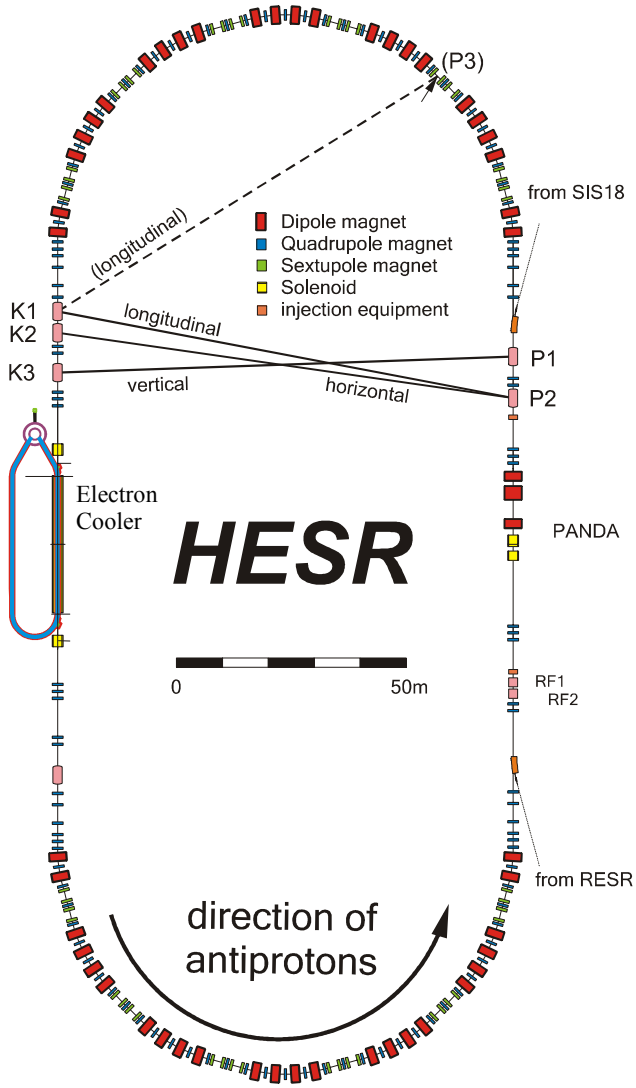

Figure 1: Schematic view of the HESR layout. Equipment for the injection from SIS18 and RESR, RF cavities (RF1, RF2), the PANDA experiment, and the electron cooler is included. Positions of stochastic cooling devices (pickup: P1–P3, kicker: K1-K3) are also indicated.

Beam Dynamics Studies

In cooler storage rings aiming for ultra-high beam quality like the HESR, the interplay of many processes determines the final equilibrium beam distribution. A by far more detailed understanding of collective phenomena in space-charged dominated cooled beams is needed than presently achieved to reach highest possible beam quality. Different software modules are being developed and im-

* Work supported by European Community RESEARCH INFRASTRUCTURES ACTION under the FP6 program: DESIGN STUDY (Contract No. 515873 – DIRAC Secondary-Beams), and by INTAS-GSI grants (Ref. No. 03-54-5584).
# a.lehrach@fz-juelich.de

proved for beam dynamics simulations at injection and during beam cooling.

Beam stability studies have been carried out including beam equilibria with electron and stochastic cooling, intra-beam scattering, and beam-target interaction. Furthermore average luminosities have been estimated assuming realistic machine cycles.

A steering concept for the HESR has been developed, utilizing the method of orbit response matrix. Orbit bumps at various positions in the ring have also been specified.

A multipole correction scheme is presently being developed. Higher-order field expansions from field calculations of HESR magnets will be utilized together with other non-linear fields like the one generated by the beam of the electron cooler.

The impedance budget of the ring is also studied. Especially the beam-position monitors, kickers, and cooling devices will have a major impact.

In addition the effect of trapped ions accumulated in the electro-magnetic potential of the circulating antiproton beam and the electron beam of the electron cooler is investigated [3].

R&D Work

Electron Cooler

High priority is assigned to the high-energy electron cooler. The main issue is the reliable operation of high-brilliance electron beams in a high-voltage environment up to 4.5 MV. An important part of the work will be to construct prototypes of several critical parts of the system. Other aspects of the electron cooling system, including the method to charge the high-voltage terminal, the problems to create the required quality of the magnetic field and the stability of the high voltage, the required ultra-high vacuum, the electron beam optics, and stability of the electron beam transport are being investigated. This work is led by TSL Uppsala.

The design of the magnet system is nearing completion. Prototypes of several solenoids are being built. Furthermore the electron gun has been designed and preparations for making the design of the collector are taking place. Tests relating to the precise regulation of the high-voltage have been carried.

Stochastic Cooling Devices

Prototyping of critical components for the stochastic cooling system is under way. Especially new high-sensitivity pickups with low-impedance requirements and higher bandwidth (2 to 4 GHz) are being developed. Hardware studies are taking place simultaneously to find the optimal solution for enhanced filter requirements.

In addition results of improved theoretical models are benchmarked with experiments utilizing the existing stochastic cooling system at COSY to ensure a proper design of the stochastic cooling system.

Magnets

With regard to maximum field strength, magnet aperture and ramping rate of the RHIC-type superconducting "cosθ"-magnets installed in the interaction regions fit the HESR requirements except for the magnet length. The maximum acceptable sagitta to get an acceptable large good field region restricts the magnetic length to roughly 1.8 m. Curved magnets will avoid this problem, but the coil arrangement is more complex. Studies of two different types of bent dipole magnets have been carried out: "cosθ" and double-helix design. Prototype work for dipole magnets will start soon. For quadrupole magnets a design study has been launched to determine a realistic assembly of dipole and quadrupole magnets and to decide whether a hybrid magnet with a sextupole coil on top of the quadrupole coil can be realized.

RF Cavities

Beam dynamics simulations indicate, that two different types of cavities are needed: one for bunch manipulation and acceleration/deceleration, and a second one for storing particles in a barrier bucket.

The first cavity will be a symmetric, magnetic alloy loaded cavity, combined with a push-pull tube-amplifier for multi-harmonic signals from 10 to 3000 V. The magnetic alloy cores (FineMet®) are on-site and will be installed as soon as the construction work is completed. The barrier bucket cavity has been designed and built as a single tank cavity. It will be driven by a transistor amplifier which allows applying voltages between 1 and 100 V. The magnetic alloy cores (VitroPerm®) are also at hand and are going to be implemented soon.

Cryogenics

To reduce static losses of the cryogenic system the number of cold-warm junctions is being minimized.

Injection septa and kickers, dipole magnets for the PANDA orbit chicane, RF cavities, stochastic kicker tanks, and the electron cooler will be operated at room temperature. The PANDA solenoid will have its own cryostat segment. All other devices will be operated at liquid Helium temperature.

References

[1] FAIR Baseline Technical Report, Volume 2: Accelerator and Science Infrastructure, GSI, March 2006.

[2] Strong Interaction Studies with Antiprotons, Letter-of-Intent, PANDA collaboration, January 2004, see http://www.gsi.de/documents/DOC-2004-Jan-115-1.pdf.

[3] P. Zenkevich, O. Boine-Frankenheim, O. Alekseev, Trapped Particles in the HESR Storage Ring, GSI-Acc-Report 2006-05-001, May 2006.

Design Status of the FAIR Proton Linac*

L. Groening[1], W. Barth[1], G. Clemente[2], P. Forck[1], M. Galonska[1], R. Gobin[3], R. Hollinger[1],O. Meusel[2], S. Minaev[4],U. Ratzinger[2], A. Schempp[2], W. Vinzenz[1], S. Yaramyshev[1]

[1]GSI, Darmstadt, Germany; [2]IAP, University of Frankfurt a.M., Germany; [3]CEA/Saclay, Gif-sur-Yvette, France; [4]ITEP, Moscow, Russia.

Introduction

The FAIR proton linac together with SIS18 and SIS100 has to provide the primary proton beams for the production of antiprotons [1]. It will deliver a 70 MeV beam of up to 70 mA to the SIS18 with a repetition rate of 4 Hz. The room temperature linac will be located north of the existing UNILAC complex. Its conceptual layout is shown in Fig. 1.

Proton Source and LEBT

At CEA/Saclay the SILHI (Source des Ions Légères a Hautes Intensitées) is operating since 1996 and its nominal beam parameters fit to the needs of the FAIR proton linac. In December 2005 beam emittances for various source and LEBT parameters were measured during a joint CEA/GSI/IAP campaign. Its evaluation in 2006 followed by additional measurements on space charge compensation in May 2006 revealed the high reliability of the set-up and confirmed experimentally the compliance of its beam properties to our requirements [2]. Accordingly, this set-up is a suitable option to be employed at the proton linac.

Operating frequency

Due to the availability of reliable 3.0 MW klystrons on the market at a frequency of 325 MHz, the layout of the RF-components of the linac was completely revised resulting in a considerable cost saving of the project. The 325 MHz rf-power sources provide about twice the peak power with respect to devices at the former frequency of 352 MHz. The number of these devices could be reduced by 40% reducing also the space requirements and civil engineering cost. Additionally, this new frequency allows for using p-linac rf-components also within a possible upgrade of the existing UNILAC Drift Tube Linac (DTL) section, as 325 MHz just corresponds to three times the Unilac operation frequency. As a consequence the proton RFQ and the DTL section had to be re-designed. The first klystron to be used at an rf-test stand has been tendered and will be delivered in early 2008.

RFQ

Although the preferred option for the RFQ was defined as a 4-rod type in 2006, an alternative 4-vane design at 325 MHz was proposed by ITEP/Moscow. The new frequency resulted in the desired reduction of both the electric surface field and of the longitudinal output emittance. The adoption of the 4-rod option should be straight forward and it is planned for 2007.

Drift Tube Linac (DTL)

Since the available rf-input peak power per load has been doubled, the number of independent rf-loads comprising the DTL was lowered from 11 to 6. Now each load consists of a pair of coupled Cross-bar H-cavities (CH). At the Frankfurt University a single CH-cavity model has been built and tested successfully [3]. It will be followed by a coupled CH-cavity model in 2007 [4]. Additionally, the number of individual DTL quadrupole types was reduced leading to an overall cost reduction. Passive DTL beam diagnostic components will be designed in collaboration with KVI, Groningen, Netherlands.

Injection into SIS18

The beam to be injected into the SIS18 must have a relative momentum spread of less then $\pm 1 \cdot 10^{-3}$. Simulations taking into account the effect of space charge forces revealed a significant growth of momentum spread during beam transport from the DTL exit to the SIS18. The transport channel has been re-designed and the last re-buncher was moved from the DTL exit to the existing transfer channel UNILAC-SIS18.

References

[1] *FAIR Baseline Technical Report*, Vol. 2, GSI Darmstadt, Germany, p. 335, (2006).

[2] R. Hollinger et al., Proc. of the XXIII Linac Conf., (2006).

[3] G. Clemente et al., Proc. of the 10th EPAC Conf., (2006).

[4] G. Clemente et al., this report.

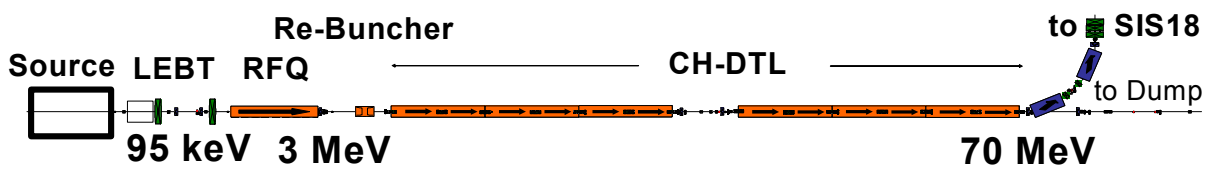

Figure 1: Conceptual layout of the FAIR proton linac.

*Supported by EU contract RII3-CT-2003-506395

Localisation of field emission and rf tuning of the 350 MHz superconducting CH-structure*

H. Podlech[1], A. Bechtold[1], C. Commenda[1], H. Liebermann[1], I. Müller[1], U. Ratzinger[1], J. Festag[2], and C. Pöppe[2]

[1]IAP, Universität Frankfurt, Germany; [2]GSI, Darmstadt, Germany

Abstract

The superconducting CH-structure is a novel multi-cell cavity for the acceleration of protons and ions in the low and intermediate energy regime [1]. A prototype cavity (350 MHz, b=v/c=0.1) with 19 cells has been built and tested several times with liquid helium at 4.5K. An effective accelerating gradient of 4.6 MV/m has been achieved which corresponds to an effective voltage of 3.7 MV[2].

Analysis of field emission

Presently the acceleration gradient is limited by field emision. Therefore a detailed analysis of the x-ray distribution has been performed with the goal to localize existing field emission centres. 30 TLD-cards (Thermo-Luminescence-Dose-meter) have been used. Figure 1 (top) shows the X-ray dose distribution along the cavity at different positions. Clearly one strong peak is visible which is one order of magnitude larger than the dose at neighbouring detectors which are shifted by one cell length $\beta\lambda/2$ and by 90 degree (Fig. 1, bottom). This measurement indicates the existence of only one strong emitter. In a next step the cavity will be treated with a mild chemistry (Buffered Chemical Polishing) and with high pressure rinsing which is the standard method to remove field emitters in superconducting cavities.

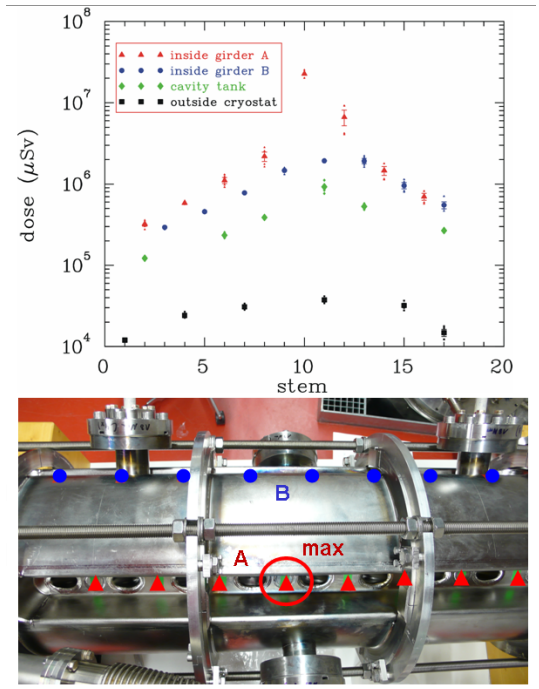

Figure 1: Measured x-ray dose at different position along the cavity (top) and positions of the x-ray dose-meter (bottom).

RF tuning

A tuning system for the superconducting CH-cavity is presently under development. It will consist of a coarse tuner with a tuning range of 600 kHz. The frequency will be shifted by applying an external force to the end cells which decreases the length of the first and the last gap. The maximum displacement is about 0.7 mm with a force of 5 KN. Additionally a fast system based on piezo-tuners will be installed to compensate frequency variations due to microphonics and Lorentz-Force-Detuning. The whole system willl be tested in a horizontal cryostat (Fig. 2).

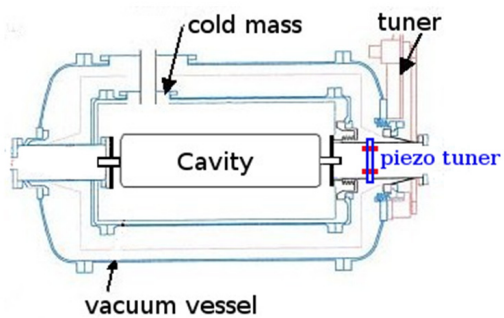

Figure 2: Schematic drawing of the horizontal cryostat with the position of the cavity and the tuning system.

References

[1] H. Podlech, "Development of room temperature and superconducting CH-structures", LINAC'04, August 2004, Lübeck, p. 28-33, http://www.JACoW.org.

[2] H. Podlech, C. Commenda, H. Liebermann, H. Klein, U. Ratzinger, A. Sauer, "First cryogenic tests of the superconducting CH-structure", EPAC'06, June 2006, Edinburgh, p. 1588-90, http://www.JACoW.org.

* Work supported by GSI, BMBF contract No. 06F134I, EU, contract No. 516520-FI6W, RII3-CT-2003-506395, EFDA/99-507ERB5005-CT990061.

Coupled CH-Cavity Development for the FAIR Proton Injector*

G. Clemente, U.Ratzinger# , IAP Goethe University, Frankfurt, Germany
L. Groening, GSI, Darmstadt

Abstract

The availability of commercial 325 MHz, 2.5 MW klystrons initiated the development of linac resonators which fit to that power level source: this will lead to a significant overall linac cost reduction. This is achieved if individual cavity modules can be rf coupled efficiently. At IAP Frankfurt a coupling cell for CH – cavity modules was designed, which at the same time can house a transverse focusing lens as well as the rf power coupler for the whole unit. A half scale model of the coupled CH modules 3 and 4 of the FAIR proton injector is under construction at IAP. Design and fabrication of a full scale high power cavity is planned for in 2007.

The Proposed Linac Design

The beam dynamics calculations lead to a limited number of gaps per acceleration section which have to be followed by a transversely focusing quadrupole lens.

Especially at the low energy end each acceleration section would need quite modest rf power levels only, when realized as an individual cavity. By rf coupling up to two of these sections and by integrating the quadrupole lens within the central coupling cell it is possible to match all cavities to the available amplifier power. Each 2.5 MW amplifier will drive one cavity via one rf power coupler in this approach.

The coupled CH-cavity concept

The original design of the CH-cavity made use of large end half drift tubes to make the end cell resonant and, at the same time, to host the magnetic lens needed for beam focusing [1]. By putting together two CH-cavities of that type and by replacing the inner end walls by a radial stem support for the big drift tube, one is approaching the coupled CH-cavity geometry as one can see from Fig.1 [2]. Taking the coupling tank diameter as well as the drift tube outer diameter as variables one finally gets the resonant coupling of both CH-cavities. The field distributions in the coupling cell were investigated by MWS field simulations and are shown in Fig. 2. The large coupling drift tube is capable to house a magnetic quadrupole triplet and/or diagnostics instrumentation as well as a cooled beam collimator. A robust radial stem is well suited for tube adjustment. Moreover, it allows comfortable access to feed all installations within the coupling tube.

Cavity Model

In order to test this new coupling concept and to validate the simulations performed with Microwave studio it was decided to build a half-scale model of the second resonator of the p-injector. This model consists in two tanks with 13 and 14 gaps respectively, coupled by a 151 mm long intetank section which includes the focusing lens. The field distribution is plotted in Fig.3

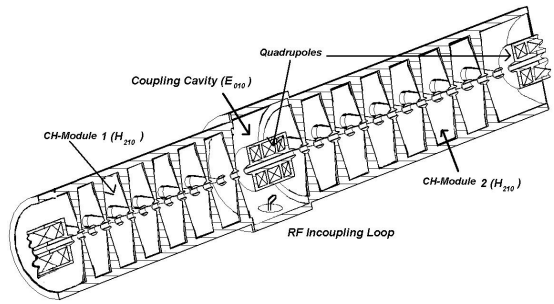

Fig.1: Sketch of a coupled cavity CH - linac

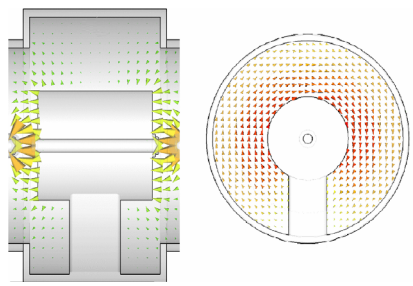

Fig.2: Coupling section between CH cavities with electric and magnetic field distribution, respectively.

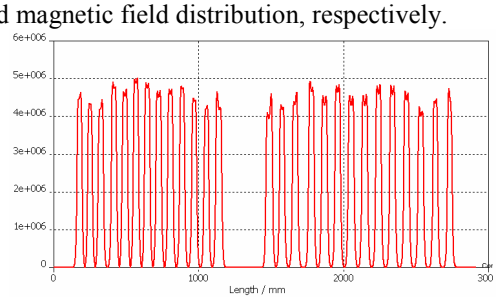

Fig.3:Axial electric field disribution for resonator 2 of the GSI proton Injector

The outer cylinder will be entirely in aluminum while all the stems and the lenses are made of massive brass. After the fabrication end, foreseen for early spring 2007, an intensive RF measurements campain will start to investigate all the properties of innovative coupling concept

References

[1] G.Clemente et al.,Proceed. of the PAC 05 Conference, Knoxville, TN, USA, p. 883 - 885.

[2] U.Ratzinger et al, Proceed. of the LINAC 06 Conference, Knoxville, TN, USA, p. 526 - 530.

*Work supported by EU Contract Nr . RII3-CT-2003-506395
#u.ratzinger@iap.uni-frankfurt.de

Design of a Target for Antiproton Production at the Future FAIR Facility*

N.A. Tahir, B. Franzke, GSI, Darmstadt, Germany
A. Shutov, I.V. Lomonosov, IPCP, Chernogolovka, Russia
R. Schmidt, Y. Kadi, CERN-AB, 1211 Geneva, Switzerland

Production, cooling and accumulation of antiprotons is a very important objective of the FAIR project. It is expected that the FAIR accelerator facility will provide a strongly focused beam of 29 Gev protons with an intensity of 2.8 $\times$ 10^{13} in a single bunch of 25 ns length. Preliminary design studies show that a total number of 1.5 $\times$ 10^{8} antiprotons will be produced within the phase space acceptance of the subsequent magnetic separator and the collector ring (CR). The production target will be irradiated with the primary beam with a repetition rate of 0.2 Hz and target survival in these experiments is an extremely important issue. In fact the same target has to be used over a period of about 6 months.

To calculate the energy loss by protons and all the secondary particles, particle interaction and transport Monte Carlo code, FLUKA [1] has been used which provides a three dimensional energy deposition profile along the proton trajectory in the production target. A cylindrical iridium target with a length of 15 cm and a radius of 1 cm has been used and the data obtained by the FLUKA code has been coupled to a two-dimensional hydrodynamic code, BIG2 [2], to study thermodynamic and hydrodynamic response of the production target. Different phases of the target material are treated in BIG2 by using an equation of state (EOS) data generated by a semi-empirical model. Since the energy deposition is a three-dimensional problem whereas the BIG2 code is two-dimensional, we study the target behavior along the cross section at a specific point inside the target (point where maximum energy deposition occurs which is at L = 2.1 cm along the beam direction). The radius of the production target is considered to be 3 mm in these calculations.

We consider four different cases namely, Case I: N = 2.8 $\times$ 10^{13}, FWHM = 0.5 mm, Case II: N = 2.0 $\times$ 10^{13},FWHM = 0.5 mm, Case III: N = 2.8 $\times$ 10^{13}, FWHM = 1.0 mm and Case IV: N = 2.0 $\times$ 10^{13}, FWHM = 1.0 mm.

We have carried out numerical simulations for all the above cases using the BIG-2. In Fig. 1 and Fig. 1, respectively, we plot temperature and pressure at t = 25 ns vs target radius at L = 2.1 cm.

It is seen from Fig. 1 that the target will survive only with the beam parameters used in case IV because the temperature remains below the melting point of iridium. However, the induced pressure is about 16 GPa and it is important to study the effect of pressure waves on the target. Moreover, during the 5 sec interval between two successive experimental shots, substantial heat conduction will take place that will reduce the temperature and the pressure significantly. To study these effects, one needs to include heat conduction and elastic-plastic effects in the simulation model. The BIG2 code is currently being upgraded to include these effects. In addition to that, a 3D code is being equipped with the necessary physics to design a viable antiproton target.

(please contact: n.tahir@gsi.de).

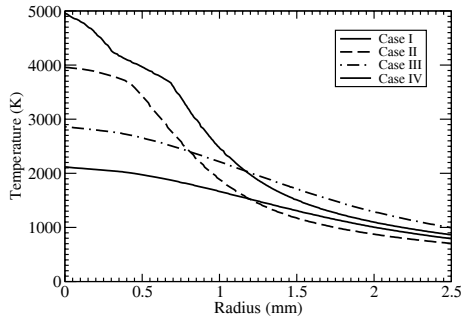

Figure 1: Temperature vs radius at L = 2.1 cm for different cases of beam parameters.

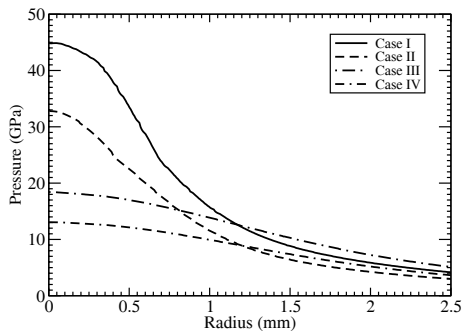

Figure 2: Pressure vs radius at L = 2.1 cm for different cases of beam parameters.

References

[1] A. Fasso et al., http:://arxivorg/abs/hep-ph/0306267 (unpublished).

[2] V.E. Fortov et al., Nucl. Sci. Eng. **123** (1996) 169.

* This work was supported by the BMBF and RFBR grant No: 06-02-04011-NNIOa, Russia

The Antiproton Separator of the FAIR Project

A. Dolinskii, B. Franzke, S. Ratschow, P. Spiller , M. Steck,
GSI, Darmstadt, Germany.

At the FAIR project 3 GeV antiprotons will be generated in collisions of 29 GeV protons with nucleons of an iridium target. Some parameters of the antiproton source are given in Table.1. The effective separation the protons and other secondary particles from the antiproton beam will be provided by an antiproton separator. The present magnet structure of the separator is shown in Fig.1.

Table 1. Parameters of the antiproton source.

Proton beam	
Kinetic energy	29 GeV
Maximum number of protons per bunch	2×10^{13}
Bunch length	25 ns
Transverse beam emittance h/v	3/1 mm mrad
Cycle time	10 s
Antiproton beam	
Kinetic energy	3 GeV
Momentum spread	±3%
Transverse emittance, h=v	200mm mrad
Yield per proton	5×10^{-6}
Maximum yield per cycle	1×10^{8}
Maximum possible stacking rate in the CR/RESR complex	3.5×10^{10} h^{-1}

The ion-optical characteristics of the separator should meet the requirements of the antiproton beam, the parameters of which are given in Table 1. The magnetic bending power is 13 Tm; the transverse acceptance is 240 mm mrad; the momentum acceptance is 6 %. These parameters require magnets with large aperture, especially in the horizontal plane (up to 400 mm). The ion optics of the antiproton separator has been calculated using CR-type bending, quadrupole and sextupole magnets [1]. The quadrupole and sexupole magnets have normal conduction coils. For the CR-type bending magnet a superferric H-type magnet design with a large useful aperture is foreseen [1]. The same type is considered to be used for the separator.

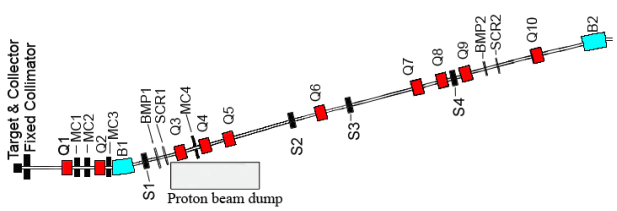

Fig.1. Layout of the antiproton separator. Abbreviations: Q1-10 – quadrupole magnets, B1-2 – dipole magnets, S1-4 – sextupole magnets, MC1-4 movable collimators, SCR1-2 fluorescene screens, BMP1-2 beam position and intensity monitor.

However, the radiation exposure of the superconducting coils might finally require normal conducting radiation-hard coils.

The large momentum spread of the antiproton beam requires compensating the chromaticity by sextupole magnets (S1–S4) placed at locations, where the dispersion is not zero. To study the expected losses of antiprotons coming out the exit of the target, and which are transported to the CR, simulation of particle tracking through the separator has been performed. The initial antiproton distribution just after the production target and subsequent magnetic horn focusing was simulated with the MARS code (Fig.2a).

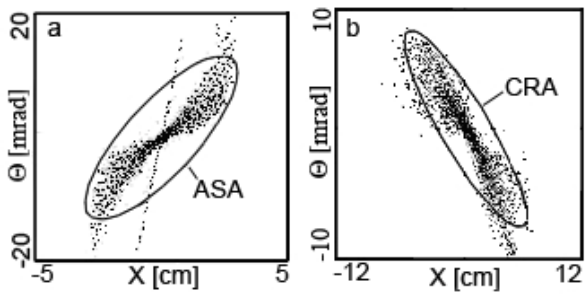

Fig.2. Antiproton distributions at: a) the production target after collecting by a magnetic horn, ASA – Antiproton Separator Acceptance; b) the matching point of the CR, CRA – Collector Ring Acceptance.

A similar antiproton distribution exists also in the vertical plane. In Fig.2a one can see also the phase ellipse, which corresponds to the separator acceptance at the target position. The ion optical parameters of this ellipse are $\varepsilon_x = \varepsilon_y$=240 mm mrad; $\beta_x \approx \beta_y \approx$4 m; $\alpha_x \approx \alpha_y \approx$-1.2. 13% of the antiprotons cannot be accepted in the separator acceptance. In Fig2b we present the antiproton distribution and phase ellipse corresponding acceptance at the matching point to the CR ring. This result was obtained after a particle tracking through the second order magnet system of the separator taking into account chromatic effects of the quadrupole magnets. In this simulation a sextupole correction has been applied. We observe that about 20% of antiproton particles are still outside of the ring acceptance. The chromatic effect of the quadrupole magnets gives additional 7% of antiproton losses, which can not be avoided with the present layout of separator magnet system shown in fig.1. Further improvement of the ion optical properties of the separator is required with respect to reduction of the particle losses.

References

[1] FAIR Baseline Technical Report, 2006.

Progress of the Super-FRS Project at FAIR*

M. Winkler[1,#], B. Achenbach[1], K.-H. Behr[1], M. Berz[2], D. Boutin[3], A. Brünle[1], H. Emling[1], H. Geissel[1], M. Gleim[1], W. Hüller[1], C. Karagiannis[1], A. Kelic[1], B. Kindler[1], E. Kozlova[1], H. Leibrock[1], Y. Litvinov[1], B. Lommel[1], S. Manikonda[2], J.A. Maruhn[4], G. Moritz[1], C. Mühle[1], G. Münzenberg[1], C. Nociforo[1], W.R. Plaß[3], A. Prochazka[1], C. Scheidenberger[1], H. Simon[1], R. Stieglitz[5], K. Sümmerer[1], N. Tahir[1], An. Tauschwitz[4], M. Tomut[1], P. Vobly[6], Z. Wang[3], H. Weick[1], J. Winfield[1], and M. Yavor[7]
[1]GSI, Darmstadt, Germany; [2]NSCL-MSU, East-Lansing, U.S.A.; [3]JLU Giessen, Germany; [4]JWGU Frankfurt, Germany; [5]FZ Karlsruhe, Germany; [6]BINP, Novosibirsk, Russia; [7]IAI RAS, St. Petersburg, Russia;

Introduction

In spring 2006 an important milestone could be achieved by the completion and issuing of the Technical Report for the Super-FRS [1] within the FAIR Baseline Technical Report (FBTR [2]). Technical refinements led to major changes in the ion-optical lattice of the Low-Energy Branch of the Super-FRS and to a rearrangement of the experimental setups using the Spectrometer and the Energy Buncher, respectively [3]. The conceptual designs and the prototype developments of various components for the Super-FRS are in progress,, i.e. the work has focused on high-power production targets, radiation resistant magnets, superferric magnets, and beam diagnostics, including a beam time for testing the first prototype beam detectors [4].

Layout of the Super-FRS

The Super-FRS consists of two separator stages; the Pre-Separator and the Main-Separator serving three experimental branches i.e. the High-Energy Branch (HEB), the Low-Energy Branch (LEB), and the Ring Branch (RB). Compared to previous designs [5] especially the layout of the LEB was modified considerably by turning the bending direction of the last dipole stage of this branch which leads to two major advantages:

1. Avoiding one intermediate image plane in front of this dipole stage and thus saving one quadrupole triplet.
2. An easier arrangement and access of the various experiments at this branch, which has to be seen in the context of the whole FAIR topology.

In addition the major experimental devices within this branch were rearranged, i.e. the energy buncher and the magnetic spectrometer, since the ion-optical function of both systems could be combined in one common magnetic stage [3]. The compromise led to a reduction of the maximum magnetic rigidity for the energy buncher from 10 to 7 Tm which causes small transmission losses, but the overall changes will lead to a considerably cost reduction. Figure 1 shows the present layout of the Super-FRS with its three branches including the energy buncher/ spectrometer at the exit of the Low-Energy Branch.

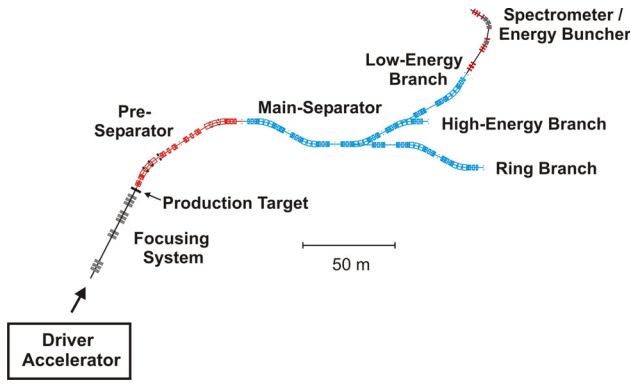

Figure 1: Layout of the Super-FRS with its three exit branches, including the new layout for the spectrometer/energy buncher behind the Low-Energy Branch [3].

High-Power Targets

Similar to the present SIS18/FRS/ESR facility, both slow and fast extraction from SIS100/300 will be used: the former, with typical extraction times of a few seconds, for counter experiments at the experimental caves, the latter for experiments with radioactive secondary beams in the storage rings where beams with a typical pulse length of ~ 50 ns are required. The optimum target thickness will range up to 8 g/cm^2 depending on the atomic number Z of the projectile and the selected energy.

Targets for slow-extracted beams

The development of a rotating graphite target wheel [2,5] was further advanced. It results in a conceptual design where several technical considerations are taken into account:

- The critical parameters (temperature, pressure/stress) of the chosen graphite grade must not be exceeded while irradiating the target material with heavy-ion beams.
- On the other hand, the operating temperature of the target material should be high to enhance the annealing of any possible radiation damage. Therefore, cooling is only foreseen by thermal radiation from the graphite surface.
- A maintenance concept must be developed that allows safe maintenance also after activation of the target assembly during long periods of high-intensity irradiation.

* Work supported by the European Community under the FP6 DESIGN STUDY (contract 515873 - DIRACsecondary-Beams).
#m.winkler@gsi.de

Liquid-metal target development

Since the highest intensity of fast-extracted ^{238}U beams with optimum focussing conditions will destroy any solid target in a single pulse, a feasibility study has been launched in order to investigate if a windowless liquid-Li jet could be used as a Super-FRS production target. This study is being conducted by the KALLA group at FZ Karlsruhe [6]. Several steps have been undertaken during the last two years (see Figure 2):

- A water loop has been constructedthat allows to investigate the flow conditions at the jet nozzle and the stability of a water jet with the required dimensions. At the same time, techniques for measuring velocity fields and jet shapes and numerical models to simulate them have been developed.
- The next step will consist of investigating the properties of a liquid-Na jet in a closed test loop. An important development is the Double-Layer Projection method (DLP) for detecting the shape of totally-reflecting surfaces.

As a third step, the liquid-Na loop can be converted to liquid Li. Important information can, however, be obtained already from the liquid-Na loop since its key flow parameters can be chosen to simulate the liquid-Li ones. Besides the experimental activities we continued also the theoretical studies concerning liquid Li targets which are summarized in [7] and [8].

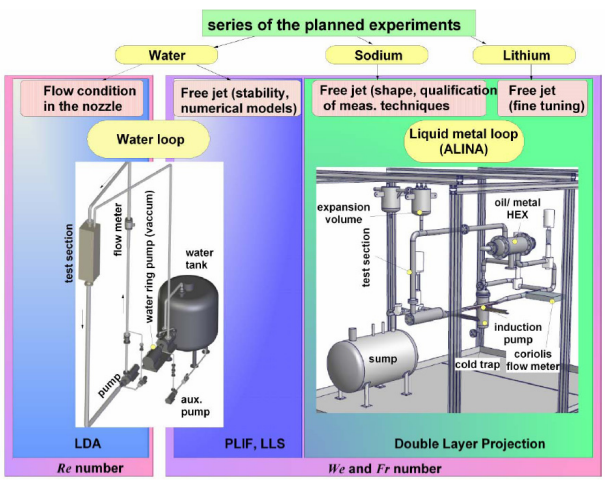

Figure 2: Schematic diagram of the different steps of liquid-metal target development for Super-FRS.

Magnet developments

The magnet developments for the Super-FRS are divided into two directions:

- Radiation resistant magnets must be used in the very first dipole stage where the production target and the beam dump will cause high radiation levels.
- All other dipole stages of the Super-FRS will be equipped with superferric magnets.

Radiation resistant magnets

The accumulated dose for magnetic elements located in the high-radiation areas of the Super-FRS is estimated to be in the order of 10 MGy/year. This requires to apply radiation resistant materials, i.e., all organic components cannot be applied. The most crucial parts in magnet design are the insulators and we consider to use Mineral Insulated Cables (MIC) [9]. A conceptual design study for a dipole magnet with an estimated overall weight of 120 tons was performed considering the possibility of remote controlled disassembling in case the magnet would fail after some years of operations.

Superferric magnets

Superferric magnets are iron dominated magnets but using super conducting coils. Thus they unify the advantages of both techniques, i.e. achieving a high field quality by iron shaping and high magnetic field gradients by applying high Ampere-turns. The specifications of the dipole magnet for the Super-FRS and the CR are very similar and thus we plan a common engineering design forfor both magnets. A prototype development is started together with the Chinese FAIR Group. A standard superferic multiplet of the Super-FRS will consist of a quadrupole triplet including correction coils and 2 sextupole magnets which are housed in one common cryostat (see Figure 3). The quadrupole magnets are characterized by very large apertures of ±190 mm and high field gradients of up to 10 T/m. A conceptual design study for such a multiplet was carried out and the next step will be the manufacturing of one prototype superferric quadrupole.

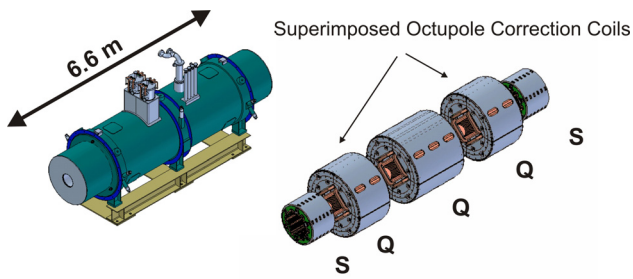

Figure 3: All magnets of a superferric multiplet for the Super-FRS will be housed in one common cryostat.

References

[1] H. Geissel et al., Nucl. Inst. & Meth. B 204 (2003) 71
[2] http://www.gsi.de/fair/reports/btr.html
[3] D. Boutin et al., this report.
[4] C. Nociforo et al., this report
[5] M. Winkler et al., GSI Report (2006-1) 47
[6] http://www.kalla.fzk.de/gsi
[7] A. Tauschwitz et al., this report
[8] N. Tahir et al., this report
[9] M. Winkler et al., IEEE Trans. on Appl. Supercond., Vol. 16 (2006) 415

Ion-Optical Design of an Energy Buncher and Spectrometer Stage for the Low-Energy Branch of the Super-FRS *†

D. Boutin ‡[1], C. Brandau[1,2,3], H. Geissel[1,3], S. Manikonda[4], H. Weick[3], M. Winkler[3], M. Yavor[5], D. Ackermann[3], M. Berz[4], J. Gerl[3], M. Gorska[3], G. Münzenberg[3], C. Nociforo[3], W.R. Plaß[1], Zs. Podolyák[2], J. Saren[6], and C. Scheidenberger[1,3]

[1]Justus-Liebig Univ., Giessen, Germany; [2]Univ. of Surrey, Guildford, UK; [3]GSI, Darmstadt, Germany; [4]NSCL-MSU, East Lansing, USA; [5]Inst. of Analytical Instrumentation, RAS, St. Petersburg, Russia; [6]Univ. of Jyväskylä, Finland

The Low-Energy branch of the new fragment separator Super-FRS [1], as part of the FAIR project, will be dedicated to experiments with exotic beams at low and intermediate energies (5 to 200 MeV/u) and stopped beams. For some experiments (HISPEC, DESPEC) a good mass identification is necessary, which requires a magnetic rigidity analyser. For others (MATS, LASPEC) the secondary beam will be implanted into a stopping cell which will have a finite volume, leading to the need of an energy (or range) bunching [2].

The present design is based on a two-stage combined spectrometer/buncher system. The first stage has a higher angular and momentum acceptance, but a lower resolution, optimized for the spectrometer mode. The second stage, in combination with the first stage, corresponds to the buncher mode which has been already discussed [2]. The two different optical modes are described in the following.

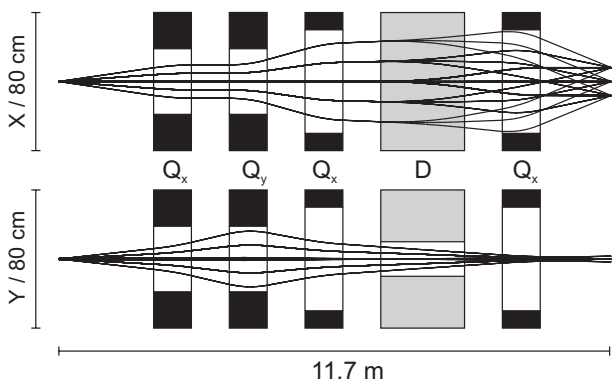

Figure 1: Optics of the spectrometer mode. The initial beam spot is (3×5) mm^2. Quadrupoles are indicated in black, dipoles in gray.

Spectrometer Mode

The first stage of the system is based on a QQQDQ spectrometer design. For the spectrometer mode, the first triplet controls the resolving power of the spectrometer, the position of the image plane and the transmission in the non-dispersive plane. The last quadrupole aims for a parallel dispersion at the image plane, located 1.5 m behind this magnet. The dipole has a deflection angle of 22.5 degrees and a maximum Bρ acceptance of 7.2 Tm. The characteristics of the system are the following: a momentum acceptance of $\pm$ 10 %, a resolving power of 1157 (with a 1 mm object size), and a corresponding angular acceptance of 40 (30) mrad in the dispersive (non-dispersive) direction. The optics of this mode is shown in Fig.1. The quadrupoles have an aperture radius of either 19 cm (Super-FRS type) or 30 cm. It is planned that the spectrometer can be rotated around a secondary target.

Buncher Mode

The system displayed in Fig.2 for the buncher mode is very similar to the system described in [3]. The main difference is that the maximum accepted Bρ has been reduced to 7.2 Tm. This allows for the reduction of field constraints on the quadrupoles, especially for large aperture ones. Further calculations are being performed to optimize the system for experimental requirements.

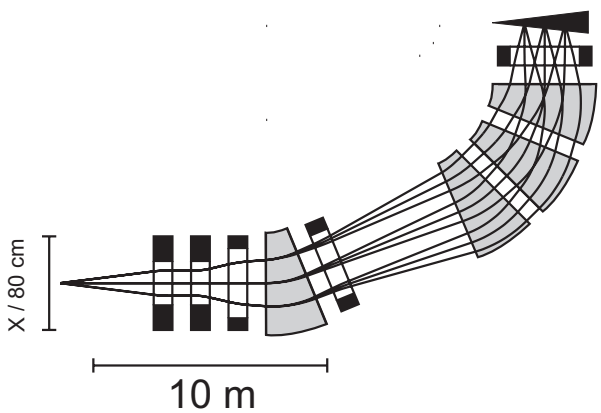

Figure 2: Optics of the buncher mode (view from the top). The first part of the system corresponds to the one described for the spectrometer mode.

References

[1] H. Geissel *et al.*, Nucl. Inst. and Meth. in Phys. Res. B204 (2003) 71.

[2] C. Scheidenberger *et al.*, Nucl. Inst. and Meth. in Phys. Res. B204 (2003) 119.

[3] FAIR Baseline Technical Report, available at http://www.gsi.de/fair/reports/btr.html

* Work supported by European Community under the FP6 program DESIGN STUDY (contract 515873 - DIRACsecondary-Beams)

† Work supported by the GSI F+E program (GI/ME2)

‡ d.boutin@gsi.de

Longitudinal Accumulation of Rare Isotope Beams in the NESR

T. Katayama[1], T. Kikuchi[2], D. Möhl[1,3], C. Dimopoulou *[1], P. Beller[1], B. Franzke[1], U. Laier[1], F. Nolden[1], G. Schreiber[1], and M. Steck[1]

[1]GSI, Darmstadt, Germany; [2]Utsunomiya University, Japan; [3]CERN, Geneva, Switzerland

A high intensity of rare isotope beams is required by the internal experiments in the NESR [1] and in particular by the electron-ion collider mode [2]. It is therefore planned to stack the RIBs longitudinally at injection energy i.e. in the range 100-740 MeV/u. The stacking will be supported by electron cooling.

The favored method of longitudinal beam accumulation is based on a barrier bucket RF system in combination with electron cooling. A broadband barrier bucket (BB) system is foreseen, which provides single sine waves of 200 ns period (5 MHz). Four cavities, each driven by a 3.5 kW solid state amplifier, result in a total voltage of 2 kV. According to dedicated beam dynamics simulations [3], this voltage is sufficient to compress cooled beams. The stacking cycle time, i.e. the time between 2 successive injections, could be about 2 s, provided that the quality of the injected pre-cooled beam from the CR allows cooling times below 1 s. This is demonstrated in Fig. 1 for a beam of $^{132}Sn^{50+}$ ions at 740 MeV/u (0.9 μs revolution period). At t=0 a bunch is injected between the BB sine pulses of 100 ns period (10 MHz). The beam immediately debunches because the barrier voltage is not sufficient to capture the particles. The BB pulses are decreased and switched off at t=0.2 s, while the beam is being continuously cooled. For the injected beam, an initial emittance of 0.5 mm mrad and momentum (energy) spread of 1.3×10^{-3} (1.5 MeV/u) was assumed. They correspond to the 2σ design values for the pre-cooled beam in CR, taking into account the transfer through the RESR to the NESR as well as an additional 30% increase of the longitudinal emittance due to diffusion processes. Parkhomchuk's formula [4] is used for the cooling rate, for an electron beam density of $3.2 \times 10^8 \mathrm{cm}^{-3}$ (1 A, 5 mm beam radius), a magnetic field strength of 0.2 T in the cooling section and an effective electron velocity corresponding to magnetic field misalignments of 5×10^{-5}. The resulting cooling time is about 0.8 s. Then, the BB pulses are adiabatically introduced into the beam and increased to 2 kV. One stays stationary while the other is shifted in phase to compress the cooled beam. At t=2 s a new bunch is injected. The process will be repeated until the required intensity of the accumulated beam is reached. With such stacking cycle times the experiments in the NESR can take full advantage of the planned cycle time of 1.5 s of SIS100, where the primary heavy ion beam is accelerated.

As an alternative, a h=1 RF system for bunching of the circulating beam and injection of a new bunch onto the unstable fixed point in longitudinal phase space is considered [5]. The RF voltage is raised so as to confine the bunch in a small fraction of the ring circumference. A new bunch is injected onto the free part of the circumference. Then the RF voltage is decreased to let the beam debunch. Continuous application of electron cooling maintains the stack and merges it with the freshly injected bunch. The present choice is a ferrite-filled RF cavity with a peak voltage of 15 kV in c.w. operation and with a frequency swing in the range 1-2.6 MHz [1]. It should be possible to modify the cavity for operation at frequencies down to 600 kHz, and thus cover the full range of injection energies at h=1, with a moderate peak voltage up to 1 kV.

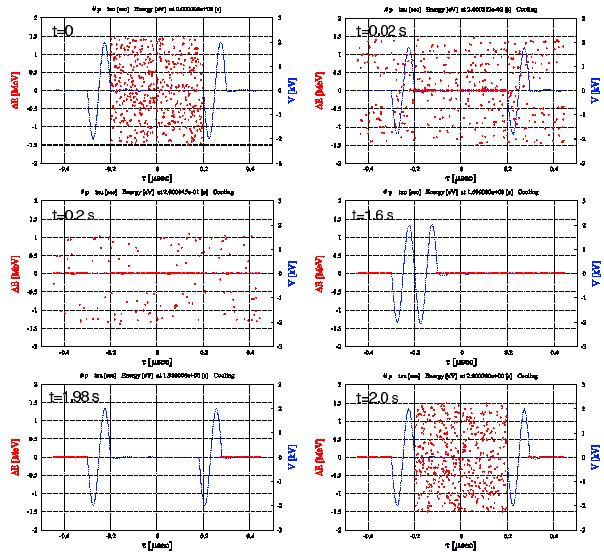

Figure 1: Accumulation of the 740 MeV/u $^{132}Sn^{50+}$ beam by Barrier Buckets and continuous application of electron cooling. Solid lines: barrier voltage; Dots: particle distribution in the longitudinal phase space. Top left to bottom right: beam injection, debunching, cooling, application of the BB pulses, compression of the stack by moving one barrier, new injection into the gap between the barriers.

These feasibility studies show that for both stacking methods the maximum useful accumulation time is limited by the lifetime of the ion beam, either due to nuclear decay or due to recombination with electrons of the cooling system. Machine experiments are prepared in the ESR as a proof of principle and for comparison of the two schemes.

References

[1] FAIR Baseline Technical Design Report, GSI (2006).

[2] I.A. Koop et al., Proc. of the 8^{th} Europ. Part. Acc. Conf., Paris (2002) 620.

[3] T. Katayama, private communication, unpublished reports.

[4] V.V. Parkhomchuk, Nucl. Instr. Meth A 441 (2000) 9.

[5] D. Möhl, private communication, unpublished reports.

* c.dimopoulou@gsi.de

Stochastic Cooling Hardware Developments for FAIR*

F. Nolden[1], S. El Hanaoui[1], U. Jandewerth[1], I. Nesmiyan[1], P. Petri[1], C. Peschke[1], and M. Steck[1]
[1]GSI, Darmstadt, Germany

Here we report on the development of slotline structures, optical notch filters, and cryogenic testing.

The development of slotline structures [1] was continued. Models were built in order to improve the sensiitivity per unit length, with a flat response in the 1-2 GHz band. They are measured on a movable test stand with a near-field field probe. The measurements are compared to model calculations, and the model geometry is optimized experimentally as soon as field models turn out to be of too small accuracy. This optimization process will be finished in spring 2007, when tests of several slotlines in a row are planned. Figure 1 shows the field probe above a test slotline.

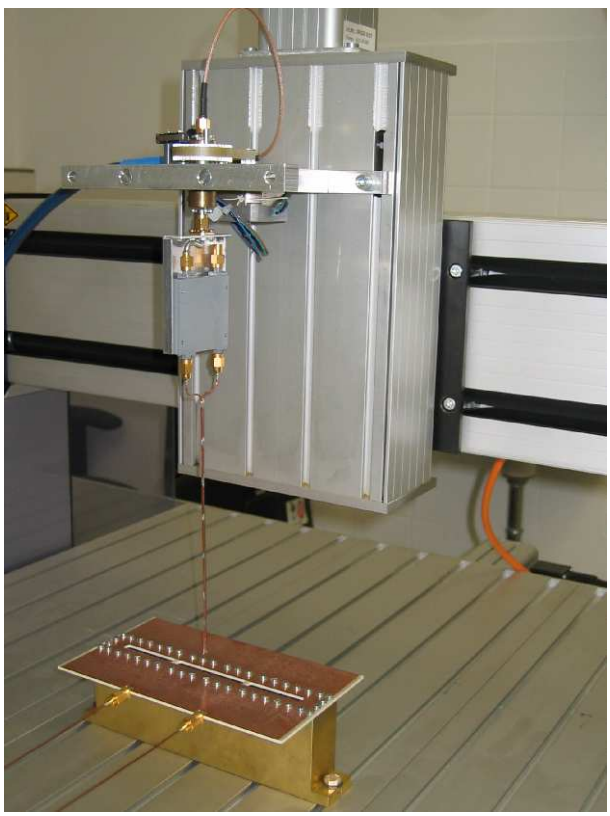

Figure 1: Field measurement of slotline structure

A novel optical notch filter is being developed. The splitting into two different lines is performed optically instead of using microwave power splitters in order to reduce asymmetry (Fig. 2). Therefore two optical receivers are necessary before signal subtraction in a microwave 180^0 hybrid. A first test was successful, the necesssary correction equalizers will be relatively easy to design. Fig. 3 shows a preliminary test assembly without equalizers and with no temperature stabilization, which has been added meanwhile.

It is planned to install a prototype into the ESR. A substantial reduction of the equilibrium nomentum spread is expected. A theoretical study of notch filter cooling and Palmer cooling of multi-component heavy-ion beams was published [2].

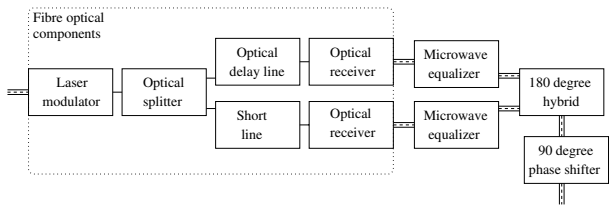

Figure 2: Schematic diagram of novel optical notch filter

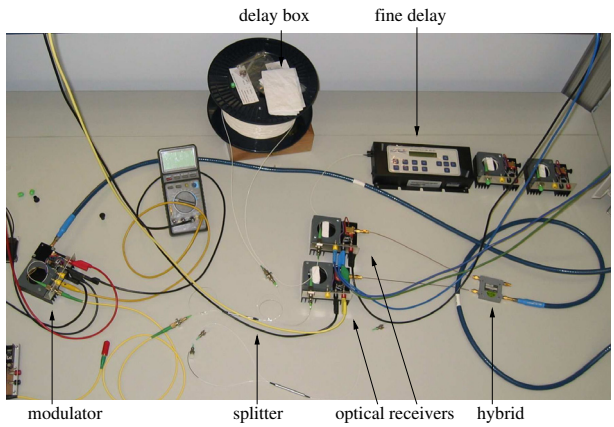

Figure 3: First test of optical notch filter

A cryogenic test stand has been built into a tank inherited from CERN. Test structures and preamplifiers can be cooled down inside the tank to temperatures below 20 K, in order to test the cryogenic pick-up tanks which will be developed for FAIR.

References

[1] C. Peschke, F. Nolden, and L. Thorndahl, Pick-up and Kicker Electrodes for the CR, Cool05 Workshop on Beam Cooling and Related Topics, AIP Conf. Proc. 821 (2005), 221-225

[2] F. Nolden, C. Peschke,and L. Thorndahl, On Stochastic cooling of multi-component fragment beams, Nucl. Inst. Meth. A 564 (2006) 87-93

* Work supported by EU, EURONS contract No. xyz.

Investigation of Slotted Slow-Wave Structures for Stochastic Cooling

T. Lau[1], T. Weiland[1], and F. Nolden[2]

[1]Technische Universität Darmstadt, Institut für Theorie Elektromagnetischer Felder (TEMF); [2]GSI, Darmstadt, Germany

In the new international project FAIR at GSI stochastic cooling of secondary particles will be an important technical element. Therefore, an investigation of kicker and pickup slow-wave structures similar to the devices investigated by Faltin [1] and McGinnis [2] have been performed with the help of the simulation package CST PARTICLE STUDIO™ [3].

Slow-wave structures as pickups are more sensitive in the region of a few Gigahertz than broad band loops. Especially, they don't need binary combiner boards and thus prevent the associated problems with them. The working

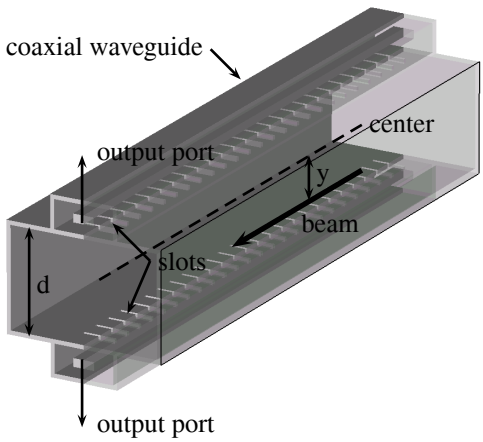

Figure 1: Schematic drawing of a slow-wave pickup with coaxial output waveguides.

principle of slot coupled slow-wave structures as pickup is as follows: The electromagnetic energy from the wake field of the beam couples via the slots into the output waveguides. Beside the coupling, the slots also reduce the phase velocity of the output waveguide which is greater than the speed of light. If the phase velocity in the output waveguides coincides with that of the beam in the beam pipe, than the electromagnetic waves emerging from the slots interact constructively in the output waveguides and a large signal is obtained. The signal difference of the two output waveguides is a measure for the transverse beam offset.

Following [2] the transverse impedance for the slow-wave pickup structures is defined by

$$Z = \frac{P}{I^2 (y/d)^2}, \tag{1}$$

with P the total power out of the output of the difference port, I the beam current, d the transverse dimension of the beam pipe and y the transverse beam offset.

In a first step the device investigated by McGinnis (see table 1) was simulated to verify the numerical simulation. Unfortunately, this structure is designed for highly relativistic beams and the coupling for slower beams, e.g. $\beta = 0.75$, is not efficient. This is seen in Fig. 2 where the obtained impedances for $\beta = 1$ and $\beta = 0.75$ are shown. For $\beta = 0.75$ the loss in impedance is roughly three orders in magnitude higher than in comparison to $\beta = 1$, because the phase velocity of the output waveguide is not matched with that of the beam and the spectrum is shifted. In order to adapt this structure for beam velocities typical used at GSI the geometry is currently redesigned. For this purpose the dimensions and the coupling between the output waveguide and the beam pipe are investigated.

height of output waveguide	20.32 mm
width of output waveguide	40.64 mm
height of beam tube	40.64 mm
width of beam tube	40.64 mm
thickness of slots	0.5 mm
length of slots	17.526 mm
width of slots	2.032 mm
distance of slots	3.048 mm
number of slots	50

Table 1: Dimensions of McGinnes type structure.

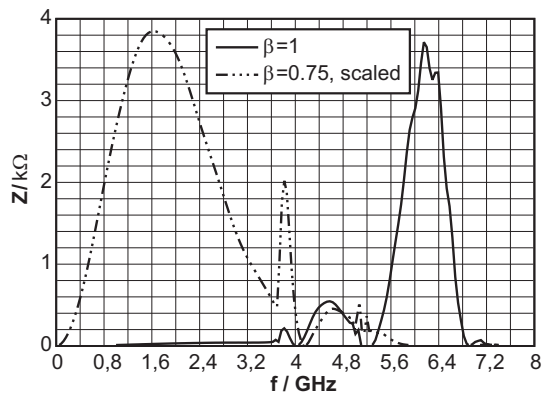

Figure 2: Impedances for the investigated structure. For $\beta = 0.75$ the result is scaled by a factor of 500.

References

[1] L. Faltin, "Slot-Type Pick-Up and Kicker for Stochastic Beam Cooling", Nuclear Instruments and Methods, vol. 148, p. 449, 1978

[2] D. McGinnis, "Slotted Waveguide Slow-Wave Stochastic Cooling Arrays", PAC 1999, 1999, New York

[3] CST GmbH, "CST PARTICLE STUDIO User Guide", CST GmbH, Darmstadt, Deutschland

Studies of coherent transverse beam stability for the FAIR synchrotrons

V. Kornilov, O. Boine-Frankenheim
GSI, Darmstadt, Germany

Collective instabilities are a potential limiting factor for the performance of the FAIR rings at GSI Darmstadt. Here, we discuss results of numerical investigations for SIS 100 and for the SIS 18 Upgrade together with experimental investigations in the SIS 18 synchrotron.

Within our experimental investigations, the first measurement of the transverse Beam Transfer Function (BTF) in SIS 18 were performed [1] on October 25, 2006. The BTF is obtained by exciting a beam with a periodic signal and measuring the resulting beam response (amplitude and phase). The BTF signal contains a wealth of important information on beam and machine properties. The beam response was measured with the Schottky probe and compared with the excitation using a network analyzer in a frequency sweep.

The inversed BTF, represented in the complex plane, gives the stability diagram, which provides threshold of instabilities. Figure 1 presents raw data (black line) for the stability diagram in the impedance plane $V + iU \propto Z^{\perp}$, measured for the slow wave at the harmonic number $m = 24$. The experimental stability diagram is compared with three theoretical distributions. We conclude that the Gaussian distribution is the most suitable one to describe the particle momentum distribution. Using these BTF measurements, the vertical tune, the momentum spread and the chromaticity were obtained too [1].

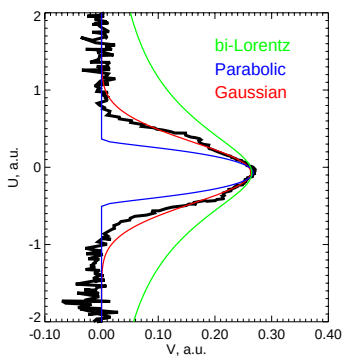

Figure 1: Measured (black line) and theoretical stability diagrams, which are inversed BTF

Considering our numerical and analytical investigations, firstly we note that Landau damping does not provide sufficient transverse stabilization in the SIS–synchrotrons, which is due to weakly-relativistic beams and small beam aperture/radius ratios. Other damping mechanisms, as due to nonlinearities (amplitude-dependent incoherent tune) may then become decisive for the FAIR rings. To the incoherent tune spread can contribute internal effects (nonlinear space charge) or external nonlinearities (e.g., octupoles in the lattice). This tune spread provides nonlinear Landau damping, which influences the collective beam motion. Additionally, there exists a complex interplay between internal and external nonlinear damping mechanisms. So far, only a few analytical works have been done and there is still some uncertainty about nonlinear Landau damping.

For the first step, we use the approach from [2], where a dispersion relation is constructed,

$$\int \frac{\mathrm{d}\psi_0}{\mathrm{d}a} \frac{[\Delta Q_{\mathrm{coh}} - \Delta Q_{\mathrm{inc}}(a)]a\mathrm{d}a}{\Omega/\omega_0 - (Q_0 + \Delta Q_{\mathrm{inc}})} = 1 \,, \qquad (1)$$

where ΔQ_{coh} is the coherent tune shift (i.e., $\propto Z^{\perp}_{\mathrm{coh}}$), $Q_0(a)$ includes only tune shifts due to external nonlinearities and $\Delta Q_{\mathrm{inc}}(a)$ is the tune shift induced by internal effects only (here, nonlinear space-charge).

As a computational tool accounting nonlinear beam dynamics, the particle tracking code `PATRIC` [3] is used. Series of simulations have been performed [4] for varying both $\mathcal{R}e(Z^{\perp})$ and $\mathcal{I}m(Z^{\perp})$ to study comprehensively the stability properties.

Our first comparison is for the case of internal effects alone. Simulations with the code `PATRIC` did not show any damping [4], which supports the prediction of the dispersion relation Eq. (1) [2]. We conclude that the incoherent tune spread due to internal effects does not provide any stability. In the case of external nonlinearity alone we found an agreement between Eq. (1) and `PATRIC` simulations.

Next, we consider the combination of both nonlinearities. According to Eq. (1), an addition of the nonlinear space-charge effect to the external nonlinearity results in a strong enhancement of the stability, whereas the size of the stable area remains unchanged in $\mathcal{R}e(Z^{\perp})$ and greatly enlarges in $\mathcal{I}m(Z^{\perp})$. Our simulations [4] confirm the enlargement of the stability along $\mathcal{I}m(Z^{\perp})$, but they disagree regarding the extent of the stability area in $\mathcal{R}e(Z^{\perp})$. Reasons for the discrepancy may be connected with the facts that the dispersion relation Eq. (1) is a one-dimensional approximation of the 2D problem and the approach of Ref. [2] is based on heuristic argumentation.

References

[1] V. Kornilov, O. Boine-Frankenheim, W. Kaufmann, P. Moritz. GSI-Acc-Note-2006-12-001, GSI Darmstadt, (2006)

[2] D. Möhl, H. Schönauer. Proc. IX Int. Conf. High Energy Acc., Stanford, 1974, p. 380 (1974)

[3] O. Boine-Frankenheim, V. Kornilov. Proc. of ICAP2006, 2-6 Oct., Chamonix Mont-Blanc, (2006)

[4] V. Kornilov, O. Boine-Frankenheim and I. Hofmann. Proc. of ICFA-HB2006, May 29 - June 2, Tsukuba, Japan, (2006)

Studies of non-linear and collective effects relevant for HESR*

S. Sorge[†1], O. Boine-Frankenheim[1], and A. Lehrach[2]
[1]GSI, Darmstadt, Germany; [2]FZ Jülich, Germany

Introduction

The HESR will be optimized to satisfy high beam quality requirements, i.e. $\Delta p/p \sim 10^{-5}$ for the envisaged high antiproton currents. Cold beams react very sensitive to external perturbations and the possible heating of the beam due to them. In this work the perturbation of the beam due to the influence of the electron cooler acting as a non-linear lens and intra-beam scattering (IBS) are the subject of detailed investigations, using particle tracking codes.

Nonlinear-lens effect of the electron cooler

The space charge field of the electron beam acts as a non-linear lens, as it was observed in CELSIUS [1]. The resulting tune spread together with the induced resonance lines can lead to 'electron heating'. For that reason, we started to investigate the influence of the electron lens using the MAD-X tracking code. With MAD-X we can study electron-lens effects using the full HESR lattice. To extend MAD-X for this purpose, the `beambeam` element, being created to describe the interaction between two particle beams in a collider, was extended by two electron current density profiles, a trapezoidal one having a flat top, and a hollow parabolic one. In particular, the flat top profile is characteristic for an electron cooler.

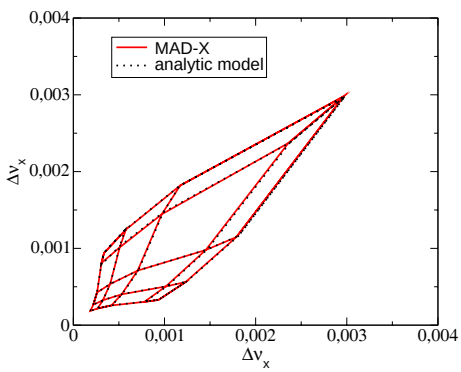

Figure 1: Footprints of the tune deviation due to an electron beam with trapezoidal radial current profile. A bare tune $\nu_x = 12.16, \nu_y = 11.23$ and a charge corresponding to an electron current $I_e = 0.2$ A and a cooler length $L_{\rm cool} = 15$ m (see table 2.11.11 of [2]) were used.

In a first step, calculations for testing and validating the extended `beambeam` element were performed. One set of machine tunes, $\nu_x = 12.16, \nu_y = 11.23$, was used. The non-linear tune shifts and tune footprints obtained from MAD-X for a simplified lattice containing a single δ-like `beambeam` kick were compared with the results of the analytical work in Ref. [1]. A very good agreement was found, as the example shown in figure 1 demonstrates.

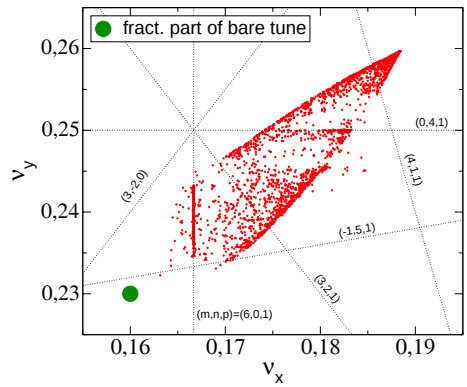

Figure 2: Tune footprints calculated with a single electron kick (left) and a sequence of 15 electron kicks (right) with trapezoidal density. A bare tune of $\nu_x = 12.16, \nu_y = 11.23$ and a charge corresponding to $I_e = 1$ A and $L_{\rm cool} = 30$ m were used. These values taken from table 2.11.11 of [2] denote maximal possible values.

In addition, resonance excitation due such a nonlinear-lens kick was analysed. Figure 2 shows a tune footprint calculated for a trapezoidal electron density in the cooler beam.

IBS measurement using transverse beam echoes

The measurement of transverse beam echoes is a possible method to determine diffusion processes like intra-beam scattering (IBS). This was done in RHIC for conditions similar to those in HESR. We evaluated these echoes using a tracking code. To include IBS, we used a strongly simplified model applying a diffusion coefficient being constant in space and time. We found, that IBS rates being much larger than expected are necessary to explain the decrease of the echo amplitude due to IBS. The results were presented at the 9th ICAP conference in Chamonix, see [3].

References

[1] V. Ziemann, TSL-note 98-43, Uppsala, Sweden, 1998, and Nucl. Instr. and Meth. A, **556** (2006) 45

[2] FAIR Technical Baseline Report, GSI, Darmstadt, 2006

[3] S. Sorge *et al.*, "Analysis of measured transverse beam echoes in RHIC", Proc. of the ICAP, Chamonix, France (2006)

*Work was supported by EU design study (contract 515873-DIRACsecondary-Beams

[†] S.Sorge@gsi.de

Kicker Coupling Impedances: Comparison between simulations and experimental measurements

E. Arévalo, B. Doliwa, and T. Weiland
Technische Universität Darmstadt, Institut für Theorie Elektromagnetischer Felder (TEMF)

Here we report numerical results on the window-frame SIS-100 injection device at GSI. Details about the computational approach and definitions of the longitudinal ($Z_{||}$), horizontal (Z_x) and vertical (Z_y) impedances can be found in Refs. [1, 2, 3, 4] and references therein. We merely remark that the modeling and discretization were carried out in CST MICRO WAVE STUDIO ®[5], whereas the simulations relie upon a combination of Python and C++ code.

The GSI SIS-100 Kicker

The fast kicker modules SIS-100 Kicker represent a potential source for beam instabilities in the planned Facility for Antiproton and Ion Research FAIR. Here, Z_x is dominated by the inductive coupling of the beam to the pulse-forming network (PFN). We note that the behavior of Z_x can be described by the parametrization $Z_x = a + b/(c + Z_g)$, where the unknown terms a, b, and c are estimated by three frequency sweeps with different values of of the PFN impedance Z_g. An excellent agreement has been observed between simulations and parametrization for a wider frequency range and different values of Z_g [1].

We have also considered the influence of the particle velocity, $v = \beta c$ on Z_x. Notice that it is possible to show analytically that $Z_x \sim \beta$ for small ω. Since the excitation current is proportional to $\exp(-ik_z z)$, where $k_z = \omega/\beta c$, the scaling $Z_x \sim \beta$ is expected as long as $k_z z L \ll 1$, where L is the length of the kicker module. This behavior is observed in Fig 2. Curves for $\beta \geq 0.5$ superimpose after division by β. For lower β, i.e. $\beta = 0.2$, this scaling rule breaks down. This shows the necessity to perform separate simulations for different β, and then interpolate the values to consider all possible cases.

It is also worth to mention that in order to validate our code we have simulated an extraction kicker at the Spallation Neutron Source (SNS) accumulator ring from which experimental measurements are available [6]. Here, we have observed that our simulations predict quantitatively well the behavior of the experimental vertical impedance [3, 4].

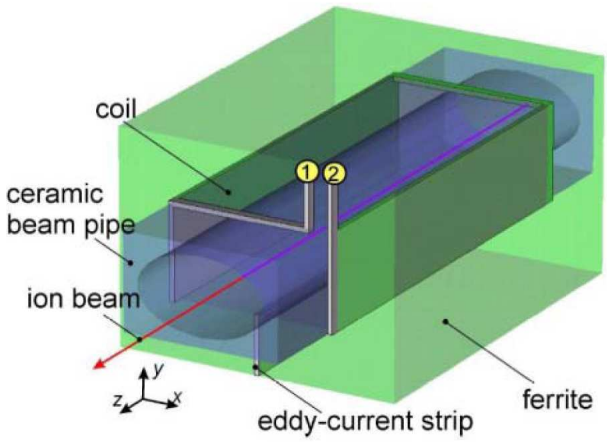

Figure 1: SIS-100 Kicker: The ceramic beam pipe is of elliptical cross section. Eddy-current strips have been added to reduce $Z_{||}$ and Z_y. Metal parts and model boundary are assumed to be perfectly conducting. The PFN is applied between the terminals (1) and (2).

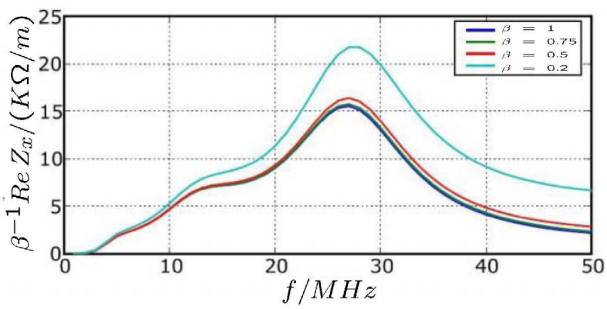

Figure 2: Real part of Z_x/β for $Z_g = \infty$ at different beam velocities $v = \beta c$ with $\beta = 1, 0.75, 0.5$, and 0.2.

References

[1] B. Doliwa, H. De Gersem, T. Weiland, *Numerical Impedance Calculations for the GSI SIS-100/300 Kickers*, Proceedings of the 10th European Particle Accelerator Conference (EPAC 2006), June 2006, pp. 2179-2181.

[2] B. Doliwa, H. De Gersem, T. Weiland, T. Boonen, *An Optimized Electromagnetic 3D Field Solver for Frequencies Below the First Resonance*, Special Issue of IEE Proceedings Science, Measurement and Technology on Computational Electromagnetics, November 2006.

[3] E. Arévalo, B. Doliwa, T. Weiland, *Transverse coupling impedance of a ferrite kicker magnet: Comparison between simulations and measurements*, Proceedings of the 9th International Computational Accelerator Physics Conference (ICAP 2006), October 2006.

[4] B. Doliwa, E. Arévalo, T. Weiland, *Numerical Calculation of Kicker Coupling Impedances*, submitted for publication (2007).

[5] CST GmbH. Bad Nauheimer Str. 19, 64289 Darmstadt.

[6] D. Davino and H. Hahn, "Improved analytical model of the transverse coupling impedance of ferrite kicker magnets", Phys. Rev. ST Accel. Beams 6 (2003) 012001.

Status of FAIR RF System Development*

H. Klingbeil, P. Hülsmann
GSI, Darmstadt, Germany

OVERVIEW

Several new types of RF systems have to be developed for FAIR [1]. The following list of systems represents the latest planning:

- SIS12/18 h=2 system
- SIS12/18 bunch compressor
- SIS100/300/NESR accelerating system
- SIS100 barrier bucket system
- SIS100 bunch compressor
- CR debuncher system
- NESR high harmonics system
- NESR barrier bucket system

For the RESR, it is planned to use one of the existing SIS18 ferrite cavities.

In the following, a status will be given for each of these systems. Since not all development projects of the GSI RF department are directly related to a specific cavity system, a second section is dedicated to these cavity-independent projects.

CAVITY SYSTEM DEVELOPMENT

The development of the SIS12/18 h=2 system is funded in the scope of the EU FP6 construction program. The starting point was a concept worked out by GSI and a detailed design study performed by Hitachi. In the first phase of the EU FP6 task, a detailed technical concept document based on a two-unit solution was completed [2]. Since the technological effort and the infrastructure requirements for such a system are very high, it was decided to realize a three-unit system. This approach relaxes the requirements for each individual unit, and the overall power consumption is reduced. Detailed specifications are currently being worked out, and first call for tenders are prepared.

The system integration of the SIS12/18 bunch compressor system is in progress. Installation in the synchrotron is scheduled for the long shutdown period at the end of 2007.

For the SIS100/300/NESR accelerating system a detailed design study has been completed by BINP [3]. Currently, the manufacturing documents are under preparation. It is planned to initiate a call for tenders for the first prototype system in 2007.

For both barrier bucket systems (SIS100 and NESR), a technical concept is available [4]. A broadband test cavity will be realized in 2007 and 2008 in order to reduce the technical risk for the NESR barrier bucket system.

The detailed design of the SIS100 bunch compressor system will not be started before reliable measurement data of the SIS12/18 bunch compressor are available. This strategy was chosen due to resource and risk limitations.

For the CR debuncher system, the detailed status is presented in a different contribution of the GSI annual report at hand.

A first design concept for the NESR high harmonics cavity is available.

GENERAL RF PROJECTS

One of the main challenges of the FAIR project for the RF department is the handling of the large variety of systems with the limited resources. Therefore, standardization and maintenance aspects play an important role [5].

In the scope of the project "Digital RF control systems", many electronics and software components have been developed based on FPGA and DSP technology. The main design criterion was modularity, and it will therefore easily be possible to use these components in various FAIR RF control systems.

An "RF maintenance and diagnostics" project has been initiated. One objective of this project is to allow remote management of the firmware of all programmable components. Furthermore, it will be possible to collect and analyze diagnostics information from any relevant RF component on site.

The status of the "Bunch Phase Timing System" project BuTiS is presented as a separate contribution of the GSI annual report at hand.

References

[1] H. H. Gutbrod (Editor in chief): "FAIR Baseline Technical Report", Volume 2, March 2006.
[2] P. Hülsmann, S. Schäfer, M. Zelensky: "Technical Concept h=2 Cavity", Rev. 1.4, 08.11.2006.
[3] V.S.Arbuzov, Yu.A. Biruchevsky, E.I.Gorniker, Ya.G. Kruchkov, S.A. Krutikhin, G.Ya. Kurkin, V.N. Osipov, V.M. Petrov, A.M. Pilan: "Intermediate Specification of the FAIR SIS100/300 and NESR RF System", December 2006.
[4] G. Schreiber: "Technical Concept Barrier Buckets", Rev. 0.92, 18.01.2006.
[5] H. Klingbeil et al.: "Standardization Aspects of FAIR RF Systems", Rev. 0.90, 13.09.2006.

* Work partly funded by EU, FP6 contract No. 515873 and 515876.

CONCEPTUAL DESIGN OF THE COLLECTOR RING RF SYSTEM

U. Laier, P. Hülsmann
GSI, Darmstadt, Germany

This paper will give a brief introduction to the design sketch of the RF system intended to operate in the Collector Ring (CR) [1] of FAIR [2]. The requirements imposed on the system are summarized and a conceptual design of this RF system is presented. More details can be found in [3-5].

Requirements

The CR is designed for fast precooling of rare isotopes and antiproton beams. Prior to stochastic cooling the relative momentum spreads of the incoming beams have to be reduced from 3% (antiprotons) and 1.5% (rare isotopes) down to 0.7% (antiprotons) or 0.4% (rare isotopes) respectively. This is achieved by means of a two step process. First, the bunch is rotated in phase space by a quarter of a synchrotron period in a mismatched bucket; afterwards it is adiabatically debunched. Additionally, the RF system at hand will also be used to rebunch the beam to allow a bunch to bucket transfer from CR to a subsequent ring.

According to single particle beam dynamic simulations [4] the CR debuncher RF system has to operate between 1.18 MHz and 1.38 MHz. At 1.18 MHz it has to provide a total voltage of 400 kV in pulsed and 20 kV in continuous operation. All changes in the operational frequency will be slow (timescale 5 min). No in situ vacuum system baking is needed. The total installation length amounts to five times 2 m. The beam pipe of the cavities must have a cylindrical diameter of at least 150 mm.

The RF system will be installed in a two stage process, the first stage only accounts for half of the cavities (200 kV pulsed, 10 kV continuous), resulting in a reduced capture range of the RF system.

System Design

It is planned to build inductively loaded coaxial resonators similar to the SIS18 bunch compressor [6]. These cavities will allow pulsed as well as continuous operation. When choosing the material of the magnetic cores to be used, one has to keep in mind that due to the limited installation length a gradient of 40 kV/m has to be achieved. Furthermore, it is imperative to account for fast changes of the gap voltage associated with the bunch rotation. Due to the limited maximum flux density and the fairly high Q value, the use of ferrite material was ruled out.

It is planned to use VitroVac 6030F, an amorphous magnetic alloy. This material, which was used to build the SIS18 bunch compressor, combines a fairly high μQf value with a considerably low Q value and it is able to withstand sufficient magnetic flux to allow the required gradients.

To fit the cavities in the available installation length ten resonators each with a length of less than 1 m will be built. Figure 1 shows, how the cavity will be driven by a push-pull amplifier consisting of two TH555A tubes operating in class A. Each tube will be inductively coupled to one half of the cavity.

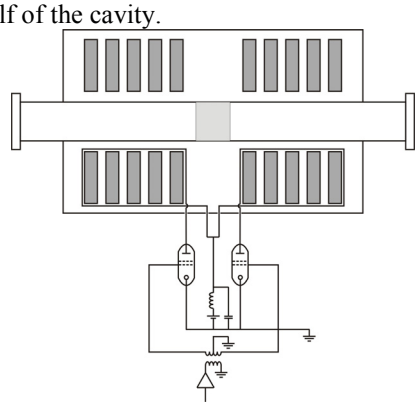

Figure 1: Sketch of cavity and amplifier.

Since no fast frequency changes are required and due to the broadband nature of the magnetic alloy it is possible to omit biasing of the ring cores. The slow frequency shifts will be obtained by remotely increasing the capacitance in parallel to the gap.

The design presented here relies on ten of the aforementioned ring cores (inner radius 145 mm, outer radius 313 mm, thickness 25 mm). This results in a reasonable capacitance limit of 500 pF to account for core, gap and stray capacitances as well as tube capacitances. The shunt impedance amounts to about 1 kΩ leading to a cavity power demand of 800 kW in pulsed and 2 kW in continuous operation. The average power of 240 W per ring core will be removed using forced air cooling.

References

[1] F. Nolden, K. Beckert, P. Beller, U. Blell, C. Dimopoulou, A. Dolinskii, U. Laier, G. Moritz, C. Muehle, I. Nesmiyan, C. Peschke, M. Steck, *'The Collector Ring CR of the FAIR Project'*, Proc. of the EPAC2006, Edinburgh (2006).

[2] W. Henning et al., *'FAIR Technical Baseline Report'*, GSI Darmstadt (2006).

[3] J. Hottenbacher, P. vom Stein, *'FAIR CR Cavity Study Final Report'*, Conceptional Design Study performed by ACCEL, Bergisch-Gladbach (2006).

[4] U. Laier, *'Design Considerations of the RF Systems in the Collector Ring'*, GSI Darmstadt (2005).

[5] U. Laier, *'Design Considerations of the CR Debuncher RF System'*, GSI Darmstadt (2005).

[6] P. Hülsmann, G. Hutter, W. Vinzenz, *'The bunch compressor system for SIS18 at GSI'*, Proc. of the EPAC 2004, Lucerne, Switzerland.

BuTiS – Development of a Bunchphase Timing System

P. Moritz
GSI, Darmstadt, Germany

Overview

The precision Bunchphase Timing System (BuTiS) is required to synchronize the distributed rf accelerating cavities in the SIS100/300 synchrotrons as well as particle bunch transfers within the other accelerators and storage rings of the FAIR facility.

System Components

The time and frequency synchronization of the accelerator rf systems on the GSI-FAIR complex have to span local distances exceeding the kilometer range. A star-type signal distribution system fed by a central frequency and time reference generator can provide the necessary signals with the required accuracy.
The "BuTiS"-system concept [1], comprises the building blocks:

Time- and frequency reference

- Central frequency- and time reference generator

Optical signal transport and distribution

- Optical transmitters and receivers
- Distribution of the "BuTiS"-signal by optical fibers
- Fiber delay measurement and correction

Signal delegation

- Signal splitting of the reference signals at target locations
- Interfacing and integration into central control system including resynchronization of the digital data that controls the rf frequencies in realtime.

Global synchronization

- Locking the central reference to global time (UTC)

Development status of the components

Time- and frequency reference

A versatile, highly stable frequency- and time reference synthesizer is manufactured together with an external contractor, WORK Microwave GmbH. It is a multifrequency synthesizer that generates coherent sinewaves at frequencies of 10 MHz and 200 MHz, and coherent time impulses (ticks) at a rate of 10 µs. The synthesizer does include remote access via LAN as well as an external phaselock reference input for 10 MHz. The prototype was demonstrated in Dec. 2006. The 200 MHz signal is required to lock all Direct Digital Synthesizers (DDS) of the accelerator rf systems synchronously. It is the master clock. The 10 µs time reference ticks are required to remove time ambiguity in the data transfers to the widely spread DDS rf generators within the FAIR complex. The 10 MHz component is provided for locking standard test and measuring equipment to the main reference. This reference synthesizer model can also be utilized as local reference source. At the destination, it can be run in a fly-wheel mode, being phaselocked to the "BuTiS" reference. Due to the inherent stability of the internal timebase, disruptions of the external reference lasting for minutes do not interrupt the synchronization of the rf systems.

Optical reference signal distribution

The reference signals from the central multifrequency reference are transported by the optical distribution system. This system is worked out under a doctor´s student contract. The working frequencies of the rf systems call for a time uncertainty of less than 200 ps to maintain proper phase relationship between the cavities. The local distances between these rf systems underlie temperature variations. The absolute lengths of the distribution paths are not identical. Thus, methods to continuously measure the individual distribution path lengths and compensate the resulting local time differences have to be found. The low time jitter values of the reference generator has to be maintained as well. The exceptional flat frequency response, paired with reasonable thermal stability, call for single mode optical fiber transmission links. The results found so far are very encouraging [2], and others report similar performance [3,4].

Signal delegation

A central aspect of synchronizing digital rf generators is the timing of the data that determines frequency of the generators. In SIS 100, the velocity of a particle bunch traveling from cavity to cavity requires a certain phase-shift of the individual cavity rf. This has to be controlled in realtime. Fortunately, a DDS rf-generator does translate prestored digital data values for phase and frequency into an analog sinewave at exactly that clock signal edge when it receives a data load command. Then, rf phase and frequency of the generated rf become deterministic properties. The 200 MHz DDS main clock allows a 5 ns coarse time resolution, the phase can be aligned in 2^{14} steps (1.2ps @ 50 MHz). This capability can be used to compensate the reference distribution delay time as well as the cavity phase shift created by the moving particles. The work on this item has started.

References

[1] P. Moritz, "Technical Concept Bunchphase-Timing-System "BuTiS", GSI Darmstadt, 2005.
[2] M. Bousonville, "Promotion Statusbericht Konzept und Projektplanung", TU Darmstadt, 2007
[3] B.G. Taylor; CERN; "Timing Distribution at the LHC"; Proc. 8th WS on Electronics for LHC Experi ments, Colmar, 2002
[4] Naito et. al. ; KEK; „RF Reference Distribution using Fibre-Optic Links for KEKB Accelerator", PAC 2001, Chicago, 2001.

Reconfigurable Computing Systems for Digital RF Closed-Loop Controls*

P. Zipf[†1], A. Guntoro[1], M. Glesner[1], and H. Klingbeil[‡2]

[1]Institute of Microelectronic Systems, Darmstadt University of Technology, Germany; [2]GSI, Darmstadt. Germany

Project Overview

For the development of the SIS100/300 accelerator, the required beam stability and manipulation tasks can only be accomplished by specific control mechanisms. Digital algorithms enable a much higher precision and flexibility for processing, filtering, open and closed-loop control of signals than analogue techniques. Their main workload is characterised by the processing of continuous data streams.

The software-driven processing of data streams using digital signal processor (DSP) systems, as currently used by the GSI for building the cavity synchronisation system, poses a capacity limit due to the block-wise computations and limited I/O bandwidth of the processors. The availability of reconfigurable hardware (field-programmable gate arrays, FPGA) opens new opportunities for the provision of computing power: Hardware functionality can be "programmed" into an FPGA on demand, a technique known as *structural programming*. Like this, stream-based algorithms, e.g., a FIR filter, can be directly implemented in fast hardware structures. Instead of loading and executing instructions working on stored data, the streams can directly be fed into the functional unit, e.g., working as a pipeline.

The primary objective of our work is the development of optimised hardware architectures for this kind of system, based on the migration of initial software solutions into faster FPGA hardware.

Structure And Development

The system hardware from Sundance consists of two DSP processors, connected by a Xilinx Virtex II FPGA which also handles all external interfaces (Fig. 1). DSP A,

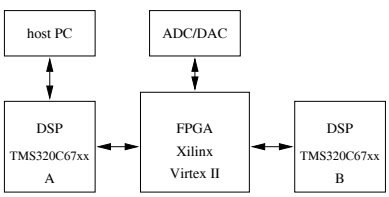

Figure 1: System architecture with two DSPs and FPGA.

running a real time operating system, communicates with the host, while DSP B does the signal processing.

The development strategy is to stepwise replace software algorithms on DSP B by optimised hardware designs placed inside the communication FPGA. Thus, the workload of DSP B is migrated to the FPGA releasing the DSP for further tasks. This strategy also ensures that the laborious hardware development is only started when a new algorithm is already tested and reference results exist.

Hardware Implementations

The first two functionalities implemented as hardware modules are a phase detector [1, 2] and an amplitude calculation. The phase detector as described in [1] requires an $arctan$ calculation which was replaced by look-up tables with precomputed values in our implementation. Different bit widths and table sizes were implemented and compared, resulting in an optimal solution at 12 bit precision and 256 table entries (range between 0 and $\pi/4$). This solution achieves a maximal error of 0.222 degrees and uses 5.37% of the FPGA slices, 5.92% of the flip-flops, and 3.46% of the 4-LUTs. The computation is implemented as a 7-stage pipeline, where each stage but the division takes one clock cycle; the division takes 18 cycles.

The amplitude calculation is needed for the DDS to tune the oscillator parameters. It is based on the CORDIC algorithm and its implementation also covers a reimplementation of the phase detection unit. To improve throughput, the algorithm is implemented in a 4-stage pipeline. A pre- and post-processing stage are used to adapt the input and output to the CORDIC quadrant limitation. The CORDIC stage calculates the CORDIC iterations inside a micro-pipeline with 16 stages (for 16 bits resolution). The CORDIC algorithm requires 478 slices (4%), 788 flip-flops (3%), and 792 4-LUTs (3%). All modules are running at 100 MHz.

Future Work

Additional hardware modules, like a FIR filter currently under development, will exceed the available FPGA resources and an alternative has to be found. We plan to investigate the possibility to use a Virtex II Pro FPGA, which also contains 2 on-chip PowerPC processors. This can be used to further improve the computing power and provides enough additional resources for future extensions. The main challenge will be the integration of this FPGA into the existing system.

References

[1] H. Klingbeil, "A Fast DSP-based Phase-detector for Closed-loop RF Control in Synchrontron", IEEE Transactions on Instrumentation and Measurement, Vol. 24, No. 3, June 2005.

[2] A. Guntoro, P. Zipf, O. Soffke, H. Klingbeil, M. Kumm, M. Glesner, "Implementation of Realtime and Highspeed Phase Detector on FPGA", Int'l Workshop on Applied Reconfigurable Computing, March 2006, Delft, The Netherlands.

* Work supported by GSI, contract DA/GLE

† zipf@mes.tu-darmstadt.de

‡ h.klingbeil@gsi.de

Development of FAIR superconducting magnets and cryogenic system

Egbert Fischer, Eric Floch, Guenther Hess, Hanno Leibrock, Juris Kaugerts, Marion Kauschke, Gebhard Moritz, J. Macavei, Carsten Muehle, Pierre Schnizer, Claus Schroeder, Andrzej Stafiniak, Kei Sugita, Birgit Weckenmann, Yu Xiang , GSI Darmstadt, Germany

Introduction

R&D continued during 2006 for FAIR superconducting magnets, for the main dipoles, quadrupoles, and now the correctors and the corresponding cryogenic distribution system as well. Design of cryostat components, such as interconnections and cold-warm-transitions of beam tubes, has started. R&D was conducted by GSI employees, in collaborations, or by contracts, funded by GSI or the European Union (EU FP6 Design study). Most of the results are documented in the GSI FAIR Baseline Technical Report (FBTR).

Superconducting Magnets

Rapidly Cycling Synchrotron Magnets

An overview of the status of the R&D is given in ref. [1].

SIS 100

Main dipole

The eddy current effects were calculated and explained [2]. Studies on mechanical stability of the coil and conductor demonstrated that the coil will survive 20 years of fast cycling operation. [3, 4].

In 2006 the FAIR Synchrotron group determined that an increased beam acceptance is required for the dipole. Therefore, we had to go from a straight magnet to a curved design. Since the magnet could be made 10% longer, the nominal field came down to 1.9 T, resulting in better field quality.

The conceptual design of full length dipoles was finished [5, 6], the cooling of such a magnet was tested at JINR (Dubna), and two magnets were ordered BINP (Novosibirsk), and BNG (Würzburg).

Main quadrupole

The conceptual design of the magnet, with a 6-turn coil was finished. The magnet is ready to be built. [7]

SIS 300

Main dipole

Technical design work for the 6T, two coil layer 1 T/s straight dipole was finished by IHEP, Protvino [8]. The 3D end design was developed by CERN [9]. Design of the tooling for a 1 m model dipole will be finished in 2007 and the model dipole will be built and tested, to validate fast cycling cosθ dipole design concepts. The Minimum Quench Energy (MQE) of a cable similar to the envisaged cable for this model dipole was measured for different values of the cable adjacent strand resistances [10].

The recently adopted lattice design change (Doublet to FODO) requires a larger beam acceptance for the SIS 300 synchrotron and therefore a larger effective aperture for the dipole. The design of a one coil layer, 4.5 T, 1 T/s, 7.8 m long curved (R= 66 m) dipole was conceived to meet this need. The technical feasibility of the design was demonstrated [11, 12] and the field quality consequences due to the curvature were found to be negligible. A conceptual design, with a temperature margin around 1 K, is still under investigation by INFN. In parallel with the magnet design development, INFN is pursuing the development of a 2.5μm filament size wire, based on a Cu-Mn interfilamentary matrix. A trial billet has been produced and tested.

Magnets for the Storage rings and the Super-FRS

Super-FRS / CR

The technical design of the CR/Super-FRS dipole was finished by the FAIR China Group. The construction of a model coil has started. The stamping tool was ordered.

The quadrupoles (with embedded octupoles) and sextupoles of the Super-FRS form a multiplet. Toshiba finished a conceptual design study for such a multiplet. The technical part of a contract for the production of a prototype quadrupole has been worked out.

NESR / RESR

Conceptual Design work of the superferric dipole is close to completion.[13] The total costs (construction and operation over 20 years) of such a magnet system were compared with those of a resistive version and were similar.

Quench detection and protection

The detection and protection schemes were established for SIS 100, SIS 300, the CR ring, the Super-FRS and the HEBT-lines and were reviewed at an expert meeting. Magnet protection bypass diode stacks were tested and diodes irradiated at ITEP [14].

Test Facility for model and prototype magnets

Test dipole GSI 001 was successfully tested (training, loss measurements) at the GSI test facility, with forced flow 2-phase and single phase cooling. The cryo-plant, with the required distribution and feed boxes, reached the design goals. The anti-cryostat is ready for installation. Most

parts of the mole were assembled and it will be operational in September of next year. The 'stretched wire' will be tested in March of next year.

Cryogenics

During last year the heat load list for the cryogenic system was updated [15][16]. The cryogenic distribution system was modified to reflect the new topology of FAIR. The location and size of the building for the cryogenic infrastructure (compressor buildings and refrigerators) was finalized. Given these locations, a new layout of the cryogenic distribution system could be started and the first steps were taken to determine the final traces of the cryogenic pipelines.

In addition to the global distribution system, the local distribution systems for CR, Super-FRS and HEBT were discussed. For CR and Super-FRS, different cooling schemes were compared and the thermo-siphon scheme with a common header for a group of magnets was chosen. For the HEBT, a new concept for the cryogenic and electrical supply of the magnets was found, by separating feed boxes for helium and electrical feed boxes.

The efficiency of the cooling of the SIS300 coil was evaluated by numerical simulations [17]. The cooling of the adopted SIS 100 magnet was recalculated.

Cryostats

Cryostat designers started the design of magnet cryostats, special ring cryostats, the magnet interconnection regions and the Cold-Warm-Transitions (CWT) of the beam pipes. A MoU with Cracow Technical University is in preparation, for support in this field.

References

[1] Fast-Pulsed Superconducting Magnets, C. Muehle, Proceeding of HB2006, Tsukuba, Japan, June 2006

[2] Analysis of the Eddy Current Relaxation Time Effects in the FAIR SIS 100 Main Magnets, E. Fischer, R. Kurnyshov, P Shcherbakov, Proceedings of ASC 06, Seattle, USA, Sep. 2006

[3] Mechanical Coil Structure of the FAIR SIS 100 Magnets, G. Moritz, E. Fischer, H. Khodzhibagiyan, A. Kovalenko, A. Nyilas, R. Burgmer, D. Krischel, P. Schmidt, W. Gärtner, M. Gehring, W. Walter and A. Wessner, Proceedings of ASC 06, Seattle, USA, Sep. 2006

[4] E. Bobrov, High-Cycle Fatigue and Fracture Mechanics Evaluations of the Conductor for the Fast Cycling SIS100 Synchrotron, GSI Internal Report, October 2006

[5] Full lenght Superferric Dipole and Quadrupole Prototype Magnets for the SIS100 at GSI: Status of the Design and Manufacturing, A. Kovalenko, N. Agapov, A. Alfeev, H. Khodzhibagiyan, G. Kuznetsov, V. Seleznev, A. Shabunov, A. Starikov, E. Fischer, G. Moritz, C. Mühle, P. Spiller, A. Kalimov, Proceedings of EPAC 06, Edingburgh, GB, June 2006

[6] Status of the Design of a Full Length Superferric Dipole and Quadrupole Magnets for the FAIR SIS 100 Synchrotron, E. Fischer, G. Moritz, C. Muehle GSI; A.Alfeev, H. Khodzhibagiyan, A. Kovalenko, G. Kuznetsov, V. Seleznev, A. Kalimov; Proceedings of ASC 06, Seattle, USA, Sep. 2006

[7] Analysis of the Superferric Quadrupole Magnet Design for the SIS Accelerator of the FAIR Project E. Fischer, G. Moritz, R. Kurnyshov, A. Kovalenko, H. Khodzhibagiyan, P. Shcherbakov, Proceedings of EPAC 06, Edingburgh, GB, June 2006

[8] Magnetic and Thermal Characteristics of a Model Dipole Magnet for the SIS 300, S. Kozub, L. Tkachenko, V. Zubko, E. Floch, J. Kaugerts, G. Moritz, B. Auchmann, S. Russenschuck, D. Tommasini, Proceedings of ASC 06, Seattle, USA, Sep. 2006

[9] Coil end design for the FAIR SIS 300 dipoles based on Differential Geometry
B. Auchmann, S. Russenschuck, J. Kaugerts, G. Moritz, Proceedings of ASC 06, Seattle, USA, Sep. 2006

[10] Cable Design for FAIR SIS 300, J. Kaugerts, G. Moritz, M. N. Wilson, A. Ghosh, A. den Ouden, I. Bogdanov, S. Kozub, P. Shcherbakov, L. Shirshov, L. Tkachenko, D. Richter, A. Verweij, G. Willering, P. Fabbricatore, G. Volpini, Proceedings of ASC 06, Seattle, USA, Sep. 2006

[11] Babcock Noell Nuclear, "Studie über die Herstellung gekrümmter Dipole für den SIS 300-Speicherring", Report S.919016, 2006

[12] ASG, STUDIO DI FATTIBILITA' PER LA COSTRUZIONE DEI DIPOLI CURVI PER PROGETTO DISCORAP/SIS 300, Report 700RM11439, 2006

[13] Design of a warm iron superferric dipole for the NESR at the FAIR facility, M. Cortes, E. Floch, H. Leibrock, J. Lucas, G. Moritz, M. Pinilla, Proceedings of ASC 06, Seattle, USA, Sep. 2006

[14] Irradiation of Bypass Diodes up to 2.2E14 Neutron/cm2 and 1.3 kGy for the FAIR Project, E. Floch, E. Mustafin, G. Moritz, H. Ramakers, A. Golubev, S. Borovlev, V. Rogov, G. Smirnov, Yu., Titarenko, V. Batyaev, A. Kantsyrev, N. Markov, A. Smolyakov, D. Hagedorn, A. Gharib, Proceedings of ASC 06, Seattle, USA, Sep. 2006

[15] Kauschke, M., Xiang, Y., Schroeder, C., Quack, H., Kutzschbach, A., Cryogenic Distribution System for FAIR, presented at CryoPrague 2006

[16] Kauschke, M., Xiang, Y., Schroeder, C., Kryosystem für FAIR, DKV-Tagung 2006

[17] Xiang, Y., Kauschke, M., Moritz, G., Kaugerts J., Supercritical Helium Flow Cooling for SIS 300, presented at CryoPrague 2006

Transient Finite-Element Simulation of the Eddy-Current Losses in the Beam Tube of the SIS-100 Magnet during Ramping

H. De Gersem*, S. Koch†, T. Weiland, TEMF TU Darmstadt, Germany

The SIS-100 magnet is designed such that a sufficient field quality is guaranteed in a broad range of operation modes [1]. The field quality during ramping is influenced by the eddy currents generated in the conductive beam tube. The eddy-current losses in the beam tube are computed on the basis of a transient 2D finite-element model. The mesh is adaptively refined (Fig. 1). The backward Euler method with a fixed time step is used for time integration. The ferromagnetic saturation of the iron yoke results in nonlinear systems of equations which are here linearised by the Newton method. The tolerances on the mesh refinement, the time integration and the nonlinear loop are 0.1%. The 2D model is validated by a parameter variation and an analytical model studying the closing paths of the currents at the end parts of the beam tube.

Simulations are carried out for the geometry and the cycle described in [2]. The material data are taken from [3]. The eddy-current losses amount to 8.68 J and 14.56 J per cycle for an elliptical beam tube made of stainless steel, with a major axis of 115 mm, a minor axis of 60 mm and with a thickness of 0.3 mm or 0.5 mm, respectively.

The field quality is measured at a reference radius of 25 mm and compared to a configuration without beam tube. The time dependence of the field quality is shown in Fig. 2a and Fig. 2b for the sextupole and decapole field components respectively. Both indicate significant differences at low aperture fields, especially for the sextupole component at the beginning of the ramping. Also without conductive beam tube and for low field values, the relative sextupole and decapole components depend on the magnitude of the field, which indicates the presence of a nonlinear effect. When the magnet operates at an injection field of 0.253 T, the magnetic flux density in the bridge of the iron yoke is already 1 T (Fig. 3). Hence, the saturation pattern in and around this bridge changes immediately at the start of the ramping, resulting in a changing field quality.

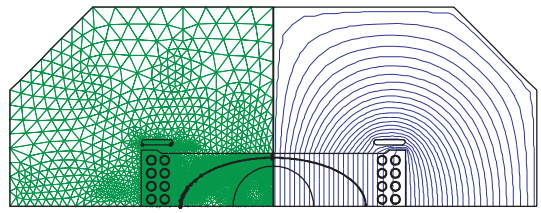

Figure 1: SIS-100 dipole magnet: mesh and magnetic flux lines at a maximum aperture field of 1.9 T.

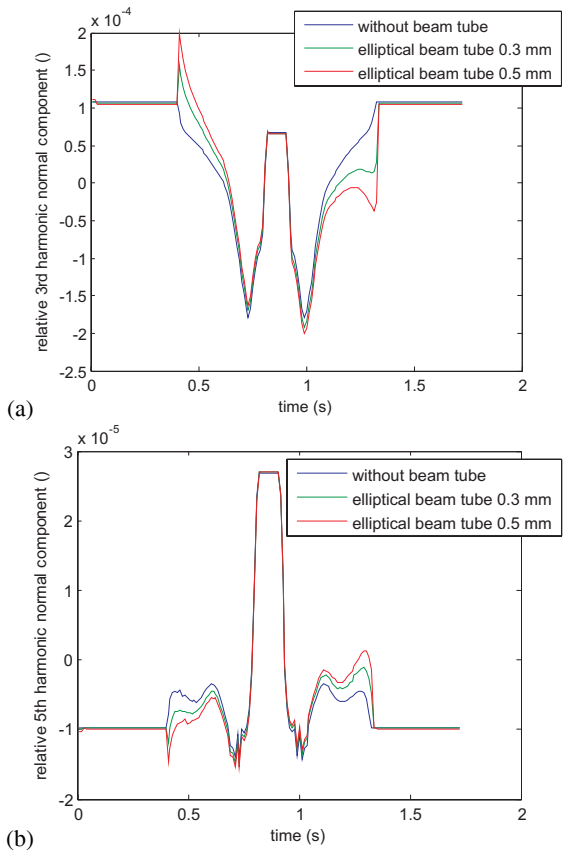

Figure 2: Comparison of the (a) sextupole and (b) decapole field components during ramping.

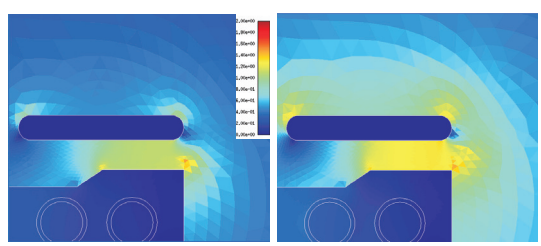

Figure 3: Magnetic flux density in the bridge of the iron yoke at aperture fields of 0.25 T and 0.36 T.

References

[1] A.D. Kovalenko, A. Kalimov, H.G. Khodzhibagiyan, G. Moritz, and C. Mühle. Optimization of a superferric Nuclotron type dipole for the GSI fast pulsed synchrotron. *IEEE Trans. Appl. Supercond.*, 12(1):161–165, 2002.

[2] Development contract on a superconductive curved dipole magnet for SIS100, Annex A, Technical Specification, Fig. 3 and Table IV, August 2006.

[3] FEM calculations on SIS100 dipole, FAIR Baseline Technical Report.

* Supported by GSI, Darmstadt
† Supported by DFG under contract GraKo 410.

Transverse BIF Profile Monitor - System Development for FAIR *

F. Becker[1], C. Andre[1], P. Forck[1], and D.H.H. Hoffmann[1,2]
[1]GSI, Darmstadt, Germany; [2]Technical University Darmstadt, Institut für Kernphysik, Darmstadt, Germany

The planned facility for antiproton and ion research FAIR at GSI will accelerate high intensity beams from protons to Uranium ions in the energy range of 100 MeV/u to 30 GeV/u. In the transport lines between the synchrotrons and in front of production targets precise alignment is required. Conventional intercepting diagnostics will melt due to the beam energy deposition. For transverse profile determination, we investigate a non-intercepting Beam Induced Fluorescence (BIF) Monitor. The residual gas N_2 is excited to fluorescence levels by atomic collisions with beam ions. By single photon detection via a double MCP image intensifier coupled to a digital CCD camera the beam profile is determined [1]. The BIF method was applied successfully at the GSI heavy ion LINAC for various ion species and energies between 4 and 11.4 MeV/u [2]. Now we investigate its application for higher energies as extracted from the heavy ion synchrotron SIS-18 [3].

Our experimental studies aimed to determine the photon yield and background contribution for different ion species (Xe, Ta, U) at beam energies from 60 to 750 MeV/u. In Fig.1 the signal amplitude (top), background level (middle) and signal to background ratio (bottom) are plotted as a function of energy. The measured signal strength corresponds to a Bethe-Bloch fit. The measured background level corresponds to the calculated cross section of neutron production which rises approximately proportional to the square of the energy and the number of nucleons [4]. Therefore the signal to noise ratio decreases with the energy, see Fig.1 (bottom) & Fig.2. It can be improved by appropriate neutron shielding or short gating times to exclude delayed neutrons [3]. Even though the recorded beam profile widths correspond to those achieved with standard methods within 10%, it is crucial to understand the excitation mechanisms. Cross sections of nitrogen fluorescence by proton impact were achieved from spectroscopic analysis. Beside the dominant N_2^+ bands due to atomic collision also N_2-bands were observed and a two-step process was identified as their excitation mechanism [5]. For 200 MeV/u Au^{65+}ions we mapped the spectral response using narrow band 10 nm interference filters and associated it with nitrogen transitions see Tab.1. Since the vacuum pressure affects the occurrence and the mean free path of secondary e^- and the beam's E-field will displace charged particles as e^- and N_2^+, profile distortions might occur. For next machine experiments focus will be on the influence of pressure and the beam's charge density on fluorescence spectra and profile distortion.

* Work supported by EU, project FP6-CARE-HIPPI

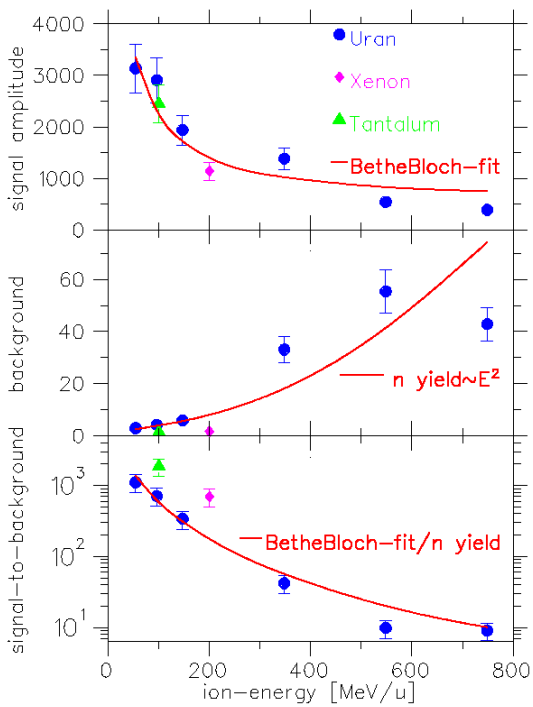

Figure 1: Energy variation for U, Xe and Ta ions.

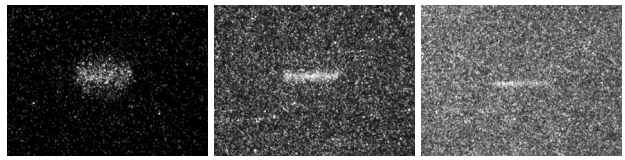

$4{\cdot}10^8$U@60MeV/u $1{\cdot}10^9$U@350MeV/u $1{\cdot}10^9$U@750MeV/u

Figure 2: Images of an Uranium beam at different energies and a N_2 pressure of $2{\cdot}10^{-3}$ mbar - slow extraction mode.

Table 1: Comparison of relative N_2 and N_2^+ transition intensities: 200 MeV/u Au^{65+}, p =$1{\cdot}10^{-2}$mbar (SIS-18, Nov. 2006) ↔ 200 keV protons, p =$2{,}6{\cdot}10^{-2}$mbar [5].

filter λ_0	molecule	Au^{65+} (2006)	p ([5], 1961)
390FS10	N_2^+ (0-0)	50±7,5%	72%
430FS10	N_2^+ (0-1)	29±4,4%	19%
470FS10	N_2^+ (0-2)	5±0,8%	4%
337FS10	N_2 (0-0)	16±2,4%	≈4%

References

[1] P. Forck et al., *Proc. DIPAC05*, Lyon, p. 223 (2005).
[2] P. Forck, A. Bank, *Proc. EPAC 02*, Paris, p. 1885 (2002) and A. Bank, P. Forck, *Proc. DIPAC 03*, Mainz, p. 137 (2003).
[3] F. Becker, C. Andre, P. Forck, D.H.H. Hoffmann *Proc. EPAC06*, Edinburgh, p. 1013 (2006)
[4] T. Kurosawa et al., *Phys. Rev.* **C 62**,044615 (2000).
[5] R.H. Hughes et al., *Phys. Rev.* **123**, 2084 (1961), L.W. Dotchin et al., *J. Chem. Phys.* **59**, 3960 (1973).

Numerical Calculations of Displacement Sensitivity for SIS100 BPMs *

P. Kowina, P. Forck, W. Kaufmann, A. Peters, J. Schölles, and A. Stafiniak
GSI, Darmstadt, Germany

Abstract

In the simulations, the linear cut Beam Position Monitor (BPM) based on a metal coated ceramics is considered. High displacement sensitivity was achieved by reduction of plate-to-plate cross talk caused by coupling capacities.

Parameters of SIS100 BPMs

For the foreseen bunch frequencies of 0.5 MHz $< f_b <$ 2.7 MHz and aspired bunch lengths the designed BPM should show a good response in the frequency range from $\sim$ 0.1 MHz to 100 MHz. For such frequencies and the bunches much longer than the BPM length the linear–cut BPM is preferred. In order to reach the desired accuracy of 100 μm [1], the mechanical stability has to be about 50 μm. The design based on a metal coated Al_2O_3 ceramics gives the required mechanical stability in the cryogenic environment. The model considered in the simulation is shown in Fig. 1. The elliptic ceramic pipe is coated on the inner side with 30 μm of PtAg metal layer. In this metal coating the electrode shapes are formed by cutting out grooves. The available detector length of 300 mm is sufficient to mount vertical and horizontal plates (together with relevant guard rings) in series within one unit. For most intense beams, the expected peak voltage of BPM signals reaches 1.8 kV [2]. Therefore, the relative distances between electrodes, guard rings etc. have to be large enough to prevent discharges.

Simulation results

For all simulations CST Studio Suite 2006 was used. All simulations were performed using the time domain solver in the bandwidth corresponding to a frequency range from DC to 200 MHz. The BPM was treated as a coaxial TEM wave guide with the ion beam approximated by a cylinder of a Perfect Electric Conductor (PEC) [2]. The main goals in optimization were: i) high displacement sensitivity (defined in Ref. [2]), ii) linearity of the position determination and iii) reduction of misalignment of the electrical center with respect to the geometrical center of the BPM.

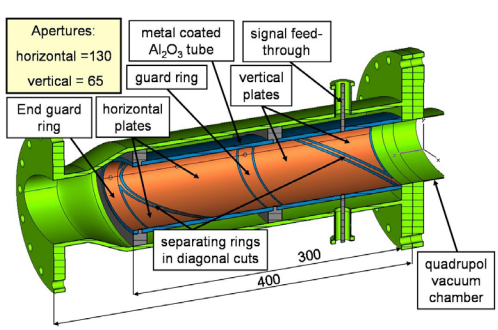

Figure 1: Model of the BPMs used in the simulations.

* Work funded by EU-Design Study contract No. 515873.

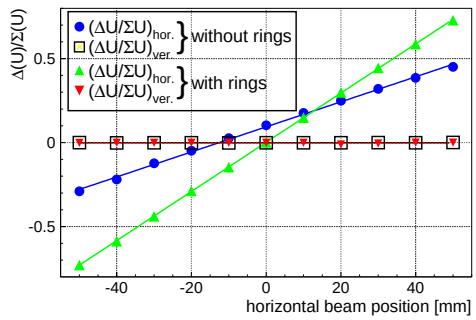

Figure 2: Displacement sensitivity for the BPM without and with separating ring and guard ring.

The influence of the end guard ring and separating rings positioned in the diagonal cut between the adjacent plates was investigated in detail. The simulated beam position was swept in the horizontal plane in the range ± 50 mm in 10 mm steps. For each beam position the BPM response in both horizontal and vertical planes was calculated from the S-parameters expressed in the frequency domain [3]. The results are presented in Fig. 2.

For both BPM configurations the position determination is linear — maximum deviations from the linear fit over the whole ± 50 mm displacement range are smaller than $\pm 2\%$ for the BPM without and $\pm 0.5\%$ for the BPM with rings, respectively. The offset of the electric center of the BPM without rings is about 13 mm whereas the offset for the BPM with rings is consistent with zero. It indicates, that a guard ring at the end of the BPM electrodes (see Fig. 1) is mandatory.

The displacement sensitivity, as given by the slope of curves in Fig. 2, depends strongly on plate–to–plate coupling. For the ceramic based BPMs large ceramic permittivity ϵ_r=9.6 leads to high coupling capacity that diminishes the difference signal and deteriorates the displacement sensitivity. An insertion of a separating ring in between the two adjacent horizontal plates reduces the coupling from $-9,5$ dB to -21 dB. This increases the displacement sensitivity by a factor of two [2]. Hence, the separating ring is required in the BPM designs based on ceramic solution. The frequency response of investigated BPM was analyzed and is discussed in details in Ref. [2]. It is shown that the displacement sensitivity is almost frequency independent in the relevant frequency range.

The simulations will be continued for alternative geometries. In parallel, the mechanical features of the single BPM components in the cryogenic environment will be investigated.

References

[1] A. Galatis et al., EPAC'06, Edinburgh, June 2006, p. 1019.
[2] P. Kowina et al., EPAC'06, Edinburgh, June 2006, p. 1022.
[3] P. Kowina et al., DIPAC'05, Lyon, June 2005, p. 114.

Dynamic 11kA Power Converter for Prototype Testing of Superconducting FAIR Magnets

H. Welker, H. Ramakers, G. Breitenberger GSI Darmstadt

In 2006 the set up of one test bench for superconducting magnets of FAIR was finished at GSI. A second one is under construction. After commissioning of both test stands magnetic measurements of up to 8 superconducting magnets per month will be possible.

The dedicated power converter must supply DC currents and ramped currents up to 11000A and provide output voltages up to +/-100V. This gives an effective apparent power of 1.3 MVA. The maximum value for the rate of current change is 18kA/s for positive and negative current ramps. To avoid tracking errors on the current ramp and to reduce current ripple the power converter is equipped with a dynamic active filter.

A similar power converter topology with active filter is in use in GSI since 1990 [1]. It consists of a 12 pulse silicon controlled rectifier (SCR), which carries the bulk of the load current, and a parallel active filter (PE) witch carries only a small current, but controls the accuracy and stability of the load current. The power converter which is installed at the test bench is based on a newer design of a power converter with active filter. As described in [2] the active filter is set up as a switch mode power converter. The main advantage is the reduction of conduction losses in the semiconductors of the active filter and leads to a more compact design of the system.

Figure 1 shows the principle circuit diagram of the power converter. Because of the large power the SCRs are connected to the 20kV voltage level via 2 identically build transformers which are phase shifted by +/- 15° el by phase rotation of the primaries. Two smoothing reactors decouple the SCRs and the active filter PE, because both units are voltage sources by principle. The PE is connected to the 400V AC system and is designed for a nominal current of 100A. At the output of the PE a small passive LC-filter suppresses the switching frequency of 100 kHz. Whereas the configuration described in [2] needs a passive filter for the SCR there is no need for SCR filtering in the GSI approach because of the new developed control strategy.

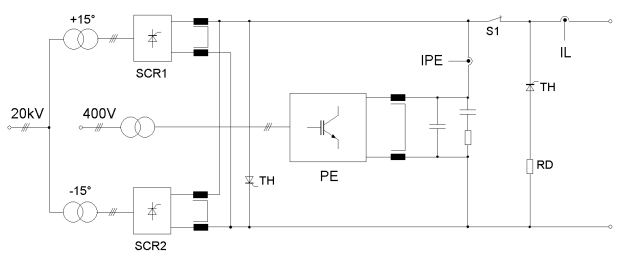

Figure 1: Principle circuit diagram of power converter

By avoiding a passive LC-filter for the SCR the power converter and a magnet as its load are a First Order System in terms of control theory. This simplifies the control, and tracking errors on the current ramp can be avoided.

Figure 2 shows the compact power part of the PE in the 11kA power converter.

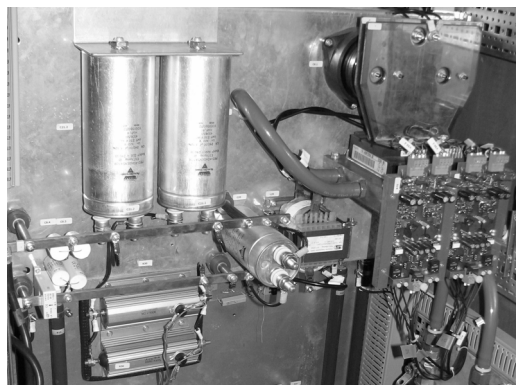

Figure 2: Power part of active filter in 11kA converter

The power converter is equipped with a quench protection system to protect the magnet in case of a quench and to reduce heat dissipation into the cryogenic system. The main parts of this system are a dump resistor which can absorb energy of 1.1 MJ and an electronic switch (S1 in Figure 1). The voltage regulation of the electronic switch ensures that the load voltage does not exceed a value of 800V. In 2007 this switch will be replaced by a prototype electronic switch with integrated redundancy in case of malfunctions. It is designed to protect a magnet string in the SIS100 synchrotron of FAIR. This kind of switch was developed in cooperation with TU Darmstadt.

The first commissioning of the power converter with active filter was done in summer 2005 with a resistive magnet and currents smaller than 1kA. The specified values for the total current deviation were fulfilled ($2.5 \cdot 10^{-4}$ relative). Operation at full current was done in short circuit operation without active filter. At the end of 2006 a first commissioning with a superconducting magnet (L = 2.8 mH, I_N = 7000A) was done. Quenches were initiated in DC operation and in ramped operation, too. For those tests the maximum current was limited to 7.2kA.

References

[1] R.Fink, R.Wagnitz/AEG, G.Breitenberger and H.Ramakers/GSI, “New principle for power supplies for synchrotron magnets without tracking errors”, EPAC 1990, Nice, June, Vol. 2

[2] F.Völker, G.Coudert, H.Muller/CERN, and A.Coraluppi/OCEM „Power Converter of the main dipole an quadrupole magnet strings of the antiproton decelerator at CERN“ EPAC 2000, Vienna.

Development of a Multigap-Pseudospark Switch for the PFN of the SIS100/300 Kicker Magnet Pulse Generator

I. Petzenhauser[1], K. Frank[1], B.J. Lee[1] and U. Blell[2]

[1]Friedrich-Alexander-University of Erlangen; [2]GSI, Darmstadt

In Erlangen multigap Pseudospark switches are under development to meet the requirements of the pulse forming network (PFN) for the SIS100/300 kicker magnets which are: hold-off voltage > 70 kV, peak current of ~ 6 kA and pulse duration of up to 6 µs. In the final phase of development a three-gap switch will be used. As reliable triggering is a key problem, different trigger methods were investigated to provide reliable breakdown of the switch acceptable delay and jitter values. A novel scheme, the carbon nanotube trigger system provided very good switching characteristics, but still suffers from very low lifetime (< 10^6) due to erosion in the ambient gas atmosphere (D_2 ~60 Pa) in the switch. A quite different and already widely tested system of the so-called high-dielectric trigger module was significantly improved by using thicker dielectric discs (6 mm instead of 1 mm) and new materials. Such a high-dielectric trigger module with a flat and partly metallized electrode (e.g. by a grid or " metal fingers"), and a dielectric in between is shown in Figure 1.

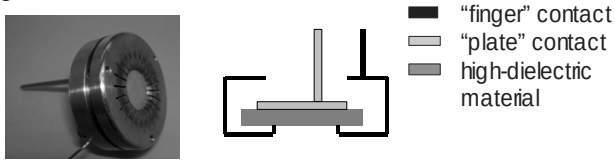

Figure 1: High-dielectric trigger module

To operate the trigger an high voltage pulse (4-6 kV) is applied to one of the electrodes. At the triple points (where gas, metal and dielectric meet) a surface plasma is created and the emitted electrons (and photons) trigger the switch. The best results were achieved with a negative trigger pulse on the finger contacts and a 50 Ω resistance between the plate contact and ground. The pulse duration of the trigger pulse plays only a minor role, a reduction from 1 µs to 100 ns didn't change the results significantly. Actually new dielectric materials have been tested only under laboratory conditions, but a lifetime increase of at least one order of magnitude was already demonstrated with any material degradation. In 2006 the first sealed-off prototype of a two-gap switch, filled with D_2 was built, shown in Figure 2. To have the later possibility of changing parts of the switch a modular construction was preferred. A commercial zirconium-based reservoir (SAES ST172) is used to adjust the gas pressure within the switch. The reservoir can reversibly store and release hydrogen or deuterium. Depending on the heater current the pressure can be varied between <0,01 Pa and >100 Pa. By the Paschen law the gas pressure is directly correlated with the hold-off voltage of the switch. D_2 was used, due to its higher voltage hold-off capability /1/. Figure 3 shows the results of own measurements of the hold-off voltages of hydrogen and deuterium in a one gap pseudospark switch. A ratio between the hold-off voltages of D_2 and H_2 of ~1,2 was found, which is in quite good agreement with data in literature [1].

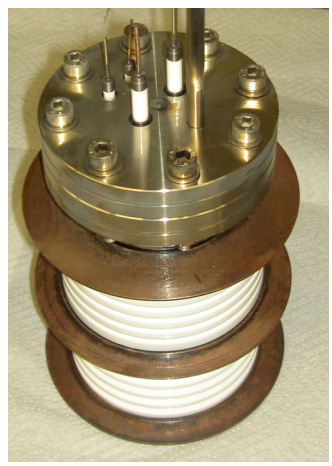

Figure 2: Prototype of a sealed-off twogap Pseudospark switch

The CF-flange at the top of the switch allows to change the trigger module and the gas reservoir.

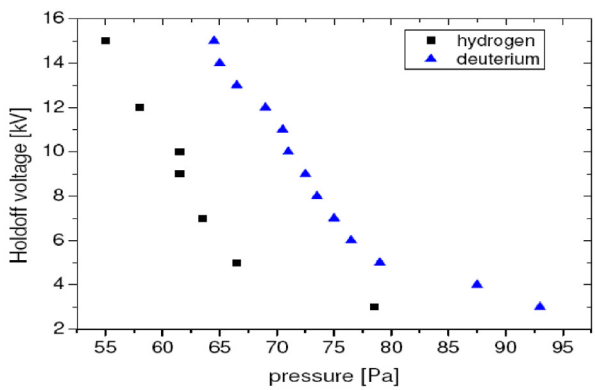

Figure 3: Paschen breakdown in H_2 and D_2 (single gap)

References

[1] J. Armstrong, T. K. Bennett, "Electric Breakdown in deuterium and hydrogen at low pressures", J. Appl. Phys.. **82** (5), pp. 2147-2149 (1997)

A long-term stable cold-cathode gauge for the special use in insulating vacuum systems of cryostats in superconducting accelerators

S. Wilfert[1], C. Edelmann[2]
[1]GSI, Darmstadt, Germany; [2] Otto-von-Guericke University Magdeburg, Germany

Abstract

The pressure conditions in insulation vacuum systems of superconducting accelerator rings or nuclear research plants is often controlled and monitored by cold-cathode gauges (hereafter CCGs). However, due to high outgassing rates of the super insulation material foils (MLI) normally used for thermal insulation, the residual gas atmosphere is dominated by high portions of hydrocarbons. If a CCG is operated in such a hydrocarbonous gas atmosphere, its mean useful life-time is substantially limited by a contamination of the gauge head. Consequently, the pressure reading of the gauge becomes erroneous and unreliable [1-3]. At the worst, the gauge can completely fail. To increase the useful operating-time of a CCG we developed an improved cold-cathode gauge of inverted magnetron-type which was specially designed for the long-term operation at high pressures or/and in gas atmospheres with high contents of hydrocarbons.

Basic Concept for a CCG with low-contamination rate

In order to increase the useful life-time of a cold-cathode gauge one has to avoid the entrance of hydrocarbonous gases into the measuring cell as far as possible. As successfully demonstrated by Haefer [4], this can be easily realized by the means of an ion baffle using a magnetically confined cold-cathode discharge. In such an ion baffle hydrocarbonous gas components will be effectively cracked due to polymerization reactions. Thus, it is obvious to integrate such an ion baffle into a classical cold-cathode gauge structure.

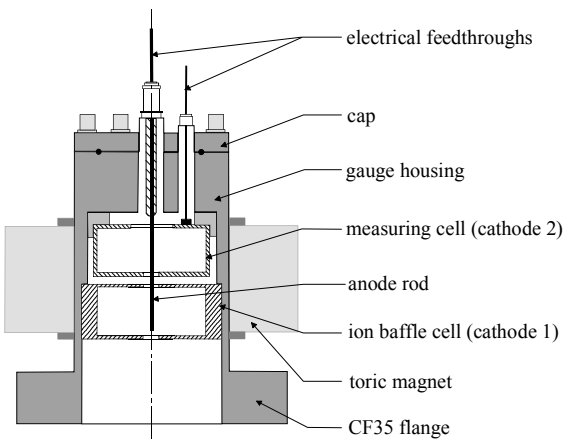

Figure 1: Schematic view of the inverted double-magnetron gauge with low contamination rate

The basic idea for a CCG with low contamination rate is thus a modification of the classical inverted magnetron structure: According to our suggestion [5], our gauge head has two electrically separated cathode cylinders. In both cells burn two independent gas discharges (cf. Figure 1). Whereas the discharge zone positioned directly at the gauge entrance works only as an ion baffle and its discharge current is not measured, only the second discharge zone located more interior is used as gauge for pressure measurement. This special double-plasma configuration has the crucial advantage that the plasma zone at the entrance of the gauge protects the inside one (which represents the measuring cell) against disturbing contamination by condensable vapors or hydrocarbons.

Experiments and Results

In order to demonstrate the efficiency of the improved vacuum sensor concept we have constructed a prototype and tested the gauge in a long-term test. For this reason, the gauge was operated continuously over a measuring period of 1.000 hours (6 weeks) at approximately constant pressures near the upper pressure measurement limit of the gauge. The test run has been carried out at a vacuum system whose residual gas atmosphere was highly contaminated with hydrocarbons. These vacuum conditions were specially suited to accelerate artificially the contamination process in the gauge head. Before the long-term operation, the gauge was calibrated under clean vacuum conditions. After the test-phase, the gauge was re-calibrated in order to verify changes in the characteristic curves. The comparison of the gauge characteristics before and after the long-term test indicates clearly that the gauge characteristics could be reproduced with a relatively high accuracy, the measured deviations still lay within in the typical range of measuring accuracy of CCGs. Compared to the most commercially available cold-cathode gauges, the improved cold-cathode gauge has at least a 3 times higher useful life-time [6].

References

[1] S. Wilfert, N. Schindler, Appl. Phys. A78 (2004), 663
[2] N. Schindler, S. Wilfert, Appl. Phys. A78 (2004), 691
[3] S. Wilfert, J. Vac. Soc. Jpn. 46(1) (2003), 31
[4] R. A. Haefer, Vakuum-Technik 11 (1962), 41
[5] Chr. Edelmann and S. Wilfert,
Patent DE 102 43 634 A1, WO 2004/4029572 A1 (2004)
[6] S. Wilfert and C. Edelmann,
Vakuum in Forschung und Praxis 18 (2006), 12-18

Residual activity induced by U ions of energy 500 MeV/u in a Cu target *

E. Mustafin[1#], H. Iwase[1], E. Kozlova[1], D. Schardt[1], A. Fertman[2], A. Golubev[2], R. Hinca[3], M. Pavlovic[3], I. Strasik[3], N. Sobolevskiy[4]

[1]GSI, Darmstadt, Germany; [2]ITEP, Moscow, Russia; [3]STU Bratislava, Slovakia; [4]INR RAS, Moscow, Russia

Measurement

Measurements of the residual activity induced by U ions of different energies in Cu and stainless steel targets have been taken at GSI Darmstadt. In this paper we present the results of measured residual activity induced by U ions with E = 500 MeV/u in a Cu target and discuss possible "hands-on" maintenance problems in the tunnel of the SIS100 synchrotron of FAIR.

The cylindrical Cu target was assembled of discs of the diameter of 50 mm and different thickness. The U beam spot was less than 11 mm in diameter. The total thickness of the Cu target was twice the range of the U ions, thus the beam stopped completely inside the target. Analyses of the gamma-spectra of the activated discs allowed to identify the radioisotope concentration in each disc and to plot the depth profile for each isotope.

The following set of radioisotopes was detected in the discs:

a) produced by fragmentation of the target and projectile nuclei: ^{7}Be, ^{22,24}Na, ^{28}Mg, ^{42,43}K, ^{44m,46,47,48}Sc, ^{48}V, ^{48,51}Cr, ^{52,54}Mn, ^{52,59}Fe, ^{55,56,57,58,60}Co, ^{57}Ni, ^{62,65}Zn

b) produced by fragmentation of the projectile nuclei only (i.e. ^{238}U) and their half-lives: ^{99}Mo - 65.94 h , ^{103}Ru - 39.26 d, ^{126}I - 13.11 d , ^{126}Sb - 12.46 d, ^{127}Xe - 36.4 d, ^{131}I - 8.02 d, ^{131}Ba – 11.5 d, ^{140}Ba – 12.75 d, ^{237}U – 6.75 d

c) the daughter product of produced isotopes: ^{140}La – the daughter product of ^{140}Ba), ^{44}Sc – the daughter product of ^{44m}Sc.

Typical measured depth profile for target activation is presented in Fig.1 on the example for ^{58}Co isotope.

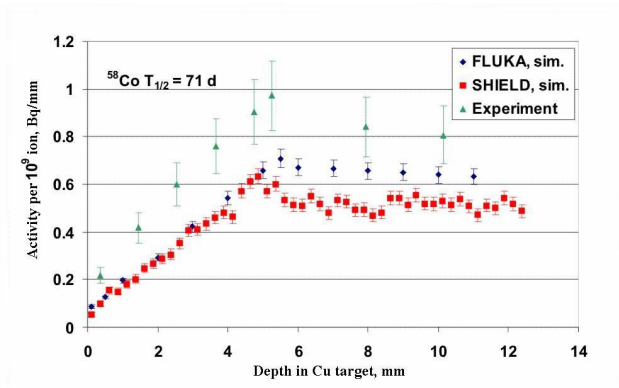

Figure 1: Depth profile of the activity of ^{58}Co.

In this case the measured and calculated activities were in agreement with each other within a factor of 2. For some isotopes the discrepancy between the calculated and measured values and also the discrepancy between the two codes FLUKA [1] and SHIELD [2] were up to a factor of 5.

Estimates of the residual activity in SIS100

The knowledge of the residual activity of individual isotopes allowed us to estimate the radiation risk due to the residual activity for the "hands-on" maintenance in the SIS100 slow extraction area, where a 5% loss of the total beam intensity of $3 \cdot 10^{11}$ s^{-1} U ions is expected.

The time-evolution of the gamma-dose obtained from residual activities induced in a Cu target is shown in Fig.2. It was assumed that the beam loss was distributed uniformly along the beam pipe over the 30 m distance downstream the electrostatic extraction septum.

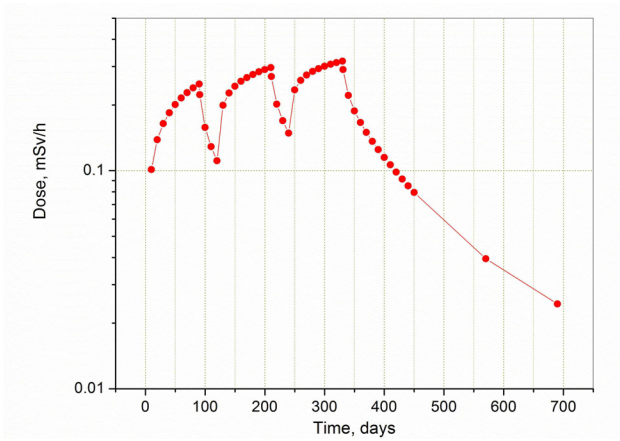

Figure 2: Calculated dose rate in the slow extraction section of SIS100 (at 1 m distance from the vacuum tube).

The calculation is given for three machine runs. Each run lasts three month with one month break between the runs. The dose rate saturates after one year at the level of about 0.4 mSv/h. This is below the 3 mSv/h access limit set by the German Radiation Protection Ordinance.

One should note that for the hot beam spots and for higher energies of the lost beam the residual activity level may become much higher.

References

[1] A. Fasso, A. Ferrari, J. Ranft, P.R. Sala, FLUKA: present status and future developments, in: A. Menzione, Scribano (Eds.), Proc. of the IV International Conference on Calorimetry in High Energy Physics, La Biodala, Italy, 21–26 September 1993, World Scientific, Singapore, pp. 493–502..

[2] N. M. Sobolevsky, "The SHIELD transport code: a tool for computer study of interaction of particles and nuclei with complex media", in Proc. of the 3rd YUNSC 2000, Belgrade, 2001, page 539.

* Work supported by GSI-INTAS Project #03-54-3588

#e.mustafin@gsi.de

Monte-Carlo shielding calculations for the target area of the SuperFRS*

G. Fehrenbacher[1], E. Kozlova[1], and T. Radon[1]
[1]GSI, Darmstadt, Germany

Introduction

First results of the shielding optimization for the Super-FRS target area have been performed with the Monte-Carlo transport code FLUKA2006.3 [1]. FLUKA is a code able to simulate interaction and transport of hadrons, heavy ions and electromagnetic particles from a few keV (or thermal neutron) to cosmic ray energies in nearly all materials [2].

Shielding

Shielding calculations are done for the following scenario: a graphite target is hit by a 1 GeV/u ^{238}U beam with an intensity of 10^{12} particles per second. The target is a wheel with radius of 22.5 cm and it is subdivided into three rings, each 16 mm wide, with thicknesses of 21.6, 32.4 and 43.2 mm, corresponding to 4, 6, 8 g/cm^2 [3]. For a conservative case the thickest part of the target with a thickness of 8 g/cm^2 is chosen.

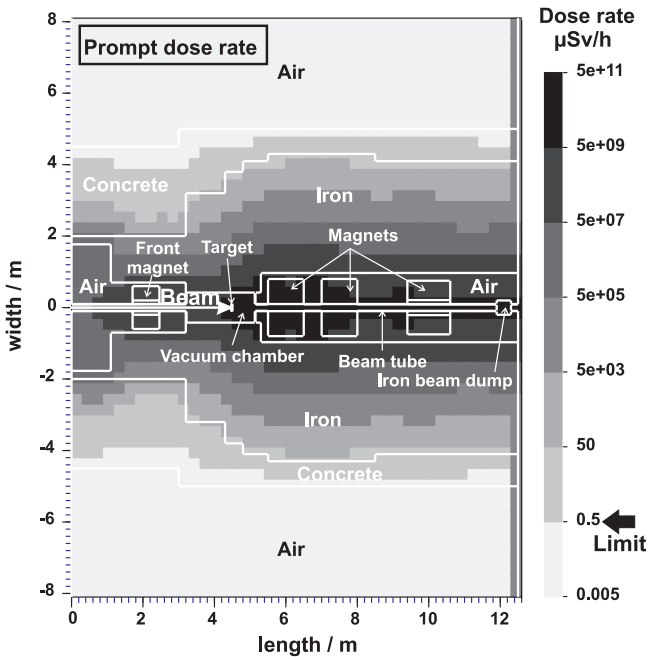

Figure 1: Plot of the prompt dose rate for the Super-FRS target area (top view, the beam height is 1.5 m).

Due to the space limitation the shielding walls should not increase the width 5 m (see Fig. 1). In this case for achievement outside the shielding the dose rate low then 0.5 μSv/h inside the concrete iron was introduced. Another variant of the shielding with predominately concrete has been calculated too.

* Work supported by EU, EURONS contract No. 506065.

Activity

The residual dose distribution for the same shielding layout is calculated. The irradiation profile assumed here is two times 60 days of Super-FRS operation with 1 Gev/u 10^{12} uranium ions per second, interrupted by 120 days without beam. The following cooling time is 4 month. The residual dose rate for such condition is estimated (see Fig. 2).

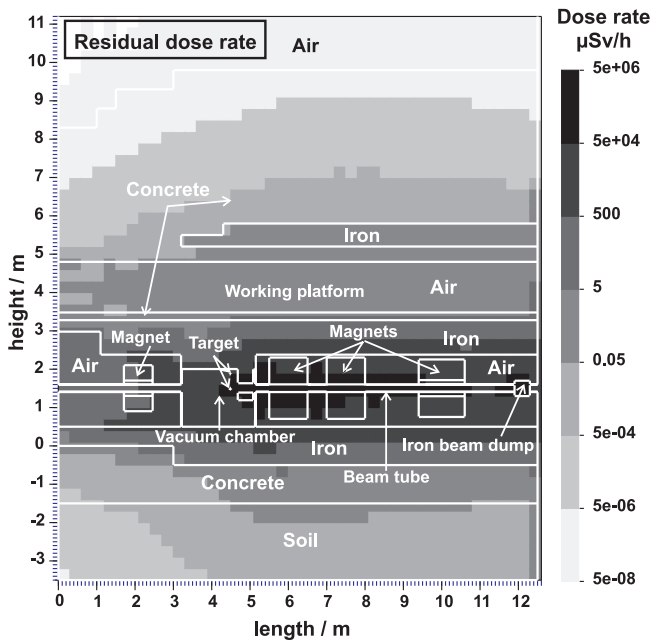

Figure 2: Residual dose rate distribution for the Super-FRS target area (side view).

Conclusion

The shielding for the Super-FRS target area is optimized. The desirable limit of the prompt dose rate of 0.5 μSv/h outside the shielding is accomplished. The residual dose rate after 4 month of cooling is ever acceptable for long term maintenance work on the working platform (see Fig. 2).

References

[1] www.fluka.org

[2] F. Ballarini *et al.*, *Nuclear models in FLUKA: present capabilities, open problems and future improvements*, presented at ND2004, Santa Fe, October (2004) (SLAC-PUB-10813)

[3] *Technical Report on the Design, Construction, Commissioning and Operation of the Super-FRS of FAIR*, Super-FRS/NUSTAR Collaboration, www.gsi.de/nustar, October (2005)

Research programme hadrons and nuclei

Accelerator Operation Report

U. Scheeler, D. Wilms
GSI, Darmstadt, Germany

This report describes the operation statistics of the accelerator facility in the year 2006. The data has been collected with the help of the program PROST [1].

General overview

In 2006 four beam time periods were scheduled. The first beam time period started on January 11th and lasted until March 17th. After one week of shutdown the second block started on March 29th and lasted until June 5th, whereas SIS operation has already been stopped one week earlier. Within the following shutdown the upgrade of the SIS power connection has been performed. Operation started again on June 21st. The third block ended on August 17th, followed by a shutdown of two months, used mainly for SIS upgrade activities. An extension of the UNILAC operation for 5 weeks began on September 29th. UNILAC, SIS and ESR operation started again on November 8th. This last beam time period lasted until December 20th.

Table 1: Overall beam time of the accelerator facility

	Total beam time 2006	Target time 2006	Target time 2005
UNILAC	6760 h	5208 h	6132 h
SIS	7012 h	4937 h	6315 h
ESR		1382 h	1374 h

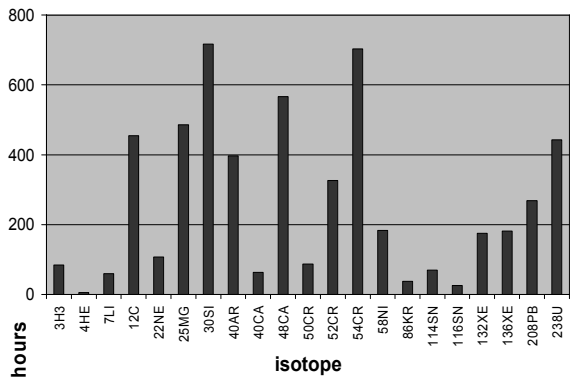

Figure 1: Accelerated isotopes for UNILAC experiments

Table 1 shows total beam time and achieved target time for different experimental areas. In 2006 the UNILAC has been operated for 6480 h and the SIS for 5432 h. One has to mention, that the total beam time for each machine is higher than the operation time due to the time-sharing operation mode. The difference in operation time of UNILAC and SIS is caused by the above mentioned extended UNILAC beam time in October. Comparing to the 6928 h of operation in 2005 this is a substantial decrease, particularly for SIS. Hence much less beam time was scheduled this year due to longer shut down periods. Nevertheless, the UNILAC operation time achieves the long-term annual level of about 6400 hours.

Over the year 2006 26 different isotopes were accelerated serving 20 low energy experiments at UNILAC and 26 high energy experiments at SIS. As shown in figure 1, UNILAC experiments mainly requested light and medium heavy elements, whereas the synchrotron users preferred lead, uranium and carbon beams (figure2).

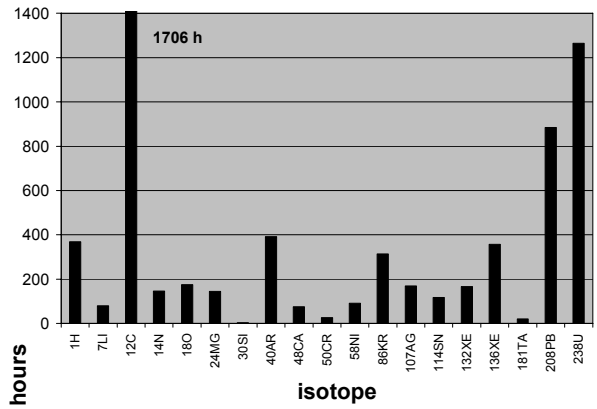

Figure 2: Accelerated isotopes for SIS experiments

UNILAC Operation

The beam time for the UNILAC experiments is summarized in table 2. The efficiency of accelerator operation is indicated by the ratio of "hours per category" to "total amount of beam time" and is given as a percentage value.

Table 2: Beam delivered to UNILAC experiments

	(h)	Percentage
Target time for exp. runs	5208	77.0%
Beam for experiment tests	61	0.9%
Accelerator development	171	2.5%
Accelerator tune-up	446	6.6%
Ion source replacement	240	3.6%
Unscheduled down time	447	6.6%
Retuning	66	1.0%
Stand-by	121	1.8%
Total beam time	**6760**	

The fraction of target time in 2006 dropped to 77 %, i.e. shows a decrease compared to the value of 85% reached in 2005. More time was needed for ion source replacement and machine tune up. The unscheduled down time doubled during the year 2006, a large fraction of this is caused by failures of RF-systems (163 hours) due to high duty cycle operation. In addition difficult operation conditions of the ion sources caused 98 hours of unscheduled down time. The remaining unscheduled down time could be attributed to vacuum problems (57h), controls (38h), infrastructure (14h) and other failures (77 h).

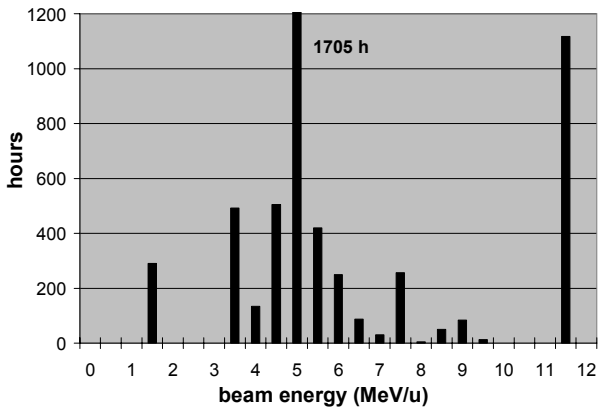

Figure 3: Beam energies of the UNILAC experiments

In Figure 3 the target time of the UNILAC experiments (without beam injected into SIS) is plotted versus beam energy. Beam energies in the range of 4 to 5 MeV/u were mainly delivered to experiments for super heavy element synthesis. Nuclear chemistry experiments were done at an energy of 7.5 MeV/u and beams of energy of 11.4 MeV/u were used for experiments in biology and material science.

Table 3: UNILAC beam delivered to SIS in 2006

	(h)	Percentage
Beam available for SIS injection	7165	90.3%
Accelerator development	17	0.2%
Ion source replacement	134	1.7%
Accelerator tune-up	236	3.0%
Unscheduled down time	346	4.4%
Retuning	38	0.5%
Total beam time	**7936**	

Table 3 shows the delivered beam for SIS injection. The beam time for injection decreased in 2006 due to the shorter operation time of SIS18. The main part of unscheduled down time (120 hours) was caused by RF-system failures. Problems of the injectors caused 75 hours of interruption.

SIS Operation

The operation statistics for SIS is shown in table 4. Compared to the year 2005 the total target time considerably decreased mainly due to longer shut-down periods. The target time for the ESR and for patient treatment remained nearly constant. In accordance with UNILAC operation, an increase of tune-up time and unscheduled down time was also observed at SIS. Unscheduled down time added up to 278 hours, in detail: 123 hours for power supplies, 37 hours for vacuum systems, 31 hours infrastructure, 14 h for controls, 13 h for RF-systems, and 60 h for other failures.

Table 4: SIS operation time in 2006

	(h)	Percentage
Beam for target area	3691	52.6%
Therapy	1177	16.8%
Beam for experiment tests	69	1.0%
Total target time SIS	4937	70.4%
Target time ESR	1382	19.7%
Accelerator development	170	2.4%
Accelerator tune-up	154	2.2%
Unscheduled down time	278	4.0%
Standby	92	1.3%
Total beam time	**7012**	

Figure 4 shows the beam time of the SIS versus beam energy. Besides therapy treatment and ESR operation, which requested beam energies in the range of 200 to 400 MeV/u, the fragment separator was the main user of the synchrotron beam with beam energies above 500 MeV/u. Beams with highest energies were delivered to Caves B, Cave C and to the HADES cave for pion production.

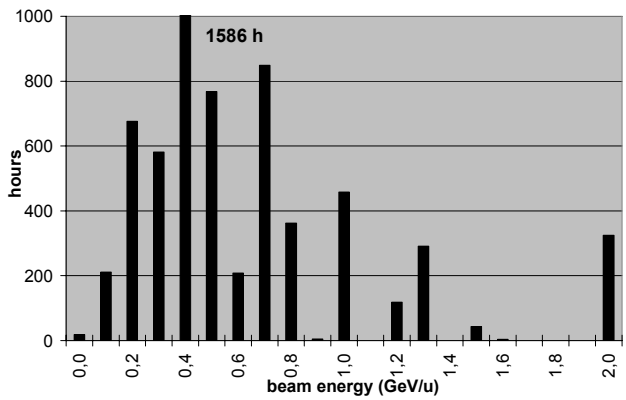

Figure 4: Beam energies at SIS

References

[1] **PR**ogramm für **O**perating und **ST**atistik

UNILAC Status and Developments

W. Barth, W. Bayer, L. Dahl, P. Gerhard, L. Groening, S. Yaramishev, GSI, Darmstadt, Germany

Status of Operation

In 2006 mainly a carbon beam from the Electron Cyclotron Resonance (ECR) ion source was accelerated via the high charge state injector (HLI) in the UNILAC for the SIS-injection as in the years before [1]. Additionally several UNILAC experiments used the beam with a duty factor of up to 30 %. Furthermore the ECR source was in operation for the production of various isotopes (^{7}Li, ^{26}Mg, ^{30}Si, ^{48}Ca, ^{50}Ti, ^{54}Cr, ^{114}Sn, ^{136}Xe) as well. Mainly experiments for the Super Heavy Element synthesis (SHE) and the nuclear chemistry including the newly established UNILAC-experiment behind the separator TASCA (Trans Actinide Separator and Chemistry Apparatus) requested beam time for the Experimental hall. In addition, ion beams from the ECR were injected into the SIS (FRS, tests "safety and radiation protection", ESR-experiments). The Penning (PIG) ion source provided Ca, Ti, Al, Ar, Cr, Ni, Sn beams with medium intensity, especially while the ECR was used for the irradiation of patients. For heavy ions (^{197}Au, ^{208}Pb, ^{238}U) beams from the PIG source were accelerated via HSI in the UNILAC with short pulses mostly for the injection into the SIS 18. Additionally, ^{238}U and ^{208}Pb beams were delivered for material research experiments in the experimental hall. The MUlti Cusp Ion Source (MUCIS) provided high current beams for different high energy experiments with high intensities (H_2, ^{14}N, ^{18}O, ^{40}Ar, ^{84}Kr, ^{136}Xe). The Metal Vapour Vacuum Arc (MEVVA) ion source delivered ^{24}Mg, ^{58}Ni and ^{107}Ag for SIS-injection. As in the year before due to serious problems with the delivery of uranium cathodes no high current uranium beam operation was performed. Alternatively, ^{181}Ta was in use to deliver the SIS-machine experiments with a high intensity heavy ion beam. In general the UNILAC operated with high reliability even in June/July when “three beam-operation” was accomplished during the treatment of patients. [1], [2]

Machine Experiments

For high current beam tests at the UNILAC mainly an argon beam from the MUCIS was delivered to the High Current Injector – more than 10 emA of Ar^{10+} (corresponding to 21 emA of $^{238}U^{28+}$ in terms of space charge) were injected into the Alvarez-DTL. The HIPPI (High Intensity Pulsed Proton Injector, CARE, contract number RII3-CT-2003-506395)-experiments were prepared in March and accomplished in June and November/December 2006. [3]

Machine experiments with a low current Pb^{4+} beam (below 1 mA) were performed in March. The HSI-beam transmission was optimized manually and reached the 100%-level. This was mainly obtained by tuning the LEBT-elements and with a changed RFQ rf phase of 17 degree; the rf phases of the Superlense and both IH tanks were not changed.

The measured (low intensity-) beam emittance is significantly small. However the transmission with calculated quadrupole gradients was much lower. This can be explained by a simplified treatment of beam line elements (TRACE-3D code) as well as by the inadequate imput distribution.

The new gas stripper-box

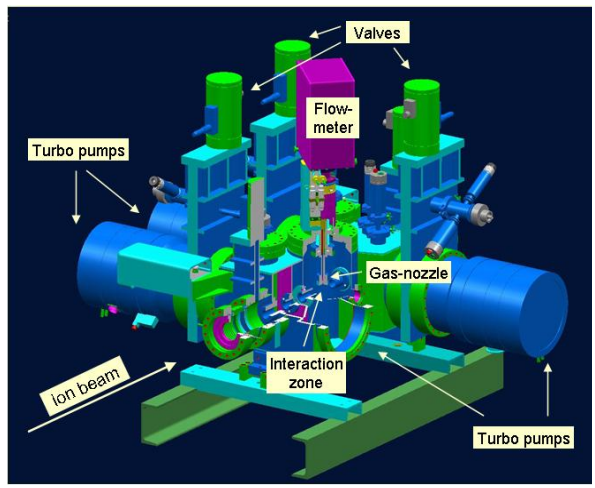

Fig. 1: New gas stripper box.

With a reduction of the available apertures in the old stripper box, it was possible to increase the stripper gas density by 50 %. For medium intense uranium beams this leads to the expected gain for the desired charge state 28+ (up to 12.8 % of the total particle number). The desired equilibrium charge state distribution was reached for a 70 % higher gas density. During long term operation the pumping speed of the old vacuum pumps was not sufficient to compensate this gas load. For high current operation, as required for FAIR, the defocusing effect of the space charge forces leads to particle loss in the transport section after the stripping area [4]. In the new gas stripper box (as shown in Fig. 1) the high stripper gas density for the necessarily enlarged apertures is provided by enhanced vacuum pumping speed.

References

[1] U. Scheeler and D. Wilms, Accelerator Operation Report, (this report)
[2] W. Barth, et. al., UNILAC Status and Development, scientific report 2004, p. 307-308
[3] W. Bayer, et. al., Preparation Status of the HIPPI Experiments, (this report)
[4] W. Barth, et. Al., Development of the UNILAC towards a Megawatt Beam Injector, LINAC2004, Lübeck, Germany, p. 246-250 (2004)

SIS18 Status Report

P. Spiller, U. Blell, O. Boine-Frankenheim, H. Eickhoff, P. Forck, G.. Franchetti, B. Franczak, H. Klingbeil, C. Omet, H. Reich, H. Ramakers, A. Redelbach, U. Scheeler, P. Schütt

Ion Beam Intensities

The intensity of accelerated beams, especially of low-Z ions could be increased significantly and the space charge limit has almost been reached. Figure 1 shows the maximum number of particles per machine cycle. In the intermediate and high-Z range, multi-multi-turn injection is often used to enhance the intensity if the primary intensities are to low. This is typically the case if a Penning source must be used, or operation with a rare isotope is requested. If the MEVVA source can be used, e.g. for production of Ta or U ion beams, the shown intensities can be reached within a single multi turn injection.

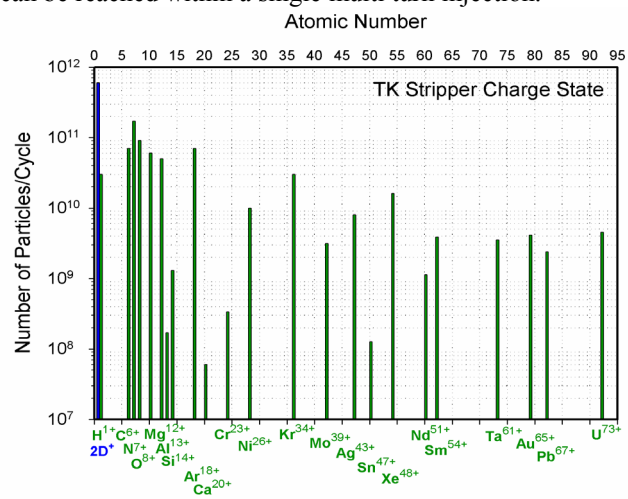

Figure 1: Maximum accelerated number of ions per cycle.

Beam Dynamics

The measurement campaign dedicated to resonance and impedance effects has been enhanced. The planned high current operation for FAIR is prepared by transverse BTF measurements. The experimental results were compared with theoretical expressions, and the betatron tune, chromaticity and the momentum spread have been determined and the origin and type of Landau damping was identified. The enhanced beam losses in connection with synchrotron motion, including space charge tune shift and resonances was a matter of extensive machine studies. This loss mechanism is of major importance for the SIS100 stacking process.

Operation with fast magnet ramps

The new GSI power grid connection has been completed in June. The new link to a local power station, which is exclusively used by GSI, enables a fast ramping of the SIS-18 magnets. In order to investigate undesirable (and unexpected) perturbations in the surrounding power grid, test runs with high power cycles have been performed. No significant influence in the external power grid was observed. However, in the internal 20 kV pulse power grid voltage oscillations were observed which lead to minor problems with the power supply of correction elements. Loss free beam acceleration could be demonstrated up to 4.5 T/s. For higher ramp rates, the total installed Rf acceleration voltage is insufficient.

Dynamic Vacuum and Ionization Beam Loss

The influence of the ramp rate on ionization beam loss at operation with intermediate charge state heavy ions has been investigated. The cross section for ionization decreases with energy such that it was expected, that the total beam loss can be reduced by faster machine cycles. Figure 2 shows the fractional loss of U^{28+} beams for different mechanisms as a function of the ramp rate. It could be proven that the amount of ionization beam loss, which is the most severe loss mechanism for the FAIR project, decreases with the ramp rate.

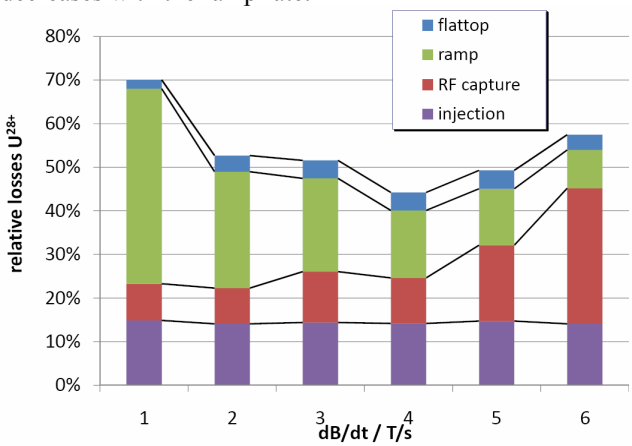

Figure 2: Fractional beam loss for different mechanisms as a function of the ramp rate.

SIS18 upgrade

In the first shut down dedicated to the SIS18 upgrade program, a first vacuum sector has been equipped with new, NEG coated magnet chambers. Furthermore a new high current DC transformer for the measurements of beam currents up to 5 A was installed and successfully commissioned. In parallel, the design, technical planning and prototyping for the planned upgrade measures for the next years have been continued. The design for the new inflector magnet, the electrostatic septum and the collimator prototypes was finished and procurement has started. The production of the new set of quadrupole chambers at the Budker Institute is being prepared. For the new h=2 MA acceleration cavities a technical design proposals was finished and an offer for production from an industrial manufacturers has been obtained.

References

SIS18 home page:
http://www-aix-usr.gsi.de/~siscoord/sis.p14.htm

Using Local Bumps for correcting the SIS18 Closed Orbit

A. Parfenova, G. Franchetti, B. Franczak, M. Kirk, C. Omet, A. Redelbach
GSI, Darmstadt, Germany

In the framework of the SIS18 upgrade several measurement campaigns on the closed orbit (CO) and its correction were carried out in February-May 2006. The CO correction is important for machine operation: the better the CO is corrected, the fewer beam loss occurs during operation due to increase of the machine's acceptance. CO errors are also relevant for feed down effects of multipoles, which may excite dangerous resonances [1]. In the SIS18 24 analog beam position monitors (BPMs), 12 in each plane, are used for the CO diagnostics [2]. For the CO control and correction 6 horizontal and 12 vertical steerers are available. The CO was monitored with the POSI program [3]. The horizontal and vertical CO was corrected using a three-steerer local bump method [4]. Taking any three steering magnets with corresponding bump angles (θ_1, θ_2, θ_3) the condition of the local bump leaves unchanged the orbit at steerers 1 and 3 so that the CO outside of the steerer region 1-3 remains unchanged. This requirement sets a constraint between the angles (θ_1, θ_2, θ_3) according to

$$\begin{aligned} \theta_2 &= -\theta_1 \sqrt{\frac{\beta_1}{\beta_2}} \frac{\sin \psi_{31}}{\sin \psi_{32}} \\ \theta_3 &= \theta_1 \sqrt{\frac{\beta_1}{\beta_3}} \frac{\sin \psi_{21}}{\sin \psi_{32}} \end{aligned} \quad (1)$$

where θ_1 is an arbitrary angle, β_i is the β-function at the ith steering magnet, $\psi_{ij} = \psi_i - \psi_j$ is the phase advance from the ith to the jth steering dipole. It is not necessary that all three steerers are located in neighbouring periods. Due to the SIS18 symmetry in location of steerers in every period, the bump angles are dependent only on the phase advance between the steering dipoles, which could be written as $\psi_{ij} = (j - i)\Delta\psi$, where $\Delta\psi = 2\pi Q/N$, $N = 12$ is the number of periods, and Q is the horizontal/vertical tune. For three neighbouring steerers symmetrically located, the local bump condition (1) becomes

$$\begin{aligned} \theta_2 &= -2\theta_1 \cos \Delta\psi \\ \theta_3 &= \theta_1 \end{aligned} \quad (2)$$

where θ_1 is an arbitrary angle. Therefore for applying Eq. 2 no optical functions are needed: only the phase advance between steering dipoles $\Delta\psi$. The method used is the following: the uncorrected CO shift x_0 in one BPM located between steerers 1 and 3 is measured with the POSI. By varying θ_1 and applying (θ_1, θ_2, θ_3) obtained from Eq. 2 we estimate $\partial x_0/\partial\theta_1$. As the dynamics is linear, the CO at the BPM location is related to θ_1 via

$$x = x_0 + \frac{\partial x_0}{\partial \theta_1}\theta_1 \quad (3)$$

By requiring $x = 0$ we correct the CO and find $\theta_1 = -x_0/(\partial x_0/\partial\theta_1)$. Using this value in Eq. 2 we perform the correction. By repeating this procedure to all steerers in groups of three the CO was consequently corrected at all positions in each plane. In Fig. 1a is shown the uncorrected horizontal and vertical CO at injection energy 11.4 Mev/u, for $Q_x = 4.17$, $Q_y = 3.35$. In Fig. 1b the CO after the correction is presented. The vertical CO was brought to a straight line with nearly zero mm displacement. The horizontal correction was performed not as accurate as the vertical one because of the lack of steerers (only 6 in this plane). The CO was also corrected for the extraction energy. It was also checked that the correction setting found keeps the CO corrected over a wide range of energies [100;1000] Mev/u. We have also checked the robustness of the correction by changing the tune from (4.29, 3.29) to (4.17, 3.35), the present high intensity working point, and kept the correction steerers unchanged. We found no relevant CO changes. Tests performed with optimized multiturn injection have shown that when the CO is corrected the beam intensity increased at least by a factor of 2 as a result of an obtained larger machine acceptance.

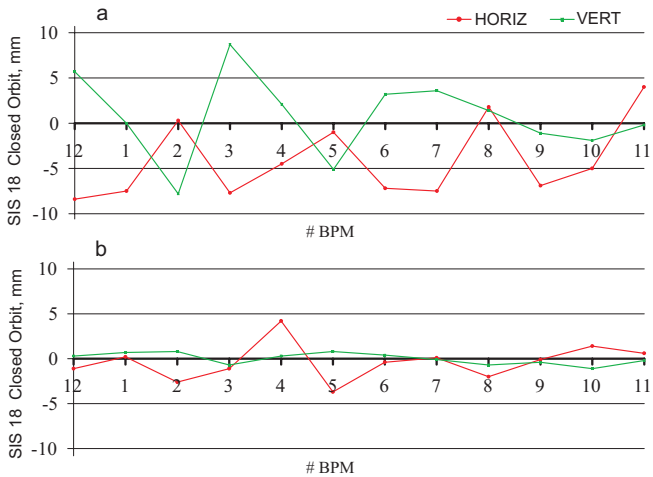

Figure 1: The horizontal and vertical CO at injection energy a) before correction; b) after the correction.

In December 2006 the implementation of the CO correction using a three-bump local orbit distortion method was implemented in SIS18 [5].

References

[1] G. Franchetti et al., GSI-Acc-Note-2005-12-001.

[2] P. Kowina et al., Proceedings of DIPAC-2005.

[3] `http://bel.gsi.de/mk/operating/posi/posi.html`.

[4] A. Parfenova et al., GSI-Acc-Note-2006-11-001.

[5] A. Redelbach, CO-Korrektur mit MIRKO bzw. SIST (2006), `\\Winfilesva\scratch\Redelbach\Documents\COC\Auto_COC.pdf`.

ESR Operation and Development

K. Beckert[1], C. Dimopoulou[1], V. Gostishchev[1], F. Nolden[1], P. Petri[1], U. Popp[1], M. Steck[1], and I. Gerritsen[2]
[1]GSI Darmstadt; [2]University of Ulm

1 ESR Operation and Main Experiments

The ESR storage ring was operated for experiments in various modes, which had been developed in previous years and which were mainly tuned according to the requirements of the different experiments. The standard storage mode in combination with cooling covered a range of beam energies from 59 to 400 MeV/u. For the experiment probing time dilation a $^{7}Li^{1+}$ beam at 59 MeV/u was stored and cooled with the electron cooling system. In the internal target straight section the Li-beam was merged with co- and counter-propagating laser beams. The overlap of the laser and ion beam was adjusted by means of mechanical scrapers. The number of ions in the metastable state, however, was still too low to permit the high precision measurement of the beam velocity required for this experiment. The same techniques of beam overlap control and fluorescence light detection were applied in laser cooling experiments with $^{12}C^{3+}$ at 123 MeV/u. In this experiment electron cooling was used as pre-cooling for the laser cooling. Systematic measurements should provide a better understanding of laser cooling at relativistic beam energies.

The highest beam energies were used for experiments with rare isotope beams from the fragment separator FRS. At 400 MeV/u the combination of stochastic pre-cooling and final electron cooling results in shortest total cooling time and optimum final beam quality.

Stored beams at the injection energy were also used for experiments at the internal target. The FOCAL experimental setup installed at the internal target was commissioned with an electron cooled beam of bare lead ions at 219 MeV/u which collided with krypton atoms in the gas jet.

The lithium-like $^{114}Sn^{47+}$ ion at an energy of 300 MeV/u was used to study electron emission from the internal target operated with hydrogen. The electrons where analyzed after a magnetic separator dipole which is installed about 3 m downstream the interaction point. As the magnetic deflection field for electrons of the same velocity as the ion beam is rather low, the closed orbit distortion of the ion beam caused by the spectrometer dipole could be compensated by horizontal correction magnets.

Experiments at the ESR also used the deceleration mode. Bare uranium ions were injected at 324 MeV/u and decelerated to 15 MeV/u for recombination experiments at the electron cooler. Electron cooling at an intermediate energy of 30 MeV/u was applied to reduce the emittance for best efficiency of deceleration. X-ray detectors installed close to the toroids at the entrance and exit of the cooler section were used as detectors for high resolution spectroscopy of recombination radiation.

The experiments employing the isochronous mode for mass measurements of short-lived unstable nuclei were continued. An optimized injection scheme was used which injects the beam onto a central orbit to avoid field errors far from the central orbit. The necessary displacement of the orbit at the injection kicker, which is located at an outer radial position, was achieved by a local orbit bump.

2 ESR Modifications and Machine Development

In the the internal target straight section additional glass windows were installed for detection of fluorescence light after excitation of ions by a laser beam. During a shutdown in October the scattering chamber of the internal target was replaced by a new one. This reaction miscroscope chamber is designed for the installation of position sensitive detectors for slow recoil ions and electrons created in collisions between the fast projectiles and the target atoms. A set of Helmholtz coils was installed which generate a homogeneous magnetic field parallel to the beam to guide the emitted electrons to the detector.

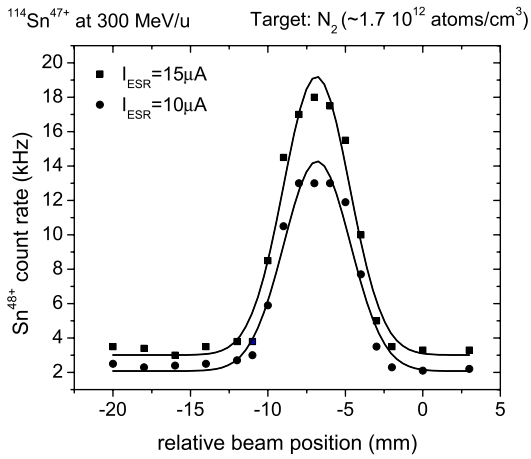

Figure 1: Count rate of ionized beam particle downstream the internal gas target as a function of the horizontal beam position. A Gaussian fit agreed with a FWHM target diameter of 5 mm.

The internal target was equipped and tested with a 50 μm diameter nozzle. As the gas flow is mainly determined by the skimmer geometry, which is unchanged, the same gas jet diameter of 5 mm at the interaction point was observed as previously with a 100 μm nozzle (Fig. 1). The smaller nozzle allows a reduction of the gas consumption and gas load to the ultra high vacuum system, particularly favorable when operated with noble gases. For operation with hydrogen gas the input pressure can be increased resulting in an increased target thickness.

Machine experiments studying the effect of the internal target and the electron cooling system on the stored beam were continued. More data on the equilibrium between target and cooling and on the influence of the target on a beam without cooling were collected and compared to the results of simulation codes [1].

In preparation of experiments studying the accumulation of heavy ion beams by a combination of barrier buckets and electron cooling, one of the two identical rf cavities was modified for broadband operation. Experiments to study longitudinal accumulation schemes are scheduled for the beginning of 2007.

References

[1] V. Gostishchev et al., contribution to this scientific report.

CODE BENCHMARKING STUDIES WITH THE ESR INTERNAL TARGET

V. Gostishchev[1,#], C. Dimopoulou[1], K. Beckert[1], P. Beller[1], A. Dolinskii[1], F. Nolden[1], M. Steck[1], A. Smirnov[2], A. Sidorin[2], I. Meshkov[2], and G. Trubnikov[2]
[1]GSI, Darmstadt, Germany; [2]JINR, Dubna, Russian Federation

Nuclear physics and fundamental interaction studies in collisions of rare isotope or antiproton beams with dense targets play a central role in the NESR and HESR storage rings of the future FAIR facility [1]. For instance, high luminosities are expected in experiments with a hydrogen pellet target in the HESR. Therefore, it is important not only to understand but also to predict the influence of a dense target on the stored beam and to investigate the interplay between phase space cooling, intrabeam scattering (IBS) and target effects. Some experiments with gas targets in light ion storage rings were carried out earlier [2]. Measurements of equilibrium horizontal emittance ε_x and momentum spread $\Delta p/p$ were performed before at the ESR [3].

The new experiments were carried out with a stored coasting beam of bare lead ions (Pb^{82+}) with an intensity of about 10^8 particles and a kinetic energy of 400 MeV/u. The ESR electron cooler was used to reduce the phase space density of the injected beam, to provide a high quality, dense stored beam and to compensate heating by the target. Four target gases (N_2, Ar, Kr, Xe) were used in the gas-jet, with densities in the range $2.5–8\times10^{12}$ atoms/cm^2 (gas-jet diameter ≈ 5 mm).

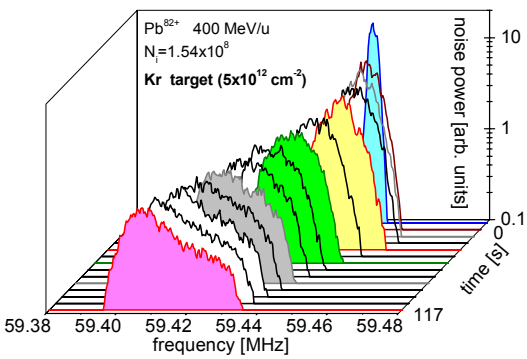

Figure 1: Schottky spectra recorded every 9 s during the blow-up measurement with the electron cooler off. Target is on for t ≥ 30 s.

The study was focused on two main procedures. For both procedures, the corresponding measurements without target were performed, thus allowing to identify and evaluate target effects. First, in the blow-up measurements the energy loss and the phase space growth of the beam due to the target have been measured as a function of time within a time interval of 2 min. Initially, the beam was cooled down to equilibrium state. At t=0 the electron cooler was switched off. Then, after about 30 seconds delay to allow for the relaxation of the beam phase space due to IBS, the Kr gas-jet target was switched on. The evolution within approximately 120 s of the longitudinal Schottky noise power spectrum for the 30th harmonic of the revolution frequency was recorded. A typical measurement is shown in Fig. 1 with a time step of 9 s. After the target was switched on (t ≥ 30 s), the position of the peak shifted to lower frequencies i.e. to lower energy due to energy loss and the width of the distribution increased due to energy straggling.

In another series of measurements at a fixed ion beam intensity of 1.58×10^8 particles, the beam parameters at the equilibrium between electron cooling, IBS and the target effects were measured for various electron currents in the cooler in the range 10 − 800 mA. These data in comparison with BETACOOL [4] simulations are shown in Fig.2. The non-magnetised model (NM) and Parkhomchuk model were used for the evaluation of cooling effects. The NM is in better agreement with experiment because it reproduces the measured dependence of emittance and momentum spread on electron current for the case without target and predicts the equilibrium states when the target is on [5].

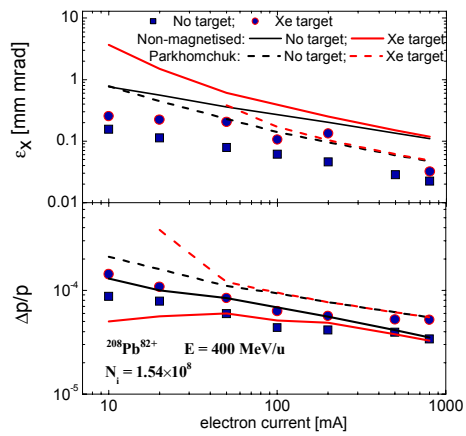

Figure 2: Equilibrium horizontal emittance and momentum spread (r.m.s. values) versus electron current of the cooler for Xe target (2.5×10^{12} atoms/cm^2).

REFERENCES

[1] An International Acc. Facility for Beams of Ions and Antiprotons, Conceptual Design Report, GSI, 2001.

[2] C. Ekström, NIM A 362 (1995) 1.

[3] GSI Scientific Report (2005) 125.

[4] BETACOOL, http://lepta.jinr.ru/betacool.htm.

[5] V. Gostishchev et al. Proc. of the 10th Europ. Part. Acc. Conf., Edinburgh (2006), http://accelconf.web.cern.ch/

#V.Gostishchev@gsi.de

Ion Source Development and Operation

P. Spädtke, M. Galonska, B. Gutermuth, F. Heymach, R. Hollinger, R. Lang, K. D. Leible, J. Mäder, K. Ochs, J. Roßbach, P. Schäffer, S. Schäffer, M. Stork, K. Tinschert, and C. Vierheller
GSI, Darmstadt, Germany

ECR Ion Source (ECRIS)

Regular operation at the High Charge State Injector (HLI) was performed for $^{7}Li^{1+}$ (6 d), $^{12}C^{2+}$ (97 d), $^{22}Ne^{3+}$ (8 d), $^{25}Mg^{4+}$ (12 d), $^{30}Si^{6+}$ (26 d), $^{48}Ca^{7+}$ (27 d), $^{54}Cr^{7+}$ (23 d), $^{54}Cr^{8+}$ (2 d), $^{114}Sn^{16+}$ (7 d), $^{136}Xe^{18+}$ (4 d). $^{136}Xe^{19+}$ (7 d). and $^{136}Xe^{21+}$ (3 d).

After the successful test to evaporate natural SiO from the ECR standard oven (STO) for the production of a $^{28}Si^{5+}$ beam, a beam of $^{30}Si^{6+}$ could be provided from the ECRIS at the HLI for an experiment on super heavy elements (SHE). Highly enriched ^{30}SiO has been used to provide a beam of high stability and intensity for nearly 4 weeks (see Fig. 1). The average material consumption of 1.7 mg/h was considerably low leading to a good efficiency.

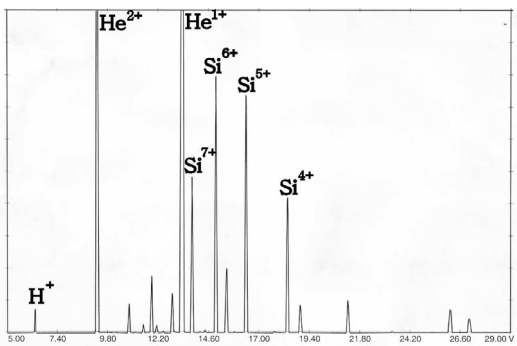

Figure 1: Charge state spectrum of the analyzed ion beam ($^{30}Si + O + He$); full scale = 100 μA

Highly enriched metallic ^{114}Sn has been used for the first time to provide a beam of $^{114}Sn^{16+}$ at medium intensity level. After $^{26}Mg^{5+}$ had been provided several times in the past years, in 2006 a $^{25}Mg^{4+}$ beam has been requested for experiments on nuclear chemistry. Again highly enriched metallic material of ^{25}Mg has been used for evaporation from the STO at low temperature level. The ECRIS has been optimized for high beam intensities to fulfill the experimental requirements. Fig. 2 shows a charge state spectrum of the analyzed beam which is already optimized on $^{25}Mg^{4+}$ and $^{25}Mg^{5+}$, respectively. The particle intensity of the charge states 4+ and 5+ is in the same range (40 μA).

A special request was made by an experiment performing laser spectroscopy at the ESR, which intends to use He–like $^{7}Li^{1+}$ in the long-lived metastable ions $^{3}S_1$–state as ion beam. As the plasma of an ECRIS with its electron energy distribution ranging up to 100 keV and more contains some amount of such metastable ions, a fraction of those can be found in the extracted ion beam [1]. Therefore a test experiment has been performed to determine the amount of metastable $^{7}Li^{1+}$–ions in the ion beam in the ESR, while the ECRIS was operated with LiF as it had been done previously. In contradiction to the assumption the fraction of metastables was too small for the dedicated experiment. In order to change the plasma conditions in the ECRIS Li_2CO_3 has been used instead of LiF as evaporation source for a second test run. However, the fraction of metastable ions in the ESR again was not sufficient for the experimental requirements. Further investigations to determine the fraction of metastables directly after the mass to charge analysis of the extracted ion beam are planned.

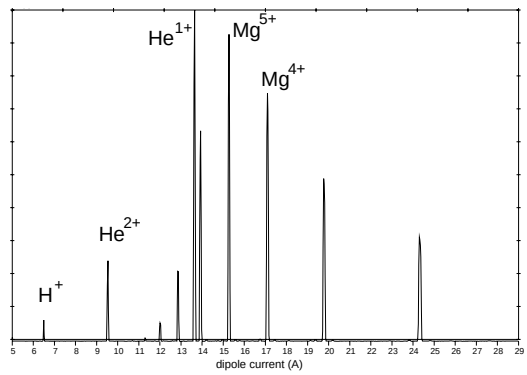

Figure 2: Charge state spectrum of the analyzed ion beam ($^{25}Mg + He$); full scale = 200 μA

Penning Ion Source (PIG)

Regular operation was performed for: $^{12}C^{1+}$ (8 d), $^{40}Ar^{1+}$ (24 d), $^{40}Ca^{3+}$ (5 d), $^{50}Cr^{2+}$ (6 d), $^{52}Cr^{2+}$ (17 d), $^{58}Ni^{3+}$ (7 d), $^{116}Sn^{5+}$ (4 d), $^{132}Xe^{6+}$ (15 d), $^{208}Pb^{3+}$ (35 d), $^{238}U^{4+}$(66 d).

As alternative for the ECR ion source for the above mentioned Li-experiment the PIG ion source has been chosen. The amount of metastables ions is still to be measured. Material for the required sputter electrodes has been ordered to perform ion source tests in the nearest future.

High Current Ion Sources (MEVVA/MUCIS)

Regular operation was performed for: $^{1}H_3^{1+}$ (18 d), $^{14}N_2^{1+}$ (11 d), $^{18}O_2^{1+}$ (13 d), $^{24}Mg^{1+}$ (9 d), $^{40}Ar^{1+}$ (26 d), $^{58}Ni^{2+}$ (6 d), $^{86}Kr^{2+}$ (19 d), $^{107}Ag^{2+}$ (10 d), $^{132}Xe^{3+}$ (10 d), $^{136}Xe^{3+}$ (19 d), $^{181}Ta^{3+}$ (3 d).

For both projects, the UNILAC upgrade program for high current uranium ion beams, and the 70 mA, 70 MeV proton beam injector for FAIR, specific features of a new compact LEBT have been studied.

At the High Current Test Bench first measurements of the ion beam quality behind a solenoid were performed using a pepper pot device to measure different 2D phase space projections and using a viewing target to measure the real space profile.

A CHORDIS with the regularly used 13-hole extraction system, delivering a 60 mA helium beam at 25 kV, was used in front of a 2-solenoid transport system. A ring structure of the ion beam can be observed on the target when the focus of the ion beam is behind the viewing target, see Fig. 3, left. This ring structure, created by each single beamlet, was already predicted by 2D-simulation with AXCEL; the corresponding abberations are generated within the extraction system.

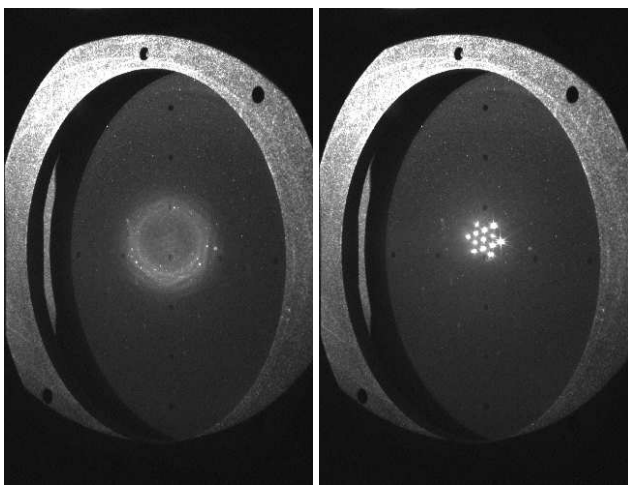

Figure 3: Viewing target behind the solenoid. Left: focus is behind the plate. Right: focus is on the plate.

With the focus directly is on the viewing plate, the exact structure of the 13-hole extraction system was projected in a very brilliant way, shown in Fig. 3, right.

This is a strong hint that solenoids can be used for beam transport even when the filling degree is very high.

To achieve a sharp image of the extraction system a correct focal strength has to be applied. As a result this is not a free parameter for the following beam transport system any more.

Ongoing simulations with KOBRA3 could reproduce these experimental results with the assumption of full space charge compensation within the 10 ms pulse of the ion beam.

High current test injector (HOSTI)

For commissioning measurements of both RFQs, for the therapy accelerator facilities at HIT in Heidelberg, and at CNAO in Pavia, Italy, respectively, the HOSTI has been temporarily modified to host the RFQs. During the exchange of both RFQs the location of the ion source has been changed to the inside of the Faraday cage. The required proton beam intensity has been provided by a MUCIS during all the time without any problem, beside the necessary filament replacement. Beam diagnostics and data acquisition were commissioned in parallel.

Uranium Material for all Ion Sources

The supply of uranium cathodes (all ion sources use metallic uranium, depleted to $\leq 0.3\%$ U^{235}) turned out to be a problem in the past years because of the material properties. Sintered material turned out not to be appropriate, metallic material of the required purity was not available. Because of its sensitivity to the atmosphere, the material becomes brittle during operation. Fortunately, a manufacturer was found who is capable of producing uranium cathodes, which are successfully tested in PIG and MEVVA ion source operation. These cathodes have been tested in October 2006. The PIG ion source performance with theses cathodes is just as good as with the former electrodes. A 7 days test run with the MEVVA ion source has shown promising results. The fraction of U^{4+} was about 60 % compared to 67 % which have been reached until 2003. An ion beam current of nearly 10 mA of U^{4+} was achieved in regular operation and a maximum current of 15 mA could be measured in the current transformer UL5DT8 (instead of the former 18 mA in regular operation with a maximum of 25 mA). The pulse-to-pulse stability and the long term stability were satisfactory during the test run while the long-term behavior and the life time of the ion source still must be investigated in a future test beam time.

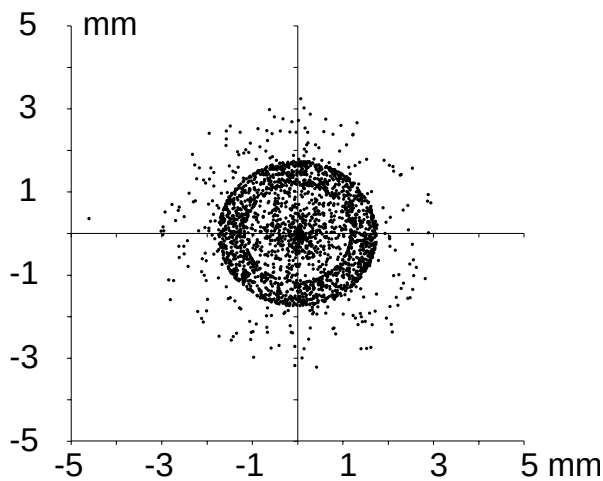

Figure 4: Simulated ring structure of the ion beam behind a solenoid.

References

[1] A. Müller, private communication

Status of the 28 GHz Superconducting ECR Ion Source Project ISIBHI–MSECRIS*

K. Tinschert, GSI, Darmstadt for the ISIBHI collaboration [1]

During the reporting period the work on the project was characterized by design, construction and starting procurement of the main components of the MS-ECRIS (Multi-Purpose Superconducting ECR Ion Source) and its ancillary equipment.

Superconducting Magnets and Cryostat

In the design review with ACCEL Instruments [2], who will deliver the magnet system and the cryostat, its final parameters and design were fixed. The warm bore has an inner diameter of 202 mm. The 3 solenoid coils generating the mirror field will provide field maxima of 4.5 T at the injection, 3.2 T at the extraction, with a minimum axial field variable between 0.3 and 0.9 T. The maximum radial field is expected to be above 2.7 T. The ribbon-linked wire of the hexapole coils consists of 5 NbTi wires (1.20 mm$\times$0.75 mm) The solenoid coils are made from single cylindrical wires (0.80 mm diameter). A sophisticated winding technique will avoid excessive magnetic fields and forces in the conductor. Particularly at the coil heads a cos(3Θ)-shape solution was adopted to minimize the field inside the conductor. A total cooling capacity of 3.0 W is provided by 2 cryocoolers. The quench detection system (QDS) will switch off the magnets in case of quench, without any damage to the magnets. Fig.1 shows the layout of the magnet system in the cryostat assembled with neighboring components. More details are described in [3].

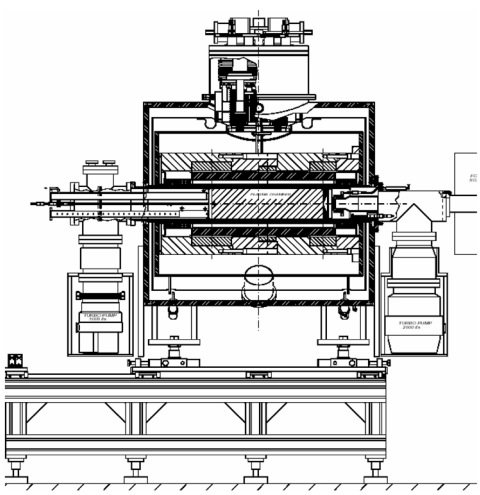

Figure 1: Schematic view of the MS-ECRIS with the cryostat on its support. Length of the cryostat: 1300 mm

RF system and mechanical design

The 28 GHz gyrotron generator is presently under refurbishment and will be equipped with a new main power supply. According to numerical calculations the optimum location of the waveguide in the injection flange has been defined. Further feedthroughs for biased disk, 14-18 GHz rectangular waveguide, evaporator ovens, water cooling and plasma diagnostics are incorporated in the injection flange.

The design of the plasma chamber (length: 1150 mm, inner diameter: 180 mm) is adapted to the requirements of RF power dissipation, of X-ray shielding and of electrical insulation. The extraction system consists of the plasma electrode, fixed in the plasma chamber, and of a movable system of screening and ground electrode. An efficient water cooling is applied to the plasma chamber and to the extraction system to handle the high dissipated power.

Experimental Setup

The preparation of the test stand has been started. The support for cryostat, injection box and extraction box is under construction. It will enable a longitudinal movement of the source along the axis for 1.2 m via a rail system.

To investigate the anisotropic beam profile and emittance, pepperpot devices will be used instead of slit-grid devices. Besides simple pepperpot devices already in use at the ECR injector setup at different positions along the beamline another versatile emittance meter also based on the pepperpot principle is under construction.

References

[1] K. Tinschert, P. Spädtke, R. Lang, J. Mäder, J. Roßbach, GSI, Darmstadt, Germany; G. Ciavola, S. Gammino, L. Celona, F. Consoli, G. Gallo, D. Mascali S. Passarello, INFN-LNS, Catania, Italy; M. Cavenago, A. Galatà, INFN-LNL, Legnaro, Italy; H. Koivisto, P. Suominen, O. Tarvainen, JYFL, Jyväskylä, Finland; C. Barué, M. Lechartier, R. Leroy, GANIL, Caen, France; J. P. M. Beijers, S. Brandenburg, H. R. Kremers, KVI, Groningen, Netherlands; D. Vanrooyen, TSL, Uppsala, Sweden; D. Küchler, CERN, Geneva, Switzerland; D. Hitz, P. Seyfert, CEA, Grenoble, France; L. Schachter, S. Dobrescu, NIPNE Bucharest, Romania

[2] ACCEL Instruments GmbH, Friedrich–Ebert–Str. 1, D–51429 Bergisch Gladbach

[3] G. Ciavola et al.; Rev. Sci. Instr. 77 (2006) 03A303

* Work supported by EU, EURONS contract No. 506065.

Beam Profile Analysis at the ECR Injector Setup (EIS)

P. Spädtke[1], L. Celona[2], W. Kaufmann[1], R. Lang[1], J. Mäder[1], J. Roßbach[1], J. Stetson[3], and K. Tinschert[1]

[1]GSI Darmstadt Germany; [2]INFN Catania Italy; [3]MSU East Lansing USA

To improve the beam transport from the source to the first accelerating structure, especially with respect to the planned upgrade of the HLI with a 28 GHz MS-ECRIS, measurements at the test bench were made. The EIS test bench is an exact copy of the first part of the existing injection beam line, established in 1989, and improved in 2001 by adding a solenoid behind the extraction system to increase the beam line acceptance, and to allow the matching of the extracted beam with different divergence angles to the following beam line. Due to the symmetry conditions of the plasma confinement (magnetic mirror with hexapolar cusp field) a contribution to the beam emittance can be expected. In the present setup no elements are available for observation or correction of this effect. We installed viewing plates instead of grid profile monitor into the beam line at three different places: directly behind extraction, between solenoid and quadrupole singlet, and at the focal point of the dipole magnet. The BaF coated targets are placed at an angle of 45^o with respect to the beam axis into the beam line. The front side of the target is observed with a CCD-camera through a vacuum window.

Measurements

The first target can be used to check the influence of source parameters on the beam quality. The traces of the extracted beam seems to be triangular and hollow. The heaviest masses do have the largest diameter, whereas lighter particles are already over-focused within the extraction system.

Ramping the magnetic solenoid directly behind the ion source focuses each single mass-to-charge ratio individually on the second viewing target. From these measurements the beam diameter for different focusing strengths as shown in Fig. 1 can be estimated, see Fig. 2. The strong influence of the hexapole becomes evident. If its influence could be corrected at this stage the beam transport could be improved substantially.

Figure 1: Beam profile of a 1 mA, 15 keV He^+ beam on the viewing target behind the solenoid with increasing focusing strength of the solenoid from left to right.

The ion beam can be used as probe to investigate the ion source properties. Starting from a typical working point of the CAPRICE ion source, the magnetic flux density of both mirror coils, the gas pressure, the rf-power, and the extraction gap width has been changed individually while the beam response on the viewing target has been recorded. One should keep in mind, that most of these parameters also influence the plasma generation and cannot be considered as free parameter.

There are also hints that depending on the frequency different rf-modes will heat the electrons differently. First results indicate that the intensity distribution within the beam can be influenced by tuning the frequency in a very narrow range of ± 40 MHz at 14.5 GHz.

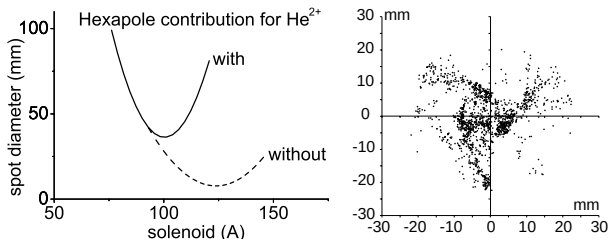

Figure 2: Left: beam diameter as function from focusing strength with and without the contribution of the hexapole. Right: simulated beam (Ar^{3+}) in a real space projection directly behind extraction, showing the good agreement between simulation and experiment.

Simulation

For the simulation of the extraction of an ion beam from an ECRIS a correct model has to be used. The movement of ions can be assumed to be collision free because the ion Lamor radius becomes small, which is different from the model used so far. Electrons within the plasma chamber are assumed to have a radial location according to their energy. Ions can be created at these locations according to the electron distribution, different charge state distributions and neutrals distribution, and their specific cross section for generation. In addition to the requirement for the production of ions the mirror condition of the magnetic confinement has to allow extraction. An example of such a simulation is shown in Fig. 2. The phase space coordinates generated by this simulation with KOBRA3 can be traced through the full beam line for the actual optical setting to design possible hexapole correction schemes, or to proof the degree of space charge compensation.

The HITRAP RF System

W. Vinzenz, G. Eichler, W. Hartmann, W. Hartmann(Mz), M. Hörr, J. Mohr, M. Pilz, A. Pitzen, G. Rudolph, R. Scholz and A. Windolf
GSI, Darmstadt, Germany

Introduction

This report describes the RF supply for the HITRAP facility, used for deceleration of heavy highly-charged ions from 4MeV/u to 6 keV/u. At least one IH, one RFQ and three bunching cavities, located in the former reinjection channel from ESR to SIS18, have to be supplied with RF power up to 200 kW peak at 108 and 216 MHz. [1]

Technical realization

After some modifications, two of the 200 kW tube amplifiers, no longer used at the UNILAC, will provide sufficient pulse power for the IH (approx. 180 kW) and the RFQ (approx. 80 kW). The maximum deliverable pulse length is 1.5 ms at a repetition rate of 1s (duty cycle ~ 0.15%). These amplifiers are sharing the needed power supplies for two tube sections (driver and final stage) each. Because of the very low duty factor one 'single line' supply unit is powerful enough to operate in a partitioned mode.

The 200 kW tube amplifiers (already serviced, one tested up to 190 kW and the second still at the test bench) will be moved to the HITRAP platform end of March 2007.

Further a so called Double-Drift-Buncher (DDB) located in front of the IH and a Rebuncher structure in between the IH and RFQ have to be supplied with 2 kW peak at 108 MHz. One 2 f -Buncher in between DDB and IH is supplied with 2 kW peak at 216 MHz. In order to feed these three Bunchers, two 2 kW solid-state amplifiers at 108 MHz and one similar in design at 216 MHz were specified and purchased after a call for tender.

As the frequency of 216 MHz has previously not been used at GSI some equipment had to be developed or redesigned. A frequency doubler 108 / 216 MHz and the appropriate LLRF amplification and distribution were made by the GSI LINAC RF group. In case of the LLRF controls we decided to stay at the same design like the 108 MHz equipment. The required modifications at the LLRF function blocks were made by IBT Darmstadt. A lot of additional control electronic equipment as well as Simatic S7 PLC controls incl. software and touch screen operation were developed and put in operation by RF group members. All these devices are plugged in a separate test bench for functional tests at the moment. The racks for all the LLRF and the 2 kW amplifiers (1) are already installed on the HITRAP platform. Also the RF cabling for power and tank probe signals is done whereas the connectors will be mounted after placing the cavities. New electronics for the cavity tuning systems (HICAT type) are ordered and will be delivered in February 2007.

The connection to the GSI control system will be made by a redesigned Interface unit used at the UNILAC. Due to the long beam pulse breaks (up to some seconds) a free running timing generator creates the needed warm-up-pulses for the RF amplifiers. This function will be switched off synchronized by the ESR timing if bunches are ready to be decelerated by HITRAP.

References

[1] Th. Beier et al. “HITRAP Technical Design Report" GSI Darmstadt , October 2003

Figure 1: 2 kW Amplifier rack

Results of HIPPI Machine Experiments

W. Bayer, W. Barth, L. Dahl, P. Forck, P. Gerhard, L. Groening, I. Hofmann and S. Yaramishev
GSI Darmstadt

Introduction

At GSI heavy ion beams are accelerated by the UNIversal Linear ACcelerator UNILAC and the heavy ion synchrotron SIS 18. The UNILAC was originally designed for low current operation. To fill SIS 18 up to the space charge limit the high current injector HSI was mounted in 1999 and upgraded in 2004 [1, 2]. Presently the highest achieved number of $^{238}U^{28+}$ ions at SIS injection amounts to $1 \cdot 10^{11}$ per 100 μs (4.5 emA). For the future accelerator complex of FAIR the UNILAC has to deliver up to $3.3 \cdot 10^{11}$ particles of $^{238}U^{28+}$ per 100 μs (15 emA) to SIS 18 with normalised transverse emittances of $\beta\gamma\,\epsilon_x = 0.8\,\mathrm{mm\,mrad}$ and $\beta\gamma\,\epsilon_y = 2.5\,\mathrm{mm\,mrad}$ [2]. As the Alvarez quadrupoles do not provide for adequate phase advances σ_0 for highly space charge dominated beams, it can be assumed, based on calculations with the multiparticle simulation code PARMILA, that just about $1.9 \cdot 10^{11}$ particles of $^{238}U^{28+}$ per 100 μs (8.4 emA) are contained within these emittances. In order to meet the FAIR requirements a dedicated upgrade of the UNILAC is essential [3], one aim is to improve the high current beam brilliance by increasing σ_0 of the Alvarez DTL.

Within the beam dynamics work package of the European JRA "High Intensity Pulsed Proton Injector" (HIPPI) investigations of space charge forces during the acceleration of high intensity beams are funded. It is intended to benchmark different simulation codes against each other [4] and to compare them with experimental data. The UNILAC with its various beam diagnostics devices offers excellent possibilities doing that. For the first time exclusive beam time (96 shifts) for UNILAC machine was requested and approved for 2006 by the scientific advisory committee.

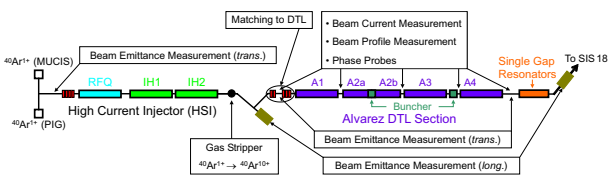

Figure 1: Overview of the experimental setup.

Experimental Setup

An overview of the experimental setup is shown in Fig. 1. All high current measurements were performed with a 7 emA $^{40}Ar^{10+}$ beam which is adequate to 15 emA $^{238}U^{28+}$ concerning space charge forces but due to the lower mass over charge ratio the DTL quadrupoles can be operated at higher phase advances.

In preparation for the measurements (transverse emittance as function of rf phase, beam energy and σ_0) the UNILAC was optimised for low (0.2 emA) and high (7.1 emA) $^{40}Ar^{10+}$ beam intensities:

- setup of the HSI for minimal longitudinal emittance,
- matching the beam to the first Alvarez tank,
- minimisation of energy parasites behind DTL,
- optimisation of the two bunchers in the DTL section to minimise the longitudinal emittance.

Preliminary Results

Results of former measurements presented in [5] showed a transverse emittance growth for low beam intensity of factor 2 while in DYNAMION [6] calculations no emittance growth was predicted. The improved beam quality was confirmed in a measurement for an optimised UNILAC setup as shown in Fig. 2. The remaining transverse emittance growth of about 1.2 appears mainly in the 1st DTL section and most probably results from a longitudinal mismatch to tank A1 due to indications of a large phase width.

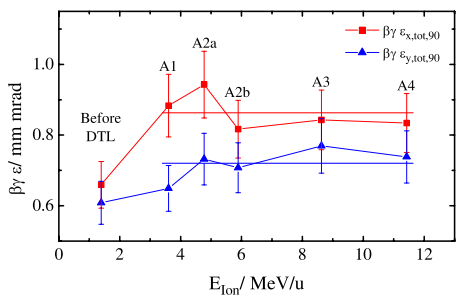

Figure 2: Measured transverse 90 % total emittances as function of beam energy for 0.2 emA $^{40}Ar^{10+}$ [7].

The accurate evaluation of the high intensity data is still in progress. As a preliminary result for the high current case a minimum transverse emittance growth factor of about 2.1 ($\sigma_0 = 60°$) was measured. About 70 % of the beam intensity delivered by the UNILAC is inside the acceptance of SIS 18.

Additionally, simulations with DYNAMION will be performed for a more detailed understanding of the results.

Acknowledgement

We acknowledge the support of the European Community-Research Infrastructure Activity under the FP6 Structuring the European Research Area programme (CARE, contract number RII3-CT-2003-506395).

References

[1] W. Barth, Proc. LINAC 2000, p. 1033
[2] W. Barth *et al.*, Proc. LINAC 2004, p. 246
[3] W. Barth *et al.*, Proc. LINAC 2006, to be pub.
[4] A. Franchi *et al.*, GSI Report 2004, p. 319
[5] W. Bayer *et al.*, GSI Report 2005, p. 87
[6] S. Yaramyshev *et al.*, Nucl. Instr. and Meth. A **558** (2006) 90.
[7] W. Bayer *et al.*, Proc. LINAC 2006, to be pub.

First measurements with the BPM High Performance Baseband Digitalization*

Andreas A. Galatis[1,2], K. Lang[1], P. Forck[1], W. Kaufmann[1], P. Kowina[1], J. Schölles[1], A. Peters[1], and A. Zoubir[2]

[1]GSI, Darmstadt, Germany; [2]TUD, Signal Processing Group, Darmstadt, Germany

Task for BPM Digitalization

The present Beam Position Monitor (BPM) electronics lacks a reliable evaluation for bunch-by-bunch measurements and has to be renewed. After the data collection and offline evaluation in 2005, the completed prototype 125MSa/s ADC-board connected to a high performance Xilinx Virtex II Pro FPGA was tested. The hardware is described more detailed in [1]. Dedicated fast online algorithms, as described in [2] where implemented and tested at SIS18 and at the CERN PS in the second half of 2006. For accurate calculation of the transverse bunch position, well defined integration windows are needed. The determination of the position using the integral value minimizes the noise in the gained position signal. The baseline of the signal is a property that also alters the position signal and therefore should be restored adequately. Main aspect of the first tests was the proof of concept in terms of online calculation feasibility.

Methods

Integration window length and baseline shift are time varying parameters and can be bunch specific. The time variation is mainly due to the changing bunch parameters during the acceleration procedure. The baseline shift is unavoidable due to analogue signal processing in the signal path and mainly depends on the bunch properties. For the window generation a free-running algorithm was developed. It does not use external parameters to determine the window starting and ending points. It makes use of the fact that the BPM signal is approximately linear between the particle bunches and almost Gaussian inside them. An accumulated signal is generated from the original signal, which has flat regions outside bunches and steep increases and decreases during bunch passage. To flatten the signal and therefore remove some noise we apply a median filter over 5 values. This smoothing-method avoids a division, which otherwise would have negative effects on computational speed. For the baseline restoration, its contribution from the prior and post bunch signal can be used. The predefined integration windows are used to distinguish between baseline region and bunch. After calculating the mean of the two signals, we add the inverted result to the actual bunch signal.

Results implementing these methods in sequence on an $^{238}U^{73+}$ beam at 750MeV/u can be seen in Figure 1 and in [2]. The baseline restored sum of two opposing plates

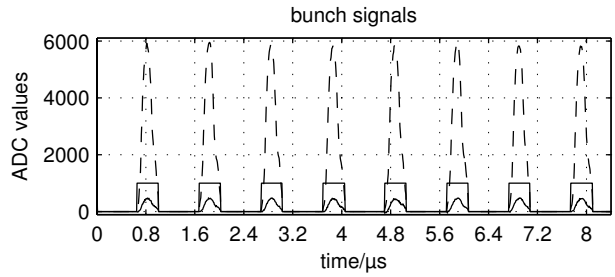

Figure 1: Raw data of the bunches from the acceleration of a U^{73+} beam recorded with 8 ns per sample. The baseline restored sum (dashed) and difference (full) signals and the calculated window (rectangular) are shown.

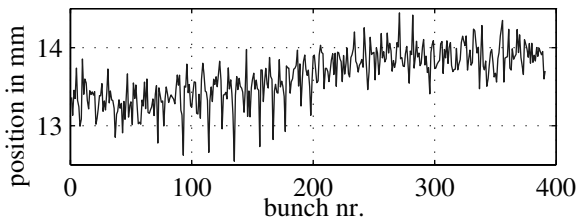

Figure 2: Calculated beam position.

and the corresponding difference is shown together with the integration window. In Figure 2 we see the calculated position from a longer data string, part of which was shown in Figure 1. Another approach using static window generation was implemented and tested [3].

Results

Measurements at CERN PS and GSI SIS18 where carried out, using two identical hardware platforms with different software implementations. Both methods showed their strengths in the respective machines. The method from [3] is very sensitive to the type of beam and initial frequency tracking. During those particular tests the calculated σ of the position data was about 0.3mm. In 2007 hardware components for the 12 BPMs in SIS18 will be delivered and we will work on a centralized data acquisition system.

References

[1] A. Galatis et al, "Beam Position Monitor System Development for FAIR", GSI Scientific Report 2005

[2] A. Galatis et al, "Digital Techniques in BPM Measurements at GSI-SIS", Proc. of EPAC '06

[3] J. Belleman, "A New Trajectory Measurement System for the CERN Proton Synchrotron", Proc. of DIPAC '05

* Founded by EU FP6-Design Studies SIS100_5

NEG Coating of the Dipole Chamber for the SIS 18 Upgrade*

M.C. Bellachioma, J. Cavaco, J. Kurdal, H. Reich-Sprenger, and D. Schäfer
GSI, Darmstadt, Germany

Abstract

The dipole and quadrupole chambers of the 12 sectors of the heavy ion synchrotron (SIS 18) will be coated with a Ti-Zr-V thin film by magnetron sputtering [1]. The NEG coating is necessary to provide uniform pumping speed along the chambers to contribute to the reduction of the base pressure of the SIS 18. In order to coat those vacuum chambers a new dipole coating facility was built at GSI, and, at the end of 2006, the first two coated dipoles were installed in the sector S05/S06. The coating facility, its operating mode, and the first results obtained will be presented.

NEG Coating Production

The dipole coating facility shown in Fig.1 was designed and commissioned in the first half of 2006. The design of the facility had to take into account the special geometrical dimensions of the dipole chambers. Those pipes, made from stainless steel, are in fact 3m long, have an elliptical cross section, and are characterised by 0,3 mm wall thickness and a 15° bending angle. For an easier integration of the dipole chambers into the sputtering system, a horizontal configuration of the facility was chosen.

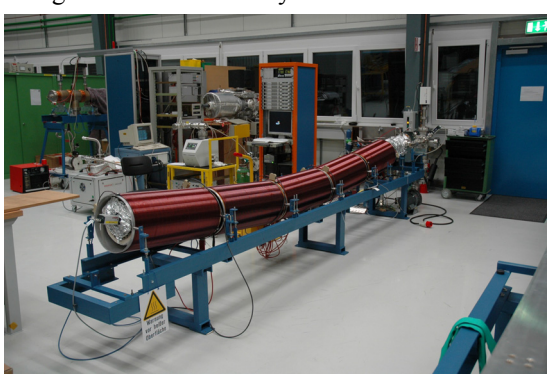

Figure 1: Picture of the experimental set-up.

The coating facility consists of a UHV pumping system (equipped with a residual gas analyser, a wide range gauge and a Kr injection line), a manifold, and five coils. To obtain a uniform film thickness, the use of two cathodes, mounted at about 40 mm from the centre of the dipole chamber, respectively, was foreseen. The two electrical cathode feedthroughs are located opposite to each other at the lateral side of the manifold and they are fed by 1,5 kW dc power supply.

The solenoids are 800 mm long having 350 mm internal diameter and they can provide a maximum magnetic field of about 180 Gauss. They are individually powered to allow also the generation of an inhomogeneous magnetic field if, in future, the coating of vacuum chambers with a non constant aperture has to be performed. The coating process for the dipole chambers takes about 10 hours to achieve the thickness of 1µm. A current of about 0,14 A/m for a voltage of 500V is applied at each feedthrough. During the sputtering process the temperature of the dipole chambers is kept at 100°C and the process parameters are monitored and recorded by computer.

Copper samples are coated simultaneously with the dipole chambers, and used to analyse the film thickness by means of scanning electron microscopy (SEM) and the elemental composition by means of energy dispersive X-ray spectroscopy (EDX). The correct activation behaviour of the produced NEG film is stated by the reduction of the oxygen peak area as function of the temperature, as proven from the XPS (X-ray photoelectron spectroscopy) results (see Fig.2).

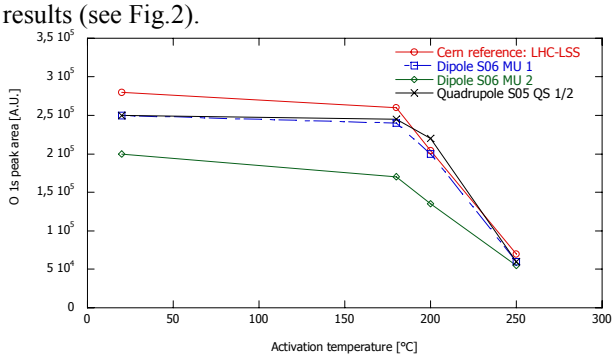

Figure 2: Reduction of the oxygen peak area as a function of the temperature. The results obtained for the chambers coated for the SIS 18 upgrade are comparable with those measured for a chamber coated for LHC.

Commissioning of the First Coated Dipole Chambers in the SIS 18

The first two coated dipole chambers and one coated quadrupole chamber were mounted in the sector S05/S06 at the end of 2006. After the bakeout and the activation of the coated pipes, pressures of about $2x10^{-10}$ mbar and $3x10^{-11}$ mbar were measured at the two ends of the sector, respectively. These pressure values can be compared with those measured at the end of a similar heating cycle at the extreme ends of the uncoated sector S07/S08: $3x10^{-10}$ mbar and $5x10^{-10}$ mbar, respectively. The pressure difference at the two sides of the sector S05/S06 can be explained after recording a mass spectrum: a significant gas load due to a not completely successful bakeout cycle of a new insertion (unplanned repair of a Q-kicker module). After several weeks of operation the total pressure in the NEG coated sector dropped to the low 10^{-11}mbar region at both sides. A new activation of the NEG surfaces during the next shutdown should lead to a further improvement of the total pressure value in this sector. In the frame of the SIS 18 upgrade project the assembling of additional ten coated dipole chambers is foreseen within 2007.

References

[1] C. Benvenuti et al., Vacuum 60 (2001) 57-65.

* Work supported by EU design study, DIRAC-PHASE-1 RP6 SIS 18-2 contract No. 515876.

Desorption Yield Measurements of Copper Characterized using UHV-ERDA *

H. Kollmus[1], M.Bender[1], W. Assmann[2], R. Dörner[3], and H. Reich-Sprenger[1]
[1]GSI, Darmstadt, Germany; [2]LMU, München, Germany; [3]IKF, Frankfurt, Germany

Ion-induced desorption is a serious luminosity limitation for high current and low charge state heavy ion accelerators [1]. In order to find low desorbing materials for the loss regions of SIS18 a dedicated experimental program was started measuring desorption yields of different materials, which are *in-situ* well characterized using UHV Elastic Recoil Detection Analysis (ERDA).

Two targets, with a size of 50 x 50 mm^2, were cut out of the same piece of 99.95% oxygen free high conductivity (OFHC) copper. Target (A) was lapped in the target laboratory of GSI using a ceramic (Al_2O_3) paste and cleaned in HNO_3 acid in order to remove a possible oxide layer and polishing grains. After preparation the sample was mounted in the UHV-ERDA chamber with minimal exposure to air. Target (B) was polished with a standard polishing paste (Fe_2O_3, grain size $\leq 10\mu$m in a Stearin matrix) which is used for copper coated accelerator cavities. After polishing the target was cleaned in an ultrasonic bath, flushed with demineralized water and dried under atmosphere for 4 h at 250° C.

The desorption yield and ERDA measurements were performed at the high charge state injector (HLI) of GSI using a 1.4 MeV/u $^{136}Xe^{21+}$ beam. From the raw ERDA spectra, compare [2], element specific depth distributions can be derived using the KONZERD code [3] as shown in Fig. 1. Here the depth distributions of copper, oxygen and carbon for the both samples are shown: whereas sample (A) is a pure metallic copper with only minor oxygen contamination on the surface, target (B) has a highly oxidized surface. For both targets the carbon contaminations is below 1 %. The thickness of the Cu_2O oxide layer on target (B) is around 450 nm. The corresponding pressure rise under ion bombardment is shown in Fig. 2. A significant higher pressure rise was observed for target (B). At the end of each desorption yield measurement we have applied a positive or negative bias voltage to the target in order to measure the influence of secondary, charged particles (electrons and ions) to the pressure rise. A pressure increase is clearly visible and is slightly more pronounced for a positive bias voltage. Here secondary ions emitted from the target gain 2000 keV kinetic energy in the electric field and are accelerated towards the chamber wall resulting in a low energetic ion stimulated desorption. The effective desorption yield for sample (A) was measured to be $\eta_{eff} \approx 360$ and for sample (B) $\eta_{eff} \approx 1500$ taken from the peak maximum. For more details see [4].

Hence, the desorption yield of the oxidized copper is around 4 times higher compared to an almost clean copper. This results and the measured $(dE/dx)^2$ dependency reported in [1] shows that desorption is directly linked to the electronic sputtering: the higher the sputter rate of the target the higher the desorption yield of the adsorbed gas. The higher sputter yields for the oxidized copper can be explained by the Thermal Spike Model [5]. Since the copper oxide is an insulator the mobility of the electrons and therefore the thermal conductivity is strongly reduced compared to a metal.

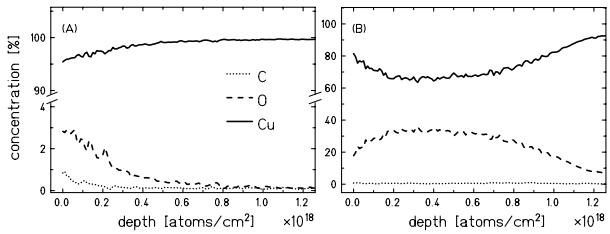

Figure 1: Depth distribution of copper, oxygen and carbon for sample (A) and (B).

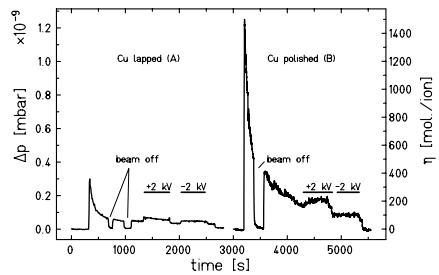

Figure 2: Desorption yield measurement of both targets.

Results and interpretation have clear consequences for materials and material treatments used for accelerator beam tubes or beam loss collimators: It should be a highly conductive material with very little impurities. It should have a clean metallic surface. Favorably it should be made out of a low Z material to minimize the electronic energy loss close at the surface. Perpendicular impact should be ensured and the amount of adsorbed gas should be reduced to a minimum, e.g., by a special bake out procedure.

References

[1] H. Kollmus et al., AIP CP773 (2005) 207-210

[2] H. Kollmus et al, GSI Scientific Report 2005 (2006)

[3] A. Bergmaier et al, NIM **B** 99 (1995) 488

[4] M. Bender et al., NIM **B** (2007), doi:10.1016/j.nimb.2006.12.101

[5] M. Toulemonde et al., NIM **B** 212 (2003) 346-357

* We acknowledge the support of the European Community-Research Infrastructure Action under the FP6 "Structuring the European Research Area" program (DIRACsecondary-Beams, contract number 515873)

Ionization Beam Loss and Collimation in SIS18

C. Omet*, P. Spiller, and H. Kollmus
GSI, Darmstadt, Germany

Introduction

Ionization of beam ions, especially at operation with intermediate charge states, combined with a strongly dynamic residual gas pressure may create major beam loss. The first experimental evidence has been obtained in SIS-18 machine experiments in 2001 with U^{28+}-ion beams. Operation with intermediate charge states is in general required to minimize the incoherent space charge tune shift in SIS-18 and SIS-100. The booster operation of SIS-18 for the FAIR accelerator facility [1] requires acceleration of more than 10^{11} U^{28+}-particles per SIS-18 machine cycle. In 2001, more than 90% of the injected 10^{10} beam ions were lost within $\approx$ 100 ms. Consequently a UHV upgrade program has been defined, aiming for a minimization of the pressure dynamics during intermediate charge state operation. In order to verify the proposed measures, a simulation code for ionization beam loss and dynamic vacuum effects has been developed. It could be shown that heavy ion beam acceleration with a reasonable low amount of loss and the desired intensity is feasible but requires a dedicated collimation system to control the ion induced desorption gases.

Code Benchmarking and Simulations

To benchmark the simulation results and the present understanding of the pressure dynamics, we continued with machine experiments [2] and verified the theoretical models of beam loss and desorption implemented in StrahlSim [3]. During a run in 2006, 5*10^9 U^{28+} particles have been injected at 7.1 MeV/u and were accelerated to 90 MeV/u. Both Rf cavities were used to produce an acceleration voltage of 28 kV. In parallel, the vacuum pressure in SIS-18 was measured.

As in previous experiments, due to ion induced desorption effects the pressure revealed a strongly dynamic behavior. However, the clear but in this case low pressure rise and the observed beam loss was not well in consistence with the theoretical predictions. To obtain a better agreement, the measured pressure should have been at least a factor of 2 higher. The discrepancy could be explained by the present distribution of the pressure gauges in SIS-18. The pressure gauges are situated near the UHV pumps and therefore do not deliver a representative measurement of the average machine pressure.

In order to verify the applied models for the energy dependency of the ionization and capture cross sections, machine experiments were conducted with acceleration at different ramp rates between 1 and 6 T/s. As expected and predicted with StrahlSim, higher ramp rates result in a lower amount of ionization beam loss. The charge exchange cross sections have a significant energy decrement, i.e. at faster ramping the time at lower beam energies is shorter.

Collimator Prototype

For the reduction of the ionization beam loss, a dedicated collimator system has been proposed [4]. The goal is to prevent the pressure bump created by ion impact from interacting with the revolving beam. On the other side the amount of gas produced shall be minimized. According to recommendations from the GSI atomics physics group, the dependency of the cross sections as a function of energy has been modified. After implementation in the STRAHLSIM code, the intensity evolution in a SIS-18 booster cycle, with and without collimation system has been re-calculated. In parallel, the design of a prototype collimator was completed (see fig. 1). The design allows testing of two optional geometries: a wedge- and block-shaped collimator block, both coated with a low-desorption yield 100 μm Au surface. The collimators are surrounded by a NEG-coated secondary chamber to provide a large local pumping speed for the control of the desorption gases. The prototypes will include various sensors for total pressure measurements (in the secondary and primary chamber) and partial pressure analysis. Two prototypes will be built and installed in SIS-18 in the winter shutdown 2007.

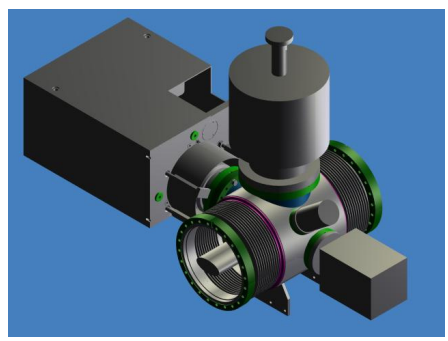

Figure 1: 3D-model of the SIS-18 collimator prototype

References

[1] GSI. FAIR Baseline Technical Report. `http://www.gsi.de/fair/reports/btr.html`, 09 2006.

[2] C. Omet, P. Schütt, and P. Spiller. Maschinenexperimente vom 24.10.2006: Schnelle Rampen, Umladungsverluste und dynamisches Vakuum. Internal report, GSI, 12 2006.

[3] C Omet, P Spiller, J Stadlmann, and D H H Hoffmann. Charge change-induced beam losses under dynamic vacuum conditions in ring accelerators. *New Journal of Physics*, 8(11):284, 2006.

[4] P. Spiller. Vorschlag für einen Kollimatorpumpstand zur gezielten Beseitigung von Desorptionsgasen. Internal Note GSI-SIS18-02-02, GSI, 02 2002.

* c.omet@gsi.de

Work supported by EU CNI (Construction) Contract "DIRAC-PHASE-1" - Contract number 515876 -

RBS Investigations of Layered Targets for SIS18 Beam Loss Collimators *

M. Bender[1], H. Kollmus[1], W. Assmann[2], R. Dörner[3], B. Kindler[1], B. Lommel[1], and H. Reich-Sprenger[1]

[1]GSI, Darmstadt, Germany; [2]LMU, München, Germany; [3]IKF, Frankfurt, Germany

Since two years an UHV Elastic Recoil Detection Analysis (ERDA) set-up is available at the high charge state injector (HLI) of GSI and mainly used for desorption studies [1, 2]. ERDA with high Z beams starting from Xe up to Au is especially suited for the investigation of light element desorption by heavy ion beams from metallic surfaces. To measure high Z target coatings like gold, Rutherford Backscattering Spectrometry (RBS) is more appropriate being the complementary ion beam analysis technique to ERDA. It has a high sensitivity to heavy elements and uses hydrogen or helium ion with a few MeV, typically. Sensitivity and depth resolution, however, are increased with little heavier projectiles such as C which can be frequently used in parasitic mode during the cancer therapy. Typically three month per year the HLI of GSI is exclusively used to produce a 1.4 MeV/u C^{2+} beam. Therefore, we have established heavy ion RBS at the UHV set-up and extended our analysis capability.

Copper coated with 50 - 100 nm gold may be used for the new SIS18 beam loss collimators. Clean metallic copper turned out to have a comparable low desorption yield as long as no oxide layer has grown on the surface. To prevent copper from oxidation it will be cleaned in vacuum and *in-situ* terminated with a thin gold layer. After coating the copper can be exposed to air and mounted inside SIS18. Like each UHV device the collimator has to be bakeable up to 300° C. RBS was used to measure the long term behavior and stability of the gold layer during a typical UHV bake-out cycle.

Results of recent RBS investigations on gold coated copper are shown in Fig. 1. The x-axis shows the scattered projectile ion energy which corresponds to the depth distribution of different elements. Since copper and gold have a quite different mass they are well separated in the energy spectrum (a). The dotted and the dashed-dotted line represents the energy of a projectile ion scattered at a copper and a gold atom, respectively, on the sample surface. From this energy distribution the film thickness can be derived using, e.g., the simulation code SIMNRA [3]. In spectrum (a) one can clearly see the gold layer of 200 nm thickness on top of the copper and no copper on the surface. Spectra (b) to (d) are now different snapshots of the sample during the 300° C heating cycle: in (b) the copper starts to diffuse into the gold towards the surface. In (c) copper is diffused into the gold layer to the sample surface and the gold starts to diffuse into the copper bulk. In (d) –the sample was now

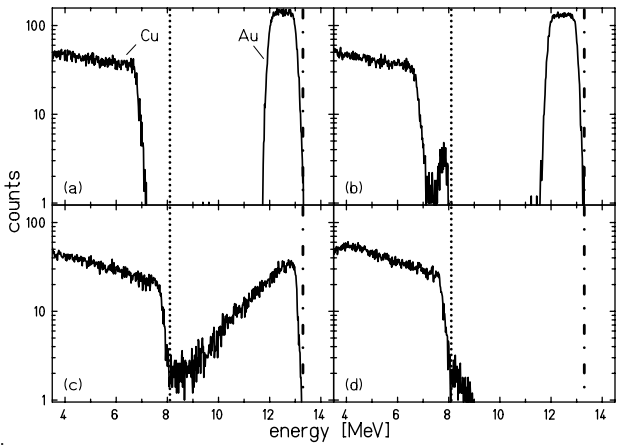

Figure 1: RBS measurements of copper with 200 nm gold coating using 16.8 MeV $^{12}C^{2+}$ ions and a scattering angle of 170 degrees: (a) as prepared, (b) - (c) after heating at 300° C for different times (see text).

at 300° C for about 100 h– the gold is almost completely inside of the copper substrate.

To avoid this in-diffusion of the gold overlay, work is in progress to find a suitable diffusion barrier and to test the stability of the gold layer during repeated heating cycles by RBS and by additional ERDA and pressure rise measurements its desorption behavior.

The new RBS capability was also used for the characterization of thin film coatings, like NEG getters. Here we are able to measure the stoichiometry of the getter components and the film thickness. Up to now the stoichiometry of the NEG was measured at CERN using XPS and the thickness using SEM. Now both can be determined with high accuracy using RBS and complemented by ERDA where the pumping properties for light elements and the diffusion of the oxide during activation can be seen.

References

[1] H. Kollmus et al., GSI Scientific Report 2005 (2006)

[2] H. Kollmus et al., GSI Scientific Report 2006

[3] M. Mayer, Report IPP 9/113, Max-Planck-Institut für Plasmaphysik, Garching, Germany (1997)

* We acknowledge the support of the European Community-Research Infrastructure Action under the FP6 "Structuring the European Research Area" program (DIRACsecondary-Beams, contract number 515873)

Radiation Hardness of PS Magnets during β-beam Operation*

M. Kirk, P. Spiller, C. Omet, J. Stadlmann, GSI, Darmstadt, Germany
M. Benedikt, Geneve, CERN

The EURISOL β-beam project addresses the design of accelerators for the production of high flux neutrino beams. With the aim to exploit the existing PS and SPS synchrotrons at CERN, it is proposed to create neutrinos and antineutrinos from high intensity radioactive beams. Boosted to high relativistic energies in the SPS and then injected into an elongated storage ring, narrow cones of neutrinos are produced. The He and F isotopes are intended to be produced by the planned EURISOL facility. The present candidates are $^{6}He^{2+} \rightarrow {}^{6}Li^{3+}+\beta^{-}+\nu$ and $^{18}Ne^{10+} \rightarrow {}^{18}F^{9+}+\beta^{+}+\bar{\nu}$ which would achieve a reasonable decay rate at γ=100 in the decay ring.

The irradiation of accelerator components due to beam loss is a serious issue. Short term irradiation studies [1] have shown that the coil's insulation, an epoxy fibre glass, has a functional lifetime corresponding to a physical dose in the range 20-40 MGy. The exact dose depends on the type of insulator. For long term exposures (years) however the remnant dose is significant. A nominal safety limit of 10 MGy which includes the remnant dose is therefore chosen. The combined function magnets in the PS, which currently are not shielding by collimators, should have lifetimes of tens of years. To a large part it is the neutron yields that contribute to the dose. The Monte Carlo transport program FLUKA [2] was selected as it is valid even beyond γ=100. The GSI accelerator code *StrahlSim* [3] provided the loss distribution at the collimator. The collimator, a 1m long lead block, was placed 10cm from the front face of the magnet and shields the magnet from the β-decay daughter nuclei. Initially Li was considered. The energy of the Li-ions was assumed monochromatic and the energy chosen was 7.8 GeV/u; the top energy of the PS. The PS dipoles have curved pole surfaces to create the combined focussing and deflection of the beam. Although the coil's geometry and material composition (i.e. water, copper, insulation) is detailed, each pole is defined by just 5 planes as shown in figure 1.

With the presence of the collimators the largest dose received is that in the front parts of the coil, particularly in the insulator where the primaries first impinge. If the dose in a region only ~1mm^3 in size exceeds 10 MGy the coil is considered defect. The spatial dose distribution over the insulation was thus evaluated over a grid with bin dimensions 1cm x 1cm x 2mm. The appropriate dimensions of the grid depend on the irradiation pattern. To this end, a life time with the collimator of ~36 years was determined which is not much longer than the 10 physics years for β-beam experiments. Perhaps this lifetime will be longer if a more realistic irradiation pattern is chosen.

However, the absence of collimation avoids secondary yields in the collimator which otherwise would impact on the coil downstream. The same sub region, as before, receives the largest dose. The overall variation of the dose however differs.
Consequently the life time of the coil is much longer, in fact much longer also compared to the time of operation it took for the need to replace the coils in the PS dipoles. Therefore, a comparison against proton irradiation is important.

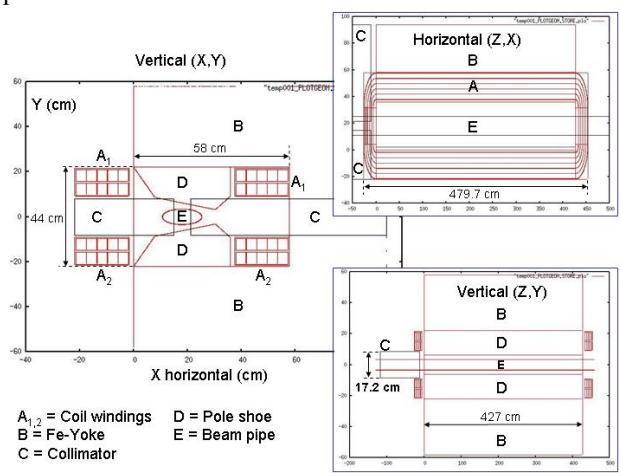

Figure 1: Cross sections through the target geometry.

So far only irradiation with Li has been investigated. Lifetimes for F-ion irradiation should also be estimated. Improvements to the model should be made since the quoted lifetime for the collimated geometry is marginally acceptable. For one, the layers of lamination, an epoxy resin, for the Fe-yoke should be included, as its dose rate may increase if the collimators are removed. A more realistic pipe geometry and beam distribution should also be considered. Inclusion of the magnetic field should be implemented since this will also affect the irradiation pattern. It could be that at lower energy collimation is feasible. This shall be investigated.

References

[1] A. H. Sullivan, A Guide to Radiation and Radioactivity Levels near High Energy Particle Accelerators, Nuclear Technology Publishing, Ashford, Kent, TN23 1JW, England, 1992
[2] FLUKA: a multi-particle transport code, A. Fasso, A. Ferrari, J. Ranft, and P. R. Sala, CERN-2005-10 (2005), INFN/TC_05/11, SLAC-R-773
[3] C. Omet et.al., New Journal of Phys., 8 (2006)284

*Work supported by the EU FP6 EURISOL design study.

Measurement of the fluence response of a passive neutron dosemeter in the energy range from thermal to 19 MeV

G. Fehrenbacher[1], F. Gutermuth[1], E. Kozlova[1], and T. Radon[1]
[1]GSI, Darmstadt, Germany

Introduction

Radiation fields outside the shielding of high energy particle accelerators are frequently dominated by the neutron component which extends over a wide energy range. At GSI for the neutron monitoring a passive thermoluminescent based dosimeter is used. The sensitive elements are pairs of TL 600/700 thermoluminescence elements. They are surrounded by a polyethylene moderator (PE). In order to improve the response to high energy neutrons the moderator is equipped with a lead layer [1].

In this work, the dosemeter response was measured in quasi-monoenergetic neutron fields of the accelerator facility of PTB in Braunschweig and in the thermal neutron field of the GKSS research reactor FRG-1 in Geesthacht.

Measurements

At PTB there are two ion accelerators, a Van-de-Graaf generator and a cyclotron. Neutrons in the energy range from 0.144 MeV to 19 MeV are produced by the accelerators using the ^{7}Li(p,n)^{7}Be, ^{3}H(p,n)^{3}He, ^{2}H(d,n)^{3}He, ^{3}H(d,n)^{4}He reactions. The measurements were carried out in forward direction with respect to the incoming beam. The neutron fluence is monitored by two long counters [2].

The measurement of the dosemeter response to thermal neutrons was performed at the GeNF laboratory at the GKSS research centre [3]. The dosimetry installation is operated by means of a xy-scanner perpendicular to the neutron beam. This scanner is necessary because the beam size is only approximately 35x35 mm^2 and the dosemeter diameter is 32 cm. Homogenous irradiations are achieved by application of quasi-Lissajous figures of the scanner. The energy distribution of the neutron field can be described by a Maxwellian distribution with a mean value of 45 meV and a kT value of 22.5 meV.

Results

The results of measurements are shown in Fig. 1 together with MC calculation. The fluence response of the TLD based system was calculated by means of the MC codes FLUKA [4] and MCNP [5]. The deviation of the measured response to the calculated one amounts to 27% at thermal energies and 5% to 14% for the accelerator neutron energies (0.144 MeV to 19 MeV). Therefore, it can be stated that the comparison of measured and calculated response shows a good agreement. The energy dependence of the detector for the fluence response are shown together with the function for the conversion of fluence to ambient dose equivalent from ICRP [6] and the high energy extension

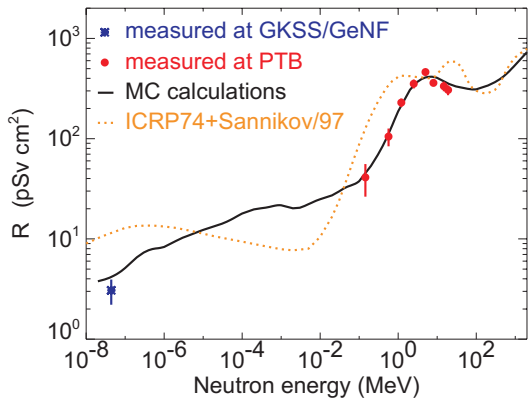

Figure 1: Measured response to thermal neutrons (asterisk) and to the accelerator produced neutrons (points). Calculated fluence responses (solid line) and the fluence-to-dose conversion function for ambient dose equivalent H*(10) due to ICRP74 [6] and [7] (dashed line).

from Sannikov and Savitskaya [7]. The detector shows an under-response for thermal neutrons and in the range of 0.1 MeV and an over-response in the keV range. The maximum deviation of the response of the device from the conversion function amounts to a factor of three. It would be desirable to determine the experimental response to monoenergetic neutron with energies from 20 MeV up to 300 MeV.

References

[1] F. Gutermuth *et al.*, *The response of various neutron dosemeters considering the application at a high energy particle accelerator*, Kerntechnik, 68, 172-179 (2003).

[2] R. Nolte *et al.*, *Quasi-monoenergetic neutron reference fields in the energy range from thermal to 200 MeV*, Radiat. Prot. Dosim. 110, Nos 1-4, 97-102 (2004).

[3] R. Böttger *et al.*, *The PTB thermal neutron reference field at GeNF*, PTB Report, PTB-N-47 (2004).

[4] A. Fasso *et al.*, *FLUKA: A multi-particle transport code CERN-2005-10 (2005)*, INFN/TC-05/11, SLAC-R-773

[5] J. F. Briesmeister (ed.), *MCNP - A General Monte Carlo N-Particle Transport Code*, Version 4B. Report LA-12625-M (Los Alamos National Laboratory) (1997).

[6] ICRP, *Conversion Coefficients for use in Radiological Protection against External Radiation*. Publication 74. Ann. ICRP 26(3/4) (Oxford: Pergamon Press) (1996).

[7] A. V. Sannikov, E. N. Savitskaya, *Ambient dose equivalent conversion factors for high energy neutrons based on the ICRP60 recommendations*, Radiat. Prot. Dosim. 70, Nos. 1-4, 383-386 (1997).

Schottky mass measurements of neutron-deficient ^{152}Sm projectile fragments

Yu.A. Litvinov[1,2], H. Geissel[1,2], K. Beckert[1], P. Beller[1], F. Bosch[1], D. Boutin[1,2], C. Brandau[1], L. Chen[1,2], C. Dimopoulou[1], R. Knöbel[1,2], C. Kozhuharov[1], J. Kurcewicz[3], S.A. Litvinov[1,2], M. Mazzocco[1], C. Nociforo[1], F. Nolden[1], W.R. Plass[1,2], C. Scheidenberger[1,2], M. Steck[1], B. Sun[1,4], H. Weick[1], and M. Winkler[1,2]

[1]GSI, Darmstadt; [2]JLU, Giessen; [3]Warsaw Univ.; [4]PKU,Beijing

The mass surface consisting of 373 different neutron-deficient nuclides has been measured with the time-resolved Schottky Mass Spectrometry (SMS) at the FRS-ESR facility recently. Exotic nuclei were produced in fragmentation of ^{152}Sm projectiles, separated in-flight with the FRS, and injected, stored, and electron-cooled in the ESR.

The masses of ^{84}Zr, ^{92}Ru, ^{94}Rh, ^{107,108,110}Sb, ^{111,112,114}I, ^{118}Ba, ^{122,123}La, ^{124}Ce, ^{127}Pr, ^{129}Nd, ^{132}Pm, ^{134}Sm, and ^{137}Eu nuclides have been determined for the first time. In addition, masses for ^{111,112}I and ^{113}Xe could be obtained by connecting known α-decay energies to the corresponding directly measured daughter nuclei. It is interesting to note that in former experiments the limit for the observation of *one single* stored ion was at about Zinc (Z=30) [1]. In the present experiment, however, single stored Magnesium (Z=12) ions were identified due to the improved signal-to-noise ratio.

The present mass accuracy of the time-resolved SMS is about 30 μu [1]. By restricting to a small frequency range, one can minimize ion-optical nonlinearities and achieve a mass accuracy as small as $\Delta m/m = 4.3 \cdot 10^{-8}$. In the example shown in Figure 1, we used the well-known masses of ^{93}Tc ($ME = -83603(4)$ keV) and ^{93g}Mo ($ME = -86803(4)$ keV) in order to determine the mass of the isomeric state ^{93m}Mo. The obtained mass value is compared to the literature in Fig. 2. For selected cases this evaluation method is very powerful, however, one does not use the advantage of the broad-band frequency recording which enables a simultaneous mass measurement of hundreds of nuclides with a relative accuracy of $1.5 \cdot 10^{-7}$ [1].

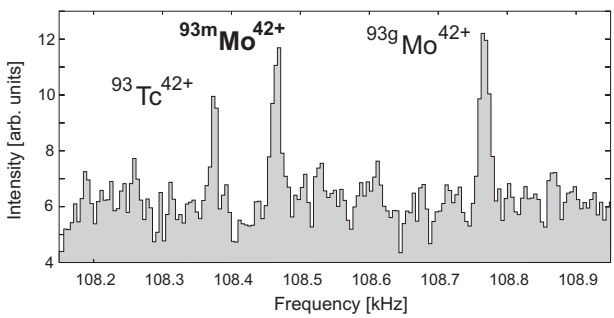

Figure 1: Example of a narrow Schottky frequency spectrum of ^{93}Tc and ^{93g}Mo and ^{93m}Mo isobars. The mass value of ^{93m}Mo has been determined based on the reference mass values of ^{93}Tc and ^{93g}Mo [2].

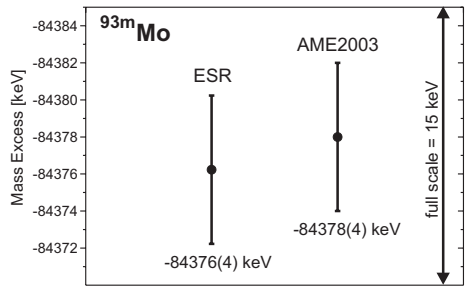

Figure 2: Comparison of the measured value for ^{93m}Mo with the one from AME 2003 [2]. The achieved mass accuracy of $\Delta m/m = 4.3 \cdot 10^{-8}$ was limited by the uncertainties of the reference masses.

The mass surface measured in this experiment largely overlaps with our previous measurements [1, 3, 4]. On the one hand this is important for the consistency check of the data. On the other hand, the results of different measurements can be combined into a common network analysis, similar to the one described in Refs. [1, 3]. Such network analysis connects all nuclides by means of measured revolution frequency relations. All precisely known masses and Q-values of different reactions will be used for calibration purposes. Each of these values contributes to constrain the entire system. All our measured masses cover already now about 50% of the known mass surface. It is possible to incorporate in this analysis also the frequency relations from the Isochronous Mass Spectrometry (IMS) [5]. This is important in view of the present FRS-ESR research program and, in particular, for the data which will be provided by the future NUSTAR/ILIMA project at FAIR.

References

[1] Yu.A. Litvinov et al., Nucl. Phys. A756 (2005) 3.

[2] G. Audi et al., Nucl. Phys. A729 (2003) 3.

[3] T. Radon et al., Nucl. Phys. A677 (2000) 75.

[4] H.Geissel et al., AIP Conf. Proc., Vol. 831 (2006) 108.

[5] M. Hausmann et al., Nucl. Instr. Meth. A 446 (2000) 569.

Orbital electron capture decay in hydrogen-like $^{140}Pr^{58+}$ ions.

Yu.A. Litvinov[1,2], F. Bosch[1], H. Geissel[1,2], J. Kurcewicz[3], N. Winckler[1,2], L. Batist[4], K. Beckert[1], P. Beller[1], D. Boutin[1,2], C. Brandau[1,2], L. Chen[2], C. Dimopoulou[1], T. Faestermann[5], L. Grigorenko[6], P. Kienle[5,7], R. Knöbel[1,2], C. Kozhuharov[1], S.A. Litvinov[1,2], L. Maier[5], M. Mazzocco[1], G. Münzenberg[1], A. Musumarra[8], C. Nociforo[1], F. Nolden[1], Z. Patyk[9], M. Pfützner[3], W.R. Plass[2], C. Scheidenberger[1,2], M. Steck[1], B. Sun[1,10], H. Weick[1], and M. Winkler[1]

[1]GSI, Darmstadt; [2]JLU, Giessen; [3]Univ. Warsaw, Poland; [4]PNPI, Gatchina, Russia; [5]TU, München; [6]JINR, Dubna, Russia; [7]SMI, Wien, Austria; [8]INFN-LNS, Catania, Italy; [9]SINS, Warsaw, Poland; [10]PKU, Beijing, China

For the first time the nuclear electron-capture decay rate of hydrogen-like ions have been measured. The selected example was $^{140}Pr^{58+}$ decaying to the nuclear ground state of fully-ionized $^{140}Ce^{58+}$ ions.

Radioactive ^{140}Pr ions have been produced by fragmenting an intense beam of ^{152}Sm projectiles, accelerated by the SIS to 508 MeV/u, in a 1 g/cm^2 thick ^{9}Be target. The hydrogen-like $^{140}Pr^{58+}$ ions were separated in-flight from contaminations as $^{140}Nd^{58+}$ and $^{140}Ce^{58+}$ ions, by using the Bρ-ΔE-Bρ separation method [1] at the FRS and injected into the ESR within 500 ns. Stochastic pre-cooling and electron cooling were applied to the stored $^{140}Pr^{58+}$ ions. The electron cooling [2] forces all stored ions to the same mean velocity and thereby reduces the initial velocity spread of a few 10^{-2} to roughly $5 \cdot 10^{-7}$. The stochastic cooling device [3] provides fast pre-cooling at a fixed fragment velocity, corresponding to 400 MeV/u, thus reducing the overall cooling time to about 2 seconds. The unambiguous identification of cooled $^{140}Pr^{58+}$ ions and their decay measurement has been performed with the time-resolved Schottky Mass Spectrometry [4].

Example of measured decay- and growth curves is shown in Fig. 1. Feeding of $^{140}Pr^{58+}$ or $^{140}Ce^{58+}$ ions via radioactive decays or atomic charge-exchange reactions of other stored ion species has been experimentally excluded by blocking the corresponding orbits with mechanical slits.

In total four measurements of the EC decay of $^{140}Pr^{58+}$ ions have been performed, where the intensity of the injected mother ions has been varied from several ten ions to about 1000 ions. Decay curves of the mother ions have been fitted with an exponential function:

$$N_{Pr}(t) = N_{Pr} \cdot e^{-\lambda t} \qquad (1)$$

where N_{Pr} is the number of mother ions, t is the time after injection, and the decay constant λ is the sum of the EC decay constant λ_{EC}, the β^+ decay constant λ_{β^+}, and the atomic losses due to collisions with rest gas ions or pick-up of electrons in the cooler λ_{loss} ($\lambda = \lambda_{EC} + \lambda_{\beta^+} + \lambda_{loss}$). The latter is much smaller than λ_{EC} and λ_{β^+}. The intensity increase of the $^{140}Ce^{58+}$ ions is determined solely by λ_{EC}. The loss of stable $^{140}Ce^{58+}$ is determined only by λ_{loss}. In order to determine λ_{β^+}, fully-ionized $^{140}Pr^{59+}$ ions have been stored in the ESR and their decay has been measured. Since there are no orbital electrons, the nucleus can only decay via the β^+ decay-channel. The measured decay-constant is then the sum $\lambda_{\beta^+} + \lambda_{loss}$.

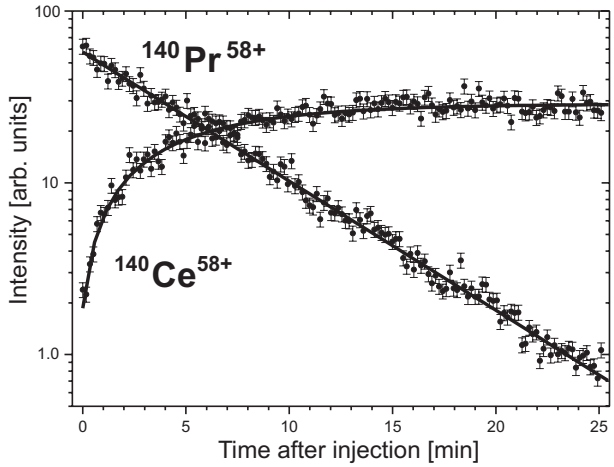

Figure 1: Intensities of $^{140}Pr^{58+}$ and $^{140}Ce^{58+}$ ions as a function of time for one injection into the ESR. The data points are shown in the laboratory frame (Lorentz factor γ=1.43.)

All measurements have shown consistent results. The half-life of hydrogen-like $^{140}Pr^{58+}$ amounts to 3.13(14) min, which is to be compared to 3.39(1) min known for the neutral atom [5].

Although the number of electrons is reduced from 59 in the neutral atom to only one, the electron-capture decay rate increases. To explain this curious observation, one has to take into account the spin orientations of the nucleus as well as of the leptons involved and the conservation of the total angular momentum in this decay. Similar effects have been seen in muon capture [6].

References

[1] H. Geissel, *et al.*, Nucl. Instr. and Meth. **B70**, 286 (1992).

[2] M. Steck *et al.*, Nucl. Instr. and Meth. **A532** (2004) 357.

[3] F. Nolden *et al.*, Nucl. Instr. and Meth. **A532** (2004) 329.

[4] Yu.A. Litvinov, *et al.*, Nucl. Phys. **A756** (2005) 3.

[5] G. Audi *et al.*, Nucl. Phys. **A729** (2003) 3.

[6] H. Primakoff, Rev. Mod. Phys. **31** (1959) 802.

β-decay half-lives of heavy neutron-rich nuclei in the N≈126 region

T. Kurtukian-Nieto*[1], J. Benlliure[1], K.-H. Schmidt[2], L. Audouin[3], B. Blank[4], F. Becker[2], E. Casarejos[1], M. Fernandez-Ordoñez[1], J. Giovinazzo[4], D. Henzlova[2], B. Jurado[4], J. Pereira[1], F. Rejmund†[3], and O. Yornadov[2]

[1]USC, Santiago de Compostela, Spain; [2]GSI, Darmstadt, Germany; [3]IPN, Orsay, France; [4]CENBG, Gradignan, France

The astrophysical r-process is responsible for the synthesis of approximately half of the heavy nuclei in the Universe. One of the main problems we have to overcome to fully understand the observed r-process abundances is the lack of information on the nuclei participating in this process, in particular for the heaviest ones. The production of heavy neutron-rich nuclei in the laboratory has been a challenging problem in the last decades, and the vast majority of very neutron-rich r-process nuclei is not experimentally accessible. In particular the waiting-point around N=126, in the heavy neutron-rich region, remain as an unexplored territory. However, the possibility of accelerating heavy ions at relativistic energies made it possible to investigate, during the last years, reaction mechanisms leading to the production of heavy neutron-rich nuclei, such as cold-fragmentation reactions[1].

In this work we concentrate on the measurement of β half lives of heavy neutron-rich nuclei approaching N=126. β-decay half-lives are of importance not only because they play an important role in the understanding of the progress and time scale of the stellar nucleosynthesis processes and consequently in the final abundance patterns, but also because they can be used to benchmark nuclear models far from stability.

The experiment was performed at the Fragment Separator (FRS). A beam of ^{208}Pb ions at 1 A GeV was delivered by the GSI heavy-ion synchrotron SIS, and directed to a beryllium target. The isotopic identification was achieved by determining both the atomic number Z and the mass-over-charge ratio A/Z of each nucleus by means of the measurements of the magnetic rigidities, time-of-flight (ToF) and energy loss of each fragment passing through the FRS. The ions at tens of $A \cdot MeV$ were implanted in an active stopper; a highly-pixelated Si detector stack which allows for the correlation in time and space of the signal from the implanted ion with the subsequent signal produced by the β-decay. The use of a mono-energetic degrader at the FRS provides a horizontal dispersion and a narrow range distribution of fragments in the active stopper.

A fragment-β-correlated time spectrum was generated by histogramming the differences between the time of the β-events and the correlated implantation events. In order to be able to disentangle the background from the real events, the fragment-β correlations were performed in a time reversed sequence. In order to determine the half-life of the selected nuclides, we performed sets of Monte-Carlo simulations with a given efficiency and lifetime, and we calculate the χ^2 from the measured and simulated ratio of the spectra of time correlations in forward- and backward-directions for each set of simulations.

The measured half-lives are systematically compared in figure1 with two theoretical models: the revised version of the Gross Theory[2] and the microscopic approximation of P. Möller et al.[3], which deals with the GT transtitions wihin the RPA and the first-forbidden(ff) transitions within the statistical Gross Theory. Generally, both models overestimate the half-lives of the nuclides, and in the case of the P. Möller model it is by orders of magnitude. These differences could be attributed to the presence of high-energy first-forbidden transitions, which reduce the total β-decay half-lives for nuclei crossing the closed-shells. These comparisons show the necessity for measuring more half-lives of nuclides far from stability in order to test the validity of nuclear and β-decay models, and to provide a basis for choosing a reliable extrapolation.

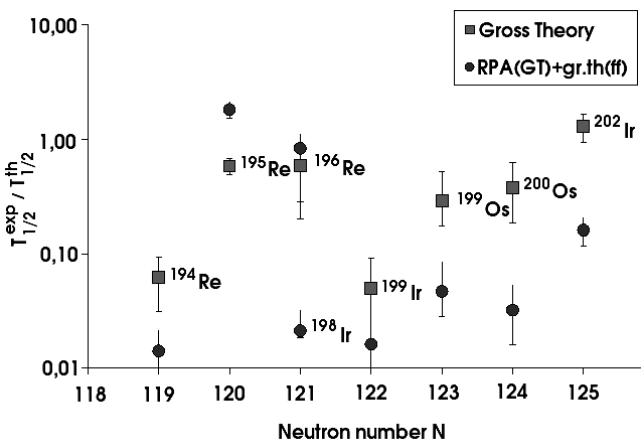

Figure 1: Ratios of experimental half-lives to theoretical calculations: from the revised Gross Theory calculations[2] and the microscopic model of Möller[3]

References

[1] J. Benlliure, K.-H. Schmidt et. al. Nucl. Phys.A660 (1999) 87

[2] T.Tachibana, M.Yamada, Proc. Int. Conf on exotic nuclei and atomic masses, Arles, 1995, p.763

[3] P. Möller, B. Pfeiffer and K.-L. Kratz. Phys. Rev. C 67, 055802 (2003)

* Teresa.Kurtukian@usc.es

† Present address:GANIL,Caen, France

Discovery of a new long-lived isomeric state in ^{125}Ce

B. Sun[1,2], Yu.A. Litvinov[1,3], P.M. Walker[4], K. Beckert[1], P. Beller[1], F. Bosch[1], D. Boutin[1,3], C. Brandau[1], L. Chen[1,3], C. Dimopoulou[1], H. Geissel[1,3], R. Knöbel[1,3], C. Kozhuharov[1], J. Kurcewicz[5], S.A. Litvinov[1,3], M. Mazzocco[1], J. Meng[2], C. Nociforo[1], F. Nolden[1], W.R. Plass[1,3], C. Scheidenberger[1,3], M. Steck[1], H. Weick[1,3], and M. Winkler[1,3]

[1]GSI, Darmstadt; [2]PKU,Beijing; [3]JLU, Giessen; [4]Univ. Surrey; [5]Warsaw Univ.

Scottky Mass Spectrometry [1] is a powerful tool for the direct mass measurement. A recent experiment [2] in 2005 has been devoted to mass measurements of neutron-deficient medium-heavy nuclei. The exotic nuclei have been produced via fragmentation of 615 MeV/u ^{152}Sm projectiles in a thick 4 g/cm^2 ^{9}Be production target, then separated in-flight with the fragment separator FRS and injected into the storage-cooler ring ESR. More than 350 neutron-deficient nuclei have been unambiguously identified in the measured frequency spectra. Here we report on the discovery of a new long-lived isomeric state in ^{125}Ce in this experiment.

The ^{125}Ce ions have been observed in the spectra in two charge states, namely 14 times as fully ionized ^{125}Ce^{58+} and 7 times having one bound electron ^{125}Ce^{57+}. In all these cases, several ions of ^{125}Ce were injected into the ESR, which have been assigned to an unresolved mixture of the ground and isomeric states. An obvious advantage of measuring single ions is that a single ion can belong to one state only. In this way ground or isomeric states can be assigned even for very small excitation energies, which cannot be resolved when both states are present simultaneously [3]. A single stored ^{125}Ce ion in the isomeric state is shown in Fig. 1. In the beginning of the measurement also ions in the ground state are present, thus making a common frequency peak. After about 100 s most of the ions have decayed. The last single ion can be identified as being in the isomeric state since its frequency has shifted, reflecting a slightly higher mass-to-charge ratio. No other fragments in different charge states can account for this frequency line. In another measurement, after about 60 s a single stored ion in the ground state has been observed. The frequency difference between the ground and isomeric states can clearly seen by comparing with the neighboring frequency of ^{69}Ge^{32+}.

For the lifetime determination, Schottky frequency spectra averaged over 2-s periods have been produced. The time of decay measured for the ion in the isomeric state in the laboratory frame is 269 ± 1 s, which in the rest frame of the ion corresponds to 193 ± 1 s (Lorentz factor $\gamma = 1.39$). Following Ref. [4] we estimate the mean lifetime of the isomer to be $\tau = 193^{+924}_{-88}$ s.

The excitation energy $E^* = 103 \pm 12$ keV has been determined by calibrating the frequency spectra with neighboring ^{41}K^{19+}, ^{82}Sr^{38+}, ^{69}Ge^{32+}, and ^{56}Fe^{26+} ions which have well-known mass values [5]. According to the Weisskopf estimate [7], a hindered E3 ($\tau_W(E3) = 14$ s) or M3 ($\tau_W(M3) = 115$ s) transition can be assigned for the de-excitation of this isomeric state.

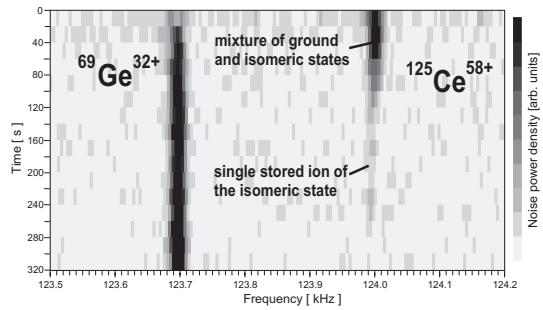

Figure 1: Sixteen sequential Schottky frequency spectra. At first, the frequency of ^{125}Ce^{58+} ions corresponds to an unresolved mixture of the ground and isomeric states. After about 100 s, only one ion of ^{125}Ce in the isomeric state is left.

There are no experimental single-particle states that seem likely to give rise to an M3 transition. However, the deduced energy and multipolarity E3 are in good accord with a "missing" transition, that would complete the low-energy part of the level structure deduced in Ref. [6] using γ-ray spectroscopic data. They identify a 1/2$^+$ bandhead, 92 keV above the (7/2$^-$) ground state, but their technique was not sensitive to the associated (E3) transition. Allowing for an E3, 92 keV electron conversion coefficient of $\alpha = 43$ [8], the present lifetime of 193 s for bare ions corresponds to 4.4 s for neutral ions.

In summary, these isomer data are interpreted as arising from an E3, 1/2$^+$ to 7/2$^-$ transition, which can be used to constrain the γ-ray spectroscopic data.

References

[1] Yu.A. Litvinov, *et al.*, Nucl. Phys. **A756** (2005) 3.

[2] Yu.A. Litvinov, *et al.*, arXiv:/nucl-ex/0509019.

[3] H. Geissel, Yu.A. Litvinov, J. Phys. **G31** (2005) 1779.

[4] K.-H. Schmidt, *et al.*, Z. Phys. A **316** (1984) 19.

[5] G. Audi, *et al.*, Nucl. Phys. **A 729** (2003) 3.

[6] C.M. Petrache, *et al.*, Eur. Phys. J. A **14**, 439 (2002).

[7] R.B. Firestone et al., Table of Isotopes, 8^{th} edition (John Wiley & Sons Inc., New York, 1996).

[8] F. Rösel, *et al.*, At. Data Nucl. Data Tab. **21** (1978) 91.

Isomerism in ^{94}Rh

L. Batist[1,2,#], A. Blazhev[3,4], J. Döring[3], H. Grawe[3], M. Kavatsyuk[3,5], O. Kavatsyuk[3,5], R. Kirchner[3], M. La Commara[2], C. Mazzocchi[3], I. Mukha[3,6], C. Plettner[3], E. Roeckl[3], M. Romoli[2]

[1]PNPI, St. Petersburg, Russia; [2]Università "Federico II" and INFN, Napoli, Italy; [3]GSI, Darmstadt, Germany; [4]University of Sofia, Bulgaria; [5]National Taras Shevchenko University of Kyiv, Ukraine; [6]University of Seville, Spain

The total absorption spectrometer (TAS) [1] mounted at the GSI on-line mass separator [2] was generally used for measuring β-intensity distributions of nuclei far from stability. Another particularly interesting application is, however, to investigate the structure of individual (low-lying) states of the β-decay parent and daughter nucleus, including isomers. As an example, we present here the results on low-lying ^{94}Rh levels obtained by studying the decay of 9-s ^{94}Pd [3]. The K_α(Rh) X-rays and a 54.6-keV γ-ray line, observed in the well-shielded germanium detector of TAS (see Fig. 1), are characterized by a half-life of 0.48(3) μs. The latter result was obtained by inspecting their time distribution relative to the time of registering γ-ray events in the NaI detector of TAS (see Fig. 2). From the intensity of delayed K_α(Rh) X-rays and 55-keV γ-rays the internal conversion coefficient was determined to be α_K = 9.5(20), indicating E2 multipolarity of the 55-keV transition. These results, together with data on β-intensity distributions, yield the tentative spin and parity assignments of (8^+) and (4^+) for the 71-s and 26-s states, respectively, and (2^+) for the newly observed 0.48-μs isomer of ^{94}Rh. There is an indication from experiment that the (8^+) level is 100(300) keV lower than the (4^+) state. A comparison of the experimental data with shell-model predictions, displayed in Fig. 3, can be used for defining the merits and deficiencies of the theoretical predictions as well as tasks of future experiments on ^{94}Pd and ^{94}Rh [3]. The data presented here prove that TAS together with its ancillary detectors is indeed a powerful tool for isomer spectroscopy.

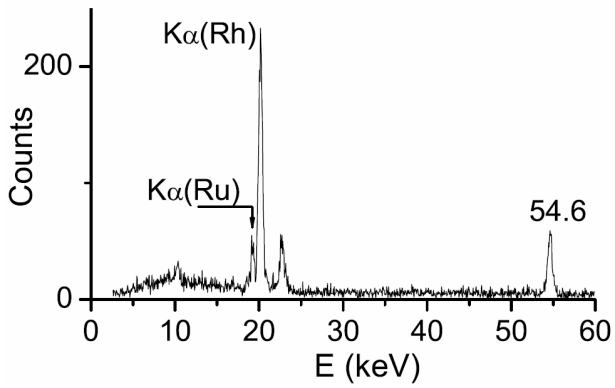

Figure 1: Low-energy part of the spectrum registered by the germanium detector.

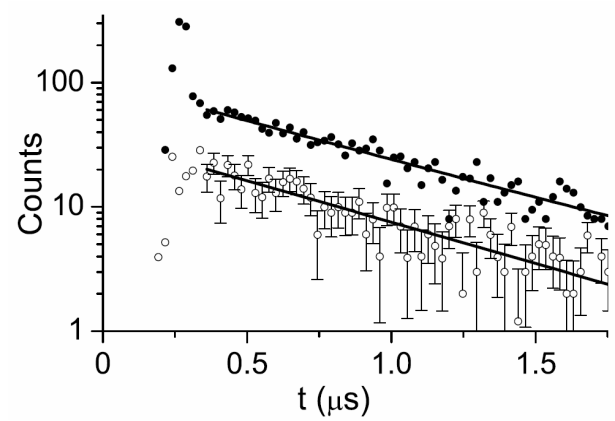

Figure 2: Time distribution of events obtained as delayed coincidences between γ-rays registered in the NaI detector and Kα(Rh) X-rays (filled circles) and 55-keV γ-rays (open circles) observed in the germanium detector.

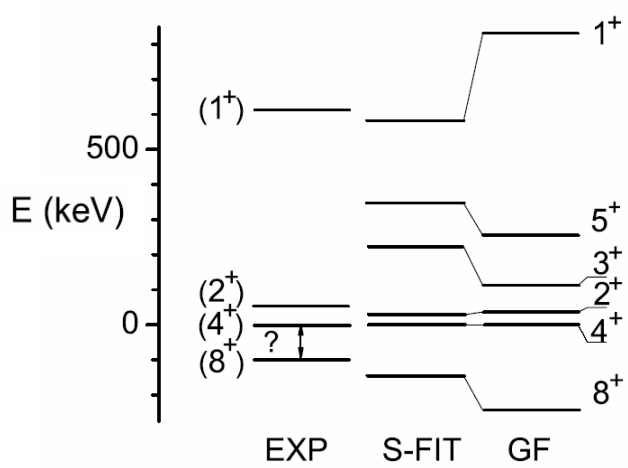

Figure 3: Experimental data on low-lying ^{94}Rh states in comparison with the corresponding shell-model predictions obtained by using the S-FIT [4] or Gross-Frenkel (GF) [5] interaction.

References

[1] M. Karny et al., Nucl. Instr. and Meth. in Phys. Res. B 126, 411 (1997).
[2] E. Roeckl et al., Nucl. Instr. and Meth. in Phys. Res. B 204, 53 (2003).
[3] L. Batist et al., Eur. Phys. J. A 29, 175 (2006).
[4] I. P. Johnstone, L. D. Skouras, Eur. Phys. J. A 11, 125 (2001).
[5] R. Gross, A. Frenkel, Nucl. Phys. A 267, 85 (1976).

#batist@pnpi.spb.ru

The Stopped Beam RISING Experimental Campaign (S244, S299, S300, S305)*

P.H. Regan[1], A.M. Bruce[2], M. Górska[3], A. Jungclaus[4], M. Pfützner[5], Zs. Podolyák[1], D. Rudolph[6], S. Pietri[1], J. Gerl[3], H.J. Wollersheim[3], P. Bednarczyk[3], H. Schaffner[3], I. Kojouharov[3], W. Grebocz[3,7] N. Kurz[3], W. Prokopowicz[3] for the RISING Collaboration

[1]University of Surrey; UK; [2]University of Brighton, UK; [3]GSI, Germany; [4]Universidad Automada, Madrid, Spain; [5]IEP, Warsaw, Poland; [6]Lund University, Sweden; [7]IFJ Cracow, Poland.

The aim of the *RISING* (Rare Isotope Spectroscopic INvestigations at GSI) collaboration is to use GeV range beams from the GSI/SIS synchrotron to study the internal structure of exotic nuclei produced through projectile fragmentation and fission reactions. These production techniques, coupled to a powerful germanium array from the decommissioned Euroball setup, plus the use of the FRS fragment separator for the selection and identification of the produced ions makes a very powerful tool for the study of such nuclei. The RISING setup moved to the Stopped Beam isomer spectroscopy configuration for the first time in February 2006.

To date, six separate experiments have been performed using this array (three in February/March 2006, two in July 2006 and one in December 2006). Gamma-ray transitions depopulating isomeric states were observed using the fragmentation isomer spectroscopy technique (see, e.g., [1]). The physics aims of the campaigns addressed thus far have concentrated on the evolution of shell closures around doubly magic nuclei using ^{136}Xe (experiment *S305*); ^{208}Pb (*S299*) primary beams, *N*=*Z* symmetries along the proton drip-line using ^{58}Ni and ^{107}Ag beams (*S244*), and isomeric decays from shell model and deformed states in very neutron-rich fission fragments produced using a ^{238}U beam (*S244* and *S300*). Individual reports for each of these experiments are presented in this Annual Report [2].

In its Stopped Beam configuration, the RISING array surrounds a passive stopper made of either perpex, copper or beryllium, which is positioned in the final focal point of the FRS. The array comprises 105 germanium crystals contained in fifteen, seven-element cluster detectors from the former Euroball array. The detectors were placed in a compact configuration in three angular rings of five detectors at 51˚, 90˚, and 129˚ relative to the primary beam axis at an average distance from the centre of the array of 22 cm. Each individual germanium detector had two parallel pre-amplifier outputs which were sent to two separate branches of the data acquisition. One was a fully digital branch and provided the input signal for 105 channels within 30 Digital Gamma Finder (DGF-4C) modules. The individual DGF channel triggers were validated by a master trigger signal generated from a fast plastic scintillator detector at the final FRS focal point. This signal was sent to a DGF channel in each crate in order to provide an internal check of the synchronization of the DGF clocks and also to provide a time-difference measurement between the arrival of an ion in the plastic scintillator and the measurement of a delayed γ ray via the DGF γ-time signal. The clock frequency of the DGF modules was 40 MHz, corresponding to a 25 ns time step.

The array performance was measured using radioactive sources both before and after the experimental beam periods. The experimental conditions were found to produce an energy resolution of less than 3 keV at 1.3 MeV.

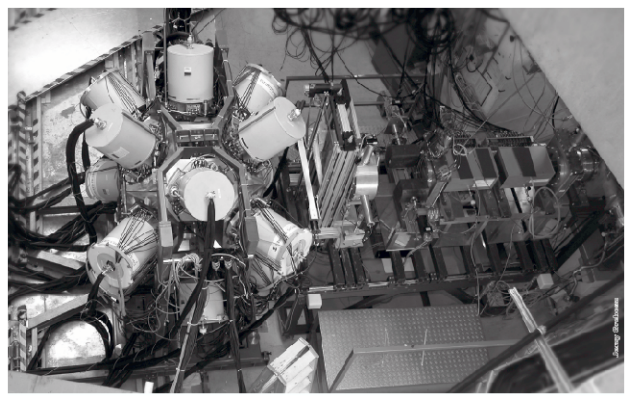

Figure 1: Photograph of the Stopped Beam RISING spectrometer at the end of the FRS beam line.

The source measurements suggest a typical γ-ray photopeak efficiency of approximately 10% at 1.3 MeV. Specific details of the characteristics and in-beam performance of the RISING array can be found in [3]. The next phase of the Stopped Beam RISING project will include the study of β-delayed spectroscopy of heavy, neutron-rich nuclei using a position sensitive silicon detector array to correlate detected β-particles with specific implanted heavy-ions. The first experiments using this development are scheduled to run at GSI in early 2007.

References

[1] M. Caamano *et al*., Eur. Phys. J. **A23** (2005) 201; K.A. Gladnishki *et al*., Phys. Rev. **C69** (2004) 024617; M. Pfützner *et a*l., Phys. Rev. **C65** (2002) 064604.

[2] P.H. Regan *et al;* (S244) Zs. Podolyák *et al.*, (S299); D. Rudolph *et al*., (S244); A.M. Bruce *et al*., (S300); A. Jungclaus, M. Górska, M. Pfützner *et al*., (S244 and S305); this GSI annual report.

[3] S. Pietri *et al*., Acta Phys. Pol. **B** (2007), in press; ibid, Nucl. Inst. Meth. Phys. Res. **B** (2007), in press.

Identification of a 10^+ Isomer in ^{54}Ni: Proton Decay 'in the Mirror' (S244)

D. Rudolph[1], R. Hoischen[1,2], M. Hellström[1], S. Pietri[3], Zs. Podolyák[3], P.H. Regan[3], A.B. Garnsworthy[3,4], S.J. Steer[3], F. Becker[2], P. Bednarczyk[2,5], L. Caceres[2,6], P. Doornenbal[2], J. Gerl[2], M. Górska[2], J. Grębosz[5,2], I. Kojouharov[2], N. Kurz[2], W. Prokopowicz[2,5], H. Schaffner[2], H.J. Wollersheim[2], L.-L. Andersson[1], L. Atanasova[7], D.L. Balabanski[7,8], M.A. Bentley[9], A. Blazhev[10], C. Brandau[2,3], J.R. Brown[9], C. Fahlander[1], E.K. Johansson[1], and A. Jungclaus[6]

[1]Department of Physics, Lund University, S–22100 Lund, Sweden; [2]Gesellschaft für Schwerionenforschung mbH, D–64291 Darmstadt, Germany; [3]Department of Physics, University of Surrey, Guildford, GU2 7XH, UK; [4]WNSL, Yale University, New Haven, CT 06520-8124, USA; [5]The Henryk Niewodniczański Institute of Nuclear Physics (IFJ PAN), PL–31-342 Kraków, Poland; [6]Departamento de Fisica Teórica, Universidad Autonoma de Madrid, E–280 49 Madrid, Spain; [7]Faculty of Physics, University of Sofia, BG–1164 Sofia, Bulgaria; [8]Institute for Nuclear Research and Nuclear Energy, Bulgarian Academy of Sciences, BG-1784 Sofia, Bulgaria; [9]Department of Physics, University of York, York, Y01 5DD, UK; [10]Institut für Kernphysik, Universität zu Köln, D–50937 Köln, Germany

Studies of isospin symmetry by means of γ-ray spectroscopic methods of isobaric analogue states has made significant progress during the past decade — the description of so-called mirror-energy difference (MED) has moved forward from a qualitative to a quantitative understanding [1, 2]. The different spatial distributions of the protons in the respective mirror states give rise to isospin breaking Coulomb effects and nuclear components [3, 4], which allows for subtle nuclear structure investigations on the basis of modern large-scale shell-model calculations [5]. Experimentally, these advances are mainly linked to 4π Ge-detector instruments in conjunction with ancillary systems. Lately, these combinations pushed for isospin $T_z = \pm 1$ or $T_z = \pm 3/2$ mirror systems [1] and electromagnetic decay properties; for example, isoscalar and isovector effective charges in the fp shell could be derived [6].

Within the RISING Stopped Beam Campaign (March 2006) [7] we undertook a search for a presumed 10^+ isomeric state in the $T_z = -1$ nucleus ^{54}Ni, which should be the analogue to a well established $\tau = 525(10)$ ns, 10^+ state in its $A = 54$ mirror ^{54}Fe [8]. The main goals were MED investigations towards the upper fp shell, and the extension of the results of Ref. [6] by comparing $B(E2; 10^+ \rightarrow 8^+)$ and $B(E4; 10^+ \rightarrow 6^+)$ strengths.

The upper spectrum in Fig. 1 reveals six delayed γ-ray transitions at 146, 451, 1227, 1327, 1392, and 3241 keV, all having the same lifetime of $\tau \sim 220$ ns. The 451, 1227, and 1392 keV represent the known $6^+ \rightarrow 4^+ \rightarrow 2^+ \rightarrow 0^+$ cascade in ^{54}Ni. The new 146 and 3241 keV lines are the $10^+ \rightarrow 8^+$ and $8^+ \rightarrow 6^+$ transitions; they are found in coincidence with the known cascade, which is proven by Fig. 1(b). Here, another weak but distinct line can be discriminated at 3386 keV, which marks the $10^+ \rightarrow 6^+$ $E4$ branch of the isomeric decay.

Interestingly, the 1327 keV line seen clearly in Fig. 1(a) is absent in Fig. 1(b). Since it exhibits (within uncertainties) the same half-life as the other transitions and because it fits in energy, we associate it with the $9/2^- \rightarrow 7/2^-$ ground-state transition in ^{53}Co, which must be emitted subsequent to a 1.28 MeV direct proton decay of the 10^+ isomer in ^{54}Ni. This marks the first (indirect) evidence for proton emission following a fragmentation reaction and brings the associated research field back to its roots: direct proton decay was first observed in ^{53m}Co in 1970 [9].

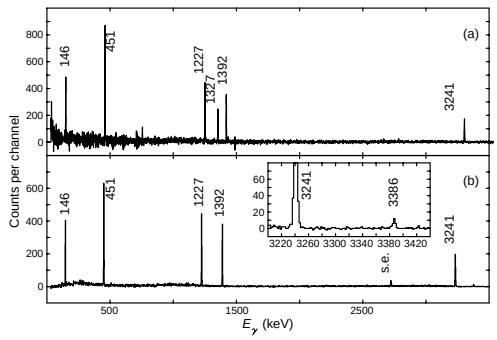

Figure 1: (a): γ-ray singles spectrum in the time range 0.05 μs $\leq t \leq$ 1.0 μs following the implantation of ^{54}Ni ions. (b): $\gamma\gamma$ correlation spectrum in coincidence with one of the 451, 1227, or 1392 keV transitions. Timing conditions as in (a) are applied, but less restrictive FRS gates.

This work is supported by the European Commission contract no. 506065 (EURONS), the Swedish VR, EPSRC (United Kingdom), the German BMBF, the Polish Ministry of Science and Higher Education, the Bulgarian Science Fund, the Spanish MEC, and the U.S. DOE.

References

[1] M.A. Bentley and S.M. Lenzi, Prog. Part. Nucl. Phys., in press.

[2] J. Ekman *et al.*, Mod. Phys. Lett. A **20**, No. 39, 2977 (2005).

[3] A.P. Zuker *et al.*, Phys. Rev. Lett. **89**, 142502 (2002).

[4] J. Ekman *et al.*, Phys. Rev. Lett. **92**, 132502, (2004).

[5] E. Caurier *et al.*, Rev. Mod. Phys. **77**, 427 (2005).

[6] R. du Rietz *et al.*, Phys. Rev. Lett. **93**, 222501 (2004).

[7] P.H. Regan *et al.*, this Annual Report.

[8] J. Huo *et al.*, Nucl. Data Sheets **68**, 887 (1993).

[9] K.P. Jackson *et al.*, Phys. Lett. **33B**, 281 (1970).

Isomer Spectroscopy Using Relativistic Projectile Fragmentation at the *N*=*Z* Line for *A*~80-90 Using RISING (S244a)*

P.H. Regan[1], A.B. Garnsworthy[1,2], S. Pietri[1], L. Caceres[3,4], M .Górska[3], D.Rudolph[5], Zs.Podolyák[1], S.J.Steer[1], J.Gerl[3], H.J.Wollersheim[3], F.Becker[3], P.Bednarczyk[3], P.D.Doornenbal[3,13], H.Geissel[3], H. Grawe[3], J.Gręboszˊ[3,6], R.Hoischen[5], A.Kelic[3], I.Kojouharov[3], N.Kurz[3], F.Montes[3], W.Prokopowicz[3], T.Saito[3], H.Schaffner[3], S.Tashenov[3], A.Heinz[2], M.Pfützner[7], T.Kurtukian-Nieto[8], G.Benzoni[9], M.Hellström[5], A.Jungclaus[4], L.-L.Andersson[5], L.Atanasova[10], D.L.Balabanski[10], M.A.Bentley[11], B.Blank[12], A.Blazhev[13], C.Brandau[1,3], J.Brown[11], A.M.Bruce[14], F.Camera[9], W.N.Catford[1], I.J.Cullen[1], Zs.Dombradi[15], E.Estevez[8], C.Fahlander[5], W.Gelletly[1], G.Ilie[13], E.K.Johansson[5], J.Jolie[13], G.A.Jones[1], M.Kmiecik[6], F.G..Kondev[16], S. Lalkovski[10,14], Z.Liu[1], A.Maj[6], S.Myalski[6], S.Schwertel[17], T.Shizuma[1,18], A.J.Simons[1], P.M.Walker[1], E.Werner-Malento[3,7] O.Wieland[9]

[1]University of Surrey, UK; [2]Yale University, USA; [3]GSI, Darmstadt, Germany; [4]Universidad Autonoma, Madrid, Spain; [5]Department of Physics, Lund University, Sweden; [6]IFJ, Kraków, Poland; [7]IEP Warsaw University, Poland; [8]Universidad de Santiago de Compostela, Spain; [9]INFN, Milano, Italy; [10]Faculty of Physics, University of Sofia , Bulgaria; [11]Dept. of Physics, University of York, UK; [12]CENBG, Bordeaux, France; [13]IKP, Universität zu Köln, Germany; [14]University of Brighton, UK; [15]Debrecen, Hungary; [16] Argonne National Laboratory, USA; [17] Technische Universität München, Germany; [18]Japan Atomic Energy Agency, Kyoto, Japan

The first experiment using the RISING array in its Stopped Beam configuration investigated nuclear structure along the *N*=*Z* line approaching ^{100}Sn. Specifically, decays from isomeric states in the *N*=*Z* nuclei ^{82}Nb and ^{86}Tc were used to shed light on the competing roles of *T*=1 and *T*=0 proton-neutron pairing in nuclei. The nuclei of interest in were populated following the projectile fragmentation of a 750 MeV/u ^{107}Ag primary beam on a 4g/cm^2 beryllium production target with typical intensities of 1x10^9 to 3x10^9 particles per extraction spill, which was 10 seconds long. Standard time of flight, position, and energy loss parameters were used to provide unambiguous particle identification through the FRS (see Fig. 1).

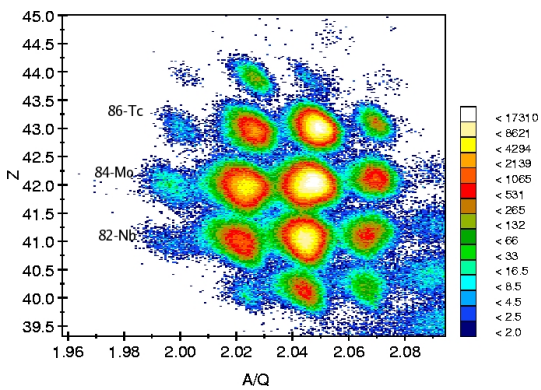

Figure 1: Calibrated identification spectrum centred on the *N*=*Z* line following the fragmentation ^{107}Ag.

At the end of the FRS, the ions passed through a variable thickness aluminium degrader such that the ions of interest came to rest in a passive stopper placed in the centre of the RISING array. In this experiment, the stopper was made from a multi-layered perspex block of total thickness 7 mm. Delayed γ rays were then detected using the RISING array. Examples are provided in Fig. 2.

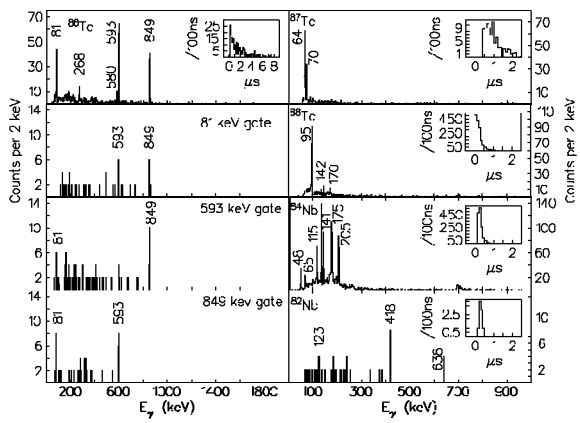

Figure 2: Time and γ-ray spectra associated with decays from isomeric states populated following the fragmentation of ^{107}Ag. (Left) Singles and γ-ray coincidence spectra associated with the isomer in ^{86}Tc. (Right) Singles spectra showing the γ-ray transitions and decay curves for isomeric decays in ^{87,88}Tc and ^{82,84}Nb.

The data are currently under final analysis and initial results have already been submitted for publication [1]. Decay schemes for the heavy odd-odd *N*=*Z* nuclei ^{82}Nb and ^{86}Tc could be constructed for the first time.

References

[1] P.H. Regan *et al.*, Nucl. Phys. A (2007), in press.

Identification of new isomeric states in the region around doubly-magic ^{132}Sn populated in the fragmentation of ^{136}Xe (S305)

A. Jungclaus[1], L. Caceres[1,2], M. Górska[2], M. Pfützner[3], S. Pietri[4], E. Werner-Malento[2,3], D. Rudolph[5], P. Detistov[6], S. Lalkovski[7], V. Modamio[1], J. Walker[1], P. Bednarczyk[2,8], P. Doornenbal[2], J. Gerl[2], J. Grebosz[2,8], I. Kojouharov[2], N. Kurz[2], W. Prokopowicz[2], H. Schaffner[2], H.J. Wollersheim[2], K. Andgren[9], J. Benlliure[10], A.M. Bruce[6], E. Casarejos[10], B. Cederwall[9], B. Hadinia[9], M. Hellström[5], R. Hoischen[5], G. Ilie[11], A. Khaplanov[9], M. Kmiecik[8], A. Maj[8], F. Montes[2], S. Myalski[8], Z. Podolyák[4], G. Simpson[12], S. Steer[4], S. Tachenov[2], R. Kumar[2,13], and S. Mandal[14]

[1]Universidad Autónoma de Madrid, Madrid, Spain; [2]GSI, Darmstadt, Germany; [3]University of Warsaw, Warsaw, Poland; [4]University of Surrey, Surrey, UK; [5]Lund University, Lund, Sweden; [6]University of Sofia, Sofia, Bulgaria; [7]University of Brighton, Brighton, UK; [8]University of Cracow, Cracow, Poland; [9]KTH Stockkholm, Stockholm, Sweden; [10]Universidad de Santiago de Compostela, Santiago de Compostela, Spain; [11]Universität zu Köln, Köln, Germany; [12]ILL Grenoble, Grenoble, France; [13]Inter University Accelerator Centre, New Delhi, India; [14]University of Delhi, New Delhi, India

The experiment S305 within the RISING stopped beam campaign has been devoted to the search for new isomeric states in nuclei around the doubly magic ^{132}Sn. The nuclei of interest were produced by the fragmentation of a ^{136}Xe primary beam provided by the SIS accelerator at GSI on a beryllium target at an energy of 700 MeV/u. The reaction products were identified ion by ion in the FRS using the Bρ - ΔE - Bρ method. Finally the ions were slowed down in a degrader and implanted in a passive stopper in the final focal plane of the FRS. γ-rays emitted in the decay of isomeric states have been measured in coincidence with properly identified and implanted ions using the RISING Ge-array. The latter comprises fifteen Cluster detectors from the former EUROBALL, i.e. 105 Ge crystals, arranged in three rings of five detectors each. This high granularity, which drastically reduces the problems caused by the so-called "prompt flash", combined with the high detection efficiency guaranteed the success of the RISING stopped beam experiments. The timing of the observed γ-rays has been determined in three independent ways, namely using the internal clock of the DGF modules (time stamping in steps of 25 ns) and two conventional timing branches with a short (t $\leq$ 1 μs) resp. long range (t $\leq$ 0.8 ms) [1]. It was therefore possible to detect isomeric decays over a large dynamic range.

The main goal of this experiment has been the identification of an expected 8^+ isomer in ^{130}Cd - searched for already in a series of experiments performed at GSI, MSU and ILL Grenoble. Most of the beam time has therefore been spent on an FRS setting centered on this nucleus. Some time, however, has been devoted to the study of the lighter Cd isotopes using a setting centered around ^{126}Cd. In these two settings seventeen new (unpublished) isomeric decays have been observed in the Ag, Cd, In and Sn isotopes as indicated in Fig. 1. Some of the γ-transitions observed in these decays had already been seen in experiments during the isomeric campaign at GSI some years ago (mainly In isotopes) [2] and in a recent experiment performed at MSU (mainly Ag and Cd isotopes) [3]. However, in these former experiments no definite conclusions concerning the decay schemes could be drawn due to a lack of statistics.

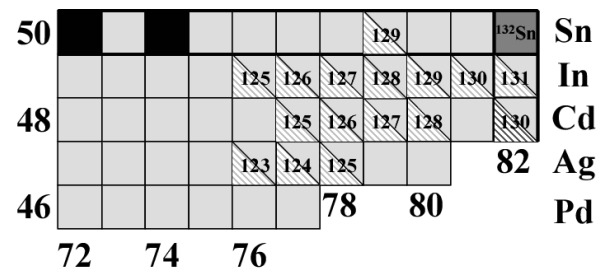

Figure 1: Nuclei in which new isomeric states have been identified in experiment S305 (triangles).

As an example we will discuss here the case of ^{128}Cd. Before our experiment only two γ-rays (645 and 784 keV) had been observed in an β-decay experiment at ISOLDE [4]. We now observed five additional γ transitions in coincidence with ^{128}Cd ions implanted in the stopper. A careful analysis of their decay curves has shown that they are emitted following the decay of two different isomeric states with lifetimes of approximately 5.3 μs and 500 ns.

This work is supported by the European Commission contract no. 506065 (EURONS), the Spanish Ministerio de Educación y Ciencia under contract FPA2005-00696 and within the programa Ramón y Cajal, the Swedish VR, EPSRC (United Kingdom), the German BMBF, the Polish Ministry of Science and Higher Educacion and the Bulgarian Science Fund.

References

[1] S. Pietri et al., Eur. Phys. J A, in press.

[2] M. Hellström et al., Proc. of the Int. Workshop on Gross Properties of Nuclei and Nuclear Excitations Hirschegg, 2003.

[3] B.E. Tomlin, PhD thesis, MSU 2006, unpublished.

[4] T. Kautzsch et al., Eur. Phys. J. A9, 201 (2000).

Investigation of nuclear structure around ^{132}Sn by fission of ^{238}U (S244)

M. Pfützner[1], M. Górska[2], L. Cáceres[2,3], E. Werner-Malento[1,2], A. Jungclaus[3], S. Pietri[4], Zs. Podolyák[4], H. Grawe[2], P. Detistov[5], S. Lalkovski[6], V. Modamio[3], J. Walker[3], P. Bednarczyk[2,7], P. Doornenbal[2,8], J. Gerl[2], J. Grębosz[2,7], I. Kojouharov[2], N. Kurz[2], W. Prokopowicz[2], H. Schaffner[2], S. Tachenov[2], H.J. Wollersheim[2], G. Benzoni[9], A.M. Bruce[6], E. Casarejos[10], F. Crespi[9] , M. Hellström[11], R. Hoischen[11], G. Ilie[8], M. Kmiecik[7], R. Kumar[2,12], A. Maj[7], S. Mandal[13], F. Montes[2], S. Myalski[7], D. Rudolph[11], G. Simpson[14], and O. Weiland[9]

[1]Warsaw University, [2]GSI, Darmstadt, Germany; [3]Universidad Autónoma de Madrid, Madrid, Spain; [4]University of Surrey, Surrey, UK; [5]University of Sofia, Sofia, Bulgaria; [6]University of Brighton, Brighton; [7]University of Cracow, Cracow, Poland; [8]Universität zu Köln, Köln, Germany; [9]University of Milan, Milan, Italy, [10]Universidad de Santiago de Compostela, Santiago de Compostela, Spain; [11]Lund University, Lund, Sweden; [12]Inter University Accelerator Centre, New Delhi, India; [13]University of Delhi, New Delhi, India, [14]ILL Grenoble, Grenoble, France

Nuclear structure studies in vicinity of the doubly magic nuclei located far off stability gained recently an increased interest with the new approach of shell evolution phenomena [1]. In addition, for the most exotic nuclei shell quenching is expected as a consequence of a change of the nuclear potential from Woods-Saxon to Harmonic Oscillator like shape [2,3]. Based on these works a question was posed if for ^{132}Sn core possibly shell quenching could be observed.

The experiment was performed as a continuation of a previous study [4] and focused on the ^{132}Sn region utilizing significantly increased ^{238}U beam intensity at GSI and an improved experimental setup. The main goal of the experiment was the search for isomeric states in nuclei closest to the magic nucleus in order to extract information on sustainability of the Z=50, N=82 shell gap. The experiment was combined with the S305 experiment pursuing similar goals. The comparison of two different production methods yielded additionally information on reaction mechanisms which is of importance for future projects. The experiment was performed within the RISING Stopped Beam Campaign (July 2006). Experimental details are described in Ref. [5]. The FRS [6] was set for nuclei arriving to the final focal plane according to their Z versus A/Q values as shown in Fig. 1. The decay of the isomeric states which survived the flight time through the FRS was measured in the RISING array.

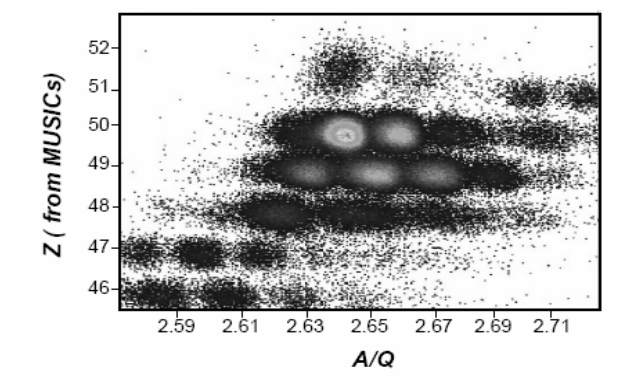

Figure 1: Nuclei observed at the final focal plane of the FRS according to their Z and A/Q.

Two of the many spectacular results of the two combined experiments were the observation of isomeric states in ^{130}Cd [7] and ^{131}In. The isomeric decay of ^{131}In consists of just one γ-ray transition at about 3.8 MeV energy as shown in Fig. 2. It probably represents the N=82 core excitation as the ½⁻ state is known as β emitter at ~300 keV. Based on that result the N=82 shell gap energy can be estimated after a detailed analysis of the still preliminary data. The shell model interpretation of the N=82 core excitation of ^{132}Sn is a challenge to infer adequate realistic interactions and to develop powerful codes.

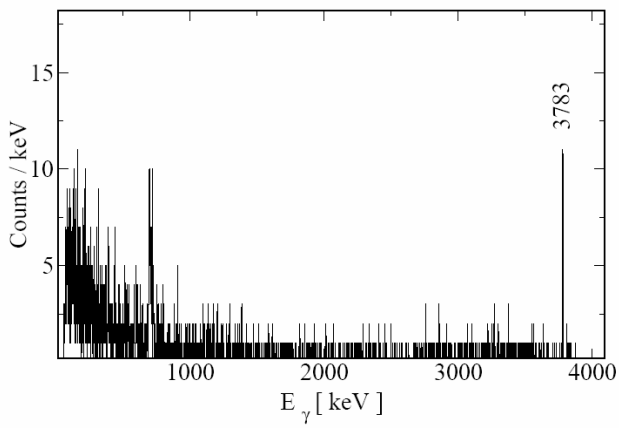

Figure 2: γ-ray spectrum of the isomeric decay in ^{131}In.

This work is supported by the European Commission contract no. 506065 (EURONS), the Spanish Ministerio de Educación y Ciencia under contract FPA2005-00696 and within the programa Ramón y Cajal, the Swedish VR, EPSRC (United Kingdom), the German BMBF, the Polish Ministry of Science and Higher Education and the Bulgarian Science Fund.

References

[1] T. Otsuka et al., Phys. Rev. Lett. 95 (2005) 232502
[2] T.R. Werner, J. Dobaczewski, W. Nazarewicz Z. Phys. A358 (1997) 169
[3] B.Pfeiffer et al., Nucl. Phys. A693 (2001) 282
[4] M. Hellström et al., Proc. of the Int.Workshop on Gross Properties of Nuclei and Nuclear Excitations Hirschegg, 2003.
[5] P.Regan et al., this Annual Report
[6] G. Münzenberg, Nucl. Instr. Meth., B70 (1992) 265
[7] A. Jungclaus et.al., this Annual Report

Lifetime measurements within the g-RISING campaign at GSI[$]

R. Lozeva[1,2,#], G. Neyens[1], G. Simpson[3] and N. Vermeulen[1] for the g-RISING collaboration[+]
[1]IKS, K.U. Leuven, Leuven, Belgium; [2]U. Sofia , Sofia, Bulgaria; [3]ILL and LPSC IN2P3-CNRS, Grenoble, France.

Introduction and experimental technique

Recent experiments on the magnetic moments of μs isomeric states, within the framework of the g-RISING campaign [1] at GSI, have additionally allowed new measurements of isomeric lifetimes in the very neutron rich side around the doubly magic ^{132}Sn. These nuclei, which are very difficult to study, were produced by relativistic fission of ^{238}U. Thus, the current motivation is to search for new high-spin isomers, as the reaction populates higher spins on average than other methods used in the past (β decay, neutron-induced fission, deep inelastic reactions). Since the nuclei in this vicinity have a particularly simple structure, only a few particles and/or holes outside a doubly magic core, their investigations enable stringent tests of nuclear shell model theories.

The present work reports on μs lifetime measurements of isomeric states in Sn and Sb isotopes based on an event-by-event time correlation between the fragments and the delayed γ-rays de-exciting the isomers in a range between ~200 ns (limited by the flight time of the ions trough the FRS [2]) and 20 μs. Except the accurate measure of the already known lifetimes in this region several new isomeric states are found.

Analysis and results

The isotope cocktail obtained in the fission reaction is demonstrated on Figure 1 by an identification plot, representing the element number (Z) vs. the mass over charge ratio (A/q) [2].

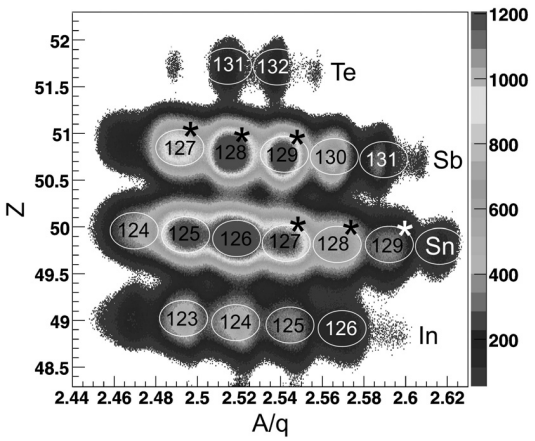

Figure 1: An identification plot from a relativistic fission reaction. Encircled are all nuclei possessing known μs isomers. Nuclei with new isomers are marked with stars.

All isotopes with μs isomers are encircled and their lifetimes studied in the current analysis. Very often a single isotope has several isomers in the μs region with various values in the literature. A summary of the available knowledge i.e. for the Sn isotopes is compared with the present study in Table 1. In addition to the already known isomeric decays several new ones are observed. They are marked on Figure 1 and Table 1 with stars. Two of them are predicted as the $(27/2^-)$ $h_{11/2}^{-\nu}$ seniority (ν=3) isomers [5] and seen already in the lighter Sn nuclei [6]. The half-lifes of these new isomeric states are found to be in the range 200 ns – 1 μs [12].

Sn	Isomer	$T_{1/2}$ [μs] literature	$T_{1/2}$ [μs] this work
124	10^+ 7^- 5^-	45(5) [3] 3.1(5) [4] 0.27(6) [4]	44.9(6.7) 3.05 (4) 0.31(10)
125	$27/2^-$ $19/2^+$	0.23(3) [5,6] 6.2 (7) [5]	0.27 (11) 6.12 (95)
126	10^+ 7^-	7.6 [7] 7.7 (5) [6] 6.6 (1.4) [4]	7.72 (12) 6.66 (79)
127	$(27/2^-)$* $(23/2^+)$ $19/2^+$	- 1.26(15) [7] 4.5(3) [5,6] 4.8 (3) [7]	0.26 (4) - 4.61 (45)
128	10^+ *	2.69(23) [8] 3.4 [9] -	3.41 (48) 0.30 (7)
129	$(27/2^-)$* $23/2^+$ $19/2^+$	- 2.0(2) [7] 2.4(2) [10] 3.2(2) [7] 3.6 (2) [10] 3.7(2) [5] 3.9(4) [11]	0.25 (9) 1.32 (71) 3.46 (38)
130	10^+	1.5(2) [11] 1.61(15) [8]	1.54 (27)

Table 1: Isomeric half-lifes for the studied Sn nuclei.

References

[1] G. Neyens et al, Act. Phys. Pol. B (2007), in press
[2] H.J. Wollersheim et al, Nucl. Instr. Meth. A 537 (2005) 637
[3] R. Broda et al, Phys. Rev. Lett. 68 (1992) 1671
[4] B. Fogelberg et al, Nucl. Phys. A 323 (1979) 205
[5] J. Pinston et al, Phys. Rev. C 61 (2000) 024312
[6] C. Zhang et al., Phys. Rev. C 62 (2000) 057305
[7] H. Gausemel et al., Phys. Rev. C 69 (2004) 054307
[8] B. Fogelberg et al, Nucl. Phys. A 352 (1981) 157
[9] J. Pinston et al, J. Phys. G 30 (2004) R57
[10] J. Genevey et al., Phys. Rev. C 65 (2003) 034322
[11] M. Hellström et al, Proc. Int. Workshop on Gross Prop. of Nucl. and Nucl. Exc., Hirschegg, Austria, Jan. 2003, p. 72
[12] R. Lozeva et al, in preparation

[$]Work supported in part by EU, EURONS contract No. RII3-CT-2004-506065.
[#]radomira.lozeva@fys.kuleuven.be
[+]See annex.

Isomeric states populated in the fragmentation of ^{208}Pb (S299) *

Zs. Podolyák[1], S.J. Steer[1], S. Pietri[1], P.H. Regan[1], D. Rudolph[2], E. Werner-Malento[3,4], T. Shizuma[1,5], S. Myalski[6], A.B. Garnsworthy[1], R. Hoischen[2,3], M. Górska[3], J. Gerl[3], H.J. Wollersheim[3], F. Becker[3], P. Bednarczyk[3,6], L. Cáceres[3,7], P. Doornenbal[3], H. Geissel[3], J. Gręboszz[3,6], A. Kelic[3], I. Kojoukharov[3], N. Kurz[3], F. Montes[3], W. Prokopowicz[3,6], T. Saito[3], H. Schaffner[3], S. Tachenov[3], A. Heinz[8], M. Pfützner[4], T. Kurtukian-Nieto[9], G. Benzoni[10], A. Jungclaus[7], D.L. Balabanski[11,12], C. Brandau[1,3], A.M. Bruce[13], W.N. Catford[1], I.J. Cullen[1], Zs. Dombrádi[14], E. Estevez[8], W. Gelletly[1], G. Ilie[15,16], J. Jolie[15], G.A. Jones[1], M. Kmiecik[6], F.G. Kondev[17], S. Lalkovski[18,13], Z. Liu[1], A. Maj[6], S. Schwertel[19], P.M. Walker[1], and O. Wieland[10]

[1]Univ. of Surrey, UK; [2]Lund Univ., Sweden; [3]GSI, Darmstadt, Germany; [4]Warsaw Univ., Poland; [5]JAEA, Kyoto, Japan; [6]INP, Kraków, Poland; [7]Univ. Autonoma, Madrid, Spain; [8]Yale Univ., New Haven, USA; [9]Univ. de Santiago de Compostela, Spain; [10]INFN, and Univ. Milano, Italy; [11]INRNE, Sofia, Bulgaria; [12]Univ. Camerino, Italy; [13]Univ. Brighton, UK; [14]ATOMKI, Debrecen, Hungary; [15]Univ. Köln, Germany; [16]NIPNE, Bucharest, Romania; [17]Argonne Nat. Lab., USA; [18]Univ. Sofia, Bulgaria; [19]TU München, Germany

Heavy nuclear species were populated in the projectile fragmentation of an E/A=1 GeV, ^{208}Pb beam. The nuclei of interest were studied within the RISING stopped beam campaign [1]. The experiment's main aim was the study of the structure of the neutron-rich N=126 nucleus, ^{204}Pt. ^{204}Pt has four protons less than the doubly magic ^{208}Pb, and its yrast structure is expected to be dominated by the proton-hole orbitals $\pi d_{3/2}$, $\pi s_{1/2}$, $\pi h_{11/2}$ and possibly $\pi d_{5/2}$. Two isomeric decays have been observed (see fig.1.). Based on the comparison with the two proton-hole nucleus ^{206}Hg [2] and shell model calculations it is expected that the two states have spin-parities of 5^- and 10^+, respectively.

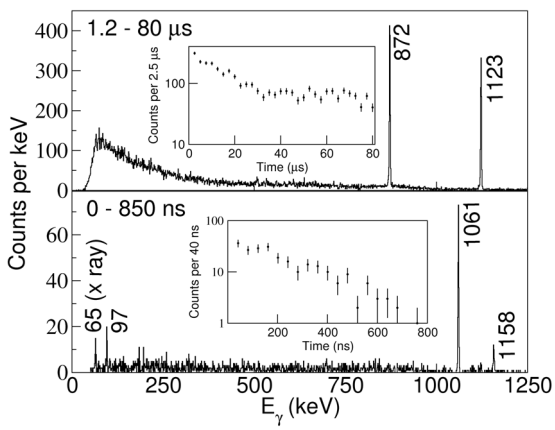

Figure 1: Delayed γ-ray spectra assigned to ^{204}Pt over two different time regimes. The lower and upper panels show the decay from the (10^+) and (5^-) isomers, respectively

In addition, the observation of the previously identified isomers will provide information on the angular momentum population within the relativistic-energy fragmentation process. Isomeric ratios will be determined for nuclei produced in different reaction mechanisms, such us 'cold fragmentation (^{204}Pt, ^{206}Hg) and 'hot fragmentation' (^{190}Pb). Decays from the previously reported isomeric $I = 27$ and $I = (49/2)$ states in ^{148}Tb [3] and ^{147}Gd [4], respectively, have also been observed. These isomeric decays represent the highest discrete spin states observed to date following a projectile fragmentation reaction.

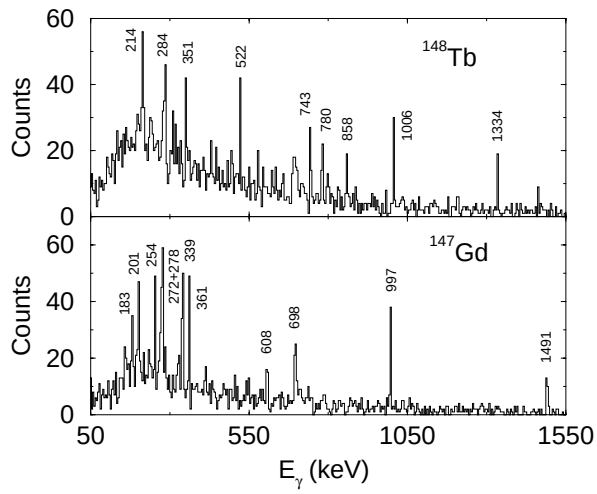

Figure 2: Delayed gamma-ray spectra associated with ^{148}Tb and ^{147}Gd. The transitions labeled with their energies in keV originate from the decay of the high spin isomers I=27$\hbar$ in ^{148}Tb [3] and I=49/2$\hbar$ in ^{147}Gd [4], respectively.

References

[1] P.H. Regan *et al.*, this Annual Report.

[2] B. Fornal *et al.*, Phys. Rev. Lett. **87** (2001) 212501.

[3] E. Ideguchi *et al.*, Z. Phys. **A352** (1995) 363.

[4] R. Broda *et al.*, Z. Phys. **A285** (1978) 423; Z. Phys. **A305** (1982) 281.

* Work supported by EU, EURONS contract No 506065.

g-factor measurement of the $19/2^+$ isomer in ^{127}Sn*

L. Atanasova[1], D. L. Balabanski[2,3], M. Hass[4], R. Lozeva[1,5], G. Neyens[5], G. Simpson[6,7] and N. Vermeulen[5] for the g-RISING Collaboration[#]

[1]University of Sofia, BG-1164 Sofia, Bulgaria; [2] INRNE, BAS, BG-1784 Sofia, Bulgaria; [3]Universitá di Camerino, 62032 Camerino, Italy; [4]Weizmann Institute of Science, Rehovot 76100, Israel; [5] IKS, K.U. Leuven, 3001 Leuven, Belgium; [6]LPSC, 38026 Grenoble Cedex, France; [7]Institut Laue-Langevin, 38042 Grenoble, France;

We report results from a *g*-factor measurement of the $19/2^+$, $T_{1/2}$ = 4.5(3) μs isomer in ^{127}Sn [1,2]. Such studies deliver valuable information about the structure of the neutron-rich nuclei in the vicinity of the doubly-magic ^{132}Sn. The experiment was done in relativistic projectile fragmentation within the RISING project [3]. The method of Time-Differential Perturbed Angular Distributions (TDPAD) was used for the measurement of the *g* factor of interest. It is based on the measurement of the Larmor precession of a spin-oriented nuclear ensemble in an external magnetic field. In order to preserve the spin orientation obtained in the reaction, fully-stripped ions are separated at relativistic energies. Thus, ions heavier than A = 80 produced and separated as fully-stripped fragments, are available only at GSI.

The neutron-rich nuclei around A ≈130 were populated in relativistic projectile fragmentation of a ^{136}Xe beam at E/A = 600 MeV on a thin 1024 mg/cm^2 Be production target. The fully-stripped ions with energy of 300 MeV per nucleon were separated, tracked and identified on an event-by-event basis with the FRS at GSI and its ancillary detectors. At the final focal plane of FRS the ions were implanted in a high-purity 2 mm annealed Copper plate, which provided a perturbation-free environment for the isomeric decay. A constant magnetic field B = 0.12 T in the vertical direction was provided. Coincidences between the ion signals from the FRS detectors and the decay γ rays, detected with eight Cluster Ge detectors mounted in the horizontal plane, were recorded within a time window of 12 μs and analysed with the CRACOW software [4]. The magnitude and sign of the alignment of the nuclear spin ensemble depends on the longitudinal momentum distribution [5], which was measured by the position sensitive scintillator detector in the second focal plane of FRS. The experimental set-up is discussed in more detail in Ref. [6].

The angular distribution of the intensity of the γ decay varies with the Larmor frequency $\omega_L = -g\mu_N B/\hbar$. To extract the *g* factor from the measured time spectra, they are combined in *R(t)* functions for each γ transition, which do not depend on the isomeric decay constant. Theoretically it has highest amplitude for the detectors placed at 90° with respect to each other and at 45° to the beam axis in horizontal plane: $R(t,\omega_L) = 3A_2B_2\sin(2\omega_L t)/(4 + A_2B_2)$, where A_2 is the angular distribution coefficient, depending on the details of the γ decay, B_2 is the orientation parameter, depending on the degree of alignment produced in the reaction.

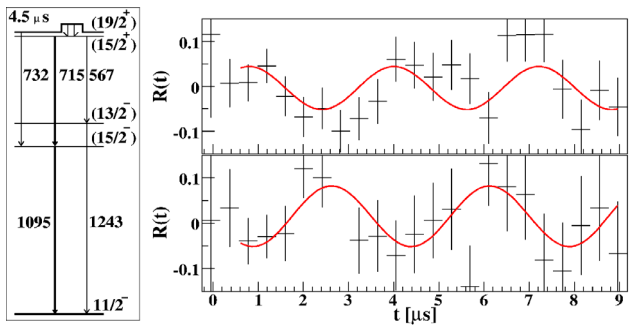

Figure 1: Left: Partial level scheme of the decay of the $19/2^+$ isomer in ^{127}Sn [1]; Right: *R(t)* functions for the 1095 keV transition (up) and for the 715 keV transition (down) at the wing of the momentum distribution.

The *R(t)* functions for the 1095 keV and 715 keV γ rays in the outermost wing of the momentum distribution are presented on Figure 1. They display opposite phase, which is in disagreement with the published level scheme [1]. For the *R(t)* function of the 715 keV transition ~ 10^4 photopeak events were used in the data analysis, which sets the limit for such experiments. The obtained absolute value of the *g* factor is $|g| \approx 0.16$. It is in agreement with theoretical calculations based on the empirical *g* factors and the assumption for the main component of the wave function based on systematics: $g(s_{1/2}^{-1}h_{11/2}^{-2}) \approx -0.156$, and with large-scale shell model calculations. These results will be discussed in detail elsewhere [7].

The results from the g-RISING campaign for the *g* factor of the $19/2^+$ isomer in ^{127}Sn show that significant alignment (~10%) is observed in the wing of the momentum distribution. The present experiment provides a benchmark (in terms of intensity of the isomeric beam and number of detected γ rays) for further studies of electromagnetic moments of isomers in nuclei farther away from stability.

References

[1] J.A. Pinston et al., Phys. Rev. C **61** (2000) 024312.
[2] J.A. Pinston and J. Genevey, J. Phys. G **30** (2004) R57.
[3] H.J. Wollersheim et al., NIM A **537** (2005) 637.
[4] J. Grebosz, Comp. Phys. Communications (2006) (in print).
[5] I. Matea et al., Phys. Rev. Lett. **93** (2004) 142503.
[6] G. Neyens et al., Acta Phys. Pol. B (2006) (in print).
[7] L. Atanasova et al. (2007) in preparation.

* Work supported in part by EC EURONS RII3-CT-2004-506065 project, the Bulgarian National Science Fund grant VUF06/05 and the Polish Ministry of Science and Higher Education grants 1-P03B-030-30 and 620/E-77/SPB/GSI/P-03/DWM105/2004-2007.
[#]See annex

g-factor measurements in neutron-rich Sn isotopes using relativistic isomeric beams produced by U-fission at RISING, GSI*

G. Ilie[1,2], J. Jolie[1], G. Neyens[3], G. Simpson[4,5], R. Lozeva[3,6], and N. Vermeulen[3]

[1]IKP, Koln, Germany; [2]NIPNE, Bucharest, Romania; [3]IKS, Leuven, Belgium; [4]ILL, Grenoble, France; [5]LPSC, Grenoble, France; [6]Univ. Sofia, Sofia, Bulgaria **for the g-RISING collaboration**†

Nuclei far from the valley of stability have become more accessible in recent years through the use of radioactive ion beams. The measurement of the magnetic moments of excited nuclear states, expressed by the g-factor, is a key topic to study the detailed structure of such nuclei and to investigate the single-particle configuration of nuclear states. High-spin isomers in the region of doubly-magic nuclei often have a rather pure single-particle configuration, for which the g-factor is a very good observable to determine the valence nucleon configuration [1].

The present study of the magnetic moments in the neutron-rich nuclei around ^{132}Sn was performed using the FRS-RISING setup at GSI [2]. For the measurement of the g-factors, the method of time-differential observation of the perturbed angular distribution (TDPAD) of deexciting γ-rays has been applied. This technique is based on the interaction of the magnetic moment with an external magnetic field.

The nuclei of interest were produced in a relativistic fission reaction of a primary ^{238}U beam from the SIS with an energy of ≈750 MeV/u and an average intensity of 10^8 ions per second impinging on a thin ^{9}Be (1g/cm^2) production target placed in front of the fragment separator FRS. The reaction products were selected and identified in the FRS by their magnetic rigidity and their specific energy loss in the degraders. Scintillators, multi-wire-proportional-counters and the ionisation chamber MUSIC were used to identify the ions in A and Z and to track their positions [2].

The final reaction products were stopped in a 2 mm thick Copper foil which was used as an implantation host and provided a perturbation-free environment for the implanted isomers. The plate was placed between the poles of an electromagnet and a magnetic field B≈0.70T was applied perpendicular to the beam axis plane and was periodically reversed. After implantation the nuclei of interest were identified based on an event-by-event time correlation. Coincidences between particle signals from the FRS detectors and the delayed γ-rays deexciting the isomers were recorded. The γ-rays emitted by the isomeric levels were measured by 8 Euroball Ge-Cluster detectors of the RISING setup [2], mounted in a ring in the horizontal plane and placed at 45 degrees with respect to the beam line and at relative angles of 30 degrees to each other.

The aim of this experiment was to measure the spin-alignment in projectile fission at relativistic energies, as well as the g-factor of these isomeric states in neutron-rich Sn isotopes. The results for the (19/2$^+$) isomeric state with a $t_{1/2}$=4.5(3)μs in ^{127}Sn [3] will be reported here.

In the offline analysis we formed time gated energy spectra and energy gated time spectra for each of the detectors using the SPY/CRACOW software [4]. From the energy gated time spectra we deduced the lifetime and we found a value in agreement with the previous values from the literature [3]. For the determination of the g-factor we used the time spectra obtained for each of the two magnetic field orientations to form the experimental R(t) function:

$$R_{exp}(t) = \frac{N_\uparrow(t,\theta,\omega_L) - N_\downarrow(t,\theta,\omega_L)}{N_\uparrow(t,\theta,\omega_L) + N_\downarrow(t,\theta,\omega_L)} \qquad (1)$$

which is no longer dependent on the isomeric decay constant. This $R_{exp}(t)$ function has the highest amplitude for the detectors at $\pm 45^0$ and $\pm 135^0$ and for these detectors it is fitted with the theoretical function:

$$R_{theor}(t) = \frac{3A_2B_2}{4 + A_2B_2}\sin(2\omega_L t) \qquad (2)$$

$\omega_L = \frac{gB\mu_n}{\hbar}$ is the Larmor frequency from which we can deduce the g-factor. The absolute value of the g-factor deduced from the fit is $|g|$≈0.16 which is in agreement with the empirical g-factor for a $\nu(h_{11/2}^{-2}s_{1/2}^{-1})$ configuration, g_{emp}=0.16. As an example the Figure 1 shows an autocorrelation analysis of the data (note that this does not show the real amplitude).

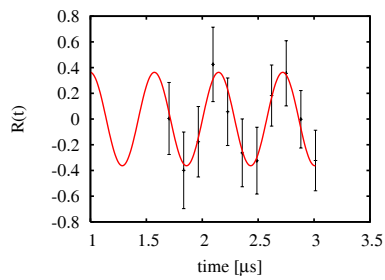

Figure 1: Preliminary result of the autocorrelation analysis for the (19/2$^+$) isomer in ^{127}Sn.

References

[1] G. Neyens, Rep. Prog. Phys. **66**, 633 and pg. 1251 (2003).

[2] H.J. Wollersheim et al., Nucl. Instrum. Meth. Phys. Res. **A 536**, 637 (2005)

[3] J.A. Pinston et al., Phys. Rev **C 61**, 024312 (2000) .

[4] J. Grebosz, Computer Phys. Communications (2006), in print.

* Work supported by EU, EURONS contract No. RII3-CT-2004-506065 and BMBF grant 06KY205I.

† See annex.

Pygmy dipole resonance in ^{130,132}Sn isotopes and the neutron skin thickness

A.Klimkiewicz and N.Paar for LAND-FRS S221 Collaboration

The pygmy dipole resonance (PDR) manifests itself as a concentration of dipole strength near the neutron separation threshold below the giant dipole resonance (GDR) domain. It is related to structural changes in nuclei with a large neutron excess giving rise to a neutron skin. According to theoretical calculations, a very precise measurement of the neutron skin thickness in heavy doubly magic nuclei like ^{208}Pb or ^{132}Sn would help in constraining the neutron matter equation of state [1, 2]. At present, the neutron matter radius in nuclei as a fundamental ground-state property cannot be approached experimentally in a straightforward way and its extraction from experimental data involves a certain model dependence [3]. Existing results on the neutron skin thickness are limited to stable nuclei. As suggested in [4], the pygmy dipole strength modes provides insight into the skin thickness as both quantities are strongly correlated with the symmetry energy.

Low-lying E1 strength was observed in exotic ^{130,132}Sn isotopes in a kinematically complete measurement performed at the LAND facility based on the relativistic Coulomb excitation in inverse kinematics [5]. Dipole strength distributions were deduced from the measured energy-differential cross sections obtained in an invariant-mass analysis applied to decay products and covered excitation energies ranging from the neutron separation threshold up to 25 MeV, including thus the GDR. The dipole response emerging below the GDR is characterized by exhausting 7(3)% and 4(3)% of the Thomas-Reiche-Kuhn sum rule for ^{130}Sn and ^{132}Sn, respectively. In the same mass region, stable N=82 isotones investigated in (γ,γ') reactions revealed a concentration of dipole strength below the neutron threshold absorbing, however, a much smaller fraction of the sum rule, below 1% [6]. We only briefly mention that, in addition to ^{130,132}Sn, we measured the pygmy strength in neighbouring odd nuclei, which facilitate a comparison with the N=82 data [6] in an identical excitation energy range. The resulting systematics reveals a clear trend of strength increasing with the $N-Z$ asymmetry, for details see [7].

In this report we focus on the following issues : constraining parameters describing the symmetry energy and extraction of the neutron skin thickness in ^{130,132}Sn from our data. Both goals were reached by using the relativistic quasiparticle random phase approximation (RQRPA) [9] with differently parametrized nucleon-nucleon interactions, corresponding to a softer or stiffer neutron matter equation of state, i.e. by varying the a_4 parameter (i.e. the symmetry energy at equilibrium density, see e.g. [3]) and, correlated to it, the slope of the symmetry energy. In each case the parameter set was calibrated to accurately reproduce the ground-state properties, like binding energies or charge radii, for a standard set of stable nuclei. An almost linear correlation between the ratio of the non-energy weighted strength absorbed by the PDR to that of GDR and the neutron skin thickness has been found. By comparing the experimental values of this ratio with that from the RQRPA, the parameters of the symmetry energy were fixed. For instance an average value $\bar{a}_4 = 31.8 \pm 1.3$ MeV in good agreement with considerations presented in [10] has been obtained. Using this result subsequently the neutron skin thickness of $\delta r(^{130}\text{Sn}) = 0.23 \pm 0.03$ and $\delta r(^{132}\text{Sn}) = 0.24 \pm 0.03$ fm were derived following a trend established by a measurement in stable Sn isotopes [8], see Fig.1. Results for the pygmy resonance in ^{208}Pb [11] are found to be consistent with the present analysis.

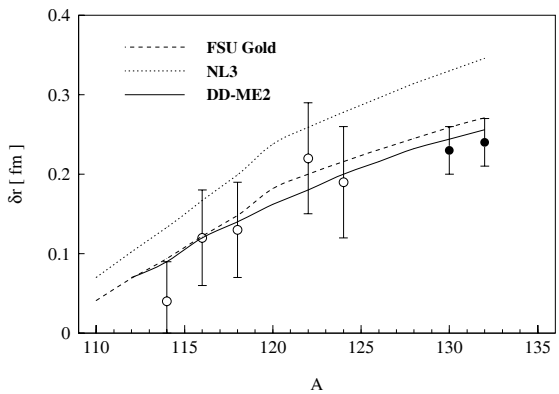

Figure 1: Neutron skin in Sn isotopes. The data for stable Sn isotopes (open circles) [8] are compared to our values (filled circles) for unstable ones. Theoretical predictions are from [4, 9].

References

[1] R.J.Furnstahl, Nucl.Phys.A 706(2002)85

[2] B.A.Brown, Phys.Rev.Lett. 85(2000)5296

[3] A.E.L.Dieperink *et al*., Phys.Rev.C 68(2003)064307

[4] J.Piekarewicz, Phys.Rev.C 73(2006)044325

[5] P.Adrich *et al*., Phys.Rev.Lett. 95(2005)132501

[6] S.Volz *et al*., Nucl.Phys.A 779(2006)1

[7] K.Boretzky *et al*., COMEX2 proceedings (to be published)

[8] A.Krasznahorkay *et al*., Phys.Rev.Lett. 82(1999)3216

[9] N.Paar *et al*., Phys.Lett.B 606(2005)288

[10] D.Vretenar, T.Nikšić and P.Ring, Phys.Rev.C 68(2003)024310

[11] N.Ryezayeva *et al*., Phys.Rev.Lett. 89(2002)272502

Two-proton fragmentation of ^{20}Mg and ^{17}Ne studied by fragment tracking with micro-strip detectors at FRS*

I. Mukha[1,2,#], K. Sümmerer[3], L. Acosta[4], M.A.G. Alvarez[1]; E. Casarejos[5]; A. Chatillon[3]; D. Cortina Gil[5]; J. Espino[1]; A. Fomichev[6]; J.E. Garcia-Ramos[4]; H. Geissel[3]; J. Gomez-Camacho[1]; L. Grigorenko[6]; J. Hoffmann[3], O. Kiselev[3,7]; A. Korsheninnikov[2]; N. Kurz[3]; Yu. Litvinov[3]; I. Martel[4]; C. Nociforo[3]; W. Ott[3]; M. Pfützner[8]; C. Rodriguez[5]; E. Roeckl[3]; M. Stanoiu[3]; H. Weick[3]; P. Woods[9]

[1]University of Sevilla, Spain; [2]Kurchatov Institute, Moscow, Russia; [3]GSI, Darmstadt, Germany; [4]University of Huelva, Spain; [5]University of Santiago de Compostela, Spain; [6]JINR, Dubna, Russia; [7]University of Mainz, Germany; [8]University of Warsaw, Poland; [9]University of Edinburgh, UK.

We report preliminary results for the fragmentation reactions ^{20}Mg→^{18}Ne+2p and ^{17}Ne→^{15}O+2p. The secondary ^{20}Mg and ^{17}Ne beams were produced by impinging a 591 A MeV ^{24}Mg primary beam with 5•10^9 ions/spill on a 4 g/cm^2 ^{9}Be target at the fragment separator FRS. The average intensities of the resulting 400 A MeV ^{20}Mg and ^{17}Ne secondary beams at the mid-plane of the FRS amounted to 400 and 800 ions/spill, respectively. Special ion-optical settings were applied: the first half of the FRS was tuned to an achromatic mode using a wedge-shaped degrader, while its second half was set for high acceptance in angle and momentum. A 6x6 cm^2 DSSD detector with 32x32 strips was used to track the secondary ions onto a 2 g/cm^2 ^{9}Be secondary target positioned at the mid-plane of the FRS.

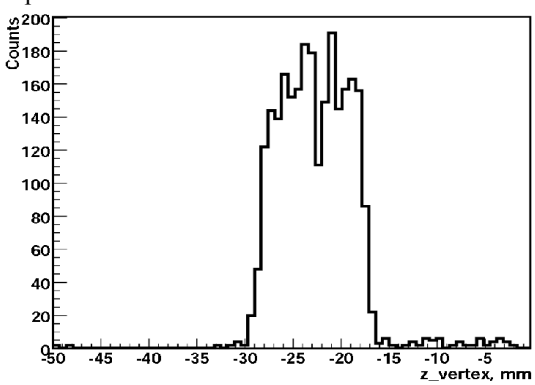

Figure 1: Profile of the ^{17}Ne→^{15}O+p+p fragmentation-vertex distribution along the beam direction as measured by the micro-strip detectors. The width of the intense bump matches the thickness of the secondary target.

Downstream from the reaction target, the break-up products of ^{20}Mg and ^{17}Ne were tracked by a newly developed detector array [1] consisting of four large-area (7x4 cm^2), 0.3 mm thick silicon micro-strip detectors with a pitch of 0.1 mm. The detector performance is reported in [2]. The detectors were used to measure energy loss and position of hits corresponding to the ejection of two protons and a heavy-ion residue, allowing the reconstruction of all fragment trajectories, their reaction vertices, angular distributions of the reaction products or proton-proton (p-p) correlations. This required careful relative alignment of the detectors with the help of reconstructed tracks; the achieved accuracy was 100 μm for protons and 15 μm for ^{15}O or ^{18}Ne.

The reaction vertices were reconstructed with an RMS uncertainty of 0.2 mm along the beam direction. Fig. 1 shows the profile obtained by demanding triple p+p+^{15}O events that correspond to fragmentation of ^{17}Ne in the 11 mm thick secondary target. Events outside this area are due to a background caused by events with delta electrons which mock up protons and thus lead to false triple-coincidence events.

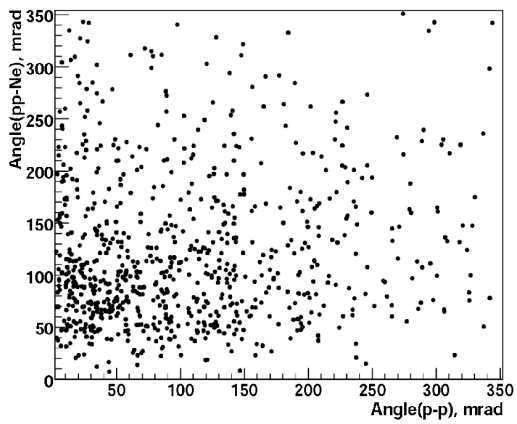

Figure 2: Proton-proton correlations observed for the ^{20}Mg→^{18}Ne+p+p reaction. The cluster of events at low p-p and intermediate pp-Ne relative angles reflects a strong p-p final-state interaction.

Fig. 2 displays the angular p-p correlations derived from the analysis of ^{20}Mg→^{18}Ne+p+p events. A strong p-p interaction corresponding to a 'di-proton' where two protons are emitted together with a relative orbital angular momentum of zero should manifest itself by small p-p and intermediate pp-Ne relative angles; the clustering of events in Fig. 2 indicates such an attraction. Similar behaviour is observed in the fragmentation ^{17}Ne→^{15}O+p+p which is in-line with the previous works [3,4].

References

[1] http://dpnc.unige.ch/ams/GSItracker/www.
[2] M. Stanoiu *et al*., contribution to this report.
[3] T. Zerguerras *et al*., Eur. Phys. J. A **20** (2004) 389.
[4] L.Grigorenko *et al*., Phys. Rev. C **71** (2005) 051604 .

* Work supported by EU, EURONS, contract No. 506065, and FPA-05958 (MEC, Spain).
#mukha@us.es

Fragment production in the spallation reaction of 500 *A* MeV ^{136}Xe with ^{1}H

L. Giot[1,], P. Napolitani[2], M. F. Ordonez[3], D. Henzlova[1,11], L. Audouin[2], J. Benlliure[3], A. Boudard[4], E. Casajeros[3], J. E. Ducret[4], T. Enqvist[5], A. Heinz[6], V. Henzl[1,11], A. Junghans[7], B. Jurado[8], A. Kelić[1],A. Krasa[11], T. Kurtukian[3], S. Leray[4], J. Pereira[3], R. Pleskač[1], F. Rejmund[9], M. V. Ricciardi[1], C. Schmitt[10], C. Stephan[2], K.-H. Schmidt[1], L. Tassan-Got[2], C. Villagrasa[4], C. Volant[4], A. Wagner[7] and O. Yordanov[1]*

[1] GSI, 64291 Darmstadt, Germany, [2] IPN Orsay, France, [3] Univ. of Santiago de Compostela, Spain, [4] DAPNIA/SPhN CEA/Saclay, France, [5] CUPP Project, Finland, [6] Yale University, USA, [7] FZ Dresden, Germany, [8] CENBG, France, [9] GANIL, France, [10] IPNL, France, [11] NPI, Czech Republic

[*] Present address: Subatech - Ecole des Mines, F-44307 Nantes-cedex 3, France

The complete understanding and modelling of proton-induced spallation reactions is a major goal both for fundamental research and technical applications. The spallation reactions have attracted interest to develop intense neutrons sources needed for accelerator-driven systems (ADS) for incineration of nuclear waste [1,2], material physics and biology [3] and also to produce high-intensity radioactive beams [4]. In addition, spallation reactions are a subject of interest in astrophysics to understand the origin of cosmic rays and their reactions with the hydrogen and helium nuclei in the interstellar medium [5]. All these perspectives have triggered a long-range research program [6] at GSI, devoted to reach a full comprehension of the proton and deuteron-induced spallation reactions by measurements of evaporation residues and fission fragments. To complete the study on the energy dependence of the spallation process, the spallation reactions of ^{136}Xe on protons at 500 *A* MeV and 1000 *A* MeV [7] were performed at GSI. The new data will help to develop improved models with better predictive power for spallation reactions involving nuclei spanning a wide mass range. In this paper, we will describe the experimental technique and the results obtained for the spallation of ^{136}Xe on protons at 500 *A* MeV.

Experiment and data analysis

The experiment was performed at the Fragment Separator (FRS) at GSI. Deflection of ions in the dipoles of the FRS, and the energy loss in two ionization chambers were used to identify in mass and atomic number every residue of the reaction. The achieved resolution in atomic number amount to $\Delta Z \approx 0.4$, and in mass $A/\Delta A \approx 400$. Moreover, high-precision information on the kinematical properties of each residue has also been obtained. Measured yields were corrected for the transmission losses, for the losses due to the secondary reactions in different layers of matter, and for the losses due to the dead-time of the data acquisition system. The production cross sections were obtained after normalizing these yields to the number of atoms in the liquid hydrogen target and to the number of impinging beam particles.

Results

The measured cross sections of the isotopes of the elements between Z = 33 and Z = 56 produced in the ^{136}Xe + ^{1}H spallation reaction at 500 *A* MeV are presented on Fig. 1 as a cluster plot on the chart of nuclides. The results of the experiments showed that the nuclide cross sections strongly decrease below Z = 40 and fall below the detection limit of the experimental set-up (~ 3 µb) for elements below Z = 33. The measurement covers a range in cross section of more than 4 orders of magnitude between 70mb and 3 µb. The single and double charge-pickup channels were also observed.

With data previously measured, these data will improve the present knowledge on spallation process, especially in its dependence on mass or on energy of the system.

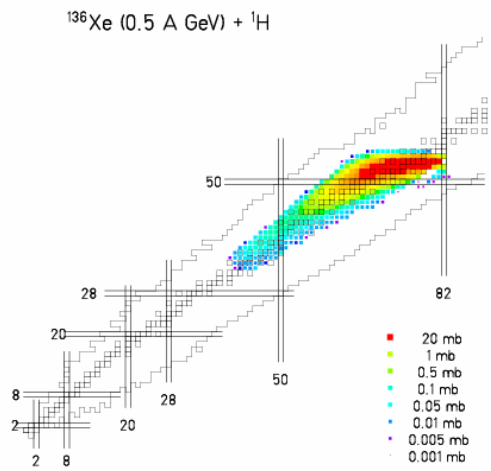

Fig. 1 Residual nuclide cross sections measured in the spallation reaction of ^{136}Xe + ^{1}H at 500 *A* MeV.

Acknowledgements

This work was financially supported by the FP6 European Community Programme (Contract No FI6W-516352).

References

[1] C. Bowman et al., Nucl. Instr. Meth. A320, 336 (1992)
[2] C. Rubbia et al., Report CERN/AT/95-44/(ET), 1995
[3] The ESS project, http://neutron.neutron-eu.net/n\ess/
[4] www.ganil.fr/eurisol/Final-Report.html.
[5] J. R. Arnold et al., J. Geophys. Res. 66 3519 (1961)
[6] http://www.gsi.de/charms/
[7] P. Napolitani et al, in preparation

Production of heavy neutron-rich nuclei "south" of lead

T. Kurtukian-Nieto[1], J. Benlliure[1], L. Audouin[2], B. Blank[3], F. Becker[4], E. Casarejos[1], D. Cortina[1], J. Giovinazzo[3], D. Henzlova[4], B. Jurado[4], M. F. Ordoñez[1], F. Rejmund[5], K.-H. Schmidt[4], O. Yordanov[4]

1 Universidade de Santiago de Compostela, E-15782 Santiago de Compostela, Spain, 2. Institut de Physique Nucléaire, F-91406 Orsay cedex, France, 3 Centre d'Etudes Nucléaires Bordeaux-Gradignan, F-33175 Gradignan, France, 4, Gesellschaft für Schwerionenforschung mbH, D-64291 Darmstadt, Germany, 5 Grand Accélérateur National d'ions Lourds, F-14000 Caen cedex, France

The properties of nuclei along the N = 126 neutron shell, "south" of lead are extremely interesting for the production of heavy elements in stellar nucleosynthesis through the r-process. Nuclei in this region have been produced using a 1 A GeV ^{208}Pb beam by cold projectile-fragmentation reactions in a beryllium target, where mostly protons are abraded from the projectile, while the excitation energy induced is low, partly even below the particle evaporation threshold. Neutron-rich projectile residues were analysed by the magnetic spectrometer FRS and identified in mass and atomic number, see Fig. 1.

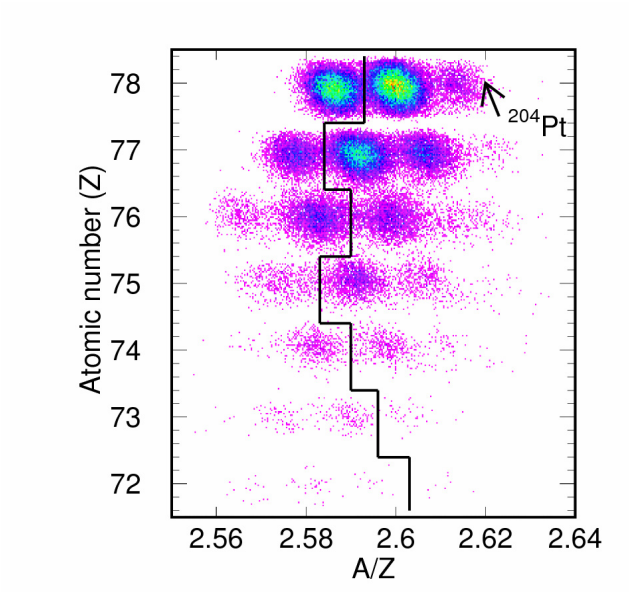

Figure 1: Identification matrix showing part of the most neutron.-rich nuclei produced in this experiment. The black lines represent the present limits of known nuclei.

The production cross sections of more than 190 neutron-rich isotopes of elements from lead down to ytterbium were measured with an uncertainty around 15%. 25 of those have been produced and identified for the first time.

Fig. 2 shows the isotopic distributions for some selected elements in comparison with different model calculations. The semi-empirical formula EPAX v.2 [1] in general fails in the description of the data; in particular the most neutron-rich nuclei are considerably overestimated. Much better agreement is found for the COFRA code [2], which is an analytical formulation of the abrasion-ablation model [3]. The good description of the data confirms that that reaction channels leading to the production of the most neutron-rich nuclei are due to large fluctuations in both the N/Z and the excitation energy of the pre-fragment.

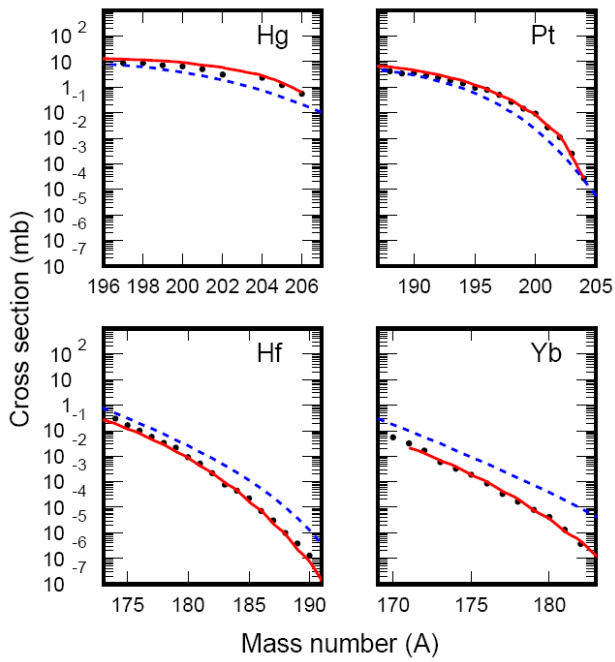

Figure 2: Isotopic production cross sections of some selected residual elements measured in this experiment compared to two model calculations, EPAX [1] (dahsed line) and COFRA [2] (solid line).

Our experiment has proven that cold fragmentation is a suitable reaction mechanism for the production of extremely neutron-rich nuclei, which are too heavy to be produced as fission fragments. This opens a way for investigating the properties of heavy nuclei close to the r-process path.

References

[1] K. Sümmerer and B. Blank, Phys. Rev. C 61 (2000) 034607.
[2] J. Benlliure et al.,Nucl. Phys. A 660 (1999) 87.
[3] J.-J. Gaimard and K.-H. Schmidt, Nucl. Phys. A 531 (1991) 709.

Study of the de-excitation channels in the reaction $^{56}Fe + p$ at 1 GeV per nucleon with the SPALADIN set-up at GSI *

J.-É. Ducret[1], É. Le Gentil[1], T. Aumann[2], C.-O. Bacri [3], J. Benlliure[4], M. Böhmer[5], A. Boudard[1], E. Casarejos[4], L. Donadille[1], M. Fernandez-Ordoñez[4], R. Gernhäuser[5], H. Johansson[2], A. Kelić[2], K. Kezzar[1,2], R. Krücken[5], T. Kurtukian-Nieto[4], A. Lafriakh[3], F. Lavaud[1], A. Le Fèvre[2], S. Leray[1], J. Lukasik[2], W.-F. J. Müller[2], P. Pawlowski[7], S. Pietri[1], F. Rejmund[6], C. Schwarz[2], C.Sfienti[2], H. Simon[2], W. Trautmann[2], C. Volant[1], and O. Yordanov[2]

[1]DAPNIA/SPhN, CEA-Saclay, France; [2]GSI, Darmstadt, Germany; [3]IPN, CNRS-IN2P3, Orsay, France; [4]University of Santiago de Compostela, Spain; [5]TU München, Garching, Germany; [6]GANIL, CEA/DSM & IN2P3-CNRS, Caen, France; [7]Institute of Nuclear Physics, Krakow, Poland

Spallation is the reaction of a light hadron with an atomic nucleus. As such, it can be seen as a way to study the de-excitation mechanism of a hot nucleus with small reaction effects like compression and high angular momentum. Its detailed understanding is also necessary for its different applications in astrophysics, spatial technology, medicine and the design of accelerator driven systems (ADS). Spallation reactions can be described in a two-step model, starting with an intranuclear cascade (INC) phase during which the incoming proton loses part of its initial kinetic energy in collisions with nucleons of the target. The INC leads to the formation of a hot system, the prefragment, whose decay is described by statistical models in a second step.

The SPALADIN collaboration [1] has measured the spallation reaction $^{56}Fe+p$ in inverse kinematics detecting in coincidence the charged fragments, both light and heavy, and the neutrons. Because of the inverse kinematics, most of the INC particles are not detected and low center-of-mass energy fragments are measured with full efficiency. The detection set-up was described in [2, 3]. It was based on the *ALADiN* magnet set-up of the Cave B of GSI (*TP MUSIC 4*, the *ToF* wall & *LAND*) with specific residue tracking detectors behind the liquid hydrogen target. To reduce the detection bias a low-selectivity trigger was used: A beam trigger and/or one neutron in *LAND*.

The analysis of the 1 GeV per nucleon data has been completed [3] and the comparison with reaction models is being performed. The results in Fig. 1 show the contributions of the different identified final states to the production cross-sections of elements characterized by their charge Z. The data (graph on the bottom-right) and the curves in the other plots of this figure) point to the importance of asymmetric splittings of the prefragment for the production of fragments with $Z \leq 10$. This explains why GEMINI [4] coupled with INCL4 [5] provides a better description of the data than the two other de-excitation codes SMM [6], & GEM [7] combined with INCL4. Other observables of the experiment are presently investigated. As shown on Fig. 1 above $Z \geq 10$, events are mainly one-residue events.

* Work supported by the European Union under contract RII3-CT-2004-506065

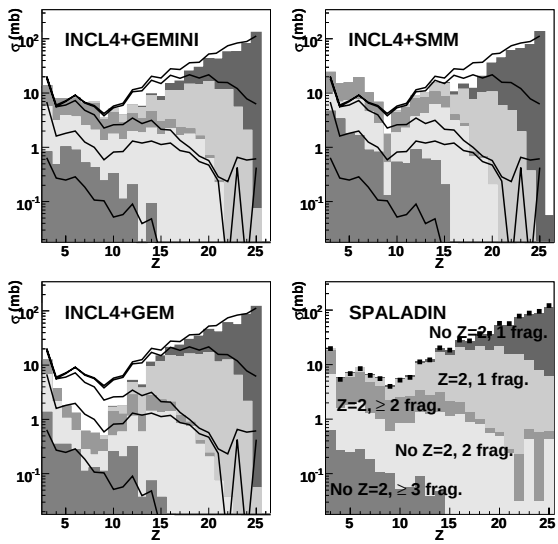

Figure 1: Contributions of the different final states to the element production cross-sections, calculated with the GEMINI, SMM and GEM (histograms), coupled to INCL4, are compared to the experimental data given by the solid lines and by the plots of the bottom-right graph.

The experiment on the system $^{56}Fe+p$ will be followed with almost the same set-up, but in Cave C, by two others, recommended by the EA of GSI: *S293* and *S304*. *S293* will be a study of the fission channels in the spallation of heavy nuclei; *S304* will allow to study the evolution of the prefragment decay with its size and excitation energy.

References

[1] J.-É. Ducret *et al.*, Proposal S248, GSI-EA (2000)

[2] J.-É. Ducret *et al.*, GSI Scientific Report 2003, p. 45

[3] É. Le Gentil, Doctorate Thesis, Uni. Evry, France (2006)

[4] R.J. Charity *et al.*, Nucl. Phys. **A483**, 371 (1988)

[5] A. Boudard *et al.*, Phys. Rev. **C66**, 044615 (2002)

[6] J.P. Bondorf *et al.*, Phys. Rep. **257**, 133 (1995)

[7] S. Furihata *et al.*, Nucl. Instr. Methods **171**, 251 (2000)

Experiment on Fission Transients in Highly Fissile Spherical Nuclei produced by Fragmentation of Radioactive Beams

C. Schmitt[1,#], P. Nadtochy[1], A. Heinz[2], B. Jurado[1], A. Kelić[1] and K.-H. Schmidt[1]
[1]GSI, Darmstadt, Germany; [2]Yale University, CT 06520, U.S.A.

While transferring energy between the collective and intrinsic degrees of freedom of the system, viscosity intricately influences nuclear dynamics. Fission of highly excited spherical nuclei provides optimal conditions for probing this dissipation phenomenon. In nuclei, when the system is initially well-localized around its spherical ground-state minimum, any shape evolution is exclusively initiated by dissipative forces. A finite time, referred as the transient time τ_{trans}, is then required for populating the states at the fission barrier [1]. Information on the strength β of nuclear viscosity *at small deformation* can be directly inferred from τ_{trans}. Most direct probes of fission times are pre-scission multiplicities of light particles and γ-rays as they can be associated with a clock (see [2] and therein). Yet, they give access to the *total* reaction time encompassing, in addition to τ_{trans}, the compound nucleus formation time, the statistical decay time and the saddle-to-scission time. Hence, experiment is not able to isolate the various stages of the process, and the analysis relies on the interplay of complex influences caused by the poorly known dependences of dissipation on deformation, temperature, angular momentum and fissility. This difficulty explains the still vivid debate on both the origin and magnitude of nuclear viscosity. We presently report on the *first* realization of experimental conditions which are ideal for isolating the early τ_{trans} contribution. Highly fissile nuclei characterized by well-defined initial conditions - in excitation energy, angular momentum and deformation - have been produced by fragmentation of radioactive beams. In addition, the width of the fission-fragment charge distribution σ_Z, which is sensitive to the limited region inside the fission saddle [3], has been accurately measured, yielding a chronometer at the saddle.

The above ideal scenario was successfully realized by an intense experimental effort invested at GSI [4]. Fragmentation of a primary stable ^{238}U beam at 1 *A* GeV in a beryllium target produces a large variety of nuclei among which 45 radioactive highly fissile spherical astatine up to thorium isotopes. The latter, separated and identified with the Fragment Separator, acted as secondary relativistic beams. Fragmentation of these projectiles in a secondary lead target yields pre-fragments with high excitation energies [5], small angular momenta [6] and still nearly spherical shapes [7]. The pre-fragment finally de-excites by a competition between fission and evaporation. Both fission fragments were detected simultaneously and accurately identified in atomic number thanks to the use of a double-ionisation chamber ($\Delta Z_{1,2}$ = 0.4 for FWHM).

The measurement of the sum Z_1+Z_2 of the charges of the two fragments allows judiciously classifying the data, since Z_1+Z_2 is correlated to the initial excitation energy E_{prf} of the pre-fragment [3] – the lower the Z_1+Z_2, the higher the E_{prf}. In Fig. 1. the experimental σ_Z is seen to increase with decreasing Z_1+Z_2, i.e. increasing temperature. To investigate the slope of this rise, we use the reaction code ABRABLA which reliability has been widely assessed for the present purpose [8]. As seen in Fig. 1. a good agreement is achieved with β=(4.5±0.5)·10^{21}s^{-1} independent on Z_1+Z_2 i.e. independent on E_{prf} [9]. That corresponds to a transient time of $<\tau_{trans}>$ = (3.3±0.7)·10^{-21}s. Also displayed, are the predictions of Bohr-and-Wheeler transition state model [10] and Kramers diffusion picture [11]: Both overestimate the experimental σ_Z due to the absence of the transient delay.

The control of the initial conditions achieved in our experiment constitutes a step further as compared to previous works, and the result points out the *undeniable* manifestation of transient effects at high excitation energy. The magnitude extracted for the dissipation strength at small deformation is an information of importance for our microscopic understanding of nuclear viscosity.

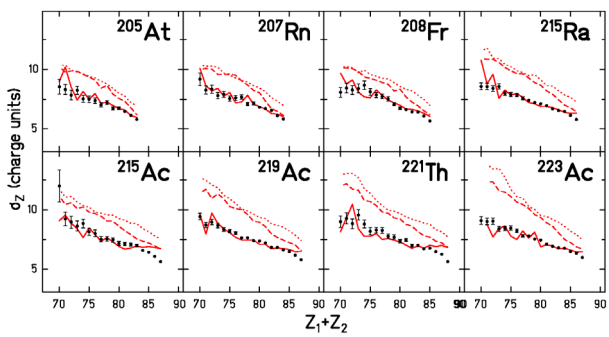

Figure 1: Width σ_Z as a function of Z_1+Z_2 for a sample of spherical beams as indicated. The data (dots) are compared with Bohr-and-Wheeler- (dotted lines), Kramers- (dashed lines) and ABRABLA $\Gamma_f(t)$- (full lines) predictions. In the two latter cases, β is set to 4.5·10^{21}s^{-1}.

References

[1] K.H. Bhatt et al., Phys. Rev. C33 (1986) 954.
[2] P. Paul et al., Ann. Rev. Nucl. Part. Sci.44 (1994) 45.
[3] B. Jurado et al., Nucl. Phys. A757 (2005) 329.
[4] K.-H. Schmidt et al., Nucl. Phys. A665 (2000) 221.
[5] K.-H. Schmidt et al., Phys. Lett. B300 (1993) 313.
[6] M. de Jong et al., Nucl. Phys. A613 (1997) 435.
[7] P.N. Nadtochy, in preparation.
[8] www w2k.gsi.de/charms/Publications/publica.htm.
[9] C. Schmitt et al., to be submitted to PRL.
[10] N. Bohr et al., Phys. Rev. 56, 1939, p. 426.
[11] H.A. Kramers, Physica VII 4 , 1940, p. 284.

The HypHI project at GSI and FAIR: Hypernuclear Spectroscopy with Stable Heavy Ion Beams and Rare-Isotope Beams *

T.R. Saito† [1,2], M. Kavatsyuk[1,3], O. Lepyoshkina[1,2], S. Minami[1,2,4], C. Rappold[1,5], P. Achenbach[2], S. Ajimura[4], T. Fukuda[6], J. Hoffmann[1], N. Kurz[1], Y. Mizoi[6], T. Nagae[7,8], D. Nakajima[7,8], J. Pochodzalla[2], A. Sakaguchi[4], and the HypHI collaboration

[1]GSI, Darmstadt, Germany; [2]IKPH, Joh. Gutenberg-Universität, Mainz, Germany; [3]Univ. Kyiv, Kiev, Ukraine; [4]Osaka Univ., Osaka, Japan; [5]Univ. Louis Pasteur, Strasbourg, France; [6]Osaka Elect.-Comm. University, Neyagawa, Japan; [7]KEK, Tsukuba, Japan; [8]Univ. Tokyo, Tokyo, Japan

The HypHI project aims to perform hypernuclear spectroscopy with stable heavy ion beams and rare-isotope beams at GSI and FAIR [1, 2]. With heavy ion beams impinged on stable target materials, hypernuclei can be produced as projectile fragments with a coalescence of hyperon(s) produced in the participant region of the collision [3, 4]. Since the velocity of produced hypernuclei is as large as the one of projectiles, hypernuclei can live longer in the laboratory system by the Lorentz factor. At 2 A GeV the mean-life of hypernuclei (typically about 200 ps at rest) will be approximately three times longer than at rest, therefore, the decay of hypernuclei takes place well behind the target. At 20 A GeV, hypernuclei mean-life is longer as 20 ns, therefore, separation of hypernuclei with magnetic spectrometer could be feasible. With heavy ion induced reactions, produced hypernuclei can be distributed from neutron- to proton-drip lines, therefore, studies of hypernuclei at extreme isospins will be reachable. At 20 A GeV, direct measurements of hypernuclear magnetic moments will be feasible by measuring perturbed asymmetry of π^- emission from the hypernuclear decay.

The project is divided in four phases [1]. The first Phase 0 experiment at GSI aims to prove the principle of the project with an invariant mass method for ${}^{3}_{\Lambda}$H, ${}^{4}_{\Lambda}$H and ${}^{5}_{\Lambda}$He hypernuclei with a ^{6}Li beam at 2 A GeV on a carbon target [5]. Phase 1 at GSI will study proton rich hypernuclei. The Phase 2 and 3 experiments suggest to be taken place at FAIR. Phase 2 for neutron rich hypernuclei is planned with R3B, and a hypernuclear separator with heavy ion beams at 20 A GeV is planned to be developed in Phase 3 for measurements of hypernuclear magnetic moments.

The HypHI collaboration is currently working on the Phase 0 experiment which is planned in 2008 in cave C with the ALADiN dipole magnet. A carbon target will be placed in front of the ALADiN magnet with a distance of 2.35 m from the magnet center. In front of the target, there is a polycrystalline diamond detector as a start counter of Time-Of-Flight (TOF) measurements. Between the target and the ALADiN magnet, there will be three arrays of scintillating fiber detectors with two-dimensional position sensitivity. The array located right behind the target measures the position of the primary vertex and energy deposition of particles from the target. Two other arrays measure secondary decay vertexes of emitted particles from Λ-hyperons and hypernuclei behind the target. Developments of these fiber detectors are discussed in these Scientific Reports by ref. [6]. Behind the ALADiN magnet, there are two TOF walls. Negatively charged pions are measured by the exiting ALADiN TOF wall, and positive charged particles are measured by a newly developed TOF wall refereed as TOF+. Details on TOF+ is discussed in these Scientific Reports by ref. [7]. The trigger system consists of three levels, with tracking trigger by fiber detectors for secondary decay vertexes, π^- trigger by the ALADiN TOF wall and $Z = 2$ particle trigger by TOF+ [2]. A total trigger efficiency of 7 % is observed by Monte Carlo simulations, discussed in these Scientific Reports by ref. [8]. The expected performance in the Phase 0 experiment has been investigated by means of Monte Carlo simulations for ${}^{4}_{\Lambda}$H, and a clear invariant mass peak on the background with a resolution of approximately 3 MeV in σ has been observed. Details of simulations are also discussed in these Scientific Reports by ref. [8]. In addition to these detectors described above, a K^+ detector in the ALADiN magnet and three layers of drift chambers will be employed. Monte Carlo simulations including all the detectors are still in progress.

References

[1] A Letter Of Intent of the HypHI project, the HypHI collaboration, submitted to GSI PAC EA30 as LOI40.

[2] T.R. Saito *et al.*, proceedings of HYP2006, October 2006, Mainz, to be published in Eur. Phys. J.

[3] S. Avramenko, *et al.*, Nucl. Phys. **A547** (1992) 95c.

[4] M. Wakai, H. Bando and M. Sano, Phys. Rev. **C38** (1988) 748.

[5] A proposal of the HypHI Phase 0 experiment, the HypHI collaboration, submitted to GSI PAC EA33 with a realization as S319.

[6] O. Lepyoshkina *et al.*, and the HypHI collaboration, in these Scientific Reports.

[7] C. Rappold *et al.*, and the HypHI collaboration, in these Scientific Reports.

[8] S. Minami *et al.*, and the HypHI collaboration, in these Scientific Reports.

* The HypHI project is granted by the Helmholtz Association and GSI as Helmholtz-University Young Investigators Group VH-NG-239 with Mainz University

† t.saito@gsi.de

Study of hypernuclei with heavy Ion beams (HypHI) :Experimental design with Monte Carlo simulation *

S. Minami† [1,2,3], M. Kavatsyuk[2,4], O. Lepyoshkina[1,2], C. Rappold[2,5], T.R. Saito[2], P. Achenbach[1], S. Ajimura[3], T. Fukuda[6], Y. Mizoi[6], J. Pochodzalla[1], A. Sakaguchi[3], and the HypHI collaboration*

[1]Johannes Gutenberg-Universität, Mainz, Germany; [2]GSI, Darmstadt, Germany; [3]Osaka University, Toyonaka, Japan; [4]Taras Shevchenko National University of Kyiv, Kyiv, Ukraine; [5]Universite Louis Pasteur Strasbourg, Strasbourg, France; [6]Osaka Electro-Communication University, Neyagawa, Japan

The HypHI project aims to study exotic hypernuclei produced as projectile fragments by heavy ion collisions [1]. In the initial phase (phase-0), a feasibility will be demonstrated by identifying mesonic decays of the lightest hypernuclei, ${}^{3}_{\Lambda}\mathrm{H} \rightarrow {}^{3}\mathrm{He} + \pi^-$, ${}^{4}_{\Lambda}\mathrm{H} \rightarrow {}^{4}\mathrm{He} + \pi^-$ and ${}^{5}_{\Lambda}\mathrm{He} \rightarrow {}^{4}\mathrm{He} + \mathrm{p} + \pi^-$ [2]. The experimental design of the phase-0 has been studied with the help of Monte Carlo (MC) simulations and the results are summarized in this report.

The detector system has been designed to track decay products of hypernuclei produced as projectile fragments by collisions of a ^{6}Li beam of 2 *A* GeV and a ^{12}C target. Figure 1 shows the detector setup which consists of 3 layers of scintillating fiber detectors, TR0, TR1 and TR2, to measure trajectories and decay vertices, TOF-start and TOF-walls to give velocity, energy deposit and position information, and the ALADiN dipole magnet to analyze momentum [3]. Hadronic reactions at the target were simulated with the ultrarelativistic quantum molecular dynamics model (UrQMD) [4], and nuclei in projectile fragments were formed by binding nucleons with projectile rapidity. Geant4 was used to simulate reactions of outgoing particles from the target through the detector system.

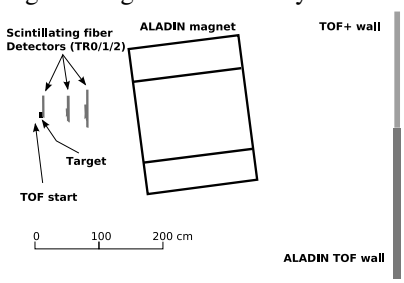

Figure 1: The detector setup for the phase-0 experiment.

Detailed MC simulations in the case of ${}^{4}_{\Lambda}\mathrm{H}$ have been performed, and resulting momentum resolutions of decayed particles are 320 MeV/c in σ for α and 8.2 MeV/c for π^-. The spatial resolution of decay vertices, which is very crucial to reduce background, was found to be 5 mm in σ along the beam axis, and 0.3 mm along axes perpendicular to the beam. Background processes and events with ${}^{4}_{\Lambda}\mathrm{H}$ are simulated separately and normalized assuming a production cross section of ${}^{4}_{\Lambda}\mathrm{H}$ is 0.1 μb [5]. The reconstructed invariant mass spectrum is shown in Figure 2, in which a clear peak whose width is 3.0 MeV/c^2 in σ can be observed on top of broad background. It is planned to use a beam intensity of 10^7 particles per second and a target thickness of 8 g/cm^2, which will give a few thousand reconstructed ${}^{4}_{\Lambda}\mathrm{H}$ per week according to the MC simulation. The estimated yield is high enough to study production cross sections and to demonstrate the feasibility of the project.

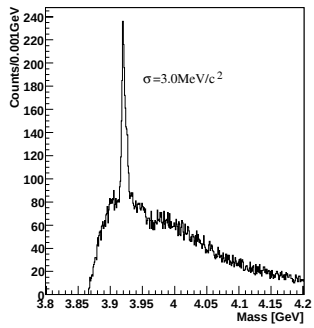

Figure 2: The invariant mass spectrum for ${}^{4}_{\Lambda}\mathrm{H}$.

An efficient trigger system is essential because of an expected high reaction rate. The trigger system was designed to select events with decay vertices in a decay volume located between TR0 and TR1, which can be achieved by requesting special hit patterns on TR0, TR1 and TR2. The decay modes of interest contain α and π^- in the final state, therefore the trigger was designed to request at least one hit with large energy deposit by α at the positive side of the TOF-wall and at least one hit at the negative side. The MC simulation shows that the efficiency to select ${}^{4}_{\Lambda}\mathrm{H}$ is 7.0% with the trigger algorithm. The trigger rate of 340 Hz was obtained which fulfills the constraint given by the DAQ.

References

[1] T.R. Saito *et al.*, proceedings of HYP2006, October 2006, Mainz, to be published in Eur. Phys. J.

[2] The HypHI collaboration, A proposal of the HypHI Phase 0 experiment, submitted to GSI PAC EA33 with a realization as S319.

[3] O. Lepyoshkina *et al.* and the HypHI collaboration, in these Scientific Reports. ; C. Rappold *et al.* and the HypHI collaboration, in these Scientific Reports.

[4] M. Bleicher, *et al.*, J. Phys. G **25** (1999) 1859.

[5] S. Avramenko, *et al.*, Nucl. Phys. **A547** (1992) 95c. ; M. Wakai, H. Bando and M. Sano, Phys. Rev. **C38** (1988) 748.

* The HypHI project is supported by the Helmholtz Association and GSI as Helmholtz-University Young Investigators Group VH-NG-239 with Mainz University

† s.minami@gsi.de

Stopping High-Energy Ions in Cryogenic Helium Gas*

S. Purushothaman[1], P. Dendooven[1,*], I. Moore[2], H. Penttilä[2], J. Ronkainen[2], A. Saastamoinen[2], J. Äystö[2], N. Takahashi[3], K. Gloos[4], C. Scheidenberger[5]

[1]KVI, University of Groningen, The Netherlands; [2]Department of Physics, University of Jyväskylä, Finland; [3]Osaka Gakuin University, Japan; [4]Department of Physics, University of Turku, Finland; [5]GSI, Darmstadt, Germany.

A variety of scientific disciplines makes use of radioactive isotopes in the form of a low-energy ion beam or an ion or atom cloud in a trap. As in-flight radioactive ion beam facilities produce and select isotopes at high energy, ion catcher techniques to transform high-energy ions into low-energy ones are essential. The extremely high ion energies at planned facilities causes technical as well as principle problems for the standard ion catcher technique using noble gases at room temperature.

We are investigating the use of cryogenic noble gases as stopping media. The feasibility of the cryogenic approach was demonstrated earlier using alpha-decay recoil ions from a ^{223}Ra source [1]. More recently, we investigated the effect of ionisation of the helium gas, as this determines the maximum beam intensity the system can handle. A 13 MeV proton beam from the cyclotron at the University of Jyväskylä, Finland, was used to ionise the helium gas just above the ^{223}Ra source (figure 1). The combined efficiency of survival and transport over several centimetres of the recoil ions was measured as a function of ionisation density (i.e. beam intensity), electric field strength, and helium pressure and temperature.

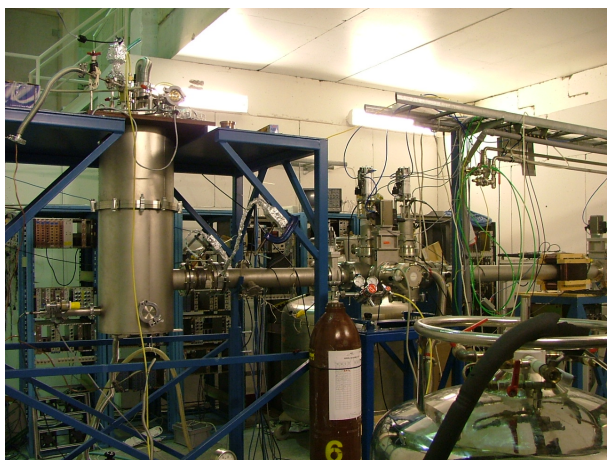

Figure 1: Cryostat coupled to a beam line at the Accelerator Laboratory of the University of Jyväskylä.

Figure 2 compares part of our results to the efficiency of extracting ions as a low-energy beam for a variety of room-temperature systems. At low ionisation density, the efficiency saturates to a maximum of a few 10s of percent. The saturation efficiency we obtained (30%) is the same as in the earlier experiment without ionising beam [1]. The extreme purity of cryogenic noble gases allows to conclude that the maximum efficiency is determined by the cross section of the relevant charge exchange reactions during slowing down of the ions in the stopping gas.

Our results demonstrate the importance of a high electric field to quickly pull ions and electrons apart and as such reduce the neutralisation probability. Part of the different behaviour of the room-temperature systems may be related to space-charge limitations in the extraction of ions through a small hole; an issue not relevant for our results as we do not extract ions from the stopping gas.

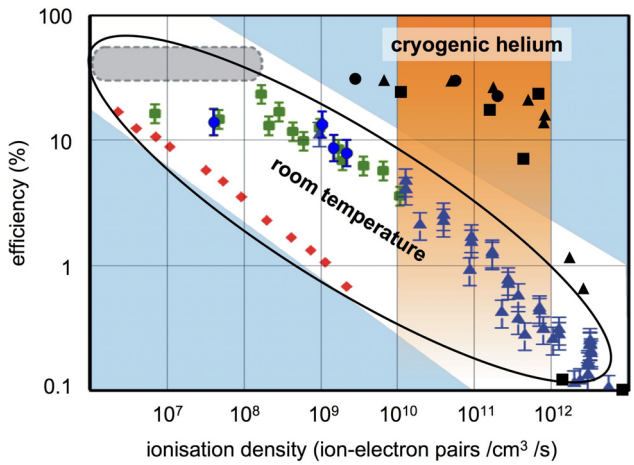

Figure 2: Survival and transport efficiency at low temperature, high density (circles: 77 K, 0.18 mg/cm^3, triangles: 10 K, 0.18 mg/cm^3, squares: 10 K, 0.54 mg/cm^3) and high electric field (160 V/cm) compared to a compilation [4] of extraction efficiencies from systems at room temperature, lower density (0.02-0.10 mg/cm^3) and smaller electric field (10-25 V/cm).

We have shown that cryogenic helium at high density and high electric field is a promising medium for the transformation of very high-energy ions into low-energy ones. It has the advantage of very high gas purity and small size. Next, a cryogenic gas catcher in which high-energy heavy ions will be stopped and extracted as a low-energy beam will be designed and tested. In connection with FAIR, we also plan to further develop the use of superfluid helium as ion catcher stopping medium [2,3].

References

[1] P. Dendooven et al., Nucl. Instrum. Meth. A 558 (2006) 580.
[2] W.X. Huang et al., Europhys. Lett. 63 (2003) 687
[3] P. Dendooven et al., AIP Conference Proceedings 831 (2006) 439.
[4] D. Morrissey at al., RNB-7 Proceedings, to be published in Eur. Phys. J. A.

* dendooven@kvi.nl

Nuclear Structure within the Fermionic Molecular Dynamics Approach

T. Neff[1,2], S. Bacca[1], and H. Feldmeier[1]
[1]GSI, Darmstadt, Germany; [2]NSCL, Michigan State University, 48823 East Lansing, MI, USA

The Fermionic Molecular Dynamics (FMD) model has been used successfully for the description of light nuclei in the p- and sd-shell. One important feature is the versatility of the Gaussian single-particle basis that allows to include shell effects as well as clustering and halos.

Hoyle-State

Recently we used the FMD model to study the conjecture that the first excited 0^+ state in ^{12}C (Hoyle state) forms a dilute self-bound gas of α-clusters [1]. The Hoyle state plays a prominent role as a prototype for α-cluster states. Even the most recent no-core shell model calculations fail to describe these states due to insufficient model space sizes. While cluster models have been used for the description of the Hoyle state for a long time [2], they rely on very simple effective interactions and fail to provide a consistent picture with the low lying states.

In our calculation we use the FMD model with an effective nucleon-nucleon force derived from the realistic Argonne V18 interaction by means of the Unitary Correlation Operator Method. A phenomenological two-body correction term is added to account for missing three-body forces. We diagonalize the Hamiltonian in a basis of 42 FMD configurations obtained by Variation after Projection on angular momentum 0^+ with constraints on radii and intrinsic quadrupole deformation and 165 explicit α-cluster configurations. These α-cluster configurations cover the model space of the microscopic α-cluster model. For the ground state we find an overlap of 0.52 with the α-cluster space. This illustrates the importance of shell model like configurations where the α's are broken by the spin-orbit force. The Hoyle state has a much more pronounced α-structure with an overlap of 0.85. To test our wave functions we calculate the densities and form factors for the FMD and also for a microscopic α-cluster model and compare with electron-scattering data in Fig. 1. The FMD results confirm the interpretation of the Hoyle-state as a dilute gas of α-clusters as proposed by the pure α-cluster models.

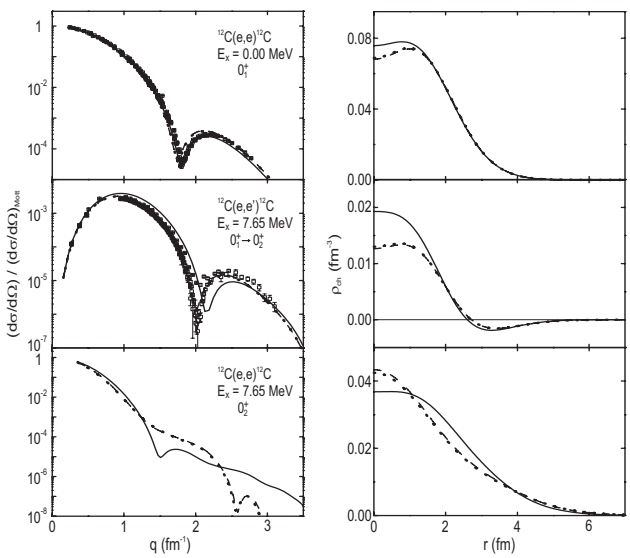

Figure 1: Measured and calculated (FMD solid lines, α-cluster dashed lines) electron scattering cross sections in ^{12}C for the ground state, the transition from the ground into the Hoyle and for the Hoyle state (left). Corresponding charge densities (right).

Isospin degree of freedom

As one of the new developments in FMD the isospin orientations of the nucleons are treated as variational parameters. This allows for intrinsic correlations among spatial, spin, and isospin degrees of freedom, which are mainly induced by the exchange of the pseudoscalar isovector pion. While the short-range part of the tensor correlations is treated explicitly with the Unitary Correlation Operator Method the long-range tensor correlations are incorporated by an intrinsic many-body state which breaks parity and charge number. In the calculation the variation of the single-particle degrees of freedom is done after restoring the symmetries by projecting on parity, total spin and charge number. The non-vanishing spin- and isospin vector-densities of the intrinsic state (see Fig. 2) illustrate the presence of the virtual pion field.

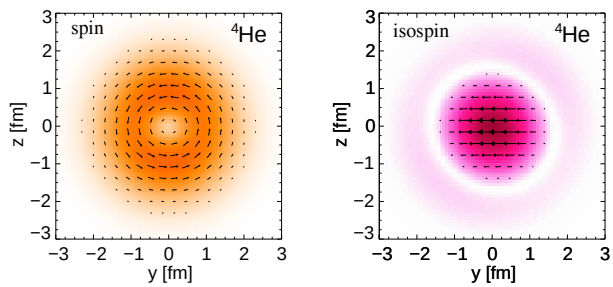

Figure 2: Spin- and isospin-density in ^{4}He. Arrows denote projections on the yz-plane while colour coding is according to absolute values.

References

[1] M. Chernykh, H. Feldmeier, T. Neff, P. von Neumann-Cosel, and A. Richter, Phys. Rev. Lett. **98**, 032501 (2007) .

[2] M. Kamimura, Nuc. Phys. **A351**, 456 (1981) .

Benchmarking V_{UCOM} in the No-Core Shell Model *

R. Roth[1] and P. Navrátil[2]

[1]Institut für Kernphysik, TU Darmstadt, Germany; [2]LLNL, Livermore, CA 94551, USA

One of the prime goals of modern nuclear theory is the description of low-energy nuclear structure on the basis of QCD-motivated realistic nucleon-nucleon interactions. For p-shell nuclei this can be achieved, e.g., within the ab initio no-core shell model (NCSM), which provides an essentially exact solution of the quantum many-body problem [1]. However, to cover the nuclear chart beyond the p-shell one has to resort to approximate many-body schemes. In contrast to the NCSM, those approaches cannot describe the strong short-range correlations induced by realistic interactions and, therefore, rely on effective interactions.

One scheme to derive a universal phase-shift equivalent effective interaction is the unitary correlation operator method (UCOM) [2]. The short-range central and tensor correlations are described explicitly by a system-independent unitary transformation. The unitary transformation of the Hamiltonian defines the correlated interaction V_{UCOM}. Unlike the bare NN potential, the Argonne V18 potential in our case, the correlated interaction has two important properties: (i) It is a soft interaction, which does not induce strong short-range correlations anymore. In the language of the shell-model the matrix elements of the interaction are pre-diagonalized and lead to a rapid convergence with increasing model-space size. (ii) The size of the net three-body interaction, which is the sum of the bare three-body interaction and the repulsive three-body terms induced by the unitary transformation, can be controlled via the range of the tensor correlation operator. In particular one can choose the correlation operator such that the net contribution of the total three-body interaction to the energy is minimal. This was done in NCSM calculations for three- and four-body systems [2]. Heavier nuclei have been studied using this V_{UCOM} in Hartree-Fock-based approaches employing perturbation theory or RPA ring summations to include long-range correlations [3].

Here we employ the ab initio NCSM to obtain detailed spectroscopic information for p-shell nuclei based on V_{UCOM}. In order to enhance convergence further, the Lee-Suzuki transformation has been used. All calculations have been performed using the ANTOINE code [4].

Figure 1 depicts the spectra of ^{6}Li and ^{10}B obtained with V_{UCOM} for different model-space sizes ranging from $0\hbar\omega$ to $14\hbar\omega$ and $8\hbar\omega$, respectively. The right-hand column represents the experimental spectrum. For both cases, the spectra are very stable w.r.t. model-space size and oscillator frequency and in good agreement with experiment. Also the absolute ground state energy agrees well with experiment. This result is remarkable given that we use a pure two-nucleon interaction, V_{UCOM}, for these calculations. For all bare realistic NN interactions it is known that neither the ground-state energy nor the structure of the spectrum are reproduced without including a three-nucleon interaction. One example is the ground state spin of ^{10}B which is wrongly predicted to be 1^+ when omitting the three-body interaction [5]. The correlated interaction V_{UCOM} reproduces these subtle phenomena already on the two-body level through its momentum dependence. This demonstrates that the UCOM transformation provides a powerful and practical way to reduce the impact of the three-body potential by transforming it into a momentum dependence.

* Supported by DFG through SFB 634. This work was partly performed under the auspices of the U. S. Department of Energy by the University of California, Lawrence Livermore National Laboratory under contract No. W-7405-Eng-48.

References

[1] P. Navrátil et al.; Phys. Rev. Lett. 84, 5728 (2000); Phys. Rev. C 68, 034305 (2003).

[2] R. Roth et al.; Phys. Rev. C 72, 034002 (2005).

[3] R. Roth et al.; Phys. Rev. C 73, 044312 (2006); C. Barbieri et al.; arXiv: nucl-th/0608011.

[4] E. Caurier, F. Nowacki; Acta Phys. Polonica 30, 705 (1999).

[5] P. Navrátil et al.; arXiv: nucl-th/0701038.

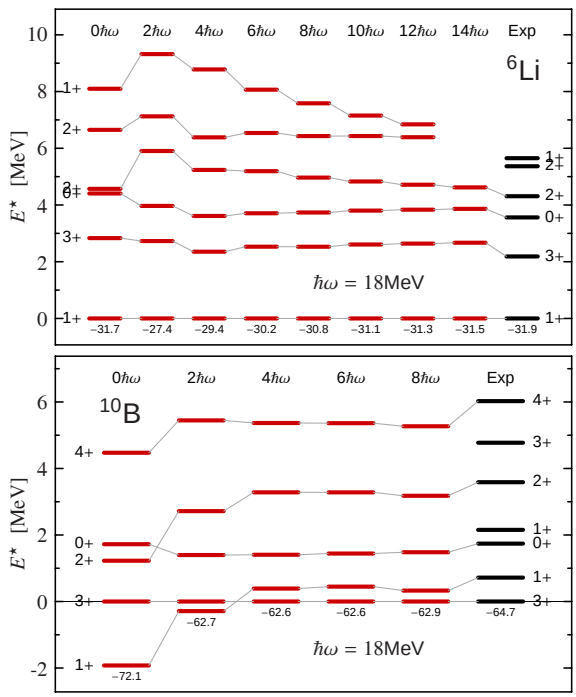

Figure 1: Spectrum of ^{6}Li (top) and ^{10}B (bottom) obtained within the NCSM for different model-space sizes using V_{UCOM}. The absolute ground state energies in [MeV] are given at the bottom.

Phenomenological Three-Body Interactions in the UCOM Framework *

A. Zapp, H. Hergert, P. Papakonstantinou, and R. Roth
Institut für Kernphysik, Technische Universität Darmstadt, Germany

In the Unitary Correlation Operator Method (UCOM) the short-range central and tensor correlations induced by the nuclear interaction are treated explicitly by a unitary transformation. This method is employed to transform the Argonne V18 potential into a phase-shift equivalent correlated interaction V_{UCOM} which is used for the following calculations [1].

Previous investigations of ground states and collective excitations based on the two-body interaction V_{UCOM} revealed systematic deviations of different observables for heavier nuclei. Figure 1 shows the binding energies per nucleon (upper part) and charge radii (lower part) of closed-shell nuclei obtained in a Hartree-Fock (HF) calculation using V_{UCOM} (disks). The range of the tensor correlator was fixed in few-body calculations ($I_\vartheta = 0.09$ fm^3) [1]. The HF approximation underestimates the binding energies, since long-range correlations cannot be described. Their inclusion within many-body perturbation theory leads to a good agreement of the binding energies with experiment [2]. Furthermore, the charge radii are clearly too small for heavier nuclei and the inclusion of long-range correlations via perturbation theory does not lead to a substantial improvement. Besides ground-state properties, collective excitations were investigated within the Random Phase Approximation (RPA) [3] using V_{UCOM}. An example is shown in Figure 2, where the response function of the isoscalar quadrupole resonance of ^{90}Zr is displayed. The solid line represents the results with the two-body interaction V_{UCOM}. The strength is concentrated at energies which are too high compared to experiment.

* Supported by DFG through SFB 634.

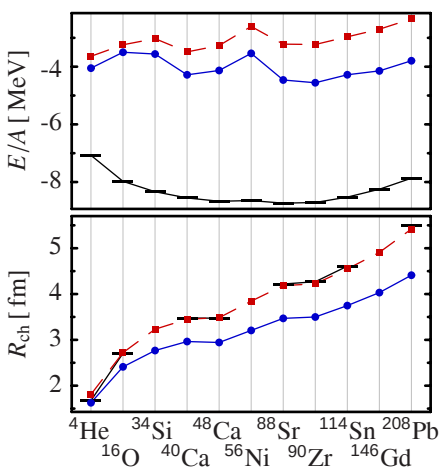

Figure 1: Binding energies and charge radii of selected closed-shell nuclei resulting from HF calculations with a two-body interaction (disks) and a two- plus three-body interaction (square symbols). The bars indicate the experimental values.

Here we study the impact of a simple three-body interaction on the radii and strength distributions. As a first ansatz, the correlated two-body interaction is supplemented by a three-body contact interaction with a strength parameter C_3. The three-body matrix elements are calculated in the harmonic-oscillator basis and included in our HF and RPA codes [4]. Using a long-range tensor correlator ($I_\vartheta = 0.20$ fm^3) in conjunction with a repulsive three-body interaction ($C_3 = 2500$ MeVfm^6) in HF leads to the binding energies and radii depicted by the square symbols in Fig. 1. Obviously the charge radii are now in good agreement with experiment. Again, the binding energies are underestimated on the HF level – it is expected that many-body perturbation theory would lead to an agreement with experiment. The collective response obtained in an RPA calculation including the three-body interaction (dashed line in Fig. 2) is shifted towards lower energies improving the agreement with experiment – further improvement can be achieved by increasing the single-particle space.

In summary, the inclusion of a simple repulsive three-body interaction seems to cure the discrepancies observed with the two-body interaction V_{UCOM} for heavier nuclei. As a next step we will use a finite-range three-body force, which then allows systematic calculations beyond Hartree-Fock, in order to provide a quantitative description of ground states and collective excitations.

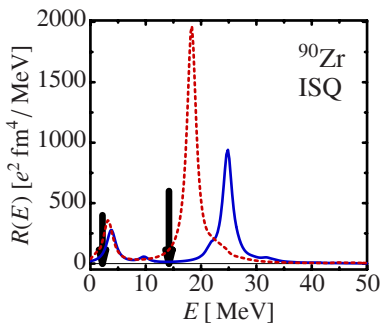

Figure 2: Isoscalar quadrupole resonance of ^{90}Zr resulting from RPA calculations with a two-body interaction (solid line) and a two- plus three-body interaction (dashed line). The arrows indicate the experimental centroids.

References

[1] R. Roth et al., *Phys. Rev.* **C 72**, 034002 (2005).
[2] R. Roth et al., *Phys. Rev.* **C 73**, 044312 (2006).
[3] N. Paar et al., *Phys. Rev.* **C 74**, 014318 (2006).
[4] A. Zapp, diploma thesis, TU Darmstadt, 2006.

Photodisintegration of light nuclei with the V_{UCOM} potential.

S. Bacca (GSI, Darmstadt, Germany)

An exact calculation of the photodisintegration cross section of ^{3}He and ^{4}He is performed using as interaction the correlated Argonne V18 potential, constructed within the Unitary Correlation Operator Method (V_{UCOM}) [1]. Calculations are carried out making use of the Lorentz Integral Transform technique [2] in conjunction with an hyperspherical harmonics basis expansion. The purpose is to perform for the first time a test of the V_{UCOM} potential in a continuum reaction, where many disintegration channels are open, and simultaneously to study the capability of describing electromagnetic reactions via a non-local two-body interactions. Few-particle systems, where the quantum many-body problem of nucleons can be solved exactly, constitute an optimal setting to probe different potentials. The total photoabsorption cross section is given by

$$\sigma_\gamma(\omega) = 4\pi^2 \alpha \omega R(\omega)\,,$$

where α is the electromagnetic coupling constant and, at low photon energy ω, $R(\omega)$ is the inclusive unpolarized dipole response function, generally defined as:

$$R(\omega) = \frac{1}{2J_0+1} \sum_{M_0} \sum_f \left| \langle \Psi_f | \hat{D}_z | \Psi_0 \rangle \right|^2 \delta(E_f - E_0 - \omega)\,.$$

Here, J_0 and M_0 indicate the total angular momentum of the nucleus in its initial ground state and its projection, while $|\Psi_{0/f}\rangle$ and $E_{0/f}$ denote ground and final states and their energies, respectively. Finally, $\hat{D}_z$ is the unretarded dipole operator.

In Fig. 1 the result of σ_γ obtained with the V_{UCOM} potential for ^{3}He and ^{4}He [3] are presented in comparison with other realistic potential predictions: the local two-body Argonne V18 interaction (AV18) and the AV18 potential with the inclusion of the Urbana IX three-body force (AV18+UIX). The comparison between the AV18+UIX potential model and V_{UCOM} allows to investigate, whether the omission of a genuine three-body force can be replaced by a non-local interaction on a continuum observable. Interestingly, for high photon energies V_{UCOM} and AV18+UIX predictions of the cross section are very similar: V_{UCOM} simulates very well the missing genuine three-body force, improving the agreement with AV18+UIX with respect to the bare AV18 result. In the same figure we also present a comparison with the available experimental data. In case of the three-body nucleus the error bars of the data from Fetisov *et al.* [4] are unfortunately too big to allow a discrimination among the different potential models. In case of the alpha particle the experimental situation is more involved. Close to threshold several data were taken in different experiments. Unfortunately even the recently published data

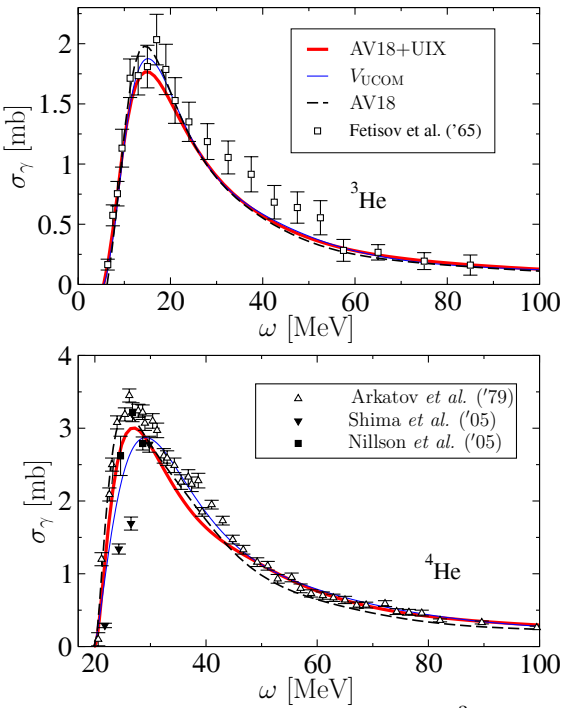

Figure 1: Photoabsorption cross section of ^{3}He and ^{4}He with different potentials in comparison with experiments.

from Nilsson *et al.* [5] and Shima *et al.* [6] show fairly large discrepancies. Only the data from Arkatov *et al.* [7] cover a larger energy range. They present a rather high peak cross section, which favors the AV18+UIX potential model in the peak and the V_{UCOM} in the energy region $30 \leq \omega \leq 45$ MeV; both potentials describe well data at high energies. These microscopic calculations offer valuable information for astrophysical studies, where nuclear absorption of γ-rays may become an important diagnostic tool for the environments of compact astrophysical sources. They can help to investigate interstellar gas, mostly isotopes of hydrogen and helium, surrounding the astrophysical γ-ray source.

References

[1] H. Feldmeier, T. Neff, R. Roth, and J. Schnack, Nucl. Phys. **A632**, 61 (1998); T. Neff and H. Feldmeier, Nucl. Phys. **A713**, 311, (2003).

[2] V. D. Efros, W. Leidemann, and G.Orlandini, Phys. Lett. B **338**, 130 (1994).

[3] S. Bacca, nucl-th/0612016.

[4] V. N. Fetisov, *et al.*, Nucl. Phys.**A71**, 305 (1965).

[5] B. Nilsson, *et al.*, Phys. Lett. B **626**, 65 (2005).

[6] T. Shima, *et al.*, Phys. Rev. C **72**, 044004 (2005).

[7] Yu. M. Arkatov, *et al.*, Yad. Konst. 4, 55 (1979).

Self-consistent Green's function and RPA studies of nuclei

C. Barbieri[1], N. Paar[2,3], R. Roth[2], and P. Papakonstantinou[2]
[1]GSI, Darmstadt, Germany; [2]TU, Darmstadt, Germany; [3]University of Zagreb, Croatia

Correlation energies from HF+RPA theory

The Hartree-Fock (HF) equations were solved for the V_{UCOM} [1] interaction in a basis of harmonic oscillator states [2]. This model explains about half of the total binding. The remaining correlation energy was evaluated using many body perturbation theory (MBPT) and standard random phase approximation (RPA) equations. In the latter case, we used the formula

$$E_{RPA} = -\sum_{\nu} \hbar\omega_{\nu} \sum_{p,h} |Y^{\nu}_{ph}|^2 \; - \; E^{(2)}_{PT} \; , \qquad (1)$$

where $E^{(2)}_{PT}$ is the contribution to the total binding energy in second order perturbation theory. A perturbative expansion of the RPA equations shows that *(i)* the sum in Eq. (1) must *also* include charge exchange modes and *(ii)* $E^{(2)}_{PT}$ is double counted and must be subtracted [3]. This leads to an improved description of the binding energies of most closed shell nuclei, up to ^{208}Pb, as shown in Fig. 1 [3]. The fair agreement between MBPT and RPA shown in the figure gives further evidence that the V_{UCOM} could be treated perturbatively.

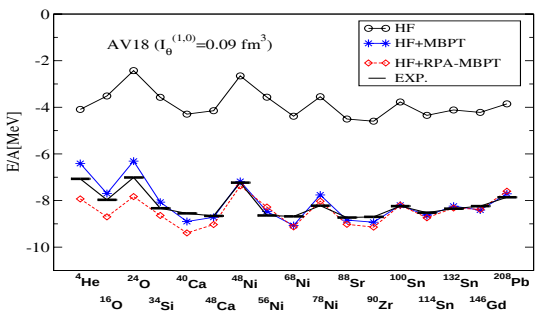

Figure 1: Nuclear binding energies per nucleon obtained from MBPT and RPA [3].

Binding and single particle energies

Since the same interaction is used in solving both the HF and RPA equations, the above HF+RPA scheme is fully consistent in the sense of Baym-Kadanoff theory [4]. Hence it satisfies basic conservation laws and sum rules. Analogously, in the framework of many body Green's functions one requires that the irreducible self-energy is expanded directly in terms of the single particle propagator that solves the corresponding Dyson equation. We refer to this scheme as self-consistent Green's functions (SCGF).

To demonstrate the relevance of self-consistency, the Table reports the binding energy of ^{16}O obtained from the intrinsic Hamiltonian, $H_{int} = T_{rel} + V$. Two different functional forms of the relative kinetic energy were used,

$$T_{rel} = \frac{A-1}{A} \sum_i \frac{\mathbf{p}_i^2}{2\,m} - \sum_{i<j} \frac{(\mathbf{p}_i \cdot \mathbf{p}_j)^2}{m\,A} \qquad (2)$$

$$= \sum_{i<j} \frac{(\mathbf{p}_i - \mathbf{p}_j)^2}{2\,m\,A} \; . \qquad (3)$$

Results are given for different approximations of the self-energy: HF (which is self-consistent), second order PT, and the same second order diagram but fully self-consistent [5].

E_B(MeV)	HF	2^{nd} ord. PT	2^{nd} ord. SC
Eq. (2)	-56.3	-125.4	-114.2
Eq. (3)	-56.3	-140.3	-114.3

In a more sophisticated approach, the three-particle irreducible (3PI) propagator is evaluated by coupling single particles to both giant resonances and paring excitations [6, 7]. Recently, it has become possible to perform full SCGF calculations with large bases (up to 8 oscillator shells) [8]. When a G-matrix interaction is used the resulting single particle (SP) spectrum is nearly independent of the oscillator length (right side of Fig. 2).

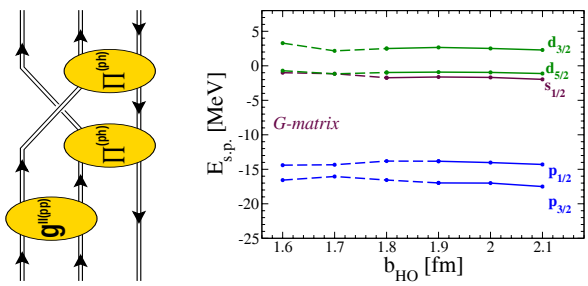

Figure 2: Left: Particle-phonon expansion of the 3PI propagator [6]. Right: corresponding neutron SP spectrum for ^{16}O [8].

References

[1] T. Neff and H. Feldmeier, Nucl. Phys. **A713**, 311 (2003).
[2] N. Paar, *et al.* Phys. Rev. C **74**, 014318 (2006).
[3] C. Barbieri, *et al.* `nucl-th/0608011`.
[4] G. Baym and L.P. Kadanoff, Phys. Rev. **124**, 287 (1961); G. Baym, Phys. Rev. **127**, 1391 (1962).
[5] C. Barbieri, to be published.
[6] C. Barbieri, W. H. Dickhoff, Phys. Rev. C**63**, 034313 (2001).
[7] W. H. Dickhoff and C. Barbieri, Prog. Part. Nucl. Phys. **52**, 377 (2004).
[8] C. Barbieri, Phys. Lett. **B643**, 268 (2006).

Phonon-coupling analysis of pygmy dipole resonances.

E. Litvinova[1], J. Daoutidis[1], P. Ring*[1], and D. Vretenar[2]
[1]Technische Universität München, Germany; [2]University Zagreb, Croatia

Abstract

An extension of Covariant Density Functional Theory is used to analyze the E1 strength distributions in the doubly magic nuclei, for which data on pygmy dipole resonances (PDR) have recently been reported. Particle-vibration coupling based on relativistic random phase approximation (RRPA) is included in a fully consistent way and the effect of two-phonon admixtures on the low-lying E1 strength is investigated.

Low-lying dipole strength in neutron rich nuclei

In recent years the study of the multipole response of nuclei far from the β-stability line and the possible occurrence of exotic modes of excitation has gained great interest both on the experimental as on the theoretical side. For neutron-rich nuclei, the pygmy dipole resonance (PDR), i.e. the resonant oscillation of the weakly-bound neutron skin against the isospin saturated proton-neutron core has been investigated. The onset of low-lying E1 strength has been observed not only in exotic nuclei with a large neutron excess, e.g. for neutron-rich oxygen isotopes [1], but also in stable nuclei with moderate proton-neutron asymmetry, like ^{44,48}Ca and ^{208}Pb [2]. Very recently the dipole strength distribution above the one-neutron separation energy was also measured in the unstable ^{130}Sn and the doubly-magic ^{132}Sn [3]. In addition to the giant dipole resonance (GDR), evidence was reported for a PDR structure at excitation energy around 10 MeV both in ^{130}Sn and ^{132}Sn, exhausting a few percent of the E1 energy-weighted sum rule.

Relativistic RPA plus phonon-coupling model

We have applied the relativistic RPA plus phonon-coupling model [4, 5] in the analysis of low-lying E1 strength distributions in ^{208}Pb and ^{132}Sn, for which data on pygmy dipole resonances (PDR) have recently been reported. The theoretical analysis is fully consistent: the same effective nuclear interaction is used both to determine the spectrum of positive- and negative-energy single-nucleon Dirac states, and as the residual interaction which determines the collective phonon states in the relativistic RPA. The calculated E1 photoabsorption cross sections, the excitation energies and widths of the giant dipole resonances (GDR) reproduce the available data. The PDR represents a resonant oscillation of the neutron skin against the isospin saturated proton-neutron core, and the corresponding RRPA state is characterized by a coherent superposition of many neutron particle-hole configurations. We find that

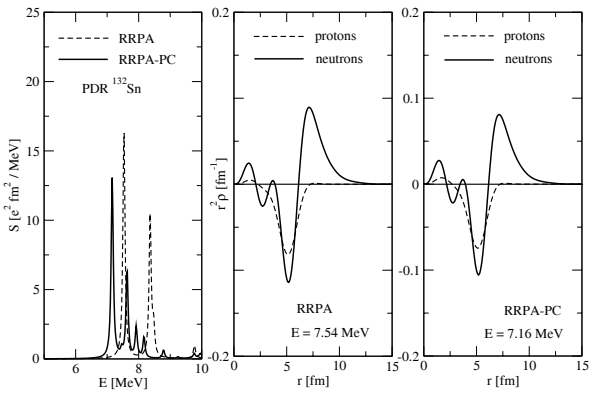

Figure 1: The low-energy portion of the E1 strength distribution in ^{132}Sn, calculated with the relativistic RPA (dashed), and with the RRPA extended by the inclusion of particle-phonon coupling (solid, RRPA-PC). In the panels on the right the proton and neutron transition densities for the peaks at 7.54 MeV (RRPA) and 7.16 MeV (RRPA-PC), are plotted as functions of the radial coordinate.

this picture remains essentially unchanged when particle-vibration coupling is included. The effect of two-phonon admixtures is a small shift of PDR states to lower excitation energy and, in the case of ^{132}Sn (see Fig. 1), the PDR strength is fragmented. Even though the PDR calculated in the extended model space of $ph\otimes$phonon configurations contains sizeable two-phonon admixtures, it basically retains a one-phonon character and its dynamics is not modified by the coupling to low-lying surface vibrations.

The results presented in Fig. 1 are obtained in the spectral representation of RRPA using an oscillator basis. The full influence of the continuum should be studied in the framework of relativistic continuum RPA including phonon coupling. Investigations in this directions are in progress.

References

[1] A. Leistenschneider *et al.*, Phys. Rev. Lett. **86**, 5442 (2001).

[2] T. Hartmann *et al.*, Phys. Rev. Lett. **93**, 192501 (2004).

[3] X. Adrich *et al.*, Phys. Rev. Lett. **95**, 132501 (2005).

[4] S. P. Kamerdzhiev, G. Y. Tertychny, and V. I. Tselyaev, Phys. Part. Nucl. **28**, 134 (1997).

[5] E. Litvinova and P. Ring, Phys. Rev. **C73**, 044328 (2006).

* ring@ph.tum.de

Shell model applications in nuclear structure and astrophysics

J.J. Cuenca Garcia[1], K. Langanke[1], A. Lisetzky[1], G. Martínez-Pinedo[1], C. Özen[1], and I. Petermann[1]
[1]GSI, Darmstadt, Germany

The erosion of shell gaps due to nucleonic excitations is one of the most interesting facets of modern nuclear structure. While most of the research has been concentrated on neutronrich nuclei, examples for cross-shell correlations are also known close to double-magic nuclei. For example, the M1 strength distribution for ^{38}Ar, a nucleus with two proton holes in the sd shell, shows a strong fragmentation, in strong contrast to sd shell model calculations which predict the strength to be located in a single transition. We have performed shell model calculations for ^{36,38}Ar which consider all correlations of the valence nucleons in the $s_{1/2}, d_{3/2}, f_{7/2}, p_{3/2}$ orbitals and their coupling to the spin-orbit partners by 1-particle-1-hole excitations and achieve a good reproduction of the energy spectra and M1 strength distributions (see Fig. 1) [1]. The strong fragmentation has been explained by particle-hole excitations across the $N = 20$ shell gap.

Sizable low-lying Gamow-Teller GT$_-$ strength has been proposed as a signal for the survival of SU(4) symmetry and as a potential hint for strong proton-neutron pairing [2]. As SU(4) symmetry can only completely be fulfilled in $N = Z$ nuclei, we have tested this conjecture by calculating the GT$_-$ distributions for the $N = Z + 2$ nuclei ^{46}Ti, ^{50}Cr, ^{54}Fe and ^{62}Zr. Although we find modest low-lying strength, the SU(4) symmetry is already quite strongly broken in these nuclei, mainly due to the spin-orbit interaction [3]. Additionally we have analyzed the shell model M1 and GT distributions for selected pf shell nuclei for dominating energy scales on the basis of a wavelet analysis and have studied the connection of these scales with the different parts of the interaction [4].

Nuclei with magic neutron numbers play the role of waiting points in the astrophysical r-process making their halflives particularly important for the matter-flow to heavier nuclei. For the $N = 82$ r-process nuclei halflives have only be determined for ^{130}Cd and ^{129}Ag, while those for the more proton-deficient have to be modelled. We have calculated the halflives for the $N = 82$ waiting points with $Z = 42 - 48$ within large-scale shell model calculations finding a good agreement with the two measured halflives, simultaneously reproducing relevant nuclear structure information [5].

The Shell Model Monte Carlo (SMMC) approach allows the calculation of nuclear properties at finite temperature in extremely large model spaces and accounting for the relevant correlations among nucleons. SMMC is particularly useful for the calculation of nuclear level densities [6]. We have performed such studies for several medium-mass nuclei with 50 active valence protons and neutrons within the complete pf- and sdg-spaces. In particular we have been able to demonstrate the effect of pairing on the level density [7]. Moreover we have studied the parity-dependence of the level density [8] which is quite relevant for the application of the statistical model to astrophysical reactions.

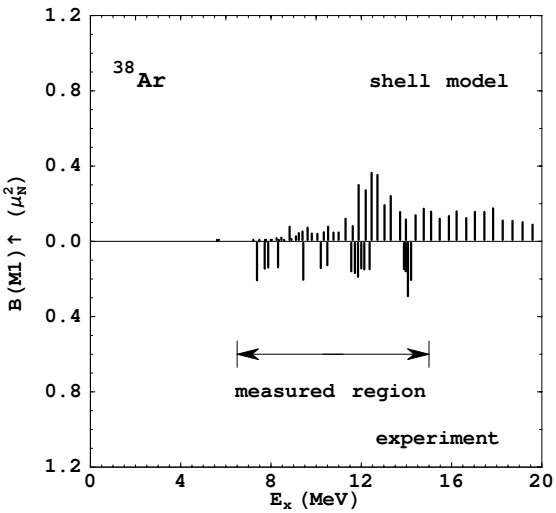

Figure 1: Comparison of shell model M1 strength distribution with the experimental data [9]

References

[1] A. Lisetzky, E. Caurier, K. Langanke, G. Martinez-Pinedo, P. von Neumann-Cosel, F. Nowacki and A. Richter, Nucl. Phys. A (in print)

[2] F. Iachello, in *Shell Model and Nuclear Structure*, ed. A. Covello, (World Scientific, Singapore, 1988) p. 407

[3] I. Petermann, G. Martinez-Pinedo and K. Langanke, submitted to Nucl. Phys.

[4] I. Petermann, diploma thesis, Technische Universität Darmstadt

[5] J.J Cuenca Garcia, G. Martinez-Pinedo, K. Langanke and F. Nowacki, submitted to Phys. Rev. C

[6] H. Nakada and Y. Alhassid, Phys. Rev. Lett. 79 (1997) 2939

[7] K. Langanke, Nucl. Phys. A778 (2006) 233

[8] C. Özen, K. Langanke, G. Martinez-Pinedo and D.J. Dean, to be published

[9] C.W. Foltz *et al.*, Phys. Rev. C49 (1994) 1359

Towards a microscopic description of nuclear reactions

T. Neff[1,2], H. Feldmeier[1], and K. Langanke[1]
[1]GSI, Darmstadt, Germany; [2]NSCL, Michigan State University, 48823 East Lansing, MI, USA

Low-energy nuclear reactions play an important role in many astrophysical scenarios. In many cases experimental data are not available at the energies important for the astrophysical processes. From the theory perspective such reactions have been investigated mainly with cluster models [1]. These models suffer from very simplified effective interactions and rather restricted model spaces for the interaction region. Nowadays *ab-initio* methods are actively pursued. Within the no-core shell model or the Green's Function Monte Carlo Method the same realistic two- and three-body forces can be used for the structure and the reaction calculations. However in both approaches the description of the asymptotic region is a very challenging problem.

With the Fermionic Molecular Dynamics (FMD) model we aim at a consistent description of bound states, resonances and scattering states starting from realistic nucleon-nucleon interactions. The important short-range central and tensor correlations are treated explicitly with the Unitary Correlation Operator Method, providing an effective low-momentum interaction. As no explicit three-body forces are included up to now and due to limitations of the FMD model space an empirical correction term is added to the two-body force.

In the FMD the many-body basis is constructed with Slater determinants of Gaussian wave packets that are projected on angular momentum and total linear momentum to restore the symmetries of the Hamiltonian. For the description of the asymptotic scattering states FMD ground states are joined taking the distance as generator coordinate. To obtain resonance or scattering solutions appropriate boundary conditions have to be included. In the many-body approach of FMD this is not a trivial problem and a new method utilizing a Collective Coordinate approach has been developed.

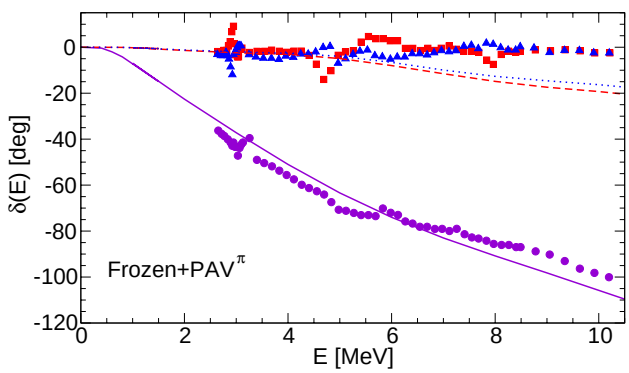

Figure 1: Phase shifts for the positive parity states ($1/2^+$, $3/2^+$ and $5/2^+$ correspond to solid, dashed and dotted lines, respectively) in the ^{3}He-α elastic scattering and comparison with experiment.

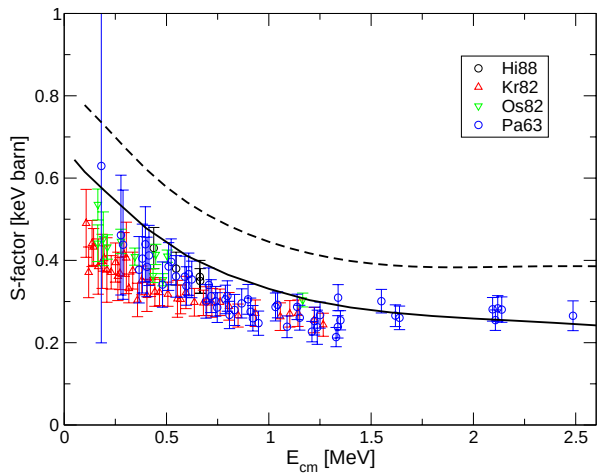

Figure 2: Astrophysical S-factor for ^{3}He(α,γ)^{7}Be. In the interaction region one configuration (dashed line) or two configurations (solid line) have been added to the antisymmetrized channel states $\mathcal{A}\left|^3\mathrm{He}\right\rangle \otimes \left|^4\mathrm{He}\right\rangle$ to improve the $3/2^-$ and $1/2^-$ bound states.

The ^{3}He(α,γ)^{7}Be *reaction*

In this reaction the ^{3}He and ^{4}He nuclei are captured from positive parity scattering states into the $3/2^-$ and $1/2^-$ bound states. In the FMD approach we use multiconfiguration FMD states for the ^{3}He and ^{4}He nuclei. For the ^{7}Be bound states two configurations obtained in a variation after angular momentum projection calculation or alternatively a single configuration obtained in a variation after parity projection procedure is used. A small fine-tuning of the interaction is necessary to reproduce the essential threshold energies. The calculated phase shifts agree very well with experimental data (see Fig. 1). With the many-body scattering solutions and the bound states, both obtained as eigenstates of the same many-body Hamiltonian, the capture cross section is calculated. As can be seen in Fig. 2 the energy dependence of the cross section is correctly reproduced. Also the branching ratio to $3/2^-$ and $1/2^-$ agrees with experimental data. Improvements in the description in the interaction region bring the normalization of the cross section closer to the data. Further improvements are under investigation.

References

[1] A. Csótó, K. Langanke, Few-Body Systems **29** (2000) 121

A New Equation of State for Astrophysical Applications

S. Typel[1] and T. Klähn[1,2]
[1]GSI, Darmstadt, Germany; [2]Universität Rostock, Germany

The equation of state (EoS) of hot and dense matter is an essential ingredient in many astrophysical models, e.g. in supernovae and compact star calculations. The thermodynamical properties and the composition of the matter have to be known in a wide range of density ($10^{-8} \lesssim n/n_{\rm sat} \lesssim 10$), temperature ($0 \le T \lesssim 50$ MeV) and proton fraction ($0 \le Y_p \lesssim 0.6$). Despite the large number of available EoS from various theoretical models, there are few [1, 2, 3] that are practically applied in astrophysical model calculations. Many studies focus only on certain aspects in a limited range of n, T and Y_p and the relevant thermodynamical quantities are not readily available in a simple form for astrophysicists. In addition, the model parameters are not well constrained by the experimental data that are nowadays available, the description is partially not self-consistent or too simplified. These deficiencies call for a development of an improved EoS that is practical and easy for the application in astrophysics.

In the present approach, the model includes the most relevant particles (protons, neutrons, light and heavy clusters, photons, electrons, myons, neutrinos). Exotic species, e.g. hyperons or quarks, and the transition to quark matter will be considered in a later stage of the development. The non-hadronic contributions have simple thermodynamics and are assumed to be distributed homogeneously in space. The hadronic part presents the main challenge. Its contribution to the EoS is calculated in a relativistic mean-field (RMF) model with density-depending nucleon-meson couplings (as suggested by Dirac-Brueckner calculations) that is able to describe the properties of atomic nuclei (binding energies, spin-orbit splittings, charge and diffraction radii, surface thickness, neutron skin thickness) with great precision and only a few parameters [4].

The determination of the model parameters is further constrained by information from astrophysical observations (maximum neutron star mass, neutron star cooling, mass-radius relation, gravitational mass-baryon number relation) and heavy-ion collisions (elliptic flow, subthreshold kaon production, isoscaling in fragment isotope yields) according to a recently developed test scheme [5]. The large body of data from the various fields is sensitive to different properties of the EoS at low and high densities for symmetric and neutron-rich matter. As a consequence, e.g., the isospin dependence and the stiffness of the EoS are rather well constrained.

At densities below nuclear saturation, the matter becomes inhomogeneous and clusters appear. Heavy nuclei arrange on a regular lattice with a surrounding gas of nucleons and light clusters. The properties of the heavy clusters are calculated in a self-consistent Thomas-Fermi approach with the RMF density functional (beyond the local density approximation) using the Wigner-Seitz appromation for the lattice cells. The density distributions in previous models [1, 2] were treated not self-consistently with simple parametrized shapes and simplifications in the energy functional. The long-range nature of the Coulomb interaction leads to an important contribution by the correlation energy depending on the shape.

A major improvement as compared to earlier models is the description of light clusters. At very low densities the equation of state can be calculated systematically in the form of a virial expansion [6]. This approach has been employed recently for a system of neutrons, protons and α-particles based on available experimental data for bound state energies and scattering phase shifts in the calculation of the second viriral coefficient [7]. The results constitute a benchmark for the EoS at very low densities but there are severe limitations for an application at higher densities where the formation of additional clusters and the medium effects on their properties have to be considered. The formation of several different clusters requires a reorganization of the virial expansion avoiding a double counting of bound state contributions. With increasing density, the effetive nuclear interaction will change and, more importantly, the Pauli blocking of states leads to the Mott effect, i.e. the bound systems dissolve in the medium. These effects are taken into account by introducing effective quasi-particle quantities and medium-dependent virial coefficients. The model is inspired by a thermodynamic Green's function approach for the calculation of the second virial coefficient at finite densities [8]. In the present model the correct transition to homogeneous matter is observed at high densities that cannot be described by a conventional second-order virial EoS.

References

[1] H. Shen et al., Prog. Theor. Phys. 100 (1998) 1013, Nucl. Phys. A 637 (1998) 435.

[2] J. M. Lattimer and F. D. Swesty, Nucl. Phys. A 535 (1991) 331.

[3] W. Hillebrandt et al., Astron. Astrophys. 133 (1984) 175.

[4] S. Typel, Phys. Rev. C 71 (2005) 064301.

[5] T. Klähn et al., Phys. Rev. C 74 (2006) 035802.

[6] G. E. Beth and E. Uhlenbeck, Physica 3 (1936) 729, Physica 4 (1937) 915.

[7] C. J. Horowitz and A. Schwenk, Nucl. Phys. A 776 (2006) 55.

[8] M. Schmidt, G. Röpke and H. Schulz, Ann. Phys. 202 (1990) 57.

Simulation and Analysis of Breakup Reactions with the Program CDXS+

S. Typel[1]
[1]GSI, Darmstadt, Germany

Electromagnetic breakup reactions of stable and exotic nuclei at medium to high projectile energies provide a wealth of information for nuclear structure and astrophysics. E.g., it is possible to study ground-state spectroscopic factors, nucleon-core interactions [1] or to extract low-energy radiative capture cross sections [2]. In order to prepare the actual experiments and to analyze the obtained data, a careful theoretical description of the breakup process and a detailed simulation according to the calculated cross sections is required.

To this end, the FORTRAN code CDXS+ was developed. It is easy to apply, runs independently of any special library, and contains many features that are relevant in the modeling of the projectile and projectile-target systems. The code is contained in a single file. The application and the underlying theoretical methods are summarized in the program manual [3]. The output contains detailed information on many properties of the considered nuclear system.

Bound and continuum states of the projectile system are described in a potential model by solving the Schrödinger equation for the relative motion of the fragments. There are various choices, e.g., for the representation of the wave functions, the angular momentum coupling, or the functional form of the central and spin-orbit potentials. Alternatively, it is possible to use asymptotic forms of the wave functions with an effective-range approximation for the phase shifts. From the matrix elements for electromagnetic multipole operators, reduced transition probabilities, photoabsorption and radiative capture cross sections can be found for the dissociation of the projectile into fragments and vice versa.

The central reaction calculation concentrates on the electromagnetic dissociation of the projectile during the scattering on a heavy target in the semiclassical approximation with either non-relativistic or relativistic Coulomb excitation functions. A correction for diffraction effects due to the wavelike nature of the projectile can be considered in an eikonal approximation. In addition, it is possible to include the breakup contribution by the nuclear interaction with the target. Here, a prior-form distorted-wave Born approximation for the relevant T-matrix element with eikonal wave functions for the projectile-target relative motion is employed. The relevant optical potentials can be specified in different functional forms or they can be derived from systematic double folding potentials. Their quality can be checked by comparing experimental data with elastic scattering cross that are provided by the program. For the breakup reaction, there is a choice from many different single, double and triple differential cross sections with various options for the independent kinematical quantities. In addition, corrections for the experimental efficiency and finite resolution can be applied.

The most general triple differential cross section can be converted into an event distribution in a Monte-Carlo simulation. The generated distribution can be analyzed with the program in the same way as in an actual experiment by extracting histograms for various kinematical quantities. The event distribution can also serve as an input for additional GEANT simulations in order to consider the properties of the experimental setup in more detail.

The program CDXS+ is currently applied in the simulation of various breakup reactions that have been or will be performed at GSI. It is expected that the Coulomb breakup of ^{6}Li can provide important information on the low-energy cross section of the ^{2}H(α,γ)^{6}Li capture reaction that is relevant in Big-Bang nucleosynthesis. From an earlier Coulomb dissociation experiment with 26 A MeV ^{6}Li [4], data for the astrophyscal S factor were extracted that are considerably larger than theoretical estimates at low energies. In the analysis of the GSI experiment with a 150 A MeV ^{6}Li beam it is important to clarify the strength of the nuclear breakup contribution.

The code is also used in preparing the future GSI breakup experiment with ^{27}P. Here the goal is to obtain more precise information on the radiative proton capture reaction on ^{26}Si as compared to an earlier experiment at RIKEN [5]. The reaction ^{26}Si(p,γ)^{27}P is considered relevant in the synthesis of ^{26}Al in novae. It is planned to observe the non-resonant direct E1 capture and the unknown resonant M1 contribution of the $\frac{3}{2}^+$ continuum state.

In a third application, the feasibility of an ^{16}O breakup experiment with ^{12}C and ^{4}He as fragments is studied in order to improve the information on the E2 contribution to the ^{12}C(α,γ)^{16}O reaction cross section. Here, the contamination by nuclear breakup is the essential problem because of the high Q-value leading to a rather small flux of virtual photons. The specific kinematical condition at GSI with a high-energy ^{16}O projectile beam could be more advantegeous than earlier attempts at lower energies [6].

References

[1] S. Typel and G. Baur, Phys. Rev. Lett. 93, 142502 (2004); C. Nociforo et al., Phys. Lett. B 605, 79 (2005); U. Datta Pramanik et al., J. Phys. G: Nucl. Part. Phys. 31, S1583 (2005).

[2] F. Schümann et al., Phys. Rev. C 73, 015806 (2006).

[3] S. Typel, CDXS+ Manual, unpublished.

[4] J. Kiener et al., Phys. Rev. C 44, 2195 (1991).

[5] Y. Togano et al., Nucl. Phys. A 758, 182c (2005).

[6] F. Fleurot, PhD Thesis, KVI Groningen (2002).

The fission rate in multi-dimensional Langevin calculations

P. N. Nadtochy, A. Kelić and K.-H. Schmidt
GSI, Darmstadt, Germany

Experimental indications of fission as a slow and highly dissipative process have come from the multiplicities of prescission particles [1] and γ-rays [2]. As the quantitative estimations of nuclear dissipation found from different theoretical models differ substantially [3], it becomes important to understand the reasons, which lead to different predictions of theoretical models. One would like to conclude on the validity of the physics considered in these models by comparing these predictions with experimental data. For this purpose, however, one should be sure that technical restrictions of the model calculations do not have any significant influence on the results. One of these restrictions is the dimensionality of the model space, which is the subject of the present work. Experimental data on nuclear dissipation have often been interpreted using one-dimensional Langevin models, where only one parameter is used for the description of the possible shapes of the fissioning nucleus. However, almost all the problems of collective nuclear dynamics are essentially multi-dimensional. Therefore, such an important characteristic as the fission rate is investigated in the present work using Langevin calculations with different numbers of collective coordinates involved in the dynamical consideration for the two most frequently used dissipation mechanisms: one-body and two-body. In order to investigate only the influence of the dimensionality of the model on the calculated results, we carry out one-dimensional, two-dimensional, and three-dimensional Langevin calculations with some simplifications. We started modelling the fission process from the compound nucleus in spherical shape. The calculations have been done for zero angular momentum. The evaporation of the prescission light particles was not considered in the present analysis. Shell corrections have also been neglected. Of course, all these effects have important influence on the fission process, but in the present study we are particularly interested in the importance of the dimensionality of problem, and, therefore, we want to keep all other effects as simple as possible. Technical details on the calculations can be found in ref. [4]. The results of the calculations for the nucleus ^{248}Cf at two excitation energies are presented in Fig. 1 for the case of the one-body dissipation. One can see from this figure that the transient time depends on the number of collective coordinates involved in the Langevin calculations. The lowest transient time is obtained in one-dimensional calculations, and this tendency is independent on excitation energy. One can also see in Fig. 1 that the stationary value of the fission rate increases after introducing new collective coordinates in the dynamical consideration: The stationary value of the fission rate in the one-dimensional case is lower than in the two-dimensional and three-dimensional cases. This effect is more pronounced at high excitation energy. The same qualitative conclusions were obtained in case of two-body dissipation.

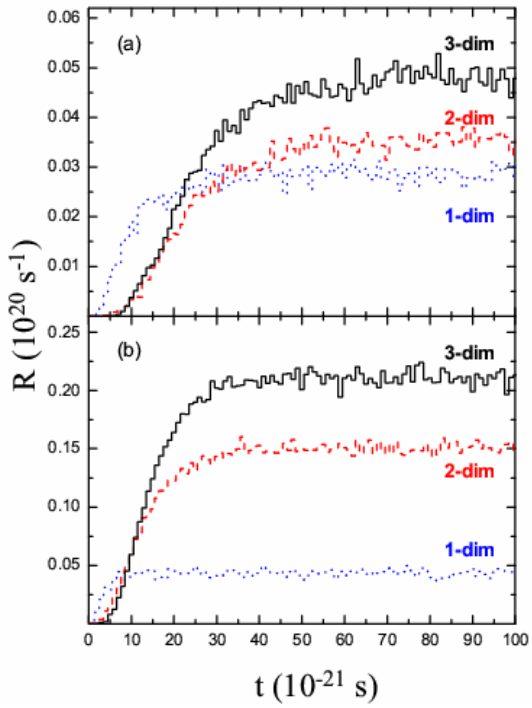

Figure 1: The fission rate calculated for the nucleus ^{248}Cf in the case of one-body dissipation for excitation energy E=30 MeV (a) and E=150 MeV (b). The solid, dashed, and dotted curves correspond to the three-, two-, and one-dimensional Langevin calculations, correspondingly.

These results are particularly important for the conclusions about nuclear dissipation, deduced from the comparison of experimental results with model calculations, which are performed in restricted deformation space. One may suppose that qualitatively the same conclusion is valid for other problems in statistical physics and chemistry on the decay of metastable states of multi-dimensional systems, which might be revisited with the powerful modern tools of Langevin calculations.

Acknowledgment

One of us (P.N.N.) is grateful to the Humboldt foundation for the financing of the stay at GSI, Darmstadt.

References:

[1] D.J. Hinde et al., Nucl. Phys. A 502 (1989) 497c.
[2] M. Thoennessen et al., Phys. Rev. Lett. 59 (1987) 2860.
[3] D. Hilscher and H. Rossner, Ann. Phys. 17 (1992) 471.
[4] P. N. Nadtochy and G. D. Adeev, Phys. Rev. C 72 054608 (2005).

The role of fission in the r-process

G. Martínez-Pinedo[1], K. Langanke[1], A. Kelić[1], K.-H. Schmidt[1], D. Mocelj[2], I. Panov[2], F.-K. Thielemann[2], N. T. Zinner[3], and B. Pfeiffer[4]

[1]GSI, Darmstadt, Germany; [2]Universität Basel, Basel, Switzerland; [3]University of Aarhus, Aarhus, Denmark; [4]University of Mainz, Mainz, Germany

The r-process is responsible for the synthesis of at least half of the elements heavier than Fe. It is associated with explosive scenarios where large neutron densities are achieved allowing for the series of neutron captures and beta decays that constitutes the r-process [1, 2]. The r-process requires the knowledge of masses and beta-decays for thousands of extremely neutron-rich nuclei reaching even the neutron-drip line. Moreover, in order to synthesize the heavy long-lived actinides, U and Th, large neutron-to-seed ratios are required ($\sim$ 100) allowing to reach nuclei that decay by fission. Fission can be induced by different processes: spontaneous fission, neutron-induced fission, beta-delayed fission and, if the r-process occurs under strong neutrino fluxes, neutrino-induced fission. The role of fission in the r-process has been the subject of many studies in the past (see ref. [3] and references therein), however, often only a subset of fission-inducing reactions was considered and a rather simplistic description of fission yields was used. It should be emphasized that, if fission really plays a role in determining the final abundances of the r-process, one needs not only fission rates but equally important are realistic fission yields as they determine the final abundances. Our goal has been to improve this situation by putting together a full set of fission rates including all possible fission reactions listed above. For each fissioning nucleus the fission yields are determined using the statistical code ABLA [4, 5]. The fission yields change from nucleus to nucleus and in a given nucleus depend on the excitation energy at which fission is induced.

Figure 1 shows the results of our calculations for two different mass models. While the FRDM mass model shows a similar trend with increasing neutron-to-seed ratio, the ETFSI-Q mass model is clearly different. This difference is due to the fact that the ETFSI-Q mass has a quenched shell gap for $N = 82$ and $N = 126$, while the other two mass models show strong shell gaps even close to the drip line. In the ETFSI-Q mass model the $N = 82$ waiting point is practically absent for the conditions of figure 1. This allows all matter to pass through $N = 82$, incorporating most neutrons in heavy nuclei and leaving very few free neutrons to induce fission events. In the other mass model, a smaller amount of matter passes the $N = 82$ and $N = 126$ waiting points. Once this matter reaches the fissioning region a large abundance of neutrons is still present that creates new neutrons by fission allowing the r-process to last for a longer time and produce a larger fraction of fission fragments. This explains why the FRDM mass model produces larger amounts of matter in the range $A = 130$–190, and implies that the shell structure at $N = 82$ is essential for determining the role of fission in the r-process.

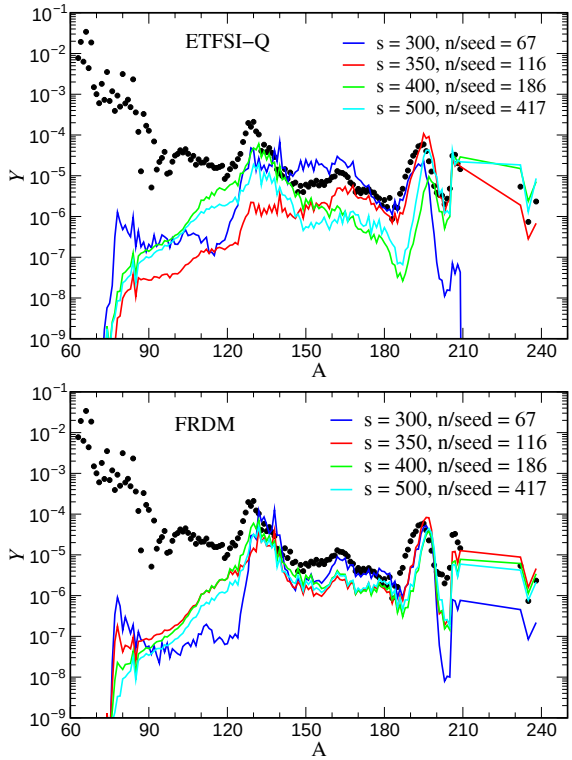

Figure 1: Final r-process abundances (at 1.6 Gy) obtained in several adiabatic expansions using two different mass models (FRDM [6] and ETFSI-Q [7]). The solid circles correspond to a scaled solar r-process abundance distribution [8].

References

[1] J. J. Cowan, F.-K. Thielemann, J. W. Truran, Phys. Repts. **208** (1991) 267.

[2] J. J. Cowan, F.-K. Thielemann, Physics Today (2004) 47.

[3] I. V. Panov, E. Kolbe, B. Pfeiffer, T. Rauscher, K.-L. Kratz, F.-K. Thielemann, Nucl. Phys. A **747** (2005) 633.

[4] J.-J. Gaimard, K.-H. Schmidt, Nucl. Phys. A **531** (1991) 709.

[5] J. Benlliure, A. Grewe, M. de Jong, K.-H. Schmidt, S. Zhdanov, Nucl. Phys. A **628** (1998) 458.

[6] P. Möller, J. R. Nix, K.-L. Kratz, At. Data. Nucl. Data Tables **66** (1997) 131.

[7] J. M. Pearson, R. C. Nayak, S. Goriely, Phys. Lett. B **387** (1996) 455.

[8] J. J. Cowan, *et al.*, Astrophys. J. **521** (1999) 194.

Astrophysical and Nuclear physics aspects of the νp-process

G. Martínez-Pinedo[1], K. Langanke[1], C. Fröhlich[2], M. Liebendörfer[2], F.-K. Thielemann[2], R. Buras[3], and H.-Th. Janka[3]

[1]GSI, Darmstadt, Germany; [2]Universität Basel, Basel, Switzerland; [3]Max-Planck-Institut für Astrophysik, Garching, Germany

Recent hydrodynamical studies of core-collapse supernovae have shown that the bulk of neutrino-heated ejecta during the early phases (first second) of the supernova explosion is proton-rich [1, 2, 3]. Nucleosynthesis studies in this environment have shown that these ejecta could be responsible for the solar abundances of elements like ^{45}Sc, ^{49}Ti and ^{64}Zn [4, 5]. Once reactions involving alpha particles freeze out, the composition in these ejecta is mainly given by $N = Z$ alpha nuclei and free protons. Proton captures on these nuclei cannot proceed beyond ^{64}Ge due to the low proton separation energy of ^{65}As and the fact that the beta-decay half-life of ^{64}Ge (64 s) is much longer than the typical expansion time scales (a few seconds).

Two recent studies [6, 7] have shown that the inclusion of neutrino interactions during the nucleosynthesis permits a new chain of nuclear reactions denoted νp-process in ref. [6]. In this process nuclei form at a typical distance of $\sim$ 1000 km from the proto-neutron star where antineutrino absorption reactions proceed on a time scale of seconds that is much shorter than the typical beta decay half-lives of the most abundant nuclei present (eg. ^{56}Ni and ^{64}Ge). As protons are more abundant than heavy nuclei, antineutrino capture occurs predominantly on protons via $\bar{\nu}_e + p \rightarrow n + e^+$, causing a residual density of free neutrons of 10^{14}–10^{15} cm^{-3} for several seconds, when the temperatures are in the range 1–3 GK. These neutrons can easily be captured by neutron-deficient $N \sim Z$ nuclei (for example ^{64}Ge), which have large neutron capture cross sections. The amount of nuclei with $A > 64$ produced is then directly proportional to the number of antineutrinos captured.

The νp-process acts in the temperature range of 1–3 GK. The amount of heavy nuclei synthesized depends on the ratio of neutrons produced via antineutrino capture to the abundance of heavy nuclei (this is similar to the neutron-to-seed ratio in the r-process, see also discussion in [7]). This ratio is sensitive to the antineutrino flux and to the proton-to-seed ratio. The first depends mainly on the expansion time scale of matter and its hydrodynamical evolution. The second is very sensitive to the proton richness of the material and its entropy. Figure 1 shows the nucleosynthesis resulting from several trajectories corresponding to the early proton-rich wind from the protoneutron star resulting of the explosion of a 15 M$_\odot$ star [1]. (These trajectories have also been studied in reference [7].) No production of nuclei above $A = 64$ is obtained if antineutrino absorption reactions are neglected. Once they are included production of elements above $A = 64$ takes place via the chain of reactions discussed in the previous paragraph. This allows to extend the nucleosynthesis beyond Zn producing elements like Ge whose abundance is roughly proportional to the iron abundance at low metallicities [8]. The production of light p-process nuclei like ^{84}Sr, ^{94}Mo and ^{96,98}Ru is also clearly seen in figure 1. However, ^{92}Mo is still underproduced. This could be due to the limited knowledge of masses around ^{92}Pd [7]. The current mass systematics [9] predict a rather low proton separation energy for ^{91}Rh that inhibits the production of ^{92}Pd. Future experimental work in this region should clarify this issue.

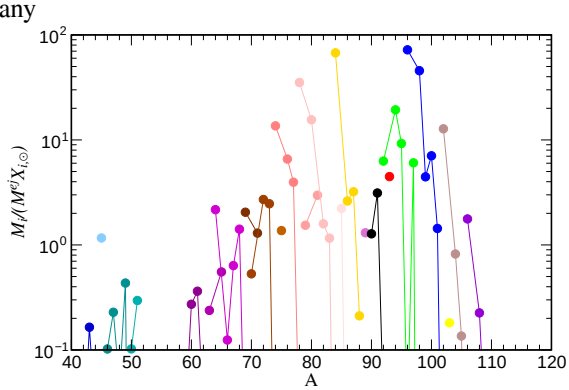

Figure 1: Integrated production factors corresponding to the early proton rich wind obtained in the explosion of a 15 M$_\odot$ star [1]. In each panel the radius, entropy and Y_e values of matter when the temperature reaches 3 GK are shown.

References

[1] R. Buras, M. Rampp, H.-T. Janka, K. Kifonidis, Astron. & Astrophys. **447** (2006) 1049.

[2] M. Liebendörfer, A. Mezzacappa, F.-K. Thielemann, O. E. Bronson Messer, W. Raphael Hix, S. W. Bruenn, Phys. Rev. D **63** (2001) 103004.

[3] T. A. Thompson, E. Quataert, A. Burrows, Astrophys. J. **620** (2005) 861.

[4] C. Fröhlich, *et al.*, Astrophys. J. **637** (2006) 415.

[5] J. Pruet, S. E. Woosley, R. Buras, H.-T. Janka, R. D. Hoffman, Astrophys. J. **623** (2005) 325.

[6] C. Fröhlich, *et al.*, Phys. Rev. Lett. **96** (2006) 142502.

[7] J. Pruet, R. D. Hoffman, S. E. Woosley, H.-T. Janka, R. Buras, Astrophys. J. **644** (2006) 1028.

[8] J. J. Cowan, C. Sneden, Nature **440** (2006) 1151.

[9] G. Audi, A. H. Wapstra, C. Thibault, Nucl. Phys. A **729** (2003) 337.

Complete and incomplete fusion in $^{25}Mg+^{206}Pb$ reactions

S. Heinz, F.P. Heßberger, D. Ackermann, S. Hofmann, J. Khuyagbaatar, R. Mann, B. Sulignano
GSI, Darmstadt, Germany.

In heavy ion collisions at energies around the Coulomb barrier reaction products emerge from the following processes: (1) complete fusion with full linear momentum transfer and subsequent particle emission and (2) reactions with partial momentum transfer, where only a part of the projectile reacts with the target nucleus. Each of these processes leads to a characteristic velocity distribution of the reaction products. Therefore, the determination of the production cross-section as a function of the isotope velocity helps to identify which process was the origin of the observed reaction products.

At the velocity filter SHIP we investigated the processes (1) and (2) using the reaction $^{25}Mg+^{206}Pb$ at 5.9×A and 8.7×A MeV with the following goals:

a) Determination of the relative contributions from processes (1) and (2) as a function of the beam energy.

b) Investigation of different beam-target combinations with a stepwise increase of the projectile mass. So far, process (2) was studied at SHIP only with beams up to Ne [1].

c) Investigation of processes (2) especially at beam energies around and below the Coulomb barrier. Former experiments have been performed at energies well above the barrier.

Several reaction products from At to Th have been identified by their α-decays. As an example in Fig. 1 the production cross-section times efficiency (σε) of ^{214}Ra is shown as a function of the isotope velocity v normalized to the compound nucleus (^{231}Pu) velocity v_{CN}.

At 8.7×A MeV a broad distribution around $v/v_{CN}=1$ can be seen (Fig.1, top). Its origin is the production of ^{214}Ra via complete fusion and subsequent 6p5n (or α4p3n) emission at E*=120 MeV.

Further, a pronounced peak at $v/v_{CN}=0.5$ is visible in the spectrum. The low velocity of these events clearly points to their production via an incomplete fusion process. In this case one projectile fragment is emitted in forward direction while the other one fuses with the target nucleus. This results in the significant shift to lower velocities of the heavy recoil product. In the case of ^{214}Ra the observed nucleus is produced by transfer of e.g. a ^{13}C cluster and subsequent emission of 5 neutrons. The large quadrupole deformation of ^{25}Mg ($ß_2=0.33$ [2]) is probably the reason for a relatively easy breakup of the projectile.

The lower graph shows the velocity distribution for 5.9×A MeV. Here, a peak is visible at $v/v_{CN}=1.4$. Since at SHIP only reaction products emitted under angles of up to ±2° with respect to the beam axis are detected, the observed peak can be explained by assuming a central collision in which a C cluster is transferred from the Mg projectile to the target and the projectile residue (also carbon) is scattered backwards. Due to momentum conservation

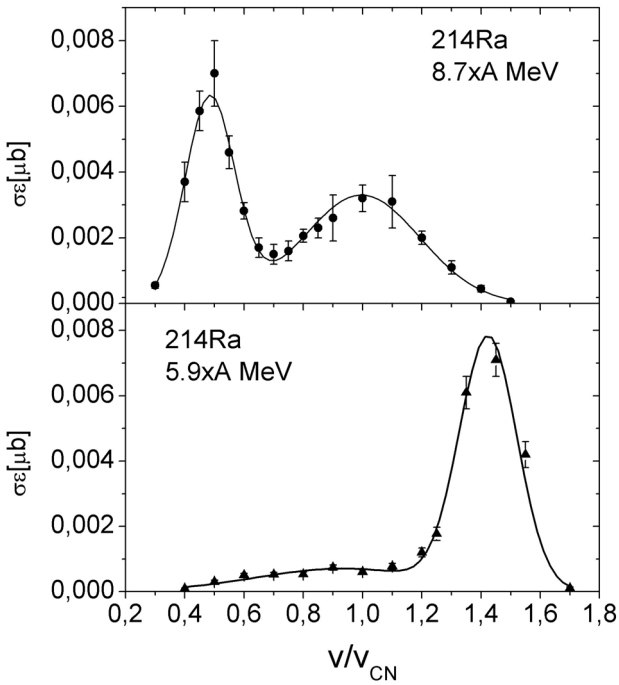

Figure 1: Velocity distribution of ^{214}Ra nuclei produced in $^{25}Mg+^{206}Pb$ collisions at 8.7×A and 5.9×A MeV.

the backward scattered C cluster leads to a momentum transfer to the target-like nucleus which leads to the observed velocity of ~40% above the compound nucleus velocity.

Additionally, we found at 5.9×A MeV also ^{214}Ra nuclei with velocities around v/v_{CN}~1 and further down to about 40% of the compound nucleus velocity. Consequently ^{214}Ra is also produced via compound nucleus formation with an excitation energy of E*=55 MeV with subsequent particle emission and via incomplete fusion.

Details of the kinematics of these processes, e.g. a possible resonance phenomenon leading to ^{12}C emission in forward direction at the higher bombarding energy, are subject to further studies which are also aiming to reproduce the measured cross-sections.

In addition, experiments are planned to measure an excitation function of the observed processes and to study the results using different projectiles.

References

[1] F.P. Heßberger et al., Z. Phys. A 348 (1994) 301.
[2] P. Möller et al., At. Data and Nucl. Data Tables 59 (1995) 185.

Investigation of the di-nuclear system U+U

S. Heinz[1], W. Mittig[2], A.C.C. Villari[2] and the E511 collaboration
[1]GSI, Darmstadt, Germany; [2]GANIL, B.P. 55027 14076 Caen Cedex France.

In heavy ion collisions at Coulomb barrier energies the two collision partners can be brought into nuclear contact. During their closest approach the two nuclei form a di-nuclear system (nuclear molecule) which is seen by the electrons as a common charge centre. The lifetime of the di-nuclear system (nuclear contact time) is correlated with the energy dissipation during the collision. While the contact times in quasi-elastic collisions are 10^{-22} to 10^{-21} s, for collisions with high energy dissipation one should expect lifetimes which are 10 – 100 times longer. Correlated with these long contact times is a large mass flow between the two nuclei which can lead to the exchange of up to 20 protons and as many neutrons as was shown in previous experiments for different collision systems up to U+U [1,2].

In April 2006 we started new investigations of the system U+U at the VAMOS spectrometer of GANIL, which have mainly two objectives:

a) Due to the high mass flow expected during nuclear contact, two reaction products can emerge. One has a proton number below uranium and the other one the complementary proton number beyond uranium. In this case we could obtain neutron rich nuclei in the transuranium region, which are otherwise experimentally not accessible.

b) If we can observe nuclear contact times of at least 10^{-20} s in very heavy collision systems like U+U, the respective reactions could be used as a "trigger" for a fundamental, experimentally hitherto unobserved phenomenon: The decay of an overcritical vacuum in a static electric field by the emission of e+e- pairs.

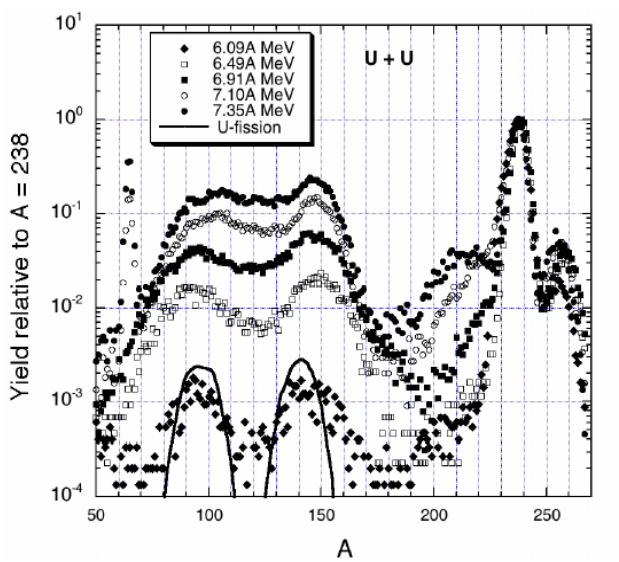

Figure 1: Mass spectra for the system U+U at different beam energies.

Our first experiment was aimed to measure an excitation function for the production of different transfer products as well as their angular distributions which should give us information about the lifetime of the di-nuclear system. We investigated five different beam energies from 6.09 to 7.35×A MeV. The corresponding mass spectrum is shown in Fig. 1. Besides a double humped distribution at 70<A<170 corresponding to fission fragments of uranium and a peak at A=238 from uranium elastic and inelastic scattering we observed a broad bump in the region 190<A<230 which contains transfer products with masses lower than uranium. This bump enhances significantly as a function of beam energy (Fig. 2) and develops a maximum around Pb-like products at A~210 for beam energies above 7xA MeV (see Fig. 1). Masses heavier than uranium were not detected definitely. The origin of the peak at A=256 is not yet determined; most probably it is an artefact of the detection system.

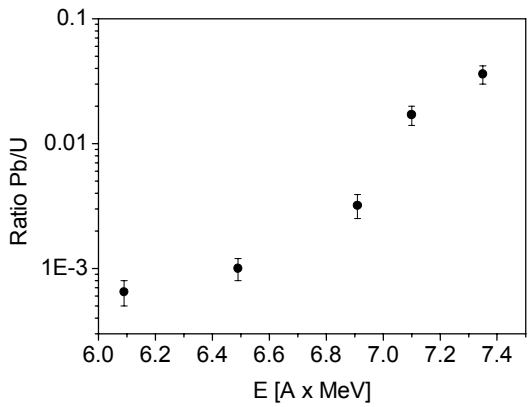

Figure 2: Excitation function for Pb-like products. The yield is normalized to elastically scattered U ions.

Pb-like fragments could be an indication of nuclear contact times significantly longer than 10^{-21} s. Since for di-nuclear systems with moderate excitation energy shell effects should be important, one could expect asymmetric fission of the system with preferential emission of nuclei close to the doubly magic nucleus ^{208}Pb - if the system lives long enough to thermalize. To isolate the reactions with the longest contact times, the angular distribution of the Pb-like fragments as well as their energy has still to be analyzed. According to calculations of [3] one should find these events at scattering angles < 60° and small kinetic energies.

References

[1] H. Freiesleben et al., Z.Phys. A292 (1979) 171
[2] K.E. Rehm et al., Nucl. Phys. A366 (1981) 477
[3] V.I. Zagrebaev et al., Phys. Rev. C73 (2006) 03160

Isomeric states in ^{213}Th and ^{214}Th

J. Khuyagbaatar[1], S. Hofmann[1], F.P. Hessberger[1], D.Ackermann[1], S. Antalic[2], H.G. Buckhard[1], S. Heinz[1], B. Kindler[1], A.F. Lisetskiy[3], B. Lommel[1], R. Mann[1], K. Nishio[4], H.J. Schött[1] and B. Sulignano[1]

[1]GSI, Darmstadt, Germany, [2]Comenius University, Bratislava, Slovakia, [3]University of Arizona, USA, [4]Japan Atomic Energy Agency (JAEA), Tokai, Japan

The isotopes ^{213}Th and ^{214}Th were produced via the 5n and 4n channel of the ^{164}Dy(^{54}Cr,xn)$^{238-x}$Cm fusion-evaporation reaction at SHIP [1].

Three previously unknown γ lines with energies of 623.2, 639.0 and 830.1 keV, which are in coincidence to each other, were assigned to ^{214}Th. These three γ lines were also in coincidence with a γ line at 89.1 keV. The relative intensities of these four γ lines are 1, (1.04±0.12), (1.02±0.12) and (0.049±0.016), respectively. The multipolarity of all transitions is assigned to E2 on the basis of the relative intensities, experimental upper half-life limits and Weisskopf estimations.

The half-life of the isomeric state in ^{214}Th was measured for the first time. It is (1.24±0.12) μs. This value is the average of the values for the three high energy γ rays. Taking these values we determined the value for the reduced transition probability B(E2) for de-excitation of the isomeric state.

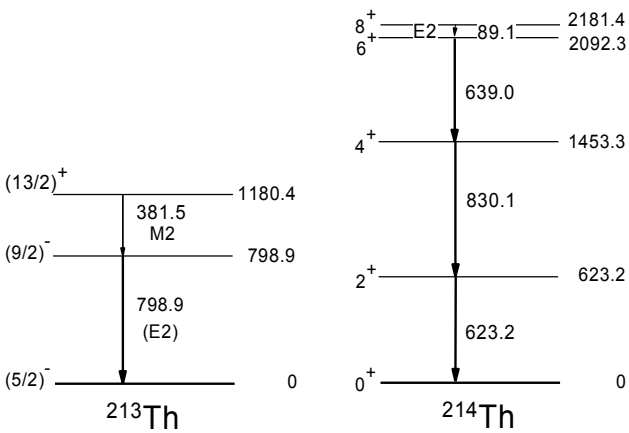

Figure 1: Suggested decay schemes for ^{213}Th and ^{214}Th. Energies are given in keV. The ordering of the 623.2 and 639.0 keV γ transitions in ^{214}Th is tentative.

The suggested decay schemes of the isomeric states are presented in Fig. 1. These schemes are based on γ−γ coincidences, relative intensities and the systematics of isomeric states in N=123, 124 isotones.

To understand the origin of the 8^+ isomeric state in ^{214}Th we have performed shell model calculations using the method given in [2]. The results of our calculations are shown in Fig. 2. Two different calculations were made to describe the behaviour of B(E2;$8^+ \rightarrow 6^+$) values in the isotones N=124, 126. The open triangles mark transitions between pure $(1h_{9/2})_{8+}$ proton states (in the seniority scheme) and the open circles mark transitions between $(1h_{9/2}2f_{7/2})_{8+}$ and $(1h_{9/2})_{6+}$ states. The solid circles denote experimental data taken from literature.

Comparing theoretical calculations with experimental data we conclude that the experiment is best reproduced by assuming a mixed configuration $\pi\{1h_{9/2}\times 2f_{7/2}\}$. Therefore, we conclude that the 8^+ isomeric state in ^{214}Th is formed by breaking a pair of protons in the $1h_{9/2}$ orbit.

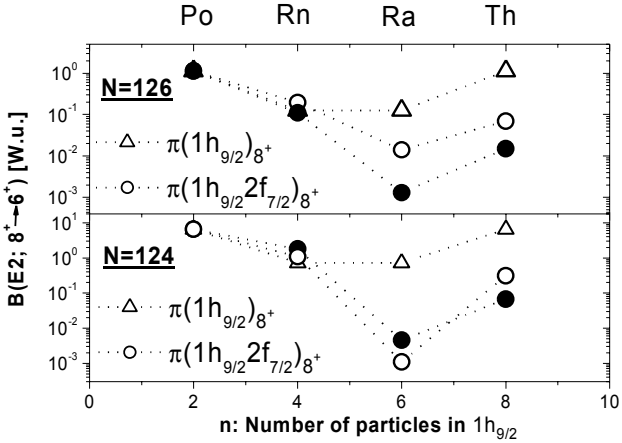

Figure 2: Experimental and theoretical B(E2;$8^+ \rightarrow 6^+$) values for N=126, 124 isotones of Po, Rn, Ra and Th (^{214}Th from our experiment). All calculated values are normalized to Po. The dashed curves are drawn to guide the eye.

Two new γ lines with energies 381.5 and 798.9 keV were assigned to ^{213}Th. The intensity of the 798.9 keV γ line was 1.65 relative to the intensity of the 381.5 keV γ line. A half-life of (1.7±0.6) μs was measured for the first time for the isomeric state. The suggested decay scheme of the isomeric state in ^{213}Th is shown in Fig. 1. It is based on the systematics of level schemes of neighbouring odd N nuclides.

The α decay energies of the ^{213}Th and ^{214}Th ground-states are almost equal. We measured values of (7.69±0.02) MeV and (7.68±0.02) MeV, respectively, in agreement with literature data [3].

The analysis of the data is being continued and detailed report on the decay schemes is in preparation.

References

[1] S. Hofmann and G. Münzenberg, Rev. Mod. Phys, **72**, (2000) 733.

[2] E. Caurier, F. Nowacki, Acta Physica Polonica B 30 (1999) 705.

[3] Table of Isotopes, edited by R.B. Firestone 8th edition, Wiley, 1996.

Production of ^{234}Cm and ^{235}Cm using the reaction ^{208}Pb(^{30}Si,xn)$^{238-x}$Cm

J. Khuyagbaatar[1], K. Nishio[2], S. Hofmann[1], D. Ackermann[1], S. Heinz[1], F. P. Hessberger[1], R. Mann[1], and B. Sulignano[1]

[1]GSI, Darmstadt, Germany; [2]Japan Atomic Energy Agency (JAEA), Tokai, Japan

Neutron deficient Cm isotopes were produced at SHIP [1] using the fusion-evaporation reaction ^{208}Pb(^{30}Si,xn)$^{238-x}$Cm. The ^{30}Si beam with a charge state 6+ was prepared from ^{30}SiO (99.5%), at the High Charge State Injector. We used two different beam energies: 5.00·A MeV and 5.27·A MeV to produce ^{235}Cm and ^{234}Cm, respectively. The ^{208}PbS target with an average thickness of 412 μg/cm^2 was irradiated for each beam energy about one day. The identification of the Cm isotopes was made by using the α–α correlation method. The result of the analysis using a time window of 1500 s and a position window of 0.5 mm is shown in Fig. 1. One member of each event was taken in the pause between the beam pulses, in order to minimize the number of accidental coincidences.

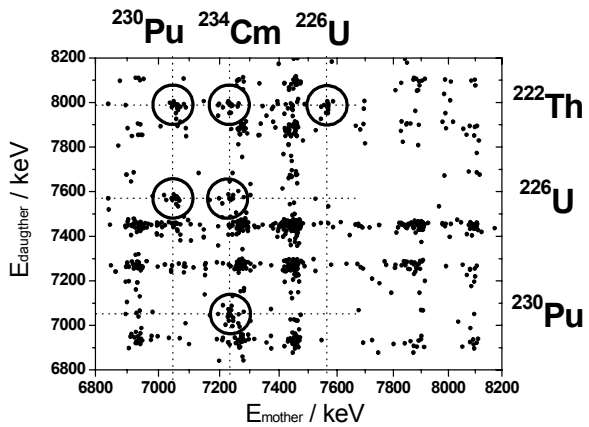

Figure 1: Two dimensional α – α correlation spectrum for the decay chain of ^{234}Cm→ ^{230}Pu→^{226}U→^{222}Th.

However, accidental coincidences with α decays of the transfer reaction products ^{211}Po, ^{211m}Po and ^{211}Bi are still high, because the cross-section for transfer reactions is a few orders of magnitude higher than that of the fusion-evaporation reactions of interest. All possible combinations of mother–daughter α–α correlations within the α decay chain of ^{234}Cm are shown in Fig. 1 (circles).

The α decay energy of ^{234}Cm is (7.24±0.02) MeV. A half-life of (70±20) s was determined from the correlation analysis of evaporation residues and α decay. The α decay of the daughter ^{230}Pu was identified at an energy of (7.06±0.02) MeV and a half-life of (127±17) s. Four spontaneous fission events were observed during the irradiation. They were also attributed to the decay of ^{234}Cm. Our new results for these isotopes are in agreement with our previous data [2].

The identification of the new isotope ^{235}Cm was made by using the same method. We observed six α decay chains which were tentatively assigned to ^{235}Cm (^{235}Cm→^{231}Pu→^{227}U→^{223}Th). In four cases the first generation α energy was (6.67±0.02) MeV, in two cases (6.98±0.02) MeV. The suggested decay scheme of ^{235}Cm is presented in Fig. 2.

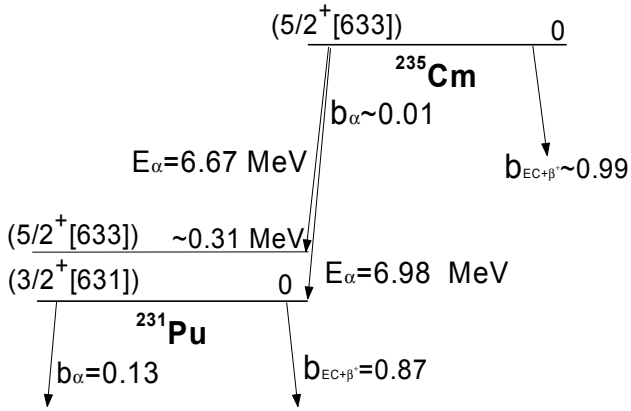

Figure 2: Suggested decay scheme for ^{235}Cm. Spin and parity of the states are extrapolated from systematics.

The main decay mode of the ^{235}Cm ground-state is electron capture and β^+-decay. We did not measure internal conversion electrons. Some of the decay characteristics were obtained from the theoretical predictions. The α decay branch is only ~1 %, which is dominantly populating an excited state of ^{231}Pu at (310±20) keV. The half-life of ^{235}Cm was not measured, because we did not identify the implanted evaporation residues at the high background produced by correlation with α decay of ^{235}Cm.

We plan to confirm the suggested decay scheme of ^{235}Cm in a future experiment (GSI proposal, U228). In this study we will synthesize ^{243}Fm in the reaction ^{208}Pb(^{40}Ar,3n)^{243}Fm. The isotope ^{235}Cm will be produced by the α decay chain ^{243}Fm→^{239}Cf→^{235}Cm.

The partial cross-section of the α decay branch of ^{234}Cm was (510±230) pb and for spontaneous fission it was (96±53) pb. The partial cross-section of the α decay branch of ^{235}Cm was estimated to be (330±130) pb.

References

[1] S. Hofmann and G. Münzenberg, Rev. Mod. Phys, 72, (2000) 733.

[2] P. Cagarda et al., GSI Rep. 2002-1 (2002) 15.

Production of seaborgium isotopes in the reaction of ^{30}Si+^{238}U

K. Nishio[1], S. Hofmann[2], F.P. Hessberger[2], D. Ackermann[2], S. Antalic[3], V.F. Comas[4], Z. Gan[5], S. Heinz[2], J.A. Heredia[4], H. Ikezoe[1], J. Khuyagbaatar[2], B. Kindler[2], I. Kojouharov[2], P. Kuusiniemi[6], B. Lommel[2], R. Mann[2], M. Mazzocco[2], S. Mitsuoka[1], A.G. Popeko[6], S. Saro[3], H.J. Schoett[2], B. Sulignano[2], A. Svirikhin[6], A.V. Yeremin[6]

[1]Japan Atomic Energy Agency, Tokai, Japan; [2]GSI, Darmstadt, Germany; [3]Comenius University, Bratislava, Slovakia; [4]Higher Institue of Technologies and Applied Sciences, Habana, Cuba; [5]Institute of Modern Physics, Lanzhou, China; [6]University of Oulu, Finland; [6]Flerov Laboratory of Nuclear Reactions, Dubna, Russia

Seaborgium isotopes were produced in the reaction of ^{30}Si + ^{238}U by using the velocity filter SHIP, and the production cross-sections were determined. The beam of $^{30}Si^{6+}$ was prepared from enriched material, ^{30}SiO (enrichment 99.5 %), at the 14 GHz ECR ion source. The beam intensities were typically 0.7 – 1.0 pμA. The experimental set-up is essentially the same as in previous experiments [1].

The uranium targets were prepared by evaporation of $^{238}UF_4$ on 45 μg/cm^2 carbon backing. The $^{238}UF_4$ target layers had thickness of 375 – 404 μg/cm^2.

The focal plane detectors were used to measure the recoil implantation and the subsequent alpha decays or spontaneous fission (sf). Behind the focal plane detector, we mounted a clover detector consisting of four Ge crystals. Due to the high multiplicity of gamma-rays emitted from the fission fragments, coincident gamma-ray are observed with a probability of 80%.

We used three different reaction energies of $E_{c.m.}$=144.0, 133.0 and 128.0 MeV, which were chosen so that the energy yields the maximum of the ER cross-sections for 5, 4, and 3n channel excitation functions according to a statistical model calculation. The accumulated beam doses were 1.8×10^{18}, 4.0×10^{18} and 1.7×10^{18}, respectively.

The observed decay chains or sf events are shown in Fig. 1. At $E_{c.m.}$= 144.0 MeV, we observed three alpha decay chains from ^{263}Sg (event number 1, 2, 3 in Fig.1), produced by five neutron emission. The energy and half-life agree with the literature values [2,3]. The cross-section for ^{263}Sg was 67(+67-37) pb. We also observed sf (No. 4), which we tentatively assign to ^{262}Sg. The cross-section was 22(+51-18) pb.

At the lower reaction energy of $E_{c.m.}$= 133.0 MeV, we observed four sf events (No. 5, 6, 7 and 8). Three events from No. 5 to No. 7 have similar lifetime, and the half-life is determined to be 120(+126-44) ms. The excitation energy of the compound nucleus is 11 MeV less than in the case of 144.0 MeV reaction energy, so that we assign these events to the new isotope ^{264}Sg. We obtained a cross-section of 10(+10-6) pb for ^{264}Sg. The sf of No. 8 has longer half-life. We tentatively assign this sf to ^{261}Rf, daughter of ^{265}Sg produced in the 3n channel. The cross-section for this event was 3.5(+8.1-2.9) pb.

At the lowest energy of $E_{c.m.}$= 128.0 MeV, no decay events were measured. We determined an upper cross-section limit of 15 pb at 68% coincidence level.

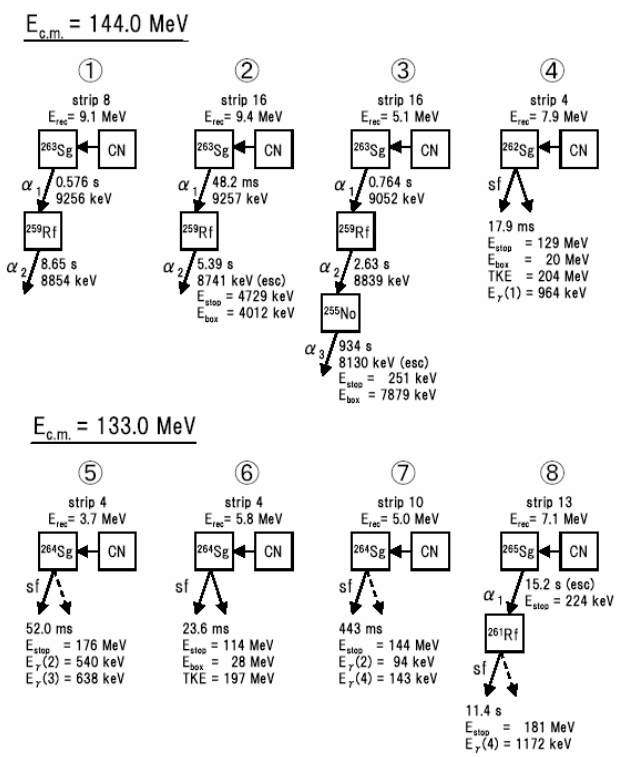

Figure 1: The observed decay chains or spontaneous fission events in the reaction of ^{30}Si+^{238}U.

The cross-sections are compared to a statistical model calculation which takes into account the prolate deformation of ^{238}U in the capture process. It is found that the collision of ^{30}Si with the equotorial side of ^{238}U results in complete fusion without any significant fusion hindrance, whereas competition between fusion and quasifission is present at collisions with the tips of ^{238}U. Detailed discussion is given in our publication [4].

References

[1] S. Hofmann and G. Münzenberg, Rev. Mod. Phys, **72**, 733 (2000).
[2] A. Ghiorso *et al*., Phys. Rev. Lett. **33**, 1490 (1974).
[3] S. Hofmann, Rep. Prog. Phys. **61**, 693 (1998).
[4] K. Nishio *et al*., Eur. Phys. J. A, **29**, 281 (2006).

Doubly magic ^{270}Hs

J. Dvorak[1], R. Krücken[1], F. Nebel[1], Z. Novackova[1] , A. Semchenkov[1, 2], A. Türler[1], B. Wierczinski[1], A. Yakushev[1], W. Brüchle[2], E. Jäger[2], M. Schädel[2], B. Schausten[2], E. Schimpf[2], M. Chelnokov[3], V. Gorshkov[3], A. Kuznetsov[3], A. Yeremin[3], R. Dressler[4], Ch. E. Düllmann[5, 6], K. Eberhardt[7], P. Thörle[7], Y. Nagame[8], Z. Qin[2, 9], M. Wegrzecki[10]

[1]TU Munich, Garching, Germany; [2]GSI, Darmstadt, Germany; [3]JINR, Dubna, Russia; [4]PSI, Villigen, Switzerland; [5]LBNL, Berkeley, CA, USA; [6]UC Berkeley, CA, USA; [7]U Mainz, Germany; [8]JAEA, Tokai-mura, Japan; [9]IMP, Lanzhou, P. R. China; [10]ITE, Warsaw, Poland

Superheavy elements owe their existence exclusively to nuclear shell effects which stabilize them against spontaneous fission (SF). Theoretical predictions locate the center of stability at the hypothetical doubly-magic spherical nucleus with Z=114 and N=184 [1]. Calculations with the inclusion of higher orders of deformation [2] suggest the ground state shell correction energy of deformed nuclei around Z=108 and N=162 to reach values as large as for ^{298}114. The increased stability leads to local minima at the N=162 neutron shell and a large difference in Q_α values between Ds and Hs isotones. This is clearly visible in Figure 1, but so far no experimental α–decay energies are available for N=162 nuclei.

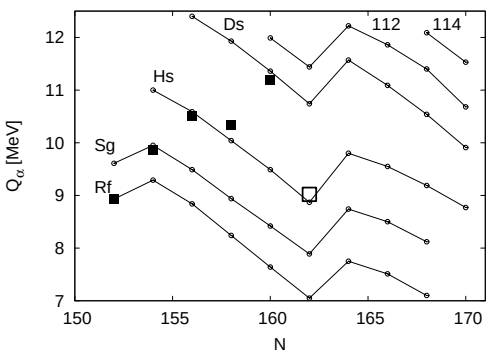

Figure 1: Q_α values from theoretical calculations and experimental data; the value for ^{270}Hs (open square) is from this work.

In [3, 4], two decay chains were tentatively assigned to ^{270}Hs based on the previously reported decay properties. However, this tentative assignment was not conclusive as the reported ^{270}Hs decay chains, consisting of α–α–SF decay sequences, were very similar to the ones assigned to ^{269}Hs. In this work we report the first synthesis and identification of the even-even nucleus ^{270}Hs and the observation of its α–decay to ^{266}Sg [5]. Contrary to earlier reports [6,7] ^{266}Sg is not decaying by α–particle emission but by SF with a relatively short half-life.

A rotating ^{248}Cm target was bombarded with a $^{26}Mg^{5+}$ ion beam at the UNILAC, GSI Darmstadt. Beam energies of 145 MeV and 136 MeV (center of target) were used to produce Hs isotopes in the 5n and 4n evaporation channels, respectively. Typical beam intensities on target were 0.8 particle-μA. Integrals of 1.46×10^{18} and 2.02×10^{18} $^{26}Mg^{5+}$ ions were accumulated at 145 and 136 MeV, respectively. An efficient rapid chemical separation method [3] together with the on-line detection system COMPACT [8] was used for the isolation and detection of Hs.

Seven decay chains attributed the decay of ^{269}Hs are described in [9]. Four α–SF chains exhibit a narrow distribution of α–particle energies with E_α=8.89±0.03 MeV. They were terminated by SF with an average lifetime of ~0.5 s. Three out of four chains were detected at the lower beam energy at the expected maximum of the 4n evaporation channel. This sequence is different from all known decay patterns. As the detection efficiency for an α-particle is 80%, there is a less than 0.1% probability that these observed α–SF chains are incomplete α–α–SF ones, where always the same α–particle was missed. We assign these four chains to the decay of the new isotope ^{270}Hs and its daughter ^{266}Sg. From the measured data Q_α=9.02±0.03 MeV and a half-life of 22 s for ^{270}Hs were derived. Measured decay properties of the observed isotopes are summarized in Tab 1.

Tab.1. Decay properties of Hs and Sg nuclei.

Z	*A*	Decay mode	Half-life	E_α
108	269	α	–	9.07±0.03 8.92±0.03
108	270	α	–	8.89±0.03
106	265	α	$14.9^{+9.1}_{-4.1}$ s	8.68±0.04
106	266	SF	444^{+444}_{-148} ms	

The α–decay energy of doubly-magic ^{270}Hs is in good agreement with theoretical calculations, which take into account shell stabilization of deformed nuclei. ^{270}Hs is the first experimentally observed even-even nucleus on the predicted N=162 neutron shell.

References

[1] A. Sobiczewski, Acta Phys. Pol. B 29, 2191 (1998).
[2] Z. Patyk *et al*., Nucl. Phys. A 533, 132 (1991).
[3] Ch.E. Düllmann *et al*., Nature 418, 859 (2002).
[4] A. Türler *et al*., Eur. Phys. J. A 17, 505 (2003).
[5] J. Dvorak *et al*., Phys. Rev. Lett. 97, (2006) 242501.
[6] Yu.A. Lazarev *et al*., Phys. Rev. Lett. 73, 624 (1994).
[7] A. Türler *et al*., Phys. Rev. C 57, 1648 (1998).
[8] J. Dvorak *et al*., GSI Report 2004, p. 183.
[9] J. Dvorak *et al*., GSI Report 2004, p. 71.

Radiochemical search for ^{268}Hs with COMPACT

J. Dvorak[1], R. Krücken[1], Z. Novackova[1], R. Schuber[1], A. Semchenkov[1,2], A. Türler[1], A. Yakushev[1], W. Brüchle[2], Ch.E. Düllmann[2], E. Jäger[2], M. Schädel[2], B. Schausten[2], E. Schimf[2], Z. Qin[2,3], R. Dressler[4], A. Kuznetsov[5], M. Chelnokov[5], K. Eberhardt[6], P. Thörle[6], and Y. Nagame[7]

[1]TU München, Germany; [2]GSI, Darmstadt, Germany; [3]IMP, Lanzhou, P. R. China; [4]PSI, Villigen, Switzerland; [5]JINR, Dubna, Russian Federation; [6]U Mainz, Germany; [7]JAEA, Tokai-mura, Japan

A rapid radiochemical technique has successfully been used to discover doubly-magic ^{270}Hs [1]. The experimental setup, based on the detection system COMPACT is described in [2]. Several successful experiments were done in the last three years [1, 3] at GSI. Here we present our recent experiment aimed at the chemical separation of ^{268}Hs, produced in the nuclear reaction ^{248}Cm(^{25}Mg, xn)$^{273-xn}$Hs. The nuclide ^{268}Hs is unknown. It is expected to decay by α-particle emission with a half-life of less than one second to 37-ms spontaneously fissioning ^{264}Sg. To be sensitive to such short-lived isotopes, the overall transport time of produced Hs nuclides from the target to our detection system was minimized and a value of less than 1 s was reached.

There are two main contributions to the overall transport time. These are the time necessary for (i) completion of the chemical reaction and (ii) transport of the nuclides. Chemical reactions can be accelerated by increasing the temperature. In our experiment, the recoil chamber and quartz filter, where oxidization occurs, were heated to 400 °C and 650 °C, respectively. To minimize the transport time, the distance between the recoil chamber and the detector setup has to be minimized. Because of the high radiation close to the target during irradiation, the chemical detection system is usually placed in separate room behind a thick concrete wall. This, however, increases the length of the transport line up to tens of meters, preventing the investigation of short-lived nuclei. Placing the COMPACT, surrounded by shielding, directly in the irradiation cave has allowed reduction of the transport line length to 4 m. This corresponds to a transport time of less than one second. The shielding of the COMPACT consisted of a 40-cm thick concrete wall, a 15-cm thick boron-paraffin layer, and a 7-cm thick Pb layer. This shielding proved to be satisfactory, as no electronic noise was observed and the background of events detected in the detector did not increase significantly compared with previous studies, when COMPACT was located outside of the irradiation cave. The experiment was operated remotely from the experiment control room.

With beam intensities of 1.5 particle-μA, an integral of 3.61×10^{18} particles was accumulated during nine days of irradiation. The lab-frame beam energy in the center of the target was 140 MeV, where HIVAP predicts the maximum cross section of $\sim$1 pb for ^{268}Hs. No events that could be attributed to the decay of ^{268}Hs or ^{269}Hs were detected.

For cross section calculations of the short-lived ^{268}Hs, knowledge of the mean transport time is necessary. This was estimated from measurements with short-lived Os isotopes. In bombardments of an enriched ^{152}Gd target with a chopped (1 s on/59 s off) ^{25}Mg beam, the isotopes ^{171}Os and ^{172}Os with half-lives of 8.3 and 19.2 seconds, respectively, were produced. The time dependence of the counting rate of the ^{171}Os and ^{172}Os decays was examined and is presented in Figure 1.

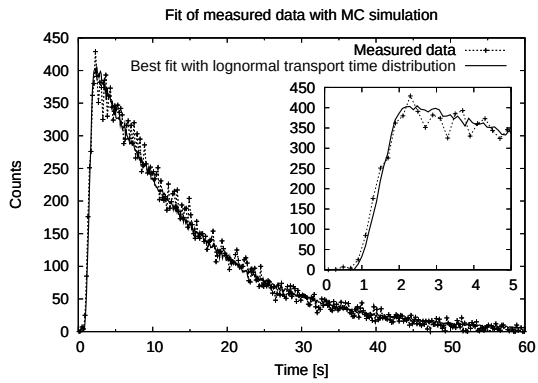

Figure 1: Time dependence of detected $\alpha-$decays of ^{171,172}Os in the detector and fit from a Monte Carlo simulation. Zero corresponds to the start of the irradiation.

A Monte Carlo simulation was performed, modelling the transport of the activity in the transport line. A lognormal shape of the transport time distribution was deduced from this model. We determined the parameters from a best fit procedure of the observed time dependence of detected $\alpha-$decays. A mean transport time of $\sim$ 1 second was calculated, in agreement with expectations.

Because the transport time is of the same order as the expected half-live, the overall detection efficiency depends on the half-life of the nuclide. A one event cross section limit of 0.8 picobarn (63.2% c.l.) has been reached for Hs isotopes with an assumed half-life of one second in this experiment. We conclude that the chemical approach allows the investigation of Hs isotopes with a half-life of one second below the one picobarn level.

References

[1] J. Dvorak *et al.*, Phys. Rev. Lett. 97 (24) (2006) 242501.

[2] J. Dvorak *et al.*, GSI Sci. Rep. 2004, p. 183

[3] J. Dvorak *et al.*, GSI Sci. Rep. 2004, p. 71

Search for the "Missing" α-Decay Branch in ^{239}Cm

Z. Qin[1,3], D. Ackermann[1], W. Brüchle[1], F.P. Hessberger[1], E. Jäger[1], P. Kuusiniemi[1], G. Münzenberg[1], D. Nayak[1], E. Schimpf[1], M. Schädel[1], B. Schausten[1], , A. Semchenkov[1] B. Sulignano[1,2], X.L. Wu[1,3], K. Eberhardt[2], J.V. Kratz[2], D. Liebe[2], P. Thörle[2], Yu. N. Novikov[1, 4]

[1]GSI, Darmstadt, Germany, [2]Johannes Gutenberg-Universität, Mainz, Germany,
[3]IMP, Lanzhou, P.R. China, [4]Petersburg Nuclear Physics Institute, Gatchina, Russia

Our first series of experiments yielded an upper limit of $3x10^{-5}$ for the α-decay branch of ^{239}Cm [1,2] produced in the ^{12}C + ^{232}Th reaction. In these experiments, only α-spectra were evaluated as the γ-spectra were not clean enough to identify γ-lines from the decay of ^{239}Cm or its daughter ^{239}Am. Due to the use of 3.9 µm thick Cu catcher foils in a rotating catcher wheel behind a rotating target setup, γ-spectra dominantly showed lines from the decay of ^{153}Sm, ^{150,151}Pm, and ^{147,149}Nd. Those homologous rare earth elements, produced in fission with cross sections of about 5 mb, were stopped in the Cu catcher but were only partly separated in the chemical procedure. ^{71,72}As and ^{69}Ge, produced in reactions of ^{12}C with the Cu catcher, created an additional background.

In recent experiments, 1 µm thick Cu foils produced by the GSI target laboratory were used in 120-150 mbar He in stationary target-catcher setups. These foils are sufficiently thick to stop all fusion products (0.3 µm range) but thin enough to let most fission products pass (3-6 µm range) and to minimize interaction of the ^{12}C beam with the Cu catcher. This provided a breakthrough and allowed identifying the 188 keV γ-line assigned to ^{239}Cm [3] as well as γ-lines of the EC-decay daughter ^{239}Am. ^{239}Cm was produced in ($\leq$ 0.4 μA_{part}) ^{12}C + ^{232}Th reactions. A faster and more efficient chemical separation procedure was applied [4]. Instead of two different elution media with 0.25M and 0.30M α-HIB, the whole separation was conducted with 0.40M α-HIB at pH=4.6. Figure 1 shows improved elution curves from a cation exchange resin. Since this time all samples contained only small amounts of Sm and Pm, we added ^{244}Cm as a tracer making the yield determination even more reliable. Overall yields varied between 75% and 90%.

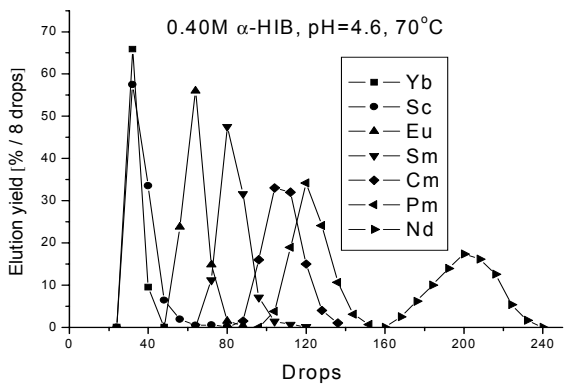

Figure 1: Chromatogram with tracer elements. Drops 80 to 150 were selected as the Cm fraction.

We performed irradiations at 74, 70, and 66 MeV ^{12}C energies in the middle of the 360 µg/cm^2 Th targets. 74 MeV was selected because at this energy, HIVAP calculations predict the highest ^{239}Cm cross section. However, as we cannot exclude that α-events observed around 6.4 MeV stem from tailing of the 6.52 MeV α-lines of ^{238}Cm, which is abundantly produced at this energy and which has a similar half-life, no attempt was made to determine an α-decay branch in ^{239}Cm from this experiment.

70 MeV was selected because interfering ^{238}Cm should be produced less by a factor of 80, whereas production of ^{239}Cm should drop by a factor of 1.7 only. Finally, 66 MeV was chosen because ^{240}Cm has its production maximum there. This allowed to check if events around 6.4 MeV can be produced by α-β-pileup. Though the ^{240}Cm activity was higher than in the other experiments, not a single α could be detected between 6.35 MeV and 7.0 MeV during the first day of measuring time. The 188 keV γ-line, assigned to ^{239}Cm [3], was measured in experiments at 70 and 74 MeV irradiation energy. In addition, the 229 and 278 keV γ-lines of the daughter product ^{239}Am were detected. Since at 70 MeV irradiation energy, HIVAP predicts a factor of 2000 lower cross section for ^{239}Am as compared to ^{239}Cm, we feel safe to attribute all measured ^{239}Am to ^{239}Cm daughters. As the absolute intensity of the ^{239}Cm 188 keV γ-line is not known, we started our analysis with the assumption of 100% abundance. Based on this, we calculated how much ^{239}Am is produced in the ^{239}Cm EC-decay. As the experimentally observed amount of ^{239}Am at 70 MeV is a factor of 2.8±0.8 higher, we concluded that the 188 keV γ-line has an intensity of about 36%. The error (90% c.i.) includes uncertainties in the half-life of ^{239}Cm between 2 and 4 h and in the Cm-Am separation yield between 30% and 70%. The 70 MeV experiments yielded five α-decays between 6.36 and 6.45 MeV within the first 10 h of measurement. An average background of 0.625 events, determined in a long background measurement without a sample, was subtracted (note that the background with a sample could be somewhat higher). This yields a ratio of α-decay to EC decay of $\leq 1.9x10^{-5}$ (90% c.i.) and $\leq 1.4x10^{-5}$ (68.3% c.i.) for the decay of ^{239}Cm.

References

[1] Z. Qin et al., GSI Scientific Report 2004, p.190
[2] Z. Qin et al., GSI Scientific Report 2005, p.197
[3] E. Browne, Nucl. Data Sheets 98, 665 (2003).
[4] Z. Qin et al., GSI Scientific Report 2004, p.191.

Magnetic Field Simulations of the TASCA Magnets

A.Belov[1], T. Belyakova[1], M. Karpakova[1], V. Kukhtin[1], E. Lamzin[1], S. Sytchevsky[1], W. Brüchle[2], E. Jäger[2], E. Schimpf[2], M. Schädel[2], A. Semchenkov[2,3], C. Mühle[2], F. Klos[2], A. Türler[3], A. Yakushev[3]
[1]Efremov Institute, St. Petersburg, Russia, [2]GSI, Darmstadt, Germany; [3] TU Munich, Garching, Germany

To optimize and improve the new separator **TASCA** (**T**rans**A**ctinide **S**eparator and **C**hemistry **A**pparatus) [1], 3D magnetic field measurements and simulations of the TASCA dipole magnet (C-type) and quads were performed.

All field calculations were made with the finite-element code KOMPOT [2, 3]. KOMPOT simulates various 3D stationary field distributions. The code has rich graphic tools (Fig.1, 2) for building finite-element models. The postprocessor is capable to produce distributed and integral magnetic characteristics. For example, field maps or magnetic fluxes and EM forces for a given region are created. The graphical interface makes it possible to visualize calculated field distributions in any region of interest and to compare it with data measured at the GSI.

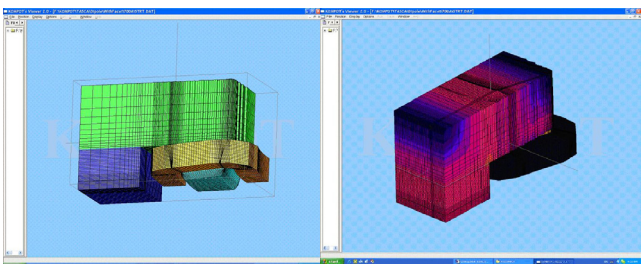

a) b)

Figure 1:a) 3D-graphic presentation of the C-magnet; b) Magnetic field distribution on the magnet surface.

The model developed for the C-magnet was reduced to one quarter of the magnet (Fig.1). The mesh had ≈0.5M nodes. More than 30 runs were carried out: a) with currents varying from 50 A to 700 A; b) with 700 A to optimize pole shapes; c) for the optimized poles shape with the currents up to 850 A.

Comparisons between measurements and simulations show good agreement. Computational model and magnetic measurement data allow calculating magnets with required magnetic field distributions. In addition, the synergism between model calculation and measurement does yield much better and much more economic results in magnet design and optimization. The magnetic field simulations provide the 3D field map in the working area of the dipole magnet and the corresponding optical characteristics for the entire envisioned induction (current) range.

In addition 3D field simulation has been performed for the quadrupoles [2, 3] in order to obtain magnetic field maps for (i) a single quadrupole magnet, (ii) two quads turned by 90 degrees relative to each other around their common axis and (iii) two quads taking into account the magnetic permeability of the duct and a valve (Fig.2).

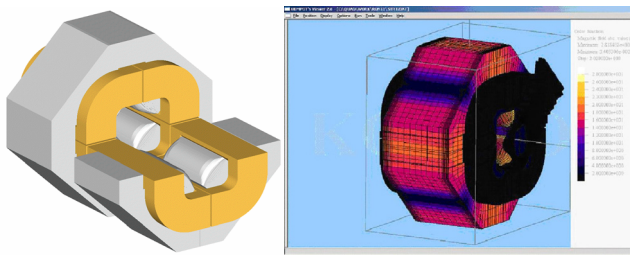

a) b)

Figure 2: a) Computational model of a doublet of quads. b) Magnetic field distributions on the surfaces of a single quadrupole with a valve.

The calculation mesh of doublet of quads contains ≈0.5M finite elements (Fig.2a). This model was used as reference to calculate the field for a set of coil currents from 200 to 650 A. The FE model allowed calculation of a precise field map for two nearby quads. The 3D field distribution was obtained in each quad, in between quads and in the region from the quad edge to the external boundary. The field of a single quad can be assessed assuming negligible interference of the magnet ends.

The second calculation model accounts for the influence of the duct and the vacuum valve (Fig.2b). Direct subtraction of field maps obtained with two different models (with and without the duct) using the same FE mesh revealed minor deviations of field and field gradient in the working area of the quads. Both the field and gradient deviations were found to be below 0.05%. As the vacuum valve introduces an asymmetry in the magnet system, an FE mesh should be built over the entire R^3 area that necessitates significant increase in computational resources. To study the influence of the valve a dedicated FE model was developed. The model has $>0.4\cdot10^6$ finite elements. From the measured data provided by GSI, the vacuum valve permeability was taken constant as $\mu_{VL}=1.4$. An additional calculation at $\mu_{VL}= 1.0$ gave assessment for the vacuum valve influence. The resultant field deviations with valve and without valve in the working area were as low as $\Delta B = 2$ G, and deviations of the field gradient were within 0.1%.

The calculated field maps were used as inputs for the TASCA trajectory analysis.

References

[1] M. Schädel et al., GSI Scientific Report 2005, p. 262.
[2] A.Belov, et al., KOMPOT/M 1.0: computer code for 3D simulation of magnetostatic field, RF Registration Certificate N2003612492
[3] N.I.Doinikov, et al., On computation of 3-D magnetostatic fields of electrophysical apparatus magnet systems, IEEE Transact. On Magnetics, v.28, No.1, January 1992, pp.908–911C.

TASCA Monte-Carlo Simulation Program and Program for Studying Ion-Optical Parameters of Dipole and Quadrupole Magnets from Field Maps

K.E. Gregorich[1], A. Semchenkov[2,3], T. Belyakova[4], V. Kukhtin[4], E. Lamzin[4], S. Sytchevsky[4], W. Brüchle[2], Ch. E. Düllmann[2], E. Jäger[2], E. Schimpf[2], M. Schädel[2], J. Dvorak[3], A.Türler[3], A. Yakushev[3]

[1]LBNL, Berkeley, U.S.A., [2]GSI, Darmstadt, Germany; [3]TUM, Garching, Germany; [4]Efremov Institute, St. Petersburg, Russia

Ion-optical calculations are often performed as a first step when designing magnetic systems. As a second step Monte-Carlo simulations are performed of **EV**aporation **R**esidue (**EVR**) trajectories through the separator, varying parameters like target thickness, gas pressure and magnet field. Such a program is very useful to optimize all system parameters and to plan and to prepare experiments.

The new **T**ASCA Monte-Carlo **SIM**ulation program (**TSIM**) is based on the **B**erkeley Gas-filled Separator **SIM**ulation program (**BSIM**) [1]. TSIM uses magnetic field maps of the TASCA dipole and quadrupole magnets, simulated by the program KOMPOT [2].

Trajectories are simulated in three steps. As a first step the event generator code **TRIMIN** (**TRIM IN**put code) generates EVRs in the target material. The following tools and input parameters are used to characterize these EVRs: a) the energy loss for the primary beam in the target material is calculated by SRIM [3] or LISE [4]; b) Gaussian type distributions with realistic widths are assumed for the primary beam energy and angular spread; c) a beam energy is randomly chosen within the excitation function for every EVR birth. A depth in the target material corresponding to this energy is determined; d) initial position of compound nuclei trajectories and recoil energies are simulated. They are modified by neutron evaporation with a kinetic energy of ~2 MeV emitted in random direction.

As an output TRIMIN gives recoil energies, position distributions and angular distributions for the EVRs inside the target, which are used as an input for the second step of the simulation process. Here EVRs are transmitted from their initial target position through remaining target material using the SRIM code [3]. The output file with recoil energy distributions and angle distributions of EVRs exiting the target serves as an input file for the last step of the TSIM calculation. This part of the simulation program, based on the original BSIM program, was adapted for TASCA taking especially into account the TASCA geometry like target position, dimensions of ducts and the detector position with variations of the detector size. Transmitting EVRs through the gas-filled separator, straggling, energy loss and charge-exchange are taken into account.

Fig.1 shows simulated trajectories of EVRs from the Ca + U reaction with TASCA; i.e. the dipole magnet followed by the first horizontally focusing quad and the second vertically focusing one; see refs. [5, 6] for more information. TSIM can be used to optimize target thickness or duct shapes and it can also be used to find the best gas pressure for a specific reaction and magnet settings.

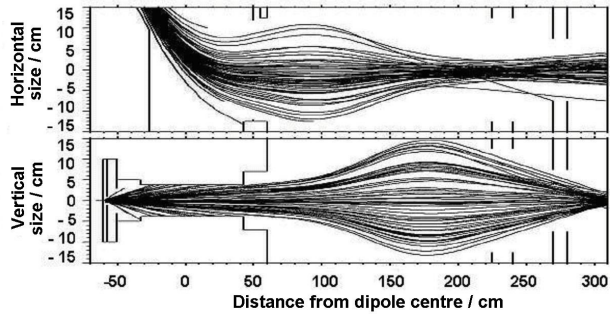

Figure 1: EVR trajectory simulations in TASCA projected in the horizontal (upper panel) and vertical (lower panel)

The newly developed KOMPOT [2] postprocessors allow calculating ion-optical parameters of the dipole magnet (**MOPS** code – **M**agneto-**O**ptical **P**arameters **S**imulation) and of quads (MOPS2 code) from field maps of the working area of the magnets. As program input data we have used the magnetic field map. The dipole magnet parameters calculated by MOPS are: a) magnetic field distribution and its series expansion in the medium plane; b) magnetic length distribution and its series of expansion in dependence on radius c) bending angle for the central trajectory and bending angle distributions at the entry and the exit; d) series of expansion for bending angles; g) edge angle distribution and the series of expansion at the entry and at the exit of the magnet; e) field distribution along the central trajectory; f) series of expansion for edge field at the entry and at the exit of the magnet.

MOPS2 allows determining ion-optical parameters of quads, based on calculated or measured distribution of magnetic field in the working area of the quads, such as: a) magnetic field and field gradient in the middle point; b) magnetic field and gradient distribution in the medium plane; c) series of expansion for field and gradient distributions; d) magnetic length for the central trajectory; e) magnetic length distribution depends on extension from the central axis; f) series of expansion for magnetic length; h) field gradient distribution on the central trajectory.

References

[1] K.E. Gregorich et al. Eur. Phys. J. A 18, 633 (2003).
[2] A. Belov et al., contributions to this report.
[3] J.F. Ziegler, Nucl. Instr. and Meth. in Phys. Res. B 219, 1027 (2004).
[4] O.Tarasov, D.Basin, LISE++ home page. ftp://ftp.nscl.msu.edu/pub/lise
[5] A. Semchenkov et al., contributions to this report.
[6] Ch.E. Düllmann et al., contributions to this report.

First TASCA Commissioning Experiments in the Small Image Size Mode

A. Semchenkov[1,2] , D. Ackermann[1] , W. Brüchle[1] , Ch. E. Düllmann[1] , E. Jäger[1] , E. Schimpf [1] , M. Schädel[1] , J. Dvorak[2] , R.Schuber[2] , A. Türler[2] , A. Yakushev[2] , K. E. Gregorich[3], M. Leino[4] , J. Uusitalo[4], J.-P.Omtvedt[5]

[1]GSI, Darmstadt, Germany; [2] TU Munich, Garching, Germany; [3] LBNL, Berkeley, U.S.A.; [4] JYFL, Jyväskylä, Finland; [5]University of Oslo, Norway

Ion-optical calculations with the code **TRANS**PORT (**TRANS**) (test reaction 235 MeV ^{48}Ca + $^{238}UF_4$ (0.5 mg/cm^2) ==> ^{283}112) were used as a first step to optimize and to built TASCA [1,2]. As a next step the **T**ASCA Monte-Carlo **SIM**ulation program (**TSIM**) was developed and was applied [3] showing good agreement with previous results. Results for TASCA in the **S**mall **Im**age Size **M**ode (**SIM**) are compared in Table 1. Smaller values obtained with the more realistic TSIM are mainly due to straggling and to charge-exchange processes in the gas. A typical product distribution in the focal plane is shown in Figure 1. Based on these simulations we opted for a window with 3 cm in diameter for the SIM **R**ecoil **T**ransfer **C**hamber (**RTC**) [4].

Table 1: Result of TRANSPORT ion-optical calculations and TASCA Monte-Carlo simulations for products from the Ca + U model reaction; see text for details.

Model	TRANS	TSIM
Solid angle / msr	≈ 4.3	≈ 4.2
Transmission / %	≈ 40	≈ 35
Horizontal image size / cm	≈ 3	≈ 4
Vertical image size / cm	≈ 3	≈ 4
Image area / cm^2	≈ 7	≈ 13

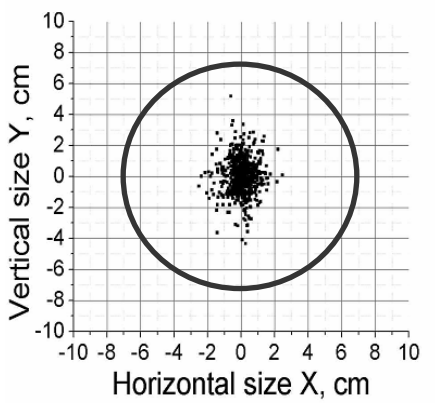

Figure 1: Evaporation residue distribution in the TASCA focal plane obtained from a Monte-Carlo simulation of the ^{48}Ca + ^{238}U model reaction. The circle depicts the 15 cm diameter RTC flange.

First TASCA commissioning experiments in the SIM were successfully performed with the reaction 230 MeV ^{54}Cr + ^{nat}Gd (0.6 mg/cm^2) ==> $^{208-211}$Ra. The Ra distribution in the (8x3.6) cm^2 16-strip silicon **F**ocal **P**lane **D**etector (**FPD**) is shown in Figure 2. Without any significant influence on the transmission the distribution maximum was found 0.5 cm to the left and 0.5 cm below the FPD center position. A comparison between Monte-Carlo simulated and experimental data is shown in Figure 3. The shapes of distributions from the experiment and from TSIM are the same; the smaller number of alphas as compared with recoils is due to a lower efficiency. The 0.5 cm horizontal shift corresponding to ≈ 0.5% in rigidity shows that the dipole magnet settings were slightly off. However, a 0.5% deviation does not influence the experimental result drastically as the momentum acceptance of TASCA in SIM is ± 10% [5]. In general, we observe an excellent agreement between theoretical model calculations and experimental data.

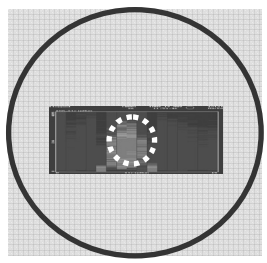

Figure 2: $^{208-211}$Ra distribution (color coded) in the FPD. The reaction was ^{54}Cr + ^{nat}Gd. The circle depicts a 15 cm diameter flange, the dashed line the ø 3 cm RTC window.

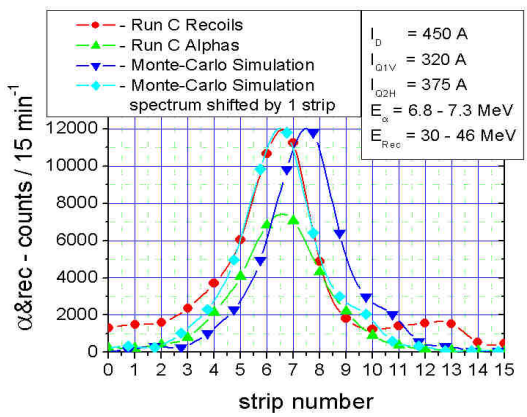

Figure 3: Results from the ^{54}Cr + ^{nat}Gd ==> $^{208-211}$Ra test reaction compared with a Monte-Carlo simulation. Shown is the horizontal distribution in the FPD.

References

[1] A. Semchenkov et al., GSI Scientific Report 2004, p. 332.
[2] M. Schädel et al., GSI Scientific Report 2005, p. 262.
[3] K.E. Gregorich et al., contribution to this report.
[4] Ch.E. Düllmann et al., contribution to this report.
[5] A. Semchenkov et al., contribution to this report.

TASCA as a Preseparator: Recoil Transfer Chamber Commissioning

Ch.E. Düllmann[1,*], D. Ackermann[1], W. Brüchle[1], F.P. Heßberger[1], E. Jäger[1], J. Khuyagbaatar[1], M. Schädel[1], B. Schausten[1], E. Schimpf[1], H.-J. Schött[1], A. Semchenkov[1,2], J. Dvorak[2], A. Gorshkov[2], R. Schuber[2], A. Türler[2], A. Yakushev[2], K. Eberhardt[3], H. Hummrich[3], J.V. Kratz[3], J.P. Omtvedt[4], K. Opel[4], J.M. Gates[5,6], K.E. Gregorich[5], R. Dressler[7], R. Eichler[7,8], Z. Gan[9]

[1]GSI, Darmstadt, Germany; [2]TU Munich, Garching, Germany; [3]U Mainz, Germany; [4]U Oslo, Norway; [5]LBNL, Berkeley, CA, USA; [6]UC Berkeley, CA, USA; [7]PSI, Villigen, Switzerland; [8]U Berne, Switzerland; [9]IMP Lanzhou, P.R. China.

One of the main foreseen applications of the gas-filled TransActinide Separator and Chemistry Apparatus (TASCA) [1] recently installed at GSI is its use as a physical preseparator for chemistry experiments [2,3]; see configuration shown in Figure 1. EVaporation Residues (EVRs) are guided to the focal plane of the separator where they penetrate a thin window separating TASCA's low pressure regime from the 1 bar regime in the Recoil Transfer Chamber (RTC) in which the EVRs are thermalized. Construction of the interface between these two regimes, the RTC window, presents a technical challenge as the following requirements have to be met: i) the window has to withstand the high pressure difference, ii) it has to be gas tight, iii) it has to be so thin that slow EVRs from asymmetric hot fusion reactions can penetrate into the RTC which necessitates using a support grid, and iv) the transparency of this grid has to be high to provide maximum transmission. As has been described before [4] two different ion optical modes are available at TASCA. For both TASCA modes, the Small Image Mode (SIM) as well as the High Transmission Mode (HTM), flanges accommodating RTC windows that match the corresponding image sizes in the focal plane [4] have been built at the TU Munich. Windows made from Mylar foils with thicknesses of 3.3 µm and less are supported by a honeycomb 80%-transparency stainless steel grid. Two RTCs were built, the HTM one (140x40 mm^2) at U Mainz and the SIM one (30 mm ∅) at U Oslo. Both are built in a modular way that allows easy changes of depth and gas flow pattern, see Fig. 2 for the HTM RTC. Additionally, catcher foils can be installed and removed quickly to determine the activity entering the RTC. First commissioning took place in Oct./Nov. 2006 in a ^{40}Ar beamtime.

The HTM RTC was tested with products of the reaction ^{nat}Gd(^{40}Ar,xn)$^{\sim 194}$Pb which were transported with a He/KCl gas-jet to a radiochemical lab located about 13 m away. Aerosol particles were collected on a glass fiber filter that was placed in front of a low energy photon counter for γ counting. Unlike in experiments without preseparation, where the γ spectrum was dominated by lines from unwanted isotopes such as ^{49}Cr or ^{43m,44}Sc produced in reactions of the beam with various parts of the target setup [5], in these tests only γ lines from Pb isotopes and their daughters could be identified, proving the advantage of preseparation. The SIM RTC was tested with short-lived partially α-decaying Hg isotopes from the ^{144}Sm(^{40}Ar,xn)$^{184-x}$Hg reaction. Preseparated Hg atoms were transported with a pure He jet to the Cryo On-line Multidetector for Physics And Chemistry of Transactinides (COMPACT) [6] that registered their α-decay. Only α lines from Hg isotopes and their daughters were visible.

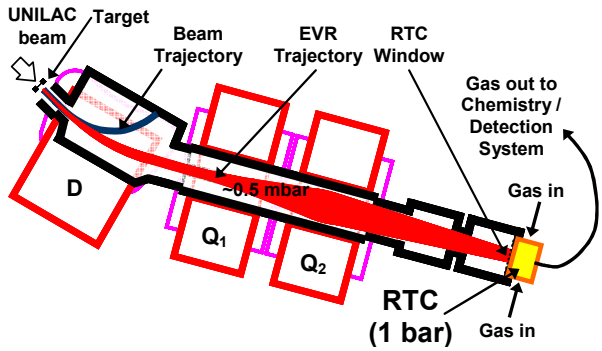

Figure 1: TASCA in the preseparator configuration

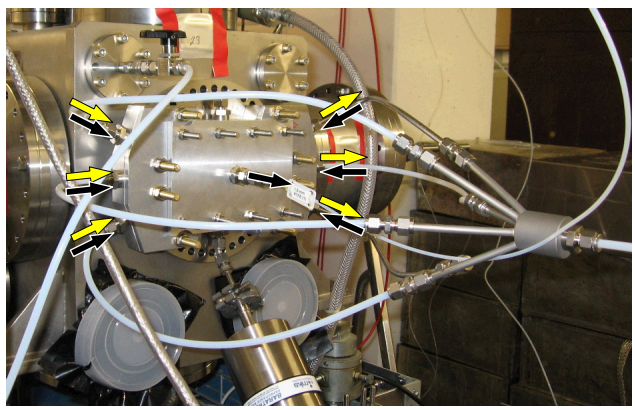

Figure 2: The HTM RTC mounted at TASCA. The two gas flow regimes are indicated by light and dark arrows.

References

[1] M. Schädel *et al.*, GSI Sci. Rep. 2005, Report 2006-1, 2006, p. 262; see also http://www.gsi.de/TASCA.
[2] Ch.E. Düllmann *et al.*, NIM. **A551** (2005) 528.
[3] J.P. Omtvedt *et al.*, J. Nucl. Radiochem. Sci. **3** (2002) 121.
[4] A. Semchenkov *et al.*, GSI Sci. Rep. 2004, Report 2005-1, p. 332.
[5] H. Hummrich, Doctoral thesis, U Mainz, 2006.
[6] J. Dvorak *et al.*, GSI Sci. Rep. 2004, Report 2005-1, p. 183.

Acknowledgements: Thanks to Inge Mikalsen at the University of Oslo and the staff of the mechanical workshop at U Mainz for fast building of the two RTCs.

*c.e.duellmann@gsi.de

Fully Relativistic *ab initio* Dirac-Coulomb Calculations of Atomic Properties of Hg and Element 112

V. Pershina[1], A. Borschevsky[2], E. Eliav[2], and U. Kaldor[2]
[1]GSI, Darmstadt, Germany; [2]Tel Aviv University, Israel

For accurate calculations of the electronic structures of the heaviest elements and their compounds, where relativistic effects are of paramount importance, the usage of fully relativistic quantum chemical methods within 4-component approximation is highly desirable. Such a usage encountered until recently difficulties for many electron systems with respect to the treatment of the electron correlation. Meanwhile, this problem has been tackled, and the latest version of the DIRAC package offers possibility of calculating the electronic structure of the heavy element compounds using the DC (Dirac-Coulomb) Hamiltonian and treating the electron correlation at various levels of theory including the most sophisticated, such as the Coupled Cluster Single Double (Triple) excitations [CCSD(T)] [1]. Meanwhile, optimal basis sets for the heaviest elements have also been developed [2]. In this work, we have made use of the recent developments in the DIRAC program and calculated atomic properties of Hg and element 112 at a very advanced level of theory.

In the basis of the DC method lies the many-electron relativistic Dirac-Coulomb Hamiltonian

$$H_{DC} = \sum_i h_D + \sum_{i<j} 1/r_{ij} \,, \qquad (1)$$

where

$$h_D = c\vec{\alpha}\cdot\vec{p} + \beta c^2 + V_{nuc} \,. \qquad (2)$$

The atomic orbitals are four-component spinors

$$\phi_{nk} = \begin{pmatrix} P_{nk}(r) \\ Q_{nk}(r) \end{pmatrix} , \qquad (3)$$

where $P_{nk}(r)$ and $Q_{nk}(r)$ are large and small component, respectively. The Faegri uncontracted 26s23p18d13f5g2h basis set was used for element 112 [2], while the Visscher polarized basis sets was used for Hg [3].

The calculations of polarizability (α) were performed at the DC single reference CCSD(T) level with the use of the finite field method. The strengths of the field were chosen as 0.0001, 0.001 and 0.01 a.u. Results for α are given in Table 1 along with the other best calculated properties of Hg and element 112. These properties are needed for calculations of the energy of physisorption of these elements on inert surfaces like quartz or ice. Ionization potentials (IP) were calculated at the Dirac-Coulomb-Breit Fock-Space CC (DCB FSCC) level [4]. The atomic radii (AR) were determined as a half of the bond lengths R_e in the dimers Hg_2 and $(112)_2$ calculated using the 4c-DFT method (4-component Density Functional Theory method, the spin-polarized version, non-collinear approximation) [5,6]. Also, AR calculated on the basis of R_{max} of the outer electron orbital are similar [7]. Results are summarized in Table 2. For comparison, non-relativistic values are also given there.

Table 1. Atomic properties of Hg and element 112 needed for calculations of the energy of physisorption

Property	Hg		Ref.	element 112		Ref.
	nr	rel		nr	rel	
IP, eV	8.98	10.44	cal.[4]	8.25	11.97	cal.[4]
		10.43	exp.			
α, a.u.	57.83	33.94	this		25.38	this
		33.91	exp.[8]	74.66	25.8	cal.[9]
AR, a.u.	3.91	3.43	calc. [6]	4.32	3.26	[6]
		3.43	exp.[10]		3.22	[7]

One can see that agreement between the present calculated DC CCSD(T) and experimental value [8] for α(Hg) is excellent. This guarantees high accuracy of the results for element 112. With the newly calculated values of IP, α and AR, the energy of physisorption of Hg and element 112 on quartz was calculated as ΔH_{ads}(Hg) = -40.8 kJ/mol using a model of atom-slab interaction [7]. This value agrees very well with the measured ΔH_{ads}(Hg) = -42 ± 2 kJ/mol. Accordingly, ΔH_{ads}(112) = -45.8 kJ/mol. The obtained results indicate that relativistically, element 112 will be stronger adsorbed on inert surfaces than Hg. Non-relativistically, ΔH_{ads}(112) = -40.2 kJ/mol, which means that non-relativistically, element 112 would have been less strongly adsorbed than Hg. Thus, relativistic effects make element 112 less, not more, volatile than Hg upon adsorption on inert surfaces.

References

[1] DIRAC 04, written by H.J. Ja. Jensen, *et al*. (2004).
[2] K. Faegri, Theor. Chim. Acta, 105 (2001) 252 .
[3] L. Visscher, private communication.
[4] U. Kaldor and E. Eliav, Adv. Quant. Chem. 31 (1998) 313.
[5] J. Anton *et al*. Phys. Rev. A 69 (2004) 012505.
[6] J. Anton *et al.* Chem. Phys. 311 (2005) 97.
[7] V. Pershina and T. Bastug, Chem. Phys. 311 (2005) 139.
[8] D. Goebel and U. Hohm, J. Phys. Chem. 100 (1996) 7710.
[9] M. Seth, Doctoral Thesis, University of Auckland, 1998.
[10] R. D. See, *et al*. J. Chem. Phys. 88 (1988) 4650.

Non-collinear relativistic DFT calculations for small molecules with superheavy elements 111 and 113

C. Sarpe-Tudoran[1], J. Anton[1], B. Fricke[1], V. Pershina[2]
[1]Universität Kassel, Institut für Physik, 34109 Kassel, Germany; [2]GSI Darmstadt, Germany

During the last 15 years a lot of effort has been invested in the experimental investigation of the chemical behaviour of superheavy elements. One was able to show that the general feature of the elements 104 to 108 is to follow the trend of the continuation of the Periodic Table [1]. Details of the experimental methods and results can be found in the recent review by Schädel [2].

These elements are so heavy that any non-relativistic calculation can not give a realistic prediction so that a full relativistic calculation is the only appropriate method. Details of the theoretical methods and results can be found in the review by Pershina [3].

The theoretical as well as the experimental effort now concentrates on the investigation of the chemical behaviour of the elements beyond 110. In this region of elements up to now nothing is known experimentally. The nuclear chemists concentrate on the chemistry of element 112. They have set up an experiment to investigate the adsorption of this element relativ to the homologue Hg and the noble gas Rn. Positive results of those experiments have recenly been reported [4].

During the last years we have investigated theoretically the adsorption energy of element 112 and Hg on a Au surface. The newest results predict an adsorption energy of about 0.7 eV [5] which is somewhat below Hg but reasonably higher than that of Rn.

Because all these elements between 110 and 119 now become interesting, the effort from the theoretical side concentrates on the calculation of small molecules with superheavy elements. These kind of calculations together with analogue calculations for their homologues allow further predictions of their chemical behaviour. Various methods have been used so far. A few references including results for even heavier elements can be found in Ref. [6-10].

Our method of calculation is a full relativistic 4-component molecular code which now includes the possibility to calculate these systems in a non-collinear fashion. This method allows the magnetic density distribution to show in different directions in different regions of the molecule. This is connected with different total energies and thus modifies the binding energies of the molecules compared to the collinear method which is used up to now.

Table 1 lists the binding energies D_e, the bond distances R_e and frequencies ω_e for a few superheavy molecules with element 111 and 113. For the diatomic molecule $(111)_2$ the potential energy curve in different approximations is given in Fig. 1. These values are important ingredients in order to understand the chemical behaviour of these elements which are dominated by large direct relativistic effects for the $7p_{1/2}$ electrons and large spin-orbit splitting of the 7p-shell in the case of element 113.

Table 1: Bond lengths, R_e, bond energies, D_e, and vibration frequences, ω_e, for a number of diatomic molecules of elements 111 and 113

Molecule	R_e (Å)	D_e (eV)	ω_e (cm^{-1})
(111)H	1.52	2.85	2804
(111)F	1.94	2.65	597
(111)Au	2.57	1.34	150
(113)H	1.78	1.70	1606
(113)F	2.23	3.42	375

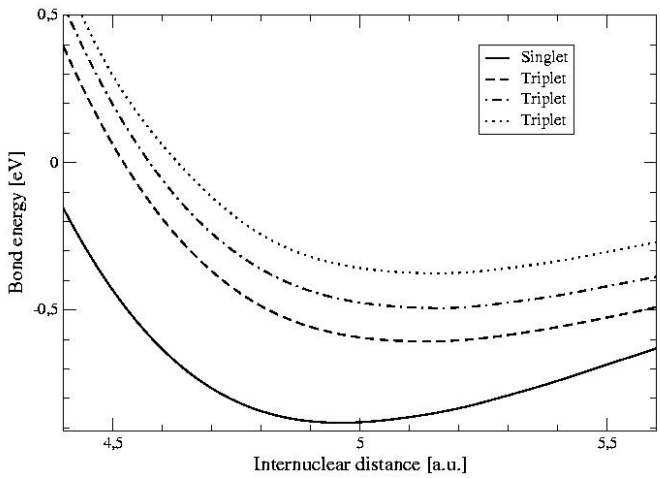

Figure 1: Potential energy curve for the system $(111)_2$ with a large triplet splitting

References

[1] B. Fricke, Struct. Bond. 21 (1975) 89.
[2] M. Schädel, Angew. Chem. Int. Ed. 45 (2006) 368.
[3] V. Pershina, Chem. Rev. 96 (1996) 1977.
[4] H. W. Gäggeler, R. Eichler PSI Press release 31. May 2006.
I5] C. Sarpe-Tudoran *et al*., J. Chem. Phys., submitted.
[6] M. Seth et al., Chem. Phys. Lett. 250 (1996) 461; J. Chem. Phys. 106 (1997) 3623; 109 (1998) 3935; 111 (1999) 6422.
[7] J. Anton *et al*., Chem. Phys. 311 (2005) 97.
[8] W. Liu *et al*., J. Chem. Phys. 116 (2002) 3626.
[9] N. S. Mosyagin *et al*., J. Chem. Phys. 124 (2006) 224302.
[10] C. S. Nash *et al*., J. Phys. Chem. A 103 (1999) 632.

Fully Relativistic Density-Functional-Theory Calculations for Intermetallic Compounds of Pb and Element 114

V. Pershina[1], J. Anton[2], B. Fricke[2]
[1]GSI, Darmstadt, Germany; [2]University of Kassel, Germany

Theoretical predictions of adsorption behaviour is very important for chemical identification of the heaviest elements using gas-phase chromatography techniques or electrochemical deposition from aqueous solutions. Earlier, we have predicted the adsorption enthalpy ΔH_{ads} and the temperature T_{ads} for element 112 with respect to that of Hg on gold (100) surface [1,2]. Recent experiments have confirmed theoretically predicted similarity of element 112 with Hg [3]. This work is an initial step in the long-term project on predicting adsorption behaviour of element 114 with respect to that of Pb on various metal surfaces. Here, we present calculations of binding energies D_e and other spectroscopic properties of the dimers of Pb and element 114 with group 10, 11 and 14 elements.

The calculations were performed using the 4-component Density Functional Theory method (4c-DFT) in the spin-polarized version (non-collinear approximation) [4]. The results for group 10 and 11 dimers are summarized in Table 1. Results for the dimers of Pb and element 114 with group 14 elements are given in Table 2.

Table 1. Optimized bond lengths (R_e), binding energies (D_e) and harmonic vibrational frequencies (w_e) for PbM and 114M, where M are group 10 and 11 elements

Molecule	R_e, a.u.	D_e, eV	w_e, cm^{-1}
PbNi	4.50	1.80	-
PbPd	4.73	1.95	201.77
PbPt	4.63	3.53	213.49
PbCu	4.80	1.60	-
PbAg	5.05	1.22	-
PbAu	4.99	2.15	152.73
114Ni	4.70	0.25	-
114Pd	5.08	0.79	137.82
114Pt	4.84	1.11	157.37
114Cu	5.20	0.47	-
114Ag	5.50	0.30	-
114Au	5.44	0.73	96.70

The results of Table 1 show that element 114 should form relatively strong bonding with the group 10 and 11 transition elements which is about 1 eV weaker than that of the corresponding Pb compounds. Bonding of both Pb and element 114 with Pt should be the strongest among these transition metals, while that with Ag should be the weakest. With group 14 elements (Table 2), Sn and Pb, element 114 should also form rather strong bonding, about 1 eV weaker than that of Pb. R_e of the 114 compounds are respectively longer. The bond in $(114)_2$ is stronger than the pure van der Waals one (Fig. 1).

Table 2. Optimized bond lengths (R_e), binding energies (D_e) and harmonic vibrational frequencies (w_e) for PbM and 114M, where M are group 14 elements

Molecule	R_e, a.u.	D_e, eV	w_e, cm^{-1}	Ref.
PbSn	5.50	2.93	-	this
PbPb	5.62	1.18	107	this
	5.53	0.86±0.01	110	exp. [5]
114Sn	5.80	1.83	-	this
114Pb	6.00	0.406	-	this
(114)(114)	6.60	0.13	26	this

The present results show similar trends for D_e, R_e, and w_e of PbM and 114M as a function of the second metal atom M. The trends in D_e for PbM are also similar to ΔH_{ads} of Pb on the corresponding metal surfaces [6]. The calculated D_e for the dimers can be used for first estimates of $\Delta H_{ads}(114)$ on the corresponding metal surfaces, as it was done for element 112 [7]. We share the opinion of [8] that the DFT results for various systems are systematic and offer consistent trends in properties.

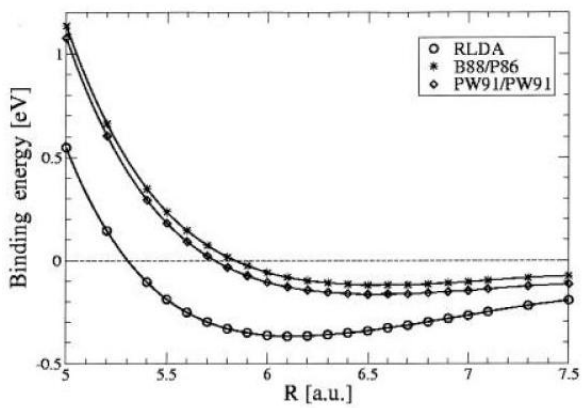

Fig. 1. Binding energy of $(114)_2$ as a function of the bond length R_e calculated in various DFT approximations. The highest level of approximation is B88/P86.

References

[1] V. Pershina *et al*. Nucl. Phys. A734 (2004) 200.
[2] C. Sarpe-Tudoran, J. Chem. Phys. submitted.
[3] H.W. Gäggeler, R. Eichler *et al*., PSI press release 31. May 2006.
[4] J. Anton *et al*. Phys. Rev. A 69 (2004) 012505.
[5] K. Pitzer *et al*. J. Phys. Chem. 86 (1982) 3068.
[6] F. Haenssler *et al*. PSI Annual report 2005, p. 3.
[7] V. Pershina *et al*. Chem. Phys. Lett. 265 (2002) 176.
[8] W. Liu *et al*. Adv. Quant. Chem. 39 (2001) 325.

Fast electrochemical deposition of Bismuth

H. Hummrich, J.V. Kratz
Institut für Kernchemie, Johannes Gutenberg-Universität Mainz, Germany

Fast electrochemical deposition is a promising method for the aqueous chemistry of the superheavy elements [1]. To perform electrodeposition experiments, the knowledge of basic electrochemical parameters like deposition potentials and the deposition velocity is necessary. To prepare experiments with element 115, its homolog Bi was investigated.

Experiments were performed with carrier free ^{212}Bi ($t_{1/2}$ = 60 min, E_γ = 727 keV). 1 ml of a solution of ^{212}Pb in 0.5 M HCl was obtained via the emanation method [2]. The solution was passed through a column (d = 8 mm, l = 15 mm) filled with the cation exchanger Dowex 50x8 (100 - 200 mesh). Under the given conditions ^{212}Pb is retained, whereas ^{212}Bi forms an anionic chloro complex and passes the column. A total elution volume of 2 ml was sufficient to elute 90 % of the activity. The eluate was evaporated to dryness and dissolved in 1 ml 0.1 M HCl.

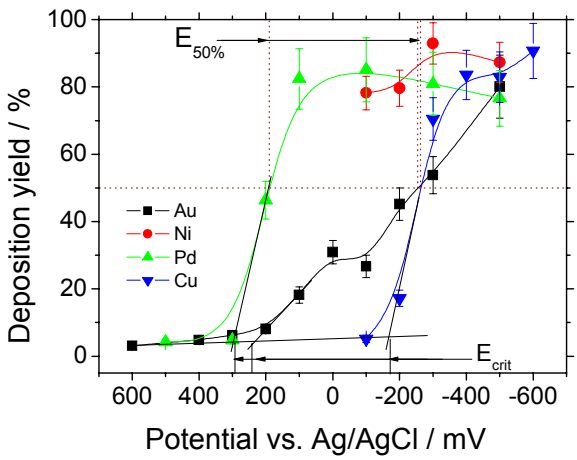

Figure 1: Potential curve for the electrochemical deposition of ^{212}Bi on various electrodes from 0.1 M HCl.

Electrochemical deposition experiments were performed using a potentiostatic setup with an electrochemical cell for fast electrochemical depositions [3]. The electrolyte was 0.1 M HCl, the working electrode material was varied. 1 ml electrolyte containing ^{212}Bi was electrolysed for 10 min, starting at the electrode rest potential which is obtained without applying external current. The deposited activity was measured for 1 min by γ-spectrometry and then electrolysis was resumed at a more negative potential etc.

Table 1: E_{crit} and $E_{50\%}$ values for the deposition of Bi from 0.1 M HCl on various electrode materials

Electrode	E_{crit}	$E_{50\%}$
Au	+250	-240
Pd	+290	+180
Cu	-180	-260
Ni	spontaneous deposition	

Potential curves for the deposition of Bi on Au, Ni, Pd, and Cu are shown in Fig. 1. The critical potential (E_{crit}), at which a significant deposition sets in, and the potential for the deposition of 50 % of the atoms in solution ($E_{50\%}$), are indicated. Numbers are given in Table 1. In agreement with literature [4], a nearly complete deposition of Bi on Ni is already observed at the rest potential (spontaneous deposition). For the deposition on Cu and Pd, s-shaped curves are obtained. The corresponding E_{crit} and $E_{50\%}$ values for the deposition on Pd and Cu differ more than 400 mV, meaning that the interaction of Bi and Pd is much stronger than the interaction of Bi with Cu. The deposition yield for the deposition on Au increases only slowly with decreasing potentials, resulting in a big difference in E_{crit} and $E_{50\%}$. This can be taken as is a sign for a hindrance in the electrodeposition process.

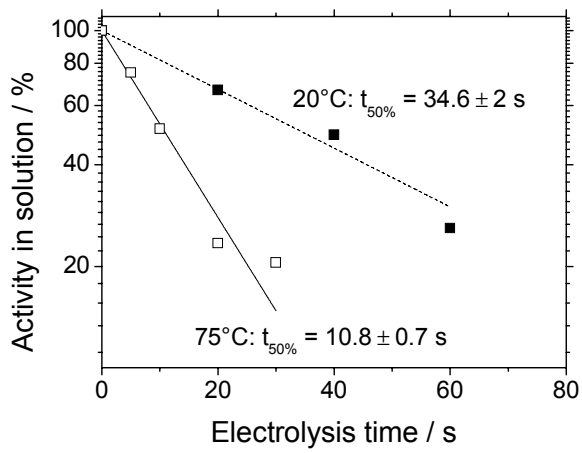

Figure 2: Electrodeposition velocity for the spontaneous electrodeposition of ^{212}Bi on Ni from 0.1 M HCl at room temperature (filled squares) and at 75 °C (open squares).

The electrodeposition velocity was determined for the spontaneous deposition of ^{212}Bi on Ni. Electrolysis was performed for a certain time and the deposited activity was measured. The time for the deposition of 50 % of the atoms in solution ($t_{50\%}$) was 35 s at room temeperature. This value could be lowered to 11 s by increasing the electrolyte temperature to 75 °C.

If isotopes of element 115 with a half-live in the range of 10 s were available, electrodeposition experiments should be performed with Ni or Pd electrodes.

References

[1] H. Hummrich et al., GSI Sci. Rep. 2005, p. 205
[2] H. Hummrich et al., Jahresbericht des Instituts für Kernchemie, Uni Mainz 2002, A10
[3] H. Hummrich et al., GSI Sci. Rep. 2004, p. 188
[4] S.C. Ehinger, R.A. Pacer, F.L. Romines, J. Radioanal. Nucl. Chem. Articles 98, 39 (1986)

Discriminant Analysis and Secondary Beam Charge Recognition

J. Łukasik, W. Trautmann, and the ALADIN Collaboration
GSI, Darmstadt, Germany

Discriminant analysis (DA) is a statistical technique for predicting a class membership for a set of vectors of observations, based on a set of variables known as predictors. The model is built on a set of observations for which the classes are known (a training set). For the training set, DA searches for a transform, or a reference frame, which makes the classes most distinct, i.e. which maximizes the between-class variance, $\boldsymbol{\sigma}_{inter}$, while minimizing the within-class variance, $\boldsymbol{\sigma}_{intra}$, (see e.g. [1]). Defining the within-class variance as a sum of individual covariance matrices for the N classes of interest: $\boldsymbol{\sigma}_{intra} = \sum_{k=1}^{N} \boldsymbol{\sigma}_k$ and the between-class variance as a complement: $\boldsymbol{\sigma}_{inter} = \boldsymbol{\sigma}_{tot} - \boldsymbol{\sigma}_{intra}$, where $\boldsymbol{\sigma}_{tot}$ is the covariance matrix for the whole training set, the searched for reference frame is found as a set of eigenvectors solving the generalized eigenvalue problem: $(\boldsymbol{\sigma}_{tot}^{-1} \cdot \boldsymbol{\sigma}_{inter})\vec{v} = \lambda\vec{v}$. The $N-1$ eigenvectors reduce the dimensionality of the problem and span the subspace in which the classes are best separated.

DA has a broad range of applications: from its pioneering application in plant taxonomy [2] through applications, e.g., in image recognition and marketing to those in nuclear physics [1, 3]. We found it also very well suited for recognizing the charge of secondary beams from the GSI fragment separator (FRS) used as projectiles in the S254 experiment [4]. In this experiment, a primary ^{142}Nd beam was used to produce the exotic ^{124}La and ^{107}Sn projectiles focused finally on the Sn targets in Cave B. In order to avoid background for the experiment from reactions up-stream, the amount of material along the beam path had to be minimized. In particular, ionization chambers, often used in secondary-beam experiments to determine the Z of the incoming beam, were not used in this experiment. The charge of the beam entering Cave B could only be measured for the projectiles which did not interact with the target, using the MUSIC IV tracking chamber down-stream of the ALADIN magnet. Those events (scaled down) were used as the training set. After realistic simulations of the beam transport, it was found that the most promising observable to determine the projectile Z could be the position of the beam at the target, measured with the position-sensitive plastic scintillator detector installed there for the tracking.

The upper part of Fig. 1 shows the position measured with the plastic scintillator at the target for non-interacting projectiles. The middle group contains all the La projectiles (Z=57), the left peak contains all the heavier and the right one all the lighter projectiles. The average efficacy of charge recognition using this method was found to be about 70%. For other "scalar" observables the efficacies are even lower, e.g., only about 30% using the energy loss in the position detector and only about 60% using the high-

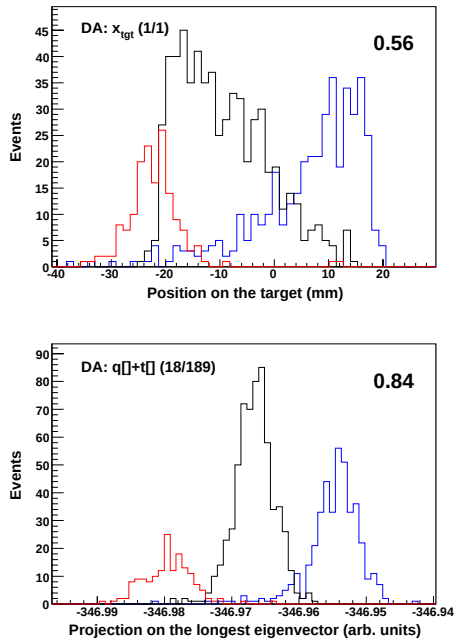

Figure 1: Charge distributions as obtained using the position of the beam at the target (top) and the DA with 189 dimensional input vectors of observations projected on the longest eigenvector (bottom). The numbers (top-right) specify the discrimination power [3] for the two methods.

resolution A/Z information obtained from the time at S8 and the position at S2 at the FRS. The lower part of the figure shows the same three classes of charge but now the distributions are drawn as projections on the longest eigenvector obtained using the DA technique with the 189 dimensional input vectors of observations. These input vectors contain the information obtained from all the up-stream detectors, i.e. the times and amplitudes of the S2 and S8 FRS scintillators and from the start and position detectors in front of the target. The 18 raw signals were, in addition, combined into pair products to maximize the DA efficiency (see e.g. [3]), altogether resulting in 189 input variables. The so obtained average efficacy of charge recognition reaches about 90%. Using also the measured projectile A/Z, isotopically pure beams can thus be selected.

References

[1] P. Désesquelles, Ann. Phys. Fr. **20** (1995) 1.

[2] R.A. Fisher, Annals of Eugenics, **7** (1936) 179.

[3] P. Désesquelles *et al.*, Phys. Rev. C **62** (2000) 024614.

[4] C. Sfienti *et al.*, Nucl. Phys. A **749** (2005) 83c.

Genuine Flow Systematics for Au+Au at Intermediate Energies

J. Łukasik, W. Trautmann, and INDRA-ALADIN Collaboration
GSI, Darmstadt, Germany

Collective flow observables are being of interest since the beginning of experimental studies of heavy ion collisions, mainly due to their presumed link to the question of nuclear equation of state. The present study is an extension of the ones outlined in [1] of the Au+Au collisions measured at GSI, at energies 40-150 AMeV, using the INDRA detector. Unlike the previous studies, the present one takes into account the corrections for the reaction plane dispersion, being of increasing importance below about 100 AMeV, and the instrumental effects, mainly the multi-hit corrections. The method of correcting for the reaction plane dispersion taking into account the correlation between the sub-events has been outlined in [2] and described in more detail in [3]. The corrections change the measured results for the directed flow by factors of up to two in the region of vanishing flow and thus are non-negligible.

The results presented below come from the review chapter on flow and stopping from [3] which aimed to supply the "theory-ready" excitation functions of directed and elliptic flow, for the Au+Au system, covering and merging the energy regions studied by the INDRA-ALADIN and the FOPI collaborations. In the overlap region, the agreement of the corrected results from the two experiments is remarkably good for both, the directed and elliptic flow.

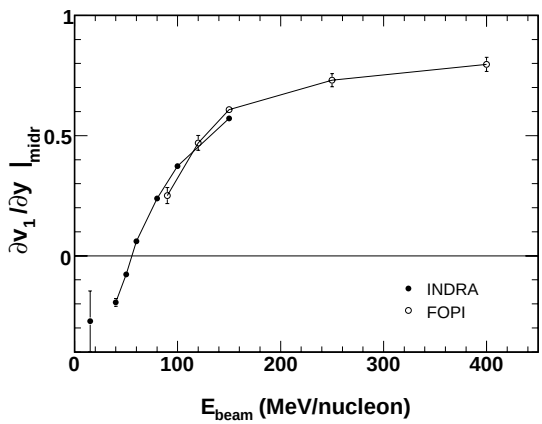

Figure 1: Slopes of directed flow $\partial v_1/\partial y$ for $Z = 2$ particles integrated over $p_{\rm T}$ for mid-central collisions (2–5.5 fm). The open and filled symbols represent the FOPI [4] and the INDRA data, respectively.

The excitation function of the slope of the directed flow, $\partial v_1/\partial y$, at midrapidity for $Z = 2$ (Fig. 1) is seen to rise monotonically with energy over the full range of 15 to 400 MeV per nucleon which is covered by the two experiments. The trends presented for uncorrected data [1], including the sign-change, are preserved, however the absolute values changed due to the applied corrections. The excitation function does not show an indication of a minimum and changes sign between 50 and 60 MeV per nucleon.

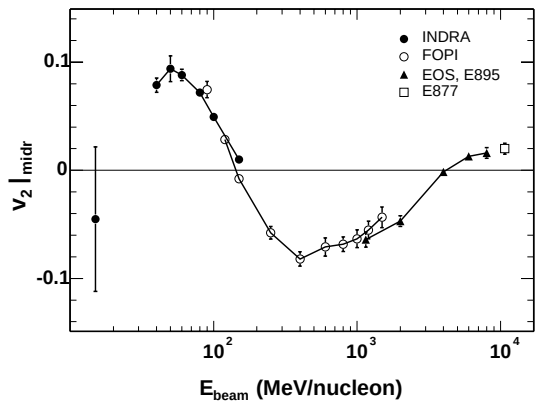

Figure 2: Elliptic flow parameter v_2 at mid-rapidity for collisions at intermediate impact parameters (about 5.5-7.5 fm) as a function of incident energy, in the beam frame. The filled and open circles represent the INDRA and FOPI [5] data, respectively, for $Z = 1$ particles, the triangles represent the EOS and E895 [6] data for protons and the square represents the E877 data [7] for all charged particles.

Elliptic flow (Fig. 2) for $Z = 1$ varies as a function of energy from a preferential in-plane, rotational-like emission ($v_2 > 0$) to an out-of-plane, or 'squeeze-out' ($v_2 < 0$) pattern, with a transition energy at about 150 AMeV. For higher energies, the strength of the collective expansion overcomes the rotational-like motion, leading to an increase of out-of-plane emission. A maximum is reached at about 400 AMeV, followed by a decrease towards a transition to again preferential in-plane emission at relativistic energies [6, 7].

References

[1] J. Łukasik, W. Trautmann et al., GSI Scientific Reports 2003 and 2004.

[2] J. Łukasik and W. Trautmann, GSI Scientific Report 2005.

[3] A. Andronic *et al.*, Eur. Phys. J. A **30**, (2006) 31, and in *Dynamics and Thermodynamics with Nuclear Degrees of Freedom* ed. by Ph. Chomaz *et al.*, Springer, Berlin Heidelberg New York, 2006

[4] A. Andronic *et al.*, Phys. Rev. C **64**, (2001) 041604.

[5] A. Andronic *et al.*, Phys. Lett. B **612** (2005) 173.

[6] C. Pinkenburg *et al.*, Phys. Rev. Lett. **83** (1999) 1295.

[7] P. Braun-Munzinger and J. Stachel, Nucl. Phys. A **638** (1998) 3c.

Isospin Effects in Spectator Fragmentation at Relativistic Energies *

C. Sfienti, S. Bianchin, M. De Napoli and W. Trautmann for the ALADiN2000 Collaboration
GSI, Darmstadt, Germany

A systematic study of isotopic effects in the break-up of projectile spectators at relativistic energies has been performed with the ALADiN spectrometer at the GSI laboratory [1, 2]. Besides a primary beam of ^{124}Sn, also secondary beams of ^{124}La and ^{107}Sn produced at the FRS fragment separator have been used in order to extend the range of isotopic compositions.

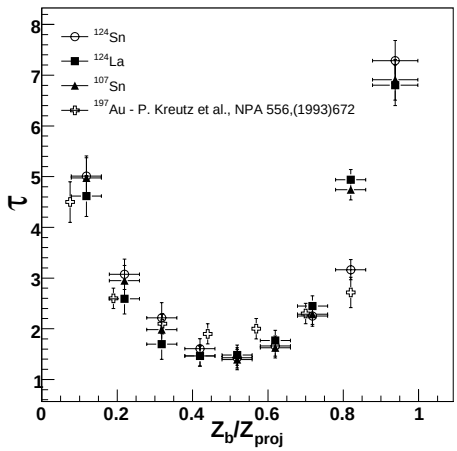

Figure 1: The extracted τ parameters as a function of $Z_{\rm bound}$ for ^{124}La, ^{124}Sn and ^{107}Sn at 600 AMeV, compared with earlier data for ^{197}Au obtained at the same energy.

The gross properties of projectile fragmentation are very similar for all the studied systems [1], as demonstrated for the τ parameterization ($\sigma(Z) \propto Z^{-\tau}$) of the charge yields $\sigma(Z)$ in Fig. 1. The fitting range was $3 \leq Z \leq 15$. The τ parameters follow a nearly universal curve with a minimum near the reduced $Z_{\rm bound}/Z_{\rm proj}$=0.5. Specific isotopic effects, even though small, can nevertheless be observed: in particular, the hierarchy of τ for the neutron-poor ^{124}La and ^{107}Sn and neutron-rich ^{124}Sn and ^{197}Au systems for $Z_{\rm bound}/Z_{\rm proj} > 0.5$ is opposite to the standard predictions of the Statistical Multifragmentation Model SMM. It can, however, be explained with a weak isotopic dependence of the surface-term coefficient in the liquid-drop description of the fragment masses at low excitation energy which gradually disappears with increasing excitation of the fragmenting system [3].

The mean N/Z of the isotope distributions of light fragments in the range $3 \leq Z \leq 13$ for two different $Z_{\rm bound}$ cuts is presented in Fig. 2. The values obtained for ^{124}Sn are larger than those for ^{124}La or ^{107}Sn (not shown) as expected from the different N/Z of the original projectiles. Their odd-even variation is, however, much more strongly

* Work supported by the European Community under contract No. HPRI-CT-1999-00001

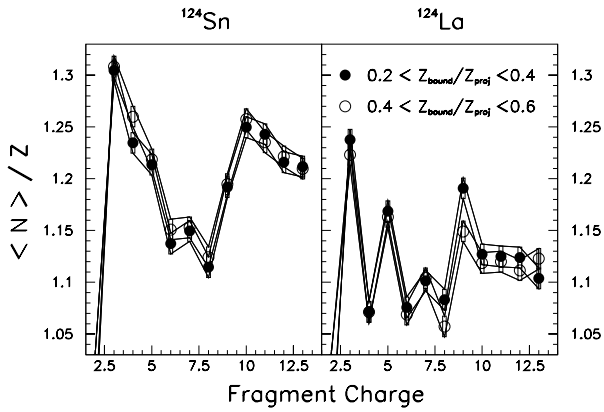

Figure 2: Mean values $< N >/Z$ of light fragments with $3 \leq Z \leq 13$ produced in the fragmentation of ^{124}Sn and ^{124}La at 600 A MeV for two different bins in $Z_{\rm bound}$.

pronounced for the neutron-poor cases. The strongly bound α-type nuclei (even-even $N = Z$) attract a large fraction of the product yields during the secondary evaporation stage [4]. This effect is, apparently, larger if already the hot fragments are close to $N = Z$ symmetry, as it is expected for the fragmentation of ^{124}La and ^{107}Sn [5].

The observed patterns are very systematic, as confirmed by comparing with earlier inclusive data obtained with the FRS [4]. They exhibit at the same time nuclear structure effects characteristic for the isotopes produced and significant memory effects of the isotopic composition of the excited system from which they originate. A precise modeling of these secondary processes is, therefore, necessary for quantitative analyses.

In the case of the ^{124}La, moreover, a small difference in the mean N/Zs for the two $Z_{\rm bound}$ cuts is observed which is absent for ^{124}Sn. This characteristics is predicted by the SMM [5]. In the statistical scenario, this difference arises from the dependence of the number of neutrons which will have to be carried by the light fragments on the Z spectrum of heavy fragments and on their capability of carrying neutrons which increases with fragment mass. The observation of this effect supports the idea of overall equilibrium of the system at breakup.

References

[1] C. Sfienti et al., GSI Scientific Report 2004, p.122.
[2] C. Sfienti et al., Nucl. Phys. A 749 (2005) 83c.
[3] A. S. Botvina et al., Phys. Rev. C 74, 044609 (2006).
[4] M. V. Ricciardi et al.,Nucl. Phys. A 733 (2004) 299.
[5] N. Buyukcizmeci et al., Eur. Phys. J. A 25 (2005) 57.

Modification of surface energy in nuclear multifragmentation

A.S. Botvina[1,2], N. Buyukcizmeci[3], M. Erdogan[3], J. Łukasik[1,4], I.N. Mishustin[5,6], R. Ogul[1,3], and W. Trautmann[1]

[1]GSI, Darmstadt, Germany; [2]INR, Moscow, Russia; [3]Selçuk University, Konya, Turkey; [4]NINP, Kraków, Poland; [5]FIAS, Frankfurt, Germany; [6]KI, Moscow, Russia

A break-up of nuclei into many fragments (multifragmentation) has been observed in nearly all types of nuclear reactions when a large amount of energy is deposited in nuclei. According to the present understanding, multifragmentation is a relatively fast process, with a characteristic time around 100 fm/c, where, nevertheless, a high degree of equilibration (chemical equilibrium) is reached. The previous ALADIN experiments have provided extensive information about multifragmentation of projectiles in peripheral nucleus-nucleus collisions at high energy [1]. It was established that the statistical multifragmentation model (SMM) [2], which assumes a thermal equilibration among hot fragments in a freeze-out volume at subnuclear densities, describes the data successfully [2, 3]. The multifragmentation reaction can be considered as an experimental tool to study the properties of hot fragments and the phase diagram of nuclear matter at densities $\rho \approx 0.1 - 0.3\rho_0$ ($\rho_0 \approx 0.15$ fm^{-3} is the normal nuclear density) and temperatures around $T \approx$ 3–8 MeV which are expected to be reached in the freeze-out volume. This part of the phase diagram is also very important for processes during the supernova II explosions and neutron star formation. Properties of fragments imbedded in hot dense environments may be modified in comparison with isolated fragments. As was established previously [4], the symmetry energy of fragments decreases when the multifragmentation channels become dominating with increasing excitation energy.

By using the SMM approach we address the surface energy of fragments in multifragmentation [5]. For this purpose, a new analysis of the ALADIN data obtained with ^{238}U, ^{197}Au and ^{129}Xe projectiles [1] was performed. In addition to the previous analyses [2, 3] we have examined a dependence of the τ parameters, characterizing $Z^{-\tau}$ fit of the fragment yields, on the bound charge $Z_{\rm bound}$ contained in the observed fragments. The values of $Z_{\rm bound}/Z_0 \approx 0.9$ (Z_0 is the projectile charge) correspond to low excitation energies, where the system decays mainly via compound nucleus channels, while at $Z_{\rm bound}/Z_0 \approx 0.5 - 0.6$ the excitation energy is high and multifragmentation dominates. The surface free energy in the SMM is parametrized as $F^{\rm surf}_{A,Z} = B(T)A^{2/3}$, where $B(T) = B_0[(T_c^2 - T^2)/(T_c^2 + T^2)]^{5/4}$. Here $B_0 \approx$18 MeV is the surface coefficient for isolated cold nuclei, and $T_c \approx$18 MeV is the critical temperature for the nuclear liquid-gas phase transition in infinite matter. Finally we have found that the surface energy coefficient B_0 can be extracted from the experimental data, and its evolution with isospin at different excitation energies can be investigated by comparing sources with different isotope content [5].

In Figure 1 we show the behavior of the surface coefficient B_0 versus the neutron to proton (N/Z) ratio during the fragmentation. Around the onset of multifragmentation (low excitation energies), there is a decrease of B_0 with N/Z that resembles the trends obtained for cold isolated nuclei. However, B_0 becomes nearly independent of the neutron richness when multifragmentation dominates. In this case nuclear fragments are primarily produced in a hot medium which represents a liquid-gas coexistence region. Modification of their properties can be explained by 'in-medium' interaction.

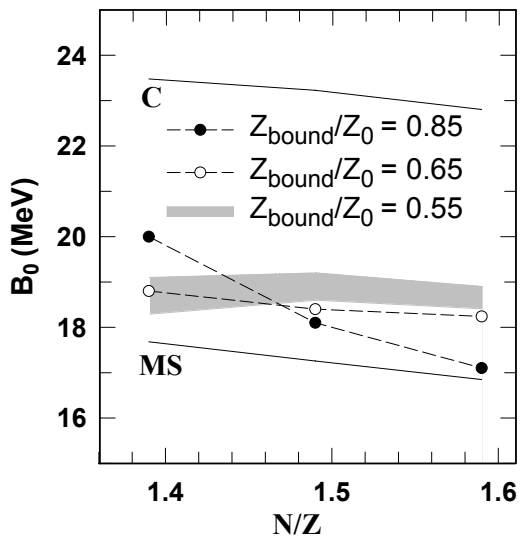

Figure 1: The extracted B_0 for sources with different N/Z ratios at the onset ($Z_{\rm bound}/Z_0$=0.85 bin), and at the region of full multifragmentation ($Z_{\rm bound}/Z_0$=0.65 and 0.55 bins). The width of the shaded band represents limits given by our method for the lowest bin. The B_0 obtained from Cameron (C) and Myers-Swiatecki (MS) mass formulae for cold nuclei are shown by solid lines for illustration.

References

[1] A. Schüttauf et al., Nucl. Phys. **A**607 (1996) 457.

[2] J.P. Bondorf et al., Phys. Rep. 257 (1995) 133.

[3] H. Xi et al., Z. Phys. **A**359 (1997) 397.

[4] A. Le Fèvre et al., Phys. Rev. Lett. 94 (2005) 162701.

[5] A.S. Botvina et al., Phys. Rev. **C**74 (2006) 044609.

Measurement of Charged Kaon Flow in Ni + Ni Collisions at 1.93A GeV*

Y. J. Kim[†1], A. Andronic[1], N. Herrmann[2], K. D. Hildenbrand[1], B. Hong[3], P. Koczon[1], Y. Leifels[1], X. Lopez[1], M. Kiš[1], W. Reisdorf[1], A. Schüttauf[1], X. Zhang[1], and the FOPI Collaboration

[1]GSI, Darmstadt, Germany; [2]Universität Heidelberg, Heidelberg, Germany; [3]Korea University, Seoul, Korea

Sub- or near- threshold charged kaon production is a sensitive tool to study nuclear matter properties in heavy-ion collisions [1]. Many theoretical models showed that studying the production and propagation of charged kaons in heavy-ion collisions at the SIS energy regime allows to address the question of the modification of hadron properties in dense baryonic nuclear matter (for the most recent review, see Ref. [2]). Recent calculations have emphasized that the directed and the elliptic flows of both K^+ and K^- as a function of rapidity are sensitive to the depth and the details of the $K^\pm$ in-medium potentials [3].

The FOPI collaboration performed a high statistics experiment by using Ni + Ni collisions at 1.93A GeV. In this experiment, 151200 K^+ and 7700 K^- were measured in 69 M central events, corresponding to a reaction cross section of 560 mb. In order to identify charged kaons, the momentum measured with the CDC is correlated with the velocity measured with the time-of-flight plastic BARREL, which allows us to separate pions, kaons, and protons up to the laboratory momentum of 0.5 GeV/c (for more details, see Refs. [4]).

The experimental results for directed and elliptic flows are summarized in Fig. 1. The upper plot presents the directed flow (v_1) and the lower plot shows the elliptic flow (v_2) of $K^\pm$ in the BARREL acceptance as a function of the normalized rapidity $y^{(0)}$, which is the particle rapidity divided by the projectile rapidity in the center-of-mass system. For the comparison, the figure also includes the v_1 parameter of protons in the CDC acceptance, which exhibits a monotonic increase towards mid-rapidity, characterizing the in-plane collective flow. We found that the K^+'s show a slight anti-flow, whereas the K^-'s show flow. Similar trends are predicted by the transport calculations for the existence of a repulsive K^+N and an attractive K^-N mean fields [3]. In the lower plot of Fig. 1, the results of $K^\pm$ elliptic flow (v_2) as a function of $y^{(0)}$ are shown together with the results from the KaoS collaboration [5]. The experimental data from FOPI and KaoS show clearly opposite elliptic flow of K^+ and K^-: $v_2 < 0$, out-of-plane emission, for positive kaons and $v_2 > 0$, in-plane emission, for negative kaons.

The systematic errors of the directed and elliptic flows for $K^\pm$ were evaluated for the following three dominant sources: the flattening of the reaction plane for detector biases, the influence of various cut conditions ($e.g.$, the matching conditions between CDC and BARREL and the variation of the particle identification window, etc.), and the effect of the pion contribution to the kaon flow. The estimated systematic errors for the directed and elliptic flows of $K^\pm$ are similar or smaller than the statistical errors shown in Fig. 1.

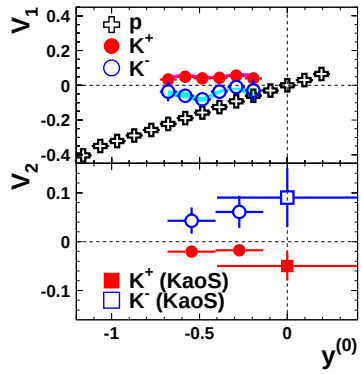

Figure 1: The experimental results of the charged kaon flow as a function of the normalized rapidity. The results contain particles in the transverse momentum divided by particle mass $p_t/m \geq 0.5$. In the upper plot of the figure is plotted directed flow of protons (crosses), K^+ (closed circles), and K^- (open circles). The error bars associated with symbols indicate the statistical uncertainties. The systematic errors are indicated by the shaded bands. In the lower plot is shown the elliptic flow of K^+ (closed circles) and K^- (open circles) together with the KaoS results (closed squares for K^+ and open squares for K^-) [5]. KaoS results are measured in the different centrality range (3.8 fm $<$ b $<$ 6.5 fm) and detector acceptance (-0.4 $< y^{(0)} <$0 .4, 0.2 GeV/c $< p_t <$ 0.8 GeV/c). The error bars associated with symbols indicate the statistical uncertainties only.

In summary, we presented the first results of the directed flow for K^- at SIS energies and the elliptic flows of $K^\pm$ in different rapidity regions. In comparison to filtered theoretical calculations, the experimental results on both K^+ and K^- flow indicate the existence of in-medium effects.

References

[1] R. Barth *et al.*, Phys. Rev. Lett. **78** (1997) 4007.

[2] C. Fuchs, Prog. Part. Nucl. Phys. **56** (2006) 1.

[3] A. Mishra *et al.*, Phys. Rev. C **70** (2004) 044904.

[4] J. Ritman *et al.*, Z. Phys. A **352** (1995) 355 ;
P. Crochet *et al.*, Phys. Lett. B **486** (2000) 6;
K. Wisniewski *et al.*, Eur. Phys. Journ. A **9** (2000) 515.

[5] F. Uhlig *et al.*, Phys. Rev. Lett. **95** (2005) 012301.

* Work supported by KOSEF contract No. F01-2006-000-10035-0 and BMBF contract No. 06HD953

† Y.-J.KIM@gsi.de

Measurement of Σ(1385) in Al+Al collisions at 1.9A GeV

X. Lopez[1], N. Herrmann[2], P. Crochet[3], and the FOPI Collaboration

[1]GSI, Darmstadt, Germany; [2]Physikalisches Institut, Heidelberg, Germany; [3]LPC Clermont-Ferrand, France

The FOPI Collaboration performed a high statistic experiment to study the strangeness production in Al+Al collisions at 1.9A GeV. The high statistics data (300 million of events) allow the reconstruction of the Σ(1385) hyperon resonance at SIS energies for the first time. This measurement corresponds to sub-threshold production since the threshold beam energy for Σ^* production in the elementary reaction is $E_{\rm thr.} = 2.33$ GeV. Recent theoretical calculations predict an important coupling of the K^- with Σ(1385) (called Σ^* in the following), Λ(1405) and Λ(1520) resonances in the medium [1, 2]. Therefore, measurement of the sub-threshold Σ^* production cross-section may carry important information regarding the complex reactions involved in the sub-threshold K^- production.

The Σ^* is an isospin triplet state and while the Σ^{*0} cannot be reconstructed with our apparatus (decay into Λ and π^0), the charged meson decay products $\pi^\pm$ of $\Sigma^{*\pm}$ are identified with the FOPI detector. The Σ^* are reconstructed from a topological analysis of their double two body decay:

$$\begin{aligned} \Sigma^{*\pm} \rightarrow \quad & \Lambda + \pi^\pm \qquad (\mathrm{BR} = 88\%, c\tau = 5\ \mathrm{fm}) \\ & \hookrightarrow \ p + \pi^- \ (\mathrm{BR} = 64\%, c\tau = 7.89\ \mathrm{cm}). \end{aligned}$$

The invariant mass spectra of Σ^{*-} and Σ^{*+} resonances are shown in the upper and lower part of Fig. 1, respectively. The combinatorial background is determined with the event mixing method relying on the correlation of a Λ from one event with pions from an other event. In addition, the two events are aligned to the reaction plane in order to have the same reference system for both particles. In the invariant mass range between 1.35 and 2 GeV/c^2, 16 excited states of Σ s have been already measured [3]. Therefore, the normalization of the mixed background was applied in the invariant mass range [1.25 ; 1.32] GeV/c^2 (grey area in upper panels of Fig. 1) in order to avoid biases in the normalization of the combinatorial background due to the so-called bumps. After background subtraction (Fig. 1, lower panels), the remaining peak in the mass spectra is fitted with a Breit-Wigner function and about 1350 $\Sigma^{*\pm}$ are found for the applied set of analysis cuts. The mean mass and width values are in good agreement with the Particle Data Group [4] within the statistical error. At higher invariant masses some excited states are visible as it was reported by the STAR Collaboration [5] which is the only other available measurement of Σ^* production in heavy ion collisions.

The measurement of the Σ^* is used as a test case to perform the analysis of other wide baryonic resonances as for example the K(892). Sub-threshold measurement of Σ^* resonances will constrain model predictions concerning sub-threshold strangeness production.

This work was partly supported by the German BMBF under Contacts No. 06HD953 and agreement between GSI and IN2P3/CEA.

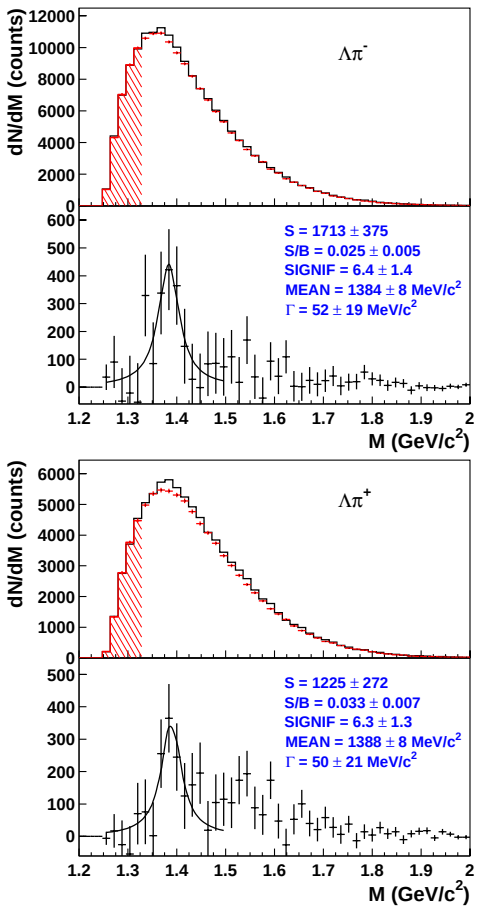

Figure 1: *Invariant mass spectra of $\Lambda\pi^-$ (π^+) pairs on upper and lower parts, respectively, measured from Al+Al collisions ($\sigma_{geo} \leq 315$ mb). The solid histogram and crosses denote the data and the scaled mixed-events background, respectively (upper panels). The lower panels show signals after background subtraction. The following characteristics of the signals are shown: number of counts in the signal (S), signal-to-background ratio (S/B) and significance (SIGNIF). The fitted parameters of the Breit-Wigner function (mean mass value and width) are also mentioned.*

References

[1] M.F.M. Lutz *et al.*, Nucl. Phys. A **700**, (2002) 193.

[2] J. Schaffner-Bielich *et al.*, Nucl. Phys. A **669**, (2000) 153.

[3] W.-M. Yao *et al.*, J. Phys. G **33**, (2006) 1.

[4] S. Eidelman *et al.*, Phys. Lett. B **592**, (2004) 127.

[5] J. Adams *et al.*, Phys. Rev. Lett. **97**, (2006) 132301.

Status of the HADES physics program and the upgrade project

The HADES collaboration

Summary

In 2006 the analysis of the ^{12}C+^{12}C data taken at a beam energy of 2 AGeV was finalized and the results for electron pair production published. The data exhibit an extra yield above the contribution expected from hadron decays after freeze-out for invariant masses above $M_{e^+e^-} > 150$ MeV/c^2. A comparison to the DLS data, which was measured in the system ^{12}C+^{12}C at 1.04 AGeV, reveals that the yield observed beyond the contribution from the η Dalitz decay increases with the beam energy like pion production. Further information on the origin of this excess is expected from the final results of the HADES run on ^{12}C+^{12}C at 1 AGeV and from studies of dielectron production in elementary reactions at low beam energies (1.25 GeV). The latter were started with a $p+p$ run in May 2006 and will be continued in April 2007 with a $d+p$ experiment, which will provide sensitivity to iso-spin effects in resonance production. This experiment will be followed by a high-resolution $\omega \rightarrow e^+e^-$ measurement in $p+p$ reactions at 3.5 GeV providing a reference for later studies of the ω line shape in $p+A$ reactions. The HADES upgrade program is well progressing. It will put the spectrometer in the condition to cope with the highest particle multiplicities and will further increase its rate capability.

Electron pair production in ^{12}C+^{12}C collisions at 2 AGeV

The excess yield observed by the DLS collaboration in light collision systems at around 1 AGeV [1] is a long standing puzzle to the extent, that by now it could not be satisfactorily explained by any theoretical calculation [2][3]. In contrast to the situation at SPS energies, a broadening of the ρ spectral function due to the surrounding medium as observed in the $In+In$ system by the NA60 collaboration [4] and in $Pb+Au$ collisions by the CERES collaboration [5], cannot explain the measured yield.

For our data we define the excess yield in the same way like it is derived by the other collaborations. We compare the measured yield, to which we apply a correction for the detector and reconstruction efficiency but none for the finite acceptance of the spectrometer [6], to a calculated yield assuming free decay of π and η mesons. In this approach we consider the dielectron decay of ρ mesons, the Dalitz decay of baryonic resonances and *N-N* bremsstrahlung as contributions from the early phase of the reaction. The longer-lived vector meson ω (ϕ production is not considered) plays an intermediate role and is counted as a conventional source although its production cross section at this low energy is barely known. The result is shown in fig. 1 (a). The contribution to the cocktail from the conventional sources (full lines, cocktail A) is based on experimental data and m_t scaling in case of the ω. The contribution from non-conventional sources is calculated assuming m_t scaling and taking into account a phase space driven population of the broad resonances, as can be inferred from the skewed mass distribution of electron pairs from ρ decay. The lower panel (fig. 1 (b)) shows the relative enhancement above the conventional sources (i.e. cocktail A). Since the measured yield shows a nearly exponential fall-off above an invariant mass of 150 MeV/c^2 (π-Dalitz

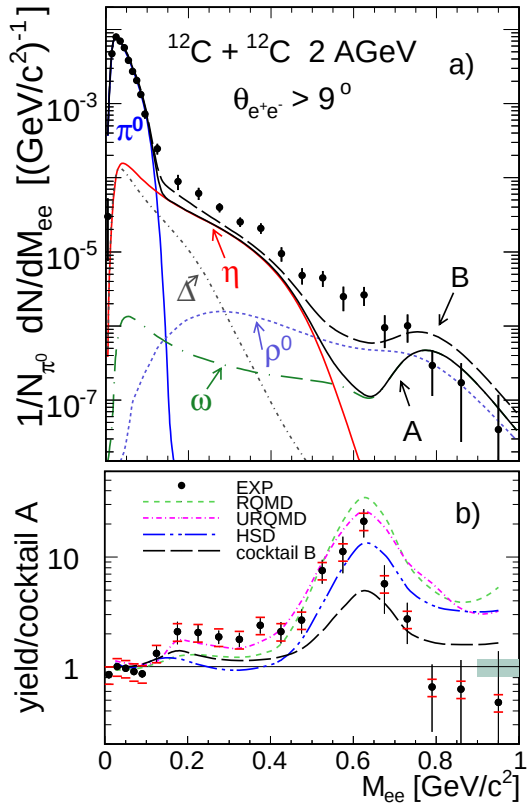

Figure 1: Dielectron yield (corrected for reconstruction efficiencies) in the acceptance of the HADES [7]. In the upper panel (a), the measured yield is compared to a cocktail assuming decay of particles in the vacuum. The cocktail is divided into contributions expected from particles with $\tau > \tau_{fireball}$ (full lines, cocktail A) and particles/resonances with $\tau \leq \tau_{fireball}$. The sum of both defines cocktail B. In the lower panel (b) the experimental yield is divided by cocktail A to show the relative enhancement above the conventional sources. The various lines display in addition the prediction of microscopic transport models (see text).

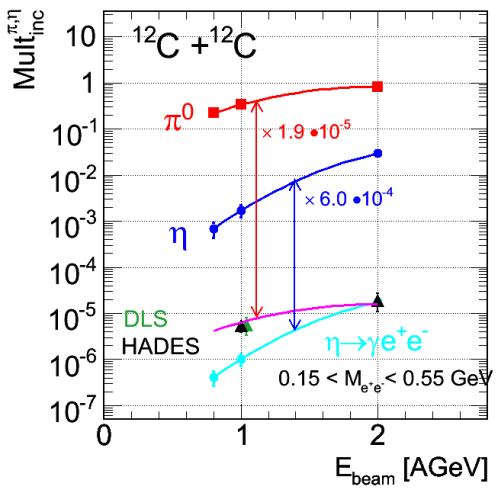

Figure 2: Excitation function of the multiplicity of excess pairs (triangles) in the mass range $150 < M_{e^+e^-}/\mathrm{MeV}/c^2 < 550$ in ^{12}C+^{12}C collisions compared to light hadron production. The data points are from TAPS (π_0-full squares, η-full circles), DLS (dielectrons at 1.05 AGeV) and HADES (2.0 and 1.0 AGeV). The line labelled $\eta \rightarrow \gamma e^+e^-$ represents the expected yield of Dalitz pairs in the indicated invariant mass range assuming the multiplicity measured by the TAPS collaboration.

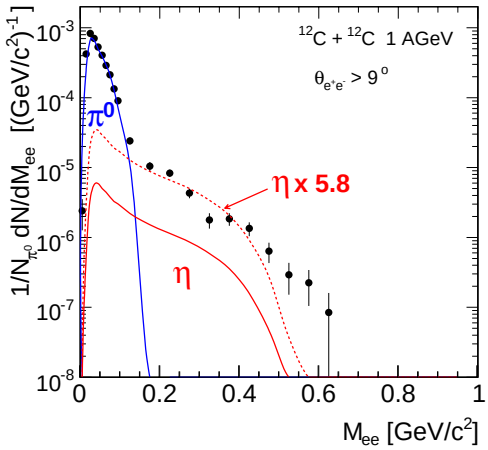

Figure 3: Invariant mass distribution of electron pairs emitted into the acceptance of HADES in ^{12}C+^{12}C collisions at 1 AGeV. The data are not corrected for detector and reconstruction efficiency. The full lines represent the expected yield for meson decay base on π^0 and η measurements of the TAPS collaboration. The dashed line shows the η scaled as to fit the data.

region), the relative yield has a maximum in the invariant mass region where the contribution from η Dalitz decay declines (i.e. around 600 MeV/c^2).

The excess yield is compared to the expectation of the full cocktail (B) and to predictions of the three microscopic transport models HSD [8], UrQMD [9] and RQMD [10]. While the overall trend is reproduced by the model calculations, a closer look discloses differences in the description of the excess. They originate mainly from differences in the treatment of the decay of baryonic resonances (mainly $\Delta(1232)$). In the vector meson pole region, all calculations lie above the data. A possible explanation for this observation could be a smaller contribution from ω decay as compared to predictions of the m_t scaling.

To link this result to the observation of the DLS collaboration we integrate the measured yield in the mass range from 150 to 550 MeV/c^2 and extract the contribution to the integral from η Dalitz decay. We find for the ratio of the total integrated yield to the integrated η yield F(2.0) = 2.07 $\pm$ 0.21(stat) $\pm$ 0.38(sys). The same analysis applied to the DLS result yields F(1.04) = 6.5 $\pm$ 0.5(stat) $\pm$ 2.1(sys). It is interesting to subtract the η yield from the total yield and to compare the excitation function of the resulting excess yield to the measured excitation function of light meson production (fig. 2). Within the experimental errors, the excess scales precisely like π production. This pattern possibly points to the origin of the excess yield since pion production at this low energies is known to be dominantly coming from the excitation and decay of baryonic resonances. Due to severe phase space limitations a sound theoretical description of electron pair production at these energies requires a proper treatment of off-shell propagation of resonances and vector mesons. Furthermore, the role of the coupling of baryonic resonances to vector mesons, in particular the ρ, has to be quantitatively understood. Please also note that the strong increase of the excess yield from 2 to almost 6 in case of DLS occurs because it is defined above the η production, which is strongly suppressed by phase space at the lower beam energy.

We hope to find more evidence for such a scenario from the results of our ^{12}C+^{12}C run at 1.0 AGeV. A preliminary spectrum obtained before final calibration of the data and with a preliminary alignment of the spectrometer shows a similar enhancement as obtained by the DLS collaboration. In fig. 3 we depict the preliminary spectrum obtained in the experimental run of August 2004. The spectrum is not yet corrected for efficiency. The cocktail was calculated in the same way as discussed before and the detector response was obtained by processing the generated events through the full analysis chain.

As a matter of fact, a comparison of the DLS result with our data is not straightforward. The DLS spectrometer has a two-arm geometry and its trigger required an electron (or positron) candidate in each of the two arms. The HADES trigger is based on one electron track candidate only. Moreover, the acceptance for low-momentum tracks in DLS is larger compared to HADES. Consequently, the phase space coverage for low-mass electron pairs is significantly different in the two experiments.

Status of the ongoing analysis

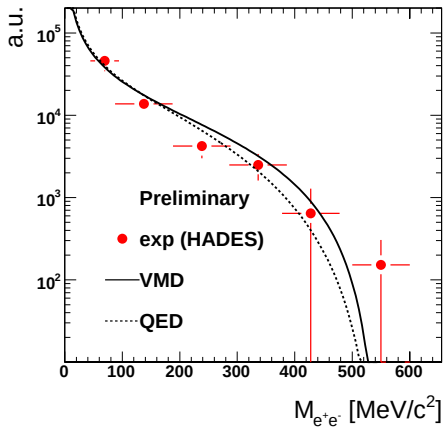

Figure 4: Invariant mass distribution $M_{e^+e^-}$ for the decay $\eta \rightarrow \gamma e^+e^-$ (statistical errors only). The dashed line shows the prediction for a pure QED (no form-factor) and the solid line represents the full Vector Meson Dominance (VMD) calculation [11].

The second round of data processing for the ^{12}C+^{12}C at 1 AGeV was started and final results are expected for the 2^{nd} quarter of 2007.

The analysis of the $p+p$ experiment at 2.2 GeV turned out to be essential to understand the electron/positron reconstruction in HADES and to cross-check the alignment of the spectrometer. The exclusive channels $pp \rightarrow (pp\eta) \rightarrow pp\gamma e^+e^-$ and $pp \rightarrow (pp\eta) \rightarrow pp\pi^+\pi^-\pi^0$ could be reconstructed in both a hadronic and a leptonic final state by exploiting missing mass techniques [6]. The obtained invariant mass distribution for the virtual photon in the leptonic decay channel of the η is shown in fig. 4.

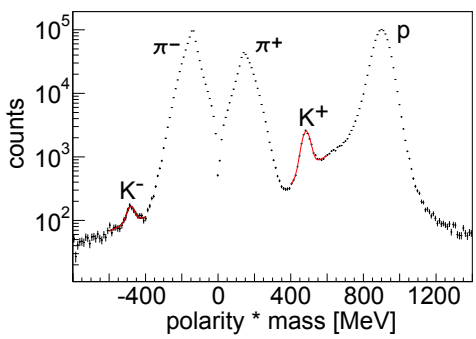

Figure 5: Kaon signals in the mass distribution of reconstructed tracks. It is derived after applying a condition on the correlation of momentum and energy loss in the drift chambers.

In August 2005 data with high statistics were taken for the collision system $Ar + KCl$ at 1.75 AGeV. Emphasis in the analysis of this run is also put on the reconstruction of hadrons containing strangeness. To improve the reconstruction, for the first time also energy loss information obtained from the multi-wire drift chambers (MDCs) is included in the particle identification process. The front-end electronics of the MDCs do not provide an analogue signal proportional to the charge deposit in the drift cells. We obtain this information from the logical timing signal, which provides the time-over-threshold. It was shown that if the arrival time distribution of the primary electrons at the signal wire is unfolded, a quantity nearly proportional to the energy loss, can be obtained [12]. In a new approach, this variable is further linearized by a minimization procedure.

By this procedure both K^+ and K^- mesons can be reconstructed. A very preliminary result depicted in fig. 5 shows a mass distribution obtained after applying a condition on the the energy loss - momentum correlation. Contributions from K^+ (2000 counts) and K^- mesons (170) are clearly visible based on a subset of 180 out of 2700 files totaly available (i.e. 7% of the total statistics). The processing of all statistics (7 Tbyte) has been started in January 2007.

pp and dp runs

A systematic investigation of electron pair production in elementary reactions of protons and neutrons on a proton target has been started with a run in April 2006 measuring p+p at 1.25 GeV kinetic energy, i.e. just below the production threshold for η mesons. In this kinematic situation one does not expect contributions to the invariant mass spectrum of dielectrons from conventional sources above the π^0 Dalitz region. The most abundant source here is then Δ Dalitz decay. However, it was conjectured that higher lying baryonic resonances can also contribute to the mass region below the vector meson pole mass due to off-shell propagation of intermediate vector mesons [13]. Furthermore, contributions of *N-N* bremsstrahlung (in particular the validity of a dominance of the dipol radiation) can be investigated by comparison of dielectron yields in pp and pn reactions (see below).

A beam of up to 2 10^7 protons per second was incident on a 5 cm liquid hydrogen target. During data taking the DAQ was running with up to 17 kHz event rate ($\sim$ 50% dead time) and in total $\approx 7.710^8$ events were taken during a period of 9 days. This program will be continued with a 5 week long beam time in April/May 2007. Neutron induced reactions will be measured using a deuterium beam at 1.25 AGeV. The main interests here are the investigation of the iso-spin effects in baryonic resonance excitation (mainly Δ) and of the off-shell production of vector mesons [14]. pp and pn reactions can be separated measuring the spectator proton in a Forward Hodoscope Wall (FHW) covering the polar angle region between 1° and 5°.

Moreover, in the second part a 3.5 GeV proton beam will be used to study omega production and in particular its vacuum line shape. The spectrum will serve as a reference for further in-medium studies of the line shape in $p + A$ reactions. It will also be possible to address the ω transition form factor were until now the validity of the VMD is

uncertain [11].

Status of the detector upgrade

The HADES collaboration plans a major upgrade of the spectrometer during the SIS shut-down in the second half of 2008. The upgrade includes the replacement of some detector systems and the installation of a new data acquisition system. The most important action is the replacement of the inner time-of-flight system (TOFINO) which, for the reason of an limited budget at the time of construction, has too low granularity not matched to the rest of the spectrometer. We foresee a RPC detector system at the position of the TOFINO detector which will comprise 1200 individual shielded detector elements housed in six gas boxes (see fig. 6). In measurements with prototypes a time resolution of $\sim$ 70 ps was obtained for rates up to 1 kHz/cm^2 and with a common correction for pulse height effects on the timing. The read-out chain consists out of a discrete preamplifier circuit and discriminator stage providing a t_0 measurement and a Δt (time over threshold) information proportional to the integrated charge in the signal. The time information is digitized with a new trigger and read-out board[1] (TRB), which is independent of VME and features 4 HPTDC time converter chips, programmable logic and an Etrax chip computer. The board can operate as an independent sub-event builder and can send data directly to the HADES event builder. The infrastructure for mass production of the RPC detector cells in Coimbra was installed in summer 2007 and the first two complete modules, housing 400 detector cells, should be ready by summer 2007.

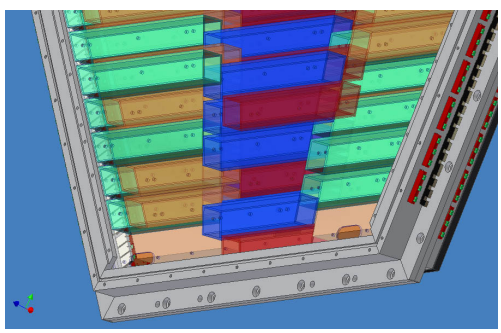

Figure 6: Technical drawing of the RPC gas box and the included single cell RPC modules. The RPC cells will be arranged in two layers to realize a dead-zone free geometry.

The HADES spectrometer will be complemented by the FHW to provide particle detection in the forward polar angle region. This systems was recycled from the forward wall operational at the KaoS spectrometer. All 288 scintillators have been equipped with new multipliers and the elements will be housed in a new support structure.

Over the last years a steady increase of voltage instabilities in the first layer of the MDCs was observed. An inspection of one of the modules gave evidence for aging effects, like a loss in mechanical tension of the aluminium field wires as well as deposits on the wires. To be prepared for future runs we decided to rebuild all modules of the first layer using copper beryllium wires instead of aluminium wires. The new modules will be produced in the detector laboratory of the Forschungszentrum Dresden-Rossendorf. Inspired by the very successful operation of the RPC prototype read-out board (TRB), a new concept for the future HADES DAQ system was developed, going beyond the replacement of critical hardware components as originally planned. The aim is to replace all VME based sub-event builders by read-out boards based on a generic TRB board currently being tested. This technology will also allow to implement a new LVL2 trigger distribution with a star-like architecture and optical links with much improved flexibility and monitoring capability. It will then also be possible to include drift chamber information in the trigger decision.

To improve the beam focus at the HADES target position for secondary π beams, third quadrupole will complement the doublet just in front of the spectrometer. This magnet and the respective power supply were part of the CELSIUS inventory and are currently adopted to the GSI magnet and beam line control system. A test run with this new installation is foreseen for autumn 2007.

[1] see separate contribution to this annual report

References

[1] R. J. Porter *et al.* [DLS Collaboration], Phys. Rev. Lett. **79**, 1229 (1997) [arXiv:nucl-ex/9703001].

[2] E. L. Bratkovskaya, W. Cassing, R. Rapp and J. Wambach, Nucl. Phys. A **634**, 168 (1998) [arXiv:nucl-th/9710043].

[3] R. Holzmann *et al.* [TAPS Collaboration], Phys. Rev. C **56**, 2920 (1997).

[4] R. Arnaldi *et al.* [NA60 Collaboration], Phys. Rev. Lett. **96**, 162302 (2006) [arXiv:nucl-ex/0605007].

[5] G. Agakichiev *et al.* [CERES Collaboration], Eur. Phys. J. C **41**, 475 (2005) [arXiv:nucl-ex/0506002].

[6] HADES coll., GSI Scientific Report 2005

[7] G. Agakichiev *et al.* [HADES Collaboration], Accep. for publication in PRL.

[8] W. Cassing and E. L. Bratkovskaya, Phys. Rept. **308**, 65 (1999).

[9] D. Schumacher, S. Vogel and M. Bleicher, arXiv:nucl-th/0608041.

[10] M. D. Cozma, C. Fuchs, E. Santini and A. Fassler, Phys. Lett. B **640**, 170 (2006) [arXiv:nucl-th/0601059].

[11] L. G. Landsberg, Phys. Rept. **128**, 301 (1985).

[12] J. Markert, Doct. Thesis, Univ. Frankfurt (2005).

[13] C. Fuchs, M. I. Krivoruchenko, H. L. Yadav, A. Faessler, B. V. Martemyanov and K. Shekhter, Phys. Rev. C **67**, 025202 (2003) [arXiv:nucl-th/0208022].

[14] E. L. Bratkovskaya, W. Cassing and U. Mosel, Nucl. Phys. A **686**, 568 (2001) [arXiv:nucl-th/0008037].

Two- and three-particle azimuthal correlations of high-p_t charged hadrons in Pb-Au collisions at 158A GeV beam energy*

S. Kniege, H. Appelshäuser, and M. Ploskon for the CERES collaboration
University Frankfurt a.M., Germany

Azimuthal correlations of hadrons with high transverse momenta serve as a measure to study the energy loss and the fragmentation pattern of jets emerging from hard parton-parton interactions. Results from the CERES experiment on two- and three-particle correlations in Pb-Au collisions will be presented for different centralities of the collisions. A study of the correlations for different charge combinations of trigger and associated particles reveals charge ordering in the fragmentation process and sensitivity of the correlation function to the type of the leading hadron. Furthermore, a strongly non-Gaussian shape on the away-side of the two-particle correlation function is observed in central collisions, indicating significant interactions of the partons with the medium. Mechanisms like elastic scattering of the initial partons or the evolution of a mach cone [1] in the medium can lead to similar modifications of the jet structure on the away-side. An analysis based on three-particle correlations is presented which helps to shed light on the origin of the observed away-side pattern.

The study of jet properties in Heavy Ion Collisions can be performed by measuring the excess of particle pairs with high transverse momenta over the uncorrelated background by a correlation function $C_2(\Delta\phi) = S(\Delta\phi)/B(\Delta\phi)$ with $\Delta\phi = \phi_t - \phi_a$. One partice, denoted as the trigger particle (ϕ_t), is chosen to be a high transverse momentum particle (2.5<p_t<4.0 GeV/c (region A)) assumed to be close to a parton emerging from a hard collision. The (jet-) associated particles (ϕ_a) are investigated by measuring

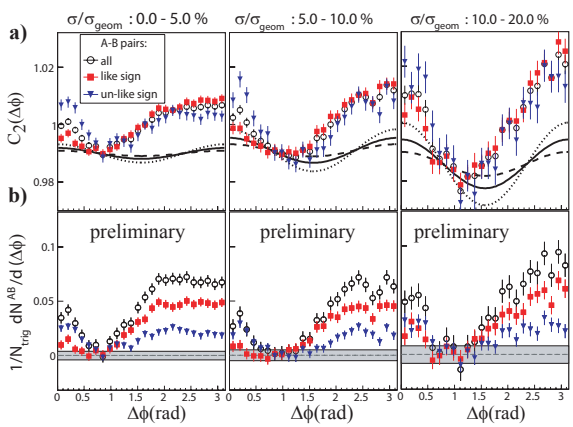

Figure 1: Two-particle correlation function a) and conditional yield b) for different centralities and charge combinations (black line: flow contribution with estimated error) (color online).

the differences in the azimuthal angles $\Delta\phi$ of all particles from a lower momentum region (1.0<p_t<2.5 GeV/c (region B)) resulting in the signal distribution $S(\Delta\phi)$. As a reference accounting for acceptance effects a background distribution $B(\Delta\phi)$ is constructed taking trigger and associated particles from different events. Besides the jet-like correlations, $C_2(\Delta\phi)$, there are correlations arising from the initial anisotropies of the collision zone resulting in an elliptic flow of the particles (black lines in Fig. 1(a)). In a two source approach the flow contribution is subtracted from the correlation function. After normalisation we obtain the conditional yield $1/N_{\text{trig}} \cdot dN^{\text{AB}}/d(\Delta\phi)$ reflecting the jet associated particles per trigger [2]. As can be seen in Fig. 1(b), the structure on the away-side deviates significantly from a Gaussian shape indicating medium effects on the emerging partons. In addition, a difference of the yields for different charge combinations of trigger and associated particles is observed. To further investigate the jet structure on the away-side correlations among the associated particles were studied.

Different scenarios like an event-by-event deflection of jets or the emission of particles in a cone could lead to similar structure on the away-side of the two-particle correlation function $C_2(\Delta\phi)$. In order to disentangle those scenarios correlations among the associated particles can be measured by determining the relative angle $\Delta\phi_{1,2}$ of two associated particles in one event relative to a (third) trigger particle and constructing the corresponding correlation function $C_3(\Delta\phi_1, \Delta\phi_2)$ as described above. The deflection

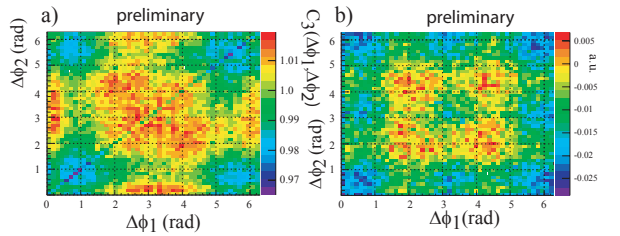

Figure 2: Three-particle correlation function (a) and jet yield (b) after subtraction of the contributions from two-particle correlations (color online).

of jets would result in pairs of associated particles being close by to each other thus populating dominantly the diagonal of the correlation function whereas a cone-like emission would give rise to off-diagonal structures. As for the two-particle correlation function non-jet correlations have to be subtracted from the measured correlation function. In Fig. 2 the correlation function (a) as well as the yield after subtraction of two-particle correlation contributions (b) are shown. In Fig. 2(b) clear off-diagonal components are visible. This gives strong indication that already at SPS energy medium effects on high-p_t particles are observed. Further investigations are needed to substantiate these findings.

References

[1] H. Stöcker, Nucl. Phys. A **750**, 121 (2005), J. Casalderrey-Solana, E. V. Shuryak and D. Teaney, Nucl. Phys. A **774**, 577-580 (2006).

[2] M. Ploskon *et al.* [CERES Collab.], Nucl. Phys. A **783**, 527-530 (2007).

* This work was supported by BMBF and GSI-F&E.

Two-particle correlations in Pb+Au collisions at the top SPS energy

D. Antończyk[1] and D. Miśkowiec[1]

for the CERES collaboration

[1]GSI, Darmstadt, Germany

Two-particle correlations are an excellent tool to examine the space-time evolution of the emitting source in heavy ion collisions [1]. In particular, the collective expansion of the source created in a collision with a finite impact parameter should lead to geometric asymmetries in the freeze-out hypersurface. To detect them, the correlation functions should be studied as a function of the pair emission angle relative to the reaction plane. In addition to the Hanbury-Brown-Twiss (HBT) two-particle correlations, the non-identical ones provide access to the information about average freeze-out positions or times of the two particle species [2].

The CERES spectrometer at the CERN SPS was dedicated to the study of the dilepton production in the collisions between heavy nuclei. After upgrade in the 1998 by a radial Time Projection Chamber (TPC) the CERES spectrometer opened the possibility of measuring charged hadrons. More information about the experimental setup as well as the data-set used here can be found in [3]. The high event statistics, collected in the final run of the CERES experiment in the fall of 2000 at the top SPS energy of 158 GeV per nucleon, and the good understanding of the experiment's resolution and of the Coulomb correction allowed to employ two sophisticated correlation techniques, the reaction plane dependent pion-pion HBT radius analysis and the pion-proton Coulomb correlation analysis [5]. The analysis of identical pions, performed in the longitudinal co-moving frame (LCMS), yielded HBT radii which, in their centrality and transverse momentum dependence, are in good agreement with the previous preliminary analysis of a subset of the data [4] and with the results of other experiments. The results support the collision picture with strong longitudinal and transverse expansion. To detect the azimuthal anisotropy of the pion source created in a collision with a finite impact parameter, the two-pion correlation were calculated in eight bins of the emission angle with respect to the reaction plane $\Phi^* = \Phi_{pair} - \Psi_{RP}$. The HBT radii plotted versus Φ^* were then fitted with $R_i^2 = R_{i,0}^2 + 2R_{i,2}^2 \cos(2\Phi^*)$ where i denotes $(out, side, long)$. The normalized second Fourier components obtained are shown in Fig. 1. The pion-proton correlation analysis, performed on the data-set collected by CERES spectrometer, allowed to measure a difference between the average freeze-out position or time of the two particle species in five bins of the pair transverse momentum. The description of the method used for this analysis was presented in [6]. The final results of this analysis, expressed in the spatial displacement between the proton and pion sources, are shown in Fig. 2. The displacement is similar to the spatial displacement seen in UrQMD (green line) and is well described

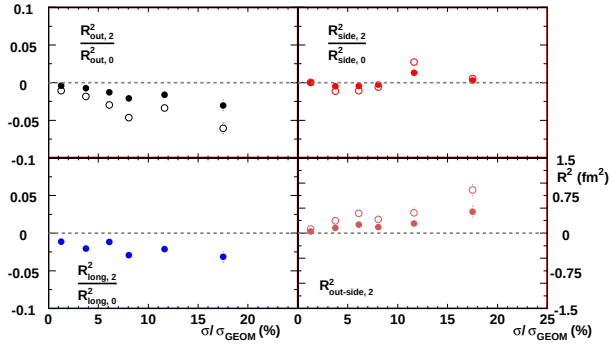

Figure 1: Fourier coefficients of azimuthal oscillations of HBT radii as a function of the event centrality. The full (open) symbols correspond to the 2^{th}-order Fourier coefficient uncorrected (corrected) for the influence of the finite reaction plane resolution.

by the parameterization $\Delta x = \frac{R_G\,\beta_\perp\,\beta_0}{\beta_0^2 + T/M_\perp}$ [7], with the pair transverse velocity $\beta_\perp$ and transverse mass $m_\perp$. The geometrical radius $R_G \sim 7.5$ fm and the transverse flow velocity $\beta_0 \sim 0.65 - 0.70$ were adjusted such as to match the transverse momentum dependence of R_{side}. This indicates that the finite displacement between the sources of pions and protons, to first order, has a similar origin as the $P_\perp$ dependence of the R_{side}, namely the transverse flow. The sign of the displacement indicates that the proton source is located at a larger radius than the pion source, or that protons are emitted earlier than pions.

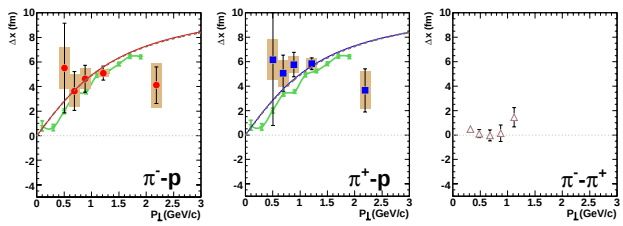

Figure 2: The source displacement as a function of the pair transverse momentum.

References

[1] M. A. Lisa et al., Ann.Rev.Nucl.Part.Sci. 55 (2005) 357-402

[2] R.Lednický et al., Phys. Lett. B373 (1996) 30

[3] D.Miśkowiec, Nucl. Phys. A774 (2006) 43-50; A. Marin, J. Phys. G30(2004) S709

[4] D.Adamova et al., Nucl. Phys. A714 (2003) 124-144

[5] D.Antończyk, PhD Thesis, TU Darmstadt (2006)

[6] D.Antończyk, GSI Scientific Report 2005, 230

[7] R.Lednický, Phys. Atom. Nucl. 67 (2004) 72-82

Charged kaon analysis within the CERES experiment

M. Kalisky for the CERES Collaboration[1]
[1]GSI, Darmstadt, Germany

Strangeness production in heavy ion collisions has raised and continues to raise interest both in experimental and theorist communities [3], [4]. In this report the status of the analysis of charged kaons registered via three charged pions decay is presented. After the upgrade of the CERES (NA45) [1] experimental setup in 1998 with a radial Time Projection Chamber (TPC) [2], the accessible physics region was extended to hadrons. In this analysis only the TPC information is being used. The data sample contains 30 million events of 7% most central Pb-Au collisions at a beam energy of 158 AGeV.

The analysis is based on the decay properties of charged kaons. K^+ decay into π^+ π^+ π^- with a branching ratio of 5.59%. Long lifetime ($c\tau$ = 3.713 m) allows for a strong background suppression via secondary vertex reconstruction. Small difference of the mass of the kaon in comparison to the sum of masses of 3 pions compresses the accessible kinematic phase space such that the pions after decay form a rather narrow cone; this opens up another possibility for the background suppression.

Because of a very high combinatorial background (due to three particle combinations) which results a very low signal to background ratio of $\sim 10^{-7}$ if no cuts are applied, it was inevitable to study the possible cuts with a Monte Carlo (MC) simulation prior to data analysis. These cuts include single track cuts (distance of the tracks from the event vertex in the transverse plane), pair cuts (difference in polar angle between the two tracks), and also 3 particle cuts (position of the reconstructed secondary vertex, quality of the secondary vertex and distance of the reconstructed kaon track to event vertex in the transverse plane). Efficiency determination is another important task of the MC. For this K^+ or K^- decays are embedded into experimental data and further analyzed (overlay MC). With this procedure the efficiency corrections can be obtained so it is possible to estimate the p_t spectra and absolute yield of kaons in the data.

The invariant mass distributions of K^+ and K^- for 3.8 millions 5% most central events are shown in Fig. 1. Measured peak position of 496.3 +/- 0.3 MeV/c^2 (for both K^+ and K^-) deviates from the PDG value by 2.5 MeV/c^2. The deviation can be reproduced by MC. The Signal-to-Background for the whole phase space is about 4 for K^+ and about 2 for K^-. The statistics of about 80k K^+ and 40k K^- expected for the full data set allows for differential studies. From the fits without additional efficiency correction a K^-/K^+ ratio can be obtained and is equal to value of 0.52 +/- 0.02 which is consistent with the existing data and the theoretical predictions [5].

In Fig. 2 the p_t versus rapidity distributions of the OMC and experimental data are shown. The mid-rapidity is at

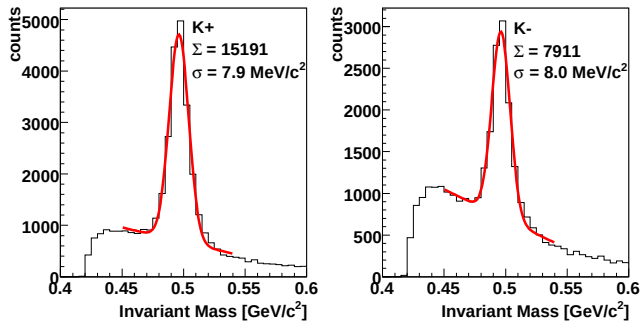

Figure 1: K+ (left) and K- (right) signal integrated over accessible p_t and rapidity.

2.913. The shape of the distributions is given both by the kinematics of the kaon decay and by the acceptance of the TPC which is $\sim$ 0.14 - 0.26 rad in the azimuthal angle.

The next steps of the analysis include the efficiency and acceptance correction with realistic assumption of p_t spectra and rapidity distribution of the kaons. Final results will be an independent verification of the results presented in [6] for the top SPS energy.

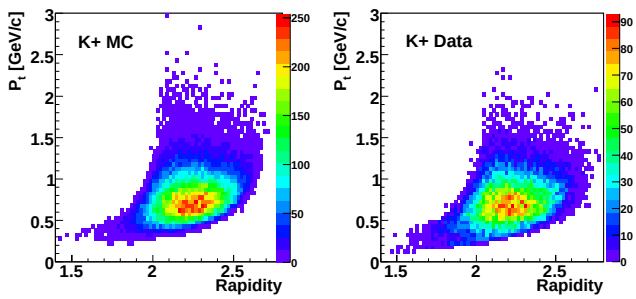

Figure 2: Simulated K+ (left) and measured K+ (right) phase space distributions.

References

[1] CERES/NA45 experiment; http://www.physi.uni-heidelberg.de/physi/ceres/

[2] A. Marin, J. Phys. G30 (2004) S709-S716.

[3] A. Andronic and P. Braun-Munzinger, Lect. Notes Phys. 652: 35-68, 2004.

[4] H. Stroebele, Nucl. Phys. A 749 (2005) 33c-41c.

[5] A. Andronic, P. Braun-Munzinger, J. Stachel; Nucl Phys. A 772 (2006) 167.

[6] A. Mischke, Eur. Phys. J. C33(2004) S621-S623.

Energy Dependence of Multiplicity Fluctuations in Central Pb+Pb Collisions

B. Lungwitz[1], C. Alt[1], C. Blume[1], P. Dinkelaker[1], D. Flierl[1], V. Friese[2], M. Gaździcki[1], M. Hauer[1], C. Höhne[2], S. Kniege[1], D. Kresan[2], M. Mitrovski[1], R. Renfordt[1], A. Sandoval[2], T. Schuster[1], R. Stock[1], C. Strabel[1], H. Ströbele[1,2], M. Utvic[1], A. Wetzler[1], and the NA49 Collaboration

[1]Fachbereich Physik der Universität Frankfurt; [2]GSI, Darmstadt, Germany

At high energy densities a new phase of matter, the quark-gluon-plasma (QGP), is expected to be formed. The energy dependences of various observables show anomalies at low SPS energies which might be related to the onset of deconfinement [1]. Both the onset of deconfinement and an approach to the critical point of strongly interacting matter might lead to an extraordinary increase of multiplicity fluctuations. In addition to the effects mentioned above also the normal statistical fluctuations are interesting to study, since the size of the multiplicity fluctuations depends on the nature of the particle ensemble (micro-canonical, canonical, grand-canonical) [5]. This motivates a detailed study of the energy [2, 3] and centrality [4] dependence of multiplicity fluctuations measured by the scaled variance $\omega = Var(n)/ < n >$.

For the study of the energy dependence of multiplicity fluctuations, very central $Pb + Pb$ collisions were selected, for which the fluctuations in the number of participants can be neglected. The multiplicity distribution of negatively charged hadrons at top SPS energy in the most central Pb+Pb collisions at $158A$ GeV is shown in figure 1 in comparison with a Poisson distribution, which is close to the prediction of the grand canonical model. The measured distributions are significantly narrower than the Poissonian ones at $20A$, $30A$, $40A$, $80A$ and $158A$ GeV[2]. The energy dependence of scaled variance for negatively charged hadrons is shown in figure 2, left. The detector acceptance changes with energy so that a direct quantitative comparison of scaled variance at different energies is not possible. A comparison to string hadronic models show that UrQMD reproduces the data on scaled variance, although the mean multiplicity is overpredicted (see figure 2, right). The Venus model underpredicts the mean multiplicity and overpredicts ω at higher energies. In [5] it is shown that the measured fluctuations are smaller than predicted by the canonical and grand-canonical model, but seem to be in agreement with the micro-canonical model.

The data on energy dependence of multiplicity fluctuations show no indication for a maximum, as expected for the onset of deconfinement or the approach to the critical point. The UrQMD model, which does not include such effects, follow the data. The suppression of fluctuations in comparison to the grand-canonical model can be explained by charge and energy-momentum conservation [5].

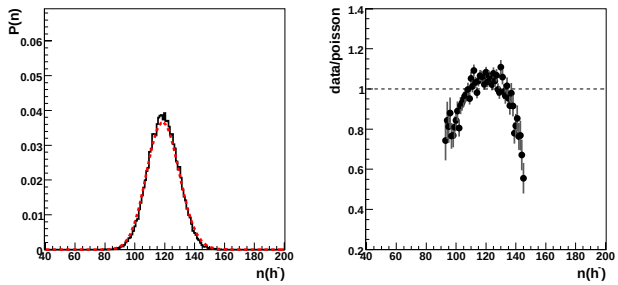

Figure 1: Left: multiplicity distribution of negative hadrons in central $Pb + Pb$ collisions at $158A$ GeV. The red line indicates a Poisson distribution with the same mean multiplicity. Right: ratio of the measured multiplicity distribution to Poisson distribution.

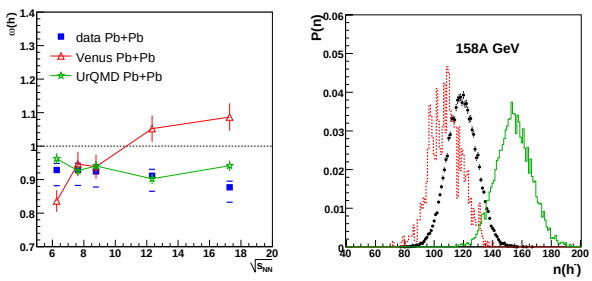

Figure 2: Left: Energy dependence of multiplicity fluctuations of h^- in $Pb + Pb$ collisions in comparison to string-hadronic models Venus and UrQMD. Right: Multiplicity distributions of negatively charged hadrons in the most central ($C < 1\%$) $Pb+Pb$ collisions at $158A$ GeV; data - black circles, Venus model - dashed red line and UrQMD - solid green line.

References

[1] M. Gazdzicki *et al.* [NA49 Collaboration], "Report from NA49," J. Phys. G **30** (2004) S701 [arXiv:nucl-ex/0403023].

[2] B. Lungwitz [NA49 Collaboration], arXiv:nucl-ex/0610046.

[3] B. Lungwitz [NA49 Collaboration], arXiv:nucl-ex/0610047.

[4] C. Alt [NA49 Collaboration], arXiv:nucl-ex/0612010.

[5] V. V. Begun, M. Gazdzicki, M. I. Gorenstein, M. Hauer, V. P. Konchakovski and B. Lungwitz, arXiv:nucl-th/0611075.

Spectra of baryons from NA49

C. Alt[1], A. Argyrakis[1], C. Blume[1], P. Dinkelaker[1], V. Friese[2], M. Gaździcki[1], C. Höhne[2], M. Kliemant[1], S. Kniege[1], D. Kresan[2], B. Lungwitz[1], M. Mitrovski[1], R. Renfordt[1], T. Schuster[1], R. Stock[1], C. Strabel[1], H. Ströbele[1], M. Utvić[1], A. Wetzler[1], and and the NA49 Collaboration[1]

[1]Fachbereich Physik der Universität Frankfurt, Germany; [2]GSI, Darmstadt, Germany

New results on the rapidity dependence of (anti-) proton production at 20A - 80A GeV together with previously published results on (anti-) hyperons [1, 2] allow to construct *total* net-baryon rapidity distributions $\mathrm{d}N_{(\mathrm{B}-\bar{\mathrm{B}})}/\mathrm{d}y$. The contributions of unmeasured baryons (n, $\Sigma^{\pm}$, Ξ^0) are estimated using the particle ratios from a statistical model fit [3]. The resulting spectra are shown in Fig. 1 together with data at lower [4] and higher [5] energies. The shapes exhibit a clear evolution from Gaussian-like shapes at low energies to a two bump structure at high energies.

The difference between the energy carried by all (net) baryons before and after a nuclear collision is often used as a measure of stopping. It can be calculated from the rapidity distributions and mean transverse masses of the net baryons:

$$E_{\mathrm{inel}} = \frac{\sqrt{s_{\mathrm{NN}}}}{2} - \frac{1}{N_{(\mathrm{B}-\bar{\mathrm{B}})}} \int_{-y_p}^{y_p} \langle m_{\mathrm{t}} \rangle \frac{\mathrm{d}N_{(\mathrm{B}-\bar{\mathrm{B}})}}{\mathrm{d}y} \cosh y \, \mathrm{d}y \quad (1)$$

The inelasticity $K = 2\,E_{\mathrm{inel}}/(\sqrt{s_{\mathrm{NN}}} - 2m_{\mathrm{p}})$, derived from equation (1), is found to be approximatly energy independent with a value of $K \approx 0.7 - 0.8$ (not shown) which is large compared to the inelasticity in p+p interactions (≈ 0.5 at high energies).

Figure 2 shows new NA49 results on Λ and $\bar{\Lambda}$ production in minimum bias Pb+Pb reactions, together with preliminary Ξ^- data for the same datasets [6]. While there is no system size dependence of the $\langle N_{\mathrm{w}} \rangle$-normalized rapidity densities for Λ and $\bar{\Lambda}$, a weak rise can be observed in the case of the Ξ^-.

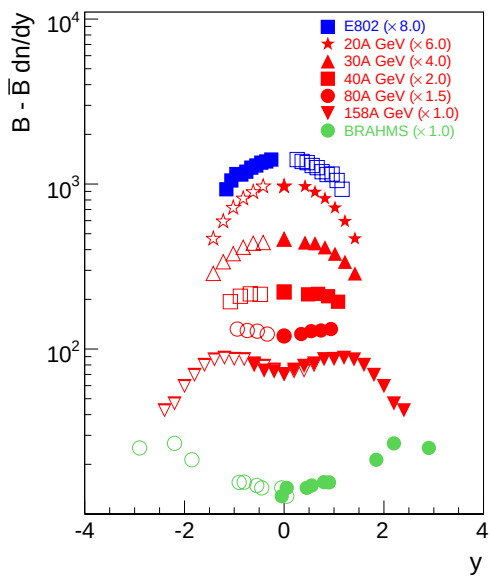

Figure 1: The rapidity distributions of net-baryons at SPS energies [2] together with results from the AGS [4] and from RHIC [5] for central Pb+Pb/Au+Au collisions.

References

[1] C. Alt et al. (NA49), Phys. Rev. **C 73** (2006), 044910.
[2] H. Appelshäuser et al. (NA49), PRL **82** (1999), 2471.
[3] F. Becattini et al., Phys. Rev. **C 73** (2006), 044905.
[4] L. Ahle et al. (E802), Phys. Rev. **C 60** (1999), 064901.
[5] I.G. Bearden et al., (BRAHMS), PRL **93** (2004), 102301.
[6] M. Mitrovski et al.(NA49), J. Phys. **G 32** (2006), s43.

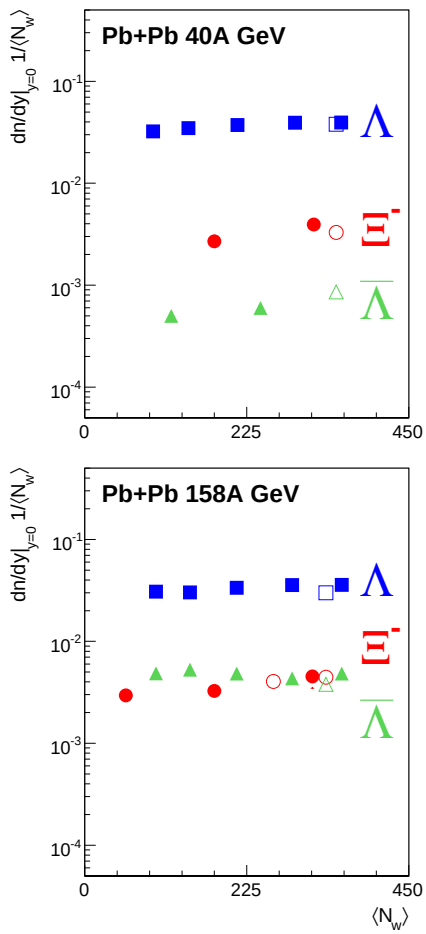

Figure 2: The rapidity densities of Λ, $\bar{\Lambda}$, and Ξ^- at midrapidity ($|y| < 0.4$ for Λ ($\bar{\Lambda}$), $|y| < 0.5$ for Ξ^-) for minimum bias Pb+Pb collisions as a function of $\langle N_{\mathrm{w}} \rangle$. Open symbols represent the results for central Pb+Pb reactions.

System-size dependence of strangeness production in high-energy A+A collisions and percolation of strings

C. Höhne[1], F. Pühlhofer[2], and R. Stock[3]

[1]GSI Darmstadt; [2]Philipps-Universität Marburg; [3]Johann Wolfgang Goethe-Universität Frankfurt

The CERN-NA49 Collaboration has recently published the yields of a series of strangeness-carrying particles (charged kaons, Λ, ϕ, in addition charged pions for normalization) in central C+C and Si+Si collisions at the top SPS energy ($\sqrt{s_{NN}} = 17.3$ GeV) [1]. Together with earlier data for p+p, S+S and Pb+Pb the systematics of strangeness production as a function of the size of the collision system was obtained. For all individual particles, including the ϕ-meson, the pion-normalized yields show a steep increase starting at p+p followed by a saturation at about 60 participating nucleons. A similar behavior is observed in the centrality dependence of the $\langle K^+\rangle/\langle\pi^+\rangle$ ratio in Au+Au collisions at $\sqrt{s_{NN}} = 200$ GeV measured by the PHENIX collaboration at RHIC [2]. In general, a strangeness enhancement in large systems compared to small ones is expected from a statistical treatment of the interacting matter: the production of strange quarks or hadrons containing such quarks is suppressed in small reaction systems due to phase space limitations that arise as a consequence of strict flavor conservation. So far, the reaction volume was usually assumed to be simply proportional to the total number of nucleons participating in the collision. This, however, lead to a strangeness saturation already at less than 10 participants in the model, e.g. [3].

Here, we present briefly the results of a study published recently [4] in which the relation between the reaction volume V and the number of colliding nucleons $N_{\rm wound}$ is investigated more carefully. Starting from a microscopic model of a nucleus-nucleus interaction the density of the individual N+N collisions is calculated. As the longitudinal dimension of the reaction zone in the center-of-mass system is below 1 fm in particular at the lighter systems at top SPS and higher energies, we do not subdivide this longitudinal dimension any further but integrate over it. With this simplification, one obtains a 2-dimensional distribution of N+N interactions in the transverse plane. It is then assumed that due to the statistical overlap of the associated strings clusters of highly excited and strongly interacting matter are formed. The technique applied is a percolation model. In general, these clusters consist of subgroups of the participating nucleons. Only with heavy collision partners a single cluster comprising nearly all participants is formed. Assuming that a cluster of overlapping strings can be considered as a coherent entity, the clusters are then assumed to hadronize independently. The resulting particle compositions are calculated from the statistical model, i.e. the effect of canonical strangeness suppression is used, though at a different level. The strangeness suppression factor η (as defined in [3]) is obtained for the individual cluster volumes, and averaging over many collisions for a specific system a volume-weighted mean is derived. η represents the predicted relative strangeness production. Experimentally, it is approximated by $E_s = \frac{\langle\Lambda\rangle+2(\langle K^+\rangle+\langle K^-\rangle)}{\langle\pi\rangle}$ (SPS) or $\langle K^+\rangle/\langle\pi^+\rangle$ (RHIC). In order to apply the chosen statistical hadronization scheme the cluster sizes in the transverse plane are transformed to 3-dimensional hadronization volumes V assuming a linear relationship.

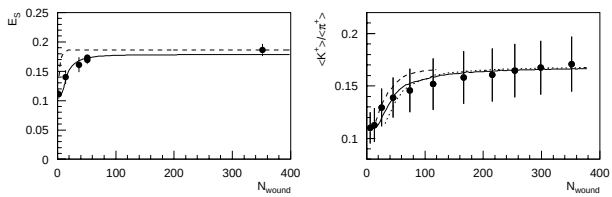

Figure 1: System-size dependence of strangeness enhancement. Left: E_s measured by NA49; Right: $\langle K^+\rangle/\langle\pi^+\rangle$ measured by PHENIX. The solid lines represent results from the percolation model; for other details see text.

Results from the model described above are presented in figure 1 in comparison to the mentioned data from SPS and RHIC. In both figures the solid lines show the calculations for the presented data. In the left frame, the dashed line shows the result of the statistical model with the commonly assumed linear relationship between V and the number of participating nucleons $N_{\rm wound}$. In the right frame, the short dashed line shows the expected E_s for centrality dependent Pb+Pb collisions at $\sqrt{s_{NN}} = 17.3$ GeV which will be measured by NA49. The long dashed line shows a prediction for Cu+Cu at $\sqrt{s_{NN}} = 200$ GeV.

The fact that for small collision systems several hadronizing volumes are formed instead of one large cluster leads to a softening of the system size dependence of relative strangeness production, and the theoretical results come into agreement with the experimental data.

We thank our NA49 colleagues, in particular V. Friese, M. Gazdzicki and P. Seyboth, for valuable discussions.

References

[1] C. Alt et al., Phys. Rev. Lett. 94 (2005) 052301.

[2] S.S. Adler et al., Phys. Rev. C 69 (2004) 034909.

[3] J. Rafelski and M. Danos, Phys. Lett. B 97 (1980) 279. A. Tounsi and K. Redlich, J. Phys. G: Nucl. Part. Phys. 28 (2002) 2095.

[4] C. Höhne et al., Phys. Lett. B 640 (2006) 96-100.

Online monitoring for the ALICE-TPC commissioning*

S. Kniege[1], H. Appelshäuser[1], R. Bramm[2], L. Musa[3], and R. Renfordt[1] for the ALICE collaboration
[1]University Frankfurt, Germany; [2]GSI, Darmstadt, Germany; [3]CERN, Geneva, Switzerland

Introduction

ALICE [1] is A Large Ion Collider Experiment which will start operation in 2007 in the course of the CERN LHC program. The main tracking device of the experiment is a cylindrical Time Projection Chamber [2] (TPC). A ROOT based software module was developed to monitor online the data stream from the TPC during the commissioning phase at CERN in 2006. The main features of the program as well as results from tests during the commissioning phase will be presented.

The ALICE-TPC

The ALICE-TPC is designed to detect up to 20000 charged tracks emerging from Pb+Pb collisions at a center of mass energy of $\sqrt{s_{NN}}$ = 5.5 TeV. Given the length of 510 cm and an outer radius of 250 cm it comprises a total sensitive drift volume of 88 m^3 filled with a gas mixture of $NeCO_2N_2$ (85/10/5). The drift field of 400 V/cm is provided by a central high voltage electrode and terminated by multi-wire proportional pad chambers mounted on the endcaps on both sides of the TPC. The readout is segmented into 36 sectors with a total of 557568 pads where 128 pads are read out by one Frond End Card (FEC). Baseline correction, tail cancellation and zero suppression can be performed online by the ALTRO chip [3] of the FEC.

Commissioning and Monitoring

After the installation of the FECs a commissioning phase started where two sectors were tested at a time in different operational modes. Cosmic tracks were recorded as well as tracks injected to the drift volume by a Laser system to check the alignment of the detector components. In addition, signals could be induced directly to the cathode plane of the chambers by a calibration pulser.
The primary goal of the online monitoring during the commissioning was to check the functionality of the TPC readout chain, the mapping of the readout components and the proper decoding of the data. After decoding the data a fast baseline subtraction

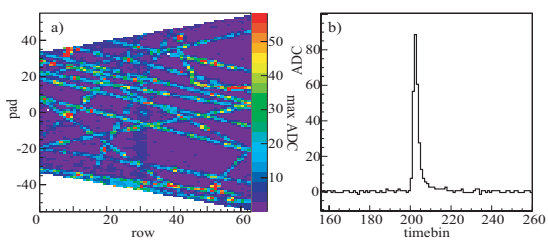

Figure 1: Maximum ADC values for one Read Out Chamber (ROC) (a) and time profile for one selected pad (b)

algorithm based on a truncated mean method was applied to remove the pedestals for each channel. The maximum ADC value was displayed in a histogram (Fig.1a) with a link to an executable showing the time profile (Fig.1b) for each pad. Moving the mouse along a track one could thus easily follow the profile of a track in time and space. Fits could be performed to all channels in order to display the arrival time of the signals. Hence an immediate coarse picture of the alignment of detector components and gain differences of single channels could be obtained. In addition, the width of the baseline σ was calculated for each channel and displayed according to Fig.1a. Knowing the FEC positions in the detector from the installation and the mapping of the readout chips and connectors on the FECs it was possible to isolate signals on a given selection of components. It was thus possible to identify single malfunctioning channels and replace the corresponding FEC.
The performance of the TPC is mainly determined by the noise level induced on the channels. With a design signal-to-noise ratio of 30:1 and a dynamic range of the Analog to Digital Converter (ADC) in the ALTRO of 2 V the noise level σ should not exceed 1 ADC count. However at the beginning of the commissioning phase a significant fraction of pads exeeded this design value (Fig.2a). It could be shown that the high noise level was mainly

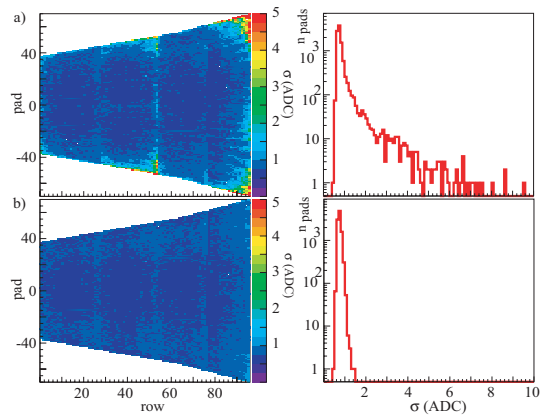

Figure 2: Width of the baseline σ in one ROC before (a) and after (b) the change of the ground cables and the readout scheme.

due to the digital current arising from the synchronous readout of the channels and the insufficient cross section of the ground cables. The Front End Electronics allowed to apply a time offset in the readout to groups of channels in order to reduce the instantaneous digital currents. In addition, increasing the diameter of the ground cables reduced the noise level on the channels significantly so that the design requirements were fulfilled (Fig.2b).

References

[1] ALICE Technical proposal, Dec. 1995, ISBN 92-9083-077-8.

[2] ALICE-TPC Technical Design Report, Dec. 1999, ISBN 92-9083-155-3.

[3] L. Musa et al, ALICE-TPC Readout Chip Users Manual, June 2002 http://ep-ed-alice-tpc.web.cern.ch/ep-ed-alice-tpc/doc/ALTRO_CHIP/UserManual_draft_02.pdf.

* This work was supported by BMBF and GSI-F&E.

Results from the ALICE-TPC laser calibration system

J. Wiechula[1]
[1]GSI, Darmstadt, Germany

A cylindrical Time Projection Chamber [1], is the main tracking device of the dedicated heavy ion LHC experiment ALICE at CERN.

Each end of the cylinder holds a readout plane which is subdivided into 18 segments in azimuth and two parts in radius (s. fig. 1). Both readout planes thus consist of 18 inner- and 18 outer multiwire proportional readout chambers (IROC and OROC, respectively) with cathode pad readout. A Central (high voltage) Electrode (CE) divides the TPC into two readout sides (A- and C-Side).

On either readout side a system of micro-mirror bundles distributes a laser beam in four planes along the beam direction. The resulting 168 laser rays can be used to measure, the residual misalignment between adjacent readout chambers. A projection on the transverse-plane of the star-like pattern of laser rays is shown in fig. 1.

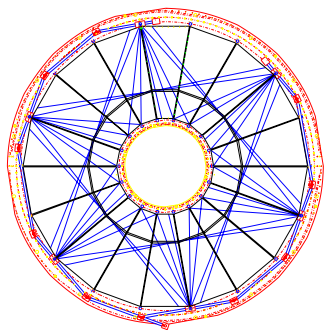

Figure 1: Endplate with positions of the laser rays

In addition to the signals from the laser tracks nearly each of the $\approx$ 550.000 readout pads receives a signal from the CE. It arises from photoelectrons from scattered laser light. This information will also be used for the alignment.

With the laser system it is also possible to determine the electron drift velocity in the detector gas (Ne-CO_2-N_2) [2] which is very sensitive to changes in temperature, pressure and gas composition. The drift velocity is needed to calculate the absolute position in beam direction from the drift time and can also be used to monitor the gas quality.

To determine the drift velocity the difference in arrival times Δt_{arr} of electrons from the CE and the laser beam plane closest to the readout plane was determined. Only the outermost 20 cm of the laser rays from one micro-mirror bundle were used. The positions of the laser rays with respect to the CE Δl are known from the technical drawings. The drift velocity is calculated as $v_{drift} = \Delta l / \Delta t_{arr}$.

Fig. 2 shows the results of the drift velocity measurements as a function of the date during the commissioning phase of the TPC [3]. The results are compared with measurements from the drift velocity monitor goofie [4]. Both measurements agree within less than 1 %.

As an example for alignment measurements fig. 3 shows the radial dependence of the drift distance, shifted by the measured mean drift distance, between the ROCs and the CE for two opposing sectors. To determine the drift distance from the measured drift time, the derived drift velocity as described above was used. The steps at $r = 133$ cm correspond to the transition from IROC to OROC and have the main reasons: a different response time of the electronics due to different pad capacities of IROC and OROC, mechanical alignment and field distortions. The origin of the slope, which is seen in all sectors and is negative on the opposite readout side, is still under investigation. Edge effects from field distortions are visible at the inner and outer radii of the TPC.

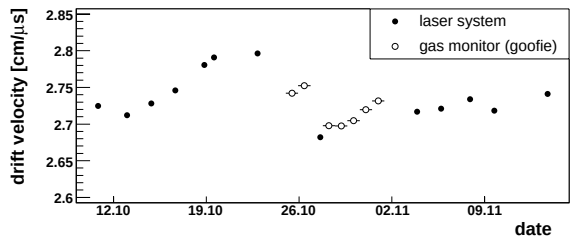

Figure 2: Drift velocity measurements as a function of the date. Comparison between results from the laser system and the gas quality monitor goofie.

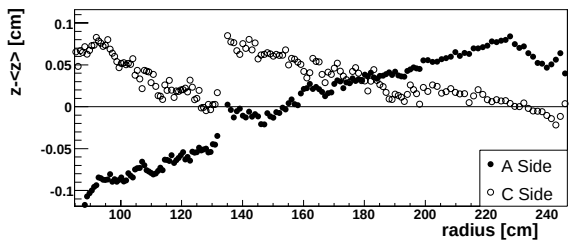

Figure 3: Measured position of the central electrode as a function of the radius for two opposing sectors.

References

[1] ALICE TPC Technical Design Report, CERN/LHCC 2000-001

[2] C. Garabatos, Nucl. Instr. and Meth. A 535 (2004) 197.

[3] P. Braun-Munzinger et al., "Commissioning of the ALICE Time Projection Chamber", GSI Scientific Report 2006

[4] J. Castillo et al., "Experience with the Goofie during the TPC commissioning", GSI Scientific Report 2006.

Hadronic sources of the event-by-event fluctuations of the K/π ratio

D. Kresan[1] and V. Friese[1]
[1]GSI, Darmstadt, Germany

Large event-by-event fluctuations are expected to be an experimental signature of the QCD critical point. As one candidate for such fluctuations, the ratio of the yields of strange to nonstrange mesons, in particular the kaon to pion ratio, has been proposed [1]. This observable has been measured by the NA49 collaboration at CERN-SPS in central Pb+Pb collisions from 20 to 158 AGeV [2]. The K/π fluctuations were obtained to be positive and increasing towards smaller beam energies. The p/π fluctuations, in contrast, are negative throughout all energies. This has been attributed to the influence of resonance (Δ) decays introducing a correlation (negative fluctuation) of protons and pions. It is obvious that hadronic effects like resonance decays and hadronic interactions result in non-vanishing fluctuations also in the K/π ratio, which should be studied in detail in order to correctly interpret the experimental data.

Fig. 1 shows the results of calculations with the string-hadronic transport model UrQMD, taking into account the detector acceptance, in comparison to the NA49 data. While the p/π fluctuations are well reproduced, the K/π data deviate from the model at lower beam energies. The influence of the detector acceptance is noticeable but not dramatic in case of K/π.

It should be noted that the ratio referenced above is the ratio of charged kaons over charged pions, i. e. $(K^+ + K^-)/(\pi^+ + \pi^-)$. Interestingly, all single particle ratios (K^+/π^+, K^-/π^- and vice versa), not measured by NA49, show negative fluctuations in the model. This suggests a significant influence of resonances as in the case of p/π. Indeed, about half of all charged kaons produced by UrQMD originate from the decay of K^*.

Positive fluctuations in the ratio of the sum of kaons over the sum of pions can be introduced by decays producing kaon or pion pairs, like e. .g. $\phi \rightarrow K^+K^-$ or alternatively

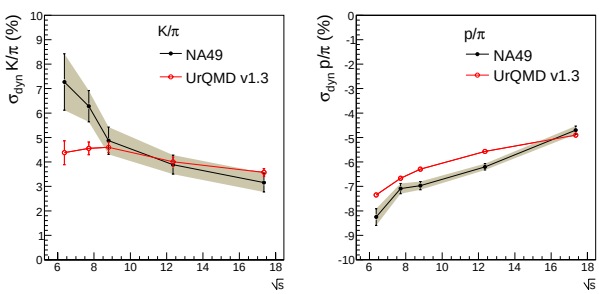

Figure 1: Dynamical fluctuations of (left) the K/π and (right) the p/π ratio as function of collision energy. The open circles denote results obtained with UrQMD, the closed one experimental results.

$\phi \rightarrow \rho\pi^0 \rightarrow \pi + \pi^-\pi^0$. For this decay, an analytical formula can be derived for the fluctuations in full phase space:

$$\sigma^2_{dyn} = \frac{2\cdot <\phi> \cdot BR_{KK}}{<N_K>^2} + \frac{2\cdot <\phi> \cdot BR_{\pi\pi}}{<N_\pi>^2} - 2\frac{Cov(N_K, N_\pi)}{<N_K><N_\pi>}$$

Here, $N_{K,\pi}$ denotes the multiplicity of primary particles. Since pions are more abundant than kaons, and the branching ratio of ϕ into kaons is larger, the first term dominates.

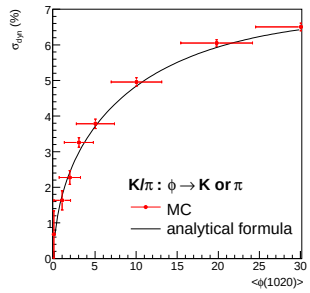

Figure 2: Dynamical fluctuations of the kaon to pion ratio obtained by the generic model as function of the ϕ yield

In order to systematically study the influence of resonance decays to the fluctuation signal, a generic decay model was developed which generates resonance decays in an environment of primary particles with given mean multiplicities and phase space distributions. Fig. 2 shows the fluctuations induced by the ϕ decay obtained from this model in full phase space as a function of the ϕ multiplicity. The yields of kaons and pions were taken from UrQMD at 25 AGeV. It can be seen that the fluctuation signal is a strong function of the ϕ yield. Accurate knowledge of the latter is thus mandatory in order to decouple the hadronic contribution to the fluctuations from possible critical phenomena.

The results of our model in full phase space agree with the analytical formula as shown in fig. 2. However, it also allows to account for limited detector acceptance. In the future, we will thus apply the generic resonance model to all beam energies measured by NA49, using experimental data on pion, kaon and resonance yields and distributions and taking into account the detailed detector acceptance.

References

[1] S. Jeon and V. Koch, Phys. Rev. Lett **85** (2000) 2076

[2] C. Roland (for the NA49 collaboration), J. Phys. G: Nucl. Part. Phys. **31** (2005) 1075

Study of the ηN scattering amplitude through the associated photoproduction of ϕ- and η-mesons in the region of the N*(1535) resonance *

M.F.M. Lutz[1] and M. Soyeur[2]
[1]GSI, Darmstadt, Germany; [2]DAPNIA, CEA/Saclay, France

The quantity of interest in this work is the s-wave η-nucleon scattering amplitude displayed in Fig 1. The real and imaginary parts of this amplitude are derived in the relativistic coupled-channel scheme of Ref. [1]. The corresponding η-nucleon scattering length is $a_{\eta N}$=(1.03 + i 0.49) fm. The range of values found in the literature for Re $a_{\eta N}$ (from $\sim$ 0.3 to $\sim$1 fm) is however very broad and reflects the indirect nature of the determination of Re $a_{\eta N}$ from η-meson production reactions.

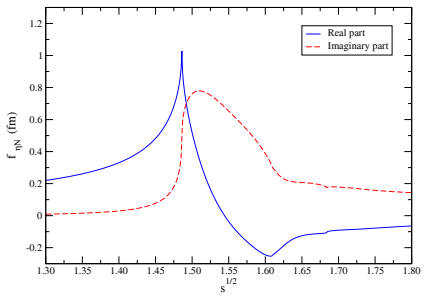

Figure 1: Real and imaginary parts of the s-wave ηN scattering amplitude (from Ref. [1])

The purpose of this calculation [2] is to show that the $\gamma p \to \phi\eta p$ process in specific kinematic conditions is most sensitive to the η-nucleon scattering at threshold, so that accurate data on this process could help determining $a_{\eta N}$.

These kinematic conditions are twofold. On the one hand the ηp invariant mass in the final state should be close to its threshold value and not much larger than the N*(1535) resonance mass. On the other hand the initial photon energy should be sufficiently high, typically in the range $4 < E_\gamma^{Lab} < 5$ GeV, in order to reach low (absolute) values of the squared 4-momentum transfer from the initial photon to the final ϕ-meson ($|t| < 1$ GeV^2).

In these conditions, we expect the $\gamma p \to \phi\eta p$ reaction cross section to be dominated by the η t-channel exchange, offering the possibility to test the η-nucleon scattering amplitude. Both π- and η-exchanges can contribute (see Fig. 2). The dominance of the η-exchange comes mainly from the very unfavourable ratio $(g_{\phi\pi\gamma}/g_{\phi\eta\gamma})^2$ which is of the order of 1/29 [2]. The s-wave $\pi\, p \to \eta\, p$ amplitude is also significantly smaller than the $\eta\, p \to \eta\, p$ amplitude. The relative sign of the coupling constants $g_{\phi\pi\gamma}$ and $g_{\phi\eta\gamma}$ is not fully determined. We have therefore calculated the interference between the π- and η-exchanges with both signs.

* Work supported by the European Community-Research Infrastructure Activity under the FP6 "Structuring the European Research Area" programme (Hadron Physics, contract number RII3-CT-2004-506078)

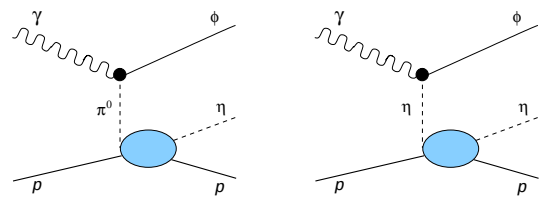

Figure 2: π^0- and η-exchange contributions to the $\gamma\, p \to \phi\, \eta\, p$ process.

A typical result of our calculation (based on the $\pi p \to \eta p$ and $\eta p \to \eta p$ amplitudes derived in Ref. [1]) is shown in Fig. 3. The calculation confirms that the π^0-exchange term is negligible while the $\pi^0 - \eta$ interference is not. As the $\pi p \to \eta p$ scattering amplitude in the N*(1535) resonance region is rather well-known, accurate data on the $\gamma\, p \to \phi\, \eta\, p$ reaction at $E_\gamma^{Lab} = 4$-5 GeV and low t would put additional constraints on the η-proton scattering amplitude close to threshold. The expected cross sections are small but do not appear out of reach of present experimental facilities. The measurement of the $\gamma p \to \phi\eta p$ reaction in these kinematics could be performed at JLab.

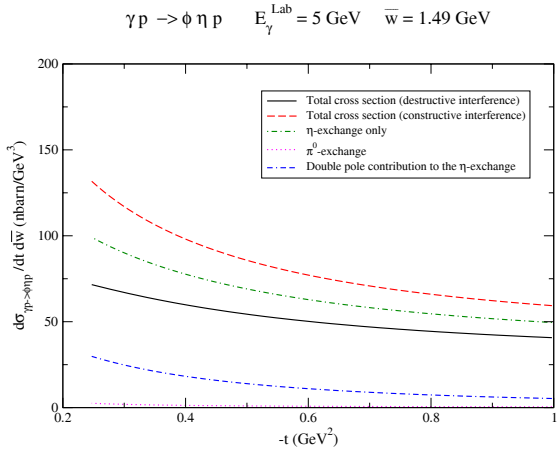

Figure 3: Differential cross section $d\sigma_{\gamma\, p\to\phi\, \eta\, p}/dt\, d\bar{w}$ at $E_\gamma^{Lab} = 5$ GeV for a total center of mass energy of the ηN pair of 1.49 GeV (from Ref. [2]). The meaning of the lines is given in the insert.

References

[1] M.F.M. Lutz, Gy. Wolf, B. Friman, Nucl. Phys. A 706 (2002) 431; ERRATUM-ibid A 765 (2006) 495.

[2] M.F.M. Lutz, M. Soyeur, Nucl. Phys. A 773 (2006) 239.

Discontinuous quark-mass dependence of baryon octet and decuplet masses

A. Semke and M.F.M. Lutz, GSI, Darmstadt, Germany

The present-day interpretation of QCD lattice simulations requires a profound understanding of the dependence of observable quantities on the light quark masses. A powerful tool to derive such dependencies is the chiral Lagrangian, an effective field theory based on the chiral properties of QCD. The application of strict chiral perturbation theory to the SU(3) flavor sector of QCD is plagued by poor convergence properties for processes involving baryons [1]. Thus it is important to establish partial summation schemes that enjoy improved convergence properties and that are better suited for chiral extrapolations of lattice simulations.

A recent novel scheme was suggested in [2, 3], the construction of which was guided by keeping manifestly covariance, analyticity and causality. The computation of the baryon octet and decuplet masses in this scheme was worked out recently indicating convincing convergence properties of the chiral loop expansion [2].

It is the purpose of the present work to confront the results of [2] with recent lattice QCD simulation of the MILC collaboration [4, 5], that use dynamical u-,d- and s-quarks in the staggered approximation. We do not aim at a quantitative extrapolation of the lattice simulation, which would require a continuum limit extrapolation and a quantitative control of systematic errors. Rather, we want to use the available partial lattice results to make predictions for future QCD lattice simulations and possibly obtain rough constraints on some chiral parameters.

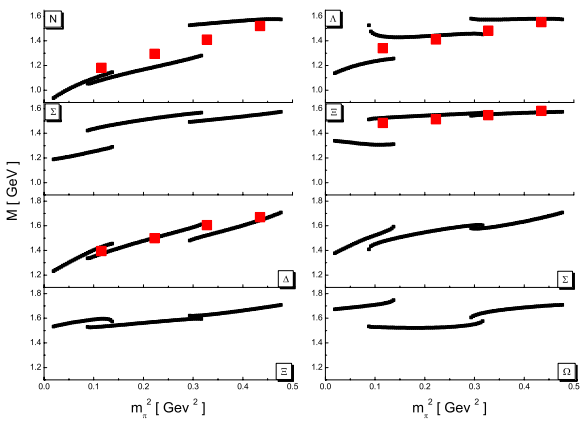

Figure 1: The pion mass dependence of baryon octet and decuplet masses predicted by the chiral loop expansion [3]. The solid squares are lattice simulations points from [4].

We evaluated the baryon octet and decuplet self energies at the one-loop level applying the relativistic chiral Lagrangian. Adjusting the Q^2 counter terms an excellent representation of the physical baryon octet and decuplet masses is obtained. The size of the pion-nucleon sigma term was estimated by including in the fit the baryon octet and decuplet masses at the SU(3) symmetric point defined by $m_\pi \simeq 690$ MeV. For the latter the MILC collaboration suggests the values $M_{[8]} \simeq 1575$ MeV and $M_{[10]} \simeq 1710$ MeV. As a result we predict $\sigma_{\pi N} \simeq 54$ MeV. The kaon-nucleon sigma terms are $\sigma_{K^- p} \simeq 380$ MeV and $\sigma_{K^- n} \simeq 355$ MeV.

Given this scenario the pion-mass dependence of the baryon octet and decuplet masses were evaluated. The latter are a solution of a set of coupled and non-linear algebraic equations. This is a direct consequence of self consistency imposed on the partial summation, i.e. the masses used in the loop functions are identical to those obtained from the baryon self energies. As a striking consequence we predict a discontinuous dependence of the baryon masses on the pion mass (see Fig. 1). Typically the baryon masses jump at pion masses as low as 300 MeV. Most spectacular is the behavior of the Ξ mass. At small pion masses it decreases with increasing pion masses. At a critical pion mass of about 300-400 MeV it jumps up to a value amazingly close to the prediction of the MILC collaboration. For all baryon masses for which the MILC collaboration published simulation points our results are reasonably close to the lattice estimates, given the present uncertainties from finite lattice spacing, the staggered approximation and the theoretical uncertainties implied by higher order contributions to the baryon self energies.

It is interesting to speculate on the physics behind such an unexpected quark-mass dependence of the baryon masses. A discontinuous behavior may signal a new type of phase transition - or perhaps only some so-far unknown instability of QCD for certain parameter choices. One may argue that in the intermediate quark-mass region a ghost state appears causing an instability. At present we can not exclude the possibility that our results merely indicate that the chiral extrapolation stops making sense at quite small quark masses. On the other hand further chiral correction terms may connect the various branches in a smooth manner providing a quite non-liner quark mass dependence of the baryon masses.

References

[1] E. Jenkins, Nucl. Phys. **B 368** (1992) 190.

[2] A. Semke and M.F.M. Lutz, Nucl. Phys. **A 778** (2006) 153.

[3] A. Semke and M.F.M. Lutz, nucl-th/0606027.

[4] C. Bernard et al., Phys. Rev. **D 64** (2001) 054506.

[5] C. Aubin et al., Phys. Rev. **D 70** (2004) 094505.

Antikaons in dense matter from a chiral unitary approach

L. Tolós[1,2], A. Ramos[3], and E. Oset[4]

[1]FIAS, J. W. Goethe-Universität, Frankfurt (M), Germany; [2]GSI, Darmstadt, Germany; [3]Universitat de Barcelona, Barcelona, Spain; [4]Universitat de Valencia-CSIC, Valencia, Spain

The interaction of the $\bar{K}$ with nuclei has received lots of attention over the last years. The modified $\Lambda(1405)$ in the medium governs the $\bar{K}N$ interaction close to threshold and gives rise to an attractive $\bar{K}N$ interaction in agreement with phenomenology of kaonic atoms. Further theoretical advances have been performed by adding the p-wave contribution to the $\bar{K}N$ optical potential in connection to heavy-ion experiments, which provide an excellent scenario for testing high-momentum kaons and, therefore, further partial-wave contributions.

The self-energy of the $\bar{K}$ in the nuclear medium has been obtained using a chiral unitary approach which incorporates the s- and p-waves of the $\bar{K}N$ interaction. The main contribution to the p-wave amplitudes comes from the Λ, Σ and Σ^* pole terms [1]. The in-medium effective $\bar{K}N$ interaction is built solving the coupled-channel Bethe-Salpeter equation which incorporates, in a self-consistent way, Pauli blocking effects, meson self-energies modified by short-range correlations and baryon binding potentials. The in-medium amplitudes are calculated using a similar unitarization procedure as in free space. The evaluation of the free space amplitudes rely on the factorization of the on-shell interaction kernel out of the loop function. While the on-shell factorization is still valid for in-medium s-wave amplitudes, the medium corrections for p-waves are calculated using the full off-shell momentum contribution of the vertices (see details in [2]).

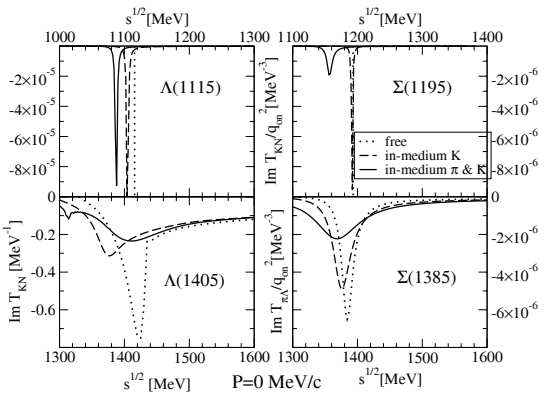

Figure 1: $\Lambda(1115)$, $\Lambda(1405)$, $\Sigma(1195)$ and $\Sigma^*(1385)$

In Fig. 1 we display the $\Lambda(1115)$, $\Lambda(1405)$, $\Sigma(1195)$ and $\Sigma^*(1385)$ by showing the imaginary part of the in-medium effective amplitude as function of c.m. energy $\sqrt{s}$ for a total momentum $P = 0$. The free amplitudes (dotted lines) are compared to the in-medium ones at ρ_0 dressing the antikaons self-consistently (dashed lines) and also considering the in-medium effects on pions (solid lines). The $\Lambda(1115)$ acquires an attractive shift of -28 MeV when pions are dressed due to the pion-mediated $\Lambda N \to \Sigma N$ transition. This is in agreement with hypernuclear spectroscopy data. The $\Lambda(1405)$ is generated dynamically close to the free position and gets strongly diluted when pions are dressed due to $\Lambda N N^{-1}$ and $\Sigma N N^{-1}$ decay channels. The $\Sigma(1195)$ shows an attraction of -35 MeV for this later case. The $\Sigma^*(1385)$ stays close to the free position for both approaches and increases the width from 30 MeV in free space to 80 MeV when pions are dressed.

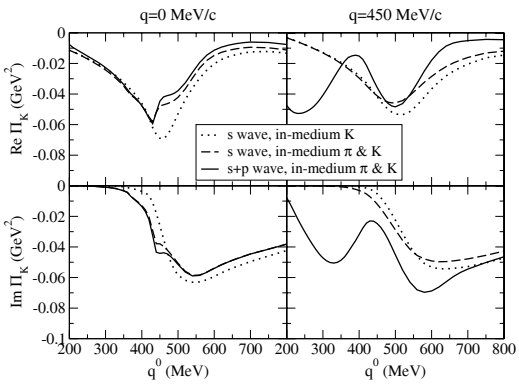

Figure 2: $\bar{K}$ self-energy for two momenta.

The self-energy of $\bar{K}$ at ρ_0 as function of energy is shown in Fig. 2 for two momenta. We show the s-wave component only dressing kaons (dotted lines), dressing also pions (dashed lines) and the p-wave contributions for the latest approach (solid lines). At zero momentum, we observe a small imaginary part at subthreshold coming from $\bar{K}NN \to \Sigma N$, ΛN. The small p-wave strength is due the Fermi motion of nucleons which produces a slight repulsion in the real part of the self-energy since the energies that come into play are above the Λ, Σ and Σ^* excitations. At finite momentum of 450 MeV/c, the imaginary part shows the ΣN^{-1} component at 300 MeV and the $\Sigma^* N^{-1}$ one around 550 MeV. In this case, the p-wave components determine the imaginary part. The corresponding optical potential changes from (-40,-30) MeV at $\rho_0/2$ to (-70,-80) MeV at $2\rho_0$ for $\vec{q} = 0$ with or without including the pion dressing while the imaginary part remains sizeable. Therefore, deep and bound $\bar{K}$ states are not expected, in agreement with previous self-consistent calculations.

References

[1] D. Jido, E. Oset and A. Ramos, Phys. Rev. C **66** (2002) 055203.

[2] L. Tolos, A. Ramos and E. Oset, Phys. Rev. C **74** (2006) 015203.

Spurious modes in the self-consistent treatment of vector mesons

F. Riek[1], H. van Hees[2], and J. Knoll[1]

[1]GSI, Darmstadt, Germany; [2]Texas A&M University, College Station, Texas 77843-3366, USA

In self-consistent Dyson resummation schemes applied to vector mesons special care has to be taken about the four-transversality of the self-energy and the propagators. Such approaches, although being conserving on the expectation-value level, suffer from the violation of Ward-Takahashi identities at the two-point and higher-order vertex-functions level. So far in the literature two schemes have been proposed to deal with this problem [2, 1]. We carefully reinvestigated both methods and found problems arising from kinematical singularities, unless further conditions are imposed on the resulting polarisation tensor. In particular singularities in the polarisation tensor occur which lead to *spurious and thus unphysical* modes: a massless mode in the approach of [1] while the projection method introduced by two of us [2] has no problems at the light cone but introduces artifacts at zero energy which also spoil the results.

In the approach proposed in [1] a naive projection scheme is used. In any iteration step of the self-consistent calculation the undesired four-longitudinal components of the polarisation tensor, $\Pi^{\mu\nu}(q)$ (e.g. of the ρ-meson), are simply cut off. Since the pertinent projectors, however, are singular on the light-cone, the spatially longitudinal component of the polarisation tensor becomes divergent there,

$$\mathrm{Im}\ \Pi_L^{\mu\nu}(q) \stackrel{q^2\to 0}{\longrightarrow} \epsilon(q)\frac{q^\mu q^\nu}{(q^2)^2}, \qquad (1)$$

implying the following behaviour for the spatially longitudinal spectral function of the vector meson in the vicinity of the light cone:

$$A_L^{\mu\nu}(q) \stackrel{q^2\to 0}{\longrightarrow} \frac{2\epsilon q^\mu q^\nu}{4m_\rho^4\vec{q}^2(q^0-|\vec{q}|)^2+\epsilon^2}. \qquad (2)$$

Thus these components show a strong peak along the light cone, c.f. the result for A^{00} in Fig. 1. Note that $A^{00}(q) = \frac{\vec{q}^2}{q^2}A_L(q)$ drops to zero at vanishing spatial momentum $\vec{q}$. This light-cone structure represents a zero-mass mode with amazing stamina. This fictitious mode always emerges unless the unprojected tensor is *exactly* four-transversal on the light-cone. Two of us (HvH and JK) [2] suggested an alternative method for the construction of a four-transversal polarisation tensor which definitely avoids the above stated light-cone singularity, since there $\Pi_L(q)$ vanishes by construction. For details we refer to refs. [2, 3]. It should be mentioned though that due to the $1/q_0^2$ factor in the construction of $\Pi^{00}(q) = q_i q_k \Pi^{ik}/q_0^2$, this method leads to a singularity in A^{00} at vanishing energy $q_0 = 0$. Numerical investigations on the example of the ρ meson show that the spurious modes in both methods seriously spoil the physical results in cases where the ρ meson significantly contributes to the self-energies of the other particles in the system such as, e.g., the pionic modes [5].

Similar problems with kinematical singularities also appear in the relativistic treatment of particles with spin 3/2 such as the Δ resonance. There the problems are even more subtle and complex. All such cases should therefore be carefully investigated and appropriately adjusted in order to comply with supplementary analytical constraints that cure the occurrence of spurious modes.

References

[1] J. Ruppert and T. Renk, Phys. Rev. C **71** (2005) 064903.

[2] H. van Hees and J. Knoll, Nucl. Phys. A **683** (2000) 369.

[3] F. Riek and J. Knoll, Nucl. Phys. A **740** (2004) 287.

[4] F. Riek, H. van Hees and J. Knoll, arXiv:nucl-th/0607023.

[5] F. Riek, Ph-D Thesis, TU-Darmstadt Feb. 2007

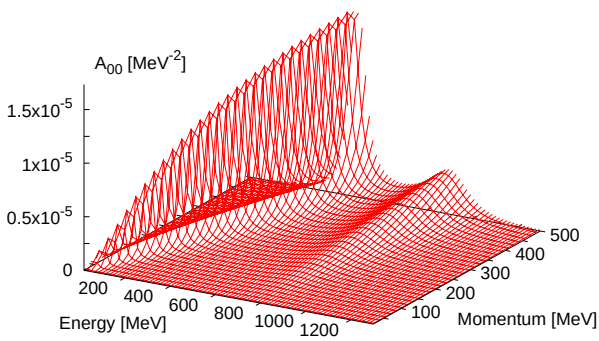

Figure 1: Time-time component, $A^{00}(q)$, of the ρ-meson spectral function at $T = 160$ MeV as a function of energy and three momentum for the Ruppert-Renk projection method.

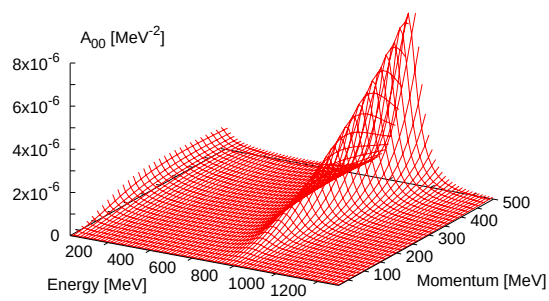

Figure 2: Same as in Fig. 1 for the method by van Hees and Knoll with spurious contributions close to zero energy.

Λ-hyperons in symmetric nuclear matter

H. Đapo*[1], B.-J. Schaefer†[2], and J. Wambach[1,3]

[1]Institut für Kernphysik, TU Darmstadt, Germany; [2]Institut für Physik, Karl-Franzens-Universität Graz, Austria; [3]GSI, Darmstadt, Germany

The study of the hyperon-nucleon (YN) interaction is essential to an understanding of the physics of octet baryons and nuclear systems with strangeness. In addition, the YN interaction also determines the properties of hypernuclei, double hypernuclei and the behavior of dense nuclear matter. Unfortunately, experimental data of the YN interaction are rare compared to the nucleon-nucleon case. There exist only a very limited amount of scattering data with which one constructs high quality potentials such as the Nijmegen soft core potential NSC97, NSC89, the Jülich one-boson-exchange potential and the recently constructed chiral effective field theory potential with cutoffs between 550 and 700 MeV [1].

The focus of this work is a comparative analysis of all these various potentials and determine their differences as well as their similarities. Based on a Renormalization Group (RG) approach an effective low-momentum YN interaction $V_{\text{low }k}$ is obtained by using these potentials as initial condition for solving the corresponding RG equations [2]. From these different $V_{\text{low }k}$'s we calculate in Hartree-Fock approximation the single particle potential (SPP) for the Λ-hyperon in symmetric non-strange nuclear matter. This allows us to investigate the density dependence of the SPP without any hyperon-hyperon (YY) interactions, which are not well known generally. The resulting various SPP's for vanishing hyperon momentum as function of the density are shown in Fig. 1.

The SPP is given by an integration over the diagonal elements of the effective low-momentum potential matrix. This also establishes a simple connection between the SPP and the $V_{\text{low }k}$. In addition, some experimental data e.g. from the (π^-, K^+) spectra are available and allow a comparison. It is found that the depth of the SPP at saturation density ρ_0 is -30 MeV [3].

As one can see in the figure most of the different effective YN interactions give different result in magnitude as well as the shape of the curves. The common feature is that all Nijmegen models and the chiral effective theory agree up to, and slightly above, the saturation density. The agreement of all the Nijmegen models is expected since all are based on a similar footing. Interesting is the agreement with the model using chiral effective theory in leading order. This chiral potential and all NSC97 potentials cross the only known experimental point at saturation density ρ_0.

For higher densities it is obvious that none of the potential agree with each other. Note, that these differences do not influence the behavior of hypernuclei strongly. But on the other hand, these differences can have drastic consequences for neutrons star with hyperons because the Λ particle abundance and concentration will strongly depend on the depth of the SPP.

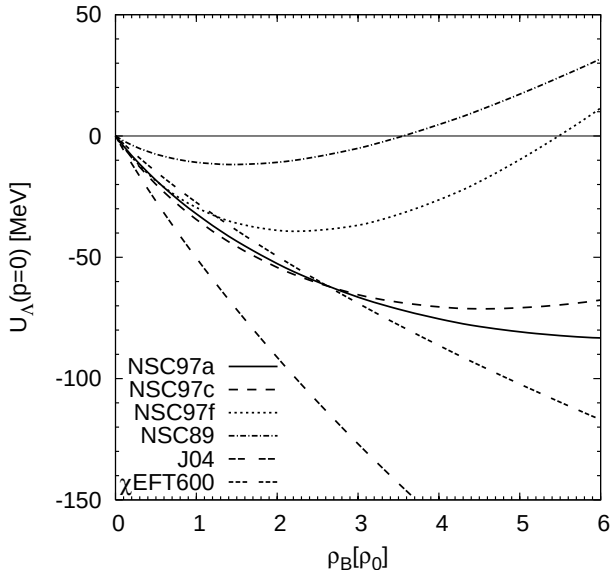

Figure 1: Density dependence of the Λ-hyperon single particle potential for vanishing momentum in symmetric nuclear matter.

We conclude from this analysis that there is a need for more experimental data in order to constrain the YN interaction. Additionally, it is seems that the leading order contribution to the ΛN potential are sufficient to reasonably describe the Λ hyperon properties.

This investigation can easily be extended to non-symmetric nuclear matter and also the inclusion of the Σ hyperons becomes feasible. Furthermore, the construction of β stable nuclear matter with nucleons and hyperons is also possible if the YY interaction is neglected.

References

[1] T. A. Rijken, V. G. J. Stoks, and Y. Yamamoto, Phys. Rev. **C59**, 21 (1999); P. M. M. Maesen, T. A. Rijken, and J. J. de Swart, Phys. Rew. **C40**, 2226 (1989); J. Haidenbauer and U.-G. Meißner, Phys. Rew. **C72**, 044005 (2005); H. Polinder, J. Haidenbauer, and U.-G. Meißner, nucl-th/0605050 (2006).

[2] B.-J. Schaefer, M. Wagner, J. Wambach, T. T. S. Kuo, and G. E. Brown, Phys. Rev. **C73**, 011001 (2006)(R); M. Wagner, B.-J. Schaefer, J. Wambach, T. T. S. Kuo, and G. E. Brown, Phys. Rev. **C74**, 054003 (2006).

[3] P. Saha et al., Phys. Rev. **C70**, 044613 (2004).

* haris@physik.tu-darmstadt.de

† bernd-jochen.schaefer@uni-graz.at

The phase diagram of the three flavor quark-meson model

M. Wagner*[1], B.-J. Schaefer†[2], and J. Wambach[1,3]

[1]Institut für Kernphysik, TU Darmstadt; [2]Institut für Physik, Karl-Franzens-Universität Graz, Austria; [3]GSI, Darmstadt

The investigation of the phase diagram of strongly interacting matter is subject of current (e.g. RHIC, BNL) and future experiments (e.g. FAIR, GSI). With these experiments different regions of the phase diagram are accessible at finite baryon chemical potential μ_B and finite temperature T. On the other hand, there are also strong efforts to understand the phase structure theoretically. For example, lattice simulations perform well at zero chemical potential and finite temperatures. For three quark flavors the phase transition is found to be a rapid crossover [1]. Lattice simulations at non-zero chemical potentials struggle with the fermion sign-problem. Although there are several methods available to circumvent this problem the predictive power of such lattice simulations is still very limited.

Therefore phenomenological model studies based on effective field theory are required in order to access the region of heavy-ion collision experiments in the phase diagram. These models (e.g. NJL, quark-meson model) incorporate the chiral symmetry of the underlying QCD. For the two lightest quark flavors (u, d) this symmetry is a good one and for three flavors (u, d, s) still an approximate symmetry. Lattice studies indicate that the confinement-deconfinement transition coincides with the chiral symmetry restoration. Model calculations, limited to two quark flavors mostly, are performed typically in mean-field approximations, which break down near the phase boundary because of strong fluctuations.

We start our investigation with an mean-field analysis in the three flavor quark-meson model. In order to calculate the partition function we omit the integration over the mesonic degrees of freedom and replace the fields by their constant expectation values $\phi = \langle\phi\rangle$. In this way the mesonic fluctuations are neglected while the integration over the quark- and antiquarks is performed. Within the Matsubara formalism two different quark chemical potentials are introduced: One for the light quarks μ and one for the strange quarks μ_s.

In Fig. 1 two phase diagrams in the (T, μ)-plane for $\mu_s = 0$ are shown. The lower curve is calculated in the chiral limit, where the explicit symmetry breaking is absent and all quark masses vanish. Based on universality arguments Pisarski and Wilzcek [2] argued that the chiral phase transition is always of first order in the chiral limit. We also found this result in our calculation. The upper curve in Fig. 1 is obtained for finite constituent light quark masses ($m_u = m_d = 300\,\text{MeV}$) and a predicted strange quark mass ($m_s = 434\,\text{MeV}$). For these values we find a smooth cross over transition for $\mu < 264\,\text{MeV}$ (dashed line). For larger chemical potentials the transition is first order. For $\mu_c^c = 264\,\text{MeV}$ and $T_c^c = 110\,\text{MeV}$ we find a critical point corresponding to a second order transition. Our value of the critical temperature $T_c \approx 178\,\text{MeV}$ at zero chemical potential for finite quark masses is in accordance with the one of former lattice calculations ($T_c \approx 173 \pm 10\,\text{MeV}$, see e.g. [3]). In the last year new lattice simulations reported a higher value ($T_c = 192 \pm 11\,\text{MeV}$,[4]), which is also still in agreement with our value. The latest value though indicates a significantly lower temperature ($T_c \approx 151 \pm 6\,\text{MeV}$, [5]).

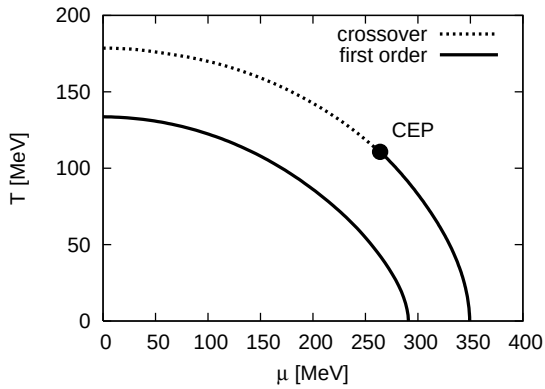

Figure 1: Phase diagrams for realistic pion masses (upper curve) and for the chiral limit (lower curve). The label CEP denotes the critical end point.

This work forms the basis for a more sophisticated treatment within the functional renormalization group (FRG) method which goes beyond the mean-field approximation. Studies with the FRG in an effective two-flavor quark-meson model show the importance of fluctuations especially in the vicinity of a phase transition [6, 7]. The FRG provides an effective and reliable tool to determine the phase structure in an efficient way.

References

[1] Y. Aoki, G. Endrodi, Z. Fodor, S. D. Katz, and K. K. Szabo, Nature **443**, 675 (2006a).

[2] R. D. Pisarski and F. Wilczek, Phys. Rev. **D29**, 338 (1984).

[3] F. Karsch, J. Phys. **G31**, S633 (2005).

[4] M. Cheng et al., Phys. Rev. **D74**, 054507 (2006).

[5] Y. Aoki, Z. Fodor, S. D. Katz, and K. K. Szabo (2006b), hep-lat/0609068.

[6] B.-J. Schaefer and J. Wambach (2006), hep-ph/0603256.

[7] B.-J. Schaefer and J. Wambach, Nucl. Phys. **A757**, 479 (2005).

* mathias.wagner@physik.tu-darmstadt.de

† bernd-jochen.schaefer@uni-graz.at

Susceptibilities in a Chiral Model with Polyakov Loops*

C. Sasaki[1], B. Friman[1], and K. Redlich[2]

[1]GSI, Darmstadt, Germany; [2]Institute of Theoretical Physics, University of Wroclaw, Wrocław, Poland

Enhanced fluctuations are characteristic for phase transitions. Thus, the exploration of fluctuations is a promising tool for probing the phase structure of a system. The phase boundaries can be identified by the response of the fluctuations to changes in the thermodynamic parameters. In this work [1] the fluctuations in various channels near the phase boundary are explored by using the Nambu–Jona-Lasinio (NJL) type model.

The quark number susceptibility χ_q is of particular interest for exploring the tricritical point (TCP) since χ_q is expected to diverge at the TCP according to universality arguments. In Fig. 1 we show the critical region in the mean field approximation, where the χ_q, due to fluctuations, exceeds the free one by more than an order of magnitude. The different critical exponents along the phase boundary and perpendicular to it are reflected in the shape of the critical region. It is elongated along the phase boundary, where the singularity is strongest. We find that the critical region

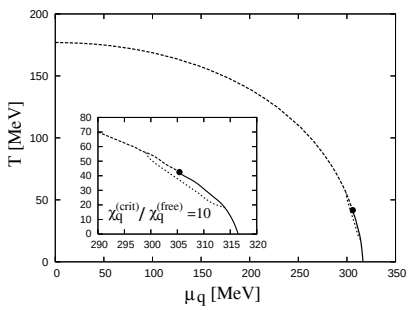

Figure 1: The critical region in the T-μ plane obtained in the NJL model. The TCP indicated by a dot is located at $(T_c = 42, \mu_c = 305)$ MeV.

extends over $\Delta T \simeq 30$ MeV, corresponding to a change of the collision energy $\Delta\sqrt{s} \sim 1$ A·GeV. Consequently, this crude estimate implies that in order to observe effects of critical fluctuations in A–A collisions one would need to measure an excitation function with an energy step $\Delta\sqrt{s}$ smaller than 1 A·GeV.

Recently, color degrees of freedom were introduced in the NJL Lagrangian through an effective gluon potential expressed in terms of Polyakov loops (PNJL model) [2]. In Fig. 2 we show the chiral and Polyakov loop susceptibilities χ_{mm} and $\chi_{l\bar{l}}$ computed at $\mu = 0$ in the PNJL model in the chiral limit within the mean field approximation. The peak of $\chi_{l\bar{l}}$ is much broader and the susceptibility remains finite at all temperatures. This is due to the explicit breaking of the $Z(3)$ symmetry by the presence of quark fields

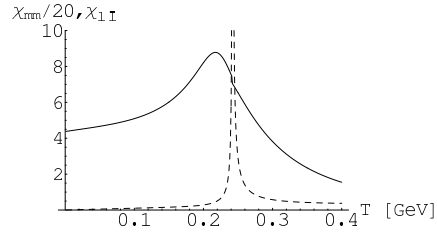

Figure 2: The chiral χ_{mm} (dashed-line) and the Polyakov loop $\chi_{l\bar{l}}$ (solid-line) susceptibilities in the chiral limit as functions of temperature T for $\mu = 0$.

in the PNJL Lagrangian. Nevertheless, $\chi_{l\bar{l}}$ still exhibits a peak structure that can be considered as a signal for the deconfinement transition in this model.

In Fig. 3 we show the resulting phase diagram for the PNJL model. The boundary lines of deconfinement and chiral symmetry restoration do not coincide. There is only one common point in the phase diagram where the two transitions appear simultaneously. Recent LGT results both

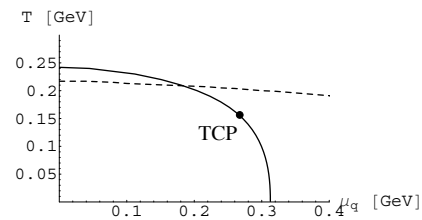

Figure 3: The phase diagram of the PNJL model in the chiral limit. The solid (dashed) line denotes the chiral (deconfinement) phase transition respectively. The TCP (bold-point) is located at $(T_c = 157, \mu_c = 266)$ MeV.

at vanishing and at finite quark chemical potential show that deconfinement and chiral symmetry restoration appear in QCD along the same critical line [3]. In general it is possible to choose the PNJL model parameters such that the both critical temperatures coincide at $\mu = 0$.

References

[1] C. Sasaki, B. Friman and K. Redlich, hep-ph/0611143; hep-ph/0611147.

[2] P. N. Meisinger and M. C. Ogilvie, Phys. Lett. B **379**, 163 (1996); K. Fukushima, Phys. Lett. B **591**, 277 (2004); C. Ratti, M. A. Thaler and W. Weise, Phys. Rev. D **73**, 014019 (2006).

[3] F. Karsch and E. Laermann, Phys. Rev. D **50**, 6954 (1994); C. R. Allton *et al.*, Phys. Rev. D **66**, 074507 (2002).

* Supported in part by the Virtual Institute of the Helmholtz Association under the grant No. VH-VI-041.

A chiral effective quark-meson model with the Polyakov loop

B.-J. Schaefer* [1], J.M. Pawlowski[2], and J. Wambach[3,4]

[1]Universität Graz, Austria; [2]Universität Heidelberg, Germany; [3]TU Darmstadt; [4]GSI, Darmstadt, Germany

The phase diagram of Quantum Chromodynamics (QCD) is governed by two symmetries, chiral symmetry in the limit of vanishing quark masses where the theory is invariant under chiral $SU(N_f) \times SU(N_f)$ flavor rotations, and a global $Z(N_c)$ symmetry associated with the center of the color $SU(N_c)$ gauge group in the absense of dynamical quarks. Then, the center symmetric phase has confinement whereas the center broken phase is deconfined.

In the real world with finite but sufficiently small quark masses with two or three flavors chiral symmetry is spontaneously and explicitly broken. At high temperatures and/or densities a chiral phase transition occurs to a partially restored chiral quark-gluon plasma (QGP) phase. The chiral condensates $\langle \bar{q} q \rangle$ serves as an order parameter for the different phases.

The order parameter for the center symmetry is the thermal average of the Polyakov loop $\Phi(A_0)$ which relates to the exponential of the free energy of a static quark. At low temperature and suffciently large quark mass the Polyakov loop vanishes, and we are in the confined phase with infinitely large free energy for a static quark. At high temperature or high energies the theory is deconfined.

By now the confinement-deconfinement phase transtion in the static quark limit is well-simulated within a simple field theoretical model for the Polyakov loop [1], the parameters of which are fitted to lattice data. However, in the presence of dynamical quarks center symmetry is explicitly broken and no order parameter exists for the deconfinement transition.

In turn, hadronic properties at low energies and the chiral phase transition at finite temperature and/or density are well-described by means of chiral effective models such as the linear quark-meson model [2]. The parameters are fixed such that chiral symmetry is broken in the vacuum. But those models lack a dynamical gauge sector important for the accurate description of the QCD phase diagram.

The Polyakov-quark-meson (PQM) model is a synthesis of the chiral quark-meson model with Polyakov loop dynamics, e.g. [3]. The basic ingredients of the model are constituent quarks, meson fields such as the σ- and π-fields, and an effective Polyakov loop potential which preserves center symmetry. A Dirac term in the action couples the quarks to the Polyakov loop via the temporal component of the gauge field. The parameter of the Polyakov loop potential are fixed by requiring that the equation of state on the lattice obtained in pure gauge theory is reproduced. In particular, in this case a first-order deconfinement phase transition is seen at $T_c \sim 270$ MeV and $\mu = 0$.

The presented model is fitted to the vacuum for physical pion masses in mean-field approximation and compared to the quark-meson model without the Polyakov dynamics in the same approximation.

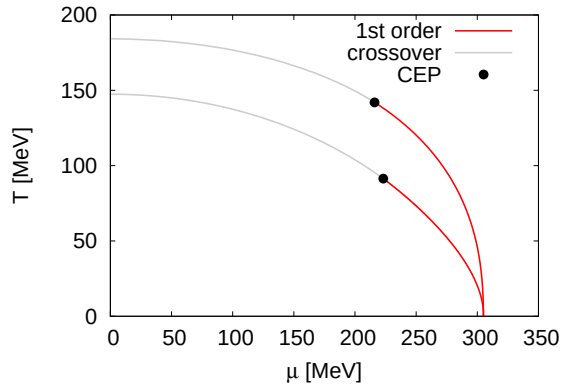

Figure 1: Phase diagrams of the two flavor quark-meson model with Polyakov loop (upper curve) and without Polyakov loop dynamics (lower curve). The label CEP denotes the critical end point.

In Fig. 1 the resulting two-flavor phase diagrams in the (T, μ)-plane for the pure quark-meson model (lower curves) [2] and for the PQM model (upper curves) are shown. The coupling of quarks to Polyakov loop changes the first-order deconfinement transition to a smooth crossover and shifts the critical temperature down to $T_c \sim 185$ MeV. In the PQM model the boundary lines of the deconfinement and chiral transition coincide at the T-axis. From RG arguments an explicit N_f- and μ-dependence of the Polyakov loop potential parameters is inferred resulting in a very good coincidence of the boundary lines of both transitions in the phase diagram [4]. The chiral transition temperature in the present model is increased throughout the phase diagram in comparison to the quark-meson model (see Fig.). For the future this analysis establishes a starting point towards the fully dynamical QCD by removing more and more of the effective model constraints.

References

[1] R. D. Pisarski, Phys. Rev. **D62**, 111501 (2000).

[2] B.-J. Schaefer and J. Wambach, Nucl. Phys. **A757**, 479 (2005); B.-J. Schaefer and J. Wambach, `hep-ph/0603256`.

[3] C. Ratti, M. A. Thaler and W. Weise, Phys. Rev. **D73**, 014019 (2006); C. Sasaki, B. Friman and K. Redlich, `hep-ph/0611147`.

[4] J. M. Pawlowski, B.-J. Schaefer and J. Wambach, in preparation (2007).

* bernd-jochen.schaefer@uni-graz.at

Polyakov loop, Quasiparticles and QCD Phase Diagram

S. Rößner[1], C. Ratti[2], and W. Weise[1]
[1]Technische Universität München, München, Germany; [2]ECT*, Villazzano (Trento) Italy

QCD thermodynamics has been the subject of intense investigations in recent years. In order to interpret corresponding lattice QCD results the Polyakov-loop extended Nambu Jona-Lasinio (PNJL) model is a promising field theoretical quasiparticle model [1, 2, 3, 4] combining the two principal non-perturbative features of low-energy QCD: confinement and spontaneous chiral symmetry breaking. In the PNJL model quarks develop quasiparticle masses by propagating in the chiral condensate, while they couple at the same time to a homogeneous background (temporal) gauge field representing Polyakov loop dynamics. Recent investigations [2, 3] have focused on PNJL calculations in comparison with lattice QCD thermodynamics including finite quark chemical potentials μ. An example is shown in Fig. 1.

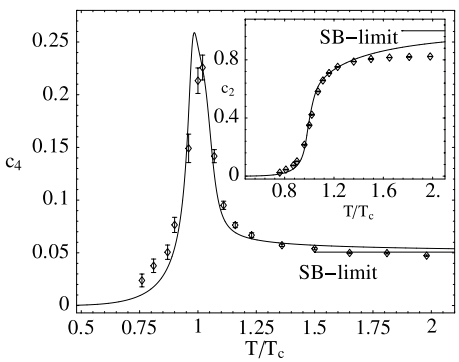

Figure 1: PNJL result for the fourth moment of the pressure with respect to μ/T compared to lattice data [5]. The inset shows the corresponding second moment of the pressure.

Of particular interest is the location of the critical endpoint at which the chiral and deconfinement crossover transitions at lower μ turn into a first-order phase transition above some critical μ. In Fig. 2 we show the phase diagrams in the (T, μ)-plane derived from the PNJL model [2] using different current quark masses. The change of the critical endpoint with varying quark mass mainly reflects the dependence of the critical chemical potential on the quark mass. The presence of the diquark dominated phase at large μ stabilizes the temperature of the critical endpoint at rather high values.

We have recently explored [3] the quark number susceptibilities. This observable is particularly interesting since it is known to diverge at the critical temperature for a first order phase transition. The observed peak in the lattice results for this observable [5] has been often interpreted as a signal of the tricritical point in the QCD phase diagram. Within our model [3] we have compared the full result for χ_q with the truncated one given by a Taylor expansion.

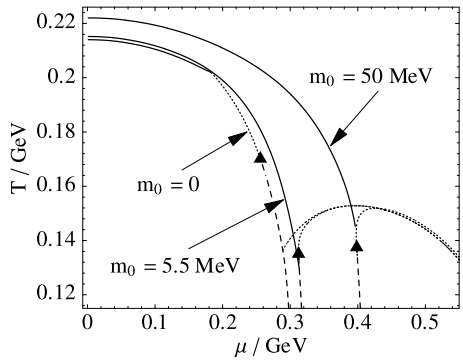

Figure 2: Phase diagram predicted by the PNJL model including scalar diquarks. The graph illustrates the current quark mass dependence of the phases and the critical point.

The conclusions that we can draw are the following: the PNJL model gives a good description of the lattice data for a large variety of thermodynamical quantities. The comparison between the full PNJL results at finite chemical potential and the truncated ones show good convergence of the Taylor series up to $\mu/T \leq 0.4$ - 0.6. For larger values of μ/T, significant discrepancies are observed between full and truncated results in the region around the phase transition, in particular for the quark number susceptibilities. The singular behaviour of the susceptibilities observed in the expanded result is not present in the full calculation. The transition predicted by our model for $\mu/T = 1$ is still a crossover, reflected by the finite height of the peak in the corresponding quark number susceptibilities.

The good agreement of the calculated quark number susceptibilities with results from lattice calculations [5] encourages us to study isovector susceptibilities in the framework of the PNJL model. Further developments now aim for an extension of the present framework to $N_f = 3$ in order to explore the rich structure of colour superconducting (diquark) phases with three quark flavours and the additional effects of Polyakov loop dynamics.

References

[1] P. N. Meisinger and M. C. Ogilvie, Nucl. Phys. Proc. Suppl. **47** (1996) 519; Phys. Lett. B **379** (1996) 163. K. Fukushima, Phys. Lett. B **591**, 277 (2004).

[2] S. Rößner, C. Ratti and W. Weise, arXiv:hep-ph/0609281.

[3] C. Ratti, S. Rößner and W. Weise, arXiv:hep-ph/0701091.

[4] C. Ratti, M. A. Thaler and W. Weise, Phys. Rev. D **73** (2006) 014019 [arXiv:hep-ph/0506234].

[5] C. R. Allton *et al.*, Phys. Rev. D **71** (2005) 054508 [arXiv:hep-lat/0501030].

Equation of State for Hot and Dense Matter in the SHMC Model*

A.S. Khvorostukhin[2], V.D. Toneev[1,2], and D.N. Voskresensky[1,3]

[1] GSI Darmstadt, Germany; [2] JINR Dubna, Russia; [3] MEPhI Moscow, Russia

Suitable equations of state (EoS) of hadronic matter should comply with experimental information extracted from the description of the global characteristics of atomic nuclei, neutron stars and heavy ion collisions. As suggested in [1] a relativistic mean-field model EoS satisfies the majority of existing constraints at zero temperature. Our considerations here generalize the model [1] to finite temperatures. We include low-lying non-strange and strange baryon resonances (p, n, Δ, Λ, Σ, Ξ, Σ^*, Ξ^*, and Ω) and their antiparticles, as well as σ, ρ, ω meson excitations constructed on the ground of mean fields, and the (quasi)Goldstone excitations of π, K and η mesons. Their high mass partners in the SU(3) multiplet K^*, η' and φ are added. The model exploits the Brown-Rho scaling hypothesis and scales mass-terms of σ, ω and ρ fields as well as the baryon masses by a universal σ mean-field dependent scaling function Φ. In order to obtain a reasonable EoS, the meson-baryon coupling constants are also scaled with the σ mean field. All states are treated within a quasiparticle approximation. We call this approach the scaling hadron mass-couplings (SHMC) model [2].

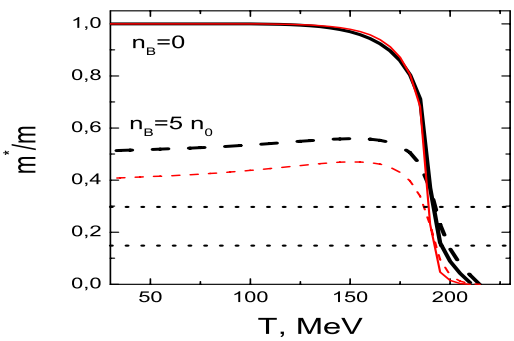

Figure 1: Temperature dependence of the effective masses of the nucleon, ω, ρ excitations (thick lines), and of the σ excitations (thin lines) at two baryon densities, $N = Z$. Levels of value m_π and $2m_\pi$ are shown by dotted lines.

Different phases can be realized within the SHMC model. As it is seen from Fig. 1, the mass of the σ excitation may fall below the value m_π at $T = T^{\rm chir}$. In models with inherent chiral symmetry this would be the chiral symmetry restoration point. In a narrow interval of temperatures $170 \lesssim T \lesssim 210$ MeV the nucleon-ω-ρ and σ excitation masses drop to zero (at $T_{c\sigma} \simeq 210$ MeV for the case $n_B = 0$) and similarly for finite n_B. Masses of higher lying resonances also drop but do not vanish at $T_{c\sigma}$. The effective mass of the σ excitation ($m_\sigma^{\rm part*}$) is getting imaginary at $T > T_{c\sigma}$. The stability is achieved due to the self-interaction between the σ-particle excitations.

* Work supported by DFG project 436 RUS 113/558/0-3

The temperature dependence of the EoS at T near $T_{c\sigma}$ is suggestive of a "phase boundary" behavior, quite different from that of the ideal gas. In case $n_B = 0$ and $T \gtrsim 170$ MeV the pressure calculated in the SHMC model results to be much higher than that predicted by lattice simulations. Yet it can be adjusted to cope with the QCD lattice data up to higher temperatures, if the strengths of the couplings of the σ meson with baryon resonances are reduced. This fact is clearly seen from the isentropic evolution path

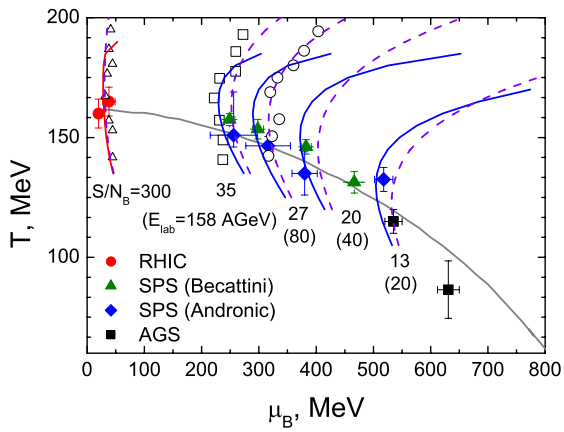

Figure 2: Isentropic trajectories for ultrarelativistic central Au+Au collisions at different bombarding energies calculated in the SHMC model (solid lines) and with suppressed baryon couplings (dashed lines). Filled symbols are from the 4π particle ratio analysis. Open symbols are the lattice 2-flavor QCD results. The thin line represents the freeze-out curve. References to all data can be found in [2].

in the (T, μ_B)-plane as obtained from the SHMC EoS shown in Fig. 2 (dash lines). The entropy per baryon participants S/N_B was estimated in [3] within the 3-fluid hydrodynamic model assuming a first order phase transition scenario to a quark-gluon plasma. It is of interest that the data sets analysed by Andronic and Becattini strongly correlate with the freeze-out curve $\bar{E}/\bar{N} = 1$ GeV. The calculated trajectories for isentropic expansion exhibit some flattening above the freeze-out curve near the expected phase boundary. Such a behavior resembles that of a smeared first-order phase transition. For suppressed baryon couplings (besides nucleons) by a factor 1/3, the trajectories turn out to be very close to those of the lattice QCD results.

References

[1] E.E. Kolomeitsev *et al.*, Nucl. Phys. **A759** (2005) 373.

[2] A.S. Khvorostukhin *et al.*, nucl-th/0612058.

[3] M. Reiter *et al.*, nucl-th/9801068.

Modelling the transition from partonic to hadronic matter with PHSD

W. Cassing[1] and M. Kant[1]
[1]Univ. of Giessen, Giessen, Germany

The dynamics of ultra-relativistic nucleus-nucleus collisions at Super-Proton-Synchrotron (SPS), Relativistic-Heavy-Ion-Collider (RHIC) or future FAIR energies are of fundamental interest with respect to the properties of hadronic/partonic systems at high energy densities. Here we address the transition from partonic to hadronic matter within the Parton-Hadron-String-Dynamics (PHSD) transport model [1]. This novel transport approach is an extension of the familiar Hadron-String-Dynamics (HSD) model [2] and includes additionally an early partonic phase with an equation of state from lattice QCD and quasi-particle properties for massive quarks, antiquarks and gluons that have been obtained from fits to lattice results [3]. The partons are treated as broad quasi-particles and propagated off-shell with strict flavor current conservation. On the partonic side elastic and inelastic interactions are included ($qq \leftrightarrow qq$, $\bar{q}\bar{q} \leftrightarrow \bar{q}\bar{q}$, $gg \leftrightarrow gg$, $gg \leftrightarrow g$, $q\bar{q} \leftrightarrow g$ etc.) exploiting 'detailed-balance' with cross sections extracted in Ref. [3]. The transition from partonic to hadronic degrees of freedom is simulated by the fusion of off-shell partons (e.g. $q + \bar{q} \leftrightarrow M$ or $q + q + q \leftrightarrow B$) to color neutral mesonic (M) or baryonic (B) resonances of finite width fulfilling energy and momentum conservation. The respective matrix element in either direction is a function of the local energy density ϵ that dissolves hadrons above $\epsilon_c = 1$ GeV/fm^3 or fuses partons below ϵ_c. On the hadronic side PHSD treats explicitly the familiar baryon octet and decouplet and selected higher resonances as well as their antiparticles. On the meson side it includes the pseudo-scalar and vector meson nonets as well as some higher meson resonances (a_1 etc.). Hadrons of even higher mass are treated as 'strings' that reflect the continuum excitation spectrum of mesons or baryons and decay to the known hadrons within HSD [2].

The present study addresses equilibration processes as well as the controlled cooling of partonic systems to hadrons in equilibrium. To this end a finite box of size $V = 1000$ fm^3 (with periodic boundary conditions) is considered and two shifted Fermi-ellipsoids of baryons are assumed as initial condition with an energy density well above ϵ_c. Initial hard baryon-baryon interactions are treated as in HSD, i.e. via the string excitation and decay (FRITIOF) or 'perturbative' QCD (PYTHIA) for 'hard' collisions for $\sqrt{s} \geq 10$ GeV [2]. The particles produced are dissolved to massive off-shell partons (see above) for $\epsilon > \epsilon_c$ and propagated with their elastic and inelastic interactions. The system then equilibrates within a few fm/c which is controlled by the anisotropy in momentum space and the relative rate of forward and backward partonic reaction channels. After 20 fm/c - when the system is safely in equilibrium - the size of the volume V is adiabatically increased such that the energy density in the finite box is decreased continuously while keeping the total energy conserved (in line with the PHSD transport dynamics). In this way the system stays in local equilibrium and the calculated pressure P and energy density ϵ can be scanned (as a function of time) and compared to respective calculations from lattice QCD (lQCD) [4] that also correspond to thermodynamic calculations in equilibrium. The resulting equation of state (EoS) P/ϵ versus ϵ is displayed in Fig. 1 (dashed line) in comparison to the respective results from lQCD (solid line) from [4]. It is seen that the numerical EoS matches the lQCD result for $\epsilon > 1.5$ GeV/fm^3 but leads to a larger pressure for smaller energy densities due to the formation of hadrons for $\epsilon \approx 1$ GeV/fm^3. We note that due to local fluctuations in the energy density $\epsilon(x)$ - for different cells in space - the phase transition is washed out for the total system. We conclude that PHSD can be viewed as a dynamical model also for the partonic stage with a proper EoS that will allow to investigate relativistic nucleus-nucleus collisions from FAIR to RHIC energies and to look for specific observables that are sensitive to the phase transition between the partonic and hadronic phase.

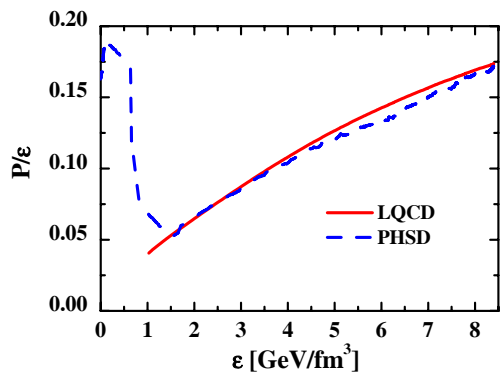

Figure 1: Comparison for the ratio of pressure P over energy density ϵ versus ϵ from PHSD (dashed line) with the same quantity from lattice QCD (solid line) [4] in thermal equilibrium.

References

[1] W. Cassing, ECT* Workshop *Parton Propagation through Strongly Interacting Matter*, Sept. 2005, http//conferences.jlab.org/ECT/program.html

[2] W. Cassing, E. L. Bratkovskaya, Phys. Rep. 308 (1999) 65.

[3] A. Peshier, W. Cassing, Phys. Rev. Lett. 94 (2005) 172301.

[4] Z. Fodor, S. D. Katz, K.K. Szabo, Phys. Lett. B 568 (2003) 73.

Neutron matter at finite temperature

L. Tolós[1,2], B. Friman[2], and A. Schwenk[3]

[1]FIAS, J.W. Goethe-Universität, Frankfurt am Main; [2]GSI, Darmstadt; [3]TRIUMF, Vancouver, Canada

The nuclear equation of state plays a central role in the physics of neutron stars and core-collapse supernovae. Renormalization group methods coupled with effective field theory offer a systematic approach to nuclear matter: For low-momentum interactions $V_{\mathrm{low}\,k}$ with cutoffs around $2\,\mathrm{fm}^{-1}$, the strong short-range repulsion in conventional nucleon-nucleon (NN) interactions and the tensor force are tamed [1]. At sufficient density, Pauli blocking eliminates the shallow bound states, and thus the particle-particle channel becomes perturbative in nuclear matter [1]. In addition, the corresponding leading-order chiral three-nucleon (3N) interaction becomes perturbative in light nuclei for $\Lambda \lesssim 2\,\mathrm{fm}^{-1}$ [2]. Consequently, the Hartree-Fock (HF) approximation is a good starting point, and perturbation theory (in the sense of a loop expansion) around the HF energy becomes tractable [1].

At finite temperature, the loop expansion around the HF free energy can be realized by the perturbative expansion of the free energy [3], where we treat the momentum dependence of the self-energy perturbatively. The free energy $F(N)$ up to second order (for details see [4]) is given by

$$F(N) = F_0(N) + \Omega_1(\mu_0) + \Omega_{2,\mathrm{n}}(\mu_0) + \left[\Omega_{2,\mathrm{a}}(\mu_0) - \frac{1}{2}\,\frac{(\partial\Omega_{1,\mathrm{NN}}/\partial\mu)^2}{\partial^2\Omega_0/\partial\mu^2}\bigg|_{\mu_0}\right] + \ldots\,, \quad (1)$$

where μ_0 is the chemical potential of a non-interacting system with the same density $\rho = N/V$ as the interacting one, $N = -[\partial\Omega_0/\partial\mu]_{\mu_0}$, and $F_0(N) = \Omega_0(\mu_0) + \mu_0 N$ is the free energy of the non-interacting system. The above expansion ensures the correct $T \to 0$ limit [3].

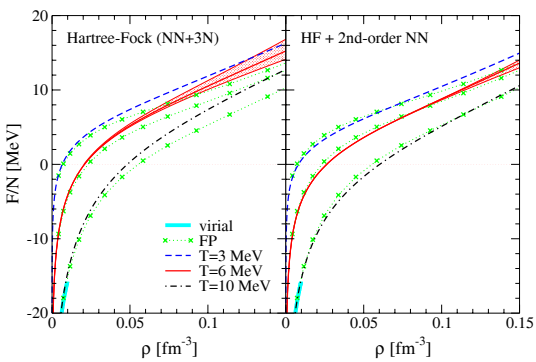

Figure 1: The free energy per particle F/N [4].

The free energy per particle [4] is shown in Fig. 1 for temperatures $T = 3\,\mathrm{MeV}, 6\,\mathrm{MeV}$ and $10\,\mathrm{MeV}$, where the low-momentum interaction $V_{\mathrm{low}\,k}$ is obtained from the Argonne v_{18} potential for a cutoff $\Lambda = 2.1\,\mathrm{fm}^{-1}$. For the 3N contribution at the HF level, we find that only the c_1 and c_3 terms of the long-range 2π-exchange part survive (for details on the 3N interaction, see [1, 2]). For the $T = 6\,\mathrm{MeV}$ results, we provide error estimates by varying the cutoff over the range $\Lambda = 1.9\,\mathrm{fm}^{-1}$ (lower curve) to $\Lambda = 2.5\,\mathrm{fm}^{-1}$ (upper curve). As expected the error grows with increasing density. From Fig. 1, we observe that the equation of state becomes significantly less cutoff dependent with the inclusion of the second-order NN contributions. We also compare our results for the free energy to the model-independent virial equation of state [5] and to the variational calculations of Friedman and Pandharipande [6] (FP, based on the Argonne v_{14} and a 3N potential). We find a very good agreement with the virial free energy, and for the densities in Fig. 1 similar results as FP.

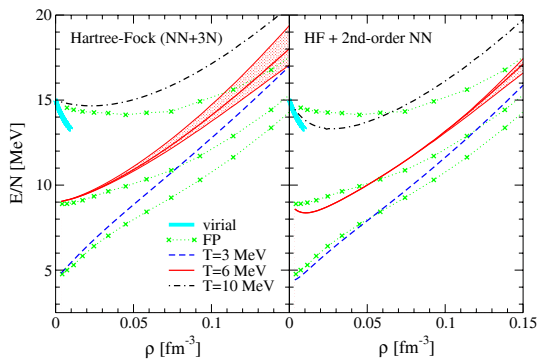

Figure 2: The energy per particle E/N [4].

Our results [4] for the energy per particle are presented in Fig. 2. As for the free energy, we observe additional binding and a significantly reduced cutoff dependence at second order. In contrast to the variational calculation of FP [6], the low-density behavior at second order is in good agreement with the virial equation of state [5]. This highlights the importance of a correct finite-temperature treatment of second and higher-order contributions.

References

[1] S.K. Bogner, A. Schwenk, R.J. Furnstahl and A. Nogga, Nucl. Phys. **A763** (2005) 59.

[2] A. Nogga, S.K. Bogner and A. Schwenk, Phys. Rev. **C70** (2004) 061002(R).

[3] W. Kohn and J.M. Luttinger, Phys. Rev. **118** (1960) 41; J.M. Luttinger and J.C. Ward, Phys. Rev. **118** (1960) 1417.

[4] L. Tolós, B. Friman and A. Schwenk, nucl-th/0611070; and in preparation.

[5] C.J. Horowitz, A. Schwenk, Phys. Lett. **B638** (2006) 153.

[6] B. Friedman and V.R. Pandharipande, Nucl. Phys. **A361** (1981) 502.

Dependence of the $^1S_0$ superfluid pairing gap on nuclear interactions

K. Hebeler[1], A. Schwenk[2], and B. Friman[1]
[1]GSI, Darmstadt; [2]TRIUMF, Vancouver, Canada

Nucleon-nucleon (NN) interactions are well constrained for relative momenta $k \lesssim 2\,\mathrm{fm}^{-1}$ by existing scattering data [1]. The model dependences for larger momenta can be seen, for instance, in the $^3P_2$ superfluid pairing gaps for Fermi momenta $k_F > 2\,\mathrm{fm}^{-1}$ [2]. In Ref. [3], we study in detail the dependence of the $^1S_0$ superfluid gap on nuclear interactions at the BCS level, and on the resolution scale.

For the RG evolution to low-momentum interactions $V_{\mathrm{low}\,k}$, we define a reduced interaction $v(k,k')$ through $V(k,k') = f(k')\,v(k',k)\,f(k)$, where $f(k)$ denotes a sharp or smooth regulator with variable cutoff Λ. Starting from an NN interaction with large cutoff $v(k,k') = V_{\mathrm{NN}}(k,k')$, we use the RG equation [4]

$$\frac{dv(k',k)}{d\Lambda} = \frac{1}{\pi}\int_0^\infty p^2 dp \left[\frac{v(k',p)\frac{d}{d\Lambda}[f^2(p)]\,t(p,k;p^2)}{p^2-k^2} + \frac{t(k',p;p^2)\,\frac{d}{d\Lambda}[f^2(p)]\,v(p,k)}{p^2-k'^2}\right] \qquad (1)$$

to generate (hermitian) low-momentum interactions, that preserve the low-momentum fully-on-shell T_{NN} matrix as well as the deuteron binding energy.

Our results for the density dependence of the neutron-neutron (nn) $^1S_0$ superfluid gap Δ [3] are shown in Fig. 1 for sharp cutoffs $f(k) = \Theta(\Lambda - k)$ with $\Lambda = 2.1\,\mathrm{fm}^{-1}$, derived from various charge-dependent NN interactions. We find that the gap is practically independent of the NN interaction used, and therefore strongly constrained by the scattering phase shifts. Consequently, the uncertainties in $^1S_0$ superfluidity are due to an approximate treatment of induced interactions and dispersion effects, which go beyond the BCS level, as well as due to three-nucleon (3N) interactions. As shown, isospin symmetry breaking leads to small but significant charge dependences in the pairing gaps.

Next, we study the dependence of the $^1S_0$ gap on the cutoff starting from the N^{3}LO chiral interaction. Our results for three densities and different smooth exponential regulators $f(k) = \exp[-(k^2/\Lambda^2)^n]$, as well as for a sharp cutoff, are shown in Fig. 2. As long as the cutoff is large compared to the dominant momentum components in the Cooper bound state, the gap depends very weakly on the cutoff. Below this scale, which depends on the density and the smoothness of the regulator, the strength of the bound state decreases, since the momentum modes that build up the Cooper pairs are integrated out. From Fig. 2, we observe that the cutoff dependence is very weak for sharp or sufficiently narrow smooth-cutoffs with $\Lambda > 1.6\,\mathrm{fm}^{-1}$.

The weak cutoff dependence indicates that, in the $^1S_0$ channel, the contribution of 3N interactions is small at the BCS level. Note that the 2π-exchange part of the corresponding low-momentum 3N interactions is cutoff independent up to the regulator functions. Finally, we emphasize that our results are obtained at the BCS level, and thus should be considered as a theoretical benchmark and not as a prediction of the physical pairing gap.

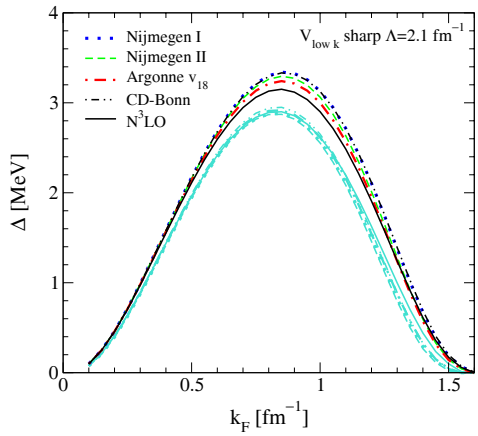

Figure 1: The $^1S_0$ superfluid gap Δ versus Fermi momentum k_F. The lines indicated in the legend are the neutron-proton gaps, whereas the grey lines show the nn gaps.

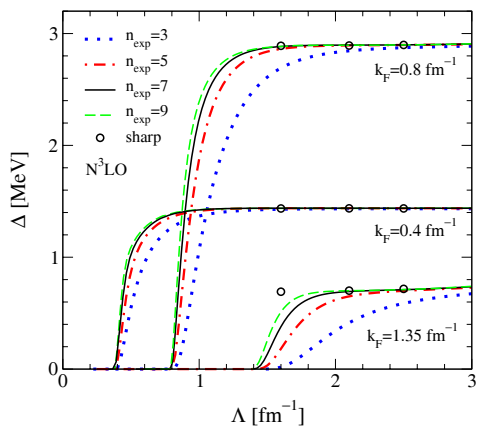

Figure 2: Results for the $^1S_0$ nn gap as a function of the cutoff Λ for three densities and various regulators.

References

[1] S.K. Bogner, T.T.S. Kuo and A. Schwenk, Phys. Rept. **386** (2003) 1.

[2] M. Baldo *et al.*, Phys. Rev. **C58** (1998) 1921.

[3] K.Hebeler, A. Schwenk and B. Friman, nucl-th/0611024.

[4] S.K. Bogner, R.J. Furnstahl, S. Ramanan and A. Schwenk, Nucl. Phys. **A** in press, nucl-th/0609003.

Goldstone bosons in the color-flavor locked phase

V. Werth*[1], M. Buballa[1], and M. Oertel[2]

[1]Institut für Kernphysik, Technische Universität Darmstadt, Germany; [2]Observatoire de Paris-Meudon, France

It is believed that the ground state of strongly interacting matter at highest densities and low temperatures is a color superconductor in the color-flavor locked phase (CFL) [1]. In that phase the formation of the diquark condensates breaks the original $SU(3)_{color} \times SU(3)_L \times SU(3)_R$ symmetry (in the chiral limit) down to $SU(3)_{color+V}$. Breaking of chiral symmetry leads to the appearance of pseudoscalar Goldstone bosons.

The properties of the Goldstone bosons have been investigated first within low-energy effective theory (EFT) approaches [2, 3, 4]. These results become exact in the weak-coupling regime at asymptotically high densities. It has been predicted that kaon and pion condensation may occur as a consequence of the stress imposed by a non-zero strange quark mass or a non-zero electron chemical potential [4].

In Ref. [5], we have explicitly constructed CFL Goldstone bosons in a three-flavor Nambu–Jona-Lasinio type model. Our Lagrangian consists of a free part and of scalar and pseudoscalar quark-quark interactions. So far, we did not take into account quark-antiquark interactions. However, as in the CFL phase baryon number is not conserved, "mesons" are essentially diquarks, and it is sufficient to consider quark-quark interactions only. The mesonic excitations are then obtained as solutions of a Bethe-Salpeter equation for the quark-quark scattering matrix $\mathcal{T}$.

We begin our discussion with the case of equal masses for up, down, and strange quarks. In this case, all considered meson masses are degenerate and given by the q_0-values for the poles in $\mathcal{T}$. In agreement with the EFT predictions of Ref. [3], we find a linear dependence of the meson mass on the quark mass, $m_{meson} = a\ m_{quark}$. The slope a, however, does in general not agree with the expression given in Ref. [3]. For instance, for a gap parameter $\Delta \approx 77\,\mathrm{MeV}$, the slope of our calculation is approximately 35% smaller than the one obtained in EFT. We have repeated this comparison for smaller values of Δ, i.e., for a weaker quark-quark interaction. The deviation then gets reduced and practically vanishes at $\Delta \approx 10\,\mathrm{MeV}$. This is expected because the expressions of Ref. [3] apply to the weak-coupling regime.

As a next step we keep m_u and m_d constant, but vary the strange quark mass m_s. The previously degenerate solutions for the poles of $\mathcal{T}$ then split into three branches, which are plotted in Fig. 1 as functions of the strange quark mass (points). Since we still have chosen equal masses for up and down quarks, π^- and π^+, K^- and $\bar{K}^0$, and K^+ and K^0, respectively, remain degenerate. Again, we compare our results with the predictions of EFT [4]. If we use our value of a instead of the EFT one (see previous paragraph), the m_s dependence of the poles is perfectly described by the EFT formula (lines in Fig. 1), without any further adjustments.

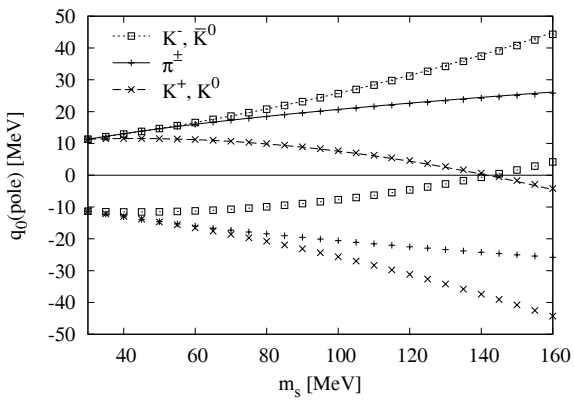

Figure 1: Meson properties for $T = 0$ and $\mu = 500\,\mathrm{MeV}$. Pole positions as functions of the strange quark mass m_s for $m_u = m_d = 30\,\mathrm{MeV}$, points: our calculation, lines: fit with EFT.

For the parameters chosen in Fig. 1, $q_0(pole)$ becomes zero for K^+ and K^0 at $m_s \approx 142\,\mathrm{MeV}$. At this point kaon condensation sets in. For higher strange quark masses the CFL phase is no longer the correct ground state and the shown results have no physical meaning.

We also calculated the pion decay constant f_π. We again find that it is smaller than the EFT prediction, but approaches the EFT value for small gap parameters Δ.

As a next step we should include more interactions, e.g., quark-antiquark interactions, which are responsible for dynamical mass generation, or instanton induced interactions, which are expected to increase the meson masses considerably.

References

[1] M. G. Alford, K. Rajagopal, and F. Wilczek, Nucl. Phys. B **537**, 443 (1999).

[2] R. Casalbuoni and R. Gatto, Phys. Lett. B **464**, 111 (1999).

[3] D. T. Son and M. A. Stephanov, Phys. Rev. D **61**, 074012 (2000).

[4] P. F. Bedaque and T. Schäfer, Nucl. Phys. A **697**, 802 (2002).

[5] V. Werth, M. Buballa, and M. Oertel, hep-ph/0611392.

* verena.werth@physik.tu-darmstadt.de

Hadronic Matter is Soft

C. Hartnack[1], H. Oeschler[2], and J. Aichelin[1]
[1]SUBATECH, Nantes, France; [2]Institut für Kernphysik, TU Darmstadt, Germany

For many years one of the most important challenges in nuclear physics has been to determine the nuclear equation of state (EoS). The study of monopole vibrations is limited to small variations in density. Presently, the most promising approach is to use heavy ion reactions in which the density of the colliding nuclei changes significantly. Two principal experimental observables have been suggested: (i) the in-plane sidewards flow of nucleons in semi-central heavy ion reaction at energies between 100 A MeV and 400 A MeV and (ii) the production of K^+ mesons in heavy ion reactions at energies around 1 A GeV. The latter method is most promising. Two effects link the yield of produced K^+ mesons with the stiffness of the EoS. If less energy is needed to compress matter (i) more energy is available for K^+ production and (ii) the density which can be reached in these reactions will be higher. In order to minimize

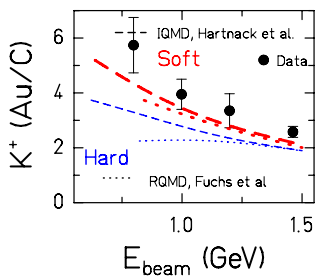

Figure 1: The ratio of the K^+ multiplicities per A obtained in Au+Au and in C+C reactions (Ref. [1]) is compared to different calculations (IQMD, dashed lines and RQMD dotted lines). The use of a hard EoS ($K_N = 380$ MeV) is denoted by thin (blue) lines, a soft EoS ($K_N = 200$ MeV) by thick (red) lines [1].

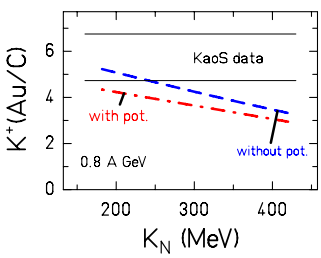

Figure 2: The double ratio $[M/A(\text{Au+Au})]/[M/A(\text{C+C})]$ calculated within the IQMD model (with and without KN potential) as a function of K_N at 0.8 A GeV. The experimental value is given as band. This allows to estimate upper limits for K_N.

the systematic errors it is better to compare ratios of cross sections rather than absolute values. Figure 1 shows the comparison of the measured ratio of the K^+ multiplicities as a function of the beam energy obtained in Au+Au and C+C reactions [1] together with transport model calculations. The data demonstrate an increase towards lower incident energies. The calculations show that this increase depends on the stiffness of the EoS. The thick lines refer to a soft EoS, while the thin lines showing a much smaller increase, represent a hard EoS. This observable is rather stable; two different models as shown in the Fig. 1 exhibit very similar trends. The sensitivity is illustrated in Fig. 2 comparing calculated ratio as a function of the compression modulus K_N with the measured value. This gives an upper limit for K_N of 240 MeV [2].

The conclusion that nuclear matter is best described by a soft EoS, is supported by another observation, the dependence of the K^+ yield on the number of participating nucleons $A_{\rm part}$ as shown in [1]. This method is based on a parametrization of the K^+ multiplicity by $M_{K^+} = A^{\alpha}_{\rm part}$. The experimental value for α of 1.34 ± 0.16 obtained at 1.5 A GeV [3] allows to conclude again that the EoS is rather soft with an upper limit of K_N of 320 MeV considering the experimental and theoretical uncertainties.

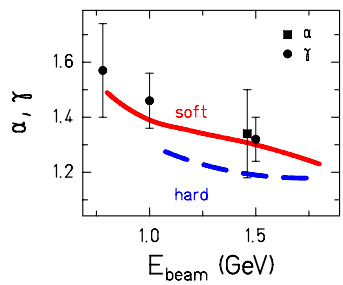

Figure 3: α and γ as a function of the beam energy summarizes the dependence of the stiffness of the EoS.

The measured dependence of the K^+ multiplicities with system size can also be parameterized by $M \sim A^{\gamma}$ giving $\gamma = 1.32 \pm 0.06$ for 1.5 A GeV beam energy [3]. As both the system-size and the $A_{\rm part}$ dependence are very similar, Fig. 3 summarizes these results showing both α and γ as a function of the beam energy. The preference of a K_N value around 200 MeV reflecting a soft EoS is striking. In [2] the robustness of this conclusion is studied in detail by varying the KN potential, the Δ life time and other parameters.

References

[1] C. Sturm et al., Phys. Rev. Lett. **86** (2001) 39; C. Fuchs et al., Phys. Rev. Lett **86** (2001) 1974; C. Hartnack, H. Oeschler, J. Aichelin, Phys. Rev. Lett. 96 (2006) 012302.

[2] C. Hartnack, H. Oeschler, J. Aichelin, Phys. Rep. in prep.

[3] A. Förster et al., (KaoS Collaboration), Phys. Rev. **C** (2007) in print.

Chemical Equilibrium in Collisions of Small Systems

I. Kraus[1], J. Cleymans[1,2,3], H. Oeschler[1], K. Redlich[2,4], and S. Wheaton[1,3]

[1]Institut für Kernphysik, Darmstadt University of Technology, Germany; [2]GSI, Darmstadt, Germany; [3]Department of Physics, University of Cape Town, South Africa ; [4]Institute of Theoretical Physics, University of Wrocław, Poland

The Statistical Model is recognized as a powerful approach to describe particle yields established at chemical decoupling. It has to be formulated in the canonical ensemble with respect to strangeness conservation if the number of strange particles becomes small. However, in some cases canonical suppression under the assumption of strangeness chemical equilibrium in the whole fireball volume was found not to be sufficient to reproduce the observed yields. It has been proposed to introduce a non-equilibrium factor γ_S as additional fit parameter. Here we focus on an alternative approach: Strangeness conservation happens in subvolumes.

Canonical suppression which refers to small systems is demonstrated in Fig 1. The left hand panel illustrates ratios of various particles with different strangeness. It shows that the grand-canonical limit is reached at radii of a few fm and that the suppression becomes stronger with increasing strangeness content. On the right hand side, the suppression of ratios of particles with a difference of $\Delta S = 1$ shows that it is similar but not identical, it depends on the strangeness content of both hadrons, not only on the difference. The latter is true for the suppression caused by the undersaturation parameter γ_S.

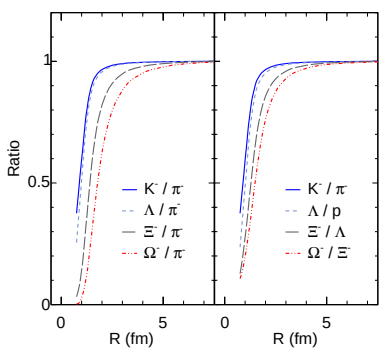

Figure 1: Different particle ratios as a function of the radius R of a spherical volume. The temperature T = 170 MeV and the baryon chemical potential μ_B = 255 MeV were chosen according to the thermal conditions at top SPS energy. All ratios are normalized to the grand-canonical limit in order to demonstrate the effect of canonical suppression.

In our approach strangeness equilibration happens only within subvolumes V_C of the system. Consequently, there are two volume parameters in the model. The overall volume of the system, which determines the particle yields, and the correlation (cluster) volume V_C causing a canonical suppression of strange particles. A particle with strangeness N_S can appear anywhere in the volume V, however, it has to be accompanied within the subvolume V_C by other particles carrying strangeness $-N_S$ to conserve strangeness.

Using the Statistical Model [1] extended by clusters with local strangeness conservation data from SPS [2] have been fitted [3]. The obtained freeze-out temperatures T barely depend on system size and also the baryon chemical potential is flat if total yields are considered. Yet, μ_B decreases towards smaller systems in fits to midrapidity densities indicating a stronger stopping in larger systems.

The obtained cluster radius, R_C (assuming spherical geometry), varies between 0.7 fm and 1.4 fm in all data sets under study (Fig. 2). The observed increase of strange to non-strange particle ratios by a factor of 2 from p-p to Pb-Pb reactions is reflected in the observed increase in the radii of the subvolumes.

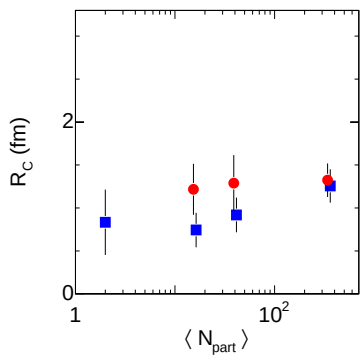

Figure 2: Cluster radius R_C as a function of the number of participants from fits to midrapidity densities (circles) and integrated yields (squares) from p-p and central C-C, Si-Si and Pb-Pb collisions.

While in the smallest system this correlation radius is about the fireball radius, larger systems exhibits a radius up to six times smaller than the fireball dimension. The fact that R_C is of the order of 1 fm and only weakly increasing with system size, could indicate that the R_C is the length of strangeness correlation in a system. This is an surprising result and requires further studies.

References

[1] S. Wheaton and J. Cleymans, hep-ph/0407174.

[2] I. Kraus (NA49 Collaboration), J. Phys. G **31** S147 (2005), [nucl-ex/0412050]; C. Alt et al. (NA49 Collaboration), Phys. Rev. C **73** 044910 (2006).

[3] I. Kraus, H. Oeschler, K. Redlich, Eur. Phys. J. C (2006) s10052 and to be published.

Collective Flow in Heavy-Ion Collisions from AGS to SPS Energies*

Yu.B. Ivanov†[1,2] and V.N. Russkikh‡[1,2]
[1]Kurchatov Institute, Moscow, Russia; [2]GSI, Darmstadt, Germany

The collective transverse flow was analysed within the model of 3-fluid dynamics (3FD) [1]. Model parameters of our previous paper [1] were used, which were fixed to reproduce a great body of experimental data in the incident energy range $E_{\rm lab} \simeq$ (1–160)A GeV. These parameters have been varied only in order to study sensitivity to stiffness of the equation of state (EoS). Thus, in addition to the default choice of the EoS with an intermediate incompressibility of $K = 210$ MeV [1] calculations were also performed for a hard (380 MeV), soft (130 MeV), and extra-soft (100 MeV) choice.

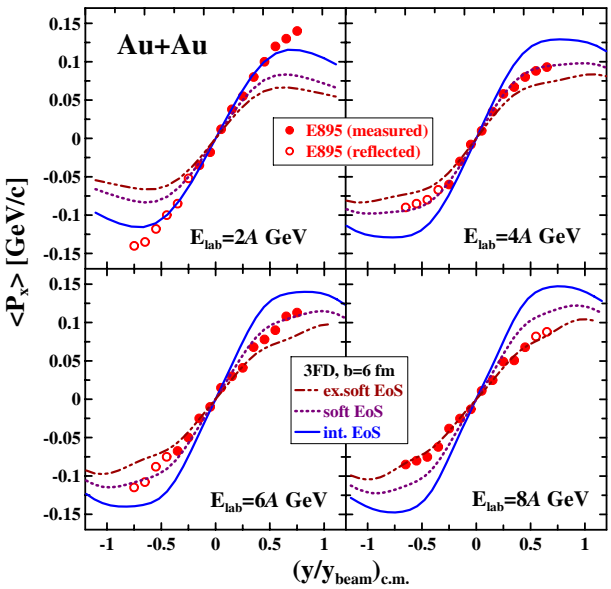

Figure 1: Directed flow of protons as a function of rapidity for mid-central Au+Au collisions at $E_{\rm lab} = 2A, 4A, 6A$ and $8A$ GeV. The 3FD results for three EoS's are presented at the impact parameter $b = 6$ fm. Data are from Ref. [2].

It was found that with the incident energy rise the flow data favor an augmented softening of the EoS. This EoS behavior essentially occurs within the AGS energy range, as it is illustrated in Fig. 1. At higher (SPS) energies the same extra-soft EoS remains preferable. This observation indirectly agrees with those obtained in the RQMD, UrQMD, JAM and HSD transport models. In these models an effective softening of the EoS occurs at the early stage of the collision, because of the implemented gradual (governed by form-factors) or abrupt switching off of mean-field interactions, or by the fact that mean fields turn out to be essentially reduced because of string formation. With this mechanism of effective softening these models efficiently reproduce the directed flow in the whole incident-energy range with the same mean-field interaction. In Ref. [3] this mechanism was summarized as "a transition from hadronic to string matter". As it was stated in Ref. [3], this "transition from hadronic to string matter" practically saturates at the top AGS energy. This agrees with our observation that no extra softening of the EoS is further required at SPS energies beyond that at top AGS energy. The transverse flow is very sensitive to the character of the *nonequilibrium* distributions of the transverse-momentum at the initial stage of the collision.

Alternatively the required EoS softening can be associated with a deconfinement transition. Therefore, other, more sophisticated EoS's, including scenario of a phase transition to the quark-gluon plasma phase, should be tested within 3FD simulations. The present calculations provide a natural benchmark for the future analysis.

The flow is an "early-stage" observable, i.e. it is determined by the early-stage evolution of the collision. Our calculations with different freeze-out criteria (different freeze-out energy densities $\varepsilon_{\rm frz}$) confirm this conjecture. The directed flow turns out to be fairly insensitive to such modifications. This low sensitivity on the freeze-out stage is not surprising. The directed flow is a measure of the *collective momentum* accumulated by matter during the expansion stage. The driving force of this collective momentum is the pressure gradient created at the early compression stage of the collision. If the freeze-out occurs not too early (e.g., not right after the compression stage), this pressure gradient has enough time to accelerate the matter, and hence the late-stage evolution does not noticeably change the earlier-accumulated collective momentum. The elliptic flow is a more subtle quantity. It is a measure of the difference of the in- and out-of-plane flows. Therefore, its sensitivity to the late stage is slightly enhanced.

A detailed report on this work can be found in Ref. [4].

References

[1] Yu.B. Ivanov, V.N. Russkikh, and V.D. Toneev, Phys. Rev. C **73** (2006) 044904.

[2] H. Liu *et al.* (E895 Collab.), Phys. Rev. Lett. **84** (2000) 5488.

[3] P.K. Sahu, W. Cassing, U. Mosel and A. Ohnishi, Nucl. Phys. **A672** (2000) 376.

[4] V.N. Russkikh and Yu.B. Ivanov, Phys. Rev. C **74** (2006) 034904.

* Work supported by DFG project 436 RUS 113/558/0-3
† Y.Ivanov@gsi.de
‡ russ@ru.net

Statistical hadronization of J/ψ in Au+Au collisions at $\sqrt{s_{NN}}$=200 GeV

A. Andronic[1], P. Braun-Munzinger[1,2], K. Redlich[3], and J. Stachel[4]
[1]GSI, Darmstadt, Germany; [2]Technical University of Darmstadt, Germany; [3]University of Wrocław, Poland;
[4]University of Heidelberg, Germany

Since its proposal twenty years ago [1] as a crucial observable for the diagnosis of the Quark-Gluon Plasma (QGP) produced in ultra-relativistic nucleus-nucleus collisions, the J/ψ meson has been the focus of intense experimental and theoretical efforts. The original idea of J/ψ melting in QGP [1] was more recently challenged with the idea that J/ψ production takes place at the chemical freeze-out [2], which appears to be coincident with the hadronization transition.

We present a comparison of statistical hadronization model (SHM) predictions to the recent data from RHIC [3] concerning the centrality and rapidity dependence of J/ψ production. We investigate the yields relative to those expected from binary scaling of production in pp collisions [5], as quantified by the observable:

$$R_{AA}^{J/\psi} = \frac{\mathrm{d}N_{J/\psi}^{AuAu}/\mathrm{d}y}{N_{coll} \cdot \mathrm{d}N_{J/\psi}^{pp}/\mathrm{d}y} \qquad (1)$$

where $\mathrm{d}N_{J/\psi}/\mathrm{d}y$ is the rapidity density of J/ψ yield integrated over transverse momentum and N_{coll} is the number of binary collisions for a given centrality class. We have recently presented [4] a comprehensive summary of the statistical hadronization model for charmed hadrons, as well as of the influence of the input parameters on its results.

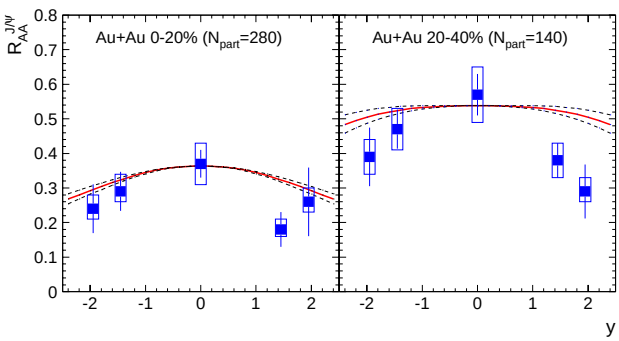

Figure 1: Rapidity dependence of $R_{AA}^{J/\psi}$ for two centrality classes. The data at RHIC are from PHENIX [3]. Besides the statistical and systematical errors (denoted by the bars and boxes), a global systematic error of the order of 10% for the data has to be additionally applied.

In Fig. 1 we present the rapidity dependence of $R_{AA}^{J/\psi}$. Our calculations reproduce the $R_{AA}^{J/\psi}$ data well. We note that a constant $R_{AA}^{J/\psi}$ value or with a minimum at midrapidity is expected within the melting model [1]. The maximum of $R_{AA}^{J/\psi}$ at midrapidity is in our model due to the enhanced regeneration yield, determined by the rapidity dependence of the charm cross section. In details, our model is in very good agrement with the data for the central bin (0-20%), while predicting for the mid-central (20-40%) centrality class a somewhat flatter shape than observed in the data. The error of the experimental J/ψ data in pp [5] used in our model plays a rather minor role, as denoted by the dashed lines in Fig. 1.

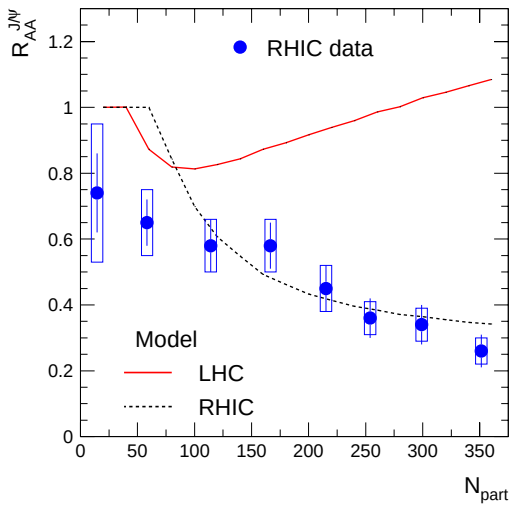

Figure 2: Centrality dependence of the $R_{AA}^{J/\psi}$ for RHIC and LHC energies.

The centrality dependence of $R_{AA}^{J/\psi}$ at midrapidity is shown in Fig. 2. Our calculations approach the value in pp collisions around N_{part}=50, which corresponds to an adopted minimal volume for the creation of QGP of 400 fm^3 [4]. The model reproduces very well the decreasing trend versus centrality seen in the RHIC data [3]. Note that in our model this suppression arises entirely as a consequence of the still small number of charm quarks ($\mathrm{d}N_{c\bar{c}}/\mathrm{d}y$=1.6). It is important to stress that at the LHC energy ($\sqrt{s_{NN}}$=5.5 TeV) the charm production cross section is about 10 times larger and, as a result, an opposite trend is predicted, see Fig. 2.

References

[1] T. Matsui, H. Satz, Phys. Lett. B 178 (1986) 416. F. Karsch, D. Kharzeev, H. Satz, Phys. Lett. B 637 (2006) 75.

[2] P. Braun-Munzinger, J. Stachel, Phys. Lett. B490 (2000) 196; Nucl. Phys. A690 (2001) 119c.

[3] A. Adare et al. (PHENIX), nucl-ex/0611020.

[4] A. Andronic, P. Braun-Munzinger, K. Redlich, J. Stachel, nucl-th/0611023.

[5] A. Adare et al. (PHENIX), hep-ex/0611020.

Electric Charge and Baryon Number Fluctuations in Pb+Pb Collisions at SPS energies

V.P. Konchakovski[1,2,3], M.I. Gorenstein[1,3], E.L. Bratkovskaya[3], and H. Stöcker[3,4]

[1]Bogolyubov Institute for Theoretical Physics, Kiev, Ukraine; [2]Shevchenko National University, Kiev, Ukraine; [3]FIAS, Frankfurt, Germany; [4]Institut für Theoretische Physik, Uni. Frankfurt, Germany

The order of phase transitions is reflected essentially in a rapid change of susceptibilities of matter in thermodynamic equilibrium with temperature T and chemical potential μ. On the other hand, the susceptibilities are a measure for fluctuations in the degrees of freedom considered such that fluctuation measurements might yield critical information on susceptibilities if hadronic rescattering does not wash out the fluctuations originating from the phase transition. In particular one expects to find large fluctuations in the vicinity of the tri-critical point. Quite early, it has been suggested to measure relative charge fluctuations since these should be significantly smaller in a QGP as compared to a hadron gas [1, 2]. However, various experimental investigations at the SPS and at RHIC have demonstrated that strong resonance interactions and decays destroy the signal substantially. Furthermore, fluctuations in conserved quantities - like charge - depend strongly on the actual phase space measured. It is therefore mandatory to use transport simulations in order to properly account for detector geometries and centrality classes of events in accordance with the experimental setup and analysis. Morover, the microscopic transport models allow to investigate the sensitivity of event-by-event observables to the early stage dynamics.

As an example, we present here the first microscopic event-by-event HSD calculations [4] of the charge fluctuations $\Delta\Phi_q$ defined as

$$\Delta\Phi_q = \Phi_q - \Phi_{q,\mathrm{GCC}}, \qquad (1)$$

$$\Phi_q = \sqrt{\frac{\langle Z^2\rangle}{\langle N\rangle}} - \sqrt{\overline{z^2}}, \quad z = q - \overline{q}, \quad Z = \sum_{i=1}^{N}(q_i - \overline{q}),$$

where q denotes a single particle variable, i.e. electric charge q; N is the number of particles of the event within the acceptance, and over-line and $\langle ... \rangle$ denote averaging over a single particle inclusive distribution and over events, respectively. The trivial fluctuations due to the global charge conservation (GCC) is

$$\Phi_{q,\mathrm{GCC}} = \sqrt{1-P} - 1, \quad \text{where} \quad \mathrm{P} = \frac{\langle \mathrm{N_{ch}}\rangle}{\langle \mathrm{N_{ch}}\rangle_{\mathrm{tot}}} \qquad (2)$$

with $\langle N_{ch}\rangle$ and $\langle N_{ch}\rangle_{tot}$ denoting the mean charged multiplicity in the detector acceptance and in full phase space (excluding spectator nucleons), respectively.

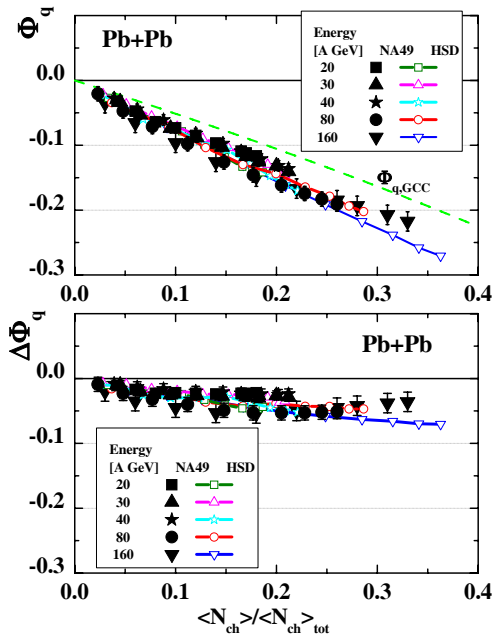

Figure 1: The dependence of Φ_q (top) and $\Delta\Phi_q$ (bottom) on the fraction of accepted particles for central Pb+Pb collisions at 20-158 AGeV. The NA49 data [3] are shown as full symbols, whereas the open symbols (connected by lines) reflect the HSD results. The dashed line shows the dependence expected for the case if the only source of particle correlations is due to the global charge conservation $\Phi_{q,GCC}$.

The HSD results [4] show a good agreement with the NA49 data at SPS energies (Fig. 1). Thus, this observable is dominated by the final stage danymics, i.e. the hadronization phase and the resonance decays, and rather insensitive to the initial QGP dynamics. On the other hand, it has been shown in [4] that the measurement of the net baryon number fluctuations helps to quantify the mixing of initial baryon currents.

References

[1] S. Jeon and V. Koch, hep-ph/0304012.

[2] E. Shuryak, J. Phys. G 30 (2004) S1221.

[3] C. Alt et al. [NA49 Collaboration], Phys. Rev. C 70 (2004) 064903.

[4] V.P. Konchakovski, M.I. Gorenstein, E.L. Bratkovskaya, and H. Stöcker, Phys. Rev. C 74 (2006) 064911.

Charmonium dynamics in nucleus-nucleus collisions at SPS and FAIR energies

O. Linnyk*[1], E. L. Bratkovskaya[1], W. Cassing[2], and H. Stöcker[1]

[1]FIAS, Universität Frankfurt, D-60438 Frankfurt, Germany; [2]Institut für Theoretische Physik, Universität Giessen, D-35392 Giessen, Germany

Charmonium production and suppression in In+In and Pb+Pb reactions at SPS energies has been investigated in the HSD transport approach within the 'hadronic comover model' as well as the 'QGP threshold scenario' [1]. As found in Ref. [1] the comover absorption model – with a single parameter $|M_0|^2$ for the matrix element squared for charmonium-meson dissociation – performs best with respect to all data sets for J/Ψ suppression as well as for the Ψ' to J/Ψ ratio for Pb+Pb (Figs. 1, 2).

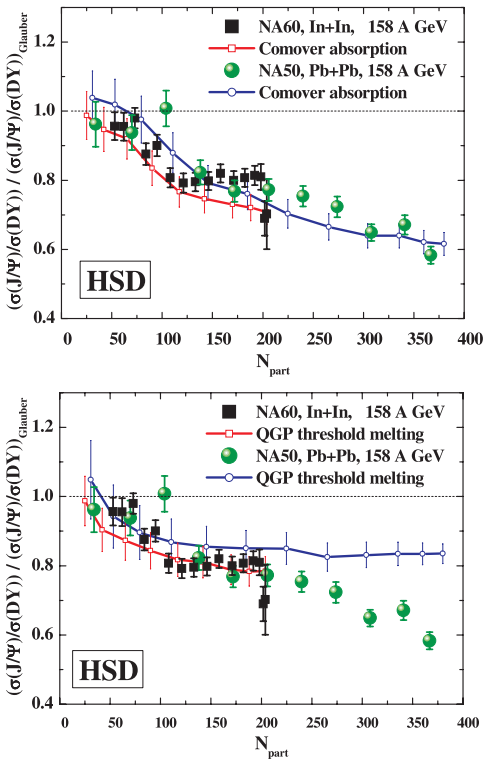

Figure 1: The ratio $B_{\mu\mu}\sigma(J/\Psi)/\sigma(DY)$ versus the number of participants N_{part} in In+In (red line with open squares) and Pb+Pb reactions (blue line with open circles) at 160 A·GeV relative to the normal nuclear absorption The full dots and squares denote the respective data from the NA50 and NA60 Collaborations. The calculations reflect the comover absorption model (upper part) and the 'QGP threshold scenario' (lower part) with $\varepsilon_{J/\Psi} = 16$ GeV/fm^3, $\varepsilon_{\chi_c} = 2$ GeV/fm^3, $\varepsilon_{\Psi'} = 6.55$ GeV/fm^3 while discarding comover absorption. The figure is taken from Ref. [1].

The 'QGP threshold scenario' roughly reproduces the J/Ψ suppression for both systems at 160 A·GeV but fails in the Ψ' to J/Ψ ratio, since too many Ψ' already melt away for a critical energy density of 2 GeV/fm^3 at 160 A·GeV. Only when assuming the Ψ' to dissolve above ∼6.5 GeV/fm^3 a reasonable description of all data is achieved in the 'QGP threshold scenario'; this threshold, however, is not in accordance with present lattice QCD calculations such that the 'threshold scenario' meets severe problems.

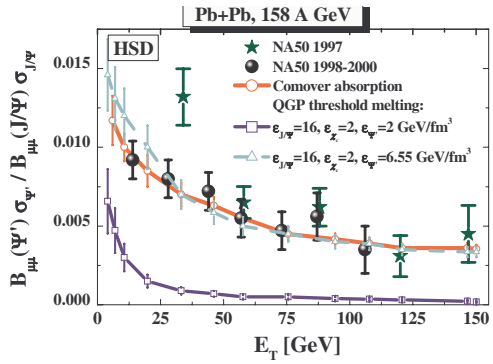

Figure 2: The ratio Ψ' to J/Ψ versus the transverse energy E_T for Pb+Pb at 160 A GeV. The full dots and stars denote the data from the NA50 Collaboration [2]. The HSD result for the comover absorption model is shown as the red line, whereas the blue line indicates the 'QGP threshold scenario' with $\varepsilon_{J/\Psi} = 16$ GeV/fm^3, $\varepsilon_{\chi_c} = 2$ GeV/fm^3 = $\varepsilon_{\Psi'}$ and light blue with $\varepsilon_{J/\Psi} = 16$ GeV/fm^3, $\varepsilon_{\chi_c} = 2$ GeV/fm^3 and $\varepsilon_{\Psi'} = 6.55$ GeV/fm^3 while discarding comover absorption. The figure is taken from Ref. [1].

On the other hand the different scenarios can clearly be distinguished at FAIR energies (of about 25 A·GeV) where the centrality dependence of the J/Ψ survival probability and the Ψ' to J/Ψ ratio are significantly lower in the comover absorption model. Indeed, the average comover density decreases only moderately with lower bombarding energy, whereas the region in space-time with energy densities above critical values of *e.g.* 2 GeV/fm^3 ceases to exist below about 20 A·GeV even in central collisions. It would be ideal to measure the J/Ψ survival probability and the Ψ' to J/Ψ ratio in central Au+Au collisions, where clear steps would indicate the presence of 'melting thresholds', while a smooth excitation function would be in favor of the comover absorption approach.

References

[1] O. Linnyk, E.L. Bratkovskaya, W. Cassing, and H. Stöcker, nucl-th/0612049.

[2] B. Alessandro *et al.*, NA50 Collaboration, nucl-ex/0612013.

* linnyk@fias.uni-frankfurt.de

Propagators of 2d Landau-gauge Yang-Mills theory

Axel Maas*[1]
[1]GSI, Darmstadt, Germany

In two-dimensional Yang-Mills theory many quantities can be determined exactly. In particular, no propagating modes exist, and thus the theory is perfectly confining. It is also related to topological field theories [1]. In Landau gauge, this is manifest already in perturbation theory, where one has an explicit version of Kugo-Ojima confinement by the quartet mechanism [2].

On the other hand, the Gribov-Zwanziger confinement scenario is also applicable to this theory [3]. As in higher dimensions it can be used to obtain predictions for the infrared critical behavior of correlation functions, especially the ghost and gluon propagators. If the scenario is correct in two dimensions, this would be very advantageous. On the one hand, it would permit to study the connection between the Gribov-Zwanziger confinement scenario, the Kugo-Ojima confinement scenario, and topological aspects. However, it is not a-priori clear how results will translate to higher dimensions. On the other hand, it will be possible to study finite volume effects with much higher resolution that in higher dimensions [4]. These effects are currently under active debate (see, e.g., [5]), and any possibility to study them quantitatively is valuable.

Unfortunately, it is not (yet) known how to calculate the Landau gauge correlation functions analytically. A possibility to obtain them are lattice calculations.

Results for the gluon propagator and the ghost dressing function are given in figure 1. Clearly, an infrared suppressed gluon propagator (at large volume) is seen as well as a infrared enhanced ghost dressing function. This is in qualitative agreement with the Gribov-Zwanziger scenario. In particular this implies that of the two infrared exponents found in [3], only the non-trivial one is realized.

Hence, this supports the existence of a Gribov-Zwanziger mechanism also in two-dimensional Yang-Mills theory. It will thus be an interesting laboratory to study the aforementioned effects. A quantitative analysis of the infrared effects as well as an extension to other quantities of interest, like vertices and the Faddeev-Popov operator, is straight-forward [4]. This may open up an interesting road to connect various aspects of confinement and to understand more quantitatively finite volume and other lattice artifacts.

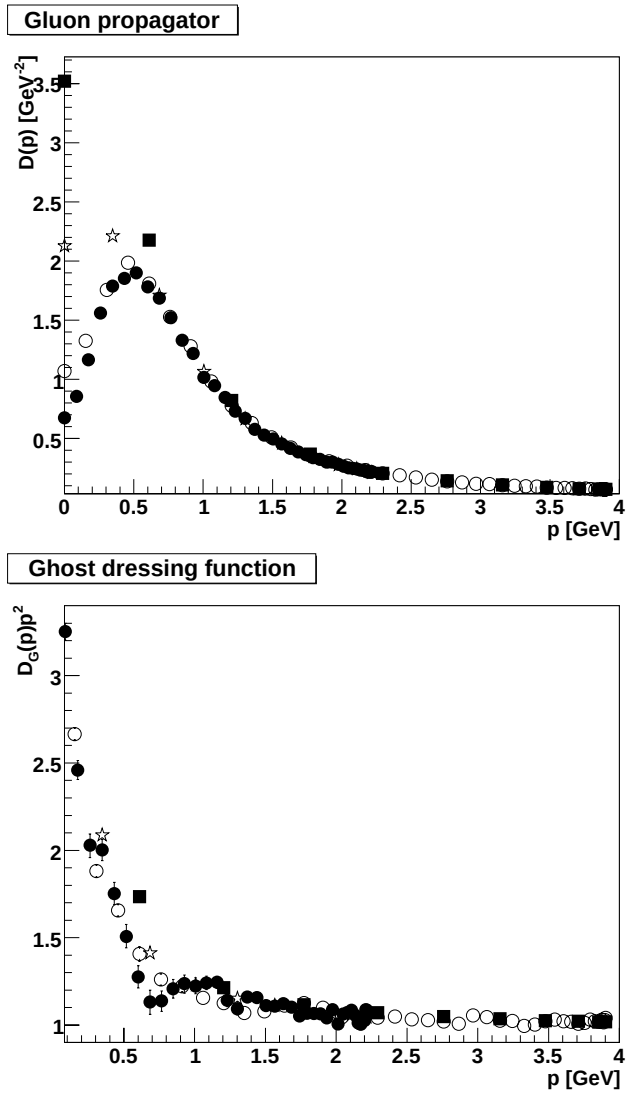

Figure 1: The gluon propagator (top) and ghost dressing function (bottom). Full circles, open circles, open stars, and full squares denote results from a (14.2 fm)^2, (8.08 fm)^2, (3.56 fm)^2, and (2.02 fm)^2 lattice, respectively. Momenta are measured along the x-axis and the scale has been set using the exact continuum result for the string tension [6] set to (440 MeV)^2. More details can be found in [4].

References

[1] D. Birmingham, M. Blau, M. Rakowski and G. Thompson, Phys. Rept. **209** (1991) 129.

[2] T. Kugo and I. Ojima, Prog. Theor. Phys. Suppl. **66** (1979) 1.

[3] D. Zwanziger, Phys. Rev. D **67** (2003) 105001 [arXiv:hep-th/0206053].

[4] A. Maas, in preparation.

[5] C. S. Fischer, A. Maas, J. M. Pawlowski and L. von Smekal, arXiv:hep-ph/0701050.

[6] H. G. Dosch and V. F. Muller, Fortsch. Phys. **27** (1979) 547.

* Present address: Institute of Physics, Slovak Academy of Sciences, Dúbravská cesta 9, SK-845 11 Bratislava, Slovakia

Hamiltonian Lattice Gauge Theory Near The Light Cone

D. Grünewald* †[1], H.-J. Pirner[1], E.-M. Ilgenfritz[2], and E. Prokhvatilov[3]

[1]Institut für Theoretische Physik, Universität Heidelberg, Germany; [2]Institut für Physik, Humboldt-Universität zu Berlin,Germany; [3]Department of Theoretical Physics, St. Petersburg University, Russia

Many physical observables are related to vacuum expectation values of light-like Wegner-Wilson loops. For example, the meson-meson scattering amplitude is governed by the correlation function of two Wegner-Wilson loops lying on the light-cone [1]. Furthermore, a model independent, non-perturbative, quantum field theoretical definition of the jet-quenching parameter $\widehat{q}$ [2] relates the logarithm of the thermal expectation value of a light-like Wegner-Wilson loop to $\widehat{q}$. The jet-quenching parameter is the essential parameter used in parton energy loss models which successfully describe the large suppression of hadron spectra, its dependence on the centrality and orientation to the reaction plane in heavy ion collisions.

The theoretical challenge is the non-perturbative determination of these vacuum expectation values. The computational methods of lattice gauge theory are in principle capable of accomplishing this even by first principle calculations which makes them very appealing. However, there is a problem in the implementation of light-like Wegner-Wilson loops in Euclidean lattices. This problem is cured if one formulates the theory on the light front. In light cone (LC) coordinates, the lightlike Wegner-Wilson loops are stretched along the coordinate axes and are easy to implement.

A lattice approach to LC QCD turns out to be problematic. Attempts to combine the method of discretized LC quantization with a transversal lattice [3, 4] do not have a continuum limit. Also, the Monte Carlo sampling of the Euclidean path integral, does not apply to the LC framework, because the Euclidean LC action has complex parts. Therefore the integrand of the path integral is not positive definite and can not be interpreted as a probability density. Similar problems are known for QCD at finite baryonic density which is often referred to as the sign problem. So far, a convenient solution has not been found. In the Hamiltonian formulation one is faced with the problem, that the LC Hamiltonian is extremely non-local due to the resolution of a constraint equation. This non-locality yields bad numerical convergence.

We propose to circumvent the problem of the inversion of a constraint equation and therefore the problem of non-locality of the Hamiltonian by using near light cone (NLC) coordinates [5, 6]

$$\begin{aligned} x^+ &= \frac{1}{\sqrt{2}}\left[\left(1+\frac{\eta^2}{2}\right)x^0 + \left(1-\frac{\eta^2}{2}\right)x^3\right] \\ x^- &= \frac{1}{\sqrt{2}}\left[x^0 - x^3\right] \end{aligned} \qquad (1)$$

which interpolate smoothly between equal time theories and the LC by varying η. Here x^0 and x^3 denote the ordinary Minkowski time and longitudinal coordinate. The transversal coordinates remain unchanged. Using the NLC Hamiltonian, the basic idea is to construct the ground state wavefunctional of NLC lattice gauge theory for fixed distance η to the LC. This wave functional can be used to measure expectation values of Wegner-Wilson loops close to the LC. The corresponding expectation values on the LC are obtained via a limiting procedure.

In our work [7], we perform a first exploratory investigation of the NLC QCD lattice Hamiltonian and its ground state. We start from the lattice NLC Lagrangean, i.e. we write the Lagrangean in terms of link variables, the lattice analog of the gauge field. The lattice Lagrangean is constructed in such a way that we recover the continuum NLC Lagrangean in the limit of a vanishing lattice constant. We extract the lattice NLC Hamiltonian from the transfer matrix in analogy to the Creutz procedure [8] for equal time theories. We solve analytically the stationary lattice Schrödinger equation for the ground state in the strong and weak coupling limit. These two extremal solutions motivate a simple two parameter gaussian wavefunctional for the ground state valid in the whole coupling range. This gaussian wavefunctional is optimized for its parameters with respect to the energy expectation value by the Ritz variational principle. The analytical results for the ground state energy in the strong and weak coupling limit are nicely reproduced by the variational solution showing that the trial wavefunctional effectively describes the ground state.

References

[1] E. R. Berger and O. Nachtmann, Eur. Phys. J. C **7** (1999) 459 [arXiv:hep-ph/9808320].

[2] H. Liu, K. Rajagopal and U. A. Wiedemann, Phys. Rev. Lett. **97** (2006) 182301 [arXiv:hep-ph/0605178].

[3] M. Burkardt, Phys. Rev. D **49** (1994) 5446 [arXiv:hep-th/9312006].

[4] S. Dalley and B. van de Sande, Phys. Rev. D **59** (1999) 065008 [arXiv:hep-th/9806231].

[5] E. V. Prokhvatilov and V. A. Franke, Sov. J. Nucl. Phys. **49** (1989) 688 [Yad. Fiz. **49** (1989) 1109].

[6] F. Lenz, M. Thies, K. Yazaki and S. Levit, Annals Phys. **208** (1991) 1.

[7] to be published.

[8] M. Creutz, Phys. Rev. D **15** (1977) 1128.

* daniel@tphys.uni-heidelberg.de

† Supported by EU project EU RII3-CT-2004-506078 and GSI

Dynamics of spatially constant Yang-Mills fields

Hans-Peter Pavel*[1,2]

[1]GSI Darmstadt, Germany; [2]TU Darmstadt, Germany; [3]Bogoliubov Laboratory of Theoretical Physics, Dubna, Moscow Region, Russia

Spatially constant Yang-Mills fields [1] are expected to play an important role in the infrared region of QCD. The low energy spectrum of SU(2) Yang-Mills quantum mechnics of spatially constant fields has been first obtained by [2] using the variational approach based on gauge invariant trial states. To obtain sufficiently accurate values also for other charateristics of the corresponding eigenstates we consider here the symmetric gauge [3]

$$A_{ai}\left(q,S\right)=O_{ak}\left(q\right)S_{ki}\ , \tag{1}$$

with the orthogonal matrix $O(q)$, parametrized by the three gauge angles q_i, and the positive definite, symmetric 3×3 physical matrix S. Restricting to the case of non-coinciding eigenvalues $0<\phi_1<\phi_2<\phi_3$ (principle orbits) of S, and performing the principal-axes transformation

$$S=R(\alpha,\beta,\gamma)\ \mathrm{diag}\ (\phi_1,\phi_2,\phi_3)\ R^T(\alpha,\beta,\gamma)\ , \tag{2}$$

we obtain the physical Hamiltonian (in a box of size=a)

$$H=\frac{1}{2}\sum_{\mathrm{cyclic}}^{3}\left[-\frac{\partial^2}{\partial\phi_i^2}-\frac{2}{\phi_i^2-\phi_j^2}\left(\phi_i\frac{\partial}{\partial\phi_i}-\phi_j\frac{\partial}{\partial\phi_j}\right)+\xi_i^2\frac{\phi_j^2+\phi_k^2}{(\phi_j^2-\phi_k^2)^2}+\frac{g^2}{a^3}\phi_j^2\phi_k^2\right]\ , \tag{3}$$

with the intrinsic angular momenta ξ_i along the principal axes. The wavefunctions Ψ are normalised as

$$\int d\alpha\sin\beta d\beta d\gamma\int_{0<\phi_1<\phi_2<\phi_3}d\phi_1 d\phi_2 d\phi_3\prod_{\mathrm{cyclic}}^{3}\left(\phi_j^2-\phi_k^2\right)|\Psi|^2\ =\ 1\ . \tag{4}$$

In [4] all eigenstates of the corresponding harmonic oscillator problem (replacing in (3) $g^2\phi_j^2\phi_k^2$ by $\omega^2\phi_i^2$) up to 30 nodes are calculated analytically and used as trial states for the above Yang-Mills problem (3). The obtained energy spectrum for the lowest 0^+ and 2^+ states is obtained with high accuracy (see Fig. 1) in an very effective way and in agreement with the result of [2]. Furthermore the expectation values of of the fields ϕ_i and $B_i=g\phi_j\phi_k$ (i,j,k cyclic) are calculated and plotted in Fig. 2 and Fig. 3 repectively for both spin-0 (•) and spin-2 (○). We find that practically all excitation energy, independently of whether vibrational or spin excitation, goes into an increasing $\langle\phi_3\rangle$ whereas $\langle\phi_1\rangle$ and $\langle\phi_2\rangle$ as well as $\langle B_3\rangle$ remain practically unchanged at their vacuum values. In all three figures the numerical errors are inside the lines/symbols.

* H.P.Pavel@theory.gsi.de

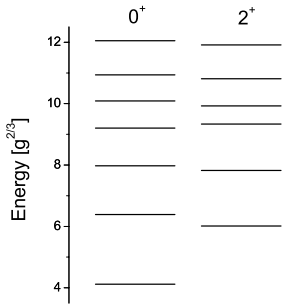

Figure 1: The lowest 0^+ and 2^+ energy levels.

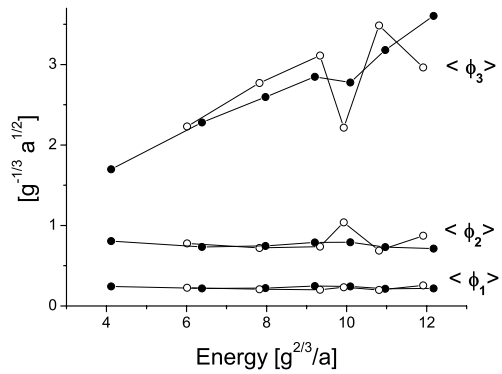

Figure 2: $\langle\phi_i\rangle$ vs energy for the 0^+ (•) and 2^+ (○) states.

References

[1] G.Z. Basean, S.G. Matinyan and G.K. Savvidi, JETP Let. **29**, 587 (1979).

[2] M. Lüscher and G. Münster, Nucl. Phys. **B232** (1984) 445 .

[3] A.M. Khvedelidze and H.-P. Pavel, Phys. Rev. D **59**, 105017 (1999).

[4] H.P. Pavel, arXiv: hep-th/0701283 (2007).

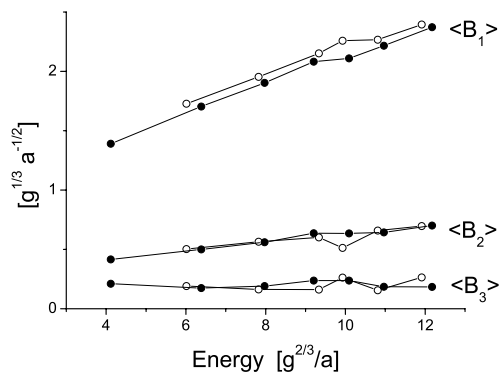

Figure 3: $\langle B_i\rangle$ vs energy for the 0^+ (•) and 2^+ (○) states.

Self-Similarity Approach in Relativistic Nuclear Physics

A. A. Baldin, E. G. Baldina
Joint Institute for Nuclear Research, Dubna, Russia

The basics of the self-similarity approach in relativistic nuclear physics are presented. The general functional self-similar solution describing interaction of relativistic nuclei is obtained.

Self-Similarity

Self-similarity is a special symmetry of solutions, where a change in scales of independent variables can be compensated by a self-similarity transformation of other dynamical variables. General steps towards a self-similar solution are:

(i) Determination of the space of parameters of the problem;

(ii) Finding/guessing the symmetry of this space, determination of invariants of this space;

(iii) Writing physical laws/dependences as correlations between these invariants (we assume analytical character of physical laws);

(iv) Using additional principles, such as the correlation depletion principle, intermediate asymptotic, etc., depending on a particular problem analyzed.

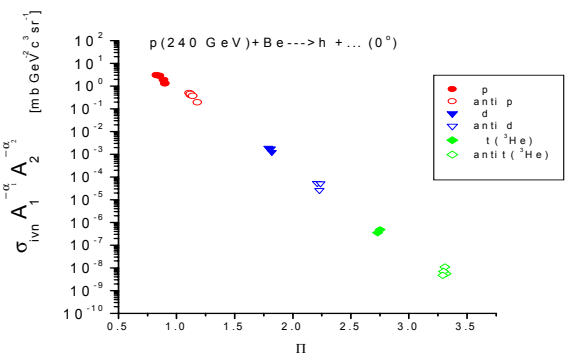

Figure 1. Antimatter production.

Bjorken Variable - Dimensional Self-Similarity

The classical Bjorken x variable is easily obtained from self-similarity considerations.

Consider the electron-proton interaction under the condition $P^2 >> M^2$, i.e. in the ultrarelativistic limit [1].

The 4-momentum conservation is written as:

$$P_1 + xP_2 = P_1' + \sum P_i' \qquad (1)$$

where subscript "1" denotes the electron, subscript "2" the proton, and prime marks quantities attributed to particles after the interaction. Rearranging Eq. (1) and raising it to the second power, we obtain

$$(P_1 + xP_2 - P_1')^2 = (\sum P_i')^2, \qquad (2)$$

or, using the notation $q = P_1 - P_1'$,

$$(q + xP_2)^2 = (\sum P_i')^2 \qquad (3)$$

Neglecting cross products in the right-hand side of (3) due to the correlation depletion principle, we obtain

$$q^2 + 2xP_2q + x^2P_2^2 = M^2, \qquad (4)$$

where M^2 is the squared mass of all produced particles. By neglecting masses in the limit $P^2 >> M^2$, we obtain

$$x = -q^2/2P_2q. \qquad (5)$$

General Self-Similar Solution for Nucleus-Nucleus Collisions - Functional Self-Similarity

A general self-similar solution [2, 3] including the Bjorken solution as a particular case, is obtained as follows.

We consider two interacting nuclei and assume that fractions X_1 and X_2 of masses (or fractions of momenta) of these nuclei participate in the interaction. The 4-momentum conservation is written as:

$$X_1P_1 + X_2P_2 = P_1' + P_2' + P_3 + \sum P_i' \qquad (6)$$

Here, P_3 is the 4-momentum of the particle of interest produced in the reaction (note that conservation of quantum numbers should be taken into account explicitly by addition of corresponding terms to the right-hand side of Eq. (6)).

Again, we neglect terms of relative motion of produced particles and masses of all particles not registered, and seek the self-similar solution in the form

$$E\frac{d^3\sigma}{dp^3} = C_1 A_1^{\alpha(X_1)} A_2^{\alpha(X_2)} f(\Pi) \qquad (7)$$

where $\Pi = \frac{1}{2}\left(X_1^2 + X_2^2 + 2X_1X_2\gamma_{12}\right)^{\frac{1}{2}}$.

The fractions X_1 and X_2 are found by minimization of Π.

$$E\frac{d^3\sigma}{dp^3} = C_1 A_1^{1/3(1+X_1)} A_2^{1/3(1+X_2)} \exp(-\Pi/C_2) \qquad (8)$$

This self-similar solution describes quantitatively a wide variety of experimental data on cumulative, twice cumulative particle production, and antimatter production [4-6] (Fig. 1).

Thus, even small mass difference essentially influences reaction mechanisms, and the assumption $P^2 >> M^2$ is not valid even for very high momenta.

References

[1] V.A.Matveev, R.M.Muradyan, A.N.Tavkhelidze, Lett. Nuovo Cim.,v.5 (1972), 907.
[2] A.A.Baldin Phys. Part. Nucl., 56 (3) (1993).
[3] A.M.Baldin, A.A.Baldin, Phys.Part.Nucl., 29 (3), 577 (1998).
[4] A.A.Baldin et al. Nucl. Phys., A519 (1990) 407.
[5] A.A.Baldin et al., JINR Rapid Comm., 3 (92) (1992) 20.
[6] A.A.Baldin, E.G.Baldina, et al., Phys.Part.Nucl., 1 (4/121) (2004), 7.

Synthetic-diamond detectors for charged-particle beams dosimetry

B. Voss*, M. Rębisz , A. Heinz
GSI, Darmstadt, Germany.

Introduction

Hadron cancer-therapy with high-energetic heavy-ions (HI) as available at the SIS facility at GSI Darmstadt [1] as well as the research with beams stopped in biological material as realized at the UNILAC at GSI in general require the precise knowledge of beam conditions and its composition as well as the applied dose within less than 1% in most cases. At these sites beam preparation, its application and the validation of the dose is controlled and steered online by sets of detectors with gaseous active media or solid state detectors with electrons and ions generated in the active detector volume or emerging from it or by scintillating screens which emit light recorded by cameras or similar devices. Online dose determination is done by small-volume ionization chambers placed in water- or solid-material phantoms as well as offline with radiographic films or nuclear track detectors measuring the (optical) density of the tracks generated by the traversing particles. All systems show strong non-linear behaviour as a function of the dose or dose rate. They also suffer from a limited dynamic range, saturation and a limited resolution in time and space and are subject of saturation, generation of background or show a threshold behaviour ignoring signals below a certain limit. Thus they involve a considerably large amount of corrections and calibrations which are usually done during time consuming quality checks before the irradiations. It is the aim of our work to gain efficiency by unambiguously counting the number of particles impinging on a certain area online with an accuracy of 1% instead of using integration methods.

Material and measurements

We present investigations on the performance of beam-monitors based on single-crystal diamond produced by chemical vapour deposition (scCVD) operated as single-particle counters. The size of the diamond sample was 3.95×3.95 mm^2, its thickness 483 µm. We applied Ti (20 nm) / Pl (30 nm) / Au (100 nm) electrodes of 3 mm diameter in parallel-plate geometry.

Experiments have been performed with high-energy carbon beams (88-430 MeV/u) as well as with low-energy (11.4 MeV/u) heavy charged-particles from ^{12}C up to ^{238}U. At the therapy facility the dose is delivered dynamically point-by-point, with overlapping positions leading to homogeneously irradiated volumes scanning an area of 9 cm^2. At the UNILAC the ions were stopped in a few micrometers of the detector material. Here an area with a diameter of 45 mm was homogenously irradiated in a fixed-field mode. The particle fluences used varied between 10^4 up to 10^9 particles/cm^2/second. In both energy regimes high-bandwidth electronics have been used to count the number of impinging particles. In order to process the signals obtained from the diamond detectors, an electronic based on a discrete high-bandwidth amplifier (DBA) [2] and alternatively a specially designed ASIC [3] was used.

Results

The counting efficiency has been measured to be 100 % with an error of 7 % for therapeutic carbon ions as shown in fig. 1 as an example as well as for low energetic ions.

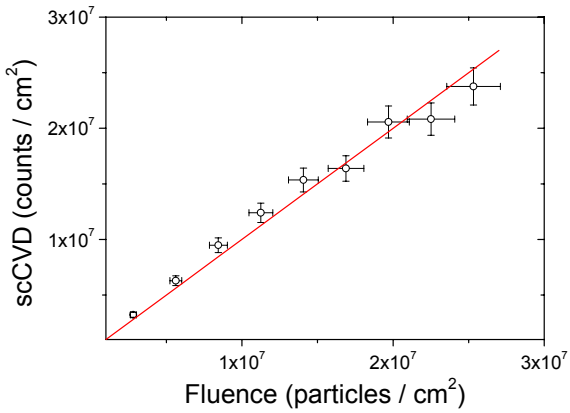

Figure 1: Efficiency of the scCVD diamond detector for carbon ions with an initial energy of 399 MeV/u. The linear fit reveals a counting efficiency of 100 ± 7 %. The error is mainly introduced by the calibration procedure.

Conclusions

Using scCVD diamond for the online-counting has been proven to increase the sensitivity and efficiency as compared to poly-crystalline material which we used in former experiments [4], where we reported a counting efficiency of up to 95 % for ^{12}C ions with an initial energy of 88 MeV/u under therapy conditions. However, the accuracy of these measurements has still to be improved in order to cope with the needs of medical devices.

For high intensities of high-energy beams the output pulse width should be in the nanosecond range. Using high-quality scCVD material this may be achieved with detector thicknesses below 100 µm. Another possibility could be single-crystal like 'sc*'CVD material with slightly worse charge collection efficiency still preserving a good S/N ratio.

References

[1] G. Kraft, Nucl. Instr. and Meth. in Phys. Res. A 454 (2000) 1-10.
[2] P. Moritz et al.. Diam. Relat Mater 10 (2001) 1765
[3] F. Anghinolfi et al., Nucl. Instr. and Meth. in Phys. Res. A 533 (2004) 183-187.
[4] M. Rębisz et al., Diam. Relat Mater 15 (2006) 822-826.

*B.Voss@GSI.de

Development of Single-Crystal CVD-Diamond Detectors*

M. Pomorski[1], E. Berdermann[1], W. de Boer[2], A. Caragheorgheopol[3], M. Ciobanu[1], B. Lommel[1], A. Martemiyanov[1], M.Traeger[1] for the NoRHDia Collaboration and H. Weick[1] for the FRS Group
[1]GSI, Darmstadt, Germany; [2]University of Karlsruhe, Germany; [3]IFIN-HH Bucharest, Romania

SIS Beam Tests

Single-Crystal CVD-Diamond Detectors (SC-DD) of ~ 300µm thickness have been tested in Cave A with proton beams of E_p > 1AGeV as start detectors for minimum ionizing particles. Fast charge-sensitive amplifiers developed at GSI and Bucharest were used. At particle rates up to 1MHz, stable operation and detection efficiency of ~100% are observed. The measured time resolution of $\sigma \geq 330$ps is not satisfying. The next step will be the test of 'sandwich' detectors providing shorter rise time at higher S/N ratio.

In FRS [1] experiments, the energy-loss (ΔE) and the Z-resolution of three SC-DD of 400µm thickness, a size of 4x4mm^2 and an active area of 3mm in diameter were measured using ^{132}Xe projectiles of different energies: 334 AMeV, 740 AMeV and 1.2 AGeV, respectively. The fragments produced on a ^{9}Be target of 4g/cm^2 were identified via Bρ, ToF measured with lucite scintillators between S2 and S4, and ΔE into two MUSIC detectors placed at S4 in front and behind the diamonds.

Even for the primary xenon beams the beam spot onto the diamonds was larger than the size of the active detector area. Due to 'boarder' events of different timing and shape, low-energetic tails appear in the raw energy spectra. However, for all three projectile energies the preliminary online data analysis shows an unexpected good ΔE/E resolution of 1%-2%, which is comparable to the resolution of the ionization chambers. In fragmentation spectra (Fig. 1) all particles are clearly identified with a $\Delta Z/Z \leq 1$.

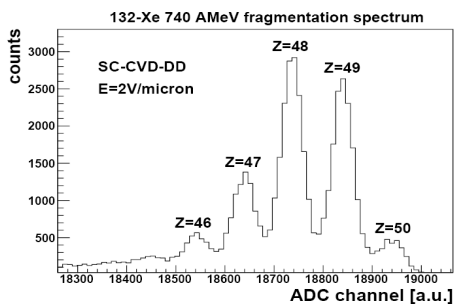

Figure 1: Fragmentation spectrum (raw data, centred on $^{112}_{48}$Cd) measured with a SC-DD of 400µm thickness.

Absence of pulse-height defects is indicated, found to affect significantly the performance of silicon detectors used for comparison in the same experiment.

Independent of the applied electric field E_D, the ^{132}Xe-induced transient current signals recorded without amplification with a 1 GHz DSO, show a bandwidth limited uniform rise time of ~ 550ps. At operation bias, the FWHM of the signals is below 3 ns, whereas the decay time of ~ 6ns is longer than in measurements with α-particles. This signal shape is typical for space charge limited transport in modified internal fields.

* Supported by EU, Hadron Physics, Project RII3-CT-2004-506078

First Tests of Heavily Irradiated SC-DD [2]

Different dose of 26 MeV protons has been applied on SC samples at Karlsruhe's cyclotron: 6.4*10^{13} pcm^{-2} on BDS14, 6.1*10^{14} pcm^{-2} on EBS3 and 1.2*10^{16} pcm^{-2} on BDS13, respectively. Note that all SC-DD tested were pre-irradiated with unknown heavy ion fluencies.

In contrast to damaged silicon sensors, significant suppression of the leakage current occurs in the case of SC-DD. Figure 2 shows ^{241}Am-α-induced Transient Current (TC) signals in BDS14 and EBS3 before (dashed lines) and after (solid lines) irradiation. For both types of drifting charge carriers, exponential signal decay proportional to the amount of created defects is obtained. Amplitudes, rise time and drift velocity remain almost unchanged, suggesting thus the creation of neutral defects.

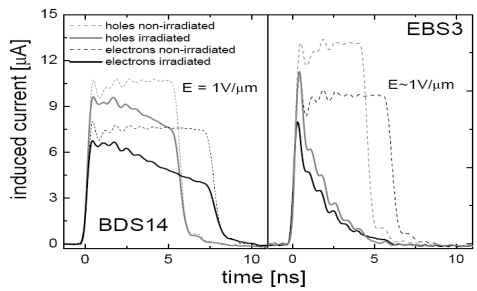

Figure 2: TC signals of SC-DD before (dashed lines) and after (solid lines) heavy p_{26MeV} irradiation.

Phenomena known from Poly-Crystalline Diamond Detectors (PC-DD) were observed in SC-DD after irradiation: Polarization, stated by the progressive decrease of stopped particles amplitudes, and priming, indicated by the recovery of the charge-collection efficiency back to nearly 100% by filling of traps with traversing ^{90}Sr electrons. After ~ 10^{16}pcm^{-2} however, electrons of $E_{ß} > 1$MeV are detected with ~ 96% efficiency and most probable value of 2200e$^-$. Concluding: The dominating Coulomb force at $E_p << 100$MeV, i.e. only a factor 6/14 lower for $^{12}_{6}$C than for $^{28}_{14}$Si , limits the high radiation resistance measured at higher energies for PC-DD [3]. In this energy range of large inelastic cross-section and heavier nuclear fragments in case of $^{28}_{14}$Si , SC-DD are expected to be at least one order of magnitude harder than silicon detectors.

References

[1] H. Geissel at el., NIM B70, 286-297 (1992)
[2] M. Pomorski et al., Diam. Rel. Mat. (2007) in press
[3] The RD42 Collaboration, LHCC report 2006

Infrared spectroscopy of chromium film growth on single-crystal diamond*

R. Lovrincic and A. Pucci
Kirchhoff Institut für Physik, Universität Heidelberg, Germany

Single crystal diamonds are very favourable as detector material for several reasons [1]. Exact knowledge about the crystal surface is essential in order to control the electronic properties of the diamond. Another decesive and so far non-standardised step towards satisfying detector performance is the fabrication of electrodes. Therefore we study as first part of our research regarding the metal-diamond interface the growth of chromium as contact material on diamond.

The free electron response of a metal can be well described with the Drude dielectric function

$$\epsilon = \epsilon_\infty - \frac{\omega_\mathrm{p}^2}{\omega(\omega + i\omega_\tau)}, \qquad (1)$$

where ω_τ is the relaxation rate of the free electrons, ω_p the plasmafrequency, and ϵ_∞ describes the background polarizability. The approximations underlying the Drude model are valid for energies well below the interband transitions. For chromium, this limit is at about $1500\mathrm{cm}^{-1}$ [2]. The real dielectric function and hence the real conductivity of thin films is strongly influenced by their morphology and crystalline structure. This is taken into account by adding a thickness dependent relaxation rate $\omega_{\tau\mathrm{s}}(d)$ to the bulk rate. In order to describe the measured data satisfactorily, we also have to consider the thickness dependence of the plasma frequency.

The in-situ experiments were performed in an ultra-high vacuum chamber that is connected to a Fourier-transform infrared spectrometer and an IR-detector. The pressure during Cr deposition was $2 \cdot 10^{-10}$mbar. The diamond substrate had been cleaned by using a 240°C hot mixture of H_2SO_4 and KNO_3, subsequent rinsing in pure water, and heating to about 250°C in UHV for several hours to remove residual hydrocarbons. Chromium was deposited by thermal evaporation at a rate of about 0.07nm/min. The deposiston rate was calibrated with a quartz micro balance. The substrate was kept at room temperature. The IR-spectra measured during evaporation are normalized to a reference spectrum taken before Cr deposition.

Figure 1 shows the change of relative transmittance during the growth of Cr on C(100). The transmission stays frequency independent up to a thickness of about 2.4nm, a behaviour well known for amourphous layers [3]. Beyond this point, the decrease in transmission is stronger for smaller wavenumbers indicating metallic behaviour. Based on equation (1) we fitted the measured spectra with $\omega_{\tau\mathrm{s}}(d)$ and β as ratio of the film plasma frequency to the bulk one derived from the data in [2]. Figure 2 shows these two parameters versus film thickness. For $d < 2.4\mathrm{nm}$ the film

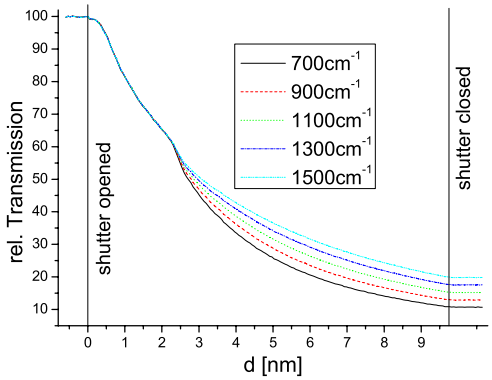

Figure 1: Transmittance change with average Cr thickness d on C(100) for the 5 wavenumbers as given. Deposition starts at 0 nm and ends at 9.7 nm.

can not be regarded as a Drude-type metal since both parameters take too high values, similar to results for Pb on Si(111)-7x7 [3]. But for $d > 2.4\mathrm{nm}$, the model describes the data very well and provides reasonable values. As the film becomes thicker β approaches one within measurement errors. However, also at the highest thickness, $\omega_{\tau\mathrm{s}}$ still gives a total relaxation rate three times bigger than the bulk value from [2]. This indicates a defect rich film with a clearly lower electronic conductivity than bulk Cr.

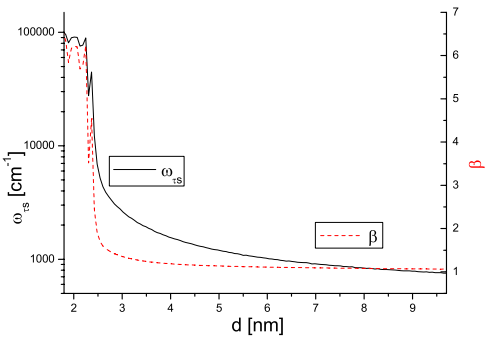

Figure 2: Deviation $\omega_{\tau\mathrm{s}}$ from bulk relaxation rate at 300 K and ratio β of film to bulk plasmy frequency versus Cr thickness

References

[1] E. Berdermann et al., phys. stat. sol. (a) **201**, p. 2521 (2004).

[2] S. S. Fouad et al., phys. stat. sol. (b) **187**, p. 99 (1995).

[3] A. Pucci et al., Phys. Rev. B **74**, p. 125428 (2006).

* Work supported by EU, project RII3-CT-2004-506078

Metallic Uranium Targets

Birgit Kindler, Willi Hartmann, Annett Hübner, Jutta Steiner, Bettina Lommel
GSI, Darmstadt, Germany.

In 2004 we reported on a new evaporation set up for uranium-compound targets, basically UF_4, for heavy-ion experiments [1]. Since for most experiments in nuclear physics and chemistry targets from metallic uranium would be preferred because side reactions are minimized, we upgraded our high-vacuum coater TF 600© from BOC Edwards© with a magnetron sputtering equipment which is suitable for deposition of metallic uranium as well as for uranium oxide or carbide as a possible alternative.

In Fig. 1 the interior of the vacuum chamber is shown with the magnetron source and the shutter and the rotating target wheel sitting above. On the left side the gas inlet is situated.

The purchase of a sputter target from metallic uranium with the required properties proved to be very difficult. After more than a year of world wide search we finally were successful to get suitable material with a content of ^{235}U less than 0.2 %, which was a requirement of the GSI-safety department, from Material Manufacturing Sciences Corporation, Oak Ridge, TN, USA. The starting material was processed in high vacuum and the oxygen content remaining in the metal was specified to be less than 25 ppm. The sputtering source was a disk of 1 inch in diameter with a thickness of 3 mm, which corresponds to about 30 g of uranium.

Figure 1: Interior of the vacuum chamber: Magnetron source, shutter, target wheel and gas inlet are shown.

The targets we produced for the SHIP experiment were deposited on 35 µg/cm² carbon backings that were heated to about 200 °C in a separate process by means of a quartz lamp. We experienced that such a heat treatment of the carbon backings improves the survival rate of the targets in the following deposition process significantly and also enhances their durability under heavy ion bombardment. Those pre-heated backings were then mounted on the target wheel inside the vacuum chamber and a layer of about 300 µg/cm² of metallic uranium was deposited with magnetron sputtering and pure argon as a sputtering gas. Without breaking vacuum an additional carbon layer of 10 µg/cm² is applied as a protection against oxidation and to reduce sputtering processes during evaporation.

The deposition of the additional carbon covering layer proofed to be essential for the stability of the uranium layers against oxidation. Breaking vacuum before the application of the covering or an oxygen contamination of the argon gas leads to a continuously alteration of the uranium layer, as can be seen in Fig.2.

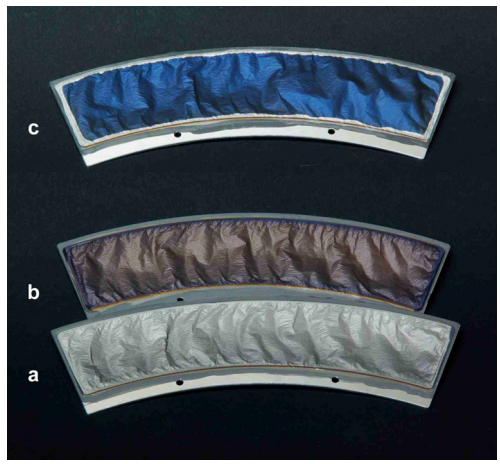

Fig. 2: Sandwich targets with C / U /C on frames used in experiments at SHIP; (**a**) Sputtering and deposition of cover layer without breaking vacuum; (**b**) venting of chamber to argon between sputtering and deposition of cover layer; (**c**) preparation the same way as (**a**) but just after changing the argon bottle.

The targets produced with this process performed excellent in various beam times of SHIP [2, 3]. They showed a high durability without noticeable material loss or deterioration.

For the TASCA set up targets of metallic uranium were sputtered on various backings with and without covering layer to test the durability of the different target-backing combinations under varying experimental conditions [4,5]. The evaluation of the results is still in progress.

References

[1] W. Hartmann; A. Hübner; B. Kindler; B. Lommel; J. Steiner, GSI Scientific Report 2004 GSI Report 2005-1, p. 306.
[2] B. Kindler et al., to be published in Nucl. Inst. and Meth. A.
[3] K. Nishio et. al., Eur. Phys. J. **A** 29, 281 (2006.
[4] B. Lommel et al., to be published in Nucl. Inst. and Meth. A.
[5] K. Eberhardt et al., contribution to this report.

Radioactive Targets for TASCA

K. Eberhardt[1], J. V. Kratz[1], D. Liebe[1], P. Thörle[1], W. Brüchle[2], Ch. E. Düllmann[2], W. Hartmann[2], A. Hübner[2], E. Jäger[2], B. Kindler[2], B. Lommel[2], R. Mann[2] , M. Schädel[2], B. Schausten[2], E. Schimpf[2], A. Semchenkov[2,6], J. Steiner[2], K. E. Gregorich[3], H.-J. Maier[4], J. Szerypo[4], R. Sudowe[5], A. Türler[6], A. Yakushev[6]

[1]Johannes Gutenberg-Universität Mainz, Germany (UMZ); [2]GSI, Darmstadt, Germany; [3]Lawrence Berkeley National Laboratory, Berkeley, USA (LBNL); [4]Ludwigs-Maximilians-Universität München, Germany (LMU); [5]University of Nevada, Las Vegas, USA (UNLV); [6]Technische Universität München, Germany (TUM)

The main components of the **T**rans**A**ctinide **S**eparator and **C**hemistry **A**pparatus **TASCA** are already installed and the separator is now in the commissioning phase. A first beam time took place in April 2006 and further commissioning experiments were performed in May and November 2006. An overview of the current status is given in separate contributions [1,2].

For the beam time in May a number of different target materials have been applied, among them a set of ^{nat}Gd-targets produced by Molecular Plating at UMZ on a 5 µm Ti-backing foil. The targets withstood a 1.43 μA_{part} Cr^{7+}-beam without damage although the use of a relatively thick Ti-backing resulted in an increased background signal. One main goal of the experiment in November was the test of different ^{238}U-targets with an intense $^{40}Ar^{10+}$-beam. Two target wheels have been irradiated – TN4 and TN8 – both consisting of three different kinds of targets.

All targets have been delivered by the GSI target laboratory. Here, the U-layer of about 500 µg/cm^2 has been produced by sputtering of depleted uranium in its metallic form with an ^{235}U content less than 0.2% [3]. Here, C and Ti, respectively, have been used as a backing material. In some cases the U-layer has been covered with a thin C layer in order to prevent losses of the target material during irradiation with the $^{40}Ar^{10+}$-beam. After a certain beam integral was applied, the targets have been inspected to check for damage. Target wheel TN4 has first been irradiated for a total of about one hour with increasing beam intensity up to 2 μA_{part}. The target segments showed severe damage with holes and cracks. TN4 was then replaced by TN8 which was irradiated for about 1.5 hours with increasing beam intensities up to 1 μA_{part}. Figure 1 shows TN8 before and after irradiation, respectively. After irradiation segment 1 (C-backing/C cover) showed a visible hole, whereas segments 2 and 3 (Ti-backing) remained mechanically stable but show intense colour changes in the central part (see fig.1).

In order to check for material losses and homogeneity, the targets with Ti-backing are currently inspected by radiographic imaging using a FLA 7000 Imager from FUJIFILM Corporation. Figure 2 shows a radiographic image of target segment #3 from target wheel TN8 with a U-content of 491µg/cm^2. Here, light grey areas correspond to the initial deposited and uniformly distributed U-layer. The dark grey area in the center part indicates the $^{40}Ar^{10+}$-beam track. Here, the higher activity origins from an activation of the Ti-backing and the U target material by the beam. Information about material losses due to the interaction with the beam is not yet available. Thus, work is currently in progress at GSI to produce U-samples as a calibration standard for quantitative measurements of target thicknesses using radiographic imaging. The targets are further inspected by α-particle counting of the U-layer in order to check for material losses. Furthermore, the targets will be inspected by electron beam diagnostics.

Figure 1: Target TN8 before (left) and after irradiation (right) with a $^{40}Ar^{10+}$-beam of 1 μA_{part} maximum intensity.

Figure 2: Radiographic image of target segment # 3 from target wheel TN 8. See text for details.

At UMZ work is currently under way to find optimum conditions for the deposition of ^{244}Pu (up to 500 µg/cm^2) on 2 µm thin Ti backing foils by Molecular Plating from isobutanolic solution. ^{244}Pu is of special interest as a target material for chemical investigations of the heaviest elements, since relatively long lived isotopes of Rf to Hs - with half-lives in the order of a few seconds - can be produced in the bombardment of a ^{244}Pu-target with beams ranging from ^{22}Ne up to ^{30}Si. ^{244}Pu is also the optimum target for production of Z=114 with a ^{48}Ca beam.

References

[1] A. Semchenkov et al., contribution to this report
[2] Ch. E. Düllmann et al., contribution to this report
[3] B. Kindler et al., contribution to this report

See also http://www.gsi.de/TASCA

Study of Ion Beam Induced Thermal Stress in Solid Graphite Target for Super-FRS Fast Extraction Scheme*

N.A. Tahir, GSI, Darmstadt, Germany
A.R. Piriz, J.J. Lopez Cela, UCLM, Ciudad Real, Spain
V. Sultanov, A. Matveichev, A. Shutov, V. Kim, A. Ostrik, I.V. Lomonosov, IPCP, Chernogolovka, Russia
D.H.H. Hoffmann, GSI and TU Darmstadt, Germany

Previously [Tahir et al., J. Phys. D: Appl. Phys. 38 (2005) 1828], 2D numerical simulations of heating of a solid graphite target by a uranium beam over an intensity range of 10^{10} - 10^{12} ions per bunch, have been presented. These simulations have been carried out using the computer code BIG-2 [Fortov et al., Nucl. Sci. Eng. 123 (1996) 169]. It has been found that the target will survive sublimation or break up due to thermal stress (static yield strength of graphite is 40 MPa) for an intensity of 10^{10} ions per bunch with an extended beam spot having σ_x = 1.0 mm and σ_y = 6.0 mm, the standard deviation of the Gaussian particle distribution in X- and Y-direction respectively (see Table 1).

Table 1: U ions, N = 10^{10}, σ_x = 1.0 mm, initial T = 300 K

σ_y(mm)	E(kJ/g)	T (K)	P (GPa)
2.0	0.233	471	1.25x10^{-1}
6.0	0.08	356	4.2x10^{-2}
12.0	0.04	327	2.0x10^{-2}

It is seen that in case of σ_y = 2 mm, 233 kJ/g specific energy is deposited in the target that leads to a temperature increase of 171 K and a thermal pressure of **125 MPa**. ANSYS code, on the other hand, predicts a similar rise in the temperature, but shows a much lower stress of **7 MPa** for the same amount of input energy. This difference is due to the fact that in Super-FRS fast extraction scheme, the bunch length is 50 ns which means that the energy is deposited instantaneously. In such a short time, there is no heat conduction nor there is any material movement due to thermal expansion. Therefore the entire energy is stored as internal energy of the target that appears as thermal pressure (pressure is energy per unit volume). This situation is fully described by the code BIG-2. Thermal pressure in the code is evaluated using the SESAME equation-of-state (EOS).

However, on time scale of several hundred micro sec after the irradiation, heat conduction becomes effective and thermal expansion takes place that lead to a reduction in temperature and pressure until a steady state is reached. It only provides information about the elastic tensions and can not treat the initial transient phase of target heating because it does not have the EOS model. The BIG-2 code, on the other hand, does not have a model of elasticity and therefore can not provide information about the thermal stress.

In order to have a complete picture of the problem, we have used a three-dimensional computer code that includes the SESAME EOS model and elastic effects using an ideal elasticity model that means Hook's law complemented with yield criterion. In Figures 1 and 2 we plot the thermal pressure and the deviatoric part at different times respectively. These figures show how the thermal pressure is converted to elastic modes.

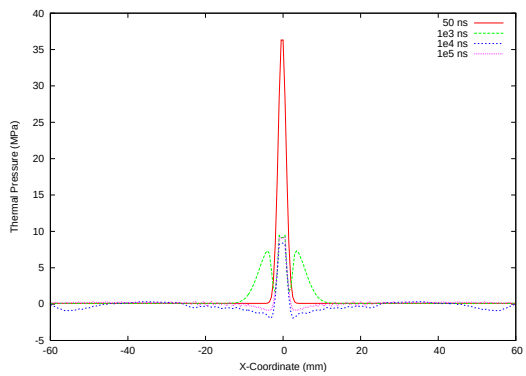

Figure 1: Thermal pressure at different times.

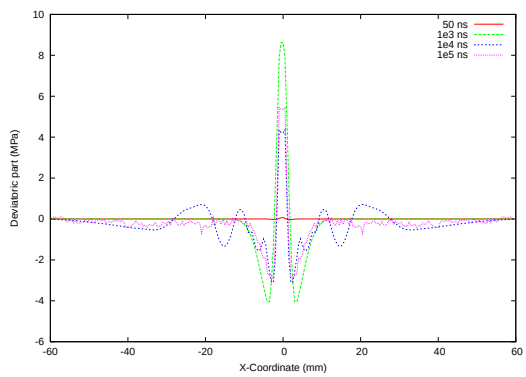

Figure 2: Deviatoric part of pressure at different times.

(please contact: n.tahir@gsi.de).

*This work was supported by the BMBF and RFBR grant No: 06-02-04011-NNIOa, Russia

Three-Dimensional Numerical Simulations of a Windowless Liquid Jet Lithium Target for the Super-FRS Fast Extraction Scheme*

N.A. Tahir, GSI, Darmstadt, Germany
V. Kim, I.V. Lomonosov, IPCP, Chernogolovka, Russia
D.H.H. Hoffmann, GSI and TU Darmstadt, Germany
A.R. Piriz, UCLM, Ciudad Real, Spain

We consider a plane slab of liquid Li that is 7 cm long, 5 cm high, 1 cm thick and the beam is directed along the target length (Z-axis). The beam consists of 10^{12} 1 GeV/u uranium ions that are delivered in a single bunch, 50 ns long. The beam focal spot has an elliptic shape with a Gaussian power profile in the radial direction. The standard deviation in X and Y directions, namely, σ_x = 2 mm and σ_y = 12 mm, respectively.

We have carried out numerical simulations of target heating using a three-dimensional computer code that is based on an individual particle in cell method. This code considers three-dimensional energy deposition by the projectile particles using a full particle tracking scheme. The physical conditions of the target are treated using a semiempirical (SE) equation of state (EOS) model that includes all the experimental data available to date. Especially, it accounts for novel high pressure experimental data and provides for more correct description of the melting region and the liquid state of Li, which is not treated so accurately in the SESAME EOS data.

The maximum temperature in the target is 950 K which is safely below the boiling temperature of Li (1643 K). The target will therefore remain in the liquid state that will avoid introduction of Li vapor into the beam line. The corresponding maximum pressure is of the order of 0.85 GPa will generate compression waves in transverse direction (along X and Y directions). Figure 1 shows pressure profiles along X-axis at different times after irradiation. Reflection of the pressure waves between the target center and the X-boundary is clearly seen. The maximum pressure that is delivered at the boundary is about 0.8 GPa that continuously decreases in subsequent reflections. Figure 2 shows pressure vs Y-coordinate at different times. It is seen that a maximum pressure of about 0.25 GPa is imparted on the boundary at 3000 ns. This is lower than the yield strength of stainless steel which means that the nozzle will survive the impact of the pressure wave.

We also did simulations using the SESAME EOS. The results are shown in Figure 6 where we present three-dimensional pressure distribution at t = 2000 ns. It is seen that in this case, one achieves negative pressures in the liquid target, which is in a state of thermodynamic equilibrium. **Obviously, this is an artefact of the SESAME**.

(please contact: n.tahir@gsi.de).

* This work was supported by the BMBF and RFBR grant No: 06-02-04011-NNIOa, Russia

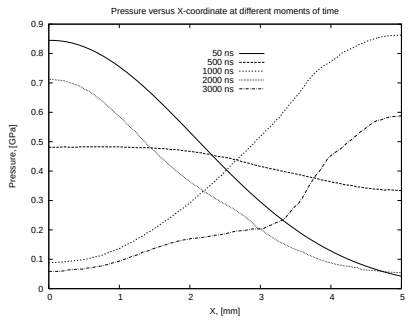

Figure 1: Pressure vs X-coordinate at different times using semi-empirical EOS data.

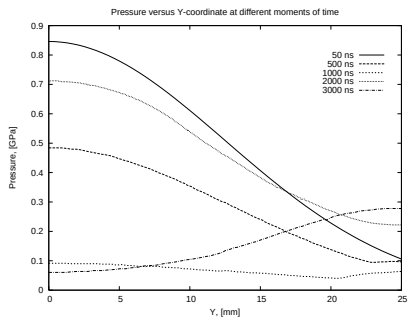

Figure 2: Pressure vs Y-coordinate at different times using semi-empirical EOS data.

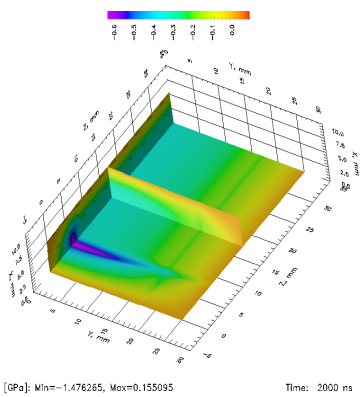

Figure 3: Target pressure at t = 2000 ns using the SESAME EOS data, strong negative pressures, an artefact of the EOS model.

PHITS simulations of radiation damage in the Super-FRS graphite target

M. Tomut[1,2,*], H. Iwase[1], A. Kelic[1], R. Neumann[1], K. Sümmerer[1] and C. Trautmann[1]
[1]GSI, Darmstadt, Germany; [2]INFIM, Bucharest, Romania.

The FAIR Super-Fragment-Separator (Super-FRS) facility will use a rotating graphite production target in the slow as well as in the fast extraction mode (for low-Z projectiles and intensities). A fine-grained isotropic graphite grade has been chosen due to its resistance to the thermal stress induced by high-power particle beams. Calculations based on properties of non-irradiated material show that it is possible for graphite to withstand energy densities of up to a few hundred J/g, but irradiation-induced changes of the thermophysical and mechanical properties may lower this value considerably. In addition, long-term radiation-induced effects have to be investigated in order to predict the lifetime of a target wheel.

Systematic information about radiation damage in materials is mostly available from neutron-irradiation experiments. In order to predict heavy-ion induced damage, we assume that the number of "displacements per atom (dpa)" is a proper scaling variable.

Dpa calculations

Dpa-values resulting from irradiating the Super-FRS graphite target with heavy ions have been calculated using the transport code PHITS [1]. A simple cylindrical-geometry model has been chosen for the target. A Gaussian-shaped beam with sizes of σ_x = 1mm and σ_y = 2mm impinges on one side of the cylinder. The fluence has been calculated by assuming an annual dose of 10^7 pulses from SIS100 with intensities of 10^{12} ions/pulse, extraction times of 1 s and a rotating frequency of the target wheel of 1 Hz. The resulting particle fluence per year is about 10^{17} ions/cm^2. Calculations have been made for ^{40}Ar, ^{136}Xe and ^{238}U ions of 1 *A* GeV energy. The 2D distribution of dpa in the cross-section of the cylindrical graphite target, at its exit end, is shown in Fig. 1 for ^{136}Xe and ^{238}U ions. For the ^{238}U beam, the highest value of dpa/year is 4×10^{-3}, which is well below the value of 1dpa corresponding to a safe operation time of the Paul Scherrer Institute graphite target E, exposed to a fluence of 10^{22} p/cm^2 of a 590 MeV proton beam.

The above calculations take into account only nuclear stopping of the heavy ions. The effects resulting from electronic energy loss may have to be considered as well, but it's not easy to quantify the number of defects created by the electronic excitation of the target atoms. For 1 *A* GeV ^{238}U ions impinging on the graphite target, the electronic linear energy transfer S_e amounts to 4 keVnm^{-1}, which is below the range of continuous track formation in highly oriented pyrolitic graphite [2]. In addition, defect clustering, which is a typical effect induced by heavy ions, takes place and may influence the thermal defect annealing significantly. The aspect of defect accumulation at large fluences needs to be addressed.

* m.tomut@gsi.de

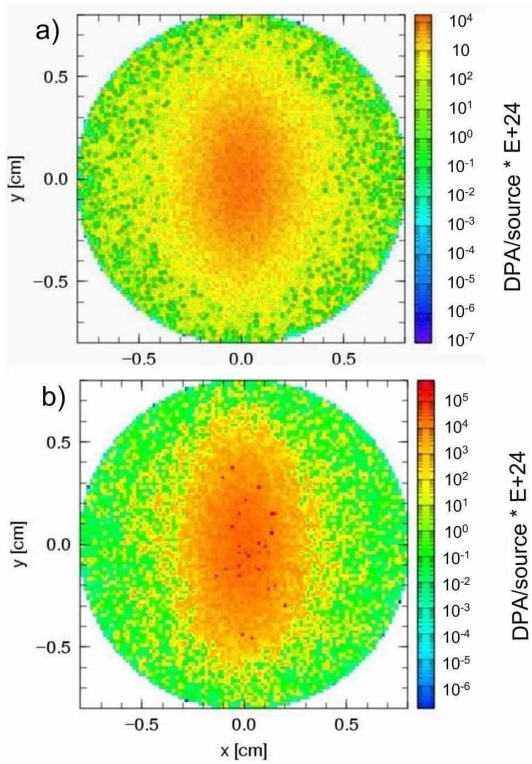

Figure 1: 2D distribution of dpa per incident ion at the exit of a cylindrical graphite target for: (a) 1 *A* GeV ^{136}Xe on a 6 g/cm^2 thick target (b) 1 *A* GeV ^{238}U on a 4 g/cm^2 thick target. The calculated dpa values were multiplied by 10^{24}.

H and He production

PHITS has also been applied to evaluate the amount of H and He gas produced in nuclear reactions in the target. H and He production has been estimated to be 50 appm/year and 5 appm/year, respectively. H is believed to diffuse out. Due to the high enthalpy of solution, He can reach high concentrations in solids and has the tendency to accumulate in bubbles between crystalline planes and at grain boundaries. This leads to additional dimensional swelling along the hexagonal axis of the graphite crystallites, to embrittlement and it will also contribute to fatigue. The heating of the target wheel by the primary beam up to temperatures of 1000 K could enhance the release of He, due to the increased He atom mobility along the basal planes.

References

[1] H. Iwase, K. Niita and T. Nakamura, J. Nucl. Sci. Tech. 39 (2002) 1142.
[2] J. Liu, R. Neumann, C. Trautmann and C. Müller, Phys. Rev. B 64 (2001) 184115.

Optimization of ion-beam profile with respect to stability of the liquid-Li target for Super-FRS

An. Tauschwitz[1], J.A. Maruhn[1], V.P. Efremov[2], H. Weick[3], and M. Winkler[3]
[1]University of Frankfurt am Main, Germany; [2]IHED, Moscow, Russia; [3]GSI, Darmstadt, Germany

At FAIR intense energetic beams of uranium will be available for experiments at Super-FRS. A small focus spot of the uranium beam is crucial to ensure the resolution of the isotopes and the transmission of the secondary beam. It is necessary to investigate the stability of the production target after the energy deposition by intense ion beams to define the beam focusing limit. A liquid lithium jet is considered as a possible target configuration for the Super-FRS [1]. To predict the integrity of the target after ion beam heating, the hydrodynamic response of the target has to be analyzed. The SIS-100 ion beam for Super-FRS will consist of 6×10^{11} ions of U^{28+} at 1 GeV/u delivered in 50-100 ns. For an ion beam deposition of about 1 kJ/g there will be no hydrodynamic motion in the target during the heating time. After the energy of the ion beam is deposited, compression and expansion (rarefaction) waves start to propagate in the target. The expanded target can become unstable, if the negative (tensile) pressures exceeds the failure stress limit. For lithium there are no data for the failure stress available in the literature. The absolute value of the failure stress decreases with temperature and depends on the purity of the material. To obtain the required data for the hydrodynamic calculations the failure stress of liquid lithium has to be measured. In the calculations reported previously [2] it was assumed, that the target remains stable until the expanded matter undergoes spinodal decomposition. The calculations were performed using a Gaussian radial profile of the ion beam current. It was shown, that for $\sigma_x = 2$ mm and $\sigma_y = 4$ mm the energy $\epsilon = 3.3$ kJ/g was deposited that corresponds to a peak temperature $T = 1560$ K. This leads to the lowest negative pressure $P = -8.6$ kbar. The situation can be improved if a rectangular radial profile of the ion beam is considered. Figure 1 shows the energy deposition along horizontal (x) and vertical (y) axis for the previously used Gaussian and idealized rectangular profiles with $r_x = 6$ mm, $r_y = 12$ mm. For the rectangular beam profile $\epsilon = 0.7$ kJ/g, $T = 704$ K. In fig. 2 the pressure distributions in the target volume are plotted. The target center lies in the origin of the coordinate system. The picture for $t = 0.6\,\mu$s shows,

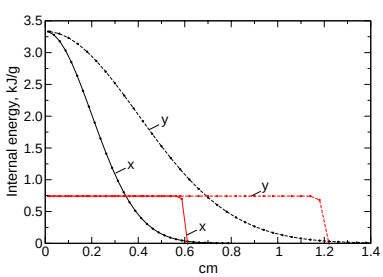

Figure 1: Specific internal energy along x and y axis after the heating with Gaussian and rectangular ion beams.

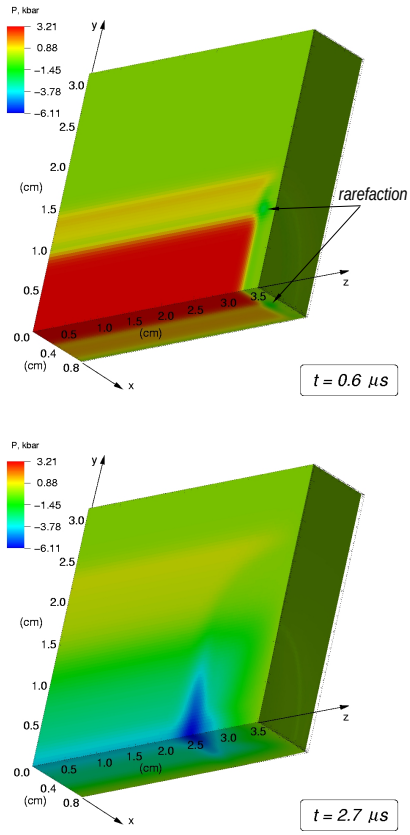

Figure 2: Pressure distribution in the target heated with a rectangular beam. The direction of the beam is the z-axis.

that the rarefaction wave starts to propagate from the edges of the heated zone. The rarefaction wave moves along the z-axis towards the target center due to the motion of the heated free surface and converges on the beam axis (z). Along x-axis the compression wave reaches the free surface, consecutive an expansion wave moves inwards. The maximum pressure $P = -6.1$ kbar occurs on the z-axis at $t = 2.7\,\mu$s. It is seen that for the rectangular beam profile lower temperature and a lower absolute value of the negative pressure are obtained in the target. Further optimizations of the radial beam profile together with ion optic calculations have to be done. The suggested modification of the ion beam profile should also be considered for the carbon target.

References

[1] FAIR, Conceptual Design Report, 2001.

[2] An. Tauschwitz et al., GSI Scientific Report 2005, FAIR-NUSTAR-SuperFRS-05.

A Multiple-Reflection Time-of-Flight Isobar Separator*

T. Dickel[1], M. Petrick[1], W.R. Plaß[1], U. Czok[1], H. Geissel[1,2], C. Jesch[1,2], C. Scheidenberger[1,2]
[1]Justus-Liebig-Universität Giessen, Germany; [2] GSI, Darmstadt, Germany

A multiple-reflection time-of-flight mass spectrometer (MR-TOF-MS) developed previously [1,2] has been extended to work as a high-resolution mass separator capable of selecting individual isobars. For this purpose, a Bradbury-Nielsen Gate [3] has been built and installed behind the MR-TOF-MS (Fig. 1).

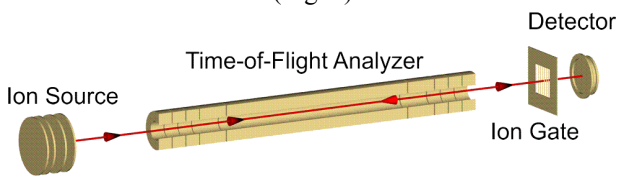

Figure 1: Schematic figure of the MR-TOF-MS and the path of the ions in the device. The analyzer has a length of 40 cm; the kinetic energy of the ions amounts to 1.5 keV.

The performance of the MR-TOF-MS was characterized using the isobaric doublet of carbon monoxide and nitrogen molecular ions. A resolving power of 62,000 (FWHM) was obtained after 1000 turns even with an uncooled ion population. In the first few turns, about 30% of the ions are lost from the device, presumably because of phase space selection. In addition, losses due to collisions with the residual gas occur, but these will be avoided in the future in a differentially pumped system. Also, the ion source will be replaced by an RF trap, which will allow for the injection of externally created ions and for ion cooling and hence further improved mass spectrometer performance. In an initial experiment, a resolving power of about 100,000 has been achieved by reducing the beam diameter in the present device from 6 mm to 4 mm (Fig. 2). This beam width is still significantly larger than that of ions ejected from an RF trap. Even after many turns, excellent peak shapes in terms of variance and skewness are obtained, fulfilling an important requirement for the resolution of isobars of significantly differing abundances. Depending on the number of detected ions, a mass accuracy of down to 10^{-7} can be expected. Thus, high-precision mass measurements of very short-lived nuclei with half-lives ≥ 1 ms are in reach. The MR-TOF-MS also has the advantage that all isobaric nuclides corresponding to the same mass number can be measured simultaneously, and that measurements will be possible already with 10 to 100 ions, albeit with reduced precision.

The use of the MR-TOF-MS as isobar separator has been demonstrated by removing either carbon monoxide or nitrogen ions from the beam in the ion gate after 50 turns (Fig. 3). The separation power achieved is thus about 7000 (FWHM). For a larger number of turns, the separation power will increase accordingly. From simulations it is expected that up 10^6 – 10^7 isobaric ions per second can be separated using the MR-TOF-MS.

Applications of this device are envisaged in a first stage for direct mass measurements at SHIP/SHIPTRAP and at the FRS Ion-Catcher. As a high-resolution mass separator the MR-TOF-MS can be used at SHIPTRAP and at the LEB at FAIR for MATS. At SHIP/SHIPTRAP, it will help to remove the strong isobaric contamination for experiments at the proton drip-line. In addition, the device could also be used as separator at ISOL facilities.

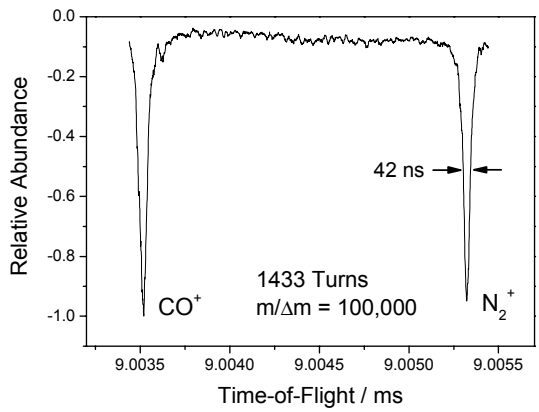

Figure 2: Mass spectrum of the isobaric doublet of CO^+ and N_2^+ obtained with the MR-TOF-MS. After 1433 turns, a peak width of 42 ns is measured, corresponding to a mass resolving power (FWHM) of about 100,000.

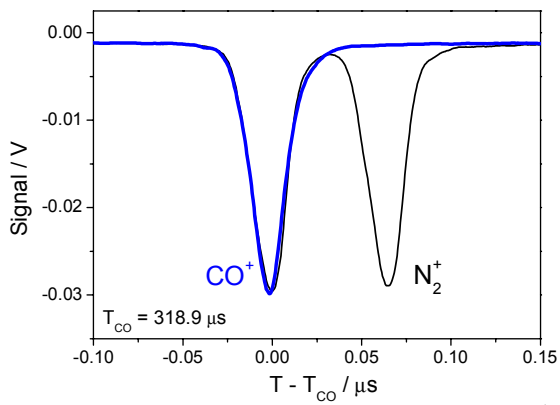

Figure 3: Separation of the isobaric doublet of CO^+ and N_2^+ in the ion gate. Using a deflection pulse at the gate, N_2^+ can be removed from the ion beam, transmitting only CO^+ (thick curve). For comparison, the spectrum without deflection is also shown (thin curve).

References

[1] T. Dickel, Diplomarbeit, Justus-Liebig-Universität Gießen, Germany, 2006.
[2] T. Dickel et al., GSI Scientific Report 2005, p. 260.
[3] N.E. Bradbury et al., Phys. Rev. 49 (1936) 388.

* Work supported by GSI (contract number GI/ME1), by the Helmholtz Association (contract number VH-NG-033) and by the BMBF (contract number 06GI185I).

Analysis of few-ion decays in the ESR

H.G. Essel[1]
[1]GSI, Darmstadt, Germany

In the ESR the revolution frequency of particles is measured by means of Schottky noise FFT (Fast Fourier Transform). This frequency reflects the particle mass. If a decay occurs and the mass changes, the revolution frequency changes as well. The FFT of noise sampled in a pick-up over a certain time interval shows the frequencies of particles in the ring. One interesting information is the exact time of the decay signaled by the appearance of a new frequency in the subsequent FFT frames. Fig.1 shows the time

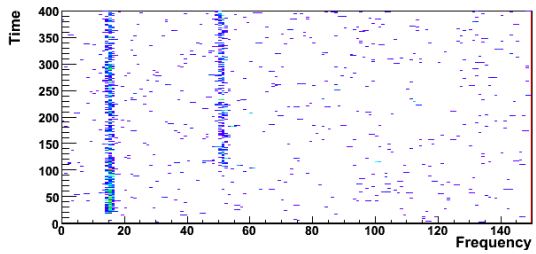

Figure 1: Single shot matrix with decay.

trace matrix of one shot generated from the raw data of a Sony/Tektronix Realtime Spectrum Analyser. It is built by lines of FFT frames of subsequent time intervals. One can easily see where the decay occurred.

Typically thousands of shots must be analyzed. Up to now the time trace matrices have been analyzed manually. To make the analysis reproducible and faster a program

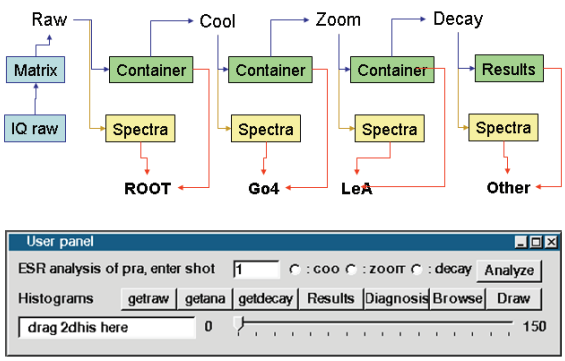

Figure 2: Analysis steps and Go4 control panel.

library has been developed to determine the decay times. The results of the manual analysis have been used as reference. The design of the software is shown in Fig. 2 as a chain of steps, each processing the output of the previous step.

Data storage, code and visualization are separated. The data of all shots of a run is stored in binary container files. The access to one shot is done by index and therefore very fast. For more detailed analysis of single shots various spectra are stored in files. The analysis code is written as functions in plain C. ROOT macros are provided to convert matrices and spectra from the files into ROOT histograms for visualization. A control panel (Fig. 2) for convenient handling of a standard analysis is provided in the Go4 browser. It executes the same macros. Pictures for printing can easily be created. Once the raw files (IQ) have been converted into the first container (Raw step), the full analysis of one shot takes about 0.2 sec.

The primary data are the FFT frames where the existence of a particle should show up as a peak. It turned out, however, that there are fake peaks and missing peaks. Therefore one needs a filter on the quality of each FFT frame and then rule out the fakes and ignore the absentees. In the ”no decay” time region the probability to find a peak is smaller than in the ”decay” region, but also in the ”decay” region there could be up to 8 subsequent missing decay peaks. A new method was introduced to describe this situation: the bonus system: To determine the first valid ”real” decay

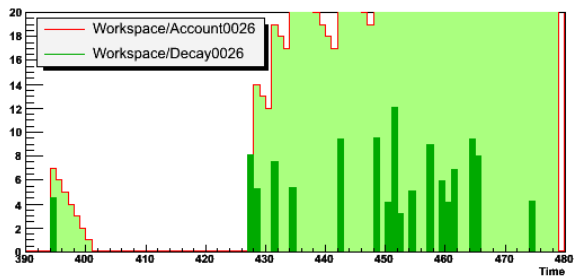

Figure 3: Account bonus mechanism.

peak which defines the decay time we must rule out fakes. We now step through the time frames and fill a confidence account spectrum, one bin per frame. A valid peak in the time frame adds a bonus (2-10) to the account (integer), a missing peak subtracts 1 if account > 0. Then the account is stored in the account spectrum bin. The time bin after the last zero in the account spectrum is the decay time. This method needs four lines of code!

The effect is that fake peaks are ignored if they are followed by n=bonus empty bins, but at the same time missing decay peaks are bridged. An account spectrum is shown in Fig. 3 together with valid frame peaks. One can easily see the mechanism (bonus 7). The proper bonus can be derived from the distribution of empty time bins in the decay track. The exact start of the track is not required for that!

The results of the software and the manual analysis agree in 75% of the shots ($\pm$ 3 frames).

GSI IT-Department Activity Report

M. Münch for the GSI IT-Department[1]
[1]GSI, Darmstadt, Germany

Overview

The GSI IT-Department provides IT services and resources for all research groups at GSI as well as the administrative and infrastructure staff. This includes central services like e-mail, central databases, printing, network access and phone just as management and support of software and hardware for all desktop workstations at GSI.

For the scientific community at GSI, compute power and large on- and near-line data storage is provided. A portfolio of scientific software and software engineering suites is available. Expertise in software development and important software packages is maintained by several R&D activities in international software projects. Research at the borderline of physics and computer sciences is done in the field of GRID computing in several initiatives.

IT plays a central role in many of the GSI wide procedures like project time recording, phone book, conference management, production of large reports (FAIR Baseline Technical Report, GSI Scientific Report) etc.

Scientific Computing

In 2006 the PANDA collaboration agreed on the use of the "FairRoot" simulation and analysis framework. Together with CBM two of the large FAIR experiments are committed to this software package maintained by the IT scientific computing group [4]. Collaborating with the PAVIA group (PANDA), a new interface to the track propagation package "Geane" is developed and is now part of VMC at CERN.

The scientific computing group is taking part in several CERN, national and international GRID initiatives [2]. On the way to fill operation of the Tier-2 center for LHC-Computing, the GSI-GRID facilities have continually and successfully taken part in the ALICE data challenges in 2006. In the European Grid Initiative "EGEE II", GSI is lead partner in "regional certification of new middle ware release" and "user training in DE/CH region". As part of the German national GRID initiative "D-GRID", GSI is concentrating on the task to make the GRID available not only for batch, but also for interactive processing.

Computing and Storage Resources

The Storage-Group right now manages 190 TByte of near line storage for usage by the compute cluster. For fast access, 16 TByte of disk cache provides a net bandwidth of 1 GByte/s for access to the data archive [3].

The Linux-Group in GSI-IT is providing compute power for large scale simulation and data analysis computations. Right now, about 260 number crunching nodes are available, most of them equipped with dual CPU dual core AMD Opteron processors. These nodes have 100 TByte of local disk space and access to central file servers providing 300 TByte on-line storage [1].

Office and Desktop Environment

About 1300 desktop workstations under MS Windows XP are now operated at GSI. Users of these machines are provided with 6.1 TByte disk space on three file servers, two of which are running as an active-active high availability cluster. Services are provided by three domain controllers, one print server, one project server, three application servers for special purposes and several license servers. For MS Windows access from remote or from non Windows PCs, six terminal servers with an extensive software suite are available via Citrix Presentation Server. All in all, 42 XEON double processor machines are providing the technical background for the Windows desktops.

In addition, around 200 desktop workstations are running under Linux, using the Linux server environment [1] for technical, scientific and daily work.

Central Services

An MS Exchange Server, consisting of a two node high availability cluster, is providing 1762 mail boxes which occupy 600 GByte of disk space. All mail boxes and user data is participating in a daily backup schedule, using 70 TByte of tape space right now. Administration of more than 2500 network attached devices and more than 2000 user accounts is done in central databases.

Three fast copy machines for large copy and print jobs in color and B&W are operated in the "Kopierzentrum". Throughout the buildings, 14 fast copy machines (three of them color) are working as print stations. In addition, 170 network printers make a hard copy device almost always available in the range of a few footsteps.

References

[1] Schön, W.; Haller, S.; Huhn, C.; Kreiser, H.; Miers, K.; Sedykh, S.; Roth, T. "The Linux farm at GSI", GSI SR 2006

[2] Malzacher, P.; Manafov, A.; Manteufel, R.; Penso, V.; Preuss, C.; Schwarz, K., "Grid Activities at GSI", GSI SR 2006

[3] Göringer, H.; Feyerabend, M.; Sedykh, S., "The GSI Mass Storage", GSI SR 2006

[4] Al-Turany, M.; Bertini, D.; Dahlinger, M.; Friese, V.; Koenig, I.; Uhlig, F., "FairRoot/CbmRoot Simulation and Analysis framework", GSI SR 2006

The Linux farm at GSI

W.Schoen[1], S.Haller[1], C.Huhn[1], H.Kreiser[1], K.Miers[1], S.Sedykh[1] and T.Roth[1]
[1]GSI, Darmstadt, Germany

Linux farm: Present status und new developments

Hardware and Numbers

In total we operate about 600 boxes in the Linux farm including 260 number cruncher in a batch queuing system providing about 100 TB of local disk space. About 200 boxes are desktop systems, fully integrated in the central linux farm. About 80 dedicated fileserver provide about 300 TB of central disk space for the data-file system. 50 boxes are dedicated for central IT services including some high-availlibility clusters for important services.
The major part of the boxes in the batch farm are single unit 19" boxes powered by dual cpu dual core opterons. This results in 4 cpus per 1HU and 124 cpus per rack – a quite high power density which is necessary to install a high amount of number crunching power in a computer room of limited size. This high spatial power density is challenging both in terms of network connections and cooling. To manage the cooling problem, special air shrouds are used to guide the air currents. In addition special air cooled racks able to handle more than 12 kW thermal output per rack are installed. In each unit up to 4 hot swappable SATA disks can be installed to provide local disk space for caching data. The major part of the farm boxes are equipped with 4 GB ecc RAM. While this is sufficient to run 4 jobs per node in parallel, for some applications, e.g. matrix inversions of multidimesional matrices, high mem queues are available with boxes up to 32 GB RAM.

Software

The Linux Farm is powered by debian-Linux (the only open source distribution – no licence is necessary to power the linux farm) including the GRID worker nodes . In 2006 we switchted the farm to debian release "sarge". First servers are already powered by the debian release "etch" in testing mode.
Our batch queue system is LSF (load sharing facility) – a commercial tool known for good scalability. The licence to run the scheduler is a non-negligible part of our buget, so in future it will be necessary to investigate scalable and powerful open source alternatives. Scientific software for simulation and analysis like Geant, Root, Paw, G04 is availlable on the Linux farm.

64 bit nodes

In addition to the standard farm computer with 32 bit operating system, we offer 64 bit queues (Debian 64). Most of the analysis software runs with significant better performace on a 64 bit system. For all applications which need more than 2^{32} bit memory, a 64 bit system is crucial. On the other hand, some experiments have not yet ported their analysis to the 64 bit system, therefore the 32 bit OS will be continued operated for some time.

Management

To improve scalability, installation and configuration was migrated to standardized open source tools which are developed and maintained by international collaborations. FAI (fully automatic installation) [1] organizes installation hosts in configuration classes according to hardware and purpose. Thus an arbitrary number of similar machines can be installed unattendedly. For each new kind of hardware an adaption of the FAI configuration files is necessary.
The configuration and the deployment of the configuration is done by cfengine [2]. In addition, all configurations and the full history of all configuration changes is kept in a subversion repository.

Monitoring

System critical parameters of the Linux farm are supervised by a system of quite advanced monitorings scripts based on Mon [3]. If a critical situation occurs the monitoring informs the administrators via email and – more important – starts to repair system critical situations without human interaction. Of course, only the most critical central services like the mail transfer agents, or the central nfs server are equipped with advanced scritps able to repair a broad range of problematic situations without human interaction. Depending of human resources, this monitoring project will spread out to more and more systems and services in the linux farm.

High Availability

Important central services (central nfs, web, mta, mass storage-entry-server,...) are implemented on dedicated hardware in a HA-cluster using hartbeat and drbd. No one failure of one of the HA systems occurred since first implementations 2004. Of course, if the network fails, even a HA system cannot operate.....

File systems

Home file system

In early 2006 a new central home system went operational. More than 2000 user home file systems are deployed over 20 RAID controllers on 10 file servers providing NFS service with a capacity of 6 TB net disk space on RAID 5. Due to the parallelism of the 10 servers, the reduced scalability of NFS is bypassed. The file system of the home directories is based on XFS. It is enhanced by the Logical Volume Manager (LVM) with

allows dynamic resizing of a mounted partition in full operation. The new home file system is scalable, powerfull and robust. A system of scripts is being developed to optimise the use of this resource using accouting information.

The new data file system

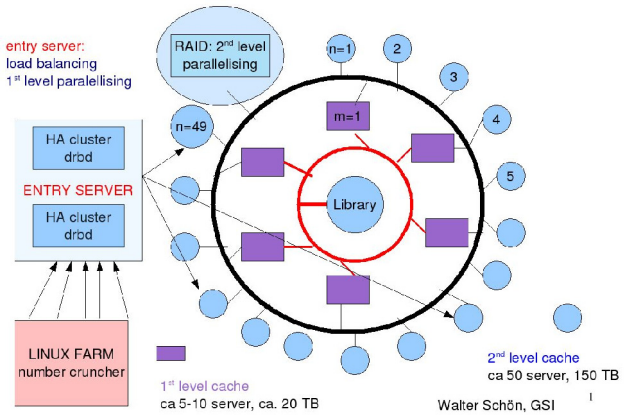

Figure 1: New data file system: Entry server spreads out data onto an ensemble of file servers. These servers communicate via gStore with the read/write cache and the tape library.

A crucial feature of GSI Linux usage is the amount of I/O produced by simulations and experiment analysis on the batch farm. The share of the theory groups in the I/O load is small because their calculations are focused on pure number crunching. While NFS is comfortable, posix compilant and a approved solution for few competing read/write accesses, its weakness is its small scalability in case of parallel access by a huge number of clients. With socket based methods implemented e.g. in gStore [4], this disadvantage of NFS can be reduced. However, the disks as mechanical systems additionally limit the performace for parallel access, so a new approach for data file system for GSI FAIR computing is necessary. The new system will use a two level parallelisation for improved performance: An entry server will spread the data file by file on an ensemble of dedicated file servers taking into account the instantaneous load of each member of the ensemble. On each file server, a high end SATA raid controller will spread the data on a bunch of disks for higher I/O performance. Of course, the entry server are of strategic importance because it contains the file catalog for the whole system. Therefore, the entry server is designed as a Linux HA-cluster (see paragraph High Avalability) . The communication of the file servers with the read/write cache and the tape library is done with gStore. A “proof of concept” system of the new data file system is under development. As the meta data system for spreading the data on the whole ensemble of file servers, xrootd is under investigation. A strong advantage of xrootd is its desaster recovery procedure: Even in the rare case of a failure of the entry server (HA), the file catalog can be reconstructed with the help of the local xrootd instance on each file server. A weak point is its nonconformity with the posix standard and a poor accounting ability, the latter being crucial in the GSI environment. A (small scale) test cluster is being set up and tested to investigate the integration with gStore and to solve the open questions concerning xrootd.

References

[1]http://faiwiki.informatik.unikoeln.de/index.php/Main_Page
[2] http://www.cfengine.org
[3] http://www.kernel.org/software/mon
[4] H.Goeringer: The GSI mass storage, Jahresbericht GSI, 2006
[5] http://xrootd.slac.stanford.edu

Grid Activities at GSI*†

P. Malzacher, A. Manafov, R. Manteufel, V. Penso, C. Preuss, K. Schwarz

Abstract

This article describes the work of the GSI Grid Group with the aim to set up an ALICE tier2 centre within the global environment of the LHC Computing Grid and to prototype a possible FAIR grid environment.

ALICE tier2 centre

The storage capacity has been increased by 30 TB disk space distributed over 5 file servers. A setup as extended xrootd cluster with a single point of entry is planned for GSI users. A part of this cluster will have additionally tape backend via gStore. From outside GSI this storage capacity is accessible as an AliEn storage element with Grid methods. First performance tests resulted in a transfer rate of 11 MB/s compared to 3-4 MB/s which was achieved when using NFS.

The existing dCache installation has been upgraded with xrootd doors including the ALICE authorisation plugin as one of the first installations within ALICE. It is currently tested in production mode by using it as a backup storage for ALICE grid jobs running worldwide.

During the second half of the year 2006 GSI participated continuously in ALICE Data Challenges. The Grid paradigm has been changed from using pure AliEn to making use of the existing LCG middleware infrastructure via an AliEn-LCG interface. To be able to run AliRoot jobs in the GSI batch farm a special high memory queue has been created. Similarly the ALICE installation at the tier1 centre at FZK/GridKa is taken care of. The contribution of GridKa to the global ALICE resources in 2006 has been 8% in average.

The EGEE project

The EGEE project came to a successful end and EGEE II started in April 2006. GSI continued participating, among others as primary partner in regional certification of new middleware releases as well as user training in the Swiss/German (DECH) Federation. The EGEE based middleware gLite came to version 1.5 and finally has been fused with the WLCG production software LCG 2.7 to gLite 3.0 at the beginning of 2006. To be able to participate in beta tests of new middleware releases GSI maintains also a pre-production testbed. All Grid systems are connected with the GSI batch farm (LSF). Next to ALICE also other Virtual Organisations (VOs) like DECH and DGTest are being supported. Both VOs are intended also for testing and training purposes.

The GSI Grid team contributes to the sub projects COD and GGUS. The complete Grid infrastructure is overseen by a small group of experts (CODs) in shift turns. Notification (in form of trouble tickets) is sent to responsible site administrators in case of operational problems. Grid users have the possibility to send trouble tickets to a global grid user support (GGUS) Those tickets are processed by grid experts on duty.

Almost all GSI Grid services are running currently on virtual nodes. For the hosting XEN servers also monitoring tools have been developed as well as methods for automatic installation (FAI). The main infrastructure consists of 5 Xen servers with 20 virtual machines with a very high reliability.

D-Grid

At GSI distributed analysis tools under usage of grid resources are being developed within work package 3 of the HEP community Grid. During the year 2006 a ROOT plug-in for the gLite middleware, TGLite, has been developed. Now using this plug-in ROOT users are able to submit jobs to a gLite flavoured Grid, query the job status and perform a range of File Catalogue operations. GSI maintains a gLite testbed for development and testing purposes.

Currently the next stage of the project is on the way, during which a prototype of a data analysis schema and tools will be created. The schema will offer users the possibility to process a distributed data analysis using TGLite and PROOF on a gLite Grid. Also deployment procedures for beta users will be implemented.

From D-Grid fundings 15 compute nodes have been bought with high memory and significant disk space attached to each node. These machines will be equipped with the D-Grid Core Middleware and then be included into the nationwide D-Grid testbed. At GSI they will be included in the LSF batch farm with proof daemons being installed in their system. This way they can be accessed via Grid/batch methods, but also they can be directly used as a PROOF analysis cluster.

Preparation for FAIR tier0

PANDA-Grid , based on the AliEn middleware and on experiences made within the ALICE experiment, has been set up and brought into operational mode. Currently 8 sites are configured and small productions consisting of PandaRoot simulation jobs have been running successfully.

* Work supported by D-Grid (BMBF, Förderkennzeichen 01AK802G), EGEE-I (European Commission under contract number IST-2003-508833) , and EGEE-II (European Union under contract number INFSO-RI-031688)

† references can be found at http://wiki.gsi.de/Grid/Links

The GSI Mass Storage

H.Göringer, M.Feyerabend, S.Sedykh
GSI, Darmstadt, Germany

The GSI mass storage provides hardware and tools for safe, reliable, and, if necessary, redundant long term storage of all user and experiment data, with fast access and available 24 hours a day and 7 days a week.

Backup/Archive functionality for user data is provided by the commercial storage manager **TSM**. Access to the mass storage for experiment data (**gStore**) is enabled with GSI made client server systems providing various user interfaces (adsmcli, tsmcli, RFIO).

gStore is based on automatic tape libraries (ATL) and data mover nodes connected via **S**torage **A**rea **N**etwork (SAN). The data movers provide large read and write disk caches to screen tape operations as far as possible from the users. Tapes and ATLs are also handled by TSM, whereas the interface to TSM (API) and the disk cache management are handled by the GSI software. Design principles and functionality of gStore are described in a previous report [1].

In 2006 there have been significant upgrades to enhance the hardware and to move services away from Windows based to Unix based systems:

- Four IBM 3592 tape drives have been installed in the IBM 3494 ATL replacing the old IBM 3590 tape drives. With new media (current capacity ~700 GB) the overall ATL capacity has been increased from 65 TB to 1.6 PB.
- A new AIX node with a TSM server managing the 3592 tape stations has been installed.
- Five new gStore data movers have been installed with Linux providing 14 TB of additional disk cache. Now the write cache is built exclusively from RAID arrays improving the security for data migration to tape.
- The gStore entry servers and disk cache managers have been moved to a new fail-safe pair of high-end Linux nodes. Besides increasing the availability of these central gStore services, the times for file queries in gStore have been reduced by nearly two orders of magnitude.
- A new TSM backup server has been installed on Linux and is in operation since spring 2006. It will replace the older backup servers on Windows and AIX in 2007, after all clients and actual data are moved away from the old servers.

An overview of the current status of the GSI mass storage can be seen in the table:

backup data	70TB LTO1	max 140 TB (2007)
experiment data	140TB LTO2 50TB 3590	max 1.6 PB (2007)
13 data movers	disk cache: 16 TB	bandwidth: 1000 MB/s

Table 1: Status GSI Mass Storage December 2006

In order to replace aged tape formats by new ones with much higher data density, and to consolidate the various server systems, the following new structure for the near future has been decided and is currently in work:

1. All **Experiment data** will be stored on the new high capacity tapes in the IBM 3494 ATL, managed by the new AIX TSM server. TSM running on AIX has been proved as very reliable in the past.
2. All **Backup data** will be stored in the Sun StorageTek L700 ATL filled with LTO2 tapes, which are currently still occupied with experiment data. The backup data will be managed by the new Linux TSM server.
3. The aged LTO1 tape drives in the other L700 ATL will be removed after all media are emptied.
4. The empty L700 ATL will be available then for redundant storage of valuable experiment data.

In order to accomplish the first two projects all existing experiment data must be copied to the new 3592 tapes. This is already done for the data accessible with adsmcli (50 TB), and currently in work for the data accessible with tsmcli (140 TB).

The gStore software is currently being enhanced to enable access to all experiment data at GSI with a single user interface, independent of their ATL location and the related TSM server. When finished the older user interfaces (adsmcli, tsmcli) will be removed, and new experiment data will be stored on 3592 tapes. Completely filled with new media, the current 3494 ATL data capacity of 1.6 PB should be sufficient for a few years.

About 340 backup clients must be moved from the old Windows and AIX TSM servers to the new Linux TSM server. Whereas most of the old backup data will be replaced automatically by new backup data, all user archive data must be migrated to the new server.

Afterwards, equipped with new tape drives, the empty L700 ATL could be moved to the "remote" computing room currently under discussion. This would be an important contribution to safe long term storage of scientific data.

First steps have been done to integrate xrootd with gStore. In a test environment developed for the Alice experiment all gStore files are available for xrootd clients. New xrootd files created in special cache areas are moved or copied to gStore asynchronously. In 2007 the integration with gStore will be implemented for the Alice Tier 2 xrootd production system and for the planned new data file system of the Linux farm [2].

[1] H.Göringer et al: The GSI Mass Storage System for Experiment Data, GSI Report 2005-1, p. 367
[2] W.Schön et al: The Linux Farm at GSI, in this report

FairRoot/CbmRoot Simulation and Analysis framework

M. Al-Turany[1], D. Bertini[1], M. Dahlinger[1], V. Friese[1], I. Koenig[1], and F. Uhlig[1]
[1]GSI, Darmstadt, Germany

Introduction

The Virtual Monte Carlo concept allows performing simulations using Geant3, Geant4 or Fluka without changing the user code [1]. This concept was used as a base for developing the CbmRoot framework for the CBM collaboration [2]. In this concept, the same framework is used for simulation and data analysis. An Oracle database with a build-in versioning management is used to efficiently store the detector geometry, materials and parameters.

As more experiments at the GSI where interested in using this framework, the framework was revised and the base packages of the framework where completely separated from the specific CBM implementation. Moreover, the framework became the new name FAIRROOT. On the Oracle server side, data bases for each experiment are running on a high availability cluster, new experiments can easily be added.

The Schematic design of the framework is shown in Fig.[1].

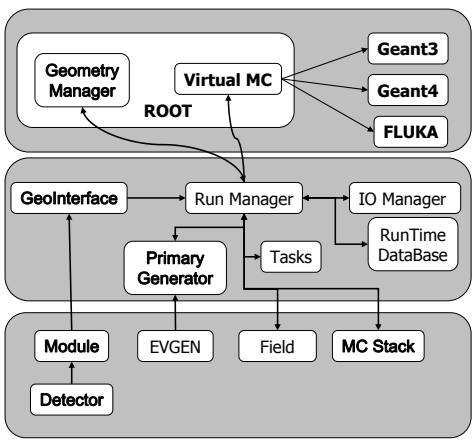

Figure 1: Schematic design of FairRoot.

New Developments

- Geane Interface:

  The Geane package allows the user to calculate the average trajectories of particles and to calculate the transport matrix as well as the propagated error covariance matrix. Geane is a set of routines worked out by the European Muon Collaboration [3, 4] and it is integrated to the GEANT3 system [5]. An interface for using geane was developed in collaboration with the Pavia group from the PANDA collaboration. The modification to the VMC classes needed for geane where also communicated to the ALICE collaboration at cern and included in the VMC distribution.

- New detector geometry reader

  A new geometry reader for the framework was developed. The input of this reader is in form of TGeoVolumes (Root Geometry format). This reader is used by the PANDA collaboration to read the detector geometries which are converted from Step file format (CAD system) to Root format.

- CMake for configuration

  CMake is a cross-platform, open-source make system [6]. CMake is used to control the software compilation process using simple platform and compiler independent configuration files. CMake generates native makefiles and workspaces that can be used in the compiler environment of user choice. Now CMake and autoconf/automake are used in parallel.

- Subversion

  The frame work is now distributed via Subversion.

summary

A VMC based framework for CBM has been implemented, the first release was in march 2004. The October 2004 release was used to produce and analyze data for the CBM technical Status report[7]. Work on digitizers and full tracking in CBM and PANDA collaborations is going on.

References

References

[1] http://alisoft.cern.ch/

[2] M.Al-Turany, D. Bertini and I. Koenig , “CBM Simulation and Analyis Framework”, GSI scintific report 2004, FAIR-EXP-07.

[3] W.Wittek, EMC Internal Reports: (*EMC/80/15, EMCSW/80/39, EMCSW/81/13, EMCSW/81/18)*

[4] A.Haas, The EMC Utility Package: (UTIL42)

[5] R.Brun, F.Bruyant, M.Maire, A.C.McPherson, P.Zanarini (DD/EE/84-1), May 1986

[6] http://www.cmake.org/

[7] CBM Collaboration Technical Status Report (GSI, Darmstadt, 2005)

Developments for a future DAQ framework DABC*

J. Adamczewski[1], H.G. Essel[1], N. Kurz[1], and S. Linev[1]
[1]GSI, Darmstadt, Germany

Requirements and concept

The **D**ata **A**cquisition **B**ackbone **C**ore *DABC* will provide a general software framework for DAQ tasks over the next years. It serves as test bed for FAIR detector tests, readout components tests, data flow investigations (switched event building) and DAQ controls. Specifically, the system must be able to handle a triggerless experiment with large data bandwidth like CBM [1]. Additionally, it is necessary to integrate the current GSI standard data acquisition system MBS [2]. The huge installed MBS equipment cannot be replaced. Instead, MBS driven front-end components (readout) should be attachable as data sources to the new framework. The DABC replaces the MBS event building functionality.

The XDAQ C++ software framework [3] developed for the CMS experiment at CERN was chosen as base for the first implementation of DABC. It features:

Task management: One node may contain several *XDAQ Executives* (processes); each *Executive* may contain *XDAQ Applications* as threads. Each application may create additional threads (*workloops*).

Data transfer management: *Peer Transport* and *Messenger* interfaces.

Hardware integration: *Hardware Access Library*.

Control support: state machines; process variable *Infospaces*; message and error loggers; web server for each *Executive*.

Evaluation and testing

The developments so far concentrated on performance and functionality evaluations.

Data transport

Data transport on a fast switched network has been investigated on a small InfiniBand (IB) linux cluster installed at GSI in 2005. An XDAQ *Peer Transport* over IB was implemented based on the uDAPL library to check the performance of IB data transfer with the XDAQ I2O messaging mechanism. For package sizes $P \geq 15$ kByte the bandwidth B saturated at $\simeq 905$ MByte$/s$ to be compared with 955 MByte$/s$ for measurements with direct uDAPL. However, the rise of the $B(P)$ curve for small packages was less steep for the XDAQ transport, since this is ruled by the minimum transfer time τ_{min} ("latency" overhead of the framework), from $(\frac{dB}{dP})_{P\to 0} = \frac{1}{\tau_{min}}$. Depending on the benchmark set up, XDAQ showed values $\tau_{min} \simeq 10 \ldots 30$ μs, well exceeding the plain uDAPL latency of $\tau_{min} \simeq 4$ μs.

Hardware access

As general software interface to attach DAQ hardware like readout boards, XDAQ provides a *Hardware Access Library* package [3]. This defines base classes for user-space communication with boards on a bus (e.g. PCI or VME). We implemented HAL *BusAdapter* and *DeviceIdentifier* classes for a generic PCI/PCIe driver of the Mannheim FPGA group[1].

The new HAL classes were tested with the available GSI *PCIGTB2* board. It was possible to access the board from an XDAQ *Application*, setting up registers and reading/writing on the *PCIGTB2* internal memory. Although the tests showed that the general HAL interface is not sufficient for all cases, (e.g. DMA; exact i/o timing), it turned out that it is well possible to implement missing features as methods of the specific *HardwareDevice* class.

Control System

XDAQ offers a http server on each node to exchange control messages and monitoring data via SOAP protocol. We developed a simple prototype of a control GUI as JAVA application. However, every update of a monitored value requires an active http/SOAP request from the GUI.

An improved approach for monitoring consists in a "publisher-subscriber"-model, where each GUI registers to be updated automatically if a variable changes in the monitored application. DIM [4] is a well established protocol library for such a usage. We developed adapter classes to run a DIM server in the XDAQ *executive*. XDAQ infospace variables are exported as DIM services. Additionally, the XDAQ application state machine can be switched by DIM commands. The DIM server provides control access from any other DIM interfaced packages, like the Labview-DIM interface of the GSI CS-framework [5] for a test control GUI, or the EPICS DIM gateway currently under development at GSI (http://wiki.gsi.de/Epics).

References

[1] "CBM technical status report", GSI, January 2005, pp.235

[2] H.G. Essel and N. Kurz, "Multi Branch System homepage", http://daq.gsi.de

[3] J. Gutleber and L. Orsini, "XDAQ framework", http://xdaqwiki.cern.ch/index.php/Main_Page

[4] C. Gaspar, "Distribution Information Management system DIM", http://dim.web.cern.ch/dim/

[5] D. Beck and H.Brand, "The CS framework", https://sourceforge.net/projects/cs-framework/

* Work supported by EU-RP6 HadronPhysics, RII3-CT-2004-506078

[1]thanks to G. Marcus, H. Singpiel, and A. Kugel, Technische Informatik V, Universtät Mannheim

Infiniband cluster for Future DAQ*

J. Adamczewski[1], H.G. Essel[1], and S. Linev[1]
[1]GSI, Darmstadt, Germany

Network requirements

The data acquisition for future experiments at FAIR requires a fast and relatively large network farm for event data transport from front-end electronics to the computing nodes where further event analysis can be performed. The CBM experiment, for example, produces about 1 TB/s of raw data rate, which should be switched in such event building network (B-Net). This requires to build a system with ∼1000 nodes, each connected to a network with 1 GB/s link performance.

Currently we are evaluating InfiniBand (IB) as probable candidate for B-Net in our first prototype of a Data Acquisition Backbone DABC (see in this report). A small test cluster of 4 nodes was installed at GSI in November 2005. Each node of that cluster is equipped with a Mellanox MHES18-XT InfiniBand Host Channel Adapter (HCA). The nominal data rate of such adapters is 1GB/s in full duplex mode.

InfiniBand software

All software required to configure and operate InfiniBand networks is collected in the OpenFabric Enterprise Distribution OFED (former OpenIB), developed by the OpenFabrics Alliance [1]. There are also software packages from hardware vendors (for instance IBGold from Mellanox), but mostly they contain the same components as the OFED package. Several user-level APIs were investigated and tested.

The low level **verbs API**, included in the OFED package as *libibverbs* library, provides direct access to InfiniBand HCA functionality from user space (so-called kernel bypass). It's most important functionality: non-blocking zero-copy data transfer, remote direct memory access (RDMA) and unreliable hardware multicast. Unfortunately, the **verbs API** is not well documented.

The user-level **direct access API (uDAPL)**, developed by the DAT collaborative [2] was inspired by IB functionality. Therefore it has many similarities with **verbs API**. Since **uDAPL** uses a peer-to-peer communication paradigm, multicast is not supported. There are several implementations of this APIs from different vendors, which are mostly compatible with each other.

Message passing interface (MPI) is widely used in the field of parallel computing. It defines an API for fast exchange of data between computing nodes. The MPI over InfiniBand Project - MVAPICH [3] provides non-blocking zero-copy data transfer, and in latest versions it even supports hardware IB multicast.

* Work supported by EU-RP6:Hadron Physics, RII3-CT-2004-506078

Benchmarking

A special test application was written to evaluate InfiniBand performance with all mentioned APIs. This test application is capable to generate different kinds of traffic patterns over InfiniBand. A time synchronization between nodes was implemented to perform time scheduled data transfers. Mostly the all-to-all traffic pattern was investigated, where each node transfers data to all other nodes according the round-robin schedule. The dependency of achieved data rates per node from packet size for different APIs is presented in table 1.

Buffer	1K	4K	16K	64K	256K
verbs	364	809	940	953	957
uDAPL	494	723	837	875	882
MPI	327	616	752	885	897

Table 1: Achieved data rates (in B/μs) in all-to-all tests

All APIs provide good performance and reach 900 B/μs for big packet sizes. While **verbs** has less API overhead, it reaches such data rate already at 8K buffer size.

Separately IB multicast was tested: **verbs** achieves 625 B/μs data rate with less than 0,01% packets lost; **MPI** only 350 B/μs, but this includes handshaking and retry when packets are lost.

Using a B-Net scheduled traffic pattern one achieves event building all-to-all traffic of 750 B/μs plus simultaneous transport multicast traffic from scheduler of 50 B/μs/node, and status traffic of 20 B/μs/node.

Future tests and developments

Our first tests show, that InfiniBand provides data rates as required for an event building network in future FAIR experiments. All investigated APIs potentially can be used in further developments of DAQ systems.

Because all our tests were performed on a small 4-nodes cluster, we cannot prove the scalability of our B-Net approach for systems with more than 100 nodes. Therefore further tests are planned in cooperation with the Forschungszentrum Karlsruhe, where several 32-nodes InfiniBand clusters are available.

References

[1] OpenFabrics Alliance website, http://www.openfabrics.org

[2] DAT Collaborative website, http://www.datcollaborative.org

[3] MPI over InfiniBand Project website, http://nowlab.cse.ohio-state.edu/projects/mpi-iba/

Enhancing the *CS* Framework for Distributed Control Systems

D. Beck, H. Brand, and S. Götte
GSI, Darmstadt, Germany

The *CS* framework is a LabVIEW based framework for developing event driven, multi-threaded control systems using an object oriented approach. In December 2006, version 3.00 of *CS* has been released. The new version is a major change addressing a couple of issues that are of prime importance for large scale distributed control systems.

Introduction

The *CS* framework is in use since a few years at about ten experiments at four institutes. Instead of supporting a maximum number of process variables, the main focus of *CS* is to provide a basis for control systems requiring a high flexibility and performance. A detailed description of *CS* is given in [1]. This text aims at describing the enhancements by the most recent version 3.00.

DIM as Communication Layer

Earlier versions of *CS* allowed for distributed control systems but required the knowledge of the node name for each process variable. Moreover, a general built-in observer mechanism where many observers may register to receive updates of one published process variable was missing.

The entire communication layer has been changed to DIM (Distributed Information Management) [2], which is a light weight protocol for inter-process communication based on TCP/IP. It follows the concept of named services. Clients may receive information from a service (observer pattern) or may send a command to a server (command pattern).

Switching to DIM as communication layer was possible after implementing a LabVIEW interface for DIM. This drastically increased the performance in the communication layer of *CS* and solved a few other problems not mentioned here. Using a *CS* system with one million DIM services was tested successfully.

Process Management

Starting with version 3.00, *CS* is complemented by a simple process management system. Typically, a couple of processes must run on each node to provide the functionality of the control system. However, each node may require a different set of processes. The process management system takes care of starting, restarting or stopping processes in distributed environments. A server publishes a list of processes for each node in the distributed system together with command line parameters and options for restarting a process in case it has been stopped or crashed. On each node a client subscribes to that list and takes care to handle the required processes. The process management system is available for MS-Windows and Linux and supports a mix of both operating systems at the same time.

Access System

A distributed control system with more than one console requires a mechanism to lock subsystems for individual operators or tasks. Such a reservation mechanism is not intended for preventing malicious attacks but for preventing accidental changes of a parameter. With *CS* 3.00, a reservation mechanism has been implemented that becomes effective when using the command pattern.

Application

The new version of *CS* represents a major change in the *CS* framework. The usage of common design patterns within *CS* has become much simpler in many cases. At the same time it was tried to provide as much backward compatibility as possible. However, experiment specific code based on the *CS* framework needs to be migrated to the new version. Thus, switching to the new version requires some work by the experiments.

At GSI, the new version is already in use at two facilities. First, the PHELIX facility [3] has the most complex control system (12 PCs) based on *CS* and represents a good test case for the new *CS* version. PHELIX started to successfully use the new version already in an early stage of its development. Second, a small test-bed of eight PCs has been set up and is permanently in operation. Its main purpose is to test scalability, stability and performance of a distributed *CS* system when being operated for many weeks. Other experiments like SHIPTRAP are about to switch to the new version in the near future. The upcoming facilities HIPTRAP and MATS at FAIR have already decided to use *CS*.

Summary

The *CS* framework has done a major step forward by adding missing features that are required for larger, distributed control system. The main change is the usage of DIM as communication layer. The software has been released in December 2007 and is already in use.

References

[1] D. Beck et al., Nucl. Instr. Meth. **A** 527 (2004) 567-579, http://wiki.gsi.de/cgi-bin/view/CSframework.

[2] C. Gaspar, M. Dönszelmann, Ph. Charpentier, International Conference on Computing in High Energy and Nuclear Physics (Padova, Italy, 1-11 February 2000), http://www.cern.ch/dim.

[3] E. W. Gaul et al., GSI Scientific Report 2002 (2003) 101-103.

Status and Improvements of Go4 Analysis Framework v3

J. Adamczewski[1], H.G. Essel[1], and S. Linev[1]
[1]GSI, Darmstadt, Germany

Status of Go4 v3

Go4 (**G**SI **O**bject **O**riented **O**nline **O**ffline) is established as standard GSI analysis framework for several experiments of atomic and nuclear structure physics, e.g. FRS, SHIP, and RISING. Go4 is based on ROOT [1] and is available for download under GPL at the Go4 homepage [2]. Go4 is installed and maintained on the GSI Linux cluster.

Go4 v3 has been released in November 2005 [3]. Go4 v3.2 released in July 2006 replaced the previous version 2.10 as stable production version. It addresses several user requests and error reports. Additionally, changes of Linux distributions and of the most recent ROOT versions required small adjustments of the release.

A Go4 workshop was held twice in June 2006 at GSI. On two days features and techniques of Go4 v3 were presented and discussed with the participants. Additionally, new Go4 tutorials were offered on the web [4].

Improvements

Analysis Framework

For simple structured analysis tasks the number of required user classes was reduced considerably: Only one method (*BuildEvent()* of class *TGo4EventProcessor*) must be implemented by the user. It contains all the analysis code. No other classes like a dummy output event class are required. The analysis can be fully configured by macros.

The *TGo4MbsFile* event source now can also read list-mode data of old event formats type *4,1* and *4,2*. These events are converted implicitly into format *10,1* for further processing.

GUI enhancements

Interactive re-bin: When a histogram is re-binned via right-mouse menu or via ROOT graphical editor, re-binning is preserved when the histogram is updated next time from analysis. Simultaneous views of the same histogram with different binning (and graphical attributes) are possible.

Viewpanel: There is a new draw options toolbox for line, marker, and fill colors of histograms and graphs. Support was added for TGraph draw modes and TGraphErrors error styles. The viewpanel menu allows to select the active object from superimposed histograms and graphs.

Zoom tools dialog was upgraded to a non modal MDI widget. It will appear always on top of workspace widgets and refers to ranges of the currently selected viewpanel pad.

Preferences menu: Added setup for histogram statistics box and Go4 marker labels.

Macro execution in GUI process

A new command line widget allows execution of ROOT commands or macros within the GUI process. Moreover, Go4 hot-start scripts may be invoked here at any time. The widget offers a file dialog to search for `*.C` and `*.hotstart` files. It also has a selector dialog of preloaded commodity functions for histogram manipulation (re-bin, addition, projection, etc.). These function template calls may be completed with existing histogram names by dragging histogram items from the browser and dropping them on the empty command argument, as shown in Fig.1.

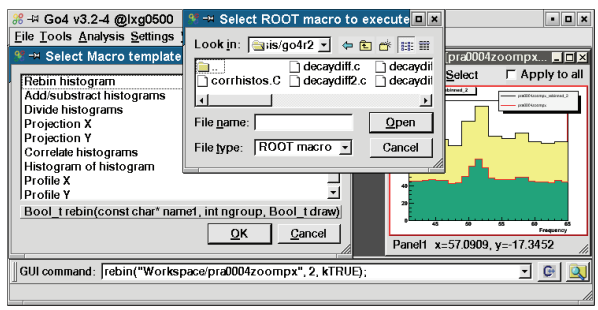

Figure 1: Go4 GUI with re-bin script example.

Methods of the Go4 GUI command interface instance *TGo4AbstractInterface* can be called in GUI macros by handle go4-> providing access to Go4 GUI views and browser objects. Additionally, all remote analysis control commands are available, like in the hot-start scripts. Macros can be written to execute inside the Go4 GUI or in CINT by checking the definition of __GO4MACRO__. The method reference of *TGo4AbstractInterface* was added to the Go4 help viewer. Example scripts are installed at `$GO4SYS/macros` location.

References

[1] R. Brun et al., "The ROOT System Homepage", http://root.cern.ch

[2] H.G. Essel et al., "The Go4 web page", http://go4.gsi.de

[3] J. Adamczewski, H.G. Essel, S. Linev, "Go4 Analysis Framework 3.0", GSI Scientific Report 2005, GSI Darmstadt , August 2006, p.270.; http://www.gsi.de/library/GSI-Report-2006-1

[4] H.G. Essel, "Go4 tutorials", http://www-linux.gsi.de/ go4/tutorial/go4.php

Silicon Micro Strip Detector Readout System

J.Hoffmann, N.Kurz, W.Ott
GSI, Darmstadt, Germany.

A readout module (SIDEREM: SIlicon DEtector REadout Module) for the silicon micro strip detector (SMSD), provided by the AMS collaboration, has been developed for the usage in GSI experiments within the MBS data acquisition system. The SIDEREM is a NIM module with an interface to a single SMSD, which provides all signals to readout a SMSD including 640 channels on the front- and 384 channels on the backside of this double sided silicon device. This interface includes also the power supply for the bias voltage of the backside (Fig. 1).

Dataflow: The analogue signals readout via multiplexing are fed into 3 parallel working ADCs on the SIDEREM and are then handed over to the onboard DSP (TMS320C6414 from Texas Instruments). The DSP optionally filters the raw data and sends it via the GTB bus into the input memory of a SAM5 VME module for further data combining and transportation. The SAM5 is finally readout by the MBS readout processor in VME BLT mode.

Altogether 15 SIDEREMS can be connected in a daisy chain to one of the two GTB ports of the SAM5 (Fig. 2). Assuming that up to 20 SAM5 may be mounted in a VME crate, this system supports the readout of one up to 600 (20*2*15) SMSD devices, scaling respectively from 1024 up to more than 600000 channels handled in a single VME crate.

Trigger System: The SIDEREM system accepts three different types of hardware triggers. Trigger type 1 produces pedestal subtracted data. It is intended as physics trigger. Type 2 delivers raw data and type 3 is mandatory for the verification of the event synchronicity. The trigger inputs are distributed on a local trigger bus. For this purpose each SIDEREM has a (local) trigger bus port. All SIDEREM modules connected to the SAM5 via GTB must, in addition, be connected to the SAM5 on this local trigger bus. It allows also for the earliest release of dead time, whenever all SIDEREM modules are ready to accept safely the next trigger.

Ancillary: For the fast data transfer from the SIDEREM modules to the SAM5 the so called "token mode" of the GTB bus is used, whereas the transparent (or address mapped) mode is used for various slow control tasks. This includes the capability to download the DSP programs for the SIDEREM and the SAM5 from the VME processor. It allows the loading of pedestal files, which are distributed from the SAM5 to all connected SIDEREM modules. Both operations are done automatically at the start up phase of the MBS DAQ. Furthermore, it is possible to set the bias voltage for the backside of the SMSD and the CCT (charge collection time) manually from the VME processor. The CCT time is used to set the optimal HOLD time after a trigger occurred, which allows the freezing of the silicon strip signal at its maximum pulse height. Finally, it is possible to readout a temperature sensor mounted on each SMSD.

This new SIDEREM system has already been used in the S271 experiment at the FRS at GSI, investigating on "two proton fragmentation" of ^{20}Mg and ^{17}Ne. It will be a key device in the LAND/R3B experiment.

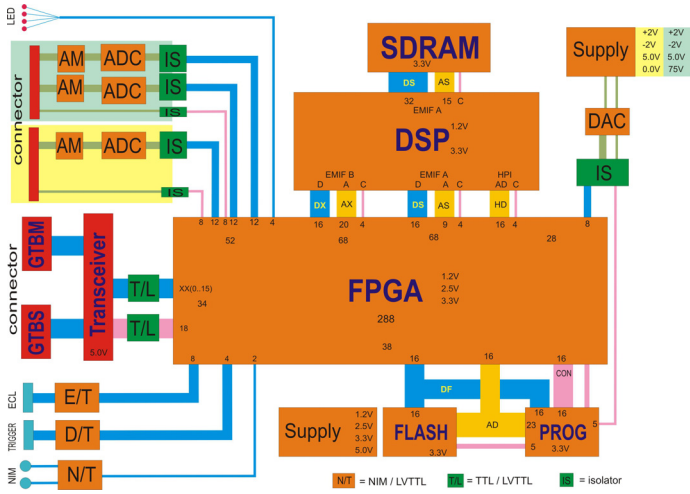

Figure 1: Block diagram of SIDEREM module

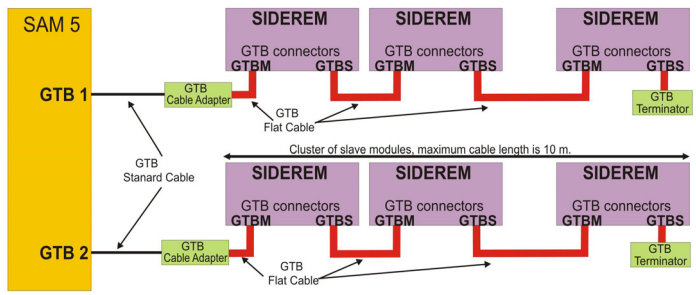

Figure 2: GTB connection scheme

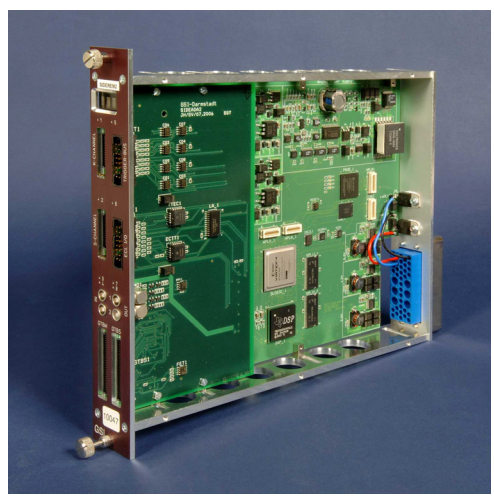

Figure 3: SIDEREM Module

Performance of Germanium detectors at high counting rates *

M. Kavatsyuk† [1,2], T.R. Saito[1,3], J. Gerl[1], I. Kojouharov[1], O. Lepyoshkina[1,3], S. Minami[1,3,4], J. Pochodzalla[3], C. Rappold[1,5], A. Sanchez Lorente[3], H. Schaffner[1], K. Szymanska[6], and Hypergamma collaboration‡

[1]GSI, Darmstadt, Germany; [2]National Taras Shevchenko University of Kyiv, Ukraine; [3]IKPH, Joh. Gutenberg-Universität, Mainz, Germany; [4]Osaka Univ., Osaka, Japan; [5]Univ. Louis Pasteur, Strasbourg, France; [6]Dipartimento di Fisica del Politecnico di Torino, Italy

Germanium detectors are widely used for γ-ray spectroscopy. However, application of such detectors is usually restricted to the low counting-rate environments as larger, high efficiency, crystals have longer charge collection times ($\leq 1\mu$s). To achieve maximum energy resolution of germanium detectors signal from preamplifier is shaped to the Gaussian form with shaping time from 3 to 6μs. The resulting total width of formed pulse is larger than 10μs. This fact increases a probability of events piled up at rates per crystal higher than few tens of kHz, which is expected in future hypernuclear γ-ray spectroscopy experiments. To solve such problems one has to use specially designed electronics (preamplifier, spectroscopic amplifiers) [1] or try to perform a pulse-shape analysis of the preamplifier signal. In the current work the second approach was chosen.

To develop a signal-analysis algorithm the high-rate measurement was performed. One representative crystal of the EUROBALL Cluster detector [2] was exposed to ^{22}Na and ^{57,60}Co γ-ray sources in a sequence of measurements, achieving 1.5, 34, 110kHz counting rate by changing the distance to the radioactive sources. The preamplifier signal was split into two separate branches. The first "analog" branch (A) consisted of timing filter and spectroscopic (SA) amplifiers, CAMAC peak-sensing ADC and constant-fraction discriminator. To achieve the best energy resolution the shaping time of SA was set to 3μs. The second "digital" branch (D) consist of 100Mhz 14 bit flash ADC SIS3301. Flash ADC was used to store pulse traces which were later processed off-line. The length of the traces was chosen to be 1.3ms and 100μs for high and low rate measurements, respectively.

The obtained traces were filtered by the Moving Window Deconvolution (MWD) algorithm [3]. However, MWD does not allow to measure the height of two neighbour pulses if they are closer in time as the length of the filter. To overcome this limitation the digitalised signals were analysed by several filters with different length. Depending on the distance between neighbour pulses (dt) analysis program selected output value of the filter with maximum length but less than dt. The output of such analysis consists of energy, time and filter length information for each event.

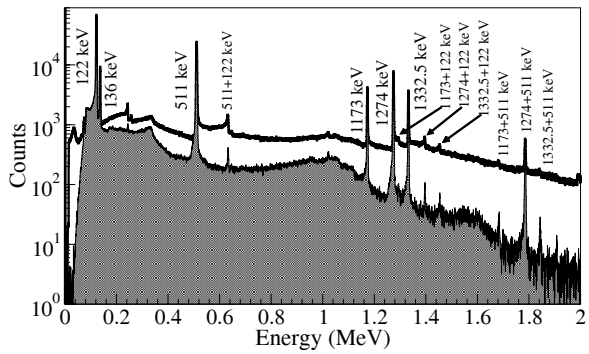

Figure 1: Gamma-ray spectrum of mixed calibration source of ^{57,60}Co and ^{22}Na obtained at 110kHz counting rate by means of analog electronics (bold line histogram) and digital signal processing (shaded-area histogram). Spectra were normalised to the area of 1332.4keV peak.

This allows to achieve maximum energy resolution in high-rate conditions as for each event shaping with optimal time constant is applied. Further in the text such analysis is referred as Multi-MWD (MMWD).

Resulting energy resolutions (FWHM at 1332keV, ^{60}Co) and fraction of rejected pulses measured for both branches are shown in the following table:

Counting rate (kHz)	Energy resolution (keV)		Pulse rejection (%)	
branch:	A	D	A	D
1.5	2.4	2.4	0	0
34	2.5	3.0	21	9
110	2.7	3.4	71	18

The analog branch provided better energy resolution, however, the probability of events piled up in analog branch drastically increases with counting rate. Figure 1 shows γ-ray spectra obtained at 110kHz rate. Due to pile up resolving the D branch provided higher peak to background ratio of 11.7 in comparison to the 2.6 obtained with analog ADC (for 1332keV ^{60}Co line).

The results of the test measurements show that the application of the MMWD analysis is very efficient for high counting rate environments.

References

[1] H. Tamura *et al.*, Phys. Rev. Lett. 84 (26) (2000) 5963.

[2] J. Eberth *et al.*, Nucl. Inst. & Meth. In Phys Res. A369 (1996) 135.

[3] A. Georgiev, W. Gast, IEEE Trans. Nucl. Sci. NS-40 (1993) 770; J. Stein *et al.*, Nucl. Instr. Meth. B 113 (1994) 141.

* This research is part of the EU I3HP RII3-CT-2004-506078 and is partially granted by the Helmholtz Association and GSI as Helmholtz-University YIG VH-NG-239 with Mainz University.

† M.Kavatsyuk@gsi.de

‡ A. Sanchez Lorente *et al.*, Performance of HPGe Detectors in High Magnetic Fields, Nucl. Inst. & Meth. In Phys Res **A**, accepted.

Final results on the Analysis of Germanium detectors in high magnetic fields*

A. Sanchez Lorente[†1], P. Achenbach[1], J. Gerl[2], M. Kavatsyuk[2], I. Kojouhavorv[2], J. Pochodzalla[1], N. Saito[2], T.R. Saito[2], H. Schaffner[2], and C. Sfienti for the HYPERGAMMA Collaboration[2]

[1]U Mainz, Germany; [2]GSI, Darmstadt, Germany

Pulse shapes of preamplifier signals for VEGA and EUROBALL detectors [1] under high magnetic field were further investigated. The analysis provides a new method which drives to recover the energy resolution under strong magnetic fields.

The observation of a simultaneous large shift and broadening of the rise time distributions [2, 3] of preamplifier signals suggests that an incomplete signal integration by shaping amplifiers could be the main origin of the observed energy shift. To verify the latter conjecture, the response to output signals of the shaping amplifier on different rise-time of input signals has been investigated with a pulse generator, and it has been confirmed that the rise-time variations are the main source of the observed energy shift and reflects the effect of the magnetic field on the charge collection process itself. Fig. 1 shows distributions of pulse heights of the output signals of the shaping amplifier measured by an CAMAC ADC as a function of measured rise-time of preamplifier signals by a flash-ADC for one of the segments of the VEGA detector at different magnetic fields, showing a strong correlation between the observables. The fit of a parabolic function to the correlation (see solid lines in Fig. 1) enables a correction of the energy spectra event-by-event for different magnetic fields. The correction functions are similar for all measurements at non-zero magnetic field, but they are shifted relative to that of the measurement at $B = 0\,\mathrm{T}$. Presently the origin of this strong shift is not understood. Fig. 2 shows the corrected γ-ray energy spectra (dashed line) for the same segment of the VEGA detector at 1.6 T in comparison to the one without correction shown by a dashed line. A significant improvement in the peak shape has been achieved. After applying the correction, an improvement on the energy resolution for the both VEGA and EUROBALL Cluster has been achieved, and the remaining degradation at fields larger than 1 T amounts to approximately 0.5 keV.

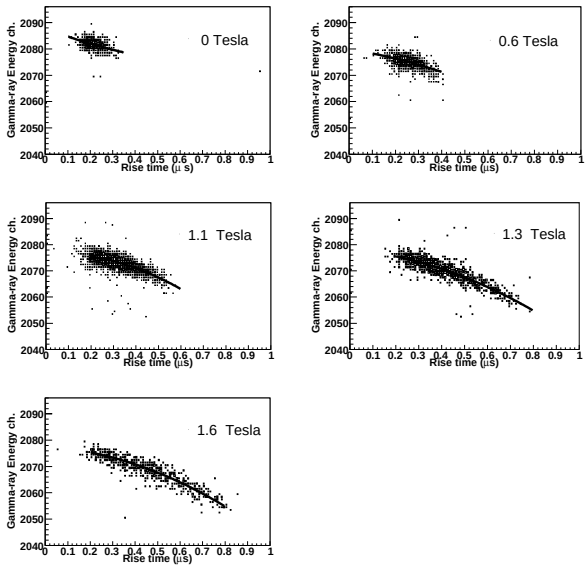

Figure 1: Correlation between the energy in channels and the rise time for the 1.332 MeV γ-rays of one of the segments of VEGA in a magnetic field. The line represents the parabolic fit function of each distribution at different values of the magnetic field.

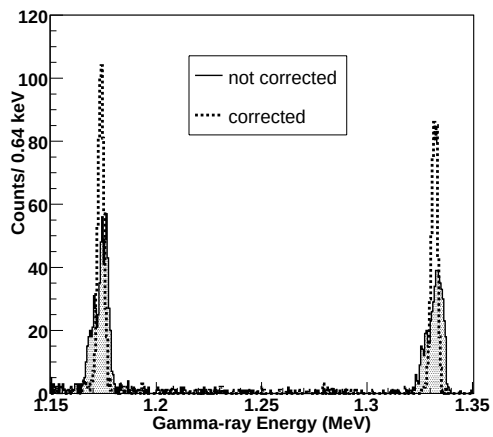

Figure 2: Two γ-ray energy spectra for ^{60}Co at maximum value of the magnetic field. The hashed spectrum presents the ADC spectrum without correction and the dashed line the corrected ADC spectrum at a field of 1.6 T.

References

[1] A. Sanchez Lorente et al., Performance of germanium detectors in high magnetic fields, in GSI Sci. Rep. 2004, p.32 and A. Sanchez Lorente *et al.*, in: GSI Sci. Report 2005, GSI, Darmstadt, 2006, p. 79, FAIR-QCD-PANDA-07

[2] A. Sanchez Lorente et al., Performance of germanium detectors in high magnetic fields, NIMA in press.

[3] A. Sanchez Lorente. PhD thesis, U Mainz.

*This research is part of the EU integrated infrastructure initiative Hadronphysics project under contract number RII3-CT-2004-506078 and by the BMBF under contract number 06MZ176.

† lorente@kph.uni-mainz.de

Mass-production of the Multi-strip Multi-gap Resistive Plate Counters (MMRPCs) and the construction of the new FOPI ToF Barrel *

M. Kiš[1], M. Ciobanu[1,2], E. Cordier[2], N. Herrmann[2], K.D. Hildenbrand [1], Y.J. Kim[1], P. Koczon[1], Y. Leifels[1], M. Marquardt[1], A. Schüttauf[1], J. Weinert[1], X. Zhang[1], and FOPI Collaboration[1]

[1]GSI, Darmstadt, Germany; [2]Physikalisches Institut, Heidelberg, Germany

In order to enlarge the charged kaons identification range up to 1 GeV/c a new ToF Barrel made of MMRPCs [1,2,3,4] was designed and built by the FOPI collaboration. The Barrel consists of 30 so-called super modules, each housing five MMRPCs, and covers a cylindrical shell of 6 m^2 surface around FOPI's Central Drift Chamber (CDC). In Fig. 1 a photo of a super module prepared for a γ source test is shown.

Figure 1: MMRPC super module mounted together with the readout electronics on a support plate.

During 2006 all 150 needed MMRPCs were produced by FOPI collaboration members in the detector laboratory of GSI. They have the following parameters: double-stack (sandwich) construction with 2×4 gas gaps of 220 μm, 16-strip anode with an effective area of 90×4.6 cm^2, an anode strip to gap ratio 1.94 mm:0.6 mm, and a 50 Ω signal line impedance. A common window (float) glass is used as a resistive plate material and the active volume of the super module is flushed with a gas mixture of freon/SF_6/isobutan (85:10:5). These counters reach a full efficiency for at electric field between 105 and 110 kV/cm.

In Fig. 2 we present the timing and efficiency performance of the production counters. The results were obtained in a proton test beam (2 GeV) with an average rate of 100 Hz/cm^2 which is similar to expected experimental conditions. The obtained time resolution in the region of full efficiency ($\varepsilon > 95\%$) is $\sigma_t < 75$ ps. Based on this results we can estimate the performance of the future FOPI ToF Barrel: a single-hit time resolution better than $\sigma_t < 85$ ps (for the whole system) with an efficiency of $\varepsilon > 99\%$. As a consequence of the multi-strip design the MMRPCs have a double-hit capability. The measured double-hit time resolution (for the whole system) is $\sigma_t < 100$ ps with of efficiency of $\varepsilon > 85\%$.

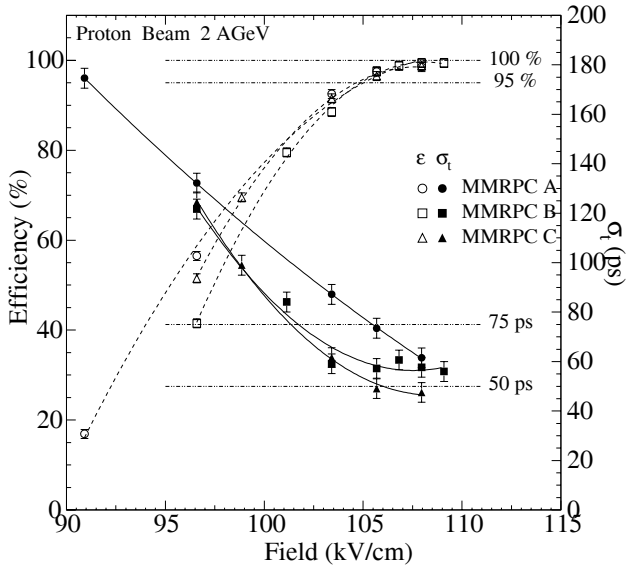

Figure 2: The time resolution (full symbols) and efficiency (hollow) of three MMRPCs as a function of an applied electric field. The curves are arbitrary fits to the data points.

The R&D phase was finished in January 2006 with a successful test of the final version of our custom design electronic readout system [4,5,6]. Subsequently all electronic for the readout of 4800 channels (trial and bulk production) was delivered by an external company[1] by the end of December 2006. Presently, the whole system is being assembled and prepared for mounting inside FOPI. The commissioning of the new ToF Barrel is planned for the first half and a first main experiment for the second half of 2007.

References

[1] E.C. Zeballos et. al., NIM A 374 (1996) 1322

[2] P.Fonte et al., NIM A 443 (2000) 201

[3] A.Schüttauf et. al., NIM A 533 (2004) 65

[4] A.Schüttauf et. al., Nucl. Phys. B (proc. Supp.) 158 (2006) 52

[5] K. Koch et al., IEEE Trans. Nucl. Sci. 52 (2005) 745

[6] M. Ciobanu et. al., submitted to IEEE Trans. Nucl. Sci. and this Annual Report

* Supported by EU/FP6 I3HP contract nr. RII3-CT-2004-506078 and BMBF contract nr. 06HD154.

[1]Productware GmbH, www.productware.de

A Drift-velocity Monitor for FOPIs Drift-chambers *

N. Zernezki[1], A. Schüttauf[1], K. D.Hildenbrand[1], Y. J.Kim[1], M. Kiš[1], P. Koczon[1], Y. Leifels[1], X. Lopez[1], M. Marquard[1], X. Zhang[1], and the FOPI Collaboration

[1]GSI, Darmstadt, Germany

We use a modified version of the Goofi-drift-monitor, developed at GSI and MPI-Munich [1][2][3] to test a new electronic chain and readout concept, which can be implement into the existing FOPI slow control system [5]. The design goal for the drift-velocity monitor is to measure the drift-velocity (v_d) with a relative error below $\frac{\Delta v_d}{v_d} \leq 1\%$ at an absolute value $v_d \sim 4\ cm/\mu s$ which is the operation value in FOPIs drift chambers. The realization of the drift-monitor is rather simple: we use a field-cage of 25 cm length and 3 proportional counters to determine the drift-velocity by a time measurement knowing the distance between the counters. Two proportional-counters (Top/Bottom) are placed within the field-cage and serve as start counters for the time measurement; the third counter (Pickup) is placed at the end of the cage and delivers the stop signals. The start signals are delivered by two Am^{241} – α-sources (4 kBq). These α-particles ionize, on their path through the field-cage, the detector gas and are finally detected in the Top and Bottom unit. The third counter (Pickup) collects the electrons which are created by the α-particles in the gas. The time difference between Top-to-Pickup and Bottom-to-Pickup is used for determining the drift-velocity.

All three proportional counters are read out by the same electronic chain using a pseudo-differential preamplifier and a shaper. The positive output signals of the preamplifier are additionally amplified to adjust their overall signal height to the range needed for the digitizer ($\pm$ 1V). The negative signals are discriminated and used to generate the trigger for the whole system. To digitize the three counter signals we use a PC based PCI-card (PCI-9812) [4] which has 4 channels with a 12 bit FADC at a sampling frequency of 20 MHz. This card is initialized and readout by a Labview program which allows to save the data to disk and to realize an online monitoring during the experiment [3]. In the current configuration of the system we are able to measure the drift-velocity within 20 min. (1000 events). This is sufficient, compared to changes of pressure or temperature which are main reason for the variations of the drift-velocity (v_d).

We tested this new system with a standard chamber gas (P10) to determine its performance during two measurement periods of 6 days. The tests were performed in an area where the counter and the gas were temperature stabilized. In Figure 1 we show the results of this tests and compare them to the inverse pressure (black solid line same plots) measured externally at the same time interval. It is

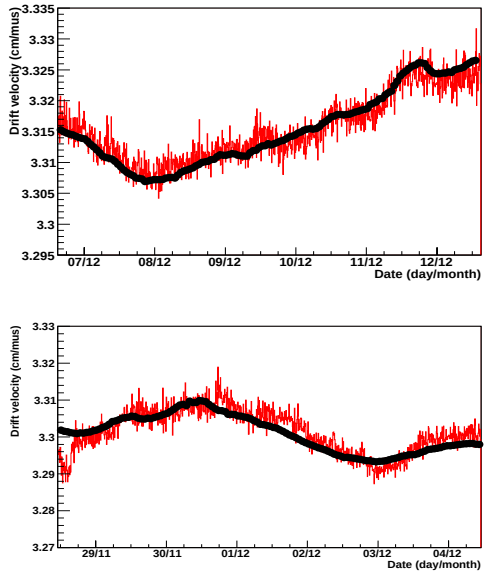

Figure 1: The two panels show the measured drift-velocity versus the time (red points) from 2 different measurement periods (6 days). On top of the measurement we plotted the inverse pressure (solid line).

obvious that the drift velocity follows directly the inverse pressure with a relative error of $\frac{\Delta v_d}{v_d} \leq 0.5\ \%$ at an absolute value of $v_d \sim 3.3\ cm/\mu s$. In summary we conclude that the new system is capable to measure the drift-velocity with the needed resolution; it will be used during the next FOPI beam-time to monitor the drift-chambers.

References

[1] C.Markert, Diplomarbeit, JWG-Universität Frankfurt am Main (1995)

[2] A.Gärtner, Diplomarbeit, Technische Universität München (2002).

[3] N.Zernezki, Diplomarbeit, Fachhochschule Darmstadt (2007).

[4] NuDAQ PCI-9812/10 20MHz Simultaneous 4-CH Analog Input Card. Users‘ Guide ADLINK Technologie Inc. Manuel Rev. 2.40: April 11, 2003

[5] P.Koczon, GSI-Annual Report 2005

* BMBF

An ASIC based fast Preamplifier-Discriminator (PADI) for MRPCs *

M.Ciobanu[1,2], A.Schüttauf[1], E.Cordier[2], N.Herrmann[2], K.D.Hildenbrand[1], Y.J.Kim[1], M.Kiš[1], P.Koczon[1], Y.Leifels[1], X.Lopez[1], M.Marquardt[1], J.Weinert[1], X.Zhang[1], and the CBM Collaboration

[1]GSI, Darmstadt, Germany; [2]Universität Heidelberg, Germany

The use of conventional integrated circuits to process primary RPC signals has reached its limit with designs like FOPI's 16 channel FEE5 [3]. To further reduce the price and power consumption per channel the natural way is a custom ASIC design. For this purpose the NINO architecture [1] used in the ALICE-ToF with its full differential structure offers a very attractive starting point for a new Preamplifier-Discriminator design.

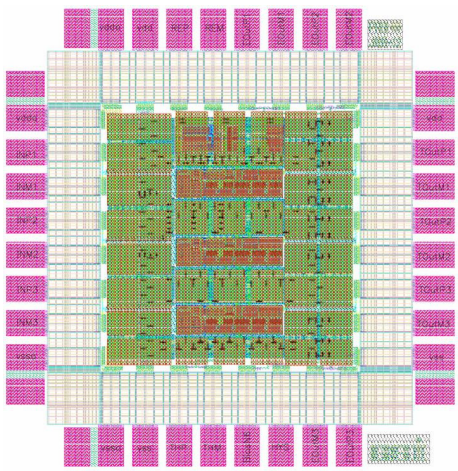

Figure 1: Asic Layout of the PADI chip with 3 channels

Taking into account the existing ideas of time measurements with fast gas detectors with up to 100000 channels within the CBM-detector at the FAIR-facility of GSI, we started to investigate, within the European project JRA-12, the development a new 4 channel PADI-ASIC in CMOS 0.18 μm technology. This chip has the following key parameters: fully differential, 50 Ω input impedance, LVDS compatible output, preamplifier gain G $\geq$ 200, preamplifier bandwidth $BW \geq 400$ MHz, peaking time $t_P \leq$ 1ns, noise related to input $\sigma_n \leq 25 \mu V RMS$, comparator gain $G \geq 200$, a DC feedback loop for offset and threshold stabilization and a threshold range related to the input of ΔU_{Thr} ~0.5-20 mV.

Based on these characteristics we designed a first version of the PADI-Chip (Fig. 1), with 3 channels in its first prototype. With the first delivered samples we have performed tests to check the basic functionality (connections, voltage, in/outputs of time and charge, thresholds). From these elementary tests we conclude that all channels are fully operational. Due to this very positive result we designed a PCB for the PADI-chip which is directly connected to our FOPI-digitizer TACQUILA3 [2].

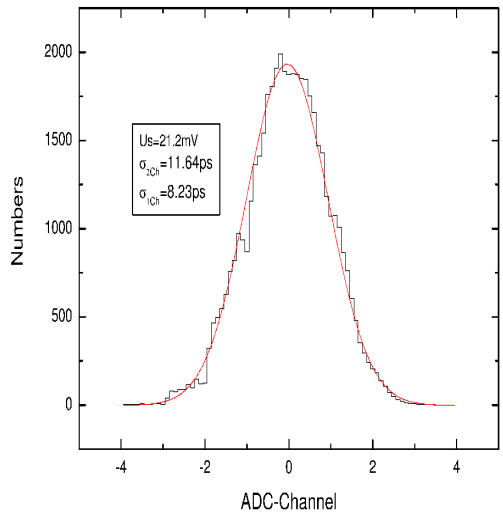

Figure 2: First timing measurement of the PADI-chip together with the TACQUILA-card. A time-resolution $\sigma_t \leq$ 10 ps has been reached for a single channel.

The combined setup (PADI-TACQUILA3) has a timing performance of $\sigma_t \leq 10$ ps for pulser signals above 20 mV (see Fig 2.). In the following measurements we will map out the overall time resolution as a function of the amplitude. We will also compare time-over-threshold (ToT) to the direct charge measurement, to learn whether the ToT measurement is applicable for the walk correction.

References

[1] F.Anghinolfi, P.Jarron, A.N.Martemiyanov, E.Usenko, H.Wenninger, M.C.S.Williams and A.Zichichi
Nucl. Inst. and Methods A, Vol. 533, Issues 1-2, 1 November 2004, 183-187

[2] K.Koch, H.Hardel, R.Schulze, E.Badura and J.Hoffmann
IEEE Transactions on Nuclear Science, Vol. 52, No. 3, June 2005, 745-747

[3] M.Ciobanu [a,b], A.Schüttauf[a], E.Cordier[b], N.Herrmann[b], K.D.Hildenbrand[a],Y.J.Kim[a], Y.Leifels[a], M.Kis[a], P.Koczon[a], X.Lopez[a], M.Marquardt[a], M.Petrovici[c], J.Weinert[a],X.Zhang[a]
sub. to IEEE Transactions on Nuclear Science 2007

* work supported by JRA12 of EU/FP6 Hadronphysics (see annex), INTAS Ref.Nr. 03-54-3891 and German BMBF contract 06 HD190I.

Design studies on Time-Of-Flight walls for the HypHI project*

C. Rappold[†1,2], M. Kavatsyuk[1,3], O. Lepyoshkina[1,4], S. Minami[1,4,5], T.R. Saito[1,4], M. Träger[1], P. Achenbach[4], S. Ajimura[5], C. Ayerbe[4], T. Fukuda[6], Y. Mizoi[6], D. Nakajima[7,8], L. Nungesser[4], J. Pochodzalla[4], A. Sakaguchi[5], and the HypHI collaboration

[1]GSI, Darmstadt, Germany; [2]Univ. Louis Pasteur, Strasbourg, France; [3]Univ. Kyiv, Kiev, Ukraine; [4]IKPH, Joh. Gutenberg-Universität, Mainz, Germany; [5]Osaka Univ., Osaka, Japan; [6]Osaka Elect.-Comm. University, Neyagawa, Japan; [7]KEK, Tsukuba, Japan; [8]Univ. Tokyo, Tokyo, Japan

The HypHI project which has been recently started aims to study hypernuclei by means of collisions of stable heavy ion and rare-isotope beams on stable target materials [1, 2]. As the first step (Phase 0), the feasibility of hypernuclear spectroscopy with heavy ion beams will be demonstrated with ^{6}Li beams at 2 A GeV impinged on a ^{12}C target by identifying $^{3}_{\Lambda}$H, $^{4}_{\Lambda}$H and $^{5}_{\Lambda}$He hypernuclei [3].

The HypHI collaboration currently works on the design study of the setup for Phase 0 based on Monte Carlo simulations with GEANT4. The current simulation program uses UrQMD calculations to generate events of nuclear collisions at the target.

The current design of the experimental setup consists of the ALADiN magnet, a diamond detector and scintillating fiber detectors in front of the ALADiN magnet, and two Time-Of-Flight (TOF) walls behind the ALADiN magnet [3]. Negatively charged pions are detected by the ALADiN TOF wall and positively charged particles by another TOF wall called TOF+ which consists of plastic scintillator bars with readout by photomultipliers. This work dedicates to the design study of TOF+.

There are several constraints in designing TOF+. Due to the intensity of projectiles as 10^7 per second a high counting rate in each plastic bar near the beam trajectory is expected. The geometry of the detector must be optimized to have less than 1 MHz counting frequency per bar in order to be lower than the maximum current accepted by photomultipliers. Moreover, the size of the detector has to be minimized with a reasonably large acceptance.

In order to satisfy those specifications, different solutions were considered. To avoid a high counting rate, a hole with a size of 7.5 cm $\times$ 6.5 cm is considered for the projectiles, and a width of 4.5 cm for each plastic bar with a thickness of 2.5 cm is chosen. In order to achieve a reasonably good position granularity, adjacent bars are overlapped by 1.5 cm, thus a position granularity is 1.5 cm. The total size of TOF+ wall is 96 cm (horizontal) $\times$ 1 m (vertical), which gives an acceptance of 92% for positively charged particles from the π^- decay channel of hypernuclei of interest. A layout of the TOF+ wall is shown in Figure 1. In the simulation, the position of the ALADiN TOF wall was also optimize to maximize the acceptance for π^- measurements.

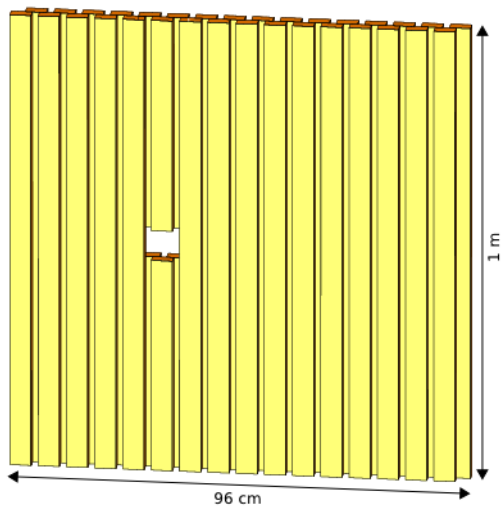

Figure 1: TOF+ wall layout

An important piece of information for the design of TOF+ is a beam spot size at the target in cave C where the experiment will be taken place. Therefore, a beam spot size is measured by a multi-wire proportional counter and emulsion films with ^{12}C beams at 2 A GeV, and a size of approximately 0.6 cm in RMS for the both horizontal and vertical directions was deduced. In the simulations, a beam with a two-dimensional Gaussian distribution with a σ of 1 cm at the target position was assumed.

Test of prototype detectors and the final design study of TOF+ is still in progress.

References

[1] T.R. Saito *et. al.*, and the HypHI collaboration, in these Scientific Reports.

[2] T.R. Saito *et. al.*, proceedings of HYP2006, October 2006, Mainz, to be published in Eur. Phys. J.

[3] A proposal of the HypHI Phase 0 experiment, the HypHI collaboration, submitted to GSI PAC EA33 with a realization as S319.

* The HypHI project is granted by the Helmholtz Association and GSI as Helmholtz-University Young Investigators Group VH-NG-239 with Mainz University

† c.rappold@gsi.de

Scintillating Fiber Detector for the HypHI Phase 0 Experiment

O. Lepyoshkina[1,2] ,M Kavatsyuk[1,3], S. Minami[1,2,4], C. Rappold[1,5], T. R. Saito[1,2], A. Achenbach[2], C. Ayerbe[2], S. Ajimura[4], T. Fukuda[6], Y. Mizoi[6], L. Nungesser[2], J, Pochodzalla[2], A Sakaguchi[4] and the HypHI collaboration.

[1]GSI, Darmstadt, Germany; [2]IKPH, Joh. Gutenberg-Universität, Mainz, Germany; [3]Kyiv University,Ukraine;[4]Osaka Univ.,Osaka,Japan;[5]Univ. Louis Pasteur, Strasbourg, France; [6]Osaka Elect. - Comm. University, Neyagawa, Japan

In order to investigate the feasibility of hypernuclear spectroscopy with heavy ion beams, the HypHI collaboration proposes an experiment defined as Phase 0 [1, 2]. For measurements of decay vertices of hypernuclei and for the tracking charged particles right behind the target a use of scintillating fiber detector is proposed. A prototype of the scintillating fiber detector has been built with Kuraray SCSRF-78 scintillating fibers with an outer diameter of 0.83mm and an active core of 0.73mm.This type of fiber has a short decay constant of 2.8 ns, high light yield and a long attenuation length more than 4m. The prototype consists out of two layers of fibers at a pitch of 0.59mm (see Fig. 1). Readout of scintillating photons is done by the Hamamatsu photomultiplier H7260 with 32 anodes.
A range of spectral response of the photomultiplier is 300-650nm. A typical gain of the photomultiplier is about $2x10^6$ at a high voltage of about 800 V.

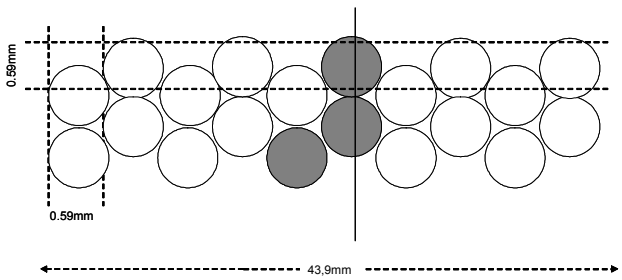

Figure 1: Fiber arrangement for the prototype.

To optimize the design of the fiber detectors, several different tests with cosmic rays have been performed. The light amplitude of each channel of the prototype was measured with CAEN Charge-to-Digital Converter QDC MOD. V792. A plastic detector placed below the fiber detector was used to create a trigger signal to the data acquisition system. Analog signal from the photomultiplier are fed into the QDC with a delay of 100ns. An energy spectrum of one of the 32 channels of fiber detector is shown in Figure 2. The energy spectrum is characterized by a shape containing two prominent peaks. The first one corresponds to a pedestal distribution, which appears due to the fact that the area of the trigger plastic detector is larger than the scintillating fiber detector; therefore a part of cosmic rays which has triggered the data system was not registered to the fiber detector. The second peak corresponds to the energy deposit distribution of cosmic rays measured by the fiber detector. A narrow pedestal distribution allows a clear separation of the cosmic ray peak from the pedestal. Measurements and data analyses are still in progress, however, the results are presented in this report have already suggested to increase the number of the layers of the fiber detector from two to four.

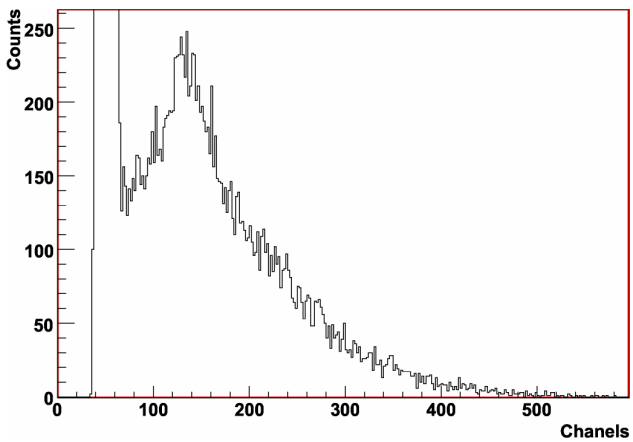

Figure2: Energy spectrum one of the channels of the fiber scintillating detector.

A beam time of three nights is planned in March 2007 to test the fiber detectors with a primary carbon beam at 2 A GeV and π^+ cocktail beam with a π^+ momentum of 1 GeV/c.

References

[1] A Letter Of Intent of the HypHI project, the HypHI collaboration, submitted to GSI PAC EA30 as LOI40.

[2] T.R. Saito et al., and the HypHI collaboration in these Scientific Reports.

* The HypHI project is granted by the Helmholtz Association and GSI as Helmholtz-University Young Investigators Group VH-NG-239 with Mainz University
o.lepyoshkina@gsi.de

Performance of a fibre detector at a ^{12}C beam of 2 AGeV energy*

P. Achenbach[†1], C. Ayerbe Gayoso[1], M. Kavatsyuk[2], O. Lepyoshkina[2], S. Minami[2], L. Nungesser[1], J. Pochodzalla[1], C. Rappold[2], and T.R. Saito[2]

[1]Inst. für Kernphysik, Joh. Gutenberg-Universität, Mainz, Germany; [2]GSI, Darmstadt, Germany

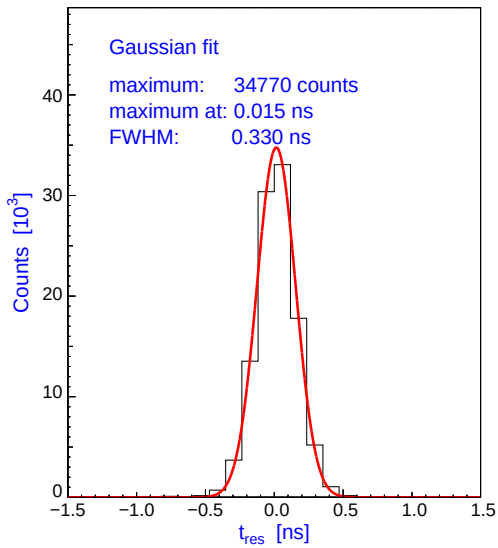

Figure 1: The residual of hit times between both detector planes. A Gaussian fit is shown with a FWHM of 330 ps.

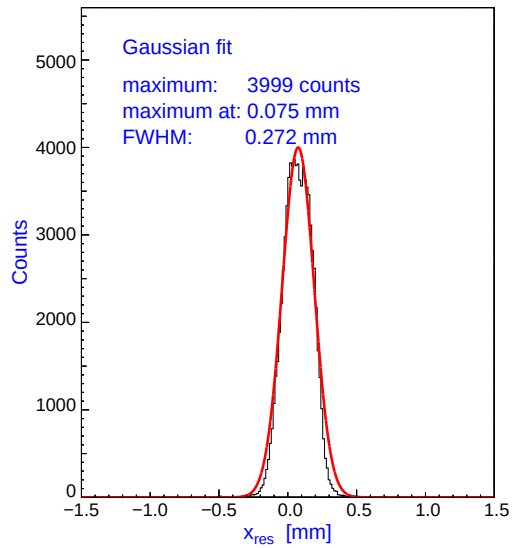

Figure 2: The residual of beam position estimates between both detector planes, using the centroid of charges. A Gaussian fit is shown with a FWHM of 0.27 mm.

The HypHI project is dedicated to hypernuclear spectroscopy with stable heavy ion beams and rare isotope beams at GSI and FAIR [1]. In its first phase it will apply scintillating fibre detectors for tracking and trigger purposes. A prototype detector with 96 read-out channels for three fibre bundles comprising 384 fibres was tested in Cave C of GSI with a ^{12}C beam of 2 AGeV energy. In each bundle 128 fibres were packed in 4 double layers with a pitch of 0.6 mm. Two bundles were aligned to a single plane perpendicular to the beam, and one bundle formed a parallel plane directly behind. Four fibres were grouped to one channel and coupled to one pixel of the photodetectors. The multi-anode photomultipliers (MaPMT) of type R7259K from Hamamatsu are fitted with a 32-channel linear array of electrodes. The effective area per channel is $0.8 \times 7\,\mathrm{mm}^2$ with a pitch of 1 mm.

For amplitude compensated timing two 32-channel discriminator boards each with 4 integrated low-walk double threshold discriminators were used. For the data shown the thresholds were set to -60 (-120) mV, and the high voltages to -500 V and -650 V. Analogue output boards with 50 Ω coaxial connectors were attached to the discriminator boards to access also the pulse heights of each channel.

A scintillation paddle was installed 2 m upstream in the beam-line to serve as a trigger counter.

In deducing the time resolution clusters of correlated hit times were searched for. The cluster with the time closest to the trigger signal time was retained, and within the cluster the time of the first arrived signal was chosen as hit time. A minimum time separation of 10 ns between clusters and a hit in a coincidence window of 20 ns width were required. The hit time residual, defined as the difference between the two hit times in the two planes of fibres, had a FWHM of 330 ps as shown in Fig. 1. The time resolution of a single detector plane was determined to be of the order of FWHM $\sim 330\,\mathrm{ps}/\sqrt{2} = 230\,\mathrm{ps}$.

Cross-talk in the MaPMT entrance window perturbed the reconstruction of the particle position. By using the pulse height information the hit channel was estimated by the centroid of charges of up to 5 neighbouring channels. The hit position residual, defined as the difference between the two estimates in the two planes of fibres, had a FWHM of 0.27 mm as shown in Fig. 2, although the estimator contained a spatial digitalisation error. The achieved accuracy was sufficient for an unambiguous identification of the hit channel leading to a spatial accuracy of $0.6\,\mathrm{mm}/\sqrt{12} \approx 170\,\mu$m (rms).

The distributions of the pulse height sums over all channels lead to a relative variation in the measured energy deposition, $\Delta E/E$, of 15 % at a high voltage of -650 V and 20 % at -850 V.

References

[1] T.R. Saito et al., "The HypHI project at GSI and FAIR", this GSI Sci. Rep. 2006.

* supported by Helmholtz Association and GSI as Helmholtz-University Young Investigators Group VH-NG-239.

† patrick@kph.uni-mainz.de

A General Purpose Trigger and Readout Board (TRB) for HADES and FAIR-Experiments *

M. Traxler[1], I. Fröhlich[4], M. Kajetanowicz[3], K. Korcyl[2], W. Krzemien[2], M. Palka[2], P. Salabura[2], C. Schrader[4], H. Stroebele[4], J. Stroth[4], P. Skott[1], A. Tarantola[4], R. Trebacz[2]

[1]EE, GSI, Darmstadt, Germany, [2]Jagiellonian University, Krakow, Poland, [3]Nowoczesna Elektronika, Krakow, Poland, [4]J.-W. Goethe-Universitaet, Frankfurt, Germany

A general-purpose trigger and readout board (TRBv2) with on-board DAQ functionality is currently being developed as a replacement of the existing HADES electronics (DAQ and parts of the FEE) as well as for the PANDA Mini Drift Chamber (MDC) readout [1]. The first version has been sucessfully integrated into the data aquisition of the HADES detector (TRBv1 [2]). While the main application of the TRBv1 was to be a 128-channel Time to Digital Converter (TDC) electronics based on the HPTDC [3] (we achieve $\sigma = 40\ ps$ resolution) to read out the HADES-RPC-detector, the TRBv2 has been designed in a way to be detector independent and thus may serve for any high-speed data acquisition by using a flexible add-on board concept.

To broaden the spectrum of possible applications in future DAQ-systems, we added a very high data-rate digital interface connector (15 Gbit/s). It gives the possibility to mount add-on boards to the TRBv2 which then provide the detector-specific interfaces (special connectors) or FEE (like ADCs) and additional computing resources (FPGAs).

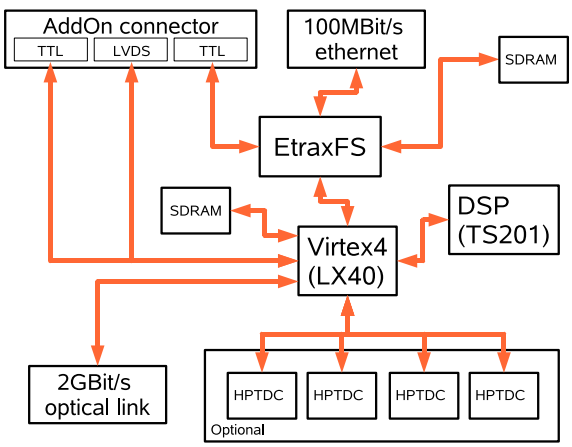

Figure 1: The TRBv2. It features 4 HPTDCs (128 channels, optional), an Etrax-FS-Processor [4] with 128 MBytes memory, Ethernet-connectivity, an optical link with 2 Gbit/s, programmable logic (Virtex 4 LX40) and a TigerSharc DSP (500 MHz, 24 MBit memory, 4 linkports).

In addition, the TRBv2 provides an optical link (2 Gbit/s) as a replacement of the HADES trigger bus and for high speed data transport (as required for example by PANDA), a large FPGA (Xilinx Virtex 4 LX40 + 128 MBytes RAM) and a TigerSharc DSP can be used as on-board resources for trigger and on-line analysis algorithms.

The TRBv2 uses an Etrax-FS processor [4] for DAQ and slow-control functionality. The processor runs a standard linux 2.6 kernel in the 128 MBytes of memory and is directly connected to the 100 Mbit/s Ethernet. The integrated three co-processors (each 200 MHz) allow a high IO bandwidth without main CPU intervention. The TRB will support EPICS to allow the integration into the HADES Slow-Control System (common project with the EE-department [5]).

An additional board has been built (HadCom), which is used to test many features of the Etrax-FS-Processor [4] as well as the communication interface between the new trigger and readout board network (TrbNet) with the existing HADES-electronics. The TrbNet will be mainly based on the 2 Gbit/s optical links but also allows the integration of VME-CPUs, the add-on boards and the front end electronics in a standardized way.

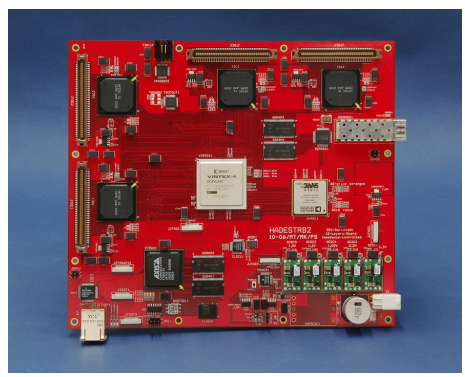

Figure 2: The prototype TRBv2 module (size: 20x23cm).

References

[1] P. Salabura, PANDA Collaboration Meeting, FEE-Session, 2006-12-11

[2] M. Traxler, 128 channel high resolution TDC with integrated DAQ-system, GSI Scientific Report (2005) 281

[3] HPTDC, J. Christiansen, Digital Microelec. Group, CERN

[4] ETRAX, AXIS Communications, Sweden

[5] http://wiki.gsi.de/Epics

* Work supported by EU FP6 grant, contract number 515876 and EU FP6 grant RII3-CT-2004-506078 (JRA1)

Commissioning of the ALICE Time Projection Chamber

P. Braun-Munzinger, J. Castillo, U. Frankenfeld, C. Garabatos, H.R. Schmidt, D. Vranic, J. Wiechula, and the ALICE collaboration
GSI, Darmstadt, Germany

The TPC is the central detector of the CERN-LHC experiment ALICE. It is the largest TPC ever built with a gas volume of ~90 m^3 and 557568 readout channels. The LHC is scheduled to commence operation in 2007 with pp-collisions.

Before installation underground inside the ALICE L3 magnet, the TPC including its auxiliary systems and services, i.e., gas system, temperature monitoring system, drift velocity monitoring system, FEC cooling, laser system, gating, chamber supply voltages, field cage high voltage, cables, DAQ and HLT have to be commissioned to ensure proper functioning of all its components.

Hardware Installation and Schedule

The insertion of the 72 *readout chambers (ROC)* into the TPC's endplate was completed in 2005 [1]. By April 2006, the 4356 *Front-End Cards (FECs)* [2] were installed and ready to be operated. At the same time a *temperature monitoring system* [3] based on 500 pt1000 sensors was mounted on the readout chambers, inside of the gas volume and onto the TPC inner and outer vessels. The *laser system* [4] close to its final configuration was ready by March. The *field cage high voltage* (100 kV) with its final setup and control was applied for the first time in May.

The 10 kA *low voltage system*, as well as the large *cooling plant* to operate all 36 sectors simultaneously, were not used on the ground level due to infrastructure limitations. They were substituted by smaller systems.

The commissioning of the TPC in a clean room on the surface level was accomplished in the period from May to December 2006.

Gas System

The gas system supplied by the CERN gas working group produced a pressure stability of 0.403 ± 0.013 mbar during commissioning. The oxygen content in the TPC was below 5 ppm, i.e. within the specified values of the Technical Design Report [5]. The knowledge of the exact gas composition (CO_2-content) was ensured by a newly installed gas chromatograph. The drift velocity and the gain of the gas could be measured "online" with high precision via a Goofie [6].

Cooling and Temperature Monitoring

A small, leakless cooling plant capable to supply two fully equipped sectors with chilled water allowed to determine its operating parameters: at a nominal water flow of 10 l/min the temperature gradient between cooling in- and outlet was below ΔT=1°C. The temperature gradient over a sector - extracted from the five probes mounted onto the Al-bodies of a single sector - was of the order of ΔT=0.1 °C. The pressure drop within a sector - an important entity for sub-atmospheric systems - was measured to be below Δp=200 mbar.

The temperature profile as measured on the TPC surface employing the pt1000-sensors is shown in Figure 1. The temperature gradients on the outer hull are due to the air conditioning inlets of the clean room. The temperature distribution on the readout plane (front-side) is due to the fact that FECs of the two rightmost sectors were powered up and their excess heat is distributed upwards. The independent regulation of the cooling circuits for the 36 sectors will allow compensating for these temperature gradients.

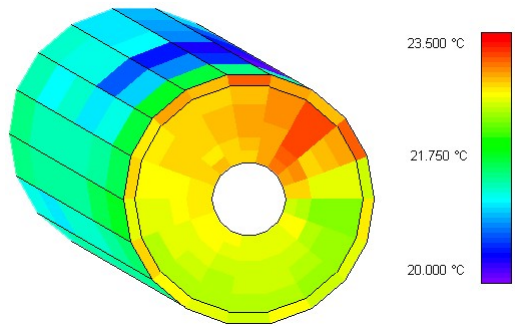

Figure 1: Temperatures on the outer hull and the readout plane of the TPC.

Laser System

Besides cosmic rays, laser beams were employed to commission the TPC's ROCs. A sketch of the laser beam distribution system (prisms, beam splitter, micro-mirror bundles and laser beams) [4] is shown in Figure 2 (left); the actually measured laser tracks are shown in Figure 2 (right).

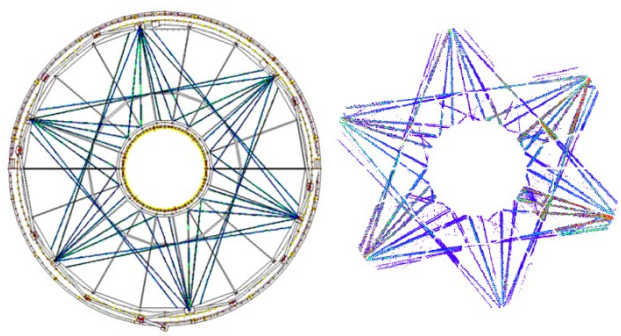

Figure 2: Left: Sketch of the laser ray distribution in the TPC. Right: Measured tracks in laser runs.

These laser tracks from the commissioning runs are used in offline-analyses to correct for residual geometrical distortions and temperature effects [7].

DAQ and HLT

The DAQ system used during commissioning corresponded largely to the final ALICE DAQ. Running since May more then 3500 runs and 24 TB of data were taken with no apparent hardware failures. The data were recorded in ROOT format and automatically migrated to CASTOR for mass storage. Online monitoring [8] allowed inspection of the data on an event-by-event basis.

The High-Level Trigger (HLT) was integrated into the data-stream and 3D-online-tracking was successfully applied.

Read-Out Chambers

All 36 sectors where subjected subsequently (always two sectors were operated simultaneously) to systematic tests to characterize the fully equipped readout chambers:

Using *cosmic ray tracks* all chambers were operated at 3 different anode voltages; at nominal voltage (MIP at 20 and 30 ADC counts for inner and outer ROC, respectively), and at nominal voltage ±50 V. The test served to verify the basic functionality of the chamber and readout chain. Figure 3 shows an example of a cosmic shower event seen in two opposite sectors.

In addition, the chambers were operated employing the *laser* at the same 3 anode voltage to verify the basic functionally of the chambers and the drift volume with well defined tracks.

In a second go-around all sectors were tested in an endurance run of at least 40 hours continuous operation.

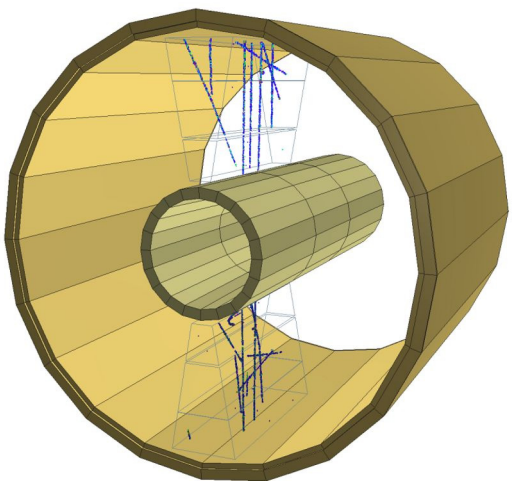

Figure 3: 3D-view of a cosmic event as seen in two TPC sectors.

Generally all chambers performed in terms of resolution and overall gain fully to specs. A few chambers exhibited gain anomalies at specific locations, which was traced back to isolated high-ohmic anode wire connection. A serious upset occurred when a single anode wire broke. This necessitated the exchange of an outer ROC, which required considerable effort to re-establish the necessary environment, i.e., clean room conditions, removal of the FECs and installation of the mounting tool. It proved, however, the principal feasibility of exchanging a chamber "in situ" without inflicting on neighbouring sectors.

Front-End Electronics

The characterization of the FECs involved the measurement of the baseline and its RMS. Tests with a *calibration cathode pulser* allowed to check the electrical connectivity, the homogeneity of the electronic gain and the relative t_0 of the readout. Non-working electronic channels were reduced to a level of 10^{-4}. The average RMS noise in the ROCs was typically 0.7 ADC counts (~680e ENC), which is fully within specs. The noise distribution over the surface is rather homogeneous with slightly higher values at the borders of the chambers.

Further tests involved data taking at high trigger rates, e.g., 10 samples/channel@ 1 kHz.

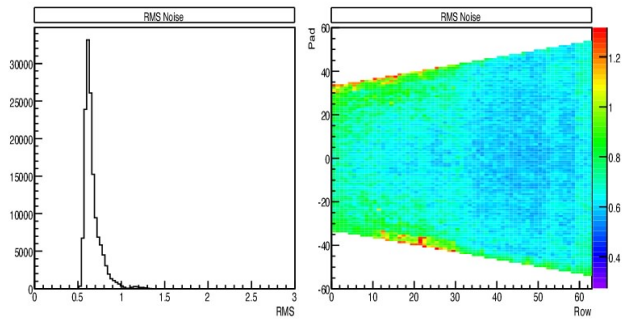

Figure 4: Left: Average RMS noise in an inner ROC in terms of ADC counts. Right: Geometrical distribution of the noise over the chamber surface.

References

[1] G. Augustinski et al., "Status of the ALICE TPC Time Projection Chamber", GSI Annual Report (2005) 282

[2] R. Campanolo et al., "Readout Electronics for the ALICE Time Projection Chamber", International Europhysics Conference on High-Energy Physics High-Energy Physics , Lisbon, Portugal (2005) 373.

[3] U. Frankenfeld, S. Popescu, H.R. Schmidt , "Temperature Monitoring System for the ALICE TPC", ALICE-EN-2005-001.

[4] G. Renault et al., "The Laser Calibration System of the ALICE Time Projection Chamber", Czechoslov. J. Phys. 55 (2005) 1674

[5] Technical Design Report, CERN/LHCC 2000-001

[6] J. Castillo et al., "Experience with the Goofie during the TPC Commissioning", GSI Scientific Report (2006)

[7] J. Wiechula et al., "Result from the ALICE TPC Laser Calibration System", GSI Scientific Report (2006)

[8] S. Kniege et al., "Online Monitoring for the ALICE-TPC", GSI Scientific Report (2006)

The ALICE TPC gas system: commissioning experience

C. Garabatos[1]
[1]GSI, Darmstadt, Germany

The ALICE TPC gas system fills the detector with the nominal gas mixture (Ne-CO_2-N_2 [90-10-5]) and circulates it at a small, fixed overpressure while continuously removing oxygen. It consists of several racks located at the gas building on the surface, at the plug half way down the cavern, and at the cavern. During commissioning in 2006, the TPC was in the surface, as was the so-called distribution rack. Like all other LHC gas systems, it was designed and assembled by the CERN PH/DT1 group, in close contact with the detector's gas link-person. The system is controlled by a PLC and has a PVSS user interface, both programmed by the CERN IT/CO group.

The system consists of several modules, each fulfilling one specific function: mixer, circulation, exhaust, analysis, purifier, and CO2 absorber. It can also be operated in different modes: purge, fill, run, and back-up. A pressure sensor located at the detector is used to regulate the circulation speed at the compressor module, thus keeping the TPC at a constant pressure at all times.

The first operation after connecting the TPC to the system is to fill the whole volume with CO_2. For this, the system is operated in purge mode, where a high flow (5 m^3/h) of CO_2 is circulated into the detector and exhausted after the compressor. After a few days, the oxygen content in the TPC gas is low enough to allow one to proceed with the next step.

The filling procedure consists of injecting a high flow of neon into the system while, after the compressor, removing CO_2 with molecular sieve cartridges. In this mode, the system operates in a closed loop. Two absorbers are used to remove CO_2: one is in operation while the other one is being regenerated, i.e., the trapped CO_2 is removed by heating the cartridge at 200 ^oC and pumping out the effluents. In this manner, no high-cost neon is wasted. This mode continues until the right ratio of Ne/CO_2 (9/1), as monitored with a CO_2 thermal conductivity analyser, is reached. This operation takes about 2 weeks, and its pace is driven by the regeneration time of the absorbers.

The filling procedure also allows one to estimate the total volume of the system, so that the next step can take place: in the so-called direct mode, the exact volume of N_2 is injected into the system in order to reach the final mixture.

Once the TPC is filled, the system is operated in run mode, where the gas is circulated at high flow (6 m^3/h) and cleaned with copper catalyser cartridges which remove O_2 and H_2O. These purifiers last for months under normal conditions. They are regenerated by flushing them with an Ar-H2 (noxal) mixture at high temperatures, thus reducing again the copper oxide.

At the same time, a small flow (60 l/h) of fresh, mixed gas is added in order to compensate for the gas exhausted through the analysis line and through leaks. The system holds a 1 m3 tank at a few bars pressure after the compressor, in order to store gas that might be needed if the ambient pressure increases. Whenever there is too much gas in the system, an exhaust flowmeter releases gas at 200 l/h.

Fig. 1 shows the stability of the overpressure in the TPC over one week of operation. The regulation parameters in the compressor module were optimised such that the deviations from nominal pressure are of the order of 0.01 mbar. One can observe that the pressure fluctuations are higher during day time, when the opening of the door of the TPC clean room, maintained at a slight overpressure, creates small ambient pressure fluctuations.

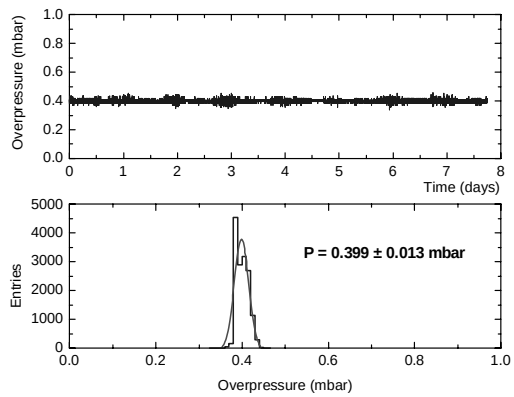

Figure 1: Time dependence of the TPC overpressure, set at 0.4 mbar. The spread, shown in the lower panel, is 0.01 mbar.

The oxygen content in the TPC was 2-3 ppm for a circulation flow a factor 3 lower than nominal. Thus, the leak rate of the device is believed to be a factor of 5 lower than specified.

The gas composition was determined by using a dedicated gas monitor detector (Goofie, see this and previous annual reports), and by analysing the gas with a gas chromatograph equipped with a double column able to separate all three TPC gases.

Failure of the gas system, e.g. due to a power cut, would issue an SMS to CERN mobile phones. In these situations the system falls into the passive back-up system, where normally opened electro-valves release CO_2 which enters the TPC if its pressure falls bellow a specified limit.

In conclusion, the first LHC gas system to be commissioned has proved to be reliable and safe.

Experience with the Goofie during the TPC commissioning

J. Castillo[1], C. Garabatos[1], and D. Antończyk[1, 2]
[1]GSI, Darmstadt, Germany; [2]University of Frankfurt, Frankfurt, Germany.

The ALICE TPC is a detector with a total volume of 88 m^2 filled with a ternary gas mixture of Ne-CO_2-N_2 [90-10-5]. To achieve its position and energy resolution requirements it is necessary to control small fluctuations in the gas composition as well as drift velocity variations [1]. A modified drift velocity monitor known as Goofie is measuring the drift velocity and also the gain. The drift velocity is obtained from the time difference between the drifting electrons produced by two emitting alpha sources, placed at known distances from a pickup detector (Fig.1).

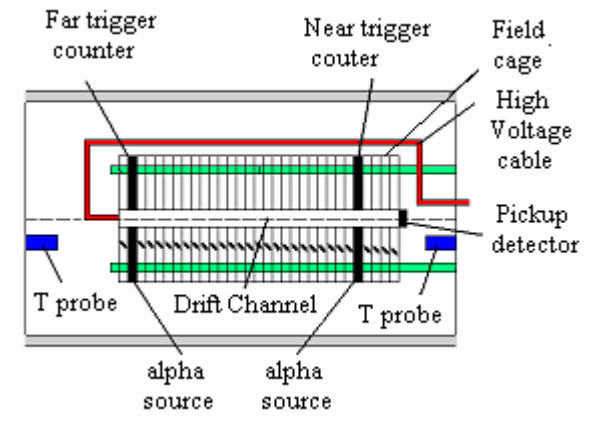

Figure 1: Layout of the Goofie, showing the position of the alpha sources, trigger counters and the pickup.

The field cage is operated at the unprecedented field of 400 V/cm [1], like in the TPC. An integrated signal of 2500 events is used for statistical considerations. The gas gain is obtained via an integration of each of the peaks of an integrated signal. Since a correlation between the gas density (T/P) and the gain and drift velocity has been proved before [1], the temperature and pressure are also recorded. The read-out board for the Goofie monitor is based on the TPC read-out front-end chain, but modified for our requirements. The signal out of three input channels (two for trigger signals, one for the pickup), trigger information and a time tag are recorded. The temperature and pressure are readout via an analogue input NI card installed directly in the PC.

During the commissioning, the Goofie was connected to one analysis line of the TPC gas system. The output events were used for creating integrated signals (2500 events) from which absolute drift velocity, gain, and a global T and P values are obtained. Once we have a significant amount of integrated signals (50) drift velocity and gain are plotted versus (T/P) and fitted with a first degree polynomial. The fit parameters are used for correcting all the subsequent data, obtaining in this way a precision of $5x10^{-4}$ in the drift velocity.

The calculation of the gas composition is based on the dependence of both drift velocity and gain on the CO_2 and N_2 fractions. The dependences lie in planes that can be fitted, and therefore a given set of values (drift velocity, gain) leads to a unique composition (CO_2, N_2). Since these dependences were calculated (using Magboltz 7.3 [2] and Garfield[3]) for another average pressure (GSI) it was necessary to shift the experimental values. The slope output of fitting lineally experimental plots of pressure versus drift velocity is used for that. Adding a constant to all pressures, new shifted drift velocity and gain were obtained. The values must be also corrected and later normalized with the central points (drift velocity and gain corresponding to Ne-CO_2-N_2 [90-10-5]). The output composition curve is shown in Fig.2. The resulting composition curve is in agreement with the real composition, while the drift velocity resolution is worse than expected, due to slight changes on the gas composition. In a future an on-line version of this method will be implemented.

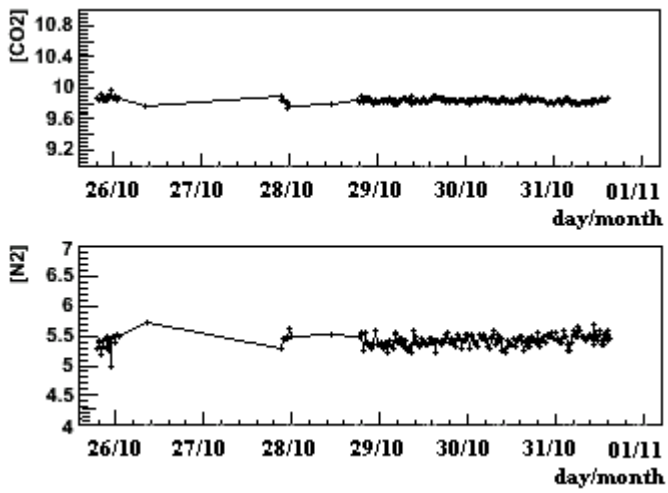

Figure 2: Calculated gas composition as a function of time during the TPC commissioning period when the Goofie was operational.

Acknowledgements

We would like to thank L. Musa, A. Junique, M. Joos, T. Morhardt and the CERN PH/DT1 group for their constant help and support.

References

[1] D. Antończyk et al., "A drift velocity monitor for the ALICE TPC", GSI Scientific Report 2004, June 2005. INSMETH-20.
[2] S.F. Biagi, MAGBOLTZ, Nucl. Inst. and Meth. A421 (1999) 234.
[3] R. Veenhof, GARFIELD, Nucl. Inst. and Meth. A419 (1998) 726.

Calibration of the ALICE Transition Radiation Detector

R. Bailhache[1] and A. Andronic[1]
[1]GSI, Darmstadt, Germany

The Transition Radiation Detector (TRD) belongs to the central barrel detectors of the ALICE experiment at the LHC at CERN. It is composed of 540 large area drift chambers, with a total of 1181952 readout pads (1728 or 2304 per chamber). To ensure the optimal performance of the detector, designed for electron/pion identification and charged particle tracking, including triggering for high-p_t electrons, a calibration procedure has been devised and tested with simulated events. Operating with a Xe-CO_2 [85-15] gas mixture at atmospheric pressure, the TRD chambers will exhibit a short-term variability in gas gain (g) and drift velocity (v_d). For these two parameters, the calibration factors will be updated per chamber at intervals of several hours. The long-term variability arises from the chamber mechanical nonuniformities and will influence the values of the gas gain and the width of the pad response function (w_{PRF}), while the time reference (t_0) is influenced by the details of signal transmission via the traces from pads to the front-end electronics. Calibration factors are foreseen in this case for each pad and the update will be done yearly. The values of g, v_d, t_0 and w_{PRF} are expected to vary, respectively, within $\pm$ 20%, 10%, 5% and 5% around their nominal values over all the detectors.

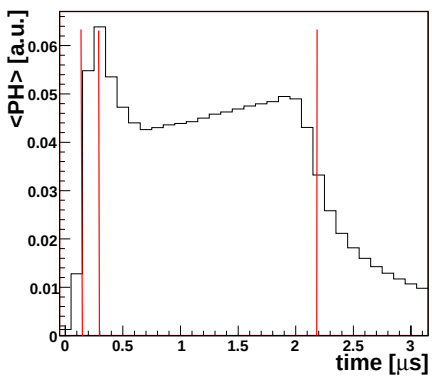

Figure 1: Average pulse height as a function of drift time. The vertical lines delimit the amplification and the drift region of the chambers.

Physics runs of pp and Pb-Pb collisions will be used to determine the calibration factors. For each chamber, or for each pad (or pad calibration group), the relevent data are accumulated in histogram, which are fitted to extract the calibration factors. For minimum bias pp (Pb-Pb) collisions, about $5{\cdot}10^4$ (10^3) and 10^8 ($2{\cdot}10^6$) events are needed to accumulate enough statistics (1000 histogram entries) for the calibration per chamber or per pad, respectively. The calibration factors are stored into the offline database to be retrieved for further iterations of raw processing.

For the gain calibration we use the deposited energy (corrected by the length of particle track), characterized by the most probable value of the energy spectrum, extracted from a fit. The drift velocity and t_0 are extracted from the average pulse height, $\langle PH \rangle$, as a function of drift time. Fig. 1 shows $\langle PH \rangle$ for simulated pions with momentum smaller than 5 GeV/c. The peak corresponds to the amplification region, where the ionization electrons from both sides of the anode wire plane are added, and is used to calibrate t_0. The plateau corresponds to the drift region of the chambers and is used to calibrate the drift velocity. The charge sharing between adjacent pads is used to achieve in the ALICE TRD a point resolution down to 300 μm [1]. The degree of charge sharing is measured by the PRF. An accurate calibration of the width of the PRF is essential to optimize the tracking capabilities of the detector.

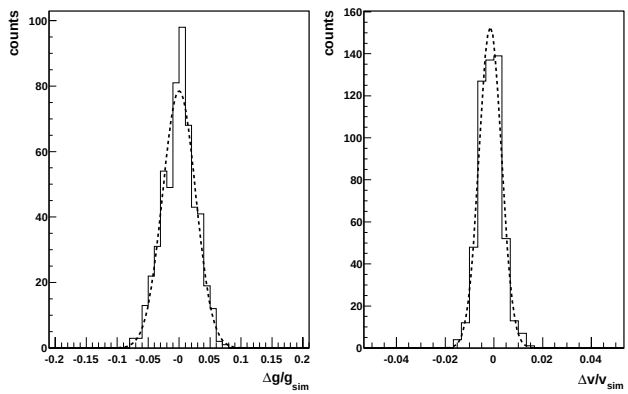

Figure 2: Accuracy of the relative gain and drift velocity calibration using the offline tracking.

The calibration procedure will run during data taking and will use the on-detector track reconstruction performed for the trigger role of the TRD [2]. Offline, the procedure will benefit from the accuracy of the global tracking in ALICE. A first test of the offline calibration procedure implemented in AliRoot [3] has been done. Fig. 2 shows the relative error between the simulated and extracted calibration factors for gain and drift velocity. The accuracies presently achieved are about 2.6% and 1%, respectively. The influence of the accuracy of the calibration on the detector performance is under study.

References

[1] C. Adler et al., Nucl. Instrum. Meth. A 540 (2005) 140.

[2] V. Angelov, Nucl. Instrum. Meth. A 563 (2006) 317.

[3] AliRoot, http://aliweb.cern.ch/offline/.

Alice TRD Manufacturing at GSI, Status of Chamber Production and Testing

G. Augustinski, J. Hehner, Ch. J. Schmidt, S. Schwab, A. Steffen and M. Träger
GSI, Darmstadt, Germany

Abstract

The Transition Radiation Detector (TRD) is one of the main detector elements of the ALICE experiment at LHC It will serve for the identification of electrons in a background of pions and additionally enhances tracking power of the overall Alice detector system.

The Alice TRD will be assembled out of 540 TRD wire chambers in 12 different sizes (+30 spares). The entire production load is distributed among fife institutions, GSI being responsible for the 152 largest modules, measuring up to 1.1 x 1.2 m^2.

During 2006, production of the first batch of chambers, comprising 60% of all chambers needed, could be finished. Production routines were backed with elaborate testing procedures that serve to establish highest quality standards for chambers released and delivered for further system integration. Statistical analysis of various characteristics has been done and will also be discussed herein.

TRD Chamber Manufacturing and Testing

A complete line of production has been set up at the GSI detector laboratory in 2005. During 2006, production-could be streamlined and brought to routine. Chambers are assembled from pre-fabricated parts like chamber side walls, various spacer ledges and the like. For each chamber, two wire planes, a cathode as well as an anode wire plane are first prepared on a specialized wire winding machine. They are then allocated and glued precisely ($\delta \sim 10\mu m$) onto the pre-fabricated chamber.

Alice TRD detector modules are designed as non serviceable, completely glue-sealed MWPC. During production, each drift chamber is tested extensively twice: Just prior to final sealing, operating potentials are applied and the chamber is inspected for potential dark currents. Dark currents, if present, can mostly be attributed to pieces of lint or dust present in the chamber and must be removed. Likewise, in this first test, gain uniformity is determined, using a mobile X-ray source or, alternatively, an ^{55}Fe radioactive X-ray source. The measurements are then employed as a guideline for corrective actions on these large wire chambers. By these means, spatial uniformity of gain to within a margin of +- 15% across the chamber could mostly be achieved. To meet these specifications caused considerable effort. The problems could be attributed to distorted chamber side walls. They disappeared with the arrival of new parts which were extruded employing different material.

Additionally a scan of very fine granularity is also performed on a line transverse to the wire orientation. Local Once neither leakage currents nor disconnected wires are detectable, a chamber can finally be sealed with glue. It is then again subjected to a final extensive testing procedure that serves as quality control prior to shipment.

Here, gain uniformity is determined for documentation purposes. Likewise, chamber gas tightness is measured through the determination of Oxygen contamination in the counting gas. Leaks detected at this stage are sealed with glue until the integral leak rate below 1 mbar l/h is attained. Finally, each chamber is continuously operated for at least 12 hours taking pulse height spectra of 55Fe X-rays. Chambers are then declared “ready for further detector integration”.

Chamber Production Status

The chamber production status at the end of 2006 is depicted in table 1.

Chamber Type	L4C1	L5C1
Ready for shipment	22	20
Shipped to IKF Frankfurt for electronics integration	8	8
Integrated into supermodule and already at the final location at LHC	4	4

Table 1

Outlook

In 2006, the TRD-project finally achieved to get the financial support for the production of the entire TRD detector system. All in all, the number of chambers to be produced at the GSI detector laboratory thus went up from 72 to 152, giving an additional 80 chambers. A second production batch is in preparation by the ALICE TRD collaboration. Several technical improvements in details realized in this batch should facilitate production. With the experience that a chamber production rate of about 1.5 per week is indeed feasible should no other unforeseen problems come up, the project will continue during all of 2007 and possibly into early spring of 2008.

References

Alice TRD Technical Design Report, CERN/LHCC 2001-021 (Oct. 2001)

Mass Test and Electronics Integration of ALICE TRD chambers at IKF Frankfurt

M. Kliemant , H. Appelshäuser , C. Blume , W. Amend , A. Fick , M. Hartig , H. Hinke , M. Kessenbrock , F. Kramer , W. Sommer , D. Wegerle , and A. Wiesenäcker
Fachbereich Physik der Universität Frankfurt

Since 2006 the IKF is one of the main production sites for the ALICE Transition Radiation Detector(TRD). In Frankfurt we build 25 ot the L0C1 chamber type. The other drift chamber types are constructed at four other production sites: at NIPNE Bucharest(Romania), at JINR Dubna(Russia), Heidelberg(Germany) and GSI. During and after the production we test the chamber quality before electronic integration. From July till December 2006, a new laboratory for the electronic integation of the TRD chambers was equipped at the IKF Frankfurt Fig. 1. The production of TDR padplanes ends in January 2007. The TRD is one of the main detectors in the ALICE experiment, the dedicated heavy ion experiment at the Large Hadron Collider(LHC) at CERN Ref. [1]. This detector is compound from 18 supermodules, each of them contains 30 TRD chambers. Each chamber has a 4.8 cm thick radiator, attached to it a gas chamber with a 3 cm long drift region and a 0.7 cm amplification gap. The induced charge is read out at the back via copper pads.

As a result of detector geometry the detector consists of 12 different chamber types. The smaler chambers have a lower number of readout chanels so the C1 chambers are fitted with eight readout boards and the C0 chambers with six readout boards, wich are build by MCM and tested in Heidelberg. All different chamber types can be equipt Ref. [3] with seven diferent types of readout boards. The readout board is a 6-layer board, which connects multichip modules. The MCM module carries a PASA and an ADC/Digital chip (TRAP). These boards have essential functions: amplifing and shaping, digitizing and sending of data. During the integration may not be none of this readout boards bent more then one percent of his length, because the board is so thin that it can't support his own weight. The slim thickness is important for a very short radiation length, to prevent the detector form secondary reactions. With some different electronic tests as pedestal-test (noise level), pulser-test and longtime stability-test we can check the performance of all MCMs on one chamber. The integration of these readout electronics and the elaborate optimisations of the noise performance done during the year 2005 are described in Ref. [2]. The most time-consuming part in the integration procedure, gluing of coling pipes on each heat generating chip Fig. 2. After gluing, each electronic test be done again, to be sure that no MCM is broken during the gluing procedure. All chambers will transfered to Münster for assembling of the supupermodules.

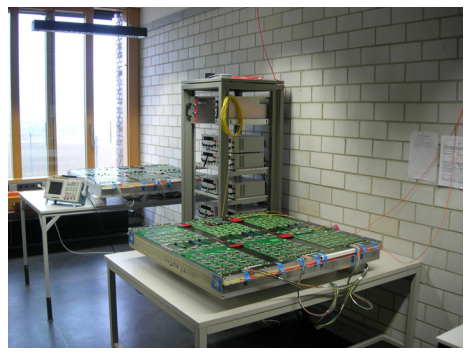

Figure 1: Electronic test stands for the ALICE TRD chambers with Pulser and low voltage suport

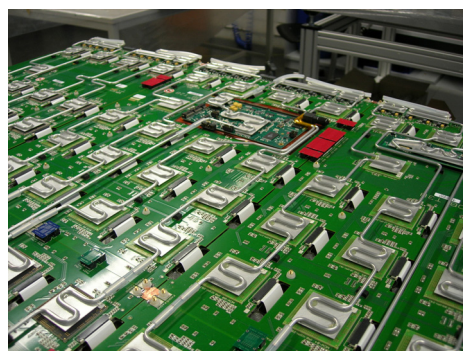

Figure 2: Cooling pipes glued on readout boards, DCS-board in background

References

[1] ALICE TRD, Technical Design Report 9, CERN/LHCC 2001-021.

[2] C.Lippmann, K.Oyama and I.Rusanov, "Electronics Integration for the ALICE TRD", GSI Scientific Report 2005, GSI Report 2006-01,p.290.

[3] I.Rusanov, J.Stachel, "The Readout Boards for the ALICE TRD", GSI Scientific Report 2005, INSTRUMENTS-METHODS-23,p.287.

Electron/pion identification with fast TRD prototypes

A. Andronic[1], H. Appelshäuser[2], V. Babkin[3], P. Braun-Munzinger[1], V. Cătănescu[4], S. Chernenko[3], C. Garabatos[1], S. Golovatyuk[3], M. Hartig[2], J. Hehner[1], A. Herghelegiu[4], M. Kalisky[1], M. Klein-Bösing[5], D. Kresan[1], C. Lippmann[1], D. Miśkowiec[1], W. Niebur[1], D. Moisa[4], M. Petriş[4], M. Petrovici[4], A. Radu[4], C.J. Schmidt[1], V. Simion[4], R.S. Simon[1], I. Rusanov[6], H.K. Soltveit[6], J. Stachel[6], F. Uhlig[1], J.P. Wessels[5], A. Wilk[5], Yu. Zanevsky[3], and V. Zryuev[3]

[1]GSI, Darmstadt, Germany; [2]University of Frankfurt, Germany; [3]JINR Dubna, Russia; [4]NIPNE Bucharest, Romania; [5]University of Münster, Germany; [6]University of Heidelberg, Germany

We report results obtained in beam tests of fast Transition Radiation Detector (TRD) prototypes. Such a TRD, envisaged for electron/pion identification, is part of the setup of the CBM detector at FAIR [1]. To cope with the envisaged rates of up to 100 kHz/cm^2, we have chosen as detectors multi-wire proportional chambers (MWPCs) of 6 mm thickness, with anode wires of 20 μm diameter with a pitch of 2 and 3 mm. Transition radiation (TR) is produced in radiators composed of polypropylene foils of 20 μm thickness (d_1), regularly spaced by a distance (d_2) of either 200 or 500 μm, with the number of foils N_f of 220 or 120, respectively. For an efficient absorption of TR, the counting gas is Xe-CO_2 [85-15]. The signals are readout on pads of 8$\times$15 mm^2 and amplified with a 16-channel ASIC preamplifier/shaper especially designed in 0.35 μm CMOS technology. The signals are sampled with a 25 MHz ADC (8 bit, nonlinear). The measurements are performed at GSI with secondary beams with momenta of 1 and 1.5 GeV/c. Two segmented scintillator detectors are used for beam definition and for rate and time-of-flight measurements. Electrons are identified with respect to hadrons using a Pb-glass calorimeter and an air-filled Cherenkov detector. The beam profile is monitored using two Si-strip detectors. The MBS data acquisition system [2] is used.

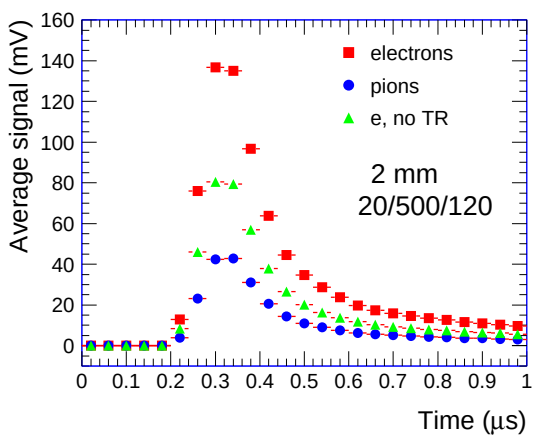

Figure 1: Average signals for pions and electrons.

An example of average signals is shown in Fig. 1 for the momentum of 1.5 GeV/c. The long tails are due to the slow-moving Xe ions created in the gas avalanche. The TR, produced only by very fast particles (γ >1000), is produced at this momentum only by electrons [3] and leads to a significant increase of the signal, which is essential for improving the electron/pion separation.

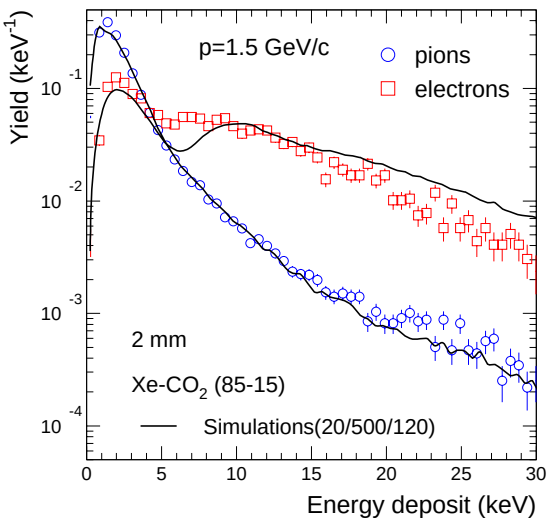

Figure 2: Measured charge spectra for pions and electrons of 1.5 GeV/c. The lines denote simulations.

In Fig. 2 we show the spectra of energy deposited in our detector for pions and electrons of 1.5 GeV/c. The Landau spectrum corresponding to the ionization energy loss (dE/dx) is, in case of electrons, complemented by the TR contribution, clearly visible in the spectrum around 10 keV. The absolute energy calibration has been done using the pion spectra with respect to simulations [4], shown in Fig. 1. These simulations reproduce very well the spectral shape for pions, but are describing the TR part only approximately. The measured TR appears to be softer than in the simulations.

The spectra measured with one layer (Fig. 2) allow us to simulate the electron identification capability of a TRD as a function of the number of layers. The results are shown in Fig. 3 for two momenta and for two radiators (characterized by $d_1/d_2/N_f$). An improvement in the e/π separation is seen at 1.5 GeV/c compared to 1 GeV/c due to the strong increase of the TR yield for electrons [3], which overcomes the relativistic rise of dE/dx of pions [4]. For higher mo-

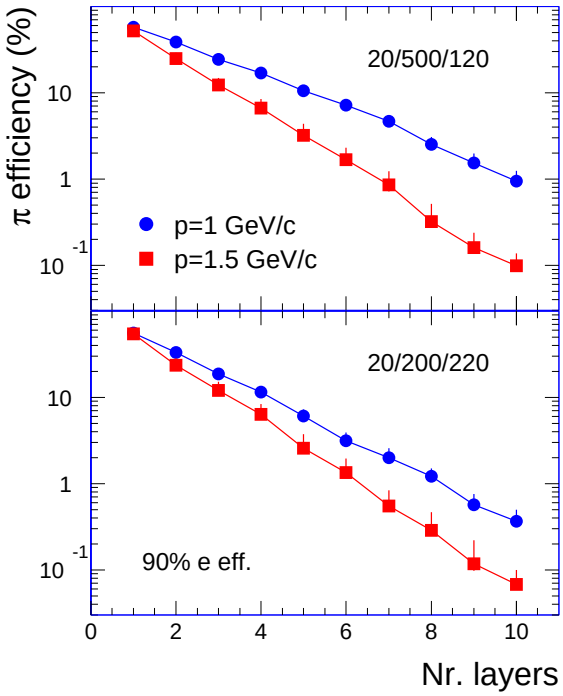

Figure 3: Extrapolated electron/pion identification performance as a function of the number of layers.

menta the e/π separation gradually degrades (a factor of 4 worse pion rejection is expected for 10 GeV/c [5]) due to the saturation of the TR yield beyond 2 GeV/c [3] and the pion dE/dx relativistic rise [4]. As seen in Fig. 3, the rejection power (expressed as π efficiency at 90% electron efficiency) is comparable for the two radiators. The radiator with larger N_f is expected to produce a larger TR yield, but it appears that its smaller foil gap (d_2=200 μm) leads to a smaller TR yield per foil compared to the radiator with d_2=500 μm. This makes the latter option a more suited choice, both because a lighter radiator is prefered in a tracking TRD (as envisaged in CBM [1]) and because of easier manufacturing and less sensitivity to foil gap nonuniformities.

In Fig. 4 we show an example of the dependence on the measured energy deposit spectra for hadrons and electrons for different local rate values. From these results we could conclude that the effect of high rates appears as pile-up, not perfectly rejected through our segmented scintillator detectors, rather than producing a reduction of the signal, expected if space charge was present.

In Fig. 5 we present the rate dependence of the electron identification with respect to hadrons as measured with one layer at the momentum of 1.5 GeV/c. While the study of e/π^- separation could only be done at low rates (10 kHz/cm^2), the high rates are achieved with a positive beam. In this case, the beam content is dominated by the protons and, due to their larger energy loss, the electron separation is in this case clearly worse. The separation is not much influenced by rate, but a degradation occurs beyond 100

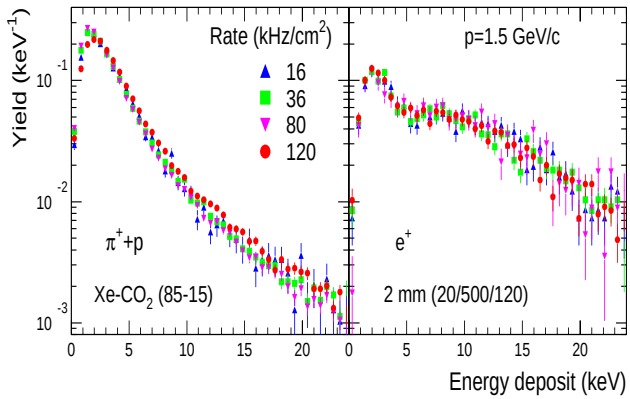

Figure 4: Energy deposit spectra for hadrons and electrons for different local rate values.

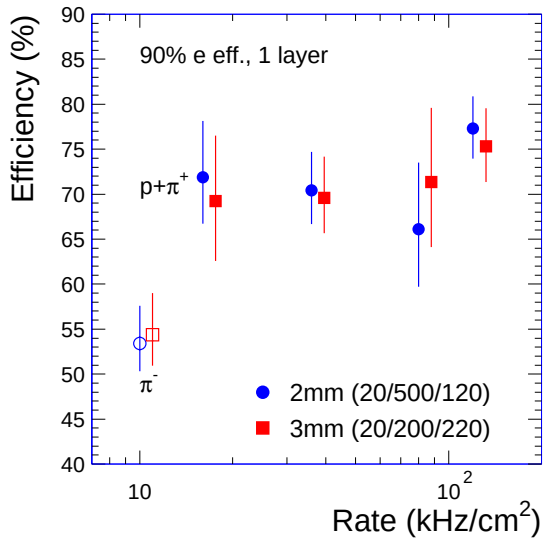

Figure 5: Rate dependence of the electron separation with respect to hadrons as measured with one layer.

kHz/cm^2. Extrapolated to 10 layers this implies a reduction of the hadron rejection by a factor of about 3 at our highest rates. The trend is similar for the detectors with anode wire pitch of 2 and 3 mm.

This work is partially funded by the EU Integrated Infrastructure Initiative Project HADRON PHYSICS under Contract No. RII3-CT-2004-506078. We acknowledge the help from G. Augustinski, M. Ciobanu, N. Kurz and Y. Leifels.

References

[1] A. Andronic, Nucl. Instrum. Meth. A563 (2006) 349.

[2] H.G. Essel, N. Kurz, IEEE Trans. Nucl. Sci. 47 (2000) 337.

[3] A. Andronic et al., Nucl. Instrum. Meth. A558 (2006) 516.

[4] A. Andronic et al., Nucl. Instrum. Meth. A519 (2004) 508.

[5] R. Bailhache, C. Lippmann, Nucl. Instrum. Meth. A563 (2006) 310.

Global Tracking Unit for ALICE TRD

J. Cuveland[1], V. Angelov[1], V. Lindenstruth[1], and F. Rettig[1]
[1]KIP, University of Heidelberg, Germany

Introduction

The ALICE TRD Detector employs 1080 optical links for data readout. The FEE chips (TRAP [1]) form a readout tree running at 8 bit 120 MHz double data rate. The tracklet and raw data are sent over the Optical Readout Interface (ORI) at 2.5 Gbit/s. The Global Tracking Unit (GTU) serves as data receiver and fast track finder and contributes to the L1 trigger decision. Finally, after L2 accept the complete event is sent optically to the DAQ.

Tracking algorithm

Tracking is performed by projecting all track segments to one virtual plane in the middle of the detector layers [2]. A track is found if the number of the tracklets in a sliding window in the virtual plane is not less than 4. The algorithm is optimized for implementation in large FPGAs.

Architecture

The GTU is built hierarchically, see Fig.1. The first stage is the TMU (Tracking Matching Unit) with 12 input optical links, a large FPGA for tracking and fast SRAM for buffering of up to 5 events. 90 such modules are connected to the 90 stacks of detector modules. Each stack consists of 6 chambers with 2 links each. The second level in the hierarchy is the SMU (concentrator board). It collects the information from 5 TMU boards or the 5 stacks in a supermodule. The 18 SMU boards send raw data to the DAQ and tracking data to the Trigger Unit Board (TRU), the final stage of the GTU. The TRU produces the TRD trigger decision and sends it to the CTP within 6.1 us after the interaction.

Developed Electronic Modules

All types of boards (TMU, SMU and TRU) have the same layout, but slightly different assembly. The first prototype was successfully tested with the first super-module as receiver of the optical links (Fig. 2). The configuration of the GTU, as well as the distribution of the BC clock and trigger is performed by DCS boards, one per SMU. The board design is close to final, some additional smaller submodules are under development.

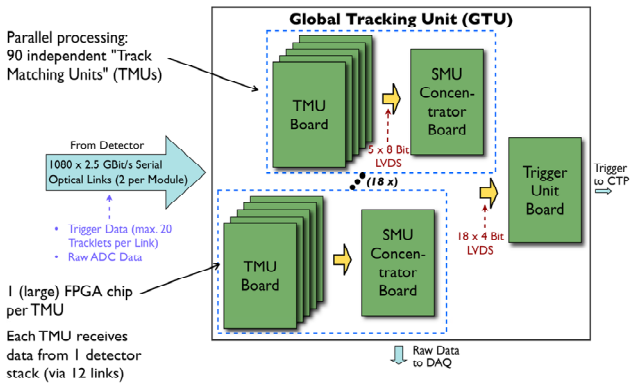

Figure 1: Global Tracking Unit (GTU) architecture.

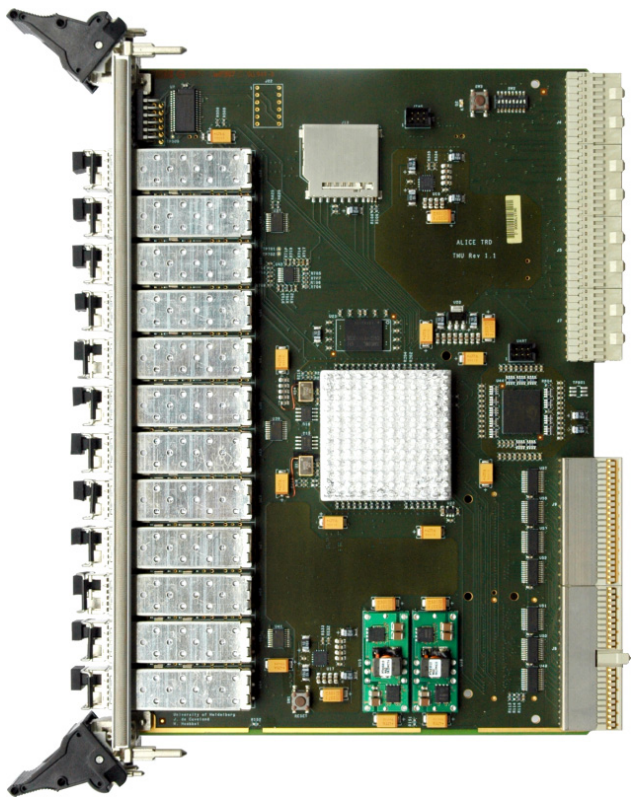

Figure 2: First prototype of the TMU. 90 of these PCBs will be used in the final setup.

References

[1] GSI Scientific Report 2004, p. 353

[2] ALICE Technical Design Report of the Transition Radiation Detector, CERN/LHCC, 2001

Construction of the First ALICE TRD Super Module

C. Adler[1], S. Altinpinar[2], A. Andronic[2], V. Angelov[3], H. Appelshäuser[4], R. Bailhache[2], A. Bercuci[2], P. Braun-Munzinger[2], C. Blume[4], V. Chepurnov[5], J. de Cuveland[3], T. Dietel[6], B. Dönigus[2], D. Emschermann[1], O. Fateev[5], C. Garabatos[2], D. Gottschalk[3], M. Hartig[4], N. Heine[6], N. Herrmann[1], M. Kessenbrock[4], V. Kiworra[3], M. Kliemant[4], T. Krawutschke[9], M.J. Kweon[1], V. Lindenstruth[3], C. Lippmann*[2], A. Marin[2], S. Masciocchi[2], J. Mercado[1], D. Miskowiec[2], K. Oyama[1], A. Petridis[8], M. Petrovici[7], S. Potirakis[8], F. Rettig[3], I. Rusanov[1], K. Schweda[1], R. Schicker[1], C.J. Schmidt[2], K. Schwarz[2], H.K. Soltveit[1], W. Sommer[4], J. Stachel[1], G. Tsiledakis[1], M. Tsilis[8], M. Vassiliou[8], W. Verhoeven[6], J.P. Wessels[6], B. Windelband[1], and Yu. Zanevsky[5]

[1]Physikalisches Institut, University of Heidelberg (Germany); [2]GSI Darmstadt (Germany); [3]Kirchhoff-Institut für Physik, University of Heidelberg (Germany); [4]Institut für Kernphysik, University of Frankfurt (Germany); [5]JINR Dubna (Russia); [6]Institut für Kernphysik, University of Münster (Germany); [7]NIPNE Bucharest (Romania); [8]University of Athens (Greece); [9]Fachhochschule Köln (Germany)

Introduction

The Transition Radiation Detector (TRD[**?**, **?**]) is one of the main detector components of the ALICE experiment[**?**] at the CERN LHC (Geneva). 18 TRD super modules will cylindrically surround the large ALICE Time Projection Chamber in the central barrel of the experiment. The TRD consists of 540 large area drift chambers and 1.18 million analog channels, which are digitized during the 2 μs drift time. 65664+5184 multi chip modules (MCMs), each equipped with a preamplifier/shaper, an ADC, digital filters and four processors, perform on-detector integrated signal processing and store and forward the event data.

The first TRD super module was constructed and delivered to CERN in 2006.

Electronics Integration and Noise Performance

The ALICE TRD is composed of large drift chambers with drift direction perpendicular to the wire planes (radial in ALICE). The drift chambers are constructed at five different production sites at NIPNE Bucharest (Romania), at JINR Dubna (Russia), at the Universities of Frankfurt and Heidelberg (Germany) and at GSI (Germany). 30 drift chambers were shipped from the different construction sites via GSI to the University of Heidelberg, where they were equipped with readout electronics and inserted into the super module hull.

Eight or six readout boards are mounted on each drift chamber, depending on the chamber type (C1 or C0). Each readout board holds 16 data taking MCMs which are directly connected to 18 readout pads each via short signal cables. Thus a C1 (C0) chamber holds 128 (96) MCMs in 16 (12) rows. The MCMs are water cooled by Al pipes running on top of each MCM. The integration of the readout electronics and the optimisations of the noise performance done during the year 2005 are described in Ref. [**?**]. Fig. **??** shows an example plot of the noise values achieved in the 128 MCMs of a C1 type drift chamber prior to installation in the super module hull. The average noise level for all drift chambers is 1.18 ADC counts (pedestal filter only), where one ADC channel corresponds to 1050 electrons. These values are very close to the expected ones and do not change significantly inside the super module.

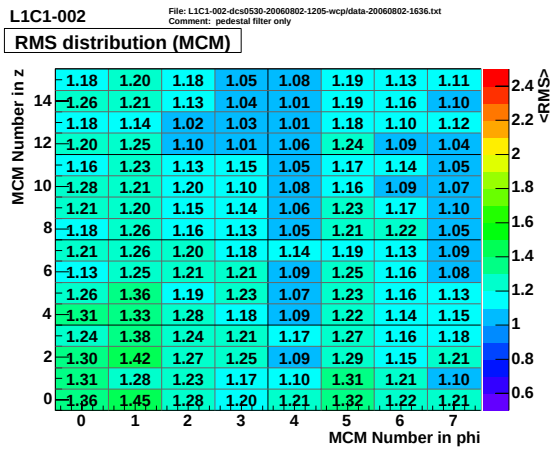

Figure 1: Noise values in the 128 MCMs of a C1 type chamber for layer one of the super module. For each MCM we show the average of 100 events, 21 ADC channels and 30 time bins. The Φ-axis runs along the wire direction across the 144 pads of one pad/MCM row. The z-axis runs along the beam axis in the ALICE experiment.

In total we suffered from 12 dead MCMs (0.32%), 127 high noise ADC channels (0.2%), adding to $12\times21+127 = 379$ unusable ADC channels (0.52%).

Super Module Assembly and Cosmics Data Readout

The 30 drift chambers are arranged inside one super module in six layers and five longitudinal (z-direction) stacks. During summer 2006, the first super module was assembled. After inserting the five chambers of one layer,

* C.Lippmann@gsi.de

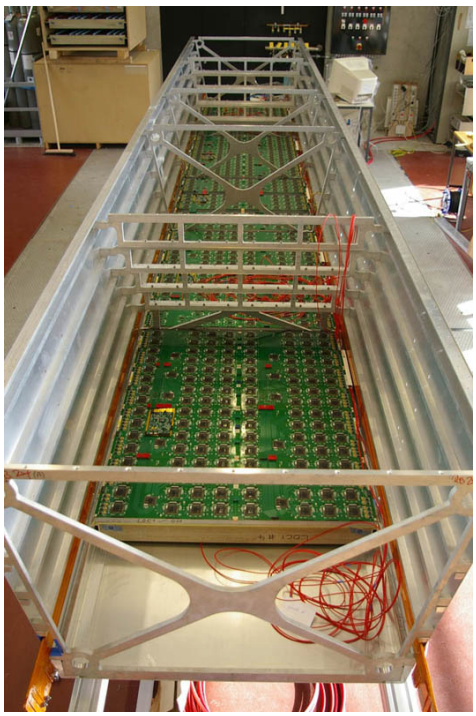

Figure 2: TRD super module hull with five drift chambers (before mounting of the cooling pipes) inserted in layer 0.

the performance of all chambers in this and the layer below was verified. Fig. **??** shows the super module with five drift chambers in layer 0.

A lot of emphasis was put on careful routing of power cables (Readout board and Detector Control System power), high voltage cables (in total 60), trigger fibers (in total 30), readout fibers (in total 60), ethernet cables and JTAG flat band cables (both for Detector Control System). Moreover 30 temperature sensors and $12 \times 6 = 72$ voltage sensors were added to the super module. The final weight of the super module is 1700 kg.

Further tests comprised a gas leak tightness test (13.5 ml/h for the full super module) and measurements of the power consumption at different trigger rates: 3323 W configured and idle, 3623 W at 1.5 kHz L1 Accept rate, and 3802 W at 150 kHz L0 Accept rate (pedestal filter only[1]).

After finalising the assembly of the super module, its performance was tested with cosmics tracks. Three scintillators were arranged so that high multiplicity cosmics events could be recorded with a rate of about two per minute. The drift chambers were filled with an Ar, CO_2 (15%) mixture and high voltage was applied by a Master/Slave distribution system specifically developed at the University of Athens, Greece (drift voltage 1450 V, anode voltage 1450 V). Fig. **??** shows one event of high multiplicity in the six drift chambers of one stack.

Super Module Installation

After transportation to CERN on September 27, the module was tested on the surface using cosmic rays before it was lowered into the ALICE cavern on October 9. The final installation took place one day later.

First beams are expected for November 2007; then two more super modules are planned to be ready. They are currently being constructed at the Universities of Frankfurt (electronics integration) and Münster (super module assembly), Germany.

[1] With tail and gain filters the values will increase slightly.

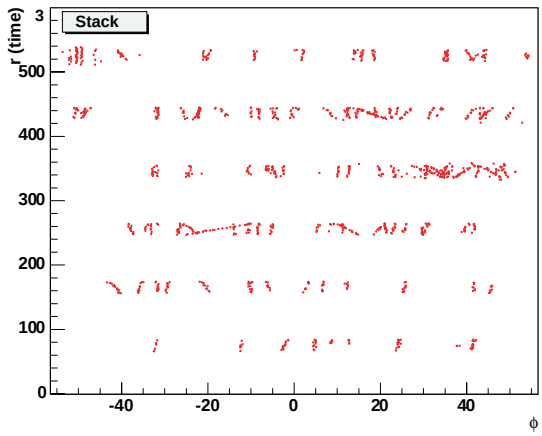

Figure 3: Cosmics tracklets in the six layers of stack three of the super module. The tracklets can be connected to form tracks. A simple reconstruction (clusterization) was applied. We show a projection of the found clusters onto the plane perpendicular to the z-axis (beam axis).

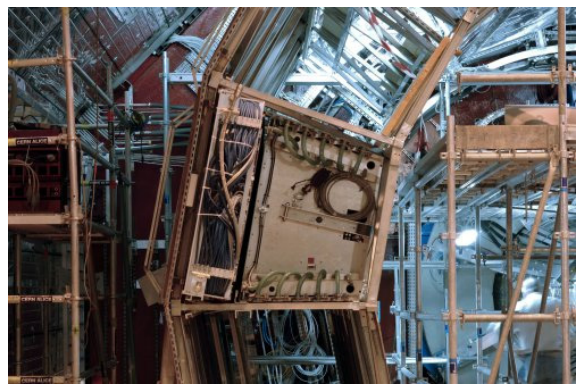

Figure 4: The first TRD super module together with a TOF module (Time Of Flight Detector, the thinner module to the left) in the *space frame* of the ALICE experiment.

References

[1] The ALICE Collaboration, "ALICE TRD Technical Design Report", *CERN/LHCC 2001-021*, ALICE TDR 9, 3 October 2001.

[2] C. Lippmann et al., "The ALICE Transition Radiation Detector", SNIC-2006-0043, Proceedings of the International Symposium on Detector Development for Particle, Astroparticle and Synchrotron Radiation Experiments (SNIC 2006), Menlo Park, California, USA, Apr. 2006. Published in eConf C0604032:0043, 2006.

[3] ALICE, A Large Ion Collider Experiment at CERN, http://aliceinfo.cern.ch/.

[4] C. Lippmann, K. Oyama and I. Rusanov, "Electronics Integration for the ALICE TRD", GSI Scientific Report 2005, GSI Report 2006-01, p. 290.

Towards high count rate, data driven Silicon strip readout electronics for CBM and other FAIR experiments*

C. J. Schmidt[1,2], K. Solvag[1,3], G. Modzel[2], H. K. Soltveit[2], S. Loechner[1], and the CBM collaboration
[1]GSI, Darmstadt, Germany; [2]Phys. Inst., Heidelberg, Germany; [3]Inst. of Phys. and Techn., Bergen, Norway;

Introduction

CBM projects a large area multi station silicon tracking station (STS) as one of its core detector systems. Due to the very high hit rates that these detectors will experience at CBM, no trigger information will be available in time to tag events of interest. Further, multi event confluence in time must be considered typical rather than exceptional. This harsh environment not only poses tough demands on front-end detector and readout technology in terms of radiation hardness but also sets the stage to a novel, purely data driven readout architecture currently under development in the EU-FP6 project DETNI [1] targeting thermal neutron scattering applications [1]. Such asynchronous, non triggered, high rates and self sparcifying front-end readout architecture cast in Silicon as a microchip is the current choice to cope with the projected challenges. CBM and GSI closely cooperate with DETNI and engaged in evaluating the first DETNI prototype microchip n-XYTER at the GSI detector lab. These studies on the 128 channel chip will then allow the development of an adapted, radiation hard, dedicated CBM-XYTER chip for the CBM Silicon Tracker System. The good adaptation to Silicon strip detectors together with the non-specialized readout has generated great interest with several major FAIR projects that see in this architecture a promising choice to satisfy their particular needs.

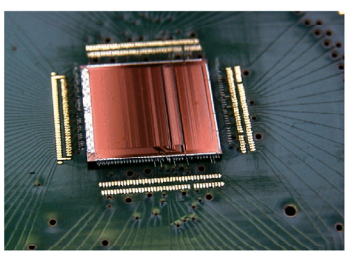

Figure 1: The n-XYTER chip

Data Driven Chip Architecture

The n-XYTER is a 128 channel front-end mixed signal ASIC design. Each channel consists of a pre-amp and two parallel shaper amplifiers, a fast one for timing and a slow one for pulse height analysis. A discriminator on the fast channel will reset a peak detector on the slow channel in time that the signal height may be detected. Simultaneously it will trigger latching a time stamp with 1ns resolution that is used to tag the data. This asynchronous opration of the front-end together with the discriminator triggered data capture is termed in short as purely data driven front-end. For every channel, both, analogue pulse height and the digital time stamp are then stored in a fifo, where it will remain until read out. Data is read out of these fifos through a token ring structure, which will un-prejudicedly read out whichever channel has data and skip non-hit channels. The chip is designed to be able to pump out data elements at an average rate of 32 MHz, each consisting of time stamp at 1ns res. and an analogue pulse height to be digitized off chip.
The n-XYTER realization shows noise figures of 1000 EMC on the fast channel (18 ns peaking time) at 30pF input capacitance, which is perfectly suited for MIP detection at standard silicon thickness. The higher resolution slow channel with a peaking time of 140ns shows noise figures of about 600 ENC at 30pF input capacitance. The comparatively high capacitance targeted is at the expense of power. For the neutron application a non-issue, power is an important specification for a CBM version of the chip. Excessive capacitance specifications can either be used to handle longer strip detectors, otherwise it could be invested in long connecting wires from silicon to front end allowing to remove necessary cooling infrastructure from within the detector.

Towards the CBM-XYTER

The chip is currently under careful investigation at the GSI-detectorlaboratory. No flaws could be revealed so far. With the slow control operative, the architecture can now be explored in depth. After the current tests on isolated functionality, the chip will then be operated with an intelligent, more complex FPGA-based readout board. It will then finally be used to set up a silicon strip detector test system. The analogue and digital tests as well as the the detector system tests will be employed to formulate modifications that address the specific needs of CBM.

References

[1] NIM A, 568 (2006), 301-308

* Work supported by EU-FP6 HADRONPHYSICS (see Annex) and EU-FP6 NMI3 DETNI
[1]DETNI is a JRA of NMI-3 focussed upon neutron det. development

Test of Transition Radiation Detectors for high rate environments

C. Garabatos[1], D. González-Díaz[1], A.Kalweit[2], F. Uhlig[1], and the CBM Collaboration
[1]GSI, Darmstadt, Germany; [2]TU Darmstadt, Darmstadt, Germany

Motivation

For the planned Compressed Baryonic Matter (CBM) experiment prototypes of Transition Radiation Detectors (TRD) were developed and tested. The TRD will be used for particle tracking and identification of high energy electrons and positrons for J/Ψ reconstruction.
Due to the fixed target geometry of the CBM experiment (see . Friese et al.,this report) particle rates of 100 kHz/cm^2 are expected for the innermost part of the first TRD station. At this rates a reduction of the effective gas gain of the TRD may appear due to build up of charge in the counting gas. Since the electron id is based on the signal amplitude, it is important for the TRD that the gain stays constant up to the highest expected particle rates. We present here results on this issue. The tested prototypes are very thin MWPC with an anode-cathode distance of only 3mm and a anode-wire pitch of 2mm with pad readout. This design is a compromise between the requirement of fast signals on the one hand and the necessity to absorb transition radiation photons on the other hand.

Setup

The measurements are performed using a X-ray tube to produce photons of an energy of 8keV which is calibrated using a ^{55}Fe source. The produced X-ray beam is collimated and attenuated with different sets of aluminum or nickel foils before entering the prototype. The size of the beam spot on the detector was measured to be 0.756 cm^2 using a Polaroid film. The gas gain is defined as

$$G = \frac{N_{e^-_{final}}}{N_{e^-_{primary}}} = \frac{I}{N_{e^-_{primary}} \cdot q_{e^-} \cdot R} \qquad (1)$$

where R is the absorbed photon rate in the detector, I the measured current and Ne the number of primary electrons produced by the X-ray photon. This number is taken from measured data [1].

Results

Figure 1 shows the measured gain as a function of the rate for a Xe-CO_2 mixture at different initial gains. The gain decreases with increasing rate due to the space-charge effect, which results in the screening of the electric field near the anode wire thus affecting the gain. The solid lines are a fit to the data using Mathieson's formula [2]

$$\ln(G/G_0)/G = KR \qquad (2)$$

where G_0 is the gain at zero rate and K is a constant which takes into account the chamber geometry and the gas properties.

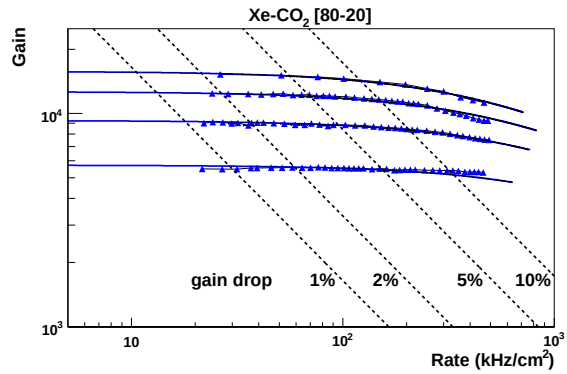

Figure 1: Gain as a function of the rate for measurements at different initial gains.

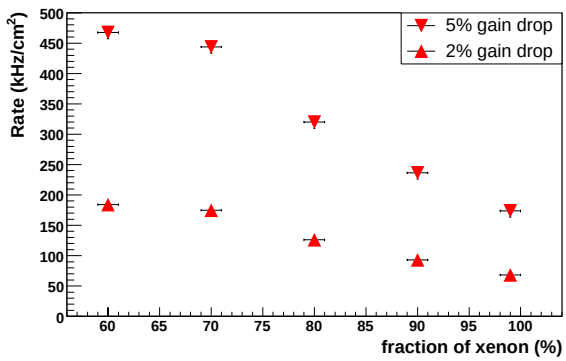

Figure 2: Rates at a gain drop of 2% and 5% and an initial gain of 5000.

Since the space-charge effect depends on the total charge in the chamber, the gain drop depends on both the initial gain and the rate. The dotted lines in Fig. 1 show constant gain drops as a function of the rate.

The energy loss of a traversing particle is smaller than the energy loss of a X-ray photon. Since in the CBM experiment the majority of particles passing the TRD will be minimum ionizing one has to calculate the rate of minimum ionizing particles which will produce the same energy loss than the X-ray photons in the test. This rates are shown in fig. 2 for different gas mixtures at an initial gain of 5000.

References

[1] F. Sauli, "Principles of operation of multiwire proportional and drift chambers", CERN 77-09 (1977) (Yellow report)

[2] E. Mathieson and G.C. Smith, Nucl. Instrum. Meth. A316 (1992) 246

Modelling of the architectural studies for the PANDA DAT system *

K. Korcyl[1], W. Kuehn[2], J. Otwinowski[1], P. Salabura[1] and L. Schmitt[3]
[1]Jagiellonian University, Krakow, Poland; [2]Giessen University, Giessen, Germany [3]GSI, Darmstadt, Germany;

We used a SystemC modeling platform [1] to investigate candidate architecture for the PANDA data acquisition and trigger (DAT) system. The system has to operate without a central trigger signal; instead a global clock will be distributed to the detector front-ends and used to mark the data [2]. The considered architecture is presented in Figure 1. The Detector Concentrator Boards (DCB), housing buffers with detector data, connect via switched networks, to farms of computing nodes, constituting three levels of the filtering system (L1, L2, L3).

The first level operates in push mode: the DCBs initiate the transfer of the time-stamped data. Only objects

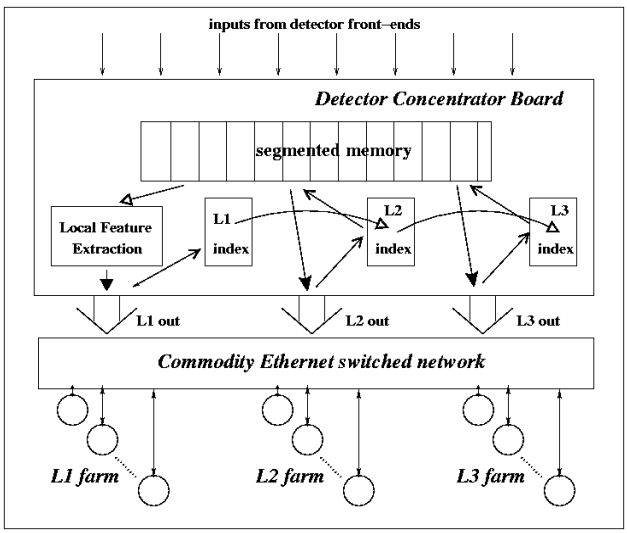

Figure 1. Investigated architecture

found in the Local Feature Extraction process are sent to L1 significantly reducing bandwidth and rate requirements. The DCBs use time stamps from the data to create the destination address of a L1 processing node. In this way all data with the same time-stamps will be sent to the same processing node. The range of time-stamps sent to the same destination can be adjusted to avoid congestion in the network (in our model we assumed 600 ns). The L1, after a fixed delay allowing for various detector characteristics and fluctuating network load, starts to correlate data. To keep the L1 latency constant we plan to execute only simplified algorithms (using FPGA based computing nodes) and leave more complicated processing for the higher levels. Only positive decisions from L1 assigning event numbers to time-stamps are broadcast to the DCBs and are sent together with L1 processing results to L2.

L2 operates in pull mode and may request sequentially from various DCBs more complete data if needed to make a decision. In this way, the requirements for bandwidth and rate are reduced. L3 performs event building for the interesting time stamps by collecting data from all the DCBs.

The DCB is the central component of the architecture, where the time stamped data from a number of front ends are received and kept during the filtering process. The main memory is segmented and the segments are released for new data when the L1 latency expires or negative decisions from the higher levels arrive. The references to segments with data are kept in internal structures indexed with time-stamps (L1) or event numbers (L2, L3). Positive decisions received by the DCBs will move references to higher level structures (L1-3 index), protecting segment data from being overwritten. Each board is equipped with three high speed links (10Gbps) to communicate with the levels of the filtering system.

In Figure 2 we present first results from modelling. The simplified setup consisted of 5 DCBs receiving data from 5 PANDA detectors with negative exponential distribution with 100 ns average (corresponding to 10 MHz interaction rate). Only 5% of the data were sent to L1 (20-

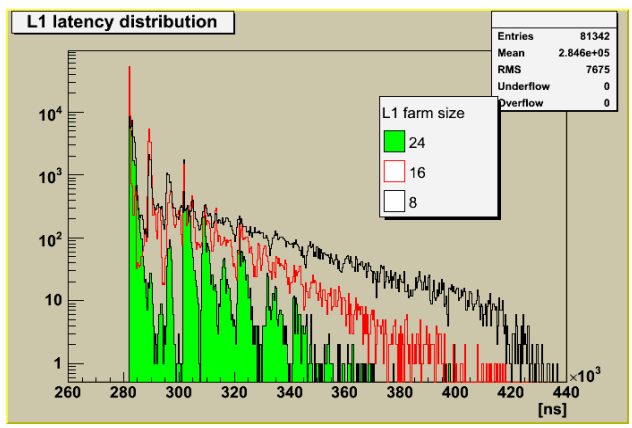

Figure 2. L1 latency distribution as function of the L1 farm size

fold reduction was assumed in local feature extraction). We used 240 µs fixed L1 delay after which 40 µs processing was started. In the figure we plot distribution of times when the positive L1 decision were received at the DCBs. As an example we show scalability of the architecture and various curves in the Figure 2 represent distributions for a variable number of the L1 processing nodes

References

[1] SystemC modelling platform; http://systemc.org.
[2] PANDA Technical Progress Report 2005

* Work supported by EU grant RII3-2004-506078

DIRC-Radiator tests for the PANDA Experiment at GSI*

G. Schepers[1], K. Götzen[1], J. Lühning[1], H. Orth[1], W. Quick[1], C. Schwarz[1], C. Sfienti[1], K. Peters[1,2], K. Dietrich[3], and A. Dikova[4]

[1]GSI, Darmstadt, Germany; [2]Johann Wolfgang Goethe-Univ. Frankfurt, Germany; [3]Univ. Hamburg, Germany; [4]Univ. Sofia, Bulgary

One of the PID-subdetectors of PANDA is a DIRC detector. With a DIRC (Detection of Internally Reflected Cherenkov photons) detector the velocity of relativistic charged particles will be measured via the determination of the angle of the Cherenkov cone. The installation of a test setup for the radiator materials and first results are reported.

Tests with laser light of different wavelengths showed that the intensity strongly depends on the laser temperature. Thus a temperature isolated and light tight box was built that includes a controlled heating system and surrounds the optical breadboard with the laser, two diodes and the radiator to be tested. The latter and one of the diodes are mounted each on two linear x-y-sledges.

To qualify and find the best radiator for the DIRC detector two main properties of the radiator material have to be tested, i.e. the percentage of Cherenkov photons lost on the way to the photon detector and the accuracy of the Cherenkov angle conservation. The observables are the absorbtion length and the internal reflection coefficient - a measure for the surface roughness - and the material homogenity.

With the stabilization of the temperature beeing better than 0.2°C the accuracy of the measurement of the intensity of the laser light was brought to an accuracy of better than 1 permille. Radiator materials were investigated, i.e. a bar from acrylic glass and a bar from fused silica (quartz). The quartz bar ($800mm \times 35mm \times 17mm$) has such a large absorbtion length that it couldn't be measured with this setup. The absorbtion length of the acrylic glass bar ($900mm \times 35mm \times 17mm$) was determined to be 10m for the red laser line at 635nm.

As a simple optical test a photo was made of millimeter patterns through both the radiators under investigation. The figure 1 shows about 40 reflexions in the quartz bar (top) and in the acrylic glass bar (bottom). The latter reveals clearly that this sample of casted acrylic glass is not suited to conserve the Cherenkov angle information.

Therefore the search for alternative materials to replace expensive fused silica radiators will be focused on extruded acrylic glass samples.

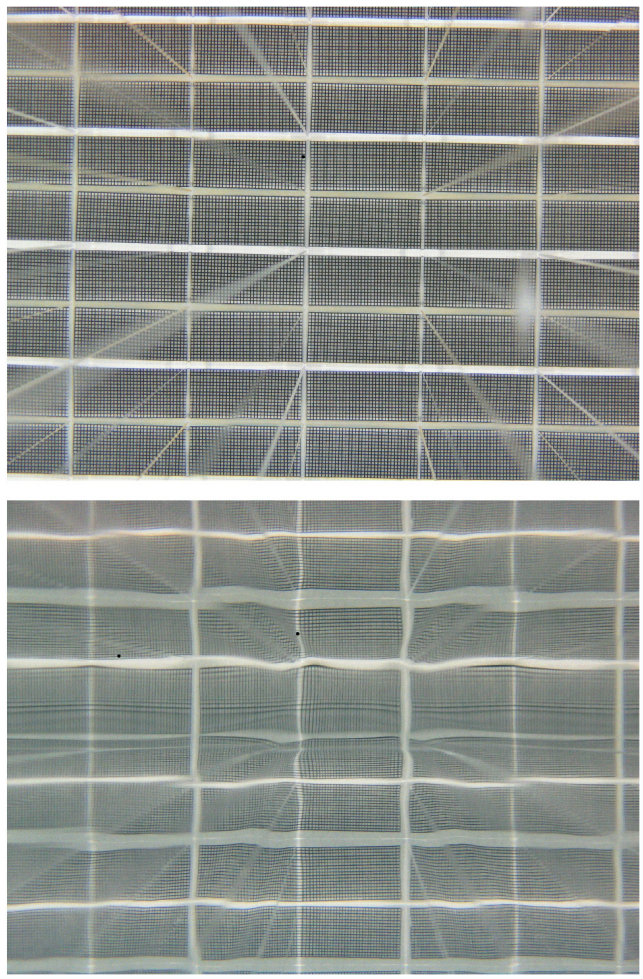

Figure 1: A picture of the internal refelexions in the quartzbar (top) shows the quality of the bar and reveals an unperfection at one of the edges. The picture of the acrylic glass bar (bottom) exposes unhomogenities in the material density.

References

[1] G. Schepers et al., Scientific Report 2005, "Towards a DIRC-Detector for the PANDA Experiment at GSI", 2005

* Work supported by the European Community RESEARCH INFRASTRUCTURES ACTION under the FP6 programme: Structuring the European Research Area - Specific Support Action - DESIGN STUDY (contract 515873 - DIRACsecondary-Beams)

Research programme in atomic physics, plasma physics and materials research

First experiments with the new ESR in-ring Reaction Microscope – Ionization dynamics in fast heavy-ion atom collisions*

D. Fischer[1,#], R. Moshammer[2], S. Hagmann[3,5], T. Ferger[2], M. Gudmundsson[1], K. Kühnel[2], M. Schäfer[2], M. Nofal[3], H. Bräuning[3], C. Brandau[3], C. Kozhuharov[3], Th. Stöhlker[3], G. Lanzanó[6], E. de Filippo[6], H. Rothard[4], and J. Ullrich[2]

[1]Stockholm University, Sweden, [2]Max-Planck-Institut für Kernphysik, Heidelberg, Germany, [3]GSI, Darmstadt, Germany, [4]GANIL, Caen, France, [5]IKF, Universität Frankfurt, Germany, [6] INFN, Catania, Italy.

When relativistic highly charged ions pass atoms at even large distances, outside their electron clouds, the target is exposed to the shortest (sub-attosecond) and most intense (more than 10^{20} W/cm^2) electromagnetic pulses available in laboratories. Thus, these "flashes of virtual light" represent a unique tool to study the many-particle quantum-dynamics of atomic systems on a time scale which is typically much shorter than the classical revolution time of bound electrons. Under these conditions, using a simple physical picture, the ionization process can be viewed as a weighted projection of the electronic bound state momentum distribution of the target onto the continuum, thus sensitively depending on the correlated many-electron initial state wave function. In order to enable such experiments, a fully equipped Reaction Microscope was installed at the gas-target section of the ESR at GSI, the first one in a storage ring world-wide. The technique allows to record kinematically complete data sets by detecting all target fragments (electrons and the recoil ion) ejected in an atomic or molecular collision (for an overview see [1]) and has been successfully applied in various campaigns at the UNILAC [2, 3]. Compared to these single-pass experiments the advantages in the ring are numerous: The very high projectile charges and velocities available at the ESR and the huge luminosity in combination with superior vacuum conditions enable to investigate multiple electron transitions and reactions with very small cross sections in unprecedented detail.

In a first commissioning experiment in December 2006 single and multiple ionization of neon and argon targets by 230 AMeV U^{90+} was investigated. In Fig. 1 the recoil ion time-of flight spectrum of argon ions is shown, which was obtained by measuring emitted electrons and recoiling target ions in coincidence. Up to 8-fold ionization of argon was observed and up to three electrons were measured in coincidence in this run.

In this pioneering experiment, the achieved momentum resolution, which is crucial to separate random coincidences and to identify different collision mechanisms, was between 1 and 2 a.u. for the recoil ions, about one order of magnitude worse than it was in earlier experiments. This can mainly be attributed to the rather large thermal and spatial spread of the ESR gas-jet and work is in progress to reduce the target temperature for the upcoming beam times. For the electrons, which were recorded at extremely low background contributions, short projectile pulses provided by the ESR (bunch-length below 5 ns) enabled us to achieve an excellent momentum resolution of 0.1-0.2 a.u.. A detailed analysis of the data is still in progress, but already within this first experiment the full operational capability of the newly installed in-ring Reaction Microscope could be demonstrated.

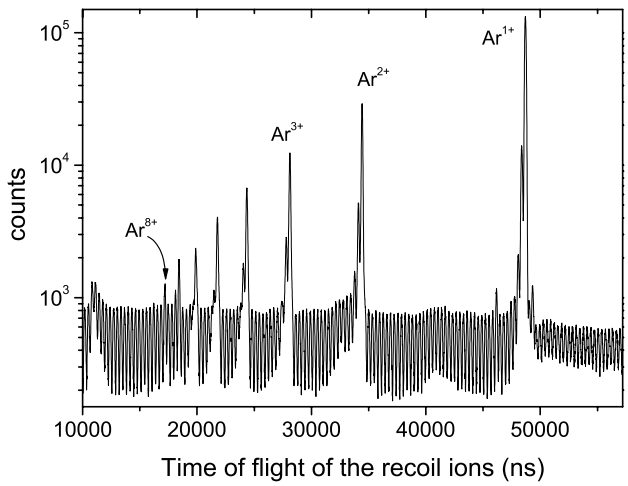

Figure 1: Time-of-flight spectrum of Ar ions created in collisions with 230 AMeV U^{90+} projectiles.

Within the extended 2007 experimental campaign, with improved resolution, we will exploit the manifold opportunities of the setup. On the one hand, as indicated above, correlated electronic ground states of atoms and molecules shall be explored and many-electron dynamics in relativistic collisions will be studied for the first time. Moreover, by investigating transitions, where the projectile charge is changed as well, like in simultaneous target and projectile ionization or in radiative as well as resonant electron transfer reactions (REC and RTE), spectroscopic information about the structure of the highly charged projectile can be obtained. By measuring the transverse momentum transfer to the target core, the impact parameter dependences of all these processes become accessible. In combination with the ESR forward electron spectrometer [4] a further increase of the versatility is reached, enabling to explore coincidences with fast emitted electrons.

References

[1] J. Ullrich et al., Rep. Prog. Phys. **66** (2003), 1463
[2] H. Kollmus et al., Phys. Rev. Lett. **88** (2002), 103202
[3] R. Moshammer et al., Phys. Rev. Lett. **83** (1999), 4721
[4] S. Hagmann et al., NIM B 205 (2003), 207

* Work supported by EU, EURONS contract No. 506065.
# fischer@physto.se

Enhancements for the Test of Time Dilation at the ESR

C. Novotny[1], B. Bernhardt[2], C. Geppert[3], G. Gwinner[4], T. W. Hänsch[2], R. Holzwarth[2], G. Huber[1], S. Karpuk[1], H.-J. Kluge[3], T. Kühl[3], W. Nörtershäuser[1,3], S. Reinhardt[5], G. Saathoff[5], D. Schwalm[5], M. Steck[3], T. Udem[2], and A. Wolf[5].

[1]Johannes Gutenberg-Universität Mainz, D-55128 Mainz, Germany; [2]Max-Planck-Institut für Quantenoptik, D-85748 Garching, Germany; [3]Gesellschaft für Schwerionenforschung, D-64291 Darmstadt, Germany; [4]University of Manitoba, Winnipeg, Manitoba, R3T 2N2, Canada; [5]Max-Planck-Institut für Kernphysik, D-69029 Heidelberg, Germany

Lorentz Invariance

The core of special relativity (SR) as a theory of local spacetime is Lorentz invariance, which is one of the most fundamental symmetries of all modern descriptions of nature. Because of this fundamental role there is much interest in experimental tests of SR.

Any deviation from SR would violate the Einstein relativity principle and can be e.g. described by a kinematical test theory (MS) [1, 2]. In the framework of this theory the time dilation effect can be used to probe the Lorentz invariance via the optical Doppler effect (so called Ives and Stilwell (IS) type experiments) [3]. Here the Doppler-shifted frequencies $\nu_{a,p}$ are compared with the rest frequency ν_0 of a moving clock. In SR, these frequencies are given by the relativistic Doppler-formula $\nu_{a,p} = \gamma_{SR}(1\pm\beta)\nu_0$, where the Lorentz factor γ_{SR} appears as a direct consequence of time dilation. The MS test theory parameterize possible deviations of time dilation by introducing a test parameter α by $\gamma = \gamma_{SR}\,(1 + \alpha\beta^2 + \ldots)$.

Storage Rings and Time Dilation

Since storage rings provide ion beams of superb quality at high velocities they allow for IS experiments with increased sensitivity. In the last decade time dilation was probed at the test storage ring (TSR) at the Max-Planck-Institut für Kernphysik in Heidelberg using metastable $^7Li^+$ ions. There an upper bound of $\alpha < 2.2 \times 10^{-7}$ has been achieved (at an ion velocity of 6.4%c) [4], which could most recently be lowered by another factor of about 2 [5]. Further improvements of this limit, however, will require higher ion velocities which are available at the ESR.

Feasibility of the time dilation experiment at the ESR with an ion velocity of v = 34%c (59MeV/u) was recently demonstrated: The lifetime of the metastable ions in the storage ring was close to the natural lifetime of the metastable state and a Doppler width of the velocity distribution of $\delta\nu$ = 1.09 GHz ± 0.08 GHz was observed (see Figure 1). But it turned out that the amount of stored ions in the metastable state is at most 0.1% of the total beam (and therefore in the range of $< 10^5$ ions).

The laser systems for parallel and antiparallel excitation of the $^7Li^+$ ions have been established. The high ion-velocity induces a Doppler-shift in the parallel excitation scheme to λ_p = 386 nm. To reach this wavelength, a laser system was developed, that consists of a frequency-doubled cw Ti:Sa laser. With an output power of about 1W from the Ti:Sa laser, the frequency-doubled light power in the ESR will be in the mW range. The 386 nm light is guided with a 20 m photonic crystal fiber to the ESR. For anti-parallel excitation, a laser system consisting of a second cw Ti:Sa laser (also pumped with another Nd:YAG laser) at a wavelength of λ_a = 780.2 nm was installed. The laser light is guided to the ESR incoupling window via a 50 m polarization-maintaining-fiber. The frequency determination of both laser systems is realised with a frequency comb synthesizer. The idea for the time dilation experiment is to simultaneously stabilize both lasers (λ_f = 771.5 nm and λ_a = 780.2 nm) to different modes of the comb. This provides the laser frequencies to an accuracy of about 200 kHz.

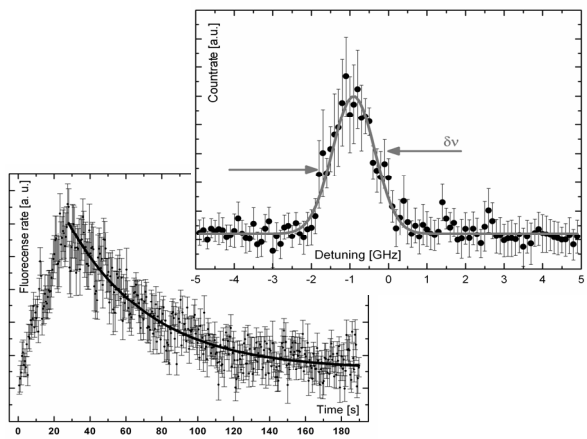

Figure 1: upper right box: velocity distribution (in terms of frequency detuning) of the metastable ions in the ESR lower left box : Life time of the metastable ions in the ESR.

For the control of the laser-laser-ion-beam overlap in the ESR, an additional observation window at a distance of six meters from the fluorescence detection region has been installed. This window has further advantages since fluorescence detection at a different position in the ESR offers the chance to gain information about systematic effects in the ring.

References

[1] H.P. Robertson, Rev. Mod. Phys. 21, 378 (1949)
[2] R. Mansouri and R. U. Sexl, Gen. Relativ. Gravit. 8, 497, 515 and 809 (1977)
[3] H. E. Ives and G. R. Stilwell, J. Opt. Soc. Am. 28 215-226 (1938)
[4] G. Saathoff *et al.*, Phys. Rev. Lett. 91 190403-(1-4) (2003)
[5] S. Reinhardt, PhD-thesis, Univ. Heidelberg (2005)

Accurate X-Ray Spectroscopy with FOCAL*

H.F. Beyer† [1], D. Attia[2], D. Banaś[3], K. Beckert[1], J. Bojowald[4], F. Bosch[1], S. Chatterjee[1], J.-Cl. Dousse[5], E. Förster[6], A. Gumberidze[1], S. Hagmann[1], S. Heß[1], J. Hoszowska[7], P. Indelicato[2], P. Jagodziński[3], H.-J. Kluge[1], Chr. Kozhuharov[1], E.-O. Le Bigot[2], D. Liesen[1], X. Ma[8], B. Manil[9], I. Mohos[4], F. Nolden[1], M. Pajek[3], U. Popp[1], D. Protić[4], R. Reuschl[1], J. Rzadkiewicz[1], A. Simon[10], A. Simionovici[11], J. Slachetko[5], U. Spillmann[1], Z. Stachura[10], M. Steck[1], Th. Stöhlker[1], S. Tachenov[1], M. Trassinelli[1], A. Warczak[10], O. Wehrhan[6], and E. Ziegler[7]

[1]GSI, Darmstadt, Germany; [2] Lab. Kastler Brossel, Université P. et M. Curie, Paris, France; [3]AS, Kielce, Poland; [4]Institut für Kernphysik, FZ Jülich, Germany; [5]Université Fribourg, Switzerland; [6]Inst. für Optik und Quantenelektronik, F. Schiller-Universität, Jena, Germany; [7]ESRF, Grenoble, France; [8]Institute of Modern Physics, Lanzhou, China; [9]CIRIL-GANIL, rue Claude Bloche, Caen, France; [10]Institute of Physics, Jagiellonian University, Cracow, Poland; [11]Laboratoire de Sciences de la Terre, ENS, Lyon, France

The twin crystal-spectrometer assembly, Bi-FOCAL, operated in the FOcusing Compensated Asymmetric Laue geometry [1] has been arranged for accurate x-ray spectroscopy at the ESR gas jet as schematically depicted in figure 1. The goal of this experiment, conducted in a joint effort with the development of suitable calorimetric low-temperature detectors [2] is the measurement of the $1s$ Lamb shift in a heavy one-electron ion as a test of QED in the domain of strong fields.

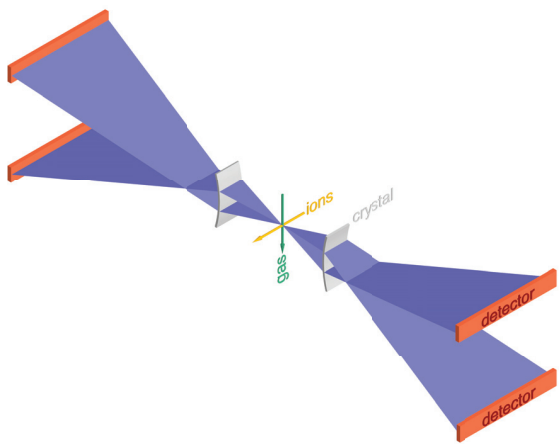

Figure 1: The Bi-FOCAL crystal spectrometer arrangement at the ESR gas jet.

In March 2006 the two kinds of spectrometers were successfully operated together during a beam time using bare Pb^{82+} ions in the ESR at a velocity corresponding to $\beta \approx 0.59$. In this run one of the FOCAL spectrometers was equipped with a new two-dimensionally position-sensitive Ge strip detector [3]. The latter has a 250 μm $\times$ 1167 μm pitch structure where the fine strips were oriented horizontally, *i.e.* perpendicular to the dispersive direction. It was demonstrated that the newly developed crystal optics [4] in concert with the position sensitive detector can cope with the low count-rate situation encountered. Background could be effectively reduced, *first* by proper shielding facilitated by the existence of a polychromatic focus and *secondly* by making use of the time and energy resolving capabilities of our detectors.

Figure 2 shows a two-dimensional image of the Lyman-$\alpha_{1,2}$ doublet of hydrogen like Pb^{81+}. The slanted lines observed for the first time are the experimental proof of the underlying x-ray-optical design. This way spectral resolving power can be retained also for fast moving sources. Coming in pairs the x-ray optics will provide Doppler cancellation capabilities. To take full advantage of these features for the next run, a second 2D detector is presently under construction. Further improvements concentrate on the long-term mechanical stability of the system required for the high accuracy demanded.

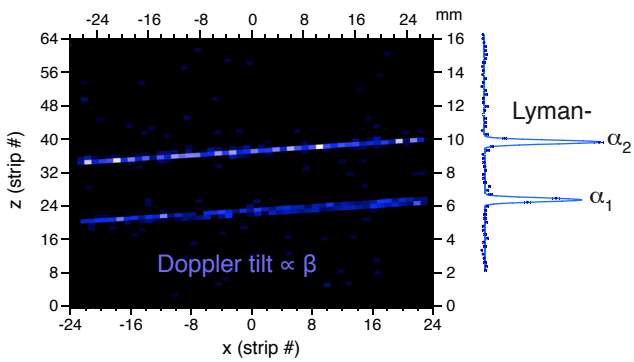

Figure 2: Lyman-α doublet of Pb^{81+} recorded with the new 2D Ge strip detector.

We thank W. Brüchle and the Institut für Kernchemie in Mainz and B. Lommel, B. Kindler and the GSI target lab for helping with the preparation of calibration sources and for the assistence in glueing our silicon crystals.

References

[1] H. F. Beyer, Nucl. Instrum. Methods. A**400** (1997) 137.

[2] P. Egelhof *et al.*, this scientific report.

[3] D. Protić *et al.* IEEE Trans. Nucl. Sc. **52** (2005) 3194.

[4] H.F. Beyer *et al.*, Spectrochimica Acta **B 59** (2004) 1535.

* Work supported by EU, Marie Curie Fellowship Programme IHP under contract number HPMT-CT-2000-00197 and EURONS contract No. 506065. D. Banas acknowledges the support by the Polish Ministry of Education and Science under Grant No. 1P03B00629.

† h.beyer@gsi.de

Study of the 2E1 Decay in He-like Tin

S.Trotsenko[1,2], A.Kumar[1,6], D.Banas[3], H.Beyer[1], H.Bräuning[1], A.Bräuning-Demian[1], A.Gumberidze[1], S.Hagmann[1,2], S.Hess[1,2], P.Jagodziński[3], C.Kozhuharov[1], M.Nofal[1,4], R.Reuschl[1,2], S.Salem[1,2], U.Spillmann[1,2], Th. Stöhlker[1,2], M.Trassinelli[1,5], L.Tribedi[6], A.Volotka[7,8], and G.Weber[1,9]

[1]GSI, Darmstadt, Germany; [2]IKF, Univ. of Frankfurt, Germany, [3] Swietokrzyska Academy, Kielce, Poland, [4]MPI, Heidelberg, Germany; [5]École Normale Supérieure, CNRS, Univ. Pierre et Marie Curie-Paris 6, France; [6]Tata Institute of Fundamental Research, India; [7]Institut für Theoretische Physik, TU Dresden, Germany, [8]Department of Physics, St. Petersburg State Univ., Russia; [9]Univ. of Heidelberg, Germany

K-shell ionization of Li-like high-Z projectiles occurring in ion-atom collisions has been found recently to be a highly selective mechanism for the population of singly excited states (1s2s) in He-like ions [1,2]. They decay to the ground state via M1 (2^3S_1-1^1S_0) and 2E1 (2^1S_0-1^1S_0) transitions (Fig. 1). Most important, this process allows one to measure the undistorted two-photon energy distribution for the 2E1 decay of the [1s2s] ($^1S_0$) state, which is of particular interest for a decisive test of theoretical predictions. A study of the two-photon decay along the isoelectronic sequence of He-like ions probes uniquely our understanding of the interplay between relativistic effects and electron electron corrections on the structure of simple few-electron atomic systems. Extending our previous experiment on He-like uranium to the medium Z regime, we present here first data of the two-photon decay energy distributions in He-like tin (Z=50).

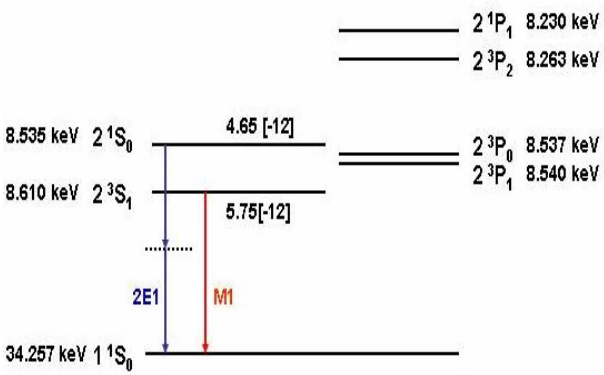

Figure 1: Binding energies of the He-like Sn levels and the decay modes of the 2^1S_0, 2^3S_1 states with their lifetimes (s) are given.

The experiment was performed at the storage ring ESR with 300 MeV/u Li-like tin ions (Sn^{47+}) colliding with N_2 and Ar targets. For the details of the experimental setup we refer to [1]. In Fig. 2a we present a preliminary spectrum measured by a Ge x-ray detector in coincidence with the up-charged Sn^{48+} ions. The spectrum is dominated by an intense line at 25.65 keV corresponding to the M1 decay of the [1s2s] $^3S_1$ state and a broad continuum towards lower energies representing the 2E1 decay of the [1s2s] $^1S_0$ level. Note, the two-photon decay shape is symmetric to the middle point where it reaches its maximum. The absence of x-rays lines from the decay of the 2p or higher states ensures that there is no intra/inter-shell excitation simultaneous with the K-shell ionization (compare [1-3]).

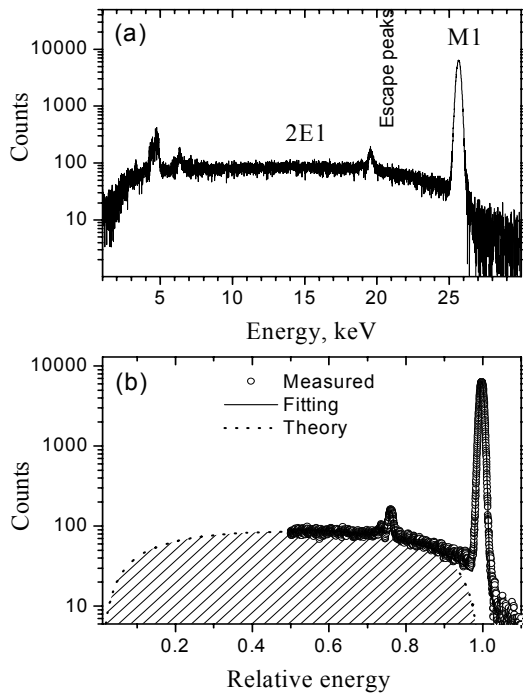

Figure 2: (a) Preliminary projectile x-ray spectra (projectile frame) for $Sn^{47+} \rightarrow N_2$ collisions measured in coincidence with ionization (Sn^{48+}). The spectrum was recoded at 35^0 observation angle (b) Higher-energy half of the spectrum along with the fitted line and theoretical distribution (see text).

Because of the symmetry of the two-photon distribution, we concentrate in our data analysis on the high energy part, above the middle point, only. Here, for a detailed analysis of the spectrum shape, only the relative detector efficiency has to be considered. As a preliminary result we compare in Fig. 2 the measured spectral distribution with a most recent theoretical prediction based on the MCDF approach (compare shaded area) [4]. The data analysis is currently in progress.

The support by the A. v. Humboldt Foundation (M.T.), the DAAD (A.K., No.: A/05/52927) and by I3 EURONS (EC contract no. 506065) is gratefully acknowledged.

[1] J.Rzadkiewicz et al., Phys. Rev. A 74 (2006) 012511
[2] D. Banas et al., Nucl. Instrum. and Methods B 235 (2005) 326
[3] Th. Stöhlker et al., Phys. Rev. A 58 (1998) 2043
[4] A. Volotka, private communication

Radiative processes studied for bare uranium ions in collisions with the H_2 target of the ESR*

G. Weber[1], Th. Stöhlker[1], D. Banas[2], S. Fritzsche[3], A. Gumberidze[1], S. Hagmann[1], S. Hess[1], C. Kozhuharov[1], M. Nofal[1], U. Popp[1], R. Reuschl[1], U. Spillmann[1], A. Surzhykov[4], and S. Trotsenko[1]

[1]GSI, Darmstadt, Germany; [2]Akedemia Swietokryzska, Kielce, Poland; [3]University of Kassel, Germany; [4]MPI für Kernphysik, Heidelberg, Germany

It was previously shown [1] that for high-Z systems the elementary process of photoionization is studied best in inverse kinematics by utilizing its time-reversed reaction, the radiative electron capture (REC) in energetic ion-atom collisions. For studying these processes the internal gas target of the ESR storage ring has been shown to provide an unique tool [2].

The experiment was performed in the ESR by using decelerated bare uranium ions at an energy of 96.6 MeV/u. In the interaction chamber of the gas target, projectile x-rays were produced in collisions with H_2 molecules. By using liquid nitrogen cooling, a density of about $2 \cdot 10^{12}$ particles per cm^3 was reached. The emitted photons were detected by an array of solid state detectors at 10°, 35°, 60°, 120° and 150° with respect to the beam axis. After passing the target chamber, the down-charged ions were separated from the beam by a dipole magnet and afterwards detected by a Multi Wire Proportional Counter (MWPC) located at the outer side of the ring.

By using the coincidence technique described in [3] we obtained the spectrum shown in figure 1. The spectrum contains several lines arising from REC into projectile K-shell, the L-subshells, and the M-shell. Even REC into the N-shell appears to be well resolved from O- and higher shells demonstrating the superior resolution achieved in this study. Electron capture into the excited states leads to the characteristic Lyman transitions, appearing well pronounced in the spectrum (Ly-α and Ly-β lines).

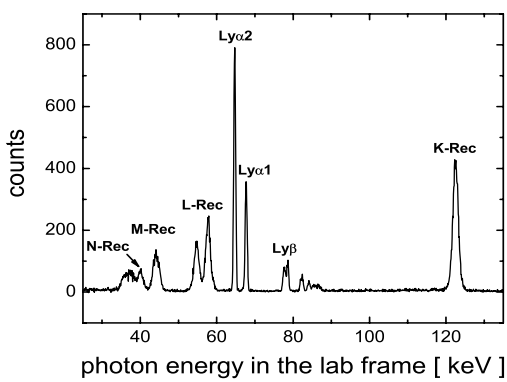

Figure 1: X-ray spectrum observed at 150 degree in the lab frame in coincidence with down-charged projectile ions.

As an example, in figure 2 the measured cross sections for REC into a) the $1s_{1/2}$ and b) the $2p_{3/2}$ state are presented for various angles in the laboratory frame. The results were normalized and compared to fully relativistic calculations (dashed lines). As can be seen in the figure, the measurements are in very good agreement with the theoretical predictions.

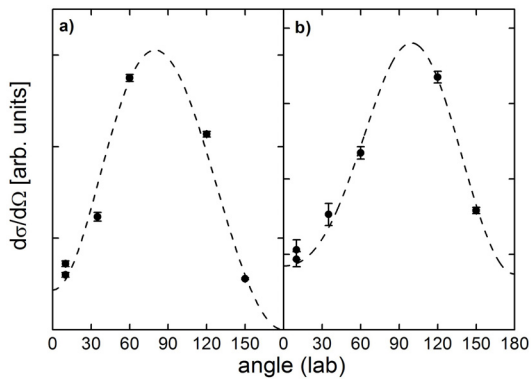

Figure 2: Measured relative REC cross sections (dots) for various angles in the lab frame in comparison to fully relativistic calculations (dashed lines): a) REC into the $1s_{1/2}$ state; b) REC into the $2p_{3/2}$ state

Recapitulating, in the present experiment the cooled hydrogen target at the ESR storage ring proofed its ability of a stable long time performance. As the experimental resolution for radiative processes occurring in heavy ions atom collisions such as REC depends essentially on the target electron momentum distribution (Compton profile), the use of hydrogen is of particular advantage. Thereby, an excellent resolution has been obtained for the REC transitions, which even allowed to distinguish REC radiation for the N- and M-shells.

References

[1] Th. Stöhlker et al., Phys. Rev. Lett. 86, 98 (2001)

[2] Th. Stöhlker et al., *X-RAY AND INNER-SHELL PROCESSES: 18th International Conference* 506, 389 (2000)

[3] G. Weber et al., submitted to Journal of Physics: Conf. Ser. (2007)

* Work supported by I3 EURONS contract No. 506065.

State-selective studies of radiative recombination at the ESR electron cooler

R. Reuschl[1,2], A. Gumberidze[1,2], Th. Stöhlker[1,2], D. Banas[3], H. Bräuning[1], C. Brandau[1], H. F. Beyer[1], S. Hagmann[1,2], C. Kozhuharov[1], A. Kubala-Kukus[3], A. Kumar[1,4], A. Simon[5], U. Spillmann[1,2], Z. Stachura[6] , M. Trassinelli[1,7], S. Trotsenko[1,2]

[1]GSI, Darmstadt, Germany; [2] IKF, University of Frankfurt, Frankfurt, Germany; [3]Swietokrzyska Academy, Kielce, Poland; [4]Tata Institute of Fundamental Research, India; [5]Jagiellonian University, Cracow, Poland; [6] INP, Cracow, Poland; [7]École Normale Supérieure, CNRS, Univ. Pierre et Marie Curie-Paris 6, France

Radiative Recombination (RR) is one of the most important processes occurring in interactions of highly-charged heavy ions with free electrons. Here, the electron transition into a bound state of the ion is accompanied by emission of a photon, carrying away the energy difference between the initial and final electron states. At very low relative energies, electrons populate very highly-excited levels in addition to the ground and low-laying states. In this regime several interesting observations have been made during the last decade which are not fully understood up to now [1,2].

In the present work we extend our former state-selective investigations of the RR process at the ESR electron cooler to the lowest beam energy used for this purpose up to now. In the following, some preliminary data and conclusions are presented.

In comparison with the previous experiment, where we used bare uranium ions (U^{92+}) at an energy of 43.95 MeV/u [3], in this study an energy of as low as 15 MeV/u was chosen at the electron cooler device of the experimental storage ring ESR. The cooling electrons recombine radiatively with the U^{92+} ions emitting x-rays, which are detected by a solid state Germanium detector mounted 4.1m downstream of the middle of the electron cooler [3]. The down-charged ions are separated from the beam in a dipole magnet of the ESR and then detected (in coincidence with the x rays) by a MWPC particle detector. Figure 1 (left side) depicts the coincidence time-spectrum obtained at 15 MeV/u. The left peak in the spectrum stems from Lyman x-ray emission (L-shell to K-shell transitions) inside the electron cooler, whereas the second peak arises from ions, which capture an electron into a highly excited state and therefore do not decay immediately via the emission of Lyman-α x rays. Instead, the electrons cascade down and the characteristic Lyman photons are emitted delayed and closer to the x-ray detector, under an increased solid angle. Therefore, the second peak appears in the time-spectrum which was not fully separated in the former experiment at an energy of 43.95 MeV/u. However, going to lower beam energies a gain in the time resolution is obtained due to the longer time of flight and the peaks appear well separated. The ratio of prompt to delayed events is higher for 43.95 MeV/u than for the lower energy. However, for the former case an error due to not fully separated peaks has to be taken into account. In addition, the relativistic solid angle correction results in a higher value for the photon emission rate of the promptly occurring events in the high energetic case. Hence, less promptly emitted photons are detected at lower energy. A correction of about 30% due to this effect has to be considered. In addition to these points, a modification of a time-pattern of the Lyman emission due to contribution from higher n states (resulting from longer time of flight) at lower energy has to be taken into account. A more detailed analysis is currently underway. From the current status we can conclude, that even at 60 % longer lifetimes (increased time of flight of about 100 ns) characteristic Lyman x-rays stemming from cascade transitions of initially highly-excited ions continue to contribute at a considerable level. Moreover, contrary to the former experiment, going to the lower energy allows us to clearly distinguish the time pattern of pure recombination events (into the K- and L-shell) from those of characteristic transitions (either prompt or delayed: due to cascades from highly excited Rydberg states) (see right side of the fig. 1). This distinctive feature may offer novel possibilities for the study of recombination processes inside the cooler with respect to the importance of high-lying Rydberg states.

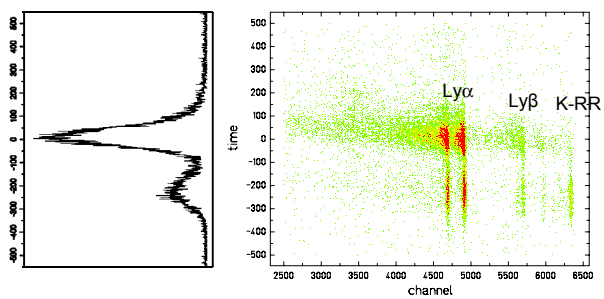

Figure 1: Coincidence time-spectrum recorded at a beam energy of 15 MeV/u (left side) and the corresponding 2D energy(channel) vs time spectrum.

Acknowledgements

The support by the A. v. Humboldt Foundation, (M.T.), the DAAD (A.K., No.: A/05/52927) and by I3 EURONS (EC contract no. 506065) is acknowledged.

References

[1] A. Wolf, et al,, Nucl. Instrum. Meth. Phys. Res. A 441, 183 (2000).
[2] A. Hoffknecht, et al., Phys. Rev. A 63, 012702 (2001).
[3] A. Gumberidze et al., Phys. Rev. Lett. **94**, 223001 (2005)

Recent Progress in Dielectronic Recombination Studies at the ESR

C. Brandau[a], C. Kozhuharov[a], D. Bernhardt[b], Z. Harman[c], A. Müller[b], K. Beckert[a], F. Bosch[a,d], S. Böhm[b], F.J. Currell[e], S. Fritzsche[d], A. Gumberidze[a], J. Jacobi[b], U.D. Jentschura[c], C.H. Keitel[c], P.H. Mokler[a,b], F. Nolden[a], R. Reuschl[a], W. Scheid[b], S. Schippers[b], E.W. Schmidt[b], U. Spillmann[a], Z. Stachura[f], M. Steck[a], Th. Stöhlker[a,g], A. Wolf[c]

[a]GSI Darmstadt, Germany; [b]Universität Gießen, Germany; [c]MPI-K Heidelberg, Germany; [d]Universität Kassel, Germany; [e]Queen's University, Belfast, U.K.; [f]IFJ Kraków, Poland; [g]Universität Frankfurt, Germany

In recent years resonance reaction spectroscopy (RRS) by means of dielectronic recombination (DR) has been developed into a versatile tool for precision spectroscopy. At the electron cooler of the ESR, three major lines of RRS experiments are presently being pursued: (a) DR measurements with a stochastically (pre-) cooled beam, (b) DR isotope shift (IS) experiments with open L-shell ions, and (c) the determination of $2s \rightarrow 2p_{1/2}$ excitation energies ('Lamb shift') in heavy Li-like ions [1 – 4]. 2006 was mainly governed by extended data analysis of previous data taking runs. Substantial progress has been achieved for all three categories:

(a) The use of a stochastically cooled or pre-cooled ion beam for DR studies has opened the door towards higher energies, thus allowing for the investigation of the most fundamental DR processes with H-like heavy ions. The prototype reaction is here the resonant capture of a free electron into one-electron uranium U^{91+} with simultaneous K→L excitation of the bound electron ('KLn DR'). Preliminary results for this reaction were reported in [1, 2]. A more refined data analysis was performed within the scope of the diploma work of D. Bernhardt [3] showing a particular sensitivity of the absolute DR rate coefficients to relativistic effects on the capture rates, i.e., the Breit interaction in the Auger matrix elements [5].

(b) For the extraction of the IS values of DR resonances associated with intra-shell $2s \rightarrow 2p_j$ excitations of Li-like neodymium isotopes $^{A}Nd^{57+}$ (A=142 and A=150) [2] a novel evaluation method has been developed. Characteristic points of the resonance spectrum like maxima, minima and inflection points values are determined from the 1st and 2nd derivatives. Using this techniques one benefits from the feature-richness of a DR spectrum (compare Fig. 1) since all characteristic values possess the same IS, i.e. the one of the corresponding core excitation $2s \rightarrow 2p_{1/2}$ or $2s \rightarrow 2p_{3/2}$. Furthermore, no prior knowledge or theoretical input about the apparatus function or the structure or shape of the DR resonances is needed. 7 independent IS measurements were performed for the energy range (0-3.5) eV, 3 for the range (12-24) eV and 1 for the energy range (25-41) eV yielding in total ~ 160 characteristic values for the $2s - 2p_{1/2}$ IS and ~ 60 for the $2s - 2p_{3/2}$ IS. The IS is about 40 meV for the $2s - 2p_{1/2}$ interval and about 42 meV for the $2s - 2p_{3/2}$ splitting, resp. The determination of the final values for the ISs and for the corresponding change in the nuclear sizes as well as the analysis of statistical and systematical errors is currently being performed.

(c) For Li-like $^{150}Nd^{57+}$ DR data were obtained up to the series limit of the $2s \rightarrow 2p_{1/2}$ excitation at about 139.2 eV (Fig. 1). This offers the opportunity for a precise determination of this energy using the method of extrapolation of Rydberg resonance energies $E_n(1s^2 2p_{1/2} n\ell_j)$ to the series limit $n \rightarrow \infty$ (see e.g. [4]). Up to now, Li-like ions provide the most stringent tests of strong field QED [6]. Our new value for Li-like Nd (Z=60) will bridge the large gap between the data for light and medium heavy elements up to xenon (Z=54) [7] and the heaviest species Au (Z=79), Pb (Z=82), and U (Z=92) [4, 6].

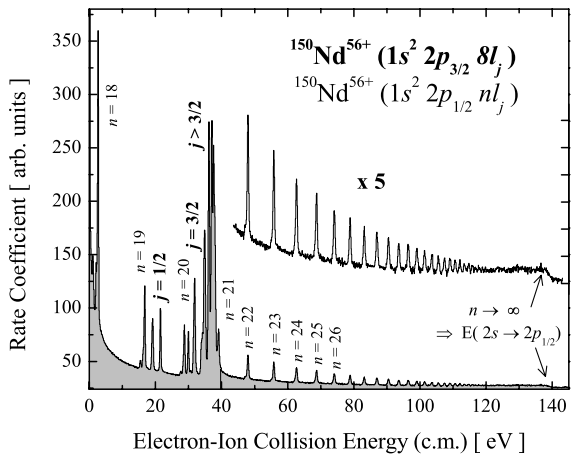

Figure 1: Dielectronic recombination of Li-like neodymium $^{150}Nd^{57+}$ in the energy range 0 - 145 eV. The initial dielectronic capture populates intermediate doubly excited states with $1s^2 2p_{1/2} n\ell_j$ ($n \geq 18$) configurations up to the $2p_{1/2}$ series limit ($\sim$ 139.2 eV) and with $1s^2 2p_{3/2} 8\ell_j$ configurations. In the insert, for a better visibility the data have been magnified by a factor of 5.

The new results are also very promising with respect to FAIR: High intensities of stable and exotic beams and a dedicated ultracold electron target at the NESR will furthermore increase precision, sensitivity and versatility of the 'swiss army knife' RRS.

References

[1] C. Brandau, et al., Rad. Phys. Chem. **75** (2006) 1763.

[2] C. Brandau, et al., J. Phys. Conf. Ser., in print.

[3] D. Bernhardt, Diplomarbeit, Universität Gießen, 2006.

[4] C. Brandau, et al., Phys. Rev. Lett. **91** (2003) 073202.

[5] P. Zimmerer, et al., J. Phys. B **24**, 2633 (1991).

[6] P. Beiersdorfer, et al., Phys. Rev. Lett. **95** (2005) 233003; V.A. Yerokhin et al., Phys. Rev. Lett. **97** (2006) 253004.

[7] D. Feili, et al., Phys. Rev. A **62** (2000) 022501.

Projectile Ionization and Electron Loss to Continuum (ELC) in Near-Relativistic Heavy-Ion Atom Collisions

M. Nofal[1,2], S. Hagmann[3], Th. Stöhlker[2,3], A. Surzhykov[1], S. Fritzsche[4], C. Kozhuharov[2], R. Moshammer[1], J. Ullrich[1], A. Gumberidze[2], U. Spillmann[2], R. Reuschl[2], S. Heß[2], S.Trotsenko[2], F. Bosch[2], D. Liesen[2], R. Dörner[3], H. Rothard[5]

[1]Max Planck Institut für Kernphysik, Heidelberg, [2]GSI, Darmstadt, [3]Institut für Kernphysik, Univ. Frankfurt, [4]Institut für Theoretische Physik, Univ. Kassel, [5]CIRIL-Ganil,Caen,France

The electron loss to projectile continuum cusp (ELC) permits to study the dynamics of the ionization for well defined shells of highly charged ions with emphasis focused on continuum states very close to threshold. This provides very sensitive tests to assess the range of validity of first order theories [1] and has recently received new attention in view of unexpected observations [2].

We have studied forward electron emission in two systems of different projectile Compton profile, U^{88+} + N_2 and Sn^{47+} + N_2 collisions at the supersonic jet-target of the ESR storage ring. We report first results for 90AMeV Be-like U^{88+} and 300AMeV Li-like Sn^{47+} measuring coincidences between electrons around $v_e \approx v_{Proj}$ and charge-exchanged projectiles having lost one electron. Electrons were analyzed with the imaging forward electron spectrometer and charge-changed projectiles were detected with a multi-wire proportional counter (MWPC) after the first dipole following the target zone.

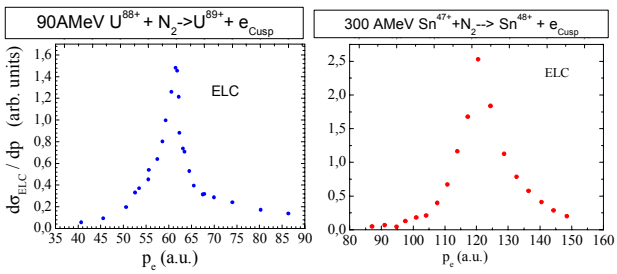

Figure 1a, b: Electron loss to continuum (ELC) cusp measured in 90AMeV U^{88+} + N_2 and in 300AMeV Sn^{47+} + N_2 collisions as function of the electron momentum p_e.

The ELC process was identified via coincidences of electrons emitted into a narrow cone around the projectile direction with charge state analyzed projectiles in charge state 89+ for incident U^{88+} (Fig 1a) and 48+ for incident Sn^{47+} (Fig 1b). In the case of U^{88+} preliminary calculations showed that the total ionization cross section for 2s ionization of the projectile exceeds the cross section for 1s ionization of the projectile by more than an order of magnitude so that the coincident electrons in the momentum range covered may be safely attributed to 2s ionization of the projectile. For 90AMeV U^{88+} the ELC-peak has a longitudinal full width half maximum (FWHM) of 5.6 a.u. of which 1.2 a.u. is instrumental. The peak is nearly symmetric close to the centre but exhibits notable slopes far away from the centre. Lacking theoretical estimates for double 2s-nl excitation we tentatively interpret the shoulders as originating from $2s^2$-2pnl excitation with subsequent autoionization.

For Sn there are at present no calculations for 1s and 2s ionization cross sections available. Considering the higher collision energy and the lower binding energies for Sn it is not possible to attribute the coincident electrons for incident Sn^{47+} to dominant 2s ionization as in the U case.

The ELC peak width for the U^{88+} projectile is longitudinally significantly narrower than for Sn even though the U(2s) and Sn(1s) Compton profile have nearly comparable width.

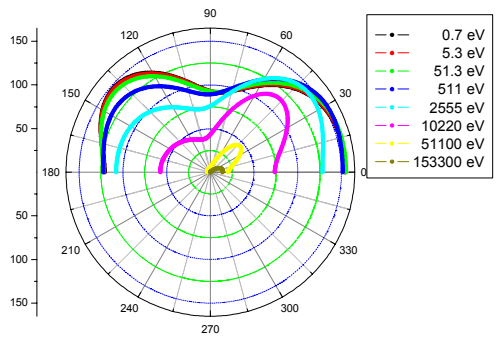

Figure 2: The theoretical DDCS for 2s ionization for U^{88+} in 90AMeV U^{88+} + N_2 as function of projectile frame emission angle and electron energy.

In order to get deeper insight into the dynamics of projectile ionization, we performed also theoretical calculations for the double differential ionization cross section DDCS [3]. In fig.2, we display the DDCS for 2s ionization of U^{88+} at 90AMeV; the emission pattern of the ejected electrons with very low kinetic energy ≤ 50eV is very smooth and exhibits only weakly enhanced humps at about 45^0 and 135^0 in the projectile frame. In fact, such double-peak structure shall reflect the radial behaviour of the 2s wavefunctions since for the ionization of the 1s state (having the same symmetry properties) the DDCS has a single maximum at about 70^0 to 90^0 depending on the continuum electron energy. With increasing electron energy, however, the second peak vanishes and the 2s DDCS exhibits a strong electron emission predominantly in the forward directions.

Support by I3-Eurons (#506065) is gratefully acknowledged.

References

1. D.Jakubassa-Amundsen, Lect. Notes in Physics **213** (1984) 17
2. A. Voitkiv, N. Gruen, J. Phys. **B34** (2001) 267
3. A. Surzhykov , S. Fritzsche, J. Phys. **B38** (2005) 2711

Radiative Electron Capture to Continuum RECC in Near-Relativistic Collisions

M. Nofal[1,2], S. Hagmann[3], Th. Stöhlker[2] ,D. Jakubassa-Amundsen[4], C. Kozhuharov[2], R. Moshammer[1], J. Ullrich[1], A. Gumberidze[3],U. Spillmann[2], R. Reuschl[2], S. Heß[2], S.Trotsenko[2], D. Banas[2], F. Bosch[2], D. Liesen[2],H. Rothard[5] , R. Dörner[3],

[1]Max Planck Institut für Kernphysik, Heidelberg, [2]GSI, Darmstadt, [3]Inst. f. Kernphysik, Univ. Frankfurt, [4] Mathematisches Institut der LMU München , [5]CIRIL-Ganil,Caen,France

Swift heavy-ion collisions offer a powerful tool to investigate a number of fundamental processes, e.g. REC/ photoionization (PI) [1] and (e,2e) for highly charged ions [2] in configurations which are not accessible otherwise. We have recently shown that the short wavelength limit of electron-nucleus bremsstrahlung (BS) [3] can be studied in a unique fashion by measuring differential cross sections for the radiative electron capture (RECC) into the projectile continuum in near relativistic collisions of highly charged ions with atoms [4]. In the projectile frame the RECC is the kinematic inverse of the electron-nucleus bremsstrahlung at the short wavelength limit (SWL) [5]: a quasifree electron from the target is decelerated from velocity v_{proj} to v≈0 while emitting a photon of energy $E_x = (\gamma-1)mc^2$. Fano and Pratt [6,7] emphasize that the short wavelength limit of BS is very closely related to PI and may serve as precision probe for the active electron's wavefunction in the extreme E-fields in the immediate vicinity of the nucleus.

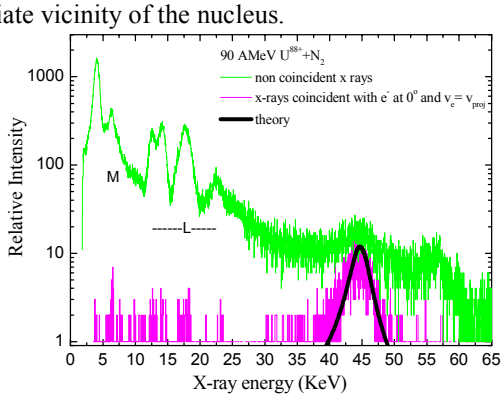

Fig.1: X-ray spectrum detected at θ=90^0 coincident with forward electrons with $v_e \approx v_{Proj}$ compared with theory, a random x-ray spectrum is included for comparison. The calculated photon spectrum is obtained from the four-fold differential cross section by integration over the forward electron acceptance cone and the energy resolution of the spectrometer.

We have investigated in the ESR the forward electron emission in 90AMeV U^{88+} +N_2 collisions and measured coincidences between electrons around $v_e \approx v_{Proj}$ and x-rays. Electrons were analyzed with the imaging forward electron spectrometer and x-rays were detected with a Ge x-ray detector at 90^0 with respect to the beam axis. In the coincident x-ray spectra (Fig.1) we observe for the very first time nearly exclusively photons from the short wavelength limit of the electron-nucleus bremsstrahlung, corroborating the identification of coincident electrons as emerging from the RECC channel. We found a strong asymmetry of the coincident RECC electron momentum distribution which is skewed towards the high energy side of the electron spectrum (Fig.2), as predicted by theory. This asymmetry is opposite to the one found for the non-radiative electron capture to the continuum ECC [5]. We note that the half width of the RECC cusp on the low momentum side is only 1.5 a.u, compared to 3.5a.u. for the nonradiative ECC.

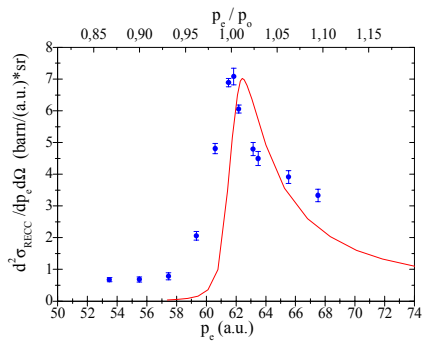

Figure 2 Radiative electron capture to the projectile continuum in 90AMeV U^{88+} + N_2 collisions as a function of the electron momentum p_e in a.u. (lower scale) or as function of the electron momentum in units of p_0, i.e. the momentum of an electron travelling with projectile velocity. The full curve represents the result of the relativistic impulse approximation folded with the instrumental resolution. The experimental cross section is normalized to the maximum of the theoretical cross section.

The shift of the peak of the theoretical curve to higher p_e is attributed to a contribution in the experimental spectrum from electrons captured into Rydberg states of the projectile and field ionized in the spectrometer. This supplemental part of the electron spectrum is centred at $\vec{v}_{electron} = \vec{v}_{projectile}$, its inclusion in a theoretical calculation, not consistently feasible within the present approach, would tend to reduce the difference between the experimental and theoretical peak positions. We will test the theoretical predictions [5] of a very strong collision energy dependence of the observed cusp asymmetry.

Support by I3 Eurons (#506065) is gratefully acknowledged.

References

1 T.Stöhlker et al. PRL**79** (1997) 3270
2. H. Kollmus et al. PRL**88** (2002) 103202
3. T. Luziejewski et al. in J. Phys.B**31**(1998) 2601
4. M. Nofal et al Annual Report GSI (2005) 304
5. D. Jakubassa, J.Phys.**B36** (2003)1971; Rad. Phys. Chem. **75** (2006) 1319; M. Nofal et al., this issue
6. U. Fano et al. Phys. Rev. **116**(1959)1168
7. R. Pratt et al. Phys. Rev. **133**(1964) B1090

Electron Capture to Continuum (ECC) in Near-Relativistic Collisions

M. Nofal[1,2], S. Hagmann[3], Th. Stöhlker[2] ,D. Jakubassa-Amundsen[4],Ch. Kozhuharov[2]
[1]Max Planck Institut für Kernphysik, Heidelberg, [2]GSI, Darmstadt, [3]Inst. f. Kernphysik, Univ. Frankfurt, [4] Mathematisches Institut der LMU München

In near relativistic collisions of heavy ions and atoms there is a transition region where radiative (RECC) and non radiative (ECC) transfer processes to the projectile appear with comparable cross sections. This is a particularly interesting case for studying the dynamics of these processes as in both cases initial and final states are the same and the only difference is the additional radiative degree of freedom in the RECC channel. Whereas the RECC is uniquely identified by coincidences between forward emitted electrons around $\vec{v}_{electron} = \vec{v}_{projectile}$ and bremsstrahlung photons, the double differential cross section DDCS for the non radiative transfer ECC $U^{88+}+N_2 \rightarrow U^{88+}+ e_{Cusp} + \{N_2^{+*}\}$ can only be derived indirectly as in a storage ring no coincidence measurement of cusp electrons with projectiles not having undergone a charge exchange in the collision is possible. We have thus measured for 90 AMeV $U^{88+}+N_2$ all pertinent channels: coincidences of electrons around $\vec{v}_{electron} = \vec{v}_{projectile}$ with bremsstrahlung photons and charge exchanged projectiles U^{89+}, U^{87+}, respectively (see fig.1). In a given number of detected forward emitted electrons the fraction of electrons associated with projectile loss (ELC) and transfer ionization (TI) is completely determined from the coincidences with the charge exchanged projectiles $n_{loss}(U^{89+})$ and $n_{capt}(U^{87+})$,respectively, and detected in multi wire proportional counters MWPC behind the first magnet downstream from the target zone. Theoretical angular distributions for electron nucleus bremsstrahlung and the simultaneously measured RECC permit to calculate the total fraction of forward electrons associated with the RECC. After subtracting these channels the relative cross section for non radiative capture to continuum ECC is derived (see fig 2).

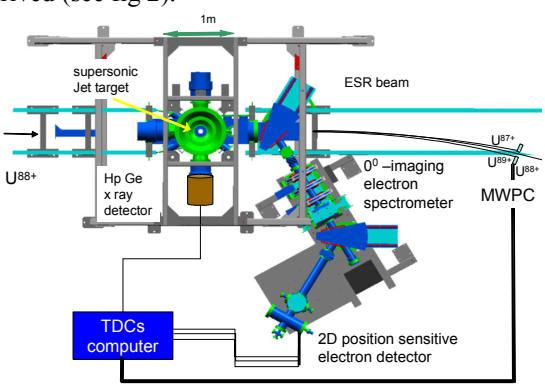

Figure 1: Top-view of the experimental set-up at the supersonic jet target area of the ESR with 0^0-forward electron spectrometer, charge exchange projectile MWPCs and the HpGe x-ray detector at 90^0 with respect to the projectile beam.

The observed FWHM of 7 au implies a significantly broader slope of the cusp than the corresponding one for the RECC which has a low momentum slope half width at half maximum of 1.5 au. We find reasonable agreement of the ECC line shape with the relativistic impulse approximation except in the high momentum slope further away from the cusp centre. In this region contributions from simultaneous excitation +capture with subsequent autoionization in the projectile (thus resulting in an unchanged charge state of the projectile) would be found. The slight asymmetry of the ECC cusp towards small electron momenta is in agreement with theory.

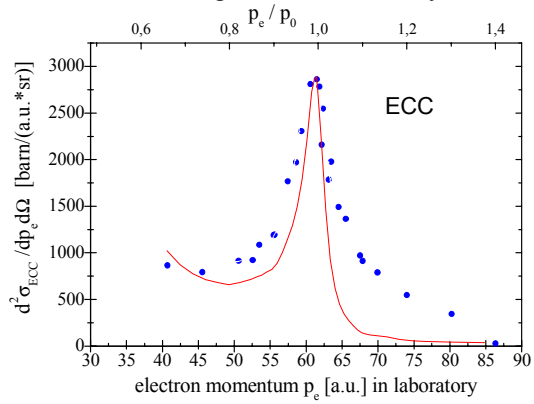

Figure 2 Non-radiative electron capture to the projectile continuum in 90AMeV U^{88+} + N_2 collisions as a function of the electron momentum in a.u. (lower scale) or as function of the electron momentum in units of p_0, i.e. the momentum of an electron travelling with projectile velocity. The full curve represents the result of the relativistic impulse approximation folded with the instrumental resolution. The experimental cross section is normalized to the maximum of the theoretical cross section.

For low collision energies in the non-relativistic regime[1] the ECC is known to exhibit a much stronger asymmetry as observed here but also with higher intensity on the low momentum side; for asymptotically high collision energies the dominance of s-continua is expected to lead to a symmetric ECC cusp[1]. In the medium collision energy range as in the current case, the weak asymmetry is, however, attributed by theory to an absence of coherence for the contributing s-, p- and d- partial waves/1/. In subsequent experiments the strongly velocity dependent asymmetry of the ECC will be investigated over a wide range of collision velocities.

References

1. J. Burgdörfer, in Lecture Notes in Physics, Vol. **213**, p 32(1984) Springer, Heidelberg

Complete Coulomb-fragmentation of N_2O in collisions with 3.6 MeV/u Au^{50+}

U. Werner[1], B. Siegmann[2], and R. Mann[3]

[1]Universität Bielefeld, Fakultät für Physik, Universitätsstr. 25, D-33615 Bielefeld; [2]Universität Dortmund, Institut für Physik, Otto-Hahn Str. 4, D-44221 Dortmund; [3]Gesellschaft für Schwerionenforschung (GSI), D-64291 Darmstadt

In continuation of our previous studies with swift highly charged Xe-ions[1] we analyzed the multiple ionization and fragmentation of N_2O in collisions with 3.6 MeV/u Au^{50+}-ions. The experiment has been performed at the UNILAC accelerator at the GSI using a position- and time-sensitive multi-particle detector [2] which allows the coincident measurement of the momenta of correlated fragment ions. Of special interest are the "Coulomb-explosion" processes, as e.g. $N_2O \longrightarrow N^{q+} + NO^+$ or $N_2O \longrightarrow N^+ + N^+ + O^+$, where the mutual Coulomb repulsion of the fragment ions plays an important role in the fragmentation dynamics. If all fragments from a particular fragmentation are detected, a kinematically complete study of the molecular break-up process is possible [3, 4] and the kinetic energy release as well as angular correlations can be derived for each individual event.

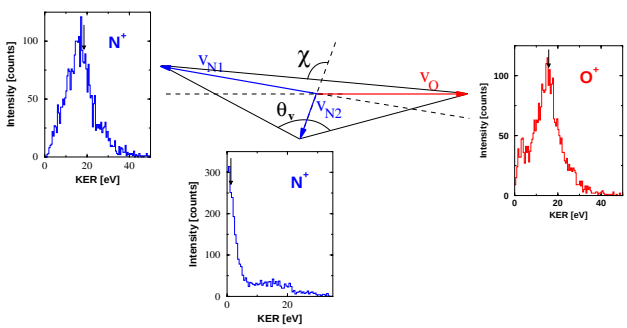

Figure 1: Fragmentation geometry (of event No. 3) and kinetic energy release (KER) distributions of coincident $N^+ + N^+ + O^+$ fragment-ions observed in collisions with 3.6 MeV/u Au^{50+}-ions. The arrows in the spectra indicate the kinetic energies corresponding to "event No. 3".

For fragmentation into three charged particles the fragmentation dynamics may be analyzed in terms of three independent parameters. A practical choice of the characteristic variables consists of the kinetic energy release and the two angles χ and θ_v in velocity space. Fig. 1 shows the definition of these angles. Although N_2O is a "linear molecule" it is initially bend due to molecular vibrations and thus the fragmentation is in general not a collinear process, i.e. the resulting θ_v values are well below 180° [4]. The geometry in Fig. 1 shows the velocity vectors and angles corresponding to a particular $N^+ + N^+ + O^+$ event and the kinetic energy distributions of the individual fragment-ions. In qualitative agreement with a simple point charge model the nitrogen ion in the middle position receives a comparatively small kinetic energy whereas the outer N^+ and O^+ ions roughly emerge with similar momenta in opposite directions (Fig. 1).

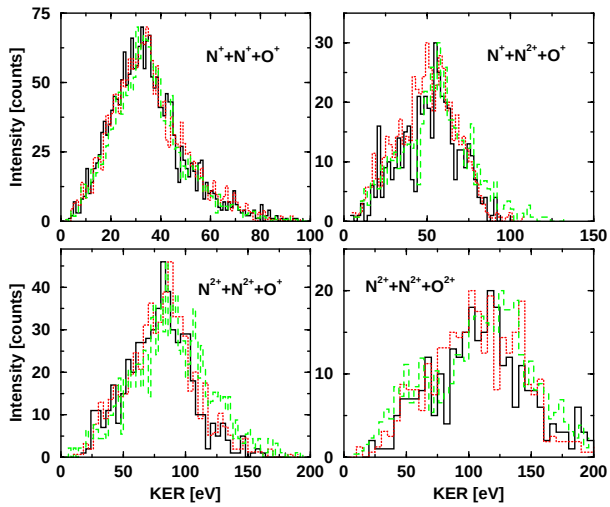

Figure 2: Total kinetic energy release (KER) of coincident $N^{p+} + N^{q+} + O^{r+}$ fragment-ions in collisions with 5.9 MeV/u Xe^{18+} (—), 5.9 MeV/u Xe^{43+} (···), and 3.6 MeV/u Au^{50+}-ions (- - -).

Fig. 2 shows the total kinetic energy release spectra of selected complete three particle fragmentation processes. Due to the asymmetric N–N–O structure the inner and outer nitrogen atoms are not equivalent, and thus three different fragmentation channels arise in case of four- and five-fold ionization. All distributions show a simple structure with one maximum. Apart from variations in the relative cross sections no striking differences between 5.9 MeV/u Xe^{18+}, 5.9 MeV/u Xe^{43+} , and 3.6 MeV/u Au^{50+}-impact was observed in the three particle processes.

References

[1] B. Siegmann, U. Werner, H.O. Lutz, and R. Mann, GSI Scientific Report 2002, 100

[2] J. Becker, K. Beckord, U. Werner and H.O. Lutz, Nucl. Instrum. Methods **A 337**, 409 (1994).

[3] U. Werner, K. Beckord, J. Becker, and H.O. Lutz, Phys. Rev. Letter **74**, 1962 (1995).

[4] B. Siegmann U. Werner, H.O. Lutz, and R. Mann, J. Phy. B **35**, 3755 (2002)

Recent results at the SHIPTRAP Penning trap mass spectrometer*

F. Herfurth[1], D. Ackermann[1], K. Blaum[1,2], M. Block[†1], A. Chaudhuri[3], M. Dworschak[1], S. Eliseev[1], R. Ferrer[2], F. Heßberger[1], S. Hofmann[1], H.-J. Kluge[1,4], A. Martín[1], G. Marx[3], M. Mazzocco[1], J. Neumayr[5], W. Plaß[6], S. Rahaman[7], C. Rauth[1], D. Rodríguez[8], L. Schweikhard[3], C. Scheidenberger[1], P. Thirolf[5], G. Vorobjev[1], and C. Weber[‡1]

[1]GSI, Darmstadt, Germany; [2]Johannes Gutenberg-Universität, Mainz, Germany; [3]Ernst Moritz Arndt-Universität, Greifswald, Germany; [4]Ruprecht Karls-Universität, Heidelberg, Germany; [5]Ludwig Maximilians-Universität, München, Germany; [6]Justus Liebig-Universität, Giessen, Germany; [7]University of Jyväskylä, Finnland; [8]Universidad de Huelva, Spain

The Penning trap mass spectrometer SHIPTRAP (fig. 1) is installed after the Separator for Heavy Ion Products (SHIP) and provides mass values for short-lived radioactive nuclei with relative uncertainties between $1 \cdot 10^{-7}$ and $1 \cdot 10^{-8}$.

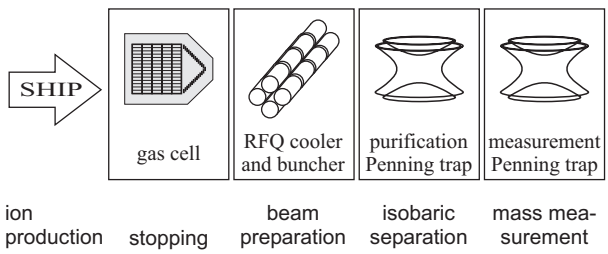

Figure 1: The functional units of the SHIPTRAP setup.

The radionuclides are produced in fusion-evaporation reactions at a few MeV/u energy. The reaction products are separated from the primary beam in the velocity filter SHIP. The energy of the reaction products is then degraded from ≈100 keV/u to ≈10 keV/u in a μm-thin titanium window before they are stopped in 50 mbar helium in a buffer-gas cell. The radioactive ions are then accumulated in a linear RFQ trap and transfered to a purification Penning trap for accumulation and mass selective cooling with a resolving power up to $m/\Delta m = 10^5$. After the transfer of the purified ion ensemble to a second (high-precision) Penning trap the ion cyclotron frequency $\nu_C = qB/(2\pi m)$, and hence, their mass, is determined. This is done with a resolving power of up to 10^6, enough to separate low-lying isomeric states.

In 2006 three experiments have been performed to access nuclei important for the astrophysical rp-process. A 0.5 mg/cm^2 thick ^{58}Ni target was irradiated with ^{58}Ni, ^{52}Cr and ^{40}Ca beams. With beam energies of 4 MeV/u for Ni and Cr, and 5 MeV/u for Ca 34 different nuclei were produced and investigated. The analysis of this data has been finished. The previously well-known masses have been reproduced and hence confirm the quality of the SHIPTRAP data together with a very good overall consistency. In total nine mass values have been measured for the first time and the SHIPTRAP values now replace the previously only estimated ones. The newly measured values also influence a number of mass values that are linked to the measured ones via α- and β-decay energy measurement. All together, the changed mass values are now used as input to astrophysical network calculations performed in collaboration with the National Superconducting Cyclotron Laboratory (NSCL) in East Lansing (USA).

In December 2006 measurements were performed to investigate the performance of the gas cell: the overall efficiency as well as the stopping range distribution. The alpha emitter ^{152}Er was produced in the reaction ^{116}Sn(^{40}Ar,4n)^{152}Er. The alpha decays counted with a silicon detector were used to monitor the beam intensity in front of, within and behind the gas cell. Furthermore, a movable silicon detector provided information on the stopping range of the Ar-beam in 50 mbar helium gas. The data are presently being analysed.

In order to increase the resolving power and the precision of a mass measurement a new excitation scheme has been investigated. In place of the ordinary quadrupolar excitation applied in the measurement trap an octupolar excitation scheme was introduced. The first results promise, aside of the expected improvement due to the higher frequency, an increased resolving power due to the narrowing of the resonance (fig. 2).

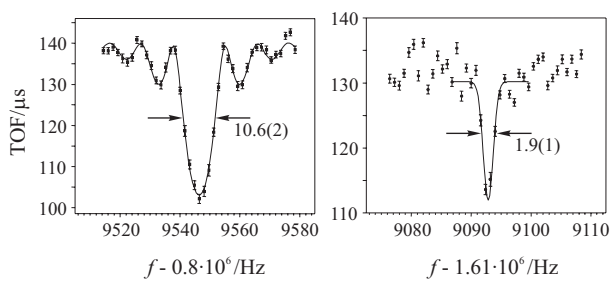

Figure 2: Time-of-flight (TOF) versus frequency curves taken with ^{133}Cs$^+$ ions for quadrupolar rf-excitation (left panel) and octupolar rf-excitation (right panel) of 100 ms duration. The solid line is a fit of the theoretical function to the quadrupolar data and a Gaussian function to the octupolar data. Also given are the full-width-half-maximum values in Hz.

* Work supported by EU, EURONS contract No. 506065., and HGF, contract number VH-NG-033 and VH-NG-037

† presently: NSCL/MSU, East Lansing, USA

‡ presently: University of Jyväskylä, Finnland

High-precision mass measurements on neutron-rich nuclides with ISOLTRAP*

A. Herlert[†1], S. Baruah[2], D. Beck[3], K. Blaum[3,4], M. Breitenfeldt[2], P. Delahaye[1], M. Dworschak[4], S. George[3,4], C. Guénaut[5], U. Hager[6], F. Herfurth[3], A. Kellerbauer[7], H.-J. Kluge[4,8], D. Lunney[9], D. Neidherr[4], R. Savreux[3], S. Schwarz[5], L. Schweikhard[2], and C. Yazidjian[3]

[1]CERN, Geneva, Switzerland; [2]Ernst-Moritz-Arndt-Universität, Greifswald, Germany; [3]GSI, Darmstadt, Germany; [4]Johannes Gutenberg-Universität, Mainz, Germany; [5]NSCL, Michigan State University, East Lansing, USA; [6]University of Jyväskylä, Finland; [7]MPI für Kernphysik, Heidelberg, Germany; [8]Ruprecht-Karls-Universität, Heidelberg, Germany; [9]CSNSM-IN2P3-CNRS, Orsay, France

The Penning trap mass spectrometer ISOLTRAP allows the investigation of short-lived nuclides with half-lives well below 100 ms and production yields of less than 1000 ions per second. Situated at the on-line isotope separator ISOLDE at CERN, several hundred exotic nuclides are available for mass measurements with a current limit of the relative mass uncertainty of 8×10^{-9}. In recent years a number of chains of neutron-rich radionuclides of different elements have been studied [1]. The corresponding atomic mass values contribute to the investigation of nuclear structure and the r-process in nucleosynthesis [2]. Furthermore, atomic masses of superallowed beta emitters have been determined, which are relevant for fundamental studies [3].

In 2006 the mass-measurement campaign concentrated on the neutron-rich nuclides $^{57-63}$Mn, $^{112-121}$Ag, and $^{114-126}$Cd, as well as the light nuclides ^{26}Al and ^{38}Ca. The latter two are of interest for testing the conserved-vector-current hypothesis of the Standard Model. In order to reach the required relative mass uncertainty of the order of 1×10^{-8}, a new excitation scheme has been applied as presented in [4].

In addition, neutron-rich iron nuclides have been studied for the first time at ISOLDE. Although refractory elements do not diffuse out of the ISOLDE targets due to their elemental properties, it was possible to produce $^{61-63}$Fe in the preparation Penning trap of ISOLTRAP (see Fig. 1 (a)) by use of the in-trap decay method [5]. Mass-selected manganese nuclides $^{61-63}$Mn from the ISOLDE target were stored in the trap and after a storage time of one second, to let the Mn ions decay, the created iron daughter nuclide ions were stored in the buffer-gas environment. As an example, the decay scheme of ^{61}Mn is shown in Fig. 1 (b). The potential well of up to 100 V and long storage times allow for an efficient collection of the daughter recoil ions. After additional cooling the iron nuclide ions were transferred to the precision trap for the determination of the cyclotron frequency. In Fig. 1 (c) a resonance of ^{61}Fe^{+} is plotted, where the solid line is the fit of the line shape to the data points. The data analysis is in progress.

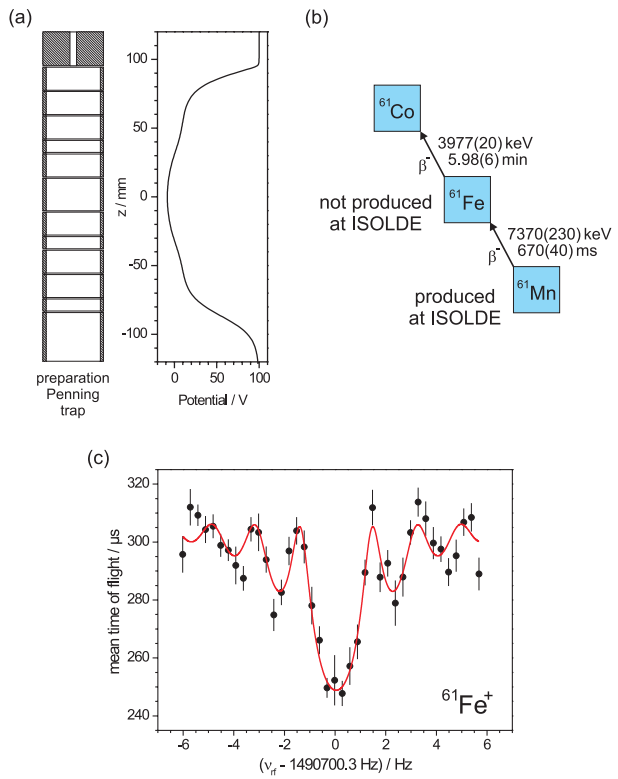

Figure 1: (a) Electrode configuration and trapping potential along the axis of the preparation Penning trap of ISOLTRAP. (b) Decay scheme of ^{61}Mn and its daughter ^{61}Fe. (c) Cyclotron resonance of ^{61}Fe^{+}, which has been produced by use of the in-trap decay method [5].

References

[1] A. Herlert *et al.*, Proceedings of Science, PoS(NIC-IX)051 (2006).

[2] P. Delahaye *et al.*, Phys. Rev. C **74** (2006) 034331.

[3] J.C. Hardy and I.S. Towner, Phys. Rev. Lett. **94** (2005) 092502.

[4] S. George *et al.*, GSI Scientific Report 2006

[5] A. Herlert *et al.*, New J. Phys. **7** (2005) 44.

* Work supported by BMBF (contracts no. 06GF151, 06MZ215, and 06GF186I), EU (contracts no. HPMT-CT-2000-00197, HPRI-CT-2001-50034, RII3-CT-2004-506065), and the Helmholtz association (contract no. VH-NG-037).

† alexander.herlert@cern.ch

High-precision mass measurements of short-lived radionuclides using time separated oscillatory fields*

S. George† [1,2], D. Beck[1], K. Blaum[1,2], M. Breitenfeldt[3], F. Herfurth[1], A. Herlert[4], A. Kellerbauer[5], H.-J. Kluge[1], M. Kowalska[4], D. Lunney[6], D. Neidherr[2], L. Schweikhard[3], C. Yazidjian[1], R. Savreux[1], and S. Schwarz[7]

[1]GSI, Darmstadt, Germany; [2]Johannes Gutenberg-Universität, Mainz, Germany; [3]Ernst-Moritz-Arndt-Universität, Greifswald, Germany; [4]CERN, Division EP, Geneva, Switzerland; [5]MPI für Kernphysik, Heidelberg, Germany; [6]CSNSM-IN2P3-CNRS, 91405, Orsay-Campus, France; [7]NSCL, Michigan State University, East Lansing, USA

The triple-trap mass spectrometer ISOLTRAP installed at the on-line facility ISOLDE/CERN is dedicated to high-precision mass measurements of radioactive nuclides. It reaches a relative mass uncertainty of below 10^{-8}. In a Penning trap an ion with a charge-to-mass ratio q/m is stored in a strong homogeneous magnetic field B_0 combined with a weak electrostatic quadrupole field. The mass measurement is performed via the determination of the cyclotron frequency $\nu_c = qB_0/(2\pi m)$. To this end, the ion motion is, after a series of preparatory steps, probed by a pulse of quadrupolar rf-radiation. The effect on the ion motion depends on the frequency, duration, amplitude and time-structure of the pulse and is detected by a time-of-flight cyclotron-resonance technique. Instead of using the conventional one-pulse excitation with a continuous external rf-field we implemented time-separated oscillatory fields, known as Ramsey's method, in order to reduce the line width of the resonance and thus the statistical uncertainty of the extracted resonance frequency [1]. In comparison to the conventional excitation scheme the statistical uncertainty has been improved by more than a factor of three using identical cycle times for the excitation and an identical frequency range. In the context of short-lived and rare produced radionuclides this opens the opportunity to reach a certain level of precision ten times faster. Cyclotron resonances of $^{38}Ca^{19}F^+$, using both the conventional scheme as well as the Ramsey type scheme, are shown in Fig. 1.

This year the new technique was applied the first time in an on-line measurement at ISOLTRAP to determine the masses of ^{26,27}Al and ^{38,39}Ca. The masses of ^{26}Al and ^{38}Ca are used for testing the conserved-vector-current hypothesis (CVC) of the Standard Model of fundamental interactions, which postulates a vector-current part of the weak interaction unaffected by the strong interaction. Thus, the decay strength of all superallowed $0^+ \rightarrow 0^+$ β-decays is independent of the nuclei except for theoretical corrections [2]. Here, a relative mass precision of 10^{-8} is required. The result of the mass measurement of ^{38}Ca [3] is in agreement with the literature value [4]. Further on we addressed the Q-value of the astrophysically important reaction $^{39}\mathrm{Ca}(\mathrm{p},\gamma)^{40}\mathrm{Sc}$. This and the other masses are presently analyzed.

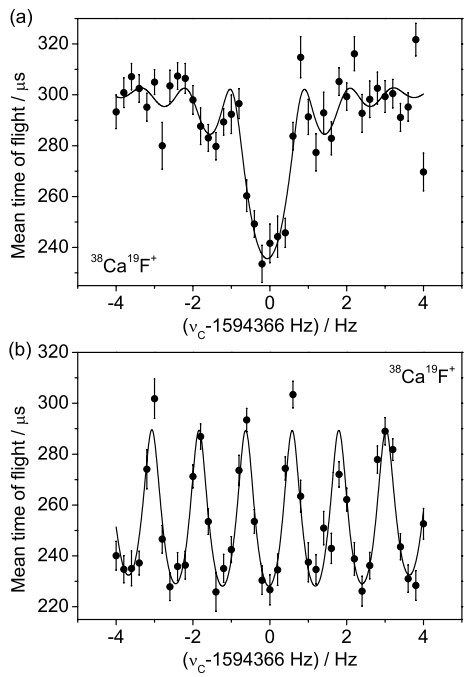

Figure 1: Time-of-flight cyclotron resonance for $^{38}Ca^{19}F^+$. For the conventional resonance (a) a continuous excitation of 900 ms is applied. In (b) the two-pulse Ramsey scheme was chosen with two 100 ms duration excitation periods interrupted by a 700 ms waiting period. The solid curve is a fit of the theoretically expected line shape to the data [5].

References

[1] G. Bollen *et al.*, Nucl. Instrum. Meth. B **490** (1992).

[2] J.C. Hardy and I.S. Towner, Phys. Rev. Lett. **94**, 092502 (2005).

[3] S. George *et al.*, submitted (2006).

[4] G. Bollen *et al.*, Phys. Rev. Lett. **96**, 152501 (2006).

[5] M. Kretzschmar, *et al.*, submitted (2006).

* Work supported by BMBF, contract No. 06MZ215 and 06GF186I, Helmholtz association, contract No. VH-NG-037.

† george@uni-mainz.de

The HITRAP Decelerator Project at GSI*

W. Barth[1], M. Bevcic[1], M. Block[1], K. Blaum[1,2], L. Dahl[1], S. Eliseev[1,3], H. Ernst[2], R. Fischer[1], P. Forck[1], G. Gruber[1], F. Herfurth[1], B. Hofmann[1,5], R. Kaminski[1], M. Kaiser[1], O. Kester[#1], H.-J. Kluge[1,4], C. Kozhuharov[1], S. Koszudowski[1,4], A. Krämer[1], G. Maero[1,4], F. Peldzinski[1], W. Quint[1,4], U. Ratzinger[5], H. Reich-Sprenger[1], A. Sauer[5], A. Schempp[5], A. Sokolov[1,3],T. Stöhlker[1,5], W. Vinzenz[1], M. Vogel[2], G. Vorobjev[1,3], D. Winters[1], H. Zimmermann[1,6]
[1]GSI Darmstadt, Germany, [2]Universität Mainz, [3]University of St. Petersburg, [4]Universität Heidelberg, [5]Universität Frankfurt, [6]LMU München

The heavy ion trap facility (HITRAP), which is shown in fig.1 and is being built in the re-injection channel between ESR and SIS will provide unique beams of highly charged ions up to bare uranium at very low energies for a large variety of experiments. At the HITRAP facility the ions, produced by the GSI accelerator facility, will be decelerated in two stages down to energies of the keV-range and will be captured in a large Penning trap [1]. In the first stage deceleration in the ESR down to 4 MeV/u will take place while electron cooling keeps the high beam quality in terms of emittance. Further deceleration down to 6 keV/u is planned with a linear rf-accelerator [2]. The HITRAP decelerator linac employs a double drift buncher (DDB) for phase focusing, an interdigital H-type (IH) structure as energy booster and a 4-rod Radio Frequency Quadrupole (RFQ). At its low energy side a de-buncher will reduce the final energy spread in order to improve the injection efficiency into the cooler Penning trap. The efforts concerning HTRAP concentrated on the infrastructure, the rf-cavity and lens design and construction, the design and construction of the low beam energy section and simulations of the cooler trap operation.

The HITRAP LINAC

After completion of the beam dynamics calculations of the HITRAP decelerator from the ESR towards the cooler trap, the design of the magnetic quadrupole lenses and the rf-cavity design has been performed using the CST Microwave Studio (MWS) code. The rf-simulations covered the two coaxial quarter wave resonators for the double drift buncher (DDB), the interdigital-H-type (IH) booster structure, a two-gap spiral re-buncher of the inter tank matching section towards the RFQ, the RFQ resonator and a two-gap spiral de-buncher at the RFQ's exit [3]. The MWS simulations are required to determine rf-parameters of the cavities such as shunt impedance, quality factor and gap voltages. In addition, the resonator geometry has been varied until the right resonance frequency was met. With MWS, the geometry of the tuner plungers, the frequency tuning range and the required coupling loop size has been determined in advance. Table 1 summarizes results of the MWS simulations. The results of the MWS simulation effort delivered the required data for the mechanical design of all cavities. Using the results of the beam dynamics calculations, the construction of the magnetic quadrupole lenses could be started.

The RFQ tank has been delivered to GSI in the beginning of 2006. After copper plating it has been shipped to Frankfurt University for assembly and rf-tuning (Fig.2). Concerning the resonant structure of the RFQ, the quadrupole electrode modulation has been milled and the stems and ground plate have been delivered to IAP Frankfurt. The surfaces of all RFQ-components have been cleaned and the assembly on an optical bench is proceeding. The final adjustment of the electrodes will follow. The two cavities of the DDB at the high-energy end of the HITRAP linac have been manufactured and delivered to GSI in September 2006 (Fig.3). Prior to the copper plating of the structures, the rf-parameters have been determined at IAP Frankfurt including bead pull measurements. The resonance frequency of the 4-gap buncher cavity without plunger was measured to be 109 MHz. Using a capacitive dummy plunger, the measured tuning range was 2.9 MHz and the tuning sensitivity 16 kHz/mm. A plunger depth of 11 cm was necessary to reach the design frequency. The variation of the gap field strength is less than 1%. The measured resonance frequency of the 2-gap buncher cavity was 216.6 MHz. An inductive tuning will be used, which allows a tuning range of 1.84 MHz. The measured tuning sensitivity was 26.3 kHz/mm and 1.7 cm plunger depth was necessary to reach the design frequency. The field flatness is significant good as well. The rf-measurements of both cavities are in very good agreement with MWS calculations.

Cavity	Shunt impedance	Q-value	required rf-power
DDB 4-gap cavity 108.408 MHz	64.8 MΩ/m	13700	1.6 kW
DDB 2-gap cavity 216.816 MHz	42 MΩ/m	10900	0.6 kW
IH-structure	285 MΩ/m	25700	175 kW
Re-buncher	10.5 MΩ/m	3900	1.5 kW
RFQ	150 kΩm	3600	120 kW
De-buncher	17 MΩ/m	1700	0.2 W

Table 1: Calculated rf-parameters of the linac cavities.

For the 2-gap spiral re-buncher of the inter tank section between IH-structure and RFQ a buncher cavity from GSI

*Work supported by the BMBF
#O.Kester@gsi.de

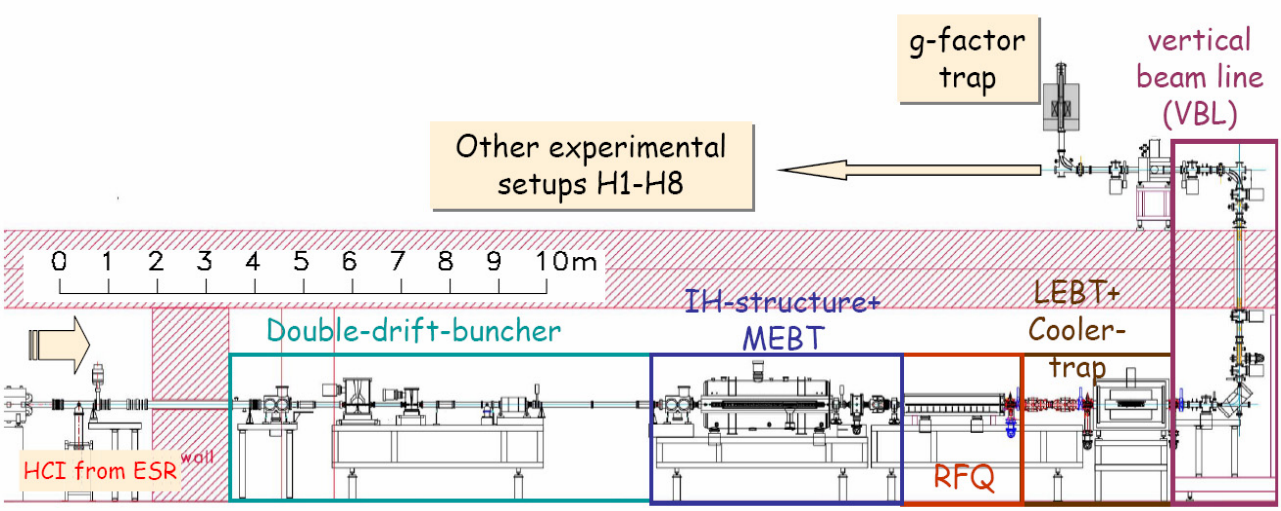

Figure 1: Overview of the HITRAP beam line in the re-injection channel.

stock has been adapted to the right beam energy range. The resonance frequency has been adjusted to 108.62 MHz by reducing the drift tube length. The gap size is 10 mm. With a capacitive dummy plunger a tuning range of 4 MHz has been determined. The final tuning is in preparation.

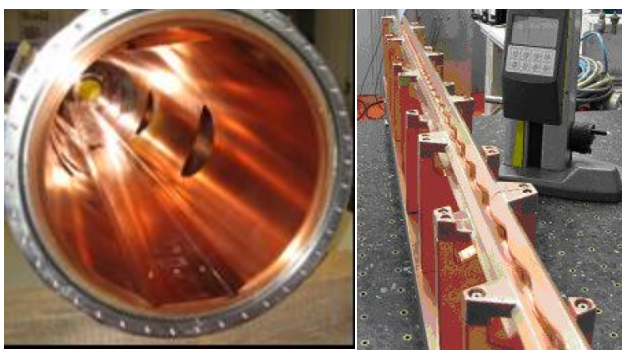

Figure 2: Pictures of the RFQ and the resonant quadrupole electrode structure.

Figure 3: Pictures of the DDB cavities. Left: 108 MHz, 4-gap buncher. Right: 216 MHz, 2-gap buncher.

The vacuum tank and the drift tube structure of the IH-structure have been ordered. In addition, the inner tank quadrupole triplet lens, which is housed in a large drift tube inside the IH-cavity, has been ordered. Design drawings of the drift tubes and the IH-vacuum tank have been submitted to GSI and the drift tube structure is in production. The design of the inner tanks lens is almost completed.

The de-buncher at the exit of the RFQ has been built in the workshop of the IAP Frankfurt and has been copper plated at GSI (Fig.4). Preliminary rf-measurements have been done before copper plating using a tuning plunger with 35 mm diameter.

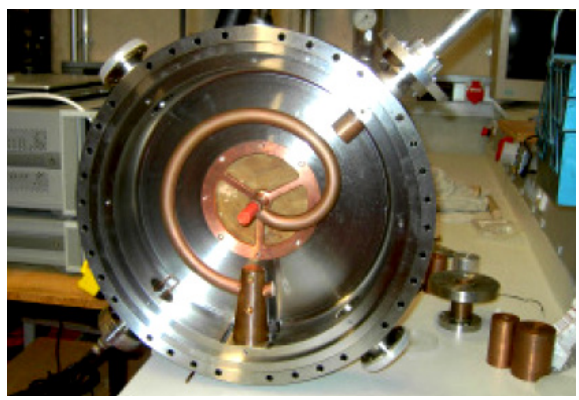

Figure 4: Picture of the De-buncher cavity, which is connected to the RFQ vacuum tank.

The measured tuning range was 2 MHz. The resonance frequency of 108.408 MHz is reached at 25 mm distance of the tuner from the spiral. The tuning sensitivity is 25 kHz/mm at this position. Due to the very low gap voltage of 400 V required for de-bunching, the resonator will be operated off resonance with a few watt rf-power.

The HITRAP low energy section

The design, construction and test of the HITRAP low-energy section are performed in parallel to the work on the HITRAP linac. The main component of the low-energy part is the cooler Penning trap. Extensive numerical simulation calculations are under progress in order to determine essential parameter of the electron cooling and resistive cooling process. In particular extraction of the cooled ion cloud and the distribution of the ions at the entrance of the vertical beam line are of further interest for beam transport calculations and the experiments.

All essential elements of the trap, the 6T-magnet, the electrode structure, the power supplies and the amplifiers are under construction. All essential parts of the magnet including the SC-coil have been completed. The low-energy beam transport line between RFQ and cooler trap has been designed in collaboration with the Fraunhofer Institut (FEP) in Dresden. Two vessels of the beam line have been delivered to GSI and are prepared for baking tests. The remaining vessels have been ordered. The complete setup is planned to be installed at the electron beam ion source "MAXEBIS" test bench at GSI. The MAXEBIS can deliver Ne or Ni-like heavy ions for offline commissioning and tests of beam line components and of the complete HITRAP low-energy section. In first MAXEBIS test-beam operations spectra of Xe and Ar-ions have been taken which revealed the A/q-values required for tests of the cooler trap for Ar [4].

The vertical beam line (VBL) and the beam lines on top of the re-injection channel will guide the ions from the cooler trap towards the experiments. The beam lines have been designed with respect to particle beam dynamics and vacuum generation. Two prototypes of the UHV-diagnostic of these beam lines has been developed and built by the KVI Groningen. The diagnostic comprises a Faraday cup and a MCP-beam-profile detection, which are mounted on a single stepper motor driven feedthrough. Measurements showed that fluorescence screens which are used at GSI are not sensitive enough to measure profiles of low energy beams with typical beam intensities which are expected in the HITRAP VBL [5]. Therefore the HITRAP low energy diagnostic will use MCP based profile diagnostic devices.

HITRAP infrastructure

The crucial element of the HITRAP infrastructure is the HITRAP supply platform located west of the Re-Injection Channel. The platform has been completed and equipped in 2006. The platform houses the HITRAP rf-system, the electric power distribution, 300 kW in total, and the cooling water distribution. Racks for the electronics of the vacuum system, diagnostics, networking, beam line elements and controls are located in two containers. The power cables towards the magnetic quadrupole lenses, the rf-power lines and low level rf-cables have been placed. In addition all required cable trays have been installed in the re-injection channel.

HITRAP commissioning

The commissioning of the HITRAP linac will be performed in steps for each section. The beam development and commissioning of HITRAP focus on the following issues:

- To measure and optimize the beam quality behind each cavity section of the HITRAP decelerator linac via emittance and energy analysis.
- To shorten the ESR cooling and ramping time to about 10 s per cycle and to compress of the ions longitudinally in a bunch of approximately 1 µs length.
- To optimize the beam transfer from the ESR towards the linac entrance and to optimize the beam transmission through the linac according to the design calculations.

For a proper tuning of the linac cavities, which comprises the right power level and the settings of the phase delay between the cavities, measurements of beam quality at the exit of the different cavities are required. The measurement of the transverse beam quality will be done via emittance measurements using the GSI emittance meter based on the "single shot pepper pot system". Measurements with the single shot pepper pot system using beams from the MAXEBIS have already been performed, but the beam intensity and beam energy were not sufficient to perform real emittance investigations. Therefore, beam tests at the HLI-UU beam line will be performed in comparison to non destructive emittance measurements using a quadrupole doublet lens and a profile monitor. The micro-bunch length will be measured with a set-up based on diamond detectors. The diamond membranes have been purchased and are available at GSI. Vacuum material and the required low loss cables for the setup are available as well and a printed board, which will carry the detectors, is in preparation. With help of the bunch length measurements the adjustment of the right phase and amplitude of the different cavities can be simplified.

References

[1] T. Beier et al., *HITRAP Technical Design Report*, GSI Darmstadt, 2003, http://www.gsi.de/documents/DOC-2003-Dec-69-2.pdf

[2] L. Dahl et al., "The HITRAP-DECELERATOR for heavy highly-charged ions", proceedings of the LINAC04, Lübeck, Germany, 2004, p.39.

[3] O. Kester et al., "Deceleration of highly charged ions for the HITRAP project at GSI", proceedings of the LINAC2006, Knoxville, TN, USA, 2006.

[4] H. Zimmermann et al., „Charge breeding exploration with the MAXEBIS", *this report*

[5] H. Ernst, "Detektorentwicklung für langsame hochgeladene Ionen für HITRAP", diploma thesis, Universität Mainz, November 2006.

A Penning trap for laser spectroscopy of cold, trapped, highly-charged ions

D.F.A. Winters[1], Z. Andjelkovic[2], Ch. Geppert[1], H.-J. Kluge[1], J. Krämer[2], M. Vogel[1], and W. Nörtershäuser[1,2]

[1]Gesellschaft für Schwerionenforschung mbH, Atomphysik, Planckstrasse 1, D-64291 Darmstadt, Germany; [2]Institut für Kernchemie, Johannes Gutenberg-Universität Mainz, Fritz-Strassmann-Weg 2, D-55128 Mainz, Germany

The HITRAP facility will soon provide highly charged ions (HCI) at very low energies and offers unique possibilities for laser spectroscopy of hydrogenlike and lithium-like heavy ions. We are currently developing a dedicated Penning trap and laser system for this task in close collaboration with the Imperial College London, and the TU Darmstadt. This trap will be operated with a Helmholtz-type superconducting magnet. A similar setup, called RETRAP, has been developed previously at Lawrence Livermore National Laboratory and was later transferred to the Lawrence Berkeley National Laboratory. It was formerly used by Prof. Dieter Schneider (LLNL/LBNL) and Prof. Dave Church (Texas A&M University) to re-trap highly-charged ions (HCI) extracted from an Electron Beam Ion Source (EBIS) [1, 2]. RETRAP uses a superconducting magnet (6 T) that has both radial and axial access to the centre of the cold (4 K) bore, which are unique features necessary for our experiments. Owing to strong support, especially by Dieter Schneider, we got the definite approval for the transfer of the RETRAP setup from LBNL to GSI in 2006.

In the past, several interesting and pioneering experiments with HCI and, for example, laser-cooled Be ions have been performed with this setup. Gruber *et al.* [3] found crystallisation of $^{136}Xe^{44+}$ inside the laser cooled Be^{+} cloud, and observed a preferential ordering of the efficiently cooled Xe-ions inside the centre of the cloud. In Februar 2007 the setup will be packed and shipped to arrive at GSI in spring 2007, where it will be installed on a platform next to the *re-injection channel* close to the new HITRAP facility [4].

The setup will then be equipped with a new Penning trap that has been developed and constructed at Imperial College in London by the group of Prof. Richard Thompson (see Fig.1). The trap will be loaded with slow, cold HCI provided by HITRAP and facilitates high-precision laser spectroscopy measurements of ground state hyperfine splittings in HCI [5, 6]. The $M1$-transitions in these ions are laser excited along the trap axis (cooled ion motion) and the fluorescence is detected perpendicular to this motion aided by the radial access of the Helmholtz-type magnet. The estimated accuracy of measurements of hydrogen- and lithium-like bismuth ions will finally allow a test of higher-order QED (calculations) up to a few percent [7, 8].

The Penning trap was gold-plated at GSI and assembled. A picture of it is shown in Fig.1. The central electrode is realized with a mesh to allow photon detection in the radial direction. To cool the ions resistively, a resonant LC circuit will be attached to the endcaps in the low-temperature environment. It is expected that ion temperatures of about 4 K can be reached, resulting in a Doppler width of a few 10 MHz. A vacuum chamber was constructed to hold the trap. It is equipped with four viewports in the radial detection and one at the lower end of the trap to shine in laser light along the trap axis. We have started to test ion loading from an external source into the trap, but in absence of the magnet, we can only operate the trap as a radiofrequency trap.

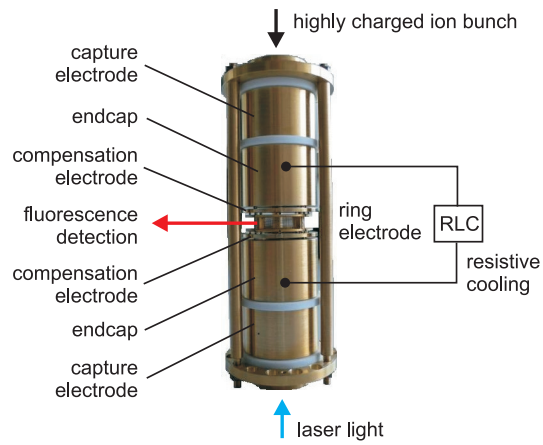

Figure 1: Photograph of the 'spectroscopy trap' for RETRAP. This experiment is part of the HITRAP projekt.

Acknowledgement

We thank Dieter Schneider for the time and work he spent for the negotiations about the RETRAP transfer.

References

[1] D. Schneider *et al.*, Rev. Sci. Instrum. **65**, 3472 (1994).

[2] D.A. Church *et al.*, Nucl. Instr. Meth. Phys. Res. B **132**, 335 (1997).

[3] L. Gruber *et al.*, Phys. Rev. Lett. **86**, 636 (2001).

[4] T. Beier *et al.*, Nucl. Instr. Meth. Phys. Res. B **235**, 473 (2005).

[5] D.F.A. Winters *et al.*, Nucl. Instr. Meth. Phys. Res. B **235**, (2005) 201.

[6] M. Vogel *et al.*, Rev. Sci. Instrum. **76**, 103102 (2005).

[7] V.M. Shabaev *et al.*, Phys. Rev. Lett. **86**, 3959 (2001).

[8] D.F.A. Winters *et al.*, Can. J. Phys. (2006) *in press*.

Charge breeding exploration with the MAXEBIS*

H. Zimmermann[#1], R. Becker[3], O. Kester[2] , J. Pfister[3], A. Sokolov[2],
D. Winters[3], M. Vogel[2], G. Vorobyev[2]

[1]Department für Physik, LMU München, Schellingstrasse 4, 80799 München, Germany
[2]GSI, Darmstadt, Planckstraße 1, 64291 Darmstadt, Germany
[3]J. W. Goethe-Universität Frankfurt, Max-von-Laue Straße 1, 60438 Frankfurt, Germany

The MAXEBIS (MAX Electron Beam Ion Source) is an ion source optimized for the production of highly charged ions. Central part of the ion source is an IrCe filament driven electron gun. The electron beam is guided by a magnetic field (max 5T) of a superconducting solenoid. Through the longitudinal and transverse confinement the EBIS ion source is ideal for charge states breeding process of externally injected ions as it is used for radioactive beam facilities like CERN/ISOLDE.

The MAXEBIS [1] has at present two tasks. It is used as a test injector for the HITRAP cooler trap [2], which is an essential part of the HITRAP project and for offline tests of the whole low energy beam line. This setup is prepared outside GSI at the Heckhalle. After the test period the MAXEBIS will be moved to GSI, and will be included in the HITRAP beam line as an offline and test injector during GSI accelerator shutdowns or for commissioning purposes. The second task is dedicated to investigations of advanced charge breeding methods in the framework of EURONS und EURISOL-DS (European Isotope Separation On-Line Radioactive Ion Beam Facility). Here the goal is to apply known ion source techniques in order to improve the critical charge breeding issues, like efficiency, beam quality and purity.

In 2006 the MAXEBIS setup has been completed and became operational for magnetic mass analysis and external injection using a surface ion source and an Ar-sputter gun. The completed setup is shown in figure 1.

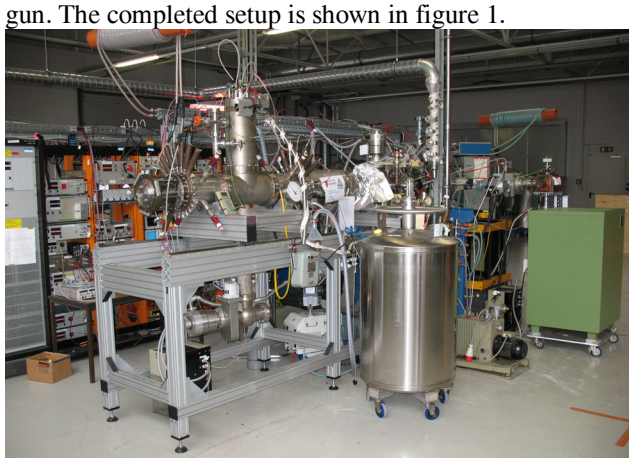

Fig. 1: Setup of the MAXEBIS for charge breeding experiments and as the test injector for the HITRAP cooler trap and RETRAP.

First injection tests have been performed and the TOF-analyser has been used to determine charge bred ions. Figure 2 shows a TOF spectrum of the extracted MAXEBIS beam while Argon ions are injected from the sputter gun. The arrow marks Ar^{9+} which is clearly visible in the spectrum. To demonstrate that the Argon peaks belong to the injected beam, the same spectrum has been taken with external Argon-beam off, which is shown in fig.3.

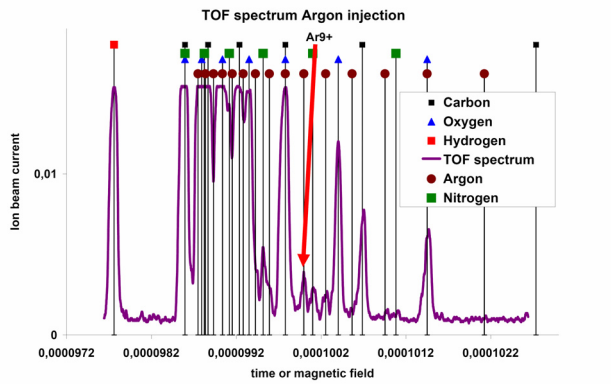

Fig.2: Argon TOF spectrum from the MAXEBIS of external injected Argon ions with max. charge state q=9+.

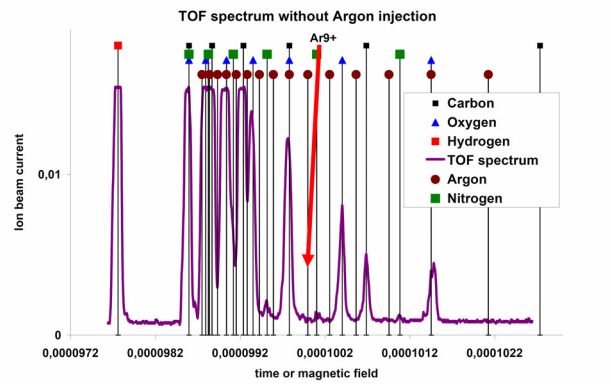

Fig. 3: TOF spectrum while a faraday cups stops the argon beam.

In conclusion, first measurements with external injection has been performed. Next steps will be measurement of efficiency and emittance during the next beam tests.

References

[1] H. Zimmermann, O. Kester, R. Becker, M. Kleinod, "Charge breeding exploration with the MAXEBIS", EPAC 2006, p. 1702

[2] F. Herfurth et al., *Highly charged ions at rest: The HITRAP project at GSI*, AIP conference proceedings Vol. 793, 2005, p.278

* Work supported by EU, EURISOL-DS, RIDS 515768
#h.zimmermann@gsi.de

Electron Cooling of highly charged ions in HITRAP*

B. Möllers, G. Zwicknagel
Institut für Theoretische Physik II, Universität Erlangen, Germany

Electron cooling of highly charged ions in HITRAP[1] is studied within the following set of coupled equations (see [2] and references therein) describing:
(i) the transfer of the energy lost by an ensemble of N_i trapped ions with charge Ze to N_e trapped electrons

$$\sum_{\mu}^{N_i} \frac{dE_\mu}{dt} = \sum_{\mu}^{N_i} M \frac{d\vec{V}_\mu}{dt} \cdot \vec{V}_\mu = -\frac{dE_e}{dt} \stackrel{!}{=} -\frac{3}{2} N_e k_B \frac{dT_e}{dt} ,$$

(ii) the heating of the electrons and their cooling by synchrotron radiation (with a time constant $\tau \approx 0.1$ s for $B = 6$ T) to an ambient temperature of $T_0 = 4$ K

$$\frac{dT_e}{dt}(t) = -\frac{2}{3k_B N_e} \sum_{\mu}^{N_i} \frac{dE_\mu}{dt}(t) \; - \; \frac{1}{\tau} (T_e - T_0) ,$$

(iii) the motion and deceleration of the ions

$$M \frac{d\vec{V}_\mu}{dt} = \vec{F}[n_e, T_e(t), \vec{B}, \vec{V}_\mu] + Ze \left(-\vec{\nabla}\Phi + \vec{V}_\mu \times \vec{B} \right) .$$

Here $\vec{F}$ is the stopping force on an ion due to collisions with magnetized electrons which is taken from the microscopic calculations of Ref.[3], and Φ is the electric potential in the trap generated by the external electrodes and the space charge field of the trapped electrons. These coupled equations are solved numerically. This provides $\vec{V}_\mu(t)$ and $T_e(t)$ which are then used for additionally calculating the radiative ion-electron recombination rate and a surviving probability $P_{\mathrm{RR},\mu}(t)$ for each ion, see [2] for details.

The potential Φ has been fully taken into account in a view test cases [4]. These calculations showed that the actual potential Φ can be replaced by an effective stopping force of $0.25 \cdot \vec{F}$, where the factor 0.25 can be interpreted as an effective extension of the electron cloud with respect to the trap length. This simplified treatment was used to calculate the time evolution of the ion energy $\langle E_i \rangle$, the electron temperature T_e and the surviving probability $\langle P_{\mathrm{RR}} \rangle$ for different highly charged ion species shown in Fig.1. These runs were performed for a cloud of $N_e = 10^{10}$ trapped electrons of a density of $n_e = 10^8$ cm^{-3} and an ensemble of 500 ions, representing (after proper scaling) $N_i = 10^5$ trapped ions. The resulting cooling times are of about half a second with radiative recombination losses of $\lesssim 15\%$. Rather remarkable are the small spreads in the cooling times (center) and recombination losses (bottom) in view of the leading order Z^2-scaling of both the stopping force and the radiative recombination rate. But the (initially) higher energy loss of the higher charged species causes a stronger heating and larger electron temperatures T_e (top), and this feeds back to the stopping force and recombination rate which are both decreasing here with increasing T_e.

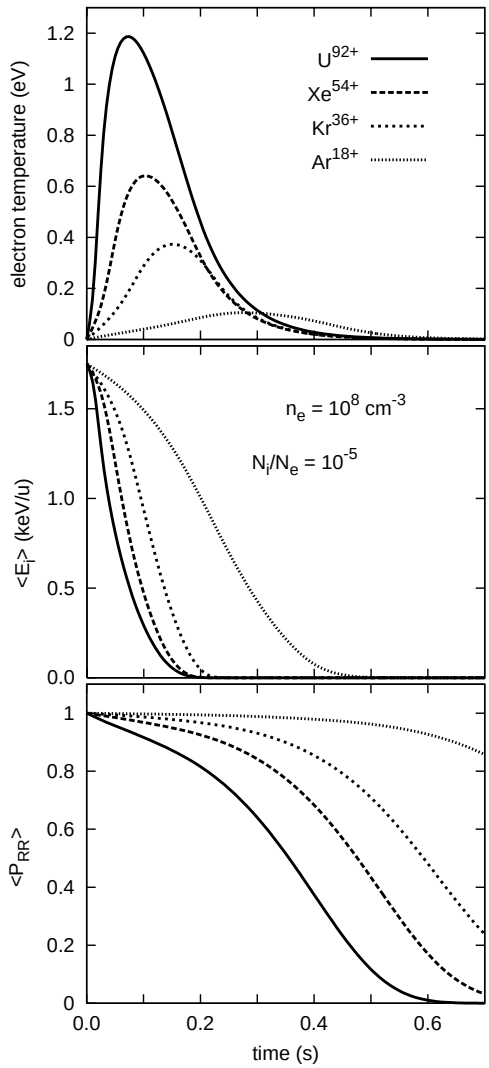

Figure 1: Temporal evolution of T_e (top), $\langle E_i \rangle$ (center) and $\langle P_{\mathrm{RR}} \rangle$ (bottom) for different highly charged ions at $B = 6$T, $n_e = 10^8$ cm^{-3}, $N_e = 10^{10}$ and $N_i = 10^5$.

References

[1] Th. Beier et al., *HITRAP, TD report*, GSI, 2003.
[2] G. Zwicknagel, in *AIP Conference Proceedings*, vol 862, ed by M. Drewsen, U. Uggerhoj, H. Knudsen (AIP, New York 2006) pp 281–291
[3] H.B. Nersisyan et al., Phys.Rev. **E61** (2000) 7022.
[4] B. Möllers, PhD-thesis, University Erlangen 2007.

*Work supported by the BMBF (06ER145)

Development of an X-Ray Crystal Spectrometer for Intra-Shell and Balmer Transitions in Highly–Charged Ions

M. Trassinelli*[1,2], A. Kumar[1,3], D. Banaś[4], H.F. Beyer[1], P. Jagodziński[4], M. Pajek[4], and Th. Stöhlker[1,5]

[1]GSI, Darmstadt, Germany; [2]Laboratoire Kastler Brossel, ENS; CNRS; Univ. Paris 6, Paris, France; [3]Tata Institute of Fundamental Research, India; [4]Świętokrzyska Academy, Kielce, Poland; [5]IKF, Univ. of Frankfurt, Germany

We present the characterization of an x-ray CCD camera of the new Bragg spectrometer for future experiments at the ESR storage ring within the SPARC collaboration [1]. Such an instrument will be specially adapted to radiation in the energy range of 1 to 10 keV. It will be used to determinate the $n = 2$ Lamb shift in highly charged ions via the high–accuracy measurements of intra-shell and Balmer (Doppler shifted) transitions. The spectrometer operates in the Johann geometry with a spherically bent Si(111) crystal and a position sensitive x-ray detector. Preliminary tests of the spectrometer movement controls have been performed in the Świętokrzyska Academy (Kielce, Poland) and two x-ray tracking simulations have been developed independently for the study of the instrument [2, 3]. In September 2006 the spectrometer has been moved to GSI and the first characterization of the position sensitive detector has been performed. The x-ray detector is a deep deleted and back illuminated Charged Couped Device (CCD) produced by Andor (DY420-BR-DD). It consists of an array of 1024×256 square pixels with a dimension of $26 \times 26 \mu\text{m}^2$. The depletion region of this detector is 40 μm, which assures a quantum efficiency of about 90% for 3-4 keV photons. As demonstrated in a recent publication [4], the charges created in the depletion region by an incoming x-ray can be collected by two and more pixels. For the correct treatment of the data, a charge distribution analysis, i.e, a cluster analysis, is required. For this propose, we have developed a new program in Fortran95 and C to readout the raw data of the CCD and further to generate energy spectra and position distributions of the detected x-rays with or without cluster analysis. Preliminary tests of the cluster analysis has been done using ^{57}Co and ^{241}Am radioactive sources. In particular for our energy range, the $K\alpha, \beta$ lines of iron and γ-rays from the cobalt source, and the L x-ray of neptunium from the americium source sere used. As shown in Fig. 1, the spectrum without cluster analysis is characterized by the presence of charge splitting events visible as an almost uniform energy distribution on the low-energy side of the Fe Kα peak. Using the cluster analysis, events corresponding to a charge deposited in two or more pixels can be taken into account to increase the signal–to–background ratio. The resolution obtained for the iron $K\alpha$ line is about 250 eV, considerably better than that presented in Ref. [4] due to the lower CCD working temperature (-76 °C in the present case). Such a low temperature has been obtained with an external water cooling system (water at 10 °C) coupled with the CCD's built-in Peltier module. In the next months we will install and use the new x-ray tube equipped with a molybdenum anode to test the Bragg spectrometer and, in particular, to characterize the silicon crystal.

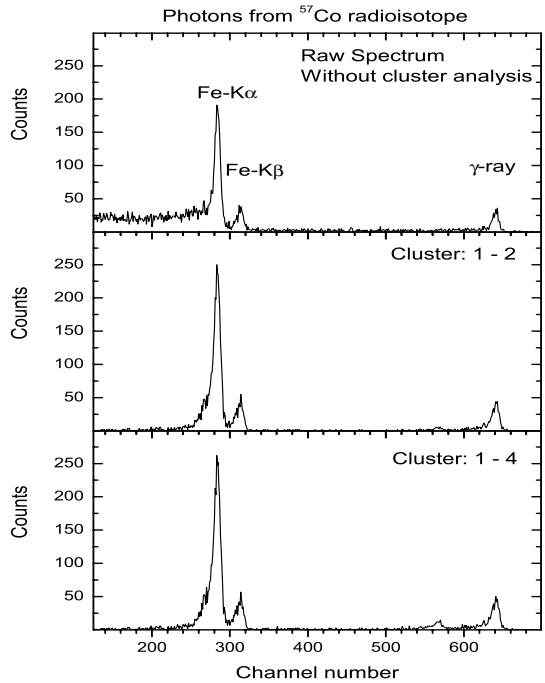

Figure 1: Energy spectrum of the $K\alpha, \beta$ iron x-ray and γ-ray lines obtained with a cobalt ^{57}Co (6.4, 7.1 and 14.4 keV). The three spectra are obtained without cluster analysis (top), considering clusters with 1 and 2 pixels (middle) and from 1 to 4 pixels (bottom).

The support by the A. v. Humboldt Foundation (M.T.), the DAAD (A.K., No.: A/05/52927), the Polish Ministry of Education and Science (D.B, P.J, M.P., No.: 1P03B-00629) and by I3 EURONS (EC contract no. 506065) is gratefully acknowledged.

References

[1] D. Banas *et al.*, GSI Scientific Report 2005 No. FAIR-APPA-SPARC-06, 2006.

[2] D. Banas *et al.*, Journal of Physics: Conference Series , in press (2006).

[3] M. Trassinelli *et al.*, Can. J. Phys., accepted (2006).

[4] F. Zamponi, T. Kampfer, A. Morak, I. Uschmann, and E. Forster, Rev. Sci. Inst.**76**, 116101 (2005).

* m.trassinelli@gsi.de

Absolute frequency measurements in iodine combining Doppler-free laser spectroscopy with a frequency comb*

Ch. Geppert[1,2], H.-J. Kluge[1], N. Miski-Oglu[2], M. Nothhelfer[2],
S. Reinhardt[3], R. Sanchez[1,2], M.Zakova[2], and W. Nörtershäuser[1,2],
[1]GSI, Darmstadt, Germany; [2]Institue for Nuclear Chemistry, University Mainz, Germany;
[3]MPI for Nuclear Physics, Heidelberg, Germany

Iodine vapour cells have been used in many classical spectroscopy experiments in the last decades. This is due to the fact that iodine vapour provides very rich absorption spectra in the visible to the infrared wavelength regime and that additionally the natural line widths of these lines are in the range of 100 kHz. This established iodine vapour as an ideal spectroscopic reference, providing accuracy better than 10^{-9}. The measurements of the charge radii of the lithium isotope chain up to ^{11}Li [1] as well as the test of time dilatation in special relativity are just two recent examples for such experiments at GSI.

For the charge radius measurement of the lithium isotopes, a two-photon spectroscopy experiment has been carried out at GSI and TRIUMF [1]. This allowed a charge radius determination with a precision better than 2%, using the charge radius of ^{7}Li measured by electron scattering experiments as an input parameter. The reference radius uncertainty currently limits the charge radii accuracy of the unstable isotopes.

During these measurements, the laser system was locked relative to the a_1 line of the $X^1\Sigma^+_g \rightarrow B^3\Pi^+_{0u}$ R(114)2-11 transition. Today, such atomic references are often replaced by photonic techniques. Since the commercial distribution of frequency combs they have been established as state of the art laser spectroscopy reference systems. In 2006 a fibre laser based frequency comb became operational at GSI. Measuring the absolute transition frequency of the iodine transition allowed us to extract the absolute frequency of the 2s-3s two-photon transition in the lithium isotopes. This is of interest since an increased accuracy in the theoretical calculation of the transition frequency will enable a determination of the absolute nuclear volume effect and, hence, an absolute charge radius based solely on optical measurements.

The measurement of the iodine transition frequency was performed with the diode laser system that was used in the on-line lithium measurements. The laser frequency was locked to the a_1 hyperfine component of the R(114)2-11 and then measured with a frequency comb (MenloSystems FC 1500) that was referenced to a FS725 rubidium standard (Stanford Research Systems). Experimental conditions like iodine pressure, cell temperature, *etc*. have been varied to investigate systematic effects. The main contribution stems from the relative uncertainty of the comb, which was estimated to ~$6\cdot10^{-10}$. The result for the absolute transition frequency is listed in Table 1.

Further checks of systematic errors were performed by measuring the transition frequency with a second setup that was operated at GSI. Here we were able to use the reference iodine cell of the lithium experiment as well as a second cell from the University of Mainz. The line was here probed with a continuous Coherent 899 titanium:sapphire ring laser system. Results from these measurements are also listed in Table 1. With the titanium:sapphire system a frequency ≈ 260 kHz higher than measured with the diode laser system was found. Even though the values agree within uncertainty it has to be considered that the dominant part in the uncertainties is of systematic origin and related to the rubidium clock that was used in both measurements. Thus, the uncertainties are correlated and cannot explain the discrepancy. We assume that it is caused by not locking the diode laser exactly to the zero crossing of the dispersion signal. Such an offset does not influence the isotope shift measurements but has to be considered in the absolute frequency determination. Thus, an additional uncertainty of about 260 kHz was assumed (second uncertainty in the table value. The additional measurement with the Mainz iodine cell showed an even higher frequency. A difference of about 250 kHz was found for three different iodine transitions that were investigated [2] and is accounted to a higher amount of impurities in the GSI cell.

Determination of the lithium frequencies must be performed on the basis of the measurement with the diode laser system and results in a transition frequency of 27206.09404 (9) cm^{-1} which is in good agreement with a previous measurement of 27206.09420 (10) cm^{-1} [3]. The uncertainty of the lithium transition frequency will be further reduced by a direct measurement of the lithium transition relative to the comb. In order to further reduce the uncertainties of the rubidium standard and therewith the frequency comb, a GPS receiver system will be installed at GSI and linked to the rubidium standard. This will provide an optical reference with a precision in the regime of 10^{-12} or better for further applications at GSI.

References

[1] R. Sanchez, *et al*., PRL **96** (2006) 033002
[2] S. Reinhardt *et al*., Opt. Comm., in print
[3] B. A. Bushaw *et al*., PRL **91** (2003) 043004

Table 1: Intercomparison of iodine frequency measurements with different experimental setups

laser system	diode laser	titanium:sapphire	titanium:sapphire
iodine cell	GSI	GSI	Mainz
frequency / kHz	**407 815 136 650 ± 240 ± 260**	**407 815 136 910 ± 300**	**407 815 137 150 ±300**

* this work is supported by EURONS (European Commission Contract No. 506065), by BMBF Contract No. 06TU203, and by the Helmholtz Association under Contract VH-NG-148

Progress towards a direct measurement of the (anti)proton *g*-factor*

S. Kreim† [1], K. Blaum[1,2], H. Kracke[1], W. Quint[2], S. Ulmer[1,3], and J. Walz[1]

[1]Institut für Physik, Universität Mainz, 55099 Mainz; [2]GSI, 64291 Darmstadt, Germany; [3]Ruprecht-Karls-Universität, 69047 Heidelberg

Determining the g-factor of a single, isolated (anti)proton in a double Penning trap results from an accurate measurement of its cyclotron and spin precession frequency. The Larmor frequency can be determined by inducing radio frequency transitions between the two spin states and detecting the resulting spin state in the magnetic bottle field of the analysis trap [1]. The spin direction is monitored by measuring the respective axial frequency non-destructively with a high-Q tank circuit. The cyclotron frequency is detected in the same manner in the homogeneous magnetic field region of the precision Penning trap. To achieve a high-precision determination of the proton g-factor long storage times are required. This is realized by performing the experiment in a closed setup at 4 K yielding an ultra-high vacuum. A low vibrational Gifford-MacMahon cooler provides the cryogenic environment.

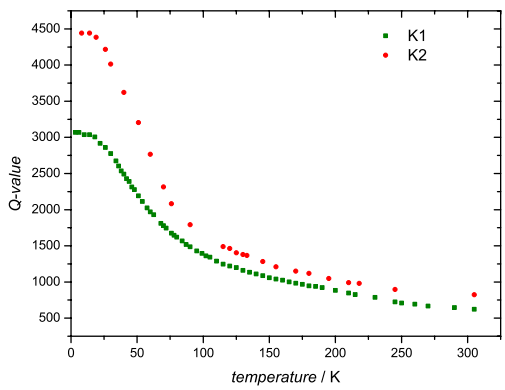

Figure 1: Q-value of differently optimized cyclotron coils depending on the temperature.

The characteristic time for these measurements is the resistive cooling time constant τ which is given by $\tau = \frac{m}{q^2}\frac{D^2}{R}$. Here, the particle's mass and charge are denoted by m and q, respectively, and R is the effective parallel resistance of the tank circuit in resonance. The effective electrode distance D is a characteristic geometric parameter, which has been calculated for both traps using SIMION. For an efficient measuring process the effective parallel resistance $R = 2\pi\nu QL = Q/(2\pi\nu C)$ has to be high requiring a high quality factor Q and inductance L as well as a low parasitic capacitance C for the detection unit. To this end, a helical resonator is used which has been optimized according to different design criteria [2]. The Q-value was increased further by the use of the type-II superconducting alloy NbTi for winding the coil. The Q-values of two differently optimized cyclotron tank circuits (K_1,K_2) - with a resonator out of copper - as a function of the temperature are shown in figure 1. With a frequency of $\nu = 81$ MHz and an inductance of $L = 1.7\,\mu$H a Q-value of 4500 was reached. The signal induced by the proton will be amplified by a first amplification stage operated at cryogenic temperatures providing a low Johnson noise as well as improving the signal-to-noise ratio. With these developments we aim for a relative uncertainty of $\delta g/g = 10^{-9}$.

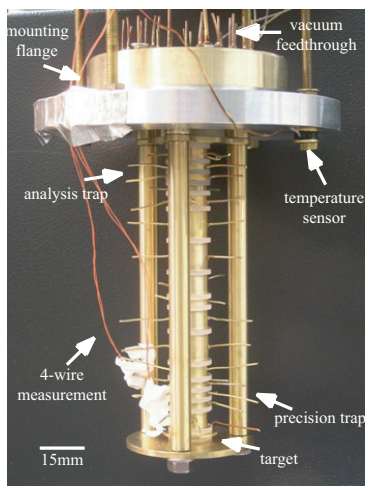

Figure 2: Double Penning trap setup.

The double Penning trap in which the experiments will take place can be seen in figure 2. To test mechanical stability and fitting accuracy, the setup has been thermally cycled for several times, the 4-wire measurement was used to look for leakage currents. Since the sealed system calls for an in-trap creation of protons, a newly developed cryogenic electron gun [3] will function as an EBIS enabling the creation of protons at the position of the precision trap. We continue to set up the experiment and plan to trap first protons by summer 2007. After having successfully performed the experiment with protons, it is possible to move the experimental setup to FLAIR at GSI to conduct the same experiment with antiprotons.

References

[1] H. Häffner, *et al.*, Eur. Phys. J. D 22, 163 (2003)

[2] W. W. Macalpine *et al.*, Proc. IRE 47, 2099 (1959)

[3] F. Maurer, *et al.*, Nucl. Instr. Meth. B 54, 234 (2005)

* Work supported by HGF under contract number VH-NG-037 and DFG under contract number QU122/3-1-2.

† kreim@uni-mainz.de

Ion trap design for a nuclear charge radius determination of ^{7,9,10,11}Be

D. Tiedemann[1], C. Geppert[2], W. Nörtershäuser[1,2] , M. Nothhelfer[1],
F. Schmidt-Kaler[3], M. Zakova[1], C. Zimmermann[4] and the BeTINa collaboration
[1]University of Mainz, [2]GSI Darmstadt, [3] University of Ulm, [4] University of Tübingen

In 1985 Tanihata and coworkers performed scattering experiments with light elements like helium, lithium and beryllium [1,2] and found, completely unexpected, a huge matter radius for some of the isotopes close to the neutron drip line, *e.g.*, ^{6,8}He, ^{11}Li, and ^{11}Be. Subsequent measurements of the magnetic dipole [3] and the electric quadrupole moments [4] excluded a large deformation of these nuclei and the picture of halo nuclei was established. Such a nucleus consists of a compact core nucleus and one or more neutrons which are only very weakly bound to this core. These neutrons have a separation energy of less than 1 MeV and wave functions that extend far away from the core.

The determination of the nuclear charge radius of such nuclei with laser spectroscopy is of particular interest, because it is a model-independent benchmark for nuclear models. This was recently demonstrated in measurements of ^{6}He [5] and ^{11}Li [6]. However, these experiments are challenges for experiment and theory with respect to the required accuracy and sensitivity. The nuclear charge radius is extracted from the measurements of the isotope shift, which is the sum of the mass and the field shift. For light elements the field effect, which includes the change of the nuclear charge radius, is 10.000 times smaller than the mass effect. Thus, the isotope shift has to be measured with accuracy on the order of a few 100 kHz. Similar accuracy must be obtained in the theoretical calculation of the mass-dependent part. So far this is only possible for three-electron systems, hence, the isotope shift for beryllium has to be measured on Be^{+} ions. Ions of the radioactive isotopes will be produced on-line at ISOLDE, precooled and accumulated in the RFQ cooler and buncher of the ISOLTRAP setup and then transferred into a linear segmented Paul Trap that has been designed for this purpose. Here, the ions will be laser-cooled down to less than 7mK to reach the required accuracy.

For this purpose two models for linear Paul Traps have been developed in the last year. The first type (Fig. 1) is based on developments in the working group of F. Schmidt-Kaler. It consists of four circuit boards with a thickness of 410 µm, which are arranged in an angle of 90 degrees to each other. The electrode structures for rf and dc voltages are applied to opposite wafers. The accuracy limit for the separation of electrodes on one wafer is given by 100 µm and allows an extreme flexibility in the shaping of different trapping potentials. This trap type has two trapping regions, one with a free field radius of 2mm and a second one with a radius of 1mm. The trap entrance and the transfer region are bevelled to maximize the capture and transfer efficiency.

The second type (Fig.2) consists of cylindrical electrodes, which can be mounted in different ways. Electrode rods with 2, 5, 10, 15 and 30 mm length were produced. The combination of these electrodes can be chosen individually depending on the requirements. This trap type combines flexibility and the presence of a very good quadrupole field over a relative large region around the trap center. Simion simulations of the capturing process of ions from external sources into the trap were performed and it was found that this should be possible with sufficient efficiency. Moreover, we have constructed a vacuum chamber, ion optics to operate the ion trap and to demonstrate ion trapping from a laser desorption ion source, as well as laser cooling and spectroscopy. First experimental tests of the trap are in preparation.

References

[1] I. Tanihata *et. al.,* PRL **55**, 2676 (1985)
[2] I. Tanihata *et. al,.* Phys.Lett. B **206**, 592 (1988)
[3] E. Arnold *et. al.,* Phys. Lett. B **197**, 311 (1987)
[4] E. Arnold *et. al.,* Phys. Lett. B **281**, 16 (1992)
[5] L.-B. Wang *et. al.,* PRL **93**, 142501 (2004)
[6] R. Sanchez *et. al.,* PRL **96**, 033002 (2006)

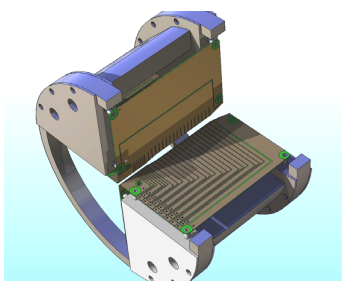

Figure 1

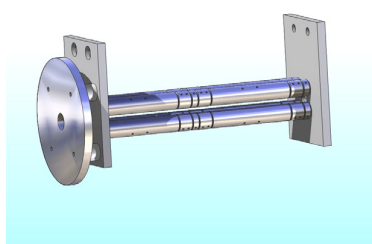

Figure 2

* this work is supported by BMBF Contract Nos. 06TU263I, 06UL264I, and 06MZ215/TP6, and by the Helmholtz Association under Contract VH-NG-148.

Detection technique with single-ion sensitivity for high-precision mass measurements on superheavy elements*

J. Ketelaer[1], K. Blaum[1,2], G. Eitel[1], S. George[1,2], R. Ferrer[1], Sz. Nagy[1], D. Neidherr[1], and the SHIPTRAP collaboration

[1]Institut für Physik, Johannes Gutenberg-Universität Mainz, Gemany; [2]GSI, Darmstadt, Germany

Introduction and motivation

Mass values contribute to a number of physical models: these range from masses of exotic short-lived nuclides being important for weak interaction studies and the Standard Model of particle physics, to stable masses as means for the definition of fundamental constants [1]. Since the discovery of the superheavy elements from $Z = 102$ to $Z = 117$, the investigations in their masses have become more and more important. They allow for tests of mass models and predictions, which deviate a lot from each other in that region.

Usually, mass measurements on radionuclides with Penning traps are performed using the destructive Time-of-Flight-Ion Cyclotron Resonance (TOF-ICR) method, where the stored and with rf fields probed ions are finally ejected out of the trap. Several hundred ions are needed to get a single spectrum, which takes typically about one hour with a production rate of a few hundred ions per second and a total efficiency of about 1%. Therefore, the TOF-ICR technique is not applicable to rarely produced superheavy nuclides with production rates of less than one per second but rather long half-lives, sometimes even in the order of seconds or minutes. Ideally suited here is the non-destructive Fourier Transform-ICR technique, investigating the image current induced by the ions in the trap electrodes. The newly developed double-Penning trap setup for SHIPTRAP featuring both common techniques is discussed here [2].

Experimental setup and results

The mass spectrometer consists of a cylindrical Penning trap to prepare the ions by buffer gas cooling and mass selective centering of the ion cloud. After that, the particles are transferred through a diffusion barrier channel with 2 mm inner diameter and 47 mm length into the hyperbolically shaped precision trap. The ring electrode of the precision trap is four-fold segmented: two segments are for excitation of the ion motion, while the others are used to detect the induced image current. The detection electrodes are connected to a superconducting helical resonator, forming an LC resonance ciruit with the intrinsic parasitic capacitances of the system. The voltage drop across this tank circuit is then amplified and finally Fourier transformed to obtain the required frequency information. Both traps are situated in a 77 K-environment, whereas the detection inductance as well as the first amplifier are placed in a liquid helium bath at 4.2 K to get the resonator superconducting and to reduce thermal noise. Besides the FT-ICR detection method, the ions can also be ejected from the trap onto a Channeltron or MCP detector to perform a Time-of-Flight measurement.

The properties of the LC detection circuit have been found to meet the requirements for the determination of the current induced by a single singly charged ion in the order of a few hundred fA. The Q-value of the helical coil, defined as the ratio between the resonance frequency and the width, is about 15000 in the unloaded situation and still above 1000 with the trap connected. The inductance of the present coil is $(337 \pm 6)\ \mu$H, which allows for tests with singly charged $^{87}Rb^+$ in a test setup at the University of Mainz. The capacitance can be adjusted around 1224 kHz by a varactor diode to shift the resonance frequency to different mass numbers. The frequency range is about 20 kHz.

Tests with the diffusion barrier channel have also been performed at different buffer gas pressures and with different sealings between the trap tube and the holder of the channel. The best results at 77 K were obtained with a ring-shaped spring covered by a teflon shield, which counteracts the thermal contraction at low temperatures. The pressure ratio between the purification trap region and the precision trap region was about 900 at a typical buffer gas pressure of $5.5 \cdot 10^{-4}$ mbar and a temperature of 77 K [3].

All parts of the setup are ready. The traps and all other electrodes are mounted and cabled. Presently, the ion transport through the trap stack in the superconducting magnet is optimised.

Outlook

For the Mainz test setup, the next steps are to store and detect ions with the conventional Time-of-Flight detection technique as well as with the here developed FT-ICR method. The single-ion sensitivity will be demonstrated soon with singly charged $^{87}Rb^+$ ions delivered by a surface ion source. Finally, the Mainz setup will move to SHIPTRAP at GSI and first mass measurements on superheavy elements, e.g. ^{254}No ($T_{1/2} = 51$ s), will be performed.

References

[1] K. Blaum, Phys. Rep. 425 (2006) 1.

[2] C. Weber, Eur. Phys. J. A 25, S01, (2005) 65.

[3] R. Ferrer et al., Eur. Phys. J. (2006) accepted.

* Work supported by the HGF under contract No. VH-NG-037 and by the BMBF under contract No. 06MZ215.

g factor of heavy ions: a new access to the fine structure constant

D. A. Glazov[1,2], V. M. Shabaev[1,2,3], A. V. Volotka[1,2], A. N. Artemyev[1,2], N. S. Oreshkina[1,2], G. Plunien[2], H.-J. Kluge[3], and W. Quint[3]

[1]St. Petersburg State University, Russia; [2]Institut für Theoretische Physik, TU Dresden, Germany; [3]GSI, Darmstadt, Germany

High-precision measurements of the g factor of H-like carbon [1] and oxygen [2] have triggered a great interest in related theoretical calculations (see Refs. [3, 4, 5, 6] and references therein). In particular, these studies provided a new determination of the electron mass to an accuracy which is 4 times better than that of the previously accepted value [7]. An extension of the g factor investigations to higher-Z ions could also lead to an independent determination of the fine structure constant α [8]. The accuracy of such a determination is, however, strongly limited by a large uncertainty of the nuclear structure effects which strongly increases when Z is growing [9]. In Ref. [10] it has been shown that the ultimate accuracy limit can be significantly reduced in the difference

$$g' = g^{[(1s)^2(2s)^2 2p_{1/2}]} - \xi g^{[1s]} \,,$$

where $g^{[(1s)^2(2s)^2 2p_{1/2}]}$ and $g^{[1s]}$ denote the g factors of the B-like and H-like heavy ions with the same nucleus, respectively. The parameter ξ here is chosen to cancel the nuclear size effect in this difference. Namely, $\xi = \Delta g_{\rm NS}^{[(1s)^2(2s)^2 2p_{1/2}]} / \Delta g_{\rm NS}^{[1s]}$, where $\Delta g_{\rm NS}$ denotes the corresponding nuclear-size correction. Due to the rather weak dependence of ξ on the nuclear charge distribution parameters, the corresponding uncertainty of g' is much smaller than that of $g^{[(1s)^2(2s)^2 2p_{1/2}]}$ and $g^{[1s]}$ alone. The reason for this lies in the specific behavior of the wavefunctions of the $s_{1/2}$- and $p_{1/2}$-states in the vicinity of the nucleus. Namely, it can be shown that in the nuclear region the product of the large and the small component of the Dirac wavefunction for these states differs mainly only by a constant factor. In one-electron approximation the g factor is given by

$$g_{\rm D} = \frac{2m\kappa c}{j(j+1)\hbar} \int_0^\infty {\rm d}r\, r^3 g_{n\kappa}(r) f_{n\kappa}(r) \,,$$

where $\kappa = (j+\frac{1}{2})(-1)^{j+l+\frac{1}{2}}$; j, l and n are the total angular momentum, the parity and the principal quantum number of the state, respectively. The nuclear-size correction enters $g_{\rm D}$ via the wavefunctions $g_{n\kappa}(r)$ and $f_{n\kappa}(r)$ obtained from the Dirac equation for the finite-nucleus potential.

In Ref. [10] we have considered the B- and H-like ions of lead, $^{208}{\rm Pb}^{77+}$ and $^{208}{\rm Pb}^{81+}$. The influence of the varying of the nuclear radius and the charge distribution model on g' has been investigated numerically. In addition to the one-electron Dirac contribution, the dominant interelectronic-interaction and QED corrections have been taken into account. The homogeneously-charged-sphere and the Fermi model with the rms radius of $5.5010(9)$ fm have been considered. It has been shown, that the parameter ξ is much more stable with respect to variations of the nuclear parameters than is the nuclear-size correction. The total relative uncertainty of g' due to the nuclear-size effect has been found to be 2.9×10^{-10}, while the uncertainty caused by the current value of $\alpha = 1/137.035\,999\,11(46)$ is 8.7×10^{-10}. We conclude: Measurements of the g factor of B- and H-like Pb to the relative accuracy of 7×10^{-10}, which is anticipated in the near future in the framework of the heavy ion trap project [11], accompanied by the theoretical calculations to the required precision, provide access to the determination of the fine structure constant with higher accuracy than that of the currently accepted value. Taking into account that the nuclear-charge-distribution uncertainty can be reduced by a factor of 3, compared to our very conservative estimate, we find that an improvement of the experimental accuracy to a 1×10^{-10} level would increase the precision of α by one order of magnitude. Concerning the accuracy this method can also compete with the new determination of α by Gabrielse and co-workers [12].

References

[1] H. Häffner *et al.*, Phys. Rev. Lett. **85**, 5308 (2000).

[2] J. L. Verdú *et al.*, Phys. Rev. Lett. **92**, 093002 (2004).

[3] V. M. Shabaev, Phys. Rev. A **64**, 052104 (2001).

[4] V. M. Shabaev and V. A. Yerokhin, Phys. Rev. Lett. **88**, 091801 (2002).

[5] V. A. Yerokhin, P. Indelicato, and V. M. Shabaev, Phys. Rev. Lett. **89**, 143001 (2002); Phys. Rev. A **69**, 052503 (2004).

[6] K. Pachucki *et al.*, Phys. Rev. A **72**, 022108 (2005).

[7] P. J. Mohr and B. N. Taylor, Rev. Mod. Phys. **77**, 1 (2005).

[8] G. Werth *et al.*, in *The Hydrogen Atom*, edited by S. G. Karshenboim *et al.* (Springer, Berlin, 2001), p. 204; S. G. Karshenboim, *ibid.* p. 651.

[9] A. V. Nefiodov, G. Plunien, and G. Soff, Phys. Rev. Lett. **89**, 081802 (2002).

[10] V. M. Shabaev *et al.*, Phys. Rev. Lett. **96**, 253002 (2006).

[11] W. Quint *et al.*, Hyperfine Interact. **132**, 457 (2001).

[12] G. Gabrielse *et al.*, Phys. Rev. Lett. **97**, 030802 (2006).

Relativistic and QED effects to the g factor of Li-like ions

D. A. Glazov[1,2], A. V. Volotka[1,2], A. N. Artemyev[1,2], V. M. Shabaev[1,2], I. I. Tupitsyn[1,2], V. A. Yerokhin[1], and G. Plunien[2]

[1]St. Petersburg State University, Russia; [2]Institut für Theoretische Physik, TU Dresden, Germany

New perspectives for testing QED effects via g factor of highly charged ions motivated numerous investigations on this subject during the last years. High-precision measurements of the g factor of light H-like ions [1, 2] provided a new determination of the electron mass to an accuracy which is four times better than that of the previously accepted value (see Ref. [3] and references therein). The analysis of corresponding experimental data stimulated a variety of accurate theoretical calculations (see, e.g., Refs. [4, 5, 6, 7, 8, 9] and references therein). Investigation of ions with more than one electron is anticipated in the nearest future. In particular, measurements of the g factor of Li-like calcium are currently in progress by the Mainz-GSI collaboration. An extension of these studies to higher Z systems will provide access to an independent determination of the fine structure constant [10].

The accuracy of theoretical values for the g factor of high-Z H-like ions is presently limited by nuclear effects. The uncertainty induced by them in the high-Z region is comparable with the binding QED correction of second order in α. At present nuclear structure effects do not allow for a theoretical description at the required level of accuracy. This represents a serious obstacle towards any further improvement of theoretical predictions and for identification of two-loop QED effects in future experiments. However, in Ref. [11] it was shown that the uncertainty due to nuclear effects can be significantly reduced in a specific combination of the g factors of H- and Li-like ions with the same nucleus. Below we briefly summarize the most accurate results for different contributions and for total values of the g factor of Li-like ions within the range $Z = 6-92$ obtained in Refs. [12, 13].

The total value of the ground-state g factor of a Li-like ion is conveniently written as

$$g = g_{\rm D} + \Delta g_{\rm int} + \Delta g_{\rm QED} + \Delta g_{\rm SQED} + \Delta g_{\rm nuc}\,.$$

Here $g_{\rm D}$ is the Dirac value for the point-charge nucleus. The interelectronic-interaction correction $\Delta g_{\rm int}$ has been obtained within a rigorous QED approach in the first order in $1/Z$. For the evaluation of higher-order contribution we have employed the large-scale configuration-interaction Dirac-Fock-Sturm method. The most accurate evaluation of the self-energy part of the one-loop QED correction was presented in Ref. [8]. References concerning other contributions to $\Delta g_{\rm QED}$ can be found in works [12, 13]. For the two-loop QED term only the analytical expansion to the order $(\alpha/\pi)^2(\alpha Z)^4$ [9] is known up-to-date. The screened QED correction $\Delta g_{\rm SQED}$ has been evaluated in framework of QED with the effective local potential that accounts for most part of the interelectronic interaction. The term $\Delta g_{\rm nuc}$ incorporates the nuclear-size, nuclear-recoil [5, 6] and nuclear-polarization [7] corrections.

Table 1: Individual contributions to the ground-state g factor of Li-like ions.

	^{40}Ca^{17+}	^{238}U^{89+}
Dirac value	1.996 426 011	1.910 722 624 (1)
Nucl. size	0.000 000 014	0.000 241 30 (43)
Interel. inter.	0.000 454 45 (14)	0.002 501 4 (38)
QED, $\sim\alpha$	0.002 325 555 (5)	0.002 446 3 (2)
QED, $\sim\alpha^2$	−0.000 003 520 (2)	−0.000 003 6 (8)
Scr. QED	−0.000 000 33 (10)	−0.000 003 1 (15)
Nucl. recoil	0.000 000 061 (2)	0.000 000 28 (69)
Nucl. polar.	0.000 000 000	−0.000 000 27 (14)
Total	1.999 202 24 (17)	1.915 904 9 (42)

Table 1 presents the most recent results [13] for the individual contributions to the g factor of the ground state of Li-like calcium and uranium. The total accuracy is mainly limited by the interelectronic-interaction contribution. Aiming for further improvement of the total theoretical accuracy, a rigorous QED evaluation of $\Delta g_{\rm int}$ to the order $1/Z^2$ and of the $\Delta g_{\rm SQED}$ beyond the local-potential approximation is desirable.

References

[1] H. Häffner *et al.*, Phys. Rev. Lett. **85**, 5308 (2000).

[2] J. L. Verdú *et al.*, Phys. Rev. Lett. **92**, 093002 (2004).

[3] P. J. Mohr and B. N. Taylor, Rev. Mod. Phys. **77**, 1 (2005).

[4] T. Beier *et al.*, Phys. Rev. A **62**, 032510 (2000).

[5] V. M. Shabaev, Phys. Rev. A **64**, 052104 (2001).

[6] V. M. Shabaev and V. A. Yerokhin, Phys. Rev. Lett. **88**, 091801 (2002).

[7] A. V. Nefiodov, G. Plunien, and G. Soff, Phys. Rev. Lett. **89**, 081802 (2002).

[8] V. A. Yerokhin, P. Indelicato, and V. M. Shabaev, Phys. Rev. Lett. **89**, 143001 (2002); Phys. Rev. A **69**, 052503 (2004).

[9] K. Pachucki *et al.*, Phys. Rev. A **72**, 022108 (2005).

[10] V. M. Shabaev *et al.*, Phys. Rev. Lett. **96**, 253002 (2006).

[11] V. M. Shabaev *et al.*, Phys. Rev. A **65**, 062104 (2002).

[12] D. A. Glazov *et al.*, Phys. Rev. A **70**, 062104 (2004).

[13] D. A. Glazov *et al.*, Phys. Lett. A **357**, 330 (2006).

Many–particle effects in relativistic heavy ion collisions

A. Surzhykov*[1], U. D. Jentschura[1], Th. Stöhlker[2], and S. Fritzsche[3]
[1]MPI–K, Heidelberg, Germany; [2]GSI, Darmstadt, Germany; [3]University of Kassel, Germany

Experiments on relativistic ion–atom collisions have a long tradition at the GSI storage ring [1, 2]. A number of case studies have been performed, for example, on electron capture as well as on ionization and excitation of heavy projectile ions. While in the past, however, most of the experiments have dealt with one–electron systems, much of today's interest is focused also on the projectiles with few bound electrons. Quite often, collisions of such few–electron heavy ions can be well understood (theoretically) within the effective single–particle approach if the Pauli principle is properly taken into account [3]. For high–Z domain, this approach is well justified because the inter-electronic effects are known to be much weaker than the electron–nucleus interaction.

Despite the good applicability of effective one–particle calculations, we discuss here case studies in which many–electron effects become important, beyond the Pauli principle and the coupling of the angular momenta. These studies concern the radiative electron capture (REC) into excited states of few–electron heavy ions [3, 4]. Following such a capture, the excited ionic states appear to be *aligned* with respect to the incident ion momentum. The alignment of the excited states—i.e., the unequal population of the sublevels with the different modulus of magnetic quantum number $|M_J|$—is known to govern the properties of the subsequent radiative decay and, hence, has been studied by us in detail. In particular, we calculated the alignment of the excited states of beryllium–like heavy ions following REC. Apart from the simple one–particle model [3], calculations have been performed also by means of Multi–configuration Dirac–Fock (MCDF) approach [4]. In this approach, both the initial and the final ionic wavefunctions are represented as a linear combination of configuration state functions (CSF) and optimized on the basis of the Dirac–Coulomb Hamiltonian. Further relativistic contributions were added by diagonalizing the Dirac–Coulomb–Breit Hamiltonian matrix.

Figure 1 displays the (degree of) alignment of the $1s^2_{1/2}2s_{1/2}3d_{3/2}\ :\ J\ =\ 2$ state of the beryllium–like gold Au^{75+} ions following REC. Due to the coupling of the electron momenta to the total angular momentum $J = 2$, two parameters $\mathcal{A}_{20}$ and $\mathcal{A}_{40}$ are required to describe the alignment of the residual ions (see Ref. [4] for more details). These parameters, which are directly related to the partial cross sections $\sigma_{|\alpha JM_J\rangle}$ for the population of the different ionic sublevels $|\alpha JM_J\rangle$, have been calculated within the effective one–particle as well as the MCDF approach for the projectile energies in the range $10 \le T_p \le 600$ MeV/u. As seen from the Figure, the

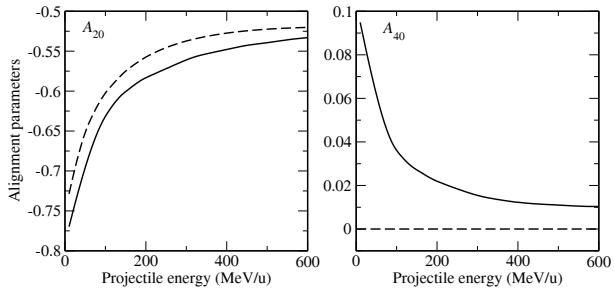

Figure 1: Alignment parameters $\mathcal{A}_{20}$ and $\mathcal{A}_{40}$ of the $1s^2\,2s\,3d_{3/2}\ \ J\ =\ 2$ state of beryllium–like gold ions following REC. Results from an effective one–particle model (– –) are compared with those from MCDF calculations (—) in Coulomb gauge.

one–particle calculations predict the large negative alignment parameter $\mathcal{A}_{20}$ while the fourth–rank parameter $\mathcal{A}_{40}$ is zero over all the energy range. A *qualitatively* different behaviour of the $\mathcal{A}_{40}$ has been obtained by means of the MCDF approach. The MCDF calculations show that REC into the $1s^2\,2s\,3d_{3/2}\ \ J\ =\ 2$ state of beryllium–like gold ions results in rather a large alignment $\mathcal{A}_{40}$, which is almost 0.1 at a projectile energy of T_p = 10 MeV/u and slightly decreases to 0.01 for higher energies. Such a—nonvanishing—parameter arises mainly due to the mixture of the $1s^2\,2s\,3d_{3/2}\ \ J\ =\ 2$ level with other levels having a strong alignment. From our calculations, in particular, we found a large admixture of about 3 % of the $1s^2\,2s\,3d_{5/2}\ \ J_f\ =\ 2$ level for which a large positive parameter $\mathcal{A}_{40}$ has been predicted before [4]. Moreover, besides the non–zero parameter $\mathcal{A}_{40}$, the configuration interaction effects also lead to an 5 % enhancement (of the absolute value) of the alignment parameter $\mathcal{A}_{20}$. These discrepancies between two theoretical approaches clearly indicates that apart from the momentum coupling and the Pauli principle, the interelectronic interaction effects may play a very important role, even in relativistic collisions of few–electron heavy ions.

References

[1] Th. Stöhlker , Phys. Scr. T80 (1999) 165

[2] S. Fritzsche, P. Indelicato, and Th. Stöhlker, J. Phys. B 38 (2005) S707

[3] A. Surzhykov, U. D. Jentschura, Th. Stöhlker and S. Fritzsche, (in preparation)

[4] A. Surzhykov, U. D. Jentschura, Th. Stöhlker and S. Fritzsche, Phys. Rev. A 73 (2006) 032716

* surz@mpi-hd.mpg.de

Photon–photon correlations in the decay of aligned hydrogenlike ions*

L. Borowska† [1,2], A. Surzhykov[3], Th. Stöhlker[4], and S. Fritzsche[1]

[1]University of Kassel, Kassel, Germany; [2]KINR, 03680 Kyiv, Ukraine; [3]MPI–K, Heidelberg, Germany; [4]GSI, Darmstadt, Germany

The two–photon decay of (hydrogenlike) atoms has been studied intensively both, by theory and experiment. However, while most investigations in the past have dealt with neutral hydrogen or low–Z ions, recent interest was focused also onto the region of high–Z ions [1]. Apart from the total decay rates and spectral distribution functions, further details about the two–photon decay can be obtained by studying the angle–angle correlations between the two emitted photons. Such angle–resolved case studies often appear to be more sensitive to relativistic and nondipole effects [2]. In all theoretical investigations on the angular correlation of the (two) emitted photons, the initially excited state of the ions was assumed to be not aligned, an assumption which is not well justified in most experiments. In fact, since the excited states are produced in radiative recombination, collisional excitation, or inner–shell ionization, they are more often then not aligned if not even polarized along the direction of the incoming ion beam.

In our recent work, we applied the density matrix theory to investigate the photon–photon angular correlations in the (two–photon) decay of aligned hydrogenlike ion. Within this theory, the population of the excited ionic states and their subsequent decay are closely related to the so–called alignment paramerers A_k. The relation between these alignment parameters and the angle–angle correlations of the subsequently emitted photons is obtained [3]

$$\frac{d^3W}{dx d\cos\theta_1 d\cos\theta_2 d\varphi_2}(x,\theta_1,\theta_2,\varphi_2) = 2\pi\,(E_i - E_f)\,\frac{E_{\gamma_1}E_{\gamma_2}}{(2\pi)^3c^2}$$
$$\times \quad \frac{1}{\sqrt{2j_i+1}} \sum_{\mu_i,\mu_f,\lambda_1,\lambda_2,k} |M_{fi}(\mu_f,\mu_i,\lambda_1,\lambda_2)|^2$$
$$\times \quad (-1)^{-j_i+\mu_i}\,\langle j_i\mu_i, j_i-\mu_i \mid k0\rangle\,\mathcal{A}_{k0} \qquad (1)$$

in the framework of second–order perturbation theory, making use of the Coulomb Green function.

To explore how the population (alignment) of the excited ionic state affects the angular correlation of the photons in the case of the two–photon decay, detailed computations have been carried for the $3d_{5/2} \rightarrow 1s_{1/2}$ decay of hydrogen–like uranium, U^{91+}. Fig. 1 displays the photon–photon correlation function (1) for the $3d_{5/2} \rightarrow 1s_{1/2}$ (two–photon) decay, following the REC into (initially) bare uranium at the projectile energy T_p = 200 MeV/u. Beside of the correlation functions for the initially 'aligned' ions (dashed line), results are shown also for the decay of unaligned ions (solid line). From the comparison of these two functions of the excited states a remarkable effect is found owing to the alignment by the electron capture. In fact,

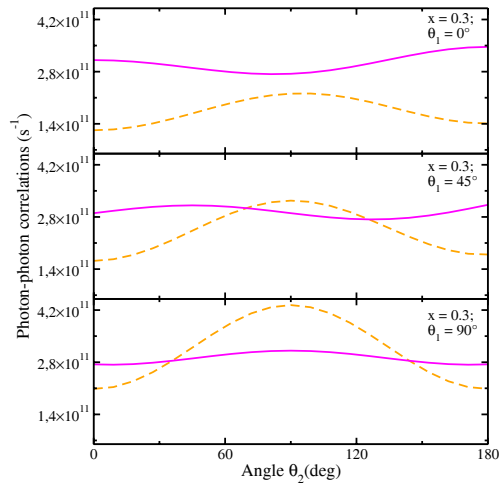

Figure 1: (color online). Photon–photon angular correlation (1) of the $3d_{5/2} \rightarrow 1s_{1/2}$ (two–photon) decay following REC into the $3d_{5/2}$ state of initially bare uranium ions at the projectile energy T_p = 200 MeV/u. The correlation functions are shown for the relative photon energy x = 0.3 and for the three (fixed) polar angles $\theta_1 = 0°, 45°, 90°$. Beside of the correlation function for an initial alignment (– –), results are shown for the two–photon decay of unaligned ions (—).

these computations differ only in the values of the alignment parameters, $\mathcal{A}_2$ and $\mathcal{A}_4$, while the size (normalization) of the correlation functions is determined by the geometry of the photon detectors. As seen from this figure, both photons are likely emitted in the parallel (or back–to–back) direction, similar as for the unaligned case, but *now* predominantly in perpendicular to the initial quantization axis (the axis of alignment). Therefore, these computations clearly indicate that the knowledge about the population mechanism and, hence, the initial alignment of the ions is essential for the analysis of any measurement of the photon–photon emission pattern.

References

[1] R. W. Dunford *et al.*, Phys. Rev. A **74**, 012504 (2006).

[2] A. Surzhykov, P. Koval, S. Fritzsche, Phys. Rev. A **71**, 022509-1 (2005).

[3] L. Borowska, A. Surzhykov, Th. Stöhlker, S. Fritzsche, Phys. Rev. A **74**, 062516-1 (2006).

* Work supported by the GSI under Project No. KS-FRI.

† lesya@physik.uni-kassel.de

Double ionization of Li-like ions by high-energy photons

A.I. Mikhailov[1], A.V. Nefiodov[1,2], and G. Plunien[2]

[1]PNPI, St. Petersburg, Russia; [2]Institut für Theoretische Physik, TU Dresden, Germany

The processes of double ionization by absorption or inelastic (Compton) scattering of a photon from atomic systems are of fundamental interest. This is due to the fact that the two-electron emission is exclusively caused by the electron-electron interaction, the accurate treatment of which is still one of the main tasks for different theoretical approaches. As a target, it is usual to use the neutral He atom in the ground state, which is supposed to be the simplest atomic system, where double ionization can occur [1, 2, 3]. Up to now no experimental data are available concerning double ionization of He in metastable states. This is connected with difficulties in preparation of any amount of such targets. However, these processes could serve as a testing ground for the study of inter-shell electron correlations.

In contrast to neutral He atoms, the use of multicharged ions as targets could provide important information about most generic features of ionization processes. In particular, it concerns the study of the universal scalings in the behavior of ionization cross sections and double-to-single ionization ratios. There also exist parametrical relationships between the cross sections for ionization of multicharged ions with different number of electrons. This opens wide perspectives for the investigation of both inner- and inter-shell electron correlations, since the experiments on stable targets can be used to test the theoretical predictions for ionization of excited states.

We have investigated the double ionization of three-electron ions by photons with high but still nonrelativistic energies ω characterized by $I \ll \omega \ll m$, where I is the ionization threshold energy and m is the electron mass ($\hbar = 1$, $c = 1$) [4, 5]. More precisely, the energy domain $\omega \gg I$ is asymptotic for the double-to-single ionization ratio only in the case of photoabsorption. In Compton scattering, the asymptotic regime is reached at higher energies $\omega \gg \eta$, where η is the average momentum of the bound electron.

For photoabsorption and Compton scattering on lithium-like ions, the universal scaling behavior of the double-to-single ionization ratios are given by [4, 5]

$$R_{\rm ph} = \frac{\sigma_{\rm ph}^{++}}{\sigma_{\rm ph}^{+}} = \frac{0.288}{Z^2}\,, \quad R_{\rm C} = \frac{\sigma_{\rm C}^{++}}{\sigma_{\rm C}^{+}} = \frac{0.147}{Z^2}\,, \quad (1)$$

respectively. In addition, one can write the following relation

$$R_{\rm ph} \simeq 2R_{\rm C}\,, \quad (2)$$

which turns out to be almost exact.

At high photon energies, the contributions arising from double photoeffect and double Compton effect can be separated experimentally, if one measures simultaneously the recoil momentum of target ions and their charge state [2, 3]. As known, in photoabsorption the target nucleus absorbs large recoil momenta $q \gg \eta$, while in Compton scattering the recoil momenta transferred to the nucleus are relatively small ($q \leq \eta$). If the distribution over the recoil momenta is not measured in the experiment, the observable quantity is the branching ratio of number of ions, the charge of which is increased by two units, to the number of ions, the charge of which is increased by one unit. To leading order of the perturbation theory over the parameter $1/Z$, this ratio reads

$$\begin{aligned} R &= \frac{\sigma_{\rm ph}^{++} + \sigma_{\rm C}^{++}}{\sigma_{\rm ph}^{+} + \sigma_{\rm C}^{+}} \simeq \quad (3) \\ &\simeq R_{\rm ph}\frac{2\sigma_{\rm ph}^{+} + \sigma_{\rm C}^{+}}{2(\sigma_{\rm ph}^{+} + \sigma_{\rm C}^{+})} \simeq R_{\rm C}\frac{2\sigma_{\rm ph}^{+} + \sigma_{\rm C}^{+}}{\sigma_{\rm ph}^{+} + \sigma_{\rm C}^{+}}\,, \end{aligned}$$

where the relation (2) has been employed. Within the non-relativistic high-energy domain, the cross section $\sigma_{\rm ph}^{+}$ for single photoeffect decreases roughly as $\omega^{-7/2}$ for growing photon energy ω. The cross section $\sigma_{\rm C}^{+}$ for Compton scattering approaches the asymptotic constant $3\sigma_{\rm T}^{+}$, where $\sigma_{\rm T}^{+}$ is the Thomson cross section for elastic scattering of a photon by a free electron. Accordingly, in contrast to the ratios $R_{\rm ph}$ and $R_{\rm C}$, the ratio R depends on the photon energy, varying within the range $R_{\rm C} < R < R_{\rm ph}$. When the photon energy increases up to $\omega \gg \eta$, the ratio (3) declines approaching the constant limit of $R_{\rm C}$.

As we have shown, the universal scaling behavior can be established for the double-to-single ionization ratios in the case of photoabsorption and Compton scattering of a high-energy photon from three-electron atomic systems. The partial contributions due to the direct and indirect ionization channels have been taken into account. We have also found parametrical relations between the cross sections for ionization processes on Li- and He-like ions with the same nuclear charge Z [4, 5]. These relations can be employed for experimental tests of theoretical predictions concerning the double ionization of low-lying excited states of He-like ions. Such experiments could become feasible using x-ray lasers within the PHELIX facilities at GSI.

References

[1] J.H. McGuire *et al*., J. Phys. B 28 (1995) 913.

[2] L. Spielberger *et al*., Phys. Rev. Lett. 74 (1995) 4615.

[3] L. Spielberger *et al*., Phys. Rev. A 59 (1999) 371.

[4] A.I. Mikhailov *et al*., Phys. Lett. A 355 (2006) 363 .

[5] A.I. Mikhailov, A.V. Nefiodov, and G. Plunien, Phys. Rev. Lett. 97 (2006) 233003.

Photon angular distribution in nuclear excitation by electron capture

A. Pálffy[1,2], Z. Harman[1], A. Surzhykov[1], and W. Scheid[2]
[1]Max-Planck-Institut für Kernphysik, Heidelberg; [2]Justus-Liebig-Universität, Giessen

In the resonant process of nuclear excitation by electron capture (NEEC), a free electron is captured into a bound atomic shell with the simultaneous excitation of the nucleus. NEEC is a process analogous to dielectronic recombination (DR), and when followed by the radiative decay of the nucleus, it is a competing resonant channel of radiative recombination (RR). Partly due to the dominant RR background, NEEC has not been observed experimentally yet, although other experimental observation of atomic physics processes with regard to the internal structure of the nucleus have been reported. NEEC is expected to allow the determination of nuclear transition energies and probabilities, the study of atomic vacancy effects on nuclear lifetimes and population mechanisms of excited nuclear levels.

Our studies regarding total cross sections for NEEC followed by the radiative decay of the nucleus and its possible quantum interference with RR are presented in Refs. [1,2]. The measurement of the angular distribution of the emitted photons in the recombination process can offer a useful method of discerning NEEC from RR [3]. In the following we investigate the photon angular distribution in the radiative decay of the nucleus following NEEC for the E2 transitions occurring in $^{238}_{92}$U. The photon emission pattern is substantially different from the one of the concurrent RR process and provides a means of discerning the two processes and to suppress the RR background.

As the properties of the radiation emitted in the nuclear decay are closely related to the alignment of the nuclear excited state, the population of these states as it arises due to the electron capture process has to be investigated. We apply a density matrix formalism to describe the alignment of vibrationally excited nuclear states formed by NEEC and the angular distribution of the de-excitation radiation. The angular differential cross section of this process is given by

$$\frac{d\sigma_{\rm NEEC}}{d\Omega}(\theta) = \frac{\sigma_{\rm NEEC}}{4\pi} W(\theta)\,, \qquad (1)$$

where $\sigma_{\rm NEEC}$ is the total cross section for NEEC followed by the radiative decay of the excited nucleus [1] and θ denotes the angle of the photon emission with respect to the direction of the incoming electron in the ionic frame. The angular distribution $W(\theta)$ for the $2^+ \to 0^+$ decay is given by

$$W(\theta) = \left(1 - \frac{\sqrt{70}}{14}\mathcal{A}_2 P_2(\cos\theta) - \frac{2\sqrt{14}}{7}\mathcal{A}_4 P_4(\cos\theta)\right), \qquad (2)$$

where the Legendre polynomials $P_k(\cos\theta)$ are weighted by the alignment parameters $\mathcal{A}_k$, which in turn are related to the cross section for the population of the different nuclear magnetic sublevels [3].

We consider the capture into the L shell of initially He-like $^{238}_{92}$U ions, as the energy of the first excited nuclear level of 44.91 keV makes the capture into the K shell of bare U impossible. The reduced transition probability $B(E2)$ for the $E2$ transition of $^{238}_{92}$U as well as the energy of the nuclear transition are taken from Ref. [4]. We envisage the scenario of a possible NEEC experiment in a storage ring, in which the radiation is emitted by the nucleus of the U^{89+} ion moving relativistically with respect to the target electrons. In Figure 1 we present the angular distribution $W(\theta_{\rm lab})$ of the photons following the electron capture into the $2s$ orbital of $^{238}_{92}$U with respect to the laboratory frame and make a comparison between the NEEC and RR photon angular distributions. While the maximum value for the RR angular distribution is at $\theta_{\rm lab} = 64°$, the emitted photons following NEEC have an angular pattern with maxima at $\theta_{\rm lab} = 46°$ and $\theta_{\rm lab} = 151°$. As the emission pattern of the gamma photons is significantly different from the one of the background RR process, photon angle-resolved measurements may prove to be the appropriate method for the observation of NEEC.

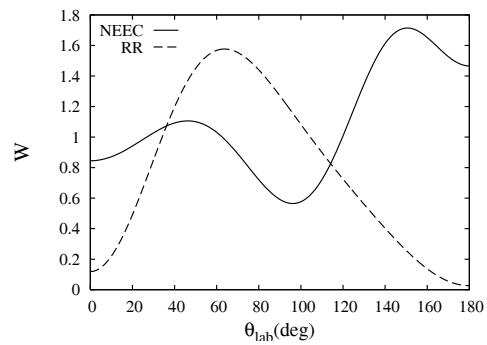

Figure 1: Angular distribution of the photons with respect to the laboratory frame for the case of RR and NEEC into the $2s$ orbital of initially He-like $^{238}_{92}$U. Both NEEC and RR angular distributions are normalized to 4π.

References

[1] A. Pálffy, W. Scheid and Z. Harman, Phys. Rev. A 73 (2006) 012715.

[2] A. Pálffy, Z. Harman and W. Scheid, Phys. Rev. A 75 (2007) 012719.

[3] A. Pálffy, Z. Harman, A. Surzhykov and U.D. Jentschura, Phys. Rev. A (2007) in press.

[4] S. Raman, C. Nestor and P. Tikkanen, At. Dat. Nucl. Dat. Tabl. 78 (2001) 1.

Hyperfine splitting in lithiumlike scandium

A. V. Volotka[1,2], D. A. Glazov[1,2], A. N. Artemyev[1,2], N. S. Oreshkina[1,2], V. M. Shabaev[1,2], I. I. Tupitsyn[1,2], and G. Plunien[1]

[1]Institut für Theoretische Physik, TU Dresden, Germany; [2]St. Petersburg State University, Russia

High-precision experiments on the ground state hyperfine splitting in highly charged ions performed at the GSI facilities and at the EBITs (see, e.g., Refs. [1, 2, 3]) have triggered intensive theoretical investigations of this effect. The error bars of the theoretical hyperfine splitting values are mainly determined by the nuclear magnetization distribution correction, the so-called Bohr-Weisskopf (BW) effect [4]. Since the total QED correction to the hyperfine splitting is of the same order of magnitude as the uncertainty of the BW correction, investigations of pure QED effects on the hyperfine structure in heavy hydrogenlike ions turn out to be unfeasible. In this context, it was proposed to consider a specific difference of the ground state hyperfine splitting in H-like and Li-like ions [5]. In this specific difference the uncertainty due to the BW effect is strongly reduced.

Recently measurement of the ground state hyperfine splitting in lithiumlike scandium has been announced [3]. In a recent work [6] we have reconsidered the theory of this effect and improved the accuracy of corresponding theoretical prediction. The ground state hyperfine splitting of a lithiumlike ion is conveniently presented as

$$\Delta E_\mu = \frac{1}{6}\,\alpha\,(\alpha Z)^3\,\frac{m}{m_{\rm p}}\,\frac{\mu}{\mu_{\rm N}}\,\frac{2I+1}{2I}\,\frac{1}{(1+\frac{m}{M})^3}\,mc^2 \times\Big[A(\alpha Z)(1-\delta)(1-\varepsilon)+\frac{1}{Z}B(\alpha Z) +\frac{1}{Z^2}C(Z,\alpha Z)+x_{\rm rad}\Big]\,.$$

Here m is the electron mass, $m_{\rm p}$ is the proton mass, μ is the nuclear magnetic moment, $\mu_{\rm N}$ is the nuclear magneton, I is the nuclear spin, and M denotes the mass of the nucleus. The one-electron relativistic factor $A(\alpha Z)$ can be analytically derived from the Dirac equation. The finite nuclear size correction δ has been evaluated numerically employing the homogeneously-charged-sphere model for the charge distribution. The BW correction ε has been calculated within the single particle nuclear model. The uncertainty of this correction is estimated to be about 50%.

The first-order interelectronic-interaction correction described by the function $B(\alpha Z)$ has been evaluated within a rigorous QED approach. Higher-order correction $C(Z,\alpha Z)/Z^2$ has been obtained in the framework of large-scale configuration-interaction Dirac-Fock-Sturm method. The term $x_{\rm rad}$ describes the QED contribution. This term has been calculated within one-loop QED approximation. The key advantage of our evaluation is the use of non-Coulomb binding potential $V_{\rm eff}$, which partly takes into account the interelectronic-interaction effect. We have used the Kohn-Sham potential, employing standard iteration procedure to achieve self-consistency. In addition, our calculations explicitly take into account the finite nuclear size and the distribution of the nuclear magnetic moment. The results of the calculation are shown in Table 1. For comparison, the results of the previous calculations [7, 8] are presented as well.

Table 1: The ground state hyperfine splitting of lithiumlike scandium [6], in meV.

Dirac value	6.9650
Finite nuclear size corr.	−0.0224(3)
BW corr.	−0.0064(32)
Interel. inter. $1/Z$	−0.8817
Interel. inter. $1/Z^2$ and higher	0.0150(2)
QED (with screening)	−0.0061(6)
ΔE_μ, total value	6.0633(33)
ΔE_μ, Ref. [7]	6.0628(60)
ΔE_μ, Ref. [8]	6.0768

The accuracy of the theoretical result obtained in [6] amounts to 0.05% which is two times better than that of the previous result of Ref. [7]. It is now determined completely by the BW correction. The improvement is achieved due to the relativistic consideration of the higher-order interelectronic-interaction corrections and non-perturbative in αZ evaluation of the QED contribution. The theoretical methods developed in this work, can also be applied to other Li- and B-like ions, including those which are of special interest for astrophysical observations [9].

References

[1] I. Klaft *et al.*, Phys. Rev. Lett. **73**, 2425 (1994).

[2] J. R. Crespo López-Urrutia *et al.*, Phys. Rev. Lett. **77**, 826 (1996).

[3] M. Lestinsky *et al.*, Proc. 38th Int. Conf. of the Eur. Group on Atomic Systems, 61 (2006).

[4] V. M. Shabaev *et al.*, Phys. Rev. A **56**, 252 (1997).

[5] V. M. Shabaev *et al.*, Phys. Rev. Lett. **86**, 3959 (2001).

[6] N. S. Oreshkina *et al.*, Opt. Spectr., in press (2007).

[7] V. M. Shabaev, M. B. Shabaeva, and I. I. Tupitsyn, Astron. Astrophys. Transact. **12**, 243 (1997).

[8] S. Boucard and P. Indelicato, Eur. Phys. J. D **8**, 59 (2000).

[9] R. A. Sunyaev and D. Docenko, private communication.

Experiments with laser-heated hohlraum targets

T. Heßling[1], A. Blažević[1], A. Pelka[2], G. Schaumann[2], D. Schumacher[2], M. Roth[2], and D.H.H. Hoffmann[2]

[1]GSI, Darmstadt, Germany; [2]TU Darmstadt, Germany

Introduction

One major research area of the plasma physics group at GSI is the energy loss measurement of heavy ions in dense, hot plasmas[1]. Heavy ions from the UNILAC pass through a plasma that is usually generated with an intense laser beam. The energy loss due to the interaction of the ions with the plasma is determined by a time of flight measurement.

Until now the experiment is done with a thin carbon foil directly heated by the *nhelix* high energy laser. This type of geometry suffers from gradients in density as well as temperature within the plasma that change considerably between two microbunches. Therefore a precise, time-resolved characterization of the key plasma parameters, like the free electron density, is necessary in order to compare experimental data with theoretical models.

Another possible setup utilizes an indirectly heated hohlraum target. The material for the interaction with the ions is placed inside a cylindrical hohlraum which has a secondary cavity attached to it, serving as a radiation converter. The laser will heat the converter volume and generate thermal radiation in the soft x-ray regime, which in turn will generate the plasma in the cylindrical hohlraum. Simulations have shown homogeneous plasma parameters during the interaction time of an ion bunch[2].

In corporation with the University of Technology Darmstadt a target facility has been set up in the "Institut für Kernphysik" where we manufacture the hohlraum targets.

Target production

In order to perform the energy loss measurement two types of hohlraums are needed: the cylindrical cavity containing a CH-foam to be heated and a spherical radiation converter attached to this. Both hohlraums can now be manufactured, two examples are shown in figure 1.

The production process starts with a brass positive form of the cavity. Onto this a thin layer of 10 μm gold is deposited by electroplating. Openings, like the laser entrance and diagnostic holes, are created lithographically, the target is coated with a photo resist that is illuminated under a microscope. Typical sizes of the openings are 130 μm for a diagnostic port and 350 μm for the laser entrance hole. At the developed areas the gold is removed by etching. As a last step the brass is etched through the holes in the gold layer.

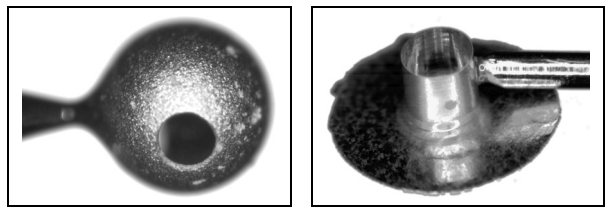

(a) spherical hohlraum, D = 760 μm (b) cylindrical hohlraum, D = 1 mm

Figure 1: Gold hohlraum targets manufactured at the University of Technology Darmstadt

Experiments

First experiments will focus on the spectral characteristics of the generated thermal radiation, aiming towards a time- and spectrally resolved measurement. The high-energy laser *nhelix* at GSI will be used for the heating.

The expected temperature with the available energy from the laser is in the range of a few electron volts. According to Planck's radiation law the wavelength of maximum emission is thereby in the ultraviolet. A spectrometer for this wavelength regime will be absolutely calibrated in intensity with a deuterium lamp. Knowing the energy in solid angle and wavelength and the radiation temperature can be deduced.

The time-resolution is achieved with a streak camera. A glass window is coated with a special layer that converts the UV light into green light detectable by the streak camera. The efficiency of the conversion is almost 100%.

The next step will be to go to higher energies and use the Phelix laser as the heating source, in order to generate a plasma volume large enough for the interaction with heavy ions. The thermal radiation will move to the soft x-ray regime and a different diagnostic is needed, which is currently designed.

References

[1] M. Roth *et al.*, "Energy loss of heavy ions in laser-produced plasmas", Europhys. Lett. **50** (2000), p. 28

[2] E. Vasina *et al.*, "Numerical investigation of Ion Beam Stopping in Indirect Laser Targets on Phelix-Unilac: Integrated 2D-Simulations", GSI Scientific Report (2000)

[3] G. Schaumann *et al.*, "Upgrade of the *nhelix* laser system at GSI", GSI Scientific Report (2004)

Development and calibration of a Thomson parabola with a MCP*

K. Harres[1], M. Schollmeier[1], J. Schreiber[2], B. M. Hegelich[3], F. Nürnberg[1], E. Brambrink[4,5], P. Audebert[5], A. Blažević[6], and M. Roth[1]

[1]Technische Universität Darmstadt, Darmstadt, Germany; [2]Ludwig-Maximilians-Universität, München, Germany; [3]Los Alamos National Laboratories, Los Alamos, USA; [4]Sandia National Laboratories, Livermore, USA; [5]Laboratoire d'Utilisation des Lasers Intenses, Palaiseau, France; [6]GSI, Darmstadt, Germany

The acceleration of ion beams by lasers has gained increasing attention over the last years. Irradiation of thin target foils with laser intensities higher than $I = 10^{18}$ W/cm^2 leads to a strong acceleration of relativistic electrons through the target in the laser direction. These electrons built up a strong electric field ($\sim$ TV/m) at the target rear surface which ionizes the atoms on the surface and accelerates them. This mechanism can be described by the *TNSA* (target normal sheath acceleration) [1] theory. For the detection and the analysis of the laser-accelerated ions a new Thomson-parabola (TP) was developed. A TP is a spectrometer that consists of parallel electric and magnetic fields which are orientated perpendicular to the beam propagation direction [2]. Inside the TP ions are deflected due to their charge-to-mass ratio. For an ideal TP with no fringe fields the deflection is given by

$$y^2 = \frac{qB^2lD}{mE}x \; . \qquad (1)$$

Here y and x are the deflections due to the magnetic and electric fields, B and E are the field amplitudes, l the field length, D the drift length between the fields and the detector and q and m are the charge and the mass of the ions respectively. A TP provides a seperation of all ions species

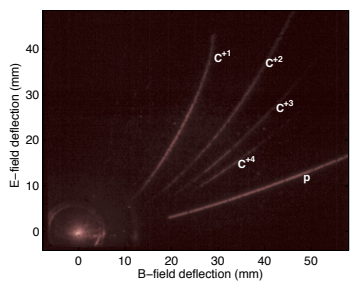

Figure 1: Proton and C^+-C^{+4} parabolas

and charge states. Every single parabola on the detector belongs to a different ion mass or charge state. The deflection along the parabolas includes the information about the ion energies. For the detection of the ions a micro channel plate (MCP) coupled with a phosphor screen was used. MCPs afford an online measurement of the accelereated ions. This is the main advantage compared to TPs with solid state nuclear track detectors [3]. Figure 1 shows an image of the phosphor screen for a laser shot onto a 20 µm thick gold foil. With the help of a tracking routine it is possible to identify the different ions. To extract the ion energy spectra from the intensities on the phoshor screen a calibration of the TP especially of the MCP was necessary. This calibration was accomplished within a laser experiment at the *LULI* 100 TW in Palaiseau, France. Besides the TP with MCP two other TPs with absolutely calibrated CR-39 detectors were used. Through a comparison between these different types of detectors it was possible to calibrate the MCP and to extract the ion energy spectra, see figure 2.

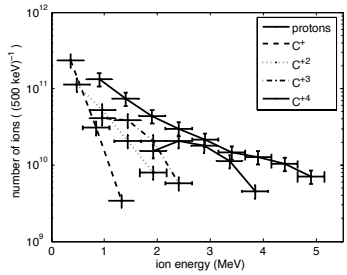

Figure 2: Energy spectra of the protons and C-ions

Independent from the target material protons from depositions on the target surface were accelerated due to their highest charge-to-mass ratio. They shield the electric field from the heavier ions. To clean up the target a CW heating laser was used that heated the target to temperatures over 1000 K. The proton line was completely removed and multiple heavy ions up to 5 MeV/u were accelerated (figure 3).

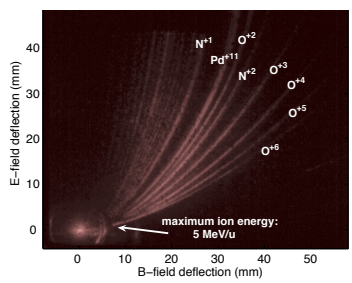

Figure 3: Oxygen, nitrogen and palladium lines from a heated 15 µm thick palladium target.

References

[1] S.P. Hatchett et al., Phys. Plasmas **7**, 2076 (2000)

[2] J.J. Thomson, Philosophical Magazine [6] **21**, 225 (1911)

[3] B.M. Hegelich, Physical Review Letters **89**, 8 (2002)

* Work supported by VIPBUL

Diamond Detectors for Longitudinal Properties of Pulsed Heavy-Ion Beams

F. Wamers[1,2], A. Blažević[2], E. Berdermann[2], B. Lommel[2], R. Knobloch-Maas[1], P. Moritz[2], G. Schaumann[1], M. Schollmeier[1], J. v. Kalben[1], B. Voss[2], E. Wörner[3], and M. Roth[1]

[1]TUD, Darmstadt, Germany; [2]GSI, Darmstadt, Germany; [3]FIAF, Freiburg, Germany

Experimental Motivation

For the investigation of the dynamics of heavy-ion beams penetrating hot dense plasma at the Z6 area at GSI an experimental setup was developed, which allows for diagnosing a directly laser-heated plasma target, and measuring the charge state and energy loss of an ion beam after / in it [1, 2]. The varying energy loss of the ion beam in the target (solid—plasma—vacuum) is determined in a TOF-like technique, in which temporal shifts (of the UNILAC period of 9.224 ns) between individual ion micro pulses are recorded. Aiming at future experiments with *in*directly heated plasma targets an *ion stop detector* was designed to match the high requirements for: *repetition rate*, *time resolution*, *high ion- & low light- sensitivity*, and *radiation hardness* as well.

Detector Design

The chosen design is based on polycrystalline CVD diamond (pcCVDD), which has previously been used for the detection of (high energy-) heavy-ions at GSI [3]. To reduce the well known phenomenon of polarisation in pcCVDD for inhomogeneous irradiation [4] the diamond was designed to be thinner than the range of ^{12}C to ^{86}Kr of $\approx$ 5 AMeV in it. FIAF[3] provided us with four thin (13 μm, 19 μm, 20.5 μm, 60 μm) pcCVDD samples, sized 10x10 mm^2. Together with the GSI's and TUD's target and detector laboratories four detectors were built: Electrodes of (20-30-100) nm Ti-Pt-Au, or 100 nm Al were sputtered onto both sides of the diamond samples (Figure 1).

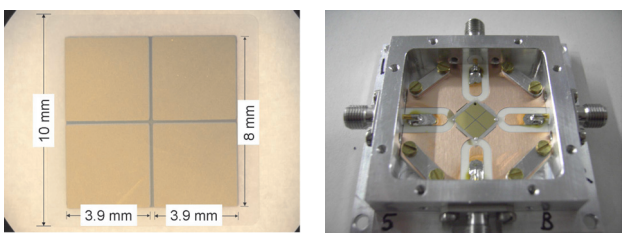

(a) 13 μm diamond sample with Ti-Pt-Au electrodes; read-out side.

(b) 13 μm detector: diamond, PCB, Al-housing, SMA connectors.

Figure 1: Two steps in the detectors' construction.

The 4-pixel read-out both offers position sensitivity and reduces the capacitance (which leads to a shorter signal fall time). The samples are connected to a 50 Ω PCB: Silver conductive glue links the single back electrode to the earth of the Al-housing; via Al-bond wires the front electrodes flow into micro-strip lines and SMA connectors. DBA4 preamplifiers (by GSI) are used for experimental operation.

Results of Tests with a ^{54}Cr Beam

The detectors were tested with macro pulses of $^{54}Cr^{21+}$ of 4.75 AMeV (ranging 25 μm in diamond). Figure. 2 illustrates the excellent performance of the 19 μm detector at a bias E-field of 1 V/μm and a preamp gain of 100:

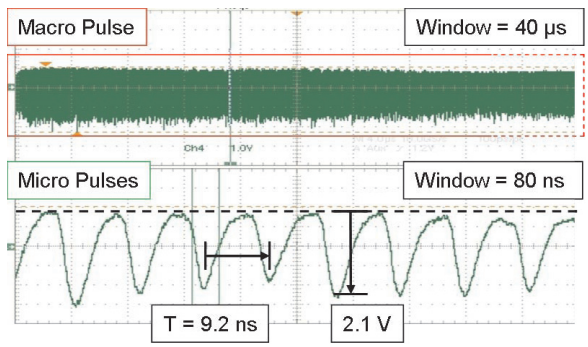

Figure 2: Zoom (bottom) into the macro structure (top) of a ^{54}Cr beam at a very low current of $\approx$ 13 pnA.

Figure. 3 shows the (σ) time resolution for determining the centre of an ion micro pulse with the 19 μm detector:

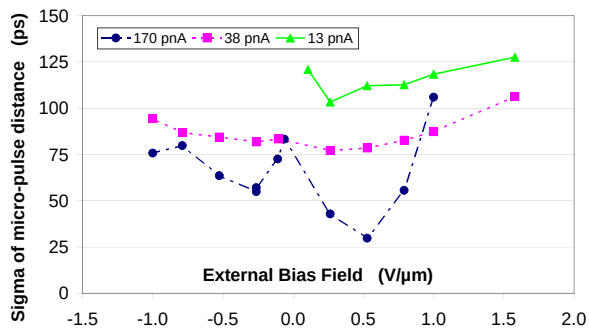

Figure 3: Δt_{tot} varying with bias and beam current.

$\Delta t_{tot} = \left(\Delta t_{beam}^2 + \Delta t_{det}^2 + \Delta t_{elec}^2 + ...\right)^{1/2}$ shows variations with beam current and detector bias. Its range of 30 ps to 120 ps is sufficient and promising for future experiments. Further analysis and tests are needed for understanding and separating the intrinsic detector response. New detector applications based on pcCVDD are planned.

References

[1] Europhysics Letters, Vol. **50** , 28-34 (2000)

[2] Laser- and Particle Beams, Vol. **23**, 503 (2005).

[3] Nucl. Phys. B (Proc. Suppl.), Vol. **78**, 533-539 (1999).

[4] NIM A, Vol. **414**, 340-356 (1998).

The diagnostic for the PHELIX* laser at the plasma physics experimental area

M. Günther[1], J. Schütrumpf[1], T. Eberl[1], A. Blažević[2], and M. Roth[1]
[1]Technische Universität Darmstadt, Germany; [2]GSI, Darmstadt, Germany

Introduction

In the near future the PHELIX laser system at the experimental area Z6 at the GSI will be employed for plasma physics experiments. The energy loss experiments as well as the generation of intense particle beams by the 100 TW laser are important applications for the PHELIX laser. It is necessary to diagnose the PHELIX laser after propagating through the transfer line between the PHELIX facility and the plasma physics experimental area (see fig. 1). Therefore, the diagnostic will be constructed inside the new Z6 clean room. The relevant parameters which should be measured are the pulse energy, the pulse shape and the wavefront as well as the near and the far field of the incoming PHELIX laser. The PHELIX diagnostic has to be constructed because of two important points: Firstly, for the reproducibility of laser plasma experiments the beam properties should be well-known. Secondly, in terms of the beam propagation through the optics of the 100 TW laser which is founded by the VIPBUL [1] at the GSI it is fundamental to know the beam properties as well. In this high intensity or energy region aberrations and similar optical effects may lead to damaged optics or unsuccessful experiments.

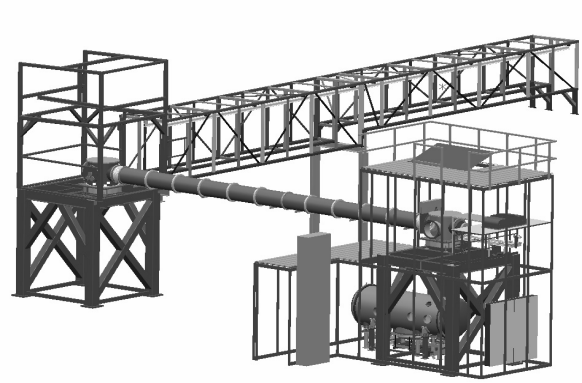

Figure 1. The transfer line between the PHELIX facility and the plasma physics experimental area and a view inside the Z6 clean room with the 100 TW pulse compressor and the diagnostics table on the right hand side. The entrance telescope is located on the right tower.

Setup and design

In front of the diagnostic the diameter of the PHELIX laser is 120 mm or 280 mm respectively. The maximum pulse energy range amounts between 500 J and 1000 J. For the 100 TW laser the 120 mm diameter beam will be used. The pulse energy of about 2% propagates through the diagnostic mirror. However, for diagnostic a realistic beam diameter is limited to 10 mm. By collimating the beam of 2% of the pulse energy a diameter less than 10 mm leads to an increased intensity. Thus the optics and the diagnostics will be damaged. To run the diagnostic it makes sense to minimize the beam diameter and to reduce the intensity. The design of the diagnostic basically consists of telescope systems to collimate the beam and two attenuators. In order to minimize the aberrations, the optical system of the diagnostic is designed by the optical design system ZEMAX#. At first a variable high energy attenuator will be employed in order to run the diagnostic beyond a wide pulse energy range. The high energy attenuator simply consists of five beam splitters which can move inside or outside the optical path respectively. Directly ahead of the diagnostics a precision attenuator is used to adjust the pulse energy exactly. The principle of the diagnostic system is designed by H.-M. Heuck and M. Hagemann [2]. However, we achieved essential improvements in the optomechanical construction and design. The spatial alignment of the diagnostic proceeds over two planes (see fig. 1 and 2). In the upper plane there is the entrance telescope which collimates the beam onto 50 mm. A 45°-mirror deflects the beam in the lower plane. A periscope adjusts the beam to the vertical positioned table with the attenuators and the diagnostics as well as the telescopes which collimates the beam up to a diameter less than 10 mm.

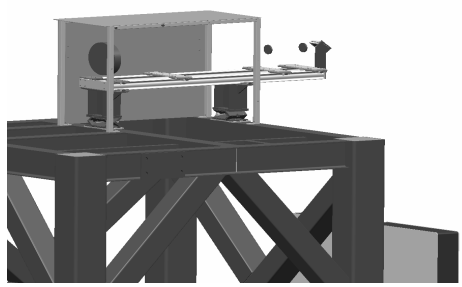

Figure 2. The entrance telescope is visible on the tower. The vertical positioned tables in the lower plane.

Status

The calculations and the design of the diagnostic system are completed. The installation will start in spring of the year 2007. The commissioning of the diagnostic system will occur in the middle of the same year.

References

[1] Virtual Institut to investigate the generation of Particle Beams by Ultra-intense Lasers, http://www.vipbul.de
[2] M. Hagemann, Aufbau und Test des Strahldiagnosesystems beim Petawatt-Laser PHELIX, diploma thesis Fachhochschule Darmstadt, 2005

* Petawatt High Energy Laser for Ion Experiments
# http://www.zemax.com

3D-flow modeling of laser-accelerated protons and electric field reconstruction

M. Schollmeier[1], H. Ruhl[2], F. Nürnberg[1], K. Flippo[4], A. Blazevic[3], J.C. Fernandez[4], C. Gautier[4], K. Harres[1], B.M. Hegelich[4], J. Schreiber[5], K. Witte[3], B. Zielbauer[3,6], and M. Roth[1]

[1]TUD, Darmstadt, Germany; [2]RUB, Bochum, Germany; [3]GSI, Darmstadt, Germany; [4]LANL, Los Alamos, NM, USA; [5]LMU, München, Germany; [6]MBI, Berlin, Germany

The irradiation of foil targets with ultra-intense short laser pulses leads to the generation of MeV ion beams from the non-irradiated target rear side [1]. The ions, mostly protons originating from contaminants, form a collimated beam with an exponential energy spectrum falling to high energies and a sharp cut-off at up to 60 MeV, depending on the laser parameters. With special target cleaning techniques it is possible to accelerate different ions, e.g. protons, carbons and oxygens simultaneously [2]. The acceleration takes place due to an electric field, generated by a dense sheath of hot electrons. This field first ionizes the atoms sitting at the rear side via field-ionization and then accelerates them. The field strength is of the order of 10^{12} V/m in a length of a few micrometers. The beam always is directed normal to the rear surface of the target with an emittance being superior compared to conventional accelerator beams [3, 4]. In the framework of the virtual laboratory *VIPBUL* [5], we want to investigate this acceleration mechanism not only for a further understanding, but also as a potential new ion source. The expansion of the beam is mainly quasineutral and very laminar. This was shown in experiments, i.e. with radiochromic film detectors [3, 7] or CR-39 as well as in 3D PIC simulations. Figure 1 shows an imprint of a 1 MeV proton beam from recent first experiments with the PHELIX laser. The target was a rear-side micro-structured Au foil with a thickness of 10 μm. The lines from the target rear side are clearly visible. This demonstrates the small transverse emittance, since the micrometer-sized structures were magnified and transported over several centimeters into the detector.

Up to now, predictions of the ion beam properties like emittance, divergence or spectrum are mainly based on simulations and very simple estimates. For R&D in direction to a new ion source a better modeling is abolutely necessary. An effective flow model by H. Ruhl, that is based on experimental data and PIC simulations, can be used to fully reconstruct the flow. This was done for a highly resolved measurement of a proton beam produced at the TRIDENT laser facility at LANL, see fig. 2 for an example of the fit to 8 MeV protons. The model is based on transfer

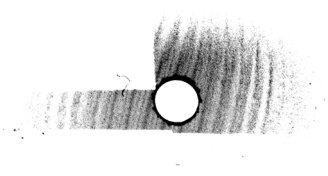

Figure 1: Imprint of a 1 MeV proton beam on CR-39, produced with the PHELIX laser (10 J stage). The white disk in the center was a hole in the detector to let the ions pass into a spectrometer. On top of the detector were Al foils for energy discrimination, visible as white (incomplete) rectangles.

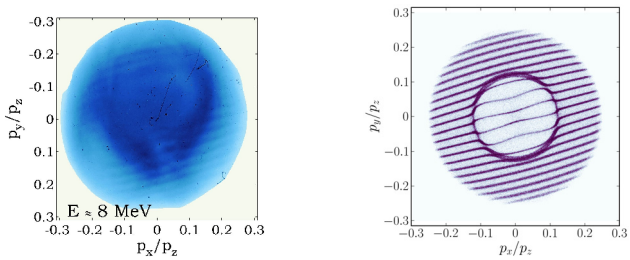

Figure 2: *left*: Imprint of 8 MeV protons in RCF. *right*: Image by the flow model.

functions $\vec{g}(\vec{x})$ that map the position of the ions to their respective momenta. It reproduces the 6D phase space of a real beam. This data can be used as a realistic parameter set for beam injection. Additionally, the eletric field by the electron pressure tensor can be calculated with

$$\Phi = -\frac{1}{2m_p q} g^2 \qquad \text{and} \qquad \mathbf{E} = -\nabla\Phi.$$

In a one dimensional approximation the field decays as

$$E(z) = \frac{2\, C_z^2 m_p c^2}{e} \frac{\ln(z/z_0)}{\ln(z_1/z_0)} \frac{1}{z},$$

where z is the expansion direction, C_z determines the expansion force and $z_{0,1}$ is the initial (final) location of the protons, respectively.

This work was supported by the virtual institute VIPBUL.

References

[1] R.A. Snavely *et.al.*, Phys. Rev. Lett. **85**, 2945 (2000)

[2] K. Harres *et.al.*, this report

[3] E. Brambrink *et.al*, GSI Ann. Rep. 2002, GSI-2003-2, 9 (2002)

[4] T.E. Cowan *et.al.*, Phys. Rev. Lett. **92**, 204801 (2004)

[5] `http://www.vipbul.de`

[6] M. Schollmeier *et.al.*, GSI Sci. Rep. 2005, **GSI-2006-1**, 330 (2006)

[7] F. Nürnberg *et.al.*, this report

3-D reconstruction of a laser accelerated proton beam using micro-structured target foils and radiochromic film detectors*

F. Nürnberg† [1], M. Schollmeier[1], K. Harres[1], A. Blažević[2], E. Brambrink[3], J. Schreiber[4], K.A. Flippo[5], B.M. Hegelich[5], C. Gautier[5], J. Fernandez[5], and M. Roth[1]

[1]TU, Darmstadt, Germany; [2]GSI, Darmstadt, Germany; [3]Sandia National Laboratories, Albuquerque, USA; [4]LMU, Mnchen, Germany; [5]LANL, Los Alamos, USA

The generation of high-current multi-MeV protons by irradiating thin foils with short-pulse, ultrahigh intensity lasers ($\tau <$ ps, $I\lambda^2 > 10^{18}$ W/cm^2 µm^2) has gained great attention in the field of laser-ion acceleration due to remarkable properties of the accelerated beam and its suitability for a new type of ion source.

The acceleration process takes place on the non-irradiated rear side of the foil. This mechanism is described by the TNSA-model [1, 2] (Target Normal Sheath Acceleration, fig.1). A rear side electrostatic field ($E > 10^{12}$ V/m)

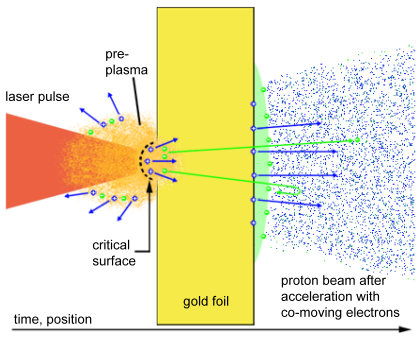

Figure 1: TNSA mechanism for laser accelerated protons.

ionizes the surface atoms and further accelerates them. The resulting beam is composed mostly of protons originating from contaminant layers of water vapor and hydrocarbons at the target surface. Presently, laser accelerated proton beams reach energies up to 60 MeV.

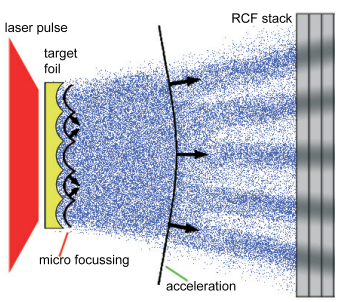

Figure 2: Development of the intensity modulation of a proton beam in the RCF stack.

An interesting fact is that protons accelerated from the rear surface of a laser-irradiated target are capable of generating images of micro-structures present on this surface [3, 4]. The protons are emitted normally to the surface. Grooved line structures at the surface effect a microfocussing of the beam (fig.2). With this feature it is possible to determine important beam characteristics such as source size, angle of beam spread and emittance.

Experiments were done at the TRIDENT laser facility, Los Alamos National Laboratory, USA (τ = 600 fs, $I\lambda^2 = 2 \cdot 10^{19}$ W/cm^2 µm^2) and with the PHELIX laser at GSI. The 10 µm thick micro-structured gold foil was fabricated at the target laboratory of TU Darmstadt. As proton detector a calibrated film stack of radiochromic films (RCF) was used. The stack arrangement of the films allows energy resolved measurements. For proton energies up to 19 MeV the source size of the proton beam shows a gaussian distribution with a FWHM of 49 µm. The angle of beam spread decreases for increasing proton energies from 40° to 4°. For increasing proton energies the transverse emittance decreases as well from 0.1 to 0.01 π mm mrad.

The spatially and energetically resolved proton distribution is determined by a weighted subtraction algorithm [5] (fig.3).

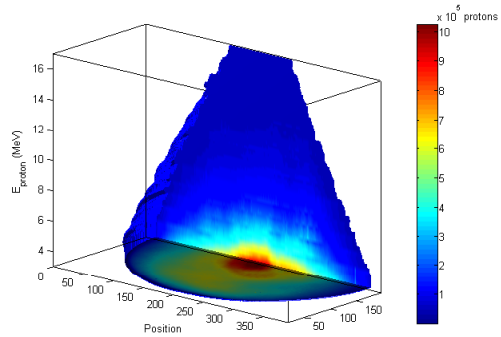

Figure 3: Proton distribution of a laser accelerated beam.

This full reconstuction of the proton beam allows to start first simulations for injecting this beam in accelerator structures as a new type of proton source.

References

[1] Snavely, R. *et al.*, Phys. Rev. Lett. **85**, 2945 (2000)

[2] Wilks, S. *et al.*, Phys. Plasmas **8**, 542 (2001)

[3] Roth, M. *et al.*, Phys. Rev. ST-AB **5**, 061301 (2002)

[4] Cowan, T. *et al.*, Phys. Rev. Lett. **92**, 204801 (2004)

[5] Nürnberg, F., diploma thesis, TU Darmstadt (2006)

* Work supported by VIPBUL

† f.nuernberg@gsi.de

Studies of *Si K*-shell spectra induced by *Ca* projectiles penetrating aerogels

J. Rzadkiewicz[1], O. Rosmej[2], A. Blazevic[2], S. Hagmann[2], V.P. Efremov[3], A. Gojska[1], D.H.H. Hoffmann[2], S. Korostiy[2], M. Polasik[4], K. Slabkowska[4], A.E. Volkov[5]

[1]The Andrzej Soltan Institute for Nuclear Studies, Poland; [2]GSI, Darmstadt, Germany; [3]Institute for High Energy Density, Moscow, Russia ; [4]Faculty of Chemistry, Nicholas Copernicus University, Poland; [5] Russian Research Centre Kurchatov Institute, Moscow, Russia

Target *K*-shell radiation induced in close collisions with heavy ions contains the information about the ionization of the stopping media in the vicinity of the ion trajectory during the first femtoseconds after the ion-atom interaction. The $K\alpha$ x-ray emission spectra of the low-density SiO_2 aerogel target bombarded by ^{48}Ca ions with initial energy of 11.4 MeV/u were measured with a high spectral ($\lambda/\delta\lambda$ = 2000) and spatial resolution (δx = 70 μm) along the ion beam stopping path. Experimental details are described in [1, 2]. The *Si* $K\alpha L^0$ diagram line and $K\alpha L^n$ (up to n=5) x-ray satellites corresponding to the radiative decays of atomic states with one hole in the *K*-shell and *n*-holes in the *L*-shell were registered [1, 2]. Fig. 1 shows the *K*-shell spectrum of SiO_2 aerogel target induced by 5 MeV/u *Ca* ions.

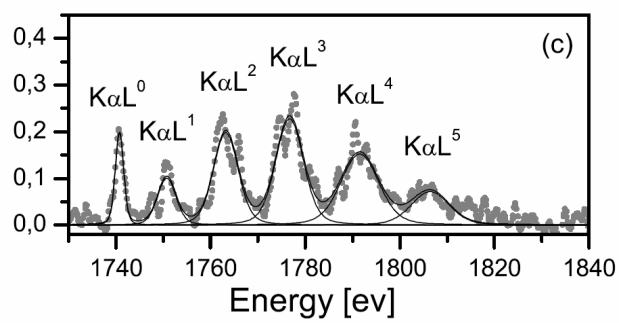

Fig.1. The $K\alpha$ spectrum of *Si* induced by *Ca* projectiles in 0.04 g/cm^3 SiO_2 aerogel at 10 mm (5.2-4.0 MeV/u) of the ion beam penetration depths. Solid lines are the result of the fitting procedure.

In this report we present the influence of the *Si M*-shell configuration on the energy shift of $K\alpha L^n$ satellites in respect to the $K\alpha L^0$ diagram line. Groups of the *L*-shell satellites were fitted using a Voigt profile (see fig.1). From the energy differences between the profile centroids corresponding to the $K\alpha L^n$ and $K\alpha L^0$ lines energy shifts of satellites with the error below 1 eV were obtained. The determined energy shifts were compared with the results of multi configuration Dirac-Fock (MCDF) calculations. It was found, that the experimental energy shifts are smaller than values obtained from free-ion MCDF theory assuming the full *M*-shell ionization of *Si*. The influence of the *Si M*-shell configuration on the energy shifts of satellites is clearly visible in the Fig. 2, where we present theoretical results of MCDF calculations [3] performed for two critical configurations, M^0 ($1s2s^22p^n3s^23p^2$) and M^4 ($1s2s^22p^n$). In all calculations a point-charge nucleus was assumed, and average-of-configuration KaL^n satellite transition energies were obtained. In the case of M^0 configuration, the L-shell vacancies cause energy shifts from about ~11 to ~70 eV. If the *Si M*-shell is completely empty the energy shifts would range from ~17 eV and ~88 eV (see Fig. 2). The emptier is *Si L*-shell, the stronger is the influence of the *M*-shell on the energy of the $K\alpha$–transition. The results of MCDF are compared with the current experiment and experiments of Kauffman et al. [4]. Analysing *Si K*-shell spectra induced under the *Cl* ion beam, Kauffman has obtained higher energy shifts of $K\alpha L^n$ satellites relative to $K\alpha L^0$ for SiH_4 gas target than for *Si*-solid. In the fig. 2 the experimental energy shifts of the *Si* $K\alpha L^n$ satellites measured for three different penetration depths of the *Ca* ions in aerogel target are as well presented. The measured energy shifts don't depend on the projectile energy (penetration depth) and are closer to the theoretical predictions assuming M^0 configuration.

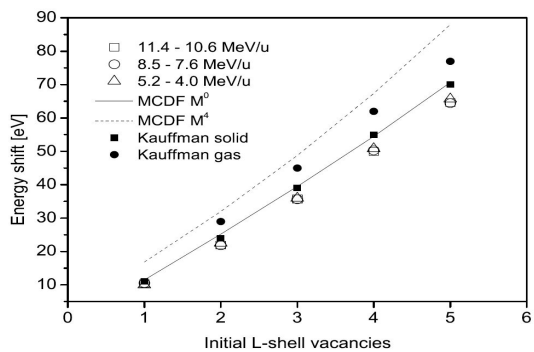

Fig.2. The experimental and theoretical energy shifts of $K\alpha L^n$ satellites. The open points - presented experiment. Full circles- SiH_4 gas and squares - solid Si target [4].The lines represent MCDF calculations, M^0 (solid line) and M^4 (dashed line).

Since the *M*-shell electrons belong to the valence band of the solid *Si,* Kauffman has supposed that in solids the *M*-shell ionization in ion-atom collisions is compensated by plasmon effect [4], which causes the electron transfer into the delocalized *Si M*-shell from the neighbouring atoms with a frequency of 10^{16} Hz.

References

[1] O. N. Rosmej et al., Phys. Rev. A 72, (2005).
[2] S. A. Pikuz Jr et al., JPhA, (2006).
[3] M. Polasik, Phys. Rev. A 39, 616 (1989)
[4] R. L. Kauffman et al, Phys. Rev.Lett. 36,1074 (1976).

Hydrodynamics of the gaseous medium heated by the ion beam

V.I. Turtikov[a], A.D. Fertman[a], B.Yu. Sharkov[a], V.P. Efremov[b], O.N. Rosmej[c], D.V. Varentsov[c], S.I. Korostiy[c,d], and D.H.H. Hoffmann[c,d]

[a]ITEP, Moscow, Russia; [b]IHED, Moscow, Russia; [c]GSI, Darmstadt, Germany; [d]TU-Darmstadt, Germany

Heavy ion beam-target interaction experiments aimed at investigation of the target density effect on the ion stopping process [1] require precise information about target parameters in the interaction region. The ion beam deposits its energy in to the excitation and ionization of the stopping media. This leads to its heating and expansion. The gas-target density varies along the ion beam stopping path, across the beam radius and in time.

In experiments carried out at UNILAC facility, the interaction of Ca ion beam with Ar and Ne gas targets was investigated [2]. The gas-target used in experiments was constructed as a massive copper cylinder 30 mm in diameter and 210 mm length. For observation of the Ca projectile velocity and charge state dynamics along the stopping path, the gas pressure in the target was kept between of 1.5-2 Bar providing the full stopping of the ion beam at the first 5-15 cm of the gas target. The 2-D visible image of the ion beam-gas target interaction region was registered using intensified gated CCD camera DicamPro. The fluorescence emission of gas atoms induced due to collision excitation by the ion beam and secondary electrons was observed throw the 180 mm long quartz window.

In the experiment we have observed the lengthening of the ion beam range in the argon gas target due to the heating of the gas media during the ion macro pulse of 5.5 ms.

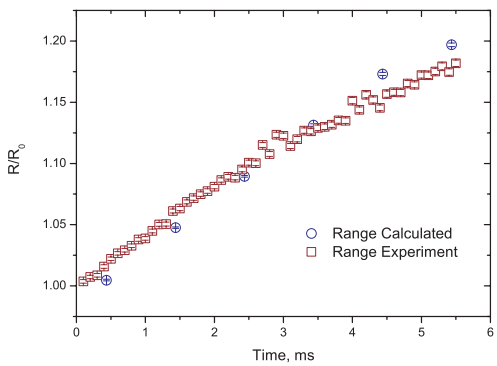

Figure 1: Relative lengthening of the ion beam range in Ar gas during the ion bream macro pulse (experiment and numerical simulation).

The ion beam range measurements over 5.5 ms with a time step of 100 μs are presented in the Figure 1. The measured values are normalized to the range length at first 100 μs of the macro bunch duration.

In order to understand the observed range lengthening phenomena, numerical simulations on hydrodynamic response of the beam-heated gas have been carried out. In the simulations, the VarJet code [3] has been employed. This code is capable of solving 2D full time-dependent Navier-Stokes equations for multicomponent gas mixtures, including viscosity, heat conductivity and diffusion effects. The initial and boundary conditions were taken as in the experiment whereas the beam-induced heating of the gas was calculated using the SRIM stopping power data and neglecting radiative energy dissipation.

The following input data for ion beam related to the experemental condition were used for a numerical simulations: 5 MeV/u energy of the Ca ions after stripping in the Havar entrance foil, 1 mm ion beam radius, homogeneous distribution of the ions across the radius, $8.6 \cdot 10^8$ particles in the macro bunch, 5.5 ms pulse duration. The value of the deposited specific energy reaches 2-3 J/g·cm^2. According to the calculations the gas temperature in the interaction region runs up to 100^o-120^o.

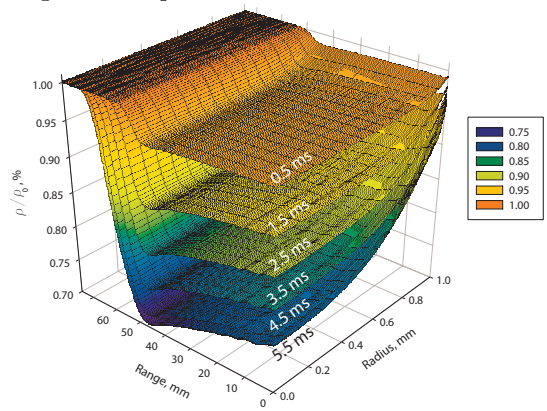

Figure 2: Calculated time dependable 2D density distribution of the Ar gas in the interaction volume. X axis - the direction of the ion beam propagation in mm, Y axis - ion beam radius, Z axis - Ar gas density normalized to the initial value.

The calculated distribution of the Ar gas density is plotted in the Figure 2 for different times during the ion macro bunch pulse. Calculation shows that the target density is changing in time across the ion beam radius and along the ion beam trajectory. Minimum of the target density (about 70% from initial value) is reached at 5.5 ms at the ion beam axis in the region of a maximum of the ion energy deposition. The heterogeneity of the target density across the ion beam radius is increasing with time and reached the maximum value of 15% at 5.5 ms. The results of the ion range simulations are shown in the Figure 1. Calculated range values are in a good agreement with measured in the experiment.

All this hydrodynamic effects in the gaseous target should be taken in to account for preparation of heavy ion beam-target interaction experiments.

References

[1] D. Gardes et al., NIM B 184 (2001) 458.

[2] S. Korostiy et al., "Calcium projectile ion radiation dynamics in the gaseous target", GSI Ann.rep. 2005.

[3] D.V. Varentsov, LPB (adopted to publishing).

Pressure dependence of excimer emission induced by an intense uranium beam

A. Adonin[1], J. Jacoby[1], V. Turtikov[2], A. Fertman[2], A. Golubev[2], D.H.H. Hoffmann[3,4], A. Ulrich[5], D. Varentsov[3], and J. Wieser[6]

[1]JWG-Uni, Frankfurt am Main, Germany; [2]ITEP, Moscow, Russia; [3]GSI, Darmstadt, Germany; [4]TUD, Darmstadt, Germany; [5]TUM, Garching, Germany; [6]Coherent, München, Germany.

In December 2005 a heavy ion beam pumped UV excimer laser has been successfully demonstrated for the first time in the experiments performed at the GSI-SIS-HHT target area [1,2]. The primary goal for this experiment was to demonstrate laser effect on the KrF^* line (λ = 248 nm) and to proof this using various methods. The dependence of spontaneous and stimulated emission from pressure and composition of the laser gas has also been studied. Unfortunately, absolute measurements were not yet possible in this pioneering experiment but the relative pressure dependencies of laser light and spontaneous emission could be studied.

A mixture of an excimer gas mixture (99,5% Kr and 0,5% F_2) and a buffer gas (pure Ar) was used as the laser medium. In order to avoid F_2 depletion due to chemical reactions, a continuous flow of gas was maintained in the laser cell. The composition of the laser gas could be varied by changing the flow rates for the excimer and buffer gases. Basically, two mixing ratios of 65/35 and 40/60 for Ar/Excimer were used and the pressure was controlled within a region from 1.2 to 2 bar by adjusting the output valve.

Examples of spectra of spontaneous emission which registered perpendicular to a laser axis are shown in Fig.1 for a mixing ratio Ar/excimer of 40/60 and different pressures. The peak at λ = 248 nm corresponds to the KrF^* laser transition and the broad-band emission from 350 to 500 nm is emitted from Kr_2F^* molecules and the low intensity peaks in the region λ > 750 nm are ArI and KrI atomic lines.

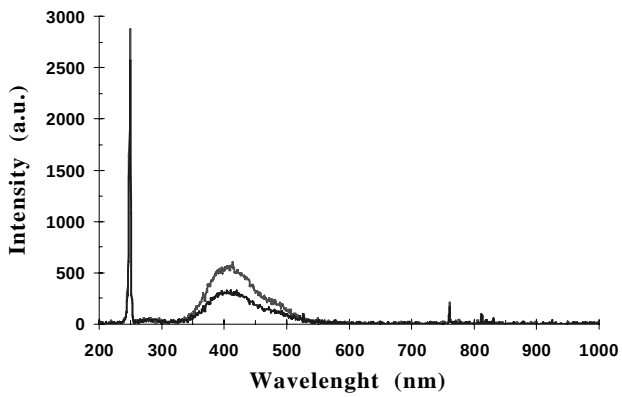

Figure 1: Spontaneous emission spectra at 1,99 bar (top) and 1,32 bar (bottom).

About 80% of the spontaneously emitted light is made up by the broad-band Kr_2F^* emission. It's two orders more intense than the atomic lines (ArI and KrI). Note, that a different pressure dependence was observed for the KrF^* and Kr_2F^* intensity.

The strongest gas kinetic channel forming Kr_2F^* molecules is via quenching of KrF^* states by rare-gas atoms in three-body reactions [3]:

$$KrF^* + 2Kr \rightarrow Kr_2F^* + Kr$$
$$KrF^* + Kr + Ar \rightarrow Kr_2F^* + Ar \quad (1)$$

These processes become very efficient at high gas pressures, in particular for pressures on the order of 1 bar and more.

Increasing pressure leads to increasing pumping power density provided by the ion beam, and, as a result, increasing population of KrF^* and Kr_2F^*. On the other hand, the rates of various quenching processes reducing a number of KrF^* and Kr_2F^* also increase. A net effect which can be observed is that the population of Kr_2F^* molecules grows faster with pressure than the population of KrF^* molecules. This is due to the three body reactions (1). This is shown in Fig.2 by plotting the ratio of light intensities of the KrF^* and Kr_2F^* emissions versus pressure.

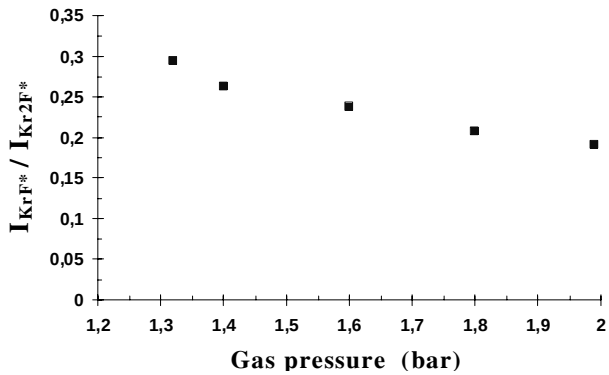

Fig. 2: Intensity ratio of the KrF^* and Kr_2F^* emissions.

In summary is shown, that information about the gas kinetic processes in the laser medium of the experiment described in ref. [1] can be obtained by studying the pressure dependence of the spontaneous emission.

References

[1] A. Ulrich, A. Adonin, J. Jacoby, V. Turtikov, et al., Phys. Rev. Lett. 06, 2006.

[2] A. Adonin, J. Jacoby, V. Turtikov, A. Fertman, et al., NIM A, 2007.

[3] Ch. K. Rhodes, Topics in Appl. Phys., Vol. 30, 1984.

Simulations of High-Energy-Density Physics Experiments at HHT Using SIS18 Uranium Beam*

N.A. Tahir, GSI, Darmstadt, Germany
A. Shutov, I.V. Lomonosov, IPCP, Chernogolovka, Russia
A.R. Piriz, University of Castilla-La Mancha, Ciudad Real, Spain
D.H.H. Hoffmann, GSI and TU Darmstadt, Germany
C. Deutsch, LPGP, University of Paris–Sud, Orsay, France

Abstract

This contribution presents numerical simulations of two recent High Energy Density (HED) physics experiments carried out at the GSI HHT experimental area using the SIS18 uranium beam. In one experiment, a solid lead target has been used while in the other case, a solid tungsten target has been considered. Our simulations show that with the existing beam parameters, one can achieve critical temperature in lead while the deposited energy is not sufficient to access the critical parameters of tungsten.

Simulation Results

During the past three years, experiments on heating of matter using the presently available uranium beams have been carried out. Several different target materials including lead, copper, tungsten, sapphire and many others have been used. In this section we present numerical simulations of two typical experiments that have recently been performed. A two-dimensional hydrodynamic computer code, BIG-2 [1] has been used to do these simulations. This code includes a semi-empirical equation-of-state model [2] to treat different phases of matter that exist during heating and expansion of the target material. For energy deposition by the projectile ions we use cold stopping [3] which is a valid approximation because the target temperature remains low in these experiments.

In most of the experiments, plane HIHEX geometry is used and the beam-target configuration is shown in Fig. 1. A thin metallic plate that is enclosed between two blocks of sapphire is irradiated with the ion beam that has an elliptic focal spot. The heated material expands and the expansion is limited by the sapphire blocks, which at the same time allow for diagnostics because of transparency of sapphire to infrared, visible and ultraviolet radiation. A beam blocker is used to avoid destruction of the sapphire plates by direct irradiation with the ion beam.

We present simulation results of two experiments in which we use lead and tungsten as target material, respectively. The beam intensity, N = 2 $\times$ 10^9 uranium ions with particle energy 350 MeV/u and a bunch length of 130 ns (FWHM). Power distribution in the beam focal spot is represented by a two-dimensional Gaussian which has FWHM_x = 0.45 mm and FWHM_y = 0.3 mm. The temporal beam intensity profile is shown in Fig. 2. Figure 3 shows the plane of experimental observation and the region of calculation, which is a quarter of the cross section.

* This work was supported by the BMBF

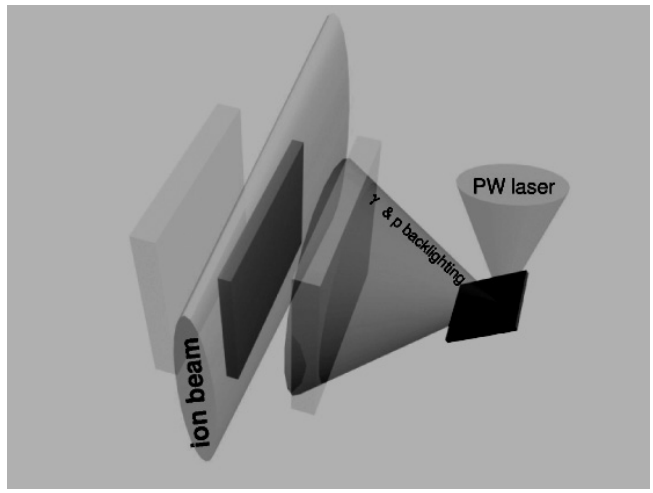

Figure 1: A schematic diagram of plane HIHEX geometry used in the current experiments.

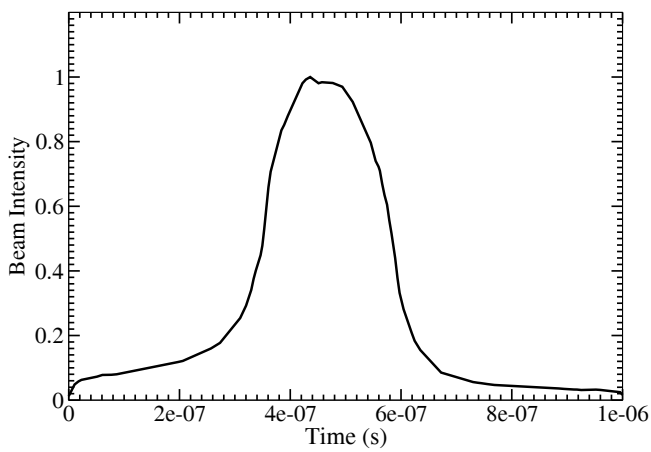

Figure 2: Temporal beam intensity profile as obtained from the accelerator and used in experiments.

Simulation results using a lead target are shown in Fig. 4 where we plot three-dimensional (pressure-volume-temperature) EOS surface of lead in red. The blue region shows the trajectories of different parts of the target that are traversed during heating and expansion. It is seen that a part of the target material passes through the critical point

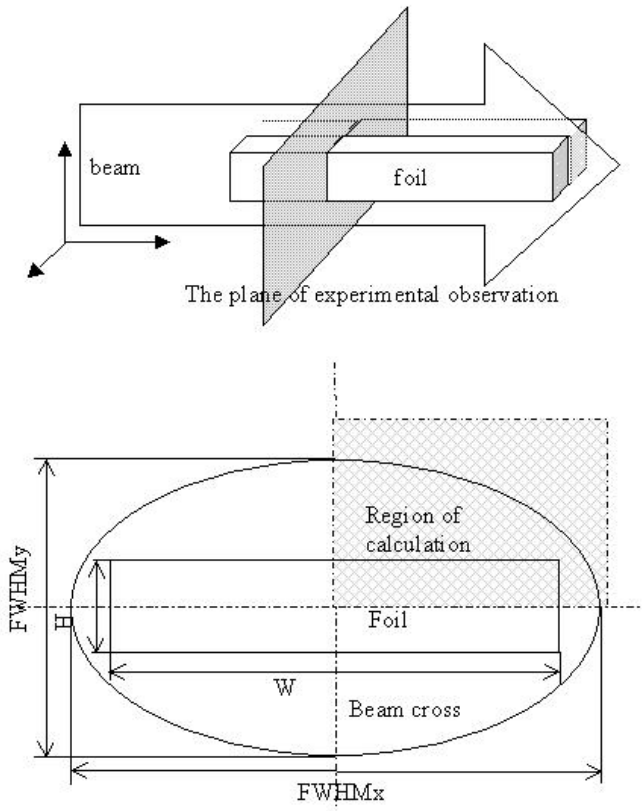

Figure 3: Beam-target geometry used in simulations of the HED matter experiments.

region which indicates that with the existing beam intensities, it is possible to access the critical point of lead.

Figure 5 shows the same variables as Fig. 9, but for a tungsten target. It is seen that with the current beam intensity, the critical point for tungsten can not be accessed. This is because the estimated specific energy to access the critical point for tungsten is 5 kJ/g which is much higher than the current level of energy deposition.

Further can be found in Ref.[4].

Conclusions

The commissioning experiments performed at the GSI HHT experimental area show that an intense heavy ion beam is a very efficient tool to induce HED states in matter. The simulations presented in this contribution show that using the moderate intensities of the uranium beam delivered by the SIS18, one can achieve the critical parameters of lead. However, for materials like tungsten which have a higher critical temperature, one needs much higher beam intensities to access the critical parameters.

(please contact: n.tahir@gsi.de).

References

[1] V.E. Fortov et al., Nucl. Sci. Eng. **123** (1996) 169.

P in Pb

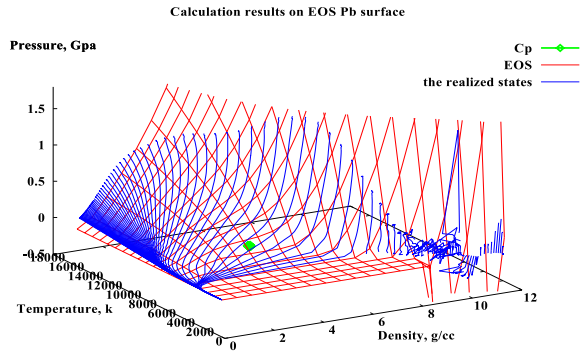

Figure 4: Red is the P-V-T surface of the EOS of lead, blue is the trajectory traversed by different parts of the target and green is the critical point.

The simulation results on EOS

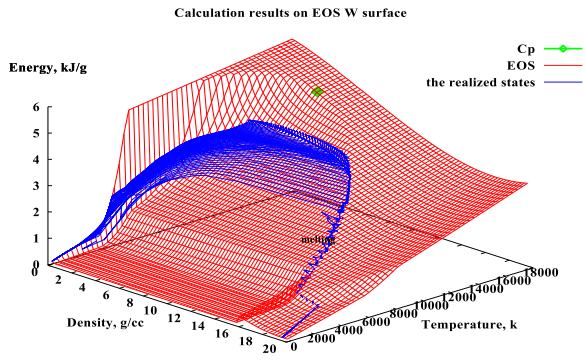

Figure 5: Red is the P-V-T surface of the EOS of tungsten, blue is the trajectory traversed by different parts of the target and green is the critical point.

[2] A.V. Bushman and V.E. Fortov, Sov. Tech. Rev. B Therm. Phys.**1** (1987) 219.

[3] J.F.Ziegler et al., The Stopping and Ranges of Ions in Solids (Pergamon Press, New York, 1.

[4] N.A. Tahir et al., Nucl. Instr. Meth. A (2007) Accepted.

Three-Dimensional Numerical Simulations of the LAPLAS Target Including Elastic-Plastic Effects

A. Matveichev, IPCP, Chernogolovka, Russia
N.A. Tahir, GSI, Darmstadt, Germany
V. Kim, A. Ostrik, I.V. Lomonosov, IPCP, Chernogolovka, Russia
A.R. Piriz, UCLM, Ciudad Real, Spain
D.H.H. Hoffmann, GSI and TU Darmstadt, Germany

Abstract

This contribution presents three-dimensional numerical simulations of the LAPLAS target [N.A. Tahir et al., Nucl. Inst. Meth. A 544 (2005) 16] including elastic-plastic effects. These calculations have shown that the shock dynamics is not significantly affected by inclusion of these new physical effects which demonstrates the validity of the previous calculations.

Introduction

The LAPLAS experimental scheme (beam-target geometry) is shown in Fig. 1. It is a multi-layered target that consists of s solid cylinder of frozen hydrogen that is enclosed in a cylindrical shell of a high-Z material like Pb or Au. One face of this target is irradiated with an intense ion beam that has an annular focal spot whose dimensions are chosen in such a way that the hydrogen is not directly heated by the ion beam. Moreover a small ring shaped part of the surrounding shell is left around the hydrogen which is called "payload". The high pressure in the beam heated region leads to a low-entropy compression of the hydrogen. Previously [1, 2, 3] we carried out two-dimensional hydrodynamic simulations of implosion of the LAPLAS target that showed that in most of the cases, the payload shell will remain in solid state and hence will retain its elastic properties. Analytic work [4] has shown that elasticity will have stabilizing effect on the Rayleigh-Taylor instability of the payload shell. In the previous simulations, elastic-plastic effects were not included. We have now carried out three-dimensional numerical simulations of the LAPLAS target implosion that also include elastic-plastic effects. These calculations show that the implosion dynamics is rather insensitive to inclusion of these additional physical effects.

Simulation Model

The simulation results presented in this section have been done using a three-dimensional computer code that is based on an individual particle in cell scheme [5]. It includes energy deposition by projectile particles using a full particle tracking scheme whereas the physical state of the target material is treated using a semi-empirical equation of state (EOS) model [6]. The elastic effects are included using an ideal elasticity model that means Hook's law complemented with yield criterion. To describe material flow in an elastic medium, Prandtl-Reuse equation of plastic flow is used:

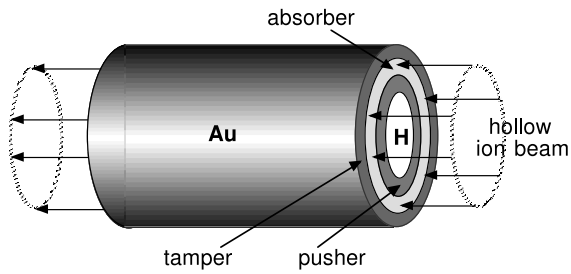

Figure 1: Beam-target geometry for the LAPLAS experimental scheme.

$$s_{ij}^{n+1} = s_{ij}^{n} + 2 \cdot G \cdot \left(e_{ij} - \frac{1}{3}\delta_{ij} Tr\hat{V} \right), \qquad (1)$$

where $e_{ij} = \frac{1}{2}\left(\frac{\partial \vec{v}_i}{\partial x_j} + \frac{\partial \vec{v}_j}{\partial x_i} \right)$ is components of strain tensor $\hat{V}$, δ_{ij} is Kronecker's delta.

To describe plastic regime of material deformation von Misses yield criterion with Wilkins normalizing procedure is used in the following form:

$$s_{ij} = \begin{cases} s_{ij}, & J < \frac{2}{3}Y_0 \\ s_{ij} \cdot \dfrac{\sqrt{\frac{2}{3}Y_0^2}}{\sqrt{J}}, & J > \frac{2}{3}Y_0 \end{cases} \qquad (2)$$

where $J = \sum_{i=x}^{z} \sum_{j=x}^{z} s_{ij}^2$ and Y_0 is yield strength.

Simulation Results

In these simulations we used a lead as well as a gold shell in the LAPLAS target with a length, L = 5 mm, inner radius = 0.4 mm and an outer radius = 3 mm. The target is driven by a uranium beam with an intensity of $5 \cdot 10^{11}$, bunch length = 50 ns having an annular focal spot with an inner radius of 1.0 mm and an outer radius of 1.5 mm.

It is to be noted that the waves propagate in an elastic medium at longitudinal speed of sound given by [7]:

$$c_l = \sqrt{\frac{B + \frac{4}{3}G}{\rho}}$$

Target	G (GPa)	B(GPa)	c_s(km/s)	c_l(km/s)
Pb	5.6	45.33	1.99958	2.15798
Au	27	175.95	3.01901	3.31349

Table 1: Values of longitudinal speed of sound

where B and G are the bulk and shear moduli respectively.

The calculated values for the longitudinal speed of sound for gold and lead are given in Table 1.

The distance between wave fronts traveling with c_s and c_l at 100 ns, $\Delta_{100\ ns}$ is 0.016 mm and 0.030 mm for lead and gold, respectively. This shows that inclusion of the elastic effects will not lead to any significant change in the shock dynamics in case of a LAPLAS implosion.

The pressure profiles achieved in numerical simulations with and without elastic effects in case of lead and gold shells are plotted in Figs. 2 and 3 respectively. It is seen that in case of lead, no difference is observed between the results including and excluding the elastic effects at this time. Fig. 3 shows a very small elastic precursor in case of gold.

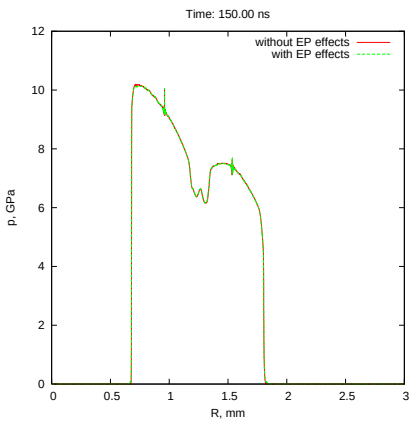

Figure 2: Pressure vs radius in case of lead at t = 150 ns.

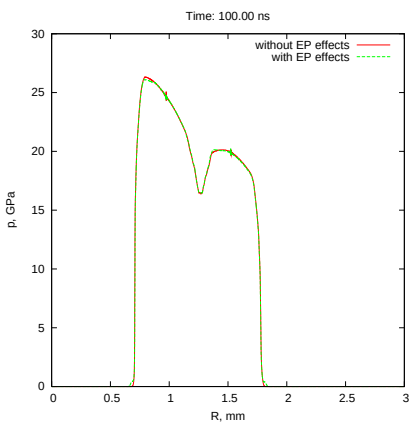

Figure 3: Pressure vs radius in case of gold at t = 150 ns.

The corresponding density profiles at t = 100 ns for lead and gold are shown in Figs. 4 and 5 respectively.

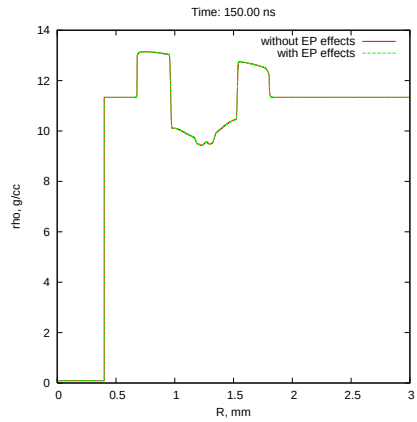

Figure 4: Density vs radius in case of lead at t = 150 ns.

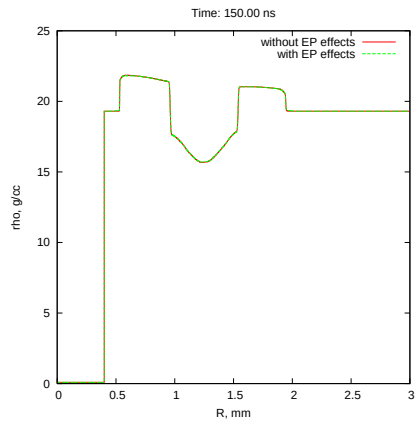

Figure 5: Density vs radius in case of gold at t = 150 ns.

It is concluded that elastic effects will not make any noticeable change in the previous simulations of the LAPLAS target.

(please contact: n.tahir@gsi.de).

References

[1] N.A. Tahir et al., Phys. Rev. E **62** (2001) 016402.

[2] N.A. Tahir et al., Phys. Rev. B **67** (2003) 184101.

[3] N.A. Tahir et al., Nucl. Inst. Meth. A **544** (2005) 16.

[4] A.R. Piriz et al., Phys. Rev. E **72** (2005) 056313.

[5] V. Kim, Private Communication (2006).

[6] A.V. Bushman and V.E. Fortov, Sov. Tech. Rev. B Therm. Phys. **1** (1987) 219.

[7] A.C. Eringen and E.S. Suhubi, Elastodynamics, Vol. 1, AP, 1974, p.100.

Richtmyer-Meshkov instability in elastic solids*

A. R. Piriz[1,#], J. J. López Cela[1], N. A. Tahir[2], and D. H. H. Hoffmann[2,3]
[1]Univ. de Castilla-La Mancha, Spain; [2]GSI, Darmstadt, Germany, [2]Technische Universität of Darmstadt, Germany

Richtmyer-Meskov (RM) instability is a well known phenomenon in hydrodynamics that occurs whenever a shock wave traverse the interface between two fluids. The LAPLAS (Laboratory of Planetary Sciences) experiment planned at GSI to be performed on the future FAIR facility for the study of high energy density states of matter, requires the low entropy implosion of a gold or lead cylinder driven by an intense ion beam in order to compress a material sample placed in the axial region. RM instability may occur during the implosion spoiling the experiment. Besides, RM determines the initial conditions for the later development of Rayleigh-Taylor instability. However, in the LAPLAS experiment the RM instability analysis must take into account that the media the process involve materials that remain in solid state during the implosion thus retaining its elastic and plastic properties. Here we have studied the RM dynamics of the interface between two perfectly elastic solids by means a simple analytical model and by two-dimensional simulation with the code ABAQUS and we find that because of the elastic properties of the material, the interface oscillates stably a characteristic period T and amplitude determined by the material properties and shock intensity.

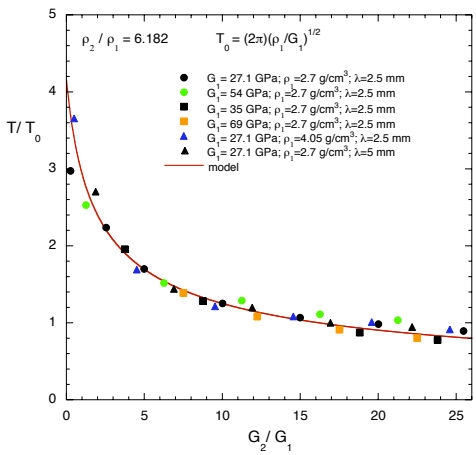

Figure 1: Oscillation period as a function of the shear moduli ratio

For the analytical treatment we assume that asymptotically, after the shock traversed the interface, the only force acting on the interface is the restoring elastic force. Thus, by using the simple method developed in Ref.[1,2] that is based in the Newton second law for the interface motion, we find an approximate analytical formula for the interface oscillation frequency $\omega = 2\pi/T$ in terms of the material parameters (densities ρ_1 and ρ_2, and shear moduli G_1 and G_2). As a first step, by considering the constitutive model for a Hookean solid, we obtain the total elastic force acting on the interface due to both materials at each side of it [3]:

$$F_y = -2(G_1 + G_2)\frac{k}{\alpha}(\xi - \xi_{0*}) \quad , (1)$$

where ξ is the instantaneous amplitude, $\xi_{0*} = \xi_0(1-v/u)$ is the post-shock initial amplitude (ξ_0 is the initial amplitude, u is the velocity of the incident shock and v is the velocity gained by the shocked interface), k is the perturbation wave number and we have assumed that the velocity field decays from the interface with a characteristic length $L = \alpha/k$. Here $\alpha = 1.55$ and it is a fitting parameter that we choose in order to best fit the numerical simulations. Therefore the interface equation of motion reads:

$$\ddot{\xi} = -\omega^2(\xi - \xi_{0*}); \quad \omega = \frac{k}{\alpha}\sqrt{\frac{2(G_1 + G_2)}{\rho_1 + \rho_2}} \quad . (2)$$

The previous equation yields the interface evolution by integrating it with the initial conditions $\xi(t=0) = \xi_0$ and $\dot{\xi}(t=0) = v_0$:

$$\xi = \xi_{0*} + \frac{v_0}{\omega}\sin\omega t \quad . (3)$$

We have performed extensive simulations with the 2D simulation code ABAQUS to validate the previous model. In Fig.1, we represented the dimensionless period T/T0 as a function of the ratio G_2/G_1 for the case $\rho_2/\rho_1 = 6.182$ and varying the rest of the parameters that appear in Eq.(2). Similar results are obtained for a given shear moduli ratio and varying the density ratio. In all the cases we find an excellent agreement between the simple model and the simulations. We have also performed simulations to determine the initial velocity v_0 which cannot be obtained from the model. We find that this velocity corresponds to the classical velocity ($G=0$) at the time $t=T$ when the system can feel the effects of the material elasticity [3]. This is an interesting result that may have implications in other RM-like flows where restoring forces are present as, for instance, in ablation fronts.

References

[1] A. R. Piriz et al. Phys. Rev. E **72**, 056313 (2005).
[2] A. R. Piriz et al. Am. J. Phys. 74, 1095 (2006).
[3] A. R. Piriz et al. Phys. Rev. E. 74, 037301 (2006).

* Work supported by JCCLM (Spain) contract No. PAI-05-071 and by BMBF (Germany).
# roberto.piriz@uclm.es

Influence of Recombination on the Free-Electron Avalanche in Laser-Irradiated Dielectrics

B. Rethfeld
GSI, Darmstadt, Germany

When transparent solids are irradiated with laser intensities above a certain threshold, strong absorption of laser energy occurs. The increasing absorptivity is caused by the formation of a free electron gas in the conduction band of the dielectric. The temporal evolution of the free-electron density in a dielectric during ultrashort pulse laser irradiation plays a fundamental role for numerous investigations. Applying a kinetic approach to describe the electron dynamics in the conduction band of a dielectric, we have shown that the simple rate equation, usually applied to describe the transient free-electron density, fails on ultrashort time scales [1]. The reason is a nonstationary shape of the electronic distribution function: since impact ionization can be performed only by electrons above a certain critical engery, the *total* free-electron density does not determine the rate of impact ionization in this case.

With the multiple rate equation (MRE), introduced in [2], I have developed a new widely applicable description, which is valid on a broad range of time scales. This system of rate equations represents the first description of the transient free-electron density which keeps track of the electrons energy distribution while maintaining the conceptual and analytic simplicity of standard rate equations. It considers the nonstationary electron energy distribution at the initial stage of ionization and provides the transition to the asymptotic avalanche regime at longer time scales. The analytic solution for the asymptotic regime yields the avalanche parameter entering the standard rate equation and the condition of its applicability.

In [2] the evolution of the free-electron density was studied for the case of irradiation of SiO_2 on timescales in the femto- to picosecond range. However, recombination processes were neglected, though they may play a considerable role. Especially for quartz, fast recombination processes on a timescale of about 150 fs are known; here ultrafast recombination in self-trapped exciton states have been experimentelly found [3].

Generally, recombination may be included in the multiple rate equation analogously to the extension of the standard rate equation as proposed in Refs. [4]. Aiming to calculate the stationary long-time behavior, we allow for reexcitation from the exciton states with a probability $W_{\rm exc}$. With the recombination time $\tau_{\rm recomb}$ a modified MRE may be formulated as:

$$\begin{aligned}
\dot n_{\rm exc} &= n_{\rm total}/\tau_{\rm recomb} - W_{\rm exc} n_{\rm exc} \\
\dot n_0 &= \dot n_{\rm pi} + 2\,\tilde\alpha\, n_k - W_{1pt}\, n_0 \\
&\quad + W_{\rm exc} n_{\rm exc} - n_0/\tau_{\rm recomb} \\
\dot n_1 &= W_{\rm 1pt}\, n_0 - W_{\rm 1pt}\, n_1 - n_1/\tau_{\rm recomb} \\
\dot n_2 &= W_{\rm 1pt}\, n_1 - W_{\rm 1pt}\, n_2 - n_2/\tau_{\rm recomb} \\
&\vdots \\
\dot n_{k-1} &= W_{\rm 1pt}\, n_{k-2} - W_{\rm 1pt}\, n_{k-1} - n_{k-1}/\tau_{\rm recomb} \\
\dot n_k &= W_{\rm 1pt}\, n_{k-1} - \tilde\alpha\, n_k - n_k/\tau_{\rm recomb}\ ,
\end{aligned} \tag{1}$$

where $n_{\rm exc}$ is the density of electrons in exciton states, $n_{\rm total} = \sum_i n_i$ and n_k the density of high-energy electrons. For the other quantities see Refs. [2].

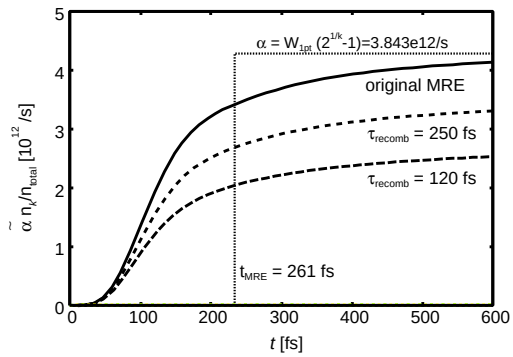

The figure shows the transient fraction of high-energy electrons, which reflects the evolution of the shape of the free-electron distribution from the initial nonstationary behavior towards the asymptotic stationary long-time behavior. A constant laser field amplitude of $E_L = 100\,{\rm MV/cm}$ was chosen and the normalized fraction $\tilde\alpha n_k/n_{\rm total}$ was calculated with the original MRE (solid line) and including recombination with different characteristic recombination times (dashed lines), respectively. For the calculation we assumed $W_{\rm exc} = W_{\rm 1pt}$. While the resulting asymptote strongly depends on the recombination time, the time to reach the stationary regime, $t_{\rm MRE}$, does not. The dotted line shows the corresponding results of the analytical estimation based on the Laplace transform of the unmodified MRE, i.e. the asymptotic value of the avalanche parameter and the transition time $t_{\rm MRE}$. Analytical estimations of the asymptotic avalanche parameter including recombination are in progress.

References

[1] A. Kaiser et al. *Phys. Rev. B* **61**, 11437, (2000).

[2] B. Rethfeld, *Phys. Rev. Lett.* **92**, 187401 (2004); B. Rethfeld, *Phys. Rev. B* **73**, 035101 (2006).

[3] P. Audebert et al., *Phys. Rev. Lett.* **73**, 1990 (1994); G. Petite et al., *NIMB* **107**, 97 (1996).

[4] M. Li et al., *Phys. Rev. Lett.* **82**, 2397 (1999); see comment G. Petite et al., *Phys. Rev. Lett.* **83**, 5182 (1999).

Investigation of the properties of a MHD plasma valve

C. Teske, M. Iberler, J. Jacoby, W. Schweizer
Inst. für Angewandte Physik, J. W. Goethe-Universität, D-60438 Frankfurt am Main, Germany

An ion beam has quite different vacuum requirements in different sections of an accelerator. Behind a stripper gas or after interaction with a gas target the vacuum conditions are poor, whereas in an accelerator module or especially in a storage ring the residual gas pressure has to be orders of magnitude better. As a new device to allow an ion beam to enter sections of different pressure we propose to investigate a new kind of plasma valve [1].

The basic principle of the MHD valve uses the Lorentz force acting upon an ionised gas between an ultra high vacuum chamber and a gas reservoir up to a pressure of several mbar. When activated, the MHD valve is composed of a discharge plasma that fills a chamber with crossed electric and magnetic fields. Gas flowing from the gas tank into the UHV chamber is ionized by the discharge. The Lorentz force acts now upon the charged particles due to the crossed electromagnetic fields and repels them back into the gas chamber. By proper adjustment of the Lorentz force, the valve can allow any desired gas flow between the two chambers, or fully block any exchange of gas. The MHD valve can even act as an efficient vacuum pump to improve the vacuum conditions in the high vacuum section. High energy particles reaching the valve from the high vacuum side will penetrate the fields and the plasma. For heavy ion beams the MHD valve would therefore act like a window.

The following Figure 1 shows the principle setup of the MHD valve.

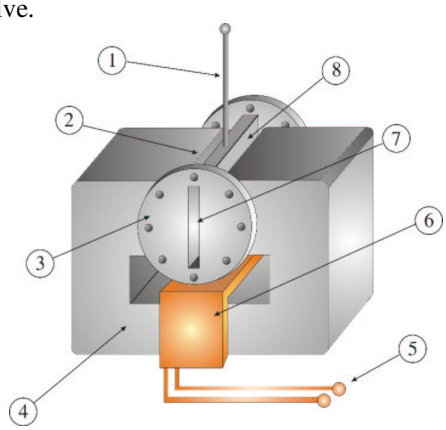

Fig.1: Schematic view on the MHD valve.
1. Electrode connection
2. Pole piece
3. Flange connection
4. Magnetic core
5. Connection to the electromagnets field coils
6. Field coil
7. Aperture opening
8. Discharge chamber

In comparison with the plasma window of *A. Hershcovitch* [2,3], which establishes a vacuum-air separation by means of a viscosity change due to an temperature gradient induced by an arc discharge, the MHD valve needs ionized gas as a result of its basic principle of operation. Because of this, the gas discharge should reach electron densities of approximately $n_e > 10^{16}\ cm^{-3}$, which is at the threshold to LTE (Local Thermal Equilibrium). The electron temperatures will be in the range of $1eV$. According to the plasma parameters a low pressure arc discharge is required with an appropriate power source.

Unlike traditional valves or membranes, a MHD valve has no moving parts and should establish a vacuum-gas separation much faster. The lack of mechanical parts should increase the reliability of the valve. In contrast to foils used at the GSI and many other facilities for vacuum-gas separation, which usually have a life time of only a few ion shots at high beam intensities and which therefore can cause severe damage and extensive maintenance of the entire accelerator system when they burst unexpected.

Until now the main construction and design of the MHD valve have been accomplished. For the power supply to maintain the arc inside the valve a 3 kW dc power supply will be used. The detailed technical design of the electrode structure in the valve is still under consideration. The aim is to reduce sputtering effects from the walls of the discharge. Due to the high power load to the walls a cooling system is mandatory. The outer structure will consist of multiple hollow, water cooled copper segments located on top of the electrodes and between the magnets, to maintain continuous operating conditions at maximum power level.

References

[1] C. Teske, M. Iberler, J. Jacoby, "Magneto-Hydrodynamisches Plasmaventil", Patent Pending, J50063, 30. June 2006.

[2] A. Hershcovitch et. al., "The Plasma Window: A Windowless High Pressure-Vacuum Interface for Various Accelerator Applications", Proceedings of the 1999 Particle Accelerator Conference, New York, 1999.

[3] A. Hershcovitch, "A plasma window for vacuum-atmosphere interface and focusing lens of sources for nonvacuum ion material modification", Review of Scientific Instruments", Volume 69, Number 2, Feb. 1998.

PHELIX Progress Report 2006

K. Witte[1], V. Bagnoud[1], A. Blazevic[1], S. Borneis[1], C. Bruske[1], J. Caird[2], S. Calderon[3], U. Eisenbarth[1], J. Fils[1,4], R. Fuchs[1], S. Götte[1], T. Hahn[1], H.-M. Heuck[1,5], C. Hildebrandt[6], D. H. H. Hoffmann[1,4], D. Javorkova[1], G. Klappich[1], J. Kluge[1], F. Knobloch[1], Th. Kühl[1,7], M. Kugler[1,6], S. Kunzer[1], M. Kreutz[1], B. LeGarrec[8], R. Lotz[1], T. Merz-Mantwill[1], E. Onkels[1], S. Radau[9], D. Reemts[1], R. M. Richard[10], M. Roth[1,4], A. Roussel[8], R. Stenner[1], A. Tauschwitz[1], R. Thiel[1], U. Thiemer[1], D. Ursescu[1], U. Wittrock[5], B. Zielbauer[1,11]

[1]GSI Darmstadt; [2]Lawrence Livermore National Laboratory/USA;[3]Pegasus Design, Inc., Pleasanton, Calfornia/USA; [4]Technische Universität Darmstadt; [5]University of Applied Sciences Münster; [6]University of Applied Sciences Darmstadt; [7]Universität Mainz, [8]Commissariat á l'Energie Atomic, [9]ROM Engineering, Inc., Tucson, Arizona/USA; [10]College of Optical Sciences, University of Arizona/USA; [11]Max-Born-Institut Berlin

Abstract

We report the major achievements of the construction of the **P**etawatt **H**igh-**E**nergy **L**aser for Heavy-**I**on E**x**periments (PHELIX) that will be capable of producing pulses up to the peak power of one PW (10^{15} W) in 500 fs and 4 kJ in 10 ns. In July and August, the commissioning of the main amplifier (MA) of PHELIX was started employing the stretched pulses of the fs-front-end (FE) which were amplified in the pre-amplifier (PA) up to 7 J. The MA was run in single-pass. The results verified the expected gain-voltage characteristics of all five 315-mm aperture Nova amplifiers and demonstrated the full functionality of all mechanical and optical components, the pulsed power, the control system, as well as the timing. We also gained first data of the beam pointing stability and the wave-front aberrations of the chain. In December, the MA was run in double-pass for the first time. To minimize the risk of damage during these first shots, the PA and MA were adjusted for generating the output energy of 133 J corresponding to 27% of the expected maximal output energy of 500 J for the 0.5 ns amplified stretched pulse. First experiments aiming at the charge-state characterization of plasmas suited for transient collisionally excited x-ray lasers were performed with 50 J.

Another important milestone was the completion of the fabrication of the PW compressor vacuum chamber that was cleaned to clean room 100-standard and stored in the PHELIX laser bay in August. The large-size multi-layer dielectric gratings were also delivered. A new single-shot autocorrelator with a dynamic range of 60-dB was developed and successfully tested [1].

The design of the beam transport to the Z6 experimental area is almost completed. For the two 520-mm diameter, 85-mm thick BK7 periscope mirrors in the laser bay tower, a six-point whiffletree back support was designed to effectively counteract the gravity sag and unavoidable deformations introduced by conventional mirror mounts.

Furthermore, the requirement document of the beam line to the PW compressor at the HHT cave was completed.

Two experimental campaigns with the PA output were carried out, one investigating the proton acceleration from the rear side of micro-structured thin foils and the other continuing the soft X-ray laser program. A major success is the demonstration of the nickel-like silver laser enabling the spectroscopy of high-Z Li-like ions in the storage ring.

The PHELIX Mission

The PHELIX project is a close cooperation with the **L**awrence **L**ivermore **N**ational **L**aboratory (LLNL) in the USA and the **C**ommissariat à l'**E**nergie **A**tomique (CEA) in France. PHELIX will offer the unique combination of highly-charged heavy-ion and high-energy laser beams thus providing the opportunity to investigate a variety of fundamental science issues in the fields of atomic, nuclear, and plasma physics.

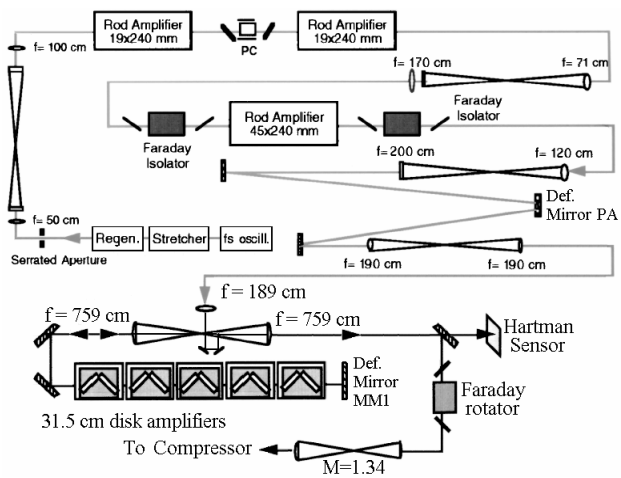

Figure 1: Schematics of PHELIX. The front-end (FE) includes the MIRA oscillator, the stretcher, and the regenerative amplifier. The pre-amplifier (PA) section consists of the serrated aperture, two 19-mm rod amplifiers, two Faraday rotators, one-45-mm rod amplifier, one Pockels cell, and four telescopes. The main amplifier (MA) consists of five 315-mm aperture Nova amplifier sections each containing two disks. The beam passing through the MA has a diameter of 26 cm which is magnified to 35 cm by the final relay telescope.

Fig. 1 shows the schematics of the fs-option of PHELIX which will deliver pulses of up to 500 J in 500 fs. The ns-

front-end will generate pulses of up to 10 ns and will thus allow a maximum energy of up to 1 kJ. The maximum energy is limited by the damage threshold of the FR-5 glass of the Faraday isolator. With the booster amplifier (not shown in Fig. 1), the energy may be increased to 4 kJ for 10-ns pulses.

MA Performance in Single and Double Pass

The purpose of the single-pass measurements carried out in July and August was fourfold: (i) to confirm the expected gain-voltage characteristics of the MA, (ii) to test the reliable functioning of all flash lamp discharge circuits and the control system of all amplifiers and Pockels cells and their proper timing, (iii) to measure the beam pointing stability and shot-induced wave front aberrations needed for the calculation of the on-target focusability, and (iv) the system's thermal recovery time from the thermal loading caused by the flash lamps and the associated deformations of the laser disks. The recovery time determines the shot repetition rate.

MA single-pass operation. The 0°-degree retro mirror (def. mirror MM1 in Fig. 1) was replaced by a 45°-diagnostic mirror guiding the beam to a full beam size calorimeter. The 2% leak of this mirror was used to measure the near and far fields as well as the pointing stability and wave front aberrations of the pulse. The campaign comprehended 22 successful shots. (i) Fig. 2 shows the MA gain and the output energy versus the voltage of the MA capacitor bank. At the envisaged voltage of 18 kV, the single-pass gain is 12 and 144 in double pass and hence sufficiently high to compensate for various losses so that chirped pulses of 500 J or 1-kJ pulses of 10-ns duration are easily achievable. (ii) After some minor improvements, all flash lamp discharge circuits, the control system, and the timing worked very reliably.

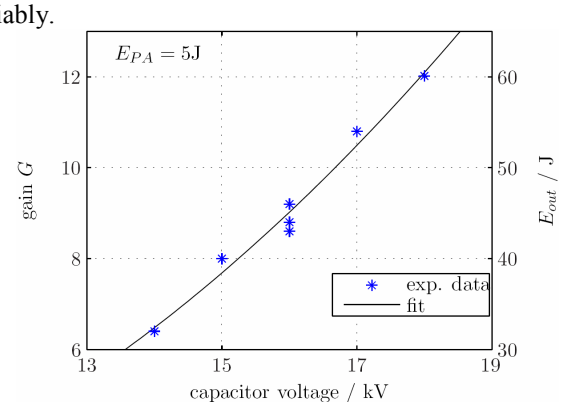

Figure 2: MA single-pass gain (scale left) and output energy (scale right) versus voltage of the capacitor bank. The MA input energy was 5 J for all shots.

(iii) Quantum-defect heating and inhomogeneous absorption of the pump light in the amplifiers cause refractive index perturbations and changes in the thickness and surface topology of the laser disks which distort the wave front (WF) of the pulse and lead also to a deflection of the beam. The frames a, b, and c in Fig. 3 show the near field (NF), the WF map, and the far field (FF) of a 50-J pulse from the MA. Besides defocus the primary aberrations are astigmatism and coma originating mainly from the PA. The defocus is easily correctable by changing the position of one of the lenses in the telescope following the 45-mm rod amplifier. The deformable mirror behind this telescope (DMPA) can compensate astigmatism and coma (see Fig. 1). The shot-to-shot WF aberrations and the beam deflection are tolerable and meet our requirements as specified in [2].

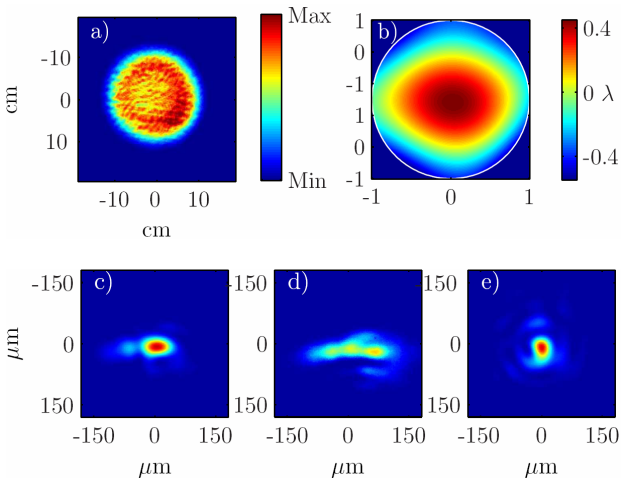

Figure 3: (a) and (c) NF and FF fluence patterns and (b) WF map of the NF at 50-J output energy from the MA. Patterns (d) and (e) show the FF generated with the FE only 1h54' and 1h19' after firing the MA, respectively. In each shot, the MA delivered 20 J. In (e) the long-term WF distortions are pre-compensated by the DM.

(iv) Besides these instantaneously occurring WF aberrations, the disks also suffer from long-term distortions due to heat transfer from the hot flash lamps. The recovery time from these distortions was measured to be 3h (see [2]). The recovery time can be significantly shortened to ~1h20' by using the DMPA (see frame d) in Fig.3).

MA double-pass operation. After several improvements of the stability of the opto-mechanics, the MA injection box, the PHELIX Control System (PCS), and the FE, the first shots with the MA run in double pass were executed in December. In order to minimize the risk of optical damage, the PA and MA were operated at a fraction of their regular pump level. Typical PA output energies and the double-pass gain in the MA were restricted to ≤ 2 J and ≤ 70, respectively. The highest output energy achieved under these conditions was 133 J corresponding to 27% of the projected output energy of 500 J. The near-field fluence pattern looked similar to that measured in the single-pass measurements whereas the far-field pattern and the wave front map clearly showed the expected increase in astigmatism and coma. A theoretical analysis on how chromatic aberrations may be compensated is presented in [3]. The uncompressed pulse had a bandwidth of 2.8 nm and a duration of 0.6 ns.

50-J pulses from the MA were focused on tantalum targets at intensities of ~10^{15} W/cm². The resulting plasma

was spectroscopically investigated as to its charge state. These measurements are related to transient collisionally excited sub-10nm X-ray lasers which are under development at GSI [4, 5].
In the next shot campaign, the output energy will be further increased and the Faraday rotator activated. This is indispensable to avoid damage from light retro reflected from the target when PHELIX is run at high output energies. The beam fluence is limited by the damage threshold of the Faraday glass which due to platinum inclusions is only 2.6 J/cm² at 0.8 ns .

Petawatt Compressor Chamber

The compressor vacuum chamber was manufactured and cleaned in August and then stored in the laser bay where it will be validated in 2007. The chamber consists of two cylinders connected by a square middle piece. Both 800 x 400 mm² The multi-layer dielectric gratings were delivered from LLNL in December 2006. However, for the first shots in the laser bay where the beam may not be magnified the 475 x 400 mm² multi-layer dielectric gratings procured from Horiba-Jobin-Yvon will be used.
A single-shot 2nd-order autocorrelator with significantly improved dynamic range of up to 60-dB was developed and successfully tested at PHELIX and at LULI. The details are outlined in [1].

The Beam Line to Z6

Fig. 4 shows the mirror tower in the laser bay and the two periscope mirrors directing the PHELIX beam to the Z6 experimental area. To avoid the gravity sag and unavoidable deformations arising from conventional mirror mounts, each of these mirrors will have a six-point whiffletree back-support. The manufacturing of the required components for the two mirrors in the laser bay tower will start in February 2007.

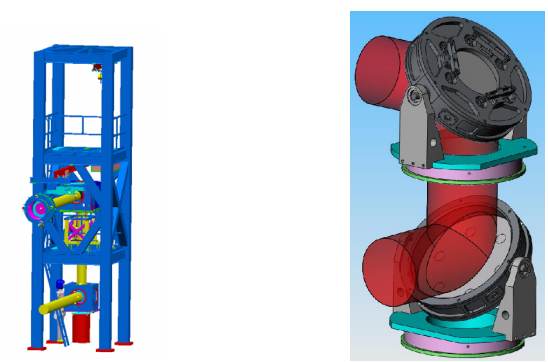

Figure 4: Mirror tower in the laser bay (left) and periscope mirrors with six-point whiffletree back support (right).

The Beam Line to HHT

The beam line from the laser bay (LB) to the experimental area in the HHT cave traverses the ESR hall over a distance of 55 m at 7 m above ground and consists of two parts, the beam lines 1 (BL1) and 2 (BL2). BL1 (see Fig. 5) connects the LB with the Petawatt compressor (PC); BL2 leads the compressed PHELIX pulse to the HHT cave located on the ground floor of the ESR (Experimental Storage Ring) hall. The BL1 combines relay imaging and spatial filtering with the beam magnification from 26 to 35 cm so that the full 800-mm length of the LLNL compressor gratings can be fully used for the generation of the PW pulse. The optical design including the damage detectors for the telescope lenses has been completed. The mechanical design is in progress.

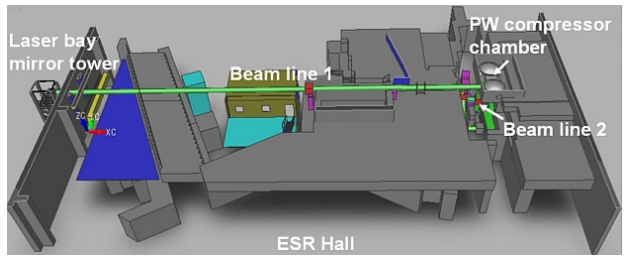

Figure 5: Beam lines BL1 and BL2 in the ESR hall. BL1 connects the mirror tower in the laser bay with the compressor chamber and BL2 the compressor chamber with the HHT cave.

Experiments with Pre-Amplifier Pulses

The PA output energy was set to 5 J yielding 3.5 J after compression. The compressed pulses were used for proton acceleration from the micro-structured rear side of thin metal foils. The proton spectrum is exponential and the cut-off energy reaches 1 MeV. The images of the target rear side generated by the proton beam on plastic CR39 sheets and radio-chromic films are being analyzed.
In another campaign, the soft X-ray laser program was continued by investigating the grazing incidence pump scheme (GRIP). In this geometry, the Ni-like silver laser [5] could be demonstrated. The wavelength of 13.5nm and the measured beam quality are suited for the planned spectroscopy of highly charged ions in the injection channel of the ESR. The long-term goal of this activity is the study of nuclear properties of radioactive isotopes within the FAIR project.

References

[1] D. Javorkova and V. Bagnoud, “A Single-Shot Autocorrelator with 60-dB Dynamic Range”, Optics Express (submitted) and this volume.
[2] H.-M. Heuck, J. Fils, et al., “Wave front measurements of the PHELIX beam”, this volume.
[3] H.-M. Heuck, P. Neumayer, T. Kühl, and U. Wittrock, “Chromatic aberration in petawatt-class lasers”, Appl. Phys. B **84**, 421-428(2006). See also: H.-M. Heuck et al., “Chromatic aberrations at PHELIX”, this volume.
[4] D. Ros, A. Klisnick et al., “Towards multi-100eV lasers generated by high-energy transient collisional pumping using the PW PHELIX beam”, this volume.
[5] B. Zielbauer, D. Ursescu, T. Kühl et al.,“A Non-Normal Incidence Pumped Ni-Like Zr XRL for Spectroscopy of Li-Like Heavy Ions at GSI/FAIR”, this volume.

Wavefront measurements of the PHELIX beam

H.-M. Heuck[1,2], J. Fils[1], P. Welp[2], V. Bagnoud[1], U. Eisenbarth[1], S. Götte[1], A. Tauschwitz[1], M. Hagemann[1], E. Onkels[1], S. Borneis[1], K. Witte[1], and U. Wittrock[2]

[1]GSI, Darmstadt, Germany; [2]FH Münster, Steinfurt, Germany

The peak intensity achievable in the focal spot with PHELIX is strongly reduced by thermo-optical aberrations. These are due to the thermal load of the pump process. Two types of aberrations are distinguished. Immediate phase distortions, also referred to as *pump-shot* aberrations, occur in the rods and disks due to quantum defect heating and inhomogeneous pump light absorption. Aberrations arising during the thermal relaxation after firing are called *long-term* aberrations. Amplifiers must cool down after a shot. While the water-cooled rod amplifiers at the pre-amplifier are cooled down in a few minutes, the air-cooled disc amplifiers at the main amplifier (MA) need several hours to relax to their initial state. By knowledge of the thermo-optical aberrations, the distorted intensity pattern in the focal spot can be predicted and the requirements be specified that have to met by adaptive optics for the correction of these aberrations.

Pump-shot and long-term aberrations

Both aberration types were measured in the MA operated in single pass [1]. To measure the pump-shot aberrations, a series of shots every 3 hours with the same laser parameters (MA energy input of 5 J, MA gain of 10, etc) was analyzed. To separate the influence of the pre-amplifier from that of the MA we had to measure the wavefront in front of and behind the MA in two different series. Both measurements are plotted in figure 1. The MA introduces mainly astigmatism, second-order astigmatism and second-order coma along the principle axis of the discs. Defocus is mainly due to the pre-amplifier. The magnitude of defocus and astigmatism is predictable and correctable with a static deformable mirror and a movable lens [2]. To compensate higher-order aberrations, the use of an actively controlled adaptive mirror is planned.

The long-term aberrations were measured every five minutes after firing with the alignment beam. The peak-to-valley (pv-)aberrations are shown in figure 2. Ten minutes after a shot, the aberrations had grown up to two wavelengths λ. After three hours the initial value is reached. These huge and strongly fluctuating aberrations limit the repetition rate of PHELIX to 1 shot in 3 hours. The thermo-optical aberrations occurring when the MA is run in the final double pass configuration will be analysed in 2007.

Adaptive optics

It is planned to compensate the long-term aberrations with an adaptive mirror. In a preliminary experiment we demonstrated that we could compensate these after 78 minutes. The application of adaptive optics is currently limited by the fast change rate of the long-term aberrations. In future we will try to compensate pump-shot and long-term aberrations simultaneously.

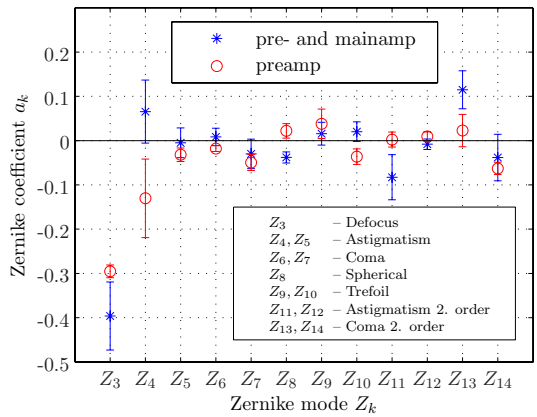

Figure 1: Comparison between pump-shot aberrations arising from pre-amplifier and from both pre- and main amplifier.

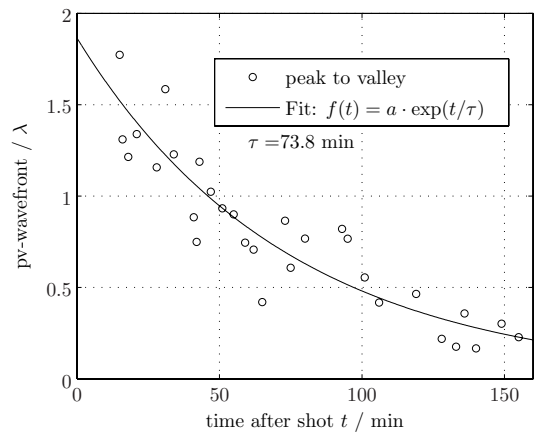

Figure 2: Long-term aberration of the main amplifier over time.

References

[1] H.-M. Heuck, "Einsatz adaptiver Optik und Kompensation chromatischer Aberration beim Petwattlaser PHELIX," Ph.D. thesis, TU Clausthal (2006).

[2] H.-M. Heuck, C. Häfner, et al., Proceedings of the 4th International Workshop on Adaptive Optics for Industry and Medicine, (Springer, Berlin Heidelberg New York, 2005).

Chromatic aberration at PHELIX

H.-M. Heuck[1,2], P. Neumayer[1], M. Hagemann[1], K. Witte[1], T. Kühl[1], and U. Wittrock[2]
[1]GSI, Darmstadt, Germany; [2]FH Münster, Steinfurt, Germany

Chromatic aberration in femtosecond lasers

The influence of the dispersion of glass seams only relevant for femtosecond lasers with a pulse length below 100 fs. This commonly used approximation holds only for visible and IR light. For UV fs-laser Z. Bor stated out that due to the large dispersion in the UV regime fs-pulses with a duration of a few hundred femtoseconds are significantly affected in lenses by the group delay [1]. When a pulse travels through a lens, the pulse is more delayed in the center than on the the edge of the lens. A previously plane pulse get curved. When a curved pulse is focused, the intensity in the focal spot is reduced. The energy from the edge of the pulse reaches the focal spot at an earlier time than the energy in the center of the pulse. For a singlet lens the radius dependent delay can be calculated:

$$T(r) = \frac{-\lambda_0}{2cf_0(n_0-1)}\frac{\mathrm{d}n}{\mathrm{d}\lambda}\cdot r^2, \qquad (1)$$

where n_0 is the refraction index of the lens material at the center wavelength λ_0, f_0 the focal length and r the radial position, c the speed of light and $\frac{\mathrm{d}n}{\mathrm{d}\lambda}$ the dispersion of the lens material. Equation 1 shows that the delay depends quadratically on the radius.

Influence of chromatic aberration at PHELIX

At PHELIX the beam diameter is expanded up to 28 cm and the radius dependend delay can not be neglected any more also in the IR regime. The delay caused by all telescope lenses between the center and the edge of the pulse is in the same order of magnitude than the ideal pulse length of 500 fs. To predict the influence of the chromatic aberration in the focal spot we have developed a numerical model based on the commercial physical diffraction propagation code GLAD and Mathematica. This model allows to calculate the propagation through an optical system, e.g. the PHELIX telescopes, with an arbitrary intensity distribution and arbitrary spatial phase aberrations.

Figure 1 shows the calculated impact of the pulse time delay for a pulse with an initial durations of 500 fs and a super-Gaussian intensity distribution. As expected, the achievable focused intensity starts to be significantly affected for a pulse time delay greater than the initial pulse duration. For PHELIX the intensity decrease is around 35%. A more detailed analysis allowing for different near field intensity shapes and with presence of spatial aberrations is given in [2].

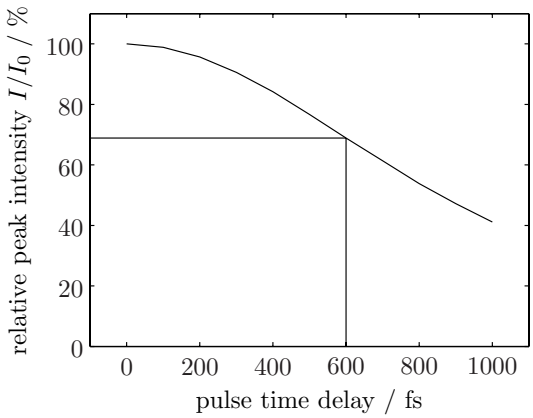

Figure 1: Peak intensity I in the focal spot normalized to that in absence of chromatic aberration I_0 versus the pulse time delay for an initial pulse durations of 500 fs

Compensation of chromatic aberrations

Chromatic aberrations can be avoided by using achromatic systems at least for all large size lenses. Even if such large achromats can be fabricated this approach would be expensive. A more cost effective and easily implemented solution is pre-compensation of the chromatic aberration of the telescope lenses at an earlier position in the beam path at a smaller beam diameter. We have developed a concept to pre-compensate the chromatic aberrations [2]. A positive diffractive lens and a negative refractive lens are combined to a nearly non magnifying telescope. The dispersion of refractive lenses is opposite and around 30 times larger than refractive lenses. This allows pre-compensating of chromatic aberration with a beam diameter of 2 cm. Such a refractive lens was presented by Kessler [3] and will increase the peak intensity of PHELIX in future. Finally, in order to allow measuring of the pulsfront delay in the amplifier chain, a self-referencing auto-correlator was developed.

References

[1] Z. Bor, "Distortion of femtosecond laser pulses in lenses and lens systems," J. Mod. Opt. **35**(12), 1907–1918 (1988).

[2] H.-M. Heuck, P. Neumayer, T. Kühl, and U. Wittrock, "Chromatic aberration in petawatt-class lasers," Appl. Phys. B **84**, 421–428 (2006).

[3] T. J. Kessler, "Diffractive Optics for Compensation of Axial Chromatic Aberration in a High-Energy, Short-Pulse Laser," in *ICUIL* (2006).

A Single-Shot-Autocorrelator with 60-dB Dynamic Range

D. Javorková[1,2,*], V. Bagnoud[1,#]
[1]GSI, Darmstadt, Germany; [2]FMPI Comenius University, Bratislava, Slovakia.

The development of single-shot, high-dynamic-range temporal measurement devices has become necessary for characterizing high-energy petawatt laser pulses. Because of the low repetition rate of such systems, no device offers high-dynamic-range measurements in a single-shot mode. In addition, investigating the unexpected temporal behavior of pulses amplified by new techniques such as analyzed in reference [1] or the alignment complexity of a large-size petawatt-class compressor require the development of a device with a high-dynamic range and single-shot operation.

We have developed a simple detection scheme that can be applied to a cross-correlator setup and improves its dynamic range by several orders of magnitude. We use an 8-bit CMOS camera that, thanks to noise reduction, yields a signal that spans over 40-dB dynamic range. With the addition of a single optical element –an optical wedge– to make a replica of the signal, we can further increase the detectable dynamic range to 60-dB without loosing the simplicity of the setup. This method is truly single shot and ideally suited for the single-shot autocorrelator setup, where the commonly admitted optical dynamic range is matched by our detection scheme.

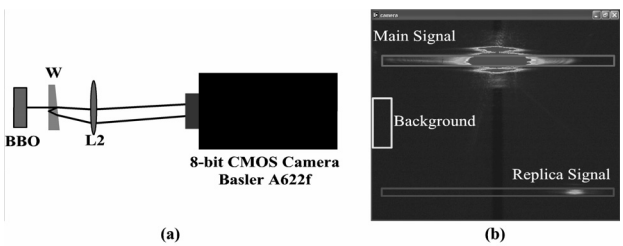

Figure 1: (a) Using a 1° uncoated wedge, a signal replica with an intensity ratio of 0.0018 is created. (b) CMOS camera image showing the three areas used for the signal retrieval.

Figure 1 shows the detection setup. The autocorrelator, not shown in the figure, is a standard single-shot autocorrelator [2], where the beam is being focused, near the crystal generating the second harmonic signal, into a line focus by a cylindrical lens. After that, the lens L2 images the crystal surface to the detector. The picture on the right (Fig. 1.b) is a snapshot of the camera readout displaying the three different areas used to compute the signal. The main area is the direct image of the crystal, where time has been mapped as a function of x (horizontal dimension). This signal area is heavily saturated but thanks to the use of the CMOS detector, the blooming effect is minimal and does not contaminate the other parts of the image. The second part of the image is the replica of the signal, which is generated by the wedged uncoated substrate located between the non-linear crystal and the imaging lens. The intensity of this signal is 0.0018 times that of the main signal and the laser intensity is adjusted so that this signal fully uses the 8-bit dynamic range of the camera. The third part is the background reference area that is used to improve the signal-to-noise ratio.

The calibration procedure includes several steps to efficiently remove the background noise, to match the 0 delay of both signal traces and to verify the wedge attenuation as well as the camera linearity, if needed. Then, an automated image analysis process retrieves the two traces and stitches them together such that the device can be used in single-shot mode, at a repetition rate up to a few Hertz for alignment or in single-event mode. The typical trace is shown in Figure 2, where the pulse has been offset temporally so that a window up to 20-ps long is available. The main result is: the detection dynamic range, from the signal peak to the detector background level is about 60 dB.

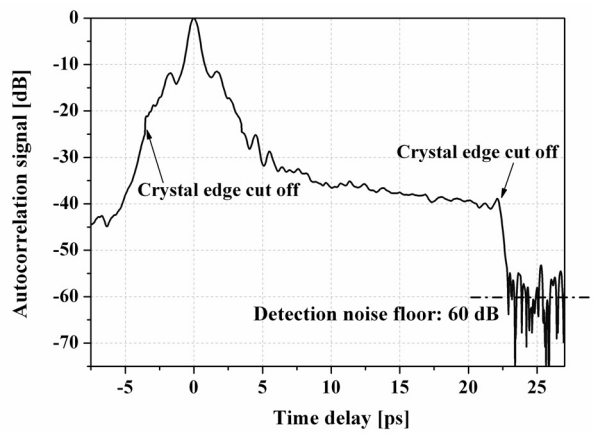

Figure 2: Autocorrelation signal of the single-shot autocorrelator using the full detection scheme. The sharp edge on the right is the cut off given by the crystal size.

This scheme is not only limited to the 2-ω autocorrelator; a 3-ω cross-correlator setup could benefit from a similar scheme, especially if the dynamic range of the detection can be extended beyond 60 dB.

References

[1] N. Forget et al, "Pump-noise transfer in optical parametric chirped-pulse amplification", Optics Letters 30, 2921-2923 (2005)
[2] F. Salin et al: "Single-Shot measurement of a 52-fs pulse", Applied Optics 26, 4528-4531 (1987)

* d.javorkova@gsi.de
# v.bagnoud@gsi.de

A Non-Normal Incidence Pumped Ni-Like XRL for Spectroscopy of Li-Like Heavy Ions at GSI/FAIR

B. Zielbauer[1,2,3], D. Ursescu[1], C. Bischoff[1], D. Zimmer[1,2], T. Kühl[1,2], V. Bagnoud[1], D. Javorkova[1], O. Rosmej[1], K. Cassou[4], S. Kazamias[4], A. Klisnick[4], D. Ros[4], K. Janulewicz[3], P. Nickles[3], G. Pert[5], P. Neumayer[6], J. Dunn[6]

[1]Gesellschaft für Schwerionenforschung (GSI), Darmstadt, Germany; [2]Universität Mainz, Mainz, Germany; [3]Max Born Insitut, Berlin, Germany; [4]Université Paris XI, Paris, France; [5]York University, United Kingdom; [6]Lawrence Livermore National Laboratory, Livermore, USA

One of the unique features of the PHELIX installation is the combination of the ultra-high intensity laser with the heavy-ion accelerator facility at GSI and its planned extension FAIR. One proposal within the SPARC program is the generation of high quality X-ray laser beams for X-ray laser spectroscopy of highly-charged ions. The long range perspective is the study of nuclear properties of radioactive isotopes within the FAIR project. A novel single mirror focusing scheme for the TCE (transient collisional excitation) XRL has been successfully implemented by the LIXAM/MBI/GSI collaboration under different pump geometries [1]. Intense and stable laser operation with Ni-like Zr and Ni-like Ag, sufficient for laser spectroscopy up to Li-like lead, was demonstrated at pump energies between 2 J and 5 J from the PHELIX preamplifier section. In a similar experimental set-up, operation of an XRL at 19 nm was achieved with 1.4 J pump energy at 10 Hz repetition rate at the Lund Laser Centre [2].

The XRL experiments at GSI were performed using the output from the pre-amplifier section of PHELIX. The pump beam of 2 to 8 J energy is split into two parts: 75% of the energy are entering in a single grating, double-pass compressor which re-compresses the pulse down to 400 fs. The remaining 25% of the energy are directly transported to the target.

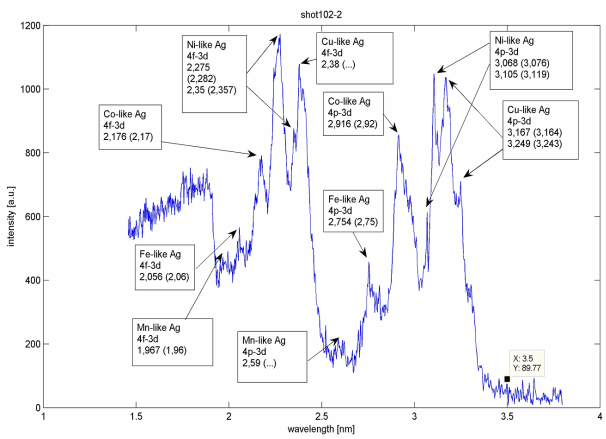

Figure 1: Emission spectrum of the laser plasma demonstrating the dominance of Ni-like lines, recorded with an XUV flat-field grating with an average line density of 2400/mm

This nanosecond pulse serves to create a plasma column several hundreds of picoseconds before the impact of the compressed pulse. Due to the ultra-high intensity of the short ps-pulse this plasma is rapidly heated, which leads to a non-stationary population inversion, with a high transient gain. The compressed pulse is focused onto the same position on the target by a single, gold coated, 6 inch diameter on-axis parabola. Tilted at an incidence angle of 9°, this naturally generates a line focus of 30 µm - 100 µm width and over 5 mm length. The XRL experiments at PHELIX were performed in two campaigns with similar set-ups. The first one was using an incident angle on target of 72° for the main pulse. In a second experimental campaign, an incidence angle on target of 45° was used. In the latter geometry, an XRL in Ni-like silver was demonstrated.

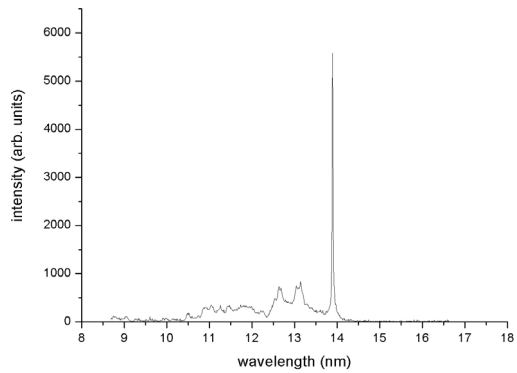

Figure 2: XRL emission of Ni-like silver at 13.9 nm (90 eV)

References

[1] P. Neumayer, W. Seelig, K. Cassou, A. Klisnick, D. Ros, D. Ursescu, T. Kühl, et al., Appl. Phys. B 78, 2004, p. 957.

[2] K. Cassou, S. Kazamias, D. Ros, F. Plé, G. Jamelot, A. Klisnick, O. Lundh, F. Lindau, A. Persson, C. G. Wahlström, B. Zielbauer, D. Ursescu, T. Kühl, Optics Letters 32, 2007 and this annual report

Supported in part by Laserlab Europe

A 10 Hz, 3 microjoule transient soft X-ray laser pumped in grazing incidence

S. Kazamias[1], K. Cassou[1], D. Ros[1], F. Plé[1], G. Jamelot[1], A. Klisnick[1], O. Lundh[2], F. Lindau[2], A. Persson[2], C.G. Wahlström[2], S. de Rossi[3], D. Joyeux[3], B. Zielbauer[4], D. Ursescu[4], T. Kühl[4]

[1]LIXAM, Université Paris XI, Orsay Cedex, France; [2]Department of Physics, Lund University, Lund, Sweden; [3]Laboratoire Charles Fabry (IOTA), Orsay Cedex, France; [4]Gesellschaft für Schwerionenforschung (GSI), Darmstadt, Germany

We present recent results on the extensive investigation of a Ni-like Mo X-ray laser pumped in the transient regime and GRIP (grazing incidence pumping) configuration. The pump laser was the 10 Hz, multi-terawatt, Ti:Sa laser system at Lund Laser Centre, Sweden. The main diagnostic was a monochromatic near-field imaging system with a 1.7 micron spatial resolution. Intense lasing was observed routinely at 18.9 nm with up to 3 micro-Joule output energy and stable operation at 10 Hz was demonstrated in 100-shot sequences. We have investigated the role of several pumping parameters, in particular the relative energy and delay between the long and short pulse. A preliminary investigation was done on the effect of a low energy prepulse. Finally, the grazing angle of the pumping pulse was systematically varied between 13° and 21°, while keeping all parameters constant. We show that this multi-parameter scan leads to a well-defined optimal zone of operation and better understanding of the GRIP configuration.

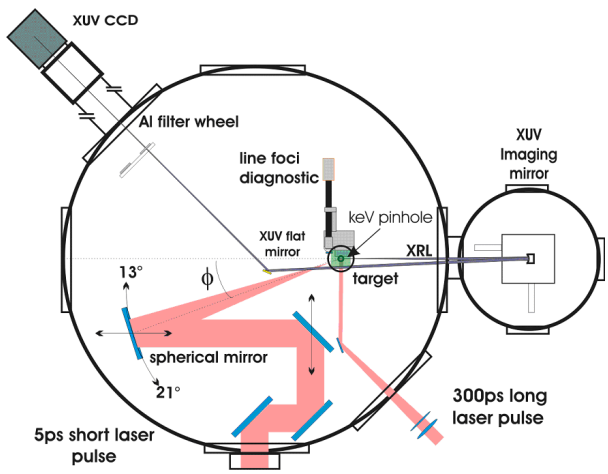

Figure 1: Experimental set-up showing the pump laser beamlines and diagnostics used to characterize the soft X-ray laser.

During a European experimental campaign in January 2006, we used the GRIP configuration to produce a saturated soft X-ray laser at 18.9 nm from a Ni-like molybdenum plasma generated with a solid target of 4 mm length [1]. A schematic view of the experimental set-up is presented in fig. 1. After the last amplification stage, the CPA Ti:Sa laser system at Lund Laser Centre delivered an energy of 1.4 J at 800 nm in a chirped, 300 ps pulse. This energy was split into two beams before it entered the compressor. One beam remained uncompressed to create the plasma and the other beam was compressed down to 5 ps to heat the plasma and pump the soft X-ray laser transition. The splitting ratio between the two pulses was adjustable to optimize the soft X-ray laser output. A low-energy pre-pulse generator was installed on the long pulse beam path. For most of the experiment, the pre-pulse preceded the long pulse by 1.3 ns and contained 7 % of its energy. All of those beams were focused in line on a 4 mm long molybdenum slab target. The effect of using a double pulse to create the preplasma has already been studied by a large number of groups [2, 3] and is widely known to increase the soft X-ray laser emission and to reduce the electron density gradient in the gain region.

For the best conditions, a soft X-ray laser beam of 3 microjoule output energy was obtained routinely at a 10 Hz repetition rate: this corresponds to a conversion efficiency of 3 10^{-6} and an average power of 30 microwatt. The brightness of this XUV source can be estimated by assuming usual values for the pulse duration and bandwidth. It is of the order of 6 10^{17} ph/s/mm^2/mrad^2/(0.1% bandwidth) for the average value and up to 10^{28} ph/s/mm^2/mrad^2/(0.1% bandwidth) for the peak one. Those values confirm that GRIP soft X-ray lasers can usefully complement third generation synchrotrons or X-ray free electron laser sources, and provide versatile sources for many applications, including XRL spectroscopy in storage rings [4]. The GSI collaborators' major contribution was the development and operation of a high-resolution keV imaging system for the plasma emission. The results of this investigation are still being analyzed.

References

[1] K. Cassou et al., Opt. Lett., 32, 139-141 (2007)
[2] P. Lu et al., Phys. Rev. A, 58, 628 (1998)
[3] J.E. Balmer et al., IEEE Journal of selected topics in Quantum Electronics 5, 1435 (1999)
[4] S. Borneis et al., Hyperfine Interactions 127, 537 (2000)

This work was supported by the Swedish Research Council, the Knut and Alice Wallenberg Foundation and through the EU Access to Research Infrastructures activity (contract RII3-CT-2003-506350, Laserlab Europe campaign led by LIXAM-France)

Propagation and absorption of the pumping laser pulses in a GRIP XRL plasma

D. Ursescu[1] , T. Kühl[1,2], B. Zielbauer[1,2,3], D. Zimmer[1,2] and G.. Pert[4]
[1]GSI, Darmstadt, Germany; [2]Johannes Gutenberg Universität, Mainz, Germany; [3]Max Born Institute, Berlin, Germany;
[4]University of York, York, U.K.

Recently, significant progress in the x-ray lasers (XRL) development was made by systematically changing the incidence angle of the main pump pulse [1, 2]. This grazing incidence pumping method (GRIP) reduced the pump energy needed to values below 1J and, as a consequence, table-top XRL systems could be demonstrated with repetition rates increased by several orders of magnitude, up to 10Hz. This approach was successful in producing XRL wavelengths as short as 10.9 nm with less than 2J pump energy [3]. In [4] it was demonstrated that the efficiency and the peak brilliance of such a GRIP XRL can be significantly improved. Up to 3-μJ energy with 1.4J pump energy and 10^{28} ph/s/mm^2/mrad^2/(0.1%bandwidth) were obtained.

The influence of the non-normal incidence angle of the MP was analyzed theoretically in [5] in the attempt of scaling the non-normal incidence pumping scheme to sub-10-nm and water-window wavelengths. The complementary theoretical study performed here is oriented toward the more detailed description of the MP incidence angle effects on the critical electron density region, where a higher XRL output could be achieved. This density region is important in sub-10nm XRL systems in order to achieve significant gain.

Further, the positive effects observed in this critical electron density region by varying the MP incidence angle can be enhanced by a variation of the PP incidence angle. It is shown here that this plasma shaping technique allows to control the electron density distribution and further plasma parameters like the distribution of the average ionization stage. Experiments reported in [6,7] show that these two angles have a key influence on the XRL output.

The possibility of gain generation closer to the critical electron density region was shown in simulations carried out with the EHYBRID 1.5D code for a set of optimized parameters.

When varying the PP incidence angle, its optimal value is found to be 75° at the MP incidence angle of 30° as shown in fig. 1. The local XRL signal is defined assuming an exponential increase of the XRL output as a function of the gain-length product. For the optimal angle of 75°, the local XRL signal is increased by a factor of 6 compared to that seen at 0° PP incidence angle. Such a configuration would be advantageous for a plasma amplifier.

In conclusion, a systematic study of the influence of the PP and MP incidence angles for a transient collisionally excited (TCE) Ag XRL was presented. A strong local XRL signal appears close to the critical electron density region at MP incidence angles around 45° which is further enlarged by a factor of 6 when the PP incidence angle goes up to 75°. This plasma shaping technique is not restricted to the TCE Ag XRL and can be beneficially used for materials other than silver as well [8, 9]. Gain generation closer to the critical density is the key for scaling TCE XRL toward sub-10 nm wavelengths. In addition, the technique is quite generally suited for controlling the electron density distribution via ionization.

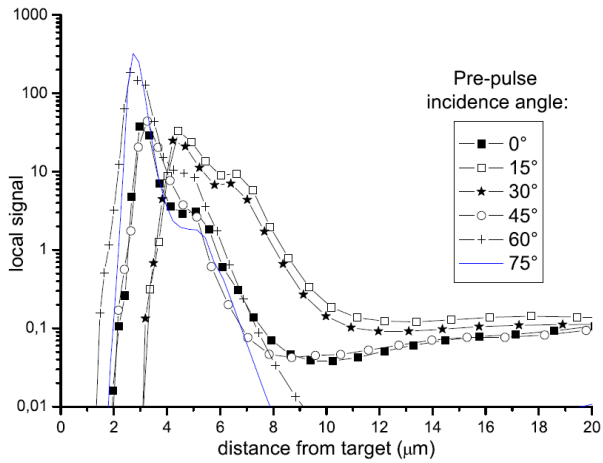

Figure 1: Local XRL signal versus the distance to the target surface for different PP incidence angles. The MP incidence angle is fixed to 30°.

References

[1] P. Neumayer, W. Seelig, K. Cassou, A. Klisnick, D. Ros, D. Ursescu, T. Kühl, et al., Appl. Phys. B 78, 2004, p. 957.
[2] R. Keenan, J. Dunn, P. K. Patel, D. F. Price, R. F. Smith, and V. N. Shlyaptsev, Phys. Rev. Lett. 94, 2005, p. 103901.
[3] J. Tummler, K. A. Janulewicz, G. Priebe, and P. V. Nickles, Physical Review E 72, 2005, p. 037401.
[4] K. Cassou, S. Kazamias, D. Ros, F. Plé, G. Jamelot, A. Klisnick, O. Lundh, F. Lindau, A. Persson, C. G. Wahlström, B. Zielbauer, D. Ursescu, T. Kühl,, Optics Letters 32, 2007.
[5] G.J. Pert, Phys. Rev. A, 73, 2006, p. 033809
[6] D. Ursescu, B. Zielbauer, T. Kühl, P. Neumayer, and G. Pert, to be submitted 2007.
[7] B. Zielbauer, D. Ursescu, T. Kühl, K. Cassou, S. Kazamias, D. Ros, F. Plé, G. Jamelot, A. Klisnick, O. Lundh, et al., to be submitted 2007.
[8] D. Ursescu, B. Zielbauer, D. Zimmer, T. Kühl, and G. Pert, PNP12 conference, Darmstadt, Sept. 2006
[9] D. Ursescu, G. J. Pert, in preparation 2007

Towards multi-100 eV X-ray lasers generated by high-energy transient collisional pumping at the new PW-PHELIX facility

D. Ros[1], C. Bischoff[2], J. Dunn[3], S. Kazamias[1], A. Klisnick[1], T. Kühl[2], A. Mayr[2], G. Pert[4], D. Ursescu[2], B.Zielbauer[2,5], D. Zimmer[2]

[1] LIXAM, Université Paris XI, Orsay Cedex, France; [2]GSI, Darmstadt, Germany; [3]Lawrence Livermore National Laboratory, USA; [4]University of York, York, U.K.; [5]Max Born Institute, Berlin, Germany

The transient collisionally pumped soft X-ray lasers [1] are generated by the interaction of two laser pulses with a solid target. The target is strongly ionized by the first long pulse (100 ps-1 ns) and the second short one (500 fs – 10 ps) induces the population inversion that is responsible for the soft X-ray laser transition. An important feature of this type of lasers is the likely extension into the regime above 100eV. A key towards this regime could be the application of non-normal-incidence pumping as first demonstrated by our experiments at the PHELIX front-end [2] and the use of pulse energies now available at PHELIX. Particularly attractive for medical and biological research would be the access to the so-called "water-window", i. e., the energy range between the K-shell absorption edges of carbon and oxygen needing 300 eV photons. For the diagnostics of Warm Dense Matter, Thomson scattering of a narrow-band laser source can deliver information on the plasma temperature and density.

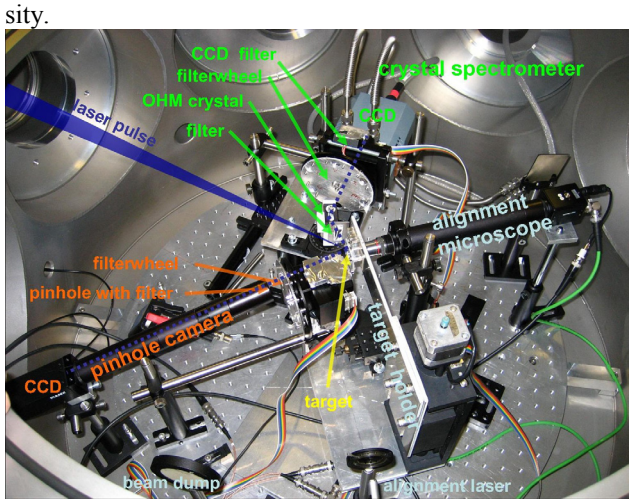

Figure 1: View of the experimental set-up. The laser beam enters from the left, X-ray emission is analysed spatially by a pinhole camera and spectrally by a crystal spectrometer.

The XRL requires a pre-pulse of 20 to 100J energy and nanosecond duration and a main pulse of around 100J in the picosecond range. During the first period of operation of the PHELIX system, ns-pulses of up to 60J were available in the PHELIX laser building. and were used in a set-up as shown in fig. 1. The main purpose of the first phase of the experiment was to test the plasma diagnostics. A crystal spectrometer and an X-ray pinhole camera are used to determine the plasma parameters. Spectra of Ag plasmas were taken at different laser energies and are currently under investigation. The important question is the development of the charge state of the plasma, which can be determined from the plasma emission lines. In addition, reference spectra from aluminium and carbon targets for the calibration of the spectrometer were produced.

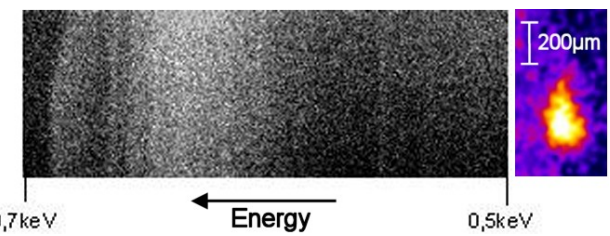

Figure 2: Spectrometer camera record with preliminary energy scale (left) and X-ray pinhole camera image (right) of a silver plasma generated by a 60 J shot.

The first experiments demonstrated the ability to produce and analyse a hot, highly charged plasma as it is necessary for the XRL laser scheme. For the final experiments, the ionisation of higher Z material has to be studied.

References

[1] A. Klisnick, J. Kuba, D. Ros, R. Smith, G. Jamelot, C. Chenais-Popovics, R. Keenan, S. Topping, C. L. S. Lewis, F. Strati, G. J. Tallents, D. Neely, R. Clarke, J. Collier, A. G. MacPhee, F. Bortolotto, K. A. Janulewicz, P. V. Nickles, "Demonstration of a 2-ps transient X-ray laser", Phys. Rev A 65, 033810 (2002)

[2] P. Neumayer, W. Seelig, K. Cassou, A. Klisnick, D. Ros, D. Ursescu, T. Kuehl, S. Borneis, E. Gaul, W. Geithner, C. Haefner, R-P. Wiewior, "Transient collisionally excited X-ray laser in nickel-like zirconium pumped with the PHELIX laser facility." Appl. Phys. B, 78 (2004), 957

This work was supported by Laserlab Europe

ILIAS - Ion and Laser beam Interaction and Application Studies

P. Mulser, Theoretical Quantum Electronics (TQE), TU Darmstadt, T. Schlegel, GSI Darmstadt

Objectives of the ILIAS study group
Founded in January 2005 it is aiming at

(i) preserving the expertise accumulated in the past by theoretical groups associated to GSI through projects combining intense heavy ion and high energy laser beams;

(ii) focussing this expertise to the new goal of establishing a GSI-specific program involving the PHELIX facility in combination with the GSI heavy ion accelerators.

The two objectives may be achieved by

- exploring the potential of intense heavy-ion and laser beams interacting with bulk matter, with mass-limited systems, and with single particles (clusters, mesoscopic systems, ions, and nuclei);
- offering theoretical assistance to the PHELIX project in planning relevant experiments and discussing them in detail with the experimentalists involved. The acronym PHELIX as used in the context here stands for all high-power laser facilities, short pulse, long pulse, and all kinds of intense laser-matter interaction research planned at GSI.
- creating a platform for activating synergies by interacting with researchers from German and European institutions.

Second year's progress
To disseminate the expertise in plasma, atomic, relativistic, and collective physics among PHELIX a weekly **workshop/seminar** has been launched at GSI in January 2005. In 2006 it has been successfully continued and intensified as a **joint venture** of the ILIAS study group, PHELIX laser project, and groups from the Plasma and Atomic Physics divisions of GSI. The workshop/seminar had 30 sessions during 2006, distributed among the subjects

> Relativistic plasma physics and fluid dynamics, theory of electron and ion acceleration by superintense laser pulses, vacuum quantum electrodynamics, relativistic wave propagation, atomic spectroscopy, Thomson scattering, search for key experiments with the PHELIX laser facility.

The **community** of actively involved German and European institutions has been enlarged by collaborations with the Universities of Düsseldorf (O. Willi, collisionless absorption), Bochum (H. Ruhl, code development, collisionless absorption), RWTH Aachen (H.-J. Kull, relativistic wave propagation, clusters), Istituto di Fisica del Plasma Piero Caldirola, Milano (M. Lontano, relativistic plasma physics), and Università Bicocca, Milano (D. Batani, fast electron transport and fast ignition). The total number of actively involved institutions and researchers at present amounts to 11 and 22, respectively.

Detailed **progress** in fundamental high-power laser-matter interaction, applied heavy ion and laser beam-matter physics and code development is reported in the ILIAS Progress Report No. 2 [1]. Complementary to traditional high-field reseach with heavy ions at GSI, intense laser field QED opens prospectives for advanced future experiments with PHELIX (see Di Piazza *et al.*, QED, nuclear and high-energy processes in extremely strong laser pulses, in [1]). Further contributions in basic research are a NO-GO theorem, a systematic investigation of relativistic wave propagation by a novel approach (Pesch, Kull), and studies on melting processes induced by lasers at different time scales [3] (Rethfeld, Anisimov in [1]; non-thermal melting). The NO-GO theorem (Mulser, Ruhl [1]) states that collisionless absorption cannot occur in regular fluid dynamics, regardless of what degree of nonlinearity the induced motion is. Detailed inspection [2] reveals that anharmonic resonance is the leading absorption mechanism in the absence of collisions. Relativistic electromagnetic wave propagation is formulated in terms of three coupled harmonic oscillator equations for the Lagrangian space coordinates and solved by analytical and numerical methods. In the field of applications, studies have been undertaken: extensively on radiation transport and hohlraum heating of matter (Schlegel, Baldina), on electron and ion acceleration by laser (Kowarsch, Scheid *et al.* [1], Blaschke *et al.* [1], Brambrink *et al.* [5, 6]), stability of foam targets (Gibbon, Olga Rosmej, Chichkov [1]), multi-electron spectra (Tomaselli, Kühl, Ursescu[1, 7]), isochoric heating with ion beams (Maruhn, Anna Tauschwitz [1], [8]), and other subjects [1, 9].

References

[1] P. Mulser, T. Schlegel (Eds), ILIAS Prog. Rep. No. 2 (2006)

[2] D. Bauer and P. Mulser, Phys. Plasmas, February issue, 2007.

[3] Baerbel Rethfeld, Phys. Rev. B 73, 035101 (2006).

[4] T. Pesch and H.-J. Kull, submitted to Phys. Plasmas.

[5] E. Brambrink, M. Roth, A. Blazevic, and T. Schlegel, Laser and Particle Beams 24, 163 (2006).

[6] E. Brambrink, J. Schreiber, T. Schlegel *et al.*, Phys. Rev. Lett. 96,154801 (2006).

[7] M. Tomaselli, T. Kühl, D. Ursescu, and S. Fritzsche, Prog. Theor. Phys. 116, 699 (2006).

[8] Anna Tauschwitz, E. Brambrink, J.A. Maruhn, M. Roth, M. Schollmeier, T. Schlegel, A. Tauschwitz, High Energy Density Physics 2, 16 (2006).

[9] G. Rascol, H. Bachau, V. T. Tikhonchuk, H.-J. Kull, and T. Ristow, Phys. Plasmas 13, 103108 (2006).

Vacuum heating vs skin layer absorption of intense fs laser pulses

D. Bauer, Max-Planck-Institut für Kernphysik, Heidelberg, P. Mulser, TU Darmstadt

Crossing of the narrow skin layer in solid targets by electrons in a time shorter than a laser cycle represents one of the numerous collisionless absorption mechanisms of intense laser-matter interaction [1, 2, 3]. This kinetic effect is studied by a test particle approach in an energy interval extending into the relativistic domain. Three main results obtained are the strong dependence of the energy gain by the single particle on the instant of injection relative to the phase of the light wave, the reflection of the particles primarily contributing to absorption well in front of the target, and absorption hardly exceeding the 10% limit. The simulation results shed new light on "vacuum heating".

Looking through the enormous amount of theoretical papers that have appeared on ultrashort intense light pulse interaction with dense matter three aspects emerge,

I. a quantitative analysis of the interaction (absorption, fast electron spectra) is not accessible to an analytical treatment but has to rely on 3-dimensional (3D) computer simulations.

II. over ten different collisionless absorption mechanisms have been proposed, none of them exceeds 5–10%.

III. the physical principle of collisionless absorption and ordering of the mechanisms under II according to their strength is missing.

The present effort tries to contribute to point III. The main aim will be to investigate which groups of particles will most contribute to absorption in which region of space, skin layer or vacuum, and to study the dynamics of electron reflection and turning point positions as a function of the relative phase of the injection instant to the laser wave. For such a purpose a test particle model is suited best. An intensity of $I = 3.51 \times 10^{18}\,\mathrm{Wcm}^{-2}$ at $\lambda = 800\,\mathrm{nm}$ (Ti:Sapphire laser) is assumed to be incident normally and under 45 degrees from $-\infty$ onto a plasma with density varying from $10n_c$ to $250n_c$, n_c critical density. Single relativistic particle dynamics is illustrated by the phase space plot of Figure 1(a). Spreading of the momenta p_l at the vacuum-target interface at $x = 0$ (LHS) is a consequence of particle injection of initial momentum p_{x0} at different phases of the laser wave at position x_0 on the RHS. The majority of particles coming back are reflected in the vacuum and have acquired almost their final energies p_{xf} already at the electron-vacuum interface. The asymptotic conservation of canonical momentum p_y is illustrated in Fig. 1(b). In contrast to standard linearized treatments neither the slow nor the energetic particles are reflected at the plasma-vacuum boundary, a fact mentioned once already in the past [3]. The majority of electrons undergo reflection in the vacuum in front of the target and absorb there also the major part of their final energy.

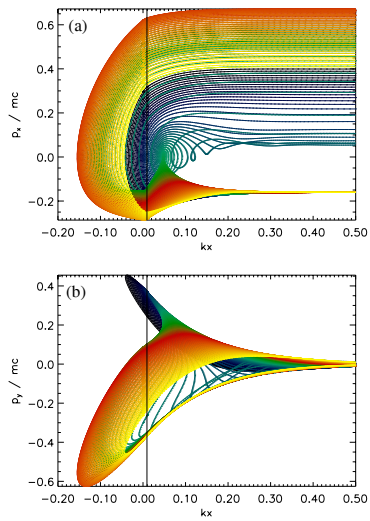

Figure 1: Particle dynamics in detail. Phase space plots p_x/mc (a) and p_y/mc (b) vs kx of 100 test particles injected with initial momentum $p_{x0}/(mc) = -0.3$ at $x_0 = 20\,\lambda_s$, λ_s skin length, at times $\omega t_0 = \pi\nu/100$, $\nu = 0, 1, \ldots, 99$ (for better visibility only phases between 0 and π are shown). Laser parameters are $I = 3.51 \times 10^{18}\,\mathrm{Wcm}^{-2}$, $\lambda = 2\pi/k = 800\,\mathrm{nm}$, and plasma density is $n_0 = 50n_c$. Reflection occurs during one half laser period predominantly in front of the target surface.

The analysis undertaken in the present paper sheds new light on the ominous term of vacuum heating. In some respect this kind of heating resembles essential aspects of the Brunel effect [4]. However, in the light of the model presented here it differs from the Brunel effect in essential aspects: (i) ponderomotive confinement of the regular electron cloud in front of the target rather than confinement by space charges; (ii) acceleration of slow as well as fast electrons occurring during a half laser period rather than extending over a whole laser period. Vacuum heating differs from absorption due to resonances of the plasma layers, and concomitant wave breaking, shown elsewhere (see NO-GO theorem, this report).

References

[1] P.J. Catto and R.M. More, Phys. Fluids **20**, 704 (1977).

[2] P. Mulser, S. Pfalzner, and F. Cornolti in *Laser Interaction with Matter*, G. Velarde *et al.* (eds.) (World Scientific, Singapore, 1989), p. 142.

[3] T.-Y. Brian Yang *et al.*, Phys. Plasmas **3**, 2702 (1996).

[4] F. Brunel, Phys. Rev. Lett. **59**, 52 (1987); Phys. Fluids **31**, 2714 (1988).

Collisionless High-Power Laser Beam Absorption: A NO-GO Theorem

P. Mulser, Tech. Universität Darmstadt, Hartmut Ruhl, Ruhr-Universität Bochum

Two decades after the invention of cirped pulse amplification the mechanism of collisionless absorption of ultrashort intense laser radiation in solid surfaces is still open to discussion. A NO-GO theorem is formulated which shows that fluid dynamics, whatsoever its degree of nonlinearity and complexity may be, does not lead to absorption in the absence of collisions. Rather is cold wavebreaking a necessary, but not sufficient, condition for irreversibility to occur. Absorption is postulated to occur due to internal plasma resonances.

When a solid target is heated up beyond an electron temperature $T_e \approx 10^3 Z^2$ eV, Z ion charge, by an intense ultrashort laser pulse, absorption by electron-ion collisions is no longer effective. Experiments show that good absorption, up to 70% and beyond, still occurs in this collisionless regime. Efficient collisionless absorption of the same order of magnitude is well confirmed by particle-in-cell (PIC) [1] and Vlasov simulations also [2]. Nonetheless, after two decades of studies no single physical effect can be addressed in a convincing way by which collisionless absorption of 50 % or higher by the free electrons in the surface plasma of the solid is accomplished [3]. In other words, collisionless absorption is well confirmed by experiments and simulations but not understood. All kinds of absorption, collisional, resonant, mode conversion, excitation, ionization, etc. are described by the cycle averaged $\boldsymbol{jE}$ term in Poynting's theorem, $\boldsymbol{j}$ total current density, $\boldsymbol{E}$ electric field. Under the influence of a harmonic laser field $\boldsymbol{E}_d \cos\omega t$, a free plasma electron oscillates at $\sin\omega t$ and harmonics of ω, and so does $\boldsymbol{j}$. In order to yield net absorption, $\boldsymbol{j}$ must contain $\cos\nu\omega t$ components (ν integer), or equivalently, a phase shift must exist between $\boldsymbol{j}$ and $\boldsymbol{E}$ differing from $\pi/2$.

A plane fully ionized overdense target is assumed to fill the half space $x \geq 0$. A plane wave $\boldsymbol{E}(\boldsymbol{x},t) = \boldsymbol{E}_0 \exp(i\boldsymbol{kx} - \omega t)$ in p or s-polarization in y-direction, wave vector $\boldsymbol{k}$ and frequency ω, is incident from $-\infty$ under angle α onto its surface. After applying a Lorentz boost in y-direction of magnitude $v_0 = csin\alpha$ the wave impinges normally onto the target and it follows under all conditions

$$\overline{j_x E_x} = \frac{\varepsilon_0}{2}\frac{1}{\tau}\int_\tau \frac{\partial}{\partial t} E_x^2 \,\mathrm{d}t \;=\; 0. \qquad (1)$$

To make a statement on $\overline{j_y E_y}$ we observe that the dynamics of a fluid element is completely determined by its Lagrangian position $\boldsymbol{\xi}(\boldsymbol{a},t) = \boldsymbol{x}(t) - \boldsymbol{a}$, with $\boldsymbol{a} = \boldsymbol{x}(t=0)$. As long as the dynamics induced by the laser is regular all physical quantities are unique functions of the displacement $\xi(a,t) = x - a$ in x-direction, $a = \boldsymbol{a}\boldsymbol{e}_x$. In its leading terms the equation of motion is given by

$$\begin{aligned}\frac{d}{dt}(\gamma_e m\frac{d\xi}{dt}) + \Omega^2(\xi)\xi &= e\frac{\gamma_0}{\gamma_e}v_0\frac{\partial}{\partial a}A_y \\ &= D(\xi,t), \quad \Omega^2 = -\frac{e^2}{|\xi|}\frac{\partial\Phi}{\partial a}.\end{aligned}$$

$D(\xi,t)$ is the driver of the anharmonic oscillator, A_y the vector potential of the laser wave and Φ the collective plasma potential. Its solution represents a rapidly oscillating motion in $\xi(a,t)$ which can be evaluated by the method of stationary phase. The result is that in the absence of internal plasma resonances ξ vanishes for $t \to \infty$. When resonances are present finite displacements survive and, as a consequence, crossing of fluid elements occurs ("cold wavebreaking"). Equivalently, the Jacobian of the mapping $(\boldsymbol{a},t_0) \to (\boldsymbol{x},t)$ becomes singular and the dynamics is no longer regular. This is the content of a remarkable NO-GO (i.e. exclusion) theorem: Whatever the degree of nonlinearity and complexity of high power laser interaction is, (I) no collisionless absorption is possible under steady state conditions in the basic geometry, considered here, in the absence of resonances, or equivalently, (II) wave breaking is a necessary consequence of collisonless absorption in an ideal fluid; it is induced by anharmonic resonance in overdense targets which is the underlying origin of collisionless absorption.

The situation with collisionless absorption by an ideal fluid is analogous to dissipation by a shock wave. The latter can be described by reversible equations which under regular flow allow adiabatic transitions only. To make account of dissipation, i.e., irreversible changes of state with corresponding increase of entropy, a discontinuity (infinite derivatives) must be introduced.

The NO-GO theorem can be viewed as the macroscopic extension of the well-known assertion that a single point charge cannot absorb a photon unless it resonates in an outer potential.

References

[1] Paul Gibbon and A.R. Bell, Phys. Rev. Lett. **68**, 1535 (1992); Paul Gibbon, Phys. Rev. Lett. **73**, 664 (1994); S.C. Wilks *et al.*, Phys. Rev. Lett. **69**, 1383 (1992).

[2] H. Ruhl and P. Mulser, Phys. Lett. **A 205**, 388 (1995); H. Ruhl, A. Macchi, and P. Mulser, Phys. Rev. Lett. **82**, 2095 (1999).

[3] D. Bauer and P. Mulser, *Vacuum heating vs skin layer absorption*, accepted by Phys. Plasmas (February issue 2007).

Fast ignition scheme: Limiting Alfvén current in the dense plasma region

Anna Antonicci, D. Batani, and P. Mulser
Dipartimento di Fisica G. Occhialini, Università Milano Bicocca, Italy

The knowledge of the maximum current (Alfvén limit) in a plasma is of fundamental importance in the context of fast ignition of fusion pellets by lasers. A relativistic electron beam embedded in a dense plasma with non-relativistic return current is calculated. with the help of the hybrid code Petra which treats the fast electrons as a relativistic PIC and the cold background plasma as a classical non-relativistic fluid.

According to numerical studies in the past, for fast thermonuclear ignition of a precompressed pellet by laser in the optical wavelenght range the intensity (energy flux density) $I = 10^{20}\mathrm{W/cm}^2$ represents an inferior limit [1]. For the deposition region of the laser beam around the critical density this implies that both currents, the direct fast electron stream as well as the charge neutralizing return current are relativistic. As soon as the direct beam of fast electrons penetrates into the pellet interior the return current can be treated as a non-relativistic classical fluid of very moderate temperature. Owing to the complexity of the problem in a first step it is legitimate to suppress the fast evolution in time (neglect of the displacement current, viceversa two-stream instability) and to limit all calculations to this region. The dynamics is driven by a parallel beam of relativistic electrons of Gaussian radius and length of 5μm and 100μm, respectively, and Gaussian energy distribution. With $\mathbf{j_f}$ the current density and η the inverse of the conductivity of the cold background electrons the governing equations are

$$\frac{\partial \mathbf{B}}{\partial t} + \mu_0 \nabla \times (\eta \nabla \times \mathbf{B}) = \nabla \times (\eta \mathbf{j_f}), \qquad (1)$$

$$\mathbf{E} = \eta(\nabla \times \frac{\mathbf{B}}{\mu_0} - \mathbf{j_f}), \qquad (2)$$

$$\frac{d\mathbf{p}}{dt} = -e(\mathbf{E} + \mathbf{v} \times \mathbf{B}). \qquad (3)$$

Eq. (3) is restricted to the relativistic electrons in the particle-in-cell (PIC) code. In the vacuum or low density plasma a beam stops propagating when its own magnetic field B turns the electrons around. Hence, the limiting Alfvén current I_A is given by

$$I_A = \frac{4\pi}{\mu_0 e} p. \qquad (4)$$

For a beam of 1 MeV electrons $I_A = 33$ kA, for 5 MeV $I_A = 166$ kA [2,3]. In the dense plasma the Alfvén limit is determined by the degree of total current neutralization and must be calculated numerically. To this end various numerical runs have been performed in an Al target of thickness $d = 100\mu$m under the assumption of cylindrical symmetry.

In Fig. 1 we show the total current I [A] (a) and the magnetic field B_θ [Tesla] (b) in space after 1 ps, and the temporal evolution of, from top to to bottom, the total energy injected minus lateral losses, the energy deposited in the target by Joule heating of the return current, the loss of the hot electrons across a coaxial test cylinder of 20 micron radius, the energy of the escaping electrons after crossing the target, the energy deposited by collisions of the fast electrons, and the losses by reflection from the entrance surface. Total current neutralization in the hot beam region is better than 10^{-3}. The calculations show that despite local violation of the Alfvén limit (4) in the lateral filaments (in red) the hot beam as a whole survives to a high degree.

In a second stage also the role of the displacement current, or equivalently, of all variants of two-stream instabilities, must be thoroughly investigated. A general conclusion which emerges already in this stage of investigations is that the Alfvén limit is less severe than criterion Eq. (4).

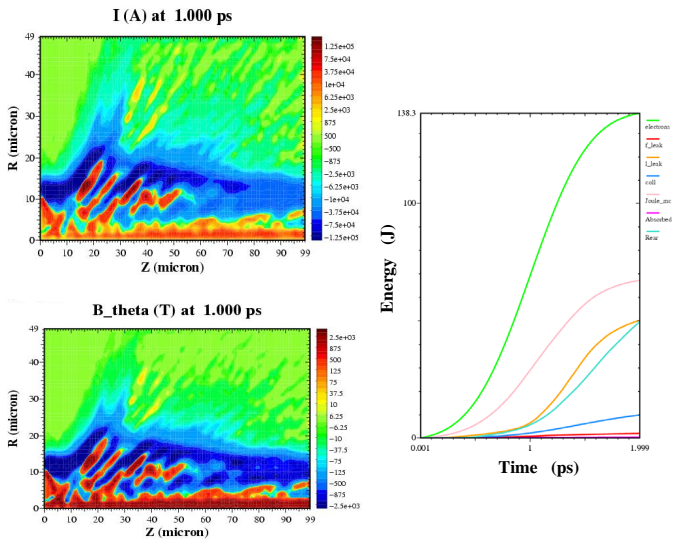

Figure 1: Total current I (a), magnetic field B_θ (b) as a function of radius $R[\mu\mathrm{m}]$ and axial length $z[\mu\mathrm{m}]$ after 1 ps, and evolution of energy deposition and energy losses induced by a parallel beam of electrons of 1.01 MeV mean particle energy and 5 micron radius during the time of 2 ps (c). Number of hot electrons is 9.9×10^{14}, total beam energy is 160 J. Locally the total current I exceeds the Alfvén limit Eq. (1). For additional data see text.

References

[1] S. Hain and P. Mulser, Phys. Rev. Lett. **86**, 1015 (2001); P. Mulser *et al.*, AIP Conf. Proc., 2001, Vol. **611**, 363-368.

[2] J. R. Davies, Phys. Rev. **E 69**, 065402(R) (2004); Laser and Particle Beams **24**, 299 (2006).

[3] D. Batani *et al.*, AIP Conf. Proc., 2004, Vol. **740**, 446-457.

Homogeneous plasma heating by laser-generated hohlraum radiation

T. Schlegel, GSI Darmstadt, E. Baldina, Joint Institute for Nuclear Research, Dubna

Radiative heating with x-rays is of large interest for dense hot matter studies. It allows to measure x-ray opacities, which are important for astrophysics, to obtain equation of state data by generating extremely uniform high-pressure shock waves or to investigate heavy ion stopping in ionized matter. To attain high spatial homogeneity of the generated plasmas in time intervals sufficiently long for observation and/or interaction, thermal x-radiation from laser-heated hohlraum targets serves as a well-suited driver.

The new program complex MULTIVF was developed to design adequate hohlraum experiments driven by the PHELIX laser. It couples the 1D hydrodynamic code MULTI [1] with a view factor code VF for radiation transport in the hohlraum [2]. We consider cavities with 2D or 3D (axially symmetric) geometry which consist of layers of optically thick material enclosing an optically thin or vacuum volume. The walls of the cavity are divided into 1D sectors modeled independently using MULTI and coupled together via view factor calculation of the whole "vacuum" cavity.

Energy deposition of fast heavy ions in hot plasmas is of special interest in inertial fusion research. The ions must be stopped in converter targets to produce a strong burst of x-rays for further fusion target heating and compression. Stopping in cold matter was carefully investigated over many decades experimentally as well as theoretically. However, ion stopping in plasmas is not really understood yet and only a few experimental results exist. The difficulty of such measurements is caused partly by the long pulse length of the ion bunches. Heavy ion pulses, passing the linear accelerator stage at GSI Darmstadt, gain energies in the range (5-10)eV per nucleon and have minimum durations of (3-4)ns. Therefore, a hot plasma target for ion stopping measurements must be kept in a nearly uniform state over times of several nanoseconds.

For our first analysis we have chosen a geometry which was already applied in opacity experiments performed at MPQ Garching [3]. A gold cavity with 3mm diameter will be irradiated now by a (150 or 300)J, Nd-glass laser pulse (wavelength $\lambda = 1\mu$m.) The pulse length was varied between 500ps and 3ns (FWHM) in the simulations assuming a sin^2-envelope. Carbon samples with different thicknesses ($0.5 - 3\mu$m; see [4]), placed at one or both diagnostic holes with 1mm diameter each, will be heated by the hohlraum radiation and afterwards crossed by a focused heavy ion beam with a width of several hundred microns.

Fig. 1 shows the radiation temperatures in dependence on time, which drive a radiative heat wave in 2μm thick carbon foils. With less deposited energy, these temperatures become smaller, however, the likewise reduced flow of wall plasma ablated mostly in the laser focal spot area will enable time intervals up to 5ns for undisturbed stopping measurements. Snapshots of plasma parameters in the carbon foils are plotted in Fig.2. The spatial uniformity of these distributions could be improved when changing to the lower laser energy, especially in case of temperature and consequently ion charge. The temporal changes became also smaller.

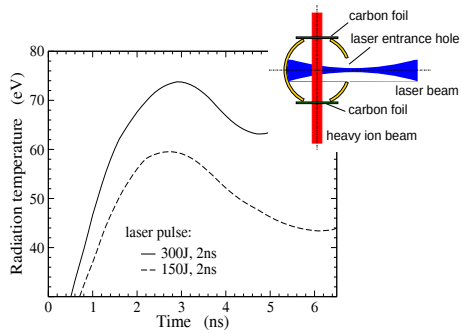

Figure 1: Radiation temperatures on the surface of carbon foils for two different laser pulses heating the cavity.

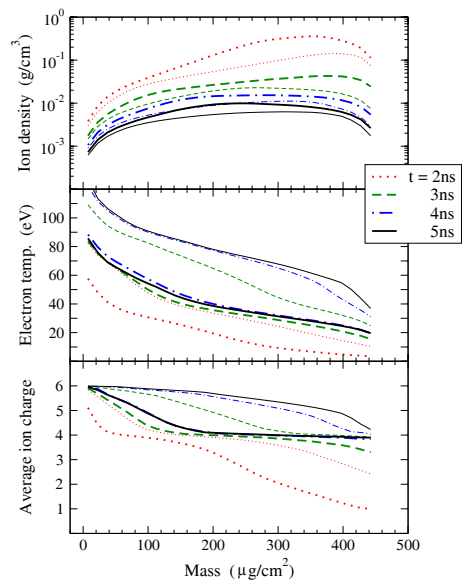

Figure 2: Plasma parameters in dependence on areal mass. Thick lines were obtained for 150J laser illumination.

References

[1] R. Ramis *et al.*, Comput. Phys. Commun. **49** (1988) 475-505.

[2] E. Baldina, Laser and Particle Beams **22** (2004) 65-68.

[3] K. Eidmann, A. Bar-Shalom, A. Saemann and G. Winhart, Europhys. Lett. **44** (1998) 459-464.

[4] M. Roth, C. Stöckl *et al.*, Europhys. Lett. **50** (2000) 28-34.

Collective Relativistic Phenomena with Femtosecond Laser Pulses

A. A. Baldin
Joint Institute for Nuclear Research, Dubna, Russia

Relativistically invariant self-similarity approach is applied for description of collective particle production by femtosecond laser pulses.

Recent outstanding advances in laser technique, namely, generation of ultrashort laser pulses ensuring intensities on the target of an order of 10^{20} W/cm^2 opened a wide class of new phenomena of production of intense and "highly-coherent" beams of radiations, including photons and charged particles (e.g., [1]).

Theoretically, the regime of "coherent" particle generation was first predicted in [2] and then confirmed numerically [3]. It is sometimes referred to as "bubble regime". Generation of positron beams by femtosecond laser pulses has also been reported [4].

A comprehensive description of particular experimental results is complicated. This motivates a desire of application of the self-similarity approach in order to reduce the number of variables considered [7].

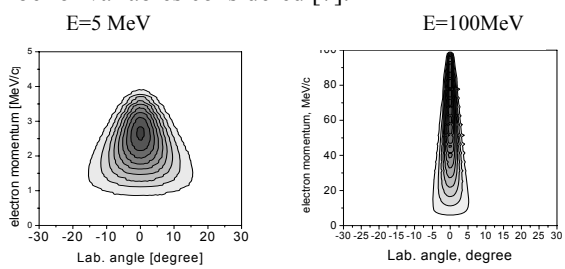

Figure 1. Isosurfaces of e- production cross sections.

A general self-similar solution constructed in [5, 6] describes quantitatively collective processes of particle production in relativistic collisions.

We extend this approach to construction of the self-similar solution describing collective interaction of a group of coherent photons with electrons similar to [5-7].

The 4-momentum conservation is written in the form:

$$E_\gamma + xP_2 = xP_2' + P_3 + P_4, \qquad (1)$$

where E_γ is the energy of the "collective photon" (group of coherent photons), and the subscripts "2", "3", "4" denote the initial accelerated electron and the final electron and positron, respectively.

The cross sections of e-/e+ production have the form

$$\sigma_{inv}{}^{e^-} = C_1 \exp(-x/C_2);\ \sigma_{inv}{}^{e^+} = C_1 \exp(-\Pi/C_2) \qquad (3)$$

where C_1, C_2 are constants, $\Pi = 0.5\left(X_1^2 + X_2^2 + 2X_1X_2\gamma_{12}\right)^{\frac{1}{2}}$.

Figure 1 shows electron production cross sections in the angle-momentum plane for initial E_γ of 5 MeV and 100 MeV.

Cross sections have clear maximums "narrowing" with increasing E_γ. Thus, for E_γ=200 MeV, about 95 % of produced e- flow unidirectionally, within a angle of 1 °. The average momentum of produced electron beam shifts from about 2.5 to 175 MeV with increasing E_γ.

Figure 2 shows (a) the invariant cross section of e+ production as a function of e+ momentum in the lab. frame for several e- kinetic energies E_{kin} and (b) the e+/e- cross section ratios for E_{kin}=10 MeV at two lab. angles. The maximum of the cross section is seen to increase and shift towards higher e+ momenta with increasing E_{kin}. The angular dependence at small angles is negligible.

These spectra are in qualitative agreement with experiment [4].

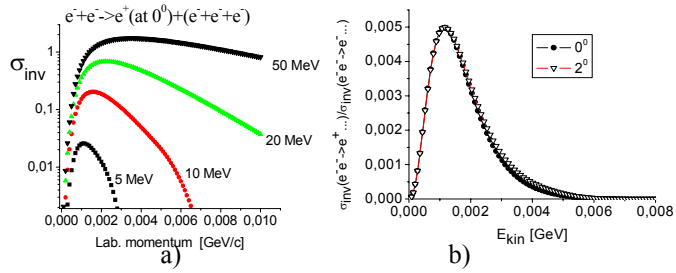

Figure 2.

The analysis of e+ production by femtosecond laser pulses shows a possibility of a dedicated study of generation of intense e+ beams for practical applications (e.g., in biology, medicine).

For optimization of particle production regimes, it is proposed to carry out experiments with simultaneous registration of e- and e+ (for every laser pulse) by two similar measurement systems for positively and negatively charged particles. Reversing poles of this magnetic spectrometer would ensure minimization of systematic errors. Measured e+/e- ratios as functions of momenta will serve as important parameters for theoretical description and practical application of such beams. Another important parameter to be studied is optimal (minimal) laser power, since particle generation has a threshold character. This requires additional study, as regards optimal target design, pre-pulse preparation, phase dependence, and so on.

References

[1] Mangles, et al. Nature, vol.43, 535-538 (2004); Geddes, et al. Nature, vol.43, 538-541 (2004); Pukhov, Malka, et al. Nature, vol.43, 541-544 (2004)
[2] A. E. Kaplan and P. L. Shkolnikov, Phys. Rev. Lett. v. 75, 2316-2319 (1995).
[3] P. L. Shkolnikov, A. E. Kaplan, A. Pukhov, J.Meyer-ter-Vehn, Appl. Phys. Lett. v. 71, 3471-3473 (1997).
[4] C. Gahn, G. D. Tsakiris, G. Pretzler, K. J. Witte, et al., Appl. Phys. Lett., vol. 77, no. 17 (2000), 2662.
[5] A.A.Baldin Phys. Part. Nucl., 56 (3) (1993).
[6] A.M.Baldin, A.A.Baldin, Phys.Part.Nucl., 29 (3), (1998), 577.
[7] A.A.Baldin, E.G.Baldina, this report.

Relativistic increase of critical electron density

M. Lontano, Istituto di Fisica del Plasma Piero Caldirola, Milano, P. Mulser, Tech. Univ. Darmstadt, T. Schlegel, GSI Darmstadt

Original quasineutrality of a plasma at rest is heavily perturbed when the electrons are induced to oscillate relativistically by a superintense laser beam. This represents one of the major difficulties when studying the propagation of intense linearly polarized electromagnetic waves in plasmas. Particular attention has to be dedicated to the effective relativistic increase of the critical density and the density of maximum laser energy deposition for applications, e.g. fast ignition studies.

When the electron particle density at rest n_0 is set into motion of relativistic velocity $\boldsymbol{v}_e$ in the lab frame it transforms into $n_e = \gamma_e n_0$, γ_e Lorentz factor [1]. The relativistic transformation of the particle density is a consequence of the well-known Lorentz contraction. In connection with magnetic fields, in order to avoid contradictions, its influence in Poisson's equation must be taken into account at arbitrary low speeds, when transforming from one reference system into another. Simple example: The magnetic field of a parallel monoenergetic electron beam vanishes in the co-moving reference system and the former Lorentz force on an electron appears now as an additional equivalent electrostatic repulsion resulting from Poisson's law. Owing to their inertia the ions can generally be considered immobile with density n_0 (charge is taken as $Z = 1$ for simplicity). As a result a strong longitudinal electric field is induced in presence of any electron motion which tries to restore the original quasineutrality. For this reason transforming electron densities just formally may produce erroneous results.

Relativistic self-focussing has been observed experimentally. For circular polarization it has been shown that the refractive index of a fully ionized plasma is given by [2],

$$\eta = \left[1 - \frac{n_e}{n_c\left(1+\boldsymbol{a}^2\right]^{1/2}}\right]^{1/2}, \quad \boldsymbol{a} = \frac{e\boldsymbol{A}}{m_e c}, \qquad (1)$$

$\boldsymbol{A}$ vector potential, n_c critical density. Hence, when compared to the non-relativistic case in presence of the circularly polarized wave $\boldsymbol{A}$, the relativistic critical density n_{cr} results as

$$n_{cr} = n_c\left(1+\boldsymbol{a}^2\right)^{1/2}, \quad \gamma_c = \left(1+\boldsymbol{a}^2\right)^{1/2}. \qquad (2)$$

γ_c is the Lorentz factor. In analogy to this expression it has been concluced by some authors that for a linearly polarized wave $\boldsymbol{a}^2$ should be replaced merely by the term $\boldsymbol{a}^2/2$, since this latter appears in the corresponding Lorentz factor γ_c for the oscillation energy [3]. However, such a simple replacement is incorrect, see [4] for relevant cases. The physical reason (not given there) is the tendency to restore quasineutrality. This may be outlined further.

In a homogeneous cold plasma the propagation of a circularly or linearly polarized monochromatic electromagnetic wave in the Lorentz gauge is governed by the wave equation for the four-quantities $A = (\boldsymbol{A}, \Phi/c)$, $J = (\boldsymbol{j}, -en_e c)$, $\boldsymbol{j} = -en_e\boldsymbol{v}_e$,

$$\left(\bigtriangledown^2 - \frac{1}{c^2}\frac{\partial^2}{\partial t^2}\right) A = -\frac{J}{\epsilon_0 c^2} \qquad (3)$$

Φ is the scalar potential, $\boldsymbol{j}$ the three-vector current density. From the conservation of the canonical momentum $\boldsymbol{v}_e$ and $\boldsymbol{A}$ are related to each other by

$$m_e\gamma_e\boldsymbol{v}_e = e\boldsymbol{A} + m_e\gamma_0\boldsymbol{v}_0, \quad \gamma_0 = \gamma(v_0). \qquad (4)$$

$\boldsymbol{v}_0$ is a constant flow velocity of the plasma. Hence, the three-current density becomes

$$\boldsymbol{j} = -\frac{e^2 n_e}{\gamma_e m_e}\boldsymbol{A} - \frac{\gamma_0}{\gamma_e}en_e\boldsymbol{v}_0 + \boldsymbol{\gamma}_0 en_0\boldsymbol{v}_0. \qquad (5)$$

Formally $n_e = \gamma_e n_0$, and (3) reduces, with a monchromatic wave of frequency ω, to the invariant steady state wave equation

$$\bigtriangledown^2\boldsymbol{A} + \frac{\omega^2}{c^2}\left(1 - \frac{n_0}{n_c}\right)\boldsymbol{A} = 0. \qquad (6)$$

From this equation any relativistic effect is canceled owing to ignoring quasineutrality and thus, relativistic self-focussing is absent, in contradiction to [2] and [4].
A monochromatic wave is switched on adiabatically and there is much time to react and to keep the electron density n_e constant in case of circular polarization. In linear polarization the time scale for restoring is much shorter and quasineutrality is therefore only partially obeyed. For this reason, i.e. the dynamic coupling of transverse and longitudinal modes, the relativistic change of the refractive index η needs further investigation. This is in particular true for the critical density where plasma resonances represent an additional complication and may be responsible for some effects observed in the experiment not yet understood [5].

References

[1] M. Lontano, S.V. Bulanov, and J. Koga, Phys. Plasmas **8**, 5113 (2002).

[2] A.I. Akhiezer and R.V. Polovin, Sov. Phys. JETP **3**, 696 (1956).

[3] L.D. Landau and E.M. Lifshitz, *The Classical Theory of Fields* (Pergamon, Oyford, 1975), 47.

[4] T. Pesch and H.-J. Kull, *Waves with constant phase velocity in relativistic plasmas* (submitted for publication).

[5] U. Teubner *et al.*, Phys. Rev. Lett. **92**, 185001 (2004).

Ion-induced damage in apatite irradiated at ambient & high pressure conditions

J. Liu[1,#], U.A. Glasmacher[2], M. Lang[3], C. Trautmann[3], K.-O. Voss[3], R. Neumann[3], G.A. Wagner[4], R. Miletich[5]

[1]IMP, CAS, Lanzhou, China; [2]Geologisch-Paläontologisches Institut, Universität Heidelberg, Germany; [3]GSI, Darmstadt, Germany; [4] MPI Kernphysik, Heidelberg, Germany; [5]Mineralogisches Institut, Universität Heidelberg, Germany

In geological minerals, tracks of fragments from spontaneous fission of U nuclei accumulate over geological time scales and are widely used for fission-track dating and thermochronology [1, 2]. In our recent studies, we tackled the problem how solids exposed to energetic heavy ions cope with the simultaneous exposure of external pressure. This combination of ion irradiation and pressure is suitable for simulating the conditions fission fragments experience in the interior of the Earth [3].

A single crystal of Durango apatite was pressurized to 10.5 GPa between two ~1.4-mm thick diamonds of a diamond anvil cell (DAC) and irradiated at the SIS with 5×10^{11} cm^{-2} Kr ions of initial energy 106 MeV/u corresponding to 25 MeV/u at the sample site. For comparison, we also exposed non-pressurized apatite samples to U ions of 11.1 MeV/u at the UNILAC.

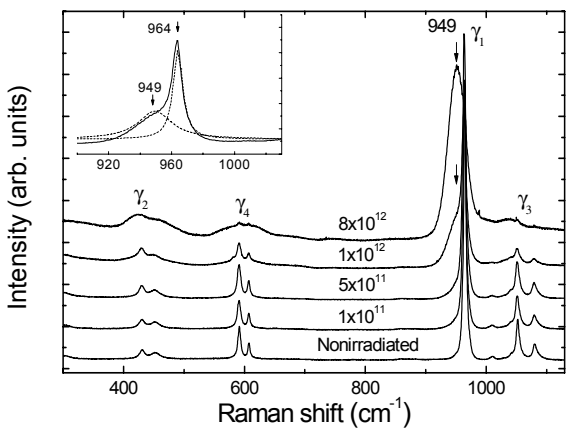

Fig. 1 Raman spectra of apatite before and after the irradiation with 2.64-GeV U ions (*dE/dx* = 34 keV/nm) at various fluences. The inset (top left) shows the splitting of γ_1 mode at fluence 1×10^{12} ions/cm^2.

Fig. 1 shows Raman spectra (HeNe laser, 632.8 nm) before and after the UNILAC irradiation with U ions at ambient conditions. The spectrum of non-irradiated apatite exhibits the intense and narrow $\gamma_1(A_g)$ band (964 cm^{-1}, symmetric stretching vibration of phosphate anions) and several smaller bands: γ_2 (430 and 453 cm^{-1}, symmetric out-of-plane bending), γ_3 (1052 and 1081 cm^{-1}, antisymmetric stretching), and γ_4 (591 and 608 cm^{-1}, antisymmetric bending). With increasing fluence, the relative intensities of γ_2, γ_3, and γ_4 with respect to γ_1 grow. Above 1×10^{12} ions/cm^2, the changes of position and width of the different bands indicate the onset of amorphization. With increasing fluence, the intensity of the 964-cm^{-1} band decreases, and a peak appears at 949 cm^{-1} (inset Fig. 1). This new band is attributed to a highly disordered structure implying distortion of the PO_4^{3-} tetrahedra and gradual disappearance of the original hexagonal crystal symmetry.

In the case of the high-pressure irradiation, Raman spectra were recorded for the irradiated apatite still mounted in the DAC (Fig. 2). With decreasing pressure, all bands shift systematically to smaller wavenumbers and some develop even a splitting. For apatite irradiated under pressure, the Grüneisen parameter, calculated from the slope of the pressure dependence of the Raman modes, is significantly smaller than values found in literature.

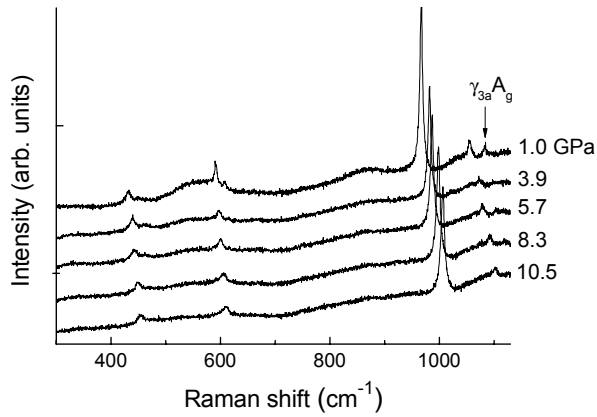

Fig. 2 Raman spectra of irradiated pressurized apatite recorded through one of the diamond anvils during pressure release (irradiation: 25 MeV/u Kr ions, 5×10^{11} cm^{-2}.

After releasing the pressure, the vibrational behavior reflected in the Raman spectra indicates that at the given fluence, apatite does not exhibit any stable phase transition when irradiated with Kr ions (*dE/dx* = 6 keV/nm) at 10.5 GPa. It also shows that ion irradiation causes less severe damage in the sample under elevated pressure than in reference samples at ambient conditions. It seems that the pressure stabilizes the crystal lattice and thus protects it against damage from heavy-ion irradiation.

References

[1] G.A. Wagner, E. Hejl, Chem. Geol. 87 (1991) 1.
[2] C. Hepburn, A.H. Windle, J. Mater. Sci. 15 (1980) 279.
[3] U.A. Glasmacher, M. Lang, H. Keppler, F. Langenhorst, R. Neumann, D. Schardt, C. Trautmann, G.A. Wagner, Phys. Rev. Lett. 96 (2006) 195701.

[#] j.liu@impcas.ac.cn
[#] Max-Planck Society fellowship is acknowledged by J.L

X-Ray Diffraction Study of Ion-Irradiated CeO_2

N. Ishikawa[1], Y. Chimi[1], O. Michikami[2], Y. Ohta[2], M. Lang[3], R. Neumann[3]
[1]JAEA, Tokai, Ibaraki 319-1195, Japan; [2]Iwate Univ., Morioka, Iwate 020-0066, Japan, [3]GSI, Darmstadt, Germany

Introduction

Nuclear fuels in light water reactors (LWR) are subjected to various high-energy particles such as neutrons and fission products (Xe, Kr, etc.). It is known that high-energy fission products create serious damage in the UO_2 crystal structure, leading to swelling and degradation of thermal properties. Cerium dioxide, CeO_2, is one of the ceramics which have the same structure (fluorite structure) as UO_2 and also a similar melting temperature. In order to investigate the damage process of UO_2 fuel ceramics, the simulation material CeO_2 is irradiated with high-energy projectiles, such as 2.7-GeV U, 200-MeV Au, and 230-MeV Xe.

Experimentals

Thin films of CeO_2 were prepared on sapphire substrates by dc sputtering. The film thickness was about 300 nm. The films were irradiated at room temperature with 2.7-GeV U from the UNILAC accelerator at GSI and with 200-MeV Au and 230-MeV Xe from the tandem accelerator at Tokai Research and Development Centre, Japan Atomic Energy Agency (JAEA-Tokai). In order to investigate the degradation of the crystal structure, X-ray diffraction (XRD) patterns were measured before and after the irradiation. The XRD peaks corresponding to (002) and (004) reflections are observed before irradiation. In this study irradiation-induced change of the (002) peak intensity is investigated. The electronic stopping power is calculated by the SRIM-2003 code.

Results and Discussion

By 2.7-GeV U irradiation the intensity of the (002) XRD peak monotonically decreases as a function of ion fluence. It is known that in most ceramic materials a high-energy heavy ion creates a track along its path. The ion-track has typically a diameter of several nanometers. The crystal structure inside the track can be amorphous or has a disordered lattice depending on ion mass, ion energy, and target material. It is expected that, if the interior of the track is sufficiently damaged, the track does not contribute to X-ray diffraction, and the XRD intensity decreases exponentially as a function of fluence. By using a simple Poisson rule the decrease in the XRD intensity can be written as

$$I(\Phi) = I_o \exp(-A\Phi), \quad (1)$$

where $I(\Phi)$ is the intensity of the XRD peak, I_o is the intensity before irradiation, A is the cross-section of a single track, and Φ is the ion fluence. As shown in Fig. 1, equation (1) holds only for 2.7-GeV U irradiation. From the above formula, a track diameter of 15 nm can be derived for 2.7-GeV U irradiation. For 200-MeV Au and 230-MeV Xe irradiations, however, equation (1) is not valid, and the decrease in XRD intensity tends to saturate in the high-fluence region. It is already known that for 210-MeV Xe irradiation [1], ion tracks are formed, but the crystal lattice inside the track is maintained. Based on this finding, the XRD peak behaviour for 200-MeV Au and 230-MeV Xe irradiations can be explained as follows. Even if ion tracks cover the whole sample, they do not completely destroy the crystal structure, and the lattice order is maintained. This leads to saturation of the intensity decrease. The degree of damage in the high-fluence region is higher for 200-MeV Au than for 230-MeV Xe. The electronic stopping powers for 2.7-GeV U, 200-MeV Au, and 230-MeV Xe irradiations are 57.3 keV/nm, 32.0 keV/nm, and 28.6 keV/nm, respectively. The degree of damage increases with increasing electronic stopping power as demonstrated in Fig 1.

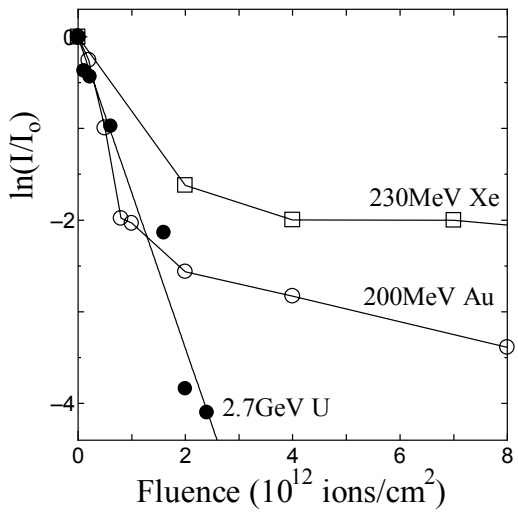

Figure 1: Logarithm of normalized XRD intensity as a function of fluence for the irradiations with 230-MeV Xe, 200-MeV Au, and 2.7-GeV U.

Reference

[1] T. Sonoda, M. Kinoshita, Y. Chimi, N. Ishikawa, M. Sataka, A. Iwase, Nucl. Instr. and Meth. B 250 (2006) 254.

Color center creation in LiF crystals irradiated with 5-MeV Au ions

K. Schwartz[1,#], A. Volkov[2], R.M. Papaléo[3], M. Sorokin[2], A. Lushchik[4], E. Vasil´chenko[4], K.-O. Voss[1], C. Trautmann[1], R. Neumann[1]

[1]GSI Darmstadt, Germany, [2]Kurchatov Institute, Moscow, Russia, [3]Catholic University of Rio Grande do Sul, Porto Alegre, Brazil, [4]Institute of Physics, University of Tartu, Estonia

Single crystals of LiF were irradiated with 5-MeV Au^{2+} ions at the Porto Alegre 3 MV Tandetron implanter applying fluences Φ between 10^{12} and 10^{14} ions/cm^2. The beam current (i) was varied from 1 to 200 (± 0.1) nA equivalent to ion flux φ [ions/cm^{2}s] = $3.1\times10^9 \cdot i$ [nA]. The range R of the ions is ~1 µm, which is much smaller than the thickness of the crystals.

The creation of color centers was investigated by optical absorption spectroscopy, with special focus on beam current (i.e., ion flux) and fluence effects.

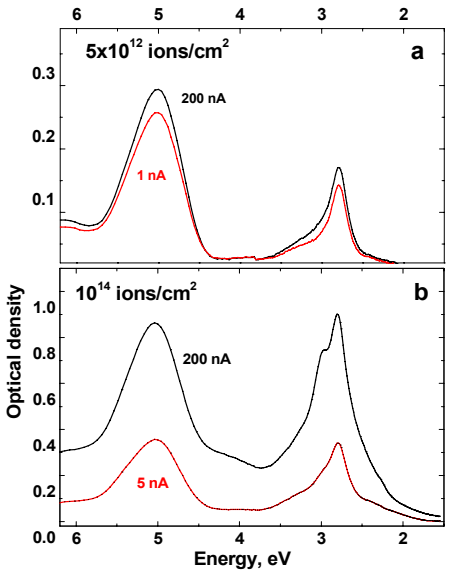

Fig. 1: Absorption spectra of LiF irradiated with 5-MeV Au ions at different fluences and beam currents.

For low fluence irradiations (up to 5×10^{12} ions/cm^2), the spectra are almost (± 10 %) independent of the beam current (Fig. 1a), whereas at higher fluences (10^{14} ions/cm^2) defect creation significantly rises with increasing i (Fig. 1b). Moreover, spectra from high-fluence and high-current irradiations are more structured, indicating the creation of more complex defect aggregates. The concentration of single F centers was determined by the Smakula-Dexter formula from the absorption maximum of the F band at 5.0 eV [1]. The absorption in the range 4.5–1.6 eV is a superposition of various color and aggregate centers (F_n, small colloids), which depend both on fluence and beam current (Fig. 1).

At high fluences, defect creation shows a strong dependence on beam current as illustrated for F centers in Fig. 2. The pronounced nonlinearity is related to track overlapping and irradiation time. At $\Phi = 5\times10^{12}$ ions/cm^2, the mean distance between neighboring tracks is $d_{ion} = (\pi\Phi)^{-1/2} \sim 2.5$ nm, which is larger than the estimated radius of the F-center halo $r_F \sim 1$ nm, whereas at $\Phi = 10^{14}$ ions/cm^2, the value of d_{ion} is ~ 0.6 nm and thus smaller than r_F. Under these conditions neighboring tacks overlap, resulting in enhanced aggregate formation. An additional factor on defect creation is the irradiation time τ, which depends on the beam current: at $i = 1$ nA the accumulation of 10^{14} ions/cm^2 requires about 9 hours, whereas at $i =$ 200 nA only 3 min are needed. Since recombination (annihilation) of electron and hole centers is smaller for shorter irradiation times, the efficiency of F and aggregate center creation increases [2].

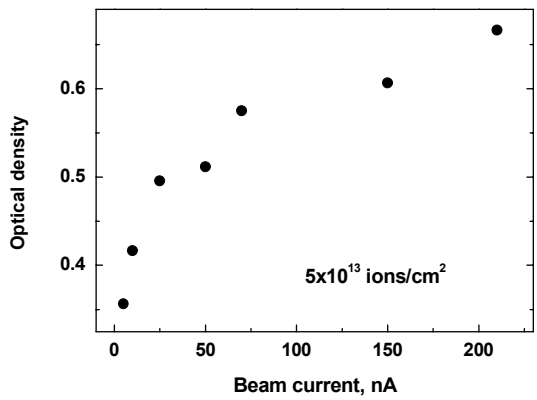

Fig. 2: Optical density of the maximum (5.0 eV) of the F center absorption band versus beam current at fluence 5×10^{13} ions/cm^2.

The high volume concentration of color centers results from the small range of the 5-MeV Au ions. For 10^{14} ions/cm^2, the volume concentration of the F-centers is $N_F \sim 8\times10^{19}$ cm^{-3}, which is much higher than typically observed for irradiations with 1-2 GeV ions [1]. Defect agglomeration in LiF irradiated with 5-MeV Au ions is more efficient [1,2]. This is also indicated by the stronger absorption in the range 5.8–6.3 eV.

It is also well-known that the kinetics of defect cluster formation depends crucially on the generation rate of defects [2,3], contributing to the dependence of the defect concentration on beam current.

References

[1] K. Schwartz, C. Trautmann, A.S. El-Said, R. Neumann, M. Toulemonde, W. Knolle, Phys. Rev. B 70 (2004) 184104.

[2] N. Itoh, A.M. Stoneham, *Materials Modification by Electronic Excitation,* Cambridge, Univ. Press, 2001.

[3] A.E. Volkov, Physica A 323 (2003) 336.

#k.schwartz@gsi.de

Monte-Carlo simulation of electronic excitations in tracks of swift heavy ions in dielectrics*

N. A. Medvedev[1], A. Volkov[2]
[1]GSI, Darmstadt, Germany; [2]Russian Research Centre 'Kurchatov Institute', Moscow, Russia

Excitation and relaxation of the electronic subsystem of solids in nanosize tracks of swift heavy ions (SHI, $E > 1$ MeV/nucl, $M \geq 20m_p$) are well separated by the following temporal stages: (a) at 10^{-17}-10^{-16} s, primary ionization of target atoms occurs in the vicinity of the projectile trajectory resulting in the first generation of fast delta-electrons. (b) Spatial spreading of these electrons and ionization of the next generation of δ-electrons take place in the time period of ~ 10^{-16}-10^{-14} sec. (c) Recombination of electronic vacancies and energy redistribution via radiation occurs on the time scale ≥ 10^{-14} sec [1,2]. Electrons also interact with ionic subsystem of target at all these stages.

The Classical Trajectory Monte-Carlo Simulation method was applied to investigate the initial two stages in silica (SiO_2) irradiated with Ca^{+19} (11.4 MeV/nucl).

This research is aimed at the determination of spatial and temporal density and energy distributions of delocalized electrons as well as of the amount of electronic vacancies in different atomic shells. The work is related to the ongoing research on ion-induced tracks in crystalline solids at GSI.

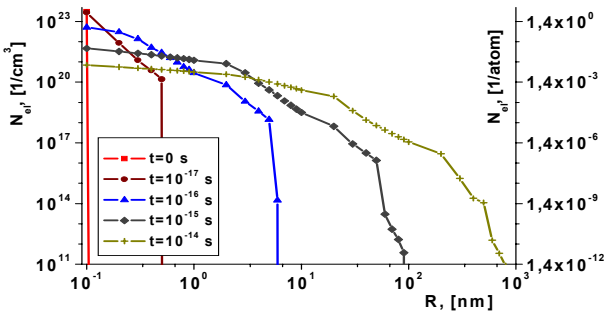

Fig. 1. Distribution of the electron density in a SHI track.

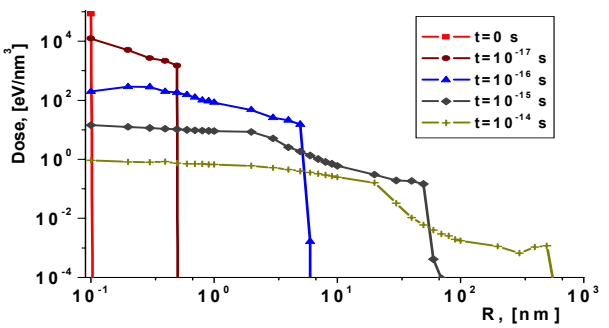

Fig. 2. Distribution of the energy density of delocalized electrons in a SHI track.

Large differences between semi-empirical calculations for δ-electron distributions [3] and the presented results were obtained. In Figs. 1 and 2 the kinetics of spreading of the excitation in the electron subsystem is presented.

Fig. 3 presents the distribution of vacancy density in different atomic shells at the time $t = 10^{-15}$ sec after the ion passage.

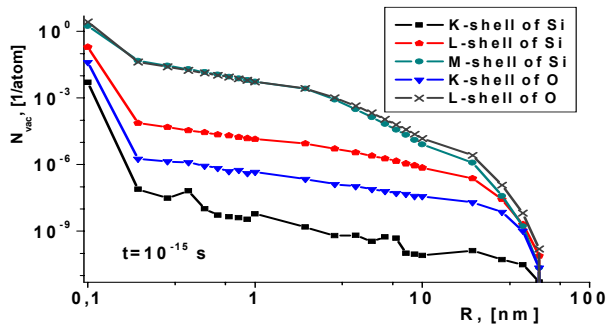

Fig. 3. Distribution of the density of vacancies in different atomic shells at 10^{-15} sec.

At this time ($t = 10^{-15}$ sec) 28.4% of the energy transferred from the projectile is trapped in the electronic vacancies.

Spatial distributions of the kinetic energy density of δ-electrons and energy density of vacancies are presented in Fig. 4.

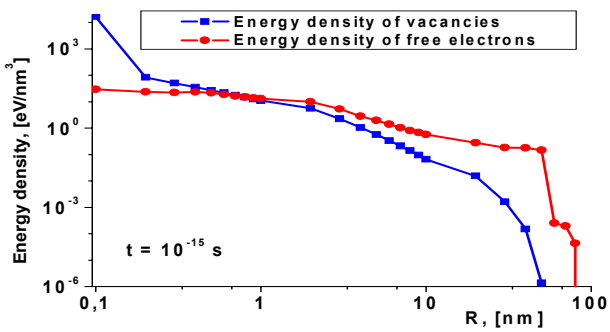

Fig. 4. Distribution of the energy densities of free electrons and vacancies in a SHI track at 10^{-15} sec.

Acknowledgments

The authors gratefully acknowledge financial support from GSI when performing part of this work in the GSI Material Research Department.

References

[1] G. Schiwietz, K. Czerski, M. Roth, F. Staufenbiel, P.L. Grande, Nucl. Instr. and Meth. B 225 (2004) 4
[2] O. N. Rosmej *et al*. Phys. Rev. A 72 (2005) 052901
[3] M.P.R. Waligórski, R.N. Hamm, R. Katz, Nucl. Tracks Radiat. Meas. 11 (1986) 309

Influence of ion-charge state on damage morphology of ion tracks in dark mica

M. Lang[1,#], W. Hasenkamp[2], N. Ishikawa[3], N. Medvedev[4], R. Neumann[1], R. Papaléo[2], C. Trautmann[1], K.-O. Voss[1], T. Yamaki[5]

[1]GSI, Darmstadt, Germany, [2]Pontifícia Univ. Católica do Rio Grande do Sul,Porto Alegre, Brazil; [3]JAEA, Tokai-mura, Japan; [4]Moscow Engineering Physics Institute & Kurchatov Institute, Moscow, Russia; [5]JAEA, Takasaki, Japan

In many dielectrics, swift heavy ions of MeV-GeV energy produce tracks of a few nm in diameter. The track morphology depends on energy loss (*dE/dx*), particularly the formation of a continuous damage trail requires a critical $(dE/dx)_c$. Below this threshold, chemical etching of discontinuous tracks exhibits inhomogeneous pore sizes and the track etching efficiency drops below unity.

In the recent past, we studied the influence of *dE/dx* and of the ion velocity on the track morphology at fixed *dE/dx* [1,2]. Here, we report how the ion charge state affects the track morphology. The experiments were performed with phlogopite, a dark mica mineral for which fission-track etching is frequently applied for dating of geological samples.

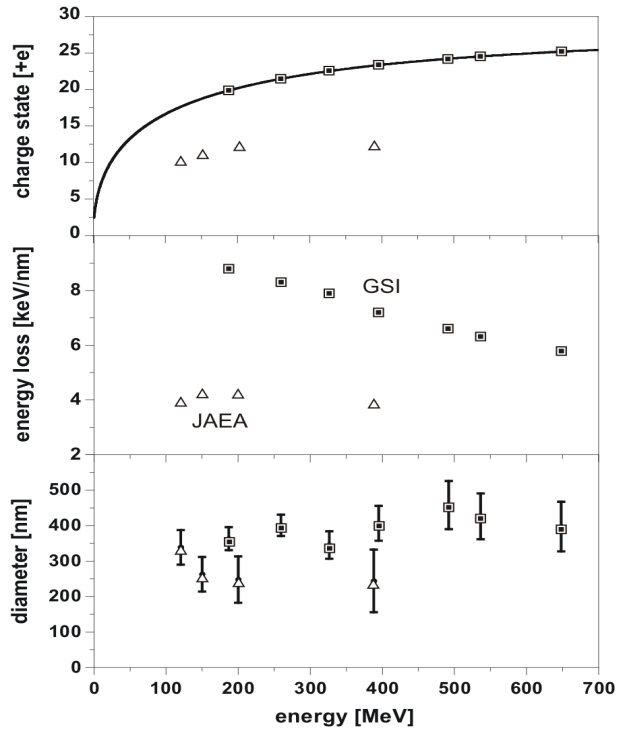

Fig. 1: (top) Ion charge state vs. kinetic energy of different irradiations at GSI and JAEA accelerators with q_{neq} (△) and q_{eq} (▣) ions. The curve represents equilibrium charge as function of energy (Barkas formula) [3]; (center) energy loss vs. energy (SRIM-code). The *dE/dx* of q_{neq} ions is estimated by correcting the corresponding equilibrium SRIM values by a factor $(q_{neq})^2/(q_{eq})^2$; (bottom) etch pit diameter vs. energy from SFM analysis.

The phlogopite samples were irradiated with ^{58}Ni ions at three different accelerators (GSI, JAEA Tokai-mura, and JAEA Takasaki) using energies from 120 to 650 MeV. In this energy regime, the charge of the ions delivered by the accelerator is in general lower than the equilibrium charge state q_{eq} at the corresponding ion velocity. The charge state of the Ni beams from both JAEA accelerators were non-equilibrium (q_{neq}), whereas at GSI, q_{eq} was adjusted by passing the ions through three Al-foils (total thickness ~3 µm) used as fluence control in front of the sample. The charge states of the different experiments are shown in Fig. 1, top.

After chemical etching in 4 % HF (RT, 3 min), the samples were inspected by scanning force microscopy (SFM) [2]. Fig. 2 shows etched tracks from q_{neq} = +15 and q_{eq} ~ +23 ions, respectively from the original surface and from a sample area covered with a 3-µm thick Al foil. The significant difference in etch-pit size and shape illustrates the direct influence of the charge state on the track morphology. Since the projectile charge is closely linked to the energy loss ($dE/dx \sim q_{eq}^2$), the energy loss of q_{neq} ions is generally smaller [3] (Fig. 1, center) and dropped, in the case shown in Fig. 2, below the critical $(dE/dx)_c$ for homogeneous damage creation. The inhomogeneous track etching results in smaller pit diameters as evident for almost all q_{neq} ions (Fig. 1, bottom).

These results demonstrate that the charge of the incoming projectile can have a significant influence on track phenomena studied on the sample surface.

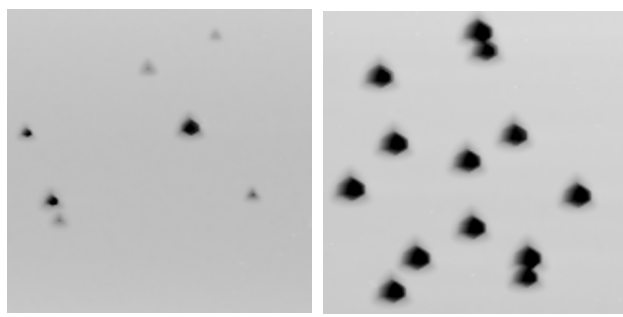

Fig. 2: SFM micrographs (3 µm × 3 µm) of etched tracks in phologopite sample irradiated with ^{58}Ni ions of q_{neq} = +15 (388 MeV) (left) original area and (right) area covered with a 3-µm Al foil in which the ions strip off electrons resulting in a equilibrium charge-state distribution around q_{eq} ~ +23 (373 MeV).

References

[1] M. Lang, U.A. Glasmacher, B. Moine, R. Neumann, G.A. Wagner, Nucl. Instr. Meth. B 218 (2004) 466.

[2] M. Lang et al., GSI Scientific Report 2005 (2006) p. 343.

[3] M. Toulemonde, Nucl. Instr. Meth. B 250 (2006) 263.

#m.lang@gsi.de

Evolution of the structure and morphology of latent tracks as a function of electronic energy deposition

A. Dunlop[1], G. Jaskierowicz[1], and C. Trautmann[2]
[1]Laboratoire des Solides Irradiés, CEA/Ecole Polytechnique, Palaiseau, France; [2]GSI, Darmstadt, Germany.

The creation of latent tracks in insulating materials exposed to energetic heavy ions has been studied in a large number of targets. In particular detailed results were obtained in yttrium iron garnet (YIG) $Y_3Fe_5O_{12}$ irradiated in a broad range of electronic energy deposition $(dE/dx)_e$ both with monoatomic and cluster ions [1-4]. By means of Transmission Electron Microscopy (TEM) and channeling Rutherford backscattering, it was demonstrated that with increasing projectile energy (i) discontinuous latent tracks appear at a threshold of $(dE/dx)_t \approx 4$ keV/nm, (ii) the track diameter increases until $(dE/dx)_e$ reaches the Bragg peak (the maximum effective diameter is estimated to be 14 nm [1]), and (iii) above the Bragg maximum, the track diameter decreases with increasing projectile velocity. This so-called "velocity effect" has been related to the evolution of the density of deposited energy [1,4]: the higher the projectile velocity, the larger the lateral spread of deposited energy resulting in a reduction of the energy density.

The aim of this work is to study the morphology and structure of ion tracks in the very high velocity regime unexplored up to now. For this purpose, small crystalline grains of YIG powder were deposited on TEM copper grids covered by a thin amorphous carbon film. The grid samples were exposed at 300 K and at normal incidence to U ions at the UNILAC and SIS applying fluences between 2 and 5×10^{10} ions/cm^2, sufficiently low to avoid spatial track overlap. The beam energy was varied between 11.1 and 417 MeV/u corresponding to $(dE/dx)_e$ ranging from 49 to 9 keV/nm, respectively.

High-resolution TEM investigations performed just after irradiation confirm that also in the high-velocity regime the track diameters decrease with increasing projectile velocity. Moreover, the track structure gradually evolves from a circular, well-defined amorphous zone into a more and more diffuse track of defective crystalline structure, and finally at very high beam velocities, the tracks show a very faint contrast in the TEM. They can only be imaged in high-resolution conditions in very thin sample regions and consist of almost perfect crystalline structures which are in perfect epitaxy with the surrounding material.

Figure 1 compares the high-resolution TEM micrographs of two tracks created at different ion velocities: at 11.1 MeV/u ($(dE/dx)_e$= 49 keV/nm), the track is continuous, amorphous and has a diameter of about 13 nm, whereas at 291 MeV/u ($(dE/dx)_e$=11 keV/nm), the track is quasi-continuous showing a non constant diameter. The damaged zone exhibits a very weak contrast and is crystalline with some point defects. The track diameter is reduced to about 3 nm.

The large differences in the morphology, size and structure of tracks produced at different beam velocities is a clear illustration that structural modifications induced by swift heavy ions become much weaker if the deposited energy is spread into a large volume thus decreasing the deposited energy density.

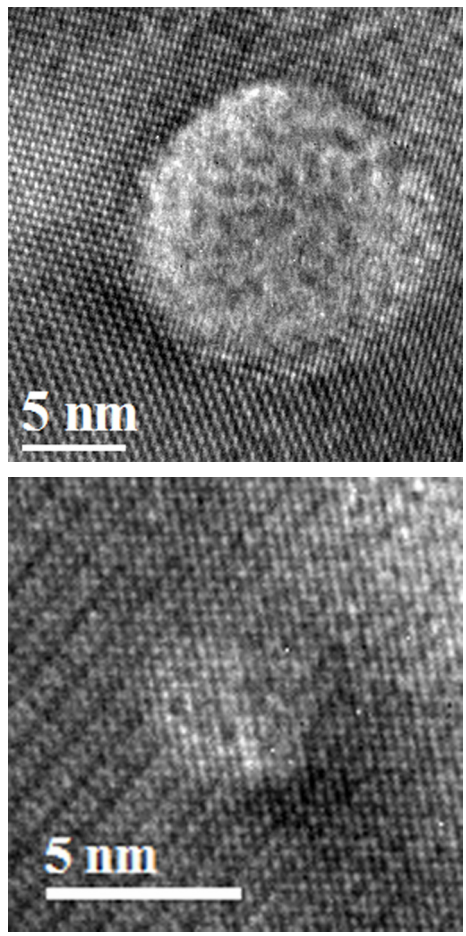

Figure 1: Bright-field high-resolution TEM micrographs of single tracks induced in YIG by U ions of (top) 11.1 MeV/u and (bottom) 291 MeV/u.

References

[1] A. Meftah, F. Brisard, J.M. Costantini, M. Hage-Hali, J.P. Stoquert, M. Studer, M. Toulemonde, Phys. Rev. B 48 (1993) 920.
[2] M. Toulemonde, F. Studer, Phil. Mag. A 58 (1988) 799.
[3] Ch. Houpert, F. Studer, D. Groult and M. Toulemonde, Nucl. Instr. Meth. B 39 (1989) 720.
[4] J. Jensen, A. Dunlop, S. Della-Negra, M. Toulemonde, Nucl. Instr. Meth. B 146 (1998) 412.

Ion-induced damage and swelling in yttria-stabilized zirconia

J.-M. Costantini[1#], C. Trautmann[2], L. Thomé[3], J. Jagielski[4], F. Beuneu[5]
[1]CEA/DEN, Saclay, France; [2]GSI, Darmstadt, Germany; [3]CSNSM, Orsay, France; [4]IEMT, Warsaw, Poland; [5]LSI, Palaiseau, France.

Cubic zirconia (ZrO_2) is considered to be a suitable refractory host (T_m~3000 K) for actinide confinement used for transmutation or high-temperature reactor projects. Literature data on radiation damage of this material are rather limited concerning studies with heavy ions [1]. Moreover, point defects were investigated only in the case of pure electronic excitations with photons [2].

This study is focusing on defect creation in zirconia exposed to energetic charged particles, in particular on the characterization of defects and the analysis of the respective roles of elastic collisions and electronic excitations in the damage processes. We also investigated beam-induced volume changes (swelling), which is an important issue for nuclear applications of this material.

Zirconia single crystals stabilized by yttrium in the cubic fluorite structure (ZrO_2: Y, with 9.5 mol% Y_2O_3) were used as received (AR) or reduced by vacuum-annealing (R). Samples with <100> and <110> orientation were exposed to electrons (1-2.5-MeV) as well as to a large variety of different energetic ions (73-MeV ^{52}Cr and 2.6-GeV ^{238}U ions at the UNILAC (GSI, Darmstadt); 145-MeV ^{13}C at the GANIL (Caen); and 180-MeV ^{32}S, 200-MeV ^{58}Ni, 230-MeV ^{79}Br, 100-MeV ^{127}I, 200-MeV ^{127}I, and 200-MeV ^{197}Au at the VIVITRON (Strasbourg).

The irradiated samples were characterized by electron paramagnetic resonance (EPR) spectroscopy, which is highly sensitive for color centers in dielectrics. The EPR spectra of all samples (irrespective of the mode of irradiation) exhibited the same main resonance lines assigned to F^+ type centers and to the so-called T (trigonal) centers (i.e. Zr^{3+} centers) [2,3]. By electrons of variable energy, the threshold energy for F^+ type center production was determined to be ~1.0 MeV, whereas electrons between 1.0 and 2.5 MeV did not induce any clear change of the production rate for T centers.

In the case of ion irradiation, the production rate of F^+ type centers as a function of fluence does not scale with the inelastic stopping power. The data rather follow the number of displacements per atom (dpa) (for dpa calculations we used an oxygen displacement energy of ~120 eV [4]). This is a strong indication for the dominant role of elastic collisions in the F^+ type center production process. However, we note that the data from the irradiation with U ions do not follow this trend.

Rutherford backscattering channeling spectrometry results show that the lattice damage increases significantly above an electronic stopping power of ~20 keV/nm (below this value, the lattice damage is less than 0.05%). Above the threshold, the damage fraction becomes larger with increases fluence but never surpasses 40%. Obviously, none of our ions induce amorphization.

This finding agrees with the observation that the out-of-plane swelling (as measured by surface profilometry) is rather low (< 0.2%) regardless of crystal orientation and thermal treatment of the samples (Fig. 1) [5]. Swelling is also found to be proportional to the F^+ type center concentration averaged over the projected range of the ions [5] and can be scaled by the estimated number of dpa. Yet, once again, the U ion data do not fit but exhibit a large slope when plotted as a function of dpa [5].

For U ions swelling yields ~0.15% at a rather low fluence of 10^{12} ions/cm^2 (corresponding low dpa). At a higher fluence of 10^{13} ions/cm^2, the <100> samples spontaneously cleaved along the <110> direction. We assume that stress phenomena become more and more dominant due to pronounced production of defect clusters. Further experiments with particularly heavy projectiles will concentrate on irradiation-induced lattice disorder.

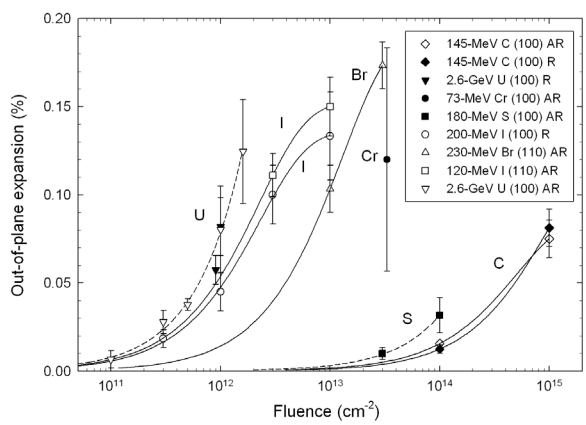

Figure 1: Out-of-plane swelling versus ion fluence for as-received (AR) and reduced vacuum-annealed (R) crystals.

References

[1] K.E. Sickafus, Hj. Matzke, Th. Hartmann, K. Yasuda, J.A. Valdez, P. Chodak III, M. Nastasi, R.A. Verall, J. Nucl. Mater. 274 (1999) 66.

[2] V.M. Orera, R.I. Merino, Y. Chen, R. Cases, P.J. Alonso, Phys. Rev. B 42 (1990) 9782.

[3] J.M. Costantini, F. Beuneu, D. Gourier, C. Trautmann, G. Calas, M. Toulemonde, J. Phys.: Condens. Matter 16 (2004) 3657.

[4] J.M. Costantini, F. Beuneu, Phys. Stat. Sol. C 2007, in press.

[5] J.-M. Costantini, C. Trautmann, L. Thomé, J. Jagielski, F. Beuneu, J. Appl. Phys. 2007, in press.

jean-marc.costantini@cea.fr

Measurements of fossil confined fission tracks in geological samples with low track densities*

Eva Enkelmann[1], Myo Min[1], Raymond Jonckheere[1,#], Christina Trautmann[2], Lothar Ratschbacher[1]
[1]Institut für Geologie, Technische Universität Bergakademie Freiberg, Germany; [2]GSI, Darmstadt, Germany

Several natural minerals contain trace amounts of uranium. Spontaneous nuclear fission of ^{238}U causes the formation of particle (fission) tracks along the trajectories of the ejected nuclear fragments. The lattice damage along a fission track is repaired at elevated temperatures, leading to a gradual reduction of its etchable length that depends foremost on the highest temperature that the track has experienced. Thus fission tracks can be thought of as maximum-reading thermometers that are generated throughout geological time.

Apatite occurs in low concentrations in most rocks and is the mineral of choice. The principal limitation of apatite T(t)-modelling is that the number of accessible tracks is low because they are situated within the interior of the grains and only etched via cracks or other tracks intersecting the mineral surface. The present experiments examine the effect of man-made ion irradiations under tilted beam incidence, producing oblique tracks that serve as etchant conduits for revealing the confined fission tracks inside the grains. The studied samples are 80-250 µm sized apatite grains from young rocks from central Myanmar, with fission-track densities between 3×10^4 and 3×10^5 cm^{-2}, corresponding to much less than 10 confined tracks for a typical sample. Polished epoxy mounts of several hundred unoriented apatite grains were irradiated at 15° from normal incidence at the UNILAC with Pb or U ions of ~800 MeV energy (range ~30 µm) and ~2×10^6 cm^{-2} fluence. Track etching was carried out with 4M HNO_3 at 25 °C in three sequential steps: t_e (etching time) = 15, 25, and 35s.

Fig. 1 shows the number of measurable confined tracks N_c as a function of t_e. In most samples, the increase of N_c is greater than the increase of t_e. On average, N_c increases ~3.5 times between t_e = 15 and 25 s and ~2 times between t_e = 25 and 35 s. The overall gain of N_c due to sequential etching between t_e = 15 and 35 s thus comes to a factor of ~7, which is still much lower than the gain from the ion irradiation itself, estimated at ~30 times. The latter first-order estimate is the average ratio of the ion track and the fission track densities. The maximum gain is achieved for the longest etching time (t_e = 35 s): N_c is on average ~200 times greater than the estimated number of confined tracks in the unirradiated samples. Increases by a factor of up to >500 were observed for some samples, but there are indications of saturation when the confined tracks start to overlap.

The variation of N_c between different samples in Fig. 1 probably results from the fact that the apatite grains in the these samples have different sizes and shapes. The presence of spurious cracks and inclusions that obscure the track end-points can also contribute to variation between the samples. For maximum gain the irradiation conditions should be tailored to the sample characteristics. Although 100 to 200 tracks are considered to be sufficient for T(t)-modelling, higher numbers could become important when attempting to model the thermal histories of individual sediment grains.

There is no indication that the ion-beam parameters influence the etchable lengths of the confined tracks. The beam orientation does, however, affect the angular distribution of confined tracks in oriented crystals [1], but this is not relevant for mounts of unoriented apatite grains. Sequential etching has no apparent effect on their angular distribution. Its effects on the length of individual tracks, mean confined track length and length distribution are not clear. Overall, the results document an isotropic increase of the mean confined track length between t_e = 15 and 25 s and an according quasi-uniform shift of the confined track length distribution towards longer lengths but no significant further increase or shift between t_e = 25 and 35 s [2].

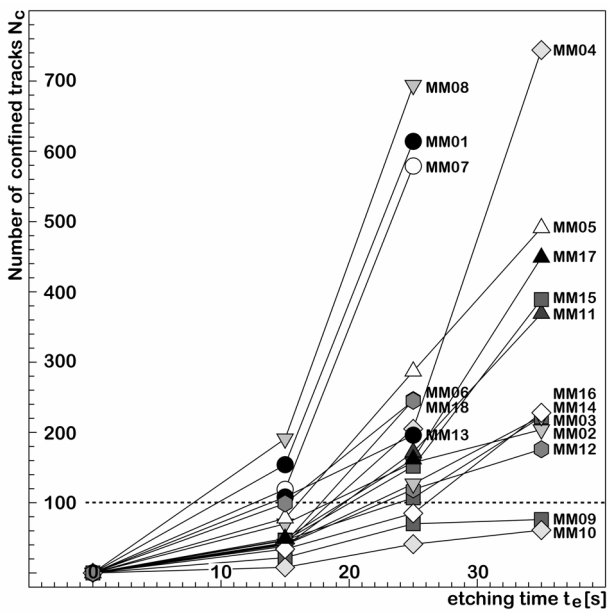

Figure 1: Number of horizontal confined tracks in 18 ion-irradiated apatite grain mounts as a function of etching time.

References

[1] R. Jonckheere, E. Enkelmann, M. Min, C. Trautmann, L. Ratschbacher, submitted. Chem. Geol.
[2] M. Min, E. Enkelmann, R. Jonckheere, C. Trautmann, L. Ratschbacher, submitted. Nucl. Instr. Meth. B.

* Work supported by DAAD and DFG grants Ra 442/20 & 442/26.
# Raymond.Jonckheere@geo.tu-freiberg.de

Laser spectroscopy and ion beam-induced luminescence of Gd^{3+} in $Gd_3Ga_5O_{12}$

T. Jenek, K.-O. Voss, R. Neumann, K. Schwartz
GSI, Darmstadt, Germany

Trivalent lanthanide ions in solids show sharp optical zero-phonon transitions within the 4f-electron subshell, since these electrons are strongly shielded by the Xe-like electronic shell [1]. Still, residual electric fields of the ligands at the rare-earth sites commonly cause Stark splittings of the otherwise degenerate fine-structure levels. Additional influences that modify the local electric fields (e.g. elevated pressure, temperature change, and lattice defects), alter these splittings accordingly. We intend to use rare-earth ions as a potential spectroscopic probe for ion beam-induced changes in solids.

Here, we report some spectroscopic results of gadolinium gallium garnet $Gd_3Ga_5O_{12}$ (GGG) that stoichiometrically contains trivalent Gd ions.

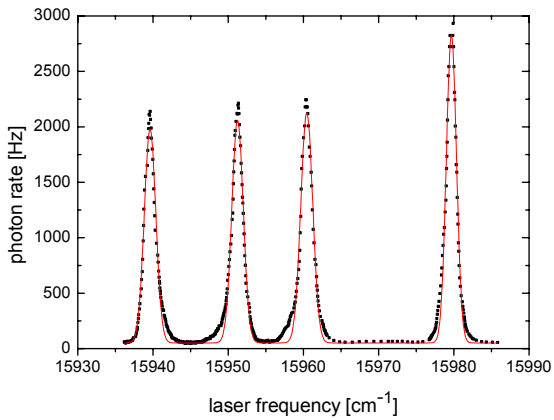

Figure 1: Two-photon excitation spectrum of the Gd^{3+} $^6P_{7/2}$ multiplet in $Gd_3Ga_5O_{12}$.

Figure 1 shows an excitation spectrum of the $^6P_{7/2}$ multiplet (being the lowest excited 4f level) of Gd^{3+} in GGG at 5 K, generated by two-photon transitions from the $^8S_{7/2}$ ground state. The lines are inhomogeneously broadened by random crystal strain to halfwidths of about 3.6 cm^{-1}. The spectrum was acquired with an intense sulforhodamine cw dye laser operated in the visible range. For this purpose, the reemitted UV fluorescence of $^6P_{7/2}$ - $^8S_{7/2}$ one-photon deexcitation (ca. 32000 cm^{-1} or 313 nm) was recorded with a cooled PMT. This one-photon transition starts from the lowest $^6P_{7/2}$ sublevel populated via radiationless relaxation. Details of the experimental setup are given in [2, 3].

When exciting a $^6P_{7/2}$ sublevel, the fluorescence intensity I vs. sample temperature T (fig. 2) shows a maximum I_0 at around 20 K, followed by a strong exponential decrease towards higher temperatures. Assuming radiationless depletion of the excited level via a thermally activated process according to a Boltzmann distribution, as described by

$$I(T) = \frac{I_0}{1+\alpha \cdot \exp\left(-\frac{Q}{kT}\right)}$$

leads to an activation energy Q = 274 (± 2) cm^{-1}, which may be provided by a single optical phonon. The intensity decrease below 15 K is not yet fully understood.

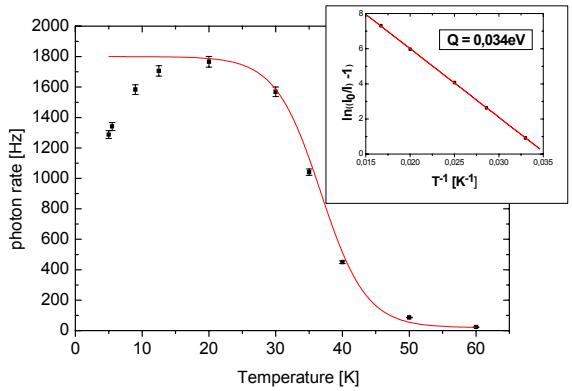

Figure 2: Thermally activated quenching of the highest $^6P_{7/2}$ sublevel with activation energy Q.

The fluorescence spectrum of GGG registered during room temperature irradiation with 100 GeV ^{238}U from the SIS synchrotron of GSI exhibits strong lines around 590 and 720 nm originating from transitions between excited states of Gd^{3+} (fig. 3). In agreement with the above findings, no $^6P_{7/2}$ - $^8S_{7/2}$ transition can be observed.

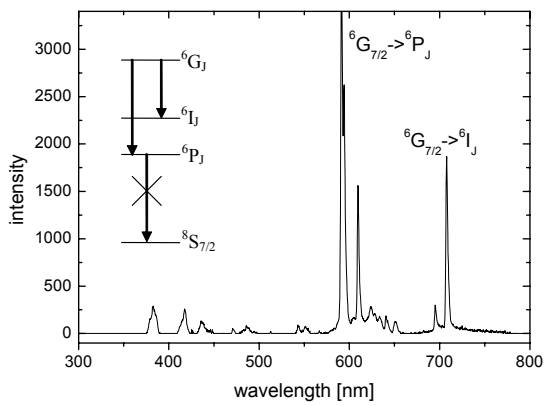

Figure 3: Fluorescence spectrum of GGG occurring under irradiation with 400 MeV/u uranium ions.

References

[1] G. Liu and B. Jacquier (Eds.), *Spectroscopic Properties of Rare Earths in Optical Materials*, Tsinghua University Press (2005).

[2] K.-O. Voss and R. Neumann, *Laser Spectroscopy of the $^6P_{7/2}$ Multiplet of Gd^{3+} in a LaF_3 Host Crystal*, GSI Scientific Report 2005 (August 2006), p. 346.

[3] K.-O. Voss, *Laser spectroscopy of Gd^{3+} ions doped into LaF_3 single crystals as probe of material parameters*, Doctoral dissertation, Heidelberg University (2006).

Material modifications induced by swift heavy ions in NbTi

A. Newirkowez[1], H. Fuess[1], R. Neumann[2], C. Trautmann[2], K.-O. Voss[2]
[1]University of Technology, Darmstadt, Germany; [2]GSI, Darmstadt, Germany

The Facility for Antiproton and Ion Research (FAIR) to be built at GSI will be equipped with superconducting magnets. Due to the high beam intensities and related beam losses, radiation damage of the Cu/NbTi superconducting wires used in the magnet coils has to be considered [1]. Radiation-induced degradation of the superconducting properties of NbTi alloy was studied in the 1970s and '80s. Using projectiles such as protons, neutrons, deuterons, and O ions, was shown to result in increased electrical resistivity and decreased critical current, superconducting transition temperature, and upper critical magnetic field [2]. These irradiations with light and/or low-energy ion beams involve small electronic energy losses.

Here we are interested in radiation effects in particular in structural changes produced with swift heavy ions (2.6-GeV U) of much higher electronic energy deposition.

A superconducting wire has typically a diameter of ~1 mm and consists of several thousand thin NbTi-filaments arranged in bundles embedded in a copper matrix for thermal stabilization (Fig. 1). The filaments are a few µm thick and are composed of β-NbTi (bcc) and α-Ti precipitate (hcp) which improve the critical current by flux-pinning. During the cold-drawing process of the filaments, the β-NbTi matrix develops a <110> crystallographic texture.

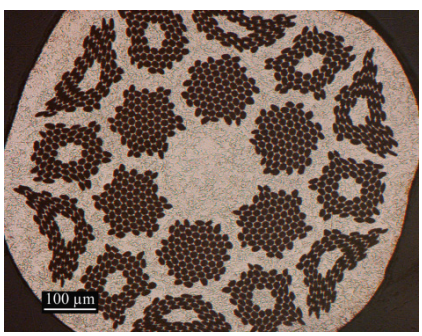

Figure 1: Optical micrograph of cross-section of multi-filamentary wire (dark: NbTi filaments, light: Cu matrix).

The irradiation of NbTi filaments was performed at the UNILAC applying fluences between 3×10^{11} and 5×10^{12} ions/cm^2 at a flux of 1 - 2×10^8 ions/cm^2·s. Before irradiation, the copper matrix was dissolved in aq. $FeCl_3$. The filaments were clamped on an Al holder and exposed to a beam of 2.6-GeV U ions at room temperature. The electronic energy loss $(dE/dx)_e$ for U in NbTi is 53 keV/nm.

Radiation-induced effects were examined using transmission electron microscopy (TEM) (Philips CM20, 200 keV), x-ray powder diffraction ($\lambda_{Mo-K\alpha1}$ = 0.70926 Å) in flat-sample transmission geometry and with four-circle diffractometry ($\lambda_{Co-K\alpha}$ = 1.78897 Å).

Figure 2 shows a selected region of the diffraction pattern of filaments irradiated with different fluences. The position of the dominant reflection of β-NbTi remains unchanged, i.e., there is no obvious change of the lattice parameters. The weak reflection of the equilibrium hcp α-Ti phase decreases already at a low fluence of 3×10^{11} ions/cm^2. By TEM, we find evidence for the hexagonal ω-Ti phase probably resulting from a transition of α- into ω-Ti [3]. Neither track formation nor any other phase transition or amorphization of the β-NbTi phase was detected.

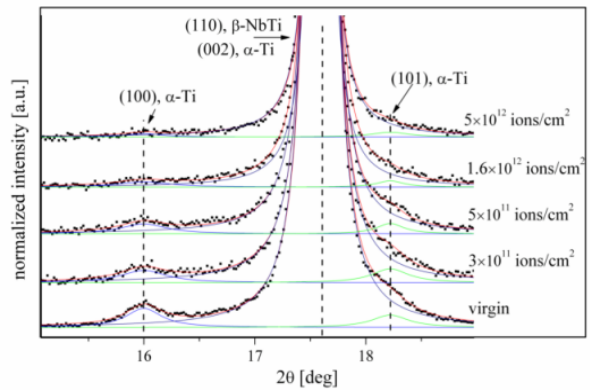

Figure 2: X-ray diffraction pattern of filaments as function of applied fluence.

Irradiated filaments showed changes of the β-NbTi texture, but quantitative analysis is problematic due to the small diameter of the filaments. We therefore measured larger foil samples with a (100)[$\bar{1}$10] texture before and after irradiation at a four-circle diffractometer. Comparing their pole figures gives evidence of irradiation-induced degradation and rotation of the azimuthal distribution of the (100) planes (Fig. 3).

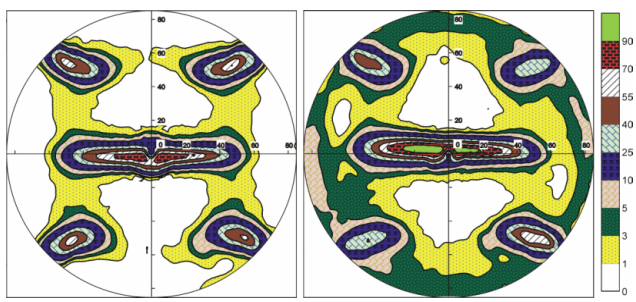

Figure 3: (100) pole figures of NbTi-foil (left: virgin, right: irradiated with 10^{12} cm^{-2} U ions).

References

[1] L. Latysheva, N. Sobolevskiy, G. Moritz, E. Mustafin, G. Walter, GSI Scientific Report 2003 (May 2004) p. 252.
[2] S.T. Sekula, J. Nucl. Mat. 72 (1978) 91.
[3] H. Dammak, A. Dunlop, D. Lesueur, Nucl. Instr. Meth. B 107 (1996) 204.

Swift heavy ion irradiation for recovery from implantation defects in GaN

A.-K. Nix[1,#], H. Höfsäss[1], S. Müller[1], C. Ronning[1], A. Kamarou[2], E. Wendler[2], W. Wesch[2], and C. Trautmann[3]
[1]Universität Göttingen, Germany; [2]Universität Jena, Germany; [3]GSI, Darmstadt, Germany

Photoluminescence of Gallium nitride can be tuned by doping with Mg-ions, e.g., by low-energy implantation. Unfortunately, the irradiation process produces lattice defects which can quench photoluminescence. In principle, thermal annealing could recover the crystal lattice, but GaN is not resistant to high temperatures and, in addition, surface melting and dopant diffusion cause problems. In this project, we are applying swift heavy ions as an alternative method to anneal implantation defects. Defect recovery with energetic ions was already investigated by RBS and TEM elsewhere [1]. Here, we are focusing on optical activation of Mg-ions.

Commercial 3-µm thick GaN-samples (provided by TDI inc., USA) on sapphire as substrate were implanted with 100-keV Mg ions or 450-keV In-ions (for comparison) with fluences of 3×10^{13} and 10^{14} ions/cm^2. The implantation depth for both ions was about 100 nm. The implanted samples were subsequently irradiated with 570-MeV Cr-ions at the UNILAC applying 5×10^{11} and 5×10^{12} ions/cm^2. The range of the energetic Cr ions is large enough (62 µm) to pass through the GaN film. The electronic energy loss in the GaN film is 7 keV/nm which is much lower than the energy loss of 200-MeV Au projectiles (34 keV/nm) for which visible track formation has been observed [2].

The implanted samples were investigated by low-temperature (12 K) photoluminescence spectroscopy using a HeCd-laser (325 nm). Spectra of Mg- and In-implanted samples before and after the irradiation with 570-MeV Cr ions are shown in Fig. 1 and 2, respectively.

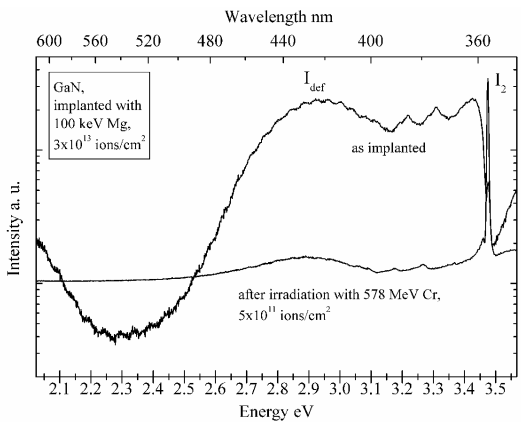

Figure 1: Luminescence spectra of Mg-implanted GaN before and after the irradiation with 570-MeV Cr ions of fluence 5×10^{11} cm^{-2}.

The comparison of the photoluminescence spectra with well-known spectra of GaN and GaN:Mg [3] gives evidence, that the near band-edge luminescence located at 3.475 eV, commonly called I_2, is reduced after implantation, especially after implantation with 10^{14} ions/cm^2. This luminescence is not visible after implantation with In, (Fig. 2, lower curve). To describe the crystal quality, the ratio of the near band-edge luminescence I_2 and the maximum value of the defect luminescence I_{def}, the broad band between 2.7 and 3.1 eV, was examined. After the MeV-ion irradiation, this ratio is increased from 0.24 to 21.26 for Mg-doping giving evidence for recovery of the damaged lattice. The recovery effect is even more visible in Fig. 2, where the near band-edge luminescence reappears and simultaneously the defect luminescence is reduced after the Cr-ion irradiation. The expected emission at 3.25 eV and its related LO-phonon replicas [3] are not visible, thus the Mg-ions were not optically activated after irradiation. The peaks at 3.18 eV and 3.26 eV probably result from specific defects produced by energetic Cr ions, because they also appear after irradiation of undoped GaN. Finally we should mention that the luminescence is hardly visible after the Cr-irradiation with 5×10^{12} ions/cm^2.

Our experiments demonstrate the possibility of lattice recovery with swift heavy ions. In future irradiations, we will vary the electronic energy loss to optimize the recovery process and achieve optical activation of dopants.

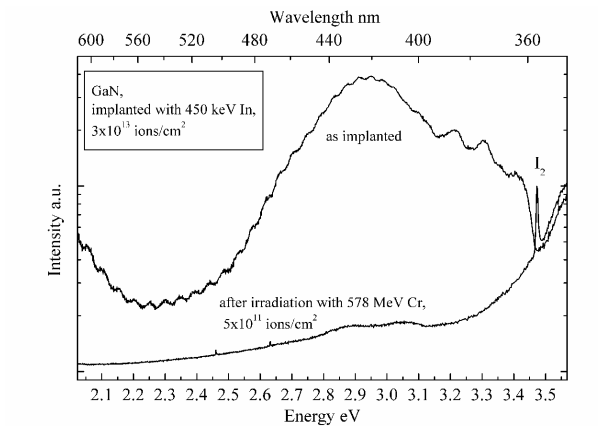

Figure 2: Luminescence spectra of In-implanted GaN before and after the irradiation with 570-MeV Cr ions of fluence 5×10^{11} cm^{-2}

References

[1] W. Wesch, A. Kamarou, E. Wendler, K. Kärtner, P.I. Gaiduk and S. Klaumünzer, Nuc. Inst. Meth. B 206 (2003) 1018.
[2] S. O. Kucheyev, H. Timmers, J. Zou, J.S. Williams, C. Jagadish and G. Li, J. Appl. Phys. 95 (2004) 5360.
[3] C. Ronning, E.P. Carlson and R.F. Davis, Physics Reports 351 (2001) 349.

#anix@uni-goettingen.de

Beam-induced outgassing of Kapton foils at low irradiation temperatures

D. Severin[1, #], E. Balanzat[2], W. Ensinger[1], R. Neumann[3], C. Trautmann[3]
[1]University of Technology Darmstadt, Germany; [2] CIRIL, Caen, France; [2]GSI, Darmstadt, Germany;.

For lifetime estimations of the new superconducting FAIR magnets, radiation degradation especially of insulating components has to be considered. This is in particular crucial because the exposure to strong radiation will occur at a low working temperature of 4.5 K.

In this study we investigated the problem of ion-beam induced outgassing and accumulation of degradation fragments in polyimide (Kapton) foils [1]. At room temperature, volatile degradation fragments are in general readily released from the polymer. However, during low-temperature irradiations, they can accumulate inside the matrix as evidenced for CO_2 molecules by means of infrared spectroscopy [2]. Larger gas concentrations and sudden release during warming up cycles of the magnets may lead to additional material destabilization.

The irradiation experiments with 50 µm thick Kapton foils were performed at 13 K in the cryostat available at the SME beamline of the GANIL. The samples were exposed to different fluences of ^{208}Pb ions of 4.3 MeV/u. Outgassing species were recorded by online residual gas analysis with a mass spectrometer (Fig. 1). All spectra were corrected by background spectra from the bombardment of the empty copper sample holder. The relative intensities of the different species do not change significantly during irradiation. In the regime of light masses ($m/z < 35$), the most prominent contributions result from hydrogen H_2 ($m/z = 2$) and a mixture of CO and N_2 ($m/z = 28$). Other smaller degradation products are different hydrocarbons C_2H_x ($m/z = 24$-30) and O_2 ($m/z = 32$). In the mass regime ($36 < m/z < 80$) heavier molecules like hydrocarbons from $C_3H_xO_y$ up to C_6H_x appear, but an unambiguous identification is not possible. It is also difficult to distinguish between small fragments produced by the ion beam and species resulting from fragmentation by the ionizing process in the mass spectrometer. Above $m/z > 81$, we observe a small peak at $m/z = 119$. This mass can be assigned to phenylisocyanate (C_7H_5NO), for which we also see a weak signal from the CO-subtracted molecule at $m/z = 91$. The detection of this fragment confirms the proposed degradation mechanism based on scission of the polyimide molecules [3].

The large outgassing yield at low irradiation temperature gives us a clear indication that small fragments are not completely frozen in, but can at least partially outgas from the polymer matrix. Figure 2 compares the mass spectra recorded at room temperature and at 13 K under similar irradiation conditions. At low temperature, the gas release is in general suppressed, predominantly for smaller species such as C_2H_x hydrocarbons.

In order to quantify the amount of gas release, we started to determine the mass loss by weighing Kapton samples before and after irradiation. First estimations from room-temperature irradiation series with U and Xe ions (11.1 MeV/u) yield a value of 0.6 % mass loss per MGy.

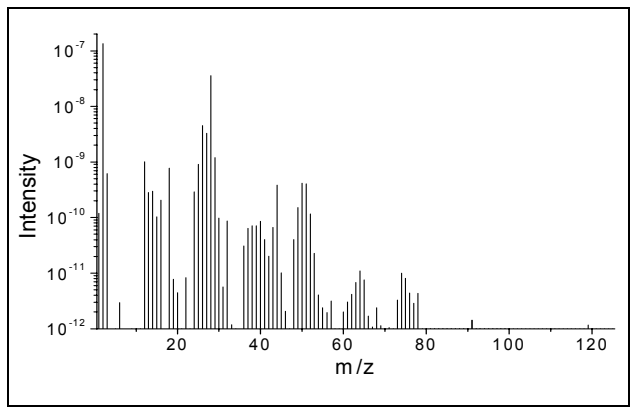

Fig. 1. Mass spectrum (log scale) of outgassing degradation fragments recorded during the irradiation of Kapton with 4.3 MeV/u Pb ions at 13 K.

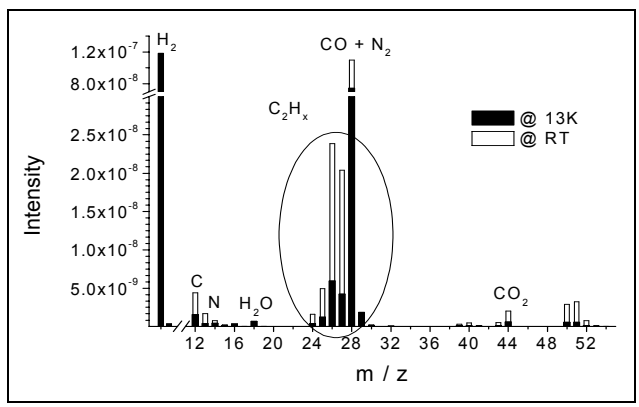

Fig. 2. Mass spectra (linear scale) recorded during irradiation at 13 K and at room temperature.

Future studies will focus on degradation effects in Kapton when exposed to high-energy and high-intensity beams of protons and neutrons with special focus on electrical and mechanical property changes. We also started to investigate the radiation stability of fibre reinforced epoxy compounds planned as structural matrix in the coils of the FAIR magnets.

References

[1] D. Severin, W. Ensinger, R. Neumann, C. Trautmann, G. Walter, I. Alig, S. Dudkin, Nucl. Instr. Meth. B236 (2005) 456.
[2] D. Severin, W. Ensinger, R. Neumann, C. Trautmann, G. Walter, E. Balanzat, GSI Scientific Report 2005 (Aug. 2006) p. 347.
[3] T. Steckenreiter, E. Balanzat, H. Fuess, C. Trautmann, Nucl. Instr. Meth. B 151 (1999) 161.

[#]severin@chemie.uni-marburg.de

Novel two-step etching process for ion tracks in polyimide

D. Dobrev, C. Trautmann, R. Neumann
GSI, Darmstadt, Germany

Polyimide is of great technical importance because of its excellent material properties (including chemical inertness and radiation resistance) which are maintained even at low and at high temperatures. When thin polyimide foils are irradiated with energetic heavy ions, long nanometric tracks are formed. Under suitable conditions, the damaged material along these tracks is dissolved and developed into micro- or nano-sized pores of high aspect ratio. In early studies aq. $KMnO_4$ and H_2O_2 were suggested as etchant [1,2]. Later, better results were obtained with NaOCl as oxidizing agent [3-5], but the situation was still not satisfying because this hypochlorite is unstable and decomposes when exposed to light and/or temperature. An additional difficulty is linked to the pH of the solution which strongly influences the etch rates of the bulk material as well as along the tracks. The controlled production particularly of highly cylindrical pores is problematic because it requires low pH values where the etch rates become extremely slow. The etching times are extended and accompanied by decomposition of NaOCl.

In this work we suggest a two-step procedure combining the initially proposed treatment with H_2O_2 at high temperature followed by etching in NaOCl at high pH and moderate temperature. As material we used 25- and 50-µm thick foils of polyimide Kapton (DuPont) and irradiated them at the UNILAC with U ions of 11.1 Mev/u energy and a fluence of 4×10^6 and 10^8 ions/cm^2.

The pre-etching was performed in an aqueous solution of 30% H_2O_2 at 90°C for different times between 1 and 3 hours. For the second etching step, the samples were immersed into a 60°C warm commercial solution of NaOCl of pH 12.5 and containing 13% active chlorine. Fig. 2 shows the resulting pore diameters as a function of etching time.

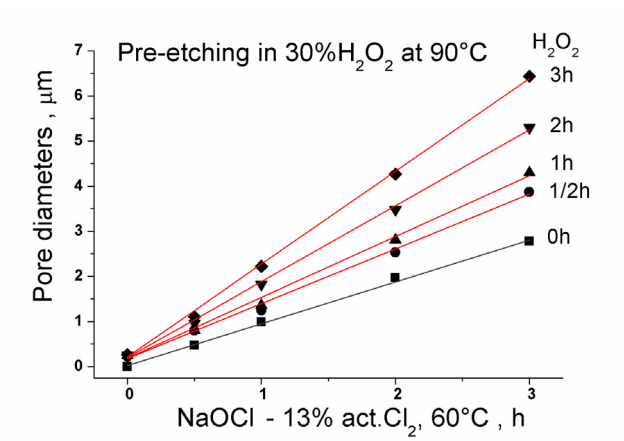

Figure 1: Pore diameter as a function of etching time of the first and second process step. The pore size was measured by scanning electron microscopy.

In order to analyse the resulting pore geometry, the membranes were galvanically filled with gold. The electrodeposition was performed using ammonium sulphite gold as electrolyte (Metakem Co) at 55°C and current density 5 mA/cm^2. Subsequently, the polyimide template was dissolved in a solution of 1 M NaOH containing 80% of ethanol at 70°C. The resulting free-standing gold structures reveal the original pore geometry (Fig. 2). As illustrated in Fig. 2, the pore shape is strongly influenced by the pre-etching step in H_2O_2. Compared to 1-step etching in NaOCl (pH 12.5, 60°C), the pretreatment leads to pores of improved cylindrical shape. The pore size of both samples is similar although the etching time in NaOCl differed by a factor of two.

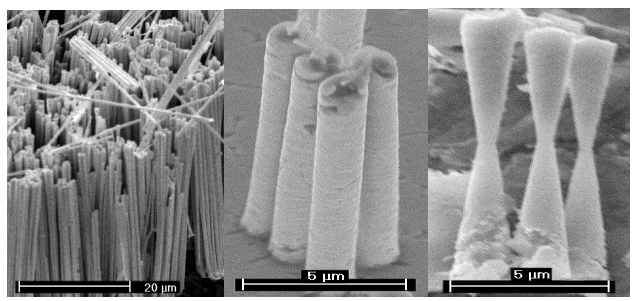

Figure 2: Gold replica of 50-µm thick Kapton foil containing 10^8pores/cm^2; left and center: cylindrical shape after 2-step etching (1 h pretreatment in H_2O_2 (90°C) followed by etching 1 h in NaOCl (pH 12.5, 60°C)); right: bi-conical shape after 2 h etching in NaOCl (pH 12.5, 60°C).

Since H_2O_2 alone does not lead to observable pores, the effect of this oxidizing agent is probably based on clearing of the track region and thus providing better access to NaOCl during the second process step and increasing the ratio of the track-to-bulk etch rate significantly. The benefit of this two-step etching process is not only the improved pore geometry but also leads to much shorter etching times without the problematic decomposition of NaOCl mentioned above. Details of the chemical activation by H_2O_2 and detrimental influence on the polyimide properties are not yet clarified.

References

[1] M. Monnin, D. Isabelle, Ann. Phys. Biol. Med. 48 (1970) 95.
[2] A.L. Velinsky et al., Polymer Sci. A 36(1994) 391.
[3] Zhu Tian-cheng, R. Brandt, P. Vater, J. Vetter, Nucl. Tracks Radiat. Meas. 15 (1988) 771.
[4] C. Trautmann, W. Brüchle, R. Spohr, J. Vetter, N. Angert, Nucl. Instr. Meth. B 111 (1996) 70.
[5] L. Klintberg, M. Lindeberg, G. Thorneli, Nucl. Instr. Meth. B 184 (2001) 536.

Preparation of ion-track membranes of poly(*p*-phenylene terephthalamide)

T. Yamaki[1], M. Asano[1], Y. Maekawa[1], Y. Suzuki[1], M. Yoshida[1], R. Neumann[2], and K.-O. Voss[2]
[1]Japan Atomic Energy Agency (JAEA), Takasaki, Gunma 370-0065, Japan; [2]GSI, Darmstadt, Germany

There have been numerous studies on ion-track membranes of poly(ethylene terephthalate) (PET) and polycarbonate (PC), which are easily prepared by ion beam irradiation and subsequent alkaline etching. More importantly, the ion-track membranes of chemically and thermally stable polyimide (PI) and polyamide (PA), with controlled pore shape and size, may be required for the design of materials that must withstand severe conditions (e.g., alkaline solution and high temperatures). PI-based microporous membranes were obtained by ion-track etching with an oxidative solution [1] and precursor method [2]. However, the ion-track membrane of PA has not yet been reported because the etching sensitivity is inversely related to polymer stability. We report here, for the first time, the investigation of ion-track etching of poly(*p*-phenylene terephthalamide) (PPTA), which is one of the PAs with the highest mechanical strength as well as chemical or thermal stability.

16-μm-thick PPTA films were bombarded by swift heavy ions from the TIARA cyclotron of JAEA and the UNILAC linear accelerator of GSI. The ion fluence was 3×10^7 ions cm^{-2}. Further irradiation conditions are listed in Table 1. The irradiated PPTA films were etched in a sodium hypochlorite (NaClO) solution at 40°C without stirring, whose pH value was adjusted at pH 9±0.5 by adding a 2 mol dm^{-3} hydrochloric acid (HCl) solution. The etched sample was washed with a large amount of water and dried at 40°C for 2 hours in vacuum. After depositing a Au coating, the surface and cross-section of the membranes were imaged with a scanning electron microscope (SEM). The conductometric method was applied to determine a track etching rate, V_t [3]. A bulk etching rate, V_b, was estimated to 0.05 μm h^{-1} by taking the decrease in film thickness during one-hour etching. Using the ratio of the two etching rates, we obtained the track formation sensitivity, Q, according to the following simple equation:

$$Q = (V_t / V_b) - 1. \quad (1)$$

Fig. 1 (a) shows SEM micrographs of the surface and cross-section of the membranes, which were obtained by the irradiation with ^{238}U ions and a 12-hour etching. This clearly confirms the perfectly cylindrical pores with a 0.3-μm diameter. The cylindrical shapes were also observed for the ^{197}Au ion irradiated films. In contrast, as shown in Fig. 1 (b), the tracks of ^{129}Xe ions were etched for 18 hours, leading to observable tracks with a surface diameter of 0.8 μm. The cross section appeared to be non-cylindrical all over the membrane cross-section. The films irradiated with ^{84}Kr and ^{102}Ru ions provided such funnel-shaped pores, too.

All results, including the linear energy transfer (LET) evaluated by a TRIM code, as well as the Q value and shape of the etched pore, are shown in Table 1. The latent tracks of the ^{84}Kr, ^{102}Ru and ^{129}Xe ions exhibited lower sensitivity to etching. This is probably the reason why funnel-shaped pores appeared in the membranes irradiated with these relatively lighter ions, where the pore diameter at the film surface increased before the formation of through-holes. However, the track sensitivity of the heavier ^{197}Au and ^{238}U ions were found to be about 4.5 times larger under the same etching conditions. The sharp increase in the Q value between the ^{129}Xe and ^{197}Au ions should be the origin of the transformation of the etched track from the funnel to cylindrical shape. This is a striking result, because the difference in the LET between these ions, which is just as much as that between the ^{197}Au and ^{238}U ions, is considered to be very small. In this case, the LET does not seem to be the only significant factor determining the sensitivity. It was reported that the damage distribution in the latent track depended on the beam energy even at a fixed value of the LET [4]. This so-called "velocity effect" in the damage creation might be manifested for the present etched tracks.

Table 1: Irradiation conditions and results.

Ion	Energy (MeV n^{-1})	LET (MeV μm^{-1})	Q	Pore shape
^{84}Kr	6.2	6.7	2.4	Funnel
^{102}Ru	3.1	9.8	6.8	Funnel
^{129}Xe	3.5	12.2	14.2	Funnel
^{197}Au	11.1	15.4	62.4	Cylindrical
^{238}U	11.1	18.3	63.4	Cylindrical

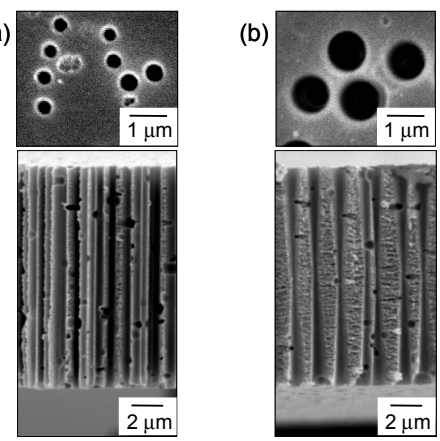

Fig. 1: SEM micrographs of the surface (top) and cross-section (bottom) of the PPTA-based ion-track membrane, which was prepared by (a) ^{238}U and (b) ^{129}Xe irradiations.

References

[1] Z. T.-Cheng, R. Brandt, P Vater, and J. Vetter, Nucl. Tracks Radiat. Meas. 15 (1988) 771.
[2] Y. Suzuki, Y. Maekawa, Y. Yoshida, M. Maeyama, and N. Yonezawa, Chem. Mater. 14 (2002) 4186.
[3] P. Apel, A. Schultz, R. Spohr, C. Trautmann, and V. Vutsadaskis, Nucl. Instr. and Meth. B, 131 (1997) 55.
[4] A. Meftah, F. Brisard, J.M. Costantini, M. H.-Ali, F. Stoquert, and M. Toulemonde, Phys. Rev. B, 48 (1993) 920.

Chemical modification of track-etched single conical nanopores inducing inversed inner wall polarity

M. Ali[1#], W. Ensinger[1], R. Neumann[2] and B. Schiedt[2]
[1]Technische Universität Darmstadt, Germany; [2] GSI, Darmstadt, Germany

Nanopores are currently considered as promising candidates for a variety of applications, including separation techniques and biological sensing [1,2]. The pore surface properties are crucial for all these applications, since they influence the transport properties (e.g. hydrophobicity, selectivity) and chemical groups on the inner pore walls may serve as binding sites for analytes [3]. Therefore, it is of highest interest to be able to control the wall properties.

Track-etched pores in polymer films open the possibility to directly chemically modify their surfaces. In polyimide (PI), mainly carboxyl groups are created during the track-etching process [4], which can be modified by different methods. One has to keep in mind, however, that most of these methods involve organic solvents, which might affect the polymer. This is of minor importance for somewhat large pores [5], but becomes crucial when going down to nanometer sizes.

The pores we were interested in here, are single conical pores in 12 µm thick PI, with only a few nm opening on one side, similar to those which have recently been used successfully for the detection of DNA molecules [6].

These pores are characterized by asymmetric I-V curves, which originate from their charged surfaces. These surface charges are influenced by the pH of the surrounding electrolyte (negative at neutral and basic pH (COO^-) and neutral at acidic pH in the I-V curves can be seen as an indication for a (COOH), and the surface charge is therefore reflected in the shape of the I-V curves at different pH values [7]. The rectification vanishes for neutral surfaces and is reversed for positive ones [8]. Therefore, changes in the I-V curves can provide an indication for a change in surface charge.

The method chosen here for modification uses only water soluble chemicals to avoid any undesirable effects on the pore shape. The reaction is the following:

The free carboxylic groups are first activated by N-hydroxysuccinimide (NHS) esters via N-(3-dimethyl-aminopropyl)-N-ethylcarbodiimide hydrochloride (EDC) [9] and subsequently react with an amine; this reaction yields amide bonds. The COO^- groups are therefore converted into NH_2 terminal groups.

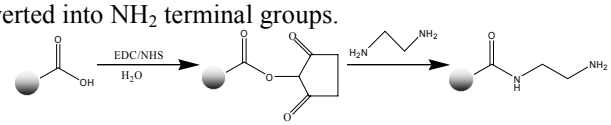

Activation was done by immersion of the samples in a 0.05 molar solution of EDC and NHS in water over night at room temperature. After washing with distilled water, the samples were further immersed in a 0.01 M solution of ethylenediamine for 24 hours. Then they were washed three times with distilled water.

M.Ali@gsi.de

To verify the success of the procedure, the I-V curves of the unmodified and modified pore were measured in 1M KCl at pH 7 and 2, adjusted by HCl. Before modification, the pore rectifies the ion current at neutral pH, and shows a linear behaviour at pH 2 (Fig. 1a), as expected for negative and neutral surfaces respectively.

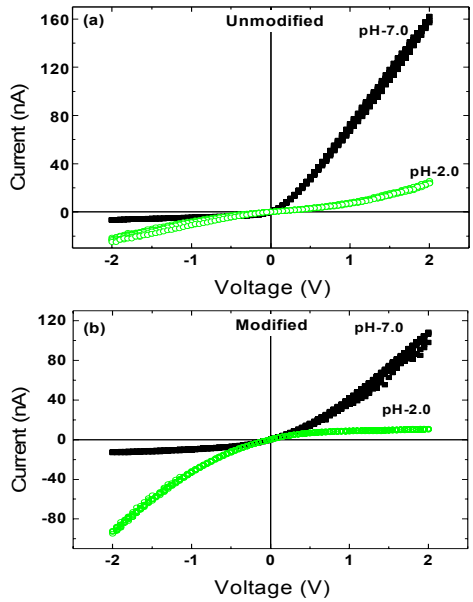

Figure 1: pH dependence of the I-V curve of a polyimide (PI) pore before a) and after b) modification with ethylenediamine.

After the modification with ethylenediamine, the pore still rectifies the ion current at neutral pH, but to a much lower degree, probably due to some unmodified carboxyl groups or due to the slightly negative behaviour of the NH_2 group, which possesses a lone pair of electrons on the nitrogen atom. At acidic pH the direction of the I-V curve reverses, i.e., rectification occurs in the opposite direction (Fig. 1b). This is a clear hint for a successful modification, because at acidic pH the nitrogen atoms are positively charged due to protonation. It can be concluded that the polarity of the pore wall was changed and, as a result, inversion of rectification occurred at low pH after modification of the pore with ethylenediamine.

References

[1] J. J. Kasianowicz et al. Proc. Natl. *Acad. Sci. USA*. **1996**, 93, 13770
[2] M. Akeson et al. *J. Biophys.*. **1999**, 77, 3227
[3] Z. Siwy et al. *Surf. Sci*. **2003**, 532–535, 1061
[4] P. Apel et al. *Nucl. Instr. and Meth. B,* **2001**, 184, 337
[5] Y. Maekawa et al. *Chem. Lett.* **2004**, 33, 151
[6] B. Schiedt.et al. *Nucl. Instr. and Meth. B,* **2005**, 236, 109
[7] Z. Siwy et al. *Nucl. Instr. and Meth. B,* **2003,** 208, 143
[8] Z. Siwy et al. *J. Am. Chem. Soc*. **2004**, 126, 1085
[9] J. Lahiri et al. *Anal. Chem*. **1999**, 71, 777

Characterization of track-etched membranes by small-angle x-ray scattering

G. Pépy[1,4,#], P. Boesecke[2], A. Kuklin[3], E. Manceau[4], N. Sertova[5], B. Schiedt[6], M. Toulemonde[5], C. Trautmann[6]

[1]Institute for Solid State Physics, Budapest, Hungary; [2]ESRF, Grenoble, France; [3]FLNP, JINR, Dubna, Russia; [4]Laboratoire Léon Brillouin, CEA Saclay, Gif sur Yvette, France; [5]CIRIL, Caen , France; [6]GSI, Darmstadt, Germany

Track-etched membranes are polymer foils irradiated with swift heavy ions and subsequently wet-etched to create pores by dissolving defects formed along the ion trajectories. Under suitable conditions, the resulting pores are of cylindrical shape and uniform in size. Such membranes are commonly used for filtration or as templates for nanowires, grown inside the pores, e.g., by electrochemical deposition.

The aim of this project is to compare nanometric pores in different polycarbonate (PC) foils and to study the effect of UV treatment. UV exposure of ion-irradiated polymers prior to chemical etching is a sensitization process widely used to improve the size distribution of pores.

The experiments were performed with two different types of amorphous PC foils (30 µm Makrofol N, 20 µm LOFO) irradiated at the UNILAC with Xe ions of 11.1 MeV/u and fluences between 3×10^8, and 10^9 ions/cm^2. Prior to etching, some of the samples were exposed to UV light (1 h from each side). Track etching was carried out in 5 M NaOH at 60 °C for 3, 5 and 8 min.

Ion-irradiated and etched membranes were analysed by small-angle x-ray scattering (SAXS) at the ID01 line of the ESRF synchrotron in Grenoble. SAXS is a non-destructive method probing large pore ensembles with a single measurement and providing three-dimensional pore information in the bulk [1], in contrast to typical microscopy techniques (e.g. scanning electron or force microscopy) that are limited to the sample surface.

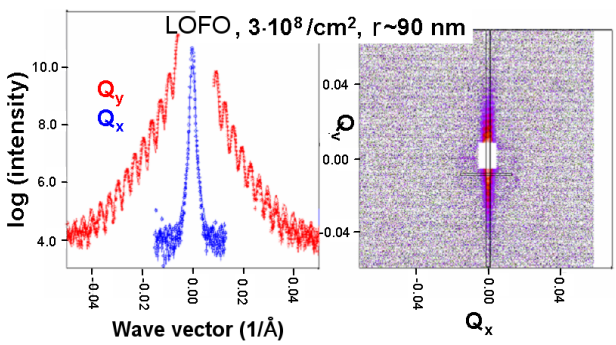

Fig. 1: SAXS data of 3×10^8 pores/cm^{-2} in LOFO polycarbonate (UV sensitized, 8 min etching). Right: anisotropic scattering pattern on 2D detector; left: x-ray intensity as a function of scattering vector for data in vertical (broad curve) and horizontal (narrow curve) rectangular filter.

A typical scattering pattern recorded with monochromatized x-rays (λ=0.088 nm) on a two-dimensional detector is shown in Fig. 1, right. Under tilted geometry, the parallel oriented pore ensemble produces a highly anisotropic pattern with two symmetric streaks. The pixel intensity of the data from the narrow rectangular-shaped filter area plotted as a function of the vertical axis exhibits pronounced oscillations (Fig. 1, left).

The data are analysed with a multipurpose XY data treatment software (PXY) [3] which allows modelling of 2-D SAXS pictures for scattering objects of simple or more complex (e.g., single/double cones or spindles) cylindrical shape with a radius r. The oscillations originate from the radial part of the Fourier transform of a cylinder mathematically described by the Bessel function [2]. The large number of oscillations is a clear indication of excellent uniformity in pore size. Comparing the oscillations of a sample with and without UV exposure, gives evidence that the UV treatment leads to a more uniform pore size distribution (Fig. 2).

Moreover, we also observe large differences between LOFO and Makrofol polycarbonate foils: the oscillations are more marked for LOFO than for Makrofol while the pore radii are smaller (between 30 and 90 nm and between 60 and 170 nm respectively) [3].

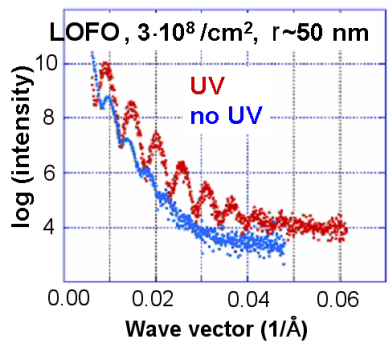

Fig. 2: SAXS intensities of LOFO samples with (upper curve) and without (lower curve) UV exposure before etching (5 min). The UV-treated sample exhibits much stronger oscillations corresponding to higher pore size uniformity.

References

[1] D. Albrecht, P. Armbruster, R. Spohr, M. Roth, K. Schaupert, H. Stuhrmann, Appl. Phys A 37 (1985) 37.

[2] G. Pépy, A. Kuklin, Nucl. Instr. Meth. B 185 (2001) 198.

[3] G. Pépy et al., SAS2006 Conference, J. Appl. Cryst. (2007), in press.

#gpepy@laposte.net

Rectification in synthetic conical nanopores

B.Schiedt[1], J. Cervera[2], S. Mafé[3], R.Neumann[1] and P. Ramírez[4,#]
[1]GSI, Darmstadt, Germany; [2] Universitat Jaume I, Castelló, Spain; [3]Universitat de València, Burjassot, Spain;
[4]Universitat Politécnica de València, Valencia, Spain

The theoretical description of ionic transport processes in nanoporous materials is a very interesting topic, since these materials have promising technological applications e.g. in sensing and filtration of molecules with size comparable to the pore diameter, and especially single pores may serve as model systems for biological ion channels. By the track-etching method [1], it is possible to produce single conical pores with nanometer sized openings on one side, showing transport properties similar to biochannels such as ionic current fluctuations [2], rectification [2], flux inhibition by divalent cations [3] and selectivity [4].

We proposed a theoretical model based on the Poisson-Nernst-Planck formalism [5] able to describe experiments on such nanopores prepared in 12 µm thick PET film (irradiation at GSI with 11.4 MeV/u U^{28+}, etching from one side with 9 M NaOH at 23 °C). Subject of the study was the concentration dependence of the rectification recorded under symmetric electrolyte conditions, 0.01 – 1 M KCl. It was demonstrated experimentally and is also assumed in our model that rectification results from electrostatic interactions of the mobile ions with fixed charges on the pore wall, which are created during the etching process. The model used here makes it possible to reproduce the experimental results using the surface charge as the only free parameter.

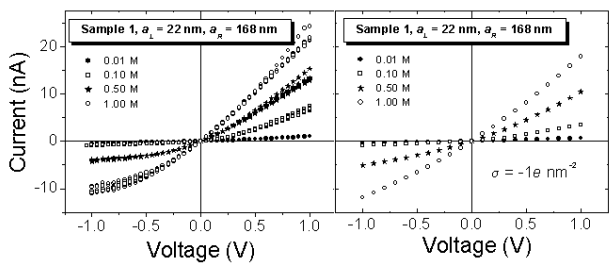

Figure 1: Experimental data (left) and calculations (right) of I-V curves for a conical nanopore with dimensions a_L = 22 nm and a_R = 168 nm at different concentrations.

This is shown in Fig. 1, where the measured and calculated I-V curves of a pore with small radius a_L = 22 nm and large radius a_R = 168 nm (sample 1) are displayed. They show the well-known asymmetry with higher current for positive potential on the small pore opening. To understand the origin of this behaviour, the average potential and concentration profiles inside the pore have been calculated for different voltages at 0.1 M (Fig. 2). The potential exhibits a clear asymmetry (with a potential well at the pore tip), which causes asymmetric co- and counter ion distributions. For positive voltages, the majority ions are driven into the pore tip by the electric field, followed by the minority ones to preserve electroneutrality. In contrast, decreased concentrations occur for negative voltages. Since the conductance of the pore is linked to the concentration of charge carriers, this leads to the observed asymmetric I-V characteristics.

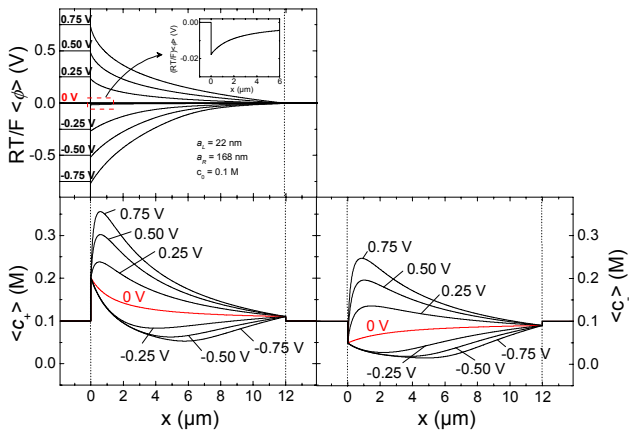

Figure 2: Average electric potential and concentrations of anions and cations inside sample 1 at 0.1 M KCl.

The degree of this rectification is given by |I(V)/I(-V)| and plotted in Fig. 3 for two pores (sample 1 and sample 2 with a_L = 3 nm and a_R = 220 nm) at V = 0.5 V against the concentration. Measurements and calculations exhibit a maximum at about 0.1 M. For higher concentrations the rectification decreases due to stronger shielding of the fixed charges.

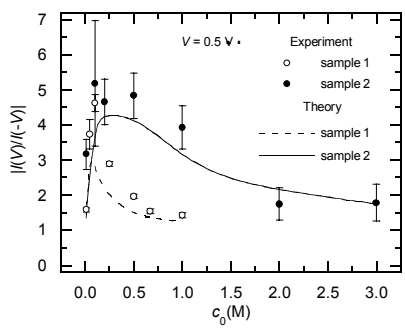

Figure 3: Measured and calculated concentration dependence of the rectification for samples 1 and 2 at 0.5 V.

References

[1] P. Apel et al., Nucl. Instr. and Meth. B 184 (2001) 337.
[2] Z. Siwy, Adv. Funct. Mat. 16 (2006) 735.
[3] Z. Siwy et al., Nano Lett. 6 (2006) 473.
[4] Z. Siwy et al., Am. J. Phys. 72 (2004) 567.
[5] J. Cervera et al., J. Chem. Phys. 124 (2006) 104706.

#patraho@fis.upv.es

Resistive Pulse Sensing of Protein and Protein/Antibody Complexes Using Single Conical Nanopores

L.T. Sexton, L.P. Horne, S. Sherrill, L.A. Baker, Y. Choi and C.R. Martin[#]
Department of Chemistry and Center for Research at the Bio/Nano Interface, University of Florida, Gainesville, FL 32611-7200, U.S.A.

Current work in the Martin group has focused on utilizing single conical nanopores prepared by the track-etch method [1] to detect proteins via the resistive pulse sensing technique by recording current-time (i-t) traces through a single pore. When an analyte passes through the pore, translocation events are observed in the i-t trace. In this study, we recorded translocation events for an individual protein and a protein/antibody complex. We then analyzed the difference between the protein and the complex events. Bovine serum albumin (BSA) and its antibody were used as a model system.

Membranes containing single nanopores were prepared by irradiating 12-µm thick polyethylene terephthalate (PET) foils with individual heavy ions (e.g. Au, Pb, U of 11.4 MeV/u) from the UNILAC. Through a chemical track etching process, using 9M NaOH and 1M formic acid, the single track was developed into a conical pore [1]. The base diameter of the resulting conical pore was ~520 nm, and the small diameter opening after etching was ~45 nm. The pores were then electrolessly gold plated and subsequently functionalized with a poly(ethylene glycol) (PEG) monolayer [2]. This was done to minimize non-specific protein absorption [3] and accomplished with a thiolated PEG chain (MW 5000). After these steps the base diameter remained approximately the same diameter because the Au layer and PEG monolayer deposited are very thin, however, the tip diameter is decreased to ~17 nm.

The PEG functionalized single conical pore was mounted in a conductivity cell, and each side was filled with 10 mM PBS buffer (pH = 7.4) that was also 100 mM in KCl. A Ag/AgCl electrode was placed on each side of the cell and connected to an Axopatch 200B (Molecular Devices Corporation, Union City, CA) patch clamp amplifier which was used to apply the desired potential, and measure the resulting ionic current flowing through the nanopore. Current time recordings were taken in the presence of (A) buffer only, (B) increasing concentrations of BSA, and (C) a solution of BSA with excess anti-BSA. Control experiments with streptavidin (SA) in the presence of anti-BSA were also done.

The translocation events for BSA showed a voltage dependence between 400-1000 mV, as well as a concentration dependence with the four concentrations used between 25-100 nM at an applied potential of 1000 mV.

After addition of excess anti-BSA (270 nM) to a solution that was 100nM in BSA facing the tip side of the conical nanopore, the duration and amplitude of events changed dramatically. Histograms of event duration for the BSA/anti-BSA complex were compared with those associated with BSA only. The event durations observed for the complex were much larger (~2213 ± 187 ms) than those for the protein only (~520 ± 11 ms), which indicates that the BSA/anti-BSA complex was formed and translocated the nanopore.

Scatter plots of event amplitude vs. event duration for BSA and the BSA/anti-BSA complex were also compared (Fig. 1). One unexpected observation is the decrease in amplitude for the events associated with the protein/antibody complex. One would expect an increase in event amplitude with a larger analyte [4]. A possible explanation for this occurrence could be due to conformational changes that must take place in order for the complex to translocate the nanopore.

Control experiments with SA and anti-BSA showed that events associated with SA do not change in amplitude or duration after addition of anti-BSA.

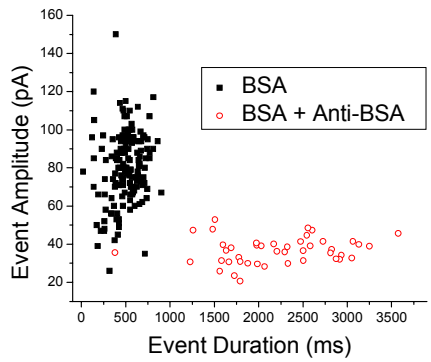

Figure 1: Scatter plot of translocation event amplitude vs. event duration for 100nM BSA (square) and 100nM BSA with 270nM anti-BSA (open circle). Applied transmembrane potential of 1000mV.

In this work we have demonstrated that our conical nanopore sensors are capable of detecting protein analytes via resistive pulse sensing. We have also shown that when the protein and antibody are combined, a significant shift in the translocation events is observed. Indeed, it should be possible to use this sensing strategy to quantitatively detect a target protein within a mixture of proteins.

References

[1] P.Y. Apel, Korchev, Y.E., Siwy, Z., Spohr, R., Yoshida, M., , *Nucl. Instr. Meth. B.* 184 (2001) 337.
[2] V.P. Menon, C.R. Martin, *Anal. Chem.* 67 (1995) 1920.
[3] Z. Yang, J.A. Galloway, H. Yu, *Langmuir* 15 (1999) 8405.
[4] C.R. Martin, H. Bayley, *Chem. Rev.* 100 (2000) 2575.

[#]crmartin@chem.ufl.edu

Burn-out current density of bismuth nanowires

T.W. Cornelius[1], M.E. Toimil-Molares[1], S. Karim[2], R. Neumann[1]
[1]GSI, Darmstadt, Germany; [2]University of Marburg, Hans-Meerwein-Str., 35032 Marburg, Germany

In the recent past, extensive studies were performed on nanoscale materials. In particular, bismuth nanowires attracted large interest because of their extraordinary properties and possible application in thermoelectric devices.

Regarding future implementations, the maximal current density j_{max} nanowires are able to carry is an important aspect. High current densities can cause voids in the wires or even lead to wire breakage. Bulk metals fail because of Joule heating at current densities of 10^3 to 10^4 A/cm^2 [1]. Bulk Bi is expected to fail at lower j_{max}, since the specific electrical resistivity of this material is more than fifty times higher than in conventional metals and the melting temperature amounts only to 271 °C. In microstructures another effect - electromigration – was found to cause failure [2]. This is a thermally activated process where atoms diffuse mostly at grain boundaries so that voids are formed. Failure occurs when voids coalesce so that they finally cause a breakage along the whole wire width.

In order to investigate the burn-out current density, single Bi nanowires were prepared electrochemically in ion track-etched polycarbonate (PC) membranes. The templates were fabricated by irradiating PC foils with single swift heavy ions at the UNILAC. Subsequently, the foils were etched in 2M NaOH at 50 °C. After coating one side of the membrane with a conductive layer, the wire was grown electrochemically in the single nanopore [3]. The deposition was continued until a cap was formed on top of the wire. After rinsing and drying the sample, an additional gold layer was sputtered onto the cap for electrically contacting the nanowire [4]. In order to determine j_{max} the current was ramped up in a two-contact configuration until failure occurred.

Fig. 1 displays the *I-V* curve of a single bismuth nanowire with diameter 230 nm. The breakage being indicated by the arrow is observed at I = 900 µA, i.e., j_{max} = 2.2*10^6 A/cm^2.

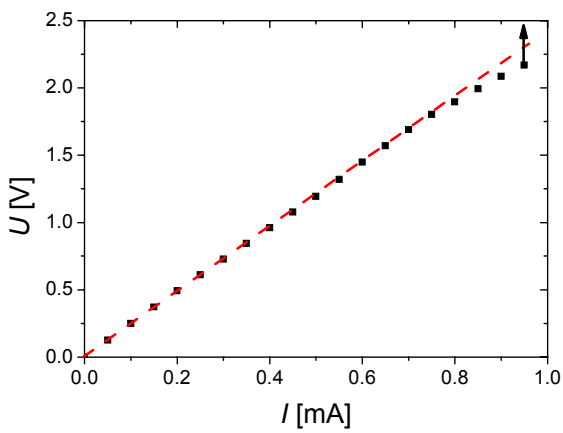

Fig. 1: *I-V* curve of a single Bi nanowire. The dashed line is a guide-to-the-eye displaying a linear ohmic behaviour.

The burn-out current density of single bismuth nanowires created under two different deposition conditions as a function of their inverse diameter is presented in Fig. 2. The plot shows that j_{max} is directly proportional to d^{-1}, i.e., wires of smaller diameters stand systematically higher current densities. Thus, while bulk metals carry current densities of up to ~ 10^4 A/cm^2 [1], our experiments reveal that wires with diameter 1 µm can carry j_{max} ~ 5*10^5 A/cm^2, the maximum current density increasing further with decreasing wire diameter. Higher current densities of up to 3.5*10^6 A/cm^2 are carried by thinner wires due to very effective heat dissipation, caused by the larger surface-to-volume ratio of the nanowire embedded in the polymer matrix.

Within the experimental uncertainty, wires created under different conditions show the same j_{max}. However, wires created at higher temperature and smaller overpotential, i.e., wires that consist of larger grains and possess lower specific electrical resistivities [4], can carry systematically higher current densities. This is due to the presence of less grain boundaries, which decreases both the effects of atom diffusion and the specific electrical resistivity, also lowering the generation of Joule heat [4].

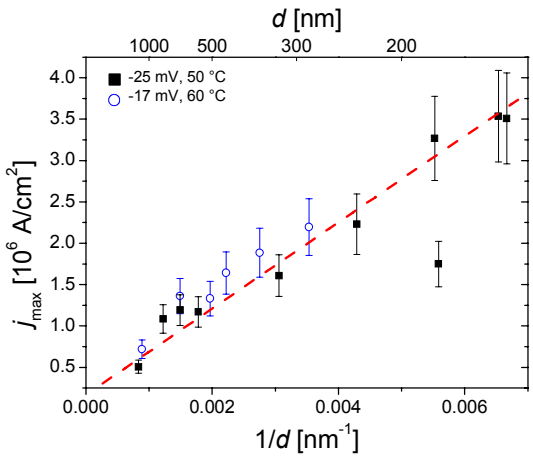

Fig. 2: Maximum current density of single Bi nanowires as a function of the inverse diameter. The dashed line represents the linear relation of j_{max} versus d^{-1}.

Our results imply that (i) j_{max} is two orders of magnitude higher for embedded Bi nanowires compared with bulk metal and (ii) j_{max} increases with diminishing d.

References

[1] P.S. Ho, T. Kwok, Rep. Prog. Phys. 52 (1989) 301
[2] J.R. Black, IEEE Trans. Electron. Devices ED-16 (1969) 338
[3] T.W. Cornelius, J. Brötz, N. Chtanko, D. Dobrev, G. Miehe, R. Neumann, M.E. Toimil Molares, Nanotechnology 16 (2005) S246
[4] T.W. Cornelius, M.E. Toimil-Molares, R. Neumann, S. Karim, J. Appl. Phys. 100 (2006) 114307

Influence of crystallinity on morphological changes in Au nanowires

S. Karim[1], M. E. Toimil-Molares[2], W. Ensinger[3], A. G. Balogh[3], T. W. Cornelius[2], R. Neumann[2]
[1]Department of Chemistry, Philipps University, Marburg, Germany; [2]GSI, Darmstadt, Germany
[3]Darmstadt University of Technology, Darmstadt, Germany

Metallic nanowires are regarded as a key component of future nanoscale devices. Strength of nanowires against surface tension effects or the so-called Rayleigh instability is crucial for the reliability of nanowire-based components. This instability stimulates a nanowire to break up into a linear row of nanospheres [1, 2]. An extensive stability analysis by Nichols and Mullins explains many aspects of this process that induces morphological changes occurring in cylindrical solid rods by mass transport either by surface or volume diffusion [3]. The analysis assumes an isotropic surface energy of the initial rod. However, the surface energy of crystalline solids is generally anisotropic varying with the crystallographic orientation. Recent theoretical investigations found that the surface energy anisotropy originating from different crystallographic orientations of nanowires can either promote or suppress Rayleigh instability [4]. Experimentally, nanowires with different crystallinity can be created depending on the fabrication conditions. Thus, nanowires provide a suitable system to experimentally investigate Rayleigh instability as a function of crystallinity. In addition, a detailed understanding of the instability is necessary to apply it as an unconventional patterning method. Here, we explored some consequences of different crystallinity of Au nanowires on the morphological changes.

We fabricated Au wires of diameter D = 87 nm by electrochemical deposition in etched ion-track membranes. By varying the deposition conditions, both polycrystalline (PC) and single-crystalline (SC) nanowires were synthesized. X-ray diffraction as well as transmission electron microscopy analysis confirmed that the SC wires are strongly <110> textured. The polymer templates were subsequently dissolved in CH_2Cl_2 and the nanowires were dispersed on SiO_2 substrates. The wafer pieces carrying the nanowires were annealed in an evacuated furnace at 600 °C for different time periods (t_a). After cooling down to room temperature, the samples were examined using high resolution scanning electron microscopy (HRSEM).

The micrographs in figure 1 illustrate the sequences of transformation of polycrystalline and single-crystalline Au wires into chains of nanospheres when annealed at 600 °C. The morphology of as-prepared polyc- and single-crystalline wires is presented in part (a) and (e), respectively. As evident in the figure, first, thickness undulations are developed on the wires causing a wire to fragment and, finally, the fragments spheroidize.

In the case of PC wires, axial perturbations developed at 1 h annealing (Fig. 1b). The wires fragmented and decayed partially into nanospheres at t_a = 2 h (Fig. 1c). Finally at 2.5 h, the wires were completely transformed into chains of nanospheres as is evident in figure 1d. The morphological evolution of SC wires at 600 °C is depicted in the figures 1e-h. The wires proved significantly more resistant to breakup compared to the PC wires. The first sign of radial perturbation in the wires appeared only at t_a = 2.5 h, fragmentation at 3 h, and the complete decay into chains of nanospheres was observed after 5 h annealing.

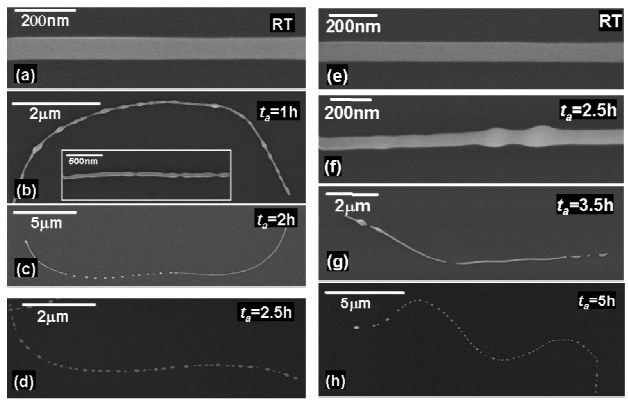

Fig.1. HRSEM images demonstrating the decay of polycrystalline (left) and single-crystalline (right) Au wires (D = 87 nm) into chains of nanospheres. The annealing was performed at 600 °C for different times indicated on the micrographs.

The mean distance between the nanospheres formed after the complete decay of both PC and SC wires is 515 ± 89 and 771 ± 162 nm, respectively. Both values are higher than predicted for materials with isotropic surface energy evolved via surface diffusion (386.7 nm).

In summary, it was demonstrated that <110> oriented single-crystalline Au nanowires are more stable against Rayleigh decay as compared to polycrystalline wires. In addition, the size and spacing of the nanospheres formed after the decay are also depend on the wire crystallinity.

References

[1] M.E. Toimil-Molares, A.G. Balogh, T.W. Cornelius, R. Neumann, C. Trautmann, Appl. Phys. Lett. 85 (2004) 5337.
[2] S. Karim, M.E. Toimil-Molares, A.G. Balogh, W. Ensinger, T.W. Cornelius, E.U. Khan, R. Neumann, Nanotechnology 17 (2006) 5954.
[3] F.A. Nichols, W.W. Mullins, Trans. Metal. Soc. AIME 233 (1965) 1840.
[4] K.F. Gurski, G.B. McFadden, Proc. R. Soc. Lond. A 459 (2003) 2575.

Antennalike plasmon resonances of single gold nanowires in the infrared

F. Neubrech[1], M. Klevenz[1], R. Lovrincic[1], G. Fahsold[1], S. Karim[3], T.W. Cornelius[2], R. Neumann[2] and A. Pucci[1]

[1]Kirchhoff-Institut für Physik, Universität Heidelberg, Im Neuenheimer Feld 227, 69120 Heidelberg, Germany; [2]Gesellschaft für Schwerionenforschung (GSI), Planckstr. 1, 64291 Darmstadt, Germany; [3]University of Marburg, Hans-Meerwein-Str., 35032 Marburg, Germany

Nanostructures, especially nanowires, are regarded as fundamental components of future key technologies. For example, metal nanowires are expected to play a decisive role for electronic devices, sensoric and analytic methods in life science. Another near future application using metal nanowires is the apertureless scanning near field optical microscopy (SNOM). This position sensitive technique allows one to detect vibrational fingerprints of single molecules on nanoantennas exploiting surface enhanced infrared absorption (SEIRA). For an efficient engineering a detailed characterization of the optical properties of nanowires is necessary. Within the framework of our studies we examined the optical properties of single metal nanowires (supported by a dielectric substrate) using infrared (IR) spectroscopic microscopy.

Gold nanowires with diameters between 50 and 200 nm were prepared by electrochemical deposition in polymeric etched ion track membranes [1]. After dissolution of the membrane, the wires were transferred onto an IR transparent substrate (e.g. KBr, CaF_2, ZnS) for spectroscopic measurements.

We performed infrared spectroscopic microscopy of single gold nanowires at the IR-beamline of the synchrotron light source ANKA (Forschungszentrum Karlsruhe). First, the wire was located and its length *(L)* was determined by microscopy with visible light. Then the IR-beam (diameter of 8.3µm in the focal plane) was centered on the selected wire and IR-transmittance spectra (sample spectra) in the spectral range from 600 to 6000 cm^{-1} were recorded. Subsequently, in order to eliminate environmental effects, reference spectra (same spectral range) were taken at some distance from the nanowire.

For nanowires with a length of a few microns we observed significant antennalike plasmon resonances in the relative transmittance spectra (ratio of the sample and reference spectra, see Fig. 1). The strongly polarization dependent resonances were observed only for the electrical field parallel to the long axis of the wire. From relative transmittance measurements the extinction cross section of a single nanowire with respect to the geometric cross-section is calculated regarding the spot size of the IR-beam, the length and diameter of the nanowire and the influence of the substrate. At the position of maximum extinction (resonance wavelength Γ) we found ratios >1, which indicate an enhanced local field in the vicinity of the nanowire [2].

The measured Γ cannot be described by the well-known $L = m \cdot \Gamma/(2n)$ dipole relation for macroscopic ideal antennas being completely embedded in a medium with refractive index n. Instead, we observed a shift towards higher resonance frequencies according to different reasons. (i) The shape of the wire (diameter) and the wire material affect the position of the resonance wavelength, which is confirmed by electromagnetic scattering simulations at single gold nanowires [2]. (ii) The polarizability of the substrate (with dielectric constant ε_s) plays a major role as we see in our experiments. In order to characterize the system completely, the polarizability of the surrounding medium (ε_m) has to be taken into account. For a rough approximation this can be done by an effective dielectric function $\varepsilon_{eff} = 1/2\ (\varepsilon_s + \varepsilon_m)$ [2]. For a demonstration of the effect of the embedding medium on the nanowire resonance curve we covered a nanowire on a ZnS substrate with paraffin wax. Due to the paraffin coverage the resonance shifts to smaller frequencies (see Fig. 1), which can be explained with the effective refractive index $n_{eff} = \sqrt{\varepsilon_{eff}}$. From our investigations of single gold nanowires we

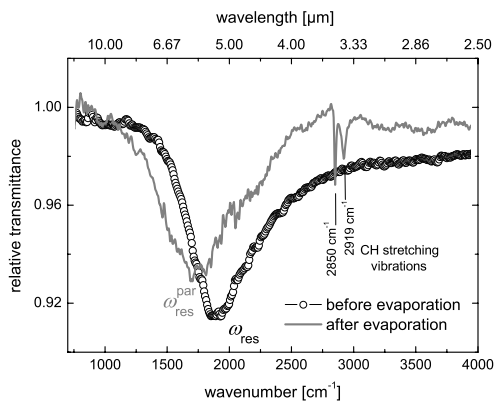

Fig. 1: Relative transmittance spectra of a single Au nanowire ($L \approx$ 1.4µm, D = 100nm) with (line) and without (dots) paraffin [2]

qualitatively know the influence of substrate and shape of the wire on the resonance frequency. In consideration of these effects we extend the $L = \Gamma/2$ dipole relation to $\omega_{res} = \pi c/(Ln_{eff})*R(L/D)$. The factor $R(L/D)$ describes the shape effects. With that relation we obtain the ratio $\omega_{res}^{par} / \omega_{res}^{air} = n_{res}^{air} / n_{res}^{par} = 0.92$ between the resonance frequencies before and after evaporating paraffin (with ε_s = 4.84 for ZnS and ε_m = 2.02 for paraffin). This ratio is in good accord with our experimental results for the resonance frequencies of several experiments [2].

We thank the IR-beamline scientists (M. Suepfle, Y.-L. Mathis, B. Gasharova and D. Moss) of the Angströmquelle Karlsruhe (ANKA) for helpful discussions and technical support. We acknowledge valuable discussions with H. Eipel (KIP).

[1] S. Karim et al., Appl. Phys. A 84, 403 (2006)
[2] F. Neubrech et al., Appl. Phys. Lett. 89, 253104 (2006)

Cadmium chalcogenides nanowires obtained in ion track templates*

I. Enculescu[1], M. Sima[1], E. Matei[1], M. Enculescu[1], T.W. Cornelius[2], R. Neumann[2]
[1]National Institute for Materials Physics, Magurele, Romania; [2]GSI, Darmstadt, Germany

Metal chalcogenide semiconductor nanowires are of particular interest for several reasons. First, II-VI semiconductors present a broad range of band gaps (from 0.15 eV in HgTe to 3.68 eV in ZnS). Second, most of them have direct energy gaps making them particularly important for electro-luminescence devices. Third, these kinds of semiconductors can be electrochemically deposited from aqueous solutions. The deposition process on macroscopic electrodes has been extensively studied in the last decades, driven by the large amount of applications that II-VI and IV-VI semiconductor devices have nowadays. Examples are the use of CdTe in a broad range of optoelectronic devices such as infrared, X-ray, and gamma ray detectors, the investigations of CdTe/CdS systems as a good alternative to silicon solar cells, and the use of ZnSe to prepare light emitting or laser diodes in the blue band. Moreover, these semiconductor compounds form solid solutions over a considerable range of compositions, and even better control over various properties and structural changes may be achieved in ternary semiconductors.

This paper presents some of our results in preparing CdS and CdTe nanowires by the template method. We used ion track-etched nanoporous polycarbonate membranes which were filled by electrochemical deposition, a method extensively used for preparing metallic nanostructures [1,2]. The bath used for deposition of CdS nanowires contains 200 mM $CdCl_2 \cdot 2H_2O$ and 10 mM $Na_2S_2O_3 \cdot 5H_2O$ at pH 2-3, the following reaction taking place at the working electrode:

$Cd^{2+} + S_2O_3^{2-} + 2e^- \rightarrow CdS + SO_3^{2-}$

Figure 1 displays a scanning electron microscopy (SEM) image of a CdS nanowire array with rectangular cross-section which was deposited at -750 mV at 90 °C.

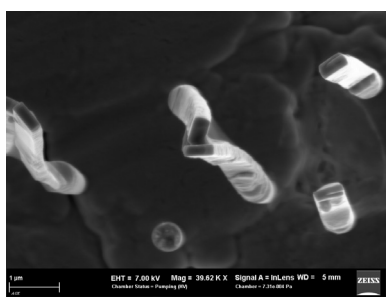

Figure 1. Array of CdS nanowires deposited in an ion track template

Deposition of CdTe nanowires was performed in a potentiostatic mode using an acidic deposition bath (1 M $CdSO_4$, 0.3 mM TeO_2 at a pH of 1.6 adjusted with H_2SO_4). The following reactions take place during deposition: $HTeO_2^+ + 3H^+ + 4e^- \rightarrow Te + 2H_2O$ and

$Cd^{2+} + Te + 2e^- \rightarrow CdTe$

The composition of the nanowires was investigated by energy dispersive x-ray analysis. The wire composition as a function of deposition potential is presented in Fig. 3. Stoichiometric composition was achieved at $U \sim 550$ mV. Lower overpotentials provide a Te excess, while an excess of cadmium is present for higher U.

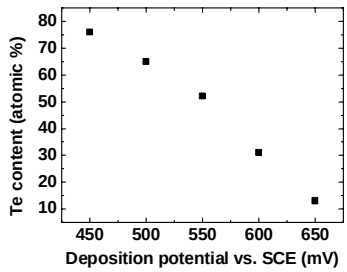

Figure 2. Cd content as a function of deposition potential for CdTe wires

A SEM image of an array of CdTe hollow rods deposited at 70°C and -550 mV is presented in Fig. 3.

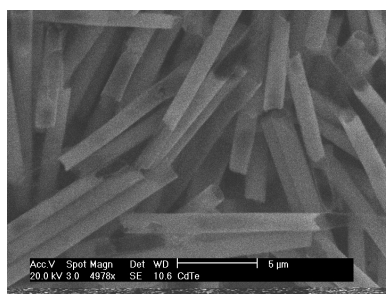

Figure 3. An array of CdTe hollow rods prepared by electrodeposition in ion track membranes.

These results demonstrate that electrochemical deposition is a promising approach towards the preparation of semiconductor nanostructures.

References

[1] M.E. Toimil-Molares, V. Buschmann, D. Dobrev, R. Neumann, R. Scholz, I. U. Schuchert, J. Vetter, Adv. Mater. 13, 62 (2001).

[2] I. Enculescu, M.E. Toimil-Molares, C. Zet, M. Daub, L. Westerberg, R. Neumann, R. Spohr, Appl. Phys. A 86, 43 (2007).

* Work supported by CEEX contract nr.1/2006
# encu@infim.ro

Textured growth of metallic fcc nanowires under direct and alternating current deposition conditions

F. Maurer[1], J. Brötz*[1], H. Fuess[1], S. Karim[2], M.E. Toimil-Molares[2], and C. Trautmann[2]

[1]Technische Universität Darmstadt, Darmstadt, Germany; [2]GSI, Darmstadt, Germany

For the fabrication of metallic nanowires, nanoporous templates are produced by irradiating polymeric foils at the UNILAC facility. After chemical etching of the ion-induced damage tracks, the cylindrical pores of the template are filled with metals by electrodeposition. The resulting nanowires have high aspect ratios (diameter a few ten nm, length a few ten µm).

Here, we investigate the textured growth of metallic face-centered cubic (fcc) nanowires, in particular Cu [1] and Au [2]. Under direct current (*dc*) growth conditions, $\langle 110 \rangle$ textured wire ensembles occur, whereas $\langle 100 \rangle$ growth directions develop under alternating current (*ac*) deposition. X-ray diffractograms of Au nanowire ensembles of different textures are shown in figure 1.

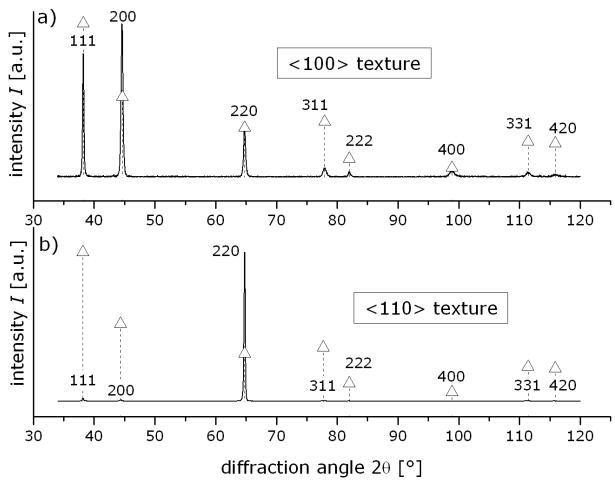

Figure 1: X-ray diffractograms of Au nanowire ensembles of a) $\langle 100 \rangle$ texture under *ac* deposition; b) $\langle 110 \rangle$ texture under *dc* deposition conditions; the dashed vertical lines with triangles atop represent the intensity distribution of a polycrystalline and untextured sample.

To explain these experimental results, the broken bond model [3] was applied to the anisotropy of single-crystalline or textured wires in combination with surface-energy minimization growth tendencies: The energy of an atomic surface is considered to be proportional to its broken-bond density. The constitution of the circular top and base planes, as well as the cylindrical mantle surfaces depend on $\langle hkl \rangle$ of the wire and can be determined from crystallographic projections [4]. The evolution of the surface energy $E_{\langle hkl \rangle}$ of an $\langle hkl \rangle$ textured fcc nanowire ensemble during growth, i.e. increasing aspect ratio h/d, is shown in Figure 2.

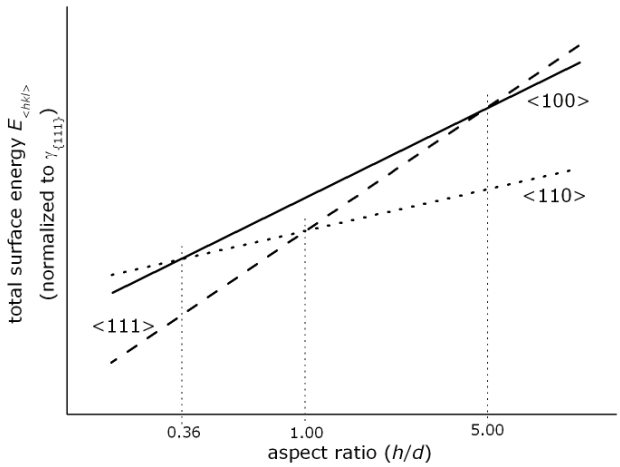

Figure 2: Evolution of surface energy $E_{\langle hkl \rangle}$ of $\langle hkl \rangle$ textured fcc nanowires with aspect ratio h/d.

Up to an aspect ratio of 1 a $\langle 111 \rangle$ texture represents the configuration of lowest energy. At higher aspect ratios the $\langle 110 \rangle$ orientation becomes the most favorable growth direction. Under *ac* conditions, lattice sites of high reactivity, i.e., lattice defects or surfaces with high number of broken bonds are preferentially dissolved during the anodic cycles of the alternating polarity. As $\{110\}$ surfaces exhibit a high number of broken bonds these lattice sites, and thus the $\langle 110 \rangle$ texture, successively disappear under *ac* conditions. In absence of $\{110\}$ surfaces, a $\langle 100 \rangle$ texture represents the orientation of lowest energy for aspect ratios larger than 5 (see Figure 2). The $\langle 110 \rangle$ texture under *dc* and the $\langle 100 \rangle$ texture under *ac* deposition conditions become stronger at smaller diameters, as the transition aspect ratios are reached earlier.

References

[1] M.E. Toimil-Molares, J. Brötz, V. Buschmann, D. Dobrev, R. Neumann, R. Scholz, I.U. Schuchert, C. Trautmann, J. Vetter; Nucl. Instr. Meth. Phys. Res. B 185 (2001) 192.

[2] S. Karim, M.E. Toimil-Molares, F. Maurer, G. Miehe, W. Ensinger, J. Liu, T.W. Cornelius, R. Neumann; Appl. Phys. A 84 (2006) 403.

[3] J.K. Mackenzie, A.J.W. Moore, J.F. Nicholas; J. Phys. Chem. Solids 23, (1962) 185.

[4] F. Maurer, J. Brötz, S. Karim, M.E. Toimil-Molares, C. Trautmann, H. Fuess; Nanotechnolgy (2007), in press.

* contact: broetz@tu-darmstadt.de

Microbeam Mapping of Charge Collection in Hexagonal Power MOSFETs and Its Relation to Single Event Burnout

J. Barak[1], D. David[1], G. Du[2], B. E. Fischer[2], A. Haran[1], M. Heiß[2], N. Refaeli[1] , and K.- O. Voss[2]
[1] Soreq NRC, Yavne, Israel, [2]GSI Materials Research, Darmstadt, Germany

Single Event Burnout (SEB) in power MOSFETs is of major concern with regard to the suitability of the MOSFET for space missions and other high particle radiation environments. Large efforts have been made to deeply understand this phenomenon, in order to develop power MOSFETs which are less sensitive to SEB [1], [2]. When an ion hits the MOSFET source, amplification of an inherent parasitic bipolar transistor (BJT) may start an avalanche process, and as a result, a breakdown, i.e. a Burnout event, may occur. The SEB cross-section depends on the bias voltage (electric field), the ion stopping power, and its hit location on the MOSFET surface. Experiments with a microbeam can yield valuable information regarding the effect of the hit location on SEB probability, unattained in wide beam tests. This information is highly important to validate the results obtained by the simulations.

The current amplification of the parasitic BJT gives rise to higher charge collection (CC). In a previous work carried out at the GSI microbeam facility [3], the mapping of the charge collection of an ST Microelectronics device revealed areas with high charge collection. These spots were related to points where the device might burn out. The charge collection spectrum was measured using a pulse-height analyzer as was done in [1].

In the present work we study an International Rectifier HEXFET technology MOSFET, IRF360. In Fig. 1 the "neck" area is shown below the gate where the MOSFET current is marked, with the N source structure on both sides. The hexagonal structure is perfect for mapping since there is no ambiguity in determining the location of each ion hit within the FET cell. For the microbeam mapping we have used Xe ions with 634 MeV.

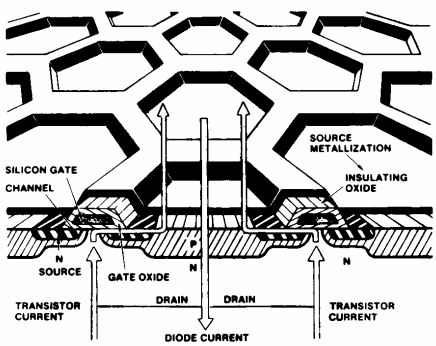

Fig. 1. The HEXFET structure (Fig. 1 in [4]).

Fig. 2 shows the charge collection spectrum for a drain to source bias (V_{DS}) of 7 V. The points sensitive to SEB are expected to be those showing high charge collection with different amplification factors. Fig. 3 shows the mapping of those ions which have high charge collection. The mapping suggests that the source area exhibits charge amplification and is the most sensitive area to SEB. Similar measurements aimed at direct mapping of SEB events with the microbeam support these findings.

We intend to continue the SEB study by mapping the charge collection and SEB using different ions, different devices, and different bias values.

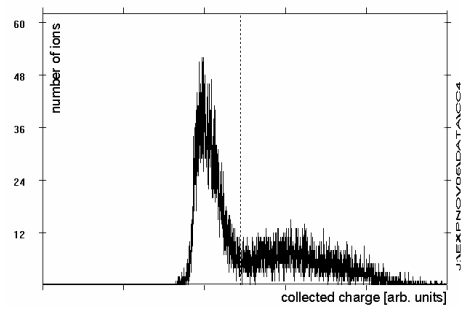

Fig. 2. The CC spectrum of IRF360 at V_{DS} = 7 V.

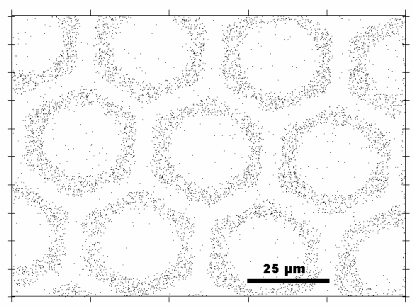

Fig. 3. Mapping of the points at V_{DS} = 7 V with charge collection above the dashed line in fig.2.

References

[1] S. Kuboyama, N. Ikeda, T. Hiro, and S. Matsuda, "Improved model for single-event burnout mechanism," *IEEE Trans. Nucl. Sci.*, vol. 51, pp. 3336–3341 Dec. 2004.

[2] S. Liu, M. Boden, D. A. Girdhar, and J. L. Titus, "Single-event burnout and avalanche characteristics of power DMOSFETs," *IEEE Trans. Nucl. Sci.*, vol. 53, pp. 3379–3385 Dec. 2006.

[3] O. Musseau, A. Torrès, A. B. Campbell, A. R. Knudson, S. Buchner, B. Fischer, M. Schlögl, and P. Briand, "Medium-energy heavy-ion single-event-burnout imaging of power MOSFET's," *IEEE Trans. Nucl. Sci.*, vol. 46, pp. 1415–1420, Dec. 1999.

[4] W. E. Abare and W. K. Martindale, "Dose rate tolerant HEXFET power supply," *IEEE Trans. Nucl. Sci.*, vol. 28, pp. 4380–4383, Dec. 1981.

Research programme biophysics and cancer therapy

Effect of UV-C- and ion-irradiation on PCNA and p21 foci formation

D. Fink, J. H. Rudolph, K. Knoop, J. Topsch, B. Jakob, G. Taucher-Scholz
GSI, Darmstadt, Germany

The cyclin-dependent kinase inhibitor p21 directly interacts with PCNA (proliferating nuclear antigen) thereby inhibiting DNA-replication. Previously, we described that PCNA and p21 also form focal protein accumulations at sites of heavy ion-induced DNA damage [1]. The function of PCNA in different DNA repair pathways is well documented whereas the role of p21 is still discussed controversially. To investigate the involvement of p21 in DNA repair, we compare the recruitment of p21 and PCNA to DNA lesions caused by different radiations in repair proficient fibroblasts (AG-cells) and in XPA (Xeroderma pigmentosum complement group A) cells. XPA-cells, due to their lack of functional XPA-protein, are defective in nucleotide-excision repair (NER), which is the main repair pathway for DNA lesions caused by UV light.

PCNA and p21 kinetics in locally UV-C light exposed fibroblasts

To evaluate the recruitment kinetics for p21 and PCNA to UV-induced DNA-damage, we locally exposed AG- and XPA cells to 100 J/m^2 of UV-C light using a microfilter-mask to produce DNA lesions only in distinct areas of the nucleus [2]. Both proteins were detected separately by fluorescence immunostaining at various time-points after irradiation.

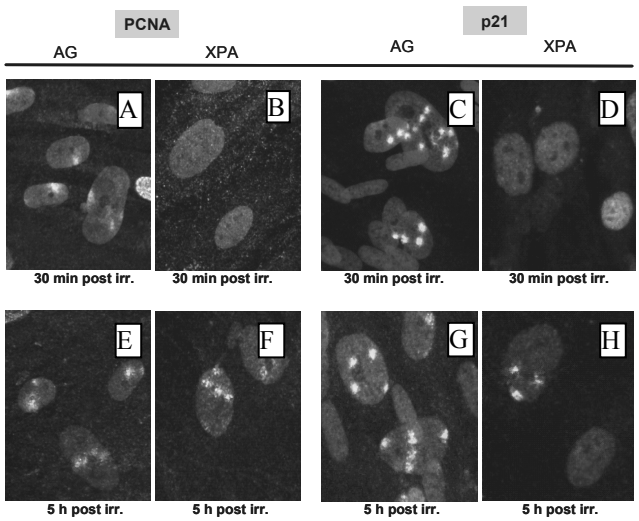

Figure 2: Detection of local accumulation of p21 and PCNA in cell nuclei of NER-proficient (AG-cells) and deficient human fibroblasts (XPA-cells) after local UV-C light exposure.

In the repair proficient AG cells, both proteins, PCNA and p21, were detectable 30 min (Fig. 1; A, C) as well as 5 h (Fig. 1; E, G) after UV exposure. In contrast, XPA cells of functional XPA protein, showed a delayed accumulation of p21 and PCNA protein at the sites of DNA-damage (Fig. 1;B,D,F,H). In agreement with literature [3], we can show that the early recruitment of PCNA and p21 proteins to UV-induced DNA lesions is related to the nucleotide-excision-repair pathway.

PCNA and p21 kinetics in fibroblasts irradiated with heavy ions

To investigate the postulated involvement of PCNA and p21 in the repair of ion-induced more complex DNA-damage, we irradiated human fibroblasts with 7.4 MeV/u argon ions (LET: 1550 keV/µm) and analysed them at different time-points by indirect immunostaining.

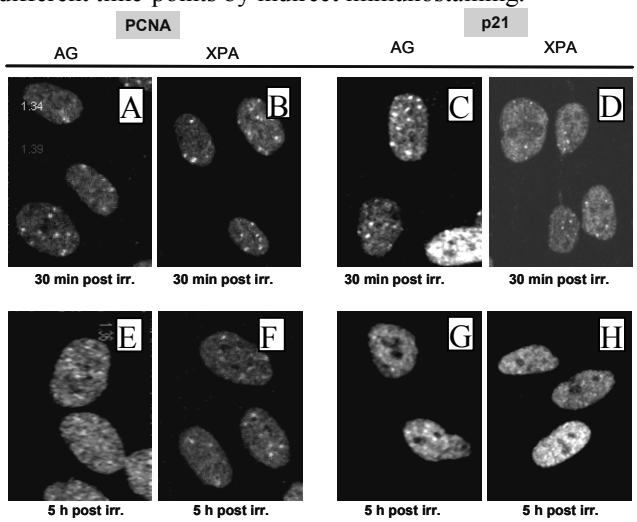

Figure 2: Detection of focal p21 and PCNA accumulations in cell nuclei of NER-proficient (AG-cells) and deficient human fibroblasts (XPA-cells) after irradiation with 7.4 MeV/u argon ions (LET: 1550 keV/µm).

Comparable to the results achieved with UV-light, 30 min post irradiation, both proteins were detected as distinct foci in normal human fibroblasts (AG-cells) (Fig. 2; A, C). In contrast to the UV-results, the NER-deficient XPA-cells (Fig. 2; B, D) showed distinct focal accumulation of both proteins 30 min after irradiation. 6 h after the exposure to argon ions, the focal accumulations of PCNA and p21 were still visible in AG-cells (Fig. 2; E, G) and in XPA-cells (Fig 2; F, H).

These results indicate a role of both proteins in NER as well as in an additional pathway related to the repair of ionizing radiation induced lesions. Further experiments have to be performed to specify this pathway in detail.

References

[1] J. H. Rudolph *et al.,* GSI Annual Report, 2006
[2] S. Katsumi *et al*., J. Inv. Dermatol., 2001
[3] P. Perucca *et al*., JCS, 2006

PCNA and p21 both accumulate very fast at heavy ion-induced DNA damage and become chromatin-associated after X-ray irradiation

J. H. Rudolph, D. Fink, C. Wiese* and G. Taucher-Scholz
GSI, Darmstadt, Germany; *LBNL, Berkeley, CA, USA

Previously, we have described that PCNA (proliferating nuclear antigen; plays a role in DNA replication and DNA repair) and p21 (mainly known as a cell cycle inhibitor) form focal accumulations at heavy ion (HI)-induced DNA lesions. The necessity of the functional interaction between p21 and PCNA was shown for p21 foci formation at HI-induced DNA lesions [1]. Furthermore, we showed that p21 is part of the chromatin-associated protein fraction after DNA damage induction with HI [2]. Here, the kinetics of the PCNA and p21 accumulation at HI-induced DNA lesions is shown to be very similar and both proteins are part of the chromatin-bound protein fraction also after DNA damage induction by X-rays.

PCNA and p21 accumulate at HI-induced DNA lesions with very similar kinetics

Human fibroblasts were irradiated with ^{24}Cr ions (11,4 MeV/u; 2×10^6 P/cm^2) followed by fixation and immunostaining of PCNA and p21 at different time-points (from 5 min up to 16 h) after exposure. At the earliest analyzed time-point, 5 min post irradiation, both proteins were detected as distinct foci (Fig. 1: panel C). Five hours after irradiation with Cr ions, still both proteins could be detected at the DNA lesions (data not shown). However, 7 h after damage induction, hardly any nucleus showed protein foci (Fig. 1 panel B).

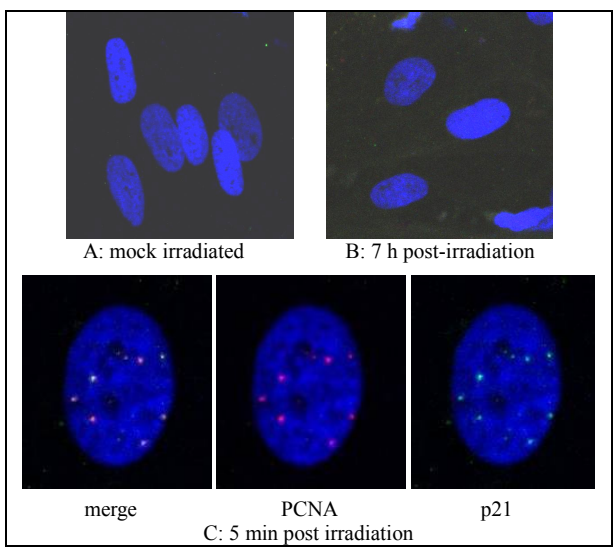

Figure 1: Human fibroblasts nuclei, irradiated with Cr ions, show early focal accumulations of PCNA and p21 that have disappeared at 7 h post-irradiation.

Also experiments with Ni and U ions showed a very similar kinetics for both proteins in foci formation after DNA damage induction by heavy ion irradiation.

PCNA and p21 are part of the chromatin-bound protein fraction after DNA damage induction by X-rays

Based on their similar accumulation kinetics at the DNA lesions and knowing that p21 has a direct PCNA binding site, a possible association of these two proteins with the damaged DNA was investigated after X-rays. Subcellular chromatin-fractionation was done after exposure of the cells to 30 Gy X-rays. An exemplary Western Blot Analysis using immunodetection against PCNA and p21 is shown in Fig. 2. The soluble chromatin fraction of mock irradiated and irradiated cells shows detectable PCNA and p21 signals (Fig. 2: lane 2 and 3). The chromatin-bound protein fraction of the mock-irradiated cells does not have any PCNA nor p21 signal (Fig. 2: lane 5). One hour after irradiation with 30 Gy X-rays, a clearly detectable PCNA signal is obtained; p21 is hardly seen (Fig. 2: lane 6). Three hours after X-ray exposure, also p21 can be detected in the chromatin-bound protein fraction (Fig. 2: lane 7).

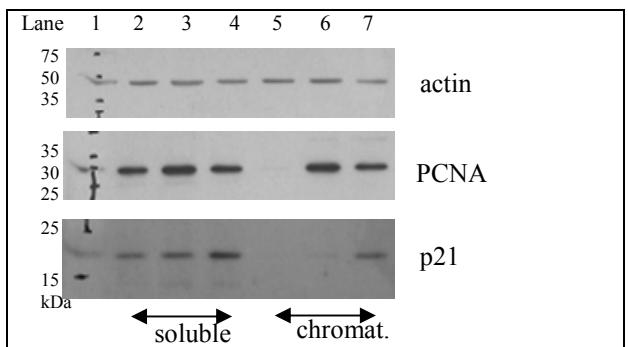

Lane
1 Molecular weight marker RPN 800 and AG lysate
2 mock-irradiated, soluble fraction
3 30 Gy X-ray 1 h post irradiation, soluble fraction
4 30 Gy X-ray 3 h post irradiation, soluble fraction
5 mock-irradiated, chromatin-bound fraction
6 30 Gy X-ray 1 h post irradiation chromatin-bound fraction
7 30 Gy X-ray 3 h post irradiation, chromatin-bound fraction

Figure 2: WB analysis of subcellular chromatin-fractionation.

The results show that p21 and PCNA are gathered at HI-induced DNA lesions with a very similar kinetics and that, as shown for HI [2], they form a chromatin-bound complex after DNA damage induction by X-rays. Studies to elucidate a possible involvement of p21 in repair of radiation induced lesions are currently being performed.

References

[1] J. Rudolph *et al.,* GSI Annual Report 2004, p. 277
[2] D. Fink *et al.,* GSI Annual Report 2005, p. 368

Transient induction of the cell cycle inhibitor CDKN1A but no DNA double-strand breaks in bystander cells after targeted exposure to heavy ions.*

P. Barberet[2], C. Fournier[1], G. Becker[1], B.E. Fischer[2], M. Heiß[2], F. Knauf[1], T. Pouthier[1], Y. Schweinfurth[1], G. Taucher-Scholz[1]
[1]GSI Biophysics and [2]GSI Material Research, Germany

Biological effects in unirradiated cells located near to irradiated cells are called bystander effects. Targeted irradiation of single cells by means of the heavy ion microprobe developed at GSI [1] was used to improve our understanding of these effects on a molecular and cellular basis. The protein of our interest was the cyclin-dependent kinase inhibitor CDKN1A (p21). Based on previous results obtained by broadbeam irradiation, we investigated the spatial distribution of the induction of p21 protein on the level of single bystander cells. We targeted single cells (3%) of a confluent monolayer of normal human fibroblasts (AG1522C) with 5 particles of carbon ions in 2 crossed lines per nucleus. Three hours after exposure we performed immunofluorescence (IF) staining for CDKN1A and 53BP1 protein. 53BP protein is recruited to sites of DNA damage immediately after irradiation by forming foci and is used to identify the targeted cells unambiguously (see figure 1a: the irradiated cell indicated with an arrow and enlarged in the box).

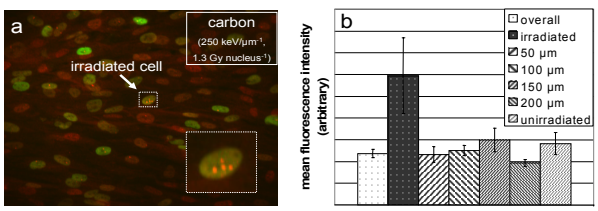

Fig. 1: Radial distribution of the expression of CDKN1A after targeted microbeam-irradiation of single cells (arrow) with carbon ions. (a) IF staining (merged) for CDKN1A (whole nucleus) and 53BP1 (foci). (b) Mean CDKN1A IF intensities according to the radial distance of up to 200 µm are shown.

The IF-intensities of CDKN1A protein per cell nucleus were quantified by means of software packages [2]. The distribution of the mean intensities according to the radial distance to the targeted cell were evaluated. The results are shown in figure 1b. Up to the radial distance of 200 µm the CDKN1A protein amount per nucleus revealed no clusters of cells bearing an increased CDKN1A protein level and the distribution of the intracellular levels of CDKN1A protein was very heterogeneous.
To see whether the overall enhancement of CDKN1A in broadbeam experiments [2] is also observed under microbeam conditions, the cells were irradiated in especially constructed divided radiation chambers [3] to separate control and bystander cells but allowing to minimize variations in IF staining. The mean value per cell nucleus comparing the overall CDKN1A levels of control and bystander cells showed a slight induction in bystander cells comparable to the broadbeam experiments [3]. As shown in figure 2, the distribution of the values for the individual cells revealed as well differences between the control and the bystander cells. The individual cells are grouped in bins by their intensity of IF staining. The mean value of the control population is indicated by vertical dashed-dotted lines. Among the bystander cells, approximately 80 % of the cells show a CDKN1A protein amount comparable to most of the control cells (below or at the mean value ±1 SD), whereas approximately 20 % of the cells have an elevated level. The observed overall enhancement of the CDKN1A level can be attributed to this subpopulation of bystander cells, but we could show that these cells are not necessarily located in the direct neighbourhood of the targeted cells.

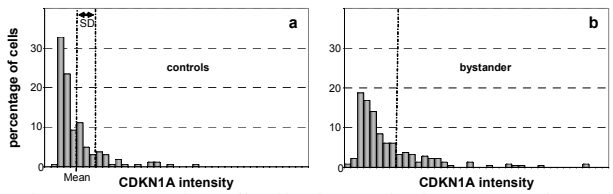

Fig. 2: Intensity distribution of the expression of CDKN1A, 3h after targeted microbeam-irradiation with carbon ions in a divided chamber. One representative data set of control mock-irradiated cells **(a)** or bystander plus irradiated cells **(b)** are shown. The mean value for the control population ±1 SD is indicated by vertical dashed-dotted lines [2].

In addition, we investigated DNA damage as a potential basis for the CDKN1A induction in bystander cells. First results on the formation of γ-H2AX foci (indicating DNA double strand-breaks) after irradiation did not show significant differences between bystander and control cells. This is consistent with our observation that the formation of micronuclei, being an indicator of chromosomal damage is not enhanced in bystander cells [4]. Taken together our data presented here suggest a CDKN1A induction that seems not to be triggered by the occurrence of DNA damage in bystander cells. As reported previously, the CDKN1A induction is transient and causes a temporary cell cycle delay but has no impact on the cellular differentiation pattern during the following days [2].

References

[1] M. Heiß *et al*., Radiat. Res., (2006) **165**, 231-239
[2] C. Fournier *et al*., Radiat. Res., (2007) **167**, 194-206
[3] P. Barberet *et al*., Radiat. Res., (2006) **166**, 682-684
[4] C. Fournier *et al*., GSI Report, (2004), 288

* work partially supported by EU Grant CELLION MRTN-CT-2003-503923 and by BMBF (grant 02S8203)

Fast recruitment of DNA-PK$_{cs}$ at DNA double-strand breaks

B. Jakob[1], J.Splinter[1], Y. Schweinfurth[1], G. Becker[1], D. Chen[2], and G. Taucher-Scholz[1]
[1]GSI, Darmstadt, Germany; [2]University of Texas Southwest Medical Center, Dallas, TX 75390-9187, U.S.A.

Introduction

DNA damage and in particular double-strand breaks (DSBs) pose a major threat to the preservation of genome integrity. Mammalian cells have developed efficient DNA repair mechanisms in response to DNA damage. In the non-homologous end-joining (NHEJ), one major pathway of DSB-repair, the DNA-dependent protein kinase (DNA-PK) is supposed to participate in the early stages of DNA end detection and processing. The DNA-PK comprises the Ku subunits (Ku70 and Ku80) and the catalytic subunit DNAPK$_{cs}$. The aim of this study was to visualize and analyse the recruitment of DNAPK$_{cs}$ to ionizing radiation induced DNA DSBs.

Results and Discussion

To measure the DNA-PK$_{cs}$ recruitment *in vivo,* we took advantage of the extremely localized dose deposition of charged particle beams. The application of this focal type of irradiation generates discrete sites of subnuclear damage including DSBs, as shown by the terminal transferase assay (Fig1).

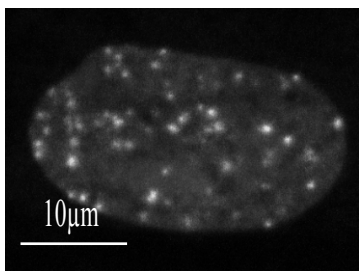

Figure 1: Human AG1522 fibroblast nucleus after irradiation with 4.1.MeV/u Bi ions. Bright spots arise from the addition of fluorescent-labelled deoxy-uridines at sites of DSBs by terminal transferase.

By upgrading and optimizing our remote controlled microscope [1] at the low energy beamline, after irradiation with low energy heavy ions it was possible to observe the development of irradiation induced protein accumulations in living V3 hamster cells expressing DNAPK$_{cs}$-YFP protein (Fig.2). The site of occurrence of these foci could be correlated to sites of ion traversals (data not shown) by the technique described in [1].

Using the fast acquisition mode (30 Hz) of the new Hamamatsu C7190-53 EBCCD, irradiation in a single macropulse and acquisition triggering, it was possible to resolve the fast recruitment kinetic of DNAPK$_{cs}$ to ion induced DSBs (Fig.3). Data analysis and application of a first order binding model revealed a recruitment time of about 12s for the initial phase (Fig.3 left). Protein accumulation started to become visible only 1 to 2 s after ion impact (Fig.3 left insert).

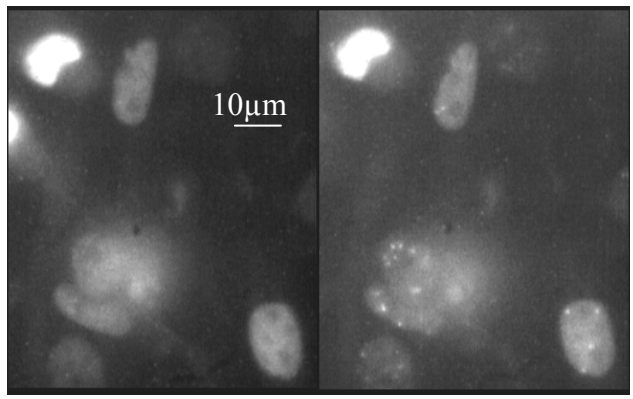

Figure 2: Living nuclei of V3 hamster cells expressing a chimeric DNAPK$_{cs}$-YFP construct, before (left) and after (right) irradiation with 4.1 MeV/u Pb ions at the beamline microscope [1]. Foci formed at the sites of ion traversals indicate recruitment of DNAPK$_{cs}$ to DSBs.

The observed kinetic behaviour thus confirms the recruitment times measured in earlier experiments using uranium ions (t = 12.8s) or UV laser irradiation [2].

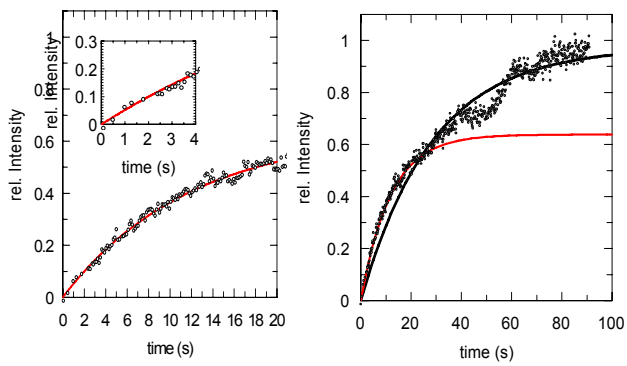

Figure 3: Recruitment kinetic of DNAPK$_{CS}$-YFP in V3 cells after irradiation with Pb. Left: Initial fast phase showing a recruitment time constant of 12s. Insert: Increased signal is already detectable about 1s after irradiation. Right: Longer measurements show a subsequent slower rise up to the saturation level (t about 28 s, for comparison, the fit of the fast phase is included)

For the first time, it was possible to observe the recruitment of DNAPK to ionizing radiation induced lesions in living cells. The quick accumulation and the lack of a lag phase implicate DNAPK$_{cs}$ as one of the fastest responding proteins after ionizing radiation. The results indicate a role in the early stages of DSB repair.

References

[1] B. Jakob et al., Rad. Res. 163 (2005) 681.
[2] N. Uematsu et al., JCB (2007), in press.

Changes in migration and beta-3 integrin expression of U87 glioma cells after conventional and heavy ion irradiation*

K. Goetze[1], W. Mueller-Klieser[1], G. Taucher-Scholz[2] and M. Scholz[2]
[1]University of Mainz, Germany; [2]GSI, Darmstadt, Germany

The formation of metastasis is one thread in clinical therapy of solid tumors and is directly linked to the migratory potential of the tumor cells. The expression of integrins and their activation through phosphorylation on the other hand play a major role in cell invasion and migration [1]. Most studies on tumor cell motility and migration are focused on their inhibition and only a few are concerned with the promotion of cell migration through standard clinical therapy. The possible side effects of radiotherapy as one possible way of curing malignant disease in clinical oncology are not well understood. After sublethal irradiation Wild-Bode et al. [2] for example, showed an enhanced migration of glioma cells and Abdollahi et al. [3] showed an upregulation of activated beta-3 integrin after irradiation of glioma cells. The informations that are currently available about the effects of particle irradiation on tumor cell migration are very scarce (Ogata et al. [4]), and the effect of integrin expression after heavy ion treatment has not yet been investigated.

Recent results in our group indicate that pro- and anti-migratory effects depend on the microenvironment of the cells and the type of radiation. We are therefore interested in the connection between cell migration, integrin expression and irradiation.

To quantify the migration of U87 human glioblastoma cells, a standardized Boyden chamber assay 24 h after irradiation was performed. The cells were treated with 10 Gy in monolayer culture under well-defined conditions using conventional (250kV X-ray) or ^{12}C particle radiation (Mid of 1cm SOBP). In parallel to the migration assay, cell lysates were prepared from untreated and irradiated cells to study the expression of activated phosphorylated beta-3 integrin in a western blot.

The effect of irradiation on tumor cell migration is shown in table 1 and depends on the type of radiation. .

Table 1: Relative cell migration of U87 cells 24h after irradiation with X-rays or heavy ions (^{12}C). (Control = 100%).

	X-ray	^{12}C
0 Gy	100%	100 %
10 Gy	123%	5%

24 h after X-ray treatment U87 cells showed an enhanced migration of 23% compared to untreated cells. Irradiation with heavy ions inhibited the cell migration almost completely to 5% of the control level, reproducibly.

Western blotting of phosphobeta-3 integrin showed an upregulated expression of this protein in U87 cells in both types of tested irradiation (Figure 1).

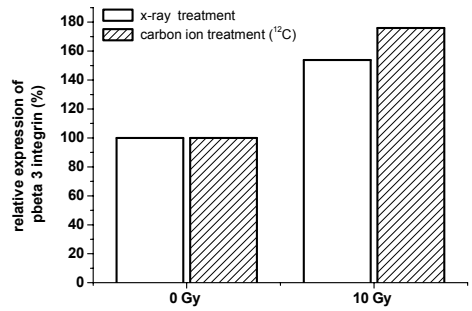

Figure 1: Relative expression level of pbeta-3 integrin 24h after irradiation with X-rays (n = 2) or heavy ions (^{12}C; n = 2).

After conventional irradiation the relative expression of activated beta-3 integrin increased to 153% compared to untreated cells. Particle irradiation increased the expression level even more to 176% compared to control cells.

These results indicate the absence of a correlation between the migration of U87 cells and the activation level of beta-3 integrins. Both tested radiation types increase the amount of phosphorylated beta-3 integrin although they have opposing effects on cell migration. Therefore the radiation induced cell migration of U87 cells might be dependent on other integrins, e.g. beta-1 integrin.

References

[1] J. D. Hood and D. A. Cheresh, Nature Rev Cancer. 2: 91-100, 2002.
[2] C. Wild-Bode, M. Weller, A. Rimner, J. Dichgans, W. Wick, Cancer Res. 61: 2744-2750, 2001.
[3] A. Abdollahi, D. W. Griggs, H. Zieher, A. Roth, K. E. Lipson, R. Saffrich, H.-J. Gröne, D. E. Hallahan, R. A. Reisfeld, J. Debus, A. G. Niethammer, P. E. Huber, Clin Cancer Res. 11: 6270-6279, 2005.
[4] T. Ogata, T. Teshima, K. Kagawa, Y. Hishikawa, Y. Takahashi, A. Kawaguchi, Y. Suzumoto, K. Nojima, Y. Furusawa, N. Matsuura, N., Cancer Res. 65: 113-118, 2005.

* Work supported by F&E grant MZ/MÜK of the GSI Darmstadt

Possible molecular pathways involved in cell death in human normal and tumour cells after exposure to carbon ion beams: Implication of TP53, ceramide and AIF*

A.E. Meijer[1], M.R. Edgren[1], B.S. Eriksson[1], G. Alphonse[2], J. Bodennec[2], M. Maalouf[2], C. Rodriguez-Lafrasse[2], G. Becker[3], C. Fournier[3] and G. Taucher-Scholz[3]

[1]Karolinska Insitutet, Department of Oncology-Pathology, Stockholm, Sweden;
[2]Molecular and Cellular Radiobiology Laboratory, Lyon-Sud, France, [3]GSI, Darmstadt, Germany.

Introduction

Knowledge of the molecular pathways involved in cell death in normal and tumour cells after exposure to accelerated ions could contribute to an improved prognosis of patients with malignant resistant tumours.

We have previously reported on a clear LET dependence for clonogenic cell survival for the human melanoma cell line AA after boron ion exposures [1, 2]. Also, the human glioma cell line M059K, proficient in DNA-PK_{cs} but mutated in TP53, are more sensitive to high LET nitrogen ions than low LET γ-rays. The M059J cell line, deficient in both DNA-PK_{cs} and TP53, does not show any difference in survival after low and high LET radiation exposure [3]. For the apoptotic responses the picture is more complex and seems to be dependent on the gene status and also the cell cycle progression in a time dependent manner [2, 4, 5]. In addition, there is evidence for caspase-independence after high LET nitrogen ion irradiation [5] but the AIF and the ceramide/SMase pathways are instead involved (data to be published).

Here we report on clonogenic cell survival for two different human cell lines. These survival data are important as a basis to assess other endpoints, i.e. apoptosis, necrosis, autophagy, senescence, cell cycle responses as well as molecular responses (TP53, ceramide and AIF), at comparable doses or survival levels.

Materials and methods

Human tumour cells, the melanoma cell line AA with wild type (*wt*) TP53, and the small cell lung cancer cell line (SCLC) U-1690 with a TP53 point-mutation, were used. Cells in monolayers were exposed to ^{12}C-ions (11.4 MeV/u or 200 MeV/u, corresponding to LET of 170 and 30 eV/nm, respectively). As reference low LET radiation X-rays were used.

Results and conclusion

The survival data presented in figure 1 show dose and LET dependence for both cell lines studied. The SF_2 values for the AA cells were 0.400, for X-rays, and 0.265 and 0.092 for carbon ions at 30 and 170 eV/nm, respectively. For the U-1690 cells the SF_2 values were 0.538, 0.308 and 0.081 for X-rays and ^{12}C-ions at 30 and 170 eV/nm, respectively. The calculated RBE values at different survival levels are shown in table 1.

These preliminary results show that irradiation with carbon ions results in important clonogenic cell death in both a dose and a LET dependent manner. The type of cell death and the molecular pathways involved have now to be investigated and compared for the different cell lines at different LET. Also, additional human normal (non-tumour) cells will be investigated.

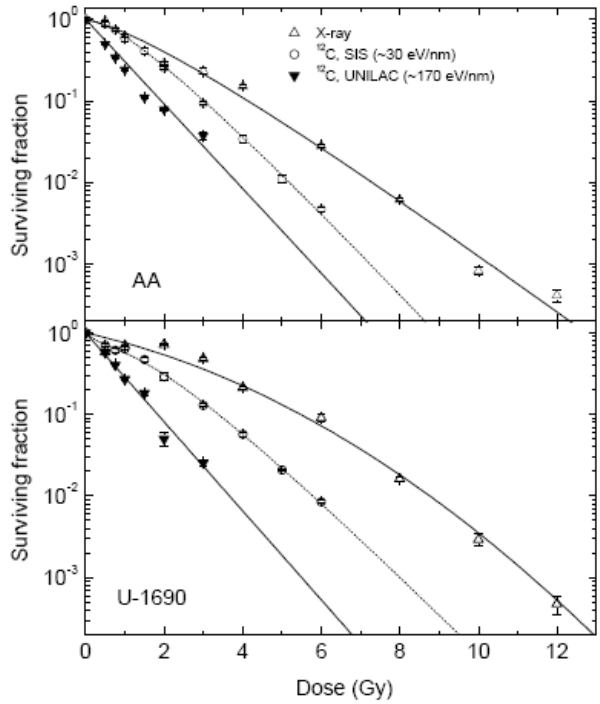

Figure 1: Survival fraction as a function of single absorbed doses of carbon ions and X-rays.

	SF	RBE U-1690	RBE AA
SIS (~30 eV/nm)	0.1	1.6	1.4
	0.2	1.6	1.4
	0.5	1.8	1.3
UNILAC (~170 eV/nm)	0.1	3.0	2.1
	0.2	3.3	2.3
	0.5	4.0	2.8

Table 1. RBE values at different survival levels.

References

[1] Persson *et al.,* Int J Radiat Biol 78:743 (2002)
[2] Meijer *et al.,* Int J Radiat Biol 81:261 (2005)
[3] Lind *et al.,* Radiat Res 160:366 (2003)
[4] Holgersson *et al.,* Int J Radiat Biol 79:611 (2003)
[5] Holgersson *et al.,* Int J Radiat Oncol Biol Phys 61:915 (2005)

* Work supported by the Swedish Cancer Society, the Stockholm Cancer Society, the King Gustaf V Jubilee Found, VINNOVA and Founds of the Karolinska Institutet.

Radiation-induced apoptosis in T-lymphocyte long-term cultures irradiated with carbon ions and X-rays*

H. Hofman-Hüther[1,#], H. Peuckert[1], and P. Virsik-Köpp[2]

[1]Dept. of Radiotherapy and Radiooncology, University of Göttingen, Germany; [2]Dept. of Environm. Medicine, University of Göttingen, Germany.

Introduction

In the present study, we investigated the delayed radiation-induced apoptosis in long-term lymphocyte cultures. The purpose of this study was to compare the efficiency of high LET carbon ions and low LET X-rays.

Material and Methods

The radiation-induced apoptosis was studied in descendants of cells from two healthy donors irradiated with 3 different doses of 100 MeV/u carbon ions or 250 kV X-rays. Lymphocytes were taken from the bulk cultures at different sampling times up to 41 days. Cells were stained with 2 µg/ml Hoechst 33342 and 10 µg/ml acridine orange. Apoptotic cells were identified by the typical morphological changes of their nucleus. 500 cells were analysed. These results were verified by TUNEL assay (data not shown).

Results

Figure 1 shows the relative percentage of apoptotic cells for both donors and both radiation qualities. The spontaneous apoptotic rate was constant in donor 2 (median = 24%). In donor 1 the initial rate of about 12% increased then to a similar level (median = 28%). The X-ray-induced apoptosis displayed a maximum on day 22 in both donors. After exposure to 100 MeV/u carbon ions, this maximum occurred later, on day 29. The delayed apoptotic response showed no clear dependence upon radiation dose, culture time, and radiation quality. The high spontaneous apoptotic rate persisting and even increasing in long-term lymphocyte cultures (as seen for our donors) makes this system quite unsuitable for the study of delayed apoptosis after irradiation with low doses. At higher doses, where significant radiation-induced apoptotic rates are induced, the system might offer a possibility to compare the effects of different radiation qualities.

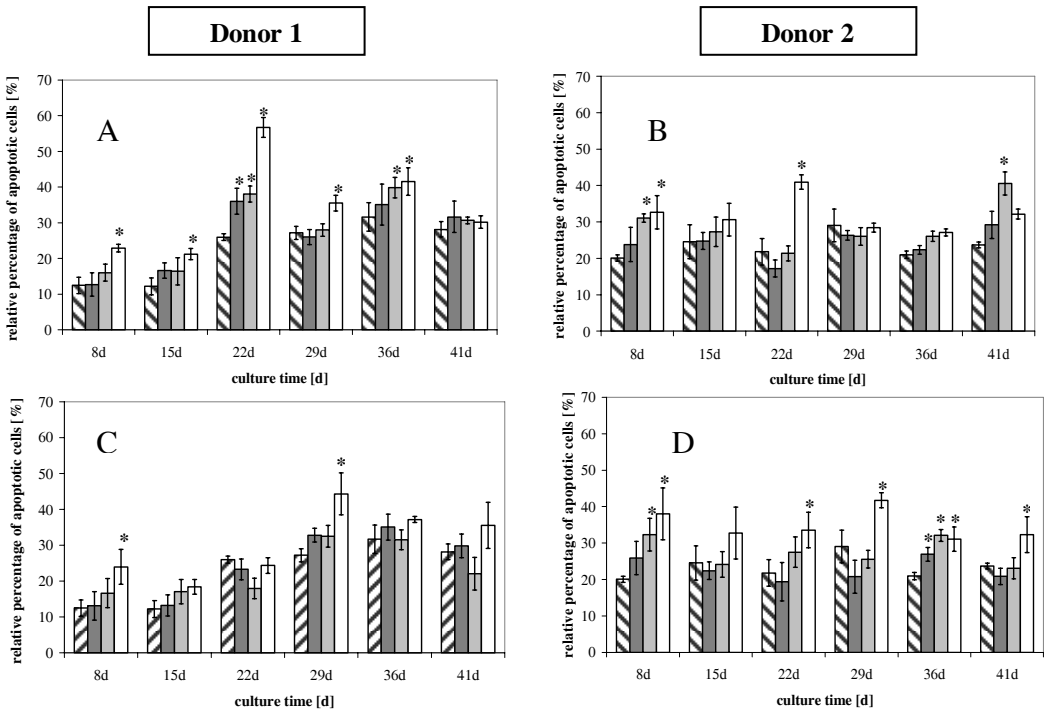

Fig.1 Relative proportions of apoptotic cells in unirradiated control cells (▨) and in cells irradiated with different doses of 250 kV X-rays (1Gy (▩), 2 Gy (▩) and 4 Gy (□)) or with different doses of 100 MeV/u carbon ions (0.25 (▩), 0.5 Gy (▩) and 2 Gy (□)) are shown for donor 1 (A and C) and for donor 2 (B and D) for X-rays and ions, respectively. At least 500 cells were analysed in each sample. Vertical error bars represent standard deviations. *(*) apoptotic rate in irradiated cells is significantly different from control rate ($\alpha = 0.05$) as tested by Dunnett´s t-test.*

* Work supported by BMBF-02S8203

#Hana.Hofman@gmx.de

DNA fragmentation – dependence on the radiation quality.

K. Psonka[1,2], Th. Elsässer[1], E. Gudowska-Nowak[1,2], and G. Taucher-Scholz[1]
[1]GSI, Darmstadt, Germany; [2]Institute of Physics, Jagiellonian University, Kraków

Introduction

Ionizing radiation produces a plethora of lesions in DNA including strand breaks (single or double) and alteration to bases. Double-strand breaks (DSBs) leading to DNA fragmentation are considered to be the most critical lesions resulting in cell killing, cancerogenesis or mutations [1] High-LET radiation produces more complex and localized damage than X-rays due to induction of spatially correlated DSBs (clusters). As we previously have shown [2], Atomic Force Microscopy (AFM) gave an opportunity to direct visualize DNA molecules and therefore to image induced DSBs in irradiated plasmid DNA solutions. Within this method induced DNA fragments can be measured and the fragments length distributions can be derived. Parallel to the experimental work, a model was developed, originally based on the framework of Local Effect Model [3], to calculate the formation of spatially correlated DSBs in plasmid DNA.

Distributions of fragment lengths – comparison of AFM and the model

To induce DSBs, plasmid supercoiled DNA (ΦX174) was irradiated in moderate radio-protective buffer (20 mM Hepes, pH 7.4). Solutions of DNA were irradiated with X-rays (low-LET radiation) or with 3.9 MeV/u Ni ions. Irradiated samples were scanned with AFM. Using established differentiation criteria for AFM, molecules with different conformation forms (supercoiled, relaxed and linear) were identified in recorded images [4]. Lengths of linear fragments produced by the radiation were measured. The recorded lengths allow to distinguish between molecules damaged by a single DSB (full plasmid length) or by multiple DSBs (several shorter fragments). Measured lengths were plotted as normalized histograms for different doses and radiation qualities.
Fig. 1 presents exemplary distributions of fragment lengths produced in ΦX174 irradiated with X-rays or Ni ions as derived from the AFM analysis. Fragmentation profiles show the dependence on the radiation quality. Irradiation with 370 Gy of X-rays produces fragments with full plasmid length whereas the same dose of ions induce fragments in the whole length range accessible to the AFM imaging. As expected the differences decrease for a high radiation dose – nevertheless the shift toward short fragments in more steeper in case of Ni ions.
In addition to the experimental approach, a semi-empirical model based on the pattern of local energy deposition, was used to calculate fragment length distributions. The model was adapted to experimental conditions taking into account constraints of AFM imaging and image processing (described elsewhere [5]). The comparison of calculated distribution to experimental data is shown on Fig. 1. Qualitatively, both distributions are in agreement. In case

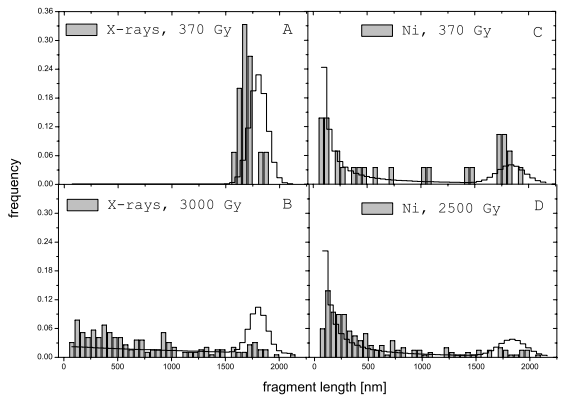

Figure 1: Distributions of fragment lengths induced by X-rays (A, B) or Ni ions (C, D) in supercoiled plasmid DNA (ΦX174) – comparison of the experimental AFM data (bars) to the model calculations (stepline).

of X-rays there is more fragments produced than predicted by the model. It can be partially explained by the fact that during the irradiation some additional lesions are induced that are transformed into further DSBs detected. On the other hand, for ions AFM analysis revealed less amount of shortest fragments ($l < 250$ nm) partially due to limitations in length detection.
Based on the model, differential effects of X-rays and ions rely only on differences in the distribution of deposited energy. Therefore, in case of particle radiation, the agreement observed between fragment length distributions and model calculations provides direct evidence for clustered DSBs on simple DNA molecules due to the inhomogeneous dose distribution based on particle track structure.

References

[1] E.L. Alpen, Radiation Biophysics, Academic Press, San Diego, 1998

[2] K. Psonka et al., GSI Annual Report, 2005, 363

[3] M. Scholz et al., Adv. Space res. 18 (1995), 5

[4] K. Psonka et al., J. Phys: Cond. Matter 17 (2005), S1443

[5] Th. Elsässer et al., this report

Fragment distributions of DNA molecules after X-ray and C^{12} ion irradiation

M. Brezeanu, F. Träger, and F. Hubenthal
Institute of Physics and Center for Interdisciplinary Nanostructure Science and Technology – CINSaT,
University of Kassel, Germany

Investigation of DNA damages induced by heavy ions is of great interest for a better understanding of the processes which appear in clinical radiotherapy and are responsible for the destruction of the cancer cells. The most serious damages of DNA molecules are double-strand breaks (DSB), i.e. the rupture of both DNA strands in the range of a few base pairs and single-strand breaks (SSB), when one of the DNA strands is broken [1]. In particular, DSBs lower effectively the cell repair rate and leads often to cell death. Thus, heavy ion irradiation of tumour cells has been used very successful in cancer therapy. However, a detailed understanding of the processes which occur on the molecular level, leading to this effective cell death, is still lacking. Conventional methods, e.g. gel-electrophoresis measurements, are suitable to analyse the percentage of supercoiled and relaxed molecules and also linear DNA fragments, but it can not provide detailed information about the fragment distribution [2]. The latter can be achieved by scanning force microscopy (SFM) which permits direct visualisation and measurement of individual DNA fragments with an accuracy of a few nanometers.

In this contribution we present a SFM analysis of radiation-induced damages in ΦX174 plasmids in 20 mM Hepes solution after X-ray and C^{12} ion irradiation at a dose of 500 Gy. For sample preparation, 3µl plasmid solution in 10 mM $MgCl_2$ [3] has been deposited on mica substrates and rested in air for 3 minutes. Subsequently, the substrates were washed with 400 µl double distilled water and dried with nitrogen. Nine samples have been prepared for each irradiated solution and around 10 images were recorded for each sample. The samples have been imaged in air with tapping mode using a CP-R microscope from Veeco Instruments. All images were recorded with a scan area of 3 µm x 3 µm and a resolution of 512 pixels x 512 pixels. The length of the fragments has been analysed using ImageJ software.

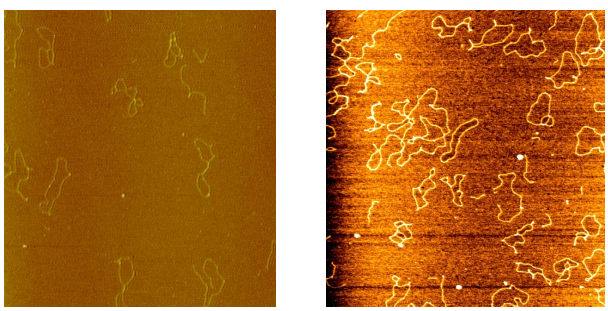

a) b)

Figure 1 SFM images of plasmids after irradiation with X-rays (a) and C^{12} ions (b); D = 500 Gy

Figure 1 depicts SFM images of ΦX174 plasmids after irradiation with X-rays (Fig 1a) and C^{12} ions (Fig. 1b). In both images a clear length distribution of the molecules can be seen. However, after irradiation with C^{12} ions a significant higher amount of small fragments were observed accompanied by a reduction of larger ones, compared to X-ray irradiation.

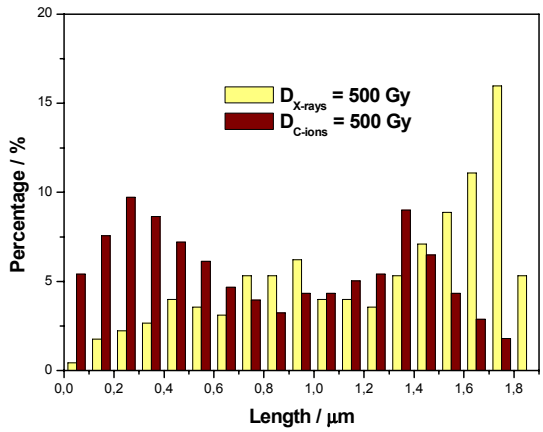

Figure 2 Fragment distributions after irradiation with X-rays and C^{12} ions at 500 Gy.

In order to obtain a fragment distribution after irradiation, 170 images have been analysed in detail and the results are presented in Fig. 2. The histograms show clearly a higher amount of small fragments (around 45% of the initial number) in the range from 50 nm to 700 nm after irradiation with C^{12} ions compared to X-ray irradiation, where only 13% are in the same length scale. Furthermore, C^{12} ions generate very small fragments with lengths below 50 nm, supposed to be due to the highly localized energy deposition. Interestingly, the fragment distribution after irradiation with C^{12} ions shows a bimodal distribution with peaks centred at 300 nm and 1400 nm. The origin of this distribution is still under investigation. In conclusion, the analysis presented in this contribution demonstrates the effectiveness of heavy ion irradiation and supports the theoretical concept of track structure for heavy ions which are supposed to be responsible for the efficiency of heavy ions in cancer therapy.

References

[1] E.J.Hall "Radiobiology for the Radiologist", J.B.Lippincott Press, 1994, p.15.
[2] D.Pang, J.E.Rodgers, B.L.Berman, S.Chasovskikh, and A.Dritschilo, Radiat. Res. 164 (2005) 755.
[3] H.G.Hansma, Annu.Rev.Phys.Chem 52 (2001) 71.

DNA Damage after High-LET Exposure

A. Krempler[1], M. Ensminger[1], G. Taucher-Scholz[2], and M. Löbrich[1]
[1]Department of Biophysics, University of the Saarland, Germany; [2]GSI, Darmstadt, Germany

It has been known for several years that high-LET-induced DSBs are generally more slowly repaired than breaks induced by photon irradiation. Moreover, the level of residual DSBs after prolonged repair incubation appears to correlate with the cell killing capacity of a given radiation quality over a substantial LET range.

One potential explanation for the slower repair after high-LET radiation relates to the spatial distribution of DSBs along ion tracks. In previous studies performed at the GSI using ion irradiation, we have investigated the cellular capacity to rejoin DSBs within fragments of different size. The results suggest that the proximity of neighboring DSBs does not significantly affect the repair process. Interestingly, for all size ranges analysed, high-LET radiation-induced fragments are removed more slowly than X-ray induced fragments of the corresponding size range [1]. This led us to the second potential explanation for the compromised DSB repair kinetics of high-LET radiations. Owing to the high ionisation density of high-LET particles, it is possible that DSBs are generally more complex with additional lesions in very close proximity to the DSB. These breaks require processing before repair. This "complexity idea" would suggest that DSBs are, on average, more complex for radiation qualities that show a high level of un-rejoined DSBs and a high cell killing effectiveness.

Recently, we have reported that ATM- and Artemis-deficient human fibroblasts show a similar, small repair defect after irradiation with X-rays or γ-rays that persists for many days [2, 3] (Fig.1A). We further demonstrated that ATM and Artemis operate in the same repair process. ATM- and Artemis-deficient cells are specifically defective in the repair of DSBs repaired with slow kinetics in repair-proficient cells. Interestingly, the fraction of breaks repaired depends upon the complexity of the DSB ends. This latter point is supported by the observation that a higher proportion of the DSBs induced by α-particles is repaired in a manner dependent upon ATM and Artemis (Fig.1B). Moreover, the process is dispensable for the repair of "clean" DSBs generated by etoposide, an inhibitor of topoisomerase II (Fig.1C). From this data we propose that Artemis, a nuclease, functions to process a fraction of non-ligatable DNA ends (approximately 10 % of the DSBs) prior to rejoining.

It is tempting to speculate that the DSBs requiring ATM and Artemis processing also determine the level of high-LET-induced cell killing. Therefore, we measure the LET-dependence of the proportion (and absolute yield) of those DSBs that require ATM and Artemis after various radiation qualities. Stationary G_0-phase primary human fibroblasts are irradiated with different ions or X-rays. After specific repair times the cells are subjected to pulsed-field gel electrophoresis. First results from the irradiation of hTert-immortalised human wild type (WT) and Artemis fibroblasts with ^{134}Xe- and ^{54}Cr-ions or 95kV X-rays suggest that the proportion of unrepaired, ATM/Artemis-dependent DSBs correlates with the LET of the radiation used (data not shown). Based on these preliminary data we will now extend the studies and use a variety of ions with different LET to quantify the proportion of complex breaks. In addition, γH2AX analysis will be used to investigate the repair of individual DSBs after low doses.

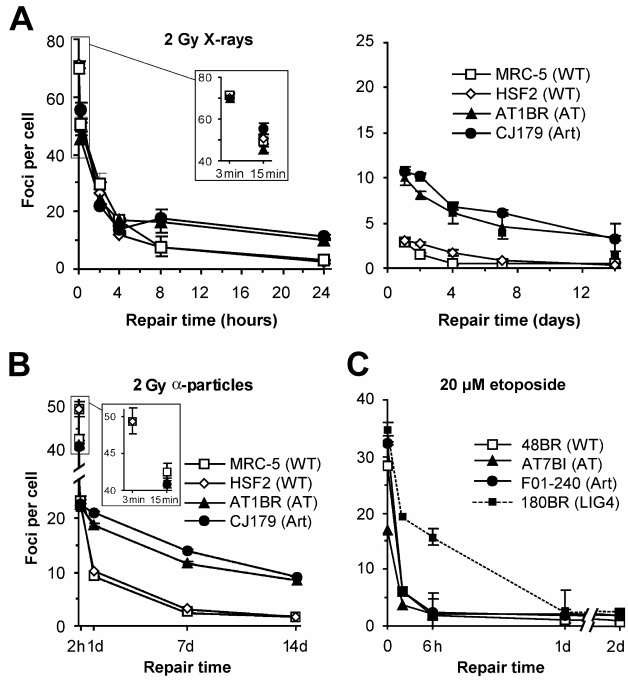

Figure 1: γH2AX analysis in WT, AT and Artemis cells after A) 2 Gy X-irradiation, B) 2 Gy α-particles or C) 20 μM etoposide (modified from [3]).

References

[1] A. Fricke, M. Kühne, and M. Löbrich, GSI Scientific Report 2006, p. 366

[2] M. Kühne, E. Riballo, N. Rief, K. Rothkamm, P.A. Jeggo, and M. Löbrich, Cancer Research 64 (2004) 500-508

[3] E. Riballo, M. Kühne, N. Rief, A. Doherty, G.C.M. Smith, M.J. Recio, C. Reis, K. Dahm, A. Fricke, A. Krempler, A.R. Parker, S.P. Jackson, A. Gennery, P.A. Jeggo, and M. Löbrich, Molecular Cell 16 (2005) 715-724

Biophysical Modelling of DNA fragmentation

Th. Elsässer[1], K. Psonka[1,2], M. Scholz[1], G. Taucher-Scholz[1], E. Gudowska-Nowak[2], S. Brons[3]
[1]GSI, Darmstadt, Germany; [2]Jagiellonian University, Cracow, Poland;[3] Heidelberg Ionen Therapie (HIT)

The induction of double strand breaks (DBSs) is considered to a severe radiation-induced damage. The investigation of fragment distributions of plasmid DNA after heavy ion irradiation can give insight into the higher fragmentation due to localized energy deposition around ion tracks. In recent years AFM pictures of fragmented supercoiled plasmid DNA were taken and analyzed. In this report, we introduce a numerical model based on the Local Effect Model (1) which predicts the experimental results under consideration of certain constraints of the detection procedure.

Theoretical Model

Heavy ion irradiation can induce DSBs in the DNA molecule which leads to a certain fragment distribution. In general it can be expressed by

$$F_D(l) = \sum_{m=0}^{\infty} f(l,m)\, p(m, \overline{n}_{DSB}), \qquad (1)$$

where p(m, $\overline{n}_{DSB}$) is the probability of m DSBs provided an average number of $\overline{n}_{DSB}$ DSBs, f(l,m) is the conditional probability of finding a fragment of length l after m DSBs and D denotes the dose. In general, Eq. (1) holds for initially supercoiled and linear molecules, whereas in the following we will restrict ourselves to the description of supercoiled molecules. We use the Local Effect Model to calculate the average number of DSBs according to the corresponding yield after photon irradiation and apply Eq. (1). The results for an irradiation of supercoiled ΦX174 DNA (total length of 5386 bp) with 3, 300, 3000 and 30000 Gy of 4 MeV/u nickel ions (LET=3950 keV/µm) (corresponding to 0.006, 0.6, 6, and 60 hits per molecule, repectively) are depicted in Fig. 1a). In general, the frequency of finding short fragments increases with dose. For doses up to 3000 Gy, the peak at full plasmid length also increases due to the production of full size linear plasmids from the supercoiled conformation. For the large energy deposition of 30000 Gy, all initially supercoiled molecules were hit more than once on average and the proportion of plasmids with the full length decreases.

Experimental constraints

For a reasonable comparison of theoretical results with experimental data we need to carefully analyze the constraints imposed by the limitations of the AFM measurement and the subsequent analysis. We need to consider the restricted image resolution which sets a lower detection limit. The binning of data has to be taken into account as well as the blurring of the full length plasmids due to the length measurement procedure. Additionally, only relative values of the different fragment lengths can be determined requiring a normalization according to the number of detected fragments. In Fig. 1b), the same fragment distributions as in Fig. 1a) are depicted including experimental constraints. Due to the lower detection limit a large proportion of small fragments is not resolved. In combination with the adapted normalization, the differences of the fragment distributions strongly decrease.

Conclusion

We have developed a theoretical model to predict the fragment distribution of linear and supercoiled DNA molecules after heavy ion irradiation taking into account the limitations imposed by the experimental detection procedure. A comparison with experiments is shown in (2). Additionally, it is a useful tool to find the best ion species to reveal the impact of localized dose deposition of heavy ion tracks on the fragment distributions.

References

1. M.Scholz and G. Kraft, Adv. Space Res. 18 (1996)
2. K. Psonka et al., this report

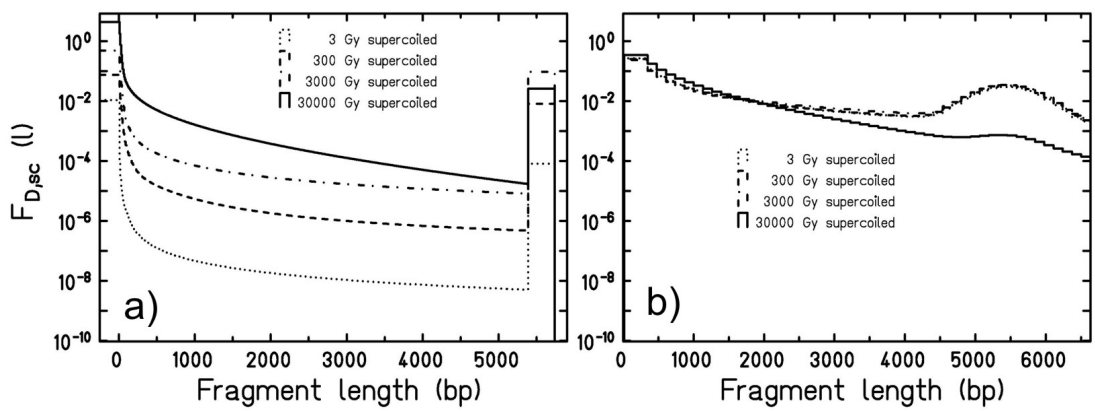

Figure 1) Frequency distribution $F_D(l)$ after irradiation with 4 MeV/u Ni. The bars at l=0 and l=L are artificially broadened for better readability. a) Theoretical prediction according to Eq. (1) b) Consideration of experimental constraints bin sizeΔl=130 bp, lower detection limit l_0=150 bp and resolution σ_l=400 bp.

Search for a chromosomal fingerprint of high LET exposure*

S. Sommer[1], M. Kreim[1], R. Lee[1], S. Ritter[1], L. Melnikova[2], E. Nasonova[2], E. Gudowska-Nowak[3]
[1]GSI, Darmstadt, Germany; [2]JINR, Dubna, Russia, [3]Jagellonian University, Krakow, Poland

Recently there has been considerable interest in identifying cytogenetic biomarkers of radiation exposure that allow both to estimate the dose to which an individual has been exposed and to determine, whether the initial exposure was to low or high LET radiation [1, 2, 3]. Taking proximity effects into account it has been hypothesized that high LET exposure will enhance the yields of intra-arm relative to inter-arm intrachanges and intrachanges relative to inter-chromosomal aberrations. However, published data are controversial.

To contribute to this issue, we reanalysed 30 data sets generated at GSI (Darmstadt) for human lymphocytes as well as for Chinese hamster cells (V79, CHO-K1, xrs5). In the experiments cells were exposed in G1-phase to heavy ions (C, Ne, Ar, Kr, Fe and Au ions) covering an LET range of 13 to 4000 keV/µm. For comparison, X-ray experiments were performed. More than 80000 first generation metaphases were scored on slides stained with the fluorescence-plus-Giemsa technique. For further details see [4, 5]. In addition, in a pilot study, the cytogenetic response of human lymphocytes to 9.5 MeV/u C ions (LET: 175 keV/µm) was investigated by multiplex fluorescence in situ hybridisation (mFISH) allowing the detection of aberrations derived from multiple breakage (complex aberrations).

Originally, as a potential fingerprint of high LET exposure, the ratio of the yield of dicentrics to centric rings, termed the F-value, has been proposed. However, as shown in figure 1, in human lymphocytes values of about 10 were found for all radiation qualities. Similarly, when the data sets for Chinese hamster cells were analysed (figure 2), no LET dependence of the F-value was apparent. Interestingly, for hamster cells the F-ratios were lower and the inter-experimental variations were larger than for human lymphocytes.

More recently further yield ratios have been suggested as possible candidates, namely the ratio of interstitial deletions to dicentrics (H-value), of interstitial deletions to centric rings (G-value) or of excess acentrics to dicentrics [1]. Analysis of our data sets revealed a weak dependence of the H- and the G-ratio on LET. In contrast, the ratio of excess acentrics to dicentrics was stable for LET values to 300 keV/µm. Thereafter, in the LET range of 300 to 4000 keV/µm the ratio increased by a factor of about 4.

Analysis of aberrations by means of the mFISH technique revealed a clearer picture. We found a significant difference in the ratio of complex to simple exchanges after X-ray compared to C ion exposure (LET: 175 keV/µm), i.e. 0.27 ± 0.06 and 2.16 ± 0.21, respectively ($t = 8.6$, $p \leq 0.01$).

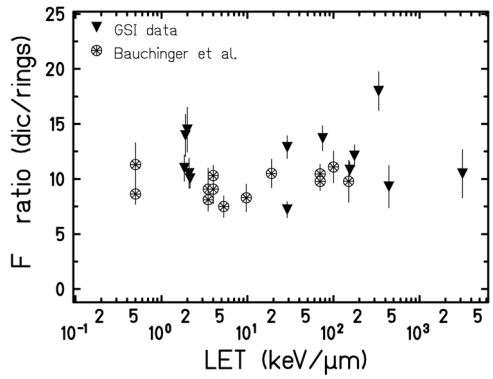

Fig. 1: F-ratios (yield of dicentrics/yield of centric rings) generated for human lymphocytes (present study and data from Bauchinger et al. [1]). Aberrations were measured in first cycle metaphases following Giemsa-staining. Standard errors are indicated by vertical bars.

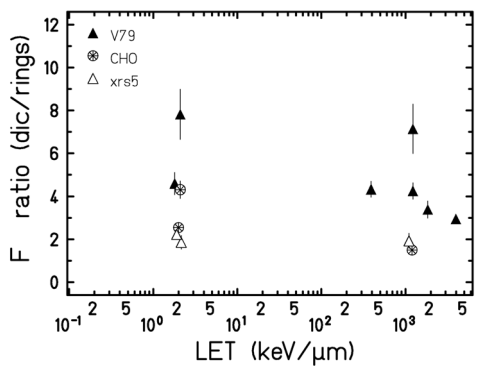

Fig. 2: F-ratios generated for 3 Chinese hamster cell lines. For details see figure caption 1.

In summary, our study shows that aberration ratios derived from solid stained metaphases do not represent practical biomarkers of high LET radiation. However, promising results have been obtained by means of mFISH.

References

[1] M. Bauchinger and E. Schmid, Int. J. Radiat. Biol. 74, 17-25 (1998)
[2] H. Wu et al., Adv. Space Res. 31, 1537-1542 (2003)
[3] R.M. Anderson et al., Int. J. Radiat. Biol. 76, 31-42 (2000)
[4] E. Nasonova and S. Ritter, Cytogenet. Genome Res. 104, 216-220 (2004)
[5] S. Ritter et al., Int. J. Radiat. Biol. 78, 191-202 (2002)

* This study was supported by BMBF (Bonn, grant 02S8203).

Induction of telomerase activity in peripheral blood mononuclear cells (PBMC) after irradiation in vitro and in vivo.

D. Milanovic, P. Maier, F. Wenz and C. Herskind
Dept. of Radiation Oncology, Mannheim Medical Center, University of Heidelberg, Germany.

Human telomerase is a specialized reverse transcriptase (hTERT) carrying its own RNA component (hTERC). This enables the enzyme to extend the leading strand of the long terminal telomere hexamer repeat sequences (TTAGGG) found on each chromosome. The telomeres are important for genomic stability by forming stable structures capping the end of the chromosomes. With few exceptions, adult normal-tissue cells express little or no telomerase, and shortening of the telomeres with each round of replication eventually leads to senescence. By contrast, telomerase is frequently found to be upregulated in cancer cells thus contributing to immortalization.

Normal lymphocytes express a low but measurable telomerase activity that is substantially increased by mitogenic stimulation with phytohemagglutinin (PHA). Radiation-induced upregulation of telomerase activity has been found in hematopoietic cell lines where it may facilitate DNA repair or contribute to genomic stability [1-3]. Recently, we demonstrated that radiation-induced upregulation of telomerase activity also occurs in human PBMC stimulated with PHA prior to irradiation in vitro [4].

Further experiments were performed to test whether telomerase can be induced in unstimulated PBMC. Figure 1 shows the telomerase activity in PBMC from three young, healthy donors without treatment, 24 hours after irradiation with 6 MV X rays in vitro and in unirradiated PBMC stimulated with PHA, respectively. The telomerase activity determined by a TRAP real-time PCR assay [4] was low compared with immortal lymphoblastoid cells (TK6 cell line). However, irradiation with a dose of 7 Gy increased the telomerase activity more than three-fold. By comparison, treatment with PHA for 72 hours resulted in approximately 40% of the activity of TK6 cells.

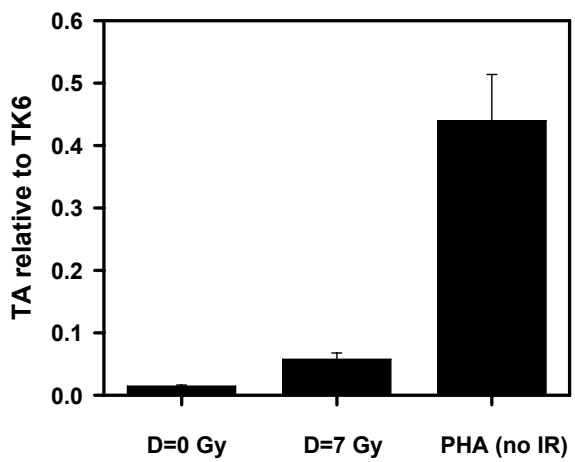

Figure 1: Increase in telomerase activity (TA) after irradiation or PHA stimulation of PBMC in vitro.

These data supported a physiological role of telomerase in the cellular radiation response, e.g. in the formation or modulation of chromosome aberrations. Therefore, we tested if enhanced telomerase activity could be detected in PBMC isolated from patients undergoing radiotherapy for prostate cancer. The data in Figure 2 showed no enhancement of telomerase activity in PBMC from irradiated patients (median dose: 53 Gy) although the activity in unirradiated, age-matched donors was apparently higher than for the young healthy donors in Figure 1. By contrast, stimulation of telomerase activity by PHA seemed to be reduced in PBMC from irradiated patients.

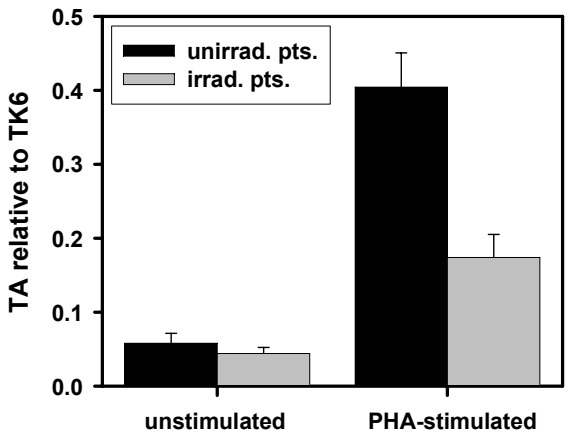

Figure 2: Telomerase activity in PBMC from 22 prostate patients after doses of 24-72 Gy of fractionated radiotherapy compared with 16 unirradiated control donors. Mean values and s.e.m. for PBMC without stimulation and after 72 hours stimuation with PHA are shown.

Possible causes for the apparent difference between the results after in vitro and in vivo irradiation are currently being studied. Furthermore, experiments to compare telomerase activity after heavy ion and X-irradiation are in progress.

Acknowledgement: This study was supported by the BMBF, Bonn (contract no. 02S8203).

References

[1] G. G. Sharma *et al.*, *Oncogene* 22, 131-46 (2003).
[2] D. Dubner *et al.*, *Int J Radiat Biol* 80, 593-605 (2004).
[3] D. Neuhof *et al.*, *Strahlenther. Onkol.* 180, 52-6 (2004).
[4] D. Milanovic *et al.*, *Radiat. Prot. Dosimetry* 2006 Dec 12 (e-pub ahead of print; advance access, http://rpd.oxfordjournals.org).

Is the shortening of chromosome ends a trigger for radiation-induced senescence or genetic instability?*

D. Krunic[2], C. Fournier[1], S. Ritter[1], S. Zahnreich[1] and P. Boukamp[2]
[1]GSI, Darmstadt, Germany; [2]DKFZ, Heidelberg, Germany.

Introduction

Telomeres are the physical ends of the linear eukaryotic chromosomes. Telomere erosion during DNA replication is considered to be the main cause of the onset of replicative senescence, an irreversible cell cycle arrest at the end of the lifespan of normal cells (1). With the help of a number of proteins, including the telomere repeat-binding factor 2 (TRF2), the telomeres form loop structures (T-loop) thereby avoiding being recognized as DNA strand breaks and preventing end-to-end telomere fusion (2). The latter is considered as a sign of genetic instability and demonstrates the crucial role of telomeres in preventing genetic instability.

Telomere fusion can lead to dicentric chromosomes without fragments. Several months after exposure to X-rays, a large amount of cells with dicentric chromosomes were detected in the progeny of irradiated fibroblasts during our longterm experiments. In other cells, replicative senescence was observed (3). This is in line with published data, reporting that both replicative senescence and genetic instability can also be induced by others than cell-intrinsic factors, among them external factors causing DNA damage (1). In our study presented here we were interested whether telomere shortening is detectable in the progeny of irradiated fibroblasts and, if so, whether the observed shortening is a basis for the occurrence of replicative senescence and genetic instability.

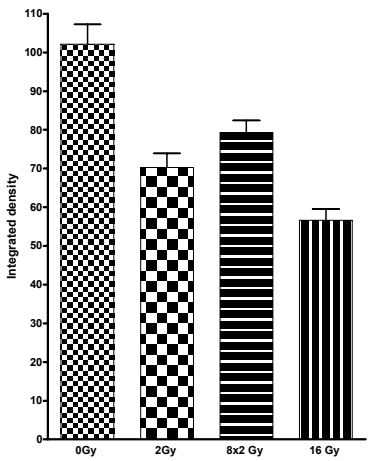

Figure 1: Integrated intensity of telomere signals per nucleus. Each data point is a mean of the values obtained at 24h, 48h and 72h after exposure to X-rays.

Materials and methods

Human fibroblasts (AG1522C) were exposed to single and fractionated doses of X-ray. Chromosomal aberrations were analysed in metaphase cells after solid staining (Giemsa). For the assessment of telomere length, fluorescence in situ hybridization, 3D image acquisition, deconvolution microscopy and image processing, as well as immunofluorescence staining for TRF2 protein were performed as described elsewhere (4).

Results and discussion

The telomere length was investigated by measuring the integrated intensity of the telomere signals per nucleus, that is proportional to the total amount of telomeric DNA and therefore to a mean telomere length of a given cell. As shown in figure 1, X-ray causes telomere shortening at in the progeny of the exposed cells. Remarkably, the values for a single and a multiple (8x) dose of 2 Gy are not significantly different. First preliminary results suggest that the shortening is detectable at later pasages up to months after irradiation (not shown). The differences in telomere length are small but significant. Besides loss of telomeric DNA, X-ray could also result in dysfunctional telomeres due to loss or modification of telomere specific proteins. In this respect TRF2 seems to play a particularly important role. To test whether TRF2 is altered upon X-ray we now aim to study TRF2 in more detail. The protocol for the TRF2 detection by immunofluorescence has already been established (see figure 2).

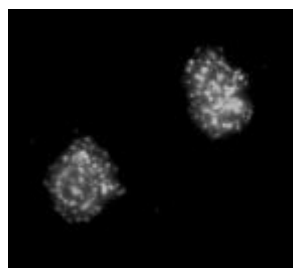

Figure 2: Immunofluorescence staining of TRF2 foci in fibroblast nuclei.

* Work supported by BMBF contract No. 02S8203.

References

[1] K. Itahana *et al.*, "Mechanisms of cellular senescence in human and mouse cells", Biogerontology 5, 2004, p. 1-10.
[2] B. van Steensel *et al.*, "TRF2 protects human telomeres from end-to-end fusions", Cell 92, 1998, p. 401-413.
[3] S. Sommer *et al.*, GSI Annual Report 2005/1 (2006).
[4] S. Ermler *et al.*, "Cell cycle-dependent 3D distribution of telomere and telomere repeat-binding factor 2 (TRF2) in HaCaT and HaCaT-myc cells ", Eur. J. Cell Biol. 83, 2004, p. 681-690.

Chromosomal aberrations and genetic instability in long-term cultures of normal human fibroblast cell lines*

S. Zahnreich[1], C. Fournier[1], P. Hessel[1], S. Ritter[1], L. Melnikova[2], and E. Nasonova[2]
[1]GSI, Darmstadt, Germany; [2]JINR, Dubna, Russia

Introduction

Former experiments have shown an increase in number of unstable chromosomal aberrations in normal human fibroblast strains with ongoing culturing time of the populations [1, 2]. These *de novo* formed unstable aberrations are an indicator of genomic instability which is considered to be one important step towards carcinogenesis. In the same experiments we observed the accumulation of stable aberrations during culturing time, in some cases as clonal aberrations in normal human fibroblasts [2]. We intend to assess whether both effects are interrelated, especially because stable aberrations and their clonal amplifications are reported to be involved in the formation of tumors, especially soft tissue sarcomas [3].

Materials and Methods

Four fibroblast cell lines originating from three different tissues were cultured up to 7 months until they reached replicative senescence (AG1521A, AG1522C/D, NHDF, IMR-90). The cells were subcultured every 2 weeks and chromosome samples were prepared. Unstable aberrations such as dicentrics, rings or breaks were scored regularly after solid Giemsa staining (100 metaphases per time point). At representative time points stable aberrations were assessed by analyzing 100 metaphases using the multiplex fluorescence in situ hybridization (mFISH).

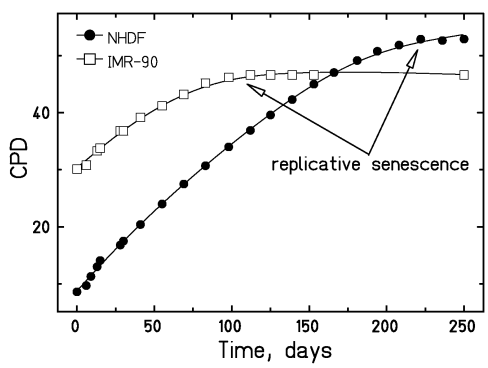

Figure 1: Proliferation of NHDF- and IMR-90 fibroblasts up to contact inhibition during cultivation and serial passaging, measured as cumulative population doublings (CPD) over 250 days.

Results and Conclusion

Figure 1 shows the proliferation of two different fibroblast cell lines. At each subcultivation the cells were counted and the number of mean population doublings was calculated. During culturing time, the activity of proliferation decreased until the cells reached the end of their replicative lifespan, the so-called replicative senescence.

An increase in unstable aberrations was detected in all cell lines shortly before the cells ceased proliferation. Chromatid type aberrations were the most frequent chromosomal aberrations, indicating genomic instability (data not shown). The analysis of stable chromosomal aberrations revealed translocations for all cell lines. Over the whole culturing time there was a basal level of 3 to 5 translocations in 100 cells. As shown in figure 2, in both cell lines the numbers of translocations per cell increased with time. In IMR-90-cells the translocations were to a large extend of clonal origin, all involving the same chromosome with a further diversification in subclones. In the second cell line (NHDF), non-clonal tranlocations together with a pronounced increase in unstable aberrations were observed. Both, the occurrence of subclones and of unstable aberrations, are a sign of genomic instability. After a short time, IMR-90 cells underwent replicative senescence, whereas NHDF-cells continued to proliferate and showed a further increase in the number of translocations and unstable aberrations (data not shown).

Genomic instability may be caused by the formation of stable aberrations but is not necessarily the consequence of their formation. Most likely, the chromosomes and gene loci involved determine the fate of the progeny of the cells leading to cell death, replicative senescence or genetic instability.

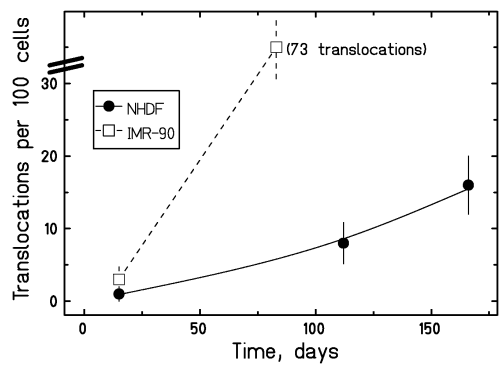

Fig. 2: Frequencies of stable aberrations (translocations, mFISH) in NHDF- and IMR-90-fibroblasts.

References

[1] Dugan and Bedford, Radiation Research 159, 2003, 301-311
[2] Sommer, S. *et al.*, GSI Annual Report 2005, 373
[3] Sharpless, N. E. *et al.*, Mol. Cell 8, no. 6, 1187-1196,2001

* Work supported by BMBF (Bonn), grant 02S8203

Effect of LET and Track Structure on the Statistical Analysis of Chromosome Aberrations: Use of the Convoluted Poisson-Neyman Distribution*

R. Lee[1], E. Gudowska-Nowak[† 1,2], E. Nasonova[1,3], M. Scholz[1], and S. Ritter[1]
[1]GSI, Darmstadt, Germany; [2]Jagellonian University, Kraków, Poland; [3]JINR, Dubna, Russia

Chromosome aberration data obtained for various types of mammalian cells after exposure to low and high LET clearly demonstrate [1] the differences in the energy deposition pattern of both radiation qualities. In the study reported here the distribution of chromosome aberrations observed in human peripheral blood lymphocytes at the first mitosis after exposure to 900 MeV/u Fe (LET=155keV/μm) ions was analyzed and compared to the effects of 250 kV X-rays [1]. After X-ray exposure the distribution of aberrations among cells was well characterized by a Poisson distribution, reflecting a simple random distribution of damages as expected according to the homogeneous pattern of energy distribution. On the contrary, after high LET exposure, the distribution of aberrations reflected the microscopic inhomogeneity of energy depositions (see Fig.1). Moreover, since in the experiments first cycle metaphase cells were collected at several sampling times, additionally insights into high and low LET induced cell cycle delays were obtained. If particle hits to the cell nucleus are viewed as independent random Poisson events with an average intensity λ, each contributing with an average number of aberrations per hit μ, the overall distribution of aberrations can be represented by a compound Poisson (Neyman-type A) statistics $P_N(k) = \frac{\mu^k}{k!} e^{-\lambda} \sum_{n=0}^{\infty} \frac{n^k}{n!} (e^{-\mu}\lambda)^n$. However, in the case of high energetic particles, the radial extension of the particle tracks cannot be neglected (cf. Fig.1) and, due to overlap effects from different tracks, the particle traversals cannot be treated as independent. In this case, the frequency of aberrations among cells is characterized by a mixture of a Neyman distribution with a *background* of a contributing Poisson-type distribution $P_{N+P}(k) = \sum_{s=0}^{\infty} P_P(s) P_N(k-s)$, representing the effects of energy released in the center part of the tracks and the outer, overlapping part of the tracks, respectively. Based on the estimate of the mean number of particle traversals after exposure to 2.3Gy Fe-ions, the parameter λ at 48 h after irradiation was set to $\lambda = 2$. Consequently, by using the estimate for the experimentally observed average number of aberrations/cell, $\langle X \rangle_{N+P} = \lambda\mu + a$ with $a = 0.25$, the value $\mu = 1.5$ aberrations per particle traversal was derived, showing almost no dose- and time-variations. In contrast, a clear time-dependence of the parameter λ (cf. Fig2) was observed, demonstrating cell cycle delay of heavily damaged cells: With increasing number of hits to a cell nucleus, more chromosome aberrations are produced in the cell [1, 2] which, in turn, was shown to correlate directly [3] with an average time to enter the mitosis.

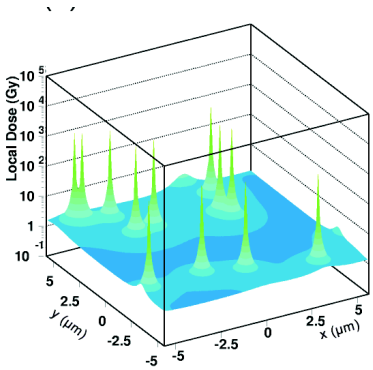

Figure 1: Microscopic dose distribution of 2.3 Gy of 990 MeV/u Fe ions 9×10^6 ions/cm^2. The estimated *background dose* is about 0.5 Gy which results in an additional 0.25 aberrations per a lymphocyte exposed

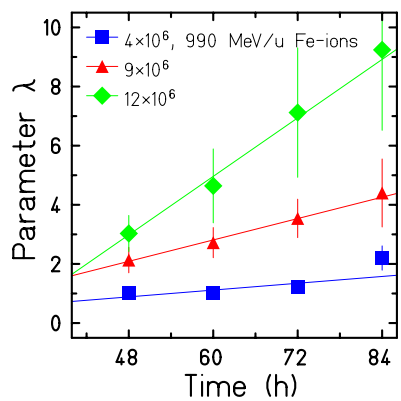

Figure 2: Evaluation of the parameter λ (i.e. a mean number of particle traversals) for human lymphocytes exposed to Fe ions by means of the convoluted Neyman-Poisson statistics fitted to frequencies of aberrations analyzed at different sampling times. Lines were fitted by a linear regression analysis.

References

[1] R. Lee *et al.*, Adv Space Res. 35 (2005) 268.
[2] M. Scholz, Adv. Polymer Sci. 162 (2003).
[3] E. Gudowska-Nowak *et al.*, Int. J. Rad. Biol. 81 (2005) 23.

* Work supported (EGN) by the EU COCOS project (MTKD-CT contract No. 2004-517186).) and BMBF 02S8203, Bonn (RL, EN)
† gudowska@th.if.uj.edu.pl

Cytogenetic damage in lymphocytes of prostate cancer patients*

S. Ritter[1], D. Becker[1], C. Fournier[1], P. Hessel[1], G. Kraft[1], S. Sommer[1], E. Nasonova[2], H. Hofman-Hüter[3], P. Virsik-Köpp[3], R. Haselmann[4] , J. Debus[4] and D. Schulz-Ertner[4]
[1]GSI, Darmstadt, Germany; [2]JINR, Dubna, Russia, [3]University Göttingen, Germany, [4]Clinical Radiology, Heidelberg, Germany

Since the start of C-ion therapy at GSI, Darmstadt, in December 1997 about 340 patients have been treated. Most patients had chordoma or low grade chondrosarcoma of the skull base. Based on the promising clinical results, namely high local control rates and mild side effects [1], the application has been recently extended to intermediate risk prostate cancer. A clinical phase I/II trial combing photon intensity-modulated radiotherapy (IMRT) and C-ion boost has been started in 2006. In parallel to this clinical trial the yields and the types of radiation-induced chromosome aberrations will be investigated in peripheral blood lymphocytes of prostate cancer patients.

Blood is unavoidably exposed during radiotherapy and the cytogenetic damage induced in lymphocytes is considered as a reliable indicator of the absorbed dose. Furthermore, with increasing LET, specific alterations in the aberration spectrum have been described [2, 3] suggesting that these changes can serve as a biomarker to distinguish between high and low LET exposures.

For the analysis of chromosomal damage in lymphocytes of prostate cancer patients blood samples (8ml) are taken before, during and at the end of therapy. Lymphocytes are isolated, cultivated *in vitro* for 48h and chromosome spreads are prepared according to standard techniques [4]. Aberrations are visualised in first generation metaphases by solid staining or painting of chromosome 2 and 4. Additionally, if sufficient metaphases are available, multiplex fluorescence in situ hybridisation (mFISH) is applied to reveal translocations induced within the whole genome.

To date, 5 patients treated with IMRT and a C-ion boost (6x3 GyE) and one patient treated solely with IMRT entered the study. Chromosome analysis after solid staining revealed a low level of aberrations (0.01-0.02/cell) in lymphocytes before therapy. As expected, cytogenetic damage increased during the time-course of radiotherapy (fig. 1). The same response was observed, when aberrations such as translocations were scored after chromosome painting (data not shown) or mFISH (fig. 2). Interestingly, complex aberrations that are discussed as a fingerprint of high LET radiation [e.g. 3] were not detected in all patients receiving a C-ion boost. As exemplarily shown in figure 2, in cells of patient 04 a low level of complex aberrations was found after the C-ion boost and at the end of therapy, while in patient 05 no complex aberrations were detected. A more detailed analysis will be performed, when a higher number of samples has been analysed.

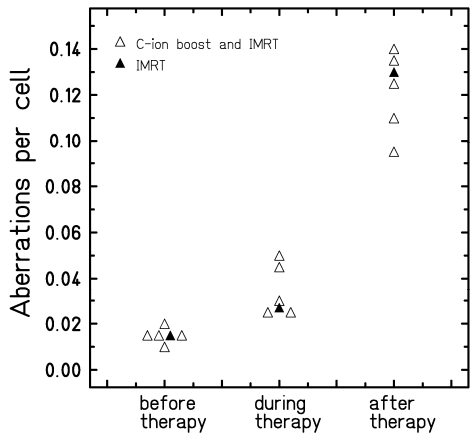

Fig. 1: Yield of aberrations in lymphocytes of prostate cancer patients measured following solid staining. Cells were analysed before therapy, during therapy (i.e. after 6 fractions) and at the end of therapy.

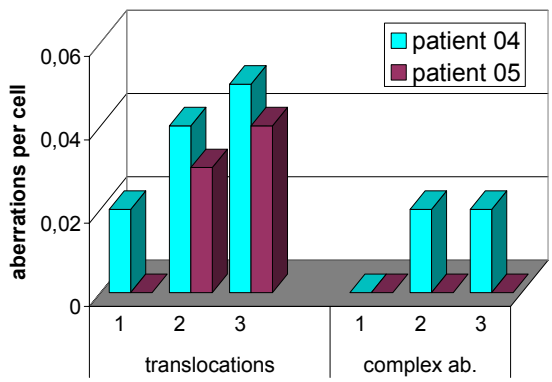

Fig. 2: Yield of translocations and complex aberrations in peripheral lymphocytes of two patients before therapy (1), after C-ion boost (2) and at the end of therapy (3). Samples were analysed by means of mFISH.

References

[1] D. Schulz-Ertner et al., Int. J. Radiation Oncology Biol. Phys. 58, 631-640 (2004)
[2] S. Sommer et al., GSI Scientific Report, this issue (2007)
[3] RM Anderson et al. Radiat. Res. 163, 26-35 (2005)
[4] E. Nasonova and S. Ritter, Cytogenet. Genome Res. 104, 216-220 (2004)

*Supported by BMBF, Bonn, under contract 02S8203.

Premature senescence in human endothelial cells exposed to carbon ions *

L. Manti[1,#], M. Durante[1], T. Elsässer[2], G. Gialanella[1], M. Pugliese[1], S. Ritter[2], P. Scampoli[1] and G. Grossi[1]

[1]Department of Physical Sciences, University of Naples Federico II and INFN, Naples Section, Italy; [2] GSI, Darmstadt, Germany

Rationale and aims

Ionizing radiation has been reported to promote a state of apparent cell-cycle arrest in both normal and tumour cell lines closely resembling the senescent phenotype [1,2]. The arrest is sometimes reversed and the cell either resumes proliferation or, alternatively, differentiates. Although DNA damage is thought to be the main effector of the senescent-like fate, the underlying mechanisms are not understood [3]. It may be triggered by oncogene(s): premature entry into senescence would thus represent a stress-induced avoidance of transformation; it could be associated with telomere shortening, in which case, since reduction of telomere length below a critical threshold is thought to result in telomere-telomere fusion, widespread genome instability and increased tumorigenic risk would ensue.

As opposed to the extensively studied cancer-related long-term effects, non-cancer radiodegenerative diseases are only recently attracting attention. The phenomenon of senescent-like response to radiation has a twofold relevance: it can help elucidate how chronic space radiation exposure may affect functions of tissues and organs, such as the cardiovascular system; in ion-based radiation treatment of tumours, it may shed light on the inescapable normal tissue complications.

The scope of this project is to investigate the ectopic onset of senescence in human umbilical vein endothelial cells (HUVECs) and its relationship with telomere length. Senescence will be revealed by positivity for β-galactosidase activity while cytogenetic analysis of telomeres will be performed by Interphase Quantitative (IQ) FISH. Karyotypic analysis will signal for acquired genomic instability.

Experimental procedure

Early passage HUVECs were irradiated at the SIS facility in Darmstadt using the therapeutic 270 MeV/amu carbon ion beam at the plateau (entrance; LET ≈ 13 keV/μm) or the spread-out Bragg Peak (SOBP; LET≈ 100 keV/μm) positions of the beam ionization path. Two doses were chosen for each position (0.5 Gy and 2 Gy). X-rays were used as a reference. Each sample was then split, serially cultivated and, at regular intervals, either harvested or replated. Acute radiosensibility was assessed by clonogenicity.

Results

Clonogenic survival was clearly LET-dependent and pronounced sublethal damage repair occurred at low LET(fig. 1).

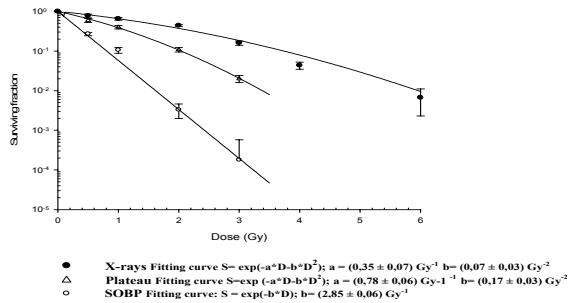

Figure 1: Clonogenic curves

β-Galactosidase tests showed that irradiated HUVECs switched to senescence earlier than did physiologically ageing controls. Initially, this occurred in an LET- and dose-dependent fashion, but a more complex pattern emerged with time (fig.2). At the plateau, which matters to normal tissue, more senescent cells were recorded compared to high dose. The opposite was true for the SOBP and X-rays.

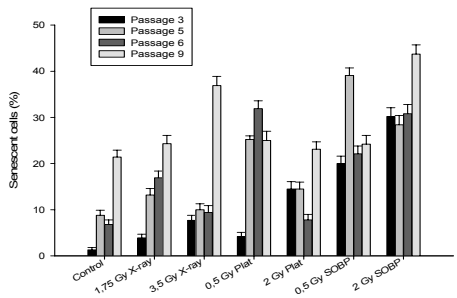

Figure 2: Cellular senescence as a function of time

Analysis of cytogenetic slides will relate these data with telomere length quantitation.

References

[1] K. R. Jones, L. W. Elmore, C. Jackson-Cook, . "p-53-dependent accelerated senescence induced by ionizing radiation in breast tumour cells. Int. J. Radiat. Biol. 81, 445-458 (2005).

[2] M. Suzuki C. Tsuruoka, Y. Uchihori, S. Ebisawa, H. Yasuda and K. Fujitaka. "Reduction of life-span of normal human fibroblasts exposed to very low dose rate charged particles". Radiat. Res., 164, 505-508 (2005).

[3] K. Suzuki, I. Mori, Y. Nakayama, M. Miyakoda, S. Kodama and M. Watanabe. "Radiation-induced senescence-like growth arrest requires TP53 but not telomere shortening. Radiat. Res. 155, 248-253 (2001).

* Work supported by EU, EURONS Chrom.Inv. Durante

#manti@na.infn.it

Neoplastic Transformation Induced by Carbon Ions*

Daniela Bettega, †[1], Paola Calzolari[1], Petra Hessel[2], and Wilma K. Weyrather[2]
[1]Dept.Physics, Univ. of Milan and INFN, Italy; [2]GSI, Darmstadt, Germany

Neoplastic transformation in vitro can be used as an indicator for risk assessment comparing different radiation types. The human hybrid (Hela X skin fibroblast) cell line, developed by Stanbridge et al [1] and Redpath et al [2] and designated CGL1 has been used to compare carbon ion irradiation to conventional radiation (15 MeV photons). Results for track segment irradiation have been reported in [3] [4].

In a next step a situation more closer to therapy has been simulated. An extended volume has been irradiated with a physical isodose of 1.5 Gy, simulating a tumor in a depth between 60mm and 100mm. Survival and transformation frequency habe been measured at 5 different positions: two in the entrance channel, one in the middle of the tumor and two after the tumor volume to measure the influence of the produced fragments. One extra point in the entrance channel has been measured for survival only. Cell were irradiated in medium filled cell culture flasks, that were combined as a stack with polyethylen slides between the flasks to get the correct distance. Ranges in the figure were corrected for water equivalence.

The results are shown in figure 1. Values and error bars are calculated from two independent experiments. The data for survival and transformation frequency in the entrance channel and in the tumor volume correspond within the normal statistical variation to that, what has been expected from the track segment data.

For the risk assessment the transformation frequency per cell at risk (the number of irradiated cells) is more relevant than the frequency per surviving cell. With the exception of the point at 50 mm (corresponding to a rim if 1 cm around the tumor volume) the transformation risk per irradiated cell is in the same range. It is remarkable that the low dose from the fragments behind the tumor volume lead to the same risk as the high doses before. This effect may be mainly contributed to the stopping α - particles, which have been shown to have a higher risk for transformation [5]. For a comparison to photons, the irradiated volumes necessary for an identical tumor dose have to be taken into acount.

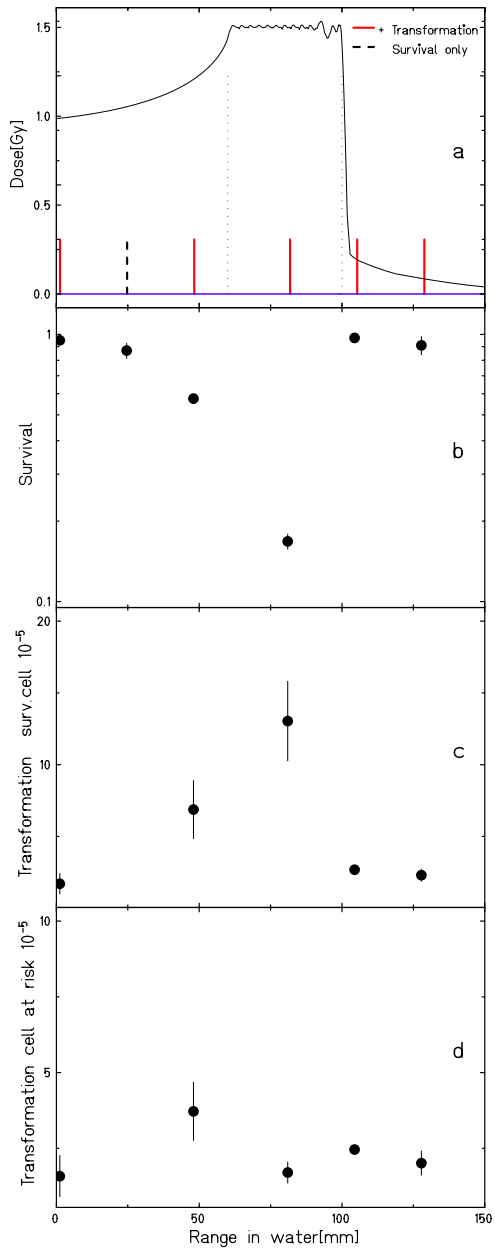

Figure 1: a) Doseprofile for the irradiated volume. Lines indicate the places where survival and transformation where measured. At the depth of 25 mm only survival has been measured.
b) Clonogenic survival.
c) Transformation frequency per surviving cell.
d) Transformation frequency calculated for cell at risk.

References

[1] Stanbridge et al , Science, 215, 252 (1982)
[2] Redpath et al, Radiat. Res. 110, 468 (1987)
[3] GSI Scientific Report 2004, 286 (2005)
[4] GSI Scientific Report 2005, 379 (2006)
[5] Bettega et al, Int.J.Radiat.Biol. 72, 532 (1997)

* Work supported by EU, EURONS contract No. 506065.
† I3-EURONS (European Commission contract no. 506065)

Investigation of cell death induced by high LET irradiation in squamous cell carcinomas for future clinical application in hadrontherapy

M.Maalouf, G.Alphonse and C.Rodriguez-Lafrasse - Laboratory of Molecular and Cellular Radiobiology - EA3738–Oullins- France
C.Fournier and G.Taucher-Scholz - GSI- Darmstadt- Germany

Increased interest in biological effects of high-LET carbon irradiation lies in the emerging development of hadrontherapy. However a number of molecular issues regarding the mechanisms of action of carbon ions remain to be clarified. Our project aims to fill in some of these gaps by analyzing the specific molecular signature of carbon irradiation in tumor cells. These studies will contribute to the comprehension of the mechanisms leading to resistance to conventional radiotherapy and will specify the elective indications for hadrontherapy. This point is crucial in order to determine the best treatment for certain types of tumours and to direct the patients towards hadron- or conventional radio-therapy.In this context and in order to verify the cellular basis of the high RBE levels, studies on the mechanisms of cell death were initiated. Therefore apoptosis and cell cycle inhibition were assessed in two head and neck squamous carcinomas (HNSCC) cell lines with different radiosensitivity. Recent clinical trials (1) had shown that the local treatment of the HNSCC by ion carbon hadrontherapy is much less efficient than for other radioresistant cancers, raising the interest for the studies in this type of cells.

In previous experiments (2), we had shown that carbon irradiation (9.8MeV/u) induces a higher level of clonogenic cell death than X-irradiation, for SCC61 (radiosensitive to X-rays) and SQ20B (radioresistant to X-rays).
Irradiations were performed at 10 Gy. As shown in figure 1, in response to high LET ions the radiosensitive cell line, SCC61, undergoes apoptosis in a time dependent manner. Four to 240 hours after irradiation the adherent and floating cells were pelleted and fixed for apoptosis quantification using propidium iodide labeling and flow cytometric analysis. The percentage of cells in sub-G1 phase, taken as an index of apoptosis, was more pronounced in response to carbon ions than to photons and it reached 78.4% at 72h and 95 % at 240h.

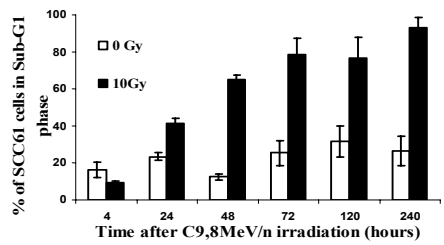

Figure 1: Kinetics for radiation-induced apoptosis (sub-G1 phase) in SCC61 exposed to carbon ions (9.8MeV/u)

On the contrary, no significant apoptosis induction was observed during the 120h following low or high LET irradiation in the SQ20B radioresistant cells (data not shown). Therefore, the proliferation activity was assessed. Growth curves were established by counting the cells at different days after irradiation. The results showed (figure 2) a very slow proliferation activity after irradiation, the number of cells remained nearly unchanged from 2 to 10 days following carbon irradiation. Similar results were observed after photon irradiation (data not shown).

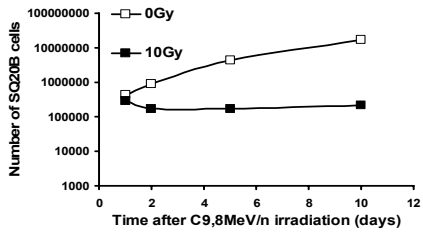

Figure 2: Number of viable SQ20B cells counted 2, 5 and 10 days after carbon irradiation

The percentage of cells in each phase of the cell cycle was then quantified by flow cytometry. In response to X-rays SQ20B showed a transient arrest in G2 phase at 24h. The G2 arrest was even more pronounced and maintained 5 days after irradiation by carbon ions (Figure 3)

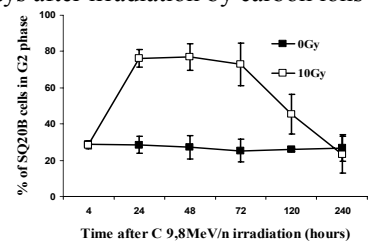

Figure 3: Percentage of SQ20B cells in G2 phase after 10Gy irradiation with carbon 9.8MeV/u.

The high efficiency of carbon irradiation in radioresistant SQ20B cells could not be explained by the induction of the apoptotic process but by a persistence of the cell cycle arrest.
We conclude that in both cell lines, carbon ion irradiation does not modify the type of cell death involved, but amplifies it. Further studies will be done to investigate the molecular mechanisms involved in the prolonged cell cycle arrest of SQ20B cells. Moreover in the radiosensitive SCC61 cell line, the potential involvement of ceramide in inducing apoptotis independently of wildtype p53 after carbon ions exposure will be studied.

References

(1) Jun-etsu Mizoe et al Int.J.Radiation Oncology Biol. Phys. 2004, 60: 358-364

(2) G.Alphonse et al. annual GSI report 2005

Carbon ion irradiation of glioblastoma cell lines combined with chemotherapy

J. Bohl[1], S. E. Combs[2], J. Debus[2], T. Elsässer[1], D. Schulz-Ertner[2] and W. K. Weyrather[1]
[1]GSI Biophysics; [2]Department of Radiation Oncology, University of Heidelberg.

Glioblastomas are the most malignant form of primary brain tumours. Despite all advances in therapy their prognosis remains poor. A new approach to overcome their high radio- and chemoresistance is the combined heavy-ion radiotherapy and chemotherapy with the alkylating agent Temozolomide (TMZ).

In this study we investigated the effect of combined carbon irradiation with chemotherapy on glioblastoma cell lines (U87-MG, LN229) and determined the relative biological effectiveness of carbon ions.

Radiobiological experiments with carbon ions have been performed at the SIS and the Unilac. We used an energy of 9.8 MeV/u on target at the Unilac with a corresponding LET on target of 170 keV/µm. For the spread-out Bragg-peak irradiation at the SIS the dose-weighted LET on target was 103 keV/µm. As a reference, irradiation experiments were performed with 250 kV X-rays. Clonogenic survival was measured after irradiation for U87-MG and LN229 cells.

Survival curves for carbon beams and 250kV x-rays as a function of dose are shown in figure 1. While typical shoulders are present in the X-ray curves, the carbon irradiation gave exponential dose curves. Table 1 shows the RBE_{α} und RBE_{10} values calculated from these curves.

Our results showed a significant increased biological effectiveness for carbon ions. The measured survival was in remarkable good agreement with the prediction according to LEM (data not shown).

In order to examine possible synergistic effects, cells were treated with TMZ for four hours followed by medium change before irradiation. The analysis of cell cycle progression by flow cytometry showed a G2/M-phase arrest after 48 hours after sole TMZ treatment (data not shown). Therefore, the irradiation for both cell lines was performed on the one hand directly after TMZ treatment and on the other hand 48 hours after treatment. Survival curves are shown in figure 2.

In combination with irradiation, TMZ treatment led to an additive effect. There was no increased radiosensitivity observed after 48 hours. LN229 cells are not only more radiosensitive than U87-MG cells, but also much more sensitive to TMZ.

Our results suggest that a treatment of glioblastomas with combined heavy-ion radiotherapy and chemotherapy might provide an opportunity for therapy. However, the differences between the investigated cell lines which reflect the diversity of glioblastomas require further research in more detail especially about the influence of TMZ on glioblastoma cells. Furthermore it is essential to investigate the effect on glioblastomas *in vivo* and to compare the radio- and chemosensitivity of the surrounding healthy tissue.

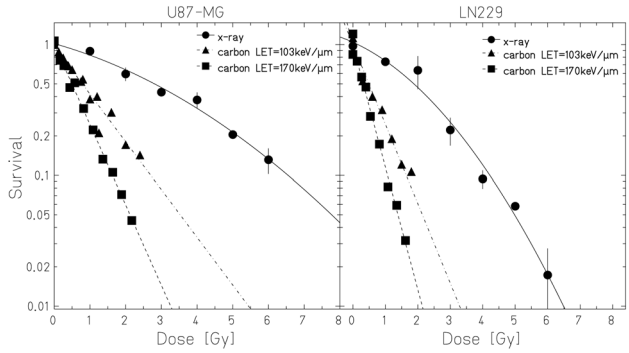

Figure 1: Survival of U87-MG and LN229 for the irradiation with carbon ions compared to x-rays. The dashed curve represents the survival after monoenergetic irradiation, dash-dotted curve represents spread-out Bragg peak irradiation.

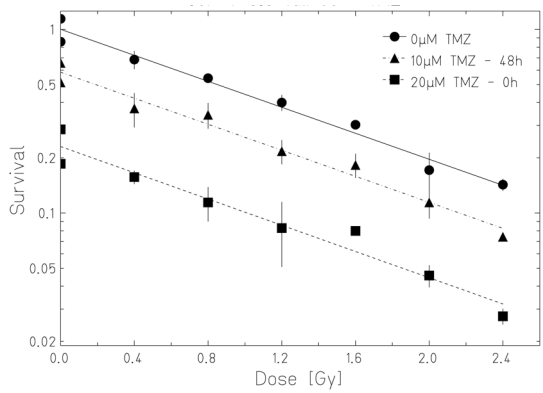

Figure 2: Survival of TMZ treated U87-MG cells for the irradiation with carbon ions. The dashed curve represents irradiation directly after TMZ treatment, the dash-dotted curve represents irradiation 48 hours after TMZ treatment.

Table 1: RBE_{α} and RBE_{10} values calculated from survival curves of U87-MG and LN229 cells after exposure to carbon ions and x-rays. Comparison between monoenergetic irradiation at the Unilac and therapy simulating spread-out Bragg peak irradiation at the SIS.

cell line	LET [keV/µm]	RBE_{α}	RBE_{10}
U87-MG	103	4.77	2.42
	170	8.04	3.99
LN229	103	5.43	2.56
	170	8.33	3.96

Phagocytotic activity of macrophages after exposure to ionising radiation*

S.Conrad[1], S.Ritter[2], and K.Nixdorff[1]
[1]Institut für Mikrobiologie und Genetik, Darmstadt; Germany [2] GSI, Darmstadt, Germany

Apoptotic cell death is a common feature after exposure to ionising radiation *in vivo* and *in vitro*. Macrophages are responsible for the phagocytotic clearance of the apoptotic cells and it was shown that phagocytosis of radiation-induced apoptotic cells can activate macrophages, leading them to the induction of an inflammatory response in the surrounding tissue by releasing cytokines [1,2]. This inflammation is responsible for the development of radiation induced side effect like pneumonia and skin fibrosis

The purpose of the present study was to measure the phagocytotic ability of irradiated macrophages *in vitro* directly by counting internalised latex beads. We used the murine RAW 264.7 cell line as a model system. The latex beads have a size of 1.1 µm in diameter, which is approximately the size of apoptotic bodies. Macrophages where irradiated with 250 kV X-rays and 9,8 MeV/u C-ions (0-32 Gy). A portion of the macrophages was activated with 1 µg/ml Lipopolysaccharid (LPS) 30min before irradiation to compare the radiation response of activated and resting macrophages. After 24h of incubation the medium was removed and replaced by medium containing latex beads in a ratio of 100 beads per macrophage. After 1h of incubation the samples were intensively washed to remove unbound and non internalised latex beads, macrophages where fixed and the number of internalised beads was counted in 200 cells per dose under a phase contrast microscope [Fig. 1]

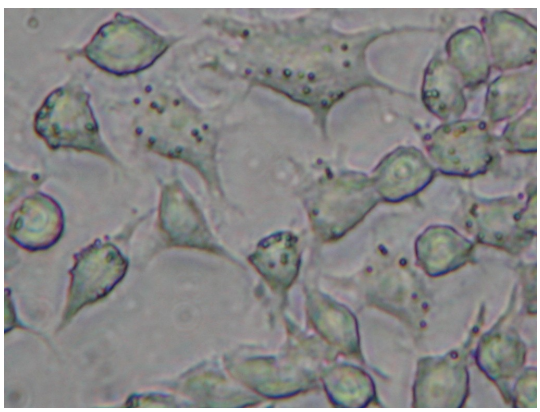

Figure 1: Irradiated RAW 264.6 macrophages (1 Gy X-ray) internalised latex beads. Beads are visible as black dots within the cells.

Figure 2 shows the results of the first experiments with stimulated and resting macrophages after X-ray irradiation. Resting macrophages phagocytised more beads with increasing dose, whereas LPS activated macrophages show a smaller increase of the phagocytic activity over the dose-range. Unirradiated resting macrophages phagocytised around 3 beads per cells, activated unirradiated cells around 7 beads per cell. Activated cells irradiated with X-ray doses between 0,25 Gy and 1 Gy show a decreased phagocytic activity which is probably coupled with an anti-inflammatory effect of low X-ray doses reported by other investigators [3].

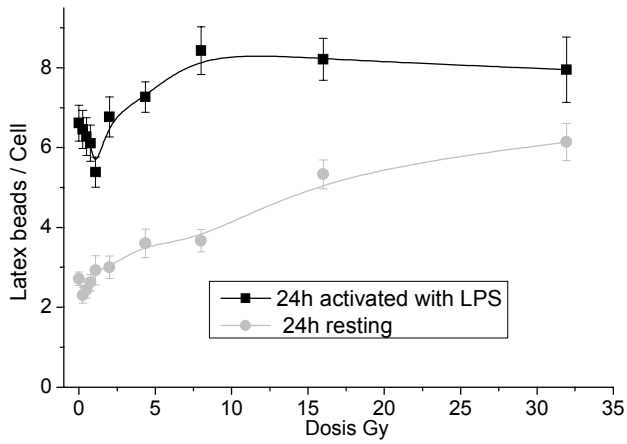

Figure 2: Number of latex beads phagocytised by macrophages. Error bars = standard error of the mean.

First results with C-ion irradiated cells also show the increased phagocytic activity but with a stronger increase (data not shown) and they also did not show the decreased phagocytic activity in the dose-range between 0,25 Gy and 1 Gy. These results indicate that ionising radiation activated the resting macrophages in a way that their phagocytic ability increased and also that LPS-activated macrophages can be activated further by radiation.

Our previous studies have shown that this activation with ionising radiation alone is not coupled with the production and release of inflammatory cytokines [4]. This indicates that cytokine production by macrophages is not a direct effect of the radiation, but potentially a result of the increased phagocytic ability of irradiated macrophages that were present in the irradiated tissue.

References

[1] E.G. Wright, P.J. Coates, Mutation Research, 597 (2006) 119-132
[2] S.A. Larimore, E.G. Wright, Oncogene 20 (2001) 7085-7095
[3] D. Schaue, K.R. Trott, Int. J. Radiat. Biol. 2002, Jul 78(7): 567-576
[4] S.Conrad, S.Ritter, K. Nixdorff, GSI Scientific Report 2004, p.287 (2005)

*This study was supported by BMBF, grant No. 02S8203

^{12}C Ions Activate the Wild-type Mouse Retina

W.G. Sannita for the ALTEA collaboration

INFN, Roma2, Roma, and Dept. of Motor Science, University, Genova, Italy;
Dept. of Psychiatry, SUNY, Stony Brook, NY, USA

Biological hazard due to prolonged exposure to space radiation is conceivably to increase onboard the International Space Station and outside the geomagnetic shield [1]. Radiation interference with brain function is also possible and could be critical. The visual system is peculiarly sensitive to cosmic radiation: most astronauts on space missions [2] and volunteers whose eyes were exposed to radiation at energies above or below the Cerenkov threshold in accelerator experiments reported phosphenes ("*light flashes*"). Relationship with particle flux and temporal correlation with HZE particles suggested retinal effects of heavy ions [2,3].

Experiments were performed at GSI, with approval by the local institutional animal care and use committees. Anesthetized (ketamine [80 mg/kg], xylazine [16 mg/kg]) adult wild-type female mice were housed in a stereotaxic platform maintaining the body temperature stable and dark-adapted. Bursts of ^{12}C ions (beam perpendicular to the retina; 1-5 ms, 10^3-10^4 particles/burst [200 MeV/n], ~3s interval between bursts) evoked a transient electrophysiological retinal response in 50% of irradiated mice, with response waveform comparable to the retinal response to light, but longer latencies and smaller amplitude. The percentage of responding mice is consistent with that (~20-50%) observed in humans [3] and may reflect physical phenomena occurring when ionizing particles impact living tissues or physiological differences in anesthesia or in the energy locally supplemented to the retina. The response amplitude correlated with the number of particles/burst, with an estimated threshold of $\approx 1x10^3$ particles/burst ((LET: $\approx$ $1.6x10^4$ KeV/μm); amplitude reached a maximum at about $2x10^3$ particles/burst (LET: $\approx$ $3.2x10^4$ KeV/μm) to then decrease with increasing particle/burst numbers. ^{12}C ion retinal activation evoked cortical responses comparable, albeit smaller and with longer latencies, to those evoked by light before and after irradiation. The retinal response amplitude of both irradiated mice and controls increased over time in the dark, suggesting negligible ^{12}C ion effects on the negative feedback mechanisms underlying dark adaptation and, by extension, on retinal sensitivity. Differences between irradiated mice and controls were not detected in retinal architecture, staining intensity and distribution of antigens at the immunocytochemistry screening analyses.

The activation by ^{12}C ions of retinal processes yielding an electrophysiological mass response in the retina and visual cortex is consistent with the suggested origin of phosphenes in space. Models of the threshold number of

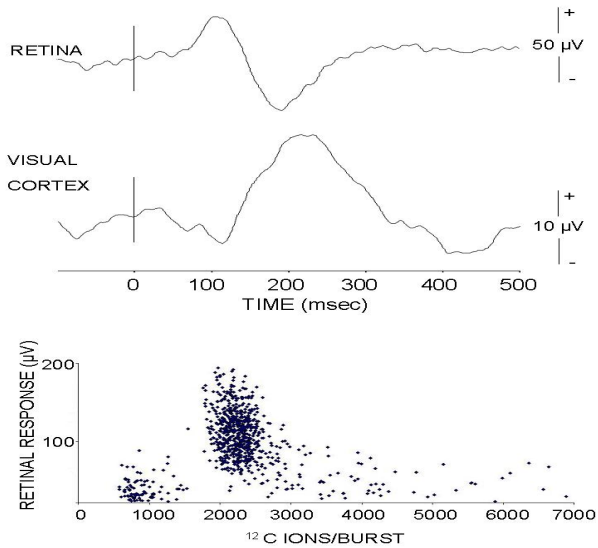

Figure 1. Average (n=10) mouse responses to ^{12}C ion (left) and retinal response amplitude vs ion number/burst in one mouse (right).

ionizations per sensitive volume induced by heavy ions, the early negative wave observed in some mice, and the cortical activation suggest outer retina effects comparable to the action of light. However, the inverted-U intensity-response function and the absence of a differential saturation of the retinal response negative/positive waves would question any selective photoreceptor activation, while recent evidence suggests the involvement of inner retinal activities, including neurons, in the generation of retinal responses [3]. Both physiological photoreceptor activation and direct (nonspecific) action on neurons appear plausible and would have implications for safety in space.

References

[1] F.A. Cucinotta, W. Schimmerling, J.W. Wilson, L.E. Peterson, P.B. Saganti, J.F. Dicello. Uncertainties in estimates of the risks of late effects from space radiation. Adv. Space Res. 34 (2004) 1383-1389

[2] C. Fuglesang, L. Narici, P. Picozza, W.G. Sannita. Light flashes in low Earth orbit: survey responses from 59 astronauts. Aviat. Space Envir. Med. 77 (2006) 449-452.

[3] W.G. Sannita, L. Narici, P. Picozza. Positive visual phenomena in space: a scientific case and a safety issue in space travel. Vision Res. 46 (2006) 2159-2165.

Modelling Irradiation-Induced Cell Cycle Delays*

A. Ochab-Marcinek[1], E. Gudowska-Nowak[†1], E. Nasonova[2,3], and S. Ritter[3]
[1]Jagellonian University, Kraków, Poland; [2]JINR, Dubna, Russia; [3]GSI, Darmstadt, Germany

In studies preceding this project we have documented [1, 2, 3] the relationship between the high lET radiation-induced mitotic delay and the expression of chromosome damage. In particular, a direct correlation between the average time to enter the mitosis and aberration burden has been claimed [3]. To further elucidate the complexity of cell cycle arrest after exposure to high LET irradiation, we have developed a Monte Carlo simulation model which combines the cell cycle progression through G_1, S and G_2/M phases with the experimental cytogenetic data [2]. Based on experimentally accessible information about the cell kinetics as measured by the mitotic index (cf. Fig.1), the aim of our project is to quantify checkpoints activity and to reproduce the cell cycle perturbations as expressed by a damage-correlated time-delay. To establish quantitative relationship between aberrations formed in interphase and visible in metaphase, cell passage through mitotic cycle stages has been simulated by means of a kinetic model in which duration of each of 4 cycle phases, $ph = \{G_1, S, G_2, M\}$, is taken as a log-normal stochastic value characterized by its mean and dispersion. For V79 Chinese hamster cells, as used in our simulations, the mean duration times [1] of the cell cycle phases are $\overline{t}_{G1} = 2.25$ h, $\overline{t}_S = 6.5$ h, $\overline{t}_{G2} = 1.5$ h, $\overline{t}_M = 0.75$h. The phase duration for an individual cell is given by a certain probability distribution $D_{ph}(\tau)$ where τ is a time which a given cell had already spent in the current phase. Consequently, a single cell of phase age τ is assumed to leave its current phase within a time interval $[\tau, \tau + d\tau]$ with probability $D_{ph}(\tau)d\tau$ and a mean number of cells $dN_{ph\rightarrow}(t)$ leaving the phase ph within an infinitesimal time interval $[t, t + dt]$ is defined by the mean flux $\frac{dN_{ph\rightarrow}(t)}{dt}$. On the other hand, if we trace the behavior of a particular cell, we can define $D_{ph}(\tau)$ as the probability distribution of leaving the phase at age τ, provided that the cell had not completed the phase earlier, i.e., $D_{ph}(\tau) = \frac{F_{ph}(\tau)}{1-\int_0^\tau F_{ph}(\tau')d\tau'}$. Knowing the mean flux we can calculate other mean quantities of interest, such as mean number of cells found in the phase ph at a given time t after irradiation (cf. Fig.2) or, when relating the delay time to mitosis with an average number of aberrations carried by a cell [3], we can predict passage of aberrant cells through subsequent phases of the cell cycle.

In order to reproduce the mean corrected mitotic index of irradiated cell populations we perform a similar fitting procedure as for the control (unirradiated cells). We make a biologically justified assumption that irradiation affects only the characteristics of G1 and G2 phases which will be reflected in fit parameters $\overline{t}_{G1}, \sigma_{G1}, \overline{t}_{G2}, \sigma_{G2}$. In fact, fits to the $F_{G2}(\tau)$ and $F_{G2}(\tau)$ distribution functions became wider when analyzing populations of irradiated cells exhibiting an apparent increase in the mean duration times of the phases. Moreover, the observed long tail of $F_{G2}(\tau)$ distribution is sugestive of a prolonged block of damaged cells in the G2 phase. The error analysis performed on simulated data allows also to draw a practical conclusion: the number of observed cells in an experimental sample should be at least 100 to obtain a relative error less than 20%.

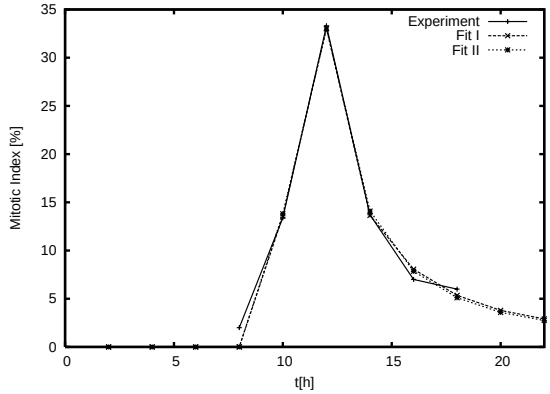

Figure 1: Mitotic index of V79 cells [2] exposed in G_1 phase to 1.96 Gy of 10.4 MeV /u Ar ions: experimental data along with fits and simulations of $N_0 = 1000$ cells.

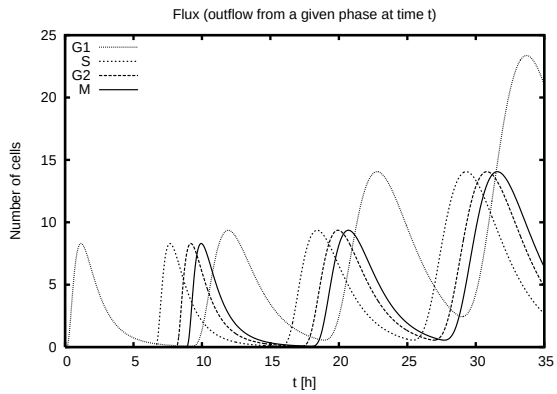

Figure 2: Exemplary flux of V79 cells from a given phase at time t. Results of MC simulations on 10^5 cells.

References

[1] M. Scholz *et al.* Int. J. Rad. Biol. 6 (1994) 59.

[2] E. Nasonova *et al.* Int. J. Rad. Biol. 77 (2001) 59.

[3] E. Gudowska-Nowak *et al.* Int. J. Rad.. Biol. 81 (2005) 23.

* Work supported by the EU COCOS project (MTKD-CT contract No. 2004-517186 and KBN Grant No 1 P03B 159 29).)

† gudowska@th.if.uj.edu.pl

Monte Carlo simulation of cell inactivation after heavy ion irradiation with the Local Effect Model (LEM) including cluster effects

Th. Elsässer and M. Scholz
GSI, Darmstadt, Germany

The Local Effect Model (LEM) represents an integral part of the heavy ion treatment planning software TRiP98 to calculate the biologically equivalent dose. Recently, the incorporation of cluster effects of single strand breaks at large local doses around the center of ion tracks was shown to be of particular importance for the prediction of the relative biological effectiveness (RBE) of the initial slope of cell inactivation experiments [1]. However, in order to apply these modifications to treatment planning, the knowledge about RBE values at doses up to a few Gy is necessary. Additionally, a refinement of the radial dose distribution seems to be appropriate.

Radial Dose Distribution

In the original dose distribution of the LEM, the radical diffusion was taken into account by using a minimal radius of 10nm below which the dose is constant. However, recent experiments suggest that the diffusion length is shorter. Therefore, we modified the physical dose distribution by reducing the minimal radius to 0.3nm according to experimental data for the dose distribution [2] and convolving the physical dose distribution D(r) with a Gaussian distribution of width σ=4nm to account for radical diffusion [5]

$$\widetilde{D}(r) = \frac{e^{-r^2/2\sigma^2}}{\sigma^2} \int_0^\infty dr' r' e^{-r'^2/2\sigma^2} I_0\left(\frac{rr'}{\sigma^2}\right) D(r') \,.$$

Cell inactivation

In order to implement the LEM into treatment planning, full survival curves must be calculated and the RBE for different survival levels is of interest. We used the mathematical method of [3] to determine the survival levels for V79 cells. For each track we compute the frequency distribution of dose per fractional area of the cell nucleus as a function of the impact parameter. The calculation of overlapping tracks corresponds to the convolution of the frequency distributions of each track. The resulting final frequency distribution contains the fractional area of the cell nucleus irradiated by a certain local dose. With this distribution we can calculate the "local" average number of lethal events for each local dose by using the response of the modified photon survival curve [5]. Integrating these average "local" events yields the total number of lethal events and finally the survival level. Fig 1 demonstrates the improvement of the modified LEM by comparing it to the original version and experimental results [4]. In general it was found that the cell survival is lower after high-LET irradiation and higher after irradiation with low-LET particles. With this method we could also prove that the approximations applied in TRiP98 are still valid for the cluster extension

Conclusion

We have shown that the cluster extension of the Local Effect Model in combination with a refined dose distribution improves the model also for full survival curves. Therefore, the modified LEM will improve the treatment planning for carbon ion therapy significantly.

References

1. Th.Elsässer and M.Scholz, GSI report 2005
2. M. N. Varma et al., *Radiat. Res.* **70,** 511-518 (1977)
3. H. Paganetti et al., Int. J. Radiat. Biol. 77, 911-928
4. W. Kraft-Weyrather, Int. J. Radiat. Biol. 75, 1357-1364
5. Th. Elsässer and M. Scholz, Rad. Res., in press (2007)

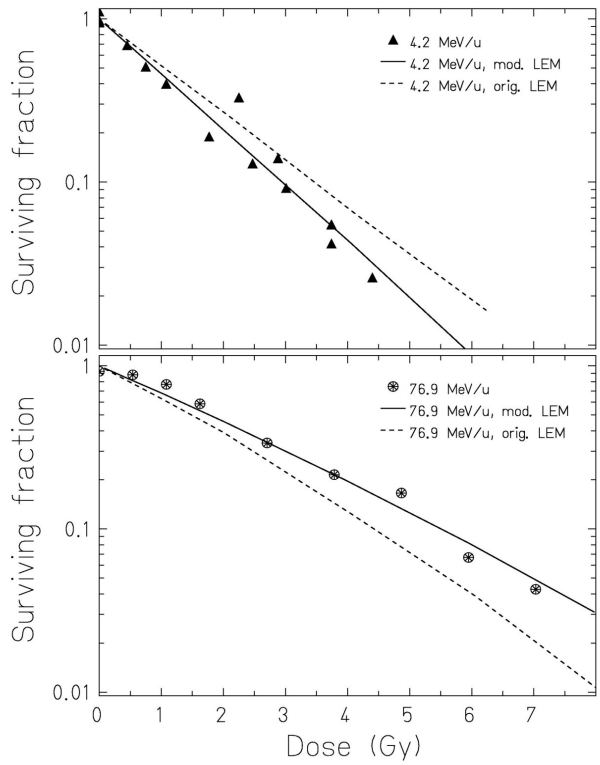

Figure 1. Cell curvival for V79 cells after irradiation with 4.2 MeV/u and 76.9 MeV/u carbon ions, respectively. Solid (dashed) lines represent the results of the modified (original) LEM.

A multidimensional system for biological dosimetry

C. von Neubeck, G. Kragl, M. Krämer and W. K. Weyrather
GSI, Darmstadt, Germany

Introduction

The software TRiP98 [1, 2] is successfully used for treatment planning. One of the major tasks of the planning procedure is the optimization step. Every further development in calculation models for treatment planning, e. g. the multiple field optimization (MFO) [3], has to be verified biologically, before the improvements can be integrated into patient treatment.

Materials and methods

Using MFO allows sparing of organs-at-risk (OAR) which are closely situated to the tumor. We chose an U-shaped target area bending around an OAR to simulate a patient situation where sharp irradiation border areas are essential. In order to reach a very high local resolution of the biological endpoint, cell survival, we developed a new phantom (figure 1) based on [4]. Chinese hamster ovary cells (CHO K1) were cultivated on polystyrene sticks. The sticks were vertically fixed between tow plates in a medium filled container and irradiated with carbon ions [5]. The dose level in the target volume was set to 6 GyE which corresponds to a survival level of 15 %. The target was irradiated in 20 layers with energies between 186.57 MeV/u and 258.15 MeV/u. After irradiation the clonogenic survival has been measured by carefully trypsinizing the cells from the sticks, cell counting and cell seeding at an appropriated number. Finally, the cells were stained after 7 days and scored for survival.

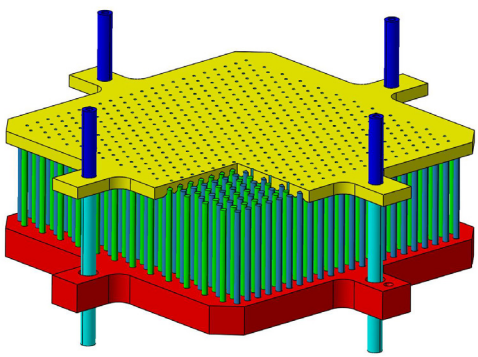

Figure 1: New phantom for biological verification. Cell carrying sticks are shown between two plates for fixation. Plates were in a defined distance via spacers.

Results

Experimental CHO K1 survival is shown in figure 3 and compared with the calculated cell survival in figure 2 for the U-shaped target. The measured cell survival is in good agreement with the calculated data. So we can demonstrate that the new phantom is suitable for biological verification of complex treatment fields with sharp dose gradient.

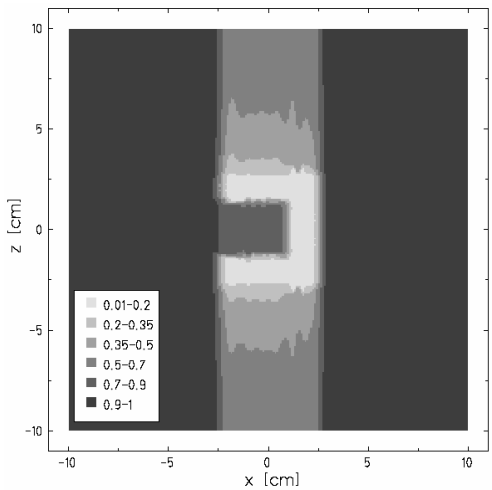

Figure 2: Calculated cell survival

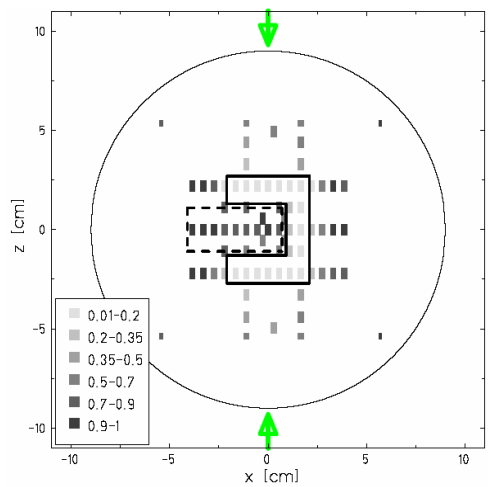

Figure 3: Measured cell survival. The target volume is indicated by solid lines and the OAR by dashed lines.

References

[1] M. Krämer et al, Phys. Med. Biol., 45/11 (2000) 3299.
[2] M. Krämer et al, Phys. Med. Biol., 45/11 (2000) 3319.
[3] GSI Report 2004
[4] A. Mitaroff et al, Radiat Environ Biophys 37 (1998) p. 47-51
[5] C. von Neubeck Diploma thesis, GSI (2006)

Experimental validation of survival calculations in the presence of motion

A. Schmidt, Ch. Bert, N. Saito, E. Rietzel, and G. Kraft
GSI, Darmstadt, Germany

Introduction

The software TRiP98 [1] is successfully used at GSI for treatment planning of stationary tumors. It is capable to calculate the absorbed dose and the biologically effective dose resulting from the superposition of usually several thousand C-12 pencil beams. Treatment is delivered with the raster scanner system [2]. If the target is subject to respiratory motion, treatment is not yet possible because target motion and scanning motion interfere and dose homogeneity is lost.

As part of the GSI motion compensation project (see [3]) TRiP98 was extended to calculate the distribution of the absorbed dose in the presence of motion [4]. Recently, we included calculation of cell survival.

Materials and methods

In the experiments a target volume of $3 \times 4 \times 1\,\mathrm{cm}^3$ was irradiated. Within the center of this volume we placed a grid of 96 cylindrical containers called wells (diameter 4.5mm) to allow for survival measurements with an adequate spatial resolution. Chinese hamster ovary cells (CHO-K1) were grown at the bottom of the well plate at standard conditions (37°C, 5% CO_2). We applied the beam using two irradiation schemes. First, the well plate was held at rest and the scanned beam delivered a homogeneous dose distribution to the target. This measurement was repeated twice and served as a static reference. Second, the well plate was moved sinusoidially (period 5 s, left-right in beams-eye-view with 2 cm amplitude) without motion compensation. 7 wells were chosen for experimental survival measurements. Selection criterion was a constant survival level within the well compared to the overall inhomogeneous survival pattern. The cells from each of these wells were carefully trypsinized, counted, and seeded at an appropriate number. After 7 days the cells were stained and scored for survival.

Results and discussion

Fig.1a shows the calculated survival for the static case. Fig.1b shows the survival measured in the wells depicted by the solid line in fig.1a in comparison to the calculation. The relatively large error bars account for the complicated cell processing procedure.

In case of uncompensated target motion interplay leads to a deteriorated survival distribution which is suitable for validating the calculation. The calculated 2D survival in case of target motion is shown in fig.2 (upper panel). Target motion leads to smearing of the survival and to an inhomogeneous interplay pattern. The comparison between experiment and calculation (fig.2, lower panel) predominantly validates the calculation. However, the experiments have to be repeated and the processing method has to be refined to gain better statistics and to acquire more data points. Finally, experiments using a motion compensation system with moving plates have to be performed.

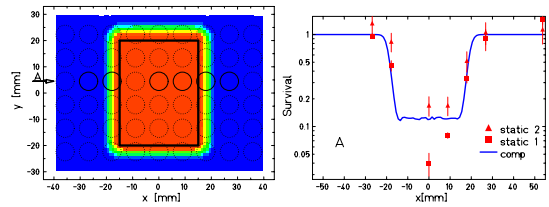

Figure 1: *a:* Calculated 2D survival distributions for the well plate at rest. The position of the wells is depicted by circles. Color coding is as in fig.2. The arrow indicates the line where the survival is measured. The PTV is indicated by the rectangle. *b:* Comparison between calculation and the two sets of measurements.

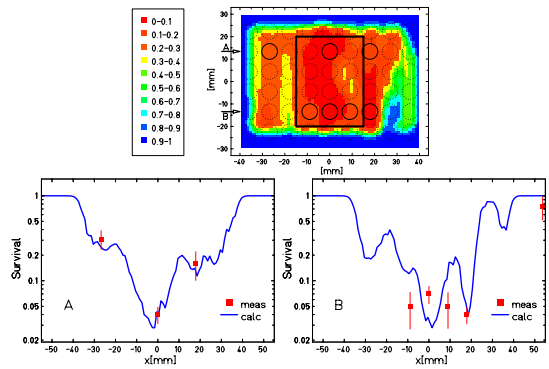

Figure 2: *Upper panel*: Calculated 2D survival for the irradiation scheme with target motion. *Lower panel*: Measured and calculated survival in comparison.

Acknowledgements

The authors thank C.v.Neubeck and M.Testa for the help during the experiments. This work is supported by Siemens Medical Solutions, Particle Therapy.

References

[1] M. Krämer et al, Phys. Med. Biol., **45** (2000) 3299

[2] Th. Haberer et al., NIM **A330** (1993) 296.

[3] N. Saito et al, This report.

[4] Ch. Bert, PhD-thesis (2006), TU Darmstadt.

Status of the 3D-online motion compensation system for ion therapy

N. Saito, C. Bert, A. Schmidt, W. Becher, E. Rietzel, D. Schardt, M. Testa, and G. Kraft
GSI, Darmstadt, Germany

Introduction

Scanned ion beam techniques proved to be an accurate method in radiation therapy with a high degree of conformity [1]. Since 1997 the carbon ion treatment unit at GSI has treated more than 330 patients with stationary tumours using a raster scanning system. In case of moving organs, however, it is necessary to mitigate interplay between organ motion and scanned beam. In order to achieve a high conformity and a homogeneous dose distribution also for moving tumours, GSI plans to compensate the organ motion in three dimensions. A prototype compensation system was developed and has been tested in different ways [2, 3, 4].

Status

The prototype motion compensation system currently consists of three LabVIEW-controlled subcomponents for motion detection, lateral compensation, and longitudinal compensation. Compensation parameters are calculated in advance as part of treatment planning. During treatment delivery, the parameters are selected from a look-up table and sent to the compensation branches. Parameter selection is based on the measured target position and the irradiated beam position.

For motion detection, a calibrated CCD camera (40 fps) is currently used to detect real time target motion by monitoring a LED which is set on a moving target. The LED position is analysed on-line, and a target position to be irradiated is predicted by taking a delay of the data transfer time into account.

For the lateral compensation the predicted displacement of the target position is sent from PC to the therapy control unit at VME. The scanning magnet is set on-line by taking the displacement into account. To improve deterministic data transfer time we exchanged the initially used TCP/IP connection [2] with a VME-PCI link bridge that maps the control system's memory on the LabVIEW-PC. With this direct connection the scanning magnets were controlled more reliably to follow the target motion in real time. The nominal and measured beam positions were compared, and the deviation between those beam positions agreed within 0.3 mm in RMS. The system has been tested also by irradiating a moving radiographic film (periodical motion to left and right with a period of about 5s). Figure 1 shows the film response for the beam scanning which was originally planned to form a homogeneous rectangle shape without motion compensation (left) and with compensation (right). The irradiation pattern of fig. 1 (left) shows the interplay between the scanning beam and the motion of the film, while the pattern in fig. 1 (right) shows a homogeneous rectangle pattern which agrees well with an irradiation pattern for a stationary target. The lateral compensation works successfully, however, the loop-time of the compensation process is influenced by tasks running on the PC which sometimes leads to false compensated beam positions. Further optimisation of software on the PC will be performed to achieve a reliable time deterministic compensation system.

The displacement of the longitudinal Bragg peak position is compensated by a wedge-type range shifter [5] installed in between beam exit window and target. Currently the range shifter consists of 2 sets of 5 PMMA wedges. Each set is placed on a linear motor with a maximum acceleration of about 1g. Based on clinical 4DCT data simulations were performed to find the acceleration required for treatment of lung tumours. The results showed that higher accelerations are required. To achieve these higher accelerations and to improve the communication between PC and motion controller we currently replace the linear motor system by a state of art servo linear motor. The new linear motor has a continuous acceleration of about 5g (10g for the thickness change) and will be tested with beam in March 2007.

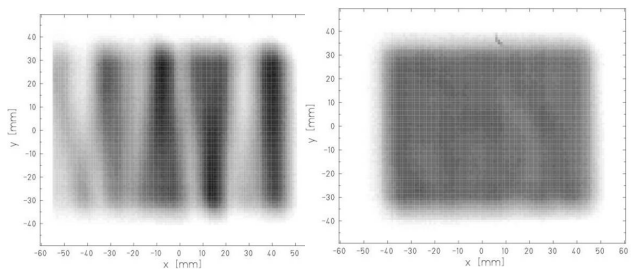

Fig. 1 : Irradiation pattern on a moving X-ray film (rectangular shape) without motion compensation (left), and with motion compensation (right).

References

[1] Gerhard Kraft, Prog. Part. Nucl. Phys. 45 (2000) s473.
[2] Sven Oliver Grözinger, Ph.D. Thesis, Technical Uni.Darmstadt, Germany (2004).
[3] Q. Li, et al. Phys. Med. Biol. 49 (2004) 3029.
[4] Christoph Bert, Ph.D. Thesis, Technical Uni. Darmstadt, Germany (2006).
[5] U. Weber *et al*, Phys. Med. Biol. 45 (200) 3627.

Acknowledgement

The authors appreciate fruitful discussions with Drs. S. Brons, S. O. Grözinger, M. Krämer, T. Haberer, and U. Weber, and lots of technical support from Drs. N. Kurz, and W. Ott. This work is supported by Siemens Medical Solutions, Particle Therapy.

Treatment planning study: Motion mitigation techniques for lung tumors

Christoph Bert and Eike Rietzel
GSI, Darmstadt, Germany

Introduction

Currently, the C-12 therapy performed at GSI cannot be applied to moving tumors because interplay between scanned ion beam and moving target does not allow controlled dose delivery. Several techniques are proposed to mitigate the influence of interplay. Among them are tracking [1], gating [2], rescanning [3], and use of margins. We used the 4D extension of GSI's treatment planning software TRiP [4] to calculate dose distributions for these mitigation techniques. Studies are based on 4DCT data from 5 lung tumor patients. Exemplary data are shown here, a detailed report will follow elsewhere.

Material and methods

For each of the patients and each mitigation technique a treatment plan was optimized. As planning target volume (PTV) we used the clinical target volume (CTV) plus margins covering the technique specific residual motion as determined by 4DCT. The treatment plan was optimized such that the energy for each pencil beam was sufficiently high to reach the corresponding grid position in any motion phase. For tracking, compensation parameters were calculated.

We computed the dose distributions of 12 motion parameter combinations for each patient and each technique (3 periods and 4 initial breathing phases). Motion amplitude was given by 4DCT and quantified by non-rigid deformation maps [5]. Particle extraction and thus beam motion were modeled according to the parameters planned for the Heidelberg ion therapy. The data shown are for motion with 4s period and 90° initial phase.

The dose distributions were analyzed by visual inspection and by dose-volume-histograms (DVH) for CTV and for the ipsilateral lung as the organ at risk.

Results and discussion

Use of internal margins did not lead to acceptable dose distributions for any patient. Despite margins, interplay caused cold and hot spots within the CTV.

Dose distributions for tracking, gating, and rescanning are shown in fig.1. The 90% iso-dose covers the CTV for all techniques as is also shown in the corresponding DVH for the CTV shown in fig. 2.

The techniques mainly differ in the dose deposited to surrounding lung tissue. In fig. 1 this can be seen e.g. for rescanning which is the technique with the largest residual motion. CTV motion was mainly in cranio-caudal direction. Since the PTV covers all positions of the CTV and since lung tissue is less dense than tumor tissue, dose contributions distal of the PTV appear at extremal CTV positions (crosses in fig. 1c). Comparison of lung DVHs (fig. 2b) quantifies this effect.

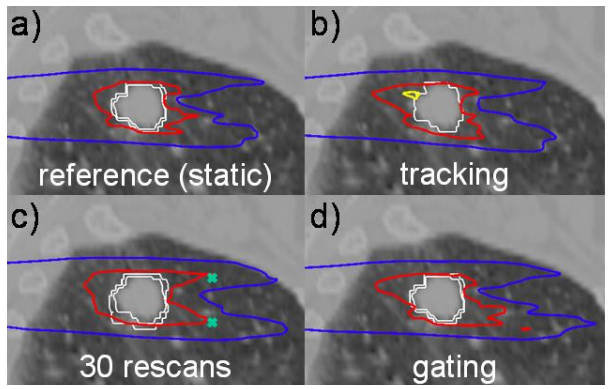

Figure 1: Shown is a sagittal slice of the CT with CTV and PTV. Overlaid are iso-dose lines for 50% and 90% of the prescribed dose.

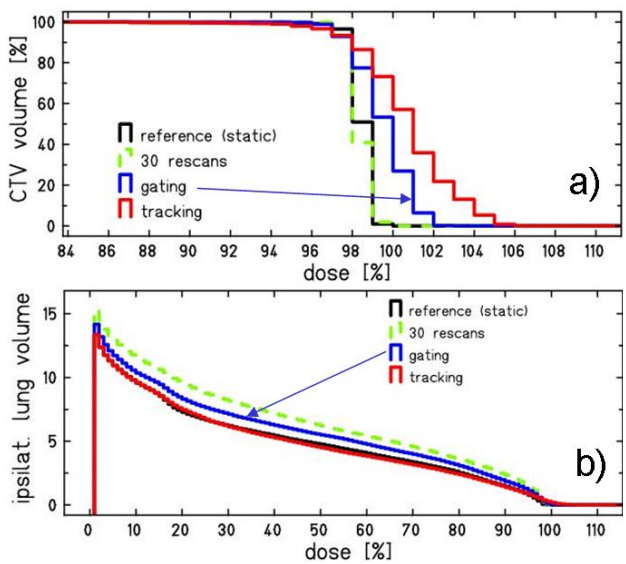

Figure 2: DVHs for CTV (a) and ipsilateral lung (b) as organ at risk for the dose data shown in fig. 1. All techniques deliver the prescribed dose level within the PTV. Gating and rescanning lead to an increased lung-dose.

Conclusion

Example data of a planning study were presented. Rescanning, gating, and tracking delivered sufficient dose to the PTV. However, gating and especially rescanning lead to an increased lung dose.

References

[1] Grözinger et al., *Phys Med Biol* 2006, **51**
[2] Minohara et al, *Int J Radiat Oncol* 2000, **47**
[4] Phillips et al, *Phys Med Biol* 1992, **37**
[5] Bert, PhD-Thesis, TU Darmstadt, 2006
[6] Rietzel et al, *Int J Radiat Oncol* 2005, **61**

Modelling therapeutical ^{3}He beams

G. Kragl[1,2], M. Krämer[1], J. Naumann[1,3], D. Schardt[1], and W. Weyrather[1]
[1]GSI, Darmstadt, Germany; [2]Technische Universität Wien, Austria; [3]HIT AG, Heidelberg, Germany

Introduction

At present various sites around the world use beams of swift protons or carbon ions for radiotherapy. The success of the GSI ^{12}C radiotherapy pilot project has triggered the planning and/or construction of numerous clinical ion facilities in Germany (Heidelberg, Marburg, Berlin) and Europe (CNAO, MedAustron, Etoile). These sites will use carbon ions and also protons as their prime modalities. There are, however, physical and radiobiological reasons to inspect other light ion species for their potential therapeutical advantages. In particular helium ions undergo less lateral scattering than protons and less nuclear fragmentation than carbon. Consequently, the HIT facility was designed to also offer helium beams as an option, which means that eventually physical and radiobiological models must be as patient-ready as they are now for ^{12}C.

Nuclear Reaction Cross Sections

The parameters of semi-empirical formulae were fitted to the few available nuclear reaction data for the ^{3}He collision with the water molecule [1]. Figure 1 shows the data together with the chosen adaption curves.

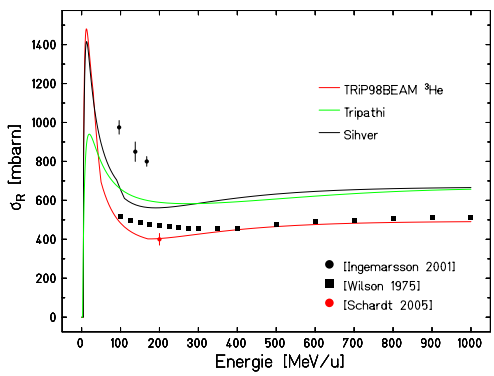

Figure 1: Reaction cross section for the nuclear reaction of ^{3}He projectiles with ^{16}O target atoms. Different models are compared with measured data [1], [3].

Depth Dose Distributions

With these base data the developer version, TRiP98BEAM, of our treatment planning system [2] was modified to generate depth dose curves and related charged particle energy spectra for ^{3}He, which subsequently can be used for treatment planning the same way as those for ^{12}C. Figure 2 shows calculation results compared with data measured at GSI.

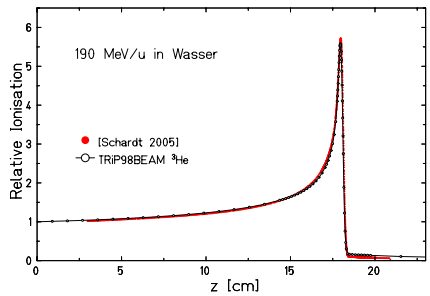

Figure 2: Depth dose profile of a ^{3}He beam in water.

Biological Dosimetry

Biological dosimetric measurements to ensure that also the biological outcome is as expected have been performed. An extended target volume was defined and irradiation was planned and performed as for a real patient. By means of a stack of culture flasks the depth survival profile was measured and compared with the planning prediction (Fig. 3). Due to the high activation of the sample a long waiting time between irradiation and trypsination was necessary. Repair processes during this time may cause increased cell survival. In addition, an adaptation of the modified biological model [5] in the low-LET range could result in a better agreement.

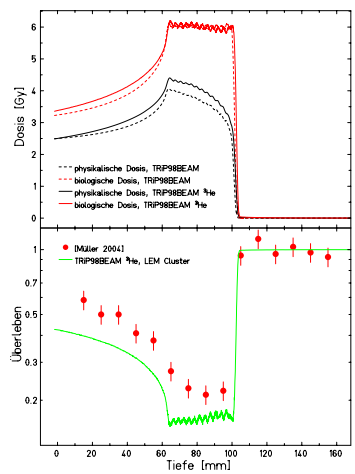

Figure 3: Physical dose, biological dose and survival of CHO cells in dependence of depth in water [4].

References

[1] G. Kragl, Diploma Thesis, TU Wien 2006
[2] M. Krämer et al, Phys. Med. Biol., 45/11 (2000) 3299
[3] H. Iwase, D. Schardt, Internal Report, GSI Biophysics 2006
[4] M. Müller, GSI Report 2004
[5] Th. Elsässer, GSI Report 2006

Analysis of the multiple scattering implementation in TRiP *

G. Iancu[1], W. Weyrather[1], and M. Krämer[1]
[1]GSI, Darmstadt, Germany

One of the main goals of any therapy treatment planning is the delivery of a conformal dose distribution in the target tissue while sparing the near seated critical ones. The multiple scattering is one of the important aspects that play a role in the modelling of the beam parameters.

TRiP

TReatment plannIng for Particles[1] is the software successfully used at GSI for therapy. While available, the Monte Carlo codes used for simulation in particle physics, are for therapy purposes rather time consuming and therefore not suitable for clinical practice. To shortcut this overhead TRiP is using a dose distribution database. This database is calculated for different ions in water and practically used energies (for ^{12}C 50-500 AMeV). For all other materials the dose distribution is derived from the water equivalent of the components.

Multiple scattering

For calculating the multiple scattering the Highland[2] parameterised form of the Moliere[3] scattering is used. This is found to be suitable in the case of small angles [4].

The procedure used follows:

- for each energy a Monte Carlo simulation is used to build an ensemble of beam particles
- using the Highland parameterisation each ensemble is then propagated through the target material. The momentum change is accounted using the Morrisey[5] formula
- the angle distribution obtained is then transformed in a spatial distribution and fitted through a double Gaussian

Figure 1 shows a plot of simulated radial dose distribution for a ^{12}C beam at 330 MeV/u in water. The depth at which the distribution is plotted is 199.63 mm and the Bragg peak depth is 201.81 mm. The difference between data integral and fit function integral is 2%.

Figure 2 is showing the ratio between the dose calculated from the double Gaussian parameterisation over the one obtained through simulation. The energy domain used in the water phantom experiment is between 320 AMeV and 345 AMeV. A systematic underestimation of the data can be observed. Nevertheless there is no important energy dependence of the effect so that the difference can be overcome through scaling. Due to symmetry reasons the main affected target areas are the ones lateral seated with respect to the beam direction.

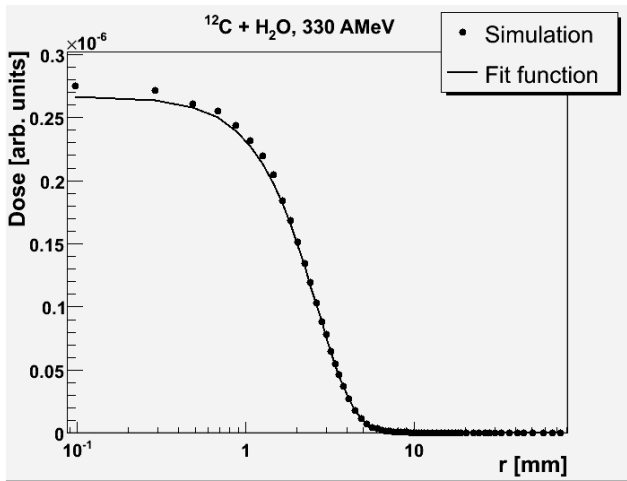

Figure 1. Radial distribution of a carbon beam at 330 MeV/u together with the fit function (see text).

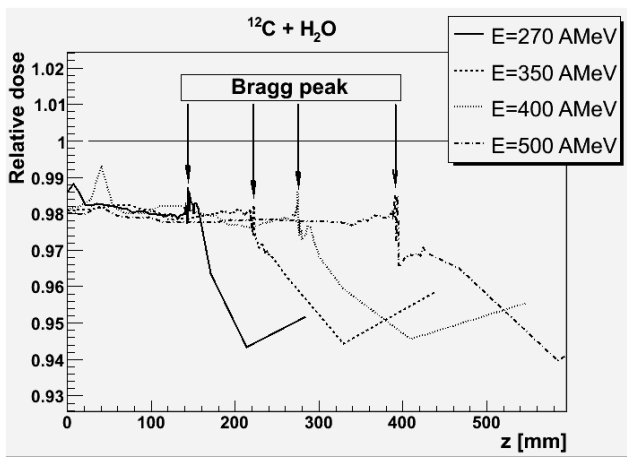

Figure 2. Dose calculated with the double Gauss parameterisation over the one obtained through MC calculation.

References

[1] M. Krämer et al. , "Treatment planning for heavy ion radiotherapy: physical beam model and dose optimisation", Phys. Med. Biol. 45 (2000) 3299-317.
[2] V. L. Highland, "Some practical remarks on multiple scattering", Nucl. Instr. and Meth. 129 (1975) p.497 and 161 (1979) p.171
[3] G. Moliere, "Theorie der Sreuung schneller geladener Teilchen", Z. Naturforschung 3a (1948) p. 78
[4] B. Gottschalk et al., "Multiple coulomb scattering of 160 MeV protons", Nucl. Instr. and Meth. B74 (1993) p. 467-490
[5] D.J. Morrisey, Phys. Rev. C39 (1989) p.460
[6] U. Weber , Doctoral thesis, Uni Kassel (1996)

Influence of the System Matrix on the Quality of the Reconstruction of In-Beam PET Data *

G. Shakirin[1,#], P. Crespo[1], and W. Enghardt[1,2]
[1]FZD, Dresden, Germany; [2]Technische Universität Dresden

At the experimental heavy ion therapy facility at the GSI Darmstadt an in-beam PET scanner is operated for quality assurance monitoring simultaneously to the therapeutic irradiation. A fully 3D maximum likelihood expectation maximization (MLEM) reconstruction algorithm has been developed and adapted to the special conditions of in-beam PET [1]. The system response function (system matrix) for that algorithm is implemented by separately calculating its components (geometry, scatter, attenuation and detector sensitivity). The system matrix itself includes the geometry component only. The geometry component of the system matrix is calculated "on-the-fly" during the reconstruction. In order to determine this component, the volume of each tube of response (TOR) is sampled by a number of lines whose endpoints are randomly distributed over the crystal surfaces. The number of lines used in the method is called a *level*. The higher the level, the more accurate and slower is the calculation. We investigated the accuracy for this approach as well as for another method for calculating of the geometry component of the system matrix based on the approximation with splines [2]. An influence of the system matrix on the quality of reconstructed images was evaluated for MLEM and ordered subsets expectation maximization (OSEM) algorithms using real treatment data collected during the therapeutic irradiations at the GSI. The accuracy of both methods for the system matrix calculation ("on-the-fly" and with splines approximation) was checked by means of analyzing the normalized mean square error (NMSE) (Fig.1 left). The method with splines approximation achieves high accuracy (*NMSE* = 0.00047) and performs with the same speed as "on-the-fly" method with level equal to 50. For visual comparison of accuracy the system matrix was calculated for one TOR with the two different methods (Fig. 1 right). The influence of system matrix on the reconstruction quality was evaluated by means of an ensemble mean square error (EMSE) [3]. The true β^+-activity distributions were generated by means of the PosGen Monte Carlo code based on real treatment data of 9 patients. EMSE was calculated for reconstructions with the MLEM algorithm (50 iterations) and with the OSEM algorithm (8 subsets, 10 iterations). EMSE does not depend significantly on the quality of the system matrix when reconstructions are performed by MLEM algorithm, but significant deviations are observed when using the OSEM algorithm (Fig. 2).

As a conclusion, it is profitable to use the splines approximation method for reconstructions with OSEM algorithm where higher quality of the system matrix leads to lower mean square error and slightly better images. However, in the specific conditions of in-beam PET (dual-head geometry and low counting statistics) the best result for reconstructions performed by the MLEM algorithm by means of EMSE is achieved with the system matrix of poor quality (with "on-the-fly" method with level = 3) and visual comparison gives no significant difference.

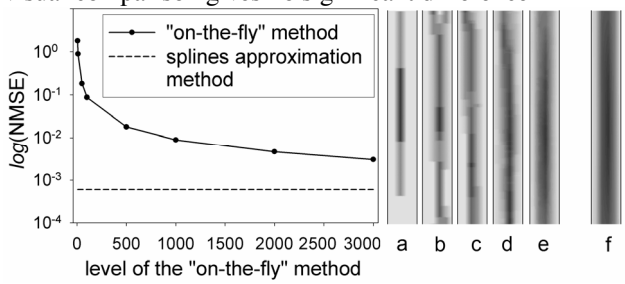

Figure 1: Left: NMSE calculated for different levels for "on-the-fly" method comparing with NMSE for splines approximation method. Right: central slice of one TOR filled with system matrix values calculated with the "on-the-fly" method with level equal to 5 (a), 10 (b), 20 (c), 100 (d), 1000 (e) and with the splines approximation method (f).

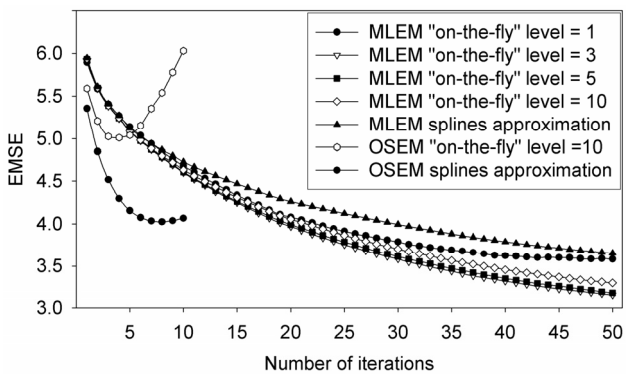

Figure 2: EMSE for images reconstructed with MLEM and OSEM (8 subsets) algorithms and different methods for calculation of the system matrix.

References

[1] K. Lauckner, "Entwicklung eines iterativen 3D Rekonstruktionsverfahrens für die Kontrolle der Tumorbehandlung mit Schwerionen mittels der PET", Thesis, Technische Universität Dresden, 1999

[2] G. Shakirin et al., "A Method of Processing of the Elements of the System Matrix for Iterative Reconstruction of PET Data", GSI Sci. Rep. 2005 p. 394

[3] H. H. Barrett and K. J. Myers "Foundations of Image Science" ISBN: 0-471-15300-1, 2003, pp. 879-883

* Work supported by the GSI, Darmstadt and the European Union
# g.shakirin@fzd.de

In-beam PET measurements of biological half-lives of ^{12}C irradiation induced β^+-activity *

F. Fiedler† [1], M. Sellesk[1,2], P. Crespo[1], R. Jülich[1], K. Parodi[3], J. Pawelke[1], F. Pönisch[1,4], and W. Enghardt[1,4]

[1]FZD, Dresden, Germany; [2]TU Bergakademie Freiberg, Germany; [3]HIT, Heidelberg, Germany; [4]TU Dresden, Germany

Introduction

The in-beam PET method is a valuable tool to measure the distribution of the delivered dose in the irradiated tissue in carbon ion therapy which has so far been applied to more than 300 patients. In order to evaluate the PET data with respect to the patient anatomy, positioning and range of the beam [2], they need to be compared with a simulation of the expected activity distribution [1]. Although these algorithms are well adapted to the therapeutic situation, there are differences that can be attributed to metabolic processes taking place in living organisms, such as the predominant perfusion-driven washout of the positron emitters. Since comprehensive data of the washout as a function of the tissue and the type of the radionuclides are not available, these processes are not taken into account in the current simulation code. In order to obtain such data, we analysed the results of a set of in-beam PET data scans taken during therapeutic ^{12}C irradiation.

Patient studies

We expect a correlation between the tissue type along the lines of response (LOR) of the positron camera and the effective half life. The only available information in this respect is provided by the planning CT, i.e. the Hounsfield unit (HU). However, the mean HU, $\overline{HU}$, along a LOR is not sufficient for classification, the standard deviation of the HU within each LOR (σ_{HU}) was additionally introduced to take into account tissue inhomogeneity (cf. Fig. 1). These two quantities were classified into 3 different regions of interest (ROI) for 14 patients. ROI I was supposed to contain rather homogeneous brain tissue (e.g. brain), ROI II was expected to include soft, but inhomogeneous tissue, and ROI III was for bone. The anatomical mapping is displayed in Fig. 2. No dependence of the effective half life on the $\overline{HU}$ and σ_{HU} was found. Therefore, we investigated the effect of the different dose levels on the effective half live by analysing two other groups of LOR. The first contained at least ten voxels with 90 % of the maximum dose. The second set of LOR contained voxel with 0 - 90 % of the maximum dose with no voxel higher than 90 %. Combining data of 55 patients, a lower effective half live for the 0 - 90 % region was found ($T_{1/2} = 71.8 \pm 0.6$ s) than for the 90 - 100 % region ($T_{1/2} = 79.5 \pm 1.8$ s) possibly due to less perfusion in the tumour.

* Work supported by GSI and EU (QLRT-2001-01574).

† f.fiedler@fzd.de

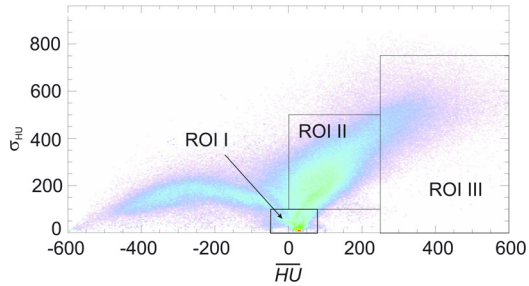

Figure 1: Two-dimensional histogram of the fraction of the LOR intersecting the planned target volume as a function of $\overline{HU}$ and σ_{HU}. The corresponding anatomical regions for a particular patient can be seen in Fig. 2.

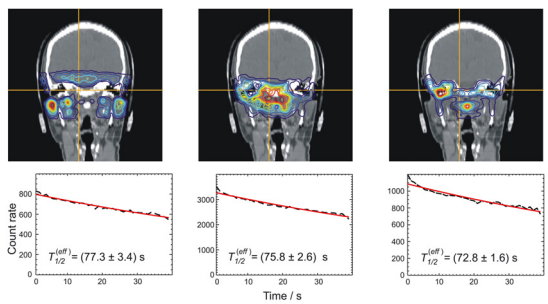

Figure 2: Effective half-lives in the patient according to the ROIs defined in Fig. 1. The left figure corresponds to ROI I, the middle to ROI II and the right to ROI III, respectively.

Conclusions

The in-beam PET data acquired during 40 s after finishing therapeutic irradiation indicate that on this rather short time scale no differentiation of tissue with respect to the washout rate of the ^{12}C beam induced β^+-radioactivity was observed. Therefore, if in-beam PET measurements can be restricted to scanning times below 100 s, the influence of tissue dependent washout processes to the spatial distribution of beam induced β^+-activity can be expected to be drastically diminished. This is expected to improve the correspondence between the measured in-beam PET images and those predicted from the treatment plan.

References

[1] F. Pönisch et al., Phys. Med. Biol. 49 (2004) 5217.

[2] W. Enghardt et al., Nucl. Inst. Meth. A 525 (2004), 284.

Neutron dose produced by 200 MeV/u ^{12}C beams stopping in water

H. Iwase, D. Schardt, F. Guthermuth
GSI, Darmstadt, Germany

To provide better data on the production of secondary particles as input for treatment planning systems for carbon ion therapy, experimental studies on ^{12}C fragmentation in water phantoms were performed at GSI. This included also measurements on the dose contribution of secondary neutrons. Systematic data on the neutron dose behind a water target were obtained in previous measurements[1], using a WENDI-II neutron dose meter[2].

Recent studies on carbon fragmentation[3, 4] have shown that more charged particels than neutrons emerge from the target at small forward angles. At 0°, the ratio of He- to H-fragments to neutrons is about 2.6 : 1.2 : 1. This means that a **neutron** dose meter placed at 0° is exposed to a mixed radiation field of charged particles and neutrons. The response of the neutron dose meter to charged particles is therefore an important question.

Response functions of WENDI-II for n, p, and ^{4}He were calculated using the PHITS code[5]. The response was assumed to be proportional to the energy deposition in the ^{3}He proportional counter in the core of WENDI-II. Fig. 1 shows the calculated WENDI-II responses per incident n, p, and ^{4}He particle respectively. The calculation predicts that the WENDI-II scores dose when it is hit by protons or ^{4}He particles with energies above 100 MeV/u.

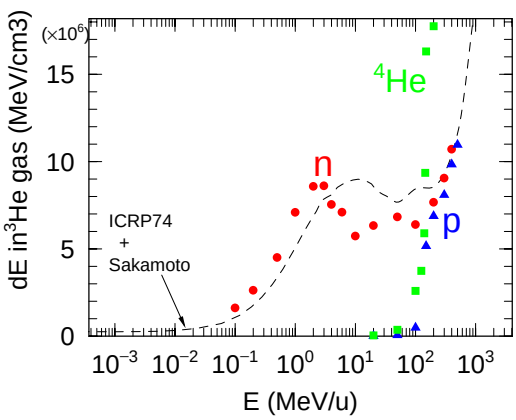

Figure 1: Response of WENDI-II to mono-energetic n, p, and ^{4}He particles

In previous experiments [3], energy spectra and angular distributions of secondary neutrons produced by 200 MeV/u ^{12}C beams stopping in a 12.8 cm thick water absorber were measured with a BaF_2 detector. Based on these neutron fluence data an estimate of the neutron equivalent dose was obtained by convolution with the fluence-to-dose conversion factor $h_\Phi(E)$. These data were compared to direct neutron dose measurements performed with WENDI-II for the same beam-target combination and at the same distance of 3m behind the target. As can be seen from Fig.2, the apparent neutron dose obtained from WENDI-II is much higher compared to the dose estimate based on the neutron fluence data, especially at small angles.

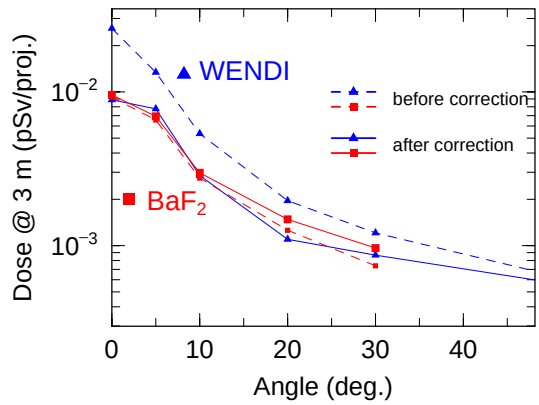

Figure 2: Results of neutron angular distributions by 200 MeV/u ^{12}C on 12.8 cm water

This discrepancy is attributed to the charged-particle response of WENDI-II. Using the response-functions for protons and helium fragments shown in Fig.1 and the spectral data of Ref.3 the WENDI-response was calculated with the PHITS code. The numbers given in table1 are proportional to the energy deposition in the ^{3}He counter tube of WENDI-II. At 0° only 34% of the measured signal stems from neutrons. This number increases to 52% at 10° and 20° and 64% at 30°. After applying these corrections to the original WENDI-II data, good agreement with the fluence-based neutron dose values is obtained. The neutron dose at 0° corresponds to a total dose of 0.5 mSv at 3m distance for a typical patient treatment with a tumor dose of 60 GyE.

Table 1: WENDI-II response to secondary fragments

Angle	Neutron	^{1}H	^{2}H	^{3}H	^{3}He	^{4}He
0	396.	115.	154.	86.	62.	368.
5	226.	48.	51.	35.	8.	33.
10	96.	40.	27.	16.	2.	4.
20	30.	21.	5.	2.	0.	0.
30	9.	4.	1.	0.	0.	0.

References

[1] H. Iwase et al., GSI scientific report 2004, pp 330 (2005).

[2] Olsher RH, et al., (2000) *Health Phys*, **79(2)**, 170-181.

[3] K. Gunzert-Marx (2003) *Ph.D. thesis, TU Darmstadt*.

[4] E. Haettner, *Master of Sci. Thesis, KTM Stockholm* (2006)

[5] H. Iwase et al., J. of Nucl. Sci. and Technol, 39, 11, 1142-1151 (2002)

Microdosimetry measurements for ^{12}C pencil beams stopping in water

S. Tsuda[1], D. Schardt[2] and F. Wissmann[3]
[1] JAEA, Ibaraki, Japan; [2] GSI, Darmstadt, Germany; [3] PTB Braunschweig, Germany.

Introduction

The inverted depth-dose profile (Bragg curve) and the small lateral spread of high-energy beams of ^{12}C ions are important advantages for the treatment of deep-seated local tumors.

The radiation field generated by heavy-ion beams in tissue is, however, rather complex, in particular due to the production of secondary nuclear fragments along the penetration path. In this work microdosimetric measurements were performed in order to characterize the radiation field of 300 MeV/u ^{12}C pencil beams in water, especially at locations off the beam axis where the small dose levels are essentially due to secondary protons and α-particles.

Experiment

Measurements were performed in the therapy room at GSI, CaveM, using a Tissue Equivalent Proportional Counter, TEPC[1)] (LET-1/2, Far West Technology, Goleta, CA, USA). The counter consists of a sphere shell made of tissue-equivalent plastic, Shonka type A150. The inner diameter of the sphere is 12.7 mm and the wall thickness 1.27 mm. The inside is filled with propane-based tissue-equivalent gas kept at 90 Torr pressure, which is equivalent to 2.7 µm in diameter of human tissue. Conversion of pulse heights into lineal energy was done using the built-in ^{244}Cm alpha source (mean energy ~5.796 MeV). Energy deposited by the alpha particles was calculated using the ATIMA code[2)]. The output signals were split and fed into three amplifiers with different gains (2.5, 25 and 400) to obtain wide range lineal energy distribution. The central horizontal section of the water phantom (30x30x30cm^3) is represented in Fig.1.

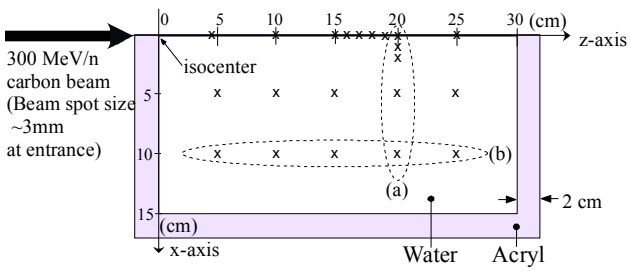

Figure 1: Horizontal section of the water phantom (half-side). Symbols, x, show the positions where lineal energy distributions were measured.

Preliminary Results

Lineal energy distributions measured along the beam axis near the Bragg peak at 15 cm and 25 cm downstream are shown in Fig.2. The distribution at 25cm depth (note the scaling factor 100) exhibits a peak at 7 keV µm^{-1}, where secondary protons and α-particles mainly contribute. These particles have wide energy distributions. Further analysis is in progress for comparing the measured y-distributions with Monte-Carlo-based model calculations.

Figure 3 shows the absorbed doses by secondary charged particles in water. It is found that the doses of secondary charged particles sharply decrease with the distance from the beam axis. The doses along the beam at 10 cm lateral distance gradually increase with depth up to 15 cm because of the increasing flux of secondary fragments which are produced along the penetration path.

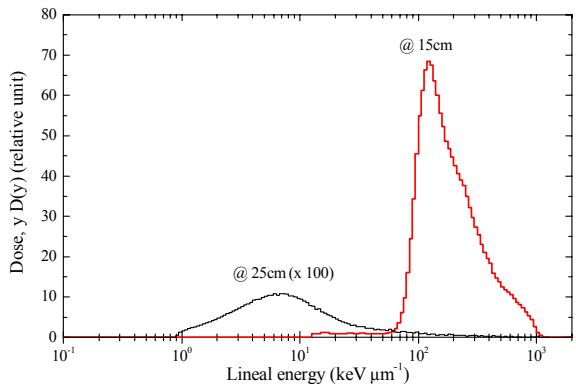

Figure 2: Lineal energy distributions measured at 15 cm and 25 cm depth on the beam axis in the water phantom.

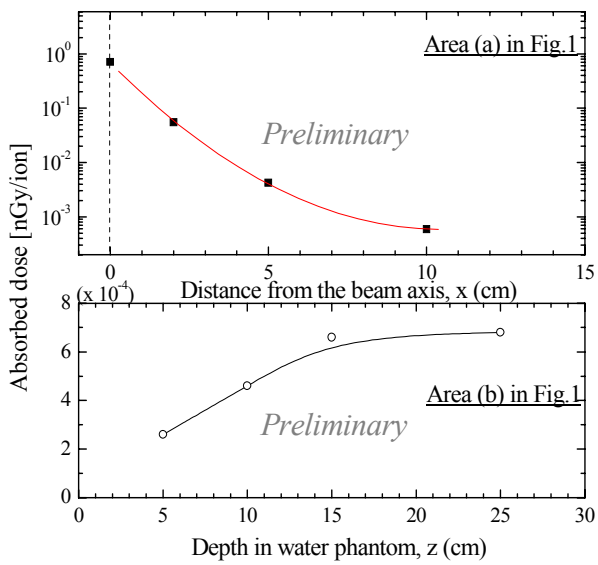

Figure 3: Absorbed doses on the positions vertical to the beam axis (a) and off the beam axis (b). See Fig.1.

[1] ICRU, Microdosimetry, ICRU Report 36 (1983).
[2] H.Geissel, et al., ATIMA, www-linux.gsi.de/~weick/atima/ (2006).

Investigation of a thermoluminescence response of diamonds to heavy-ion irradiation

M. Rębisz#, B. Voss
GSI, Darmstadt, Germany

The response of 60 commercially available synthetic polycrystalline diamonds made by Chemical Vapour Deposition (pCVD) technique and standard Thermo-Luminescent Dosimeters (TLDs) to heavy-ions was investigated. Systematically recorded dose-response curves for high-energy carbon beams (88-430 MeV/u) as well as low-energetic heavy-ions (HI) from ^{12}C up to ^{238}U with energies below 10 MeV/u allowed to determine the relative TL efficiency of dosimeters

$$\eta = \frac{\left(TL/D\right)_{HI}}{\left(TL/D\right)_{ref}}$$

defined as the ratio of the TL signal per unit dose and unit mass for heavy charged particles to the signal for sparsely ionizing radiation [1]. Measurements with a reference-radiation source have been done with ^{60}Co and an X-rays lamp. Figure 1 presents the relative efficiency of mechanical grade 'PC' diamonds and LiF dosimeters to heavy-ions.

The decrease of the TL efficiency with increasing Linear Energy Transfer (LET) is less pronounced for the diamond detectors and the efficiency is even up to 45 times higher than for LiF dosimeters after an irradiation with ^{208}Pb ions [2].

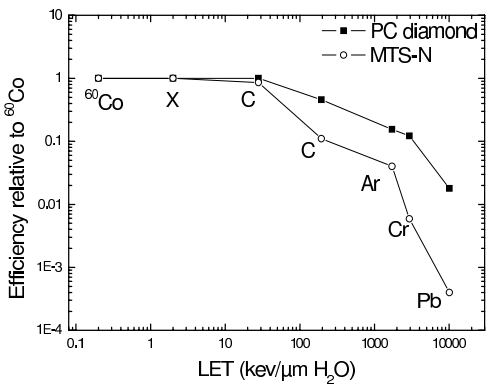

Figure 1: Experimental relative TL efficiency (η) for the CVD diamond and LiF dosimeters as a function of the calculated LET in water

There are many instances in medical dosimetry where spatial (3D or 2D) dose distributions need to be measured. For the quality control of the therapeutic-beam parameters on-line measurements of intensity and profile of the pencil beam are not sufficient and the determination of the resulting dose distribution in phantoms is also necessary to obtain. The measurements of the TL signals of the pCVD diamonds and TLD100 dosimeters for various depth in a phantom made of a stack of 60 PMMA slabs each with 5 mm thickness for the scanning ^{12}C beam are presented. Figure 2 illustrate the depth-dose distribution profiles as the results of two measurements performed with carbon ions with initial energies of 307 MeV/u and 354 MeV/u, for a dose of 1 Gy in the plateau region of the Bragg-Peak. The detectors were calibrated with a carbon beam with energy of 248 MeV/u.

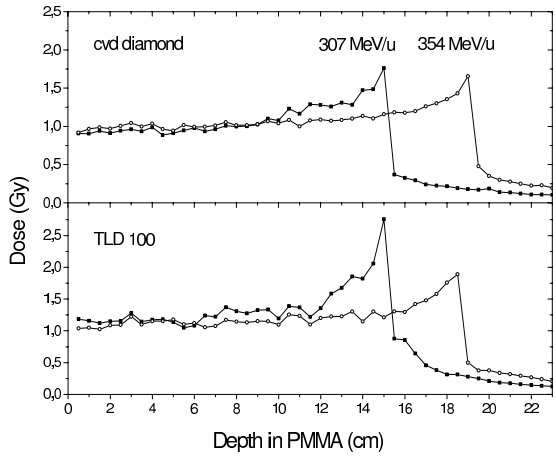

Figure 2: Depth-dose distributions for the 307 MeV/u and 354 MeV/u carbon beams measured with pCVD diamond material and TLD100 type LiF detectors.

For both tested dosimeters the Bragg-Peak with its steep fall off is clearly visible. The precision of the dose evaluation suffers from the imperfect positioning of the individual detectors in the phantom along the ions paths. The Bragg-Peak is not always recorded with the required accuracy because of the granularity in depth.

References

[1] Y.S. Horowitz, O. Avila, M. Rodriguez-Villafuerte, 2001, Nuclear Instruments and Methods in Physics Research B; 184, 85-112.

[2] M. Rębisz, B. Voss, The response of thermally stimulated luminescence in CVD diamonds to heavy charged particles, contribution to this report & Radiation Measurements 2007, in press

#M.Rebisz@gsi.de

Investigations on BeO as a dosimeter material for hadron therapy

B. Voss[*,1], M. Rębisz[1] , M. Sommer[2]
[1]GSI, Darmstadt, Germany; [2]Technische Universität Dresden, Dresden, Germany.

Introduction

Hadron cancer-therapy with high-energetic heavy-ions (HI) as available at the SIS facility at GSI Darmstadt [1] as well as the research with beams stopped in biological material as realized at the UNILAC at GSI in general require the precise knowledge of the applied dose within less than 1% in most cases. Solid state detectors based on various materials read out via thermally stimulated light emission are often used to fulfil this task [2].

Material and measurements

We present investigations on the performance of BeO dosemeters based on Thermalox 995® pellets of 4 mm diameter and 0.8 mm thickness delivered by Brush-Wellmann. Irradiations were performed at the therapy facility of GSI with carbon ions of energies between 88 and 430 MeV/u. The irradiated disc have been read out using Optically-Stimulated-Light emission (OSL) with a reader of type 'BeOmax' [3].

Results

As an example, fig. 1 shows the circular wedge-shaped 2D dose distribution for 430 MeV/u ions ranging from 0.1 to 10.6 Gy in various steps.

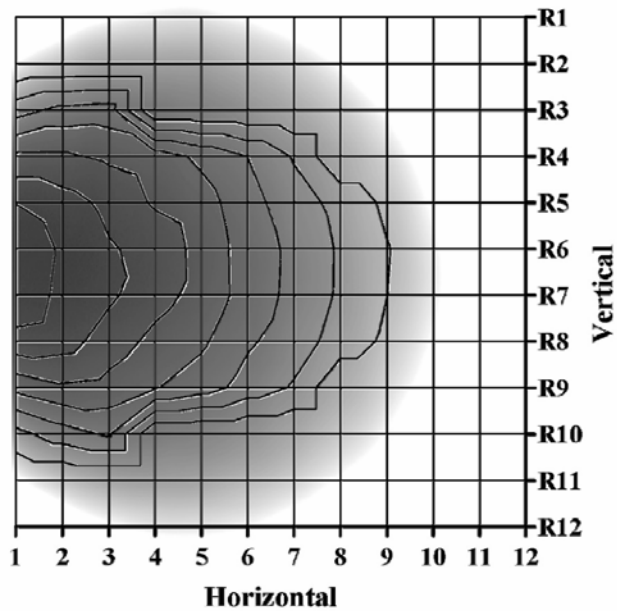

Figure 1: Contours of measured doses on top of the optical density distribution of a radiographic film for a circular dose wedge. Doses range from 0.1 to 10.6 Gy The steps in the contours stem from the placement of the limited amount of samples available.

We observe a fairly good agreement between the spatial distribution of the nominal dose delivered and the measured contours. Figure 2 shows the comparison for the horizontal cut through the centre of the distribution. Nominal and measured values show a linear dependence within an error of approximately 5%.

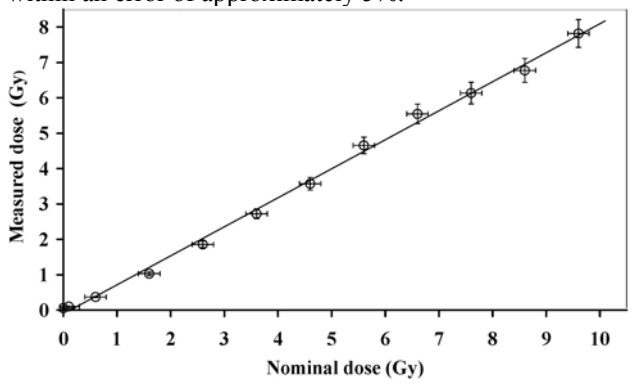

Figure 2: Comparison between measured and nominal doses for the horizontal cut through the centre of the wedge shaped irradiation (see fig. 1).

The dominant contribution to the error bars arise from the limited accuracy of the positioning (x) of the samples during the irradiation. Besides this, the variation in the individual response of the samples to photons is in the order of 20 % as usually found for solid-state dosimetric material. Unfortunately, the calibration (y) for the individual samples which has been performed with photons does not take into account effects arising form the high LET of the heavy ions inside each particle track. Here the saturation level of the material which is approx. 5 Gy for low-LET radiation is easily reached. This also leads to a loss of the measured absolute dose which is deficient by 20% if one only takes into account the first 10 s of the OSL decay curve which shows a slower degradation of the signal with time if compared to low-LET irradiated samples. This may be due to the activation of deeper traps which usually are not taken into account in the evaluation.

Conclusions

Using BeO as a dosimeter material for irradiation with heavy ions seems to be feasible. However, the accuracy of these measurements has still to be improved in order to cope with the needs of medical devices. Moreover, more precise and detailed measurements are needed as input for the development of a theoretical model including the effects of high-LET radiation.

References

[1] G. Kraft, Nucl. Instr. and Meth. in Phys. Res. A 454 (2000) 1-10.
[2] M. Rębisz, B. Voss, accepted for publication in Rad. Prot. Dosim. (2007).
[3] M. Sommer, J. Henninger, Rad. Prot. Dosim. 119 (2006) 394-397.

[*]B.Voss@GSI.de

Status Report of the HIT Project

U. Weinrich for the GSI therapy accelerator team

Abstract

Major progress of the Heidelberg ion beam cancer therapy centre took place in 2006. The assembly of the full accelerator up to the fixed beam patient treatment rooms was performed. The LINAC commissioning with beam has recently been completed and the first technical subsystems have been handled over to the HIT GmbH, the company which is charged with the operation of the facility. In January of this year the commissioning of the accelerator sections with beam has started; in addition the assembly of the Gantry could also be started.

The main focus of the present work is to establish the accelerator functionality, to lead the ion beams to patient rooms and to reach a beam quality capable for patient treatment.

Building and technical infrastructure

The building and the corresponding technical infrastructure were completed. This includes the clinical part of the building as well as the offices. The finishing of the Gantry part the building can only be started after the assembly of the main Gantry components will be performed, which is scheduled for spring 2007.

Figure 1: Overview of the building in summer 2006

Progress of the Accelerator System

By the end of the year the delivery was completed for all magnets, all vacuum chambers, the ion sources, the Linac RF system and the synchrotron RF system. Nearly all power supplies were delivered and the beam diagnostic [1] is complete with the exception of some isocenter diagnostic.

The year 2006 was marked by the assembly and adjustment work of the accelerator components, the cabling and connection work, the following commissioning of the components without beam and the integration into the accelerator control system.

Despite the compact size of the accelerator the work was done in a highly parallel manner. As an example rough assembly work took place in the Gantry room while connection work was done in the high energy beam transport line, the synchrotron components were commissioned without beam, and beam was optimised in the Linac part.

Figure 2: Fully assembled High Energy Beam Transport line

Acceptance tests of the two ECR ion sources of SUPERNANOGAN type could be successfully performed with good long term stability and ion currents, partly exceeding design currents, shown in Table 1.

Ion	Extr.voltage (kV)	Ion current (eμA)
$^{12}C^{4+}$	24	200
$^{1}H_3{}^{1+}$	24	700
$^{3}He^{1+}$	24	500
$^{16}O^{6+}$	21,3	150

Table 1: specified ion species and intensities

At the end of 2006 the beam commissioning of the Linac could be preliminary finished leading to a current of $^{12}C^{4+}$ about 30 μA after the IH-section at 7 MeV/u. [1], [3]

In parallel theoretical analysis with the DYNAMION simulation code took place to investigate the origin of the major losses mainly observed at the RFQ-section, taking into account the measured size and distribution of the emittance in front of the RFQ [4].

Furthermore the ion sources and the synchrotron RF were handed over for permanent operation towards the HIT GmbH in December 2006; the other systems of the Linac systems will follow in a rapid order. The staff of the HIT GmbH was also trained accordingly.

The Synchrotron and the High Energy Beam Transport line to the two fixed beam stations are assembled and the commissioning without beam is nearly finished.

Progress of the Gantry System

The detailed layout for the Gantry to serve the third patient treatment room was finalised by the company MT Aerospace [6] [6]

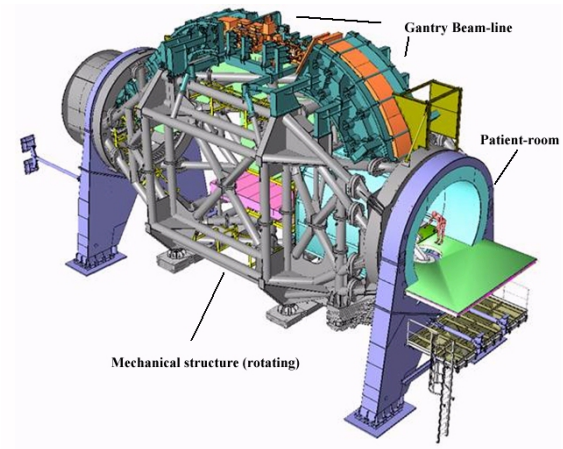

Figure 3: Final Gantry layout

The delivery of the main Gantry structure was delayed to the beginning of January 2007.
The accelerator assembly for the Gantry and quality assurance place is foreseen to be finished and connected to the existing accelerator sections in summer 2007.

Figure 4: Gantry room with main Gantry supports

A temporary wall has been installed in the High Energy beam line area, which allows that these assembly activities can be performed while the beam commissioning test in the synchrotron and High Energy beam line take place.

Accelerator and Treatment Technique

The two Patient Rooms for the fixed beam stations have been nearly fully equipped with the treatment technique components from Siemens Medical Solutions in close collaboration with the accelerator components installation.

General Project Evolution

Beam commissioning hat taken place until the end of the Linac. The main focus of the present work is to lead the ion beams to patient rooms and to reach a beam quality suited for patient treatment.

In 2006 GSI has played the major role in the commissioning of the HIT accelerator and will maintain this role for the commissioning of the Gantry as well as for the beam optimisation towards the first patient all throughout the year 2007.
A lot of intense discussion took place between GSI and the university hospital to set up the necessary procedures for the final operation such as the maintenance strategy including qualified personal and spare parts, the safety aspects, or the project documentation.
The beam commissioning activities are planned within a 2 and 3 shift organization; according to the present schedule the beam quality for patient treatments at the two horizontal treatment places should be available late summer 2007. For the Gantry branch the start of beam commissioning is scheduled at the beginning of 2008 aiming at beam properties suitable for patient treatment around middle of 2008.

Since the therapy accelerator will be approved in accordance to the European Medical Device Directive, much effort was and still has to be done into this direction as well. The according quality assurance activities for the treatment system, supplied by Siemens, will cover a significant part of the commissioning time.

References

[1] M. Schwickert, beam diagnostic for HIT, this report
[2] B. Schlitt, Linac commissioning for the HIT project, this ann. report
[3] G. Clemente et al, 'Assembly and RF Tuning of the IH-DTL for the HIT-Linac, this ann. report
[4] S. Yaramishev at al. Beam dynamics simulations for the HIT-Linac, this ann. report
[5] R. Fuchs, Die Gantry in der HICAT-Anlage, HGF-Tagung, May 2006.
[6] U. Weinrich, Gantry Design for Proton and Carbon Hadrontherapy-Facilities, EPAC 2006

Linac Commissioning for the Heavy Ion Cancer Therapy Facility HIT

M. Maier[1], B. Schlitt[1], C. Kleffner[1], W. Barth[1]
[1]GSI, Darmstadt, Germany

Abstract

The accelerator part of the clinical facility for cancer therapy HIT using energetic proton and ion beams (C, He and O) has been installed during 2006 at the Radiologische Universitätsklinik in Heidelberg, Germany [1]. The commissioning of the injector linac was performed in three steps for the LEBT, the RFQ and the IH-DTL and has successfully ended in December 2006. Some major results are briefly reported in this contribution.

Introduction

The commissioning of the linac shown schematically in Figure 1 was done in three consecutive steps as listed in Table 1 starting in April 2006 [2][3]. For each commissioning step a dedicated beam diagnostics test bench was designed to allow for beam current-, profile-, energy- and emittance measurements. Different ion species were used: H_2^+, H_3^+, $^3He^+$, $^4He^{2+}$, $^{12}C^{4+}$ and $^{16}O^{6+}$. In this contribution selected results for $^{12}C^{4+}$ are reported.

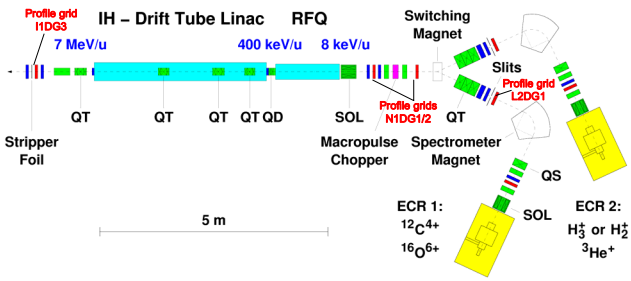

Figure 1: Overview of the injector linac (solenoids SOL, quadrupole triplets QT, doublets QD, singlets QS).

Table 1: Assembly and commissioning milestones.

November 05 – March 06	LEBT, ECRIS	installation & functional tests of components
April / May 06	ECRIS	successful beam commissioning
May – July 06	LEBT	
July / August 06	RFQ	installation of RFQ & testbench, RF commissioning
September 06	RFQ	beam acceleration to 400 keV/u
October 06	IH-DTL	completing of linac with IH-DTL & stripper-section
November 06	IH-DTL	RF commissioning
December 06	IH-DTL	first 7 MeV/u C^{6+} beams (35 eμA)

LEBT

Figure 2 shows a typical ion source spectrum obtained for carbon operation. The specified intensity of the separated $^{12}C^{4+}$ beam from the ion source is 200 eμA. The beam profiles along the LEBT are shown in Figure 3 (for the grid positions compare to Figure 1). For this setting a beam current of 184 eμA corresponding to a transmission of 92 % in the LEBT was achieved.

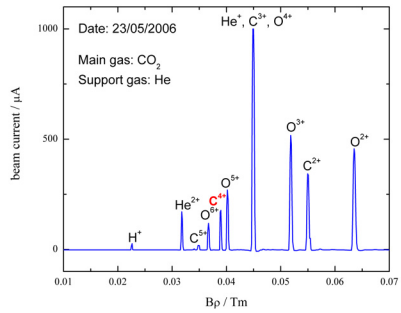

Figure 2: Ion source spectrum for carbon operation.

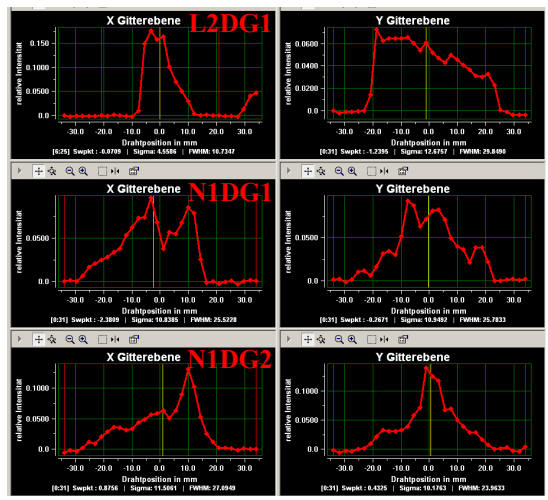

Figure 3: Beam profiles along the LEBT for $^{12}C^{4+}$.

RFQ

Before installation of the RFQ in Heidelberg, the RFQ had been investigated and tested with proton beams at a dedicated test bench at GSI [4]. As an example of measurements performed in Heidelberg, Figure 4 shows the energy of the $^{12}C^{4+}$ beam behind of the RFQ versus the tank voltage. The working point of the RFQ is marked, as well as the energy range required for injection into the adjacent IH-DTL.

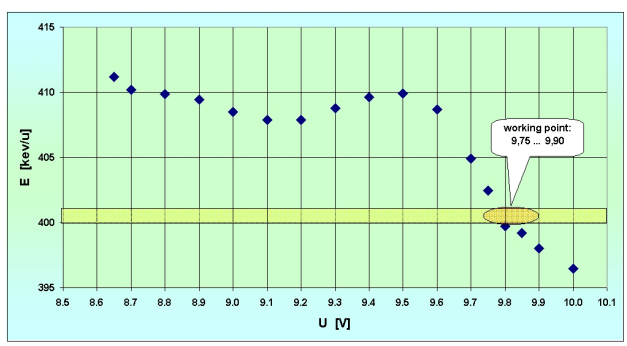

Figure 4: Beam energy measurements versus tank voltage to determine the RFQ working point for $^{12}C^{4+}$.

IH-DTL

Beam profiles and current behind the IH-DTL [5] are shown in Figure 5 and Figure 6. The beam current of 35 eμA behind the IH-DTL corresponds to a transmission of 19 % of the linac; a total $^{12}C^{6+}$ current of 50 eμA behind the stripper foil has been achieved.

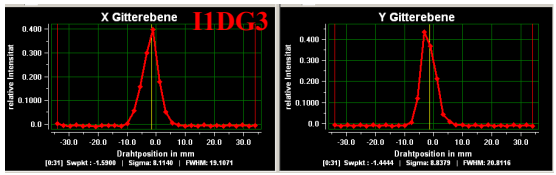

Figure 5: Beam profiles behind the IH-DTL as measured during commissioning for a $^{12}C^{4+}$ beam.

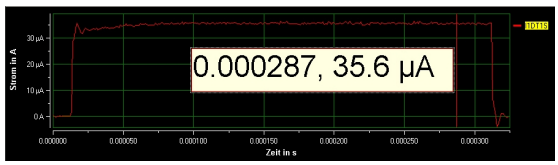

Figure 6: $^{12}C^{4+}$ beam current behind the linac. The achieved transmission is about 19 %, macro-pulse length 300 µs.

Amplitude and phase scans were performed as shown in Figure 7 to determine the working point of the IH-DTL. For each setting the energy, the transmission and the emittance of the beam were measured. This was repeated for different LEBT and RFQ settings.

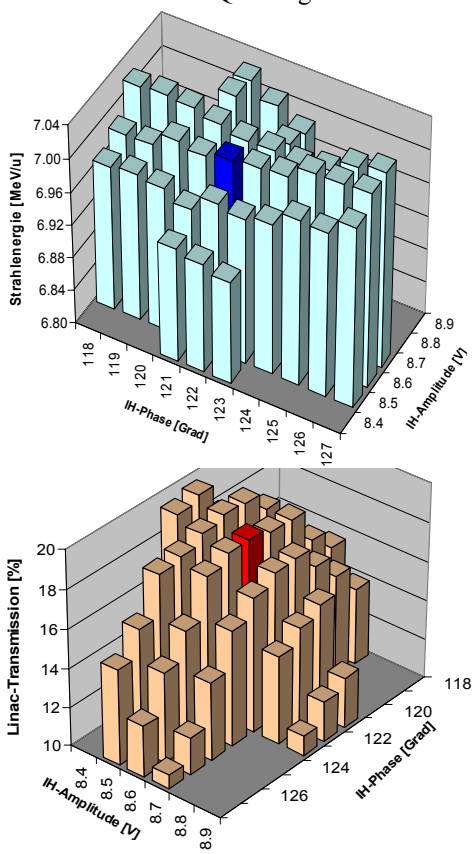

Figure 7: Energy and transmission of the $^{12}C^{4+}$ beam behind the linac depending on IH amplitude and phase.

Exemplary a measured horizontal emittance for $^{12}C^{4+}$ beam at the working point is shown in Figure 8. The main results for $^{12}C^{4+}$ are summarized in Table 2.

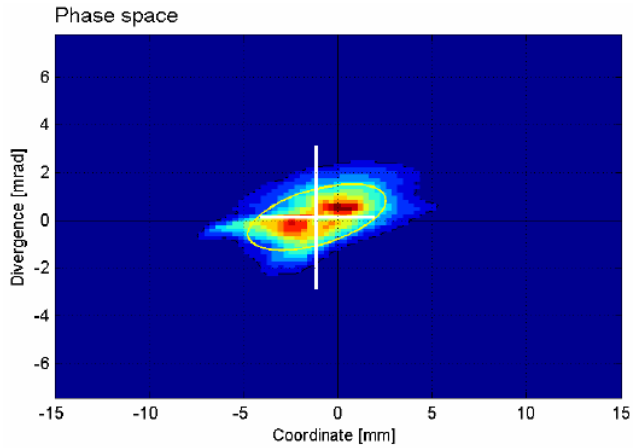

Figure 8: Horizontal emittance of the $^{12}C^{4+}$ beam behind the linac with $\varepsilon_{h,\,4\times rms}$ = 4.4 π mm mrad.

Table 2: Main results for $^{12}C^{4+}$ beam behind the IH-DTL.

E / MeV/u	$\varepsilon_{h,\,4\times rms}$ / π mm mrad	$\varepsilon_{v,\,4\times rms}$ / π mm mrad	transmission
7.00	4.4	5.3	19 % (35 eμA)

Summary and Outlook

The linac was successfully commissioned in 2006 for proton, carbon and oxygen ions. Yet the achieved beam intensities behind the linac are up to a factor of 3 below the design values. The parameter sets for $^{3}He^{+}$ and $^{16}O^{6+}$ are incomplete as these ion species were not or only partly used for the linac commissioning.

In parallel to the commissioning, extensive beam dynamics simulations in particular using the DYNAMION [6] and LORASR [5][7][8] codes have been performed for a better understanding of the measured results. Further investigations for improvement of the transmission are still going on, in particular concerning the front-end solenoid and RFQ.

The authors would like to thank all colleagues from GSI and HIT for their cooperation and support during beam commissioning.

References

[1] U. Weinrich et al., this report.
[2] M. Maier et al., *Proc. EPAC2006*, p. 1571.
[3] B. Schlitt et al., *Proc. LINAC2006*, p. 148.
[4] C.M. Kleffner et al., *Proc. LINAC2006*, p. 791.
[5] G. Clemente, H. Vormann et al., this report.
[6] S. Yaramishev et al., this report.
[7] R. Tiede, Frankfurt University, IAP Internal Note IAP-DYNA-291106, November 2006.
[8] R. Cee et al., *Proc. EPAC2006*, p. 1957.

Beam dynamics simulations for the HIT-LINAC

S. Yaramyshev, W. Barth, A. Orzhekhovskaya

Abstract

The commissioning of the injector linac of the Heidelberg ion beam therapy facility (HIT) is preliminary finished [1].

The main goal of the beam dynamics study with the DYNAMION code [2] (carried out in parallel with the commissioning) was to estimate the maximum possible transmission for the HIT front-end system, namely for the solenoid and the RFQ. The results of the simulations from ion source to the solenoid showed good coincidence with the previous calculations done during design stage

As a first step, an adequate description of the linac elements was carried out. All geometrical data, available from the external calculations, measurements, specifications and tables for the machining, were used. Dedicated subroutines of the DYNAMION code precisely calculate the 3D electrical field in the RFQ and DTL. Also the misalignments of the linac elements can be defined for the simulations.

Emittance measurements

An RFQ acceptance of 330 mm*mrad ($^{12}C^{4+}$) was calculated analytically and, as well, obtained from the dedicated simulations. The measured beam emittance after the LEBT is about 300 mm*mrad (at 90% level of intensity).

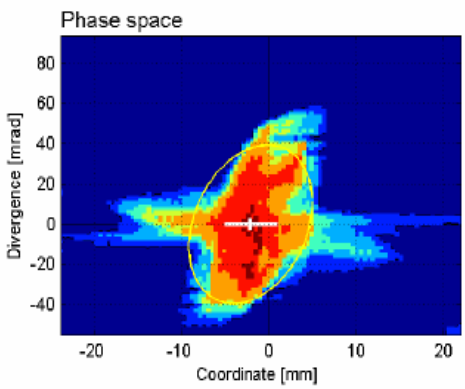

Fig. 1. Beam emittance in the horizontal phase space X-X' measured behind the solenoid.

The final beam focusing to the HIT-RFQ is made by a solenoid. During commissioning of the LEBT several measurements of the beam emittance (Fig. 1) had been done (50 cm behind the solenoid). The distance from the solenoid to the RFQ entrance is only about 10 cm. The magnetic field of the solenoid was varied in the range from 40% to 60% of the nominal value to provide for a reasonable beam size at the position of the measurement device. A dedicated procedure for reconstruction of the particle distribution from the emittance measurement data was developed.

Front-end simulations

Data of the magnetic field measurements were used for the reconstruction of the solenoidal field. A dipole component in the field distribution was observed. The solenoid was transversally tilted to compensate the influence of the field to the particle motion. Taking into account the non-uniformity of the field, the particle motion was simulated backward through the displaced solenoid and again forward, but with the design value of the solenoidal B-field.

The forward simulations through the solenoid with the measured field and the reconstructed particle distribution resulted in a total emittance growth of 15% (90% of particles). The calculated macroparticle distribution at the RFQ entrance in the horizontal phase space is shown in Fig. 2; the vertical one is similar. The ellipse represents the RFQ acceptance. As shown, a significant number of particles is outside of the acceptance due to the emittance deformation. This was illustrated by simulations for the RFQ with C^{4+} ions, when a particle transmission of about 50% was calculated (measured for C^{4+} ions is about 25%).

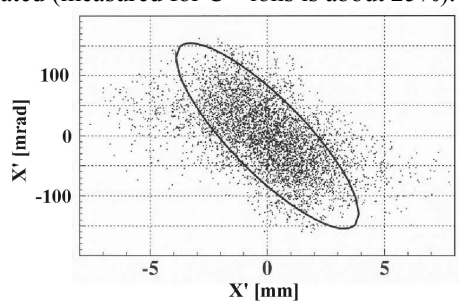

Fig. 2 Particle distribution (X-X' phase space) at the HIT-RFQ entrance.

Our recent calculations for the particle transmission through the HIT front-end don't show essential difference between ideal (axis-symmetrical) and real solenoids (with recent settings of the machine). It can be assumed that the dipole field component in the real solenoid is partly compensated by its tilt. More detailed study of the measured solenoidal field approximation and of the reconstruction of the particle distribution is possible. Nevertheless a serious increase of the calculated transmission is not expected.

The particle transmission for the whole front-end system can be significantly increased by changing the matching conditions at the RFQ entrance, what requires minor modification at the beginning of the RFQ electrodes. A similar upgrade of the HSI RFQ was successfully realized in 2004.

[1] B. Schlitt et al., LINAC-06, Knoxville, 2006
[2] S. Yaramishev et al., NIM A, Vol 558/1 (2005)

Assembly and RF Tuning of the IH-DTL for the HIT LINAC

G. Clemente [2], H. Vormann [1], Y. Lu [2], S. Minaev [3], R. Tiede [2],
B. Schlitt [1], R. Fuchs [1], C. Will [1] and U. Ratzinger [2]
[1]GSI, Darmstadt, Germany; [2]IAP, Frankfurt, Germany, [3]ITEP, Moscow, Russia .

Abstract

The 20 MV, 217 MHz IH-DTL for the HIT facility has been assembled and mechanically aligned until July 2006. RF tuning of the 3.8 m long tank with 56 gaps has been done from April to October 2006. The beam commissioning at the HIT facility in Heidelberg was performed successfully in December 2006.

Assembly

Alignment plates had to be invented to adjust the side walls of the middle frame against the stiff lower half shell of the tank. The copper plating of the cavity at GSI worked properly besides a rather thick layer on the sealings which resulted in a frequency shift of –0.7 MHz.

The three quadrupole triplet lenses inside the tank are directly connected to the lower tank half shell. The maximum transverse deviations of individual quadrupoles amount up to ±0.2 mm after the final alignment – a factor of 2 more than specified but still tolerable, as checked by LORASR beam dynamics simulations (Fig. 1).

We would like to thank our GSI colleagues T. Dettinger, N. Bönsch, J. Cavaco and N. Kischnick for their committed workmanship at copper plating and assembly.

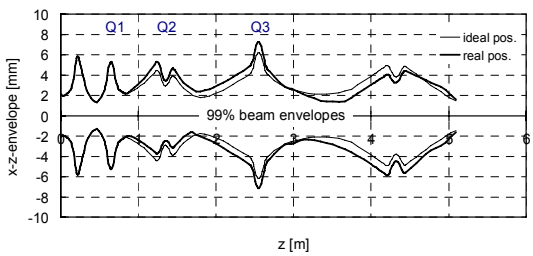

Fig. 1: Beam envelopes for ideal lense positions (thin line) and real pos. (bold line, hor. deviat. Δx [mm] Q_{11} -0.02, Q_{12} +0.05, Q_{13} -0.07, Q_{21} -0.17, Q_{22} -0.20, Q_{23} +0.02, Q_{31} -0.05, Q_{32} -0.10, Q_{33} -0.11).

RF Tuning

Usually, three goals have to be reached during the final RF tuning of an RF cavity: the requested operation frequency in combination with convenient positions of movable plungers, the quality factor to meet the power loss specifications and finally, the gap voltage distribution according to beam dynamics simulations [1].

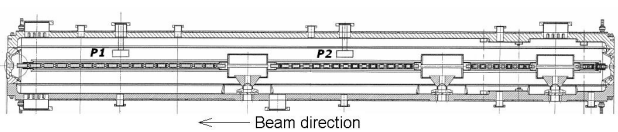

Fig. 2: Sketch of the IH-DTL. Four DTL sections are subdivided by three lenses; movable plungers P1 and P2.

The HIT IH cavity (Fig. 2) offers plane surfaces along the upper and lower half shells to mount inductively acting bodies. Besides the usual way of tuning the capacity distribution along the drift tube structure, it is now possible to tune the gap voltage distribution while moving the resultant operation frequency up or down as needed to reach the design frequency.

The RF tuning was finished successfully in October 2006, resulting in a gap field distribution as shown in Fig. 3. The sum gap voltage deviation per section is less than 1 % [2].

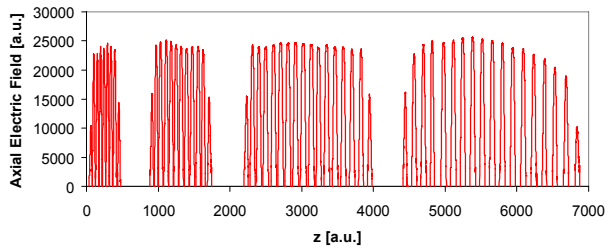

Fig 3: Resulting on axis electric field distribution, the maximum corresponds to 180 kV/cm.

Two movable plungers are mounted (Fig.2). Due to the high sensitivity of the gap voltage distribution only a small tuning range of about ±50 kHz can be recommended for stable beam operation. As the RF duty factor is below 1 % and the thermal drift was measured to be –400 Hz/K only, this tuning range is sufficient. On the other hand, the different dielectric constant causes a frequency shift of +62 kHz under vacuum conditions and must be considered at the RF tuning. Finally, it was even decided to keep one plunger fixed while the RF frequency control is performed with plunger P2 only.

List of measured parameters:

Design ion	C^{4+}
Energy range	0.4 – 7.0 *A* MeV
Quality factor	15200
Voltage gain	19.8 MV
Cavity length	3.76 m
RF power losses	≈ 850 kW
Eff. shunt impedance	≈ 125 MΩ/m

References

[1] Y. Lu, Developement of an IH-DTL Injector for the Heidelberg Cancer Therapy Project, PhD Thesis, Frankfurt University, GSI Darmstadt, July 2005.

[2] G. Clemente et al., Final Tuning and tolerances of the 217 MHz, 20 MeV IH-Linac for HICAT, Frankfurt University, IAP-ACC-071206, Frankfurt, December 2006.

Beam Diagnostics for HIT

M. Schwickert[1], S. Borger[1], R. Boywitt[1], C. Dorn[1], H. Graf[1], T. Hoffmann[1], W. Kaufmann[1], P. Kowina[1], C. Müller[1], A. Peters[1,2], H. Reeg[1], J. Schölles[1] and M. Witthaus[1]
[1]GSI, Darmstadt, Germany; [2]Heidelberger Ionen Therapie (HIT), Heidelberg, Germany.

Introduction

In 2006 the GSI beam diagnostic group delivered and commissioned the total amount of 92 Beam Diagnostic (BD) devices for the HIT facility (Heidelberger Ionen Therapie). The delivery of the BD equipment [1] is part of the GSI project to construct a dedicated accelerator facility for tumor treatment at the Heidelberg university clinics. A contract about the delivery of beam diagnostic components for HIT was signed in 2003 between the University Clinics and GSI. After successful functional acceptance tests, the relevant part of the components was used for the commissioning of the Low Energy Beam Transport (LEBT) and Linac section (see [2]).

Beam Diagnostics for Commissioning

At the beginning of 2006 the construction of the HIT accelerator building was finished. The installation of the Linac part, including all beam diagnostic equipment, was organized in three commissioning steps. Prior to each step functional acceptance tests of the included BD components had to be carried out under supervision of HIT GmbH, the operation company.

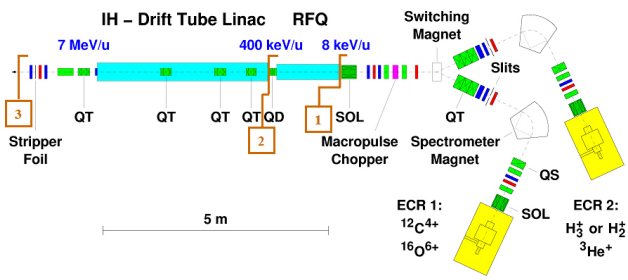

Figure 1: HIT linac (ECR: ECR ion source, SOL: solenoid, QS, QD, QT: quad singulet, duplet, triplet). The numbers indicate the positions of the test setup for the 3 commissioning steps.

The layout of the LEBT and Linac section is shown in Fig. 1. For the stepwise commissioning of 1) the ion sources and Low Energy Beam Transport (LEBT), 2) the 400 keV/u RFQ and 3) the 7 MeV/u IH-structure, measurements of all relevant beam parameters (beam intensity, profile, energy etc.) were performed using the delivered HIT BD devices.

Additionally, each step involved a dedicated diagnostic measurement setup at the end of the marked (Fig. 1) beam transport section, including a mobile setup for emittance measurements (MobEmi).

BD for commissioning of LEBT

The LEBT section was mounted in March 2006 including all BD devices and on March 30th all BD systems of the LEBT passed the functional acceptance test. Commissioning of the LEBT section was carried out from May to June 2006. This section includes 5 Faraday-cups, 2 Tantalum viewing-screens, 4 Profile grids and 2 DC-transformers. The BD components in the ion source branches were especially designed to withstand the relatively high dc-beam power of up to 360 W at a very small penetration depth of approx. 100 nm. The diagnostic setup at the RFQ input location (pos. 1 in Fig. 1) included 1 additional profile grid, 1 Faraday-cup and the MobEmi.

An important task of the LEBT commissioning was to align the ion beam with the geometrical axis of the ion optical system by using profile grids. The profile grids presented in Fig. 2 have 64 wires per plane (horizontal and vertical) with a wire spacing of 1.2 mm. For standard measurements the signals of two adjacent wires are combined, thus reducing the number of electronic channels needed.

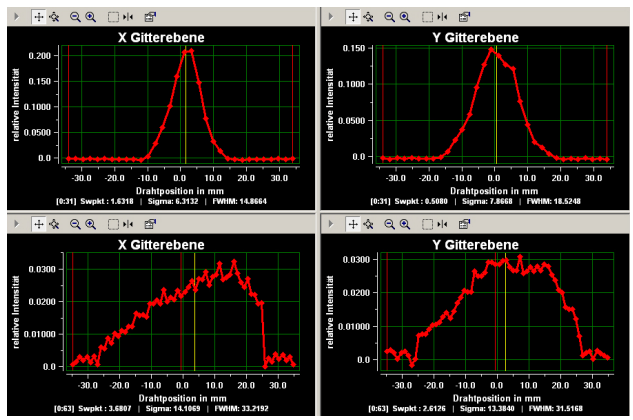

Figure 2: Online display for two profile grids; x- (left) and y-grid layer (right); vertical line: center of mass

Detection of the dc-beam current in the two source branches is performed using water-cooled Faraday-cups. Two Faraday-cups installed at the exit of each of the spectrometer magnets are used for taking the mass spectrum of the ion beam.

As a result of the LEBT commissioning a full set of operational parameters for the beam optics was elaborated and the transmission of the LEBT was maximized to more than 90% for all utilized ion species, i.e. protons, carbon and oxygen ions.

BD for commissioning of RFQ

In September 2006 the commissioning of the RFQ-structure was performed. At this stage the primary task was the precise measurement of the beam energy in order to tune the RFQ to the design energy of 400 keV/u. For this purpose the measurement setup (MobEmi) at the exit

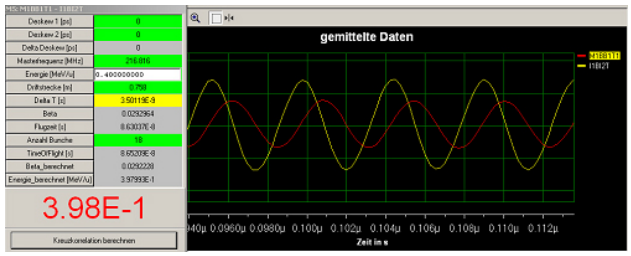

Figure 3: Online calculation of the beam energy after the RFQ (E=0.398(2) MeV/u)

of the RFQ (pos. 2 in Fig. 2) was additionally equipped with 3 phase probes for the detection of the beam energy by the time-of-flight (TOF) method. The beam energy is calculated online via a cross-correlation of the signals of two successive phase probes. Fig. 3 shows the signals measured using 4 GSa digitizer boards [3]. The phase shift of the two probe signals, reflecting the time of flight, is clearly visible in the plot.

Using profile grids before and after the RFQ a beam alignment procedure was performed also for this section. By combining the measurement results with ion optical simulations the integrity of all devices of the beam transport system, i.e. steerers, solenoid, dipoles, quadrupoles, was checked and operational parameters were derived.

BD for commissioning of IH-DTL

The commissioning of the 7 MeV/u IH-DTL was carried out in December 2006. In this case the measurement setup at the exit of the IH-DTL (pos. 3 in Fig. 2) was matched for the higher beam energy. In order to achieve an energy-resolution of $\Delta E \approx 5$keV/u the distance between the phase probes was extended.

This energy resolution is sufficient to monitor the state of the stripping foils located in the first diagnostic chamber after the quadrupole triplet at the high-energy end of the IH-DTL. The position of the foil stripper is between the two phase probes used for the TOF measurements. Therefore the energy loss of the ion beam passing the carbon stripping foil, which is a measure also for the foil thickness, can be detected using the TOF setup.

During IH commissioning the beam energy was measured as a function of the rf amplitude and phase in order to define the working point of the rf system. The 8 channel digitizers used for TOF measurements also allow the detection of the phase relation of the linac rf cavities. E.g. the decoupled rf signal of the RFQ tank can be measured together with the rf signal of the IH-DTL. This is an important means to control the phase stability of the accelerating cavities with respect to the master oscillator.

Outlook: Synchrotron Commissioning

The delivery of the BD components for the synchrotron and HEBT (high energy beam transfer) section was completed until summer. On July 25th 2006 all BD systems passed the functional acceptance test on site.

The synchrotron is equipped with 6 beam-position monitors (1 BPM per period), 6 mobile Beam-loss monitors, 1 AC- and 1 DC-transformer, 1 viewing screen for first turn analysis and 2 pairs of Schottky-pickups. The BPMs were especially designed and matched to the parameters of the HIT synchrotron [4].

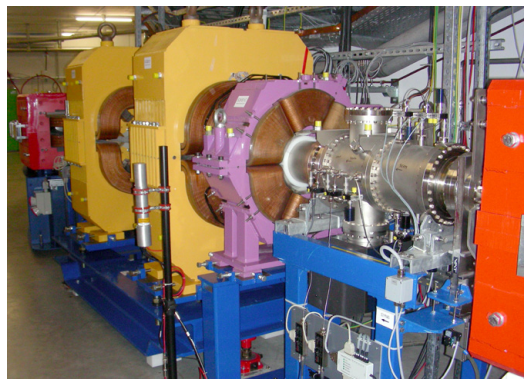

Figure 4: Synchrotron period S2: dipole, Schottky-pickups, hexapole, quadrupole (from right)

Fig. 4 shows a photo of period S2 of the synchrotron including the horizontal and vertical pairs of plates for Schottky measurements. This setup can be used also for tune measurements, by switching the rf-relais on the outside of the vacuum chamber to power amplifiers for beam excitation. In this mode the signal of one BPM will be connected to a network analyzer for the detection of the beam transfer function.

For synchrotron commissioning the first turn analysis using a viewing screen installed in period 1 (just before the re-entry into the injection septum) will be of great importance. The target material P43 of the viewing screen is optimized for the detection of low intensity ion beams and the optical decay time of 1 ms is adequate in order to preserve the time structure of the beam profile [5].

The MEBT (medium energy beam transport) section was commissioned in January 2007 and in February the first beam was injected into the HIT synchrotron. The signal of the 300 µs linac macropulse was primarily detected on the BPM in period 1. After only three more days of commissioning the first turn was achieved and the beam was detected on the first turn viewing screen. The synchrotron BD is prepared for the first multi-turn injection.

References

[1] M. Schwickert et al. „Beam Diagnostics for the HIT and CNAO medical accelerators“, GSI Scientific Report, p. 398, 2006.

[2] U. Weinrich et al., “Status of the HIT project”, this GSI Scientific Report.

[3] http://www.acqiris.com

[4] P. Kowina et al. “Optimisation of ‘shoe-box type’ Beam Position Monitors “, Proc. DIPAC2005, p. 114, Lyon, 2005.

[5] A. Peters et al. „2D-Characterization of Ion Beams using Viewing Screens”, Proc. EPAC2002, p. 1960, Paris, 2002.

Fast measurements of single Bragg peaks with an active multi-plane phantom

B. Voss*, M. Henske, A. Heinz, H.J. Junk, H. Risch
GSI, Darmstadt, Germany

Introduction

Hadron cancer-therapy [1] with high-energetic heavy-ions requires the precise knowledge of the energy of the primary beam using an method independent from the accelerator. This may be obtained by measuring the range of the impinging particles. Currently, this task is performed with a system consisting of a water column with remote controlled variable thickness flanked by two ionization chambers (IC). The energy-loss in the IC installed upstream of the setup serves to normalized the signal of the second IC to the beam intensity. Recording this quantity for various thicknesses of the water absorber allows to trace and determine the position of the Bragg-Peak, which coincides with the maximum reading of the second IC. Moreover, the shape of the curve is an additional characteristic feature to be checked. Checking the constancy of the associated material thickness is done during the preparative phase of every beam time.

The precision of this setup is limited e.g. by the accuracy of the stepper motor used to steer the thickness of the water absorber. The sum of all contributions is in the order of 100 µm. The measurement of one point of the curve requires one extraction cycle of the SIS of 5 s, which sums up to a total of 10 to 15 minutes per Bragg-Peak measurement. Thus the total constancy check requires approximately 1.5 hours of beam time for a representative set of energies. It is our aim to minimize this load to only a few seconds per energy. For this purpose, a set of staged ICs has been built which is handy enough to be used during even daily checks.

Material and measurements

The detector setup (see fig.1) with outer dimensions of 220x250x690 mm^3 and a weight of 18 kg consist of 60 Lucite© (PMMA) plates, each 5 mm thick forming the high-voltage layers of adjacent ICs. Their design is symmetric concerning high-voltage and signal layers made of 13 µm thick aluminized Mylar© foils in the centre of a twofold 3 mm active gap. The detector can be operated at max. ±1200 V with air as detector medium. The whole construction is modular for ease of maintenance and adoption to the experimental needs. The different ICs are densely flanged together in order to form one unit with a total thickness of 36.2 ±0.1 cm, which is enough to stop all primary carbon beams used for therapy at GSI. The relatively large active area of 96x96 mm^2 allows to collects all charges deposited by the pencil beam on the optical axis. Position adjustment to this axis was done with a precision below 1 mm by laser and surface masks.

The readout electronic [2] is based on a VLSI chip, working according the recycling-capacitor technique. LabVIEW-RT software is used to record and visualize the data.

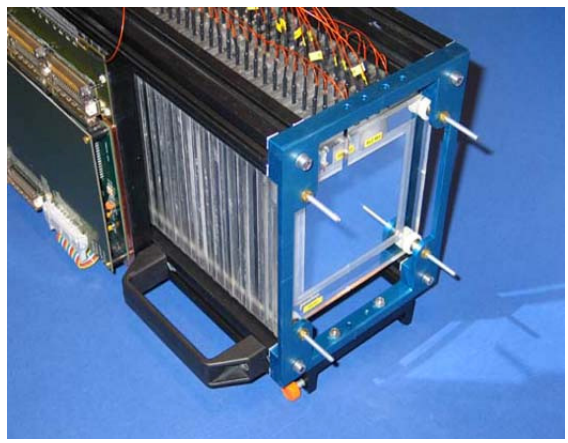

Figure 1: Front photo of the phantom.

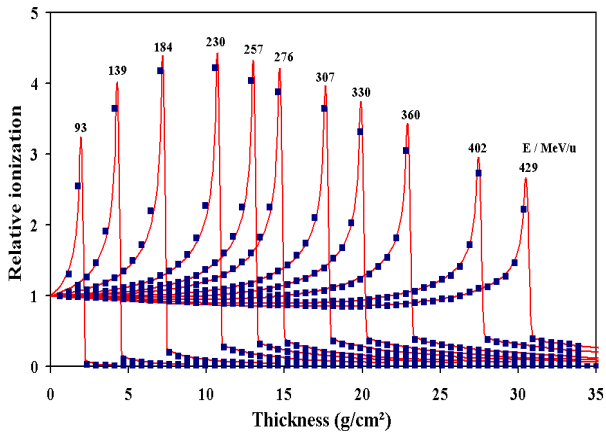

Figure 2: Measured (points) and calculated (lines) [3] Bragg-peaks for selected carbon-beam energies between 93 and 429 MeV/u.

Results, Conclusions & Outlook

Despite the fact, that data analysis is still ongoing we can state, that choosing adequate intensities of the primary beam one may separate the different Bragg-Peaks. The comparison between TRiP98Beam calculations [3] and the measurements (see fig. 2) reveal sufficient agreement. Nevertheless, the granularity of the universal, homogeneous setup is not best suited to resolve the peaks for all energies. Consequently, we will modify the setup using thinner (e.g. 7 µm) absorbers at least for a subset of the layers.

References

[1] G. Kraft, Nucl. Instr. and Meth. in Phys. Res. A 454 (2000) 1-10.
[2] G.C. Bonazzola, Nucl. Inst. and Meth. in Phys. Res. A 405 (1998) 111-120.
[3] M. Krämer et al., Radiother. Oncol. 73 (2004) 80-85.

*B.Voss@GSI.de

First measurements with a homogeneous GEM-foil detector with therapeutic beams

B. Voss[*,1], L. Doignie[2], A. Heinz[1], H. Risch[1]
[1]GSI, Darmstadt, Germany; [2]ENSICAEN, Caen, France

Introduction

There are two main motivations for the detector development we report on here. First: Hadron cancer-therapy with high-energetic heavy-ions as available at the Schwer-Ionen Synchrotron (SIS) facility at GSI Darmstadt [1] or at the dedicated facility HIT [2] in Heidelberg in general requires the precise knowledge of the beams position. Detectors based on wire planes are applicable but they introduce inhomogeneities changing the beam quality. Second: Applications where the energy-loss of traversing particles is independent from their position like the operation within high-resolution magnetic spectrometers (e.g. the FRS at GSI) require homogeneous thicknesses of all material placed in the beam. Gaseous Electron Multiplication GEM [3] in combination with foil-type signal anodes are favourable because of their improved homogeneity compared to standard multi-wire detectors which spoil the resolution of the magnetic separation.

Material and measurements

We examined the performance of a very homogeneous detector composed of two-fold amplification layers realized with four-sector GEM foils in standard configuration: 50 µm thick Kapton©, 50 µm hole diameter with 140 µm pitch. The structure of the detector layers is kept modular for easy exchange and maintenance of the signal and amplification layers.

The active area of the detectors is limited by the GEMs to 200x200 mm^2. These layers are installed in 90° configuration glued to separate PCB-frames with a distance of 4 mm. They are operated at -2.5 kV and -1.5 kV, respectively and are mounted in 4 mm distance in front of an anode with strip-design forming the signal layer. Strip width is 1.5 mm with a spacing of 0.5 mm. The signals of every strip is fed trough the detector housing giving the opportunity to apply various readout concepts. During first test in the laboratory we successfully tested a delay-line readout which minimizes the electronic complexity. The readout used in the beam experiment is based on a VLSI chip [4], working according the recycling-capacitor technique digitizing the signal of every individual strip. LabVIEW-RT software is used to record and visualize the data. Measurements have been performed at CaveM at GSI. Position spectra of carbon pencil-beams for various energies between 89 and 430 MeV/u, several beam width and intensities of up to 2x10^8 pps have been recorded.

Results, Conclusions & Outlook

The detector worked to a satisfying extent detecting the pencil-beam as shown in fig. 2. The feasibility of a GEM based device has been proven for an operation under therapy conditions with narrow pencil beams. Nevertheless, there are still various technological problems to be solved. More detailed measurements are necessary to prove the feasibility for a scanned beam applying the standard electronic [5] used at CaveM.

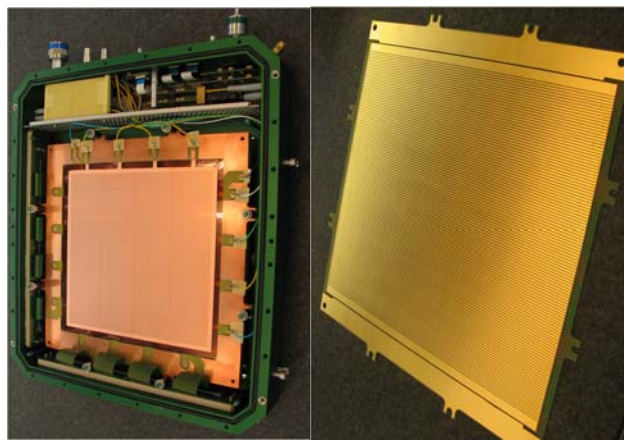

Figure 1: Picture of the GEM-foil (left) and the structure of the strip-line signal layer (right).

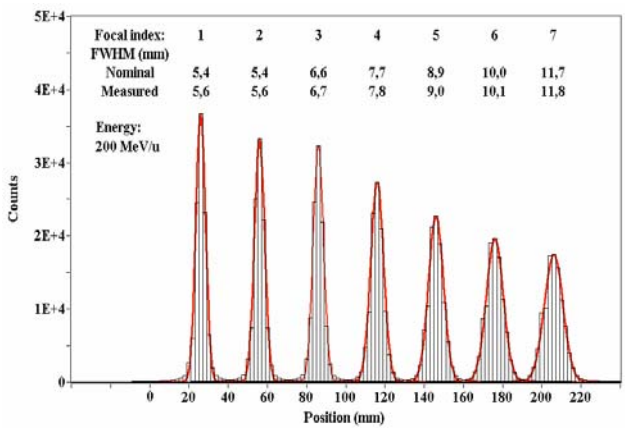

Figure 2: Examples of the charge spectra recorded on the strips (bars) of the anode layer for beam width at different positions for a beam energy of 200 MeV/u as a showcase. The Gaussian fits reveal a good agreement between the nominal and the measured width for the non-scanned beam. The intrinsic resolution of the strip-type anode has been subtracted.

References

[1] G. Kraft, Nucl. Instr. and Meth. A 454 (2000) 1-10.
[2] P. Heeg et al., Z. f. Med. Phys. 17 (4) (2007) 17 -24.
[3] F. Sauli, Nucl. Instr. and Meth. A 386 (1997) 531.
[4] G.C. Bonazzola, Nucl. Inst. and Meth. A 405 (1998) 111-120.
[5] E. Badura et al., IEEE TNS 47 (2000) 170-173.

*B.Voss@GSI.de

Measurement of the carbon ion micro-structure after KO extraction

K. Parodi[1], S. Brons[1], P. Forck[2], B. Franczak[2], T. Haberer[1], T. Hoffmann[2], D.A. Liakin[2], P. Moritz[2], D. Ondreka[2], U. Scheeler[2], and P. Schütt[2]
[1]HIT, Heidelberg, Germany; [2] GSI, Darmstadt, Germany.

Abstract: The micro-structure of carbon ion beams was measured in the energy range of therapeutic interest after knock-out extraction, which will be established at the upcoming ion beam facility in Heidelberg. The measured widths of the beam bunches were compared with those obtained after the slow resonant extraction technique, which is currently used at GSI for ion therapy. The positive implications of KO extraction for applications to in-beam PET are discussed.

The residual micro-structure (i.e., bunched structure at the sub-microsecond time scale) of the extracted beam is responsible for time-correlated prompt radiation following nuclear interactions of the primary ions in the target [1,2]. This originates a background of random coincidences in in-beam PET measurements which cannot be suppressed by standard random correction techniques well established in nuclear medicine tracer imaging [2]. To improve the very low statistics of usable events for PET imaging, solutions have been proposed which allow recovery of the subset of β^+-activity coincidences measured in the time of no ion occurrence during the micro-pulsed beam extraction (spill) [3].

The efficiency of the method depends on the ratio between the width of the micro-bunches and the radio-frequency repetition period. Previous investigations were done at GSI using the slow resonant (SR) extraction technique which is currently adopted for carbon ion therapy [2]. At the upcoming hospital based facility in Heidelberg, the knock-out (KO) extraction technique will be used. Therefore, the micro-structure of the beam after KO extraction was measured and compared with new values acquired after slow resonant extraction under the same conditions.

Low intensity (10^6 s^{-1}) carbon beams of 5 discrete energy steps (about 89, 100, 280, 321 and 426 MeV/u) were produced. Timing information of the extracted ions was obtained from the pulses of the BC400 plastic scintillation detector of the beam diagnostic system, similar to the experiment of [2]. The record of the ion arrival time with respect to the phase of the synchrotron radio-frequency was determined using the ABLASS system [4].

Preliminary time correlation results obtained from the online analysis of the ABLASS system clearly indicate a smaller beam spread (i.e., bunch width) when using KO extraction, as shown in figure 1. Also, the variation of the bunch width is found to be much more stable over the spill in the case of KO extraction, resulting in the smaller error bars of figure 1.

These beam properties would translate in a twofold advantage for in-beam PET applications. In fact, reduced bunch width for the same radio-frequency period ensures a larger fraction of usable coincident events to be recovered during the spill for the same macroscopic beam intensity and spill duration. Further, the stability of the beam micro-structure over the spill enables safe applicability of the RF-phase information to trigger the PET data acquisition for in-spill separation of the corrupted events acquired during the beam bunch from the usable coincidences acquired outside the beam appearance [3]. A more detailed off-line analysis of the newly measured data as well as a comparison with the previous SR experiment is ongoing and a quantification of the expected advantages of KO over SR extraction for in-beam PET applications will be reported soon.

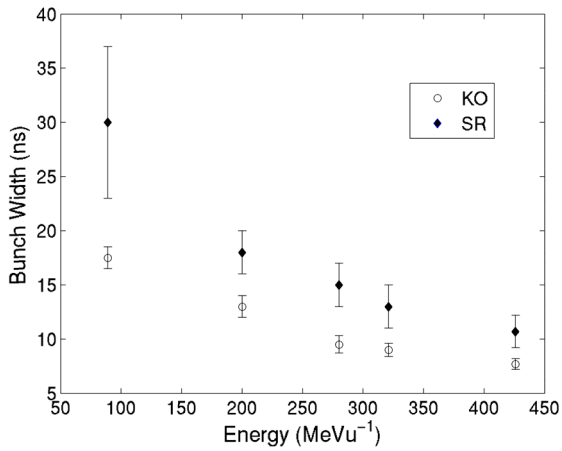

Figure 1: Bunch widths (standard deviation) from the online analysis of the ABLASS system for the data acquired after KO and SR extraction at different beam energies. The larger error bars for the SR data reflect the measured variation of the bunch width over the spill.

References

[1] J. Pawelke et al., In-beam PET imaging for the control of heavy-ion tumour therapy", IEEE Trans. Nucl. Sci. 44 (1997) 1492

[2] K. Parodi et al., "Random coincidences during in-beam PET measurements at microbunched therapeutic ion beams", Nucl. Instr. Meth. A 545 (2005) 446

[3] P. Crespo et al., "Suppression of random coincidences during in-beam PET measurements at microbunched therapeutic ion beam radiotherapy facilities", IEEE Trans. Nucl. Sci. 52 (2005) 980

[4] T. Hoffmann et al., "New spill structure analysis tools for the VME based data acquisition system ABLASS at GSI", Proc. 12th Beam Instrumentation Workshop, Batavia, 2006

Status of the Linac for the Italian Hadron-Therapy Centre CNAO

B. Schlitt, C. Kleffner, A. Reiter, H. Vormann, R. Bär, M. Hörr, G. Hutter, G. Riehl and W. Vinzenz
GSI, Darmstadt, Germany

Abstract

During 2006, the RFQ for the CNAO injector linac was tested successfully with proton beams at the RFQ test bench at GSI. Final acceptance tests of the beam diagnostics components to be delivered by GSI were also performed at the RFQ test bench. The IH tank was delivered to GSI and the drift tube structure was assembled in the tank after copper plating of all components.

Introduction

The Italian hadron-therapy centre CNAO (Centro Nazionale di Adroterapia Oncologica) [1][2] is presently under construction in Pavia, Italy, about 30 km south-western of Milan. The centre will be devoted to the treatment of deeply-seated tumours with proton and light ion beams and to clinical and radiobiological research. The design of the CNAO accelerator is based on the Proton-Ion Medical Machine Study (PIMMS) and consists of two ECR ion sources, a 7 MeV/u injector linac, which is identical to the linac of the Heidelberg ion therapy centre HIT [3][4], and a 400 MeV/u synchrotron.

In July 2004, a contract between CNAO and GSI was signed regarding the construction and commissioning of the CNAO linac. All components for the linac were ordered by CNAO from the same companies as for the Heidelberg project. GSI delivers technical support in the order processing of all linac components, is in charge of the copper plating, assembly and RF tuning of the linac structures (together with IAP), performs numerous pre-tests and will also deliver support during installation and commissioning of the linac on site in Pavia. In an addendum to this contract, the delivery of various beam diagnostics elements for the CNAO LEBT, linac and MEBT by the GSI beam diagnostics group was agreed [5][6].

RFQ Test Bench

The RFQ for CNAO was delivered by NTG in late 2005 to Frankfurt University (IAP), where the assembly, the alignment and the low-level RF tuning of the RFQ structure were done. The RFQ was delivered to GSI in April 2006. In July 2006 the CNAO 200 kW RF amplifier was delivered by THOMSON to GSI.

The test bench was modified with respect to the test bench used for the Heidelberg RFQ [7][8]. The MUCIS ion source was now installed inside the HOSTI terminal and the test bench was shifted towards the terminal. All components for the Heidelberg project were dismounted and were replaced with vacuum and beam diagnostics components for CNAO (phase probes, AC transformer, profile grid and Faraday cup). First beam tests were performed in September 2006. High power tests are planned during the RFQ commissioning in Pavia in 2007.

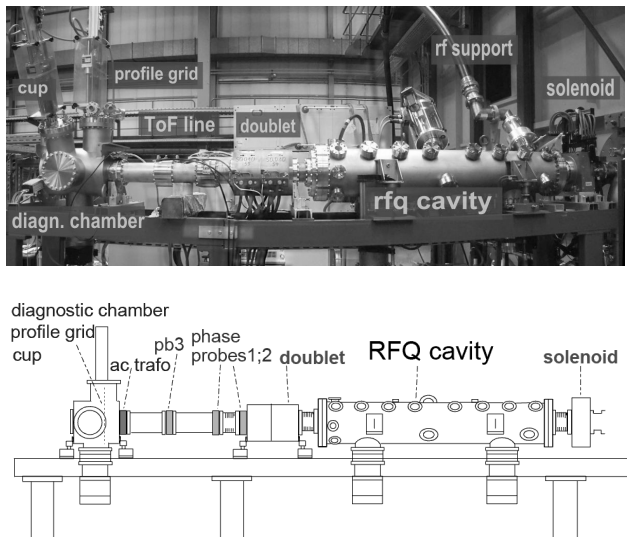

Figure 1: View and sketch of the RFQ test bench at the GSI HOSTI terminal equipped with RFQ and beam diagnostics components for CNAO.

As shown in Fig. 1, a solenoid matches the proton beams to the RFQ entrance. A magnetic quadrupole doublet focuses the accelerated beam transversely into a drift section for time-of-flight (ToF) energy measurements. The maximum distance between the capacitive phase probes was reduced to 0.4 m in order to eliminate debunching effects in the ToF measurements.

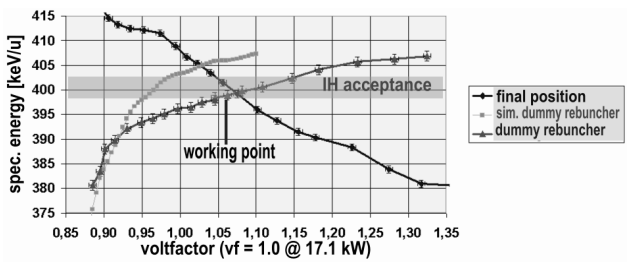

Figure 2: Measured energy of the proton beams behind of the RFQ with (internal) rebuncher in final position and without rebuncher (dummy rebuncher) vs. RF amplitude.

Various beam tests with different heights of the rebuncher drift tube support as well as without rebuncher were performed until December 2006 with proton beam currents up to 800 µA behind of the RFQ. The measured results for the final rebuncher setting and without rebuncher are shown in Fig. 2. The steep incline of the output energy of the RFQ without rebuncher below a voltfactor of 0.95 is compared to simulation results obtained with PARMTEQ. This was done in order to calibrate the nominal RF power at a voltfactor of 1.0 to 17.1 kW for proton beams. The working point is expected at a voltfactor of 1.06, resulting in a power consumption of 165 kW

for the acceleration of carbon ions. Around this working point, the output energy can be tuned to 400 keV/u and can be matched to the IH acceptance by varying the RF power (Fig. 2). The measured output energy characteristics for the final setting of the rebuncher allows for an estimation of the total effective rebuncher voltage of 27 kV for protons.

Beam Diagnostics & Linac Control System

By August 2006 all beam diagnostics (BD) items – mechanical components as well as pre-amplifier modules and PXI data acquisition (DAQ) electronics including the manual control software – were available. Two AC transformers, four phase probes and seven profile grids had been constructed, vacuum tested, and prepared for the final acceptance tests, which took place at GSI during the last week of September 2006. All hardware and software items were thoroughly inspected by members of the CNAO BD group. The programme extended from laboratory investigations concerning the rate capability of DAQ electronics or detector calibrations to beam measurements at the RFQ test bench with 8 keV protons from the ion source and 400 keV protons from the RFQ. After one week, all BD devices had passed the tests and were officially accepted by the CNAO foundation.

Much of the hardware and software integration took place at the RFQ test bench. The manual control software of the BD systems were pushed to meet the experimental requirements as a stand-alone tool not only for trouble-shooting and maintenance, but partially also for the initial phase of linac commissioning in Pavia. Thereby, the experiences gained from LEBT and linac commissioning in Heidelberg delivered valuable input to establish the range of necessary software functionalities.

The RFQ test bench further offered the possibility to test the linac control system for CNAO which was adopted from the Heidelberg project and which has to be delivered by ECKELMANN. This sub-control software will later be linked to the main CNAO accelerator control system (ACS) via a dedicated gateway that provides communication with all linac components (magnet power supplies, RF amplifiers, BD devices from GSI). Several tests to read out BD systems through the gateway and to include the CNAO timing master were successfully performed at GSI together with the CNAO ACS group. More integration tests are planned for March 2007 at GSI and later on site in Pavia immediately after installation of the components at the accelerator facility.

IH-DTL and Further Components

After first RF measurements at the PINK factory in October 2005 and succeeding vacuum tests, the IH tank was delivered to GSI in April 2006. Copper plating of the tank and some refinishing operations were performed afterwards at GSI. After installation of an additional crane in the GSI UHV laboratory ('Leichtbauhalle'), the drift tube structure was assembled within the IH tank in October 2006 (Fig. 3). First RF measurements have been performed in January 2007. Completion of RF tuning and assembly is scheduled until mid 2007.

Three solenoid magnets and one Rohrsteerer were delivered by SIGMAPHI in 2006. 17 magnet power supplies and one HV supply for the LEBT chopper were manufactured by JAEGER and were delivered to CNAO in summer 2006. Three RF amplifiers for pulse powers of 1400 kW, 200 kW and 4 kW were produced by THOMSON. Factory acceptance tests took place during 2006 and in January and February 2007. All three systems should be ready for delivery end of March 2007.

Figure 3: Open IH cavity for CNAO after copper plating and assembly of the drift tube structure. The three large drift tubes contain magnetic quadrupole triplet lenses and were produced by DANFYSIK.

Conclusions and Outlook

During 2006, most of the components for the CNAO injector linac have been completed. The components will be shipped to Pavia during spring/summer 2007. The accelerator part of the CNAO building in Pavia is almost completed yet. The installation of the accelerator as well as the commissioning of the LEBT, of the ion sources and of the linac are scheduled for 2007.

We would like to thank our partners from CNAO for the very fruitful and pleasant cooperation. Furthermore, the committed support of various GSI groups is greatly acknowledged.

References

[1] U. Amaldi, Radiotherapy and Oncology, vol. 73, Suppl. 2, December 2004, p. S191.
[2] S. Rossi, Proc. EPAC 2006, p. 3631.
[3] B. Schlitt et al., Proc. LINAC 2006, p. 148.
[4] M. Maier, B. Schlitt et al., this report.
[5] A. Peters et al., GSI Scientific Report 2005, p. 398.
[6] A. Reiter, A. Peters, M. Schwickert, Proc. EPAC 2006, p. 1028.
[7] C. Kleffner et al., GSI Scientific Report 2005, p. 400.
[8] C.-M. Kleffner et al., Proc. LINAC 2006, p. 791.

Annex

Publications to FAIR: future experiments

Compiled by K. Große

1. Reviewed publications (WoS listed)

001 Andronic, A.*; CBM Collaboration: **The TRD of the CBM experiment.** *Nuclear instruments & methods in physics research, Section A, Accelerators, spectrometers, detectors and associated equipment* **563**(2): 349–354. DOI:10.1016/j.nima.2006.02.187

002 Friese, V.*: **Strangeness and charm in the CBM experiment.** *Journal of physics G, Nuclear and particle physics* **32**(12): S439–S446. DOI:10.1088/0954-3899/32/12/S53

003 Friese, V.*: **The CBM experiment at GSI/FAIR.** *Nuclear physics A, Nuclear and hadronic physics* **774**: 377–386. DOI:10.1016/j.nuclphysa.2006.06.018

004 Geissel, H.*; Weick, H.*; Winkler, M.*; Münzenberg, G.*; Yavor, M.: **Ion-optical layout of a powerful next-generation pre-separator for in-flight separation of relativistic rare isotopes.** *Nuclear instruments & methods in physics research, Section B, Beam interactions with materials and atoms* **247**(2): 368–376. DOI:10.1016/j.nimb.2006.02.014

005 Heuser, J. M.*; Deveaux, M.*; Müntz, C.; Stroth, J.: **Requirements for the silicon tracking system of CBM at FAIR.** *Nuclear instruments & methods in physics research, Section A, Accelerators, spectrometers, detectors and associated equipment* **568**(1): 258–262. DOI:10.1016/j.nima.2006.05.238

006 Iwase, H.*; Weick, H.*; Radon, T.*; Gutermuth, F.*; Winkler, M.*; Geissel, H.*: **Calculation of activation and dose spatial distributions induced by high intensity uranium beams at the Super-FRS fragment separator at FAIR.** *Nuclear instruments & methods in physics research, Section A, Accelerators, spectrometers, detectors and associated equipment* **562**(2): 972–975. DOI:10.1016/j.nima.2006.02.117

007 Koshurnikov, E. K.; Efremov, A. A.; Lobanov, Y. Y.; Makarov, A. F.; Orth, H.; Sissakian, A. N.; Vodopianov, A. S.: **Conceptual design of the PANDA magnet system.** *IEEE transactions on applied superconductivity* **16**(2): 469–472. DOI:10.1109/TASC.2005.869643 Also part of: EXP.

008 Kühn, W.; HADES PANDA Collaboration: **Hadrons in dense matter: From HADES to PANDA.** *Acta physica Polonica B, Particle physics and field theory, nuclear physics, theory of relativity* **37**(1): 129–138. OPEN ACCESS.

009 Peters, K.*: **Hadron physics at FAIR.** *Nuclear Physics B - Proceedings Supplements* **154**: 35–41. DOI:10.1016/j.nuclphysbps.2006.01.064

010 Senger, P.*: **Dense baryonic matter.** *Acta physica Polonica B, Particle physics and field theory, nuclear physics, theory of relativity* **37**(1): 115–127. OPEN ACCESS.

011 Tahir, N. A.*; Spiller, P.* Udrea, S.; Cortazar, O. D.; Deutsch, C.; Fortov, V. E.; Gryaznov, V.; Hoffmann, D. H. H.* Lomonosov, I. V.; Ni, P.; Piriz, A. R.; Shutov, A.; Temporal, M.; Varentsov, D.: **Studies of equation of state properties of high-energy density matter using intense heavy ion beams at the future FAIR facility: The HEDgeHOB collaboration.** *Nuclear instruments & methods in physics research, Section B, Beam interactions with materials and atoms* **245**(1): 85–93. DOI:10.1016/j.nimb.2005.11.084 Also part of: 'Large-scale facilities for research with photons, neutrons and ions'.

012 Tolós, L.*; Schaffner-Bielich, J.; Stöcker, H.: **D-mesons: In-medium effects at FAIR.** *Physics letters B* **635**(2): 85–92. DOI:10.1016/j.physletb.2006.02.045

013 Tolós, L.*; Schaffner-Bielich, J.; Stöcker, H.: **Open-charm enhancement at FAIR.** *Journal of physics G, Nuclear and particle physics* **32**(12): S533–S536. DOI:10.1088/0954-3899/32/12/S71

2. Further publications[1]

001 Auchmann, B.; S. Russenschuck, J. Kaugerts, G. Moritz: **Coil end design for the FAIR SIS 300 dipoles based on Differential Geometry.** In: *Proceedings of ASC 06, Seattle, USA, Sep. 2006*,

002 Bogdanov, B.; S. Kozub, V. Pokrovsky, L. Shirshov, P. Shcherbakov, V. Sytnik, L.Tkachenko, V.Zubko, G.Moritz, J. Kaugerts: **Investigations concerned with development of SC dipole for the SIS 300 accelerator.** In: *Proceedings of RUPAC2006, Novosibirsk, Russia, Sep. 2006*,

003 Brinkmann, K.-T.; Gianotti, P.; Lehmann, I.: **Exploring the Mysteries of Strong Interactions The PANDA Experiment.** In: *Nuclear Physics News* **16***(1)*, 15p.

004 Cortes, M.; E. Floch, H. Leibrock, J. Lucas, G. Moritz, M. Pinilla: **Design of a warm iron superferric dipole for the NESR at the FAIR facility.** In: *Proceedings of ASC 06, Seattle, USA, Sep. 2006*,

005 Currell F. J. SPARC; Widmann, E. FLAIR: **Challenges for Atomic and Fundamental Physics with Highly Charged Ions and Antiprotons.** In: *Nuclear Physics News* **16***(1)*, 24p.

006 Fischer, E.; G. Moritz, C. Muehle GSI; A.Alfeev, H. Khodzhibagiyan, A. Kovalenko, G. Kuznetsov, V. Seleznev, A. Kalimov: **Status of the Design of a Full Length Superferric Dipole and Quadrupole Magnets for the FAIR SIS 100 Synchrotron.** In: *Proceedings of ASC 06, Seattle, USA, Sep. 2006*,

[1] as reported by authors.

007 Fischer, E.; P. Shcherbakov, R. Kurnyshov: **Finite Element Calculations on Detailed 3d Models for the Superferric Main Magnets of the FAIR SIS 100 Synchrotron.** In: *Proceedings of CHATS 2006, Berkeley, California, Sep. 2006*,

008 Fischer, E.; R. Kurnyshov, P Shcherbakov: **Analysis of the Eddy Current Relaxation Time Effects in the FAIR SIS 100 Main Magnets.** In: *Proceedings of ASC 06, Seattle, USA, Sep. 2006*,

009 Floch, E.; E. Mustafin, G. Moritz, H. Ramakers, A. Golubev, S. Borovlev, V. Rogov, G. Smirnov, Yu., Titarenko, V. Batyaev, A. Kantsyrev, N. Markov, A. Smolyakov, D. Hagedorn, A. Gharib: **Irradiation of Bypass Diodes up to 2.2E14 Neutron/cm2 and 1.3 kGy for the FAIR Project.** In: *Proceedings of ASC 06, Seattle, USA, Sep. 2006*,

010 Groß, K.; Eschke, J.: **Facility for Antiproton and Ion Research (FAIR).** In: *Nuclear Physics News* **16***(1)*, 5p.

011 Höhne, C.; Rami, F.; Staszel, P.: **The Compressed Baryonic Matter experiment at FAIR.** In: *Nuclear Physics News* **16***(1)*, 19p.

012 Heuser, J. M. et al.,: **A high-performance Silicon Tracker for the CBM experiment.** In: *Proceedings of Particles and Nuclei International Conference (PANIC05), Santa Fe, New Mexico, October 24-28, 2005, AIP,* AIP Conference Proceedings **842**, 1073p.

013 Kaugerts, J.; G. Moritz, M. N. Wilson, A. Ghosh, A. den Ouden, I. Bogdanov, S. Kozub, P. Shcherbakov, L. Shirshov, L. Tkachenko, D. Richter, A. Verweij, G. Willering, P. Fabbricatore, G. Volpini: **Cable Design for FAIR SIS 300.** In: *Proceedings of ASC 06, Seattle, USA, Sep. 2006*,

014 Kauschke, M.; Y. Xiang, C.H, Schroeder,: **Kryosystem für FAIR.** In: *Proceedings of Deutsche Kälte-Klima-Tagung 2006, Dresden, Germany, Nov. 2006*,

015 Kauschke, M.; Y. Xiang, C.H. Schroeder, H. Quack, A. Kutzschbach: **Cryogenic Distribution Systems for FAIR.** In: *Proceedings of Cryo Prague 2006, Prague, CZ, July 2006*,

016 Khodzhibagiyan, H. G.; Nikolai N. Agapov, Victor D. Bartenev, Valery M. Drobin, Egbert Fischer, Alexander D. Kovalenko, Gregory L. Kuznetsov, Peter I. Nikitaev, Lyudmila V. Potanina, Alexander K. Shikov, Andrei Yu. Starikov, Gennady P. Vedernikov, Nadezhda M. Vladimirova: **Superferric Quadrupole Magnet with a Pulse Repetition Rate of 10 Hz for High Energy Particle Accelerators.** In: *Proceedings of ASC 06, Seattle, USA, Sep. 2006*,

017 Kozub, S.; L. Tkachenko, V. Zubko, E. Floch, J. Kaugerts, G. Moritz, B. Auchmann, S. Russenschuck, D. Tommasini: **Magnetic and Thermal Characteristics of a Model Dipole Magnet for the SIS 300.** In: *Proceedings of ASC 06, Seattle, USA, Sep. 2006*,

018 Kozub, S.; L. Tkachenko, V. Zubko, E. Floch, J. Kaugerts, G. Moritz, B. Auchmann, S. Russenschuck, D. Tommasini: **Magnetic and Thermal Characteristics of a Model Dipole Magnet for the SIS 300.** In: *Proceedings of ASC 06, Seattle, USA, Sep. 2006*,

019 Leibrock, H.; G. Moritz, Q. Wang, P. Yuan, Ma Lizhen, S.T. Wu, J. Lucas: **Superferric magnets for SUPER-FRS and storage rings of FAIR.** In: *Proceedings of RUPAC2006, Novosibirsk, Russia, Sep. 2006*,

020 Lomonosov, I. V.; Tahir, N. A.: **Prosepcts of High-Energy Density Matter Research at the Future FAIR Facility at Darmstadt.** In: *Nuclear Physics News* **16***(1)*, 29p.

021 Marbs, A.; F. Boochs, I. Pschorn: **A Photogrammetric Alignment Approach at High-Radiation Areas of FAIR.** In: *Proceedings of IWAA2006, SLAC, Stanford, Sep. 2006*,

022 Moritz, G.; E. Fischer, H. Khodzhibagiyan, A. Kovalenko, A. Nyilas, R. Burgmer, D. Krischel, P. Schmidt, W. Gärtner, M. Gehring, W. Walter and A. Wessner: **Mechanical Coil Structure of the FAIR SIS 100 Magnets.** In: *Proceedings of ASC 06, Seattle, USA, Sep. 2006*,

023 Muehle, C.: **Fast-Pulsed Superconducting Magnets.** In: *Proceeding of HB2006, Tsukuba, Japan, June 2006*,

024 Mustafin, E.; Iwase, H.*; Kozlova, E.*; Schardt, D.*; Fertman, A.; Golubev, A.; Hinca, R.; Pavlovic, M.; Strasik, I.; Sobolevskiy, N.: **Measured Residual Radioactivity Induced by U Ions of Energy 500 MeV/u in a Cu Target.** In: Biscari, C. (Ed.): *Proceedings of 10th European Particle Accelerator Conference, Edinburgh, 2006,*, 1834p.

025 Neumann, R.; Schardt, D.; Scholz, D.; Trautmann: **FAIR Experiments in Biophysics and Materials Research.** In: *Nuclear Physics News* **16***(1)*, 35p.

026 Peters, K.: **Hadron physics at FAIR.** In: AIP Conf. Proc. **814**, 33p.

027 Peters, K.: **Hadron physics at FAIR.** In: *Proceedings Rio de Janeiro 2005, Hadron spectroscopy,*, 33p.

028 Rubio, B.; Nilsson, T.: **NuSTAR.** In: *Nuclear Physics News* **16***(1)*, 9p.

029 Vysotsky, V. A., Anatoly V. Taran, Alexander V.Rychagov, Victor E.Sytnikov, Gebhard Moritz, Marion Kauschke, Egbert Fischer, Sergei A.Egorov, Igor Yu.Rodin, Valerii E.Korsunsky, Luca Bottura, Martin N. Wilson: **The Miniature Cable-In-Conduit-Conductor a Novel Development for Use in Fast Pulsed Accelerators such as FAIR.** In: *Proceedings of ASC 06, Seattle, USA, Sep. 2006*,

030 Wirth, H.; Ina Pschorn: **HICAT - A new heavy ion cancer therapy facility.** In: *Proceedings of IWAA2006, SLAC, Stanford, Sept. 2006*,

031 Xiang, Y.MM. Kauschke, G. Moritz, J. Kaugerts: **Supercritical Helium Flow Cooling for SIS300 Superconducting Dipole of FAIR.** In: *Proceedings of Cryo Prague 2006, Prague, CZ, July 2006*,

Publications to FAIR: accelerator research & development

Compiled by K. Große

1. Reviewed publications (WoS listed)

001 Benedetto, E.; Franchetti, G.*; Zimmermann, F.: **Incoherent effects of electron clouds in proton storage rings.** *Physical review letters* **97**(3): 034801. DOI:10.1103/PhysRevLett.97.034801

002 Bogdanov, I.; Kozub, S.; Pokrovsky, V.; Shcherbakov, P.; Shirshov, L.; Sytnik, V.; Tkachenko, L.; Zubko, V.; Kaugerts, J.; Moritz, G.: **Tests of straight and bent superconducting dipoles.** *IEEE transactions on applied superconductivity* **16**(2): 399–402. DOI:10.1109/TASC.2005.864336

003 Bogdanov, I.; Kozub, S.; Shcherbakov, P.; Tkachenko, L.; Zubko, V.; Muehle, C.; Moritz, G.; Tommasini, D.: **Optimization of a dipole with partially keystoned cable for the SIS 300.** *IEEE transactions on applied superconductivity* **16**(2): 395–398. DOI:10.1109/TASC.2005.864254

004 Deppisch, F.; Päs, H.; Redelbach, A.*; Rückl, R.: **Constraints on SUSY seesaw parameters from leptogenesis and lepton flavor violation.** *Physical Review D - Particles, Fields, Gravitation and Cosmology* **73**(3): 033004. DOI:10.1103/PhysRevD.73.033004

005 Fischer, E.; Kurnyshov, R.; Moritz, G.; Shcherbakov, P.: **3-D transient process calculations for fast cycling superferric accelerator magnets.** *IEEE transactions on applied superconductivity* **16**(2): 407–410. DOI:10.1109/TASC.2005.864338

006 Kalimov, A.; Fischer, E.; Kurnyshov, R.; Moritz, G.; Muehle, C.; Shcherbakov, P.: **Design of a superferric quadrupole magnet with a high field gradient.** *IEEE transactions on applied superconductivity* **16**(2): 403–406. DOI:10.1109/TASC.2005.864357

007 Khodzhibagiyan, H. G.; Fischer, E.; Kovalenko, A. D.: **New design for the SIS100/300 magnet cooling.** *IEEE transactions on applied superconductivity* **16**(2): 411–414. DOI:10.1109/TASC.2005.864339

008 Koch, S.; De Gersem, H.; Fischer, E.; Moritz, G.; Weiland, T.: **Simulation of eddy-current losses in a fast ramped superconductive dipole magnet.** *IEEE transactions on applied superconductivity* **16**(2): 334–337. DOI:10.1109/TASC.2006.870003

009 Lehrach, A.; Boine-Frankenheim, O.*; Hinterberger, F.; Maier, R.; Prasuhn, D.: **Beam performance and luminosity limitations in the high-energy storage ring (HESR).** *Nuclear instruments & methods in physics research, Section A, Accelerators, spectrometers, detectors and associated equipment* **561**(2): 289–296. DOI:10.1016/j.nima.2006.01.017

010 Omet, C.*; Spiller, P.*; Stadlmann, J.*; Hoffmann, D. H. H.*: **Charge change-induced beam losses under dynamic vacuum conditions in ring accelerators.** *New Journal of Physics* **8**: 284. DOI:10.1088/1367-2630/8/11/284 OPEN ACCESS. Also part of: 'Large-scale facilities for research with photons, neutrons and ions'.

011 Spiller, P.*; Franchetti, G.*: **The FAIR accelerator project at GSI.** *Nuclear instruments & methods in physics research, Section A, Accelerators, spectrometers, detectors and associated equipment* **561**(2): 305–309. DOI:10.1016/j.nima.2006.01.043

012 Struckmeier, J.*; Redelbach, A.*: **Energy-second-moment map analysis as an approach to quantify the irregularity of Hamiltonian systems.** *Physical Review E - Statistical, Nonlinear, and Soft Matter Physics* **74**(2): 026209. DOI:10.1103/PhysRevE.74.026209

013 Tahir, N. A.*; Lomonosov, I. V.; Shutov, A.; Udrea, S.; Deutsch, C.; Fortov, E.; Gryaznov, V.; Hoffmann, D. H. H.*; Jacobi, J.; Kain, V.; Kuster, M.; Ni, P.; Piriz, A. R.; Schmidt, R.; Spiller, P.*; Varentsov, D.; Zioutas, K.: **Proposed studies of strongly coupled plasmas at the future FAIR and LHC facilities: the HEDgeHOB collaboration.** *Journal of Physics A: Mathematical and General* **39**(17): 4755–4763. DOI:10.1088/0305-4470/39/17/S70 Also part of: 'Large-scale facilities for research with photons, neutrons and ions'.

014 Tahir, N. A.*; Shutov, A.; Lomonosov, I. V.; Gryaznov, V.; Deutsch, C.*; Fortov, V. E.; Hoffmann, D. H. H.*; Ni, P.; Piriz, A. R.; Udrea, S.; Varentsov, D.; Wouchuk, G.: **Studies of thermophysical properties of high-energy-density states in matter using intense heavy ion beams at the future FAIR accelerator facilities: The HEDgeHOB collaboration.** *Journal De Physique. IV : JP* **133**: 1059–1064. DOI:10.1051/jp4:2006133215 Also part of: 'Large-scale facilities for research with photons, neutrons and ions'.

015 Winkler, M.; Svedentsov, M.; Behr, K. H.; Geissel, H.; Iwase, H.; Moritz, G.; Muhle, C.; Weick, H.: **Radiation resistant quadrupole magnet for the Super-FRS at FAIR.** *IEEE transactions on applied superconductivity* **16**(2): 415–418. DOI:10.1109/TASC.2005.864253

2. Further publications[1]

001 A. Lehrach, R. Maier, D. Prasuhn, Boine-Frankenheim O.*, Hasse R.W.*, Hinterberger F.: **Beam Performance with Internal Targets in the High-energy Storage Ring (HESR).** In: Biscari, C. (Ed.): *Proceedings of 10th European Particle Accelerator Conference, Edinburgh, 2006,*, 2197p.

002 Barth, W.*; Dahl, L. A.*; Groening, L.*; Yaramyshev, S.*; Ratzinger, U.: **Long-Term Perspective for the UNILAC as a**

[1] as reported by authors.

High-Current, Heavy-Ion Injector for the FAIR-Accelerator Complex. In: *LINAC2006, 2006 Linear Accelerator Conference, August 21-25, 2006 Knoxville, Tennessee, USA,*, 180p.

003 Beller, P.*; Beckert, K.*; Dimopoulou, C.*; Dolinskii, C. A.*; Nolden, F.*; Steck, M.*; Yang, J.*: **Layout of an Accumulator and Decelerator Ring for FAIR.** In: Biscari, C. (Ed.): *Proceedings of 10th European Particle Accelerator Conference, Edinburgh, 2006,*, 199p.

004 Benedikt, M.; Fabich, A.; Kirk, M.; Omet, C.; Spiller, P. J.*: **Estimation of Decay Losses and Dynamic Vacuum for the Beta-beam Accelerator Chain.** In: Biscari, C. (Ed.): *Proceedings of 10th European Particle Accelerator Conference, Edinburgh, 2006,*, 1696p.

005 Boine-Frankenheim, O.*; Hofmann, I.*; Kornilov, V.*: **Instabilities and Space Charge Effects in High Intensity Ring Accelerators.** In: Biscari, C. (Ed.): *Proceedings of 10th European Particle Accelerator Conference, Edinburgh, 2006,*, 1882p.

006 Clemente, G.; Podlech, H.; Ratzinger, U.; Tiede, R.; Groening, L.*; Minaev, S.: **Status of the 70 MeV, 70 mA CH Proton-DTL for FAIR.** In: Biscari, C. (Ed.): *Proceedings of 10th European Particle Accelerator Conference, Edinburgh, 2006,*, 1283p.

007 D'Imperio, N. L.; Luccio, A. U.; Malitsky N.; Boine-Frankenheim, O.*: **Parallel 3-D Space Charge Calculations in the Unified Accelerator Library.** In: Biscari, C. (Ed.): *Proceedings of 10th European Particle Accelerator Conference, Edinburgh, 2006,*, 2835p.

008 Fischer, E.*; Moritz, G.*; Khodzhibagiyan, H. G.; Kovalenko, A. D.; Kurnyshov, R. V.; Shcherbakov, P. A.: **Analysis of the Superferric Quadrupole Magnet Design for the SIS100 Accelerator of the FAIR Project.** In: Biscari, C. (Ed.): *Proceedings of 10th European Particle Accelerator Conference, Edinburgh, 2006,*, 2586p.

009 Forck, P.* ; Peters, A.*: **Innovative Beam Diagnostics for the Challenging FAIR Project.** In: Biscari, C. (Ed.): *Proceedings of 10th European Particle Accelerator Conference, Edinburgh, 2006,*, 1016p.

010 Franchetti, G.*; Boine-Frankenheim, O.*; Hofmann, I.*; Kornilov, V.*; Spiller, P. J.*, Stadlmann, J.*: **Considerations for the High-intensity Working Point of the SIS100.** In: Biscari, C. (Ed.): *Proceedings of 10th European Particle Accelerator Conference, Edinburgh, 2006,*, 2793p.

011 Franchetti, G.*; Hofmann, I.*: **Space Charge Induced Resonance Trapping in High-intensity Synchrotrons.** In: Biscari, C. (Ed.): *Proceedings of 10th European Particle Accelerator Conference, Edinburgh, 2006,*, 2790p.

012 Groening, L.*; Barth, W.*; Dahl, L. A.*; Vinzenz, W.*; Yaramyshev, S.*; Clemente, G.; Ratzinger, U.; Schempp, A.; Tiede, R.: **The 70-MeV Proton Linac for the Facility for Antiproton and Ion Research FAIR.** In: *LINAC2006, 2006 Linear Accelerator Conference, August 21-25, 2006 Knoxville, Tennessee, USA,*, 186p.

013 Kovalenko, A. D.; Agapov, N. N.; Alfeev, A. V.; Khodzhibagiyan, H. G.; Kuznetsov, G. L.; Seleznev ,V. V.; Starikov, A. Y.; Fischer, E.*; Moritz, G.*; Muehle, C.*; Spiller, P. J.*; Kalimov, A. K.; Shabunov, A.V.: **Full Length Superferric Dipole and Quadrupole Prototype Magnets for the SIS100 at GSI: Status of the Design and Manufacturing.** In: Biscari, C. (Ed.): *Proceedings of 10th European Particle Accelerator Conference, Edinburgh, 2006,*, 2583p.

014 Kraemer, A.; Bellachioma, M. C.; Kollmus, H.; Sprenger, H. R.*.;Wilfert, S.*: **The Vacuum System of FAIR Accelerator Facility.** In: Biscari, C. (Ed.): *Proceedings of 10th European Particle Accelerator Conference, Edinburgh, 2006,*, 1429p.

015 Krämer, D.*: **Baseline Design for the Facility for Antiproton and Ion Research (FAIR) Finalized.** In: Biscari, C. (Ed.): *Proceedings of 10th European Particle Accelerator Conference, Edinburgh, 2006,*, 205p.

016 Litvinov, S. A.*; Dolinskii, A.*; Geissel, H.*; Nolden, F.*; Steck, M.*; Weick, H.*: **The Isochronous Mode of the Collector Ring.** In: Biscari, C. (Ed.): *Proceedings of 10th European Particle Accelerator Conference, Edinburgh, 2006,*, 1618p.

017 Mikhaylov, V. A.; Alfeev, A. V.; Butenko, A. V.; Eliseev, A. V.; Khodzhibagiyan, H. G.; Kovalenko, A. D.; Kozlov, O. S.; Seleznev, V. V.; Starikov, A. Y.; Volkov, V.; Fischer, E.*; Spiller, P. J.*; Stadlmann, J.*: **Basic Aspects of the SIS100 Correction System Design.** In: Biscari, C. (Ed.): *Proceedings of 10th European Particle Accelerator Conference, Edinburgh, 2006,*, 240p.

018 Moritz, G.*: **Status of the Development of the FAIR Superconducting Magnets.** In: Biscari, C. (Ed.): *Proceedings of 10th European Particle Accelerator Conference, Edinburgh, 2006,*, 2577p.

019 Nolden, F.*; Beckert, K.*; Beller, P.*; Blell, U.*; Dimopoulou, C.*; Dolinskii, A.*; Laier, U.*; Moritz, G.*; Muehle C.*; Nesmiyan, I.*; Peschke, C.*; Steck, M*.: **The Collector Ring CR of the FAIR Project.** In: Biscari, C. (Ed.): *Proceedings of 10th European Particle Accelerator Conference, Edinburgh, 2006,*, 208p.

020 Omet, C.*; Spiller, P. J.*; Stadlmann, J.*: **Simulation of Dynamic Vacuum Induced Beam Loss.** In: Biscari, C. (Ed.): *Proceedings of 10th European Particle Accelerator Conference, Edinburgh, 2006,*, 211p.

021 Shcherbakov, P. A.; Fischer, E.*; Kurnyshov ,R. V.: **3D Field Computation for the Main Prototype Magnets of the SIS100 Accelerator of the FAIR Project.** In: Biscari, C. (Ed.): *Proceedings of 10th European Particle Accelerator Conference, Edinburgh, 2006,*, 2592p.

022 Shcherbakov, P. A.; Fischer, E.*; Kurnyshov, R.V.: **3D Magnetic Field and Eddy Current Loss Calculations for Iron Dominated Accelerator Magnets using ANSYS Compared with Results of Noncommercial Codes.** In: Biscari, C. (Ed.): *Proceedings of 10th European Particle Accelerator Conference, Edinburgh, 2006,*, 2595p.

023 Spiller, P. J.*; Barth, W.*; Dahl, L. A.*; Eickhoff, H.*; Hollinger, R.*; Spaedtke, P. S.*: **Approaches to High Intensi-**

ties for FAIR. In: Biscari, C. (Ed.): *Proceedings of 10th European Particle Accelerator Conference, Edinburgh, 2006,*, 24p.

024 Stadlmann, J.*; Blasche, K.*; Franczak, B.*; Omet, C.*; Pyka, N.*; Spiller, P.J.*; Kovalenko, A.D.: **Ion Optical Design of the Heavy Ion Synchrotron SIS100.** In: Biscari, C. (Ed.): *Proceedings of 10th European Particle Accelerator Conference, Edinburgh, 2006,*, 214p.

025 Zhabitsky, V.*; Gorbachev, E.*; Lebedev, N. I.*; Blell, U.*; Spiller, P. J.*: **Transverse Damping System at SIS100.** In: Biscari, C. (Ed.): *Proceedings of 10th European Particle Accelerator Conference, Edinburgh, 2006,*, 3014p.

Publications to the programme 'physics of hadrons and nuclei': accelerator research & development

Compiled by K. Große

1. Reviewed publications (WoS listed)

001 Becker, F.; Hug, A.; Forck, P.*; Kulish, M.; Ni, P.; Udrea, S.; Varentsov, D.*: **Design, development, and testing of non-intercepting profile diagnostics for intense heavy ion beams using a capacitive pickup and beam induced gas fluorescence monitors.** *Laser and particle beams* **24**(4): 541–551. DOI:10.1017/S0263034606060721 Also part of: 'Large-scale facilities for research with photons, neutrons and ions'.

002 Boine-Frankenheim, O.*; Hasse, R.*; Hinterberger, F.; Lehrach, A.; Zenkevich, P.: **Cooling equilibrium and beam loss with internal targets in high energy storage rings.** *Nuclear instruments & methods in physics research, Section A, Accelerators, spectrometers, detectors and associated equipment* **560**(2): 245–255. DOI:10.1016/j.nima.2006.01.131

003 Buzio, M.; Beauquis, J.; Bottura, L.; Coccoli, M.; Deferne, G.; Krotov, N.; Laface, E.; Ruccio, A.; Perez, J. G.; Missiaen, D.; Schnizer, P.; Smirnov, N.; Wildner, E.; Winkes, P.; Walckiers, L.: **Warm and cold magnetic and mechanical alignment tests of LHC short straight sections.** *IEEE transactions on applied superconductivity* **16**(2): 1395–1398. DOI:10.1109/TASC.2005.864728

004 Franchetti, G.*; Hofmann, I.*: **Particle trapping by nonlinear resonances and space charge.** *Nuclear instruments & methods in physics research, Section A, Accelerators, spectrometers, detectors and associated equipment* **561**(2): 195–202. DOI:10.1016/j.nima.2006.01.031

005 Hoffmann, D. H. H.*; Blazevic, A.*; Rosmej, O. N.*; Spiller, P.*; Tahir, N. A.*; Weyrich, K.*; Dafni, T.; Kuster, M.; Roth, M.; Udrea, S.; Varentsov, D.; Jacoby, J.; Zioutas, ; Sharkov, B. Y.: **Advances of dense plasma physics with particle accelerators.** *Journal de Physique IV - Proceedings* **133**: 49–55. DOI:10.1051/jp4:2006133011 Also part of: 'Large-scale facilities for research with photons, neutrons and ions'.

006 Hoffmann, D. H. H.*; Blazevic, A.*; Rosmej, O. N.*; Spiller, P.*; Tahir, N. A.*; Weyrich, K.*; Dafni, T.; Kuster, M.; Roth, M.; Udrea, S.; Varentsov, D.; Jacoby, J.; Zioutas, K.; Mintsev, V.; Fortov, V. E.; Sharkov, B. Y.; Maron, Y.: **Frontiers of dense plasma physics with intense ion and laser beams and accelerator technology.** *Physica scripta* **T123**: 1–7. DOI:10.1088/0031-8949/2006/T123/001 Also part of: 'Large-scale facilities for research with photons, neutrons and ions'.

007 Hofmann, I.*; Franchetti, G.*: **Self-consistent study of space-charge-driven coupling resonances.** *Phys. Rev. Top. Accel. Beams* **9**(5): 054202. DOI:10.1103/PhysRevSTAB.9.054202 OPEN ACCESS.

008 Hofmannn, I.*; Franchetti, G.*: **Nonlinear phenomena in space-charge dominated beams.** *Nuclear instruments & methods in physics research, Section A, Accelerators, spectrometers, detectors and associated equipment* **561**(2): 137–142. DOI:10.1016/j.nima.2006.01.006

009 Laidani, N.; Bartali, R.; Gottardi, G.; Anderle, M.; Chuste, G.; Bellachioma, C.*: **Production and characterization of thin a-C :(H) films for gas permeation barrier functionality against He, CO2, N_2, O_2 and H_2O.** *Journal of physics Condensed matter* **18**(26): 5945–5959. DOI:10.1088/0953-8984/18/26/014

010 Lee, S. Y.*; Franchetti, G.*; Hofmann, I.*; Wang, F.; Yang, L.: **Emittance growth mechanisms for space-charge dominated beams in fixed field alternating gradient and proton driver rings.** *New Journal of Physics* **8**: 291. DOI:10.1088/1367-2630/8/11/291 OPEN ACCESS.

011 Métral, E.; Franchetti, G.*; Giovannozzi, M.; Hofmann, I.*; Martini, M.; Steerenberg, R.: **Observation of octupole driven resonance phenomena with space charge at the CERN Proton Synchrotron.** *Nuclear instruments & methods in physics research, Section A, Accelerators, spectrometers, detectors and associated equipment* **561**(2): 257–265. DOI:10.1016/j.nima.2006.01.029

012 Nolden, F.*; Nesmiyan, I.*; Peschke, C.*: **On stochastic cooling of multi-component fragment beams.** *Nuclear instruments & methods in physics research, Section A, Accelerators, spectrometers, detectors and associated equipment* **564**(1): 87–93. DOI:10.1016/j.nima.2006.04.056

013 Sytnikov, V. E.; Vysotsky, V. S.; Rychagov, A. V.; Taran, A. V.; Moritz, G.; Kauschke, M.; Fischer, E.; Egorov, S. A.; Rodin, I. Y.; Korsunsky, V. E.; Bottura, L.; Wilson, M. N.: **Development and test of a miniature novel cable-in-conduit-conductor for use in fast ramping accelerators with superconducting magnets.** *IEEE transactions on applied superconductivity* **16**(2): 1176–1179. DOI:10.1109/TASC.2006.873237

014 Zenkevich, P.; Boine-Frankenheim, O.*; Bolshakov, A.: **A new algorithm for the kinetic analysis of intra-beam scattering in storage rings.** *Nuclear instruments & methods in physics research, Section A, Accelerators, spectrometers, detectors and associated equipment* **561**(2): 284–288. DOI:10.1016/j.nima.2006.01.013

2. Further publications[1]

001 Al-Khateeb A. M.; Daqa, W. M.; Boine-Frankenheim, O.*; Hasse, R. W.*; Hofmann, I.*: **Transverse Coupling Impedances From Field Matching in a Smooth Resistive Cylindrical Pipe for Arbitrary Beam Energies.** In: Biscari, C. (Ed.): *Proceedings*

[1] as reported by authors.

of 10th European Particle Accelerator Conference, Edinburgh, 2006,, 2853p.

002 Barabin, S.V.; Liakin D. A.; Orlov, A. Y.; Forck, P.*; Giacomini, T.*: **Testing the Silicon Photomultiplier for Ionization Profile Monitor.** In: Biscari, C. (Ed.): *Proceedings of 10th European Particle Accelerator Conference, Edinburgh, 2006,*, 1172p.

003 Barth, W.*; Bayer, W. B.*; Dahl, L. A.*; Groening, L.*; Yaramyshev, S.*: **Status of the End-to-End Beam Dynamics Simulations for the GSI UNILAC.** In: *LINAC2006, 2006 Linear Accelerator Conference, August 21-25, 2006 Knoxville, Tennessee, USA,*, 438p.

004 Barth, W.*; Dahl, L. A.*; Hofmann, S.*; Tinschert, K.*; Ratzinger, U.: **UNILAC Upgrade Programme for the Heavy Element Research at GSI-SHIP.** In: Biscari, C. (Ed.): *Proceedings of 10th European Particle Accelerator Conference, Edinburgh, 2006,*, 1565p.

005 Bayer, W. B.*; Barth, W.*; Dahl, L. A.*; Groening, L.*; Yaramyshev, S.*: **Heavy-Ion-Beam Emittance Measurements at the GSI UNILAC.** In: *LINAC2006, 2006 Linear Accelerator Conference, August 21-25, 2006 Knoxville, Tennessee, USA,*, 177p.

006 Bechtold, A.; Habs, D.; Fischbach, J.; Ratzinger, U.; Rehberg, J.; Reichwein, M.; Schempp, A.; Haeuser, J.;Kester, O. K.*: **The MAFF IH-RFQ Test Stand at the IAP Frankfurt.** In: Biscari, C. (Ed.): *Proceedings of 10th European Particle Accelerator Conference, Edinburgh, 2006,*, 1577p.

007 Bender, M.*; Kollmus, H.*; Assmann, W. A.: **Understanding of Ion Induced Desorption Using the ERDA Technique.** In: Biscari, C. (Ed.): *Proceedings of 10th European Particle Accelerator Conference, Edinburgh, 2006,*, 1423p.

008 Benedetto, E.; Franchetti, G.*; Rumolo, G.; Zimmermann, F.: **Resonance Trapping, Halo Formation and Incoherent Emittance Growth due to Electron Cloud.** In: Biscari, C. (Ed.): *Proceedings of 10th European Particle Accelerator Conference, Edinburgh, 2006,*, 2820p.

009 Boine-Frankenheim, O.; Kornilov, V.: **Implementation and validation of space charge and impedance kicks in the code PATRIC for studies of transverse coherent instabilities in the FAIR rings.** In: *Proc. of ICAP 2006, October 2-6 2006, Chamonix Mont-Blanc, France*,

010 Budz, P.; Abo-Bakr, M.; Buerkmann-Gehrlein, K.; Duerr, V.; Kolbe, J.; Krämer, D.; Rahn, J.; Wüstefeld, G.; Churkin, I. N.; Rouvinsky, E. R.; Semenov, E. P.; Sinyatkin, S. V.; Steshov, A. G.; Klein, R.; Ulm, G.: **The Magnets of the Metrology Light Source in Berlin-Adlershof.** In: Biscari, C. (Ed.): *Proceedings of 10th European Particle Accelerator Conference, Edinburgh, 2006,*, 3296p.

011 Buerkmann-Gehrlein, K.; Abo-Bakr, M.; Anders, W.; Budz, P.; Dressler, O.; Duerr, V.; Feikes, J.; Hoberg, G. H.; Krämer, D.; Kuske, P.; Lange, R.; Rahn, J.; Schneegans, T.; Schueler, D.; Weihreter, E.; Wuestefeld, G.; R.; Klein, R.; Ulm, G.: **Status of the Metrology Light Source.** In: Biscari, C. (Ed.): *Proceedings of 10th European Particle Accelerator Conference, Edinburgh, 2006,*, 1423p.

012 Calaga, R.; F. Franchi, F*; Tomas, R.: **Global and Local Coupling Compensation in RHIC using AC Dipoles.** In: Biscari, C. (Ed.): *Proceedings of 10th European Particle Accelerator Conference, Edinburgh, 2006,*, 2774p.

013 Cee, R.; Kleffner, C.M.; Maier, M. T.; Schlitt, B.; Ratzinger, U.; Schempp, A.: **Front-to-end Simulation of the Injector Linac for the Heidelberg Ion Beam Therapy Centre.** In: Biscari, C. (Ed.): *Proceedings of 10th European Particle Accelerator Conference, Edinburgh, 2006,*, 1957p.

014 Commenda, C.; Liebermann, H.; Podlech, H.; Ratzinger, U.; Sauer, A. C.; Dermati, K.*: **Status of the Tuner for the 19-Cell Superconducting CH Prototype Cavity.** In: *LINAC2006, 2006 Linear Accelerator Conference, August 21-25, 2006 Knoxville, Tennessee, USA,*, 740p.

015 Dahl, L. A.*; Barth, W.*; Kaiser, M.*; Kester, O. K.*; Kluge, H. J.*; Vinzenz, W.*; Hofmann, B.; Ratzinger, U.; Sauer, A. C.; Schempp, A.: **The HITRAP Decelerator Project at GSI.** In: Biscari, C. (Ed.): *Proceedings of 10th European Particle Accelerator Conference, Edinburgh, 2006,*, 1568p.

016 Dahl, L. A.*; Barth, W.*; Yaramyshev, S.*; Visotski, S. A.; Vorobyov, I.: **A New LEBT and RFQ Radial Matcher for the UNILAC Front End.** In: *LINAC2006, 2006 Linear Accelerator Conference, August 21-25, 2006 Knoxville, Tennessee, USA,*, 183p.

017 Forck, P.*; Andre, C.*; Becker, F.*; Iwase, H.*; Hoffmann, D.*: **Profile Measurement by Beam Induced Fluorescence for 60 MeV/u to 750 MeV/u Heavy Ion Beams.** In: Biscari, C. (Ed.): *Proceedings of 10th European Particle Accelerator Conference, Edinburgh, 2006,*, 1013p.

018 Franchetti, G.*; Hofmann ,I.*: **Scaling Laws for the Montague Resonance.** In: Biscari, C. (Ed.): *Proceedings of 10th European Particle Accelerator Conference, Edinburgh, 2006,*, 2796p.

019 Franchetti, G.; Hofmann, I.: **Towards the description of long term self-consistent effects in space charge induced resonance trapping.** In: *Proc. of ICAP 2006, October 2-6 2006, Chamonix Mont-Blanc, France*,

020 Franchi, F.*; Bayer, W. B.*, Franchetti, G.*; Groening, L.*; Hofmann, I.*; Orzhekhovskaya, A.*; Yaramyshev, S.*; Yin, X.*; Bellodi, G.; Gerigk, F.; Lombardi, A. M.; Mütze, T.; Clemente, G.; Sauer, A. C.; Tiede, R.; Duperrier, R.; Uriot, D.: **Linac Code Benchmarking for the UNILAC Experiment.** In: *LINAC2006, 2006 Linear Accelerator Conference, August 21-25, 2006 Knoxville, Tennessee, USA,*, 460p.

021 Franchi, F.*; Calaga, R.; Tomas, R.: **Fast Compensation of Global Linear Coupling in RHIC using AC Dipoles.** In: Biscari, C. (Ed.): *Proceedings of 10th European Particle Accelerator Conference, Edinburgh, 2006,*, 2071p.

022 Galatis, A. A.; Kowina, P.; Lang, K.; Peters, A.*: **Digital Techniques in BPM Measurements at GSI-SIS.** In: Biscari, C. (Ed.): *Proceedings of 10th European Particle Accelerator Conference, Edinburgh, 2006,*, 1019p.

023 Galonska, M.; Galonska, M.; Gobin, R.; Hollinger, R.*: **Computer Simulations of a High-Current Proton Beam at the SILHI-LEBT.** In: *LINAC2006, 2006 Linear Accelerator Conference, August 21-25, 2006 Knoxville, Tennessee, USA,*, 469p.

024 Gostishchev, V.*; Beckert, K.*; Beller, P.; Dimopoulou, C.*; Dolinskii, A.*; Nolden, F.*; Steck, M.*; Meshkov, I. N.; Sidorin, A. O.; Smirnov, A. V.; Trubnikov, G. V.: **Internal Target Effects in the ESR Storage Ring with Cooling.** In: Biscari, C. (Ed.): *Proceedings of 10th European Particle Accelerator Conference, Edinburgh, 2006,*, 202p.

025 Hofmann, B.; Schempp, A.; Kester, O. K.*: **An RFQ-Decelerator for HITRAP.** In: *LINAC2006, 2006 Linear Accelerator Conference, August 21-25, 2006 Knoxville, Tennessee, USA,*, 151p.

026 Hofmann, B.; Schempp, A.; Kester, O. K.*: **The HITRAP RFQ Decelerator at GSI.** In: Biscari, C. (Ed.): *Proceedings of 10th European Particle Accelerator Conference, Edinburgh, 2006,*, 1586p.

027 Hollinger, R.*; Barth, W.*; Dahl, L. A.*; Galonska, M.*; Groening, L.*; Spaedtke, P. S.*; Gobin, R.; Leroy, P.-A.; Meusel, O.: **High-Current Proton Beam Investigations at the SILHI-LEBT at CEA/Saclay.** In: *LINAC2006, 2006 Linear Accelerator Conference, August 21-25, 2006 Knoxville, Tennessee, USA,*, 232p.

028 Kester, O. K.*; Barth, W.*; Dahl, L. A.*; Herfurth, F.*; Kaiser, M.*; Kluge, H. J.*; Kozhuharov, C.*; Quint, W.*; Hofmann, B.; Ratzinger, U.; Sauer, A. C.; Schempp, A.: **Deceleration of Highly Charged Ions for the HITRAP Project at GSI.** In: *LINAC2006, 2006 Linear Accelerator Conference, August 21-25, 2006 Knoxville, Tennessee, USA,*, 189p.

029 Kleffner, C. M.*; Baer, R.*; Barth, W.*; Galonska, M.*; Heymach, F.*; Hollinger, R.*; Hutter, G.*; Kaufmann, W.*; Maier, M. T.*; Reiter, A.*; Schlitt, B.*; Schwickert, M.*; Spaedtke, P. S.*; Vinzenz, W.*; Bechtold, A.; Schempp, A.; Cee, R.; Feldmeier, E.; Vollmer, S.: **Testbench of the HICAT RFQ at GSI.** In: *LINAC2006, 2006 Linear Accelerator Conference, August 21-25, 2006 Knoxville, Tennessee, USA,*, 791p.

030 Kleffner, C. M.*; Baer, R.*; Barth, W.*; Galonska, M.*; Heymach, F.*; Hollinger, R.*; Hutter, G.*; Kaufmann, W.*; Maier, M. T.*; Reiter, A.*; Schlitt, B.*; Schwickert, M.*; Spaedtke, P. S.*; Vinzenz, W.*; Bechtold, A.; Schempp, A.; Cee, R.; Feldmeier, E.; Vollmer, S.: **Testbench of the HICAT RFQ at GSI.** In: *LINAC2006, 2006 Linear Accelerator Conference, August 21-25, 2006 Knoxville, Tennessee, USA,*, 791p.

031 Knaack, K.; Wittenburg, K.; Neubert, R.; Nietzsche, S.; Vodel, W.; Peters, A.: **A New SQUID-based Measurement Tool for Characterization of Superconducting RF Cavities.** In: Biscari, C. (Ed.): *Proceedings of 10th European Particle Accelerator Conference, Edinburgh, 2006,*, 1070p.

032 Kollmus, H.*; Bellachioma, M. C.*; Bender, M.*; Kraemer, A.*; Kurdal, J.*; Sprenger, H. R.*: **Vacuum Issues and Challenges of SIS18 Upgrade at GSI.** In: Biscari, C. (Ed.): *Proceedings of 10th European Particle Accelerator Conference, Edinburgh, 2006,*, 1426p.

033 Kowina, P.; Galatis, A. A.*; Kaufmann, J.*; Schoelles, J.*: **Numerical Calculations of Position Sensitivity for Linear-cut Beam Position Monitors.** In: Biscari, C. (Ed.): *Proceedings of 10th European Particle Accelerator Conference, Edinburgh, 2006,*, 1022p.

034 Lehrach, A.; Boine-Frankenheim, O.; Hasse. R.; Prasuhn, D.: **Beam-dynamics simulation studies for the High-Energy Storage Ring (HESR).** In: *Proc. of ICAP 2006, October 2-6 2006, Chamonix Mont-Blanc, France*,

035 Maier, M. T.*; Baer, R.*; Barth, W.*; Dahl, L. A.*; Dorn, C.*; Fleck, T. G.*; Groening, L.*; Kleffner, C. M.*; Müller, C*; Peters, A*; Schlitt, B*; Schwickert, M*; Tinschert, K*; Vormann, H*; Cee, R.; Naas, B.; Scheloske, S.; Winkelmann, T.; Ratzinger, U.; Schempp, A.: **Status of the Linac-commissioning for the Heavy Ion Cancer Therapy Facility HIT.** In: Biscari, C. (Ed.): *Proceedings of 10th European Particle Accelerator Conference, Edinburgh, 2006,*, 1571p.

036 Ratzinger, U.; Clemente, G.; Commenda, C.; Liebermann, H.; Podlech, H.; Tiede, R.; Barth, W.*; Groening, L.*: **A 70-MeV Proton Linac for the FAIR Facility Based on CH - Cavities.** In: *LINAC2006, 2006 Linear Accelerator Conference, August 21-25, 2006 Knoxville, Tennessee, USA,*, 526p.

037 Reeg, H.*; Glatz, J.*; Schneider, N.*; Walter, H.: **Machine Protection by Active Current-transmission Control at GSI-UNILA.** In: Biscari, C. (Ed.): *Proceedings of 10th European Particle Accelerator Conference, Edinburgh, 2006,*, 1025p.

038 Reiter, A.*; Peters, A.*; Schwickert, M.*: **Integrated Beam Diagnostics Systems for HICAT and CNAO.** In: Biscari, C. (Ed.): *Proceedings of 10th European Particle Accelerator Conference, Edinburgh, 2006,*, 1028p.

039 Schlitt, B.*; Baer, R.*; Barth, W.*; Fleck, T. G.*; Hoerr, M.*; Hutter, G.*;. Kleffner, C. M.*; Maier, M. T.*; Peters, A.*; Schwickert, M.*; Tinschert, K.*; Vinzenz, W.*; Vormann, H.*; Wilms, D.*; Cee, R.; Feldmeier, E.; Naas, B.; Scheloske, S.; Suhm, J.; Vollmer, S.; Winkelmann, T.; Clemente, G.; Ratzinger, U.; Schempp, A.: **Commissioning of the 7-MeV/u, 217-MHz Injector Linac for the Heavy Ion Cancer Therapy Facility at the University Clinics in Heidelberg.** In: *LINAC2006, 2006 Linear Accelerator Conference, August 21-25, 2006 Knoxville, Tennessee, USA,*, 148p.

040 Sorge, S.; Boine-Frankenheim, O.; Fischer, W.: **Analysis of measured transverse beam echoes in RHIC.** In: *Proc. of ICAP 2006, October 2-6 2006, Chamonix Mont-Blanc, France*,

041 Tomas, R.; Brüning, o. S.; Fartoukh, S. D.; Giovannozzi, M.; Papaphilippou, Y.; Zimmermann, F.; Calaga, R.; Peggs, S.; Franchi, F.*: **Procedures and Accuracy Estimates for Beta-beat Correction in the LHC.** In: Biscari, C. (Ed.): *Proceedings of 10th European Particle Accelerator Conference, Edinburgh, 2006,*, 2023p.

042 Weinrich, U.: **Gantry Design for Proton and Carbon Hadrontherapy Facilities.** In: Biscari, C. (Ed.): *Proceedings of 10th European Particle Accelerator Conference, Edinburgh, 2006,*, 964p.

043 Zimmermann, F.; Basset, R.; Benedetto, E.; Dorda, U.; Gio-

vannozzi, M.; Papaphilippou, Y.; T., Pieloni,, Ruggiero, F.; Rumolo, G.; Schmidt, F.; Todesco, E.; Abell, D. T.; Bartolini, R.; Boine-Frankenheim, O.*; Franchetti, G.*; Hofmann, I.*; Cai, Y.; Pivi, M. T. F.; Chin, Y.H.; Ohmi, K.; Oide, K.; Cousineau, S. M.; Danilov, V. V.; Holmes, J. A.; Shishlo, A. P.; Farvacque, L.; Friedman, A.; Furman, M. A.; Grote, D. P.; Qiang, J.; Sabbi, G. L.; Seidl, P. A.; Vay, J.-L.; Kaltchev, D.; Katsouleas, T. C.; Kim, E.-S.; Machida, S.; Payet, J.; Sen, T.; Wei, J.; Zotter, B.,: **Accelerator Physics Code Web Repository.** In: Biscari, C. (Ed.): *Proceedings of 10th European Particle Accelerator Conference, Edinburgh, 2006,*, 2254p.

044 Zimmermann, H. Z.; Becker, R.; Kleinod, M. K.; Kester, O. K.*: **Charge Breeding Exploration with the MAXEBIS.** In: Biscari, C. (Ed.): *Proceedings of 10th European Particle Accelerator Conference, Edinburgh, 2006,*, 1702p.

Publications to the programme 'physics of hadrons and nuclei': experiments

Compiled by K. Große

1. Reviewed publications (WoS listed)

001 Abt, I.; Adams, M.; Agari, M.; Albrecht, H.; Aleksandrov, A.; Amaral, V.; Amorim, A.; Aplin, S. J.; Aushev, V.; Bagaturia, Y.; Balagurav, V.; Bargiotti, M.; Barsukova, O.; Bastos, J.; Batista, J.; Bauer, C.; Bauer, T. S.; Belkov, A.; Belkov, A.; Belotelov, I.; Bertin, A.; Bobchenko, B.; Bocker, M.; Bogatyrev, A.; Bohm, G.; Bräuer, M.; Bruinsma, M.; Bruschi, M.; Buchholz, P.; Buran, T.; Carvalho, J.; Conde, P.; Cruse, C.; Dam, M.; Danielsen, K. M.; Danilov, M.; De Castro, S.; Deppe, H.; Dong, X.; Dreis, H. B.; Egorytchev, V.; Ehret, K.; Eisele, F.; Emeliyanov, D.; Erhan, S.; Essenov, S.; Fabbri, L.; Faccioli, P.; Feuerstack-Raible, M.; Flammer, J.; Fominykh, B.; Funcke, M.; Garrido, L.; Gellrich, A.; Giacobbe, B.; Glass, J.; Goloubkov, D.; Golubkov, Y.; Golutvin, A.; Golutvin, I.; Gorbounov, I.; Gorisek, A.; Gouchtchine, I.; Goulart, D. C.; Gradl, S.; Gradl, W.; Grimaldi, F.; Guilitsky, Y.; Hansen, J. D.; Hernandez, J. M.; Hofmann, W.; Hohmann, M.; Hott, T.; Hulsbergen, W.; Husemann, U.; Igonkina, O.; Ispiryan, M.; Jagla, T.; Jiang, C.; Kapitza, H.; Karabekyan, S.; Karpenko, N.; Keller, S.; Kessler, J.; Khasanov, F.; Kiryushin, Y.; Kisel, I.; Klinkby, E.; Knöpfle, K. T.; Kolanoski, H.; Korpar, S.; Krauss, C.; Kreuzer, P.; Krizan, P.; Krucker, D.; Kupper, S.; Kvaratskheliia, T.; Lanyov, A.; Lau, K.; Lewendel, B.; Lohse, T.; Lomonosov, B.; Manner, R.; Mankel, R.; Masciocchi, S.; Massa, I.; Matchikhilian, I.; Medin, G.; Medinnis, M.; Mevius, M.; Michetti, A.; Mikhailov, Y.; Mizuk, R.; Muresan, R.; zur Nedden, M.; Negodaev, M.; Nörenberg, M.; Nowak, S.; de Vera, M. T. N. P.; Ouchrif, M.; Ould-Saada, F.; Padilla, C.; Peralta, D.; Pernack, R.; Pestotnik, R.; Petersen, B. A. A.; Piccinini, M.; Pleier, M. A.; Poli, M.; Popov, V.; Pose, D.; Prystupa, S.; Pugatch, V.; Pylypchenko, Y.; Pyrlik, J.; Reeves, K.; Reßing, D.; Rick, H.; Riu, I.; Robmann, P.; Rostovtseva, I.; Rybnikov, V.; Sanchez, E.; Sbrizzi, A.; Schmelling, M.; Schmidt, B.; Schreiner, A.; Schroder, H.; Schwanke, U.; Schwartz, A. J.; Schwarz, A. S.; Schwenninger, B.; Schwingenheuer, B.; Sciacca, F.; Semprini-Cesari, N.; Shuvalov, S.; Silva, L.; Sözüer, L.; Solunin, S.; Somov, A.; Somov, S.; Spengler, J.; Spighi, R.; Spiridonov, A.; Stanovnik, A.; Staric, M.; Stegmann, C.; Subramania, H. S.; Symalla, M.; Tikhomirov, I.; Titov, M.; Tsakov, I.; Uwer, U.; van Eldik, C.; Vassiliev, Y.; Villa, M.; Vitale, A.; Vukotic, I.; Wahlberg, H.; Walenta, A. H.; Walter, M.; Wang, J. J.; Wegener, D.; Werthenbach, U.; Wolters, H.; Wurth, R.; Wurz, A.; Zaitsev, Y.; Zavertyaev, M.; Zeuner, T.; Zhelezov, A.; Zheng, Z.; Zimmermann, R.; Zivko, T.; Zoccoli, A.; HERA-B Collaboration: **Polarization of Λ and $\bar{\Lambda}$ in 920 GeV fixed-target proton-nucleus collisions.** *Physics letters B* **638**(5): 415–421. DOI:10.1016/j.physletb.2006.05.040

002 Ackermann, D.*: **Superheavy elements - Synthesis, structure and reaction mechanism.** *International journal of modern physics E, Nuclear physics* **15**(7): 1577–1586. DOI:10.1142/S0218301306005150

003 Adamová, D.; Agakichiev, G.*; Antonczyk, D.; Appelshäuser, H.; Belaga, V.; Bielčiková, J.; Braun-Munzinger, P.*; Busch, O.*; Cherlin, A.; Damjanovic, S.; Dietel, T.; Dietrich, L.; Drees, A.; Esumi, S. I.; Filimonov, K.; Fomenko, K.; Fraenkel, Z.; Garabatos, C.*; Glässel, P.; Hering, G.*; Holeczek, J.*; Krobath, G.; Kushpil, V.; Ludolphs, W.; Maas, A.*; Marín, A.; Milošević, J.; Miśkowiec, D.*; Ortega, R.; Panebrattsev, Y.; Petchenova, O.; Petráček, V.; Radomski, S.*; Rak, J.*; Ravinovich, I.; Rehak, P.; Sako, H.*; Schmitz, W.; Schukraft, J.; Sedykh, S.*; Shimansky, S.; Stachel, J.; Šumbera, M.; Tilsner, H.; Tserruya, I.; Tsiledakis, G.; Wessels, J. P.; Wienold, T.; Wurm, J. P.; Yurevich, S.; Yurevich, V.: **Leptonic and charged kaon decay modes of the phi meson measured in heavy-ion collisions at the CERN super proton synchrotron.** *Physical review letters* **96**(15): 152301. DOI:10.1103/PhysRevLett.96.152301

004 Ageev, E. S.; Alexakhin, V. Y.; Alexandrov, Y.; Alexeev, G. D.; Amoroso, A.; Badelek, B.; Balestra, F.; Ball, J.; Baum, G.; Bedfer, Y.; Berglund, P.; Bernet, C.; Bertini, R.; Birsa, R.; Bisplinghoff, J.; Bordalo, P.; Bradamante, F.; Bravar, A.; Bressan, A.; Brona, G.; Burtin, E.; Bussa, M. P.; Bytchkov, V. N.; Cerini, L.; Chapiro, A.; Cicuttin, A.; Colantoni, M.; Colavita, A. A.; Costa, S.; Crespo, M. L.; Dalle Torre, S.; Dasgupta, S. S.; Dedek, N.; De Masi, R.; Denisov, O. Y.; Dhara, L.; Diaz, V.; Dinkelbach, A. M.; Dolgopolov, A. V.; Donskov, S. V.; Dorofeev, V. A.; Doshita, N.; Duic, V.; Dunnweber, W.; Ehlers, J.; Eversheim, P. D.; Eyrich, W.; Fabro, M.; Faessler, M.; Falaleev, V.; Fauland, P.; Ferrero, A.; Ferrero, L.; Finger, M.; Finger, M.; Fischer, H.; Franz, J.; Friedrich, J. M.; Frolov, V.; Garfagnini, R.; Gautheron, F.; Gavrichtchouk, O. P.; Gerassimov, S.; Geyer, R.; Giorgi, M.; Gobbo, B.; Goertz, S.; Gorin, A. M.; Grajek, O. A.; Grasso, A.; Grube, B.; Grunemaier, A.; Hannappel, J.; von Harrach, D.; Hasegawa, T.; Hedicke, S.; Heinsius, F. H.; Hermann, R.; Hess, C.; Hinterberger, F.; von Hodenberg, M.; Horikawa, N.; Horikawa, S.; d'Hose, N.; Ijaduola, R. B.; Ilgner, C.; Ioukaev, A. I.; Ishimoto, S.; Ivanov, O.; Iwata, T.; Jahn, R.; Janata, A.; Joosten, R.; Jouravlev, N. I.; Kabuss, E.; Kalinnikov, V.; Kang, D.; Karstens, F.; Kastaun, W.; Ketzer, B.; Khaustov, G. V.; Khokhlov, Y. A.; Khomutov, N. V.; Kisselev, Y.; Klein, F.; Koblitz, S.; Koivuniemi, J. H.; Kolosov, V. N.; Komissarov, E. V.; Kondo, K.; Konigsmann, K.; Konoplyannikov, A. K.; Konorov, I.; Konstantinov, V. F.; Korentchenko, A. S.; Korzenev, A.; Kotzinian, A. M.; Koutchinski, N. A.; Kowalik, K.; Kravchuk, N. P.; Krivokhizhin, G. V.; Kroumchtein, Z. V.; Kuhn, R.; Kunne, F.; Kurek, K.; Ladygin, M. E.; Lamanna, M.; Leberig, M.; Le Goff, J. M.; Lichtenstadt, J.; Liska, T.; Ludwig, I.; Maggiora, A.; Maggiora, M.; Magnon, A.; Mallot, G. K.; Manuilov, I. V.; Marchand, C.; Marroncle, J.; Martin, A.; Marzec, J.; Matsuda, T.; Maximov, A. N.; Medved, K. S.; Meyer, W.; Mielech, A.; Mikhailov, Y. V.; Moinester, M. A.; Nahle, O.; Nassalski, J.; Neliba, S.; Neyret, D. P.; Nikolaenko, V. I.; Nozdrin, A. A.; Obraztsov, V. F.; Olshevsky, A. G.; Ostrick, M.; Padee, A.; Pagano, P.; Panebianco, S.; Panzieri, D.; Paul, S.; Pereira, H. D.; Peshekhonov, D. V.; Peshekhonov, V. D.; Piragino, G.; Platchkov, S.; Platzer, K.; Pochodzalla, J.; Polyakov, V. A.; Popov, A. A.; Pretz, J.; Procureur, S.; Quintans, C.; Ramos, S.; Rebourgeard, P. C.; Reicherz, G.; Reymann, J.; Rith, K.; Rondio, E.; Rozhdestvensky,

A. M.; Sadovski, A. B.; Saller, E.; Samoylenko, V. D.; Sandacz, A.; Sans, M.; Sapozhnikov, M. G.; Savin, I. A.; Schiavon, P.; Schill, C.; Schmidt, T.; Schmitt, H.; Schmitt, L.; Shevchenko, O. Y.; Shishkin, A. A.; Siebert, H. W.; Sinha, L.; Sissakian, A. N.; Skachkova, A.; Slunecka, M.; Smirnov, G. I.; Sozzi, F.; Srnka, A.; Stinzing, F.; Stolarski, M.; Sugonyaev, V. P.; Sulc, M.; Sulej, R.; Takabayashi, N.; Tchalishev, V. V.; Tessarotto, F.; Teufel, A.; Thers, D.; Tkatchev, L. G.; Toeda, T.; Tretyak, V. I.; Trousov, S.; Varanda, M.; Virius, M.; Vlassov, N. V.; Wagner, M.; Webb, R.; Weise, E.; Weitzel, Q.; Wiedner, U.; Wiesmann, M.; Windmolders, R.; Wirth, S.; Wislicki, W.; Zanetti, A. M.; Zaremba, K.; Zhao, J.; Ziegler, R.; Zvyagin, A.; COMPASS Collaboration: **Gluon polarization in the nucleon from quasi-real photoproduction of high-** p_T **hadron pair.** *Physics letters B* **633**(1): 25–32. DOI:10.1016/j.physletb.2005.11.049

005 Alessandro, B.; Antinori, F.; Belikov, J. A.; Blume, C.; Dainese, A.; Foka, P.*; Giubellino, P.; Hippolyte, B.; Kuhn, C.; Martínez, G.; Monteno, M.; Morsch, A.; Nayak, T. K.; Nystrand, J.; López Noriega, M.; Paić, G.; Pluta, J.; Ramello, L.; Revol, J.-P.; Safarik, K.; Schukraft, J.; Schutz, Y.; Scomparin, E.; Snellings, R.; Baillie, O. V.; Vercellin, E.; ALICE Collaboration: **ALICE: Physics Performance Report, Volume II.** *Journal of physics G, Nuclear and particle physics* **32**(10): 1295–2040. DOI:10.1088/0954-3899/32/10/001

006 Alt, C.; Anticic, T.; Baatar, B.; Barna, D.; Bartke, J.; Betev, L.; Białkowska, H.; Blume, C.; Boimska, B.; Botje, M.; Bracinik, J.; Bramm, R.; Buncić, P.; Cerny, V.; Christakoglou, P.; Chvala, O.; Cramer, J. G.; Csató, P.; Dinkelaker, P.; Eckardt, V.; Flierl, D.; Fodor, Z.; Foka, P.*; Friese, V.*; Gal, J.; Gazdzicki, M.; Genchev, V.; Georgopoulos, G.; Gładysz, E.; Grebieszkow, K.; Hegyi, S.; Höhne, C.*; Kadija, K.; Karev, A.; Kliemant, M.; Kniege, S.; Kolesnikov, V. I.; Kornas, E.; Korus, R.; Kowalski, M.; Kraus, I.*; Kreps, M.; van Leeuwen, M.; Levai, P.; Litov, L.; Lungwitz, B.; Makariev, M.; Malakhov, A. I.; Markert, C.*; Mateev, M.; Melkumov, G. L.; Mischke, A.; Mitrovski, M.; Molnár, J.; Mrówczyński, S.; Nicolic, V.; Pálla, G.; Panagiotou, A. D.; Panayotov, D.; Petridis, A.; Pikna, M.; Prindle, D.; Pühlhofer, F.; Renfordt, R.; Roland, C.; Roland, G.; Rybczyński, M.; Rybicki, A.; Sandoval, A.*; Schmitz, N.; Schuster, T.; Seyboth, P.; Siklér, F.; Sitar, B.; Skrzypczak, E.; Stefanek, G.; Stock, R.; Ströbele, H.; Susa, T.; Szentpetéry, I.; Sziklai, J.; Szymanski, P.; Trubnikov, V.; Varga, D.; Vassiliou, M.; Veres, G. I.; Vesztergombi, G.; Vranić, D.*; Wetzler, A.; Wlodarczyk, Z.; Yoo, I. K.; Zimányi, J.; NA49 Collaboration: **Upper limit of** D^0 **production in central Pb-Pb collisions at 158A GeV.** *Physical review C, Nuclear physics* **73**(3): 034910. DOI:10.1103/PhysRevC.73.034910

007 Alt, C.; Anticic, T.; Baatar, B.; Barna, D.; Bartke, J.; Betev, L.; Białkowska, H.; Blume, C.; Boimska, B.; Botje, M.; Bracinik, J.; Bramm, R.; Buncić, P.; Cerny, V.; Christakoglou, P.; Chvala, O.; Cramer, J. G.; Csató, P.; Dinkelaker, P.; Eckardt, V.; Flierl, D.; Fodor, Z.; Foka, P.*; Friese, V.*; Gál, J.; Gazdzicki, M.; Genchev, V.; Georgopoulos, G.; Gładysz, E.; Grebieszkow, K.; Hegyi, S.; Höhne, C.*; Kadija, K.; Karev, A.; Kliemant, M.; Kniege, S.; Kolesnikov, V. I.; Kornas, E.; Korus, R.; Kowalski, M.; Kraus, I.*; Kreps, M.; Laslo, A.; van Leeuwen, M.; Lévai, P.; Litov, L.; Lungwitz, B.; Makariev, M.; Malakhov, A. I.; Mateev, M.; Melkumov, G. L.; Mischke, A.; Mitrovski, M.; Molnár, J.; Mrówczyński, S.; Nicolic, V.; Pálla, G.; Panagiotou, A. D.; Panayotov, D.; Petridis, A.; Pikna, M.; Prindle, D.; Pühlhofer, F.; Renfordt, R.; Roland, C.; Roland, G.; Rybczyński, M.; Rybicki, A.; Sandoval, A.*; Schmitz, N.; Schuster, T.; Seyboth, P.; Siklér, F.; Sitar, B.; Skrzypczak, E.; Stefanek, G.; Stock, R.; Strabel, C.; Ströbele, H.; Susa, T.; Szentpetery, I.; Sziklai, J.; Szymanski, P.; Trubnikov, V.; Varga, D.; Vassiliou, M.; Veres, G. I.; Vesztergombi, G.; Vranić, D.*; Wetzler, A.; Wlodarczyk, Z.; Yoo, I. K.; Zimányi, J.; NA49 Collaboration: **Energy and centrality dependence of** $\bar{p}$ **and p production and the** $\bar{\Lambda}/\bar{p}$ **ratio in Pb + Pb collisions between 20A GeV and 158A GeV.** *Physical review C, Nuclear physics* **73**(4): 044910. DOI:10.1103/PhysRevC.73.044910

008 Alt, C.; Anticic, T.; Baatar, B.; Barna, D.; Bartke, J.; Betev, L.; Białkowska, H.; Blume, C.; Boimska, B.; Botje, M.; Bracinik, J.; Buncić, P.; Cerny, V.; Christakoglou, P.; Chvala, O.; Dinkelaker, P.; Dolejsi, J.; Eckardt, V.; Fischer, H. G.; Flierl, D.; Fodor, Z.; Foka, P.*; Friese, V.*; Gaździcki, M.; Grebieszkow, K.; Höhne, C.*; Kadija, K.; Karev, A.; Kliemant, M.; Kniege, S.; Kolesnikov, V. I.; Kornas, E.; Korus, R.; Kowalski, M.; Kraus, I.*; Kreps, M.; van Leeuwen, M.; Lungwitz, B.; Makariev, M.; Malakhov, A. I.; Mateev, M.; Melkumov, G. L.; Mitrovski, M.; Mrówczyński, S.; Pálla, G.; Panayotov, D.; Petridis, A.; Renfordt, R.; Rybczyński, M.; Rybicki, A.; Sandoval, A.*; Schmitz, N.; Schuster, T.; Seyboth, P.; Siklér, F.; Skrzypczak, E.; Stefanek, G.; Stock, R.; Strobele, H.; Susa, T.; Sziklai, J.; Szymanski, P.; Trubnikov, V.; Varga, D.; Vassiliou, M.; Veres, G. I.; Vesztergombi, G.; Vranić, D.*; Wenig, S.; Wetzler, A.; Włodarczyk, Z.; Yoo, I. K.; NA49 Collaboration: **Inclusive production of charged pions in p+p collisions at 158 GeV/c beam momentum.** *The European physical journal: C, Particles and fields* **45**(2): 343–381. DOI:10.1140/epjc/s2005-02391-9

009 Amsler, C.; Baker, C. A.; Barnette, B. M.; Batty, C. J.; Benayoun, M.; Blum, P.; Braune, K.; Bugg, D. V.; Crede, V.; Crowe, K. M.; Doser, M.; Dunnweber, W.; Engelhardt, D.; Faessler, M. A.; Haddock, R. P.; Heinsius, F. H.; Hessey, N. P.; Hidas, P.; Jamnik, D.; Kalinowsky, H.; Kammel, P.; Kisiel, J.; Klempt, E.; Koch, H.; Kortner, O.; Kunze, M.; Kurilla, U.; Landua, R.; Matthay, H.; Meyer, C. A.; Meyer-Wildhagen, E.; Ouared, R.; Peters, K.; Pick, B.; Ratajczak, M.; Regenfus, C.; Roethel, W.; Seth, K.; Strohbusch, U.; Suffert, M.; Thoma, U.; Uman, I.; Wallis-Plachner, S.; Walther, D.; Wiedner, U.; Zou, B. S.; Zupancic, C.; Crystal Barrel Collaboration: **Study of** $K\bar{K}$ **resonances in** $\bar{p}p \to K^+K^-\pi^0$ **at 900 MeV/***c* **and 1640 MeV/***c***.** *Physics letters B* **639**(3): 165–171. DOI:10.1016/j.physletb.2006.06.010

010 Andreyev, A. N.; Antalic, S.; Ackermann, D.*; Franchoo, S.; Heßberger, F. P.*; Hofmann, S.*; Huyse, M.; Kojouharov, I.; Kindler, B.*; Kuusiniemi, P.*; Lesher, S. R.; Lommel, B.*; Mann, R.*; Münzenberg, G.*; Nishio, K.*; Page, R. D.; Ressler, J. J.; Streicher, B.; Saro, S.; Sulignano, B.*; Van Duppen, P.; Wiseman, D. R.: α**-decay spectroscopy of the new isotope** ^{192}**At.** *Physical review C, Nuclear physics* **73**(2): 024317. DOI:10.1103/PhysRevC.73.024317

011 Andreyev, A. N.; Antalic, S.; Ackermann, D.*; Franchoo, S.; Heßberger, F. P.*; Hofmann, S.*; Huyse, M.; Kojouharov, I.; Kindler, B.*; Kuusiniemi, P.*; Lesher, S. R.; Lommel, B.*; Mann, R.*; Münzenberg, G.*; Nishio, K.*; Page, R. D.; Ressler, J. J.; Streicher, B.; Saro, S.; Sulignano, B.*; Van Duppen, P.; Wiseman, D.; Wyss, R.: α**-decay of the new isotope** ^{187}**Po: Probing prolate structures beyond the neutron mid-shell at N=104.** *Physical review C, Nuclear physics* **73**(4): 044324. DOI:10.1103/PhysRevC.73.044324

012 Andreyev, A. N.; Antalic, S.; Huyse, M.; Van Duppen, P.; Ackermann, D.*; Bianco, L.; Cullen, D. M.; Darby, I. G.; Franchoo, S.; Heinz, S.*; Heßberger, F. P.*; Hofmann, S.*; Kojouharov, I.*; Kindler, B.*; Leppänen, A. P.; Lommel, B.*; Mann, R.*; Münzenberg, G.*; Pakarinen, J.; Page, R. D.; Ressler, J. J.; Saro, S.; Streicher, B.; Sulignano, B.*; Thomson, J.; Wyss, R.: **α decay of the new isotopes ^{193,194}Rn.** *Physical review C, Nuclear physics* **74**(6): 064303. DOI:10.1103/PhysRevC.74.064303

013 Andronic, A.*; Appelshäuser, H.; Bailhache, R.*; Baumann, C.; Braun-Munzinger, P.*; Bucher, D.; Busch, O.*; Catanescu, V.; Chernenko, S.; Christakoglou, P.; Fateev, O.; Freuen, S.; Garabatos, C.*; Gottschlag, H.; Gunji, T.; Hamagaki, H.; Herrmann, N.; Hoppe, M.; Lindenstruth, V.; Lippmann, C.*; Morino, Y.; Panebratsev, Y.; Petridis, A.; Petrovici, M.; Rusanov, I.; Sandoval, A.*; Saito, S.; Schicker, R.; Soltveit, H. K.; Stachel, J.; Stelzer, H.*; Vassiliou, M.; Vulpescu, B.; Wessels, J. P.; Wilk, A.; Yurevich, V.; Zanevsky, Y.; ALICE Collaboration: **Transition radiation spectra of electrons from 1 to 10 GeV/c in regular and irregular radiators.** *Nuclear instruments & methods in physics research, Section A, Accelerators, spectrometers, detectors and associated equipment* **558**(2): 516–525. DOI:10.1016/j.nima.2005.12.188

014 Andronic, A.*; Braun-Munzinger, P.*; Redlich, K.*: **Statistical production of antikaon nuclear bound states in heavy ion collisions.** *Nuclear physics A, Nuclear and hadronic physics* **765**(1): 211–225. DOI:10.1016/j.nuclphysa.2005.10.006

015 Andronic, A.*; Braun-Munzinger, P.*; Stachel, J.: **Hadron production in central nucleus-nucleus collisions at chemical freeze-out.** *Nuclear physics A, Nuclear and hadronic physics* **772**(3): 167–199. DOI:10.1016/j.nuclphysa.2006.03.012

016 Andronic, A.*; Łukasik, J.*; Reisdorf, W.*; Trautmann, W.*: **Systematics of stopping and flow in Au plus Au collisions.** *The European physical journal A, Hadrons and nuclei* **30**(1): 31–46. DOI:10.1140/epja/i2006-10101-2

017 Antalic, S.; Streicher, B.; Hessberger, F. P.*; Hofmann, S.*; Ackerman, D.*; Saro, S.; Sulignano, B.: **Synthesis and properties of the heaviest elements.** *Acta physica Slovaca* **56**(2): 87–90.

018 Antonczyk, D.*; Baechler, J.; Bramm, R.*; Campagnolo, R.; Christiansen, P.; Frankenfeld, U.*; Gutierrez, C. G.; Ivanov, M.; Kowalski, M.; Musa, L.; Przybyla, A.; ALICE TPC Collaboration: **Performance studies with an ALICE TPC prototype.** *Nuclear instruments & methods in physics research, Section A, Accelerators, spectrometers, detectors and associated equipment* **565**(2): 551–560. DOI:10.1016/j.nima.2006.06.022

019 Antonczyk, D.*; CERES Collaboration: **Non-identical particle correlations in central Pb+Au collisions at 158 AGeV.** *Nukleonika* **51**: S47–S50.

020 Aubert, B. et. al. and the BARBAR Collaboration: **B meson decays to ωK^*, $\omega\rho$, $\omega\omega$, $\omega\phi$, and ωf_0.** *Physical Review D* **74**(5): 051102. DOI:10.1103/PhysRevD.74.051102

021 Aubert, B. et. al. and the BARBAR Collaboration: **Branching fraction limits for B^0 decays to $\eta'\eta, \eta'\pi^0$ and $\eta\pi^0$.** *Physical Review D* **73**(7): 071102. DOI:10.1103/PhysRevD.73.071102

022 Aubert, B. et. al. and the BARBAR Collaboration: **Branching fraction measurements of charged B decays to B decays to $K^{*+}K^+K^-$, $K^{*+}\pi^+K^-$, $K^{*+}K^+\pi^-$ and $K^{*+}\pi^+\pi^-$ final states.** *Physical Review D* **74**(5): 051104. DOI:10.1103/PhysRevD.74.051104

023 Aubert, B. et. al. and the BARBAR Collaboration: **Dalitz plot analysis of the decay $B^\pm \to K^\pm K^\pm K^\mp$.** *Physical Review D* **74**(3): 032003. DOI:10.1103/PhysRevD.74.032003

024 Aubert, B. et. al. and the BARBAR Collaboration: **Determinations of $|V(ub)|$ from inclusive semileptonic B decays with reduced model dependence.** *Physical review letters* **96**(22): 221801. DOI:10.1103/PhysRevLett.96.221801

025 Aubert, B. et. al. and the BARBAR Collaboration: **Measurement of $\bar{B^0} \to D^{(*)0}\bar{K}^{(*)0}$ branching fractions.** *Physical Review D* **74**(3): 031101. DOI:10.1103/PhysRevD.74.031101

026 Aubert, B. et. al. and the BARBAR Collaboration: **Measurement of branching fractions and CP-violating charge asymmetries for B meson decays to $D^{(*)}\bar{D^{(*)}}$, and implications for the CKM angle γD-*(D)over-bar(*), and implications for the Cabibbo-Kobayashi-Maskawa angle gamma.** *Physical Review D* **73**(11): 112004. DOI:10.1103/PhysRevD.73.112004

027 Aubert, B. et. al. and the BARBAR Collaboration: **Measurement of branching fractions and charge asymmetries in B decays to an η meson and a K^* meson.** *Physical review letters* **97**(20): 201802. DOI:10.1103/PhysRevLett.97.201802

028 Aubert, B. et. al. and the BARBAR Collaboration: **Measurement of branching fractions in radiative B decays to $\eta K\gamma$ and search for B decays to $\eta' K\gamma$.** *Physical Review D* **74**(3): 031102. DOI:10.1103/PhysRevD.74.031102

029 Aubert, B. et. al. and the BARBAR Collaboration: **Measurement of the η and η' transition form factors at q^2 = 112 GeV^2.** *Physical Review D* **74**(1): 012002. DOI:10.1103/PhysRevD.74.012002

030 Aubert, B. et. al. and the BARBAR Collaboration: **Measurement of the $B \to \pi\ell\nu$ branching fraction and determination of $|V_{ub}|$ with tagged B mesons.** *Physical review letters* **97**(21): 211801. DOI:10.1103/PhysRevLett.97.211801

031 Aubert, B. et. al. and the BARBAR Collaboration: **Measurement of the $D^+ \to \pi^+\pi^0$ and $D^+ \to K^+\pi^0$ branching fractions.** *Physical Review D* **74**(1): 011107. DOI:10.1103/PhysRevD.74.011107

032 Aubert, B. et. al. and the BARBAR Collaboration: **Measurement of the Spin of the Ω^- Hyperon.** *Physical review letters* **97**(11): 112001. DOI:10.1103/PhysRevLett.97.112001

033 Aubert, B. et. al. and the BARBAR Collaboration: **Measurement of the branching fraction and photon energy moments of $B \to X_s\gamma$ and $A(CP)(B \to X(s+d)\gamma)$.** *Physical review letters* **97**(17): 171803. DOI:10.1103/PhysRevLett.97.171803

034 Aubert, B. et. al. and the BARBAR Collaboration: **Measurement of the branching fraction and time-dependent CP asymmetry in the decay $B^0 \to D^{*+}D^{*-}K^0_{(S)}$.** *Physical Review D* **74**(9): 091101. DOI:10.1103/PhysRevD.74.091101

035 Aubert, B. et. al. and the BARBAR Collaboration: **Measurement of the ratio $B(B^+ \to Xe\nu)/B(B^0 \to Xe\nu)$.** *Physical Review D* **74**(9): 091105. DOI:10.1103/PhysRevD.74.091105

036 Aubert, B. et. al. and the BARBAR Collaboration: **Measurement of time-dependent CP asymmetries in $B^0 \to D^{(*)\pm}\pi^{\mp}$ and $B^0 \to D^{\pm}\rho^{\mp}$ decays.** *Physical Review D* **73**(11): 111101. DOI:10.1103/PhysRevD.73.111101

037 Aubert, B. et. al. and the BARBAR Collaboration: **Measurements of CP-violating asymmetries and branching fractions in B decays to ωK and $\omega\pi$.** *Physical Review D* **74**(1): 011106. DOI:10.1103/PhysRevD.74.011106

038 Aubert, B. et. al. and the BARBAR Collaboration: **Measurements of branching fractions, polarizations, and direct CP-violation asymmetries in $B \to \rho K^*$ and $B \to f_0(980)K^*$ decays.** *Physical review letters* **97**(20): 201801. DOI:10.1103/PhysRevLett.97.201801

039 Aubert, B. et. al. and the BARBAR Collaboration: **Measurements of branching fractions, rate asymmetries, and angular distributions in the rare decays $B \to K\ell^+\ell^-$ and $B \to K^*\ell^+\ell^-$.** *Physical Review D* **73**(9): 092001. DOI:10.1103/PhysRevD.73.092001

040 Aubert, B. et. al. and the BARBAR Collaboration: **Measurements of neutral B decay branching fractions to $K^0_S\pi^+\pi$ - final states and the charge asymmetry of $B^0 \to K^{*+}\pi-$.** *Physical Review D* **73**(3): 031101 Also part of: . DOI:10.1103/PhysRevD.73.031101

041 Aubert, B. et. al. and the BARBAR Collaboration: **Measurements of the $B \to D^*$ form factors using the decay $\bar{B}^0 \to D1*+e^-\bar{\nu}_e$.** *Physical Review D* **74**(9): 092004. DOI:10.1103/PhysRevD.74.092004

042 Aubert, B. et. al. and the BARBAR Collaboration: **Measurements of the branching fraction and time-dependent CP asymmetries of $B^0 \to J/\psi\pi^0$ decays.** *Physical Review D* **74**(1): 011101. DOI:10.1103/PhysRevD.74.011101

043 Aubert, B. et. al. and the BARBAR Collaboration: **Measurements of the decays $B^0 \to \bar{D}^0p\bar{p}$, $B^0 \to \bar{D^{*0}}p\bar{p}$, $B^0 \to D^-p\bar{p}\pi^+$, and $B^0 \to D^{*-}p\bar{p}\pi^+$.** *Physical Review D* **74**(5): 051101(R). DOI:10.1103/PhysRevD.74.051101

044 Aubert, B. et. al. and the BARBAR Collaboration: **Observation of $B^+ \to \bar{K^0}K^+$ and $B^0 \to K^0\bar{K^0}$.** *Physical review letters* **97**(17): 171805. DOI:10.1103/PhysRevLett.97.171805

045 Aubert, B. et. al. and the BARBAR Collaboration: **Observation of B^0 meson decay to $a_1(1260)^{\pm}\pi^{\mp}$.** *Physical review letters* **97**(5): 051802. DOI:10.1103/PhysRevLett.97.051802

046 Aubert, B. et. al. and the BARBAR Collaboration: **Observation of $\Upsilon(4S)$ decays to $\pi^+\pi^-\Upsilon(1S)$ and $\pi^+\pi^-\Upsilon(2S)$.** *Physical review letters* **96**(23): 232001. DOI:10.1103/PhysRevLett.96.232

047 Aubert, B. et. al. and the BARBAR Collaboration: **Observation of e^+e^- annihilations into the C = +1 hadronic final states $\rho^0\rho^0$ and $\phi\rho^0$.** *Physical review letters* **97**(11): 112002. DOI:10.1103/PhysRevLett.97.112002

048 Aubert, B. et. al. and the BARBAR Collaboration: **Precise branching ratio measurements of the decays $D^0 \to \pi^-\pi^+\pi^0$ and $D^0 \to K^-K^+\pi^0$.** *Physical Review D* **74**(9): 091102. DOI:10.1103/PhysRevD.74.091102

049 Aubert, B. et. al. and the BARBAR Collaboration: **Search for $B^+ \to X(3872)K^+$, $X(3872) \to J/\psi\gamma$.** *Physical Review D* **74**(7): 071101. DOI:10.1103/PhysRevD.74.071101

050 Aubert, B. et. al. and the BARBAR Collaboration: **Search for $B^+ \to \phi\pi^+$ and $B^0 \to \phi\pi^0$ decays.** *Physical Review D* **74**(1): 011102. DOI:10.1103/PhysRevD.74.011102

051 Aubert, B. et. al. and the BARBAR Collaboration: **Search for T, CP and CPT violation in B^0 $\bar{B}^0$ mixing with inclusive dilepton events.** *Physical review letters* **96**(25): 251802. DOI:10.1103/PhysRevLett.96.251802

052 Aubert, B. et. al. and the BARBAR Collaboration: **Search for B meson decays to $\eta'\eta^-$.** *Physical Review D* **74**(3): 031105. DOI:10.1103/PhysRevD.74.031105

053 Aubert, B. et. al. and the BARBAR Collaboration: **Search for doubly charmed baryons Ξ_{cc}^+ and Ξ_{cc}^{++} in BARBAR.** *Physical Review D* **74**(1): 011103. DOI:10.1103/PhysRevD.74.011103

054 Aubert, B. et. al. and the BARBAR Collaboration: **Search for the charmed pentaquark candidate $\Theta_c(3100)^0$ in e^+e^- annihilations at $\sqrt{s}$ = 10.58 GeV.** *Physical Review D* **73**(9): 091101. DOI:10.1103/PhysRevD.73.091101

055 Aubert, B. et. al. and the BARBAR Collaboration: **Search for the decay $B^0 \to K^0_{(S)}K^0_{(S)}K^0_{(L)}$.** *Physical Review D* **74**(3): 032005. DOI:10.1103/PhysRevD.74.032005

056 Aubert, B. et. al. and the BARBAR Collaboration: **Search for the decay $B^0 \to a_1^{\pm}\rho^{\mp}$.** *Physical Review D* **74**(3): 031104. DOI:10.1103/PhysRevD.74.031104

057 Aubert, B. et. al. and the BARBAR Collaboration: **Search for the decay $\tau- \to 3\pi^-2\pi^+2\pi^0\nu_\tau$.** *Physical Review D* **73**(11): 112003. DOI:10.1103/PhysRevD.73.112003

058 Aubert, B. et. al. and the BARBAR Collaboration: **Search for the decay of a B^0 or $\bar{B}^0$ meson to $\bar{K}^{*0}K^0$ or $K^{*0}\bar{K}^0$.** *Physical Review D* **74**(7): 072008. DOI:10.1103/PhysRevD.74.072008

059 Aubert, B. et. al. and the BARBAR Collaboration: **Searches for B^0 decays to ηK^0, $\eta\eta$, $\eta'\eta'$, $\eta\phi$, and $\eta'\phi$.** *Physical Review D* **74**(5): 051106(R). DOI:10.1103/PhysRevD.74.051106

060 Aubert, B. et. al. and the BARBAR Collaboration: **Study of $B \to D^{(*)}D^{(*)}_{s(J)}$ decays and measurement of D_s^- and $D_{sJ}(2460)^-$ branching fractions.** *Physical Review D* **74**(3): 031103. DOI:10.103/PhysRevD.74.031103

061 Aubert, B. et. al. and the BARBAR Collaboration: **Study of the $D^*_{sJ}(2317)^+$ and $D_{sJ}(2460)^+$ mesons in inclusive $c\bar{c}$ production near $\sqrt{s}$ = 10.6 GeV.** *Physical Review D* **74**(3): 032007. DOI:10.1103/PhysRevD.74.032007

062 Aubert, B. et. al. and the BARBAR Collaboration: **Study of the decay $\bar{B}^0 \to D^{*+}\omega\pi^-$.** *Physical Review D* **74**(1): 012001.

DOI:10.1103/PhysRevD.74.012001

063 Aubert, B. et. al. and the BARBAR Collaboration: **The $e^+e^- \to 33(\pi^+\pi^-), 2(\pi^+\pi^-\pi^0)$ and $K^+K^-2(\pi^+pi^-)$ cross sections at center-of-mass energies from production threshold to 4.5 GeV measured with initial-state radiation.** *Physical Review D* **73**(5): 052003. DOI:10.1103/PhysRevD.73.052003

064 Audouin, L.; Tassan-Got, L.; Armbruster, P.*; Benlliure, J.; Bernas, M.; Boudard, A.; Casarejos, E.; Czajkowski, S.; Enqvist, T.*; Fernández-Domínguez, B.; Jurado, B.*; Legrain, R.; Leray, S.; Mustapha, B.; Pereira, J.; Pravikoff, M.; Rejmund, F.; Ricciardi, M.-N.*; Schmidt, K.-H.*; Stéphan, C.; Taieb, J.*; Volant, C.; Wlazło, W.: **Evaporation residues produced in spallation of ^{208}Pb by protons at 500 A MeV.** *Nuclear physics A, Nuclear and hadronic physics* **768**(1): 1–21. DOI:10.1016/j.nuclphysa.2006.01.006

065 Bacca, S.*; Feldmeier, H.*: **Resonant tunneling in a schematic model.** *Physical review C, Nuclear physics* **73**(5): 054608. DOI:10.1103/PhysRevC.73.054608

066 Bailhache, R.*; Lippmann, C.*; ALICE TRD Collaboration: **New test beam results with prototypes of the ALICE TRD.** *Nuclear instruments & methods in physics research, Section A, Accelerators, spectrometers, detectors and associated equipment* **563**(2): 310–313. DOI:10.1016/j.nima.2006.02.157

067 Barbieri, C.*: **Single particle spectra based on modem effective interactions.** *Physics letters B* **643**(5): 268–272. DOI:10.1016/j.physletb.2006.10.054

068 Bastin, J. E.; Herzberg, R. D.; Butler, P. A.; Jones, G. D.; Page, R. D.; Jenkins, D. G.; Amzal, N.; Brew, P. M. T.; Hammond, N. J.; Humphreys, R. D.; Ikin, P. J. C.; Page, T.; Greenlees, P. T.; Jones, P. M.; Julin, R.; Juutinen, S.; Kankaanpää, H.; Keenan, A.; Kettunen, H.; Kuusiniemi, P.; Leino, M.; Leppänen, A. P.; Muikku, M.; Nieminen, P.; Rahkila, P.; Scholey, C.; Uusitalo, J.; Bouchez, E.; Chatillon, A.; Hurstel, A.; Korten, W.; Le Coz, Y.; Theisen, C.; Ackermann, D.*; Gerl, J.*; Helariutta, K.*; Hessberger, F. P.*; Schlegel, C.*; Wollerscheim, H. J.*; Lach, M.; Maj, A.; Meczynski, W.; Styczen, J.; Khoo, T. L.; Lister, C. J.; Afanasjev, A. V.; Maier, H. J.; Reiter, P.; Bednarczyc, P.; Eskola, K.; Hauschild, K.: **In-beam gamma ray and conversion electron study of ^{250}Fm.** *Physical review C, Nuclear physics* **73**(2): 024308. DOI:10.1103/PhysRevC.73.024308

069 Batist, L.; Blazhev, A.*; Döring, J.; Grawe, H.*; Kavatsyuk, M.*; Kavatsyuk, O.*; Kirchner, R.*; La Commara, M.; Mazzocchi, C.*; Mukha, I.*; Plettner, C.*; Roeckl, E.*; Romoli, M.: **Beta decay of Pd-94 and of the 71 s isomer of Rh-94.** *The European physical journal A, Hadrons and nuclei* **29**(2): 175–182. DOI:10.1140/epja/i2006-10074-0

070 Benlliure, J.; Casarejos, E.; Pereira, J.; Schmidt, K.-H.*: **Transient and quasistationary dissipative effects in the fission flux across the barrier in 1A (GeVU)-^{238}U on deuterium reactions.** *Physical review C, Nuclear physics* **74**(1): 014609. DOI:10.1103/PhysRevC.74.014609

071 Berdermann, J.; Blaschke, D.*; Grigorian, H.; Voskresensky, D. N.*: **Asymmetric neutrino propagation in newly born magnetized strange stars; GRB and kicks.** *Progress in particle and nuclear physics* **57**(1): 334–342. DOI:10.1016/j.ppnp.2006.01.009

072 Bernas, M.; Armbruster, P.*; Benlliure, J.*; Boudard, A.; Casarejos, E.; Enqvist, T.; Kelic, A.; Legrain, R.; Leray, S.; Pereira, J.; Rejmund, F.*; Ricciardi, M.-V.*; Schmidt, K.-H.*; Stephan, C.*; Taieb, J.*; Tassan-Got, L.; Volant, C.: **Very heavy fission fragments produced in the spallation reaction U-238+p at 1 A GeV.** *Nuclear physics A, Nuclear and hadronic physics* **765**(1): 197–210. DOI:10.1016/j.nuclphysa.2005.10.009

073 Blaschke, D.*; Voskresensky, D.*; Grigorian, H.: **Cooling of neutron stars with color superconducting quark cores.** *Nuclear physics A, Nuclear and hadronic physics* **774**: 815–818. DOI:10.1016/j.nuclphysa.2006.06.142

074 Botvina, A. S.*; Buyukcizmeci, N.; Erdogan, M.; Łukasik, J.*; Mishustin, I. N.; Ogul, R.*; Trautmann, W.*: **Modification of surface energy in nuclear multifragmentation.** *Physical review C, Nuclear physics* **74**(4): 044609. DOI:10.1103/PhysRevC.74.044609

075 Casarejos, E.; Benlliure, J.; Pereira, J.; Armbruster, P.*; Bernas, M.; Boudard, A.; Czajkowski, S.; Enqvist, T.*; Legrain, R.; Leray, S.; Mustapha, B.; Pravikoff, M.; Rejmund, F.; Schmidt, K.-H.*; Stephan, C.; Taieb, J.; Tassan-Got, L.; Volant, C.; Wlazlo, W.: **Isotopic production cross sections of spallation-evaporation residues from reactions of ^{238}U(1A GeV) with deuterium.** *Physical review C, Nuclear physics* **74**(4): 044612. DOI:10.1103/PhysRevC.74.044612

076 Cassing, W.; Kant, M.; Langanke, K.*; Vogel, P.: **Transport study of charged current interactions in neutrino-nucleus reactions.** *Physics letters B* **639**(1): 32–37. DOI:10.1016/j.physletb.2006.03.074

077 Cleymans, J.; Kraus, I.; Oeschler, H.; Redlich, K.; Wheaton, S.: **Statistical model predictions for particle ratios at $\sqrt{s_{NN}}$=5.5 TeV.** *Physical review C, Nuclear physics* **74**(3): 034903. DOI:10.1103/PhysRevC.74.034903

078 Cleymans, J.; Oeschler, H.; Redlich, K.; Wheaton, S.: **Comparison of chemical freeze-out criteria in heavy-ion collisions.** *Physical review C, Nuclear physics* **73**(3): 034905. DOI:10.1103/PhysRevC.73.034905

079 de Souza, R. T.; Le Neindre, N.; Pagano, A.; Schmidt, K.-H.*: **Detection.** *The European physical journal A, Hadrons and nuclei* **30**(1): 275–291. DOI:10.1140/epja/i2006-10123-8

080 Dobrovolsky, A. V.; Alkhazov, G. D.; Andronenko, M. N.; Bauchet, A.*; Egelhof, P.*; Fritz, S.*; Geissel, H.*; Gross, C.*; Khanzadeev, A. V.; Korolev, G. A.; Kraus, G.*; Lobodenko, A. A.; Münzenberg, G.*; Mutterer, M.; Neumaier, S. R.*; Schäfer, T.*; Scheidenberger, C.*; Seliverstov, D. M.; Timofeev, N. A.; Vorobyov, A. A.; Yatsoura, V. I.: **Study of the nuclear matter distribution in neutron-rich Li isotopes.** *Nuclear physics A, Nuclear and hadronic physics* **766**: 1–24. DOI:10.1016/j.nuclphysa.2005.11.016

081 Domingo-Pardo, C.; Abbondanno, U.; Aerts, G.; Alvarez-Pol, H.; Alvarez-Velarde, F.; Andriamonje, S.; Andrzejewski, J.; Assimakopoulos, P.; Audouin, L.; Badurek, G.; Baumann, P.; Becvar, F.; Berthoumieux, E.; Bisterzo, S.; Calvino, F.; Cano-Ott, D.; Capote, R.; Carrapico, C.; Cennini, P.; Chepel, V.; Chiaveri,

E.; Colonna, N.; Cortes, G.; Couture, A.; Cox, J.; Dahlfors, M.; David, S.; Dillman, I.; Dolfini, R.; Dridi, W.; Duran, I.; Eleftheriadis, C.; Embid-Segura, M.; Ferrant, L.; Ferrari, A.; Ferreira-Marques, R.; Fitzpatrick, L.; Frais-Koelbl, H.; Fujii, K.; Furman, W.; Gallino, R.; Goncalves, I.; Gonzalez-Romero, E.; Goverdovski, A.; Gramegna, F.; Griesmayer, E.; Guerrero, C.; Gunsing, F.; Haas, B.; Haight, R.; Heil, M.; Herrera-Martinez, A.; Igashira, M.; Isaev, S.; Jericha, E.; Kadi, Y.; Kappeler, F.; Karamanis, D.; Karadimos, D.; Kerveno, M.; Ketlerov, V.; Koehler, P.; Konovalov, V.; Kossionides, E.; Krticka, M.; Lamboudis, C.; Leeb, H.; Lindote, A.; Lopes, I.; Lozano, M.; Lukic, S.; Marganiec, J.; Marrone, S.; Mastinu, P.; Mengoni, A.; Milazzo, P. M.; Moreau, C.; Mosconi, M.; Neves, F.; Oberhummer, H.; Oshima, M.; O'Brien, S.; Pancin, J.; Papachristodoulou, C.; Papadopoulos, C.; Paradela, C.; Patronis, N.; Pavlik, A.; Pavlopoulos, P.; Perrot, L.; Plag, R.; Plompen, A.; Plukis, A.; Poch, A.; Pretel, C.; Quesada, J.; Rauscher, T.; Reifarth, R.; Rosetti, M.; Rubbia, C.; Rudolf, G.; Rullhusen, P.; Salgado, J.; Sarchiapone, L.; Savvidis, I.; Stephan, C.; Tagliente, G.; Tain, J. L.; Tassan-Got, L.; Tavora, L.; Terlizzi, R.; Vannini, G.; Vaz, P.; Ventura, A.; Villamarin, D.; Vincente, M. C.; Vlachoudis, V.; Vlastou, R.; Voss, F.; Walter, S.; Wendler, H.; Wiescher, M.; Wisshak, K.; nTOF Collaboration: **Resonance capture cross section of ^{207}Pb.** *Physical review C, Nuclear physics* **74**(5): 055802. DOI:10.1103/PhysRevC.74.055802

082 Domingo-Pardo, C.; Abbondanno, U.; Aerts, G.; Alvarez-Pol, H.; Alvarez-Velarde, F.; Andriamonje, S.; Andrzejewski, J.; Assimakopoulos, P.; Audouin, L.; Badurek, G.; Baumann, P.; Becvar, F.; Berthoumieux, E.; Calvino, F.; Cano-Ott, D.; Capote, R.; de Albornoz, A. C.; Cennini, P.; Chepel, V.; Chiaveri, E.; Colonna, N.; Cortes, G.; Couture, A.; Cox, J.; Dahlfors, M.; David, S.; Dillman, I.; Dolfini, R.; Dridi, W.; Duran, I.; Eleftheriadis, C.; Embid-Segura, M.; Ferrant, L.; Ferrari, A.; Ferreira-Marques, R.; Fitzpatrick, L.; Frais-Koelbl, H.; Fujii, K.; Furman, W.; Gallino, R.; Goncalves, I.; Gonzalez-Romero, E.; Goverdovski, A.; Gramegna, F.; Griesmayer, E.; Guerrero, C.; Gunsing, F.; Haas, B.; Haight, R.; Heil, M.; Herrera-Martinez, A.; Igashira, M.; Isaev, S.; Jericha, E.; Kadi, Y.; Kappeler, F.; Karamanis, D.; Karadimos, D.; Kerveno, M.; Ketlerov, V.; Koehler, P.; Konovalov, V.; Kossionides, E.; Krticka, M.; Lamboudis, C.; Leeb, H.; Lindote, A.; Lopes, I.; Lozano, M.; Lukic, S.; Marganiec, J.; Marques, L.; Marrone, S.; Mastinu, P.; Mengoni, A.; Milazzo, P. M.; Moreau, C.; Mosconi, M.; Neves, F.; Oberhummer, H.; Oshima, M.; O'Brien, S.; Pancin, J.; Papachristodoulou, C.; Papadopoulos, C.; Paradela, C.; Patronis, N.; Pavlik, A.; Pavlopoulos, P.; Perrot, L.; Plag, R.; Plompen, A.; Plukis, A.; Poch, A.; Pretel, C.; Quesada, J.; Rauscher, T.; Reifarth, R.; Rosetti, M.; Rubbia, C.; Rudolf, G.; Rullhusen, P.; Salgado, J.; Sarchiapone, L.; Savvidis, I.; Stephan, C.; Tagliente, G.; Tain, J. L.; Tassan-Got, L.; Tavora, L.; Terlizzi, R.; Vannini, G.; Vaz, P.; Ventura, A.; Villamarin, D.; Vincente, M. C.; Vlachoudis, V.; Vlastou, R.; Voss, F.; Walter, S.; Wendler, H.; Wiescher, M.; Wisshak, K.; nTOF Collaboration: **New measurement of neutron capture resonances in ^{209}Bi.** *Physical review C, Nuclear physics* **74**(2): 025807. DOI:10.1103/PhysRevC.74.025807

083 Ekstrom, A.; Cederkall, J.; Hurst, A.; Fahlander, C.; Banu, A.*; Butler, P.; Eberth, J.; Gorska, M.*; Habs, D.; Huyse, M.; Kester, O.; Niedermayer, O.; Nilsson, T.; Pantea, M.; Scheit, H.; Schwalm, D.; Sletten, G.; Ushasi, D. P.; van Duppen, P.; Warr, N.; Weisshaar, D.; IS418 REX-ISOLDE ISOLDE Collaboration: **Coulomb excitation of ^{110}Sn using REX-ISOLDE.** *Physica scripta* **T125**: 190–191. DOI:10.1088/0031-8949/2006/T125/045 Also part of: 'Large-scale facilities for research with photons, neutrons and ions'.

084 Fettouhi, A.; Geissel, H.*; Schinner, A.; Sigmund, P.: **Stopping of high-Z ions at intermediate velocities.** *Nuclear instruments & methods in physics research, Section B, Beam interactions with materials and atoms* **245**(1): 22–27. DOI:10.1016/j.nimb.2005.11.058

085 Fettouhi, A.*; Weick, H.*; Portillo, M.*; Becker, F.*; Boutin, D.*; Geissel, H.*; Knöbel, R. K.; Kurcewicz, J.*; Kurcewicz, W.; Kurpeta, J.; Litvinov, Y.*; Livesay, R. J.; Morrissey, D. J.; Münzenberg, G.*; Nolen, J. A.; Ogawa, H.; Sakamoto, N.; Scheidenberger, C.*; Stadlmann, J.*; Winkler, M.*; Yao, N.: **Gas-solid effect in mean charge and slowing down of uranium ions at 60.2 and 200 MeV/u.** *Nuclear instruments & methods in physics research, Section B, Beam interactions with materials and atoms* **245**(1): 32–35. DOI:10.1016/j.nimb.2005.11.060

086 Fröhlich, C.; Hauser, P.; Liebendörfer, M.; Martinez-Pinedo, G.; Thielemann, F.-K.; Bravo, E.; Zinner, N. T.; Hix, W. R.; Langanke, K.*; Mezzacappa, A.; Nomoto, K.: **Composition of the innermost core-collapse supernova ejecta.** *The astrophysical journal : an internat. review of spectroscopy and astronomical physics: Part 1* **637**(1): 415–426.

087 Fröhlich, C.; Hix, W. R.; Martínez-Pinedo, G.*; Liebendörfer, M.; Thielemann, F. K.; Bravo, E.; Langanke, K.*; Zinner, N. T.: **Nucleosynthesis in neutrino-driven supernovae.** *New Astronomy Reviews* **50**(7): 496–499. DOI:10.1016/j.newar.2006.06.003

088 Frohlich, C.; Martínez-Pinedo, G.*; Liebendörfer, M.; Thielemann, F.-K.; Bravo, E.; Hix, W. R.; Langanke, K.*; Zinner, N. T.: **Neutrino-induced nucleosynthesis of $A > 64$ nuclei: The ν p process.** *Physical review letters* **96**(14): 142502. DOI:10.1103/PhysRevLett.96.142502

089 Gadea, A.; Lenzi, S. M.; Lunardi, S.; Marginean, N.; Zuker, A. P.; de Angelis, G.; Axiotis, M.; Martinez, T.; Napoli, D. R.; Farnea, E.; Menegazzo, R.; Pavan, P.; Ur, C. A.; Bazzacco, D.; Venturelli, R.; Kleinheinz, P.; Bednarczyk, P.; Curien, D.; Dorvaux, O.; Nyberg, J.; Grawe, H.*; Gorska, M.*; Palacz, M.; Lagergren, K.; Milechina, L.; Ekman, J.; Rudolph, D.; Andreoiu, C.; Bentley, M. A.; Gelletly, W.; Rubio, B.; Algora, A.; Nacher, E.; Caballero, L.; Trotta, M.; Moszyński, M.: **Observation of ^{54}Ni : Cross-conjugate symmetry in $_f7/2$ mirror energy differences.** *Physical review letters* **97**(15): 152501. DOI:10.1103/PhysRevLett.97.152501

090 Gazit, D.; Bacca, S.*; Barnea, N.; Leidemann, W.; Orlandini, G.: **Photoabsorption on ^{4}He with a realistic nuclear force.** *Physical review letters* **96**(11): 112301. DOI:10.1103/PhysRevLett.96.112301

091 Gazit, D.; Barnea, N.; Bacca, S.*; Leidemann, W.; Orlandini, G.: **Photonuclear sum rules and the tetrahedral configuration of ^{4}He.** *Physical review C, Nuclear physics* **74**(6): 061001. DOI:10.1103/PhysRevC.74.061001

092 Grigorenko, L. V.*; Langanke, K.*; Shul'gina, N. B.; Zhukov, M. V.: **Soft dipole mode in ^{17}Ne and the astrophysical $2p$ capture on ^{15}O.** *Physics letters B* **641**(3): 254–259.

DOI:10.1016/j.physletb.2006.08.054

093 Gulminelli, F.; Trautmann, W.*; Yennello, S. J.; Chomaz, P.: **Challenges in nuclear dynamics and thermodynamics.** *The European physical journal A, Hadrons and nuclei* **30**(1): 1–3. DOI:10.1140/epja/i2006-10128-3

094 Höhne, C.*; NA49 Collaboration: **Results from NA49.** *Nuclear physics A, Nuclear and hadronic physics* **774**: 35–42. DOI:10.1016/j.nuclphysa.2006.06.011

095 Höhne, C.*; Pühlhofer, E.; Stock, R.: **System-size dependence of strangeness production in high-energy A+A collisions and percolation of strings.** *Physics letters B* **640**(3): 96–100. DOI:10.1016/j.physletb.2006.07.042

096 Hartnack, C.; Oeschler, H.; Aichelin, J.: **Hadronic matter is soft.** *Physical review letters* **96**(1): 012303. DOI:10.1103/PhysRevLett.96.012302

097 Hartnack, C.; Oeschler, H.; Aichelin, J.: **Recent astrophysical and accelerator-based results on the hadronic equation of state.** *Journal of physics G, Nuclear and particle physics* **32**(12): S231–S239. DOI:10.1088/0954-3899/32/12/S29

098 Hayes, A. B.; Cline, D.; Wu, C. Y.; Ai, J.; Amro, H.; Beausang, C.; Casten, R. F.; Gerl, J.*; Hecht, A. A.; Heinz, A.; Hughes, R.; Janssens, R. V. F.; Lister, C. J.; Macchiavelli, A. O.; Meyer, D. A.; Moore, E. F.; Napiorkowski, P.; Pardo, R. C.; Schlegel, C.*; Seweryniak, D.; Simon, M. W.; Srebrny, J.; Teng, R.; Vetter, K.; Wollersheim, H. J.*: **Breakdown of K selection in Hf-178.** *Physical review letters* **96**(4): 042505. DOI:10.1103/PhysRevLett.96.042505

099 Herzberg, R. D.; Greenlees, P. T.; Butler, P. A.; Jones, G. D.; Darby, I. G.; Eeckhaudt, S.; Grahn, T.; Gray-Jones, C.; Hessberger, F. P.*; Jones, P.; Julin, R.; Juutinen, S.; Ketelhut, S.; Leino, M.; Leppänen, A.-P.; Moon, S.; Nyman, M.; Page, R. D.; Pakarinen, J.; Pritchard, A.; Rahkila, P.; Sandzelius, M.; Sarén, J.; Scholey, C.; Steer, A.; Uusitalo, J.; Venhart, M.: **Isomer spectroscopy in ^{254}No.** *Physica scripta* **T125**: 73–77. DOI:10.1088/0031-8949/2006/T125/016

100 Herzberg, R. D.; Greenlees, P. T.; Butler, P. A.; Jones, G. D.; Venhart, M.; Darby, I. G.; Eeckhaudt, S.; Eskola, K.; Grahn, T.; Gray-Jones, C.; Hessberger, F. P.*; Jones, P.; Julin, R.; Juutinen, S.; Ketelhut, S.; Korten, W.; Leino, M.; Leppänen, A. P.; Moon, S.; Nyman, M.; Page, R. D.; Pakarinen, J.; Pritchard, A.; Rahkila, P.; Saren, J.; Scholey, C.; Steer, A.; Sun, Y.; Theisen, C.; Uusitalo, J.: **Nuclear isomers in superheavy elements as stepping stones towards the island of stability.** *Nature* **442**(7105): 896–899. DOI:10.1038/nature05069

101 Heßberger, F. P.*: **GSI experiments on synthesis and nuclear structure investigations of heaviest nuclei.** *International journal of modern physics E, Nuclear physics* **15**(2): 284–291. DOI:10.1142/S0218301306004119

102 Heßberger, F. P.*; Hofmann, S.*; Ackermann, D.*; Antalic, S.*; Kindler, B.*; Kojouharov, I.*; Kuusiniemi, P.*; Leino, M.; Lommel, B.*; Mann, R.*; Nishio, K.; Popeko, A. G.; Sulignano, B.*; Saro, S.; Streicher, B.; Venhart, M.; Yeremin, A. V.: **Alpha-gamma decay studies of No-255.** *The European physical journal A, Hadrons and nuclei* **29**(2): 165–173. DOI:10.1140/epja/i2006-10083-y Also part of: 'Large-scale facilities for research with photons, neutrons and ions'.

103 Heßberger, F. P.*; Hofmann, S.*; Ackermann, D.*; Antalic, S.; Kindler, B.*; Kojouharov, I.*; Kuusiniemi, P.*; Leino, M.; Lommel, B.*; Mann, R.*; Nishio, K.; Popeko, A. G.; Sulignano, B.*; Saro, S.; Streicher, B.; Venhart, M.; Yeremin, A. V.: **Alpha-gamma decay studies of ^{255}Rf, ^{251}No and ^{247}Fm.** *The European physical journal A, Hadrons and nuclei* **30**(3): 561–569. DOI:10.1140/epja/i2006-10137-2

104 Hofmann, J.*; Lutz, M. F. M.*: **D-wave baryon resonances with charm from coupled-channel dynamics.** *Nuclear physics A, Nuclear and hadronic physics* **776**(1): 17–51. DOI:10.1016/j.nuclphysa.2006.07.004

105 Holzmann, R.*; HADES Collaboration: **Measurement of the di-electron mass spectrum in ^{12}C+^{12}C collisions at 2 AGeV by HADES.** *Nuclear physics A, Nuclear and hadronic physics* **774**: 727–730. DOI:10.1016/j.nuclphysa.2006.06.124

106 Ivanov, Y. B.*; Russkikh, V. N.*; Toneev, V. D.*: **Relativistic heavy-ion collisions within three-fluid hydrodynamics: Hadronic scenario.** *Physical review C, Nuclear physics* **73**(4): 044904. DOI:10.1103/PhysRevC.73.044904

107 Jenkins, D. G.; Meadowcroft, A.; Lister, C. J.; Carpenter, M. P.; Chowdhury, P.; Hammond, N. J.; Janssens, R. V. F.; Khoo, T. L.; Lauritsen, T.; Seweryniak, D.; Davinson, T.; Woods, P. J.; Jokinen, A.; Penttila, H.; Martinez-Pinedo, G.; Jose, J.: **Reevaluation of the ^{30}P(p,γ)^{31}S astrophysical reaction rate from a study of the T=1/2 mirror nuclei, ^{31}S and ^{31}P.** *Physical review C, Nuclear physics* **73**(6): 065802. DOI:10.1103/PhysRevC.73.065802

108 Kavatsyuk, M.*; Batist, L.; Becker, F.*; Blazhev, A.*; Brüchle, W.*; Döring, J.*; Faestermann, T.; Gorska, M.*; Grawe, H.*; Janas, Z.; Jungclaus, A.; Karny, M.; Kavatsyuk, O.; Kirchner, R.; La Commara, M.; Mandal, S.*; Mazzocchi, C.*; Mukha, I.*; Muralithar, S.*; Plettner, C.*; Płochocki, A.; Roeckl, E.*; Romoli, M.; Schädel, M.*; Zylicz, J.: **Gamow-Teller beta decay of ^{105}Sn.** *The European physical journal A, Hadrons and nuclei* **29**(2): 183–188. DOI:10.1140/epja/i2006-10077-9

109 Kavatsyuk, M.*; Batist, L.; Karny, M.; Roeckl, E.*: **Decay Q-value of ^{105}Sn and of other nuclei near ^{100}Sn, measured at the GSI on-line mass separator.** *International Journal of Mass Spectrometry* **251**(2): 138–145. DOI:10.1016/j.ijms.2006.01.023

110 Kelic, A.*; Natowitz, J. B.; Schmidt, K.-H.*: **Nuclear thermometry.** *The European physical journal A, Hadrons and nuclei* **30**(1): 203–213. DOI:10.1140/epja/i2006-10117-6

111 Kelic, A.*; Schmidt, K.-H.*: **Assessment of saddle-point-mass predictions for astrophysical applications.** *Physics letters B* **634**(4): 362–367. DOI:10.1016/j.physletb.2006.02.010

112 Kindler, B.*; Ackermann, D.*; Hartmann, W.*; Heßberger, F. P.*; Hofmann, S.*; Lommel, B.*; Mann, R.*; Steiner, J.*: **Chemical compound targets for SHIP on heated carbon backings.** *Nuclear instruments & methods in physics research, Section A, Accelerators, spectrometers, detectors and associated equipment* **561**(1): 107–111. DOI:10.1016/j.nima.2005.12.232

113 Klähn, T.; Blaschke, D.*; Typel, S.*; van Dalen, E. N. E.; Faessler, A.; Fuchs, C.; Gaitanos, T.; Grigorian, H.; Ho, A.; Kolomeitsev, E. E.; Miller, M. C.; Ropke, G.; Truemper, J.; Voskresensky, D. N.*; Weber, F.; Wolter, H. H.: **Constraints on the high-density nuclear equation of state from the phenomenology of compact stars and heavy-ion collisions.** *Physical review C, Nuclear physics* **74**(3): 035802. DOI:10.1103/PhysRevC.74.035802

114 Kraft-Bermuth, S.*; Bleile, A.*; Egelhof, P.*; Ilieva, S.*; Kiseleva, A.*; Kiselev, O.*; Meier, J. P.*: **Development of an array of calorimetric low-temperature detectors for heavy ion physics.** *Nuclear instruments & methods in physics research, Section A, Accelerators, spectrometers, detectors and associated equipment* **559**(2): 519–521. DOI:10.1016/j.nima.2005.12.044

115 Kurcewicz, J.; Liu, Z.; Pfützner, M.; Woods, P. J.; Mazzocchi, C.*; Schmidt, K.-H.*; Kelić, A.*; Attallah, F.*; Badura, E.*; Davids, C. N.; Davinson, T.; Doring, J.; Geissel, H.; Gorska, M.; Grzywacz, R.; Hellström, M.*; Janas, Z.; Karny, M.; Korgul, A.; Mukha, I.*; Plettner, C.*; Robinson, A.; Roeckl, E.*; Rykaczewski, K.; Schmidt, K.; Seweryniak, D.; Sümmerer, K.*; Weick, H.*: **Production cross-sections of protactinium and thorium isotopes produced in fragmentation of ^{238}U at 1A GeV.** *Nuclear physics A, Nuclear and hadronic physics* **767**: 1–12. DOI:10.1016/j.nuclphysa.2005.12.008

116 Kuusiniemi, P.*; Heßberger, P.*; Ackermann, D.*; Antalic, S.*; Hofmann, S.*; Nishio, K.*; Sulignano, B.*; Kojouharov, I.*; Mann, R.*: **Studies of ^{213g,m}Ra and ^{214g,m} Ra by α and γ decay.** *The European physical journal A, Hadrons and nuclei* **30**(3): 551–559. DOI:10.1140/epja/i2006-10148-y

117 Langanke, K.*: **Neutrino-nucleus reactions in core-collapse supernovae.** *Progress in particle and nuclear physics* **57**(1): 324–333. DOI:10.1016/j.ppnp.2005.11.027

118 Langanke, K.*: **Shell model Monte Carlo studies of pairing correlations and level densities in medium-mass nuclei.** *Nuclear physics A, Nuclear and hadronic physics* **778**(3): 233–246. DOI:10.1016/j.nuclphysa.2006.08.005

119 Langanke, K.*: **Shell model and supernovae.** *Physica scripta* **T125**: 26–30. DOI:10.1088/0031-8949/2006/T125/006

120 Langanke, K.*; Thielemann, F.-K.; Wiescher, M.: **Special issue on nuclear astrophysics - Foreword.** *Nuclear physics A, Nuclear and hadronic physics* **777**: XIII–XV. DOI:10.1016/S0375-9474(06)00612-9

121 Laszlo, A.; Schuster, T.; NA49 Collaboration: **High P_T spectra of identified particles produced in Pb plus Pb collisions at 158 GeV/nucleon beam energy.** *Nuclear physics A, Nuclear and hadronic physics* **774**: 473–476. DOI:10.1016/j.nuclphysa.2006.06.068

122 Le Gentil, E.; Böhmer, M.; Lafriakh, A.; Pietri, S.; Aumann, T.*; Bacri, C. O.; Benlliure, J.; Boudard, A.; Casarejos, E.; Combet, M.; Ducret, J.-E.; Fernandez-Ordonez, M.; Gernhäuser, R.; Johansson, H.*; Kelić, A.*; Kezzar, K.; Krücken, R.; Kurtukian-Nieto, T.; Le Fèvre, A.*; Leray, S.; Lukasik, J.*; Müller, W. F. J.*; Rejmund, F.; Schwarz, C.*; Sfienti, C.*; Simon, H.; Trautmann, W.*; Volant, C.; Yordanov, O.*: **Exclusive measurements on ^{56}Fe+p at 1 A Gev with the SPALADIN setup at GSI.** *Nuclear instruments & methods in physics research, Section A, Accelerators, spectrometers, detectors and associated equipment* **562**(2): 743–746. DOI:10.1016/j.nima.2006.02.037

123 Leppänen, A.-P.; Uusitalo, J.; Greenlees, P. T.; Herzberg, R.-D.; Amzal, N.; Becker, F.; Butler, P. A.; Chewter, A. J. C.; Cocks, J. F. C.; Dorvaux, O.; Eeckhaudt, S.; Eskola, K.; Gerl, J.*; Grahn, T.; Hammond, N. J.; Hauschild, K.; Helariutta, K.; Heßberger, F. P.*; Houry, M.; Jones, G. D.; Jones, P. M.; Julin, R.; Juutinen, S.; Kankaanpää, H.; Kettunen, H.; Khoo, T. L.; Korten, W.; Kuusiniemi, P.; Le Coz, Y.; Leino, M.; Lister, C. J.; Lucas, R.; Muikku, M.; Nieminen, P.; Nyman, M.; Page, R. D.; Pakarinen, J.; Rahkila, P.; Reiter, P.; Sarén, J.; Schlegel, C.*; Scholey, C.; Stezowski, O.; Theisen, C.; Trzaska, W. H.; Wollersheim, H. J.*: **Recoil-fission tagging of the transfermium nucleus ^{252}No.** *The European physical journal A, Hadrons and nuclei* **28**(3): 301–306. DOI:10.1140/epja/i2006-10056-2

124 Lippmann, C.*; Riegler, W.; Kalweit, A.: **Rate effects in resistive plate chambers.** *Nuclear Physics B - Proceedings Supplements* **158**: 127–130. DOI:10.1016/j.nuclphysbps.2006.07.037

125 Lommel, B.*; Hartmann, W.*; Kindler, B.*; Steiner, J.*: **Conversion of isotopic material from metal to compound and vice versa.** *Nuclear instruments & methods in physics research, Section A, Accelerators, spectrometers, detectors and associated equipment* **561**(1): 100–103. DOI:10.1016/j.nima.2005.12.230

126 Lozeva, R.*; Gerl, J.*; Górska, M.*; Kojouharov, I.*; Mandal, S.*; Wollersheim, H.-J.*; Balabanski, D.; Becker, F.*; Grebosz, J.*; Banu, A.*; Bednarczyk, P.*; Doornenbal, P.*; Schaffner, H.*: **A novel Calorimeter Telescope for identification of relativistic heavy-ion reaction channels.** *Nuclear instruments & methods in physics research, Section A, Accelerators, spectrometers, detectors and associated equipment* **562**(1): 298–305. DOI:10.1016/j.nima.2006.02.163

127 Lukić, S.*; Gevaert, F.*; Kelić, A.*; Ricciardi, M. V.*; Schmidt, K.-H.*; Yordanov, O.*: **Systematic comparison of ISOLDE-SC yields with calculated in-target production rates.** *Nuclear instruments & methods in physics research, Section A, Accelerators, spectrometers, detectors and associated equipment* **565**(2): 784–800. DOI:10.1016/j.nima.2006.04.082

128 Lutz, M. F. M.*; Hofmann, J.*: **Dynamically generated hidden-charm Baryon resonances.** *International Journal of Modern Physics A* **21**(27): 5496–5502. DOI:10.1142/S0217751X06034665

129 Lutz, M. F. M.*; Korpa, C. L.: **Open-charm systems in cold nuclear matter.** *Physics letters B* **633**(1): 43–48. DOI:10.1016/j.physletb.2005.11.046

130 Lutz, M. F. M.*; Soyeur, M.: **Study of the η N scattering amplitude through the associated photoproduction of ϕ- and η-mesons in the region of the N*(1535) resonance.** *Nuclear physics A, Nuclear and hadronic physics* **773**(3): 239–249.

131 Lutz, M. F. M.*; Wolf, G.; Friman, B.: **Erratum: Scattering of vector mesons off nucleons (vol 706, pg 431, 2002).** *Nuclear physics A, Nuclear and hadronic physics* **765**(3): 495–495. DOI:10.1016/j.nuclphysa.2005.11.017

132 Martinez-Pinedo, G.; Liebendörfer, M.; Frekers,

D.: **Nuclear input for core-collapse models.** *Nuclear physics A, Nuclear and hadronic physics* **777**: 395–423. DOI:10.1016/j.nuclphysa.2006.02.014

133 Maruyama, T.; Tatsumi, T.; Voskresensky, D. N.*; Tanigawa, T.; Endo, T.; Chiba, S.: **Finite size effects on kaonic "pasta" structures.** *Physical review C, Nuclear physics* **73**(3): 035802. DOI:10.1103/PhysRevC.73.035802

134 Middleton, D. G.; Annand, J. R. M.; Barbieri, C.*; Barneo, P.; Blok, H. P.; Böhm, R.; Distler, M. O.; Friedrich, J.; Giusti, C.; Glazier, D. I.; Grabmayr, P.; Hehl, T.; Heim, J.; Hesselink, W. H. A.; Jans, E.; Kohl, M.; Lapikas, L.; MacGregor, I. J. D.; Martin, I.; McGeorge, J. C.; Merkel, H.; Moschini, F.; Rosner, G.; Seimetz, M.; de Vries, H.; Walcher, T.; Watts, D. P.; Zihlmann, B.: **First measurements of the ^{16}O(e, e'pn)^{14}N reaction.** *The European physical journal A, Hadrons and nuclei* **29**(3): 261–270. DOI:10.1140/epja/i2005-10314-9

135 Miśkowiec, D.*; CERES Collaboration: **Collection of CERES results.** *Nuclear physics A, Nuclear and hadronic physics* **774**: 43–50. DOI:10.1016/j.nuclphysa.2006.06.027

136 Mitrovski, M. K.; NA49 Collaboration: **Strangeness production at SPS energies from NA49.** *Journal of physics G, Nuclear and particle physics* **32**(12): S43–S50. DOI:10.1088/0954-3899/32/12/S05

137 Mukha, I.*; Roeckl, E.*; Batist, L.; Blazhev, A.; Döring, J.*; Grawe, H.*; Grigorenko, L.; Huyse, M.; Janas, Z.*; Kirchner, R.*; La Commara, M.; Mazzocchi, C.*; Tabor, S. L.; Van Duppen, P.: **Proton-proton correlations observed in two-proton radioactivity of ^{94}Ag.** *Nature* **439**(7074): 298–302. DOI:10.1038/nature04453

138 Nickel, D.; Alkofer, R.; Wambach, J.*: **Unlocking of color and flavor in color-superconducting quark matter.** *Physical Review D* **74**(11): 114015. DOI:10.1103/PhysRevD.74.114015

139 Nickel, D.; Wambach, J.*; Alkofer, R.: **Color superconductivity in the strong-coupling regime of Landau gauge QCD.** *Physical Review D* **73**(11): 114028. DOI:10.1103/PhysRevD.73.114028

140 Nickel, F.*; Behr, K.-H.*; Chulkov, L.; Geissel, H.*; Klemm, J.*; Klepper, O.; Marx, D.; Münzenberg/Munzenberg, G.; Pfeng, E.; Ruzicka, J.; Scheidenberger, C.*; Weick, H.*: **Change of the energy loss of relativistic heavy ions in a gadolinium target at and above the ferromagnetic Curie temperature.** *Nuclear instruments & methods in physics research, Section B, Beam interactions with materials and atoms* **243**(1): 103–108. DOI:10.1016/j.nimb.2005.07.225

141 Nishio, K.*; Hofmann, S.*; Heßberger, F. P.*; Ackermann, D.*; Antalic, S.; Comas, V. F.; Gan, Z.; Heinz, S.*; Heredia, J. A.; Ikezoe, H.; Khuyagbaatar, J.*; Kindler, B.*; Kojouharov, I.*; Kuusiniemi, P.; Lommel, B.*; Mann, R.*; Mazzocco, M.*; Mitsuoka, S.*; Nagame, Y.; Ohtsuki, T.; Popeko, A. G.; Saro, S.; Schött, H. J.*; Sulignano, B.*; Svirikhin, A.; Tsukada, K.; Tsuruta, K.; Yeremin, A. V.: **Measurement of evaporation residue cross-sections of the reaction ^{30}Si+^{238}U at subbarrier energies.** *The European physical journal A, Hadrons and nuclei* **29**(3): 281–287. DOI:10.1140/epja/i2006-10091-y

142 Özen, C.; Dean, D. J.: **Shell model Monte Carlo method in the pn-formalism and applications to the Zr and Mo isotopes.** *Physical review C, Nuclear physics* **73**(1): 014302. DOI:10.1103/PhysRevC.73.014302

143 Papakonstantinou, P.; Kosmas, T. S.; Wambach, J.; Faessler, A.: **Continuum random-phase approximation study of the incoherent mu(-)-e(-) conversion rate and its spurious 1(-) admixture.** *Physical review C, Nuclear physics* **73**(3): 035502. DOI:10.1103/PhysRevC.73.035502

144 Perru, O.; Sorlin, O.; Franchoo, S.; Azaiez, F.; Bouchez, E.; Bourgeois, C.; Chatillon, A.; Daugas, J. M.; Dlouhy, Z.; Dombradi, Z.; Donzaud, C.; Gaudefroy, L.; Grawe, H.*; Grevy, S.; Guillemaud-Mueller, D.; Hammache, F.; Ibrahim, F.; Le Coz, Y.; Lukyanov, S. M.; Matea, I.; Mrazek, J.; Nowacki, F.; Penionzhkevich, Y. E.; Santos, F. D.; Pougheon, F.; Saint-Laurent, M. G.; Sletten, G.; Stanoiu, M.; Stodel, C.; Theisen, C.; Verney, D.: **Enhanced core polarization in ^{70}Ni and ^{74}Zn.** *Physical review letters* **96**(23): 232501. DOI:10.1103/PhysRevLett.96.232501

145 Peters, K.*: **A primer on partial wave analysis.** *International Journal of Modern Physics* **21**(27): 5618–5624. DOI:10.1142/S0217751X06034811

146 Planeta, R.; Amorini, F.; Anzalone, A.; Auditore, L.; Baran, V.; Berceanu, I.; Blicharska, J.; Brzychczyk, J.; Borderie, B.; Bougault, R.; Bruno, M.; Cardella, G.; Cavallaro, S.; Chatterjee, M. B.; Chbihi, A.; Colonna, M.; D'Agostino, M.; DeFilippo, E.; Dayras, R.; DiToro, M.; Frankland, J.; Galichet, E.; Gawlikowicz, W.; Geraci, E.; Giustolisi, F.; Grzeszczuk, A.; Guazzoni, P.; Guinet, D.; Iacono-Manno, M.; Kowalski, S.; LaGuidara, E.; Lanzano, G.; Lanzalone, G.; Lukasik, J.; Maiolino, C.; Majka, Z.; LeNeindre, N.; Nicolis, N. G.; Pagano, A.; Papa, M.; Petrovici, M.; Piasecki, E.; Pirrone, S.; Politi, G.; Pop, A.; Porto, F.; Rivet, M. F.; Rosato, E.; Rizzo, F.; Russo, S.; Russotto, P.; Sassiv, M.; Schmidt, K.; Siwek-Wilczynska, K.; Skwira-Chalot, I.; Sochocka, A.; Sperduto, M. L.; Swiderski, L.; Trifiro, A.; Trimarchi, M.; Vannini, G.; Verde, G.; Vigilante, M.; Wieleczko, J. P.; Wilczynski, J.; Zetta, L.; Zipper, W.: **Isospin effects studied with the chimera detector at 35 MeV/nucleon.** *Acta physica Polonica B, Particle physics and field theory, nuclear physics, theory of relativity* **37**(1): 183–191. OPEN ACCESS.

147 Podolyák, Z.; Gerl, J.*; Hellström, M.*; Becker, F.*; Gladnishki, K. A.; Górska, M.*; Kelić, A.*; Kopatch, Y.*; Mandal, S.*; Regan, P. H.; Schmidt, K.-H.*; Walker, P. M.; Wollersheim, H. J.*; Banu, A.*; Benzoni, G.; Boardman, H.; Casarejos, E.; Ekman, J.; Geissel, H.*; Grawe, H.*; Hohn, D.; Kojouharov, I.*; Leske, J.; Lozeva, R.*; Mineva, M. N.; Neyens, G.; Page, R. D.; Pearson, C. J.; Portillo, M.*; Rudolph, D.; Saito, N.*; Schaffner, H.*; Sohler, D.; Sümmerer, K.*; Valiente-Dobón, J. J.; Wheldon, C.; Weick, H.*; Winkler, M.*: **High angular momentum states populated in fragmentation reactions.** *Physics letters B* **632**(2): 203–206. DOI:10.1016/j.physletb.2005.10.070

148 Przygoda, W.; Agakishiev, C.; Agodi, C.; Alvarez-Pol, H.; Balanda, A.; Bassini, R.; Bellia, G.; Belver, D.; Bielcik, J.*; Blanco, A.; Böhmer, M.; Boiano, C.; Bortolotti, A.; Boyard, J.; Brambilla, S.; Braun-Munzinger, P.*; Cabanelas, P.; Chernenko, S.; Christ, T.; Coniglione, R.; Dahlinger, M.*; Diaz, J.; Djeridi, R.; Dohrmann, F.; Duran, I.; Eberl, T.; Enghardt, W.; Fabbietti, L.; Fateev, O.; Finocchiaro, P.; Fonte, P.; Friese, J.; Fröhlich, I.;

Garzon, J.; Gernhäuser, R.; Golubeva, M.; Gonzalez-Diaz, D.; Grosse, E.; Guber, F.; Heinz, T.*; Hennino, T.; Hlavac, S.; Hoffmann, J.*; Holzmann, R.*; Ierusalimov, A.; Iori, I.; Ivashkin, A.; Jaskula, M.; Jurkovic, M.; Kajetanowicz, M.; Kämpfer, B.; Kanaki, K.; Karavicheva, T.; Kirschner, D.; König, I.*; König, W.*; Kolb, B.*; Kopf, U.*; Kotte, R.; Kotulic-Bunta, J.; Krücken, R.; Kugler, A.; Kühn, W.; Kulessa, R.; Lang, S.*; Lehnert, J.; Maier, L.; Maier-Komor, P.; Maiolino, C.; Marin, J.; Markert, J.; Metag, V.; Montes, N.; Moriniere, E.; Mousa, J.; Münch, M.*; Müntz, C.; Naumann, L.; Novotny, R.; Novotny, J.; Ott, W.*; Otwinowski, J.; Pachmayer, Y.; Perez, T.; Pechenov, V.; Pietraszko, J.*; Pinhao, J.; Pleskac, R.; Pospisil, V.; Pullia, A.; Rabin, N.; Ramstein, B.; Riboldi, S.; Ritman, J.; Rosier, P.; Roy-Stephan, M.; Rustamov, A.*; Sadovsky, A.; Sailer, B.; Salabura, P.; Sapienza, P.; Schmah, A.; Schön, W.*; Schroeder, C.*; Schwab, E.*; Senger, P.*; Simon, R.*; Smolyankin, V.; Smykov, L.; Spataro, S.; Spruck, B.; Ströbele, H.; Stroth, J.*; Sturm, C.*; Sudol, M.*; Tiflov, V.; Tlusty, P.; Toia, A.; Traxler, M.*; Tsertos, H.; Turzo, I.; Wagner, V.; Walus, W.; Willmott, C.; Winkler, S.; Wisniowski, M.; Wojcik, T.; Wüstenfeld, J.; Zanevsky, Y.; Zumbruch, P.*; HADES Collaboration: **HADES experiment: Di-lepton spectroscopy in p+p (2.2 GeV) and C+C (1 and 2 A GeV) collisions.** *Acta physica Polonica B, Particle physics and field theory, nuclear physics, theory of relativity* **37**(1): 139–151. OPEN ACCESS.

149 Redlich, K.; Friman, B.*; Sasaki, C.*: **Charge fluctuations along the QCD phase boundary.** *Journal of physics G, Nuclear and particle physics* **32**(12): S283–S291. DOI:10.1088/0954-3899/32/12/S35

150 Ricciardi, M. V.*; Armbruster, P.*; Benlliure, J.; Bernas, M.; Boudard, A.; Czajkowski, S.; Enqvist, T.; Kelić, A.*; Leray, S.; Legrain, R.; Mustapha, B.; Pereira, J.; Rejmund, F.*; Schmidt, K.-H.*; Stéphan, C.; Tassan-Got, L.; Volant, C.; Yordanov, O.*: **Light nuclides produced in the proton-induced spallation of ^{238}U at 1 GeV.** *Physical review C, Nuclear physics* **73**(1): 014607. DOI:10.1103/PhysRevC.73.014607

151 Roeckl, E.*: **One-proton and two-proton radioactivity of the (21^+) isomer in ^{94}Ag.** *International journal of modern physics E, Nuclear physics* **15**(2): 368–373. DOI:10.1142/S0218301306004223

152 Russkikh, V. N.*; Ivanov, Y. B.*: **Collective flow in heavy-ion collisions for E_{lab}=1-160 GeV/nucleon.** *Physical review C, Nuclear physics* **74**(3): 034904. DOI:10.1103/PhysRevC.74.034904

153 Schaefer, B. J.; Wagner, M.; Wambach, J.*; Kuo, T. T. S.; Brown, G. E.: **Low-momentum hyperon-nucleon interactions.** *Physical review C, Nuclear physics* **73**(1): 011001. DOI:10.1103/PhysRevC.73.011001

154 Schümann, F.; Typel, S.*; Hammache, F.*; Sümmerer, K.*; Uhlig, F.*; Böttcher, I.; Cortina, D.*; Förster, A.; Gai, M.; Geissel, H.*; Greife, U.; Grosse, E.; Iwasa, N.; Koczoń, P.; Kohlmeyer, B.; Kulessa, R.; Kumagai, H.; Kurz, N.*; Menzel, M.; Motobayashi, T.; Oeschler, H.; Ozawa, A.; Płoskon, M.; Prokopowicz, W.; Schwab, E.*; Senger, P.*; Strieder, F.; Sturm, C.*; Sun, Z. Y.*; Surówka, G.; Wagner, A.; Walús, W.: **Low-energy cross section of the ^{7}Be(p,γ) ^{8}B solar fusion reaction from the Coulomb dissociation of B-8.** *Physical review C, Nuclear physics* **73**(1): 015806. DOI:10.1103/PhysRevC.73.015806

155 Schüttauf, A.*; Hildenbrand, K. D.*; Ciobanu, M.*; Cordier, E.; Herrmann, N.; Kim, Y. J.*; Kis, M.*; Koczon, P.*; Leifels, Y.*; Petrovici, M.; Simion, V.: **Performance of the multistrip-MRPCs for FOPI.** *Nuclear Physics B - Proceedings Supplements* **158**: 52–55. DOI:10.1016/j.nuclphysbps.2006.07.033

156 Schuster, T.; Laszlo, A.; NA49 Collaboration: **High p_T spectra of identified particles produced in Pb+Pb collisions at 158 A GeV beam energy.** *Journal of physics G, Nuclear and particle physics* **32**(12): S479–S482. DOI:10.1088/0954-3899/32/12/S60

157 Semke, A.*; Lutz, M. F. M.*: **Baryon self energies in the chiral loop expansion.** *Nuclear physics A, Nuclear and hadronic physics* **778**(3): 153–180. DOI:10.1016/j.nuclphysa.2006.07.043

158 Seyboth, P.; Alt, C.; Anticic, T.; Baatar, B.; Barna, D.; Bartke, J.; Betev, L.; Bialkowska, H.; Blume, C.; Boimska, B.; Botje, M.; Bracinik, J.; Bramm, R.; Buncic, P.; Cerny, V.; Christakoglou, P.; Chung, P.; Chvala, O.; Cramer, J. G.; Csato, P.; Dinkelaker, P.; Eckardt, V.; Flierl, D.; Fodor, Z.; Foka, P.; Friese, V.; Gal, J.; Gazdzicki, M.; Genchev, V.; Georgopoulos, G.; Gladysz, E.; Grebieszkow, K.; Hegyi, S.; Höhne, C.*; Kadija, K.; Karev, A.; Kikola, D.; Kliemant, M.; Kniege, S.; Kolesnikov, V. I.; Kornas, E.; Korus, R.; Kowalski, M.; Kraus, I.*; Kreps, M.; Laszlo, A.; Lacey, R.; van Leeuwen, M.; Levai, P.; Litov, L.; Lungwitz, B.; Makariev, M.; Malakhov, A. I.; Mateev, M.; Melkumov, G. L.; Mischke, A.; Mitrovski, M.; Molnar, J.; Mrowczynski, S.; Nicolic, V.; Palla, G.; Panagiotou, A. D.; Panayotov, D.; Petridis, A.; Peryt, W.; Pikna, M.; Pluta, J.; Prindle, D.; Pühlhofer, F.; Renfordt, R.; Roland, C.; Roland, G.; Rybczynski, M.; Rybicki, A.; Sandoval, A.*; Schmitz, N.; Schuster, T.; Sikler, F.; Sitar, B.; Skrzypczak, E.; Slodkowski, M.; Stefanek, G.; Stock, R.; Strabel, C.; Ströbele, H.; Susa, T.; Szentpetery, I.; Sziklai, J.; Szuba, M.; Szymanski, P.; Trubnikov, V.; Varga, D.; Vassiliou, M.; Veres, G. I.; Vesztergombi, G.; Vranic, D.*; Wetzler, A.; Wlodarczyk, Z.; Yoo, I. K.; Zimanyi, J.: **Onset of deconfinement in Pb+Pb collisions at the CERN SPS.** *Acta physica Polonica B, Particle physics and field theory, nuclear physics, theory of relativity* **37**(12): 3429–3450. OPEN ACCESS.

159 Sfienti, C.*; Adrich, P.*; Aumann, T.*; Bacri, C. O.*; Barczyk, T.*; Bassini, R.*; Boiano, C.*; Botvina, A. S.*; Boudard, A.*; Brzychczyk, J.*; Chbihi, A.*; Cibor, J.*; Czech, B.*; De Napoli, M.*; Ducret, J.-E.*; Emling, H.*; Frankland, J.*; Hellström, M.*; Henzlova, D.*; Kezzar, K.*; Imme, G.; Iori, I.*; Johansson, H.*; Lafriakh, A.*; Le Fèvre, A.*; Le Gentil, E.*; Leifels, Y.*; Lynch, W. G.*; Lühning, J.*; Łukasik, J.*; Lynen, U.*; Majka, Z.*; Mocko, M.*; Müller, W. F. J.*; Mykulyak, A.*; Orth, H.*; Otte, A. N.*; Palit, R.*; Pawlowski, P.*; Pullia, A.*; Raciti, G.*; Rapisarda, E.*; Sann, H.*; Schwarz, C.*; Simon, H.*; Sümmerer, K.*; Trautmann, W.*; Tsang, M. B.*; Volant, C.*; Wallace, M.*; Weick, H.*; Wiechula, J.*; Wieloch, A.*; Zwieglinski, B.*: **Mass and isospin dependence in multifragmentation.** *Acta physica Polonica B, Particle physics and field theory, nuclear physics, theory of relativity* **37**(1): 193–198. OPEN ACCESS.

160 Skokov, V. V.*; Toneev, V. D.: **Dilepton production from**

hydrodynamically expanding fireball. *Acta physica Slovaca* **56**(4): 503–509.

161 Skokov, V. V.; Toneev, V. D.: **Semi-central in-in collisions and brown-rho scaling.** *Physical review C, Nuclear physics* **73**(2): 021902. DOI:10.1103/PhysRevC.73.021902

162 Soyeur, M.; Lutz, M. F. M.*: **e^+e^- pair production from nucleon targets in the resonance region.** *Acta physica Polonica B, Particle physics and field theory, nuclear physics, theory of relativity* **37**(1): 65–75. OPEN ACCESS.

163 Stefanek, G.; NA49 Collaboration: **Elliptic flow of a Λ hyperons in Pb+Pb collisions at 158 a GeV.** *Nuclear physics A, Nuclear and hadronic physics* **774**: 499–502. DOI:10.1016/j.nuclphysa.2006.06.074

164 Tolos, L.; Cabrera, D.; Ramos, A.; Polls, A.: **The effect of the in-medium Θ^+ pentaquark on the kaon optical potential.** *Physics letters B* **632**(2): 219–225. DOI:10.1016/j.physletb.2005.10.061

165 Tólos, L.*; Ramos, A.; Oset, E.: **Chiral approach to antikaon s- and p-wave interactions in dense nuclear matter.** *Physical review C, Nuclear physics* **74**(1): 015203. DOI:10.1103/PhysRevC.74.015203

166 Tsang, M. B.; Bougault, R.; Charity, R.; Durand, D.; Friedman, W. A.; Gulminelli, F.; Le Fèvre, A.*; Raduta, A. H.; Raduta, A. R.; Souza, S.; Trautmann, W.*; Wada, R.: **Comparisons of statistical multifragmentation and evaporation models for heavy-ion collisions.** *The European physical journal A, Hadrons and nuclei* **30**(1): 129–139. DOI:10.1140/epja/i2006-10111-0

167 Wagner, M.; Schaefer, B. J.; Wambach, J.*; Kuo, T. T. S.; Brown, G. E.: **Convergence of multi-channel effective interactions.** *Physical review C, Nuclear physics* **74**(5): 054003. DOI:10.1103/PhysRevC.74.054003

168 Wilk, A.; ALICE TRD Collaboration: **Analysis of the electron/pion separation capability with real size ALICE TRD prototypes using a neural network algorithm.** *Nuclear instruments & methods in physics research, Section A, Accelerators, spectrometers, detectors and associated equipment* **563**(2): 314–316. DOI:10.1016/j.nima.2006.02.165

169 Winckler, N.; Dababneh, S.; Heil, M.; Kappeler, F.; Gallino, R.; Pignatari, M.: **Lanthanum: An s- and r-process indicator.** *The astrophysical journal : an internat. review of spectroscopy and astronomical physics: Part 1* **647**(1): 685–691.

170 Yamaguchi, T.; Ohnishi, T.; Suzuki, T.; Becker, F.*; Fukuda, M.; Geissel, H.*; Hosoi, M.; Janik, R.; Kelić, A.*; Kimura, K.; Mandel, S.*; Münzenberg, G.*; Nakajima, S.; Ohtsubo, T.; Ozawa, A.; Prochazka, A.; Shindo, M.; Sitár, B.; Strmen, P.; Suda, T.; Sümmerer, K.*; Sugawara, K.; Szarka, I.; Takechi, M.; Takisawa, A.; Tanaka, K.: **Production cross sections of isotopes formed by fragmentation of similar to 1A (GeVKr)-^{80}Kr beam.** *Physical review C, Nuclear physics* **74**(4): 044608. DOI:10.1103/PhysRevC.74.044608

171 Zinner, N. T.; Langanke, K.*; Vogel, P.: **Muon capture on nuclei: Random phase approximation evaluation versus data for $6 \leq \mathbf{Z} \leq 94$ nuclei.** *Physical review C, Nuclear physics* **74**(2): 024326. DOI:10.1103/PhysRevC.74.024326

2. Further publications[1]

001 Andronic, A.; Lukasik, J.; Reisdorf, W.; Trautmann, W.: **Systematics of stopping and flow in Au+Au collisions.** In: Chomaz, P.; Gulminelli, F.; Trautmann, W.; Yennello, S. J: *Dynamics and Thermodynamics with Nuclear Degrees of Freedom,*,

002 Baur, G.; Typel, S.: **Investigation of subthreshold resonances with the Trojan horse method.** In: AIP Conference Proceedings **853**, 366p.

003 Braun-Munzinger, P.; Wambach, J.: **Extreme Materie.** In: *Physik Journal* **5***(10)*, 41p.

004 Cherubini, S.; Spitaleri, C.; Crucilla, V.; Gulino, M.; La Cognata, M.; Lamia, L.; Pizzone, R. G.; Romano, S.; Tudisco, S.; Tumino, A.; Mukhamedzhanov, A.; Trache, L.; Tribble, R.; Rolfs, C.; Typel, S.: **Trojan Horse Method: Recent Experiments.** In: AIP Conference Proceedings **847**, 263p.

005 Hammache, F.; Galaviz, D.; Sümmerer, K.; Typel, S.; Attallah, F.; Caamano, M.; Coc, A.; Cortina, D.; Geissel, H.; Hellstroem, M.; Iwasa, N.; Kiener, J.; Koczon, P.; Kohlmeyer, B. Schwab, E.; Schwarz, K.; Schuemann, F.; Senger, P.; Sorlin, O.; Tatischeff, V.; Thibaud, J. P.; Uhlig, F.; Wagner, A.; Walus, A.: **Cross section measurements of the Big Bang nucleosynthesis reaction D$(\alpha,\gamma)^6$Li by Coulomb dissociation of ^{6}Li.** In: AIP Conference Proceedings **831**, 21p.

006 Isenhower, D.; et al.: **Proposal to upgrade the MIPP experiment.** In: *FERMILAB-PROPOSAL-0960,*, 93p.

007 Kniege et al.: **Rapidity dependence of Bose-Einstein correlations at SPS energies.** In: *Kromeriz 2005, Multiparticle dynamics,* 473p.

008 Knoll, J.*; Riek, F.*; Ivanov, Y. B*; Voskresensky, D. N.*: **Dynamics of resonances in strongly interacting systems.** In: *Proceedings of 3rd Interdisciplinary Workshop on Progress in Nonequilibrium Green's Functions, Kiel, Germany, 22-26 Aug 2005,*, 357p.

009 Lippmann, C.: **The ALICE Transition Radiation Detector.** In: *ECONF C0604032:0043,2006*,

010 Lukasik, J.; Trautmann, W.: **Reaction plane dispersion at intermediate energies.** In: Conf. Proc. Vol. **91**, 387p.

011 Maruyama, T.; Tanigawa, T.; Chiba, S.; Tatsumi, T.; Endo, T.; Voskresensky, D. N.*: **Coulomb and surface effects on the pasta structure in nuclear matter.** In: *29th Johns Hopkins Workshop on current problems in particle theory: strong matter in the heavens (JHW2005),* Proceedings of Science, 10p.

012 Wambach, J.: **Modern Aspects of Nuclear Structure Theory.** In: *Prog. Part. Nucl. Phys*,

[1] as reported by authors.

Publications to the programme 'large-scale facilities for research with photons, neutrons and ions'

Compiled by K. Große

1. Reviewed publications (WoS listed)

001 Alonso, J.*; Blaum, K.*; Djekic, S.; Kluge, H.-J.*; Quint, W.*; Schabinger, B.; Stahl, S.; Verdu, J.; Vogel, M.; Werth, G.: **A miniature electron-beam ion source for in-trap creation of highly charged ions.** *Review of scientific instruments* **77**(3): 03A901. DOI:10.1063/1.2162857

002 Andriamonje, S.; Arsov, V.; Aune, S.; Autiero, D.; Avignone, F.; Barth, K.; Belov, A.; Beltrán, B.; Bräuninger, H.; Carmona, J. M.; Cebrian, S.; Chesi, E.; Collar, J. I.; Creswick, R.; Dafni, T.*; Davenport, M.; Di Lella, L.; Eleftheriadis, C.; Englhauser, J.; Fanourakis, G.; Farach, H.; Ferrer, E.; Fischer, H.; Franz, J.; Friedrich, P.; Geralis, T.; Giomataris, I.; Gnienko, S.; Goloubev, N.; Hartmann, R.; Hasinoff, M. D.; Heinsius, F. H.; Hoffmann, D. H. H.*; Irastorza, L. G.; Jacoby, J.; Kang, D.; Königsmann, K.; Kotthaus, R.; Krčmar, M.; Kousouris, K.; Kuster, M.; Lakić, B.; Lasseur, C.; Liolios, A.; Ljubicić, A.; Lutz, G.; Luzón, G.; Miller, D. W.; Morales, A.; Morales, J.; Mutterer, M.; Nikolaidis, A.; Ortiz, A.; Papaevangelou, T.; Placci, A.; Raffelt, G.; Ruz, J.; Riege, H.*; Sarsa, M. L.; Savvidis, I.; Serber, W.; Serpico, P.; Semertzidis, Y.; Stewart, L.; Vieira, J. D.; Villar, J.; Walckiers, L.; Zachariadou, K.; Zioutas, K.; CAST Collaboration: **Search for solar axions: the CAST experiment at CERN.** *Czechoslovak Journal of Physics* **56**: C203–C209. DOI:10.1007/s10582-006-0137-z

003 Apel, P. Y.; Akimenko, A. P.; Blonskaya, I. V.; Cornelius, T.*; Neumann, R.*; Schwartz, K.*; Spohr, R.*; Trautmann, C.*: **Etching of nanopores in polycarbonate irradiated with swift heavy ions at 15 K.** *Nuclear instruments & methods in physics research, Section B, Beam interactions with materials and atoms* **245**(1): 284–287. DOI:10.1016/j.nimb.2005.11.164

004 Barberet, P.*; Fournier, C.*; Knauf, F.*; Heib, M.*; Fischer, B. E.*; Taucher-Scholz, G.*: **Studies on the induction of the cell cycle regulator CDKN1A (p21) in bystander cells using the GSI heavy-ion microbeam.** *Radiation research* **166**(4): 682–684. Also part of: 'Health: Cancer research'.

005 Baur, G.; Typel, S.*: **The GSI heavy ion microbeam: A tool for the investigation of cellular response to high LET radiations.** *Acta Physica Polonica A* **109**(3): 329–334. Also part of: 'Health: Cancer research'.

006 Becker, F.; Hug, A.; Forck, P.*; Kulish, M.; Ni, P.; Udrea, S.; Varentsov, D.*: **Design, development, and testing of non-intercepting profile diagnostics for intense heavy ion beams using a capacitive pickup and beam induced gas fluorescence monitors.** *Laser and particle beams* **24**(4): 541–551. DOI:10.1017/S0263034606060721 Also part of: 'Physics of hadrons and nuclei:' Accelerator.

007 Blaum, K.*: **High-accuracy mass spectrometry with stored ions.** *Physics Reports* **425**(1): 1–78. DOI:10.1016/j.physrep.2005.10.011

008 Blazevic, A.*; Bohlen, H. G.; von Oertzen, W.; Balashov, V. V.; Stysin, A. V.: **Charge-state resolved energy spectra of swift Ne-22 ions passing through thin carbon foils.** *Nuclear instruments & methods in physics research, Section B, Beam interactions with materials and atoms* **245**(1): 41–43. DOI:10.1016/j.nimb.2005.11.062

009 Borghesi, M.; Fuchs, J.; Bulanov, S. V.; Mackinnon, A. J.; Patel, P. K.; Roth, M.: **Fast ion generation by high-intensity laser irradiation of solid targets and applications.** *Fusion Science & Technology* **49**(3): 412–439.

010 Bosch, F.*; Geissel, H.*; Litvinov, Y. A.*; Beckert, K.*; Franzke, B.*; Hausmann, M.*; Kerscher, T.; Klepper, O.*; Kozhuharov, C.*; Löbner, K. E. G.; Münzenberg, G.*; Nolden, F.*; Novikov, Y. N.; Patyk, Z.; Radon, T.*; Scheidenberger, C.*; Steck, M.*; Wollnik, H.: **Experiments with stored exotic nuclei at relativistic energies.** *International Journal of Mass Spectrometry* **251**(2): 212–219. DOI:10.1016/j.ijms.2006.01.037

011 Brambrink, E.; Roth, M.; Blazevic, A.*; Schlegel, T.*: **Modeling of the electrostatic sheath shape on the rear target surface in short-pulse laser-driven proton acceleration.** *Laser and particle beams* **24**(1): 163–168. DOI:10.1017/S026303460606023X

012 Brambrink, E.*; Schreiber, J.; Schlegel, T.*; Audebert, P.; Cobble, J.; Fuchs, J.; Hegelich, M.; Roth, M.*: **Transverse characteristics of short-pulse laser-produced ion beams: A study of the acceleration dynamics.** *Physical review letters* **96**(15): 154801. DOI:10.1103/PhysRevLett.96.154801

013 Brandau, C.*; Kozhuharov, C.*; Müller, A.; Schippers, S.; Beckert, K.*; Beller, P.*; Bernhardt, D.; Bosch, F.*; Böhm, S.; Currell, F. J.; Franzke, B.*; Gumberidze, A.*; Harman, Z.; Harman, Z.; Jacobi, J.; Mokler, P. H.*; Nolden, F.*; Scheid, W.; Schmidt, E. W.; Spillman, U.*; Stachura, Z.; Steck, M.*; Stöhlker, T.*: **First dielectronic recombination measurements with H-like uranium.** *Radiation Physics and Chemistry* **75**(11): 1763–1766. DOI:10.1016/j.radphyschem.2005.07.054

014 Cervera, J.; Schiedt, B.*; Neumann, R.*; Mafe, S.; Ramirez, P.: **Ionic conduction, rectification, and selectivity in single conical nanopores.** *Journal of Chemical Physics* **124**(10): 104706. DOI:10.1063/1.2179797

015 Chatterjee, S.*; Beyer, H. F.*; Liesen, D.*; Stöhlker, T.*; Gumberidze, A.*; Kozhuharov, C.*; Banas, D.; Protic, D.; Beckert, K.*; Beller, P.*; Krings, T.; Bosch, F.*; Franzke, B.*; Hagmann, S.*; Hoszowska, J.; Indelicato, P.; Kluge, H.-J.*; Ma, X.; Manil, B.; Mohos, I.; Nolden, F.*; Popp, U.*; Simionovici, A.; Sierpowski, D.; Steck, M.*; Spillmann, U.*; Brandau, C.*; Förster, E.; Stachura, Z.; Tashenov, S.*; Trassinelli, M.; Warczak, A.; Wehrhan, O.; Ziegler, E.; Trotsenko, S.*; Reuschl, R.*: **The FOCAL spectrometer for accurate X-ray spectroscopy of fast heavy ions.** *Nuclear instruments & methods in physics research, Section B, Beam interactions with materials and atoms* **245**(1):

67–71. DOI:10.1016/j.nimb.2005.11.074

016 Cornelius, T. W.*; Toimil-Molares, M. E.*; Neumann, R.*; Fahsold, G.; Lovrincic, R.; Pucci, A.; Karim, S.: **Quantum size effects manifest in infrared spectra of single bismuth nanowires.** *Applied physics letters* **88**(10): 103114. DOI:10.1063/1.2183823

017 Cornelius, T. W.*; Toimil-Molares, M. E.*; Neumann, R.*; Karim, S.: **Finite-size effects in the electrical transport properties of single bismuth nanowires.** *Journal of Applied Physics* **100**(11): 114307. DOI:10.1063/1.2388857

018 Delahaye, P.; Audi, G.; Blaum, K.; Carrel, F.; George, S.*; Herfurth, F.*; Herlert, A.; Kellerbauer, A.; Kluge, H.-J.*; Lunney, D.; Schweikhard, L.; Yazidjian, C.*: **High-accuracy mass measurements of neutron-rich Kr isotopes.** *Physical review C, Nuclear physics* **74**(3): 034331. DOI:10.1103/PhysRevC.74.034331

019 Delahaye, P.; Barton, C. J.; Connell, K.; Fritioff, T.; Kester, O.*; Lamy, T.; Lindroos, M.; Sortais, P.; Translrömer, G.; Wenander, F.: **Recent results with the Phoenix booster at ISOLDE.** *Review of scientific instruments* **77**(3): 03B105. DOI:10.1063/1.2165579

020 Deutsch, C.; Tahir, N. A.*: **Fusion reactions and matter-antimatter annihilation for space propulsion.** *Laser and particle beams* **24**(4): 605–616. DOI:10.1017/S0263034606060691

021 Dong, C. Z.; Zhang, D. H.; Stöhlker, T.*; Fritzsche, S.; Fricke, B.: **Relativity, electron correlation and QED effects in the $1s2s^2$ S-$2_{1/2}$ state of highly charged Li-like ions.** *Journal of physics B, Atomic, molecular and optical physics* **39**(14): 3121–3129. DOI:10.1088/0953-4075/39/14/018

022 Drukarev, E. G.*; Ma, X.*; Mikhailov, A. I.; Mikhailov, I. A.; Mokler, P. H.*: **Angular distribution of characteristic photons after radiative electron capture at strong central fields.** *Physical review A, Atomic, molecular, and optical physics* **74**(2): 022717. DOI:10.1103/PhysRevA.74.022717

023 Du*, G.*; Fischer, B.*; Barberet, P.*; Heiss, M.*: **A fast online hit verification method for the single ion hit system at GSI.** *Radiation Protection Dosimetry* **122**(1-4): 185–187. DOI:10.1093/rpd/ncl435

024 Dunford, R. W.; Kanter, E. P.; Krässig, B.; Southworth, S. H.; Young, L.; Mokler, P. H.*; Stöhlker, T.*; Cheng, S.: **Two-photon decay in gold atoms.** *Physical review A, Atomic, molecular, and optical physics* **74**(1): 012504. DOI:10.1103/PhysRevA.74.012504

025 Dunford, R. W.; Kanter, E. P.; Krässig, B.; Southworth, S. H.; Young, L.; Mokler, P. H.*; Stöhlker, T.*; Cheng, S.; Kochur, A. G.; Petrov, I. D.: **Coster-Kronig transition probability f(23) in gold atoms.** *Physical review A, Atomic, molecular, and optical physics* **74**(6): 062502. DOI:10.1103/PhysRevA.74.062502

026 Dvorak, J.; Brüchle, W.; Chelnokov, M.; Dressler, R.; Düllmann, C. E.; Eberhardt, K.; Gorshkov, V.; Jäger, E.*; Krücken, R.; Kuznetsov, A.; Nagame, Y.; Nebel, F.; Novackova, Z.; Qin, Z.*; Schädel, M.*; Schausten, B.*; Schimpf, E.*; Semchenkov, A.*; Thörle, P.; Türler, A.; Wegrzecki, M.; Wierczinski, B.; Yakushev, A.; Yeremin, A.: **Doubly magic nucleus $^{270}_{108}Hs^{162}$.** *Physical review letters* **97**(24): 242501. DOI:10.1103/PhysRevLett.97.242501

027 Eichler, R.; Brüchle, W.*; Buda, R.; Burger, S.; Dressler, R.; Düllmann, C. E.; Dvorak, J.; Eberhardt, K.; Eichler, B.; Folden, C. M.; Gäggeler, H. W.; Gregorich, K. E.; Haenssler, F.; Hoffman, D. C.; Hummrich, H.; Jäger, E.*; Kratz, J. V.; Kuczewski, B.; Liebe, D.; Nayak, D.; Nitsche, H.; Piguet, D.; Qin, Z.; Rieth, U.; Schädel, M.*; Schausten, B.*; Schimpf, E.*; Semchenkov, A.*; Soverna, S.; Sudowe, R.; Trautmann, N.; Thörle, P.; Türler, A.; Wierczinski, B.; Wiehl, N.; Wilk, P. A.; Wirth, G.*; Yakushev, A. B.; von Zweidorf, A.*: **Attempts to chemically investigate element 112.** *Radiochimica acta* **94**(4): 181–191. DOI:10.1524/ract.2006.94.4.181 OPEN ACCESS.

028 Ekstrom, A.; Cederkall, J.; Hurst, A.; Fahlander, C.; Banu, A.*; Butler, P.; Eberth, J.; Gorska, M.*; Habs, D.; Huyse, M.; Kester, O.; Niedermayer, O.; Nilsson, T.; Pantea, M.; Scheit, H.; Schwalm, D.; Sletten, G.; Ushasi, D. P.; van Duppen, P.; Warr, N.; Weisshaar, D.; IS418 REX-ISOLDE ISOLDE Collaboration: **Coulomb excitation of ^{110}Sn using REX-ISOLDE.** *Physica scripta* **T125**: 190–191. DOI:10.1088/0031-8949/2006/T125/045 Also part of: 'Physics of hadrons and nuclei': Experiments.

029 Elizarov, A. A.; Shabaev, V. M.; Oreshkina, N. S.; Tupitsyn, I. I.; Stöhlker, T.*: **The hyperfine structure of heavy hydrogen-like ions: Calculation based on experimental data on muonic atoms.** *Optics and Spectroscopy* **100**(3): 361–366. DOI:10.1134/S0030400X0603009X

030 El-Said, A. S.*; Neumann, R.*; Schwartz, K.*; Trautmann, C.*: **Swelling and creation of color centers in MgF_2 single crystals irradiated with energetic heavy ions.** *Nuclear instruments & methods in physics research, Section B, Beam interactions with materials and atoms* **245**(1): 250–254. DOI:10.1016/j.nimb.2005.11.110

031 Flippo, K. A.; Hegelich, B. M.; Schmitt, M. J.; Meserole, C. A.; Fisher, G. L.; Gautier, D. C.; Cobble, J. A.; Johnson, R.; Letzring, S.; Schreiber, J.; Schollmeier, M.; Fernandez, J. C.: **Ultrashort-laser-produced heavy ion generation via target laser-ablation cleaning.** *Journale de Physique IV* **133**: 1117–1122. DOI:10.1051/jp4:2006133227

032 Fritioff, T.; Cederkäll, J.; Weissman, L.; Barton, C. J.; Connell, K. A.; Duniec, D.; Kester, O.; Lamy, T.; Nilsson, T.; Jardin, P.; Sortais, P.; Translrömer, G.; ISOLDE Collaborat; IS397 Collaboration: **Purification of radioactive neutron-rich argon beams using an ion source in charge breeding mode.** *Nuclear instruments & methods in physics research, Section A, Accelerators, spectrometers, detectors and associated equipment* **556**(1): 31–37. DOI:10.1016/j.nima.2005.09.045

033 Fukuzumi, M.; Chimi, Y.; Ishikawa, N.; Suzuki, M.; Takagaki, M.; Mizuki, J.; Ono, F.; Neumann, R.*; Iwase, A.: **Effects of swift heavy ion irradiation on magnetic properties of Fe-Rh alloy.** *Nuclear instruments & methods in physics research, Section B, Beam interactions with materials and atoms* **245**(1): 161–165. DOI:10.1016/j.nimb.2005.11.094

034 Giselbrecht, S.; Gietzelt, T.; Gottwald, E.; Trautmann, C.*;

Truckenmüller, R.; Weibezahn, K. F.; Welle, A.: **3D tissue culture substrates produced by microthermoforming of pre-processed polymer films.** *Biomedical Microdevices* **8**(3): 191–199. DOI:10.1007/s10544-006-8174-8

035 Glasmacher, U. A.; Lang, M.*; Keppler, H.; Langenhorst, F.; Neumann, R.*; Schardt, D.*; Trautmann, C.*; Wagner, G. A.: **Phase transitions in solids stimulated by simultaneous exposure to high pressure and relativistic heavy ions.** *Physical review letters* **96**(19): 195701. DOI:10.1103/PhysRevLett.96.195701 Also part of: 'Health: Cancer research'.

036 Gregorich, K. E.; Gates, J. M.; Düllmann, C. E.*; Sudowe, R.; Nelson, S. L.; Garcia, M. A.; Dragojević, I.; Folden, C. M.; Neumann, S. H.; Hoffman, D. C.; Nitsche, H.: **New isotope ^{264}Sg and decay properties of $^{262-264}$Sg.** *Physical review C, Nuclear physics* **74**(4): 044611. DOI:10.1103/PhysRevC.74.044611

037 Habchi, C.; Nguyen, D. T.; Deves, G.; Incerti, S.; Lernelle, L.; Van Vang, P. L.; Moretto, P.; Ortega, R.; Seznec, H.; Sakellariou, A.; Sergeant, C.; Simionovici, A.; Ynsa, M. D.; Gontier, E.; Heiss, M.; Pouthier, T.; BoudoU, A.; Rebillat, F.: **Three-dimensional densitometry imaging of diatom cells using STIM tomography.** *Nuclear instruments & methods in physics research, Section B, Beam interactions with materials and atoms* **249**: 653–659. DOI:10.1016/j.nimb.2006.03.074

038 Heiß, M.*; Fischer, B. E.*; Jakob, B.*; Fournier, C.*; Becker, G.*; Taucher-Scholz, G.*: **Targeted irradiation of mammalian cells using a heavy-ion microprobe.** *Radiation research* **165**(2): 231–239. DOI:10.1667/RR3495.1 Also part of: 'Health: Cancer research'.

039 Herfurth, F.*; Beier, T.*; Dahl, L.*; Eliseev, S.*; Heinz, S.*; Kester, O.*; Kozhuharov, C.*; Maero, G.*; Quint, W.*; HITRAP Collaboration: **Precision measurements with highly charged ions at rest: The HITRAP project at GSI.** *International Journal of Mass Spectrometry* **251**(2): 266–272. DOI:10.1016/j.ijms.2006.02.012

040 Herlert, A.; Baruah, S.; Blaum, K.*; Delahaye, P.; Dworschak, M.; George, S.*; Guenaut, C.; Hager, U.; Herfurth, F.*; Kellerbauer, A.; Marie-Jeanne, M.; Schwarz, S.; Schweikhard, L.; Yazidjian, C.*: **Towards high-accuracy mass spectrometry of highly charged short-lived ions at ISOLTRAP. 251**(2): 131–137. DOI:10.1016/j.ijms.2006.01.017

041 Heßberger, F. P.*; Hofmann, S.*; Ackermann, D.*; Antalic, S.*; Kindler, B.*; Kojouharov, I.*; Kuusiniemi, P.*; Leino, M.; Lommel, B.*; Mann, R.*; Nishio, K.; Popeko, A. G.; Sulignano, B.*; Saro, S.; Streicher, B.; Venhart, M.; Yeremin, A. V.: **Alpha-gamma decay studies of No-255.** *The European physical journal A, Hadrons and nuclei* **29**(2): 165–173. DOI:10.1140/epja/i2006-10083-y Also part of: 'Physics of hadrons and nuclei': Experiments.

042 Heuck, H. M.*; Neumayer, P.*; Kühl, T.*; Wittrock, U.: **Chromatic aberration in petawatt-class lasers.** *Applied physics B, Lasers and optics* **84**(3): 421–428. DOI:10.1007/s00340-006-2230-1

043 Hoffmann, D. H. H.*: **Editorial from the Editor in Chief: Impact factors and open access publishing.** *Laser and particle beams* **24**(4): 467–468. DOI:10.1017/S0263034606060769

044 Hoffmann, D. H. H.*: **Untitled.** *Laser and particle beams* **24**(1): 1–2. DOI:10.1017/S0263034606060277

045 Hoffmann, D. H. H.*: **Untitled.** *Laser and particle beams* **24**(3): 333–334. DOI:10.1017/S0263034606060629

046 Hoffmann, D. H. H.*; Blazevic, A.*; Rosmej, O. N.*; Spiller, P.*; Tahir, N. A.*; Weyrich, K.*; Dafni, T.; Kuster, M.; Roth, M.; Udrea, S.; Varentsov, D.; Jacoby, J.; Zioutas, ; Sharkov, B. Y.: **Advances of dense plasma physics with particle accelerators.** *Journal de Physique IV - Proceedings* **133**: 49–55. DOI:10.1051/jp4:2006133011 Also part of: 'Physics of hadrons and nuclei:' Accelerator.

047 Hoffmann, D. H. H.*; Blazevic, A.*; Rosmej, O. N.*; Spiller, P.*; Tahir, N. A.*; Weyrich, K.*; Dafni, T.; Kuster, M.; Roth, M.; Udrea, S.; Varentsov, D.; Jacoby, J.; Zioutas, K.; Mintsev, V.; Fortov, V. E.; Sharkov, B. Y.; Maron, Y.: **Frontiers of dense plasma physics with intense ion and laser beams and accelerator technology.** *Physica scripta* **T123**: 1–7. DOI:10.1088/0031-8949/2006/T123/001 Also part of: 'Physics of hadrons and nuclei:' Accelerator.

048 Hoffmann, D. H.* H.*; Blazevic, A.*; Rosmej, O. N.*; Spiller, P.*; Tahir, N. A.*; Weyrich, K.*; Dafni, T.; Kuster, M; Ni, P.; Roth, M.; Udrea, S.; Varentsov, D.;. Jacoby, J.; Kain, V.; Schmidt, R.; Zioutas, K.; Mintsev, V.; Fortov, V. E.; Sharkov, B. Y.: **Particle accelerator physics and technology for high energy density physics research.** *The European physical journal D* : 1–7. DOI:10.1140/epjd/e2006-00125-0

049 Hoffmann, D. H. H.; Zioutas, K.: **Search for axions.** *Nuclear Physics B - Proc. Suppl.* **151**: 359–362. DOI:10.1016/j.nuclphysbps.2005.07.043

050 Jeppesen, H. B.; Moro, A. M.; Nilsson, T.; Ames, F.; van den Bergh, P.; Bergmann, U. C.; Bollen, G.; Borge, M. J. G.; Cederkäll, J.; Van Duppen, P.; Emhofer, S.; Forstner, O.; Fraile, L. M.; Fynbo, H. O. U.; Gomez-Camacho, J.; Habs, D.; von Hahn, R.; Huber, G.; Huyse, M.; Johansson, H. T.; Jonson, B.; Kester, O.; Lenske, H.; Liljeby, L.; Meister, M.; Nyman, G.; Oinonen, M.; Pantea, M.; Podlech, H.; Ratzinger, U.; Reisinger, K.; Rensfelt, K. G.; Repnow, R.; Riisager, K.; Richter, A.; Rudolph, K.; Scheit, H.; Schempp, A.; Schmidt, P.; Schrieder, G.; Schwalm, D.; Sieber, T.; Simon, H.; Tengblad, O.; Tengborn, E.; Turrion, M.; Weissmann, L.; Wenander, F.; Wolf, B.: **Investigation of the ^{9}Li+^{2}H → ^{8}Li+t reaction at REX-ISOLDE.** *Physics letters B* **635**(1): 17–22. DOI:10.1016/j.physletb.2006.02.034

051 Kajetanowicz, M.; Samek, S.; Sierpowski, D.; Stoehlker, T.*; Warczak, A.; Wilk, A.: **Digital processing of Ge-detector signals.** *Radiation Physics and Chemistry* **75**(11): 1972–1976. DOI:10.1016/j.radphyschem.2005.07.049

052 Kanapathipillai, M.*: **Nonlinear absorption of ultra short laser pulses by clusters.** *Laser and particle beams* **24**(1): 9–14. DOI:10.1017/S0263034606060034

053 Kankainen, A.; Batist, L.; Eliseev, S. A.*; Elomaa, V. V.; Eronen, T.; Hager, U.; Hakala, J.; Jokinen, A.; Moore, I.; Novikov, Y. N.; Penttila, H.; Peräjärvi, K.; Popov, A. V.; Rahaman, S.;

Rinta-Antila, S.; Ronkanen, P.; Saastamoinen, A.; Seliverstov, D. M.; Sonoda, T.; Vorobjev, G. K.*; Äystö, J.: **Mass measurements of neutron-deficient nuclides close to A=80 with a Penning trap.** *The European physical journal A, Hadrons and nuclei* **29**(3): 271–280. DOI:10.1140/epja/i2006-10088-6

054 Karim, S.; Toimil-Molares, M. E.*; Balogh, A. G.; Ensinger, W.; Cornelius, T. W.*; Khan, E. U.; Neumann, R.*: **Morphological evolution of Au nanowires controlled by Rayleigh instability.** *Nanotechnology* **17**(24): 5954–5959. DOI:10.1088/0957-4484/17/24/009

055 Karim, S.; Toimil-Molares, M. E.*; Maurer, F.; Miehe, G.; Ensinger, W.; Liu, J.; Cornelius, T. W.*; Neumann, R.*: **Synthesis of gold nanowires with controlled crystallographic characteristics.** *Applied Physics A: Materials Science & Processing* **84**(4): 403–407. DOI:10.1007/s00339-006-3645-6

056 Karny, M.; Batist, L.; Banu, A.; Becker, F.; Blazhev, A.*; Brown, B.; Brüchle, W.*; Döring, J.*; Faestermann, T.; Górska, M.*; Grawe, H.*; Janas, Z.; Jungclaus, A.; Kavatsyuk, M.*; Kavatsyuk, O.*; Kirchner, R.*; La Commara, M.; Mandal, S.*; Mazzocchi, C.*; Miernik, K.; Mukha, I.*; Muralithar, S.*; Plettner, C.*; Plochocki, A.; Roeckl, E.*; Romoli, M.; Rykaczewski, K.; Schädel, M.*; Schmidt, K.; Schwengner, R.; Zylicz, J.: **Beta decay of the proton-rich nuclei ^{102}Sn and ^{104}Sn.** *The European physical journal A, Hadrons and nuclei* **27**(2): 129–136. DOI:10.1140/epja/i2005-10258-0

057 Kazamias, S.; Cassou, K.; Ros, D.; Ple, F.; Jamelot, G.; Klisnick, A.; Lundh, O.; Lindau, F.; Persson, A.; Wahlström, C. G.; de Rossi, S.; Joyeux, D.; Zielbauer, B.*; Ursescu, D.*: **High-cadence XUV laser pupmped by titanium laser: Saphir, towards the LASERIX station.** *Journal De Physique. IV : JP* **138**: 13–19. DOI:10.1051/jp4:2006138003

058 Kester, O.*; Zimmermann, H.; Becker, R.; Kleinod, M.: **The Frankfurt MAXEMS setup for advanced charge breeding experiments.** *Review of scientific instruments* **77**(3): 03B102. DOI:10.1063/1.2163332

059 Kirchner, T.; Tawara, H.; Tolstikhina, I. Y.; Ulantsev, A. D.; Shevelko, V. P.; Stoehlker, T.: **Multielectron ionization of atoms by fast ions: An approximation by normalized exponentials.** *Technical Physics* **51**(9): 1127–1136. DOI:10.1134/S1063784206090040

060 Kolb, T.; Kost, F.*; Neubrech, F.*; Toimil-Molares, M. E.*; Cornelius, T.*; Neumann, R.*; Pucci, A.; Fahsold, G.: **IR spectroscopy and preparation of nanoslits in metal thin films.** *Infrared Physics & Technology* **49**(1): 29–34. DOI:10.1016/j.infrared.2006.01.027

061 L'Hoir, A.; Adoui, L.; Barrué, F.; Billebaud, A.; Bosch, F.*; Bräuning-Demian, A.*; Bräuning, H.; Cassimi, A.; Chevallier, M.; Cohen, C.; Dauvergne, D.; Demonchy, C. E.; Giot, L.; Kirsch, R.; Gumberidze, A.*; Kozhuharov, C.*; Liesen, D.*; Mittig, W.; Mokler, P. H.*; Pita, S.; Poizat, J.-C.; Ray, C.; Roussel-Chomaz, P.; Rothard, H.; Rozet, J.-P.; Stöhlker, T.; Tarisien, M.; Testa, E.; Toleikis, S.; Toulemonde, M.; Vernhet, D.: **Ion slowing down and charge exchange at small impact parameters selected by channeling: 2Superdensity effects.** *Nuclear instruments & methods in physics research, Section B, Beam interactions with materials and atoms* **245**(1): 1–14. DOI:10.1016/j.nimb.2005.11.055

062 Lindenblatt, M.; Pehlke, E.; Duvenbeck, A.; Rethfeld, B.*; Wucher, A.: **Kinetic excitation of solids: The concept of electronic friction.** *Nuclear instruments & methods in physics research, Section B, Beam interactions with materials and atoms* **246**(2): 333–339. DOI:10.1016/j.nimb.2006.01.006

063 Liu, J.; Duan, J. L.; Toimil-Molares, E.*; Karim, S.; Cornelius, T. W.*; Dobrev, D.*; Yao, H. J.; Sun, Y. M.; Hou, M. D.; Mo, D.; Wang, Z. G.; Neumann, R.*: **Electrochemical fabrication of single-crystalline and polycrystalline Au nanowires: the influence of deposition parameters.** *Nanotechnology* **17**(8): 1922–1926. DOI:10.1088/0957-4484/17/8/020

064 Logan, B. G.; Bangerter, R. O.; Callahan, D. A.; Tabak, M.; Roth, M.*; Perkins, L. J.; Caporaso, G.: **Assessment of potential for ion-driven fast ignition.** *Fusion Science and Technology* **49**(3): 399–411.

065 López Cela, J. J.; Piriz, A. R.; Serna Moreno, M. C.; Tahir, N. A.*: **Numerical simulations of Rayleigh-Taylor instability in elastic solids.** *Laser and particle beams* **24**(3): 427–435. DOI:10.1017/S0263034606060599

066 Maier-Komor, P.; Faestermann, T.; Krucken, R.; Nebel, F.; Winkler, S.; Groß, M.; Habs, D.; Kester, O.; Szerypo, J.; Thirolf, P. G.: **The vacuum system for the Munich fission fragment accelerator.** *Nuclear instruments & methods in physics research, Section A, Accelerators, spectrometers, detectors and associated equipment* **561**(1): 66–75. DOI:10.1016/j.nima.2005.12.229

067 Matveev, V. I.; Gusarevich, E. S.; Matrasulov, D. U.; Rakhimov, K. Y.; Stöhlker, T.*; Baur, G.: **Projectile electron losses in the collisions with neutral targets: sudden-perturbation approximation.** *Journal of physics B, Atomic, molecular and optical physics* **39**(6): 1447–1460. DOI:10.1088/0953-4075/39/22/C01

068 Maurer, F.; Dangwal, A.; Lysenkov, D.; Muller, G.; Toimil-Molares, M. E.*; Trautmann, C.*; Brötz, J.; Fuess, H.: **Field emission of copper nanowires grown in polymer ion-track membranes.** *Nuclear instruments & methods in physics research, Section B, Beam interactions with materials and atoms* **245**(1): 337–341. DOI:10.1016/j.nimb.2005.11.124

069 Menard, V.; Reulet, P.; Nörtershäuser, W.*; Le Masson, S.; Millan, P.: **Velocity and temperature fields measurement using thermochromic liquid crystals.** *Journal of Visualization* **9**(2): 131–131.

070 Mokler, P. H.*: **QED contributions to the atomic structure at strong central fields.** *Radiation Physics and Chemistry* **75**(11): 1730–1739. DOI:10.1016/j.radphyschem.2005.07.044

071 Nagy, S.; Fritioff, T.; Suhonen, M.; Schuch, R.; Blaum, K.*; Björkhage, M.; Bergström, I.: **New mass value for ^{7}Li.** *Physical review letters* **96**(16): 163004. DOI:10.1103/PhysRevLett.96.163004

072 Nardi, E.; Fisher, D. V.; Roth, M.; Blazevic, A.; Hoffmann, D. H. H.*: **Charge state of Zn projectile ions in partially ionized plasma: Simulations.** *Laser and particle beams* **24**(1): 131–141. DOI:10.1017/S0263034606060204

073 Nebel, F.; Zech, E.; Faestermann, T.; Krücken, R.; Maier-Komor, P.; Assmann, W.; Szerypo, J.; Groß, M.; Kester, O.; Thirolf, P. G.; Grötzschel, R.: **Time-dependent radioactivity distribution in MAFF.** *Nuclear instruments & methods in physics research, Section A, Accelerators, spectrometers, detectors and associated equipment* **561**(1): 83–89. DOI:10.1016/j.nima.2005.12.191

074 Neff, S.; Knobloch-Maas, R.; Tauschwitz, A.*; Hoffmann, D. H. H.; Yu, S. S.: **Study of kink instabilities in 1 m long, free-standing plasma channels used for ion beam transport.** *Journal of Applied Physics* **99**(12): 123304. DOI:10.1063/1.2206694

075 Neff, S.; Knobloch, R.; Hoffmann, D. H. H.*; Tauschwitz, A.*; Yu, S. S.: **Transport of heavy-ion beams in a 1 m free-standing plasma channel.** *Laser and particle beams* **24**(1): 71–80. DOI:10.1017/S0263034606060125

076 Neubrech, F.; Kolb, T.; Lovrincic, R.; Fahsold, G.; Pucci, A.; Aizpurua, J.; Cornelius, T. W.*; Toimil-Molares, M. E.*; Neumann, R.*; Karim, S.: **Resonances of individual metal nanowires in the infrared.** *Applied physics letters* **89**(25): 253104. DOI:10.1063/1.2405873

077 Neumayr, J. B.; Beck, L.; Habs, D.; Heinz, S.; Szerypo, J.; Thirolf, P. G.; Varentsov, V.; Voit, F.; Ackermann, D.*; Beck, D.*; Block, M.*; Di, Z.*; Eliseev, S. A.*; Geissel, H.*; Herfurth, F.*; Heßberger, F. P.*; Hofmann, S.*; Kluge, H.-J.*; Mukherjee, M.*; Münzenberg/Munzenberg, G.; Petrick, M.; Quint, W.; Rahaman, S.; Rauth, C.*; Rodríguez, D.*; Scheidenberger, C.*; Sikler, G.*; Wang, Z.*; Weber, C.*; Plaß, W. R.; Breitenfeldt, M.; Chaudhuri, A.*; Marx, G.; Schweikhard, L.; Dodonov, A. F.; Novikov, Y.; Suhonen, M.: **The ion-catcher device for SHIPTRAP.** *Nuclear instruments & methods in physics research, Section B, Beam interactions with materials and atoms* **244**(2): 489–500. DOI:10.1016/j.nimb.2005.10.017

078 Ni, P.; Hoffmann, D. H. H.*; Kulish, M.; Nikolaev, D.; Tahir, N. A.*; Udrea, S.; Varentsov, D.; Wahl, H.*: **Pyrometric system for temperature measurements of HED matter generated by intense heavy ion beams.** *Journal de Physique IV - Proceedings* **133**: 977–980. DOI:10.1051/jp4:2006133196

079 Ohgai, T.*; Enculescu, I.*; Zet, C.; Westerberg, L.; Hjort, K.; Spohr, R.*; Neumann, R.*: **Magneto-sensitive nickel nanowires fabricated by electrodeposition into multi- and single-ion track templates.** *Journal of Applied Electrochemistry* **36**(10): 1157–1162. DOI:10.1007/s10800-006-9200-5

080 Omet, C.*; Spiller, P.*; Stadlmann, J.*; Hoffmann, D. H. H.*: **Charge change-induced beam losses under dynamic vacuum conditions in ring accelerators.** *New Journal of Physics* **8**: 284. DOI:10.1088/1367-2630/8/11/284 OPEN ACCESS. Also part of: FAIR future experiments accelerator research and development.

081 Papakonstantinou, P.; Wambach, J.; Civitarese, O.; Kosmas, T. S.: **The role of the continuum and the spurious 1^- transitions in incoherent $\mu^- e^-$ conversion rate calculations.** *Czechoslovak Journal of Physics* **56**(5): 481–494. DOI:10.1007/s10582-006-0112-8

082 Pershina, V.*; Polakova, D.; Omtvedt, J. P.: **Theoretical predictions of complex formation of group-4 elements Zr, Hf, and Rf in H_2SO_4 solutions.** *Radiochimica acta* **94**(8): 407–414. DOI:10.1524/ract.2006.94.8.407 OPEN ACCESS.

083 Pikuz, S. A.; Efremov, V. P.; Rosmej, O.*; Blazevic, A.*; Korostiy, S.*; Fertman, A.; Simtov, A. V.; Norman, H. E.; Hoffmann, D. H. H.*: **Investigations of heavy-ion tracks' energy deposition inside solid media by methods of x-ray spectroscopy.** *Journal of Physics A: Mathematical and General* **39**(17): 4765–4769. DOI:10.1088/0305-4470/39/17/S71

084 Piriz, A. R.; Cortazar, O. D.; López Cela, J. J.; Tahir, N. A.*: **The Rayleigh-Taylor instability.** *American journal of physics* **74**(12): 1095–1098. DOI:10.1119/1.2358158

085 Piriz, A. R.; Lopez Cela, J. J.; Moreno, M. C. S.; Tahir, N. A.*; Hoffmann, D. H. H.: **Korrection: Thin plate effects in the Rayleigh-Taylor instability of elastic solids (vol 24, pg 275, 2006).** *Laser and particle beams* **24**(3): 465–465. DOI:10.1017/S0263034606069965

086 Piriz, A. R.; López Cela, J. J.; Serena Moreno, M. C.; Tahir, N. A.*; Hoffmann, D. H. H.: **Thin plate effects in the Rayleigh-Taylor instability of elastic solids.** *Laser and particle beams* **24**(2): 275–282. DOI:10.1017/S0263034606060423

087 Piriz, A. R.; López Cela, J. J.; Tahir, N. A.*; Hoffmann, D. H. H.*: **Richtmyer-Meshkov flow in elastic solids.** **74**(3): 037301. DOI:10.1103/PhysRevE.74.037301

088 Pomorski, M.*; Berdermann, E.*; Caragheorgheopol, A.; Ciobanu, M.*; Kis, M.*; Martemiyanov, A.*; Nebel, C.; Moritz, P.*; NoRHDia Collaboration: **Development of single-crystal CVD-diamond detectors for spectroscopy and timing.** *Physica status solidi A, Applied research* **203**(12): 3152–3160. DOI:10.1002/pssa.200671127

089 Rahaman, S.; Block, M.*; Ackermann, D.*; Beck, D.*; Chaudhuri, A.*; Eliseev, S.*; Geissel, H.*; Habs, D.; Herfurth, F.*; Heßberger, F. P.*; Hofmann, S.*; Marx, G.; Mukherjee, M.; Neumayr, J. B.; Petrick, M.; Plaß, W. R.; Quint, W.*; Rauth, C.*; Rodriguez, D.; Scheidenberger, C.*; Schweikhard, L.; Thirolf, P. G.; Weber, C.*: **On-line commissioning of SHIPTRAP.** *International Journal of Mass Spectrometry* **251**(2): 146–151. DOI:10.1016/j.ijms.2006.01.049

090 Rethfeld, B.: **Free-electron generation in laser-irradiated dielectrics.** *Physical review: B, Condensed matter and materials physics* **73**(3): 035101. DOI:10.1103/PhysRevB.73.035101

091 Reuschl, R.*; Gumberidze, A.*; Stöhlker, T.*; Kozhuharov, C.*; Rzadkiewicz, J.*; Spillmann, U.*; Tashenov, S.*; Fritzsche, S.; Surzhykov, A.: **The Balmer spectrum of H-like uranium produced by radiative recombination at low velocities.** *Radiation Physics and Chemistry* **75**(11): 1740–1743. DOI:10.1016/j.radphyschem.2006.05.006

092 Rodriguez, D.*; Audi, G.; Äystö, J.; Beck, D.*; Blaum, K.*; Bollen, G.; Herfurth, F.*; Jokinen, A.; Kellerbauer, A.; Kluge, H.-J.*; Kolhinen, V. S.; Oinonen, M.; Sauvan, E.; Schwarz, S.: **Accurate mass measurements on neutron-deficient krypton isotopes.** *Nuclear physics A, Nuclear and hadronic physics* **769**: 1–15. DOI:10.1016/j.nuclphysa.2006.02.001

093 Roth, M.; Audebert, P.; Blazevic, A.*; Brambrink, E.; Cob-

ble, J.; Cowan, T. E.; Fernandez, J.; Fuchs, J.; Geissel, M.; Hegelich, M.; Karsch, S.; Ruhl, H.; Schollmeier, M.; Stephens, R.: **Laser accelerated heavy particles - Tailoring of ion beams on a nano-scale.** *Optics communications* **264**(2): 519–524. DOI:10.1016/j.optcom.2005.12.085

094 Rzadkiewicz, J.*; Stöhlker, T.*; Banaś, D.; Beyer, H. F.*; Bosch, F.*; Brandau, C.*; Dong, C. Z.; Fritzsche, S.; Gojska, A.; Gumberidze, A.*; Hagmann, S.; Ionescu, D. C.*; Kozhuharov, C.*; Nandi, T.*; Reuschl, R.*; Sierpowski, D.; Spillmann, U.*; Surzhykov, A.; Tashenov, S.*; Trassinelli, M.*; Trotsenko, S.*: **Selective population of the [1s2s] ^{1}S and [1s2s] $^3S_1$ states of He-like uranium.** *Physical review A, Atomic, molecular, and optical physics* **74**(1): 012511. DOI:10.1103/PhysRevA.74.012511

095 Sahoo, B. K.*; Majumder, S.; Merlitz, H.; Chaudhuri, R.; Das, B. P.; Mukherjee, D.: **Electric dipole transition amplitudes for $^{207}Pb^+$.** *Journal of physics B, Atomic, molecular and optical physics* **39**(2): 355–363. DOI:10.1088/0953-4075/39/2/010

096 Sanchez, R.*; Nörtershäuser, W.*; Ewald, G.*; Albers, D.; Behr, J.; Bricault, P.; Bushaw, B. A.; Dax, A.*; Dilling, J.; Dombsky, M.; Drake, G. W. F.; Götte, S.*; Kirchner, R.*; Kluge, H.-J.*; Kühl, T.*; Lassen, J.; Levy, C. D. P.; Pearson, M. R.; Prime, E. J.; Ryjkov, V.; Wojtaszek, A.; Yan, Z. C.; Zimmermann, C.: **Nuclear charge radii of ^{9,11}Li: The influence of halo neutrons.** *Physical review letters* **96**(3): 033002. DOI:10.1103/PhysRevLett.96.033002

097 Schädel, M.*: **Chemistry of superheavy elements.** *Angewandte Chemie - International Edition* **45**(3): 368–401. DOI:10.1002/anie.200461072

098 Schmidt, E. W.; Schippers, S.; Müler, A.; Lestinsky, M.; Sprenger, F.; Grieser, M.; Repnow, R.; Wolf, A.; Brandau, C.* Lukic, D.; Schnell, M.; Savin, D. W.: **Electron-ion recombination measurements motivated by AGN X-ray absorption features: Fe XIV forming Fe XIII.** *The astrophysical journal : an internat. review of spectroscopy and astronomical physics: Part 1* **641**(2): L157–L160. DOI:10.1086/504038

099 Schollmeier, M.; Rodríguez Prieto, G.*; Rosmej, F. B.; Schaumann, G.*; Blazevic, A.; Rosmej, O. N.*; Roth, M.: **Investigation of laser-produced chlorine plasma radiation for nonmonochromatic X-ray scattering experiments.** *Laser and particle beams* **24**(3): 335–345. DOI:10.1017/S026303460606099X

100 Schwartz, K.*; Volkov, A. E.; Voss, K. O.*; Sorokin, M. V.; Trautmann, C.*; Neumann, R.*: **Thermal spike effect on defect evolution in NaCl irradiated with light and heavy ions at 8 and 300 K.** *Nuclear instruments & methods in physics research, Section B, Beam interactions with materials and atoms* **245**(1): 204–209. DOI:10.1016/j.nimb.2005.11.102

101 Shabaev, V. M.*; Glazov, D. A.; Oreshkina, N. S.; Volotka, A. V.; Plunien, G.; Kluge, H.-J.*; Quint, W.*: **g-factor of heavy ions: A new access to the fine structure constant.** *Physical review letters* **96**(25): 253002. DOI:10.1103/PhysRevLett.96.253002

102 Sikler, G.; Audi, G.; Beck, D.*; Blaum, K.; Bollen, G.; Herfurth, F.*; Kellerbauer, A.; Kluge, H.-J.*; Lunney, D.; Oinonen, M.; Scheidenberger, C.*; Schwarz, S.; Szerypo, J.; Weber, C.: **Erratum to: Mass measurements on neutron-deficient Sr and neutron-rich Sn isotopes with the ISOLTRAP mass spectrometer (vol 763, pg 45, 2005).** *Nuclear physics A, Nuclear and hadronic physics* **768**(1): 160–160. DOI:10.1016/j.nuclphysa.2006.01.005

103 Siwy, Z. S.*; Powell, M. R.*; Petrov, A.*; Kalman, E.*; Trautmann, C.*; Eisenberg, R. S.: **Calcium-induced voltage gating in single conical nanopores.** *Nano letters* **6**(8): 1729–1734. DOI:10.1021/nl061114x

104 Surzhykov, A.; Fritzsche, S.; Stöhlker, T.* Tashenov, S.*: **Polarization of L-shell REC photons following the capture into highly charged ions.** *Radiation Physics and Chemistry* **75**(11): 1767–1770. DOI:10.1016/j.radphyschem.2005.07.037

105 Surzhykov, A.; Jentschura, U. D.; Stöhlker, T.* Fritzsche, S.: **Radiative electron capture into high-Z few-electron ions: Alignment of the excited ionic states.** *Physical review A, Atomic, molecular, and optical physics* **73**(3): 032716. DOI:10.1103/PhysRevA.73.032716

106 Surzhykov, A.; Jentschura, U. D.; Stöhlker, T.*; Fritzsche, S.: **Kα_1 radiation from heavy, heliumlike ions produced in relativistic collisions.** *Physical review A, Atomic, molecular, and optical physics* **74**(5): 052710. DOI:10.1103/PhysRevA.74.052710

107 Szerypo, J.; Gross, M.; Grossmann, R.; Habs, D.; Kester, O.; Maier, H. J.; Thirolf, P.; Zech, E.; Faestermann, T.; Krücken, R.; Maier-Komor, P.; Nebel, F.: **Radioactivity distribution in the MAFF beamline.** *Nuclear instruments & methods in physics research, Section A, Accelerators, spectrometers, detectors and associated equipment* **561**(1): 76–82. DOI:10.1016/j.nima.2005.12.217

108 Tahir, N. A.*; Lomonosov, I. V.; Shutov, A.; Udrea, S.; Deutsch, C.; Fortov, E.; Gryaznov, V.; Hoffmann, D. H. H.*; Jacobi, J.; Kain, V.; Kuster, M.; Ni, P.; Piriz, A. R.; Schmidt, R.; Spiller, P.*; Varentsov, D.; Zioutas, K.: **Proposed studies of strongly coupled plasmas at the future FAIR and LHC facilities: the HEDgeHOB collaboration.** *Journal of Physics A: Mathematical and General* **39**(17): 4755–4763. DOI:10.1088/0305-4470/39/17/S70 Also part of: FAIR future experiments accelerator research and development.

109 Tahir, N. A.*; Shutov, A.; Lomonosov, I. V.; Gryaznov, V.; Deutsch, C.*; Fortov, V. E.; Hoffmann, D. H. H.*; Ni, P.; Piriz, A. R.; Udrea, S.; Varentsov, D.; Wouchuk, G.: **Studies of thermophysical properties of high-energy-density states in matter using intense heavy ion beams at the future FAIR accelerator facilities: The HEDgeHOB collaboration.** *Journal De Physique. IV : JP* **133**: 1059–1064. DOI:10.1051/jp4:2006133215 Also part of: FAIR future experiments accelerator research and development.

110 Tahir, N. A.*; Shutov, A.; Lomonosov, I. V.; Gryaznov, V.; Piriz, A. R.; Hoffmann, D. H. H.*; Forto, V. E.; Kain, V.; Schmidt, R.: **Potential of CERN large hadron collider to study high-energy-density states in matter.** *Journal De Physique. IV : JP* **133**: 1085–1088. DOI:10.1051/jp4:2006133220

111 Tahir, N. A.*; Spiller, P.* Udrea, S.; Cortazar, O. D.;

Deutsch, C.; Fortov, V. E.; Gryaznov, V.; Hoffmann, D. H. H.* Lomonosov, I. V.; Ni, P.; Piriz, A. R.; Shutov, A.; Temporal, M.; Varentsov, D.: **Studies of equation of state properties of high-energy density matter using intense heavy ion beams at the future FAIR facility: The HEDgeHOB collaboration.** *Nuclear instruments & methods in physics research, Section B, Beam interactions with materials and atoms* **245**(1): 85–93. DOI:10.1016/j.nimb.2005.11.084 Also part of: FAIR future experiments.

112 Tashenov, S.*; Stöhlker, T.*; Banaś, D.; Beckert, K.*; Beller, P.*; Beyer, H. F.*; Bosch, F.*; Fritzsche, S.; Gumberidze, A.*; Hagmann, S.*; Kozhuharov, C.*; Krings, T.; Liesen, D.*; Nolden, F.*; Protic, D.; Sierpowski, D.; Spillmann, U.*; Steck, M.*; Surzhykov, A.: **First measurement of the linear polarization of radiative electron capture transitions.** *Physical review letters* **97**(22): 223202. DOI:10.1103/PhysRevLett.97.223202

113 Tauschwitz, A.*; Efremov, V. P.; Jacoby, J.; Tauschwitz, A.*: **Schlieren diagnostics of fused quartz heated by intense ion beams.** *IEEE transactions on plasma science* **34**(5): 2414–2418. DOI:10.1109/TPS.2006.883388

114 Testa, E.; Dauvergne, D.; Bräuning-Demian, A.*; Bosch, F.*; Bräuning, H.; Chevallier, M.; Cohen, C.; Gumberidze, A.*; Hagmann, S.*; L'Hoir, A.; Kirsch, R.; Kozhuharov, C.*; Liesen, D.*; Mokler, P. H.*; Poizat, J.-C.; Ray, C.; Rozet, J.-P.; Stöhlker, T.*; Toleikis, S.*; Toulemonde, M.; Verma, P.*: **Electron gas polarization effect induced by heavy H-like ions of moderate velocities channeled in a silicon crystal.** *Nuclear instruments & methods in physics research, Section B, Beam interactions with materials and atoms* **245**(1): 47–51. DOI:10.1016/j.nimb.2005.11.073

115 Tomaselli, M.; Kühl, T.*; Ursescu, D.*; Fritzsche, S.: **Correlated EoM and distributions for A=6 nuclei.** *Progress of theoretical physics* **116**(4): 699–723. DOI:10.1143/PTP.116.699

116 Udrea, S.; Shilkin, N.; Fortov, V. E.; Hoffmann, D. H. H.; Jacoby, J.; Kulish, M. I.; Mintsev, V.; Ni, P.; Nikolaev, D.; Tahir, N. A.*; Varentsov, D.: **Electrical resistivity measurements of heavy ion beam generated high energy density aluminium.** *Journal of Physics A: Mathematical and General* **39**(17): 4743–4747. DOI:10.1088/0305-4470/39/17/S68

117 Udrea, S.; Shilkin, N.; Varentsov, D.; Tahir, N. A.*; Bock, R.*; Constantin, C.; Dewald, E.; Fortov, V. E.; Hoffmann, D. H. H.; Jacoby, J.; Kulish, M.; Lomonosov, I.; Mintsev, V.; Ni, P.; Nikolaev, D.; Shutov, A.: **Electrical resistivity of high energy density matter generated by high intensity heavy ion beams.** *Journal de Physique IV - Proceedings* **133**: 1089–1091. DOI:10.1051/jp4:2006133221

118 Ulrich, A.; Adonin, A.; Jacoby, J.; Turtikov, V.; Fernengel, D.; Fertman, A.; Golubev, A.; Hoffmann, D. H. H.*; Hug, A.; Krücken, R.; Kulish, M.; Menzel, J.; Morozov, A.; Ni, P.; Nikolaev, D. N.; Shilkin, N. S.; Ternovoi, V. Y.; Udrea, S.; Varentsov, D.*; Wieser, J.: **Excimer laser pumped by an intense, high-energy heavy-ion beam.** *Physical review letters* **97**(15): 153901. DOI:10.1103/PhysRevLett.97.153901

119 Urbassek, H. M.; Gu, X.; Rethfeld, B.: **Laser-irradiation-induced temperature jump at interfaces: Evidence for the Kapitza effect in molecular-dynamics simulation.** *Computational Materials Science* **38**(1): 51–55. DOI:10.1016/j.commatsci.2006.01.006

120 Verma, P.*; Mokler, P. H.*; Bräuning-Demian, A.*; Bräuning, H.; Kozhuharov, C.*; Bosch, F.*; Liesen, D.*; Hagmann, S.*; Stöhlker, T.*; Stachura, Z.; Banas, D.*; Orsic-Muthig, A.*; Schöffler, M.; Sierpowski, D.; Spillmann, U.*; Tashenov, S.*; Tolelkis, S.*; Wahab, M. A.: **Probing superheavy quasimolecular collisions with incoming inner shell vacancies.** *Nuclear instruments & methods in physics research, Section B, Beam interactions with materials and atoms* **245**(1): 56–60. DOI:10.1016/j.nimb.2005.11.161

121 Verma, P.*; Mokler, P. H.*; Bräuning-Demian, A.*; Kozhuharov, C.*; Bräuning, H.; Bosch, F.*; Liesen, D.*; Stöhlker, T.*; Hagmann, S.; Chatterjee, S.*; Gumberidze, A.*; Reuschl, R.; Schöffler, M.; Spillmann, U.*; Orsic Muthig, A.*; Tachenov, S.*; Stachura, Z.; Wahab, M. A.: **Spectroscopy of superheavy quasimolecules.** *Radiation Physics and Chemistry* **75**(11): 2014–2018. DOI:10.1016/j.radphyschem.2005.10.042

122 Werth, G.; Alonso, J.*; Beier, T.*; Blaum, K.; Djekic, S.*; Häffner, H.; Hermanspahn, N.; Quint, W.*; Stahl, S.; Verdú, J.; Valenzuela, T.; Vogel, M.*: **Highly charged ions, quantum-electrodynamics, and the electron mass.** **251**(2): 152–158. DOI:10.1016/j.ijms.2006.01.046

123 Weyrich, K.*; Wahl, H.*; Hoffmann, D. H. H.*; Golubev, A. A.; Kantsyrev, A. V.; Sharkov, B. Y.; Kulish, M.; Dudin, S.; Mintsev, V. B.; Fortov, V. E.; Gryaznov, V.: **Shockwave-driven, non-ideal plasmas for interaction experiments with heavy-ion beams.** *Journal of Physics A: Mathematical and General* **39**(17): 4749–4754. DOI:10.1088/0305-4470/39/17/S69

124 Zollondz, J.-H.; Schwen, D.; Nix, A.-K.; Trautmann, C.*; Berthold, J.; Krauser, J.; Hofsäss, H.: **Conductive nanoscopic ion-tracks in diamond-like-carbon.** **26**(5): 1171–1174. DOI:10.1016/j.msec.2005.09.107

125 Zuegel, J. D.; Borneis, S.*; Barty, C.; Legarrec, B.; Danson, C.; Miyanaga, N.; Rambo, P. K.; Leblanc, C.*; Kessler, T. J.; Schmid, A. W.; Waxer, L. J.; Kelly, J. H.; Kruschwitz, B.; Jungquist, R.; Moses, E.; Britten, J.; Jovanovic, I.; Dawson, J.; Blanchot, N.: **Laser challenges for fast ignition.** *Fusion Science & Technology* **49**(3): 453–482.

2. Further publications[1]

001 Bechtold, A.; Habs, D.; Fischbach, J.; Ratzinger, U.; Rehberg, J.; Reichwein, M.; Schempp, A.; Haeuser, J.;Kester, O. K.*: **The MAFF IH-RFQ Test Stand at the IAP Frankfurt.** In: Biscari, C. (Ed.): *Proceedings of 10th European Particle Accelerator Conference, Edinburgh, 2006,*, 1577p.

002 Bernard, J.; Tahir, N. A.; More, R. M.; Armijo, J.; Friedman, A.; Henestoroza, E.; Lomonosov, I. V.; Shutov, A.; Penn, G. E.; Piriz, A. R.; Wurtele; J. S.: **Ion Beam Driven Warm Dense Matter Studies.** In: *Bull. Am. Phys. Soc.* **48**, 284p.

[1] as reported by authors.

003 Blaum, K.; Schatz; H.: **Kernmassen und der Ursprung der Elemente.** In: *Physik Journal* **5***(2)*, 35p.

004 Blazevic A.*; Rethfeld B.*; Hoffmann D. H. H.*: **High Energy Density Matter Generated by Heavy-Ion Beams, and Application to Fusion Energy.** In: *Matematisk-fisiske Meddelelser* **52***(1)*, 109p.

005 Dahl, L. A.*; Barth, W.*; Kaiser, M.*; Kester, O. K.*; Kluge, H. J.*; Vinzenz, W.*; Hofmann, B.; Ratzinger, U.; Sauer, A. C.; Schempp, A.: **The HITRAP Decelerator Project at GSI.** In: Biscari, C. (Ed.): *Proceedings of 10th European Particle Accelerator Conference, Edinburgh, 2006,*, 1568p.

006 Düllmann, C.: **Physical Preseparation for Chemistry Experiments.** In: *Czech. J. Phys. 56, Suppl. D*, D333p.

007 Grawe,H; Blazhev,A; Gorska,M; Grzywacz,H; Mukha,I: **Nuclear Structure far off Stability - Implications for nuclear astrophysics.** In: *Eur. Phys. J A27, Supplement 1*, 257p.

008 Herlert, A.; Baruah, S.; Blaum, K.; Delahaye, P.; George, S.; Guenaut, C.; Herfurth, F. Kellerbauer, A.; Kluge, H.-J.; Lunney, D.; Schwarz, S.; Schweikhard, L.; Weber, C.; Yazidjian, C.: **High-accuracy mass measurements on neutron deficient neon isotopes.** In: *Proceedings American Institute of Physics Aegean Island of Kos, Greece, 2006,*,

009 Hoffman, D. C.; Lee, D. E.; Pershina, V.: **Transactinide elements and future elements.** In: Stoica, S.; Trache, L.; Tribble, R. E. (Eds.): *The Chemistry of the Actinide and Transactinide Elements, 3rd Edition, ED:Morss, L.; Edelstein, N. M.; Fuger, J. (Eds.),* 1652p.

010 Hofmann, B.; Schempp, A.; Kester, O. K.*: **An RFQ-Decelerator for HITRAP.** In: *LINAC2006, 2006 Linear Accelerator Conference, August 21-25, 2006 Knoxville, Tennessee, USA,*, 151p.

011 Kellerbauer, A.; Audi, G.; Beck, D.; Blaum, K.; Bollen, G.; Delahaye, P.; George, S.; Guenaut, C.; Herfurth, F.; Herlert, A.; Kluge, H.-J..; Lunney, D.; Mukherjee, M.; Rodriguez, D.; Schwarz, S.; Schweikhard, L.; Weber, C.; Yazidjian, C.: **ISOLTRAP Mass Measurements for Weak-Interaction Studies.** In: *Proceedings American Institute of Physics Aegean Island of Kos, Greece, 2006,*,

012 Kester, O. K.*; Barth, W.*; Dahl, L. A.*; Herfurth, F.*; Kaiser, M.*; Kluge, H. J.*; Kozhuharov, C.*; Quint, W.*; Hofmann, B.; Ratzinger, U.; Sauer, A. C.; Schempp, A.: **Deceleration of Highly Charged Ions for the HITRAP Project at GSI.** In: *LINAC2006, 2006 Linear Accelerator Conference, August 21-25, 2006 Knoxville, Tennessee, USA,*, 189p.

013 Kluge, H.-J.: **Fundamental Experiments at Low Energies.** In: *Proceedings Lake Souise, Canada, 2006,*, 60p.

014 Kluge, H.-J.: **Precision Experiments with Stored and Cooled Highly Charged Ions.** In: *Proceedings American Institute of Physics, Innsbruck, Austria, 2006,*, 60p.

015 Kröll, T.; Behrens, T.; Krücken, R.; Fastermann, T.; Gernhauser, R.; Mahgoub, M.; Maierbeck, P.; Münch, M.; Ames, F.; Habs, D.; Kester, O.; Lutter, R.; Morgan, T.; Pasini, M.; Rudolph, K.; Thirolf, P.; Bildstein, V.; Niedermaier, O.; Scheit, H.; Schwalm, D.; Martin, D.; Scherillo, A.; Warr, N.; Weisshaar, D.; Iwanicki, J.; Butler, P.; Cederkall, J.; Delahaye, P.; Fraile, L. M.; Georgiev, G.; Köster, U.; Sieber, T.; Wenander, F.; Franchoo, S.; Hurst, A.; Huyse, M.; Invanov, O.; Mayet, P.; Stefanescu, I.; van de Walle, J.; van Duppen, P.; Pantea, M.; Davinson, T.: **Coulomb excitation of neutron-rich Cd isotopes at REX-ISOLDE.** In: *Proceedings,* AIP Conf. Proc. 831, 119 (2006), 119p.

016 Liesen, D.; T. Stöhlker: **Quantenelektrodynamik im Test.** In: *Physik Journal* **5***(2)*, 16p.

017 Litvinov, Y. A.; Bosch, F.; Geissel, H.; Weick, H.; Beckert, K.; Beller, P.; Boutin, D.; Brandau, C.; Chen, L.; Klepper, O.; Knöbel, R.; Kozhuharov, C.; Kurcewicz, J.; Litvinov, Y. A.; Mazzocco, M.; Münzenberg, G.; Nociforo, C.; Nolden, F.; Plass, W. R.; Scheidenberger, C.; Steck, M.; Sun, B.; Winkler, M.: **New Mass and Lifetime Measurements of ^{152}Sm Projectile Fragments with Time-Resolved Schottky Mass Spectrometry.** In: *Proceedings of the VL National Conference on Nuclear Physics "Frontiers in Physics of the Nucleus" St. Petersburg, Russia, 2006,*,

018 Rethfeld, B.*: **Free-electron generation in laser-irradiated dielectrics.** In: *Proceedings of SPIE - The International Society for Optical Engineering 6261 I*,

019 Tahir, N. A.*; Hoffmann, D. H. H.*; Kadi, Y.; Schmidt, R.; Piriz, R.; Shutov, A.: **Interaction of the CERN Large Hadron Collider (LHC) Beam with Carbon Collimators.** In: Biscari, C. (Ed.): *Proceedings of 10th European Particle Accelerator Conference, Edinburgh, 2006,*, 1789p.

020 Tahir, N. A.*; Shutov, A.; Lomonosov, I. V.; Piriz, A. R.; Wouchuk, G.; Deutsch, C.; Hoffmann, D. H. H.*; Fortov, V. E.: **Numerical simulations and theoretical analysis of High Energy Density experiments at the next generation of ion beam facilities at Darmstadt: The HEDgeHOB collaboration.** In: *High Energy Density Physics* **2***(1-2)*, 21p.

021 Tahir, N. A.; Shutov, A.; Lomonosov, L. M.; Kim, V.; Fortov, V. E.; Piriz, A. R.;: **HEDgeHOB: High Energy Density Matter Generated by Heavy Ion Beams at the Future Facility for Antiprotons and Ion Research.** In: *Bull. Am. Phys. Soc.* **48**, 230p.

022 Tauschwitz, A.; Brambrink, E.; Maruhn, J. A.; Roth, M.; Schollmeier, M.; Schlegel, T.; Tauschwitz, A.: **Laser-produced proton beams as a tool for equation-of-state studies of warm dense matter.** In: *High Energy Density Physics 2*, 16p.

023 Tauschwitz, Anna; Brambrink, E.; Maruhn, J. A.; Roth, M.; Schollmeier, M.; Schlegel, T.*; Tauschwitz, Andreas*: **Laser-produced proton beams as a tool for equation-of-state studies of warm dense matter.** In: *High Energy Density Physics* **2***(1-2)*, 16p.

024 Tomaselli, M.*; Kühl, T.*; Ursescu, D.*; Fritzsche, S.: **Microscopic Cluster Theory for Exotic Nuclei.** In: *Journal of Physics: Conf. Ser.***49**, 208p.

025 Vorobjev, G.; Ackermann, D.; Beck, D.; Blaum, K.; Block, M.; Chaudhuri, A.; Di, Z.; Eliseev, S.; Ferrer, R.; Habs, D.; Herfurth, F.; Heßberger, F. P.; Hofmann, S.; Kluge, H.-J.; Maero, G.;

Martin, A.; Marx, G.; Mazzocco, M.; Neumayr, J. B.; Novikov, Y. N.; Plaß, W. R.; Rauth, C.; Rodriguez, D.; Scheidenberger, C.; Schweikhard, L.; Sewtz, M.; Thirolf, P.; Quint, W.; Weber, C.: **Mass measurements of radionuclides near the endpoint of the rp-process at SHIPTRAP.** In: *Proceedings of Science CERN, Geneva, Switzerland, 2006,*,

026 Zimmermann, H. Z.; Becker, R.; Kleinod, M. K.; Kester, O. K.*: **Charge Breeding Exploration with the MAXEBIS.** In: Biscari, C. (Ed.): *Proceedings of 10th European Particle Accelerator Conference, Edinburgh, 2006,*, 1702p.

Publications to the programme 'health' in the field 'cancer research'

Compiled by K. Große

1. Reviewed publications (WoS listed)

001 Barberet, P.*; Fournier, C.*; Knauf, F.*; Heib, M.*; Fischer, B. E.*; Taucher-Scholz, G.*: **Studies on the induction of the cell cycle regulator CDKN1A (p21) in bystander cells using the GSI heavy-ion microbeam.** *Radiation research* **166**(4): 682–684. Also part of: 'Large-scale facilities for research with photons, neutrons and ions'.

002 Baur, G.; Typel, S.*: **The GSI heavy ion microbeam: A tool for the investigation of cellular response to high LET radiations.** *Acta Physica Polonica A* **109**(3): 329–334. Also part of: 'Large-scale facilities for research with photons, neutrons and ions'.

003 Becherel, O. J.; Gueven, N.; Birrell, G. W.; Schreiber, V.; Suraweera, A.; Jakob, B.*; Taucher-Scholz, G.*; Lavin, M. F.: **Nucleolar localization of aprataxin is dependent on interaction with nucleolin and on active ribosomal DNA transcription.** *Human molecular genetics* **15**(14): 2239–2249. DOI:10.1093/hmg/ddl149 OPEN ACCESS.

004 Bert, C.*; Metheany, K. G.; Doppke, K. P.; Taghian, A. G.; Powell, S. N.; Chen, G. T. Y.: **Clinical experience with a 3D surface patient setup system for alignment of partial-breast irradiation patients.** *International journal of radiation oncology, biology, physics* **64**(4): 1265–1274. DOI:10.1016/j.ijrobp.2005.11.008

005 Bert, C.*; Rietzel, E.*; Haberer, T.; Chen, G.*; Kraft, G.*: **Treatment of moving targets with scanned ion beams: A comparison of different strategies.** *Medical physics* **33**(6): 2049–2049. DOI:10.1118/1.2240902

006 Brede, H. J.; Greif, K. D.; Hecker, O.; Heeg, P.; Heese, J.; Jones, D. T. L.; Kluge, H.; Schardt, D.*: **Absorbed dose to water determination with ionization chamber dosimetry and calorimetry in restricted neutron, photon, proton and heavy-ion radiation fields.** *Physics in medicine and biology* **51**(15): 3667–3682. DOI:10.1088/0031-9155/51/15/005

007 Eidelman, Y. A; Ritter, S.*; Nasonova, E.*, R. Lee, R.*, T. A. Talyzina, T. A. Andreev, S. G.: **Prediction of dose response for radiation induced exchange aberrations taking cell cycle delays into account.** *Radiation Protection Dosimetry* **122**(1-4): 185–187. DOI:10.1093/rpd/ncl413

008 Ellerbrock, M.; Jakel, O.; Krämer, M.; Nikoghosyan, A.; Schulz-Ertner, D.: **Clinical implementation of multiple field dose optimization in heavy ion treatment planning.** *Radiotherapy and oncology: journal of the European Society for Therapeutic Radiology and Oncology* **81**: S358–S358.

009 Elsässer, T.*; Scholz, M.*: **Improvement of the local effect model (LEM)implications of clustered DNA damage.** *Radiation Protection Dosimetry* **122**(1-4): 475–477. DOI:10.1093/rpd/ncl521

010 Galwas-Kliber, K.; Scholz, M.; Tarnawski, R.; Kummermehr, J.: **Response of a transplantable mouse mammary carcinoma to single doses of accelerated carbon ions.** *Radiotherapy and oncology: journal of the European Society for Therapeutic Radiology and Oncology* **81**: S362–S362.

011 Glasmacher, U. A.; Lang, M.*; Keppler, H.; Langenhorst, F.; Neumann, R.*; Schardt, D.*; Trautmann, C.*; Wagner, G. A.: **Phase transitions in solids stimulated by simultaneous exposure to high pressure and relativistic heavy ions.** *Physical review letters* **96**(19): 195701. DOI:10.1103/PhysRevLett.96.195701 Also part of: 'Large-scale facilities for research with photons, neutrons and ions'.

012 Grözinger, S. O.*; Rietzel, E.*; Li, Q.; Bert, C.*; Haberer, T.*; Kraft, G.*: **Simulations to design an online motion compensation system for scanned particle beams.** *Physics in medicine and biology* **51**(14): 3517–3531. DOI:10.1088/0031-9155/51/14/016

013 Heiß, M.*; Fischer, B. E.*; Barberet, P.*; Du, G.*; Jakob, B.*; Becker, G.*; Taucher-Scholz, G.*: **Update and performance of the scanning ion microprobe at GSI.** *Radiation research* **166**(4): 670–670. DOI:10.1667/RR0683.1

014 Heiß, M.*; Fischer, B. E.*; Jakob, B.*; Fournier, C.*; Becker, G.*; Taucher-Scholz, G.*: **Targeted irradiation of mammalian cells using a heavy-ion microprobe.** *Radiation research* **165**(2): 231–239. DOI:10.1667/RR3495.1 Also part of: 'Large-scale facilities for research with photons, neutrons and ions'.

015 Hofman-Hüther, H.; Peuckert, H.; Ritter, S.*; Virsik-Köpp, P.: **Chromosomal instability and delayed apoptosis in long-term T-lymphocyte cultures irradiated with carbon ions and X rays.** *Radiation research* **166**(6): 858–869. DOI:10.1667/RR0569.1

016 Jakob, B.*; Taucher-Scholz, G.*: **Interaction of heavy ions with nuclear chromatin: Spatiotemporal investigations of biological responses in a cellular environment.** *Nuclear instruments & methods in physics research, Section B, Beam interactions with materials and atoms* **245**(1): 292–297. DOI:10.1016/j.nimb.2005.11.117

017 Karger, C.; Peschke, P.; Sanchez-Brandelik, R.; Scholz, M.; Debus, J.: **Radiation tolerance of the rat spinal cord after single and fractionated doses of photons and carbon ions.** *Radiotherapy and oncology: journal of the European Society for Therapeutic Radiology and Oncology* **81**: S82–S82.

018 Karger, C. P.; Peschke, P.; Sanchez-Brandelik, R.; Scholz, M.*; Debus, J.: **Radiation tolerance of the rat spinal cord after 6 and 18 fractions of photons and carbon ions: Experimental results and clinical implications.** *International journal of radiation oncology, biology, physics* **66**(5): 1488–1497.

DOI:10.1016/j.ijrobp.2006.08.045

019 Krämer, M.*; Scholz, M.*: **Rapid calculation of biological effects in ion radiotherapy.** *Physics in medicine and biology* **51**(8): 1959–1970. DOI:10.1088/0031-9155/51/8/001

020 Loeper-Kabasakal, B.; Thamm, R.; Kampfer, S.; Wagner, F. M.; KastenmAller, A.; Lange, W.; Kneschaurek, P.: **Reactor fission neutron beam for radiotherapy.** *Radiotherapy and oncology: journal of the European Society for Therapeutic Radiology and Oncology* **81**: S361–S362.

021 Nasonova, E. A.*; Shmakova, N. L.; Komova, O. V.; Mel'nikova, L. A.; Fadeeva, T. A.; Krasavin, E. A.; Ritter, S.*: **Cytogenetic effects of low-dose radiation with different LET in human peripheral blood lymphocytes.** *Radiation an Environmetal Biophysics* **45**(4): 307–312. DOI:10.1007/s00411-006-0073-0

022 Rebisz, M.*; Martemiyanov, A.*; Berdermann, E.*; Pomorski, M.*; Marczewska, B.; Voss, B.*: **Synthetic diamonds for heavy-ion therapy dosimetry.** *Diamond and related materials* **15**(4): 822–826. DOI:10.1016/j.diamond.2005.12.022

023 Scholz, M.*; Matsufuji, N.; Kanai, T.: **Test of the local effect model using clinical data: tumour control probability for lung tumours after treatment with carbon ion beams.** *Radiation Protection Dosimetry* **122**(1-4): 478–479. DOI:10.1093/rpd/ncl426

024 Schulz-Ertner, D.; Nikoghosyan, A.; Hof, H.; Combs, S. E.; Jakel, O.; Kraft, G.; Debus, J.: **Carbon ion treatment in low-grade-chondrosarcoma of the skull base. 182**: 29–29.

2. Further publications[1]

001 Amaldi, U.; Kraft, G.: **Particle accelerators take up the fight against cancer.** In: *CERN courier* **46***(10)*, 17p.

002 Mustafin, E.; Iwase, H.*; Kozlova, E.*; Schardt, D.*; Fertman, A.; Golubev, A.; Hinca, R.; Pavlovic, M.; Strasik, I.; Sobolevskiy, N.: **Measured Residual Radioactivity Induced by U Ions of Energy 500 MeV/u in a Cu Target.** In: Biscari, C. (Ed.): *Proceedings of 10th European Particle Accelerator Conference, Edinburgh, 2006,*, 1834p.

003 Scholz, M.: **Dose response of biological systems to low- and high-LET radiation.** In: Horowitz, Y: *Microdosimetric response of physical and biological systems to low- and high-LET radiations,*

[1] as reported by authors.

Patents and patent applications

Compiled by M. Hensel, K. Große

Granted patents and inventors

D. Dobrev, R. Neumann, N. Angert, J. Vetter **Metallmembranfilter und Verfahren zur Herstellung desselben.** European patent, September 2006 (GSI No. P174).

R. Spohr, P. Apel, Y. Korchev, Z. Siwy, Y. Masaru **Verfahren zum Ätzen mindestens einer Ionenspur zu einer Pore in einer Membrane und elektrolytische Zelle zur Prparierung einer solchen.** US patent, February 2006 (GSI No. P162).

U. Ratzinger, B. Schlitt **Driftrährenbeschleuniger zur Beschleunigung von Ionenpaketen.** German and US patent, July 2006 (GSI No. P193).

K. Blasche, B. Franczak **Beschleunigeranlage für eine Strahlentherapie mit Ionenstrahlen.** German patent, December 2006 (GSI No. P219).

W. Bourgeois, R. Fuchs, P. Spiller **Isokinetische Gantry-Anordnung zur isozentrischen Führung eines Teilchenstrahls und Verfahren zu deren Auslegung.** European patent, June 2006 (GSI No. P192).

S. Giselbrecht, C. Trautmann, R. Truckenmüller **Formkörper, Verfahren zu seiner Herstellung und seine Verwendung.** German patent, February 2006 (GSI No. P223).

T. Haberer **Verfahren und Vorrichtung zum Steuern einer nach dem Rasterscanverfahren arbeitenden Bestrahlungseinrichtung für schwere Ionen oder Protonen mit Strahlextraktion.** US patent, August 2006 (GSI No. P176).

P. Mokler **Turbomolekularpumpe mit koaxial zentralem Durchgang.** US patent, August 2006 (GSI No. P180).

A. Bechthold, Ratzinger, A. Schempp, B. Schlitt **Apparatus for ion beam formation and preaccelerating of ions used in a heavy ion cancer facility.** US patent, November 2006 (GSI No. P169).

Z. Siwy, J. Behrends, N. Fertig, Prof. A. Fulinski, C. Martin, R. Neumann, C. Trautmann, E. Toimil **Nanodevice for controlling the flow of charged particles in electrolytes.** European patent, September 2006 (GSI No. P183).

P. Apel, H. Kiesewetter, R. Spohr, M. Skoczylas, C. Zet **Elektrolytische Bank.** German patent, October 2006 (GSI No. P227).

Patent applications and inventors

C. von Neubeck, W. Kraft-Weyrather, C. Gübitz **Bestrahlungsverifikationsvorrichtung für Strahlentherapieanlagen und Verfahren zur Handhabung derselben.** For German patent, March 2006 (GSI No. P238).

More information under:
<http://www.gsi.de/informationen/tt/index_e.html>

GSI as publisher

Compiled by K. Große

Augustin, I.; Eickhoff, H.; Groß, K.-D.; Henning, W. F.; Krämer, D.; Walter, G. (Eds.): **FAIR Baseline Technical Report**. September 2006.

Accelerator Reports and Notes:

Zenkevich, P.; Boine-Frankenheim, O.; Alekseev, O.: **Trapped Particles Effects in the HESR Storage Ring.** GSI-Acc-Report-2006-05-001

Strasik I.; Fertman A., Mustafin E., Kozlova E., Pavlovic M., Hinca R., Iwase H.: **Depth-profiling of the residual activity induced by 950 MeV/u Uranium ions in Copper.** GSI-Acc-Note-2006-11-002

Smolyakov A.; E. Mustafin, E.: **FLUKA-based simulation of neutron irradiation of quench protection diodes for the superconducting SIS300 magnets.** GSI-Acc-Note-2006-10-001

Bolshakov, P. R.; Zenkevich, P.: **Study of cooling equilibrium and beam tails in HESR using the MOCAC code.** GSI-Acc-Note-2006-05-001

Quatraro, D.; Franchetti, G.: **Invariance properties of orbits near a resonance.** GSI-Acc-Note-2006-11-003

Franchi, A.; Franchetti, G.; Giacomini, T.; Kirk, M.; Redelbach A.: **Measurement of emittance exchange driven by betatron coupling in SIS-18.** GSI-Acc-Note-2006-03-001

Kornilov, V.; Boine-Frankenheim, O.; Kaufmann, W.; Moritz, P.: **Measurements and Analysis of the Transverse Beam Transfer Function (BTF) at the SIS 18 Synchrotron.** GSI-Acc-Note-2006-12-00

GSI Reports:

Pfeiffer, Bernd: **Influence of mass measurements at FSR-ESR on r-process calculations.** GSI Report 2005-3.

Weyrich, K. (Ed.): **High Energy Density Physics with Intense Ion and Laser Beams: Annual Report 2005.** GSI Report 2006-2.

Große, K. (Ed.): **GSI Scientific Report 2005.** GSI Report 2006-1.

GSI Preprints:

Surzhykov, A.; Jentschura, U. D.; Stöhlker, T.; Fritzsche, S.: **Kα_1 radiation from heavy, helium-like ions produced in relativistic collisions.** GSI Preprint 2006-08.

Stöhlker, T.; Beyer, H. F.; Bräuing-Demian, A.; Brandau, C.; Hagmann, S.; Kozhuharov, C.; Kluge, H. J.; Kühl, T.; Liesen, D.; Mann, R.; Nörtershäuer, W.; Quint, W.; Schramm, U.; Schuch, R.: **Atomic Physics with Highgly-Charged Ions at the Future FAIR Facility: A Status Report.** GSI Preprint 2006-07.

Tashenov, S.; Stöhlker, T.; Bana, D.; Beckert, K.; Beller, P.; Beyer, H. F.; Bosch, F.; Fritzsche, S.; Gumberidze, A.; Hagmann, S.; Kozhuharov, C.; Krings, T.; Liesen, D.; Nolden, F.; Protic, D.; Sierpowski, D.; Spillmann, U.; Steck, M.; Surzhykov, A.: **First Measurement of the Linear Polarization of Radiative Electron Capture Transitions.** GSI Preprint 2006-06.

Armbruster, P.: **Precompound Charged Particle Emission (PCE) - A Mechanism Beyond Element Production by Complete Fusion.** GSI Preprint 2006-05.

Rzadkiewicz, J.; Stöhlker, T.; Banas, D.; Beyer, H. F.; Bosch, F.; Brandau, C.; Dong, C. Z.; Fritzsche, S.; Gojska, A.; Gumberidze, A.; Hagmann, S.; Ionescu, D. C.; Kozhuharov, C.; Nandi, T.; Reuschl, R.; Sierpowski, D.; Spillmann, U.; Surzhykov, A.; Tashenov, S.; Trassinelli, M.; Trotsenko, S.: **Selective population of the [1s2s]1S0 and [1s2s]3S1 states of He-like uranium.** GSI Preprint 2006-04.

Matveev, V. I.; Gusarevich, E. S.; Matrasulov, D. U.; Rakhimov, K. Y.; Stöhlker, T.; Baur, G.: **Projectile electron losses in the collisions with neutral targets: Sudden-perturbation approximation.** GSI Preprint 2006-03.

Surzhykov, A.; Jentschura, U. D.; Stöhlker, T.; Fritzsche, S.: **Radiative electron capture into high-Z, few-electron ions: Alignment of the excited ionic states.** GSI Preprint 2006-02.

Lukic, S.; Gevaert, F.; Kelic, A.; Riccardi, M. V.; Schmidt, K.-H.; Yordanov, O.: **Systematic comparison of ISOLDE-SC yields with calculated in-target production rates.** GSI Preprint 2006-01.

PhD, Master, Bachelor, Habilitation and Diploma theses

Compiled by K. Große

Ahrens, S.: **Multi-dimensional numerical investigation of laser induced particle acceleration.** Bachelor: TU-Darmstadt.

Alber, Ina: **Effizienz der Doppelpass Verstärkung im NHELIX-Hochenergielaser.** Bachelor: TU Darmstadt.

Altinpinar, S.: **Investigations of the performance of ALICE TRD chambers.** Diplom: TU Darmstadt.

Antonczyk, D.: **Detailed analysis of two-particle correlations in central Pb-Au collisions at 158 GeV per nucleon.** Dissertation: TU Darmstadt.

Ataie, Abdul: **RPA Theorie für schwache Zerfälle von Exotischen Kernen.** Diplom: Universität Gießen.

Bailhache, R.: **o. T.** Diplom: Ecole Centrale Paris.

Bannier, B.: **Simulations of dilectron capabilities of HADES at SIS100.** Diplom: TU Dresden.

Becker, Frank: **Ein strahlinduzierter Fluoreszenz-Monitor zur nichtinvasiven Diagnostik intensiver Schwerionenstrahlen.** Diplom: TU-Darmstadt.

Bernhardt, Dietrich: **Dielektronische Rekombination wasserstoffähnlicher Uranionen am Schwerionenspeicherring ESR.** Dissertation: Justus-Liebig-Universität Gießen.

Bert, Christoph: **Bestrahlungsplanung für bewegte Zielvolumina in der Tumortherapie mit gescanntem Kohlenstoffstrahl.** Dissertation: TU Darmstadt. GSI Diss 2006-01.

Böhmer, Michael: **Messung der Spallationsreaktion ^{56}Fe + p in inverser Kinematik.** Dissertation: Technische Universität München.

Bohl, Jessica: **Charakterisierung von zwei Glioblastomzelllinien zur Vorbereitung für die Tumortherapie mit schweren Ionen in Kombination mit Chemotherapie.** Diplom: Hochschule Darmstadt.

Busch, Oliver: **o.T.** Dissertation: TU Darmstadt.

Caceres-Monrol, Lucia: **Identification of the isomeric state in the N=Z nucleus 82Nb.** Dissertation: Autonoma University Madrid.

Cornelius, Thomas Walter: **Fabrication and Characterisation of Bismuth Nanowires.** Dissertation: Universität Heidelberg. GSI Diss 2006-09.

Deveaux, Michael: **Radiation hardness studies on monolitic active pixels sensors.** Dissertation: Univ. Frankfurt.

Doering, Matthias: **Screening of heavy quarks and hadrons at finite temperature and density.** Dissertation: Universität Bielefeld.

Dworschak, Michael: **Optimierung der Zyklotronfrequenzbestimmung und Hochpräzisionsmassenmessungen an neutronenreichen Zinnisotopen mit ISOLTRAP.** Diplom: Universität Würzburg. GSI Dipl 2006-03.

Ehmann, Christian: **Hadron Spectroskopie auf dem Gitter.** Diplom: Regensburg.

Eichstädt, F.: **In-medium properties of omega mesons.** Diplom: Universität Gießen.

Eppinger, Katrin: **Pulsformanalyse für MINIBALL zur Messung an relativistischen Schwerionen.** Diplom: Technische Universität München.

Fedoseew, Andreas: **Relativistische Quantenfeldtheorie für Korrelationen in Kernmaterie.** Diplom: Universität Gießen.

Feigh, Stefan: **Ein geometrisches Diskretisierungs- und Lösungsverfahren auf der Basis der Finiten-Integrations-Methode.** Diplom/DissertationNOCH: Technische Universität Darmstadt.

Fettouhi, Andre: **Investigation of slowing-down and charge exchange of nickel and uranium ions in gases and solids int he energy range (60-200) MeV/u.** Dissertation: Univ. Gießen.

Fraiß, Maik: **Design, Test und Implementation eines Systems zur statistischen Auswertung und Überwachung der Microsoft Umgebung bei GSI Darmstadt.** Diplom: FH Darmstadt.

Frammelsberger, Carmen: **Chirale Störungstheorie und Extrapolation von Gitter-Daten.** Diplom: Regensburg.

Franchi, Andrea: **Studies and Measurements on Linear coupling and Nonlinearities in Hardon Circular Accelerators.** Dissertation: Goethe-Universität Frankfurt am Main, URN:https://www.gsi.de/onTEAM/gsidiss/public/1155296435.html. GSI Diss 2006-07.

Fricke, Andreas: **o. T.** Dissertation: Univ. des Saarlands.

Garcia, Jose Javier Cuenca: **Shell model halflives at magic neutron number N=82.** Diplom: Universität Darmstadt.

Guebitz, Carola: **Strahlenbiologische und physikalische Messungen für die Bestrahlungsplanung mit leichten Ionen.** Diplom: TU Darmstadt.

Härtle, Rainer: **Antikaon-nuclear bound states.** Diplom:

TU München.

Haettner, Emma: **Experimental study on carbon ion fragmentation in water using GSI therapy beams.** Master: Royal Technical Highschool Stockholm (Sweden).

Henzl, Vladimir: **Spectator Response to the paricipant blast.** Dissertation: Czech Technical University Prague, Faculty of Nuclear Science and Physical Engeneering.

Henzlova, Daniela: **Systematic investigations of the isotopc distributions measured in the fragmentation of 124Xe and 136Xe projectiles.** Dissertation: Czech Technical University Prague, Faculty of Nuclear Science and Physical Engeneering. GSI Diss 2006-02.

Hertsch, Susanne: **Messung der Lichttransmission an lasergeheiztem Kohlenstoffplasma.** Bachelor: TU Darmstadt.

Heuck, Hans-Martin: **Einsatz adaptiver Optik und Kompensation chromatischer Aberration beim Petawattlaser PHELIX.** Diplom: Fachhochschule Münster.

Hoek, Matthias: **Design and Construction of a Scintillating Fibre Tracker for Measuring Hard Exclusive Reactions at HERMES (Using test beams at GSI).** Dissertation: Universität Gießen.

Huebner, Kay: **The Polyakov loop and its correlators in higher representations of SU(3) at finite temperature.** Dissertation: Universität Bielefeld.

Hug, Alexander: **Nichtinvasive Diagnostik intensiver stark fokussierter Schwerionenstrahlen.** Diplom: TU Darmstadt.

Hummrich, Holger: **Einsatz elektrochemischer Methoden fuer die Untersuchung superschwerer Elemente.** Dissertation: Johannes Gutenberg-Universität Mainz.

Isselhorst, Cartsen: **pi-pi Korrelationen in heisser und dichter Materi.** Dissertation: TU-Darmstadt.

Jakob, Bernhard: **Die Beschreibung von dichtem Wasserstoff mit der Methode der Wellenpaket-Molekulardynamik (WPMD).** Dissertation: Universität Erlangen.

Jöst, Johannes: **Entwicklung eines ADC-DAC Boards für digitale Regelungssysteme in einer DSP - Umgebung.** Diplom: FH Bielefeld.

Käsz, Manuel: **Study of Expansion of Solid Helium-4 into Vacuum.** Dissertation: J. W. Goethe-Universität Frankfurt am Main.

Kaltenbrunner, Thomas: **Gitter-Operatoren für Baryon-Wellenfunktionen.** Diplom: Regensburg.

Ketelaer, Jens: **Development of a non-destructive FT-ICR detection system for singly charged ions in a gryogenic Penning trap.** Diplom: Universität Mainz. GSI Dipl 2006-05.

Kliemt, Ralf: **Beschreibung von Proton-Antiproton-Kollisionen mit dem ROC-Modell.** Diplom: TU Dresden.

Korostiy, Svitlana: **Spectroscopic investigation of the charge dynamics of heavy ions penetrating solid and gaseous targets.** Dissertation: TU Darmstadt. GSI Diss 2006-7.

Krauß, Matthias: **Gammaspektrometrische Messungen der Aktivierungen an der Beschleunigerstruktur des GSI-Schwerionensynchrotrons und Abschätzung der nuklidspezifischen Dosisleistungen.** Diplom: Berufsakademie Karlsruh.

Kugler, Maximilian: **Entwicklung einer Klassenbibliothek zur Erstellung generischer Sequenzen im Rahmen des CS Frameworks.** : Hochschule Darmstadt. GSI Dipl 2006-04.

Laczko, Gabor: **Investigation of the Radial Ionization Distribution of Heavy Ions with an Optical Particle Track Chamber and Monte-Carlo Simulations.** Dissertation: TU Darmstadt.

Lau, Thomas: **Numerische Methoden zur Simulation teilchengenerierter elektromagnetischer Felder in der Beschleunigerphysik.** Dissertation: Technische Universität Darmstadt.

Lee, Ryonfa: **Chromosome aberrations in human lymphocytes irradiated with heavy ions.** Dissertation: TU Darmstadt.

Liebig, Clemens: **Entwicklung eines Abbildungssystems mit variabler Vergrößerung für den Einsatz eines Wollastoninterferometers als Plasmadiagnostik.** Bachelor: TU Darmstadt.

Lineva, Natalia: **o. T.** Dissertation: TU Darmstadt.

Linnyk, Olena: **Quark off-shellness effect on parton distribution functions.** Dissertation: Universität Gießen.

Löb, Daniel: **Untersuchung des Ablationsverhaltens lasergeheizter Kohlenstoffolien.** Bachelor: TU Darmstadt.

Manteufel, Robert: **Integration von Speicherressourcen in die Rechnerfarm der GSI unter Berücksichtigung von Anwendungsszenarien aus Grid-Computing.** Diplom: FH Darmstadt.

Marhauser, Marc Florian: **The quark propagator in the color-spin locked phase.** Diplom: TU-Darmstadt.

Meusel, Oliver: **Fokussierung und Transport von Ionenstrahlen mit Raumladungslinsen.** Dissertation: Goethe-Frankfurt am Main.

Milosic, Timo: **Nuclear Reactions Within Fermionic Molecular Dynamics.** Diploma: TU-Darmstadt.

Mühlbauer, Monika: **Chirale Dynamik mit Pion-Nukleon-Formfaktoren.** Diplom: TU München.

Neidherr, Dennis: **Entwicklung einer Pumpsperre für das**

Penning-Fallen-Massenspektrometer SHIPTRAP. Diplom: Universität Mainz. GSI Dipl 2006-06.

Ni, Pavel: **Temperature Measurement of High-Energy-Density Matter Generated by Intense Heavy Ion Beams.** Dissertation: TU Darmstadt.

Peschke, Claudius: **Higher-Order-Mode Dämpfer als Strahllagemonitore.** Dissertation: Johann Wolfgang Goethe Universität Frankfurt/M.

Petermann, Ilka: **Waveletanalyse von Schalenmodellrechnungen zu Riesenresonanzen.** Diplom: o. A..

Pogonyi, Eszter: **Untersuchungen zum Dosisbeitrag von sekundären Neutronen bei der Strahlentherapie mit Kohlenstoffionen.** Diplom: TU Darmstadt.

Procura, Massimiliano: **Quark mass dependence of nucleon observables and lattice QCD.** Dissertation: TU München.

Radomski, S.: **Neutral strange particle production at top SPS energy measured by the CERES experiment.** Dissertation: TU Darmstadt.

Rauch, Udo: **Der Einfluß dicht ionisierender Strahlung auf elektrische Membranintegrität von Modellzellen.** Diplom: TU Darmstadt.

Rodriguez-Prieto, Gonzalo: **Highly Charged Ion Jets from Medium Flux Laser Plasmas.** Dissertation: TU Darmstadt.

Rößner, Simon: **Field theoretical modelling of the QCD phase diagram.** Diplom: TU München.

Rustamov, Anar: **Exclusive η Meson Reconstruction in Proton-Proton Collisions at 2.2 GeV with the HADES Spectrometer and High Resolution Tracking.** Dissertation: Technischen Universität Darmstadt. GSI Diss 2006-10.

Sachez Alarcon, Rodolfo Marcelo: **Nuclear Charge Radius of the Halo Nucleus Lithium-11.** Dissertation: Universität Mainz. GSI Diss 2006-09.

Sanjari, Shahab: **Hardware and Software Implementation of a Radio Frequency High-Speed Data Conversion Unit for Digital Control Systems.** Bachelor: TU Darmstadt.

Schaller, Gernot: **On selected numerical approaches to Cellular Tissue.** Dissertation: Johann Wolfgang Goethe-Universität Frankfurt am Main.

Scheidenberger, Christoph: **Struktur exotischer Kerne und astrophysikalische Anwendungen: Massen- und Lebensdauermessungen mit gespeicherten, relativistischen Projektilfragmenten.** Habilitation: Universität Gießen.

Scherer, Stefan: **Modelling ultra-relativistic Heavy Ion Collisions with the quark Molecular Dynamics qMD.** Dissertation: Johann Wolfgang Goethe-Universität Frankfurt am Main.

Schlörit, Andreas: **Entwurf, Auslegung und Aufbau von teilbaren, geschlitzten Flusskonzentratoren für Strahlstrom-Messensorik.** Diplom: FH-Wiesbaden-Rüsselsheim.

Schöffler, Markus S.: **Grundzustandskorrelationen und dynamische Prozesse untersucht in Ion-Helium-Stößen.** Dissertation: Johann Wolfgang Goethe-Universität Frankfurt/M.

Schrader, Christoph: **Phototechnisches Ausleseverfahren für Ionenstrahlen.** Diplom: FH Wiesbaden-Rüsselsheim.

Schreiber, Gerald T.: **Barrier-Buckets am Experimentierspeichering der Gesellschaft für Schwerionenforschung.** Dissertation: Goethe-Universität Frankfurt am Main. GSI Diss 2006-05.

Srisawad, Ponrad: **Kaon and Sigma meson production in heavy ion reactions at intermediate energies.** Dissertation: Suranaree University (Thailand) and Universität Tübingen.

Stang, Denise: **Konzeption und Entwicklung eines Abbildungssystems für Laserthomsonstreuung an heißen dichten Plasmen.** Bachelor: TU Darmstadt.

Streicher, Branislav: **Synthesis and spectroscopic properties of transfermium isotopes with Z = 105, 106 and 107.** Dissertation: Comenius Universität Pressburg (Bratislava), Slowakei.

Tang, Hai: **Entwicklung einer Schnittstelle zwischen Webbrowsern und Oszilloskopen.** Diplom: FH-Darmstadt.

Thaler, Michael: **Phases of QCD: lattice thermodynamics and quasiparticle approaches.** Dissertation: TU München.

Theiß, Alexander: **Untersuchungen zum Ladungsaustausch in den Ein-Elektron-Stoßsystemen Li(2+) + Li(3+) → Li(3+) + Li(2+) und Li(2+) + 3He(2+) → Li(3+) + 3He(+).** Dissertation: Universität Giessen.

Tsiledakis, G. K.: **Scale Dependence of Mean Transverse Momentum Fluctuations at Top SPS Energy measured by the CERES experiment and studies of gas properties for the ALICE experiment.** Dissertation: TU Darmstadt.

Tsoutsouris, Efthymios: **Eigenschaften von weichmagnetischen Materialien und deren Verlustermittlung durch die Epsteinrahmen-Methode.** Diplom: Universität Kassel.

Ulmer, Stefan: **Entwicklung des experimentellen Aufbaus zur Messung des g-Faktors des Protons in einer Penning-Falle.** Diplom: Universität Heidelberg.

Ursescu, Daniel: **Grazing Incidence Pumped Zr X-Ray Laser for Spectroscopy on Li-like Ions.** : Universität Mainz. GSI Diss 2006-04.

Verbuyst, Eli: **Measuring the radiation tolerance of a CPLD.** Diplom: Fachhochschule Köln.

von Neubeck, Cläre Hanna Freiin: **Aufbau eines 3-dimensionalen Systems zur biologischen Verifikation der Bestrahlungsplanung mit Schwerionen.** Diplom: Hochschule Darmstadt.

Voss, Kay-Obbe: **Laser Spectroscopy of Gd^{3+} Ions Doped into LaF_3 Single Crystals as Probe of Material Parameters.** Dissertation: Universität Heidelberg.

Wagenknecht, Katja: **Qualitätssicherung an einem Tomotherapiegerät.** Diplom: Berufsakademie Karlsruh.

Wamers, Felix: **Entwicklung eines Detektors für gepulste Schwerionenstrahlen.** Diploma: TU Darmstadt.

Wissel, Soenke: **Mesonic correlation functions from light quarks and their spectral representation in hot quenched lattice QCD.** Dissertation: Universität Bielefeld.

Yazidjian, C.: **A new detector setup for ISOLTRAP and test of the isobaric multiplet mass equation.** Dissertation: Université de Caen (France).

Zaunick, Hans-Georg: **Erweiterung einer Teststation fr Pixelfrontends und Charakterisierung eines FE-I-Chips.** Diplom: TU Dresden.

Zeeb, Gebhard: **Einfluss schwerer hadronischer Zustände auf das QCD-Phasendiagramm und die Ausfrierbedingungen in einem hadronischen chiralen Modell.** Dissertation: Johann Wolfgang Goethe-Universität Frankfurt am Main.

Zheng, Wang: **Aufbau und Charakerisierung einer Laserablationsquelle mit Kohlenstoffclustern als Referenz für Flugzeitspektrometrie von exotischen Kernen.** Dissertation: Univ. Gießen.

International and national collaborations *

Compiled by K. Große

The FAIR Collaborations

FAIR: The BIOMAT Collaboration

The High-Energy Irradiation Facility for Biophysics and Materials Research
Spokespersons: M. Durante, Naples (Italy) S. Klaumünzer, Berlin (Germany)

Contributions in this report:
FAIR-EXPERIMENTS-34

FAIR: The CBM Collaboration

The Condensed Baryonic Matter experiment
<http://www.gsi.de/zukunftsprojekt/experimente/CBM/index_e.html>
Spokesperson: P. Senger Darmstadt (Germany)

Contributions in this report:
FAIR-EXPERIMENTS-06
FAIR-EXPERIMENTS-07
FAIR-EXPERIMENTS-08
FAIR-EXPERIMENTS-09
FAIR-EXPERIMENTS-10
FAIR-EXPERIMENTS-11
FAIR-EXPERIMENTS-12
FAIR-EXPERIMENTS-13
FAIR-EXPERIMENTS-14
FAIR-EXPERIMENTS-15
FAIR-EXPERIMENTS-16
FAIR-EXPERIMENTS-17
FAIR-EXPERIMENTS-18
INSTRUMENTS-METHODS-16
INSTRUMENTS-METHODS-26
INSTRUMENTS-METHODS-40
INSTRUMENTS-METHODS-41

FAIR: The FLAIR Collaboration

A Facility for Low-energy Antiproton and Ion Research
< http://www-linux.gsi.de/∼flair/>
Spokesperson: E. Widmann (Austria)

Contributions in this report:
FAIR-EXPERIMENTS-32

FAIR: The HEDgeHOB Collaboration

High Energy Density Matter generated by Heavy iOn Beams
<http://hedgehob.physik.tu-darmstadt.de>
Spokesperson: Hoffmann, D. H. H., Darmstadt (Germany)

Contributions in this report:
PLPY-PHELIX-09
PLPY-PHELIX-11
PLPY-PHELIX-12
PLPY-PHELIX-14

The PANDA Collaboration

<http://www.ep1.rub.de/∼panda/auto/_home.htm>
Spokesperson: U. Wiedner, Uppsala (Sweden)

Contributions in this report:
FAIR-EXPERIMENTS-02
FAIR-EXPERIMENTS-03
FAIR-EXPERIMENTS-04
FAIR-EXPERIMENTS-05
INSTRUMENTS-METHODS-23
INSTRUMENTS-METHODS-42
INSTRUMENTS-METHODS-43

FAIR: The NUSTAR Collaboration

International Nuclear Structure and Astrophysics Community GSI
<http://www.gsi.de/forschung/kp/kp2/nustar.html>

As part of FAIR-NUSTAR: The DESPEC Collaboration

Decay Spectroscopy
Spokesperson: B. Rubio, Valencia (Spain)

Contributions in this report:
FAIR-EXPERIMENTS-26
FAIR-EXPERIMENTS-27
FAIR-EXPERIMENTS-29

As part of FAIR-NUSTAR: The HISPEC Collaboration

High resolution Spectroscopy
Spokesperson: Z. Podolyak, Surrey (United Kingdom)

Contributions in this report:
FAIR-EXPERIMENTS-25
FAIR-EXPERIMENTS-28

As part of FAIR-NUSTAR: The R^3B Collaboration

Reactions with Relativistic Radioactive Beams
<http://www-land.gsi.de/r3b/>

* Only listed are colloborations contributed to this report.

Spokesperson: T. Aumann Darmstadt (Germany)

Contributions in this report:
FAIR-EXPERIMENTS-19
FAIR-EXPERIMENTS-20
FAIR-EXPERIMENTS-21
FAIR-EXPERIMENTS-22

As part of FAIR-NUSTAR: The ELISe Collaboration

ELectron-Ion Scattering in a Storage Ring (eA collider)
<http://www.gsi.de/zukunftsprojekt/experimente/elise/>
Spokesperson: H. Simon, Darmstadt (Germany)

Contribution in this report:
FAIR-EXPERIMENTS-23
FAIR-EXPERIMENTS-24

As part of FAIR-NUSTAR: The EXL Collaboration

Exotic nuclei studied in light-ion induced reactions at the NESR storage ring
<http://ns.ph.liv.ac.uk/∼mc/EXL/collaboration/EXL-collaboration.html>
Spokesperson: M. Chartier, Liverpool (United Kingdom)

Contributions in this report:
FAIR-EXPERIMENTS-30
FAIR-EXPERIMENTS-31

As part of FAIR-NUSTAR: The LEB Collaboration

Low Energy Branch
Spokesperson: C. Scheidenberger, Darmstadt (Germany)

Contributions in this report:
FAIR-ACCELERATORS-11
FAIR-EXPERIMENTS-35
FAIR-EXPERIMENTS-36

As part of FAIR-NUSTAR: The Super-FRS Collaboration

Contributions in this report:
FAIR-ACCELERATORS-10
INSTRUMENTS-METHODS-06
INSTRUMENTS-METHODS-07
INSTRUMENTS-METHODS-08
INSTRUMENTS-METHODS-09

FAIR: The SPARC Collaboration

Stored Particles Atomic Physics Collaboration
<http://www.gsi.de/zukunftsprojekt/experimente/sparc/index_e.html>
Spokesperson: R. Schuch, Stockholm (Sweden)

Contributions in this report:
ATOMIC-PHYSICS-19
ATOMIC-PHYSICS-26

FAIR: The WDM Collaboration

Radiative Properties of Warm Dense Matter Produced by Intense Heavy Ion Beams
<http://www.gsi.de/phelix/Experiments/FAIR/WDM/index.html>
Spokesperson: F. B. Rosmej

Contributions in this report:
FAIR-EXPERIMENTS-33

The SIS/ESR/UNILAC Collaborations

The ALADiN 2000 Collaboration

<http://www-kp3.gsi.de/www/kp3/aladinhome.html>
Spokesperson: W. Trautmann, Darmstadt (Germany)

Contributions in this report:
NQMA-EXPERIMENTS-01
NQMA-EXPERIMENTS-03
NQMA-EXPERIMENTS-02 (INDRA-ALADIN)

FAIR: The CHARMS Collaboration

Collaboration for High-Accuracy Experiments on Nuclear Reaction Mechanisms with magnetic Spectrometers
<http://www.gsi.de/charms/>
Spokesperson: Karl-Heinz Schmidt, GSI

Contributions in this report:
NUSTAR-EXPERIMENTS-17
NUSTAR-EXPERIMENTS-18
NUSTAR-EXPERIMENTS-20
NUSTAR-THEORY-11

The FOPI Collaboration

4π Detector System for Charged Particles
<http://www-fopi.gsi.de/>
Spokesperson: N. Herrmann, Heidelberg (Germany)

Contributions in this report:
INSTRUMENTS-METHODS-24
INSTRUMENTS-METHODS-25
NQMA-EXPERIMENTS-05
NQMA-EXPERIMENTS-06

The HADES Collaboration

<http://www-hades.gsi.de>
Spokesperson: Salabura, P.

Contributions in this report:
INSTRUMENTS-METHODS-30
NQMA-EXPERIMENTS-07

The HITRAP Collaboration

HITRAP - A Facility for Experiments with Heavy Highly Charged Ions and Antiprotons
< http://www.gsi.de/forschung/ap/projects/hitrap/index.html>
Technical Coordinator: O. Kester (GSI), Scientific Coordinator: W. Quint (GSI)

Contributions in this report:
ATOMIC-PHYSICS-15
ATOMIC-PHYSICS-16
ATOMIC-PHYSICS-18
ATOMIC-PHYSICS-24
ATOMIC-PHYSICS-25
ATOMIC-PHYSICS-30
GSI-ACCELERATORS-10

The ILIAS Collaboration

Ion and Laser beam Interaction and Application Studies
Spokesperson: P. Mulser, Darmstadt (Germany)

Contributions in this report:
PLPY-PHELIX-23
PLPY-PHELIX-24
PLPY-PHELIX-25
PLPY-PHELIX-26
PLPY-PHELIX-29

The PHELIX Collaboration

Petawatt High-Energy Laser for Heavy Ion Experiments
<http://www.gsi.de/forschung/phelix>
Spokesperson: K. Witte (GSI)

Contributions in this report:
ATOMIC-PHYSICS-28
PLPY-PHELIX-15
PLPY-PHELIX-16
PLPY-PHELIX-17
PLPY-PHELIX-19
PLPY-PHELIX-21
PLPY-PHELIX-27

The LAND-FRS Collaboration

Large Area Neutron time of flight Detector – Fragment Separator
Spokesperson: T. Aumann, Darmstadt (Germany)

Contributions in this report:
NUSTAR-EXPERIMENTS-15

The NoRDia Collaboration

Novel Radiation Hard CVD Diamond Detectors for Hadron Physics
<http://www-norhdia.gsi.de>
Cordinator at GSI: E. Berdermann.

Contributions in this report:
INSTRUMENTS-METHODS-02 (NoRHDia)
INSTRUMENTS-METHODS-03 (NoRHDia)

The RISING Collaboration

<http://www-linux.gsi.de/EB_at_GSI/index.html>
Spokesperson: H.-J. Wollersheim, GSI, Darmstadt (Germany)
Contributions in this report:
NUSTAR-EXPERIMENTS-06
NUSTAR-EXPERIMENTS-07
NUSTAR-EXPERIMENTS-08

NUSTAR-EXPERIMENTS-10
NUSTAR-EXPERIMENTS-12

The g-factors at RISING Collaboration

< http://www-linux.gsi.de/w̃olle/EB_at_GSI/G-FACTOR/>
Spokesperson: G. Neyens IKS, KU Leuven (Belgium)
Contributions in this report:
NUSTAR-EXPERIMENTS-11
NUSTAR-EXPERIMENTS-13
NUSTAR-EXPERIMENTS-14

The SHIP Collaboration

Separator for Heavy Ion reaction Products
<http:/www.gsi.de/forschung/kp/kp2/ship/>
Spokesperson: S. Hofmann, GSI Contributions in this report:
NUSTAR-SHE-01
NUSTAR-SHE-02
NUSTAR-SHE-03
NUSTAR-SHE-04
NUSTAR-SHE-05

The SHIPTRAP Collaboration

<http://www.gsi.de/forschung/ap/projects/shiptrap/>
Spokesperson: F. Herfurth, Darmstadt (Germany)
Contributions in this report:
ATOMIC-PHYSICS-12
ATOMIC-PHYSICS-23

The TASCA Collaboration

Transactinide Separator and Chemistry Apparatus
<http://www.gsi.de/tasca/>
Spokesperson: M. Schädel, GSI

Contributions in this report:
INSTRUMENTS-METHODS-05
NUSTAR-SHE-09
NUSTAR-SHE-10
NUSTAR-SHE-11
NUSTAR-SHE-12

Other collaborations e. g. at external institutions

The ALICE Collaboration

A Large Ion Collider Experiment at CERN LHC
<http://alice.web.cern.ch/Alice/AliceNew/collaboration/>
The collaborations contains 27 countries, 83 institutes, and about 1000 members. Here only the participants of the GSI are listed.
Leader at the GSI: P. Braun-Munzinger

Contributions in this report:
INSTRUMENTS-METHODS-31
INSTRUMENTS-METHODS-32
INSTRUMENTS-METHODS-33
NQMA-EXPERIMENTS-14
NQMA-EXPERIMENTS-15

The ALICE TRD Collaboration

The Transition Radiation Detector of the ALICE experiment at LHC
<http://www-alice.gsi.de/trd>
Project leader: J. Stachel, Heidelberg (Germany)
Contributions in this report:
INSTRUMENTS-METHODS-34
INSTRUMENTS-METHODS-35
INSTRUMENTS-METHODS-36
INSTRUMENTS-METHODS-38
INSTRUMENTS-METHODS-39

The CERES Collaboration

Cherenkov Ring Electron Pair Spectrometer at the CERN SPS
<http://www.physi.uni-heidelberg.de/physi/ceres/>
Spokesperson: J. Stachel, Heidelberg (Germany)

Contributions in this report:
NQMA-EXPERIMENTS-08
NQMA-EXPERIMENTS-09
NQMA-EXPERIMENTS-10

The NA49 Collaboration

Large Acceptance Hadron Detector for an Investigation of Pb-induced Reactions at the CERN SPS
<http://na49info.cern.ch/>
Spokesperson: P. Seyboth

Contributions in this report:
NQMA-EXPERIMENTS-11
NQMA-EXPERIMENTS-12
NQMA-EXPERIMENTS-13
NQMA-EXPERIMENTS-16

The ISOLTRAP Collaboration

<http://isoltrap.web.cern.ch/isoltrap>

Contributions in this report:
ATOMIC-PHYSICS-13
ATOMIC-PHYSICS-14

Other collaborations:

INSTRUMENTS-METHODS-22
INSTRUMENTS-METHODS-27 (HyPHI)
INSTRUMENTS-METHODS-28 (HyPHI)
INSTRUMENTS-METHODS-29 (HyPHI)
MATERIALS-14
NUSTAR-EXPERIMENTS-19
RADIATION-BIOPHYSICS-23 (ALTEA)

Connection between contributions to this report and experiment numbers at the GSI accelerators:

BIO-13 RADIATION-BIOPHYSICS-15
BIO-14 RADIATION-BIOPHYSICS-20
BIO-07 RADIATION-BIOPHYSICS-04
BIO-14 RADIATION-BIOPHYSICS-12
BIO-14 RADIATION-BIOPHYSICS-14
BIO-14 RADIATION-BIOPHYSICS-17
BIO-16 RADIATION-BIOPHYSICS-03
BIO-01 RADIATION-BIOPHYSICS-21
E039 ATOMIC-PHYSICS-03
E045 ATOMIC-PHYSICS-06
E065 ATOMIC-PHYSICS-07
E067 ATOMIC-PHYSICS-02
E069 ATOMIC-PHYSICS-09
E069 ATOMIC-PHYSICS-10
E070 ATOMIC-PHYSICS-01
E070 ATOMIC-PHYSICS-08
E075 ATOMIC-PHYSICS-15
P008 PLPY-PHELIX-22
R240 NUSTAR-SHE-05
S139 INSTRUMENTS-METHODS-28
S174 NUSTAR-EXPERIMENTS-09
SBIO-08 RADIATION-BIOPHYSICS-26
SBIO-09 RADIATION-BIOPHYSICS-19
S184 NUSTAR-EXPERIMENTS-17
S185 NQMA-EXPERIMENTS-02
S227 NUSTAR-EXPERIMENTS-03
S244a NUSTAR-EXPERIMENTS-08
S244 NUSTAR-EXPERIMENTS-06
S244 NUSTAR-EXPERIMENTS-07
S244 NUSTAR-EXPERIMENTS-10
S248 NUSTAR-EXPERIMENTS-19
S254 NQMA-EXPERIMENTS-01
S254 NQMA-EXPERIMENTS-03
S258 FAIR-EXPERIMENTS-36
S261 NQMA-EXPERIMENTS-05
S271 NUSTAR-EXPERIMENTS-16
S280 INSTRUMENTS-METHODS-02
S286 INSTRUMENTS-METHODS-37
S291 FAIR-ACCELERATORS-29
S299 NUSTAR-EXPERIMENTS-12
S305 NUSTAR-EXPERIMENTS-09
S310 NUSTAR-EXPERIMENTS-13
S311 NUSTAR-EXPERIMENTS-11
S311 NUSTAR-EXPERIMENTS-14
S319 INSTRUMENTS-METHODS-27
S319 INSTRUMENTS-METHODS-29
S319 NUSTAR-EXPERIMENTS-21
S319 NUSTAR-EXPERIMENTS-22
S328 FAIR-EXPERIMENTS-20
SITH EXTERNAL-HIT-08
SITH RADIATION-BIOPHYSICS-28
STHE RADIATION-BIOPHYSICS-30
STHE RADIATION-BIOPHYSICS-35
U165 ATOMIC-PHYSICS-11
U197 NUSTAR-EXPERIMENTS-05
U205 NUSTAR-SHE-06
U205 NUSTAR-SHE-07
U210 NUSTAR-SHE-08
U215 NUSTAR-SHE-04
U217 ATOMIC-PHYSICS-12
U219 NUSTAR-SHE-09
U219 NUSTAR-SHE-10
U219 NUSTAR-SHE-11
U219 NUSTAR-SHE-12
U224 PLPY-PHELIX-07
U224 PLPY-PHELIX-08
U225 NUSTAR-SHE-03
U226 PLPY-PHELIX-03
UMAT MATERIALS-24

EU projects at GSI

Compiled by R. Simon, M. Pantea, K. Große

FAIR Design Study 'DIRACsecondary-Beams'/FP6 (515873)
<http://www.gsi.de/fair/EU-Design-Study/index.html>
Coordinator: GSI, Darmstadt (Germany)
Project coordinator: J. Eschke
Steering committee: J. Eschke (GSI, chair), H. H. Gutbrod (GSI), W. F. Henning (GSI), P. Gianotti (Frascati), R. Krücken (München), R. Maier (FZJ), B. Franzke (GSI), D. Krämer (GSI)
Contact at GSI: J. Eschke, K. Berghöfer, F. Weißbach

Contributions in this report:
FAIR-ACCELERATORS-01
FAIR-ACCELERATORS-02
FAIR-ACCELERATORS-04
FAIR-ACCELERATORS-10
FAIR-ACCELERATORS-11
FAIR-ACCELERATORS-13
FAIR-ACCELERATORS-16
FAIR-EXPERIMENTS-28
FAIR-EXPERIMENTS-35
FAIR-EXPERIMENTS-37
GSI-ACCELERATORS-12
INSTRUMENTS-METHODS-43

FAIR Construction 'DIRAC-PHASE 1'/FP6 (515876)
<http://www.gsi.de/fair/EU-Construction/index.html>
Coordinator: GSI, Darmstadt (Germany)
Project coordinator: J. Eschke
Steering committee: J. Eschke (GSI, chair), H. H. Gutbrod (GSI), W. F. Henning (GSI), H. Eickhoff (GSI), J.-E. Ducret (CEA), H. Ströbele (U-Frankfurt/M.)
Contact at GSI: J. Eschke, K. Berghöfer, F. Weißbach

Contribution in this report:
FAIR-ACCELERATORS-18
GSI-ACCELERATORS-13
GSI-ACCELERATORS-14
GSI-ACCELERATORS-15
GSI-ACCELERATORS-16
INSTRUMENTS-METHODS-30
NQMA-EXPERIMENTS-07

HADRONPHYSICS/FP6 (RII3-CT-2004-506078)
<http://hadronphysics.infn.it/>
Coordinator: INFN Frascati (Italy)
Project coordinator: C. Guaraldo (LNF-INFN)
Management board: M. Anselmino (INFN), T. Johansson (Univ. Uppsala), H. Koch (Univ. Bochum), L. Riccati (INFN), G. Rosner (Univ. Glasgow), R. Simon (GSI)
Project coordinator at GSI: R. Simon

Contributions in this report:
FAIR-EXPERIMENTS-03
FAIR-EXPERIMENTS-04
FAIR-EXPERIMENTS-05
FAIR-EXPERIMENTS-06
FAIR-EXPERIMENTS-07
FAIR-EXPERIMENTS-08
FAIR-EXPERIMENTS-09
FAIR-EXPERIMENTS-10
FAIR-EXPERIMENTS-11
FAIR-EXPERIMENTS-12
FAIR-EXPERIMENTS-14
FAIR-EXPERIMENTS-15
FAIR-EXPERIMENTS-17
FAIR-EXPERIMENTS-18
INSTRUMENTS-METHODS-02
INSTRUMENTS-METHODS-17
INSTRUMENTS-METHODS-22
INSTRUMENTS-METHODS-23
INSTRUMENTS-METHODS-24
INSTRUMENTS-METHODS-26
INSTRUMENTS-METHODS-37
INSTRUMENTS-METHODS-40
INSTRUMENTS-METHODS-41
NQMA-THEORY-01

EURONS/FP6 (RII3-CT-2004-506065)
<http://www.gsi.de/informationen/jofu/EURONS/>
Coordinator: GSI, Darmstadt (Germany)
Project coordinator: A. C. Müller (IN2P3-IPNO), C. Scheidenberger (GSI, deputy coordinator)
Executive board: P. Butler (CERN), P. Van Duppen (U- Leuven), K.-D. Groß (GSI), S. Harissopoulos (NCSR Demokritos), R. Julin (Univ. Jyväskylä), S. Lenzi (INFN Padova)
Contact at GSI: I. Reinhard; M. Pantea

Contributions in this report:
ATOMIC-PHYSICS-01
ATOMIC-PHYSICS-03
ATOMIC-PHYSICS-05
ATOMIC-PHYSICS-12
ATOMIC-PHYSICS-13
ATOMIC-PHYSICS-14
ATOMIC-PHYSICS-20
ATOMIC-PHYSICS-23
FAIR-ACCELERATORS-30
FAIR-EXPERIMENTS-19
FAIR-EXPERIMENTS-20
FAIR-EXPERIMENTS-21
FAIR-EXPERIMENTS-22
FAIR-EXPERIMENTS-27
FAIR-EXPERIMENTS-30
GSI-ACCELERATORS-08
NUSTAR-EXPERIMENTS-06
NUSTAR-EXPERIMENTS-07

NUSTAR-EXPERIMENTS-08
NUSTAR-EXPERIMENTS-09
NUSTAR-EXPERIMENTS-11
NUSTAR-EXPERIMENTS-12
NUSTAR-EXPERIMENTS-13
NUSTAR-EXPERIMENTS-14
NUSTAR-EXPERIMENTS-16
NUSTAR-EXPERIMENTS-19
RADIATION-BIOPHYSICS-18
RADIATION-BIOPHYSICS-19

CARE/FP6 (RII3-CT-2003-506395)
<http://esgard.lal.in2p3.fr/Project/Activities/Current/>
Coordinator: CEA Saclay (France)
Project coordinator: R. Aleksan (CEA)
Project coordinator at GSI: H. Eickhoff
Contact at GSI: L. Groening

Contributions in this report:
FAIR-ACCELERATORS-05
FAIR-ACCELERATORS-24
GSI-ACCELERATORS-11

EGEE/FP6 (INFSO-RI-508833)
<http://public.eu-egee.org/>
Coordinator: CERN (Switzerland)
Project coordinator: B. Jones (CERN), D. Kranzlmüller (CERN)
Project coordinator at GSI: P. Malzacher
Contact at GSI: P. Malzacher

Contributions in this report:
INSTRUMENTS-METHODS-14

Laserlab/FP6 (RII3-CT-2003-506350)
<http://www.laserlab-europe.net>
Coordinator: Forschungsverbund Berlin (Germany)
Project coordinator: W. Sandner (Berlin)
Project coordinator at GSI: T. Kühl
Contact at GSI: T. Kühl
Contributions in this report:
PLPY-PHELIX-19
PLPY-PHELIX-20
PLPY-PHELIX-21
PLPY-PHELIX-22

EUROTeV/FP6 (011899 RIDS)
<http://www.eurotev.org>
Coordinator: DESY, Hamburg (Germany)
Project coordinator: E. Elsen (DESY)
Project coordinator at GSI: H. Eickhoff
Contact at GSI: P. Schütt

Cellion/FP6 (MRTN-CT-2003-503923)
Network of Excellence
<http://cellion.ifj.edu.pl>
Project coordinator: Z. Stachura (PAN)
Contact at GSI: B. Fischer

Contribution in this report:
RADIATION-BIOPHYSICS-03

EURISOL-Design Study/FP6 (515768 RIDS)
<http://www.eurisol.org>
Coordinator: INFN-LNL (Italy)
Project coordinator: Y. Blumenfeld (IPN-Orsay)
Project coordinator at GSI: K.-H. Schmidt
Contact at GSI: A. Kelic

Contributions in this report:
ATOMIC-PHYSICS-17
GSI-ACCELERATORS-17

EUROTRANS/FP6 (516520 F16W)
<http://nuclear-server.fzk.de/eurotrans/>
Coordinator: FZK, Karlsruhe (Germany)
Project coordinator: J. U. Knebel (NUCLEAR)
Project coordinator at GSI: K.-H. Schmidt
Contact at GSI: A. Kelic

EURATOM-Fellowships FISA2004/FP6 (012985 FI6W) and RESPA2004/FP6 (516352 F16W)
Project coordinator: K.-H. Schmidt
Contact at GSI: A. Kelic

Contribution in this report:
NUSTAR-EXPERIMENTS-17

Contributions to other EU projects:
FAIR-ACCELERATORS-29
FAIR-EXPERIMENTS-23
FAIR-EXPERIMENTS-24
INSTRUMENTS-METHODS-39
NQMA-THEORY-10
NQMA-THEORY-17
RADIATION-BIOPHYSICS-33

Invited talks at conferences at other institutions

Compiled by K. Große

Ackermann, D.: **Schwere Elemente - Kernmaterie unter extremen Bedingungen.** Johannes Gutenberg-Universitaet Mainz (Germany), 04.12.2006.

Ackermann, D.: **Superheavy Elements - Synthesis, Structure and Reaction Mechanism.** Conference on Nuclear Structure Physics, Shanghai (China), June 2006.

Ackermann, D.: **Superheavy Elements - Synthesis, Structure and Reaction Mechanism.** FUSION06 - Reaction Mechanism and Nuclear Structure at the Coulomb Barrier, San Servolo, Venice (Italy), March 2006.

Ackermann, D.: **Superheavy Elements - Synthesis, Structure and Reaction Mechanism.** IX International Conference on Nucleus Nucleus Collisions (NN2006), Rio de Janeiro (Brazil), August 2006.

Andronic, A.: **Hadron production at chemical equilibrium.** Brookhaven National Laboratory (USA), 16.-17.02.2006.

Andronic, A.: **Multiwire proportional drift chambers:ALICE TRD and TPC.** International Research Training Group Workshop, Heidelberg (Germany), 05.10.2006.

Andronic, A.: **Statistical hadronization of heavy quarks in nucleus-nucleus.** ECT International Workshop on Heavy Flavor Physics in Heavy Ion Collisions at the LHC, Trento (Italy), 06.-09.09.2006.

Augustin, I.: **FAIR - die Zunkunft der GSI.** GSI, Open Day, 11.09.2006.

Augustin, I.: **Status of FAIR.** MESON 2006, Krakau (Poland), 09.06.2006.

Augustin, I.: **Status of FAIR.** Syposium on Physics of High Baryon Density, Strasbourg (France), 19.09.2006.

Augustin, I.: **Status of the FAIR Project.** CAARI 2006, Ft. Worth, Texas (USA), 22.08.2006.

Augustin, I.: **The International Facility for Antiproton and Ion Research.** Info-Day, Ministry for Research and Higher Education, Warsaw (Poland), 08.12.2006.

Aumann, T.: **A next-generation setup for scattering experiments with high-energy beams.** International Workshop on Nuclear Physics with RIBF, RIKEN, Saitama (Japan), August 2006.

Aumann, T.: **Experiments with rare-isotope beams at FAIR.** Internationales Graduiertenkolleg Basel-Graz-Tübingen, University of Basel (Switzerland), May 2006.

Aumann, T.: **Prospect of Nuclear Structure Studies at the Future FAIR Accelerators.** Erice School on Nuclear Physics 2006, Erice (Italy), September 2006.

Aumann, T.: **Scattering experiments with high-energy radioactive beams at the future FAIR facility.** IX International Conference on Nucleus Nucleus Collisions (NN2006), Rio de Janeiro (Brazil), August 2006.

Aumann, T.: **Single-particle and collective properties of radioactive nuclei investigated with R3B.** GANIL, Caen (France), July 2006.

Barth, W.: **Future UNILAC design.** INTAS-final-meeting at GSI (Germany), 05.-06.09.2006.

Bayer, W.: **HIPPI Beam Dynamics Machine Experiments.** HIPPI-WP5-meeting, 27.-28.04.2006.

Bayer, W.: **HIPPI beam experiments at the UNILAC.** INTAS-final-meeting at GSI (Germany), 05.-06.09.2006.

Bender,M.: **Untersuchung der Ionenstrahl induzierten Desorption mittels UHV-ERDA.** LMU München (Germany), 05.-06.09.2006.

Bert, C.: **Treatment of moving targets with scanned ion beams.** Joint Seminar of Biological and Medical Division, National Institute of Radiological Sciences (NIRS), Chiba (Japan), 21.09.2006.

Boine-Frankenheim, O.: **Implementation and validation of space charge and impedance kicks in the code PATRIC for studies of transverse coherent instabilities in the FAIR rings.** ICAP 2006, Chamonix (France), 2006.

Boine-Frankenheim, O.: **Instabilities and Space Charge Effects in High Intensity Ring Accelerators.** EPAC 2006, Edinburgh (Great Britain), 2006.

Boretzky, K.: **Dipole response of neutron-rich Sn isotopes.** Collective Motion in Exotic Nuclei II Conference, St. Goar (Germany), June 2006.

Botvina, A. S.: **Multifragmentation of nuclei and properties of stellar matter in supernova II explosions.** Forschungszentrum Jülich, Jülich (Germany), June 2006.

Botvina, A. S.: **Properties of stellar matter in supernova II explosions.** International Workshop XXXIV on Gross Properties of Nuclei and Nuclear Excitations, Hirschegg (Germany), January 2006.

Botvina, A. S.: **Symmetry energy of fragments produced in multifragmentation and properties of stellar matter in**

supernova II explosions. Frühjahrstagung der Deutschen Physikalischen Gesellschaft, München (Germany), March 2006.

Braun-Munzinger, P.: **Der Urknall im Labor:Erforschung von Urknallmaterie mit Schwerionenstoessen.** Vorlesungsreihe im Studienstiftungs-Kolleg, Bad Honnef, April 2006.

Braun-Munzinger, P.: **Prospects and challenges for strong interaction physics with FAIR.** Graduiertenkolleg Tübingen-Basel, May 2006.

Braun-Munzinger, P.: **Quarkonium production and the statistical hadronization model.** Workshop on Heavy Flavor, Tsinghua university, Beijing (China), November 2006.

Braun-Munzinger, P.: **Quarkonium production at RHIC and prospects for LHC.** Plenary talk, QM2006 conference, Shanghai (China), November 2006.

Braun-Munzinger, P.: **Quarkonium production in nucleus-nucleus collisions from FAIR to LHC energy.** Workshop on physics in the LHC era, Valparaiso, (Chile), December 2006.

Braun-Munzinger, P.: **Relativistic nucleus-nucleus collisions.** Studienstiftungskolleg, Saarbruecken, October 2006.

Braun-Munzinger, P.: **Statistical hadronization and quarkonia production at RHIC and LHC.** Heavy Ion Forum, CERN, July 2006.

Braun-Munzinger, P.: **Thermalization, hadronization, and the QCD phase boundary.** SQM2006 conference, Los Angeles (US), March 2006.

Braun-Munzinger, P.: **Ultra-relativistic nuclear collisions and the QCD phase boundary.** Universität Mainz, Kolloquium, February 2006.

Cornelius, T. W.: **Bismuth nanowires: fabrication and characterisation.** Seminar on solid state physics, Technical University Karlsruhe, Institute of Physics, Karlsruhe (Germany), 24.04.2006.

Cornelius, T. W.: **Size effects in bismuth nanowires.** Ecole Polytéchnique Fédérale de Lausanne EPFL, Lausanne (Switzerland), 16.02.2006.

Cornelius, T. W.: **Size effects in bismuth nanowires.** Technical University of Denmark (DTU), Department of Micro- and Nanotechnology, Lyngby (Denmark),, 31.01.2006.

Dahl, L.: **Front-end upgrade overview.** INTAS-final-meeting at GSI (Germany), 05.-06.09.2006.

Dahl, L.: **GSI HITRAP.** INTAS-final-meeting at GSI (Germany), 05.-06.09.2006.

Doornenbal, P.: **Spectroscopy of 36 Ca via two-step Fragmentation.** Gamma-Ray Spectroscopy in Europe, Present and Future Challenges, Trient (Italy), May 2006.

Doornenbal,P.: **Shell Structure, Collectivity and Nuclear Shapes - RISING in-beam Experiments at Relativistic energies.** International Conference on Nuclear Structure Physics, Shanghai (China), June 2006.

Düllmann, C. E.: **Auf dem Weg zu neuen Verbindungsklassen von Transactinoiden: Vorexperimente mit flüchtigen Metallkomplexen von Hafnium und Zirkonium mit Hexafluooactetylaceton.** Seminar fuer Kern- und Radiochemie, Johannes Gutenberg-Universität Mainz (Germany), 14.06.2006.

Düllmann, C. E.: **Chemistry Experiments with Long-Lived Preseparated Transactinides - Today's Achievements and.** Workshop on Atomic Properties of the Heaviest Elements, Abtei Frauenwörth im Chiemsee (Germany), September 2006.

Düllmann, C. E.: **Physical Preseparation for chemistry experiments - an overview and an example.** 15th Radiochemical Conference, RadChem 2006, Marianske Lazne (Czech Republic), April 2006.

Düllmann, C. E.: **Physical Preseparation:a powerful new method for transactinide chemists.** International Symposium on Exotic Nuclei, 'EXON 2006', Khanty-Mansiysk (Russia), July 2006.

Düllmann, C. E.: **Report of the 'Recoil Transfer Chamber' working group.** TASCA06 - 5th Workshop on Recoil Separator for Superheavy Element Chemistry, Garching (Germany), September 2006.

Düllmann, C. E.: **Towards a new compound class of transactinides - Studies of volatile group 4 metal complexes with hexafluoroacetylactone.** Seminar des Labors fuer Radio- und Umweltchemie, Paul Scherrer Institut, Villigen (Switzerland), 23.06.2006.

Egelhof, P.: **Light Ion Induced Direct Reactions in Inverse Kinematics at Low.** Int. School of Nuclear Physics, Erice (Italy), September 2006.

Egelhof, P.: **Proton Scattering Measurements at GSI and Future Prospects at FAIR and.** IOP Meeting on Neutron Skins, Liverpool (UK), November 2006.

Elsässer, T.: **Mit schweren Ionen gegen den Krebs.** Physikalischer Verein Frankfurt, Univ. Frankfurt (Germany), 13.06.2006.

Elsässer, T.: **The Local Effect Model - Simulation of the Relative Biological Effectiveness (RBE) for Heavy Ion Treatment Planning.** Joint Seminar of Biological and Medical Division, National Institute of Radiological Sciences (NIRS), Chiba (Japan), 25.10.2006.

Elsässer, T.: **The Local Effect Model - Simulation of the Relative Biological Effectiveness (RBE) for Heavy Ion Treatment Planning.** Seminar on Medical Physics, Jagiellonian University of Cracow (Poland), 02.03.2006.

Emling, H.: **Experiments with Exotic Beams at GSI and FAIR.** DAE-BRNS Symposium on Nuclear Physics, Vadodara (India), December 2006.

Emling, H.: **Nuclear Structure from Medium-/High-Energy Reactions with RIB's.** NSCL User Workshop, East Lansing (USA), June 2006.

Emling, H.: **Pygmy Resonances.** 2nd German-Japanese Workshop on Nuclear Structure and Astrophysics, RIKEN, Saitama (Japan), September 2006.

Emling, H.: **Pygmy and Giant Dipole Resonances in Unstable Neutron-Rich Nuclei.** IReS Strassbourg (France), January 2006.

Emling, H.: **The Rare-Isotope-Beam Facility at FAIR.** Seventh International Conference on Radioactive Nuclear Beams (RNB7), Cortina d'Ampezzo (Italy), July 2006.

Eschke, J.; Friese, V.; Hne, C.; Mller, W.F.J.; Senger, P.: **The FAIR Project - Physics with CBM - The CBM Experiment.** CBM Seminar at USTC Hefei and CCNU Wuhan (China), 21.-23.11.2006.

Feldmeier, H.: **'Modern Nuclear Structure Theory - From Realistic Interactions to Nuclei'.** Beijing, University, International Summer School on Subatomic Physics (China) 21.08.2006.

Feldmeier, H.: **Halo and cluster structures in Fermionic Molecular Dynamics.** ECT* workshop in Trento, 'Physics of Halo Nuclei' (Italy), 30.10.2006.

Feldmeier, H.: **Von Schalen, Clustern und Halos, Neue Konzepte zur Lösung des nuklearen Vielteilchenproblems.** Physik Kolloquium, TU-Dresden (Germany), 02.05.2006.

Fischer, B.: **How to shoot precisely with single high energy heavy ions.** 19th International Conference on the Application of Accelerators in Research and Industry CAARI, Dallas/Fort Worth (USA),, 20.-25.08.2006.

Fischer, E.: **o.T..** ASC 2006, Seattle (USA), 2006.

Fournier, C.: **Exposure of human fibroblasts to low and high LET irradiation: occurence of premature differentiation and of genetic instability in long-term cultures.** 36th COSPAR Colloquium, Mutagenetic consequence in the space environment, Xi'an (China), July 2006.

Fournier, C.: **Studies on premature aging and differentiation in human fibroblasts after exposure to high and low fluencies of heavy ions.** The National Laboratory of Heavy Ion Accelerator, Lanzhou (China), July 2006.

Fournier, C.: **Studies on the cell cycle arrest and premature aging in human fibroblasts after exposure to high and low fluences of heavy ions.** Cancer Centre Karolinska (CCK), Stockholm (Sweden), 2006.

Fournier, C.: **Studies on the cell cycle arrest and premature aging in human fibroblasts after exposure to high and low fluencies of heavy ions.** Chinese Institute for Atomic Energy, Beijing (China), July 2006.

Fournier, C.: **Studies on the cellular bystander response after exposure to high LET irradiation.** Cospar Meeting 2006, Beijing (China), July 2006.

Franchetti, G.: **Resonance trapping due to space charge and synchrotron motion, in theory, simulations, and experiment.** ICFA Advanced beam dynamics workshop 2006, Tsukuba (Japan), 2006.

Franchetti, G.: **Towards the description of long term self-consistent effects in space charge induced resonance trapping.** ICAP 2006, Chamonix (France), 2006.

Friman, B.: **Lecture series on 'Effective Theories in Many-Body Fermi Systems'.** ECM, Facultat de Fisica, University of Barcelona (Spain), 08.-11.05.2006.

Friman, B.: **Lecture series on 'RG approach to nucleonic matter'.** ECT School on RG and EFT to Many-Body Systems, 27.02-10.03.2006.

Geissel, H.: **NUSTAR Experiments with the Oresent and Future Facilities at GSI-FAIR.** Symposium Daresbury, Daresbury (UK), February 2006.

Geissel, H.: **Precision Experiments with relativistic ions at GSI.** Seminar Universität London, London (United Kingdom), 14.09.2006.

Geissel, H.: **Present and Future Experiments with Stored Exotic Nuclei at Relativistic Energies.** Seventh International Conference on Radioactive Nuclear Beams RNB7, Cortina d'Ampezzo (Italy), June 2006.

Geissel, H.: **The Super-FRS project, overview and status.** Second international expert meeting on next generation high-intensity fragment separators, RIKEN, Saitama (Japan), February 2006.

Gonzalez Diaz, D.: **Modelling the RPC behaviour at high rates..** Universidade de Santiago de Compostela (Spain), 19.-22.09.2006.

Gorska, M.: **Nuclear structure far off stability - New results from RISING.** SENUF06 theory workshop, Tokyo University (Japan), March 2006.

Gorska, M.: **Nuclear structure far off stability - RISING Campaigns.** Zakopane'06, Zakopane (Poland), September 2006.

Gorska, M.: **Nuclear structure studies in the frame of RISING.** Institute of Experimental Physics, Warsaw University, Warsaw (Poland), December 2006.

Gorska, M.: **RISING:Phases and Recent results.** ISOLDE Workshop, CERN Geneva (Switzerland), February 2006.

Gorska, M.: **Structure of exotic nuclei observed in RISING experiments.** German-Japanese workshop 2006, RIKEN, Saitama (Japan), October 2006.

Groening, L.: **Development of the beam matching to the Alvarez.** INTAS-final-meeting at GSI (Germany), 05.-

06.09.2006.

Groening, L.: **HIPPI-experiments at the UNILAC.** HIPPI-WP5-meeting, 27.-28.04.2006.

Groening; L.: **GSI proton linac: Status quo.** INTAS-final-meeting at GSI (Germany), 05.-06.09.2006.

Guntoro, A.; Zipf, P.; Soffke, O.; Klingbeil, H.; Kumm, M.; Glesner, M.: **Implementation of Realtime and Highspeed Phase Detector on FPGA.** International Workshop On Applied Reconfigurable Computing ARC2006, Delft (Niederlande), 01.-03.03.2006.

Gutbrod, H. H.: **An International Facility for Antiproton and Ion Research in Europe.** INPAC Indien Particle Accelerator Conference (India), 04.11.2006.

Gutbrod, H. H.: **Paul Kienle and the GSI.** Paul Kienle: 75th Birthday Symposium, Austrian Academy of Science, Wien (Austria), 01.09.2006.

Gutbrod, H. H.: **Pion Freeze-Out Time in Pb-Pb Collisions at 158 A GeV/c. Studied via II-/II+ and k-/k+ Ratios.** WA98 Collaboration, CERN (Switzerland), 16.07.2006.

Gutbrod, H. H.: **Status of the FAIR Project.** 22nd Winter Workshop on Nuclear Dynamics, JINR Dubna (Russia), 19.04.2006.

Gutbrod, H. H.: **The International Facility for Antiproton and Ion Research - FAIR.** Helmholtz, Brüssel (Belgium), 18.09.2006.

Gutbrod, H. H.: **A place to test many of Walter's old and new ideas: FAIR - An International Facility for Antiproton and Ion Research.** ISHIP 2006, Frankfurt (Germany), 03.04.2006.

Gutbrod, H. H.: **Hadron Physics and Property of High Baryon Density Matter at FAIR.** International Workshop on Hadron Physics and Properties of High Baryon Density Matter, Xi'an (China), 24.11.2006.

H. Oeschler: **Centrality Dependence of Strange Particle Yields from SIS up to RHIC.** Brookhaven Nat. Lab., Upton NY (US), February 2006.

Heil, M.: **Branchings in the s-process path.** Exotic Radionuclides from Accelerator Waste for Science and Technology ERAWAST, PSI, Villigen (Switzerland), November 2006.

Heil, Michael: **The s process in massive stars.** Radioactive Beams, Nuclear Dynamics and Astrophysics, Erice, Sicily (Italy), September 2006.

Heil, Michael for the n_TOF collaboration: **Neutron capture cross section measurements for astrophysics at nTOF.** International Symposium on Nuclear Astrophysics - Nuclei in the Cosmos IX, Geneva (Switzerland), June 2006.

Henning, W.: **Bethe's Legacy in Nuclear Physics: From Nuclear Structure to Nuclear Matter.** Hans Bethe Symposium, Frankfurt (Germany), 13.03.2006.

Henning, W.: **FAIR Research and a Status Report.** Fifth International Conference on Perspectives in Hadronic Physics, Trieste (Italy), 22.-26.05.2006.

Henning, W.: **Heavy Ion Physics Gateway to the Unknown.** International Symposium on Heavy Ion Physics, Frankfurt (Germany), 03.04.2006.

Henning, W.: **Long-Term Solar Neutrino Flux and Storage Ring Physics at GSI.** Serbian Physical Society, Belgrad (Serbia), 27.03.2006.

Henning, W.: **The FAIR Project: Challenges and Opportunities.** IX International Conference on Nucleus Nucleus Collisions, Rio de Janeiro (Brazil), 28.08-01.09.2006.

Henning, W.: **The landscape of nuclei: How far, how soon?.** Nuclear Physics, the Core of Matter, the Fuel of Stars, A Symposium surveying the future of nuclear physics and celebrating 50 years of John Schiffer's research at Argonne, Chicago (USA), 21.-22.09.2006.

Henning, W.: **Von den Grundbausteinen zur komplexen Materie: Die neue Beschleunigeranlage FAIR bei der GSI Darmstadt.** TU Darmstadt, Seminar, 08.05.2006.

Heßberger, F. P.: **Experiments on Nuclear Structure and Synthesis of Superheavy Elements at SHIP.** Tours Symposium on Nuclear Physics VI, Tours (France), September 2006.

Heßberger, F. P.: **GSI Experiments on Synthesis and Nuclear Structure Investigations of Heaviest Nuclei.** Workshop on Atomic Properties of the Heaviest Elements, Abtei Frauenwörth im Chiemsee (Germany), September 2006.

Heßberger, F. P.: **Nuclear Structure Investigations in the Region of Superheavy Nuclei.** The International Conference on Nuclear Structure and Related Topics, Dubna (Russia), June 2006.

Heuser, J. M.: **Development of a Silicon Tracking and Vertex Detection System for the CBM Experiment at FAIR.** 15th International Workshop on Vertex Detectors (VERTEX 2006),Perugia (Italy), 25.-29.09.2006.

Heuser, J. M.: **The CBM Silicon Tracking System.** Presented on DETNI Collaboration Meeting, Perugia (Italy), 16.03.2006.

Heuser, J. M.: **The CBM Silicon Tracking System.** Presented on PANDA Collaboration Meeting, Dresden (Germany), 07.03.2006.

Höhne, C.: **System-size dependence of strangeness production at the SPS.** BNL workshop on Strangeness in collisions (USA), February 2006.

Höhne, C.: **The high baryon density CBM experiment and other QCD related research activites at the future FAIR**

facility in Germany. KEK, University of Tsukuba, University of Hiroshima, and RIKEN/ University of Tokyo (Japan), May 2006.

Hoffmann, Dieter H. H.: **Heavy Ion Fusion Research at GSI.** Heavy Ion Inertial Fusion HIF 06, St. Malo (France), 10.07.2006.

Hoffmann, Dieter H. H.: **Heavy Ion Matter Interaction to generate High Energy Density Matter States and the Application to Inertial Fusion Energy.** ION 06, Copenhagen (Denmark), 30.4 - 4.3 2006, 02.04.2006.

Hoffmann, Dieter H. H.: **Plasma Physics, Inertial Fusion and High Energy Density Physics.** GSI Students Program, GSI Darmstadt (Germany) 24.08.2006.

Hoffmann, Dieter H. H.: **Recent Warm Dense Matter Experiments and the propects of High Energy Density Physics at GSI and FAIR.** European Conference on Laser Interaction with Matter XXIX ECLIM, Madrid, Spain) June 11-16 2006,, 12.06.2006.

Hoffmann, Dieter H. H.: **Von Dunkler Materie, Exotischen Teilchen und der Hoffnung die Energiequelle der Sterne nutzbar zu machen.** GSI Wissenschaft für Alle‘, GSI Darmstadt (Germany), 01.11.2006.

Hoffmann, Dieter H. H. for the CAST collaboration: **Search for Axions with the CERN Axion Solar Telescope (CAST)- Staus Report-.** International Conference on High Energy Physics, Moscow (Russia), 27.07.2006.

Hofmann, S.: **Auf der Jagd nach superschweren Elementen.** Fachhochschule Darmstadt, Fachbereich Gestaltung, Darmstadt (Germany), 17.01.2006.

Hofmann, S.: **Search for SHE - Experiments.** ECOS - Town Meeting ’Opportunities with high intensity stable beams in Europe’, Paris (France), October 2006.

Hofmann, S.: **Studies of SHE at SHIP.** International Symposium on Exotic Nuclei, EXON 2006, Khanty-Mansiysk (Russia), July 2006.

Hofmann, S.: **Studies of Superheavy Elements at SHIP.** International Symposium on Heavy Ion Physics, ISHIP-2006, Frankfurt (Germany), March 2006.

Hofmann, S.: **Study of Superheavy Nuclei.** Workshop on Advanced Laser and Mass Spectroscopy, ALMAS-1;Innovative Physics Ideas, GSI Darmstadt (Germany), October 2006.

Hofmann, S.: **Superschwergewichte - Wie Atomkerne geschmiedet werden.** Universität Tübingen (Germany), 06.12.2006.

Hofmann, S.: **Von X-Strahlen zum neuen Element Röntgenium - Eine Kurze Geschichte zur Atom- und Kernphysik.** Remscheid-Lennep, anläßlich Verleihung der Röntgen-Plakette 2006, Germany, 13.05.2006.

Hollinger, R.; Barth, W.; Dahl, L.; Galonska, M.; Groening, L.; Gobin, R.; Meusel, O.: **High Current Beam Investigation at the SILHI-LEBT at CEA/Saclay.** LINAC 2006, Knoxville (USA), 2006.

Holzmann, R.: **Dilepton production:an experimental overview.** 2nd HADES Summer School, Siegen (Germany), September 2006.

Ivanov, Y.: **Hydrodynamics approach to heavy-ion collisions.** Helmholtz Int. Summer School, Dense Matter In Heavy Ion Collisions and Astrophysics, JINR LTP, Dubna (Russia), 21.08-01.09.2006.

Ivanov, Y.: **Transverse Flow in 3-Fluid Dynamics (AGS to SPS).** Workshop The Physics of High Baryon Density, ECT, Trento (Italy), 29.05-02.06.2006.

Iwase, H.: **Calculation of secondary neutron fields generated by high-energy heavy-ion reactions using the Monte-Carlo code PHITS.** International Workshop on Fast Neutron Detectors and Applications, Cape Town (South Africa), 06.04.2006.

Iwase, H.: **Energy deposition and radiation at the Super-FRS.** 11.05.2006.

Iwase, H.: **Experimental and theoretical study of the neutron dose produced by carbon ion therapy beams.** Tenth symposium on neutron dosimetry, Uppsala (Sweden) 16.06.2006.

Jacoby, J.: **Heavy Ion Beam Pumped KrF-Laser.** 16th International Heavy Ion Fusion Conference, Saint-Malo (France) 14.07.2006.

Kauschke, M.: **Kryosystem für FAIR.** DKV-Tagung Dresden (Germany), 2006.

Kauschke, M.; Xiang, Y.; Schroeder, C. H.: **Cryogenic Distribution System for FAIR.** DKV-Tagung Dresden (Germany), 2006.

Kelic, A.: **Experimental approaches to spallation reactions.** International Meeting ’Selected topics on nuclear methods for non-nuclear applications’, Varna (Bulgaria), September 2006.

Kelic, A.: **New Insight into the Fission Process by the Study of Relativistic Nuclear Collisions .** International Symposium on Exotic Nuclei, EXON 2006, Khanty-Mansiysk (Russia), July 2006.

Kelic, A.: **The role of fission in r-process nucleosynthesis.** International Symposium on Nuclear Astrophysics - Nuclei in the Cosmos - IX, CERN, Geneva (Switzerland), June 2006.

Kelic, A.: **The role of fission in r-process nucleosynthesis.** International Workshop XXXIV on Gross Properties of Nuclei and Nuclear Excitations, Hirschegg (Austria), January 2006.

Kim, Y.-J.: **Flow measurement of strangeness with FOPI at SIS.** International Workshop on Strangeness Nuclear Physics, Zhang Jia Jie, China, September 2006.

Kleffner, C.: **Strahlmessungen und Status des CNAO-RFQ für die Tumortherapieanlage in Pavia.** Beschleunigerseminar IAP Frankfurt (Germany), 29.11.2006.

Klimkiewicz, A.: **Collective dipole excitations and neutron skin thickness in the 132Sn mass region.** Chimera-GSI Workshop on Symmetry Energy in Nuclear Reactions, GSI Darmstadt (Germany December 2006.

Knöbel, R.: **Mass Measurements with Stored Radioactive Nuclei at the FRS-ESR Facility.** Tours Symposium on Nuclear Physics VI, Tours (France), September 2006.

Koczon, P.; Schweinfurth, Y.: **Heavy ion tumor therapy - experiences and perspectives.** Onkologisches Institut der Universität Warschau (Poland), February 2006.

Kollmus, H.: **Ionenstrahlinduzierte Desorption und deren Konsequenzen.** LMU München (Germany), 12.06.2006.

Krämer, D.: **FAIR - An International Facility for Antiproton and Ion Research.** RuPAC Novosibirsk, 2006.

Kraemer, M.: **Biological treatment planning for ion beams with TRiP98.** NIRS/MedAustron Satellite Meeting, Innsbruck (Austria), 26.02.2006.

Kraemer, M.: **Therapieplanung I.** Graduiertenkurs Heidelberg (Germany), April 2006.

Kraft, G.: **Heavy ion therapy, a challenge for radiobiology.** The European Radiation Research Society, Kiew, 22.08.2006.

Kraft, G.: **Schwerionentherapie an der GSI - Erfahrungen und Perspektiven.** Treffen der Direktoren der Rhön Kliniken, Weimar (Germany), 28.01.2006.

Kraft, G.: **Strahlentherapie mit schweren Ionen.** Physikalisches Kolloquium Univ. Mainz (Germany), 14.11.2006.

Kraft, G.: **The implication of Bethe's Equation to Radiation Biology and Therapy.** Bethe Festival Uni Frankfurt (Germany), 13.03.2006.

Kraft-Weyrather, W.: **Particle Radiotherapy.** Maastro Klinik; Maastricht (Netherlands), 07.06.2006.

Kraft-Weyrather, W.: **Particle radiobiology for hadrontherapy and space radiation protection.** Workshop to the Future Strategies for Space Radiation Research in Europe Taormina (Italien), September 2006.

Kraft-Weyrather, W.: **Radiobiolocigal Basis of Hadrontherapy.** European School of Oncology, Milano (Italien), February 2006.

Kraft-Weyrather, W.: **Schwerionentherapie.** Winterschule Pichl, Medizinische Physik in der Strahlentherapie Pichl (Austria), March 2006.

Kurz, A.: **Governance und Steuerung am Beispiel FAIR.** Tage des Wissenschaftsmanagements, Internationale Großprojekte der naturwissenschaftlichen Forschung, Villa Vigoni July 2006.

Kurz, A.: **Kooperation zwischen Hochschulen und außeruniversitären Forschungseinrichtungen.** Tagung des Zentrums für Wissenschaftsmanagment an der Deutschen Hochschule für Verwaltungswissenschaften, Wissenschaftsmanagement - State of the Art, Speyer (Germany), October 2006.

Kurz, A.: **Planing and construction of international large scale facilities for science.** 10th Israeli-German Administrators Meeting, March 2006.

Langanke, K.: **^{12}C (α,γ) ^{16}O: the theoretical challenge.** Workshop in honor of Charles A. Barnes 85th birthday, California Institute of Technology, Pasadena (USA), 15.12.2006.

Langanke, K.: **A FAIR Chance for Supernovae.** Colloqium, Universität Bonn (Germany), 05.05.2006.

Langanke, K.: **A FAIR Chance for Supernovae.** Colloquium, Physics Department, Dresden (Germany), 22.11.2006.

Langanke, K.: **A FAIR Chance for Supernovae.** International Symposium on Heavy-Ion Physics ISHIP, Frankfurt (Germany), 06.04.2006.

Langanke, K.: **Electron capture rates and neutrino-nucleus cross sections.** Workshop on Astrophysical Data Evaluation, Basel (Switzerland), 24.06.2006.

Langanke, K.: **Evaluation of weak-interaction rates for supernovae.** JINA workshop, Santa Barbara (USA), 10.03.2006.

Langanke, K.: **FAIR - Facility for Antiproton and Ion.** Research Colloque Ganil (France), 02.06.2006.

Langanke, K.: **Microscopic description of astrophysically important reactions.** Symposium on nuclear structure and astrophysics, Erice (Italy), 17.09.2006.

Langanke, K.: **Neutrino-nucleus reactions in supernovae IL-IAS meeting, Paris Observatory, Paris (France).** 13.12.2006.

Langanke, K.: **Nuclear Astrophysics at FAIR.** SFAIR Annual Meeting, Lund (Sweden), 14.11.2006.

Langanke, K.: **Nuclear structure, nucleosynthesis and supernovae.** Seminar, Physics Department, Heidelberg (Germany), 29.11.2006.

Langanke, K.: **R-process and nuclear structure.** RIKEN-GSI workshop on Nuclear Structure and Astrophysics, Tokyo (Japan), 06.10.2006.

Langanke, K.: **Shell model and supernovae.** Maria Goeppert-Mayer 100th birthday colloquium, Göttingen (Germany), 28.11.2006.

Langanke, K.: **Supernovae and nuclear structure.** Colloquium, Physics Department, Lund (Sweden), 15.11.2006.

Langanke, K.: **Weak interactions in supernovae.** Bethe 100. Symposium, California Institute of Technology, Pasadena (USA), 23.01.2006.

Langanke, K.: **Wir sind alle Sternenstaub.** Saturday Morning Physics, TU Darmstadt (Germany), 09.12.2006.

Lopez, X.: **Heavy ion collisions at SIS energies.** University of Split (Kroatia), May 2006.

Lopez, X.: **Les collisions d'ion lords aux 'energies du SIS.** Laboratoire de Physique Corpusculaire LPC, Clermont-Ferrand (France), February 2006.

Lukasik, J.: **Collective flow around the balance.** Frühjahrstagung der DPG, München (Germany), March 2006.

Lukasik, J.: **Flow measurements.** EXL-R3B Meeting, Milano (Italy), October 2006.

Lukasik, J.: **Isotopic flows in Xe+Sn.** CHIMERA-GSI Workshop, GSI Darmstadt (Germany), December 2006.

Lutz, F. M.: **Charm in nuclear matter.** Seminar am Forschungszentrum Jülich (Germany), 06.02.2006.

Lutz, F. M.: **Chiral dynamics and Hadrogenesis.** Graduiertenkollegs 'Eichtheorien - Experimentelle Tests und theoretische Grundlagen' Mainz (Germany), 18.07.2006.

Lutz, F. M.: **Chiral dynamics and Hadrogenesis.** Yukawa International Seminars 2006 (YKIS2006), Kyoto (Japan) 27.11-03.12.2006.

Lutz, F. M.: **Dynamically generated hidden charm baryon resonances.** International Workshop on Tau-Charm Physics, Peking (Japan), 05.-07.06.2006.

Lutz, F. M.: **Hadrogenesis and charm in nuclear matter.** The 4th PANDA physics workshop,Dresden (Germany), 06.-10.03.2006.

Lutz, F. M.: **Hadrogenesis.** Seminar am KVI (Netherlands), 27.03.2006.

Marin, A.: **Feasibility of gamma-jet correlations in ALICE detecting photons through conversions in the central barrel.** ECT Workshop, Jet physics in HIC at LHC', Trento (Italy), September 2006.

Martinez-Pinedo, G.: **o. T..** 26. International Workshop on Physics of High Energy Density in Matter, Hirschegg (Germany), 29.-03.02.2006.

Martinez-Pinedo, G.: **o. T..** 2nd International Conference on "Collective Motion in Nuclei under, 24.-27.04.2006.

Martinez-Pinedo, G.: **o. T..** 3rd ANL/MSU/INT/JINA RIA Theory Workshop, Argonne National Laboratory (USA), 04.-07.04.2006.

Martinez-Pinedo, G.: **o. T..** Finish Arctic Spring Workshop, Saariselkä (Finland), 24.-27.04.2006.

Martinez-Pinedo, G.: **o. T..** International Symposium on Nuclear Astrophysics - Nuclei in the Cosmos - IX, Geneva (Switzerland), 25.-30.06.2006.

Martinez-Pinedo, G.: **o. T..** Workshop on Advanced Laser and Mass Spectroscopy, GSI Darmstadt (Germany) 19.-20.10.2006.

Martinez-Pinedo, G.: **o. T..** Workshop on Massive Stellar Progenitors, The Final Days of Burning, Santa Barbara California (USA), 09.-10.03.2006.

Miskowiec, D.: **Pion-pion and pion-proton correlations - new results from CERES.** II. Workshop on Particle Correlation and Femtoscopy, Sao Paolo (Brazil), 2006.

Muehle, C.: **o.T..** HB2006, Tsukuba (Japan), 2006.

Neumann, R.: **Phase transitions in solids stimulated by simultaneous exposure to high pressure and relativistic heavy ions.** Deutsche Tagung für Forschung mit Synchrotronstrahlung, Neutronen und Ionenstrahlen an Großgeräten SNI 2006, University of Hamburg (Germany), 05.10.2006.

Neumann, R.: **Materialforschung mit energiereichen Schwerionen bei der GSI.** Deutsche Tagung für Forschung mit Synchrotronstrahlung, Neutronen und Ionenstrahlen an Großgeräten SNI 2006, University of Hamburg (Germany), 05.10.2006.

Neumann, R.: **Materialforschung mit energiereichen Schwerionen bei der GSI.** Friedrich-Schiller-Universität Jena, Physikalisch-Astronomische Fakultät, Jena (Germany),, 20.10.2006.

Neumann, R.: **Materialforschung mit energiereichen Schwerionen bei der GSI.** TU Darmstadt, Fachbereich Material- und Geowissenschaften, Darmstadt (Germany), 24.04.2006.

Neumann, R.: **Nanowires and IR spectroscopy.** ANKA Users' Meeting at FZ Karlsruhe (Germany), 10.10.2006.

Neumann, R.: **Quantum effects in bismuth nanowires.** Catholic University of Rio Grande do Sul, Faculty of Physics, Porto Alegre (Brazil), 16.01.2006.

Neumann, R.: **Tumor therapy with heavy ions at GSI.** Catholic University of Rio Grande do Sul, Faculty of Physics, Porto Alegre (Brazil), 17.01.2006.

Nociforo, C.: **11Be and the evolution of the shell structure.** Halo06 Workshop:The Physics of Halo Nuclei, ECT, Trento (Italy), November 2006.

Oeschler, H.: **Pourquoi est-il si difficile dobserver le Plasma de Quarks et de Gluons?.** IReS Strasbourg (France), 16.06.2006.

Oeschler, H.: **Production of strange particles from SIS up to LHC.** Brookhaven Nat. Lab., Upton NY (US), 23.03.2006.

Oeschler, H.: **Strange Particle Production from SIS up to LHC.** Institute of High Energy Physics, Beijing (China), 11.24.2006.

Oeschler, H.: **Strange Particle Production from SIS up to LHC.** Soft Physics workshop, Catania (Italy), 27.09.2006.

Oeschler, H.: **Transition from Baryonic to Mesonic Freeze Out.** Conference on Strange Quark Matter, Los Angeles (US), 26.03.2006.

P. Braun-Munzinger: **Relativistic nucleus-nucleus collisions and the QCD phase boundary.** Heavy Ion Physics symposium, Seoul (Korea), September 2006.

Pershina, V.: **Relativistic Effects on Atomic and Molecular Properties of the Heaviest Elements.** Workshop on Atomic Properties of the Heaviest Elements, Abtei Frauenwörth im Chiemsee (Germany), September 2006.

Pershina, V.: **Theoretical Chemistry for chemical identification of the Heaviest Elements.** IX International Conference on Nucleus Nucleus Collisions NN2006, Rio de Janeiro (Brazil), August 2006.

Pershina, V.: **Theoretical Predictions of Experimental Behaviour of Superheavy Elements and Relativstic Effects.** ICCMSE 2006 - International Conference of Computational Methods in Sciences and Enegineering, Chania, Crete (Greece), November 2006.

Peters, A.; Forck, P.: **Beam Diagnostics Challenges in the FAIR project at GSI.** o.O., 2006.

Peters, K.: **A Primer on Partial Wave Analysis.** Charm 2006, Beijing (China), June 2006.

Peters, K.: **Das BaBar Experiment.** Festkolloquium für Abschied H. Koch, Bochum (Germany), July 2006.

Peters, K.: **Facets of Hadron Physics.** Groningen (The Netherlands), September 2006.

Peters, K.: **Hadronenspektroskopie (3 Vorträge).** Arbeitstreffen Kernphysik, Schleching (Germany), March 2006.

Peters, K.: **Heavy States, from B-Factories to Panda.** ISHIP 2006, Frankfurt (Germany), April 2006.

Peters, K.: **Moderne Detektorentwicklung am Beispiel Panda.** Naturwissenschaftliches Kolloquium der Hochschule Darmstadt, Darmstadt (Germany), April 2006.

Peters, K.: **Physikprogramm bei BES.** Seminar für Kernphysik, Dresden (Germany), February 2006.

Peters, K.: **The BES Experiment at Beijing.** DESY Seminar, DESY, Hamburg (Germany), December 2006.

Peters, K.: **The BES Experiment at Beijing.** DESY Seminar, DESY, Zeuthen (Germany), December 2006.

Pietraszko, J. for the HADES collaboration: **Dielectron production in C+C and P+P collisions with the HADES.** 9th International Workshop on Meson Production, Properties and Interaction, Krakow (Poland) 09.-13.06.2006.

Pietraszko, J. for the HADES collaboration: **HADES at SIS100.** CBM Collaboration Meeting, Strasbourg (France), 19.-22.09.2006.

Plass, W.: **Direct Mass Measurements of Exotic Nuclei at the FRS-ESR Facility at GSI.** Conference on Trapped Charged Particles and Fundamental Physics, Vancouver (Canada), September 2006.

Plass, W.: **Mass and Lifetime Measurements at GSI fpr Nuclear Structure and Astrophysics.** 2nd German-Japanese Workshop on Nuclear Structure and Astrophysics, RIKEN, Saitama (Japan), September 2006.

Plass, W.: **Mass measurements of Exotic Nuclei.** International Summer School on Subatomic Physics, Bejing (China), August 2006.

Plass, W.: **Novel Developments for Ion-Catcher Facilities.** Gruppenseminar, Sektion Physik der Ludwig-Maximilians-Universität München (Germany), 15.05.2006.

Rethfeld, B.: **Free electron generation in laser-irradiated dielectrics.** SPIE International Conference on High-Power Laser Ablation, Taos, New Mexico (USA), 09.05.2006.

Rethfeld, B.: **Ultrakurzzeitdynamik laserangeregter Festkörper – Zeitaufgelöste Beschreibung von der Anregung bis zum Materialabtrag.** Institut fär Physik, Universität Kassel (Germany) 22.05.2006.

Rethfeld, B.: **Ultrakurzzeitdynamik laserangeregter Festkörper – Zeitaufgelöste Beschreibung von der Anregung bis zum Materialabtrag.** Seminar zur Quantenstatistik und Statistischen Physik, Institut für Physik,, 11.04.2006.

Ritter, S.: **Estimating the health risk of high LET radiation.** The National Laboratory of Heavy Ion Accelerator, Lanzhou (China), July 2006.

Ritter, S.: **Radiation risk based on cytogenetic damage.** Chinese Institute for Atomic Energy, Beijing (China), July 2006.

Ritter, S.: **Radiobiological Research at GSI: in vitro studies and cancer therapy.** Joint Institute for Nuclear Research, Dubna (Russia), 06.02.2006.

Ritter, S.: **Search for chromosomal biomarkrs specific to a prior exposure to densely inizing radiation.** Cospar Meeting 2006, Beijing (China), July 2006.

Roth, M.: **Laser accelerated Ions for Fusion.** 16th International Symposium on Heavy Ion Inertial Fusion, Saint-Malo (France), 7.1.2006.

Roth, M.: **Proton and Carbon Ion Cancer Therapy at GSI.** JST Workshop, Nara, Kansai Photon Center, (Japan) 50.61. 200.

Rustamov, A. for the HADES collaboration: **Exclusive η meson reconstruction in pp collisions at 2.2 GeV..** XLIV International Winter Meeting on Nuclear Physics, Bormio (Italy) 29.01-04.02.2006.

Saito, T. R.: **Coulomb excitation of the yrast and non-yrast 2+ states in 134Ce and 136Nd.** Gamma-ray spectroscopy in Europe, ECT, Trento (Italy), May 2006.

Saito, T. R.: **Exploring Nuclear Landscape with Strangeness.** Nuclear Physics Seminar, Giessen University, Giessen (Germany), 01.12.2006.

Saito, T. R.: **Hypernuclei and Experimental Determinations of the Hyperon-Nucleon Potentials.** Workshop on Exotic Nuclei and Neutron Stars, IPN, Orsay (France), September 2006.

Saito, T. R.: **Hyperons in Nuclear Structure.** Gudrun's Symposium, the Niels Bohr Institute, Copenhagen, Denmark, December 2006.

Saito, T. R.: **The HypHI project at GSI.** IX International Conference on Hypernuclear and Strange Particle Physics HYP2006, University of Mainz, Mainz (Germany), October 2006.

Saito, T. R.: **The HypHI project at GSI/FAIR.** Nuclear Physics Seminar, Tohoku University, Sendai (Japan), 15.12.2006.

Saito, T. R.: **The HypHI project at GSI/FAIR: Hypernuclear Spectroscopy with Stable Heavy Ion Beams and rare-Isotope Beams.** Phyiscs Seminar, IHNP, Strasbourg (France), 23.11.2006.

Saito, T. R.: **The HypHI project:Hypernuclear spectroscopy with heavy ion beams at GSI.** International workshop on Strangeness Nuclear Physic SNP2006, Zhang Jia Jie (China), September 2006.

Saito, T. R.: **The HypHI project:Hypernuclear spectroscopy with heavy ion beams at GSI.** Workshop on Quark Many Body Systems with Strangeness, Atami (Japan), December 2006.

Schädel, M.: **Physikalische und chemische Eigenschaften superschwerer Elemente.** Physikalische Kolloquium, Institut für Physik, Universität Kassel (Germany), 11.05.2006.

Schädel, M.: **Status of TASCA - an overview.** TASCA06 - 5th Workshop on Recoil Separator for Superheavy Element Chemistry, Garching (Germany), September 2006.

Schädel, M.: **Superheavy Chemistry - Achievements and Perspectives.** ASR2006 - The 6th International Symposium on Advanced Science Research 'Frontiers of Nuclear and Radiochemistry', Tokai, Ibaraki (Japan), October 2006.

Schädel, M.: **Superheavy Chemistry - Achievements and Perspectives.** ICCMSE 2006 - International Conference of Computational Methods in Sciences and Enegineering, Chania, Crete (Greece), November 2006.

Schädel, M.: **Superheavy Element Chemistry at GSI - Past, Present and Future.** The 35th RIBF Nuclear Physics Seminar, RIKEN Nishina Center for Accelerator Based Science, Wako (Japan), 30.10.2006.

Schardt, D.: **Tumor therapy with high-energy carbon ion beams.** IX. International Conference on Nucleus-Nucleus Collisions, Rio de Janeiro (Brasil) 28.08.2006.

Schardt, D.: **Zielgenaue 3D-Bestrahlung von Tumoren mit hochenergetischen Ionen OR:Deutsche Gesellschaft für angewandte Optik, Jahrestagung 2006, Weingarten (Germany).** 09.06.2006.

Scheidenberger, C.: **Atomic and nuclear interactions of swift heavy ions.** RIBF-ICW06, RIBF International Collaboration Workshop on Experiments at the RIBF, Wakoshi (Japan), November 2006.

Scheidenberger, C.: **Die Entdeckung und Erforschung extrasolarer Planeten.** Physikalische Kolloquium, Antrittsvorlesung, Justus-Liebig-Universität Gießen (Germany), 29.05.2006.

Schiedt, B.: **Characterization and application of single conical nanopores in polymer foils.** TU Darmstadt, FB Materialforschung, Darmstadt (Germany), 02.12.2006.

Schiedt, B.: **Ion track-etched nanopores in polymer foils.** Universität Osnabrück, FB Biologie, Osnabrück (Germany), 02.06.2006.

Schlegel, T.; Baldina, E.; Brambrink, E.; Ramis, R.: **Spatially homogeneous plasma heating with photons andor particles - application of a new hybrid view-factor code.** 29. European Conference on Laser Interaction with Matter (ECLIM), Madrid (Spain), 12.-16.06.2006.

Schlegel, T.; Baldina, E.; Ramis, R.: **Laser heated hohlraums for heavy ion stopping and opacity measurements.** 26. International Workshop on Physics of High Energy Density in Matter, Hirschegg (Germany), 29.-03.02.2006.

Schlitt, B.: **Status of Installation and Commissioning of the Heidelberg Ion Therapy Centre (HIT).** CNAO Project Technical Committee, University of Milano Bicocca (Italy), 18.07.2006.

Schlitt, B.: **Status of the CNAO Injector Linac,.** CNAO Project Technical Committee, University of Milano Bicocca (Italy), 18.07.2006.

Schmidt, K.-H.: **Beam Preparation for EURISOL.** EURISOL Design Study's Physics and Instrumentation Workshop, January 15-21, 2006, Trento (Italy), June 2006.

Schmidt, K.-H.: **Data Requirements for Modelling in Nuclear Astrophysics - Fission.** Data Needs in Nuclear Astrophysics, June 23-24, 2006, Basel (Switzerland), June 2006.

Schmidt, K.-H.: **New insight into the fission process from experiments with relativistic heavy ions.** 6th International Conference on Dynamical Aspects of Nuclear Fission, Smolenica Castle - Bratislava, Slowakia .10.2006.

Schmidt, K.-H.: **Relevant High-energy Data for ADS.** Second IP EUROTRANS International Training Course - Nuclear Data for Transmutation, Santiago de Compostela (Spain), June 2006.

Schmidt, K.-H.: **Signatures of multifragmentation in spallation reactions .** International Meeting "Selected topics on nuclear methods for non-nuclear applications", Varna, Bulgaria September 2006.

Schmidt, K.-H.: **Yields from extended p-driver capabilities - calculation and experimental results.** EURISOL Town Meeting CERN, Geneva (Switzerland), .11.2006.

Scholz, M.: **Biophysical Modelling in Treatment Planning for Ion Beam Therapy.** Institute of Modern Physics, Chinese Academy of Science, Lanzhou (China), 27.07.2006.

Scholz, M.: **Biophysical Modelling of Ion Radiation Effects.** Chinese Institute of Atomic Energy, Beijing (China), 20.07.2006.

Scholz, M.: **Biophysical Models in Ion Beam Therapy.** 36th COSPAR Scientific Assembly, Beijing (China), 16.07.2006.

Scholz, M.: **Ion Beam Radiobiology: From Basic Research to Applications in Tumor Therapy.** Institute of Physics, Jagellonian University, Krakow (Poland), 02.03.2006.

Scholz, M.: **Modeling of biological effects of charged particle beams as a basis for treatment planning in ion beam therapy.** Seminar at NIRS/HIMAC, Chiba (Japan), 12.07.2006.

Scholz, M.: **Selection of the weighting factor to take into account radiation quality in ion-beam therapy.** AEA/ICRU-Meeting, Columbus/Ohio (USA), 29.03.2006.

Scholz, M.: **Strahlenbiologische Grundlagen der Tumortherapie mit Ionenstrahlen.** XVI. Graduiertentage, University of Heidelberg (Germany), 19.04.2006.

Scholz, M.: **Tumortherapie mit Ionenstrahlen.** 12. Patientenforum, Wetzlar (Germany), 06.03.2006.

Schüttauf, A.: **TOF Detectors.** IRTG Fall School 2006, Heidelberg (Germany), October 2006.

Schwartz, K.: **Color center creation in LiF crystals under irradiation with 5 - 20 MeV Au ions: dependence on ion beam current and fluence.** Tartu University, Institute of Physics, Tartu (Estonia), 02.11.2006.

Schwartz, K.: **Energiereiche Ionen in Festkörpern: Strahlenschäden und Erzeugung von Nano-Strukturen.** Univ. Erlangen-Nürnberg, Institut für Werkstoffwissenschaften, Erlangen (Germany), 05.12.2006.

Semchenkov, A.: **Results from first TASCA commissioning experiments.** TASCA06 - 5th Workshop on Recoil Separator for Superheavy Element Chemistry, Garching (Germany), September 2006.

Senger, P.: **Compressed baryonic matter - Experiments at GSI and at FAIR.** Helmholtz-School on Dense Matter In Heavy Ion Collisions and Astrophysics, JINR Dubna (Russia), August 2006.

Senger, P.: **Hot and dense nuclear matter - what do we learn from heavy-ion collisions?.** Graduiertentag, December Basel (Switzerland), 15.12.2006.

Senger, P.: **Strange particles and neutron stars - experiments at GSI.** International Symposium on Heavy-Ion Physics, Frankfurt (Germany), 02.-06.04.2006.

Senger, P.: **The Compressed Baryonic Matter Experiment at FAIR.** FAIR community meeting, Daresbury Laboratory (Great Britain), 24.-25.01.2006.

Senger, P.: **The Compressed Baryonic Matter Experiment at FAIR.** International Workshop:Critical Point and the Onset of Deconfinement, Florence (Italy) 03.-06.07.2006.

Senger, P.: **The Compressed Baryonic Matter Experiment at FAIR.** International workshop BP 2006, Budapest (Hungary), 09.05-11.04.2006.

Senger, P.: **The Compressed Baryonic Matter Experiment at FAIR.** Workshop, Can we discover the QCD critical point at RHIC ?, Brookhaven National Laboratory (USA), 09.-10.03.2006.

Senger, P.: **The FAIR project.** Center China Normal University, Wuhan (China), November 2006.

Senger, P.: **The FAIR project.** Gordon Research Conference on Nuclear Chemistry, New London, N.H. (USA) 08.06.2006.

Senger, P.: **The FAIR project.** University of Science and Technology of China, Hefei (China), November 2006.

Sfienti, C.: **Gross Properties and isotopic Phenomena of Spectator Fragmentation.** IXth International Conference on Nucleus Nucleus Collisions, Rio de Janeiro (Brasil), September 2006.

Sfienti, C.: **Surveying Spectator Fragmentation at Relativistic Energy.** Frühjahrstagung der Deutschen Physikalischen Gesellschaft, München (Germany), March 2006.

Sfienti, C.: **Surveying Spectator Fragmentation at Relativistic Energy.** LXIV International Meeting on Nuclear Physics, Bormio (Italy), January 2006.

Simon, H.: **The ELISe experiment at FAIR.** IX International Conference on Nucleus Nucleus Collisions (NN2006),Rio de Janeiro (Brazil), August 2006.

Simon, Haik: **Correlations in Breakup Reactions.** Workshop:The Physics of Halo Nuclei - Halo06, Trento (Italy), November 2006.

Simon, Haik: **The ELISe Experiment at FAIR.** EMIN - 2006, XI International Seminar on Electromagnetic Interactions of Nuclei, Moscow (Russia) September 2006.

Stroth, J.: **From HADES to CBM.** ISHIP2006, Frankfurt 03.-06.04.2006.

Stroth, J.: **Low mass Lepton Pairs - Experiments.** Symposium on the Physics of High Baryon Density, Strasbourg (France), 19.09.2006.

Stroth, J.: **Low-mass electron pairs.** The Physics of High Baryon Density, Trento (Italy), 29.05-.06.2006.

Tahir, N. A.: **Prospects of High Energy Density Matter Research at the Future Facility For.** 12th International Conference on the Physics of Non 06.09.2006.

Tahir, N. A.: **Prospects of High Energy Density Matter Research at the Future Facility For.** 16th International Symposium on Heavy Ion Inertial Fusion, Saint Malo (France), 12.07.2006.

Tahir, N. A.: **Prospects of Warm Dense Matter Research at the Future Facility For Antiprotons and Ion Research (FAIR) at Darmstadt: The HEDgeHOB Collaboration.** Accelerator Driven Warm Dense Matter Workshop, Pleasanton,CA (USA), 22.02.2006.

Tahir, N. A.: **Studies of High Energy Density States in matter Using Intense Heavy Ion Beams at future FAIR Facility at Darmstadt: The HEDgeHOB Collaboration.** Pakistan Institute of Physics (PIP) International Conference, Lahore (Pakistan), 14.03.2006.

Taucher-Scholz, G.: **Live cell imaging to asses repair protein dynamics at sites of local ion-induced DNA damage.** Int. l. Workshop on Radiation Damage to DNA, Tekirova (Turkey), May 2006.

Taucher-Scholz, G.: **Molecular targets and cellular responses to ionizing radiation: the use of charged particles.** 1st Langendorff Congress, Freiburg (Germany), April 2006.

Tinschert, K.: **Ion Sources at GSI.** Institute of Heavy Ion Physics, Beijing University (China), 25.09.2006.

Toneev, V.: **Dynamics of relativistic heavy-ion collisions.** Helmholtz Int. Summer School, Dense Matter In Heavy Ion Collisions and Astrophysics, JINR LTP, Dubna (Russia), 21.08-01.09.2006.

Trautmann, C.: **How energetic heavy ions modify solids: basic aspects and applications in micro- and nanoscience.** Forschungszentrum Karsruhe (Germany), January 2006.

Trautmann, C.: **Material modifications and nanoscience with MeV-GeV ions.** ICPT Workshop on Ion Beam Studies of Nanomaterials: Synthesis, Modification and Characterization, Trieste (Italy), February 2006.

Trautmann, C.: **Material modifications with MeV-GeV heavy ions: basic aspects and applications.** University of Uppsala (Sweden), November 2006.

Trautmann, C.: **The future FAIR accelerator facility for antiproton and ion research.** Deutsche Tagung für Forschung mit Synchrotronstrahlung, Neutronen und Ionenstrahlen an Großgeräten (SNI 2006), Hamburg (Germany), 06.10.2006.

Trautmann, W.: **Isotopic effects in multifragmentation and the nuclear equation of state.** IXth International Conference on Nucleus Nucleus Collisions, Rio de Janeiro (Brasil), September 2006.

Trautmann, W.: **Isotopic effects in spectator fragmentation.** Gordon Research Conference on Nuclear Chemistry, New London (Great Britain), June 2006.

Trautmann, W.: **The symmetry energy in multifragmentation.** International Workshop XXXIV on Gross Properties of Nuclei and Nuclear Excitations, Hirschegg (Germany), January 2006.

Typel, S.: **High Density Constraints on Hadronic EoS from the Phenomenology of Compact Stars and Heavy-Ion Collisions.** IPN, Orsay (France), 03.-06.04.2006.

Typel, S.: **Indirect Methods for Nuclear Astrophysics.** 3rd VISTARS Workshop on Nuclear Astrophysics, Rußbach (Austria) 11.-18.03.2006.

Typel, S.: **Indirect Methods for Nuclear Astrophysics.** GANIL, Caen (France), 02.10.2006.

Typel, S.: **Indirect Methods for Nuclear Astrophysics.** IPN, Orsay (France), 30.03.2006.

Typel, S.: **Indirect Methods for Nuclear Astrophysics.** LNS-INFN, Catania (Italy), 06.11.2006.

Typel, S.: **New Equation of State of Hot and Dense Matter for Astrophysical Applications.** Workshop III of the Virtual Institute on Dense Hadronic Matter and QCD Phase Transitions, Rathen (Switzerland), 15.-17.10.2006.

Varentsov, V. for the HEDgeHOB collaboration: **HEDP/WDM Experiments at GSI and at FAIR.** 12th International Conf. on Physics of Nonideal Plasmas, Darmstadt 05.09.2006.

Varentsov, V. for the HEDgeHOB collaboration: **High Energy Density Physics Experiments at GSI and at FAIR OR:16th International Symposium on Heavy Ion Fusion, Saint-Malo (France).** 12.07.2006.

Varentsov, V. for the HEDgeHOB collaboration: **Warm Dense Matter Studied by Heavy-Ion Beams.** 33th EPS Conf. on Plasma Physics, Rome (Italy), 22.06.2006.

Voskresensky, D.: **Quantum kinetic theory.** Helmholtz

Int. Summer School, Dense Matter In Heavy Ion Collisions and Astrophysics, JINR LTP, Dubna (Russia), 21.08-01.09.2006.

Wambach, J.: **Modern Aspects of Nuclear Structure Theory.** International School of Nuclear Physics, Erice (Italy), 22.09.2006.

Wambach, J.: **The Phase Diagram of Strongly Interacting Matter,.** Physikalisches Kolloqium, Basel (Switzerland), 15.12.2006.

Wambach, J.: **The Phase Diagram of Strongly Interacting Matter.** ISHIP2006, Frankfurt (Germany), 03.04.2006.

Wambach, J.: **The Physics of Dense Hadronic Matter.** YKIS2006, Kyoto (Japan), 28.11.2006.

Weick, H.: **Mass and lifetime measurements in storage rings.** International Symposium on Exotic Nuclei,'EXON2006', Khanty-Mansiysk (Russia), July 2006.

Winkler, M.: **Design of Large Sector-Field High-Energy Fragment Separators with Aberration Correction.** CPO-7 - 7th Int. Conf. on Charged Particle Optics, Cambrdge (UK), July 2006.

Winkler, M.: **Radioactive beam experiments at FAIR.** Tours Symposium on Nuclear Physics VI, Tours (France), September 2006.

Yaramyshev, S.: **DYNAMION status and simulations for the UNILAC.** INTAS-final-meeting at GSI (Germany), 05.-06.09.2006.

Yaramyshev, S.: **HSI-RFQ upgrade 2004 & new HSI-RFQ.** INTAS-final-meeting at GSI (Germany), 05.-06.09.2006.

Seminars and talks at the GSI

Compiled by M. Enders, K. Große

Sahoo, B. K./GSI (Germany): **Application of Coupled-Cluster Theory to Parity Non-conservation in Atoms.** Seminar der Materialforschung, 04.01.2006.

Roth, M./Institut für Kernphysik, TU Darmstadt (Germany): **European Extreme Light Infrastructure (ELI).** Physik dichter Plasmen mit Schwerionen- und Laserstrahlen, 10.01.2006.

Tomaselli, M./TU Darmstadt, GSI (Germany): **Electron Clusters in Strong Laser Fields.** ILIAS-Seminar-Arbeitsseminar, 10.01.2006.

Vogel, P./Caltech (USA): **Another application of nuclear reactors: Study of neutrino oscillations.** GSI Kolloquium, 10.01.2006.

Kelic, A./GSI (Germany): **The Role of Fission in the r-process Nucleosynthesis.** NuSTAR Seminar, 11.01.2006.

Kirchner, T./TU Clausthal (Germany): **Rearrangement dynamics in ion-atom collisions with active electrons on both centers.** Atomphysik-Seminar, 11.01.2006.

Melde, T./Graz (Austria): **Constituent quark model in relativistic quantum mechanics.** Theorie-Seminar, 11.01.2006.

Schmidt, Alexander/GSI (Germany): **Multiple Field Optimization of Biologically Effective Dose and Experimental Verification of a Pseudo Treatment Plan.** Seminar der Materialforschung, 11.01.2006.

Adamczewski, J.: **GO4 Status.** IT/EE-Seminar, 17.01.2006.

Korostiy, S./GSI (Germany): **Spectroscopic investigation of heavy ion charge states and velocity inside solid and gaseous targets (Gas-solid effect).** Physik dichter Plasmen mit Schwerionen- und Laserstrahlen, 17.01.2006.

Lindroos, M./CERN (Switzerland): **The Technical challenges of Beta-beams.** GSI Kolloquium, 17.01.2006.

Ruhl, H./Ruhr-Universität Bochum (Germany): **Monoenergetische Protonen: Experimente und Theorie.** ILIAS-Seminar-Arbeitsseminar, 17.01.2006.

Psonka, K./GSI (Germany): **DNA fragmentation induced by ionizing radiation Atomic Force Microscopy study.** Seminar der Materialforschung, 18.01.2006.

Reinhard, S./MPI-K, Heidelberg (Germany): **Time dilation measurements with fast stored lithium ions: TSR version.** Atomphysik-Seminar, 18.01.2006.

Simon, H./GSI (Germany): **Dripline Nuclei: Properties, Means and Tools.** NuSTAR Seminar, 18.01.2006.

Severin, D./Universität Marburg (Germany): **Radiation sensitivity of insulating materials used in the superconducting magnets for the FAIR project.** Beschleuniger-Seminar, 19.01.2006.

Bauer, D./MPI Heidelberg (Germany): **Laser-Absorption und Ionisation in Clustern und Bericht vom Winter Colloquium on the Physics of Quantum Electronics 2006, Snowbird, Utah.** ILIAS-Seminar-Arbeitsseminar, 24.01.2006.

Narici, L./Rom (Italy): **ALTEA, a multiple approach program for studying the ionizing radiation effects on the Central Nervous System (CNS): ground and space investigations.** GSI Kolloquium, 24.01.2006.

Rodriguez Prieto, G./GSI Darmstadt (Germany): **Long-Pulsed Medium-Flux Laser Plasmas with High Electron Temperatures: Spectroscopic and Space Resolved Studies.** Physik dichter Plasmen mit Schwerionen- und Laserstrahlen, 24.01.2006.

van Wezel, J./FZ Karlsruhe (Germany): **PetaByte Mass Storage at GridKa: Components, architecture and experiences.** IT/EE-Seminar, 24.01.2006.

Giacri, M.-L./Saclay (France): **Creation of Photonuclear Activation Library and Measurements of Delayed Neutrons from Photofission.** NuSTAR Seminar, 25.01.2006.

Klimkiewicz, A./GSI (Germany): **Dipole response of exotic neutron-rich nuclei in the 132Sn mass region.** Seminar der Materialforschung, 25.01.2006.

Schlegel, T./GSI (Germany): **Radiative hydrodynamics in laser-heated hohlraums.** Theorie-Seminar, 25.01.2006.

Schneble, H.: **Bauleitplanung für das FAIR-Projekt unter Berücksichtigung von naturschutzfachlichen Kompensationsmaßnahmen.** Wissenschaft für alle, 25.01.2006.

Gales, S./Ganil (France): **SPIRAL2GANIL: a world leading ISOL facility in Europe at the dawn of the new decade.** GSI Kolloquium, 31.01.2006.

Grid Group: **Grid Status.** IT/EE-Seminar, 31.01.2006.

Dimopoulou, C./GSI (Germany): **Ionization and Fragmentation of Simple Molecules in a Reaction Microscope.** Atomphysik-Seminar, 01.02.2006.

Mazzocco, M./GSI (Germany): **Reactions with Light Weakly Bound RIB's at Coulomb Barrier Energies.** NuSTAR Seminar, 01.02.2006.

Raha, U./Bonn (Germany): **Hadronic atoms in effective**

field theory. Theorie-Seminar, 01.02.2006.

Meusel, O./Universität Frankfurt (Germany): **Low Energy Beam Transport Using Space Charge Lenses.** Beschleuniger-Seminar, 02.02.2006.

Mulser, P./TQE, TU Darmstadt (Germany): **Neuere Aspekte der kollektivem Ionenbeschleunigung: Analytik und Simulationen von P. Gibbon und S. Betti.** ILIAS-Seminar-Arbeitsseminar, 07.02.2006.

Ritter, H. G./LBNL (USA): **Strongly interacting matter at RHIC.** GSI Kolloquium, 07.02.2006.

Birkl, G./TU Darmstadt (Germany): **Cold and Trapped Metastable Neon Atoms - from Atomic Structure to Bose-Einstein Condensation.** Atomphysik-Seminar, 08.02.2006.

Chatillon, A./GSI (Germany): **Spectroscopy of Odd-Z Transfermium Nuclei/The Structure of ^{251}Md.** NuSTAR Seminar, 08.02.2006.

Trassinelli, M./GSI (Germany): **Quantum Electrodynamics Tests and X-rays Standards using Pionic Atoms and Highly Charged Ions.** Seminar der Materialforschung, 08.02.2006.

Göckel, H.: **Windows Server.** IT/EE-Seminar, 14.02.2006.

Morita/RIKEN (USA): **Experiments on synthesis of the heaviest elements at RIKEN.** GSI Kolloquium, 14.02.2006.

Rethfeld, B./Institut für Kernphysik, TU Darmstadt (Germany): **From solid to warm dense matter: Time travel from ultrafast laser-solid excitation to overcritical material expansion.** Physik dichter Plasmen mit Schwerionen- und Laserstrahlen, 14.02.2006.

Witte, K./GSI (Germany): **PHELIX am Target: Parameter, Experimente.** ILIAS-Seminar-Arbeitsseminar, 14.02.2006.

Geppert, C./GSI (Germany): **Laser Ion Source Developments at the University of Mainz.** Atomphysik-Seminar, 15.02.2006.

Lineva, N./GSI (Germany): **Heavy Ion Impact Induced Low Energy Electron Emission and their Transport in Solids.** Seminar der Materialforschung, 15.02.2006.

Peter, I.: **Forschung an der GSI und FAIR - ein verständlicher Überblick für Laien.** Wissenschaft für alle, 15.02.2006.

Sanz-Cillero, J.-J./Orsay (France): **Confronting resonance theory and QCD at large Nc.** Theorie-Seminar, 15.02.2006.

Strahinja, L./GSI (Germany): **Comprehensive Investigation of the Decay Losses of the Short-lived Nuclei in the ISOL Extraction Method.** NuSTAR Seminar, 15.02.2006.

Kornilov, V./GSI (Germany): **Intensity Limitations for SIS18/100 Due to Transverse Collective Instabilities.** Beschleuniger-Seminar, 16.02.2006.

Ruhl, H./Universität Bochum (Germany); Mulser, P./TQE, TU Darmstadt (Germany): **Offene Fragen der relativistischen Laser-Plasmawechselwirkung: Was lohnt für ein Experiment mit PHELIX?** ILIAS-Seminar-Arbeitsseminar, 21.02.2006.

Schaa, V.: **Joint Accelerator Conferences on Web (JACOW).** IT/EE-Seminar, 21.02.2006.

Golubev, A./ITEP, Moskau (Russia): **Experimental Investigation of Energy Deposition of Fast Ions in Cold Matter using the 'Thick Target' Approach.** Beschleuniger-Seminar, 23.02.2006.

Oset, E./Valencia (Spain): **Chiral dynamics of the Kbar nucleus interaction: critical review of deeply bound Kbar states.** Theorie-Seminar, 27.02.2006.

Tabor, S. L./Florida State University (USA): **Shifting Shells - Dependence of Shell Structure on Neutron Excess.** NuSTAR Seminar, 27.02.2006.

Duve, E.; Engel, P.: **Vorschlag einer integrierten Monitoring Lösung.** IT/EE-Seminar, 28.02.2006.

Scheid, W./Universität Gießen (Germany): **Beitrag zu Relativistischen Plasmaphysik: Vermischtes aus der Atomphysik.** ILIAS-Seminar-Arbeitsseminar, 07.03.2006.

Enculescu, M./National Institute of Materials Physics, Bucharest (Romania): **Optical properties of polymer templates for nanowire synthesis.** Seminar der Materialforschung, 14.03.2006.

Ruhl, H./Universität Bochum (Germany): **Relativistische über Laserplasmaexperimente mit PHELIX.** ILIAS-Seminar-Arbeitsseminar, 14.03.2006.

Schön, W.: **Der Aufbau der Linux Farm.** IT/EE-Seminar, 14.03.2006.

Franchi, A./GSI (Germany): **Measurement and correction of linear coupling and nonlinearities from BPM and RGM data.** Beschleuniger-Seminar, 16.03.2006.

Habermann, M./GFE (Germany): **Anwendungen von CBM Root.** IT/EE-Seminar, 21.03.2006.

Maruhn, J.: **Relativistische Fluiddynamik.** ILIAS-Seminar-Arbeitsseminar, 21.03.2006.

Dirk, O./Universität Greifswald (Germany): **Temperaturrelaxation und Stoßabsorption in Laserplasmen.** ILIAS-Seminar-Arbeitsseminar, 26.03.2006.

Adamczewsky, J.; Al Turany, M.; Göringer, H.; Malzacher, P.: **Konferenzberichte CHEP 2006.** IT/EE-Seminar, 28.03.2006.

Ratschow, S./GSI (Germany): **Beam Line Layout for the FAIR Project.** Beschleuniger-Seminar, 30.03.2006.

Bollen, G./National Superconducting Cyclotron Laboratory, Michigan State University, East Lansing, Michigan (USA): **Joint**

Symposium on Atomic Physics: "Precision Experiments with Thermalized Rare Isotope Beams from Projectile Fragmentation. Sonderveranstaltung, 31.03.2006.

Freifelder, R./Department of Radiology, University of Pennsylvania at Philadelphia (USA): **Positron Emission Tomography w. ToF, First Clinical Results.** Sonderveranstaltung, 03.04.2006.

Roth, M./TU Darmstadt, GSI (Germany): **Notes from the JST Workshop Ultra intense Lasers and medical applications (JAEA / Kansai Photon Center, 15.3.-16.3.2006).** ILIAS-Seminar-Arbeitsseminar, 04.04.2006.

Parfenova, Y./Bruxelles (Belgium): **Nucleon removal in s-d-shell nuclei (15,21,23O, 18,20N, 22F, 17Ne).** NuSTAR Seminar, 05.04.2006.

Mulser, P./TQE, TU Darmstadt (Germany): **Relativistische und nichtrelativistische ponderomotorische Laser-Plasmakopplung.** ILIAS-Seminar-Arbeitsseminar, 11.04.2006.

Das, P./VECC, Kolkata (India): **A study of change in nuclear decay rate due to hyperfine interactions using a cryogenic Penning trap.** Atomphysik-Seminar, 12.04.2006.

Witte, F.: **Dreifach ist des Raumes Maß . . . die faszinierende Wirklichkeit des dreidimensionalen Weltalls (Stereovortrag).** Wissenschaft für alle, 12.04.2006.

Lee, S.-Y./Indiana (USA): **What does it take to implement Neuronetworks in Future Accelerators?** GSI Kolloquium, 18.04.2006.

Rakhimov, K./Uzbek Academy of Sciences (Uzbekistan): **Projectile Electron Loss in the Collisions with Neutral Targets: Sudden perturbation approach.** Atomphysik-Seminar, 24.04.2006.

Chichkov, B./Laser Zentrum Hannover e.V. (Germany): **Übersicht über Plasmonics am Laser Zentrum und Vorschlag von High-Power-Experimenten.** ILIAS-Seminar-Arbeitsseminar, 25.04.2006.

Skrinsky, A./BINP-Nowosibirsk (Russia): **Electron cooling - History, Present Status, and Perspectives (Kolloquium für B. Franzke).** GSI Kolloquium, 25.04.2006.

Roth, R./Darmstadt (Germany): **Correlated Realistic Interactions for Nuclear Structure and Reactions.** NuSTAR Seminar, 26.04.2006.

Schlegel, T./GSI (Germany): **Spatially homogeneous plasma heating with lasers - application of a new hybrid view-factor code.** Atomphysik-Seminar, 26.04.2006.

Messmer, P-/Tech-X Corporation, Boulder, CO (USA): **Kinetic Modelling of Plasmas in ECR Sources.** Beschleuniger-Seminar, 27.04.2006.

Lesch, H./München (Germany): **Was sind und warum gelten Naturgesetze? Das Universum und ich! (Kolloquium für N. Angert).** GSI Kolloquium, 02.05.2006.

Piriz, R./Universidad de Castilla - La Mancha (Spain): **Richtmyer-Meskov flow in elastic solids.** Physik dichter Plasmen mit Schwerionen- und Laserstrahlen, 02.05.2006.

Heiss, M./GSI (Germany): **The heavy-ion-microprobe at GSI.** Seminar der Materialforschung, 03.05.2006.

Lüttges, S./GSI (Germany): **Vierzehn Tage Jemen oder Warum nur vormittags entführt wird.** Atomphysik-Seminar, 03.05.2006.

Ruppert, J./Durham (Great Britain): **What does the rho do? Lessons from NA60's di-muon measurement.** Theorie-Seminar, 03.05.2006.

Wiehl, N./Mainz (Germany): **The Ultracold Neutron Source at the Research Reactor TRIGA Mainz.** NuSTAR Seminar, 03.05.2006.

Brambrink, E./LULI Palaiseau (France): **Laser-driven ion acceleration and applications: Experiment and theory.** ILIAS-Seminar-Arbeitsseminar, 09.05.2006.

Kessler, G./ehem. Forschungszentrum Karlsruhe: **Requirements for Nuclear Energy in the 21st Century, Nuclear Energy as a Sustainable Energy Source.** Physik dichter Plasmen mit Schwerionen- und Laserstrahlen, 09.05.2006.

Ressmann, D.; van Wezel, J./GridKa Karlsruhe (Germany): **The PetaByte Mass Storage at GridKa.** IT/EE-Seminar, 09.05.2006.

Shotter, A./TRIUMF (Canada): **The scientific reach of TRIUMF, Canada's National Laboratory for Particle and Nuclear Physics.** GSI Kolloquium, 09.05.2006.

Antalic, S./Bratislava (Slovakia): **Nuclear Structure in Fermium Region.** NuSTAR Seminar, 10.05.2006.

Dmitrasinovic, V./Belgrade (Serbia): **D_s(2317) and D_s(2308) as candidates for open-charm tetra quarks.** Theorie-Seminar, 10.05.2006.

Nofal, M./MPI-K, Heidelberg (Germany): **The Radiative Electron Capture to Continuum Cusp (RECC) and its Relation to the Short-Wavelength Limit of Electron-Nucleus (e-n) Bremsstrahlung.** Atomphysik-Seminar, 10.05.2006.

Voss, K.-O./GSI (Germany): **Laser Spectroscopy of Gd3+ Ions Doped into SHI-Irradiated Lanthanum Fluoride Single-Crystals.** Seminar der Materialforschung, 10.05.2006.

Hahn, R. von/MPI-K, Heidelberg (Germany): **Status of the low-energy electrostatic Cryogenic Storage Ring (CSR) at MPI-K.** Beschleuniger-Seminar, 11.05.2006.

Grunder, H./ehem. Argonne National Laboratory (USA): **What can and should Nuclear Energy Contribute to the Future Energy Mix?** Physik dichter Plasmen mit Schwerionen- und Laserstrahlen, 16.05.2006.

Roth, T.; Schön, W.: **Konferenzberichte Hepix.** IT/EE-

Seminar, 16.05.2006.

Wittig, H./Mainz (Germany): **Progress in lattice QCD: of Quarks, Walls and Domains.** GSI Kolloquium, 16.05.2006.

Hanhart, C./Jülich (Germany): **Towards an understanding of the light scalar mesons.** Theorie-Seminar, 17.05.2006.

Lee, R./GSI (Germany): **Chromosome aberrations in human lymphocytes irradiated with heavy ions.** Seminar der Materialforschung, 17.05.2006.

Nishio, K./Tokai (Japan): **30Si+238U - Fusion Reaction Dynamics.** NuSTAR Seminar, 17.05.2006.

Shevelko, V. P./Lebedev Physical Institute, Moscow (Russia): **Charge-changing collisions of U28+ ions with the rest-gas atoms in the 1 MeV/u 10 GeV/u energy range (preliminary calculations).** Atomphysik-Seminar, 17.05.2006.

Brust, H./GSI (Germany): **Ideen für ein campusweites VLAN-Konzept.** IT/EE-Seminar, 23.05.2006.

Denker, A./HMI (Germany): **Swift Ion Beams for Solid State Physics and Materials Science, Medicine and Science of Art.** GSI Kolloquium, 23.05.2006.

Enculescu, I./National Institute of Materials Physics, Bucharest (Romania): **Semiconductor nanowires prepared in ion-track templates.** Seminar der Materialforschung, 23.05.2006.

Stöhlker, T./GSI and Universität Frankfurt (Germany): **X-Ray Imaging and Compton Polarimetry of Atomic Transitions in Heavy Ions.** Physik dichter Plasmen mit Schwerionen- und Laserstrahlen, 23.05.2006.

Nadtochy, P./GSI (Germany): **Three-dimensional Langevin calculations of fission-fragment charge distribution for the reaction of 238U at 1 A GeV on a CH2 target.** NuSTAR Seminar, 24.05.2006.

Nofal, M./IKF Frankfurt and GSI (Germany): **The Radiative Electron Capture to Continuum Cusp (RECC) and its Relation to the Short-Wavelength Limit of Electron-Nucleus (e-n) Bremsstrahlung.** Seminar der Materialforschung, 24.05.2006.

Stroke, H. H./New York University (USA): **At the Intersection of Atomic and Nuclear Physics.** Atomphysik-Seminar, 24.05.2006.

Krücken, R./TU München (Germany): **Nuclear Structure Studies at REX-ISOLDE and the HIE-ISOLDE project.** GSI Kolloquium, 30.05.2006.

Moses, E. I./Director NIF, LLNL, Livermore (USA): **The National Ignition Facility: Progress Toward Ignition.** Physik dichter Plasmen mit Schwerionen- und Laserstrahlen, 30.05.2006.

Thiemer, U.: **Modulare Steuerungstechnik für Experimente.** IT/EE-Seminar, 30.05.2006.

Boretzky, K.: **Dipole Response of Isospin Asymmetric Nuclei.** NuSTAR Seminar, 31.05.2006.

Gostishchev, V./GSI Darmstadt (Germany): **Measurements and simulations of gas-jet-target effects in the ESR.** Seminar der Materialforschung, 31.05.2006.

Surzhykov, A./MPI-K Heidelberg (Germany): **Many-electron effects in relativistic ion-atom collisions.** Atomphysik-Seminar, 31.05.2006.

Baym, G./Urbana (USA): **Neutron stars and the properties of matter at high densities.** GSI Kolloquium, 06.06.2006.

Burrows, A./University of Arizona (USA): **Brown Dwarfs.** GSI Kolloquium, 06.06.2006.

Kaiser, C./Physikalisches Institut, Universität Karlsruhe(Germany): **Low Temperature Measurements on Silver and Bismuth Nanowire Arrays.** Seminar der Materialforschung, 06.06.2006.

Düllmann, C./GSI (Germany): **On the Way to Long-lived Preseparated Transactinides.** NuSTAR Seminar, 07.06.2006.

Kunz, P./Universität Mainz (Germany): **Laser Spectroscopy of Heavy Elements in a Buffer Gas Cell.** Atomphysik-Seminar, 07.06.2006.

Kester, O./GSI (Germany): **Deceleration of highly charged ions within the HITRAP project at GSI.** Beschleuniger-Seminar, 08.06.2006.

Dickhoff, W. H./St. Louis (USA): **Many-body calculation of correlated nucleons.** Theorie-Seminar, 12.06.2006.

Engelen, J./CERN (Switzerland): **Status and First Physics at LHC.** GSI Kolloquium, 13.06.2006.

Flemming, H.: **Das Design des neuen TAC-Chips.** IT/EE-Seminar, 13.06.2006.

Kingsep, A. S./Russian Research Centre Kurchatov Institute, Moscow (Russia): **Inertial Confinement Fusion Activity at the Kurchatov Institute.** Physik dichter Plasmen mit Schwerionen- und Laserstrahlen, 13.06.2006.

Cornelius, T./GSI (Germany): **Bismuth nanowires: Fabrication and characterization.** Seminar der Materialforschung, 14.06.2006.

Dudek, J./Strasbourg (France): **Exotic Geometrical Symmetries in Nuclei and their Potential Impact on Large Scale Experimental Projects.** NuSTAR Seminar, 14.06.2006.

Kaiser, N./München (Germany): **Chiral dynamics of nuclear matter: quasi-particle and spin-orbit interaction.** Theorie-Seminar, 14.06.2006.

Laehde, T./Bonn (Germany): **Partially quenched chiral perturbation theory at NNLO.** Theorie-Seminar, 19.06.2006.

Adamczewski, J.; Linev, S.: **DAQ for FAIR: uDAPL and XDAQ on an InfiniBand test cluster.** IT/EE-Seminar, 20.06.2006.

Barnes, T./Oak Ridge (USA): **Recent Developments in Charmonium: the XYZ States.** GSI Kolloquium, 20.06.2006.

Duvenbeck, A./Universität Duisburg-Essen (Germany): **Computer Simulation of electronic excitation in atomic collision cascades.** Seminar der Materialforschung, 20.06.2006.

Frank, K./Universität Erlangen-Nürnberg (Germany): **Grundlagen und Anwendungen von gepulsten Hohlkathodenentladungen.** Physik dichter Plasmen mit Schwerionen- und Laserstrahlen, 20.06.2006.

Doornenbal, P./GSI (Germany): **RISING In-beam Experiments at Relativistic Energies.** NuSTAR Seminar, 21.06.2006.

Herlert, A./CERN (Switzerland): **High-precision mass measurements on exotic nuclides: recent results from the ISOLTRAP experiment.** Atomphysik-Seminar, 21.06.2006.

Sandro, C./GSI (Germany): **Radiosensitivity of human B-lymphocytes ad Macrophages following X-ray and carbon ion exposure.** Seminar der Materialforschung, 21.06.2006.

Zimmermann, H./LMU, GSI (Germany): **Charge breeding exploration with the MAXEBIS at GSI.** Beschleuniger-Seminar, 22.06.2006.

Al Turany, M.; Bertini, D.: **Entwicklungen für Simulation und Analyse in der IT.** IT/EE-Seminar, 27.06.2006.

Kessler, G./ehem. Forschungszentrum Karlsruhe (Germany): **Requirements for Nuclear Energy in the 21st Century - Nuclear Energy as a Sustainable Energy Source.** Physik dichter Plasmen mit Schwerionen- und Laserstrahlen, 27.06.2006.

Köhl, M./ETHZ (Switzerland): **Strongly Correlated Ultracold Atomic Gases.** GSI Kolloquium, 27.06.2006.

Rethfeld, B./GSI (Germany): **Zeitskalen laserinduzierter Phasenübergänge von Festkörpern.** ILIAS-Seminar-Arbeitsseminar, 27.06.2006.

Karpov, A./Dubna (Russia): **Potential Energy of Heavy Nuclear System in Fusion-fission Processes.** NuSTAR Seminar, 28.06.2006.

Malzacher, P.: **'Per Anhalter durch die Galaxis' aus der Sicht der Informatik.** Wissenschaft für alle, 28.06.2006.

Pisarski, R./BNL (USA): **A kind of 'chiral' Lagrangian for deconfinement.** Theorie-Seminar, 28.06.2006.

Trassinelli, M./GSI (Germany): **Quantum Electrodynamics Tests and X-rays Standards using Pionic Atoms and Highly Charged Ions.** Atomphysik-Seminar, 28.06.2006.

Trotsenko, S./GSI (Germany): **State Selective Production of Excited States in He- and Li-like Heavy Ions.** Seminar der Materialforschung, 28.06.2006.

Gulmelli, F./Ensicaen and University of Caen (France): **From multifragmentation to supernovae and neutron stars.** Sonderveranstaltung, 29.06.2006.

Otsuki, K./Chicago (USA): **Astrophysical site for the r-process.** Theorie-Seminar, 03.07.2006.

Höll, A./Universität Rostock (Germany): **Thomson Scattering as a Plasma Diagnostic Tool.** Physik dichter Plasmen mit Schwerionen- und Laserstrahlen, 04.07.2006.

Keitel, C./MPI Heidelberg (Germany): **QED, nuclear and high-energy processes in extremely strong laser pulses.** GSI Kolloquium, 04.07.2006.

Pereira, J./MSU (USA): **Experimental Possibilities for Nuclear Astrophysics at NSCL.** NuSTAR Seminar, 04.07.2006.

Alkofer, R./Graz (Austria): **QCD Green's functions and their application to hadron physics.** Theorie-Seminar, 05.07.2006.

Eeckhaudt, S.: **Nuclear Structure in the Nobelium Region at the Jyväskylä Gasfilled Separator RITU.** NuSTAR Seminar, 05.07.2006.

Rebisz, M./GSI (Germany): **Diamond detectors for heavy ion beams dosimetry.** Seminar der Materialforschung, 05.07.2006.

Spillmann, U./GSI (Germany): **Development of Segmented Solid State Detectors for X-ray Spectroscopy and Polarimetry.** Atomphysik-Seminar, 05.07.2006.

Huhn, C.: **Der Upgrade auf Sarge Linux.** IT/EE-Seminar, 11.07.2006.

Müller, E./Garching (Germany): **Core collapse supernovae, neutron stars and the equation of state.** GSI Kolloquium, 11.07.2006.

Ursescu, D.; Zielbauer, B./GSI (Germany): **Transient X-ray laser development at non-normal incidence pumping angles.** Physik dichter Plasmen mit Schwerionen- und Laserstrahlen, 11.07.2006.

Maruhn, J. A./Frankfurt (Germany): **TDHF in 3D with full Skyrme forces: surprises and problems.** Theorie-Seminar, 12.07.2006.

Stanoiu, M./GSI (Germany): **Use of Microstrip Si Detectors in Reactions of Astrophysical Interest and Exotic Decay Modes Experiments.** NuSTAR Seminar, 12.07.2006.

Sulignano, B./GSI (Germany): **Structure and properties of K isomers in the region of SHE.** PhD-Seminar, 12.07.2006.

Giacomini, T.; Becker, F./GSI (Germany): **IPM and BIF, non-destructive beam profile measurement for UNILAC, SIS, ESR and FAIR.** Beschleuniger-Seminar, 13.07.2006.

Novratil, P./Livermore (USA): **7Be(p,gamma) 8B S-factor from ab initio wave functions.** Theorie-Seminar, 17.07.2006.

Buervenich, T./Frankfurt (Germany): **Exotic nuclei - a challenge for mean-field models.** Theorie-Seminar, 18.07.2006.

Kumar, M./University of Allahabad (India): **Swift-Heavy-Ion Induced Effects in Nano-grains LiF Thin Films.** Seminar der Materialforschung, 18.07.2006.

Ni, P./TU Darmstadt, GSI (Germany): **Temperature measurement of high-energy-density matter generated by intense heavy ion beams.** Physik dichter Plasmen mit Schwerionen- und Laserstrahlen, 18.07.2006.

Rodriguez Prieto, G./GSI (Germany): **Highly charged ion jets from medium flux laser plasmas.** Physik dichter Plasmen mit Schwerionen- und Laserstrahlen, 18.07.2006.

Rolfs, C./Bochum (Germany): **Fusion reactions in stars.** GSI Kolloquium, 18.07.2006.

Estrada, F. J. L./Madrid (Spain): **A unified Coulomb gauge QCD approach to conventional and exotic mesons.** Theorie-Seminar, 19.07.2006.

Sauer, A./Universität Frankfurt (Germany): **The HITRAP Decelerator Project at GSI.** Atomphysik-Seminar, 19.07.2006.

Mulser, P./TU Darmstadt (Germany): **Einfluss der Zweistrominstabilität auf das Alfvn - Stromlimit.** ILIAS-Seminar-Arbeitsseminar, 25.07.2006.

Fischer, C./Darmstadt (Germany): **Dynamically induced scalar quark confinement.** Theorie-Seminar, 26.07.2006.

Goutte, H./CEA-Bruyeres-le-Chatel (France): **Microscopic potential energy surfaces and low-energy fission dynamics.** NuSTAR Seminar, 26.07.2006.

Nebel, C./Diamond Research Center, AIST, Tsukuba (Japan): **Diamond for Biosensing.** Sonderveranstaltung, 10.08.2006.

Desjarlais, M./Sandia National Lab. Albuquerque (USA): **Quantum molecular dynamics simulations in support of high energy density physics experiments on Sandia's Z machine.** GSI Kolloquium, 05.09.2006.

Fortov, V./IHED RAS, Moscow (Russia): **Charge und Density Coupling in Non-ideal Plasma.** GSI Kolloquium, 05.09.2006.

Itoh, N./Sophia University, Tokyo (Japan): **Seeing Galaxy Clusters Through Cosmic Microwave Background: Sunyaev-Zeldovich Effect.** Theorie-Seminar, 05.09.2006.

: **Tag der offenen Tür - Forschung hautnah erleben.** Sonderveranstaltung, 10.09.2006.

Hoffmann, J.; Ott, W.: **Siderem: Ein Modul zur Auslese von Halbleiterdetektoren.** IT/EE-Seminar, 12.09.2006.

Hess, S.: **Auf der Jagd nach schwarzen Löchern - Blick in die Zentren aktiver galaktischer Kerne.** Wissenschaft für alle, 13.09.2006.

Bellachioma, M. C./GSI (Germany): **Thin film getter coatings for the SIS18 upgrade.** Beschleuniger-Seminar, 14.09.2006.

Kugler, M.: **Universeller Sequenzer für das CS Framework.** IT/EE-Seminar, 19.09.2006.

Pesch, T./RWTH Aachen (Germany): **Wellen konstanter Phasengeschwindigkeit in relativistischen Plasmen.** ILIAS-Seminar-Arbeitsseminar, 19.09.2006.

Miers, K.: **Zukünftige Maßnahmen für eine verbesserte Spamabwehr.** IT/EE-Seminar, 26.09.2006.

Bazavov, A./Florida (USA): **RHIC and Non-Equilibrium Signals of the Deconfining Phase Transition.** Theorie-Seminar, 27.09.2006.

Scheidenberger, C.: **Hallo, ist da jemand? Oder: was wissen wir über Planeten bei fernen Sternen.** Wissenschaft für alle, 04.10.2006.

Bayer, W./GSI (Germany): **Status Quo of the UNILAC as a Megawatt Beam Injector for FAIR.** Beschleuniger-Seminar, 05.10.2006.

Müller, B./Duke University (USA): **Some Like It Hot: The Quark-Gluon Plasma at RHIC and LH(I)C.** Sonderveranstaltung, 09.10.2006.

Stock, R./Universität Frankfurt-M (Germany): **Hadron Production in Relativistic Nuclear Collisions.** Sonderveranstaltung, 09.10.2006.

Yang, X./IMP (China): **The vacuum system of HIRFL+CSR.** Beschleuniger-Seminar, 10.10.2006.

Barnea, N./Jerusalem (Israel): **Realistic nuclear force predictions for neutrino scattering on light nuclei.** Theorie-Seminar, 11.10.2006.

Leemans, W./LOASIS Program, LBNL (USA): **GeV electron beams from a cm-scale laser accelerator and intense radiation.** Sonderveranstaltung, 16.10.2006.

Straumann, N./Universität Zürich (Switzerland): **Dark Energy: Recent Developments.** GSI Kolloquium, 17.10.2006.

Bräuning, H./GSI (Germany): **Charge Transfer in Ion-Ion Collisions.** Atomphysik-Seminar, 18.10.2006.

Ducret, J.-E./CEA DAPNIA/SPhN (France): **Spallation Measurements in Coincidence: Why and how? First Results of the SPALADIN Experiment ^{56}Fe+p at 1 A GeV.** NuSTAR Seminar, 18.10.2006.

Yakovlev, D./St. Petersburg (Russia): **Magnetars as cooling neutron stars with internal heating.** Theorie-Seminar,

18.10.2006.

Fehrenbacher, G./GSI (Germany): **Radiation Safety Planning for FAIR.** Beschleuniger-Seminar, 19.10.2006.

Andreev, N./Institute of High Energy Density, Moscow (Russia): **Long distance propagation of short intense laser pulses.** Physik dichter Plasmen mit Schwerionen- und Laserstrahlen, 24.10.2006.

Rosmej, O./GSI (Germany); Rzadkiewicz, J./The Andrzej Soltan Institute for Nuclear Studies (Poland): **High electron temperature in the heavy ion track? Interpretation of the target K-shell spectra induced by the heavy ion beam.** ILIAS-Seminar-Arbeitsseminar, 24.10.2006.

Grigorenko, L./GSI (Germany): **Correlation Studies of the Light Exotic Nuclei: 5H and 9He. Problematic Issues of 9He and 10He Structure.** NuSTAR Seminar, 25.10.2006.

Mirtsch, F./Mirtsch GmbH (Germany): **Machbarkeitsuntersuchung zum Einsatz von dünnwandigen, wölbstrukturierten Vakuum-Röhren für einen möglichen Einsatz im SIS100.** Beschleuniger-Seminar, 26.10.2006.

Hagner, C./Universität Hamburg (Germany): **Status and Perspectives of Neutrino Oscillations.** GSI Kolloquium, 31.10.2006.

Urbassek, H. M./TU Kaiserslautern (Germany): **Sputtering by ion and cluster impact: Insight from molecular-dynamics simulations.** Physik dichter Plasmen mit Schwerionen- und Laserstrahlen, 31.10.2006.

Camano, M./USC (Spain): **Production and Characterization of the 7H Resonance.** NuSTAR Seminar, 01.11.2006.

Hoffmann, D. H. H./GSI: **Plasmaphysik: Von dunkler Materie, exotischen Teilchen und der Hoffnung die Energiequelle der Sterne nutzbar zu machen.** Wissenschaft für alle, 01.11.2006.

Udem, T./MPI für Quantenoptik, Garching (Germany): **Femtosecond Frequency Combs and Applications.** Atomphysik-Seminar, 01.11.2006.

Basko, M./Institute for Theoretical and Experimental Physics (ITEP), Moscow (Russia): **On the theory of ion acceleration by plasma expansion into vacuum.** Physik dichter Plasmen mit Schwerionen- und Laserstrahlen, 07.11.2006.

Sherrill, B./MSU (USA): **The Future of Radioactive Ion Beam Facilities in the United States.** GSI Kolloquium, 07.11.2006.

Palffy, A./Universität Gießen (Germany): **Nuclear Excitation of Heavy Ions by Electron Capture.** Atomphysik-Seminar, 08.11.2006.

Saito, T. R./GSI (Germany): **Exploring the Nuclear Landscape with Strangeness: The HypHI Project at GSI/FAIR.** NuSTAR Seminar, 08.11.2006.

Skoczen, B./Cracow University of Technology (Poland): **Reliability, Structural Stability and Interconnection Technologies in Superconducting Particle Accelerators.** Beschleuniger-Seminar, 09.11.2006.

Essel, H.: **Analysis für ESR-Experimente.** IT/EE-Seminar, 14.11.2006.

Gibbon, P./Jülich (Germany): **Mesh-free Simulation of Laser Interaction with mass-limited Targets.** ILIAS-Seminar-Arbeitsseminar, 14.11.2006.

Lu, Z.-T./University of Chicago (USA): **Time Reversal, Halo Nuclei, and Saharan WaterMany Uses of Cold, Radioactive Atoms.** GSI Kolloquium, 14.11.2006.

Meister, C.-V./Brandenburg Highschool and Science Project ”Physics of Stellar and Planetary Atmospheres” Potsdam (Germany): **Recent Problems of the Physics of Earth’s Magnetosheath.** Physik dichter Plasmen mit Schwerionen- und Laserstrahlen, 14.11.2006.

Veskovski, S./National Instruments; Brand, H./GSI (Germany): **Open National Instruments Forum.** Sonderveranstaltung, 14.11.2006.

Abe, Y.: **Mechanism for Fusion Hindrance and Synthesis of Superheavy Elements.** NuSTAR Seminar, 15.11.2006.

Henning, W. F.; Schavan, A.; Partsch, J.; Hofmann, S.; Fölsing, A.: **Taufe von Element 111.** Sonderveranstaltung, 17.11.2006.

Müller, C./MPI für Kernphysik, Heidelberg (Germany): **Lepton pair creation in strong laser fields.** ILIAS-Seminar-Arbeitsseminar, 21.11.2006.

Severijns, N./KU Leuven (Belgium): **Weak interactions studies in nuclear beta-decay.** GSI Kolloquium, 21.11.2006.

Woller, K./DESY (Germany): **Organisation des IT Betriebs bei DESY.** IT/EE-Seminar, 21.11.2006.

Zamponi, F./Institut für Optik und Quantenelektronik, Univ. Jena (Germany): **Measurement of Magnetic Fields Produced by fs Laser Pulses and Spectropolarimetry.** Physik dichter Plasmen mit Schwerionen- und Laserstrahlen, 21.11.2006.

Dorokhov, A./Moscow (Russia): **Current-current correlators within the instanton liquid model.** Theorie-Seminar, 22.11.2006.

Kowalska, M./CERN (Switzerland): **Exploring the ’island of inversion’ by laser and beta-NMR spectroscopy.** Atomphysik-Seminar, 22.11.2006.

Pleskac, R./GSI (Germany): **New Measurements of Total Fission Cross Sections at GSI.** NuSTAR Seminar, 22.11.2006.

Baboi, N./DESY (Germany): **Using Higher Order Modes in the Superconducting Tesla Cavities for Diagnostics at Flash DESY.** Beschleuniger-Seminar, 23.11.2006.

Andreev, A. A./Institute for Laser Physics SIC Vavilov State Optical Institute, St. Petersburg (Russia): **Analytical modelling and numerical simulation of fast-ion generation from a mass-limited target irradiated by an ultra-high intensity laser beam.** Physik dichter Plasmen mit Schwerionen- und Laserstrahlen, 28.11.2006.

Blaschke, D./JINR Dubna and Wroclaw University (Poland): **Laser acceleration of ion beams.** ILIAS-Seminar-Arbeitsseminar, 28.11.2006.

Göbel, E. O./PTB (Germany): **Quantum standards in the SI.** GSI Kolloquium, 28.11.2006.

Lang, D.: **WebDAV bei GSI.** IT/EE-Seminar, 28.11.2006.

Courtin, S./IPHC-ULB, Strasbourg (France): **Molecular Resonances: an Experimental Approach.** NuSTAR Seminar, 29.11.2006.

Zschornack, G./TU Dresden (Germany): **Highly Charged Ions from the Dresden EBIT: Tools for X-ray Spectroscopy, Materials Modifications and Surface Metrology.** Atomphysik-Seminar, 29.11.2006.

Schaetzel, S./DESY (Germany): **The CALICE Tracking Calorimeters for the ILC.** Sonderveranstaltung, 04.12.2006.

Geissler, M./MPI für Quantenoptik, Garching (Germany): **Electron acceleration with few cycle laser pulses.** ILIAS-Seminar-Arbeitsseminar, 05.12.2006.

Volkov, A./Russian Research Centre Kurchatov Institute, Moscow (Russia): **Material excitation in swift heavy ion tracks.** Physik dichter Plasmen mit Schwerionen- und Laserstrahlen, 05.12.2006.

Bosch, F./GSI (Germany): **Reise zum Urknall mit Hubble und COBE - Warum die Physiker glauben, dass die Welt vor 14 Milliarden Jahren entstanden ist.** Wissenschaft für alle, 06.12.2006.

Montes, F./GSI (Germany): **Heavy Element Nucleosynthesis in the Early Galaxy.** NuSTAR Seminar, 06.12.2006.

Kroyer, T./CERN (Switzerland): **Transverse Schottky Measurements in the CERN SPS and LHC.** Beschleuniger-Seminar, 07.12.2006.

Logan, G./LBNL, Berkeley (USA): **Revisiting Heavy Ion Fusion.** Physik dichter Plasmen mit Schwerionen- und Laserstrahlen, 12.12.2006.

Maruhn, J./Universität Frankfurt (Germany): **Theoriebeitrag zum Roadmap Meeting des PPAC am 13.12.06.** ILIAS-Seminar-Arbeitsseminar, 12.12.2006.

Maas, A./Sao Paulo (Brazil): **Gluons at finite temperature, confinement, screening and all that.** Theorie-Seminar, 13.12.2006.

Mazzocco, M./GSI (Germany): **Extension of the Monte-Carlo Code MOCADI to Fusion-Evaporation Reactions.** NuSTAR Seminar, 13.12.2006.

Schöffler, M. S./IKF, Universität Frankfurt-M (Germany): **Ground state correlation and dynamical processes in fast ion-helium-collisions.** Atomphysik-Seminar, 13.12.2006.

Appelshäuser, H./Universität Frankfurt (Germany): **Ultra-relativistic Heavy-Ion Collisions on the verge of LHC.** GSI Kolloquium, 19.12.2006.

Czanta, M./Fa. Merck, Darmstadt (Germany): **Liquid Crystals - From Molecules to Modern Display Application.** Atomphysik-Seminar, 20.12.2006.

Simon, H./GSI (Germany): **The End of Delay Cables.** NuSTAR Seminar, 20.12.2006.

Open workshops and meetings

Complied by M. Enders, K. Große

06.01-03.02.2006: **26th International Workshop on Physics of High Energy Density in Matter (Hirschegg).**

26.-27.01.2006: **Joint Symposium on Hadron Physics.**

8.02-03.03.2006: **7. Collaboration Meeting of the CBM Experiment at FAIR.**

06.-07.03.2006: **International RICH-Workshop of the CBM Experiment at FAIR.**

06.-10.03.2006: **XVI. PANDA Collaboration Meeting.**

11.-18.03.2006: **3rd Workshop on Nuclear Astrophysics 'VISTARS meets JINA', Russbach (Austria).**

19.-23.03.2006: **FUSION06 - Reaction Mechanisms and Nuclear Structure at the Coulomb Barrier, San Servolo, Venezia (Italy).**

20.-21.03.2006: **First Technical FLAIR Meeting on the Integration of CRYRING into FLAIR.**

24.-28.04.2006: **PANSI3 Workshop on Communicating Research Results: Activities and Techniques.**

27.-28.04.2006: **D-Grid HEPCG Workshop.**

02.-03.05.2006: **FLAIR collaboration meeting (Stefan Meyer Institute for Subatomic Physics, Vienna).**

02.05.2006: **R&D Proposal "Thin Diamond Plates" from Element Six.**

02.05.2006: **Submission Readiness Review for the DETNI n-XYTER. ASIC Laboratory University of Heidelberg (Germany).**

02.05.2006: **Workshop NMI-3 DETNI: N-XYTER, The First Dedicated Neutron Detector Readout ASIC; Post Submission Review, Summary and Outlook. HMI, Berlin (Germany).**

22.-24.05.2006: **Charge breeding and related topics.**

12.-14.06.2006: **XVII. PANDA Collaboration Meeting.**

20.-23.06.2006: **2nd International Conference on 'Collective Motion in Nuclei under Extreme Conditions' (COMEX-2), Sankt Goar (Germany).**

28.06.2006: **Workshop on the Nuclear Equation of State.**

31.08-01.09.2006: **3rd NoRHDia Workshop GSI.**

02.-05.09.2006: **XVIII. PANDA Collaboration Meeting (Wien).**

04.09.2006: **12th International Workshop on the Physics of Non-ideal Plasmas.**

18.09.2006: **Abendveranstaltung der Helmholtz-Gemeinschaft mit Präsentation von FAIR (Brüssel).**

19.-22.09.2006: **CBM Collaboration meeting.**

19.09.2006: **CBM Symposium - Physics of High Baryon Density (Strasbourg).**

21.10.2006: **2. Meeting of the GSI Users' Group Executive Committee.**

25.-29.10.2006: **XVII HADES Collaboration Meeting.**

16.-17.11.2006: **CBM Experiment - Workshop on Muon Detection.**

19.-20.11.2006: **ALMAS1: Workshop on Advanced Laser and Mass Spectroscopy.**

20.-21.11.2006: **Workshop on atomic physics experiments at HITRAP and Cave A.**

27.11.2006: **Status of CVD-Diamond Production and Future Plans of Element Six; Required Diamond Detector Materials for FAIR experiments.**

11.-12.12.2006: **Symmetry Energy in Nuclear Reactions.**

11.-15.12.2006: **PANSI3 Workshop on Communicating Research Results: Activities and Techniques.**

11.-15.12.2006: **XIX. PANDA Collaboration Meeting.**

Experiments performed at the GSI accelerator in 2006

compiled by Carsten Schwarz, beam coordinator 2006

*In all tables 1 shift represents 8 hours of beam delivered to an experiment running in main mode. Shift numbers in brackets denote parasitic shifts.

Exp	Short title	Spokespesrson	Status	Area	Ion	Shifts
U068	Bolometric detectors	Egelhof	main/parasitic	Z6	^{7}Li	12(3)
U184	Heavy elements	S.Hofmann	main	Y7	^{54}Cr, ^{48}Ca	78
U200	Nuclear Structure Investigation of No, Lr	Heßberger	main	Y7	^{48}Ca	18
U205	Decay properties near Z=108 and N=162	Türler	main	X1	^{25}Mg	29
U206	Rn isotopes	Andreyev	main	Y7	^{52}Cr	24
U207	Optical spectroscopy of Nobelium	Backe	main	Y7	^{52}Cr	6
U209	Nuclear Structure Investigation of SHE	Heßberger	main/parasitic	Y7	^{54}Cr	33(18)
U210	Missing α emitters in the transuranium region	Novikov	parasitic	X1	^{12}C	0(4)
U212	UNILAC-experiments of FP6/CARE/HIPPI	I.Hofmann	main	TK	^{40}Ar	24
U213	Ion-plasma interaction	Blazevic	parasitic	Z6	^{54}Cr	0(15)
U215	Reaction 30Si + 238U	Nishio	main	Y7	^{30}Si	72
U216	ERDA	Bender	parasitic	UU	^{12}C, ^{136}Xe	0(39)
U217	Mass measurements at SHIPTRAP	Block	main	Y7	^{40}Ar,^{40}Ca, ^{58}Ni	30
U218	Coulomb excitation of ^{112,114,116}Sn	Doornenbal	main/parasitic	X7	^{114,116}Sn, ^{136}Xe	15(3)
U219	TASCA commissioning	Schädel	main/parasitic	X8	^{30}Si,^{40}Ar,^{54}Cr	2.5(7)
U220	Incomplete fusion of ^{25}Mg and ^{206}Pb	Heßberger	parasitic	Y7	^{25}Mg	0(36)
U221	CVD detector test	Bräuning-Demian	main/parasitic	X4	^{54}Cr,^{238}U	5(6)
U226	Energy loss in laser generated plasmas	Roth	parasitic	Z6	^{40}Ar	0(6)
UBIO	Radiobiology	Scholz, Hagmann	main/parasitic	X3,X6	^{12}C,^{30}Si,^{54}Cr, ^{86}Kr,^{132,136}Xe, ^{208}Pb	39(57)
UMAT	Material science	Trautmann, Fischer	main/parasitic	X0	^{7}Li,^{12}C,^{54}Cr, ^{58}Ni,^{116}Sn, ^{132}Xe,^{208}Pb, ^{238}U	93(12)

E039	Precision X-ray spectroscopy	Beyer	main	ESR	^{208}Pb	42
E045	Two-electron Lamb shift	Stöhlker	main	ESR	^{114}Sn, ^{116}Sn, ^{238}U	39
E049	Beta decay of highly charged ions	Bosch	main	ESR	^{208}Pb	36
E053	Laser cooling of C^{3+} ion beam	Schramm	main	ESR	^{12}C	18
E055	Direct mass measurements at FRS-ESR	Scheidenberger	main	ESR	^{136}Xe,^{238}U	48
E067	Test of time dilatation at the ESR	Karpuk	main	ESR	^{7}Li	9
E070	Collision dynamics at relativistic energies	Moshammer	main	ESR	^{238}U	9

S223	Coulomb dissociation	Sümmerer	parasitic	HTC	^{12}C	0(2)
S240	Test of GLAST calorimeter	Lott	parasitic	HTC	^{12}C,^{132}Xe	0(1)
S244	The GSI FRS γ ray spectroscopy campaign	Regan	main	FRS	^{58}Ni,^{107}Ag,^{238}U	49
S245	Bound and unbound nucl. near the driplines	Jonson	main	FRS	^{40}Ar	27
S247	Nuclear density distributions	Khandzadeev	main	FRS	^{18}O	33
S249	Precise measurement of stopping power	Golubev	parasitic	HTA	^{40}Ar	0(9)
S271	Two-proton decay of ^{19}Mg	Mukha	main	FRS	^{24}Mg	18
S277	Single particle occupancies near ^{54}Ca	Krücken	main/parasitic	FRS	^{48}Ca,^{86}Kr	48(6)
S280	R&D on synthetic diamond detectors	Berdermann	main/parasitic	FRS, HTA	^{1}H,^{132}Xe	6(19.5)
S286	TRD tests	Garabatos	parasitic	HTD	^{14}N	0(30)
S291	Residual radioactivity induced by U ions	Mustafin	main	HTA	^{238}U	12
S297	Strange baryons and kaonic cluster	Herrmann	main/parasitic	HTB	^{1}H,^{12}C	12(4)
S299	Along the N=126 closed shell	Podolyak	main/parasitic	FRS	^{208}Pb,^{238}U	21(6)
S300	Shape co-existence and the possibility of X(5) behaviour in neutron rich A=100 nuclei	Bruce	main	FRS	^{238}U	21
S301	Dielectron production in pp,dp, and AA col.	Salabura	main	HAD	^{1}H	42
S302	HED matter generated by intense HI-beams	Varentsov	parasitic	HHT	^{40}Ar,^{238}U	0(53)
S305	Fragmentation of ^{136}Xe	Jungclaus	main	FRS	^{136}Xe	37
S317	High-intensity effects and beam loss issues in FAIR	I. Hofmann	main	SIS	^{40}Ar	6
S319	Testexperiment for HypHi	Saito	parasitic	HTC	^{12}C	0(3)
S328	RPC detector tests	Benlliure	parasitic	HTC	^{12}C	0(3)
SBIO	Biophysics experiments	Scholz/Schardt/ Narici	main/parasitic	HTA	^{12}C,^{18}O	13(6)
STHE	Therapy experiments	Krauss/Narici/ Schardt	main	HTA, HTM	^{12}C	11
SMAT	Material science	Trautmann	main/parasitic	HTA	^{208}Pb,^{238}U	9(27)
SiSt	Radiation safety	Fehrenbacher	main	HTA	^{12}C	14

Facts and Figures

Compiled by J. Heilmann

Gesellschafter/Shareholders since 1969, December 17th

Federal Republic of Germany	90% of budget (and of share capital)
State of Hesse/Land Hessen	10% of budget (and of share capital)

Accelerators

FAIR	Facility for Antiprotons and Ion Research		pre- construction R&D
UNILAC	UNIversal Linear ACcelerator	13 MeV/u for U	in operation since 1976
SIS	Schwer-Ionen-Synchrotron	50–1000 MeV/u for U	in operation since 1989
ESR	Experimental Storage Ring	3–400 MeV/u for U	in operation since 1990

Users of the accelerator complex

In 2006, GSI provided access to 25 experimental areas to more than 1400 scientific users.

GSI Funding in Mio. Euro

research area Structure of Matter	73.8	
research area Health	3.4	
special tasks and Helmholtz-activities	1.9	
third party funding	15.6	
total budget		**94.7 Mio. Euro**

Personnel 2006 in person years

research area Structure of Matter	416	
FAIR-activities (Structure of Matter)	138	
research area Health	29	
management and management support	70	
scientific and technical infrastructure	211	
personnel involved in projects funded by nat./internat. funding agencies	100	
total personnel		**964 person years**

Statutory organs and scientific advisory committees to GSI as of December 31, 2006

Supervisory Board/Aufsichtsrat:

Dr. B. Vierkorn-Rudolph [chair],
Bundesministerium für Bildung und Forschung, Bonn/Berlin (Germany),
as representative of the Federal Republic of Germany

Ministerialrat Dr. R. Koepke,
Bundesministerium für Bildung und Forschung, Bonn/Berlin (Germany),
as representative of the Federal Republic of Germany

Ministerialdirigent Dr. R. Bernhardt,
Hessisches Ministerium für Wissenschaft und Kunst, Wiesbaden (Germany),
as representative of the State Hessen in Germany

Prof. Dr. R. Klanner,
Universität Hamburg/DESY (Germay),
as representatives of the Scientific Council of the GSI

Scientific Directorate/Wissenschaftliches Direktorium WD:

Prof. Dr. W. F. Henning [chair]
Dr. H. Eickhoff, Prof. Dr. K.-H. Langanke, B. Schönfelder, Dr. A. Kurz

Division and Department Heads/Bereichs- und Abteilungsleiter:

Dr. D. Krämer, FAIR-Technical Division/FAIR Bereich
Dr. H. Eickhoff, Accelerator/Beschleunigerbereich
B. Schönfelder, Infrastructure/Infrastruktur
Prof. Dr. K.-H. Langanke, Research/Forschungsbereich and
Theory: Nuclear structure and astrophysics/Theorie: Kernstruktur- und Astrophysik
Prof. Dr. H.-J. Kluge, Atomic physics/Atomphysik
Prof. Dr. G. Kraft, Biophysics/Biophysik
Prof. Dr. P. Braun-Munzinger, Nuclear physics I/Kernphysik I
Prof. Dr. H. Emling, Nuclear physics II/Kernphysik II
Prof. Dr. K. Peters, Nuclear physics III/Kernphysik III
Prof. R. Neumann, Materials research/Materialforschung
Prof. Dr. D. H. H. Hoffmann, Plasma physics/Plasmaphysik
Prof. Dr. J. Stroth, HADES
Prof. Dr. J. Wambach, Theory: QCD and hadron physics/Theorie: QCD und Hadronenphysik
Prof. Dr. K. Witte, PHELIX

Scientific Council/Wissenschaftlicher Rat WR:

<http://www.gsi.de/informationen/users/EAC/wr/>

R. Klanner [chair], Universität Hamburg (Germany); D. von Harrach, Johannes-Gutenberg-Universität Mainz (USA); N. Holtkamp, Oak Ridge National Laboratory (USA); C. Leemann, Thomas Jefferson National Accelerator Facility, Newport News (USA); B. Mueller, Duke University, Durham, North Carolina (USA); H. Requardt, Siemens AG Medical Solutions, Erlangen (Germany); R. Sauerbrey, Forschungszentrum Rossendorf, Dresden (Germany); S. Myers, CERN EP, Geneva (Switzerland); B. M. Sherrill, Michigan State University, East Lansing (USA); A. Shotter, TRIUMF, Vancouver (Canada); M. Soyeur, DSM/DAPNIA/SPhN, Gif-sur-Yvette (France); D. Vernhet, Université Paris 6 et 7, Paris (France).
Secretary: K.-D. Groß

Scientific Committee/Wissenschaftlicher Ausschuss WA:

<http://www-w2k.gsi.de/wa/scientific_committee.htm>

S. Richter [chair]; A. Bräuning-Demian; T. Cornelius; B. Friman; B. Lommel; P. Malzacher; Y. Leifels; M. Kreiser (for the Betriebsrat); H. Reich-Sprenger; C. Scheidenberger; L. Schmitt; M. Scholz; P. Senger; H. Simon; J. Stadlmann; M. Traxler; A. Tauschwitz; D. Varentsov; G. Walter.

Scientific Advisory Committees to GSI

GSI General Programme Advisory Committee G-PAC:

<http://www.gsi.de/informationen/users/EAC/ea/>

J. Aichelin, SUBATECH, Nantes (France); P. Giubellino, INFN Turin, Torino (Italy); R. Hoekstra, KVI Groningen, Groningen (The Netherlands); R. Krücken, Technische Universität München, Physik-Department (Germany); M. Lewitowicz, GANIL, Caen (France); S. Paul, Technische Universität München, Physik-Department (Germany); T. Peitzmann, Utrecht University (The Netherlands); N. Pietralla, Technische Universität Darmstadt, Darmstadt (Germany); H. Schatz, Michigan State University, East Lansing (USA); M. Wada, RIKEN, Saitama (Japan); M. Weidemüller, Universität Freiburg (Germany); E. Widmann, Stefan-Meyer-Institut für subatomare Physik, Österreichische Akademie der Wissenschaften, Vienna (Austria).
Secretary: K. Füssel

GSI Phelix and Plasmaphysics Program Advisory Committee (PPAC):

<http://www.gsi.de/informationen/users/EAC/ppac/>

M. H. R. Hutchinson [Chair], Rutherford Appleton Lab (United Kingdom); S. Jacquemot, LULI, Ecole Polytechnique, Palaiseau (France); G. Logan, LBL Berkeley (USA); T. A. Mehlhorn, Sandia National Laboratories, Albuquerque (USA); R. Sauerbrey, Forschungszentrum Rossendorf, Dresden (Germany); B. Sharkov, Inst. of Theoretical and Experimental Physics Moscow (Russia).
Secretary: K. Füssel

GSI Biophysics & Radio-Biology Program Advisory Committee (Bio-PAC):

<http://www.gsi.de/informationen/users/EAC/bio-pac/>

G. Iliakis [Chair], Institut für Medizinische Strahlenbiologie Universitätsklinikum Essen (Germany); M. Durante, Universita 'Federico II', Napoli (Italy); R. Engenhardt-Cabillic, Klinik für Strahlentherapie Philipps-Universität Marburg Klinikum (Germany); B. Michael, Gray Lab (Cancer Research Trust), Mount-Vernon-Hospital, Northwood (United Kingdom); R. Okayasu, National Institute of Radiological Sciences, Chiba-shi (Japan); E. Pedroni, Paul Scherrer Institut, Villigen (Switzerland).
Secretary: K. Füssel

GSI Users' Group Executive Committee (UEC):

<http://www.gsi.de/forschung/usersgroup/index.html>

J. V. Kratz, Johannes Gutenberg-Universität, Mainz (Germany) [CHAIR]; J. Benlliure, University of Santiago de Compostela, Santiago de Compostela (Spain); B. Blank, CEN, Bordeaux (France); T. Faestermann, Techn. Univ. Müchen (Germany); J. Friese, Techn. Univ. München (Germany); U. A. Glasmacher, Ruprecht-Karls Univ., Heidelberg (Germany); J. Jacoby, Johann-Wolfgang-Goethe Univ., Frankfurt (Germany); R. Kulessa, Jagiellonian University, Krakow (Poland); L. Narici, Univ. of Rome, Rome (Italy); M. Petrovici, Nat. Inst. for Physics and Nuclear Engineering, Bucharest (Romania); P. Salabura, Jagiellonian University, Krakow (Poland) [CHAIR-ELECT]; B. Sharkov, Inst. of Theoretical and Experimental Physics, Moscow (Russia); J. Ullrich, Max-Planck-Inst. for Nuclear Physics, Heidelberg (Germany); A. Warczak, Jagiellonian University, Krakow (Poland).
Secretary: K. Füssel

Scientific Coordination:

Dr. K. D. Groß

GSI – Organigram

Gesellschaft für Schwerionenforschung mbH

Scientific Council
12 Members
Chair
R. Klanner

Scientific Committee
18 Members
Chair
1555 S. Richter

Experiment Committee
12 Members
Chair
H. Wilschut

Coordination of the FAIR Project
2458 H. Gutbrod

Scientific coordination
2535 K.-D. Groß

Public Relations
2598 I. Peter

Safety und Radiation Protection
2007 G. Fehrenbacher

Shareholders' Assembly
Federal Government / State of Hessen

Supervisory Board
Chair B. Vierkorn-Rudolph
Vice Chair R. Bernhardt

Managing Directors
W. F. Henning, A. Kurz
Management Board
W. F. Henning (Chair), A. Kurz,
H. Eickhoff, K. Langanke, B. Schönfelder

Controlling/ Accounting
2621 J. Heilmann

Legal Service
2132 A. Lambert

Patents and Technology Transfer
2385 R. Fuchs (Komm.)

Internal Audit
NN

Works Council
2503 A.Schlossarek / Chair

Equal Opportunity Committee
2026 P. Schütt / Chair

Representation of the Disabled
2524 W. Krall /Vertrauensmann

Data Protection
2855 S. Schulz

Research
2747 K. Langanke (Komm.)

- **Atomic Physics** 2722 H.-J. Kluge
- **Biophysics** 2607 G. Kraft
- **Nuclear Physics I** 2760 P. Braun-Munzinger
- **Nuclear Physics II** 2669 H. Emling
- **Hadron Physics** 2763 K. Peters
- **Materials Research** 2172 R. Neumann
- **Plasma Physics** 2664 D. Hoffmann
- **Theory** Nuclear Structure and Astrophysics 2747 K. Langanke
- **Theory** Hadrons/QCD 2753 J. Wambach
- **PHELIX** 2028 K. Witte

Scientific and Technical Infrastructure
1427 B. Schönfelder

- **Facility Management and Buildings** NN
- **Library and Documentation** 2610 K. Große
- **Information Technology** 2394 M. Münch
- **Experiment Electronics** 2496 E. Badura
- **Detector Laboratory** 2273 C. J. Schmidt
- **Target Laboratory** 2691 B. Lommel
- **Manufacturing and Central Technologies** 2385 R. Fuchs

Accelerator
2395 H. Eickhoff

- **Therapy Accelerator Heidelberg** 3858 U. Weinrich
- **Operations** 2316 D. Wilms
- **Ion Sources** 2320 P. Spädtke
- **Injectors** 2170 W. Barth
- **Accelerator Electronics** 2349 R. Bär
- **UHV/BES** 2904 H. Reich-Sprenger
- **Beam Diagnostics** 2313 A. Peters
- **HF / Accelerator Structures** 2086 H. Klingbeil
- **Electric Energy Technology** 2377 H. Ramakers

FAIR
2096 D. Krämer

- **FSY** FAIR Synchrotrons 2405 P. Spiller
- **FSR** FAIR Storage Rings 2406 M. Steck
- **FMT** FAIR Magnet Technology 2383 G. Moritz
- **FAT** FAIR Accelerator Theory 2409 I. Hofmann
- **FCC** FAIR Civil Construction NN
- **Technical Integration** NN

Administration
2646 A. Kurz

- **Personnel Department** 2611 J. Größer
- **Finance** 2597 A. Städter
- **Purchasing and Materials Management** 2577 M. Hener
- **Coordination Public Project Funding** 2848 D. Müller

update: 15th March 2007
organigram

Address: POB 11 05 52
64420 Darmstadt
Phone: 0 6159/71– 0 Fax: 0 6159/71–2785
www.gsi.de

List of Authors

— C —

— G —

— H —

— I —

— J —

— K —

— L —

— M —

— N —

— O —

— P —

— T —

— U —

— V —

— W —

— X —

— Y —

— Z —